BEI-2019

Bridge Engineering Institute Conference

July 22-25, 2019

Honolulu, Hawaii, USA

Edited by
Yail J. Kim
Isamu Yoshitake
Vanissorn Vimonsatit
Xuhui He
Yongcheng Ji

BEI
An International Technical Society

Sponsors

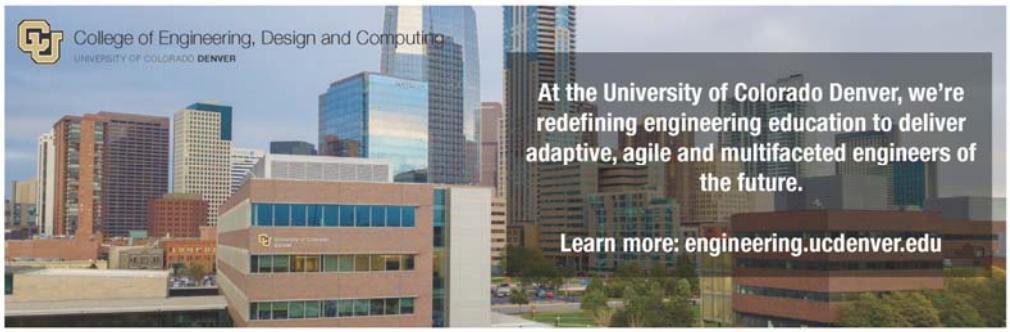
College of Engineering, Design and Computing
UNIVERSITY OF COLORADO DENVER
At the University of Colorado Denver, we're redefining engineering education to deliver adaptive, agile and multifaceted engineers of the future.
Learn more: engineering.ucdenver.edu


3 DEGREES
Bachelors
Masters
PhD
4 TRACKS
Civil Engineering
Structural Engineering
Sustainability and Innovation
Construction Engineering
10,000+
degrees conferred
ABET
ACCREDITED
Top 50%
ranked graduate program in the US
(US News and World Report, 2020)
cee.hawaii.edu

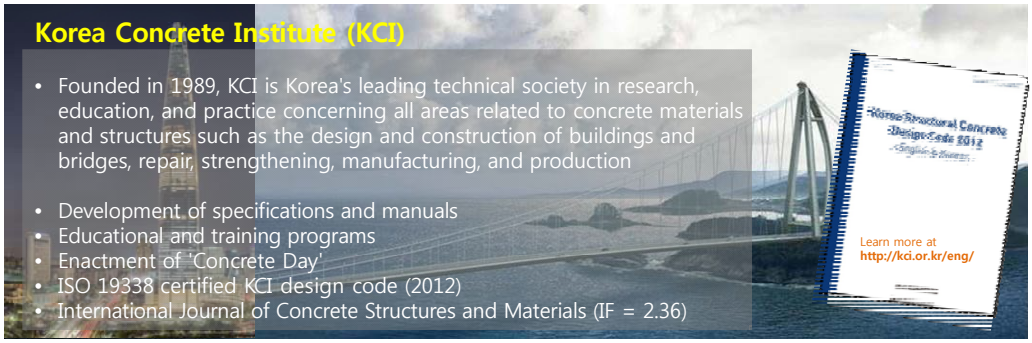
Korea Concrete Institute (KCI)
• Founded in 1989, KCI is Korea's leading technical society in research, education, and practice concerning all areas related to concrete materials and structures such as the design and construction of buildings and bridges, repair, strengthening, manufacturing, and production
• Development of specifications and manuals
• Educational and training programs
• Enactment of 'Concrete Day'
• ISO 19338 certified KCI design code (2012)
• International Journal of Concrete Structures and Materials (IF = 2.36)
Learn more at
http://kci.or.kr/eng/

Bridge Engineering Institute Conference in 2019 (BEI-2019)

Honolulu, Hawaii, USA

July 22 to 25, 2019

Edited by
Yail J. Kim
Isamu Yoshitake
Vanissorn Vimonsatit
Xuhui He
Yongcheng Ji

ISBN: 978-1-7340386-0-6

The Bridge Engineering Institute
An International Technical Society
www.beibridge.org

Table of Contents

Materials

Wind and Vibration

Monitoring and NDT

Railway Bridges

Earthquake, Dynamics, and Impact

Laboratory- and Field-Testing

The Bridge Engineering Institute, An International Technical Society

Executive Committee

Yail Jimmy Kim
President
University of Colorado
Denver
USA

Isamu Yoshitake
Vice-President
Yamaguchi University
Japan

Vanissorn Vimonsatit
Director
Curtin University
Australia

Xuhui He
Director
Central South University
China

International Advisory Committee and Secretary

Riadh Al-Mahaidi
Swinburne University of
Technology, Australia

Brahim Benmokrane
University of Sherbrooke,
Canada

Steve C.S.Cai
Louisiana State
University, USA

Nien-Yin Chang
University of Colorado
Denver, USA

Mark F. Green
Queen's University,
Canada

Issam Harik
University of Kentucky,
USA

Venkatesh Kodur
Michigan State
University, USA

Urs Meier
EMPA,
Switzerland

Hiroshi Mutsuyoshi
Saitama University,
Japan

John Myers
Missouri University
of S. and T., USA

Antonio Nanni
University of Miami,
USA

Steve Nolan,
Florida Department of
Transportation, USA

Saiid Saiidi
University of Nevada
Reno, USA

Jim Shiau
University of Southern
Queensland, Australia

Johan L. Silfwerbrand
KTH Royal Institute of
Technology, Sweden

Jongsung Sim
Hanyang University,
Korea

Ertugrul Tacioglu
University of California
Los Angeles, USA

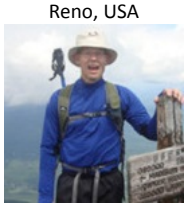

Dan Tobias
Illinois Department of
Transportation, USA

Mark Williams
Walter P. Moore
USA

Yongcheng Ji
Northeast Forestry
University, China
(Secretary)

Conference Organization

Conference Chair

Yail Jimmy Kim
University of Colorado Denver (USA)

Organizing Committee

Isamu Yoshitake (Chair)
Yamaguchi University (Japan)

Vanissorn Vimonsatit
Curtin University (Australia)

Xuhui He (China)
Central South University (China)

International Scientific Committee

Anil Agrawal (USA)
Thomas Attard (USA)
Riadh S Al-Mahaidi (Australia)
Toshihiko Aso (Japan)
Brahim Benmokrane (Canada)
Steve Cai (USA)
NY Chang (USA)
Zhengqing Chen (China)
Wonseok Chung (Korea)
Gonglian Dai (China)
Raafat El-Hacha (Canada)
Amir Fam (Canada)
Yaojun Ge (China)
Mark Green (Canada)
Issam Harik (USA)
Kent Harries (USA)
Venkatesh Kodur (USA)
Jae-Hoon Lee (Korea)
Yongle Li (China)
Urs Meier (Switzerland)
Hiroshi Mutsuyoshi (Japan)
John Myers (USA)
Hideaki Nakamura (Japan)
Antonio Nanni (USA)
Steven Nolan (USA)
Weixin Ren (China)
Saiid Saiidi (USA)
Jose Sena-Cruz (Portugal)
Jim Shiau (Australia)
Johan L Silfwerbrand (Sweden)
Jongsung Sim (Korea)
Limin Sun (China)
Ertugrul Taciroglu (USA)
Dan Tobias (USA)
Lucio Valter (Portugal)
Baolin Wan (USA)
Mark Williams (USA)
Hiroshi Yokota (Japan)

Plenary Speakers
(alphabetical order)

Professor Riadh Al-Mahaidi, Ph.D.
Swinburne University of Technology, Australia

Riadh Al-Mahaidi is a Professor of Structural Engineering and Director of the Smart Structures Laboratory at the Swinburne University of Technology, Australia. He also holds the position of Vice-President (International Engagement) at Swinburne. Prior to joining Swinburne in January 2010, he was the Head of the Structures Group at Monash University. Over the past 20 years, he focused his research and practice on life time integrity of bridges, particularly in the area of structural strength assessment and retrofitting using advanced composite materials. He currently leads a number of research projects on strengthening of bridges using fiber reinforced polymers combined cement-based bonding agents, and fatigue life improvement of metallic structures using advanced composite systems and shape memory alloys. He recently started some projects on hybrid testing of structures. He received a BSc (Hon 1) degree in civil engineering from the University of Baghdad and MSc and PhD degrees in structural engineering from Cornell University in the United States.

To date, Al-Mahaidi published over 180 journal and 230 conference papers and authored/edited 10 books and conference proceedings. He was awarded the 2012 Vice-Chancellor's Internationalization Award, the RW Chapman Medals in 2005 and 2010 for best journal publication in the Engineers Australia Structural Journal, and best paper awards at the ACUN-4 (2002) and ACUN-6 (2012) conferences. Al-Mahaidi and his research group won the 2016 Engineers Australia Excellence Award for Innovation, Research and Development (High Commendation) for the Multi-Axis Substructure Testing (MAST) System that they built at Swinburne. He was recently awarded the 2017 WH Warren Medal by the Board of the College of Civil Engineers of Australia. He was recently awarded the 2018 ARRB Research Impact Award**.** This prize is awarded to an individual researcher or research team, whose research, development and implementation efforts have made a significant improvement on operational quality and/or cost in the last 24 months, demonstrating a considerable impact within the community and industry.

Plenary Speakers
(alphabetical order)

Professor Steve C.S. Cai, Ph.D., P.E.
Louisiana State University, USA

Steve C.S. Cai, a Professional Engineer (PE) since 1995, is the Edwin B. and Norm S. McNeil Distinguished Professor in the Department of Civil and Environmental Engineering at Louisiana State University (LSU), USA. He is serving as the Coordinator of Structures Group and Director of the Bridge Innovative Research and Dynamics of Structures Laboratory. Cai was elected to be a Fellow of the American Society of Civil Engineers (ASCE) in 2010. Cai received his Ph.D. in 1993 from the Department of Civil Engineering, University of Maryland, College Park, Maryland; M.S. in 1987 from the Department of Civil Engineering, Tsinghua University, Beijing, China; and B.S. in 1983 from the Department of Civil Engineering, Zhejiang University, Hangzhou, China.

Cai began his employment at LSU as a tenure-track Assistant Professor in August, 2001, was appointed as a tenured associate professor in Aug. 2006, and was promoted to full professor in Aug. 2010. Prior to his arrival at LSU, Cai had one year of experience as a tenure-track Assistant Professor at Kansas State University (2000-2001); four years of experience as a structural researcher and development senior engineer at the Florida Department of Transportation (1996-2000); and three years of experience as a consulting engineer at Michael Baker Jr., Inc. (1993-1996). Since he joined LSU in 2001, Cai served as Principal Investigator for more than 50 federal, state government, and university funded projects. His research interests include bridge performance evaluation/instrumentation/testing, traditional and new material applications in infrastructures, performance and hazard mitigation of costal structures under wave/wind actions, and long-span bridge aerodynamics. Cai published more than 390 technical papers in journals (over 200) and conference proceedings in these research areas.

Cai is currently serving on many national and international committees. He served and has been serving on many editorial boards, such as Associate Editor of the Journal of Bridge Engineering and the Journal of Engineering Mechanics, and an editorial board member of Engineering Structures and Wind & Structures. Other major professional services encompass Secretary and Treasurer of the American Association for Wind Engineering and a member of the Engineering Project Selection Committee, East Baton Rouge Parish, representing LSU.

Plenary Speakers
(alphabetical order)

Professor Zheng-qing Chen, Ph.D.
Hunan University, China

Zheng-qing Chen (1947.10.28-), a renowned expert in bridge engineering and engineering mechanics, has been a member of the Chinese Academy of Engineering since 2015. Chen obtained his bachelor degree and master degree in solid mechanics from Hunan University in 1981 and 1984, respectively, and his PhD degree in applied mechanics from Xian Jiaotong University in 1987. Before joining Hunan University, he was a Professor and Dean of Civil Engineering at Central South University. Currently, he is a Professor in the Department of Bridge Engineering and founding Director of the Wind Engineering Research Center at Hunan University. Chen has been involved in many research areas on engineering mechanics problems related to civil structures with an emphasis on long and flexible bridges. He is a pioneer in the analysis of nonlinear behavior of cable-supported bridges in China, and his development has been applied to the nonlinear-based design of the first several modern suspension bridges built in China. He also made a significant contribution to wind engineering in both theoretical and experimental aspects. His research outcomes have been applied to a number of civil engineering structures, including the vibration control technologies for MR dampers and eddy current dampers.

Plenary Speakers
(alphabetical order)

Professor Nabil F. Grace, Ph.D.
Lawrence Technological University, USA

Nabil F. Grace is the Dean of Engineering and University Distinguished Professor at Lawrence Technological University, Southfield, MI, USA. He is also the Director of the Center for Innovative Materials Research (CIMR). The CIMR is the largest and most comprehensive testing facility in the state of Michigan. Grace's innovative research and unique deployment projects are funded by the United States Army Research Laboratory, US Department of Transportation (DOT), the State of Michigan, National Science Foundation, and several State DOTs. In the last few years, Grace received fourteen national awards for the deployment of his research findings in various infrastructures. This deployment includes the first corrosion-free highway bridge in the United States that used carbon fiber reinforced polymer (Bridge Street Bridges, Michigan), the Penobscot cable-stayed long span bridge in Maine, and M-102 Highway Bridges over the Plum Creek, Michigan. In 2017, Grace was in charge of the design, construction, instrumentation, and monitoring of the longest CFRP-prestressed concrete bridge span in the US, which was constructed over HWY I-75 in the State of Michigan. Most recently, Grace has been awarded a research contract from MDOT to develop the Design Guidelines for the use of CFRP-prestressed Strands in Prestressed Concrete Bridges. Furthermore, in 2018, Grace was awarded a pool-fund research contract from MDOT, NCDOT, MEDOT, and OHDOT to address the use of 0.7 in. CFRP strands in prestressed concrete highway bridges. Grace was awarded four US patents for his development of the unique Ductile Hybrid Fabric, Armor Structure, and New Innovative Bridge Systems. He has published over 200 technical papers and articles in national and international journals such the PCI, ACI, ASCE, and CSCE Journals, and delivered several keynote presentations in national and international conferences.

Plenary Speakers
(alphabetical order)

Professor Wei-Xin Ren, Ph.D.
Hefei University of Technology, China

Wei-Xin Ren is currently Dean of the School of Civil Engineering, Hefei University of Technology, China. He is also the Changjiang Distinguished Professor of Bridge Engineering, heading the Bridge Stability and Dynamics Laboratory with more than 10 faculty members and 40 graduate students. He received his Ph.D. in bridge engineering from Central South University, China, in 1993 and conducted two years of post-doctoral research in Tsinghua University, China. He was promoted to a full professor in 1995. He was a visiting professor in Japan, Belgium, USA, and Australia. His research interests include the broad areas of bridge and structural engineering; specifically, structural stability and dynamics, long span cable-supported bridges, damage detection, finite element modeling, and structural condition assessment and heath monitoring. Ren has published five books and more than 350 articles, including 130 refereed international journal papers. He was listed in Most Cited Chinese Researchers in the Civil and Structural Engineering area by Elsevier in 2014, 2015, 2016, and 2017. He was also listed in Most Cited World Researchers in the Civil Engineering area by Elsevier in 2016.

Invited Speaker

Professor Hong-Gun Park, Ph.D., P.E.
Seoul National University, Korea
Korea Concrete Institute

Hong-Gun Park, a member of the Presidential Advisory Council on Science & Technology (PACST) in Korea, is a Professor in the Department of Architecture & Architectural Engineering at Seoul National University, Seoul, South Korea, where he has served on the faculty since 1997. Park is a former Vice-President of the Korea Concrete Institute (KCI), and is the Director of the Korean Building Code Center at the Architectural Institute of Korea and a Vice-President of the Korean Structural Engineers Association. He is a member of two national academies: National Engineering Academic Society in Korea (NEAK) and the Korean Academy of Science and Technology (KAST). He is also a member of the CAEE Academy of Distinguished Alumni at the University of Texas at Austin, TX, USA.

Park is a Fellow of the American Concrete Institute (ACI) and serves as a member of ACI Committees 59 (International Advisory Committee), 421 (Slabs), 445 (Shear and Torsion), and International Conferences/Conventions (IC/C). He received the prestigious Chester Paul Siess Award for Excellence in Structural Research, bestowed by ACI, two times in 2009 and 2012.

Park has authored more than 230 technical papers, including 45 ACI Structural Journal papers and 40 ASCE Journal of Structural Engineering papers. His research interests include the seismic design of reinforced concrete and composite structures, constitutive modeling for nonlinear finite element analysis, and the evaluation of existing building structures. Currently, Park is leading two research projects concerning high-rise buildings and nuclear power plants, supported by the Korean government.

Park received his BS and MS in architectural engineering from Seoul National University, Seoul, South Korea, in 1985 and 1987, respectively, and his PhD in civil engineering from the University of Texas at Austin, Austin, TX, USA, in 1994. He is a registered Professional Engineer in South Korea.

Construction and Preservation

Non-Destructive Inspection of Concrete Degraded by Alkali-Silica Reaction

Atsushi Teramoto[1*], Ryota Murakami[2], Masaki Watanabe[3], and Takaaki Ohkubo[4]

[1]: Hiroshima University, Higashi-Hiroshima, Japan; email: a-teramoto@hiroshima-u.ac.jp
[2]: Hiroshima University, Higashi-Hiroshima, Japan; email: m173238@hiroshima-u.ac.jp
[3]: Hiroshima University, Higashi-Hiroshima, Japan; email: m180720@hiroshima-u.ac.jp
[4]: Hiroshima University, Higashi-Hiroshima, Japan; email: ohkubotk@hiroshima-u.ac.jp

[*]: corresponding author

Keywords: non-destructive inspection method; ultrasonic spectroscopy; alkali-silica reaction (ASR); pessimum; static elastic modulus

Abstract: In Japan, damage caused by alkali-silica reaction (ASR) has been reported to the reinforced concrete (RC) bridges, mainly in the Hokuriku region. Degradation of concrete by ASR might deteriorate the structural performance of RC bridges. Therefore, evaluation of and countermeasures against such deterioration are indispensable. In particular, a non-destructive inspection method, which could evaluate the degree of degradation without damaging the actual structure, is highly desirable. However, many unknowns remain in the quantitative evaluation of the correlation between the degree of deterioration assessed by the non-destructive method and that gained by the conventional destructive tests (compression strength and static elastic modulus). In this research, we focused on ASR as a deterioration phenomenon of concrete by conducting ultrasonic spectroscopy of specimens for different degrees of deterioration. The indicators by the ultrasonic spectroscopy were ultrasonic propagation velocity (UPV), average frequency and maximum power spectrum (MPS). All of these factors showed that tended to decrease in earlier concrete deteriorated by ASR. Conversely, with regard to the static elastic modulus, a high correlation was found between these factors, even though no correlation was found between these aspects and compressive strength. However, in the long period MPS showed better agreement than UPV. It is thought that this is due to ultrasonic transmission of alkali silica gel. From the above results, the combination use of UPV and MPS is effective measures as a non- destructive diagnosis method of bridge structure.

1. Introduction

Alkali-silica reaction (ASR) causes performance deterioration of reinforced concrete (RC) structures due to deterioration of concrete. In Japan, many cases of ASR have been reported in bridge piers, mainly in the Hokuriku region, after JIS A 5308, the Japanese regulation on control countermeasures for ASR, was specified in 1989. The pessimum effect is believed to be one of the causes of occurrence of ASR even if the above countermeasures are taken (Katayama et. al. 2004). In general, when ASR degradation is observed in important RC structures like bridges by visual inspection, a thorough evaluation with regard to whether the structure continues to satisfy the predetermined performance is required. Moreover, as ASR progresses over a long period,

performance verification during the structure's future service life is also necessary, particularly if the affected bridge serves as important infrastructure.
When conducting the performance evaluation of the structure, destructive testing such as compressive strength testing of the sampled core gained from the actual structure is generally carried out. However, the cost of collecting concrete cores is prohibitive, and a simpler structural evaluation method is required. Given the above background, the demand for a non-destructive inspection method that can evaluate the degree of degradation without damaging the actual structure is extremely high. To this end, we conducted research focusing on the ultrasonic method, one of the most well-known non-destructive inspection techniques. Although many previous studies have used the ultrasonic method (Larose 2013), less quantitative comparison exists with regard to the degree of ASR deterioration assessed by the ultrasonic method and conventional destructive testing (compressive strength and static elastic modulus). Therefore, in this research, specimens with different degrees of deterioration were prepared using the pessimum effect, and the relationship between the results of the conventional destructive test and the value measured by the ultrasonic spectroscopy method was studied.

2. Experimental Procedure

2.1 Materials and Mixture Proportions of ASR Specimens

There are various types of pessimum effects, such as those caused by aggregate type and those attributable to aggregate particle size. In this study, we used the effect of aggregate type on pessimum in order to prepare specimens with different degrees of ASR deterioration. The reactive aggregate used in this experiment was an andesite showing rapid expansion, and the non-reactive aggregate was quartz porphyry crushed stone. The reactive aggregate used in this experiment is known to have a pessimum mixing ratio of 30% as per a previous study (Kawabata et al. 2017). In this experiment, 4 mixture proportions of 10, 30, 50, and 80% were used as mixing ratios of reactive aggregate, so that different expansions due to ASR could be generated at the same age. In addition, the total amount of alkali was adjusted to 5.5 kg/m^3 with sodium hydroxide reagent to accelerate ASR. Sealing curing was carried out at 20 °C for 28 d after casting, and thereafter, wet cloth curing was carried out at 60 °C.

Table 1 Mixture Proportions

	Water	Cement	Coarse Aggregate		Fine Aggregate
			Reactive	Non-Reactive	
CS10	160	320	103	908	805
CS30	160	320	308	706	805
CS50	160	320	514	504	805
CS80	160	320	822	202	805

2.2 Change in Length

Three cylindrical specimens with φ100 × 200 mm were prepared, and the change in the lengths of the ASR specimens was measured with a contact gauge as the distance between the chips attached to the stainless steel band.

2.3 Compressive Strength Test

The compressive strength and static elastic modulus were measured in accordance with JIS A 1108 and JIS A 1149, respectively with φ100 × 200 mm.

2.4 Ultrasonic Spectroscopy Method

Prism specimens with 70 × 70 × 600 mm were prepared, and ultrasonic measurements were performed in the longitudinal direction of the specimens using an ultrasonic measuring instrument and a 54 kHz transducer (Pundit PL-200, Proceq) at specified accelerated age (0, 1, 7, 14, 35, and 70 days). Then, Fourier transformation of the waveform by ultrasonic spectroscopy was carried out.

3. Results and Discussion

3.1 Change in Length

Figure 1 shows the development of ASR-related expansion in each specimen. Figure 1 confirms that specimens show different degrees of deterioration depending on the mixing amount of the reactive aggregate.

3.2 Compressive Strength & Static Elastic Modulus

Figure 2 shows changes over time in the compressive strength and static elastic modulus, and Figure 3 shows the relationship between the mechanical properties and the deterioration due to ASR. According to Figure 2, the static elastic modulus decreases sharply with the progress of ASR in all specimens. Whereas the compressive strength shows a slight increase or stagnation, this is attributed to the greater influence of hydration due to high-temperature and high-humidity curing as compared with degradation by ASR. Figure 3, which shows the relationship between the static elastic modulus and expansion ratio, confirms that the static elastic modulus decreases with expansion and is very sensitive to ASR deterioration. In addition, it was confirmed that this relationship is not dependent on the mixing amount of the reactive aggregate.

3.3 Ultrasonic Spectroscopy

The following two indicators are used for non-destructive inspection of concrete via the ultrasonic

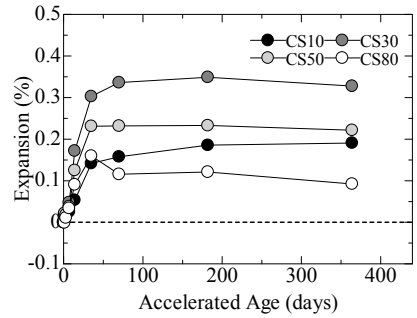

Fig. 1 ASR-induced expansion.

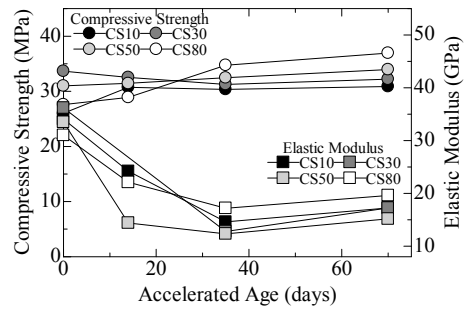

Fig. 2 Development of mechanical properties with accelerated age.

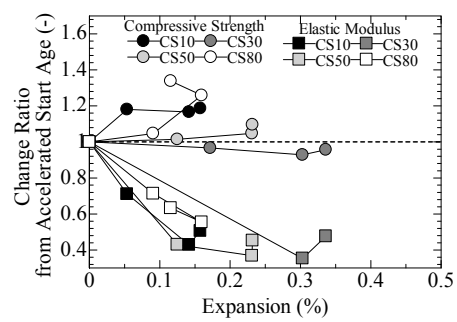

Fig. 3 Relationships between mechanical properties and expansion ratio.

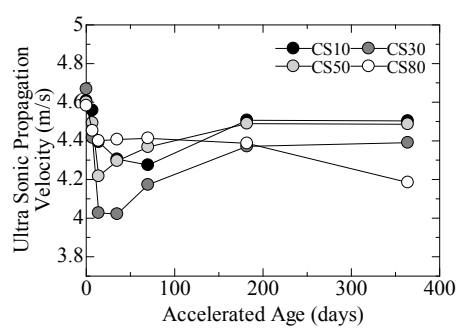

Fig. 4 Development of UPV properties with accelerated age.

method: ultrasonic propagation velocity (UPV) and Fourier spectrum of the ultrasonic waveform. In past studies, UPV has mainly been applied as an index for ASR diagnosis. (e.g., Swamy 1997). Figure 4 shows the development of UPV in each mixture. As shown in the figure, UPV decreases with the progress of ASR. However, thereafter, a tendency to gradually recover is notable except for CS80. This tendency is thought to be caused by alkali-silica gel (ASG) filling the micro-cracks caused by ASR, and past studies have confirmed the same phonomena (e.g., Mohammed 2003). However, even if the ASG transmits longitudinal waves, it cannot be expected to transmit stress. Therefore, using UPV as an indicator for mechanical properties might over-evaluate the performance of the structure. Figure 5 shows the Fourier spectrum of CS30. The figure indicates that the Fourier spectrum changes as ASR progresses; in particular, a remarkable decrease in the maximum power spectrum (MPS) is observed. Figure 6 shows the temporal change in the MPS of each mixture. It shows a uniform declining trend with ASR progression. Figure 7 shows the relationship between the MPS and static elastic modulus, and a good correlation is observed. Although omitted in this paper, the reduction of the maximum power spectrum is accompanied by the decrease of the average frequency as a result, so that the average frequency is also considered to be effective as an index showing the degree of degradation by ASR. From the above, it was shown that when applying the ultrasonic method to the deterioration diagnosis of ASR, multiple indicators such as UPV and MPS should be utilized.

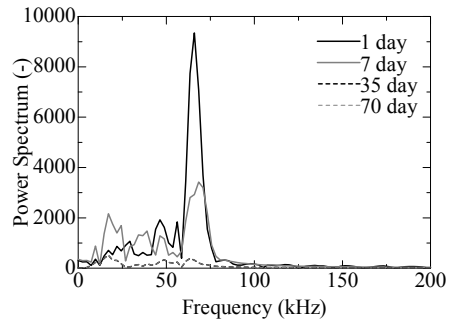

Fig. 5 Fourier spectrum (CS30)

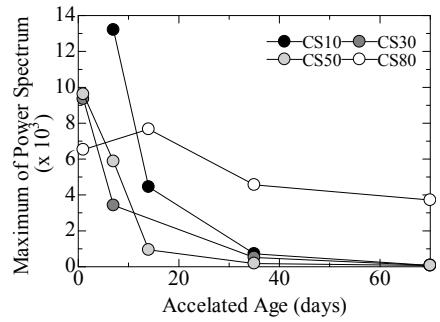

Fig. 6 Development MPS with accelerated age.

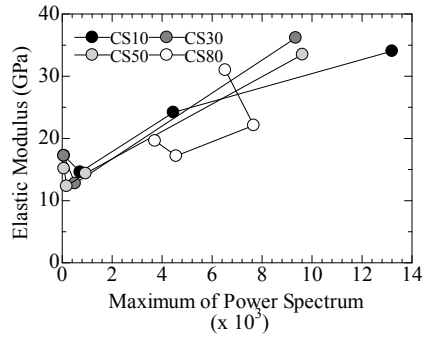

Fig. 7 Relationships between MPS and elastic modulus.

4. Conclusion

This research investigated the ultrasonic method as a non-destructive inspection technique to evaluate the mechanical properties of concrete with different degrees of ASR deterioration. The results showed that the UPV is not a best index for evaluating ASR degradation degree. The utilization of other indicators which obtained from the Fourier spectrum of the waveform by ultrasonic spectroscopy could improve the accuracy of diagnosis.

5. References

Katayama et al. 2004. Alkali-aggregate reaction under the influence of deicing salts in the Hokuriku district, Japan, Materials Characterization, 53, 105–122.

Kawabata et al. 2017. The mechanism of limited inhibition by fly ash on expansion due to alkali–silica reaction at the pessimum proportion, Cement and Concrete Research, 92, 1–15.

Larose 2013. A review of ultrasonic Coda Wave Interferometry in concrete, Cement and Concrete Research, 53, 248–255.

Mohammed et al. 2003. Alkali-silica reaction-induced strains over concrete surface and steel bars in concrete, ACI Materials Journal, 100-M16, 133–142.

Swamy 1997. Assessment and Rehabilitation of AAR-affected Structures, Cement and Concrete Composites, 19, 427-440

Deterioration of Mixed Rebar and Fiber-Reinforced Concrete Bridge Decks

Benjamin Z. Dymond[1*] and Corin Treat[2]

[1] Dept. of Civil Engineering, University of Minnesota Duluth, Duluth, MN, USA; email: dymond@d.umn.edu
[2] Meyer Borgman Johnson (MBJ), Duluth, MN, USA

*: corresponding author

Keywords: bridge decks; epoxy-coated rebar; polypropylene fibers; deterioration

Abstract: Between 1973 and 1989, approximately 600 bridge decks were constructed in Minnesota with a top layer of epoxy-coated rebar and a bottom layer of uncoated, black rebar (i.e., mixed rebar deck) to potentially reduce corrosion in the top layer of steel reinforcement. In the last five years, at least 20 bridge decks have been constructed with polypropylene fibers in the concrete mix to reduce the width and amount of cracking. This research project investigated how mixed rebar or polypropylene fibers affected the rate of deterioration in bridge decks (e.g., spalling of underside of deck concrete or unsound concrete on the top wearing surface) compared to control structure decks that were approximately the same age. The results were subdivided to indicate how the superstructure type, average daily traffic, route type, and wearing surface crack density affected the condition ratings and rate of deterioration. Based on the results, the mixed rebar decks reached worse condition states than the control structures when comparing the condition of the underside of the deck. Steel superstructures affected the deterioration of mixed rebar decks the most.

1. Introduction and Background

Long-term deterioration of concrete bridge decks is often what dictates the service life of a bridge in northern climates. De-icing chemicals used on the deck generally accelerate this deterioration. Concrete decks are typically reinforced with a layer of steel rebar in the top and the bottom of the cross section. The de-icing chemicals reach the steel rebar through cracks in the top of the concrete deck and diffusion through the concrete matrix. The steel becomes corroded from these chemicals, which causes the surrounding concrete to expand and deteriorate. The Minnesota Department of Transportation (MnDOT) has been implementing different policies to reduce concrete bridge deck deterioration by protecting the reinforcement from corrosion and reducing cracking in the concrete. In the early 1970s, epoxy-coated rebar was used in the top layer of the concrete deck with uncoated rebar in the bottom layer (i.e., mixed rebar deck) until approximately 1989 (Nelson, 2014). In the 2010s, MnDOT began using polypropylene fibers in the concrete mix to reduce the width and amount of cracking in the top of the deck.

The goal of this research was to compare the rate of deterioration of mixed rebar concrete decks and fiber-reinforced concrete decks with control group structure decks and determine the factors that have historically had the largest impact on the rate of deterioration for mixed rebar decks. This was accomplished by evaluating historical inspection data to compare how different types of decks deteriorated over time.

A bridge is currently rated using the National Bridge Inventory (NBI) system and individual element ratings. Before 2016, Commonly Recognized (CoRe) Structural Elements were used to provide the individual element ratings. The CoRe elements rate the bridge using condition states 1 to 5 or 1 to 4, with 1 being the best condition (MnDOT, 2013). In 2016, National Bridge Element (NBE) ratings replaced the CoRe Element ratings. The NBE elements rated a bridge using condition states 1 to 4, with 1 being the best condition. NBE elements identify the amount of the deck in square feet (SF) or linear feet (LF) that is in each condition state. For example, a bridge may have a total quantity of 3821 SF with 3501 SF in condition state 1 and 320 SF in condition state 2 for a certain element rating (MnDOT, 2018). This study analyzed CoRe Element #26 Top of Deck with Epoxy Rebar (No Overlay), CoRe Element #358 Cracking on the Top of Deck, CoRe Element #359 Cracking on the Underside of Deck, and NBE Element #12 Reinforced Concrete Deck (underside of deck). Data from NBE Element #12 was of primary interest because they indicated deterioration of the underside of the deck, which is the hardest surface to repair and is the surface in the closest proximity to the uncoated rebar in mixed rebar decks.

2. Methods

Approximately 471 bridges built between 1973 and 1989 with mixed rebar decks were included in the study and 35 decks with epoxy-coated top and bottom mat rebar (built between 1973 and 1990) served as the control structures. Approximately 18 fiber-reinforced decks built between 2012 and 2017 were included in the study and four non-fiber-reinforced decks with epoxy-coated top and bottom mat rebar (built between 2013 and 2016) served as the control structures. Historical inspection data were provided in two databases: (1) CoRe inspection data from 1992 to 2016 that included Elements #26, #358, and #359; (2) NBE inspection data from 2014 to 2018 that included Element #12. The data for each element were divided into subsets:

- all mixed rebar decks or all control structures
- mixed rebar decks with an Average Daily Traffic (ADT) less than 4,000, between 4,000 and 10,000, or greater than 10,000
- mixed rebar decks with current wearing surface crack density less than 0.01 LF/SF, between 0.01 and 0.1 LF/SF, or greater than 0.1 LF/SF
- mixed rebar decks carrying Interstates, U.S. Highways, State Highways, County Roads, or Town Roads
- mixed rebar decks with a reinforced concrete, steel, or prestressed concrete superstructure
- mixed rebar decks that had a skew less than or equal to 20° (not skewed) or greater than 20° (skewed)

The number of years each subset of bridges remained at each condition state was calculated for each element. The percentage of the deck in condition states 3 and/or 4 for the most recent NBE Element #12 data was calculated to determine the percentage of the underside of the deck with unsound concrete. This element in the bridge was of primary interest due to the inability to repair cracking or spalling on the underside of a bridge deck. The bridges that had at least 2% of the deck unsound were analyzed and the percentage of these bridges that had mixed rebar decks was calculated. Furthermore, the percentage of the mixed rebar decks that were in each subset were calculated as shown in Figure 1.

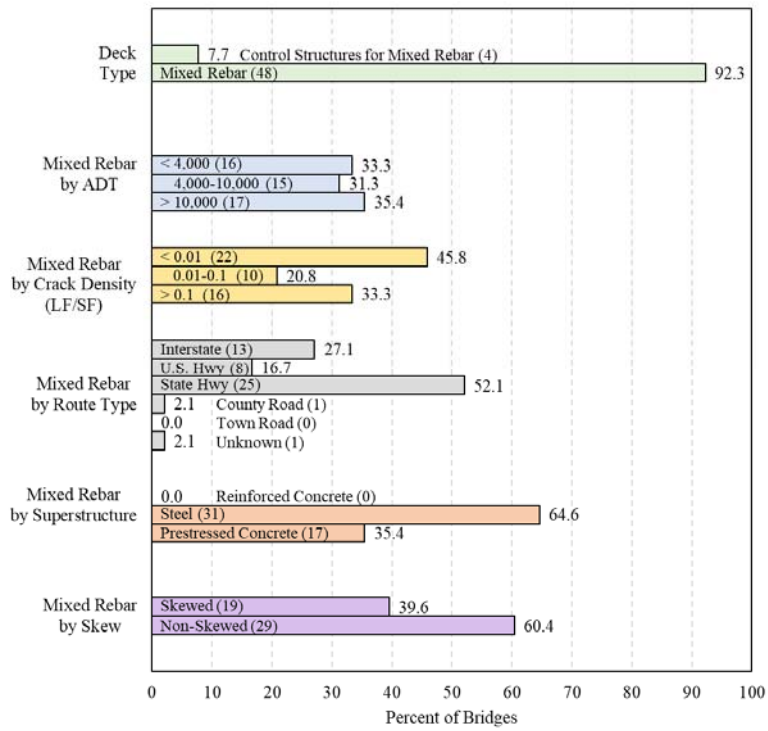

Fig. 1. Percent of bridges in each subset that have greater than or equal to 2% of the deck area in condition states 3 and/or 4 for NBE Element #12 (52 bridges). Bar chart labels include the number of bridges in each subset in parentheses.

3. Results

The following observations were drawn from analysis of the ratings.

- All mixed rebar decks spent an average of 8.5 years at condition state 2 before dropping to condition state 3 for CoRe Element #359 Cracking on the Underside of Deck.
- Approximately 30% more mixed rebar decks with steel superstructures had reached condition states 3 and/or 4 for NBE Element #12 Reinforced Concrete Deck (underside of deck) than mixed rebar decks with a prestressed concrete superstructure. Decks with steel superstructures also had a higher percentage of the entire deck area in condition states 3 and/or 4 (1.83%) than the decks with prestressed concrete superstructures (1.15%).
- Of the 52 bridge decks that had at least 2% of the deck in condition states 3 and/or 4 for NBE Element #12 Reinforced Concrete Deck (underside of deck), 92.3% were mixed rebar decks and 7.7% were the control structures. More than 50% of these mixed rebar decks carried a State Highway, had a steel superstructure, and were not skewed. The mixed rebar decks were split almost equally between each level of ADT.

4. Conclusions and Recommendations

The following conclusions were drawn from the results of this study:

- The mixed rebar decks reached worse condition states than the control structure decks when considering CoRe Elements #26 Top of Deck with Epoxy Rebar (No Overlay), #358

Cracking on the Top of Deck, #359 Cracking on the Underside of Deck, and NBE Element #12 Reinforced Concrete Deck (underside of deck).

- Average daily traffic did not appear to affect the deterioration of the deck.
- Wearing surface crack density did not appear to affect the deterioration of the deck since many of the cracks may extend only to the bottom of the 2 in. low slump concrete wearing course and not into the underlying structural slab.
- Mixed rebar decks with steel superstructures reached worse condition states than mixed rebar decks with prestressed concrete superstructures.
- Mixed rebar decks with no skew reached worse condition states than mixed rebar decks with skew considering NBE Element #12 Reinforced Concrete Deck (underside of deck). There were likely other factors not included in this study that impacted these results since it was expected that skewed decks would reach a worse condition state than decks with no skew.
- No conclusions were drawn based on the results for the fiber-reinforced decks due to the small sample size and the limited amount of data available over time.

The following recommendations were made based on the results of this study:

1. Create a new inspection rating element that quantifies the crack density on the underside of the deck for mixed bar decks. Through-deck cracking may be a key indicator for future underdeck spalling of mixed bar decks since the cracks provide a clear path for the chlorides to reach the uncoated bottom mat. This element would be less valuable for fully epoxy or black bar decks since the rebar corrosion typically occurs in the top mat of those bridge decks.
2. Consider a more robust crack sealing such as flood coating with methyl methacrylate (MMA) or applying an impermeable wearing course such as premixed polymer concrete (PPC) or epoxy chip seal on mixed rebar decks when they have been at CoRe Element #359 condition state 2 for approximately 7 years. This could reduce the number of bridges that reach condition state 3. This recommendation was based on the average number of years that a deck remained at condition state 2 for CoRe Element #359. Use of epoxy coating on both mats of rebar in bridge decks seemed beneficial as the mixed bar decks deteriorated faster.

5. References

Minnesota Department of Transportation. 2013. Bridge Inspection Field Manual Version 1.10, MnDOT Bridge Office, Oakdale, MN.

Minnesota Department of Transportation. 2018. State of Minnesota Bridge and Structure Inspection Program Manual, MnDOT Bridge Office, Oakdale, MN.

Nelson, S. L. 2014. Deterioration Rates of Minnesota Concrete Bridge Decks, Report Number MN/RC 2014-40, Minnesota Department of Transportation, St. Paul, MN.

Treatment of Alkali-Silica Reaction in Concrete Structures Using Pressurized Injection of Lithium Nitrite

Tatsuya Kitada[1*] and Kazunori Era[2]

[1]: Kyokuto Kowa Corporation, Hiroshima, Japan; email: t-kitada@kkn.co.jp
[2]: Kyokuto Kowa Corporation, Hiroshima, Japan; email: era@kkn.co.jp

[*]: corresponding author

Keywords: repair, alkali-silica reaction (ASR), lithium nitrite, pressurized injection

Abstract: The repair of alkali-silica reaction in concrete is conventionally performed using crack injection, surface coating, and other procedures. However, there has recently been increased interest in techniques using lithium nitrite. We developed a method for pressurized injection of lithium nitrite designed to make all the alkali-silica gel within the concrete non-expansive. Pressurized lithium nitrite injection is used as a radical treatment method for concrete structures that have deteriorated because of alkali-silica reaction. In this paper, we discuss the basic principles of this method and its development and application in Japan. We also present examples of its application and the results of follow-up surveys on actual structures.

1. Introduction

Alkali-silica reaction (ASR) in concrete structures has been reported in many cases of concrete deterioration in Japan and abroad. Conventionally, repair treatment is performed to block extraneous water penetration using crack injection, surface coating, and other procedures. However, structures continue to deteriorate again soon after treatment because of the strong expandability of ASR products. Under these circumstances, there has recently been increased interest in techniques using lithium ions to repair ASR damage. Various mechanisms have been proposed for inhibiting ASR expansion using lithium ions, such as making the gel non-expansive through ion exchange between the Na^+ in the alkali-silica gel and the supplied Li^+.[1)] Many studies have reported that ASR expansion does not occur in concrete that has a certain proportion or more of lithium ions mixed in beforehand.[2)]

Three types of ASR repair methods using lithium nitrite are already in use: surface coating, crack injection, and section repair. However, these methods are said to supply lithium ions in a range limited to the concrete outer surface and the areas surrounding cracks, and it does not lead to the fundamental control of ASR. Thus, we developed a method for pressurized injection of lithium nitrite to fundamentally control ASR by supplying lithium ions throughout the concrete and making all the alkali-silica gel within the concrete non-expansive. These efforts have led to the practical use of this method.

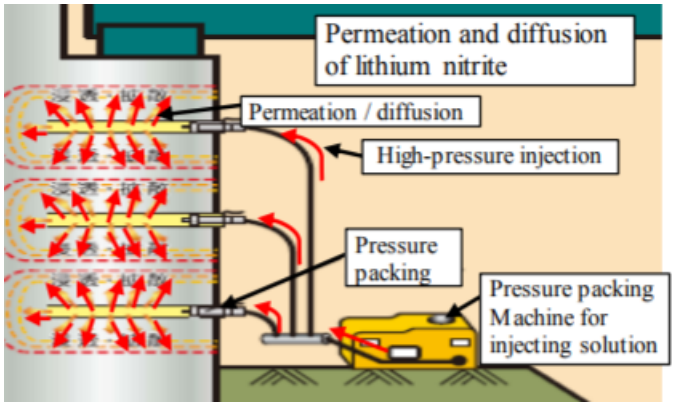

Fig. 1. Schematic diagram of the method

2. Pressurized lithium nitrite injection method

Pressurized lithium nitrite injection is a method for repairing ASR by drilling small holes in the ASR-affected concrete frame, and then pressure-injecting lithium nitrite solution through these holes to make the solution permeate into the concrete. Through pressurized injection, lithium ions are supplied over a wide extent of the concrete interior, thereby fundamentally controlling future ASR expansion by making the ASR gel non-expansive. The 20-mm-diameter holes are drilled at 500- to 1,000-mm intervals, which are set according to hole depth and structure dimensions. Injection pressure is set according to the degree of deterioration of the structure and is generally in the range of 0.5 to 1.5 MPa. The amount of lithium nitrite for pressurized injection is set for every structure according to the structure's alkali content to achieve a specific Li/Na mole ratio. A schematic of pressurized alkali nitrite injection is shown in Fig. 1.

3. Application of pressurized lithium nitrite injection method to ASR repair projects

3.1. Work examples and structures for application

As of March 2018, the injection method has been applied to more than 100 work sites in Japan, primarily on structures administered by the Ministry of Land, Infrastructure, Transport and Tourism and local governments. At every site, the structure has been assessed to have significant ASR deterioration, where the residual ASR expansion remains harmful and is expected to propagate further in the future. Some of these structures have undergone ASR repair by crack injection and surface coating methods in the past but have already deteriorated again. Structures to which this method was applied include bridge substructures (abutments and piers), bridge superstructures (reinforced-concrete girders and deck slabs), box culverts, estuary weirs, wharfs, building foundations, and steel tower foundations. Typical work examples are shown in Fig. 2 for pressurized injection on road bridge abutments (Okutani Bridge).

Fig. 2. Pressurized lithium nitrite injection on bridge abutments (Okukani Bridge)

3.2. Methods for verification of ASR repair effectiveness

(1) Residual expansion test

To quantitatively verify the inhibition of ASR expansion after pressurized lithium nitrite injection, core sampling is conducted before and after application of the method and then the residual expansion test is carried out to compare the two measurements. The JCI-DD2 method is used as the standard, with the acceleration environment set at 40°C and 95% relative humidity. A sample core 100 mm in diameter × 250 mm in length is removed from the structure by using a diamond core drill. The assessment criterion in the JCI-DD2 method is 0.05% expansion, meaning that the sample has harmful expandability when total expansion exceeds 0.05% after a 13-week acceleration period, whereas the expansion is harmless when below 0.05%.

(2) Follow-up survey of exterior damage

We regularly conduct follow-up surveys of exterior damage over the long term to look for the presence of new exterior damage and symptoms of recurrence of ASR expansion on all structures that have undergone repairs using this method. The follow-up survey of exterior damage is basically performed once per year.

3.3. Verification of effectiveness of ASR repair using pressurized lithium nitrite injection

(1) Residual expansion test results

Table 1 lists major ASR repair projects using the injection method and their residual expansion test results before and after application of the method. The structures include abutments, piers, and bridges that are currently still in service. Based on the test results of total alkali in the concrete, we pressure-injected lithium nitrite at a pressure of 0.5 to 1.5 MPa such that the Li/Na mole ratio is 0.8 to 1.0 in all the structures. It can be seen that while all of the structures showed high residual expansion before application, the residual expansion after application is considerably lower than the values before application. Because the values of the residual expansion test after application are well below the JCI-DD2 assessment criterion of 0.05% and the ability of ASR expansion to propagate in the future is evaluated as harmless, we can conclude that the pressurized lithium nitrite injection method inhibits ASR expansion in concrete structures.

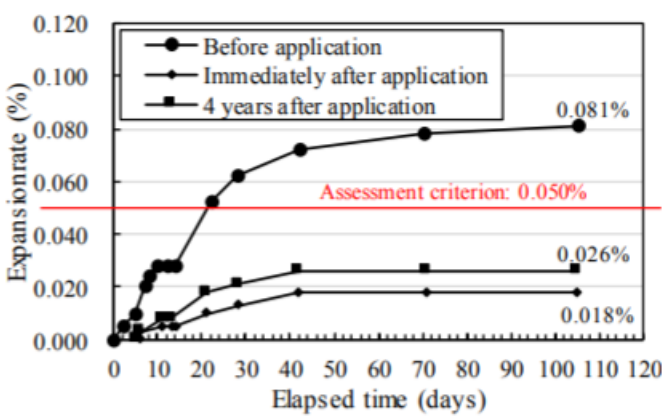

Fig. 3. Residual expansion test results (Sue Bridge)

Fig. 4. Follow-up survey of concrete exterior (Sue Bridge)

As an example, Fig. 3 shows the residual expansion test results for the Sue Bridge abutment. Results for total expansion, which is the sum of expansion during standard curing at 20°C and accelerated curing for 13 weeks at 40°C, show that while expansion was 0.081% before application, it became 0.018% immediately after application, falling to 22.2% of the value before application. Since this value is below the JCI-DD2 assessment criterion of 0.05%, we can conclude that the pressurized lithium nitrite injection inhibited ASR expansion. In addition to immediately after application, we took core samples from the bridge and carried out the residual expansion test again 4 years after application. Comparison of the expansion trends both immediately after application and 4 years later shows that, while expansion is 0.018% immediately after application, the value became somewhat higher at 0.026% 4 years after application. However, it is still much lower than the JCI-DD2 criterion of 0.05% after 13 weeks, and compared with the value of 0.081% before application, it remains at 32.1% of the original even after 4 years has elapsed after application. Thus, we can conclude that the high reduction effect on ASR expansion is still maintained.

Table 1. Major ASR repair projects

FY	Structure	Location	Residual expansion*		FY	Structure	Location	Residual expansion*	
			Before	**After**				Before	**After**
2005	Abutment	Kagawa	0.08%	**0.02%**	2014	Bridge	Shimane	Harmful	**0.02%**
2013	Abutment	Shimane	0.07%	**0.02%**	2014	Pier	Aichi	Harmful	**0.027%**
2013	Pier	Saga	0.18%	**0.01%**	2016	Bridge	Shimane	0.092%	**0.016%**
2013	Pier	Kagawa	0.21%	**0.01%**	2016	Abutment	Shimane	0.092%-	**0.018%**
2013	Pier	Kagawa	Harmful	**0.01%**	2017	Pier	Shimane	Harmful	**0.004%**
2013	Abutment	Kagawa	Harmful	**0.03%**	2017	Abutment	Shimane	Harmful	**0.011%**
2014	Bridge	Yamagata	0.28%	**0.03%**	2018	Pier	Shimane	Harmful	**0.024%**

*Assessed as harmless if residual expansion is 0.05% or less.

(2) Results of follow-up survey of exterior damage

Follow-up surveys of exterior damage have been performed on all the work sites shown in Table 1, and the results confirm that, for all the structures, no appearance or symptoms of damage that suggest ASR propagation have been found from the time of application up to the present. As an example of the follow-up survey of exterior damage, the condition of Sue Bridge before application (2005) and 10 years after application (2015) are shown in Fig. 4. On the abutment concrete surface before application, extensive map cracking, which characterizes ASR expansion, can be observed, along with water leakage found in some cracked sections and considerable moisture intrusion into the concrete coming from the bridge seat surface and back face of the abutment. Because surface coating had not been applied to the concrete surface after pressurized injection of lithium nitrite during the bridge abutment repair work, the concrete surface condition can be directly inspected during follow-up observation after application. Exterior damage surveys were carried out regularly after application. A carefully conducted close visual inspection of the abutment concrete surface 10 years after application in 2015 did not find exterior damage that can be regarded as a recurrence of ASR deterioration or its symptoms.

4. Conclusions

1) We developed the pressurized lithium nitrite injection method by focusing on making the ASR gel non-expansive by using lithium ions to repair ASR damage in concrete structures.
2) We carried out residual expansion tests before and after application of the pressurized lithium nitrite injection method to on actual structures, and these tests showed that residual expansion after application was reduced in all of the structures to values that are assessed as harmless.
3) For actual structures to which the pressurized lithium nitrite injection method was applied, we regularly conducted follow-up surveys of exterior damage over the long term. Surveys showed that no appearance or symptoms of damage that suggest recurrence of ASR deterioration has been found in any of the structures.

5. References

1) M.D.A.Thomas, R.Hooper and D.B.Stokes, "Use of Lithium-Containing Compounds to Control Expansion in Concrete Due to Alkali-Silica Reaction", Proc. Of 11th International Conference on Alkali-Aggregate Reaction, pp.783-792, 2000

2) Mitsuru Saito, Akio Kitagawa and Shigemasa Hasaba, "Effectiveness of Lithium Nitrite in Suppressing Alkali-Aggregate Expansion", Journal of the society of Materials Science, Japan, Vol.41, No.468, pp.1375-1381

Post-tensioning of Deteriorated Reinforced Concrete Bridge Girders with Unbonded Near-Surface Mounted (NSM) Shape-Memory Alloy Wires

Arkabrata Sinha[1] and Jovan Tatar[2*]

[1] Department of Civil & Environmental Engineering, University of Delaware, Newark, DE, USA; email: arka@udel.edu
[2] Department of Civil & Environmental Engineering, University of Delaware, Newark, DE, USA; email: jtatar@udel.edu

[*] : corresponding author

Keywords: shape-memory alloy; post-tensioning; repair; concrete; bridge girders; near-surface mounted

Abstract: Excessive cracking and deflections can significantly impair functionality of concrete bridge girders. In this study, a novel repair technique utilizing heat-induced post-tensioning with unbonded near-surface mounted (NSM) nickel-titanium-niobium (NiTiNb) shape-memory alloy (SMA) wires, was experimentally evaluated. SMAs are an attractive post-tensioning material because of their ability to recover seemingly plastic deformation following heating, via a property termed shape-memory effect (SME). Material characterization tests performed on NiTiNb wires with 2.5% prestrain showed that the SMA can generate recovery stress of approximately 500 MPa when actuated via Ohmic heating. Following materials characterization, the proposed post-tensioning system was experimentally evaluated in reinforced concrete (RC) girders measuring 2.3 m in length, and 23×41 cm in cross-sectional dimensions. The girders were first cracked to simulate girder damage. Cracked girders were then repaired with a varying number of NSM 4-mm NiTiNb wires which were anchored using prestressing chucks. Prestrained NiTiNb wires were actuated via Ohmic heating which triggered SME. Post-tensioning with NiTiNb resulted in crack width reduction of up to 74% and a decrease in residual midspan deflection of up to 49%. After post-tensioning, the girders were loaded up to failure. A relatively small amount of NiTiNb reinforcement increased the girder cracked stiffness (by up to 31%) and ultimate strength (by up to 45%) of the strengthened girders.

1. Introduction

Concrete bridge girders can experience serviceability issues due to excessive cracking and midspan deflection. Traditional repair techniques, such as post-tensioning using steel and carbon fiber reinforced polymer (CFRP) tendons, have proven to be expensive in terms of construction time (and resulting management of traffic costs), equipment and anchorage issues. In this paper, a novel post-tensioning technique utilizing shape-memory alloy (SMA) wires was used to reduce the crack widths and residual deflections, and strengthen damaged RC girders. The benefit of the technique is that it can be implemented without causing significant disruption to traffic flow, and with relatively simple equipment (such as open-flame torch, or electrical power source) as compared to traditional post-tensioning which requires operation of hydraulic jacks on-site.

2. Background on Shape-memory Alloys

SMAs are unique materials which can recover seemingly permanent deformation when subject to an external stimulus such as heating, by a property called shape-memory effect (SME). SMAs can reversibly transform between a high-temperature and high-stiffness phase (called austenite) and low-temperature and low-stiffness phase (called martensite) when heated and cooled through the transformation temperatures, respectively. Martensite can have two variants: (i) twinned; and (ii) detwinned. Stressing twinned martensite above the detwinning start stress (σ_s) initiates transformation to detwinned martensite and the process is complete as the stress goes beyond detwinning finish stress (σ_f) (Fig. 1a). There is a seemingly permanent strain (ε) in the detwinned martensite after removal of the stress (Fig. 1a). Subsequent heating of detwinned martensite through austenite start temperature (A_s) and above the austenite finish temperature (A_f) results in transformation from detwinned martensite to austenite, and complete shape-recovery occurs (Lagoudas, 2008). Cooling the austenite below martensite start temperature (M_s) and beyond martensite finish temperature (M_f) results in transformation to twinned martensite and the seemingly permanent deformations are regained (Fig. 1b). Shape-recovery of the SMA under restrained condition leads to the development of recovery stress which, when transferred to the concrete girders as upward corrective post-tensioning forces, closes cracks and recovers deflection as it will be demonstrated in our work. The SMA used for application in structural engineering should have high enough A_s so that the material does not get triggered accidentally by the ambient temperature during transportation and installation. The SMA should also have a low enough M_s so that the material does not lose the post-tensioning force in cold ambient temperature following shape-recovery.

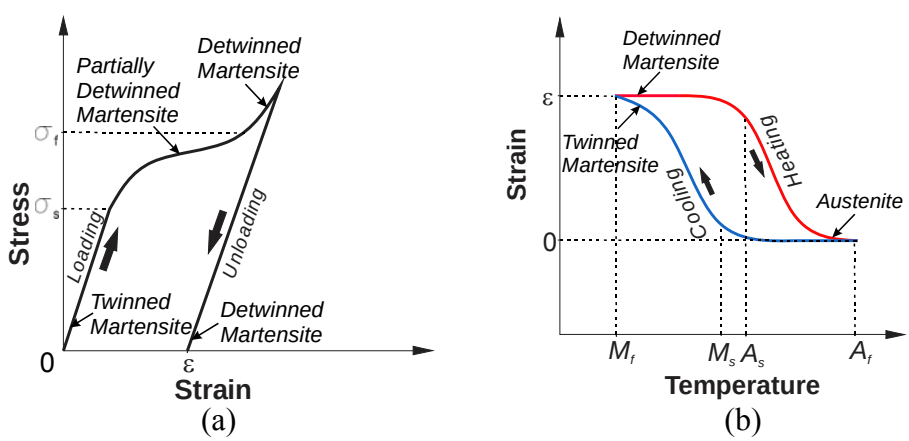

Fig. 1. Thermomechanical behavior of SMA: (a) stress vs. strain curve of martensite

demonstrating the transformation from twinned martensite to detwinned martensite with the application of stress; and (b) strain vs. temperature curve during shape-recovery (transformation from martensite to austenite).

3. Materials

A ternary alloy of nickel, titanium, and niobium (NiTiNb) was used in this research since it has a range of transformation temperatures which allows the material to stay in the high-stiffness

austenite phase. It also maintains recovery stress in the typical range of service temperatures experienced by concrete bridges in the contiguous U.S. Restrained recovery tests on 4-mm NiTiNb wires prestrained at 2.5% indicated a peak recovery stress of 503 MPa when heated above 150°C with 92% (about 462 MPa) recovery stress retained at room temperature (Fig. 2). Tensile tests on NiTiNb wires in austenite phase indicated σ_s and tensile strength of about 585 MPa and 1035 MPa, respectively, with an initial modulus of elasticity of 69 GPa.

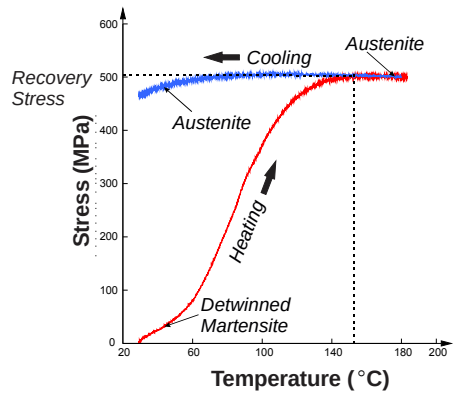

Fig. 2. Recovery stress vs. temperature of NiTiNb wires

Concrete having a 28-day compressive strength of 35 MPa with a 0.49 water-to-cementitious material ratio was used in the RC girders. The Grade 60 steel reinforcement bars had a yield stress of 476 MPa and the tensile strength of 738 MPa, as reported by the manufacturer.

4. Test Specimens

Experimental program included four lightly reinforced RC girders measuring 2.3 m in length and 23×41 cm in cross-sectional dimensions. The tensile reinforcement consisted of 3-#13 metric (#4 imperial) steel bars with 6 cm clear cover. Shear resistance was provided by #10 metric (#3 imperial) U-shaped stirrups (Fig. 3). Three RC girders were preloaded to introduce flexural cracks and residual deflection simulating a typical damaged girder. Varying number of unbonded NSM NiTiNb wires were then installed inside grooves introduced at the tension face of the cracked girders. The girders were labeled as 8-SMA, 10-SMA, and 12-SMA (where the numeric part corresponds to the number of NiTiNb wires installed). NiTiNb wires were anchored with prestressing strand chucks (Fig. 4) at girder ends. Fourth (uncracked) girder served as Control.

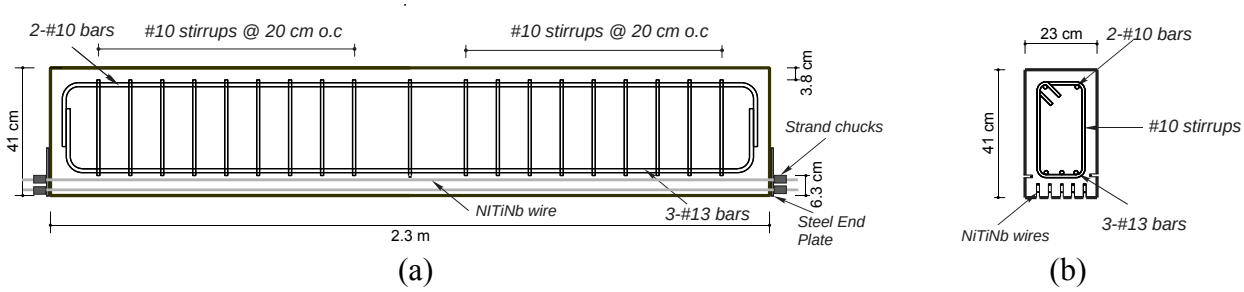

Fig. 3. Typical design of RC girders: (a) Side elevation; and (b) cross-section

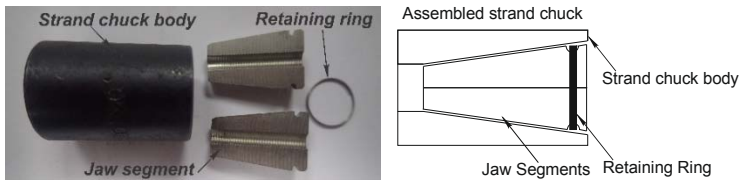

Fig. 4. Details of the prestressing strand chucks used as anchorage device

5. Experimental Procedures

The proposed post-tensioning technique was verified by conducting the following experiments: (i) post-tensioning tests on cracked RC girders; and (ii) flexural tests on post-tensioned girders.

5.1 Post-tensioning Tests on Reinforced Concrete Girders

The cracked girders were post-tensioned by heating the NiTiNb wires above 150 □C by passing a constant current using a 3000-W electrical power source. The temperature of the NiTiNb wires was monitored by affixing K-type thermocouple probes to the wires. The changes in residual midspan deflection (EMD1, EMD2) on either side of the girder and crack widths (Crack1, Crack2) were monitored using LVDTs. Strain in the top fiber of concrete on either side of the midspan of the girders (SG1, SG2) was recorded using strain gages.

5.2 Flexural Tests on Post-tensioned RC Girders

Following post-tensioning, the girders were subject to four-point flexural loading (Fig. 5) up to failure, to observe the change of yield moment, ultimate moment capacity and stiffness after post-tensioning. The load and midspan deflection were recorded throughout the tests.

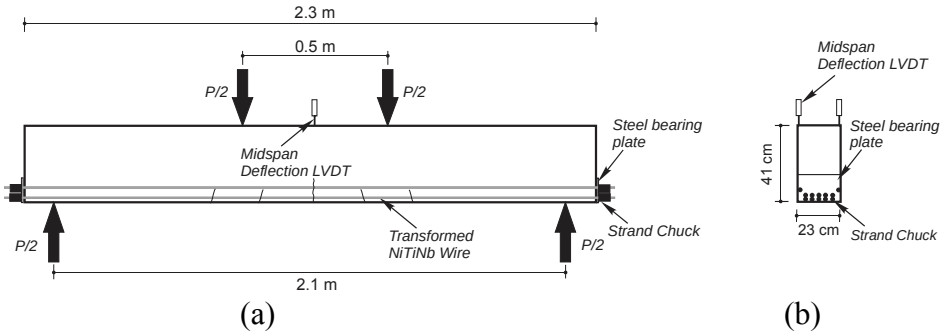

Fig. 5. Flexural test setup: (a) elevation; and (b) end view

6. Results and Discussions

6.1. Post-tensioning Tests on RC Girders

The post-tensioning results of 12-SMA girder, which are representative of the post-tensioning experiments on all three girders are discussed in this paper. Variation of crack width, residual midspan deflection, and tensile strain on top of concrete with time are shown in Fig. 6a, 6b, 6c, respectively, with the time at which the temperature of each NiTiNb wire reached 150 °C, being marked as S1, S2, etc. (where the numbers are used to identify each wire). It should be noted that

the temperature wire number 12 (S12) was not recorded due to malfunction of the data acquisition system.

The crack widths reduced by up to 74% due to compressive post-tensioning forces generated from shape-recovery of the NiTiNb wires, transferred via end anchorage. The final crack widths were within the limits according to the (ACI 224) guidelines for Control of cracking in concrete structures. The residual midspan deflection decreased by up to 49% due to the negative moment introduced by the post-tensioning forces. Increase in tensile strain (up to 120×10^{-6} mm/mm) in the top fiber of RC girders provided further evidence of successful transfer of post-tensioning (Fig. 6c).

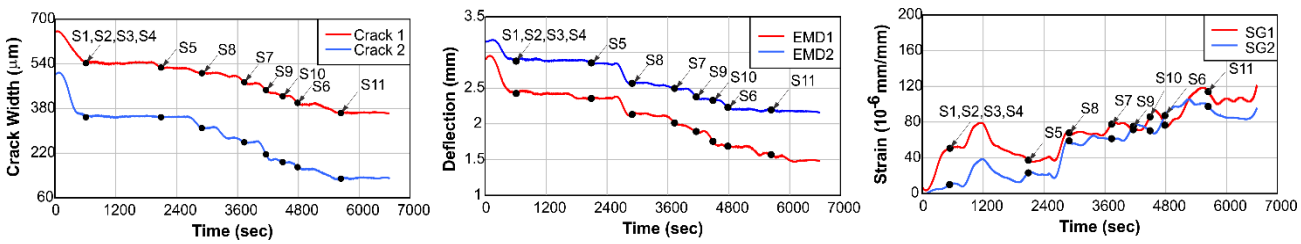

(a) (b) (c)

Fig. 6. Typical post-tensioning results showing the variation of: (a) crack width; (b) residual midspan deflection; and (c) tensile strain on top of concrete with time for 12-SMA girder

6.2. Flexural Tests on Post-tensioned RC Girders

Loading the post-tensioned girders up to failure showed an increase in the yield moment and ultimate moment capacity by up to 58% and 45%, respectively (Fig. 7) over Control girder since the NiTiNb wires carried tensile stresses. The cracked stiffness of the girders increased by up to 31% after post-tensioning damaged girders with only 0.0015 NiTiNb reinforcement ratio.

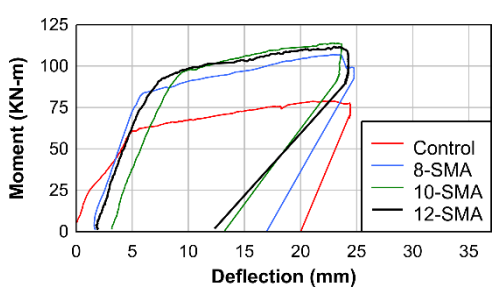

Fig. 7. Moment vs. deflection for 8-SMA, 10-SMA and 12-SMA and Control girder

7. Summary and Conclusions

The objective of this study was to verify the feasibility of using a heat-induced post-tensioning technique utilizing unbonded NSM NiTiNb wires. The post-tensioning and flexural tests on cracked RC girders indicated that the proposed post-tensioning technique was successful in strengthening the girders. The following conclusions were made based on the current experimental results:

- Post-tensioning was accomplished using simple equipment (electrical power source).
- The crack width and midspan deflection of the damaged RC girders reduced by up to 74% and 49%, respectively, as a result of post-tensioning.
- The ultimate moment capacity and the cracked stiffness of damaged RC girders increased by 45% and 31%, respectively, with a relatively small addition of NiTiNb reinforcement.

8. Acknowledgments

The authors thank the Louisiana Transportation Research Center (LTRC) for financial support.

9. References

ACI 224R-01. Control of Cracking in Concrete Structures. ACI Committee 224, Farmington Hills, Michigan, USA.

Lagoudas, D. C. 2008. Shape Memory Alloys: Modeling and Engineering Applications, Springer Science & Business Media, Berlin/Heidelberg, Germany.

Study on Discriminating Method of Bottom of Concrete Cement Concrete Road Slab in Seasonal Frozen Region

Qianqian Zhao[1], Peifeng Cheng[2*], and Wenmei Zhao[3]

[1] Northeast Forestry University; Heilongjiang Institute of Technology, Harbin, China; email: 492954791@qq.com
[2] Civil Engineering College, Northeast Forestry University, Harbin, China; email: chengpeifeng@126.com
[3] Heilongjiang Provincial Highway Survey and Design Institute, Harbin, China; email: 1054127663@qq.com

[*]: corresponding author

Keywords: seasonal frozen region; cavity beneath slab; deflection difference; transfer capacity; void region

Abstract: In order to accurately and effectively discriminate the slab bottom of cement concrete pavement in the seasonal frozen region, the recommended range of deflection judgment of cement concrete pavement in the seasonal frozen region is established. Through a similar proportion of static experiments in the typical pavement structure of the seasonal frozen region, the cement concrete pavement slab under actual working conditions is simulated to investigate the effect of load size and void region on the deflection of cement concrete slab under the same load carrying capacity. When determining the load acting on the side of the lateral hollowing plate, the side of the longitudinal hollowing plate and the corner of the plate, the difference between the plate angle under different load carrying capacity and the midpoint of the plate and the edge of the plate. The results show that the deflection value of cement concrete slab will increase with the increase of the void region at the bottom of the slab, and the increasing trend will show the shape of anti-S. When the load is applied above the vacant region, the longitudinal direction of the cement concrete slab will take off. Empty, the midpoint of the longitudinal plate edge is at the end of the cantilever beam, and the variation range is large, and the strain rate is also large. When the cement concrete slab is laterally emptied and the vacant region is small, the symmetry axis is from the load application point to the vacant side. There is obvious upward warping deformation, and the plate body voiding region is all under pressure; when the cement concrete slab angle is emptied and the load is applied above the slab corner vacant region, the intersection of the vacant boundary and the diagonal line, the rate of displacement drop is relatively fast, and the displacement of the triangular boundary is larger than the displacement of the boundary point of the horizontal edge. The recommended range of deflection judgment for the evaluation index of the bottom of cement concrete slabs in the seasonal frozen region is theoretically supported for the establishment of the method for determining the bottom void of cement concrete road slabs.

1. Introduction

Hollow bottom of cement concrete pavement is one of the most common diseases of cement concrete slabs (Hao X et al. 2017; Li J et al. 2017; Shao-Yong et al. 2017; Grandin R et al. 2017; Papamarkou Set al. 2018), which seriously affects the service life of cement concrete pavement. When the void occurs, the stress on the corner and edge of the cement concrete pavement is extremely unfavorable. Under the repeated action of the driving load, the stress state of the cement concrete slab is similar to that of the cantilever beam due to the excessive stress of the slab, strain and deflection, have a serious impact on the performance of cement concrete road panels, and even lead to road damage. In order to prolong the service life of cement concrete pavement (Hao X et al. 2017; Kang T K et al.2018), it is particularly important to accurately evaluate the voiding of cement concrete slab bottom. In the "Code for Design of Highway Cement Concrete Pavement", only the method for testing the void of cement concrete slab is given. The criterion and criterion for the determination of void are not given in the specification (Xu J H et al. 2016; Zhang Y et al.2016). The standard for judging the void of concrete slabs in the "Technical Specifications for Maintenance of Highway Cement Concrete Pavements" is that the deflection value exceeds 0.2 mm. However, due to factors such as load, climate and pavement structure, the deflection value will be affected. The actual situation of the road surface in each area is quite different (Janus M et al.2015). It is necessary to adjust the 0.2mm recommended in the specification.

Zhang Zhanjun (Zhang Zhanjun et al. 2000) based on the approximate beam method calculated by elastic substrate, proposed the ratio of the deflection value in the plate and the deflection value of the plate edge as an index to judge whether the bottom of the plate is empty or not. Ying Ronghua (Ying Ronghua et al. 2008) used the measured deflection curve and the road surface deflection basin to evaluate the basic stiffness parameters under the concrete slab when determining the condition of the plate body. The disadvantage of the above method is that the calculation is cumbersome, the use process is more complicated, and the practicability is poor. At present, the determination of the bottom of the plate in the seasonal frozen region has not yet formed a completely effective method. In the past, the evaluation of the void state is based on a single deflection value, and the single deflection value is easily affected by the variation. Many factors will affect the single deflection value, such as the pavement structure, the test season, the adjacent plate void，transfer capacity and so on. A single indicator cannot distinguish the effect of the void condition and the joint condition on the deflection, and the influence of the above factors can be eliminated when the difference in deflection is used.

2. Experimental overview

2.1. Test piece production

According to the similar principle (Li C et al. 2015), the concrete slab is reduced year by year. The model size of the cement concrete selected by the test is length × width × thickness is 50 × 40 × 2.5cm^3, and the base layer is cement stabilized gravel with a thickness of 2cm. The layer is graded with a gravel thickness of 1.5 cm, and the surface layer and the base layer and the anti-freezing mat layer and the base layer are bonded by cement mortar. Due to the same void area and load transfer capacity, the depth of the void has little effect on the deflection of the edge and corner of the cement concrete slab in the seasonal frozen region. For the convenience of analysis, the depth of the void is selected to be 5 mm, and the ratio is reduced according to the similarity

principle. The post-depletion depth is 0.5 mm. Similarly, the load ratio is reduced to 5kN, but to further analyze the deformation of the concrete slab under different loads, the load is loaded from 0.5kN to 1kN, 1.5kN, 2kN, 2.5kN, 3kN, 3.5kN, 4kN, 4.5kN and 5kN, a 2.6 x 2.6 cm^2 hammer is used to make a load application. In addition, combined with Gao Shunping (Gao Shunping, 2014) proposed), the moderate and heavy grades of the bottom of the slab are divided into corresponding concrete slabs, that is, when the concrete slab edge is 80×80cm^2, the concrete slab angle is 1/2×40×40cm^2, the concrete slab is slightly emptied; when the vacant area of the concrete slab is more than 120×150cm^2, the void area of the concrete slab angle exceeds 1/2×150×150 cm^2, the concrete slab is severely emptied, when the vacant area is between the two, a moderate vacancy occurs. Therefore, in the production of the test piece, the artificially produced paper shell is used to simulate the method of voiding the bottom of the concrete slab. In table 1, the cement concrete test pieces of different void areas are numbered, and three sets of test pieces are made for each number for comparison.

Table 1. Test cement concrete plate number

Void position	Void position /cm²	Cement concrete test piece number
No void	0	1-1
Corner clearance	1/2×40×40	2-1
	1/2×150×150	2-2
Lateral void	80×80	3-1
	120×150	3-2
Longitudinal void	80×80	4-1
	120×150	4-2

2.2. Transfer capacity determination

According to the determination of the evaluation level of the load-bearing capacity in the specification, in the production of the cement concrete slab, the test pieces with the joint transfer capacity of 0%, 30%, 55%, 75% and 90% are respectively prepared. The longitudinal and transverse joints shall be perpendicular to the longitudinal joints. The spacing between the vertical joints shall be determined within the range of the road width. The spacing of the transverse joints shall be selected according to the type and thickness of the surface layer. The ordinary cement concrete surface layer is generally cement or lime fly ash stabilized grain. The base layer is taken.

3. Arrangement of strain gauges and displacement gauges

In the test, the symmetry center of the test piece was selected as the position where the load was applied, and the strain gauge and the displacement gauge were symmetrically arranged. The bottom of the bottom is divided according to the center line, and only the strain and deflection of the symmetrical side are studied. The longitudinal hollow displacement gauge is arranged as shown in Fig. 1(a), the lateral hollow displacement gauge is arranged as shown in Fig. 1(b), and the slab angular displacement displacement gauge is arranged as shown in Fig. 1(c). For this test, the strain gauges and the displacement gauges are densely arranged on the demarcation boundary line, and the layout of the strain gauges and the displacement gauges is scaled according to the

ratio in the figure. The strain gauges for longitudinal voiding, lateral voiding, and corner voiding are laid out in the same manner as in the layout of the displacement gauge.

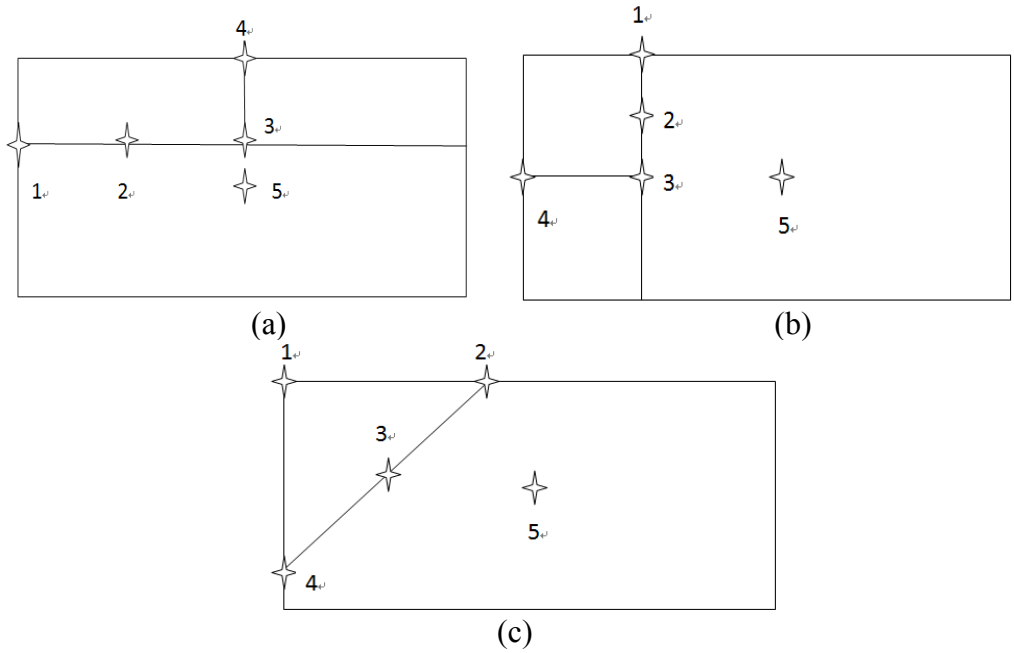

Fig. 1. Displacement meter arrangement: (a) Longitudinally disengaged displacement meter; (b) Lateral clearance displacement meter; (c) Corner angle disengagement meter layout

4. Test results analysis

Taking the longitudinal emptying area 80×80cm^2 as an example, the three sets of emptying parts corresponding to the emptying area are numbered 4-1-1, 4-1-2 and 4-1-3 respectively. In different statics, the deflection value is averaged under the action of the load, and the unreasonable data is eliminated. The remaining data processing methods of the test piece are consistent with the former. The load is applied above the longitudinal emptying area. The displacement-load curves of the concrete slabs corresponding to No. 4-1 and No. 4-2 under longitudinal clearance are shown in Figure 2:

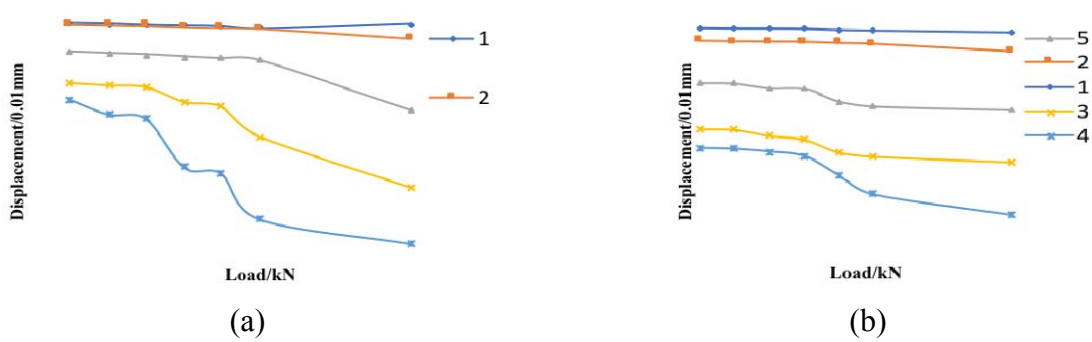

Fig. 2. Displacement-load curve of each point under longitudinal emptying conditions: (a) Displacement-load curve of each point of No. 4-1 plate; (b) Displacement-load curve of each point of No. 4-2 plate

According to the analysis of the longitudinal hollow deflection: as can be seen from Figure 2, the slope of the displacement line of the 4 point > the slope of the displacement line of the 3 point > the slope of the displacement line of the 5 point > the slope of the displacement line of the 2 point > The slope of the 1 point displacement line. The displacement of the 1 point and the 2 point are not obvious, but at this time, the strain at the fourth point and the third point is sharply increased. The 4 points are located at the end of the cantilever beam, and the variation range is large, and the strain rate changes greatly. At this time, the cement concrete slab is brittle fracture state. When the emptying area is 80×80cm^2, when the applied load is gradually loaded from 0.5MPa to 5MPa, the displacement difference between the fourth point with the largest displacement in the plate and the first point with the smallest displacement of the plate edge is 0.08~0.22mm.. When the plate side voiding area is 120×150 cm^2, when the applied load is gradually loaded from 0.5 MPa to 5 MPa, the displacement difference between the fourth point with the largest displacement and the first point with the smallest displacement exceeds 0.40 mm.

The load is applied above the lateral clearance area. The displacement-load curves of the concrete slabs corresponding to No. 3-1 and No. 3-2 under lateral clearance conditions are shown in Figure 3:

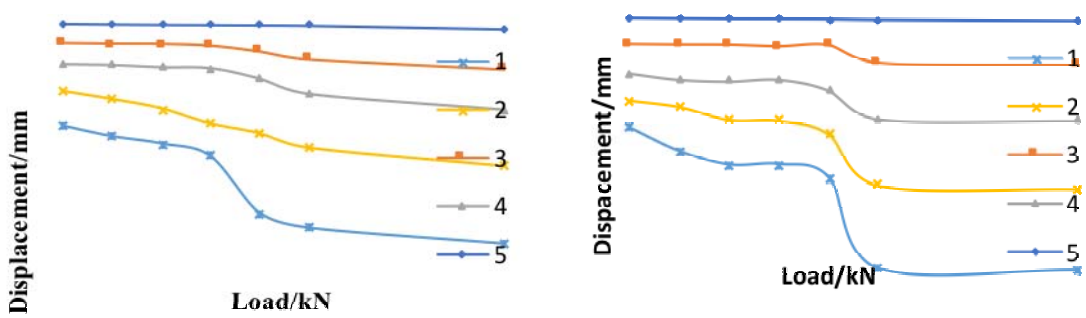

(a) (b)

Fig. 3. Displacement-load curve at each point under lateral clearance: (a) Displacement-load curve of each point of 3-1 plate; (b) Displacement-load curve of each point of 3-2 plate

As can be seen from Figs. 3, the slope of the 4 point displacement straight line > the slope of the 3 point displacement straight line > the slope of the 2 point displacement straight line > the slope of the 1 point displacement straight line > the slope of the 5 point displacement straight line. The load-displacement curves at points 4, 3, and 2 are linearly decreasing. The load-displacement curves at points 1 and 5 do not change much, and a small amount of warpage is not observed until the late stage of loading. The 4 points are located at the end of the cantilever with the largest displacement. When the vacant area is small, there is obvious upward warping deformation along the symmetry axis from the load application point to the vacant side. The strain change obtained by the strain analysis shows that the slab void area is all under pressure, due to the plate body. The non-empty area and the road surface are not constrained, so it is reasonable to have warpage of the plate itself.

In Fig. 3(a), when the area of the void area is 120 × 150 cm^2, if the load is continuously applied, micro-cracks appear on the lower surface of the cement concrete slab body, and then it is similar to the two concrete slabs which are formed from the periphery to the middle direction. The fracture causes a state in which the middle position of the symmetry axis of the concrete slab is low and the positions on both sides are high. When the emptying area is 80×80cm^2, the applied load is gradually loaded from 0.5MPa to 5MPa, the displacement difference between the 4 point with the largest displacement in the plate and the 5point with the smallest displacement of the plate edge is 0.1~0.23mm. When the plate side voiding area is 120×150 cm^2, the applied load is gradually loaded from 0.5 MPa to 5 MPa, the displacement difference between the 4 point with the largest displacement and the 5 point with the smallest displacement exceeds 0.45 mm. The displacement-load curves of the points of the concrete slabs corresponding to No. 2-1 and No. 2-2 under the angle of the plate corner are shown in Figure 4:

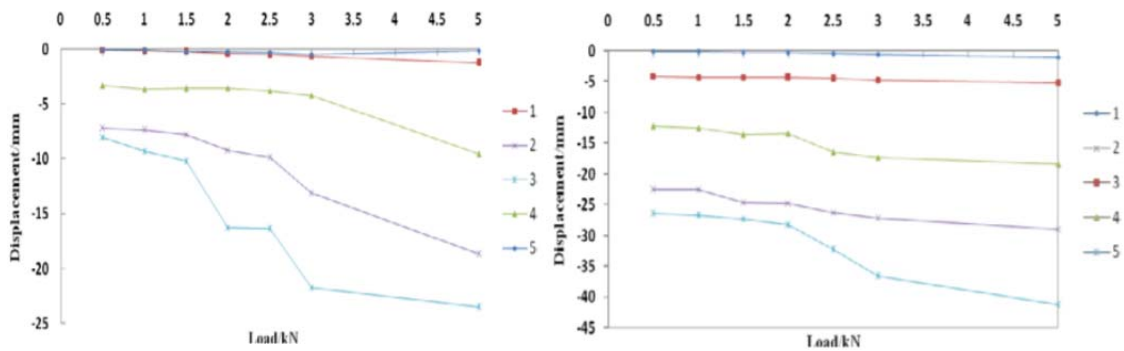

(a) (b)

Fig. 4. Displacement-load curve of each point under the condition of plate angle: (a) Displacement-load curve of each point of 2-1 plate; (b) Displacement-load curve of each point of 2-2 plate

According to the results of the plate angle vacancy displacement, it can be seen from Fig. 4(a) that when the vacant area is 1/2×40×40 cm^2, the area of the vacant area is small, so under the action of the load, the vacant area settling occurs at the 3 points, the rate of change of the 1 point of displacement > the rate of change of the displacement of the 3 point > the rate of change of the displacement of the 4 point > the rate of change of the displacement of the 2 point > the rate of change of the displacement of the 5 point, which indicates the void boundary The displacement at the intersection with the diagonal is faster, and the displacement of the triangle is such that the displacement of the longitudinal boundary is larger than the displacement of the lateral boundary.

The data shows that the longitudinal side bears a relatively large load relative to the transverse side of the concrete slab and is more prone to fracture. When the plate corner emptying area is 1/2×40×40 cm^2, when the applied load is loaded from 0.5 MPa to 5MPa, the displacement difference between the 5 point and the 1 point is 0.18 to 0.32 mm. When the plate corner emptying area is 1/2×150×150 cm^2 , when the applied load is gradually loaded from 0.5 MPa to 5 MPa, the displacement difference between the first point and the fifth point exceeds 0.51 mm.

5. Analysis of the impact of the void area

In order to further verify the influence of the void area on the deflection, the variation of the deflection under different void areas is analyzed. The curve of the deflection under the different void areas of the edge and the plate angle is shown in Fig. 5. No gap occurs when the edge of the plate has the minimum deflection value of 0.1 mm, when the siding area of the slab is developed to 1.2×1.5m^2, the cement concrete slab has the largest deflection value of 0.45 mm. As the void area increases gradually, the deflection value increases gradually, but the two are not linear. As the void area increases, the growth trend of the deflection value shows an anti-S type. Similarly, when the slab angle does not occur, the deflection value of the cement concrete slab is the smallest, which is 0.18 mm. When the siding area of the slab is developed to 1/2×1.5×1.5 m^2, the maximum deflection value of the cement concrete slab is 0.51mm. As the void area increases gradually, the deflection value increases gradually, but the two are not linear. As the void area increases, the growth trend of the deflection value shows an anti-S type.

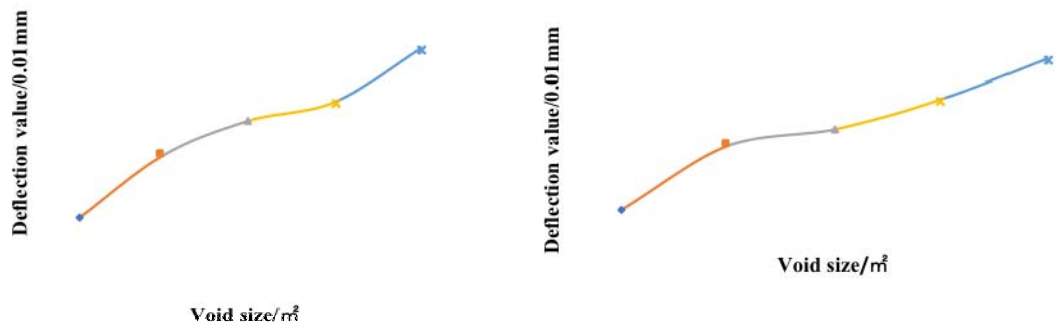

(a) (b)

Fig. 5. Relationship between the size of the void and the deflection (a) Relationship between the area of the edge of the plate and the deflection; (b) The relationship between the area of the plate and the deflection

6. Detachment discriminating recommended range

Based on the above research, the degree of voiding is divided into four grades, and corresponding the difference between the midpoint of the board and the plate, plate angle and plate bending difference are established according to different transfer capacity levels, and the recommended range of deflection judgment for the bottom void of cement concrete slab in the seasonal frozen region is formed. Therefore, the degree of voiding of the cement concrete slab in the seasonal frozen region can be determined by the difference between the edge of the plate and the plate and the difference between the plate angle and the plate, as shown in Table 2.

7. Conclusion

(1) The deflection value of cement concrete pavement will increase with the increase of the bottom void area, and the increasing trend will show the shape of anti-S.

(2) When the longitudinal direction of the cement concrete slab is emptied and the load is applied above the longitudinal vacant area, the midpoint of the longitudinal slab is at the end of the cantilever beam, and the variation range is large, and the strain rate is also large.

Table 2. Deflection for seasonal frozen area recommended range (0.01mm)

Transfer capacity		bad	poor	general	excellent
Difference between the edge of the board and the plate /0.01mm	excellent	< 10	< 8.5	< 8	< 7.5
	general	10 ~ 23	8.5 ~ 23.5	8 ~ 23	7.5 ~ 22.5
	poor	23 ~ 45	23.5 ~ 43.5	23 ~ 43	22.5 ~ 42.5
	bad	≥45	≥43.5	≥43	≥42.5
Plate angle and plate bending difference /0.01mm	excellent	< 18	< 16	< 15	< 14
	general	18 ~ 32	16 ~ 35	15 ~ 34	14 ~ 33
	poor	32 ~ 51	35 ~ 49	34 ~ 48	33 ~ 47
	bad	≥51	≥49	≥48	≥47

The displacement value of the midpoint of the longitudinal plate edge> the displacement value in the plate> the longitudinal displacement value of the boundary point.

(3) When the cement concrete slab is laterally emptied and the load is applied above the lateral vacant area, the eccentricity is small when there is a significant upward warping deformation along the symmetry axis from the load application point to the vacant side. The empty areas are all under pressure.

(4) When the angle of the cement concrete slab is hollowed out and the load is applied above the slab corner, the displacement rate of the intersection of the vacant boundary and the diagonal is faster, and the triangle is emptied to make the longitudinal vacancy boundary point The displacement is greater than the displacement of the lateral edge of the lateral edge.

(5) Through the indoor test, simulate the bottom of the typical cement concrete pavement structure in the seasonal frozen area, and analyze the deflection in the corners, slabs and plates under different vacant depths, different vacant areas and different transfer capacities. The change and the use of laboratory test verification, the recommended range of deflection judgment of cement concrete slab bottom void evaluation index in the seasonal frozen region is obtained, which provides theoretical support for the establishment of pavement condition assessment model.

8 References:

[1] Hao X, Dong J, Wei J, et al. Effect of Cu on corrosion behavior of low alloy steel under the simulated bottom plate environment of cargo oil tank. Corrosion Science, 2017, 121(2):84-93.

[2] Li J, Li Y, Sun H, et al. Cathodic Protection for External Side of Bottom Plate of Storage Tank. Journal of Petrochemical Universities, 2017, 30(1):87-91.

[3] Shao-Yong Huo, Jiu-Jiu Chen, Guang-Huang Song, et al. Asymmetric propagation of the first order antisymmetric lamb wave in a tapered plate based on time domain analysis. Acoustical Physics, 2017, 63(4):393-401.

[4] Grandin R, Doin M P, Bollinger L, et al. Long-term growth of the Himalaya inferred from interseismic InSAR measurement. Geology, 2017, 40(12):1059-1062.

[5] Papamarkou S, Christopoulos D, Tsakiridis P E, et al. Vitrified medical wastes bottom ash in cement clinkerization. Microstructural, hydration and leaching characteristics.. Science of the Total Environment, 2018, 635(4):705-715.
[6] Ahari M N , Eshghi S , Ashtiany M G . The tapered beam model for bottom plate uplift analysis of unanchored cylindrical steel storage tanks[J]. Engineering Structures, 2009, 31(3):623-632.
[7] Kang T K, Chen Y H, Chien F T, et al. Reduction of Kink Effect of Poly-Si TFT With Bottom Field Plate by Dispersing Current Density Technique. IEEE Transactions on Electron Devices, 2016, 63(7):2975-2979.
[8] Xu J H, Yi B W, Fan Y. A bottom-up optimization model for long-term CO 2 emissions reduction pathway in the cement industry: A case study of China. International Journal of Greenhouse Gas Control, 2016, 44(3):199-216.
[9] Zhang Y, Bonizzoni E, Maloberti F. Energy-efficient switching method for SAR ADCs with bottom plate sampling. Electronics Letters, 2016, 52(9):690-692.
[10] Janus M, Zatorska J, Czyżewski A, et al. Self-cleaning properties of cement plates loaded with N,C-modified TiO2 photocatalysts. Applied Surface Science, 2015, 330(14):200-206.
[11] Zhang Zhanjun, Cao Dongwei, Hu Changshun. Research on Thickness of Asphalt Pavement on Cement Concrete Bridge Deck. Journal of Chang'an University(Natural Science), 2000, 20(2): 16-19.
[12] LIU Han-qing, HUANG Wei, YANG Yue, YING Rong-hua.Application of PFWD to detect the rebound modulus of new and old subgrade pavement[J].Highway,2008(1):200-203.
[13]Li C, Tsai K, Lee H. Seismic design and testing of the bottom vertical boundary elements in steel plate shear walls. Part 2:experimental studies. Earthquake Engineering Structural Dynamics,2015,43(14);2155-2177.
[14]Gao Shunping. Analysis of the working condition of the bottom of cement concrete pavement and the technology of void evaluation[D]. Kunming University of Science and Technology, 2014.

Design and Installation of Cement Based Composite Technologies in the Strengthening of Missouri Bridge P0058

Michael Janke[1], Eli S. Hernandez[2], John J. Myers[3*], and Antonio Nanni[4]

[1] KPPF; St. Louis, MO, USA; email: mjanke@kppf.com
[2] Missouri S&T; Rolla, MO, USA; email: ehd36@mst.edu
[3] Missouri S&T, Rolla, MO, USA; email: jmyers@mst.edu
[4] University of Miami, Miami, FL, USA; email: nanni@miami.edu

[*] : corresponding author

Keywords: bridge strengthening; cementitious-repair techniques; composite design; FRCM; SRG

Abstract: With the nation's infrastructure continuing to age, technologies are being developed to strengthen structures as a more sustainable option than replacing them. The use of fiber-reinforced cementitious matrix (FRCM) composite strengthening systems is a promising new technology for adding flexural and shear capacity to existing reinforced concrete members. While cement based systems with carbon, polyparaphenylene benzobisoxazole (PBO), and steel have all been successfully implemented in a lab setting, there is not research data available for installation in the field. FRCM composites have advantages over the more widely used fiber reinforced polymer (FRP) composites such as heat resistance and compatibility with concrete substrate. FRP systems have previously been field tested, giving confidence for the growth of FRCM use. This study aimed to validate the use of cement-based systems for field implementation. Missouri Bridge P-0058, a structurally deficient bridge in southern Missouri, was recently selected and six of its twelve girders were strengthened using four different composite systems, three of which are cement-based. A parametric study was conducted to help choose the final design. This project showed that cement based composite strengthening systems are a viable technology for future field applications.

1. Introduction

Replacing thousands of bridges is both time consuming and expensive. Consequently, repairing bridges has emerged as a more sustainable option. Strengthening or retrofitting concrete structures can add capacity and increase the service life by several decades. Traditional flexural strengthening techniques include externally bonded steel plates, steel or concrete jackets, external post-tensioning, and other methods. Shear strengthening methods include external stirrups and epoxy bonded steel plates. These methods leave materials exposed to the environment, making them vulnerable to corrosion.

Since the 1980s, composite materials have become an alternative for strengthening concrete structures in the United States, Japan, Canada, and Europe. While many research projects have been conducted in university labs, more full-scale and in situ studies are needed, since

departments of transportation (DOTs) are still hesitant to implement these innovative materials. Composite materials consist of fibers that are incased in some sort of matrix. Common fiber types include carbon, glass, aramid, and PBO. When a polymeric resin is used, the material is classified as a fiber-reinforced polymer. When a cementitious material is used, the material is classified as a fiber-reinforced cementitious matrix. Both classes of composites have advantages over traditional materials such as corrosion resistance and high tensile strength. This study was conducted to validate the applicability of several composite systems for strengthening bridge girders in the field. The main objective was to demonstrate bridge girder strengthening using the FRCM and SRG technology, which to date have no reported field bridge applications in available literature.

2. Bridge Configuration

Bridge P0058, constructed in 1951, is located on Highway 142 and spans the Myatt Creek in Howell County, Missouri. This bridge consists of four simply supported reinforced concrete (RC) spans. The west spans (1 and 2) are 37.5 ft (11.43 m) long, and east spans (3 and 4) are 27.5 ft. (8.38 m) representing a total bridge length of 130.0 ft. (39.62 m). The slab thickness is 6 in. (150 mm), and three rectangular RC beams spaced 7.1 ft. (2.16 m) on center support it. In Missouri, condition assessment of bridges is conducted periodically for their deck, superstructure (sup), and substructure (sub). Bridge P0058 was selected from a list of candidate bridges considered structurally deficient according to MoDOT inspection data. In the most recent condition assessment, Bridge P0058 received a deck/sup/sub rating of 4/4/6 (where 4 means poor, and 6 means satisfactory). Due to the age and condition, Bridge P0058 is currently load posted. The total deck width is 17.2 ft. (5.23 m) with a curb-to-curb roadway of 14.0 ft (4.27 m). Fig. 1 shows the bridge's approach, and a profile view.

(a) (b)

Fig. 1. Bridge P0058. (a) Approach; (b) profile view

3. Strengthening Systems

Four different strengthening systems were recommended to improve Bridge P0058's carrying capacity. Material properties were obtained from the manufacturers or through tests performed in the lab. The following sections present detailed information about these systems.

3.1 Fiber-Reinforced Polymer

A carbon fiber reinforced polymer (CFRP) manufactured by Structural Technologies was chosen to be used on this strengthening project. The product consists of a high modulus carbon fiber (VWrap^{TM} C200HM) and an epoxy-based resin (VWrap^{TM} 770 Epoxy Adhesive). As stated in

ACI 440.2R-08, to account for long-term exposure to the environment, the material strength must be reduced based on the environmental exposure of the application.

3.2 Fabric-Reinforced Cementitious Matrix

Three different systems with cementitious matrix were proposed in this study. The fiber types used were carbon FRCM (CFRCM), PBO FRCM, and SRG (steel cords). When designing with FRCM, the properties should come from an idealized bilinear stress strain curve, and the contribution of FRCM before cracking is neglected. The idealized curve should come from statistic data from a series of coupon tests. The carbon FRCM system used is a Unidirectional Carbon Grid (CSS-UCG) produced by Simpson Strong-Tie. The PBO FRCM system consists of fibers and inorganic matrix manufactured by Ruredil. The SRG system employs a GeoSteel G600R mesh with either a cementitious matrix produced by Kerakoll S.p.A.

4. Design of Strengthening System

The design and analysis of the strengthening systems were performed according to ACI 318-14 (ACI 2014), ACI 4402R-08 (ACI 2008), and ACI 549-13 (ACI 2013).

4.1 Flexure Design

The FRCM design procedure, presented in ACI 549, is analogous to the FRP design procedure followed in ACI 440. The ultimate moment capacity is estimated based on the internal strain and stress distribution under flexure at the ultimate limit state. A trial-and-error method is used for obtaining the ultimate strength that satisfies strain compatibility and force equilibrium. Fig. 2 illustrates the steps followed in the design procedure. The nominal moment capacity, M_n, is estimated as follows:

$$M_n = f_s A_s (d - \frac{a}{2}) + A_f f_{fe} (d_f - \frac{a}{2}) \tag{1}$$

where f_s = stress in steel reinforcement; A_s = Area of longitudinal steel; d = distance from extreme compression fiber to centroid of steel reinforcement; a = depth of equivalent stress block; f_{fe} = stress in FRP/FRCM reinforcement; A_f = Area of FRP/FRCM reinforcement; and d_f = distance from extreme compression fiber to centroid of FRP/FRCM reinforcement. ACI 549.4R limits the amount of enhancement provided by the strengthening system to fifty percent (50%) of the existing flexural capacity.

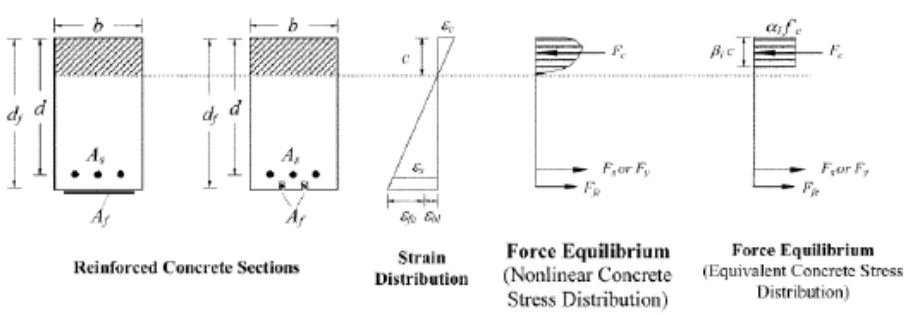

Fig. 2. Internal stress and strain distribution in flexure. Source: ACI Committee 440 (ACI 2008)

4.2 Shear Design

The total shear strength of an FRP/FRCM-strengthened concrete member with existing steel shear reinforcement is computed by adding the contribution of the FRP/FRCM strengthening system as follows:

$$V_n = V_c + V_s + V_f \tag{2}$$

where V_n = nominal shear strength; V_c = nominal shear strength provided by concrete; V_s = nominal shear strength provided by existing steel; and V_f = nominal shear strength provided by FRP/FRCM system. A reduction factor, ϕ_v, of .75 is applied to the nominal shear strength, V_n. For FRP systems, a shear strength reduction factor, ψ_v, is applied to account for the configuration of the u-wrapped system. The FRCM contribution to nominal shear is estimated as follows:

$$V_f = nA_f f_{fv} d_f \tag{3}$$

where n = number of layers of mesh reinforcement; A_f = area of mesh reinforcement by unit width effective in shear; f_{fv} = design tensile strength of the FRCM shear reinforcement; and d_f = effective depth of the FRCM shear reinforcement.

5. Summary of Strengthening Design

A parametric study was performed considering the strengthening system, span length, and numbers of plies. Table 1 lists a summary of the strengthening systems employed and the ratio the moment capacity was enhanced for each main carrying member.

Table 1. Summary of Strengthening System Design

Girder	Span 1 (long span)	Span 4 (short span)
1	CFRP Flexure: two plies (17.7% cap. increase) Shear: one ply (17-in. spacing)	SRG Flexure: two plies (3.9% cap. increase) Shear: two plies (18-in. spacing)
2	Carbon FRCM Flexure: two plies (6.3% enhancement) Shear: one ply (12-in. spacing)	SRG Flexure: two plies (3.9% enhancement) Shear: two plies (18-in. spacing)
3	Carbon FRCM Flexure: two plies (6.3% enhancement) Shear: one ply (12 in. spacing)	PBO FRCM Flexure: two plies (7.1% enhancement) Shear: two plies (18 in. spacing)

Note: for Spans 2 and 4, no strengthening system was used. All strips used for strengthening are 12-inch wide.

6. Concluding Remarks

The objective of this study was to validate cementitious composite systems for strengthening of RC members in the field. This project is the first documented field implementation of cement based strengthening systems. A parametric study was conducted to compare the theoretical performance of the different strengthening systems. This project demonstrated that cement based composite strengthening systems are a viable technology for field infrastructure applications.

7. References

American Concrete Institute (2008). "Guide for the Design and Construction of Externally Bonded FRP Systems for Strengthening Concrete Structures ." ACI 440.2R-08, Farmington Hills, MI.

American Concrete Institute (2013). "Guide to Design and Construction of Externally Bonded Fabric- Reinforced Cementitious Matrix (FRCM) Systems for Repair and Strengthening Concrete and Masonry Structures ." ACI 549.4R-13, Farmington Hills, MI.

American Concrete Institute (2014). "Building Code Requirements for Structural Concrete and Commentary." ACI 318-14, Farmington Hills, MI.

A New Temperature Model for Steel Box Girders in High Speed Railway Bridges

Gonglian Dai[1], Xinyang Chang[2*], Yimin Wen[3], and Tong Qiu[4]

[1] Department of Civil Engineering, Central South University, Changsha, Hunan, China; email: daigonglian@csu.edu.cn;
[2] Department of Civil Engineering, Central South University, Changsha, Hunan, China; email: changecho@csu.edu.cn
[3] Department of Civil Engineering, Central South University, Changsha, Hunan, China; email: wenyimin@csu.edu.cn;
[4] Department of Civil Engineering, The Pennsylvania State University, University Park, PA, USA; email: tqiu@engr.psu.edu.

[*] : Corresponding author

Keywords: high speed railway; steel box girders; temperature model

Abstract: With the increasing need of long-span bridges in high-speed railways, steel box girders with over 300-m span have been widely applied in China. Under the thermal loading including solar radiation, ambient temperature, and ground long-wave radiation, the temperature distribution of steel box girders differs widely from that of concrete girders due to the superior thermal conductivity of steel. In order to develop a better temperature model for steel box girders, a numerical model for the heat conduction of steel box girders is first established. By adopting the field-measured ambient temperature and solar radiation as thermal boundary conditions, the temperature field of steel box girder is determined independently. Temperature sensors are also installed on site to monitor the temperatures of the steel box girder in real time. It is found that the numerical results are in good agreement with the field measured data and a novel temperature model considering both uniform temperature change and temperature gradient variation of the steel box girder in high-speed railway is proposed.

1. Introduction

The study of thermal effect on bridge mainly includes two components: thermal loads on structures and structural thermal response. Since the 1960s, lots of efforts have been devoted to the study of thermal effects on bridges. Zuk (1965) was recognized as the first scholar to study thermal behavior of bridges; he concluded that the temperature distribution along a bridge depended mainly on air temperature, wind, solar radiation and bridge materials. Emerson (1973) developed a finite difference model and calculated the vertical temperature distribution in concrete deck, composite deck and steel deck. Tong et al. (2001) developed a numerical model for the analysis of temperature distribution in steel bridges. Xu et al. (2010) relied on the wind and structural health monitoring system (WASHMS) of Tsing Ma Bridge, studied the covariance between air temperature and structural uniform temperature. Ding et al. (2012) studied the temperature distribution characteristics and statistical features in the steel box girder of Runyang Suspension Bridge. Zhou et al. (2016) developed a two-dimensional heat transfer finite element model of a typical steel box section of Humber Bridge; the time-dependent temperature distribution was calculated and the vertical and transversal temperature differences

were investigated. As described above, most studies in this field were mainly focused on small and medium-span concrete and composite highway bridges. In the past two decades, with the increasing application of steel bridges in civil engineering, scholars began to conduct research on the thermal behavior of large-span steel bridges; however, similar studies on railway bridges are lacking.

2. Field Monitoring Details

In the field monitoring, 43 temperature sensors were installed in the steel box girder of Yuxi River Bridge. The temperature sensors were divided into 4 groups according to their locations: the top plate (TP), the east web plate (EW), the west web plate (WW), and the side web plate (SW), which consisted of 7, 12, 12, and 12 temperature sensors, respectively, as shown in Fig 1.

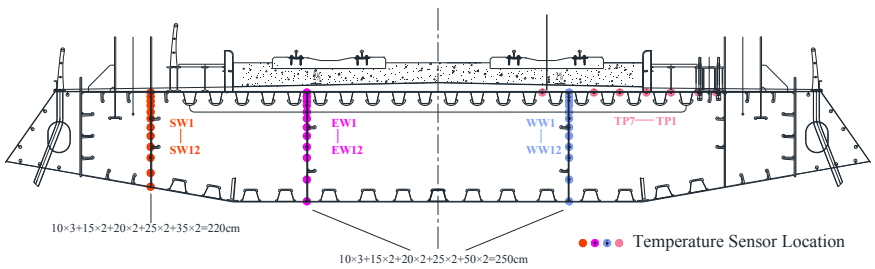

Fig. 1. Steel girder cross section and temperature sensor location

A small weather station provided by Jinzhou Sunshine Technology Co.Ltd was placed near the bridge site to monitor meteorological parameters including air temperature, solar radiation and wind speed at the bridge in real time.

3. Uniform Temperature and Temperature Gradient

The variation of uniform temperature and temperature gradient difference within the cross section both produce thermal load effects in the superstructure (BS EN 1991-1-5 2003). The uniform temperature and temperature gradient can be derived based on the equivalent deformation principle. If we know the exact vertical temperature distribution in a bridge deck $T(y)$, the uniform temperature T_u and temperature gradient T_g can be calculated as

$$T_u = \frac{1}{A}\int_h T(y)dA \tag{1}$$

$$T_g = \frac{h}{I}\int_h T(y)\cdot(y - y_c)dA \tag{2}$$

where A is the cross-sectional area, I is moment of inertia of cross section, yc is the coordinate of neutral axis in vertical direction, and h is the height of deck.

Since we get discrete temperature sensors deployed within the girder cross section, the cross section can be divided into several layers vertically with each layer having a temperature sensor in it. We can calculate uniform temperature T_u and temperature gradient T_g as

$$T_u = \frac{1}{A}\int_h T(y)dA = \frac{1}{A}\sum_{i=1}^{n} T_i A_i \tag{3}$$

$$T_g = \frac{h}{I}\int_h T(y)\cdot(y - y_c)dA = \frac{h}{I}\sum_{i=1}^{n} T_i A_i (y_i - y_c) \tag{4}$$

where A_i is the area of ith layer, T_i is measured temperature in the ith layer, y_i is coordinate of the center of ith layer, and n is the number of layer divided within the cross section.

The uniform temperature of bridge deck keeps changing, which shall be determined by the temperature distribution within the cross section in real time. The uniform temperature at every 30-minute internal from 2018/06/02 to 2019/01/20 is calculated and shown in Fig. 2.

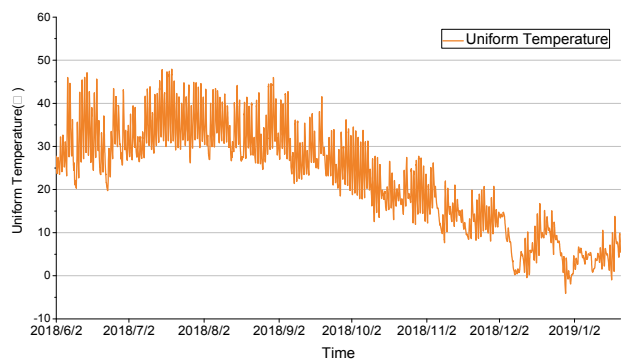

Fig. 2. Uniform temperature variation from 2018/06/02 to 2019/01/20

The uniform temperature of bridge deck varies both daily and seasonally. In a day, the uniform temperature is not constant and may change significantly, which mainly depends on the weather condition. In a year, the uniform temperature in summer is higher than that in winter, which reaches a peak of 47.9^{o}C in July and a low of -4.1^{o}C in December.

The equivalent temperature gradient varies linearly from top plate to bottom plate, which can produce the same bending deformation compared with the actual temperature load. The equivalent temperature gradient at every 30-minute internal from 2018/06/02 to 2019/01/20 is calculated and shown in Fig. 3.

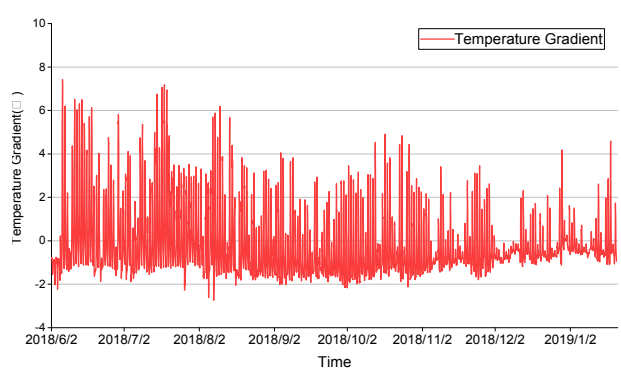

Fig. 3.Temperature gradient variation from 2018/06/02 to 2019/01/20

The positive temperature gradient values are generally larger than the negative temperature gradient values, in which the maximum positive temperature gradient reaches 7.3°C at daytime in summer and the minimum negative temperature gradient reaches -2.6 °C at nighttime in summer.

4. Numerical Analysis

A typical sunny day of 2018/07/18 was selected and the measured meteorological parameters were applied as boundary conditions in the developed FE model. The simulated results of the temperature variation at EW1, EW9, and EW12 are compared with the corresponding measurements in Fig. 4.

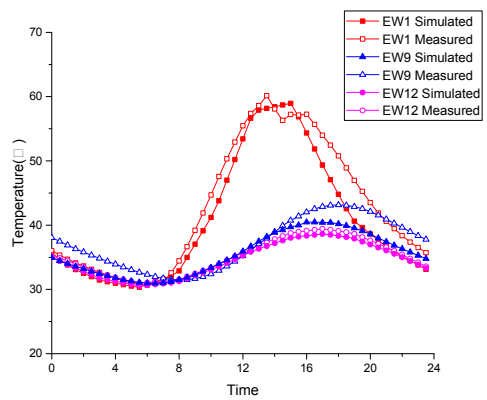

Fig. 4. Comparison between measured and simulated temperature variation

The maximum temperature of the top plate (EW1) was much higher than that of the bottom plate (EW12), and different locations reached their maximum temperature at different time. Fig.4 shows a good agreement between the simulated and measured temperature variation.

5. Conclusions and Future Work

This paper investigates the temperature distribution characteristics in a steel box girder of high-speed railway, which is in the construction stage with no ballast on the upper surface. The conclusions are drawn as follows:

1. Uniform temperature and temperature gradient of the bridge girder keep changing and may differ significantly in a day.
2. The uniform temperature in summer is much higher than that in winter, which reaches a maximum value of 47.9 °C in July and a minimum value of -4.1 °C in December.
3. The positive temperature gradient is much larger than the negative temperature gradient and the positive temperature gradient in winter is lower than that in summer.
4. The FE model which considers meteorological parameters as boundary conditions for thermal analysis is shown to accurately predict the temperature variation.

Future research on numerical simulation of the thermal response of a steel girder with ballast on top and proposing a nonlinear temperature model for steel girders are recommended.

6. References

British Standards, 2003. BS EN 1991-1-5, Eurocode 1: Actions on structures - Part 1-5: General actions - Thermal actions.

Ding Y, Li A, Wang G, 2012. Thermal field characteristic analysis of steel box girder based on long-term measurement data[J]. International Journal of Steel Structures, 12(2):219-232.

Emerson, 1973. The Calculation of the Distribution of Temperature in Bridges. TRRL Report LR 561. Transport and Road Research Laboratory, Department of the Environment, Crowthorne, Berkshire, England.

Tong M, Tham L G, Au F T K, P.K.K. Lee, 2001. Numerical modelling for temperature distribution in steel bridges[J]. Computers & Structures, 79(6):583-593.

Xu Y L et al, 2010. Monitoring temperature effect on a long suspension bridge[J]. Structural Control & Health Monitoring, 17(6):632-653.

Zhou L, Xia Y, et al, 2016. Temperature Analysis of a Long-Span Suspension Bridge Based on Field Monitoring and Numerical Simulation[J]. Journal of Bridge Engineering, 21(1):04015027.

Zuk W, 1965. Thermal behavior of composite bridges-insulated and uninsulated[J]. Highway Research Record 76:231-253.

Methods for Promoting Conversion and Determining Converted Strength of Calcium Aluminate Cement Concrete

Marwa M. Korayem[1] and Matthew P. Adams[2*]

[1] John A. Reif, Jr. Department of Civil and Environmental Engineering, New Jersey Institute of Technology, Newark, NJ, USA, email: mi45@njit.edu
[2] John A. Reif, Jr. Department of Civil and Environmental Engineering, New Jersey Institute of Technology, Newark, NJ, USA, email: adams@njit.edu

[*] : corresponding author

Keywords: rapid repair concrete; calcium aluminate cement; conversion; strength testing

Abstract: Rapid repair materials have become commonplace for bridge and pavement repairs since the need to reduce lane closure times has become more important to local economies and users. Rapid repair materials can vary in chemistry, and often, standard test methods do not apply for testing the quality of these materials. Calcium aluminate cement (CAC) concretes are high early strength systems that are particularly useful in cold environments where the system will still rapidly set and gain strength at temperatures near freezing. CAC systems undergo a unique process known as conversion, in which metastable hydrates convert to stable hydrates, resulting in an increase in porosity and strength loss. Understanding the time at which this conversion occurs, and the magnitude of strength loss is important for long-term design decisions involving repaired concrete systems. Methods promoting conversion for quality assurance testing are discussed including immediate submersion in 38°C and 50°C water baths, delayed submersion in 50°C water bath, and self-heating with the use of a semi-adiabatic box. Mechanical properties testing is discussed with a review of required modifications to existing test methods. Finally, determination of time to conversion through a concrete maturity method, non-destructive testing, and destructive testing techniques is discussed with a presentation of a novel method of using electrical resistivity to detect conversion of CAC concrete.

1. Introduction

Calcium aluminate cement (CAC) is characterized by its rapid strength gain, even at low temperatures approaching 0°C (Scrivener and Alain, 2003). This key feature has made CACs extremely useful in certain concrete repair applications, particularly in cold regions (Banfill 2014). CAC is a specialty cement that can be used in a wide range of applications and has led to an increase in interest in concrete rapid repair applications. Despite the higher cost of CAC (about 4-5 times of ordinary portland cement, OPC), it can provide solutions to specific rapid repair applications where the use of ordinary portland cement may not be feasible (Scrivener 2009). CAC has also performed well as a corrosion resistant material and has been widely used in sewer pipe lining and repair(Scrivener and Alain, 2003; Goyns and Alexander, 2014; Valix and Cheung, 2014) .

CAC composition differs significantly from ordinary portland cement (OPC). CAC contains mainly alumina and calcium oxides and little to no silica while OPC contains mainly calcium and silica oxides and little alumina (Scrivener, 2001; Scrivener and Alain, 2003). The hydration of monocalcium aluminate (CA, the main phase in the unhydrated CAC cement) initially produces CAH_{10} and C_2AH_8 which are metastable hydrates. These metastable hydrates undergo a process known as "conversion" in which the two denser stable hydrates, C_3AH_6 and AH_3, are formed. This conversion process is accompanied by the release of water, an increase in porosity, and significant reduction in its strength. Whether metastable or stable hydrates form during the hydration of CAC depends strongly on temperature, unlike the hydration of calcium silicates which produce the similar hydrates at all temperatures below 100˚C (Scrivener and Alain, 2003). If the temperature is below 15˚C the initial metastable hydrate CAH_{10} is formed, while if the temperature is above 30ºC the initial metastable C_2AH_8 is formed. If the temperature lies between 15ºC and 30ºC, then neither is preferred between the two metastable hydrates regarding the order to be formed and a reduced setting time is observed (Scrivener et al., 1999; Scrivener and Alain, 2003; Adams and Ideker, 2017). The time to conversion varies and depends mainly on the temperature history to which concrete is subjected. Previous work has shown that CAC concrete has converted within 15 minutes from being cast when placed directly in a 100˚C water bath. When placed in a water bath of 30°C, CAC was shown to not reach its minimum converted strength until 30 days after casting (Fryda et al., 2001). Some systems have lasted up to 70 years without undergoing conversion (Fryda et al.). It is important to note that the conversion process only occurs in systems that contain only CAC as the binding material. As additions are made to create binary or ternary binder systems, different hydrates will form, and conversion will not occur.

The conversion process has a significant impact on the strength of CAC systems. Due to the densification of hydrates during conversion, pore space opens up inside the bulk cement paste reducing compressive strength of the concrete (Lamour et al. 2001). Once a minimum compressive strength is reached (i.e. the system has full converted) the strength will again increase as the remaining unhydrated cement grains continue to hydrate (Scrivener & Alain 2003; Scrivener 2009). It should be noted that despite the loss in strength, good quality concrete of acceptable compressive strengths can be achieved after conversion with acceptable mixture design. The minimum converted strength should be used as the design strength for the system, however, to ensure that the system is not structurally deficient.

The standard method used for curing hydraulic cement concrete for compressive strength testing, ASTM C31 in the US, mandates that cylinders are to be cast on site and allow to cure for up to 48 hours. Then these cylinders can be placed in a water bath at 23˚C ± 2˚C until the day of testing. This method is not applicable to CAC as this curing regime will not allow for reaching the minimum converted strength within a convenient time at this given temperature. Therefore, alternative methods of curing must be used that will promote conversion. This method should ensure that the minimum converted strength that is used for design can be measured within a reasonable time period (i.e. within 28 days). This paper reviews the current methods used for promoting conversion such that the minimum compressive strength in CAC systems that are used for rapid repair of pavements and transportations structures can be measured.

2. Existing Methods of Promoting Conversion to Determine Design Strength

There are two existing methods that are used to promote conversion of CAC and to obtain the minimum converted compressive strength within a reasonable time. The first method, described in European committee for standardization, calcium aluminate cement-composition, specifications, and conformity criteria (EN 14647), is used primarily in Europe. This method states that to achieve the minimum converted strength of CAC concrete rapidly, the test specimens should be submerged directly in a 38°C water bath after cast. According to this standard, the minimum converted strength will occur at the fifth day after being cast (EN 14647, 2005). Figure 1 shows the effect of temperature on the speed of conversion.

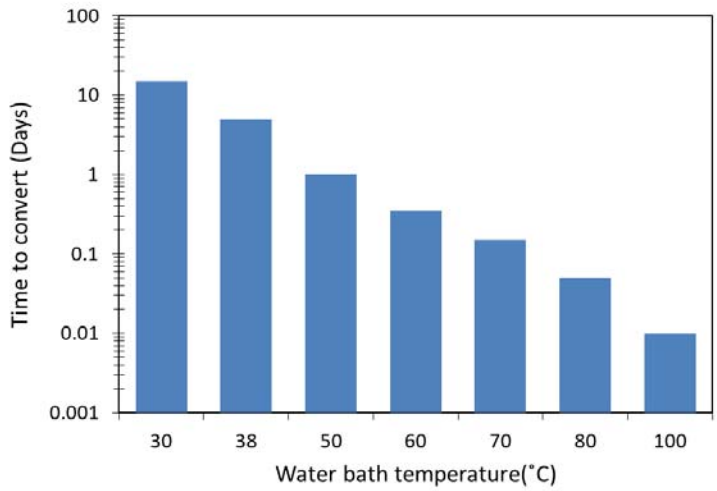

Fig. 1. The impact of temperature on time to convert in CAC systems (Fryda et al., 2001; Fryda et al., 2008; Adams et al., 2018)

The second method is described by standard SS-4491 used by the Texas Department of Transportation, in Texas, U.S.A. This method states that the specimens should be placed immediately in a heavily (semi-adiabatic) insulated box after casting. The insulated box takes advantage of the high heat of hydration produced during CAC hydration which is captured to encourage "self-heating" of the specimens (Tx DoT SS-4491, 2009). These samples that are stored in the insulated box will in turn generate heat to promote the rapid conversion of the metastable hydrates. A heavily insulted box similar to that suggested by the Texas DOT can be seen in Figure 2 (Adams, 2015).

Fig. 2. Semi-adiabatic insulated box for curing CAC (Adams, 2015)

Fig. 3. Heated curing tank at 50˚C (left) Temperature relays at temperature=50˚C±2˚C(right)

These test methods are useful for determining the converted strength of CAC concrete within a reasonable time, however, they are not field-friendly and are not practical to be used for infrastructure applications. That is because these methods do require bulky equipment, or equipment that requires a power source. It is not easy to be transported to the site, so samples can be directly placed into the heated water bath or the insulated box directly after being cast. Additionally, it is not clear if these curing methods produce a conservative estimate of the design strength. When the system is encouraged to convert even before the system has completely hardened, this may result in a different microstructure compared to a system that converts after the concrete has reached final set.

3. Proposed Method of Promoting Conversion to Determine Design Strength

Fryda et al. proposed a test method that overcomes these challenges by allowing the CAC concrete specimens to cure on site at ambient temperatures for up to 48 hours. Then the specimens can be transported to the laboratory and placed in a heated water bath at 50°C (Fryda, Charpentier and Bertino, 2008). Adams et al. suggested a modification to the method to reduce the time on site to 24 hours, and also studied the robustness of the test method with various parameters (aggregate types, curing time, w/cm ratio and the temperature of curing) in order to examine the robustness of this test (Adams, 2015; Adams et al., 2018). The proposed method suggests that when cured on site at normal ambient conditions for 24 hours, and then transported to the laboratory and placed into a water bath at 50°C, minimum converted strength will be reached at 48 hours after casting. This proposed method is convenient to be used on site as it permits the curing of the cylinders in the field at ambient temperatures and then they can be transported to the laboratory at a later time for curing till the day of testing. Therefore, no additional equipment will be required on site beyond the standard concrete sampling tools. A heated water tank for curing the CAC samples at temperature 50˚C± 2˚C in the laboratory is shown in Figure 3. This system uses two submersible heaters in a horse trough tank filled with water, a submersible circulation pump, and a programmable temperature relay to maintain temperature. The tank is then covered with insulation to better maintain temperature. A system such as this can be made for as little as $600 USD.

4. Summary and Conclusions

CAC concrete systems can be very useful in bridge and road repairs as they are known to gain early strength at very low temperatures approaching freezing. CAC systems undergo a unique process known as conversion that results in an increase in porosity and strength loss. It is crucial then to know when conversion occurs and to get the minimum converted strength for design. Different existing methods for promoting conversion including immediate submersion heated water baths and self-heating with the use of a semi-adiabatic box have shown good results. However, they are not field-friendly for repair situations and it may be difficult to have all cylinders well sealed when placed in the water tank. A recently developed accelerated method to promote conversion by allowing to cure samples for 24 hours at ambient temperatures followed by submersion in a heated water tank at 50˚C is recommended instead.

5. References

A.M.Goyns and M.G.Alexander (2014) 'Performance of various concretes in the Viginia experimental sewer over 20 years', in C.H.Fentiman, R.J.Mangabhai, and K.L.Scrivener (eds) *Calcium Aluminates:Proceedings of the International Conference, Avignon., France*. IHS BRE Press, pp. 573–584.

Adams, M. P. (2015) *Factors Influencing Conversion and Volume Stability in Calcium Aluminate Cement Systems*. Oregon State University.

Adams, M. P. *et al.* (2018) 'Evaluation of a Procedure for Determining the Converted Strength of Calcium Aluminate Cement Concrete', *Journal of Testing and Evaluation*, 46(4). doi: 10.1520/JTE20160277.

Adams, M. P. and Ideker, J. H. (2017) 'Influence of aggregate type on conversion and strength in calcium aluminate cement concrete', *Cement and Concrete Research*. Elsevier, 100(July), pp. 284–296. doi: 10.1016/j.cemconres.2017.07.007.

EN 14647 (2005) *European Committee for Standarization, Calcium Aluminate cement-Composition, specifications, and conformity criteria*. Brussels.

Fryda, H. *et al.* (2001) 'Relevance of laboratory tests to field applications of calcium aluminate cement concretes', *Calcium Aluminate Cements*, (Lmc), pp. 227–246.

Fryda, H., Charpentier, E. and Bertino, J. M. (2008) 'Accelerated Test for Conversion of Calcium Aluminate Cement', (July).

Fryda, H., Lamberet, S. and Dunster, A. (2008) 'Calcium Aluminate Cement concrete in an Old concrete structure', (July 2008), pp. 209–220.

Fryda, H., Lamberet, S. and Dunster, A. (no date) 'Calcium Aluminate Cement Concrete in an Old Marine Structure', (July 2008), pp. 209–220.

K.L.Scrivener (2001) 'Historical and Present Day Applications of Calcium Aluminate

Cements', in R J Mangabhai, F. P. G. (ed.) *Proceedings of the International conference on Calcium Aluminate Cements held at Heriot Watt University Edinburgh, Scotland, UK*. IOM Communications Ltd, pp. 3–23.

Karen Scrivener (2009) 'Advanced Concrete Technology', in *Calcium Aluminates Cements*. Elsevier, p. 2/1-2/31.

M.Valix and A.W.H.Cheung (2014) 'The impact of calcium aluminate cement and aggregates on conversion and on field performance in sewers', in C.H.Fentiman, R.J.Mangabhai, and K.L.Scrivener (eds) *Calcium Aluminates:Proceedings of the International Conference, Avignon., France*. IHS BRE Press, pp. 585–599.

P.F.G.Banfill (2014) '10 years exposure of ciment fondu mortars in a marine environment', in CH, F., RJ, M., and KL, S. (eds) *Calcium Aluminates: Proceedings of the International conference, Avignon*. IHS BRE Press, pp. 545–555.

Scrivener, K. L. and Alain, C. (2003) 'Calcium Aluminate Cements', in *Lea's Chemistry of Cement and Concrete, Elsevier Science*.

Scrivener, K. L., Cabiron, J. L. and Letourneux, R. (1999) 'High-performance concretes from calcium aluminate cements', *Cement and Concrete Research*, 29(8), pp. 1215–1223. doi: 10.1016/S0008-8846(99)00103-9.

Tx DoT SS-4491 (2009) *Texas Department of Transportation*. Austin, TX.

V.H.R.Lamour *et al.* (2001) 'Mechanical Properties of Calcium Aluminate Cements', in Mangabhai, R. J. and Glasser, F. P. (eds) *Proceedings of the International conference on Calcium Aluminate cement Held at Heriot Watt University Edinburgh, Scotland, UK*. IOM Communications Ltd, pp. 199–213.

Chloride Concentration Analysis for Concrete Bridge Decks Rehabilitated Using Partial-Depth Hydrodemolition

W. Spencer Guthrie[1*], Elizabeth A. Roper[2], and Dale P. Bentz[3]

[1] Department of Civil and Environmental Engineering, Brigham Young University, Provo, Utah, USA; email: guthrie@byu.edu
[2] Department of Civil and Environmental Engineering, Brigham Young University, Provo, Utah, USA; email: newbillbiz@gmail.com
[3] Retired, Frederick, Maryland, USA; email: bentzcarey@peoplepc.com

[*] : corresponding author

Keywords: bridge deck; chloride concentration; concrete; hydrodemolition; surface treatment

Abstract: Partial-depth hydrodemolition is an increasingly popular method of rehabilitating concrete bridge decks exhibiting damage from chloride-induced corrosion of the top mat of reinforcing steel. For typical bridge decks in Utah, USA, the objective of this research was to investigate the effects of partial-depth hydrodemolition and overlay treatment timing on chloride concentration profiles in concrete bridge decks for depths of concrete removal below the top mat of reinforcing steel. The research results are intended to provide engineers with guidance about the latest timing of hydrodemolition that can maintain a chloride concentration level below the corrosion threshold of 1.2 kg of chloride per cubic meter of concrete at the depths of both the top and bottom mats of reinforcing steel. Numerical modeling generated chloride concentration profiles through a 75-year service life, given a specific original cover depth (OCD), treatment time, and surface treatment usage. The results indicate that, when a surface treatment is used, the chloride concentration at either the top or bottom mat of reinforcing steel does not reach or exceed 1.2 kg of chloride per cubic meter of concrete after hydrodemolition during the 75 years of simulated bridge deck service life. The results also indicate that, when a surface treatment is not used, the chloride concentration at the top mat of reinforcement exceeds 1.2 kg of chloride per cubic meter of concrete within 10, 15, and 20 years for OCD values of 51, 64, and 76 mm, respectively.

1. Introduction

Chloride-induced corrosion of reinforcing steel is one of the leading causes of concrete bridge deck deterioration (Hema et al., 2004). As concrete is relatively weak in tension, the tensile forces exerted by the expansive rust cause the surrounding concrete to crack. Eventually, such cracking can lead to delaminations and potholes on the bridge deck surface, which decrease the structural integrity, ride quality, and service life of the bridge deck.

Repair of these distresses requires removal and replacement of the damaged concrete. One technique that is especially useful for partial-depth concrete removal is hydrodemolition (Wenzlick, 2002). This technique, which is becoming an increasingly common practice, involves removal of deteriorated concrete from the top surface of a concrete bridge deck using high-pressure water jets. Following removal of the old concrete, a new concrete overlay is placed to

restore or increase, as needed, the original deck thickness and specified design strength. A surface treatment is commonly applied to the new deck surface to prevent future ingress of chloride ions and/or water (Birdsall et al., 2007).

Unlike traditional concrete removal techniques such as milling, which is limited to depths shallower than the top mat of reinforcing steel (Guthrie et al., 2008), hydrodemolition can be used to remove concrete from around and even below the top mat of reinforcing steel. Thus, bridge decks that may no longer be suitable for repair using traditional concrete removal techniques, due to the development of critical chloride concentrations at depths deeper than the top mat of reinforcing steel, may still be good candidates for repair using hydrodemolition. In these cases, depending on the chloride concentrations at the time of hydrodemolition and the depth of concrete removal below the top mat of reinforcing steel, the service life of the deck may be significantly extended. Specifically, a sufficient quantity of chloride ions must be removed from the deck so that, after application of a surface treatment preventing further chloride ingress, equilibration of the remaining chloride ions in the repaired deck does not result in a chloride concentration greater than or equal to the generally accepted corrosion threshold of 1.2 kg of chloride per cubic meter of concrete at the top or bottom mat of reinforcing steel.

The objective of this research was to investigate the effects of partial-depth hydrodemolition and overlay treatment timing on chloride concentration profiles in concrete bridge decks for depths of concrete removal below the top mat of reinforcing steel. The research results are intended to provide engineers with guidance about the latest timing of hydrodemolition that can maintain a chloride concentration level below 1.2 kg of chloride per cubic meter of concrete at the depths of both the top and bottom mats of reinforcing steel. The scope of this research included numerical modeling of chloride concentration using inputs typical of concrete bridge decks in Utah, USA.

2. Procedures

Numerical modeling of chloride concentration was performed using a software program developed by the National Institute of Standards and Technology (Bentz, 2007) to investigate the effects of partial-depth hydrodemolition and overlay treatment timing on chloride concentration profiles in concrete bridge decks for depths of concrete removal below the top mat of reinforcing steel. The program uses the one-dimensional approximation for diffusion based on Fick's second law to simulate the diffusion of chlorides through concrete and considers several user-specified internal and external variables that affect chloride diffusion and binding. In the modeling, average monthly temperatures representing typical Utah conditions were used together with cyclic loading of chlorides on the top surface of the bridge deck to simulate the seasonal exposure of bridges in Utah to deicing salt in the absence of a surface treatment; after a simulated surface treatment application, the chloride concentration at the top surface of the bridge deck was specified to be zero, as the treatment, if maintained over time, should prevent future ingress of chloride ions and/or water. Specific values of the inputs are documented separately (Roper, 2018).

For typical bridge deck thicknesses of 203, 229, and 254 mm, corresponding OCDs of 51, 64, and 76 mm were used in the simulations. Using these parameters, each simulation differed based on total duration of chloride exposure, time at which hydrodemolition is performed, OCD, depth

of removal by the high-pressure water jets, and application of a surface treatment on the rehabilitated concrete deck. Specifically, crossing the various levels of the experimental factors in a full-factorial structure generated a total of 36 unique combinations, or scenarios. These included OCDs of 51, 64, and 76 mm (with corresponding removal depths of 86, 98, and 111 mm that include the OCD, the diameter of a 16-mm reinforcing bar, and an additional removal depth of 19 mm below the top mat); treatment times of 25, 30, 35, 40, 45, and 50 years following deck construction; and the presence or absence of an applied surface treatment after hydrodemolition. The numerical modeling for each scenario was performed for a simulated 75-year service life, as recommended by the Federal Highway Administration (FHWA, 2011).

Modeling of the decks without treatment was performed first to develop a baseline chloride concentration profile to which the chloride concentration profiles for various treatment times were compared. Modeling was then performed for each unique combination of OCD, treatment time, and surface treatment application to produce chloride concentration profiles that would be expected after rehabilitation was performed. The latest timing of rehabilitation that maintained a chloride concentration level below 1.2 kg of chloride per cubic meter of concrete at the depths of both the top and bottom mats of reinforcing steel was identified for each unique combination of OCD and surface treatment application.

3. Results

The numerical modeling performed to investigate the effects of different partial-depth hydrodemolition and overlay treatment times on chloride concentration profiles in concrete bridge decks generated chloride concentration profiles through a 75-year service life given a specific OCD, treatment time, and surface treatment usage. From these profiles, graphs of chloride concentration over time at the depths of both the top and bottom mats of reinforcing steel were prepared for each OCD value and surface treatment usage included in the modeling. For each treatment year, the chloride concentration figures were used to determine the maximum chloride concentration that would occur at both mats of reinforcing steel after hydrodemolition and the deck age at which these maximum values occurred. In addition, when the maximum chloride concentration was greater than the threshold of 1.2 kg of chloride per cubic meter of concrete, the deck age at which this threshold was first reached was also determined.

Results were computed for a bridge deck with an applied surface treatment for OCD values of 51, 64, and 76 mm, respectively, with specific values given separately (Roper, 2018). The results indicate that, when a surface treatment is used, the concentration at either the top or the bottom mat of reinforcing steel does not reach or exceed 1.2 kg of chloride per cubic meter of concrete after hydrodemolition during the 75 years of simulated bridge deck service life.

Results were also computed for a bridge deck without an applied surface treatment for OCD values of 51, 64, and 76 mm, respectively, with specific values again given separately (Roper, 2018). The results indicate that, when a surface treatment is not used, the chloride concentration at the top mat of reinforcement exceeds 1.2 kg of chloride per cubic meter of concrete within 10, 15, and 20 years for OCD values of 51, 64, and 76 mm, respectively.

The results of the numerical modeling clearly suggest that a surface treatment should be applied as part of the rehabilitation process to seal the deck against future chloride ingress. Although the

results indicate that the chloride concentration at the bottom mat of reinforcement does not reach or exceed 1.2 kg of chloride per cubic meter of concrete during the 75 years of simulated bridge deck service life, the top mat of reinforcing steel will experience chloride-induced corrosion beginning 10 to 20 years after rehabilitation without an applied surface treatment.

4. Conclusion

Partial-depth hydrodemolition and overlay treatment should be considered as an effective means of removing chloride-contaminated concrete from immediately around and even below the top mat of reinforcing steel and allowing mechanical interlock with the new concrete overlay placed after hydrodemolition. For bridge decks typical of those in Utah, treatment times from 25 to at least 50 years can be specified to achieve significant extensions in deck service life. To maximize deck service life, a surface treatment should be applied to seal the rehabilitated concrete deck against further chloride ingress after hydrodemolition and overlay treatment.

5. Acknowledgements

The authors gratefully acknowledge the Brigham Young University Office of Research and Creative Activities and the Utah Department of Transportation for funding this research.

6. References

Bentz, D. P. 2007. Prediction of a chloride ion penetration profile for a concrete. <http://concrete.nist.gov/~bentz/clpen2.html> (May 1, 2018).

Birdsall, A. W., Guthrie, W. S., and Bentz, D. P. 2007. Effects of initial surface treatment timing on chloride concentrations in concrete bridge decks, Transportation Research Record, 2028, 103-110.

Federal Highway Administration (FHWA). 2011. Bridge preservation guide, Publication No. FHWA-HIF-11042, Washington, DC.

Guthrie, W. S., Nolan, C. D., and Bentz, D. P. 2008. Effect of initial scarification and overlay treatment timing on chloride concentrations in concrete bridge decks, Transportation Research Record, 2220, 66-74.

Hema, J., Guthrie, W. S., and Fonseca, F. 2004. Concrete bridge deck condition assessment and improvement strategies, Report No. UT-04.16, Utah Department of Transportation, Salt Lake City, UT.

Roper, E. A. 2018. Chloride concentration and blow-through analyses for concrete bridge decks rehabilitated using hydrodemolition, M.S. thesis, Department of Civil and Environmental Engineering, Brigham Young University, Provo, UT.

Wenzlick, J. D. 2002. Hydrodemolition and repair of bridge decks, Report No. RDTO2-002, Missouri Department of Transportation, Jefferson City, MO.

Steel

Test Study on Fatigue Performance of Welded Details on the Orthotropic Steel Decks

Meiling Zhuang[1,2] and Changqing Miao[1,2]

[1] Key Laboratory of Concrete and Prestressed Concrete Structure of Ministry of Education, Southeast University, Nanjing 210096, China; email: 18036558037@163.com
[2] School of Civil Engineering, Southeast University, Nanjing Jiangsu 210096, China

[*] : corresponding author

Keywords: orthotropic steel bridge deck; welding seams; fatigue stress spectra; fatigue life

Abstract: To study the fatigue performance of welded details on the orthotropic steel decks, the standard box girder section on the steel box girder of Taizhou Bridge is taken as the research object in this paper. Through the load test of the Taizhou Bridge, the stress response test of the orthotropic steel box girder under the vehicle load is performed. Based on the Miner linear cumulative damage theory, the S-N curve of the Eurocode3 specification is referenced, and the fatigue life calculation formula of the welding details is determined according to the actual structural features. The fatigue life evaluation of the four typical welding details in the steel box girder is performed. The research results show that the stress measurement points on the four typical welding details are mainly based on low amplitude stress cycles, Most of the stress amplitudes are in the range of 2-10 MPa, among which the stress amplitude of the welding details at the U-rib butt joint is larger; the fatigue life of weld seams in the 14mm thick top plate is smaller than that of the 16 mm thick top plate corresponding to the fatigue life of the weld seams; The U-ribbed butt welded joints and the openings of the diaphragms were prone to fatigue failure. Among them, the welding details of the 14mm thick U-rib butt joints first appeared fatigue failure; The arrangement of the diaphragm can effectively increase the fatigue life of the top-U rib weld and improve the fatigue performance at this detail.

1. Introduction

The study of fatigue effects of orthotropic bridge decks abroad is relatively early, and design specifications have been compiled, such as BS5400 in the United Kingdom, AASHTO in the United States, and Eurocode3 in Europe. In recent decades, the application of orthotropic steel bridge decks in China's large-span highway bridges has developed rapidly, but the fatigue research and design specification lags behind the construction of bridges, and fatigue design is usually performed with reference to foreign regulations [1-9].

Many weld joints in orthotropic deck are fatigue-sensitive parts. Domestic and foreign investigations and studies have shown that the following parts of the fatigue disease accounts for more than 90% of the total disease, which is the fatigue vulnerable parts of the steel box orthotropic steel bridge deck [1-2]: ①U-rib ribbed slot; ②Diaphragm and U -rib welds; ③Steel box girder deck and U -rib; ④U-rib butt joint. At present, the fatigue life of the above four types of key weld details is less studied based on the real-bridge load test,.

In order to improve the anti-fatigue design of steel box orthotropic steel bridge decks, this article focuses on the details of the above four key welds, and evaluates the fatigue performance of each welding detail under 14mm and 16mm thick decks combined with the dynamic test of Taizhou Bridge. Firstly, according to the Miner linear fatigue damage theory and the S-N curve in the European Eurocode3 specification, the cumulative fatigue damage calculation method for the welding details of flat steel box girders is established. Secondly, based on the stress data measured at each welding detail, a simplified rain flow counting method was used to obtain the stress amplitude spectrum and the numbers of stress cycles. Finally, predict the fatigue life of each welding detail and find out relative fatigue delicate welding position.

2.Fatigue stress monitoring

According to the load test of Taizhou Bridge, the stress distribution test and stress response test of welding details in the steel box girder were performed. The test selects five test sections in the N26 hoisting girder section (two standard A girder sections) near the L/4 side as shown in Fig.1 , the strain monitoring was performed on the welding details of the U-rib-deck, U-rib-U rib, diaphragm plate-deck, diaphragm plate-U rib, and diaphragm plate opening. The measurement points were symmetrically arranged on the 14mm and 16mm thick deck as shown in Fig.2. Among them, without the diaphragm, the top plate is arranged with two kinds of one-way and two-way strain gages, so as to monitor the cross-bridge direction and along-bridge strain of the top deck-U rib. The U-rib-U ribs are arranged in longitudinal bridge to one-way strain gauges.

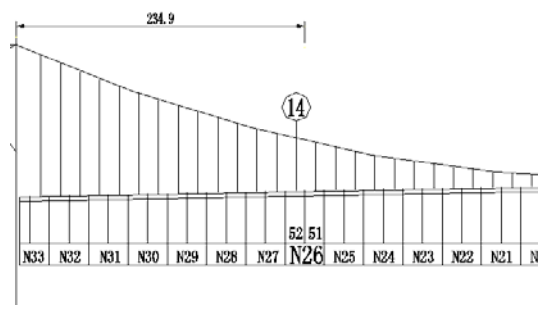

Fig. 1. Steel box girder section of Taizhou Bridge

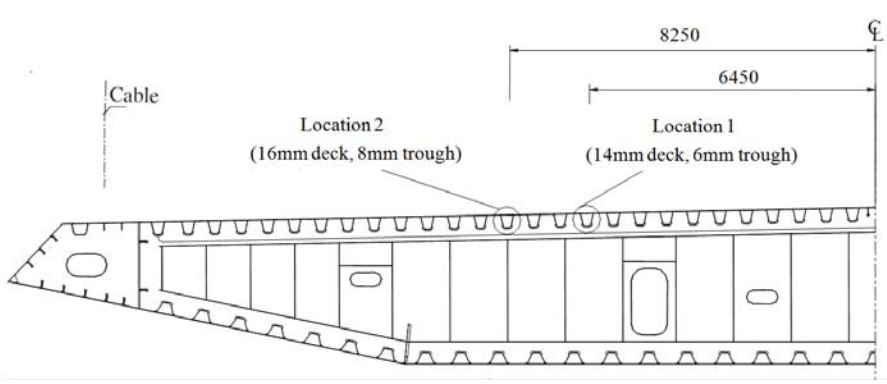

Fig. 2. Transverse location of measuring points（Unit：m）

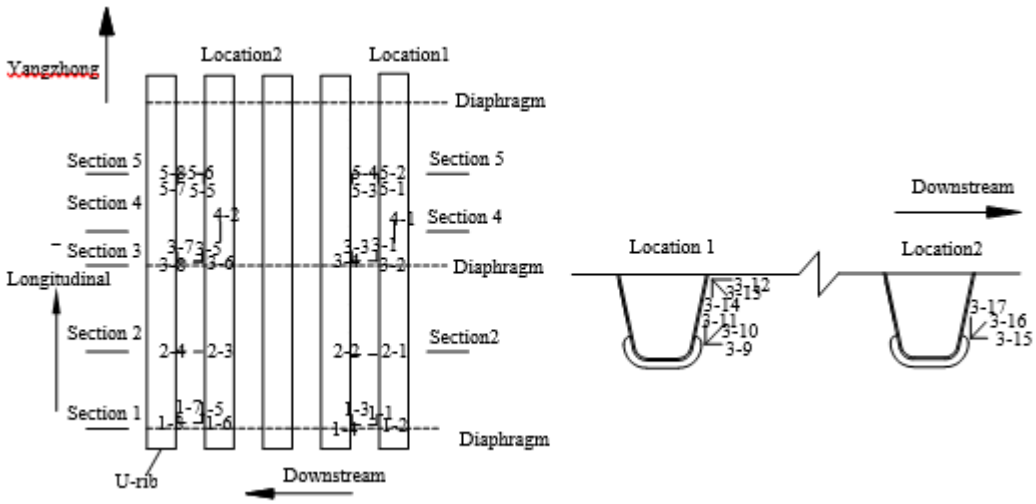

(a) Weld details (b) Diagram on Section 3

Fig. 3. Strain gauges layout

Due to the complicated stress distribution of the welding details at the diaphragm, in the position of the diaphragm, strain flowers are arranged on the diaphragm, and two kinds of strain gauges are arranged on the top plate, one-way and two-way. The location and number of the girder sections and measuring points in the steel box girder is located are shown in Fig. 3. (In Fig. 3 show that the strain gauge is bidirectional point, along the bridge of 1-1, 1-2 for the transverse direction; 3-9/3-10/3-11 indicate that this position is a strained flower, and the cross-bridge strain is measured from 3-9, the oblique 45-degree strain can be obtained from 3-10, and the vertical-bridge strain from 3-11.)

The site uses the Donghua DH 3817 and TEST 3827 dynamic and static signal test instruments to collect data. Each instrument has 8 test channels, and the instruments are connected in series. Strain gage connection mode selection 1/4 bridge, and for temperature compensation. The sampling frequency is 100Hz. The trial-loaded vehicle uses a three-axle truck with a total weight of 300 kN. The specific vehicle parameters are shown in Fig. 4(a). According to the data measured while driving in a fleet, the team had a total of 13 vehicles, each with a 20-m spacing along the bridge, with a vehicle speed of 40 km/h and driving at the same time. The horizontal cross-bridge to the loading position is shown in Fig. 4(b).

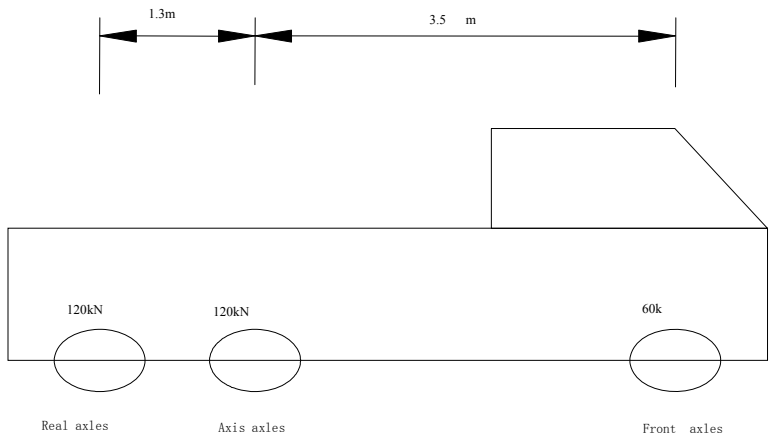

(a) Test loading vehicles

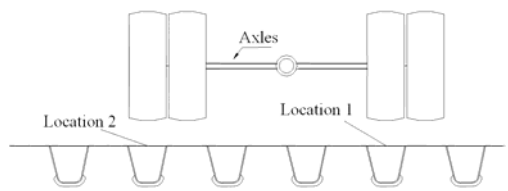

(b) Loading locations

Fig. 4. Test loading vehicles and locations

3. Fatigue life evaluation of weld details

For the measured strain-time curve by the test, the fatigue stress spectrum of each measuring point is obtained through the simplified rain flow counting method [10], and the numbers of stress amplitude cycles at each level is obtained. The research results show that the stress measurement points on the four typical welding details are mainly based on low amplitude stress cycles, most of the stress amplitudes are in the range of 2-10 MPa, among which the stress amplitude of the welding details at the U-rib butt joint is larger. Based on the Miner criterion and the *S-N* curve of the Eurocode3[11], the formula for calculating the fatigue life of each detail can be obtained:

$$L = \frac{1}{D} = \frac{1}{\sum_{S_i \geq \Delta\sigma_D} \frac{n_i S_i^3}{K_C} + \sum_{Sj < \Delta\sigma_D} \frac{n_j S_j^5}{K_D}} \tag{1}$$

$$K_C = \Delta\sigma_C^3 \cdot 2 \times 10^6 \tag{2}$$

$$K_D = \Delta\sigma_D^5 \cdot 5 \times 10^6 \tag{3}$$

In the formula: S_i is the stress cycle greater than or equal to $\Delta\sigma_D$, S_j is the stress cycle less than $\Delta\sigma_D$, n_i, n_j are the numbers of action cycles greater than or equal to $\Delta\sigma_D$ and less than $\Delta\sigma_D$, respectively. The fatigue life of each detail is calculated from equation (1), as shown in Table 4.

Table 4. Fatigue life of weld details on sections

Sections	Deck thickness	Measuring point location	Details of the type	Fatigue life
Section 1	14	1-1/1-2	Deck-U-rib	1071642547
		1-3/1-4	Deck-U-rib	1360453537
	16	1-5/1-6	Deck-U-rib	1971387733
		1-7/1-8	Deck-U-rib	4797787764
Section 2	14	2-1	Deck-U-rib	183330018
		2-2	Deck-U-rib	123410797
	16	2-3	Deck-U-rib	231167355
		2-4	Deck-U-rib	127050660
Section 3	14	3-1/3-2	Deck-U-rib	728034140
		3-3/3-4	Deck-U-rib	6516799068
		3-9/10/11	diaphragm plate opening	9446049
		3-12/13/14	Deck-U-rib - Diaphragm	32821058
	16	3-5/3-6	Deck-U-rib	842560218
		3-7/3-8	Deck-U-rib	11880713528
		3-15/16/17	diaphragm plate opening	9585804
Section 4	14	4-1	U-rib butt joint	2330774
	16	4-2	U-rib butt joint	4449858
Section 5	14	5-1/5-2	Deck-U-rib	13257040
		5-3/5-4	Deck-U-rib	34920151
	16	5-5/5-6	Deck-U-rib	378725039
		5-7/5-8	Deck-U-rib	1391102158

4. Conclusion

Research indicates:

(1) The stress measured points are mainly based on low-amplitude stress cycles, and most of the stress amplitudes are in the range of 2 to 10 MPa, the welding details stress at the U-rib butt joint is larger among the stress amplitudes.

(2) The fatigue life of each weld seam at 14mm thick deck is smaller than that at at 16mm thick deck corresponding to the fatigue life of the weld.

(3) U ribs butt welded joints, openings in the diaphragm easy to fatigue damage. Among them, the 14mm thick U-ribbed butt weld details first appeared fatigue failure.

⑷ The arrangement of the diaphragm can effectively increase the fatigue life of the top-U rib weld and improve the fatigue performance at this detail.

5. Acknowledgments

This research has been supported by the National Natural Science Foundation of China (Grant No.51778135), the Natural Science Foundation of Jiangsu Province (Grant No.BK20160207) and Aeronautical Science Foundation of China (Grant No. 20130969010), the Fundamental Research Funds for the Central Universities and Postgraduate Research & Practice Innovation Program of Jiangsu Province (Grant No.KYCX18_0113 and KYLX16_0253).

6. References

1. Zeng Z B．Classification and reasons of typical fatigue cracks in orthotropic steel deck*Steel Construction*，2011，26 (2) : 9-15，26.
2. Zhang Q H, Cui C, Bu Y Z, et al. Fatigue tests and fatigue assessment approaches for rib-to-diaphragm in steel orthotropic decks. *Journal of Constructional Steel Research*, 2015, 114:110-118.
3. Liu Y, Xiao X, Lu N, et al. Fatigue Reliability Assessment of Orthotropic Bridge Decks under Stochastic Truck Loading. *Shock and Vibration*,2016, 2016, 2016(3):1-10.
4. Chang K O, Bae D. Proposed revisions to fatigue provisions of orthotropic steel deck systems for long span cable bridges. *International Journal of Steel Structures*, 2014, 14(4):811-819.
5. Yang S L, Zhou S. Current Research of Fatigue Damage in Orthotropic Deck Plates of Long Span Steel Box Girder Bridges in China[J]. *Bridge Construction*, 2017, 47(4):60-65.
6. TongGuo, Yu-WenChen. Fatigue reliability analysis of steel bridge details based on field-monitored data and linear elastic fracture mechanics. *Structure & Infrastructure Engineering*, 2013, 9(5):496-505.
7. Chang K O, Bae D. Proposed revisions to fatigue provisions of orthotropic steel deck systems for long span cable bridges. *International Journal of Steel Structures*, 2014, 14(4):811-819.
8. Zhang Q H, Cui C, Bu Y Z, et al. Fatigue tests and fatigue assessment approaches for rib-to-diaphragm in steel orthotropic decks. *Journal of Constructional Steel Research*, 2015, 114:110-118.
9. Liu Y, Xiao X, Lu N, et al. Fatigue Reliability Assessment of Orthotropic Bridge Decks under Stochastic Truck Loading. *Shock and Vibration*, 2016, (2016-11-29), 2016, 2016(3):1-10.
10. American Association of State Highway and Transportation Officials. AASHTO LRFD Bridge Design Specification[S]. 2007: Washington, D.C.
11. Eurocode 3. Design of Steel Structures Part 2: Steel Bridges.

Full-Scale Tests' Best Practice Revealed

Anders Carolin[1*]

[1] Trafikverket, Luleå and Sweden; email: anders.carolin@trafikverket.se

[*] : corresponding author

Keywords: full-scale tests; ultimate limit state; bridges; failures

Abstract: Testing full scale-bridges to failure are expensive and difficult to perform, yet needed to meet tomorrow's expectations from society. Experience from several full-scale tests of different kinds, performed last ten years, including mistakes and successes is condensed down to a minimum of suggestions that should be considered during planning of tests. The suggestions are grouped into the four categories; why, what, how and when, all of them with different view-points. If only one mistake can be avoided by inspiration from suggested methodology it will be judged as a great success.

1. Introduction and method

Full-scale tests of bridges to failure can be considered as top of civil engineering and the most attractive kind of research. Tests include structural engineering, monitoring engineering, computational engineering, and guessing, Sustainable bridges 2007. The interest from media for full-scale tests shows that there is a societal interest as well. Full-scale tests to failure are spectacular, costly and have the signature of one-shot opportunity. Still after many performed tests Paulsson et al. 2016 and Täljsten et al. 2018, every time they have an almost mystic aura. In the following, practical advices and experience from performed tests are given. Experience is based upon several performed full-scale tests related to ultimate limit stage, either directly by loading to failure, Puurula et al. 2015, Häggström et al. 2017, Bagge et al. 2018 or indirectly by study of dynamics Zangeneh et al. 2018 or fatigue consumption Wang et al. 2019.

2. Needs for full-scale tests

Societies need due to several reasons extend the economical service life of existing structures, Sustainable bridges (2007). This must be done without jeopardizing safety or availability. Relatively often it is desirable to increase loads or speeds on existing structures compared to what they were intentionally built for. With higher loads and longer usage probability of deterioration increase. Existing codes for designing new structures, models and tools are not good enough for evaluation of existing structures. New structures can be built according to design codes, guidelines and handbooks. Listed documents necessarily don't describe true bearing capacity very well but must always be conservative, possible to obey and eliminate questions of interpretation. There are numerous examples of existing structures that do not fulfil requirements of design codes whilst still carrying very high loads. We should not blame the codes, instead we must understand that codes are not intended to describe a bearing capacity of an existing structure. Even if we do have significant understanding and tools to describe bearing capacity, these are often based on laboratory reduced scale tests in good condition. Full-scale tests are needed to calibrate models and understand scale-effects including deterioration,

dynamics, and fatigue. The reason for the test must be explained, almost to such level that the test is not required anymore.

3. Ambition of the tests

Numerous examples of needs for research that requires full-scale testing can easily be found, e.g. at BEI-2019 conference. When performing a test a clear list of a few items that definitely shall be answered from the test must exist. The purpose of a short list is to ensure that items are continuously considered during all phases: planning, performance and evaluation. Typical problems with need for further understanding may be: remaining stress in posttensioned concrete; bearing capacity of alkali-silica-reaction damage structures, structures with corroded steel reinforcement; bearing capacity of substructures; dynamic behavior and damping; transformation of global load to local load effects; deformation in ULS; ductility and so on. Full analyses before the test are needed and should have all answers for the tested configuration. The test should only be of confirmative nature.

4. Performing the test

When selecting configuration, it must be chosen to ensure expected failure. In case of two likely failure modes, set-up should be changed to get a clear understanding of one problem and to avoid discussion on what were the causes and what were the consequences. Studied problem should if possible be isolated to avoid having uncontrolled mixtures of failure modes or phenomena. Sometimes bridges need strengthening for certain failure modes in order to ensure the interesting failure. Loads are to be applied beyond maximum carrying capacity, deformation to be increased when capacity reduces.

4.1. Loading

The practical side of applying load is often the most challenging part of a full-scale test to failure. Required loads are not only very large, they must also be well-defined, controllable, and possible to monitor and model. Gravity loads are not recommended to use, as they are difficult to control and monitoring when large deflections forms. In Fig. 1, a well proven method of applying loads is shown.

Fig. 1. Example of loading: hydraulic jacks (left) pulling ground anchored strands (right) creating a downward force. Method used in Puurula et al. 2015, Häggström et al. 2017 and Bagge et al. 2018.

Steel strands have been anchored in bedrock with concrete mortar and hydraulic jacks are pulling strands creating a downward force. Limited stroke of jacks in combination with large structural deformation during test and elasticity of strands require a set up that allows resetting of jacks whilst strand tension remains. Elasticity of strands do give a limitation to deformation control of test when ultimate loads are passed that however in most cases are acceptable. Bridge dynamics, a ultimate limit state criterion, can be studied without taking structures to failure by applying different frequencies in control ways. In Fig.2, two examples that have been used successfully to introduce resonance are shown. Counter rotating masses are normally relatively light equipment limited by frequency dependent force. A more powerful equipment is to use fully controllable hydraulic jack that pushes the structure at selected points on the structure. This has the advantage of not disturbing traffic on the structure as it works from underneath, and that equipment is relatively easy to handle. Large forces, elastic deformations and sudden failure means that large amount of stored energy will be released explosively and adequate safety measures are critical.

Fig. 2. Examples of dynamic loading: (left) Häggström et al. 2017 counter rotating masses; (right) Zangeneh et al. 2018 hydraulic jack with full control of frequencies and amplitudes.

4.2. Monitoring

To maximize results from full-scale tests careful planning of monitoring systems are required. Depending of studied details, need of sensors will vary from traditional laboratory capabilities to ability to capture very large deformations and loads. Number of sensors should also be overdetermined, as some sensors likely are to malfunction and that events must be recorded by several sensors in order to support conclusions. To verify cross-section models, often used in analytical calculations, cross-section data is needed and must be recorded. To verify numerical models, global behavior is very useful and global deformations and behavior must be recorded throughout the test. Experience gives that existing tests may be evaluated in new ways and also in combination with each other long after planned research has finished and therefore it is recommended that a certain amount of, what can be considered to be, unnecessary sensors are installed. Full-scale tests of structures also give the possibility to test monitoring technology. The monitoring technology are developing several times faster than structural engineering. For structural engineers to adopt new technology full-scale tests provide very useful opportunities. Novel technologies, compared to strain gauges or LVDT:s, which can be considered are photogrammetry for deformation, speckle pattern recognition for strain monitoring, amplified

video deformation for resonance modes, airborne cameras, laser scanning and several more. An effective method to avoid monitoring mistakes is to make a pre-analysis and presentation of results on fake data from planned sensors.

5. Planning the test

Full-scale tests should always be perform when possible including: costs, time, seasons, procurement rules, and logistics. Testing opportunity may arise when an old structure is taken out of service by one of several reasons. In such case full-scale failure test should be proceeded by in service tests. In service tests also requires planning, monitoring and detailed analysis as described under "What". A decision to do a full-scale test is required at least six months in advance, preferable some 12 months. For the execution of the test, a rule of thumb is that it always takes more time than planned.

6. Discussion and Conclusion

Given considerations have been found the hard and expensive way. All may not be fully applicable in all cases, should be seen as inspiration for discussions when planning test on real structures, and may save large amount of resources and improve outcomes.

7. References

Bagge, N., Popescu, C., and Elfgren, L. 2018. Failure tests on concrete bridges: Have we learnt the lesson? Structure and Infrastructure Engineering, 14(3) 292-319.

Häggström, J., Blanksvärd, T., and Täljsten, B. 2017. Bridge over Åby River – Evaluation of full scale testing. Research Report, Luleå University of Technology, 180 pp.

Paulsson, B., Bell, B., Schewe, B., Jensen, J. S., Carolin, A., and Elfgren, L. 2016. Results and Experiences from European Research Projects on Railway Bridges. 19th IABSE Congress Stockholm, 2570-2578.

Puurula, A., Enochsson, O., Sas, G., Blanksvärd, T., Ohlsson, U., Bernspång, L., Täljsten, B., Carolin, A., Paulsson, B., and Elfgren, L. 2015. Assessment of the Strengthening of an RC Railway Bridge with CFRP Utilizing a Full-Scale Failure Test and Finite-Element Analysis, J. Struct. Engineering, ASCE, 11 pp.

Sustainable Bridges. 2007. Assessment for Future Traffic Demands and Longer Lives. Four guidelines and 35 background documents are available at www.sustainablebridges.net

Täljsten, B., Blanksvärd, T., Sas, G., Bagge, N., Nilimaa, J., Popescu, C., Elfgren, L. and Carolin, A. 2018. Bridge tested to failure in Sweden, IABSE Conf. 2018, Copenhagen, Denmark. 7pp.

Wang R., Leander J., and Karoumi R. 2019. Comparison of simulation methods applied to steel bridge reliability evaluations. 13th Int. Conf. on Applications of Statistics and Probability in Civil Engineering (ICASP13), South Korea.

Zangeneh A., Svedholm C., Andersson, A., Pacoste C., and Karoumi, R. 2018. Identification of soil-structure interaction effect in a portal frame railway bridge through full-scale dynamic testing. Engineering Structures 159, 299-309.

Rust Rating System using Image Analysis for Weathering Steel Bridges

Toshihiko Aso[1*], Yuto Tokieda[2], Keiji Tajima[3], Yasunori Nakamura[4], and Kazuo Sakamoto[5]

[1] Dept. of Civil and Environmental Engineering, Yamaguchi University, Ube, Japan; email: aso@yamaguchi-u.ac.jp
[2] Graduate school of Sciences and Technology for Innovation, Yamaguchi University, Ube, Jap; email: n; email: i037ve@yamaguchi-u.ac.jp
[3] Dept. of Civil and Environmental Engineering, Yamaguchi University, Ube, Japan; email: tajima@yamaguchi-u.ac.jp
[4] Kozo Keikaku Engineering Inc., Tokyo, Japan; email: yasu@kke.co.jp
[5] Kozo Keikaku Engineering Inc., Tokyo, Japan; email: saka@kke.co.jp

*: corresponding author

Keywords: weathering steel; rust; corrosion; rating; image analysis

Abstract: To avoid unexpected corrosion on weathering steel bridge, inspection for growth of rust is very important. In rust inspection, five level rust rating is used in Japan. This study aims to construct automatically rust rating system for cellophane tape test. In this system, captured rust is converted to digital image by scanning or photo shot. Binarization processing and separation processing are applied to the obtained image to separate rust particles. Each rust particle was converted to equivalent circle which area of circle is same of rust particle area, equivalent diameter of each converted circle could be computed. From equivalent diameters of all rust particles, equivalent diameter size accumulation curve was obtained. From the comparison of many types of such equivalent diameter size accumulation curve, we found diameter at 40% and 100% can be expressed characteristics of rust. Comparison of the results of the proposed image analysis and the visual inspection by the senior inspector showed good agreement.

1. Introduction

In many steel structures, painting has been used to prevent corrosion on its surface. However, corrosion protection performance of painting is deteriorated with age, so repaint is necessary. It means painting require high maintenance cost. Therefore, other corrosion protection technique has been developed. For example, hot dipping, thermal spraying and weathering steel. Weathering steel is a Steel alloy containing Cu, Cr and Ni in an appropriate amount and forming dense rusts on the surface by repeating moderate dry and wet in the atmosphere. On weathering steel, dense and protective rust layer are formed on surface of steel. So, steel surface is protected from attack of corrosive air and water by the rust. On the other hand, rust on ordinary steel is porous and there are many cracks in the rust. So, water, salt and oxygen are reach steel surface easily. From the difference of rust property, corrosive rate of weathering steel could be reduced.

In Japan, all bridges must inspect in every 5 years. To avoid unexpected corrosion on weathering steel bridge, inspection of corrosion is very important. This paper proposes new technique for rust rating of non-painted weathering steel bridges for inspection.

2. Rust level and inspection

Table 1 shows rust rating of weathering steel in Japan (Japan road association, 2014). Level 5 to Level 3 are assumed as normal rust. Level 2 is a rust which need detailed inspection. In Level 1, it is the most serious level, thick and loose laminar rust has formed. Figure 1 displayed typical images of these five-level rust. Cellophane tape test has been used for rust inspection of weathering steel bridges. In this test, Cellophane-Tape (Scotch tape) is pressed against surface of weathering steel to capture rust. After removal, the tape is attached to a sheet such as OHP sheet. After that, inspector rating the captured rust according to rating table. This test has an advantage of convenience and it could be archiving a captured rust. Due to rust rating is performed by visual inspection, it is not very easy to inexperienced inspector. Therefore, this test has possibility of human error when inspector does not have enough experience.

Table 1. Rust level

Level	Attribute	Description	Rust thickness (mm)
5	Acceptable	Very thin	<200
4	Acceptable	Average rust size < 1mm diameter	<400
3	Acceptable	Average rust size 1 - 5 mm diameter	< 400
2	Detailed inspection	Granule size 5 – 25 mm with rust flakes	400 - 800
1	Critical	Thick and loose laminar, very severe corrosion	< 800

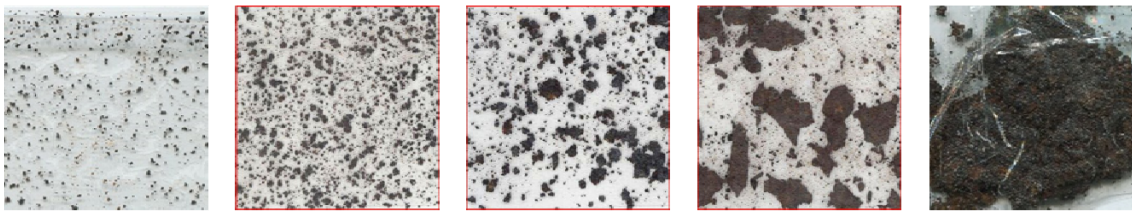

Level 5 Level 4 Level 3 Level 2 Level 1

Fig. 1. Rust images

3. Rust rating by image analysis

In this study, to avoid human error in rust inspection, automatically rating system for cellophane tape test was constructed. In this system, captured rust is convert to digital image by scanning or photo shot. Each rust particle assumed to circle which has same area of the rust particle as shown in Fig.2. Then compute equivalent diameter of the circle of all particles. From the all equivalent diameters, equivalent diameter size accumulation curve could be obtained. Figure 3 shows equivalent diameter size accumulation curves of Level 4 and Level 2, respectively. Distribution of equivalent diameter of particles are different in these two figures. From the comparison of many types of these curves, it became clear that diameter at 40% and 100% can be expressed characteristics of each rust level.

Figure 4 indicates distribution of equivalent diameter at 40% and 100% on accumulation curve of Level 4 rust. In these figures, the total number of samples is 149. At 40% of accumulation curve, equivalent diameter of less than 2.0mm is 144 samples, that is 97% of all samples.

Furthermore, there are 135 samples with equivalent diameter of less than 4 mm at cumulative percentage of 100%. These diameters could assume as characteristic diameter of Level 4 rust. With the same consideration, threshold diameters of each rust level were determined as shown in Table 2. In this table, Level 5 and Level 1 does not described. Because Level 1 is a laminar rust, it is easy to visual inspection, Level 5 indicates very small rust powder, it is no need for separate Level 5 and Level 4.

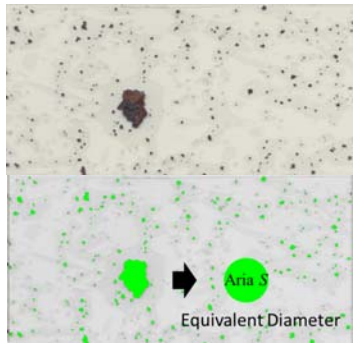

Fig. 2. Conversion of rust particle to circle

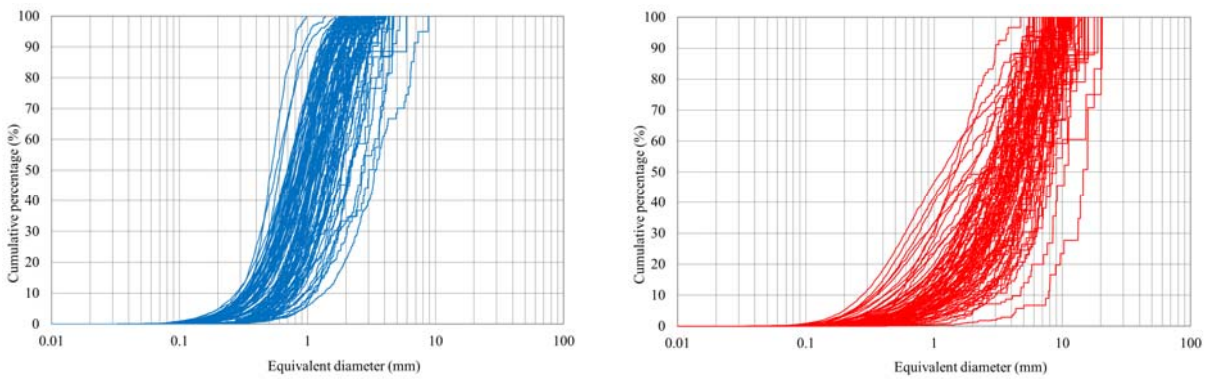

(a) Level 4 (b) Level 2

Fig. 3. Accumulation curves

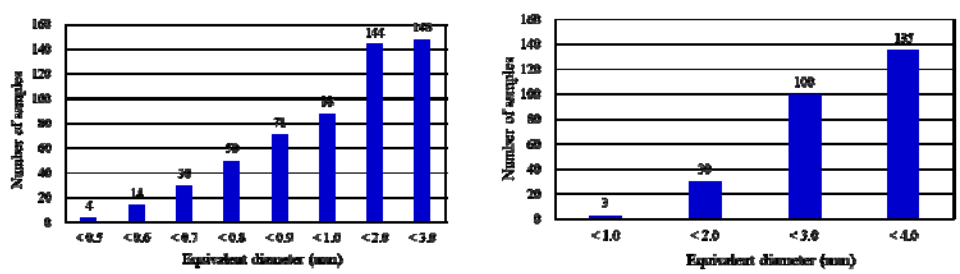

(a) 40% (b) 100%

Fig. 4. Distribution of equivalent diameter of Level 4 rust

Table 2. Criteria of rating

Level	Equivalent diameter at 40% on Cumulative percentage (mm)	Equivalent diameter at 100% on Cumulative percentage (mm)
4	lass than 2mm	
3	2mm - 4mm	3mm - 8mm
2	more than 4mm	more than 8mm

Figure 5 displays analysis flow of proposed method. In this study, binarization was computed by iterative selection method (Ridler, 1978). Table 3 shows a comparison between estimation from image analysis and judgement from visual inspection by senior inspector. For example, there are 34 samples which experienced inspector judged level 3, proposed system judged Level 4. Total concordance rate is 74% for 377 samples. Especially, at Level 2, which is a border of abnormal rust, concordance rate is 88%. This table indicates almost good agree between estimation and judgements. Figure 6 shows error occurrence image that is inspector rated Level 4 but image analysis estimated Level 2. This error occurred by discoloration of sampling tape. To reduce such error, adaptation of other algorithm of binarization and particle deviation should be tested.

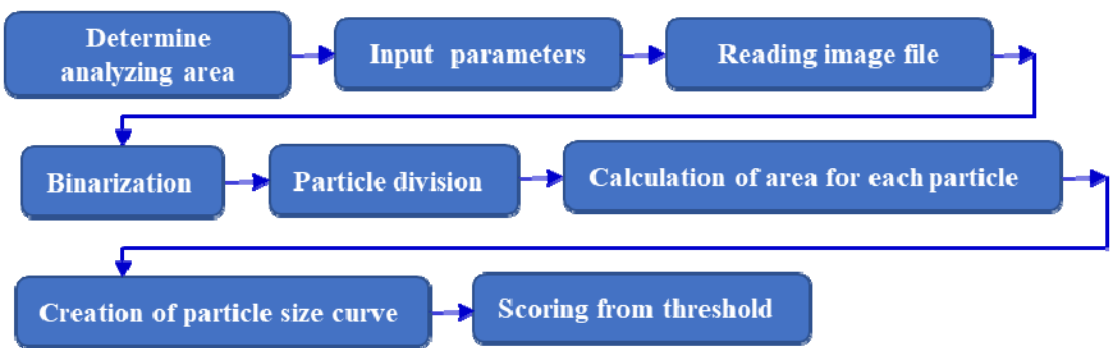

Fig. 5. Analysis flow

Table 3. Comparison of rust level between experienced engineer and image analysis

		Image analysis estimation		
		Level 4	Level 3	Level 2
Experienced inspector	Level 4	90.6% (135/149)	8.7% (13/149)	0.7% (1/149)
	Level 3	26.8% (34/127)	43.3% (55/127)	29.9% (38/127)
	Level 2	1.0% (1/101)	10.9% (11/101)	88.1% (89/101)

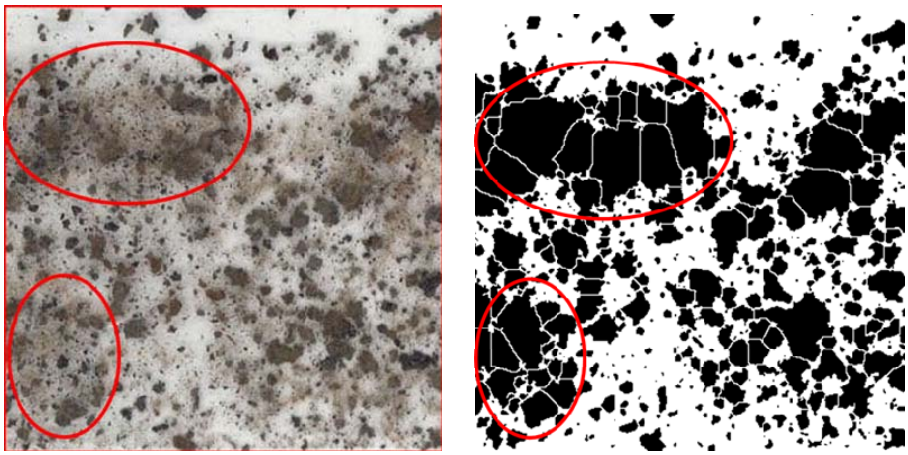

Fig. 6. Images of error occurrence

4. Conclusion

This study constructed automatically rust rating system using image analysis for inspection of weathering steel bridges. From the results of comparison, this system could adapt to practically use.

5. Acknowledgements

This research was carried out as "Study on development of maintenance and repair technique of weathering steel bridges", commissioned research of National Institute for Land and Infrastructure Management, under technology research and development system of Committee on Advanced Road Technology established by Road Bureau of Ministry of Land, Infrastructure and Transport.

6. References

Japan road association, 2014, Corrosion protection manual for highway steel bridges.

Ridler, T.W. and Calvard, S., 1978, Picture thresholding using an iterative selection method, IEEE Transactions on Systems, Man and Cybernetics, 8, 630-632.

Data-Driven Identification for Early-Age Corrosion-Induced Damage in Metallic Structures

Zi Zhang[1], Hong Pan[2,3], and Zhibin Lin[4*]

[1] Department of Civil and Environmental Engineering, North Dakota State University, Fargo, ND 58108 USA; email: zi.zhang@ndsu.edu
[2] School of Civil Engineering, Jinggangshan University, Ji'an, Jiangxi 343009, China; email: tjhp@gmail.com
[3] Department of Civil and Environmental Engineering, North Dakota State University, Fargo, ND 58108 USA; email: hong.pan@gmail.com
[4] Department of Civil and Environmental Engineering, North Dakota State University, Fargo, ND 58108 USA; email: zhibin.lin@ndsu.edu

[*] : corresponding author

Keywords: oil/gas pipelines and bridges; structural health monitoring; early-age corrosion; data-driven approaches; acoustic signal

Abstract: Corrosion is one of leading causes of structural malfunction or even failures of metallic structures, such as oil/gas pipelines and bridges. Rapidly detecting corrosion-induced damage in these large-scale structures are critical steps to assess their conditions and provide timely maintenance/mitigation. Despite great effort in corrosion detection methods and technologies through physics, most are limited due to incapability in accounting for early-age corrosion, particularly under the dynamic field conditions, where structures are often exposed to high uncertainties. In this study, we propose the data-driven approaches using signal process to identify sensitive features that could be better classified for early-age corrosion. Acoustic signals of steel samples under accelerated corrosion tests from the literature were used for a case study. The results showed that the proposed features could effectively assist data classification for early-age corrosion. Moreover, different noise levels were introduced to quantitatively evaluate the effectiveness of the feature extraction methods

1. Introduction

Metallic civil structures, including highway bridges and oil/gas pipelines, are key lifelines for economy and society need. are vulnerable to corrosion-induced damage (Wang et al., 2016; Pan et al., 2017; Gui et al., 2017; Pan et al., 2018; Lin et al., 2018). In recent years, severe corrosion-induced bridges and oil/gas pipelines accidents have raised widespread attention to safety issue, while structural health monitoring (SHM) and rapid detecting damage could provide effective solutions for enhancing the health state of these critical civil structures. Acoustic emission (AE) is a widely accepted as one of non-destructive testing approaches in SHM. It uses elastic waves to propagate though the structure and detects the active damage. The advantage of AE is that it can locate the damage without intruding into the structure. Corrosion is a significant problem for the structural health monitoring, especially for the steel structures. In order to avoid the corrosion damages, numerous scholars make efforts on corrosion detection and many monitoring methods have been developed. Comparing with other detection methods (such as chemical analysis or

electrochemical techniques), acoustic emission provides a direct, real-time and sensitive measure to expose the corrosion happened. Seah et al. (1993) illustrated that the AE technique could monitor and predict the rate of corrosion. Ramadan et al. (2008) used acoustic emission to analyze the microprocess of stress corrosion cracking of stainless steel. Their results demonstrated that AE could detect the crack growth. Alvarez et al. (2008) measured the intergranular stress corrosion cracking propagation thought the mean amplitude and rise-time of the AE signal. AE techniques were applied to identify the onset of corrosion in rebar and detected the cracking due to expansion of corrosion (Kawasaki et al., 2010). Kawasaki et al. (2013) proposed that acoustic emission could quantitatively evaluate the corrosion process in concrete due to expansion of corrosion products.

Along this vein, we investigate the data-driven approaches using signal process to identify sensitive features that could be better classified for early-age corrosion-induced damage. A case study of corrosion characteristics generated from different metals was used for acoustic signals. Features were extracted using frequency and time-frequency analyses, while the uncertainty was simulated by inclusion of different noise levels.

2. Cast study

A case study was used from the literature (Chang, 2014), where four different metals, X52 steel and LY12CZ aluminum alloy and hydrogen embrittlement of AZ31B magnesium and 7075-T6 aluminum alloys, were subjected to NaCl solution and then corrosion fatigue cycles. Their signals were collected by AE system (Chang, 2014), as shown in Fig. 1.

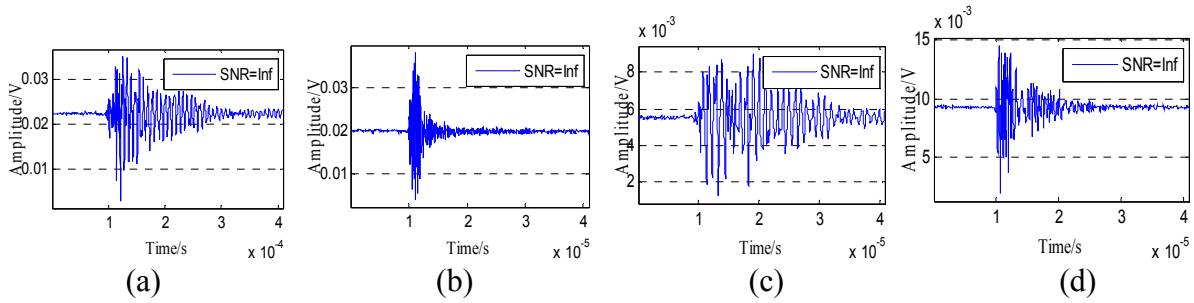

Fig. 1. AE signals: (a) X52 steel; (b) LY12CZ; (c) AZ31B; and (d) 7075-T6

Uncertainty was simulated by the inclusion of different noises using signal to noise ratio (SNR). The SNR is defined by $SNR_{dB} = 10\log_{10}(\frac{P_{signal}}{P_{noise}})$, where P_{signal} and P_{noise} = signal and noise, respectively. Four different SNRs, 30db, 50dB, 80dB, and 100dB, are used in this study.

3. Results and Discussion

3.1. Features using frequency and time-frequency analysis

As shown in Fig. 2, AE signals were processed by frequency analysis. Clearly, except LY12CZ alloy, other three metals exhibited identical features in terms of frequency range and characteristics. Moreover, AE signals were decomposed in time-frequency domain, as typically illustrated in Fig. 3. Thus, the features could be defined in the time-frequency representation

points as $Feature_i = \frac{\sum_{i=1}^{N} TFR_i}{N}$, where the N is representing the number of time-frequency representation point and TFR_i is the time representation point in the time-frequency in Fig. 3. Different boxes through the whole time-frequency domain could be used to select the sensitive damage features. The box information represents all the information of the response of the data covering all the main frequency field. The significant difference in data trend to allow clear identification for undamaged or damaged cases.

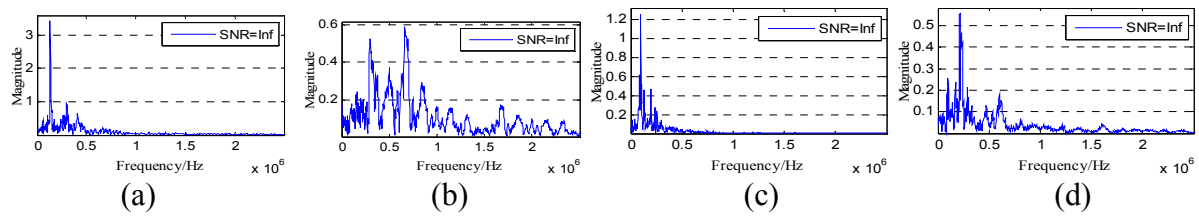

Fig. 2. Frequency of AE signals from: (a) X52 steel; (b) LY12CZ; (c) AZ31B; and (d) 7075-T6

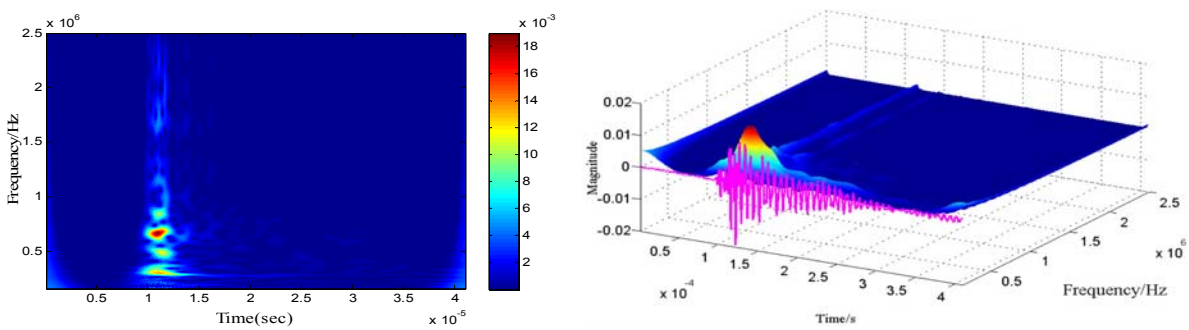

Fig. 3. Time-Frequency analysis of AE signals fromX52 steel

3.2. Impacts of noise level to the features

Uncertainty was simulated by inclusion of noise levels. The influence of different ratio of noise made it separately, as shown in Fig. 4. Particular separation from initial intact signal was noticed when features were under the SNR of 50dB. Clearly, the increase of noise levels raised the challenge in the damage identification. For example, frequency was not clear when SNR=30dB.

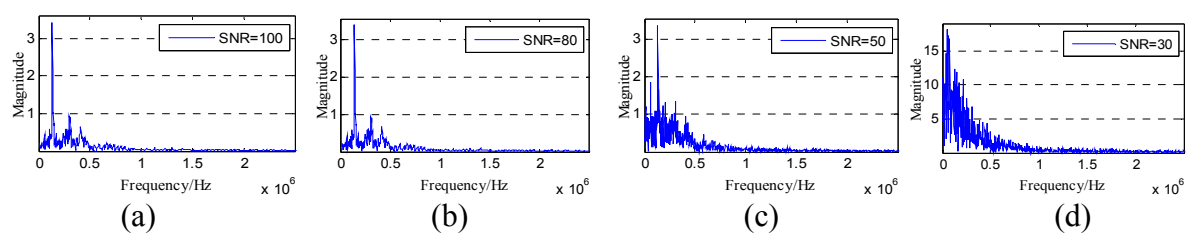

Fig. 4. Signals of X52 steel under noise level of (a) 100dB; (b) 80dB; (c) 50dB; and (d) 30dB

4. Conclusions

We investigated the features generated from AE signals under frequency domain, or time-frequency domain. Clearly the corrosion-induced damage exhibited identical features, while inclusion of high level of noise could significantly affect the data classification.

5. Acknowledgments

The authors gratefully acknowledge the financial support provided by ND DOC Venture Grant, USDOTs (DTPH5616HCAP03, 693JK318500010CAAP and 693JK31850009CAAP). The work presented in this paper was also conducted with partial support from North Dakota State University and the Mountain-Plains Consortium, a University Transportation Center funded by the U.S. Department of Transportation. The results, discussion, and opinions reflected in this paper are those of the authors only and do not necessarily represent those of the sponsors.

6. References

Alvarez, M., Lapitz, P., Ruzzante, J. 2008. AE response of type 304 stainless steel during stress corrosion crack propagation, Corros. Sci. 50, 3382–3388.

Gui, G., Pan, H., Lin, Z., Li, Y., Yuan, Z. 2017. Data-driven support vector machine with optimization techniques for structural health monitoring and damage detection. KSCE Journal of Civil Engineering, 21, 523–534.

Kawasaki Y, Tomoda Y, Ohtsu M. 2010. AE monitoring of corrosion process in cyclic wet–dry test. J Constr Build Mater 24(12), 2353-7.

Kawasaki, Yuma, et al. 2013. Corrosion mechanisms in reinforced concrete by acoustic emission.Construction and Building Materials, 48, 1240-1247.

Lin, Z., Pan, H., Wang, X., Li, M. 2018. Data-driven structural diagnosis and conditional assessment: from shallow to deep learning. In Sensors and Smart Structures Technologies for Civil, Mechanical, and Aerospace Systems 2018, International Society for Optics and Photonics, 10598, 1059814.

Pan, H., Ge, R., Xingyu, W., Jinhui, W., Na, G., Zhibin, L. 2017. Embedded Wireless Passive Sensor Networks for Health Monitoring of Welded Joints in Onshore Metallic Pipelines. In ASCE 2017 Pipelines.

Pan, H., Gui, G., Lin, Z., Yan, C. 2018. Deep BBN Learning for Health Assessment toward Decision-Making on Structures under Uncertainties. KSCE Journal of Civil Engineering 22, 928–940.

Ramadan, S., Gaillet, L., Tessier, C., Idrissi, H., 2008. Detection of stress corrosion cracking of high-strength steel used in prestressed concrete structures by acoustic emission technique, Appl. Surf. Sci. 254, 2255–2261.

Seah, K. H. W., et al. 1993. The correlation of acoustic emission with rate of corrosion. Corrosion Science 34 (10), 1707-1713.

Wang, X., Qi, X., Lin, Z., Wang, J., Gong, N. 2016. Electrochemical Characterization of the Soils Surrounding Buried or Embedded Steel Elements. In ASCE Pipelines, 110–116.

Wang Xingyu, Xiaoning Qi, Zhibin Lin and Dante Battocchi. 2018. Graphene-Reinforced Composites for Protective Coatings for Oil and Gas Pipelines. Nanomaterials, 8, 1-14

Wang Xingyu, Xiaoning Qi, Zhibin Lin and Dante Battocchi. 2019. Characterization of Graphene Reinforced Epoxy Coatings for Internal

Structural Consequences of Grout Deterioration in the Grouted Shear Stud (GSS) Connection

Arjun Jayaprakash[1*], James Nau[2], Mohammad Pour-Ghaz[3], and Mervyn Kowalsky[4]

[1] NC State University, Raleigh, USA; email: ajayapr@ncsu.edu
[2] NC State University, Raleigh, USA; email: nau@ncsu.edu
[3] NC State University, Raleigh, USA; email: mpourgh@ncsu.edu
[4] NC State University, Raleigh, USA; email: kowalsky@ncsu.edu

*: corresponding author

Keywords: grouted shear stud connection; large scale testing; artificial damage simulation; steel bridge substructures; seismic design

Abstract: The grouted shear stud (GSS) connection for steel bridge substructures was developed, for utility in seismic design, as a ductile alternative to the column to cap-beam directly welded connection. The GSS connection utilizes plastic hinge relocation to eliminate brittle cracking at the weld region and provides full strength and ductility capacity for steel bridge columns. However, the grout material used as part of the GSS connection is susceptible to damage through years of exposure, especially in extremely cold climates. This study investigates the effect of grout deterioration on the overall structural behavior of steel bridge substructure systems by artificially simulating grout damage states in a series of large-scale tests. This paper discusses preliminary results from two large scale tests performed on two-column steel bridge bent specimens. The first was a control specimen which was a newly constructed bridge bent that utilized the GSS connection. Expanded polystyrene beads were added to the grout in the GSS connection for the second specimen to simulate a state of damage caused by cold-climate exposure, i.e., a reduced strength and stiffness. Preliminary results indicate that the global behavior of steel bridge substructures is not significantly affected by grout deterioration in the GSS connection.

1. Introduction

The Grouted Shear Stud (GSS) connection is a novel steel bridge column-to-cap beam connection with potential utility in seismic design. The components of the GSS connection include a round steel pile column, a steel pipe stub of larger diameter and a steel cap beam as shown in Fig. 1(a). The pipe stub is shop welded to the cap beam. The cap beam-stub assembly is then lowered onto the erected piles to make a socket type connection. The annular region between the pile and larger diameter pipe stub is then filled with high strength grout to complete the connection. In contrast to conventional column-to-cap beam directly welded connections, the GSS connection relocates the plastic hinge to the steel column section thereby utilizing its full capacity and ductility before failure. Complete discussion of the GSS connection may be found in Fulmer et al. (2015, 2016). This report summarizes two large scale tests of two-column steel bent specimens that utilize the GSS connection. The objective of these tests was to determine if damage to the GSS connection due to long-term exposure to extreme cold climatic conditions could potentially reduce the seismic performance of the bent. Each test utilizes a different level

of deterioration (LoD) for the grout in its connections, i.e., effective damage states are simulated for the GSS connection in each test. Differences in their performance under cyclic quasi-static lateral loading were investigated. The first test was a control test. The GSS connections in the first test specimen were initially undamaged. The second test had GSS connections that had reduced grout compressive strength (f'_c) and elastic modulus (E) representative of a moderate-to-high level damage due to freeze-thaw exposure.

2. Experimental setup

The test specimens were large scale two-column steel bents as shown in Fig. 1(b). The steel bent was supported by two base shoes through pin connections. The height of the center of the cap-beam from the pins was 11'2" (3.40 m) and the center-to-center distance between the two columns was 12' (3.66 m). The base shoes were pre-stressed to the laboratory strong floor utilizing 1-3/8" (35 mm) diameter Dywidag bars. A 440-kip (1957 kN) actuator connected to a plate, mounted on the laboratory strong wall, was used to apply quasi-static cyclic lateral loading. A three-cycle-set loading history was utilized. To make meaningful comparisons, both tests followed the same displacement history. After initial elastic cycles, three cycles at each ductility level (μ1, μ1.5, μ2, μ3 and so on) were applied until test termination. The criterion for termination was either rupture of the pile column wall or an overall strength drop below 50%.

(a) (b)

Fig. 1. (a) Constituents of the GSS connection; (b) Experimental setup for Tests 1 and 2.

3. Artificial Damage Simulation for Test 2

Years of exposure to cold climate tend to reduce the structural properties, such as compressive strength (f'_c) and elastic modulus (E), of cementitious grouts. Simulating this reduction in grout properties to effectively represent the long-term damage state of grout was essential to define the level of deterioration (LoD) variable for Test 2. A few studies (Babu et al. 2005, Bucher 2009) in the past have found that adding expanded polystyrene (EPS) aggregates to a cementitious mixture could reduce its structural properties E and f'_c. Therefore, the addition of EPS was the chosen method to simulate reduced properties, for this study. Note that LoD in these tests refer to the state of the bottom half of the GSS connections in the two-column bent specimens with respect to parameters f'_c and E. Almost all of the durability damage is assumed to be focused in the bottom half of the connection. Moreover, the contribution of the top half of the connection in force transfer is minimal. Fig. 2 shows the state of the grout in the connections of the Test 2 specimen. The y-axis is the depth of the location of measurement from the bottom of the cap beam. The x-axis show values of compressive strength [Fig. 2(b)] and elastic modulus [Fig. 2(c)] normalized to the same quantities in Test 1. Compressive strength of 2” x 2” (50mm x 50mm)

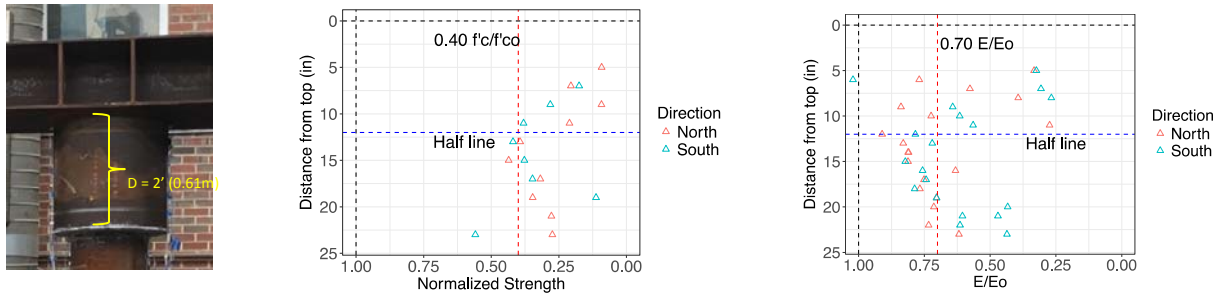

(a) (b) (c)

Fig. 2. Results of grout properties from the GSS connection of Test 2: (a) GSS connection depth; (b) Compressive strength profile obtained from cubic samples; (c) Dynamic elastic modulus profile obtained from disc samples; (1 in = 25.4 mm).

cubic samples taken during casting was measured per ASTM C109 (2018). The elastic modulus was measured from disc samples utilizing the method proposed by Leming et al. (1998). On average, the GSS connection in Test 2 had a reduction in strength of 60% and elastic modulus of 30% compared to Test 1 in the bottom half of the connection.

4. Results and Discussion

Test 1 achieved a drift of 9% while Test 2 achieved 11% drift [Fig. 3(a)]. A comparison of the cyclic force-displacement hysteresis curves for the two tests are shown in Fig. 3(b). Tests 1 and 2 showed similar structural behavior. During the elastic cycles, Test 2 specimen had a slightly reduced stiffness compared to Test 1 specimen [Fig. 4(a)]. This was expected since the grout in Test 2 was "deteriorated". However, this reduction is barely noticeable on the complete force-displacement hysteresis curve. In the early inelastic cycles (μ1 and μ2), the curvature demand in the plastic hinge region for Test 1 columns was higher than that of Test 2. This resulted in a slightly larger energy dissipation by Test 1 specimen compared to Test 2 [Fig. 4(b)]. During μ3 cycles, Test 1 specimen started losing its load carrying capacity as the plastic hinge was fully developed [Fig. 4(c)]. The section just below the plastic hinge pinched and therefore reduced the section modulus. Moreover, high strain demands caused the steel material to flow and thereby reduced the wall thickness. During μ4 cycles, both Test 1 and Test 2 started to show similar behavior once again [Fig. 4(d)]. Some differences here included a slightly higher load carrying capacity and a reduced reloading stiffness of Test 2 specimen. Loosely speaking, Test 2 specimen was more flexible and ductile than Test 1 specimen.

(a) (b)

Fig 3. (a) The maximum drift achieved by Test 2 was 11% at a ductility of 5; (b) A comparison of the force-displacement hysteresis of two tests; (1 in = 25.4 mm, 1 kip = 4.45 kN).

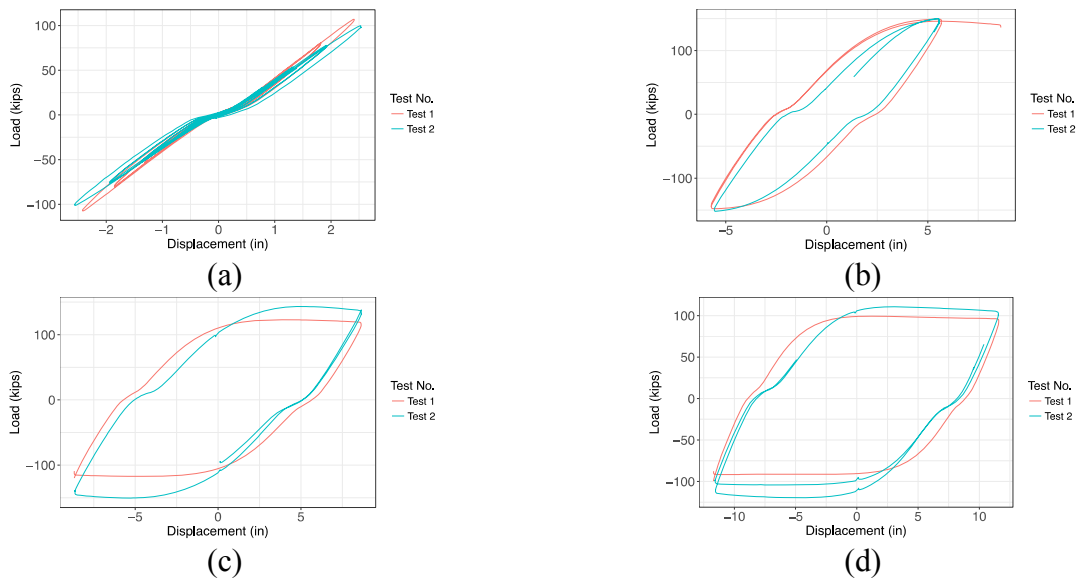

Fig. 4. Comparison for hysteretic loops at different ductilities: (a) F_y cycles; (b) μ2 cycles; (c) μ3 cycles; (d) μ4 cycles; (1 in = 25.4 mm, 1 kip = 4.45 kN).

Despite the grout properties being reduced considerably, the difference in the overall structural behavior of the two-column bent specimen was of no real significance. Results suggest that a moderate-to-high level of durability damage within the GSS connection in steel bridge substructures is of little to no concern from the perspective of its global structural behavior under lateral loading. However, this cannot be stated conclusively without further investigation. Two additional large scale tests of similar nature are planned to be executed in March-April 2019.

4. References

ASTM C109. 2016. Standard Test Method for Compressive Strength of Hydraulic Cement Mortar, ASTM International, West Conshohocken, PA.

Babu, D.S., Babu, K.G., and Wee, T. 2005. Properties of lightweight expanded polystyrene aggregate concretes containing fly ash. Cement and Concrete Research 35(6), 1218-1223.

Bucher, B.E. 2009. Shrinkage and shrinkage cracking behavior of cement systems containing ground limestone, fly ash, and lightweight synthetic particles. Thesis, Purdue University.

Fulmer, S., Kowalsky, M., & Nau, J. 2015. Grouted shear stud connection for steel bridge substructures. Journal of Constructional Steel Research 109, 72-86.

Fulmer, S., Kowalsky, M., Nau, J., & Marx, E. 2016. Development of a ductile steel bridge substructure system. Journal of Constructional Steel Research 118, 194-206.

Leming, M.L., Nau, J.M., & Fukuda, J. 1998. Non-destructive determination of dynamic modulus of concrete disks. Materials Journal 95(1), 50-57.

Fatigue Evaluation of Diaphragm Cutout on an Orthotropic Steel Bridge with Heavy Freight Transportation

Zhiwen Zhu[1*], Jianpeng Li[2], and Ze Xiang3

[1] Department of Civil and Environmental Engineering, Shantou University, Shantou, China; email: zhuzw@stu.edu.cn
[2] College of Civil Engineering, Hunan University, Changsha, China;
email: lijianpeng@hnu.edu.cn
[3] College of Civil Engineering, Hunan University, Changsha, China; email:1024291686@qq.com

[*] : corresponding author

Key words: steel bridge; fatigue; diaphragm cutout; vehicle loading spectrum; fatigue truck; overweight

Abstract: In order to investigate the diaphragm cutout cracking at an orthotropic steel bridge on heavy freight transportation highway, vehicle loading spectrum and fatigue truck models based on weight-in-motion(WIM) system, as well as the girder section model and sub-model based on ANSYS, were established to evaluate the fatigue performance of steel bridges. The traffic database was used to present ten representative vehicle models, with vehicle gross and axle weight, axle spacing, as well as vehicle and axle load distribution on each lane included, from which the vehicle loading spectrum was proposed. Based on the rule of equivalent fatigue damage, the six-axle representative truck, which was the dominant vehicle type on fatigue loading, was used as a prototype to derive the proposed standard and simplified standard fatigue truck models. Then the fatigue truck models were applied to the models to acquire stress responses and fatigue assessment of the cutout. The study shows that the average daily truck traffic was significantly large on the highway, and a high fraction of the trucks impose on the bridge with overweight gross weight and axle weight, as well as the truck passage concentrated on part of the lanes. As the local effect was significantly on orthotropic deck, the transverse and longitudinal stress influence line of cutout were short, and the stress response of diaphragm cutout could only identify axle-group, instead of individual axles of the axle-group. Diaphragm cutout was controlled by the in-plane deformation, increasing the thickness of diaphragm could effectively reduce stress, but would increase the out-of-plane stress. Fatigue life evaluation results were accordance with the actual bridge cracking time that between 6 to 10 years, it was suggested that offsets the lane line position and transfinite vehicle rectifying works would extend the fatigue life of the bridge. The research presented in this paper would provide important information for fatigue design and evaluation of steel bridges, especially the orthotropic steel bridge decks on heavy freight transportation highway in China.

1. Introduction

Orthotropic steel bridge is not only light and expedient construction, they also offer a smooth ride and protect the diaphragm from leakage. Furthermore, the orthotropic deck together with the stiffening girders form a torsion tube that increase the torsion stiffness of the bridge, and significantly improve its aerodynamic stability (AASHTO 2010). A concern of orthotropic steel bridges is details that are prone to fatigue cracking, which resulting from the complicated welded details combined with stresses that can be more difficult to quantify (Federal Highway Administration 2012). Over the years, many laboratory tests and field measurements have been carried out all over the world as to investigate the mechanism of various detail cracking (Connor et al. 2006; Fanjiang et al.2004; Fisher et al.1990; Kozy et al.2010; Tsakopoulos et al.2005; Zhou et al.2006). Many considerations have been obtained and the bridge engineering benefits a lot. The primary focus is in resolving the stress concentration at critical details to prevent fatigue cracking (Shao et al.2013; Li et al.2014; Xiao et al.2008; Hyong-Bo Sim et al.2012), especially for the rib-to-diaphragm intersections, where three-dimensional stresses are generated by the in-plane flexure of the diaphragm response combined with the out-of-plane twisting from the rib rotations. The rib was initially made discontinuous to fit between the diaphragms, current practice is typically to make them continuous through cutout in the web plates of the diaphragms. A stress-relieving cutout on the diaphragm around the rib should reduce the stress concentration at the rib-to-diaphragm intersections (Federal Highway Administration 2012). It should be recognized however, owing to the complexity of the problem and the unique features of each bridge, there has not worldwide consensus yet been established for the shape of the cutout, the challenge remains for fatigue damage assessment at this detail. Early reported diaphragm cutout cracking includes Westgate bridge in Australia, Humen bridge in China and so on (Zhu et al. 2015).

In this paper, fatigue cracks were observed at diaphragm cutout on a self-anchored suspension bridge, which was open to traffic at the end of 2006, as shown in Fig.1(a). The first crack was observed on base metal at diaphragm cutout in September 2013 during a bridge routine inspection. The fatigue crack is closely monitored and further inspection at the beginning of 2014 found more cracks on the same detail, as shown in Fig. 1(b). Then temporarily stop holes were drilled at the crack tip and regular inspections were carried out as to make sure if the cracks would propagate beyond the stop holes (Zhu et al. 2015)

(a) (b)

Fig. 1. Diaphragm cutout cracking of the steel bridge: (a) Fatigue crack; (b) Drilled stop hole at tip of crack

It is observed that the truck loads have been increasing in both magnitude and volume in China. Truck over weight-limit may accelerate wearing damage or affect durability of the highway structures (Han et al.2015). Further, increasing truck weight may also impose higher load-carrying requirements for new and renewed bridges. As a result, it will cost more to construct new bridges and upgrade existing bridges to prevent strength deficiency and increased fatigue. For fatigue assessment, it requires a reasonable knowledge of the live-load spectra produced in service. Weigh-in-motion (WIM) has been developed as an extensive measurement device to monitor gross vehicle weight, axle weight and axle spacing, as well as vehicle and axle load distribution on each lane of passing vehicles(Zhou et al. 2015). The use of WIM databases can achieve more accurate truck loading, in particular, it would enable comprehensive statistics on truck-bridge loading to be obtained for use in highway bridge design or fatigue rating of existing bridges.

In this paper, the fatigue standard fatigue truck model and its simplified truck model were developed from vehicle load spectrum based on weight-in-motion(WIM) system. Then the girder section model and sub-model based on ANSYS, were carried out to evaluate the fatigue performance of the steel bridges. The steel bridge is located in Guangdong Province China mainland, is a self-anchored structure with one single main tower and one suspended span of 350m, as shown in Fig. 2(a). The box girder is 3.5m high and the total width is 26.1m. Five traffic lanes are arranged on the deck, including the overtake lane, fast speed lane, two heavy traffic lane and high speed lane, from right to left in Fig. 2(b). The orthotropic steel deck(OSD) system includes a 16mm deck plate, 10mm close ribs, 12mm diaphragm at hanger and 10mm at others. Detail OSD structural information is shown in Fig. 2(c).

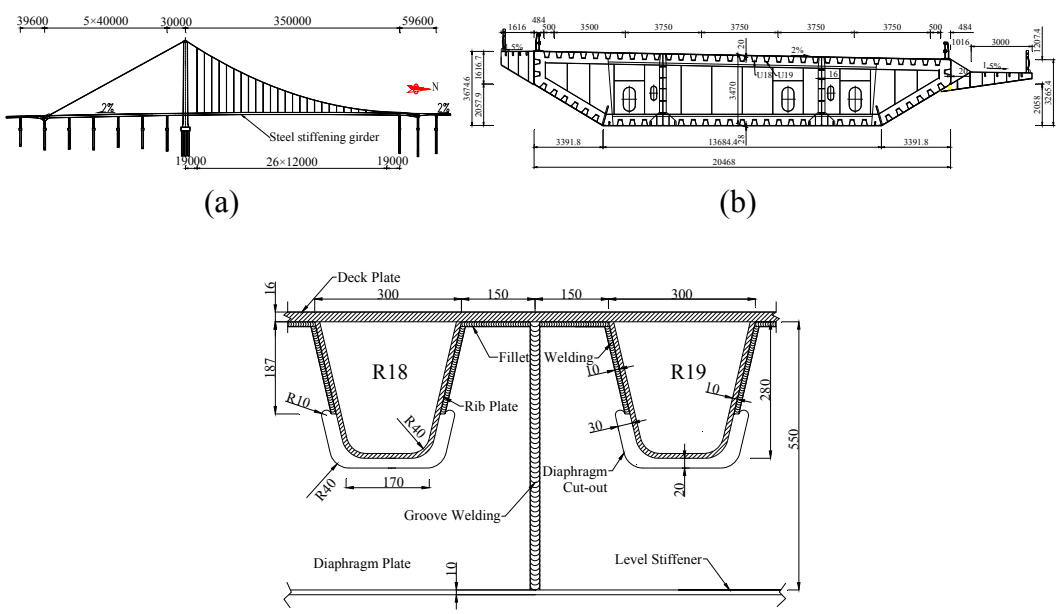

Fig. 2. Bridge layouts (Unit: mm): (a) Bridge elevation; (b) Cross-section of steel box girder; (c) Structural detail of OSD

2. WIM databases

The WIM system was located on the steel bridge in South China highway, the bridge was on the city ring fast trunk road which was open to traffic at the end of 2006. The number of average daily truck passage was significantly large on the highway, and the fraction of truck passage in all traffics was remarkably high. In order to investigate vehicle loading spectrum and fatigue truck models on this heavy freight transportation highway, the traffic data from the WIM system was used to present ten representative vehicle models, with vehicle gross and axle weight, axle spacing, as well as vehicle and axle load distribution on each lane included, from which the vehicle loading spectrum was proposed targeting to evaluate the fatigue performance of this orthotropic steel bridges, and can also be used for freight of heavy road vehicle load spectrum research in China to provide the reference. This paper used the traffic data in August 2013, eliminated a week's abnormal data due to traffic control, as shown in Fig. 3. It can be seen that the traffic flow was stable in common condition, and the average daily traffic was 45065. Further traffic classification according to the axle number, is shown in Fig. 4. The maximum volume of traffic was 2-axle vehicle with daily traffic of 39965, and the variability was large as it was mainly comprised of cars and minivans. Trucks with more than 3 axles were shown in Fig. 4, in which the traffic of other truck was small.

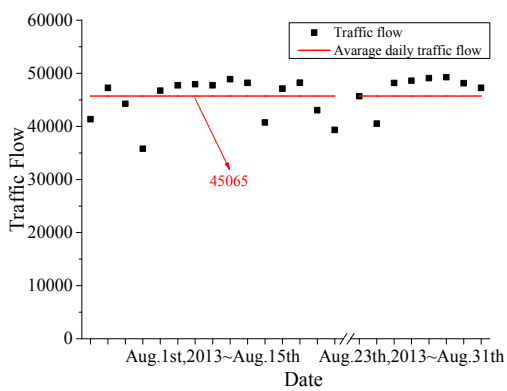

Fig.3. Traffic data statistics

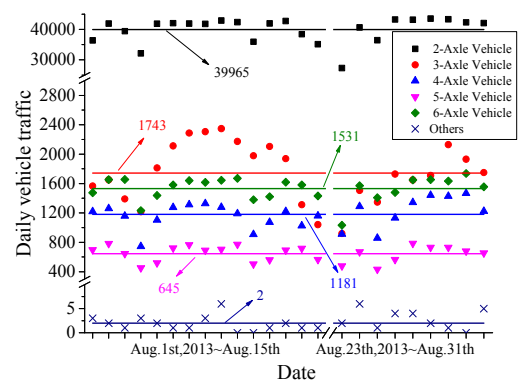

Fig.4. Vehicles with different axle number

The explicit detail of WIM data is shown in Table 1. This paper listed 11 simplified models refer to conferences [6] and [7], the traffic database from WIM was classified based on axle-number and axle-spacing , as shown in Table 1 and Table 2. As shown in Table 1, the variation of axle-spacing was small for most vehicle types, but a few individual truck with small volume was much high, such as the axle-spacing variation was reached 3.5m of type 3-axle(5), as it was small volume, which should have little influence on the whole samples, and could be classified into similar models according to the axle-spacing. The average gross vehicle weight(GVW) was high for trucks, and the volume of average daily truck traffic(ADTT) was 10516, which was account for 23.3% of the total traffic. It can be seen that the average daily truck passage was significantly large on the highway, both magnitude and volume were significantly greater than the AASHTO LRFD recommended daily one-direction trucks and proportions, that the highway freight was very busy.

Table 1. Average daily traffic flow data by WIM (Unit: m)

Vehicle type	number	Ave_{L1} (m)	Var_{L1} (m)	Ave_{L2} (m)	Var_{L2} (m)	Ave_{L3} (m)	Var_{L3} (m)	Ave_{L4} (m)	Var_{L4} (m)	Ave_{L5} (m)	Var_{L5} (m)	Ave_{GVW} (kN)	Var_{GVW} (kN)	Model
2-axle(1)	218	1.4	(0.1)									4	(13)	V1
2-axle(2)	21592	2.6	(0.1)									17	(10)	
2-axle(3)	12740	3.2	(0.2)									41	(31)	V2
2-axle(4)	5397	5.1	(0.8)									146	(69)	V3
2-axle(5)	19	4.2	(0)									145	(49)	
3-axle(1)	287	1.9	(0.1)	5.3	(0.4)							238	(91)	V4
3-axle(2)	1	4.9	(0.5)	8.1	(0.3)							206	(80)	
3-axle(3)	10	2.8	(0.8)	7.8	(2.1)							219	(120)	
3-axle(4)	1433	3.3	(1.3)	2.7	(2.0)							240	(96)	V5
3-axle(5)	13	4.8	(3.5)	2.7	(2.8)							152	(154)	
4-axle(1)	476	1.8	(0.3)	4.5	(0.3)	1.3	(0)					342	(126)	V6
4-axle(2)	242	4.1	(0.2)	7.8	(0.6)	1.3	(0.3)					351	(128)	V7
4-axle(3)	450	2.8	(0.8)	6.1	(1.6)	1.3	(0.1)					354	(153)	
4-axle(4)	9	3.2	(2.6)	4.1	(3.7)	2.0	(1.3)					108	(149)	
4-axle(5)	2	2.9	(0.6)	6.7	(2.3)	2.9	(0.7)					77	(118)	
4-axle(6)	2	2.6	(0.8)	2.8	(2.7)	4.4	(2.3)					75	(108)	
5-axle(1)	619	3.5	(0.2)	7.2	(0.9)	1.3	(0)	1.3	(0)			405	(193)	V8
5-axle(2)	1	4.5	(3.0)	2.4	(0.7)	6.2	(2.0)	1.4	(0.2)			344	(240)	V9
5-axle(3)	9	3.4	(0.4)	1.4	(0.1)	6.9	(1.2)	2.8	(0.5)			649	(200)	
5-axle(4)	14	3.2	(0.5)	1.5	(0.5)	6.7	(1.7)	1.4	(0.3)			490	(255)	
5-axle(5)	3	2.9	(1.6)	4.2	(3.4)	4.1	(3.2)	2.4	(1.5)			267	(229)	
6-axle(1)	1220	3.3	(0.2)	1.3	(0)	7.3	(1.7)	1.3	(0)	1.3	(0)	535	(268)	V10
6-axle(2)	35	1.9	(0.8)	2.6	(0.8)	7.7	(2.5)	1.4	(0.8)	1.3	(0.3)	482	(229)	V11
6-axle(3)	276	1.8	(0.2)	2.6	(0.1)	8.2	(1.7)	1.3	(0)	1.3	(0)	531	(233)	

Notes： L_i-- the ith axle spacing；GVW—gross vehicle weight；
Ave—average of axle spacing or gross vehicle weight；Var--variance of axle spacing or gross vehicle weight

3. Fatigue vehicle loading spectrum

Load intensity and load frequency are the main parameters of vehicle load spectrum. Fatigue load spectrum should not only consider the vehicle load itself, the response characteristics of structure under vehicle load should also be considered. When a truck passed, for far away from the wheel load components, such as suspender, cable and girder, that would only produce one stress cycle. For directly bearing components, such as deck and diaphragm, that would produce repeatedly stress cycles. The former fatigue load model was corresponding to gross vehicle weight, while the latter should be refined to the axle load and axle spacing, and also the vehicle distribution should be considerate at the same time.

3.1 Representative vehicle model

The axle spacing is an important classification basis of representative vehicle model, which is explicated as the weighted average of axle spacing in the same classification vehicles:

$$L_i = \sum_{j=1}^{n} L_{ij} / n \tag{1}$$

where L_{ij} is the ith axle spacing of the jth vehicle in the same classification; n is the total number of vehicle in this classification; L_i is the ith axle spacing of the representative vehicle models. From Table 1 and Table 2, one can see that the average GVW of V1 was small than 30kN but up to 20000 of daily traffic, account for 48.5% of the total traffic. It could be neglected in the fatigue vehicle spectrum as could not cause bridge fatigue damage (Han et al. 2015). The other truck model with more than seven-axle could also be neglected as its low frequency in the lane. The daily traffic of Model V9 was only 26, it was classified as its representativeness in China, such as Dongfeng truck listed in the reference [6]. The daily traffic of 2-axle truck of V2 and V3 was 18156, then the daily traffic of 3-axle truck of V4 and V5 was 1742, while the daily traffic of 4-axle truck of V6 and V7 was 1181, and the daily traffic of 5-axle truck and 6-axle truck were 645 and 1438 respectively. The axle group was defined as the axle spacing less than 1.3m, such as two-axle group of 4-axle truck V6 and V7, three-axle group of 6-axle truck V10 and V11. The explicit details are shown in Table.2.

Table 2. Representative vehicle models

Model	Number	Representative vehicle models /m
V1	21810	
V2	12740	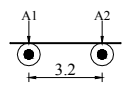
V3	5416	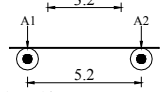
V4	297	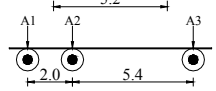
V5	1445	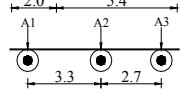
V6	476	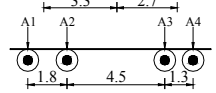
V7	705	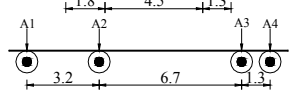
V8	619	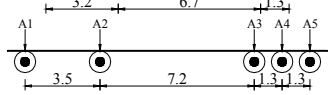
V9	26	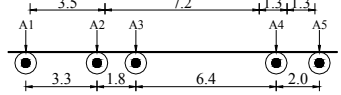
V10	1220	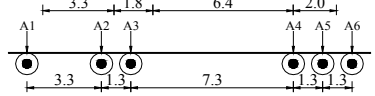
V11	311	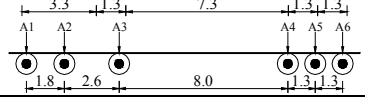

3.2 Gross vehicle weight (GVW)

The gross vehicle weight (GVW) is directly reflect the load intensity, which is the important parameter of fatigue assessment in main components of bridge. According to the AASHTO procedure, an equivalent truck weight W_{ev} is calculated based on equivalence in fatigue accumulation.

$$W_{ev} = [\sum f_i W_i^3]^{1/3} \quad (2)$$

where f_i is occurrence frequency of trucks with a gross vehicle weight of W_i. As mentioned above, the vehicle weight less than 30kN was removed when calculating the equivalent vehicle weight and the equivalent axle load in this paper. As shown in Fig.5, the increasing of gross vehicle weight with the increasing number of axles. The minimum equivalent gross vehicle weight was 77kN of V2 model, while the maximum was 645kN of V10 model. Although there was small daily traffic of V9 model, its equivalent GVW reached 631kN. Almost all represented models were shown in multimodal distribution of GVW, except the V2 was single peak and partial distribution. The most significant reason was the overweight of the trucks, that should induced multiple peaks of load distribution at the normal load and overloaded conditions. More details are shown in Table.3

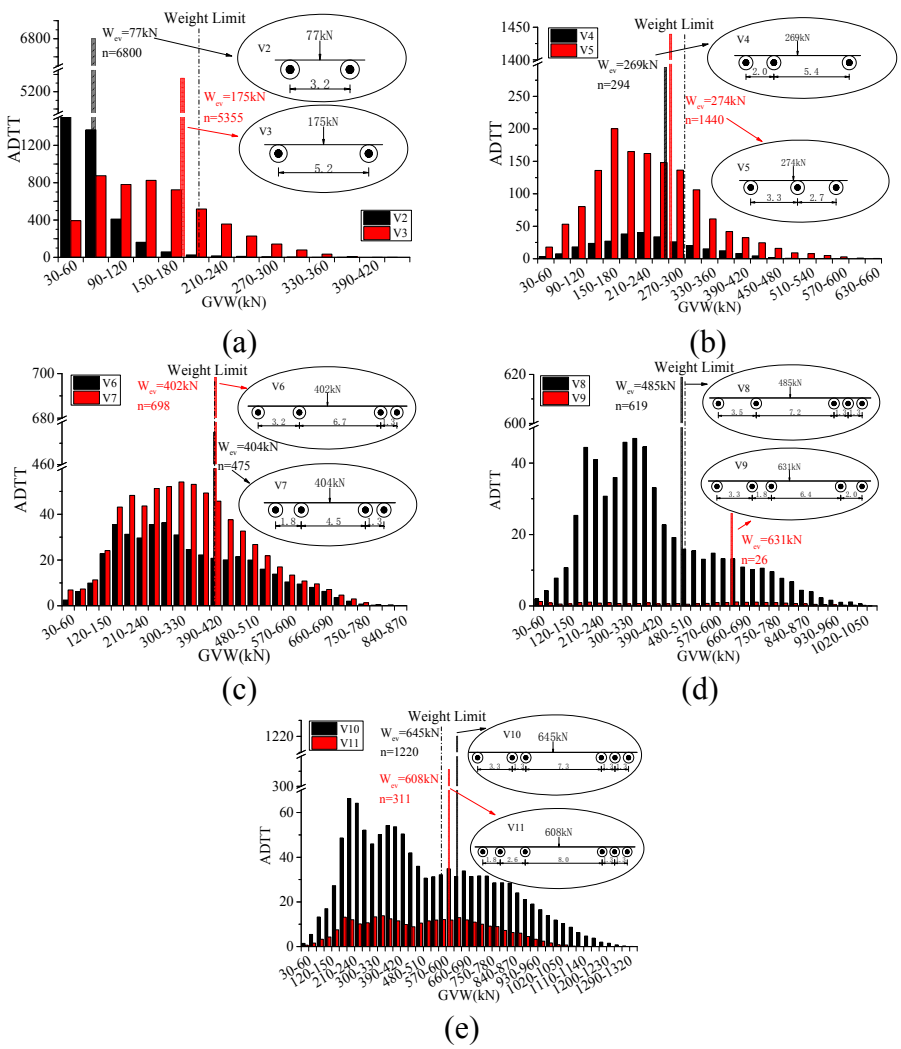

Fig. 5. Gross vehicle weight (kN) and axle spacing(m) of representative vehicles: (a) V2 and V3 ; (b) V4 and V5; (c) V6 and V7; (d) V8 and V9; (e) V10 and V11

Trucks operating with a weight above the legal limit are referred to as overloads or overweight loads, their weights and sizes have been regulated in some jurisdictions of the China. According to ministry of transport of the People's republic of China, a clear weight limits were set as in Table 3. The truck overloading were very serious, the average gross vehicle weight were all exceed the corresponding weight limit, and the maximum gross vehicle weight was even twice more than the weight limit. The maximum overloaded rate of V9 model reached 69.2%, even the 2-axle representative vehicle model V3 had 29% of the overloaded rate. The average GVW and maximum GVW were respectively 208kN and 445kN of the minimum model V2, that indeed equal to the AASHTO LRFD fatigue vehicle. So it's unreasonable to neglect two-axle trucks at overloaded situation for AASHTO LRFD. For the maximum equivalent GVW of six-axle trucks, the overloaded rate was above 65%. The maximum GVW of more than 3-axle truck models were significantly more than 550kN of the largest weight limit, particularly the 5-axle truck and 6-axle truck were all over 1000kN, and the maximum GVW was reached 1325kN of V10 model, about 2.4 times more than the weight limit. The gross vehicle weight and axle weight must be comprehensively taken into account in bridge fatigue evaluation, especially the heavy freight transportation highway with high fraction of the trucks of overweight gross weight and axle weight.

Table 3. Overloaded vehicles statistic

Model	Weight Limit (kN)	Number	Overloaded Rate (%)	Maximum GVW (kN)	Average GVW(kN)
V2	200	191	1.5	445	208
V3	200	1571	29.0	412	221
V4	300	138	46.5	595	304
V5	300	455	31.5	656	335
V6	400	211	44.3	846	482
V7	400	338	47.9	851	470
V8	500	287	46.4	1071	567
V9	500	18	69.2	1032	656
V10	550	800	65.6	1325	679
V11	550	211	67.8	1292	651

3.3. Axle weight (AW)

As the influence line is short for fatigue details of orthotropic steel deck, a truck passing may produce repeatedly stress cycles, that's mean the number of stress cycle is depend on the axle number. Meanwhile the stress range is directly related to axle load. The equivalent axle weight is explained as:

$$A_{ej}=[\sum f_i(A_{ij})^3]^{1/3} \tag{3}$$

where A_{ej} is equivalent axle weight of jth axle, f_i is frequency of occurrence of ith truck with axle weight of A_{ij}, A_{ij} is j^{th} axle weight of ith truck. The axle weight distribution and its equivalent axle weight of representative vehicle were plotted in Fig.6. By compare with the AASHTO LRFD fatigue model HS-15 with 26kN of front axle and 54kN of the others, most equivalent axle

weight of fatigue truck models were significantly high, that the maximum axle weight was 155kN for the second axle of V8. Even for the rear axle of 2-axle truck V3 was reached 121kN. This further illustrated that the fatigue damage introduced by 2-axle truck shouldn't be neglected, it's not comprehensive to just consider the trucks with more than 3-axle trucks at the overloaded condition, which defined by AASHTO LRFD. In addition, the individual axle weight of axle-group was basically identical, which the difference was not greater than 10kN. Therefore, the equivalent axle load could be proportional distributed according to the distribution proportion of vehicle axle weight.

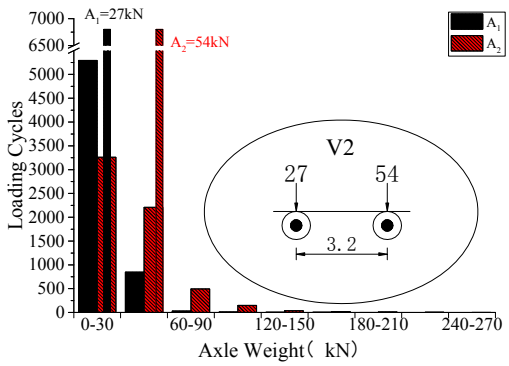

(a)

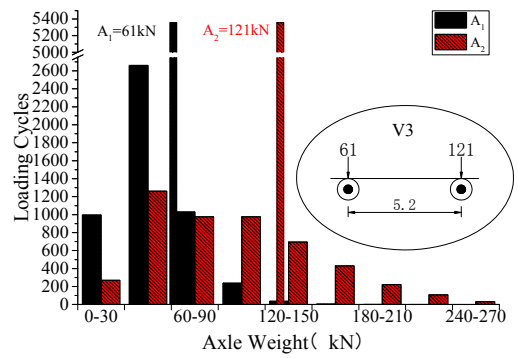

(b)

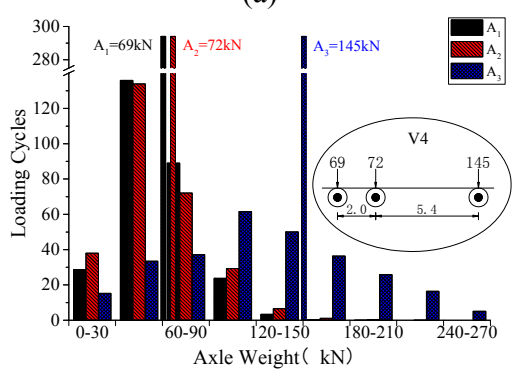

(c)

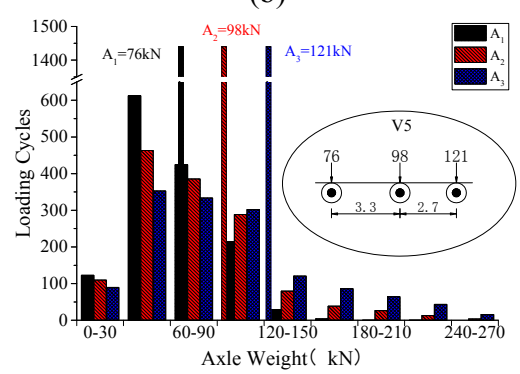

(d)

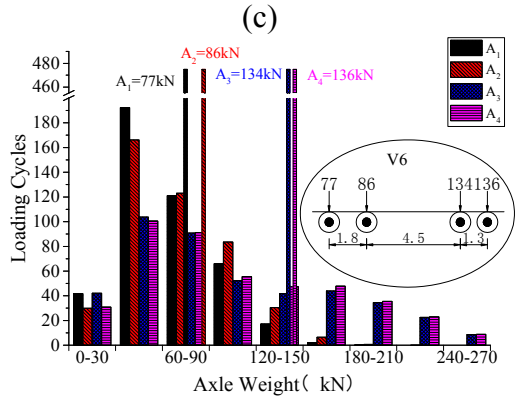

(e)

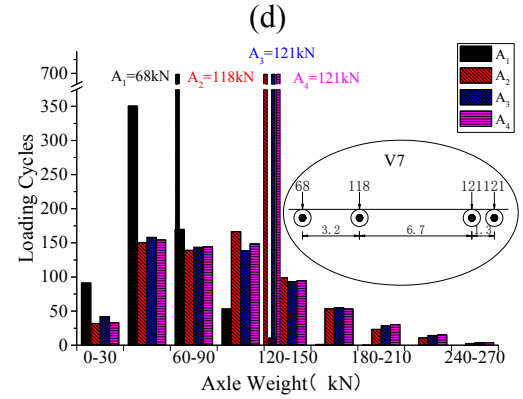

(f)

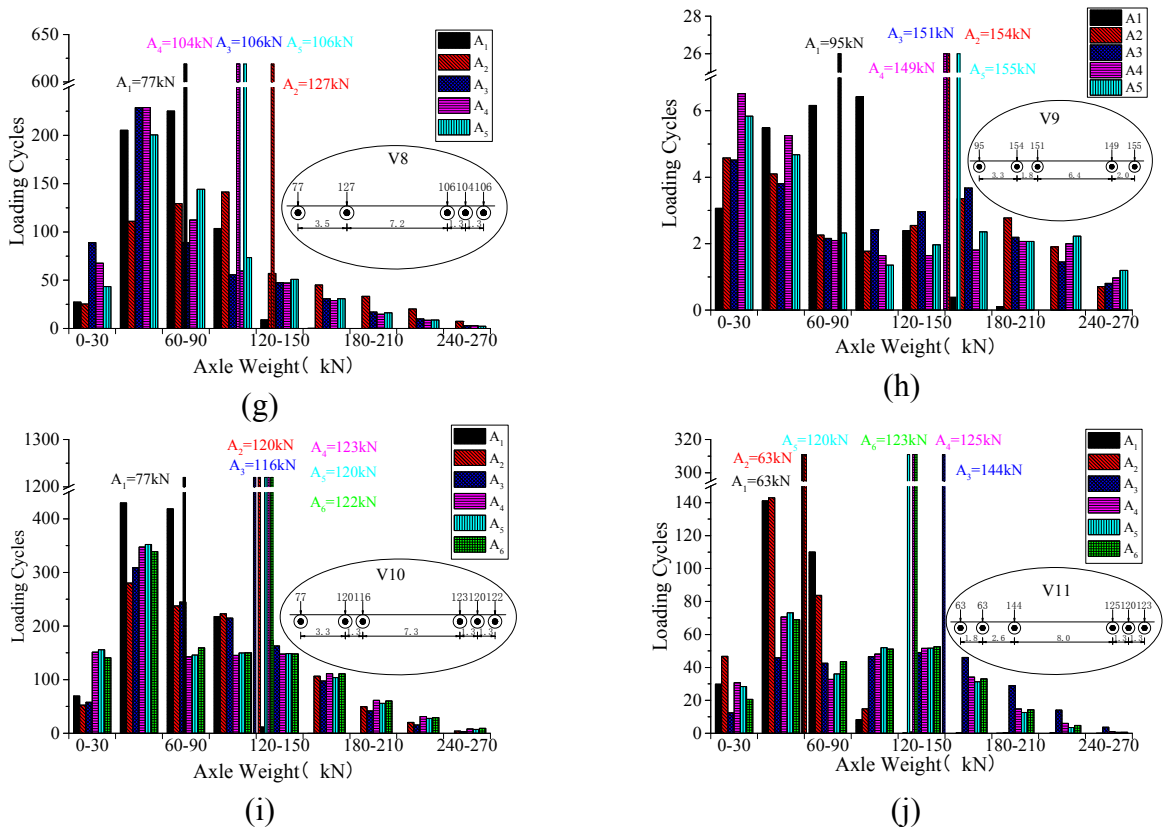

Fig. 6. Axle weight (kN) distribution and equivalent axle weight (kN) of representative vehicles: (a) V2; (b) V3; (c) V4; (d) V5; (e) V6; (f) V7; (g) V8; (h) V9; (i) V10; (j) V11

3.4. Vehicle distribution

The truck passage concentrates on part of lanes would generally characterized by non-uniform distribution, thus may cause fatigue cracking concentrated on these heavy traffic concentrates lanes, it's necessary to study the vehicle load spectrum of bridge along the lateral distribution characteristics. In this paper, five traffic lanes were arranged on the deck, including the overtake lane, fast speed lane, two heavy traffic lane and high speed lane, from left to right in Fig. 2(b). Table.4 shows the vehicle lateral distribution, which out bracket number is vehicles account for the total traffic, and in bracket number is vehicles account for the corresponding considered type. V1 was mainly driving on lane 1 and lane 5, while V2 was mainly distributed on lane 1 and lane 3. More than 2-axle trucks with heavy gross vehicle weight mainly driving on lane 3 and lane 4, particularly the lane 3 was the most heavy traffic lane. It was note that although the V3 model was 2-axle truck, as its serious overloaded that couldn't be ignored on fatigue evaluation.

3.5. Axle weight distribution

Axle load distribution along lanes directly reflects the load intensity and load density. Fig. 7 shows the axle weight distribution based on vehicle spectrum listed in Table 4, and the corresponding equivalent axle weight is calculate according to Equation 3. As vehicle weight

less than 30kN of model V1 and model V2 were mainly driving on lane 1 and lane 5, the corresponding equivalent axle weight were small, that lane 1 was 31kN and lane 2 was 9kN.

Table 4. Vehicle distribution on lanes

Model	Lane 1		Lane 2		Lane 3		Lane 4		Lane 5		One-direction vehicle	
	Number	Rate	Number	Rate	Number	Rate	Number	Rate	Number	Rate	Number	Rate
V1	6102	13.5(28.0)	1481	3.3(6.8)	2441	5.4(11.2)	2047	4.5(9.4)	9738	21.6(44.7)	21809	48.4
V2	4802	10.7(37.7)	1179	2.6(9.3)	2988	6.6(23.5)	1782	4.0(14.0)	1990	4.4 (15.6)	12740	28.3
V3	196	0.4(3.6)	387	0.9(7.2)	3064	6.8(56.6)	1748	3.9(32.3)	21	0(0.4)	5416	12.0
V4	12	0(3.9)	18	0(5.9)	173	0.4(58.4)	94	0.2(31.5)	1	0(0.3)	297	0.7
V5	63	0.1(4.3)	345	0.8(23.9)	633	1.4(43.8)	401	0.9(27.7)	4	0(0.3)	1445	3.2
V6	17	0(3.5)	67	0.1(14.0)	230	0.5(48.3)	162	0.4(34.1)	1	0(0.1)	476	1.1
V7	18	0(2.6)	47	0.1(6.6)	398	0.9(56.4)	242	0.5(34.3)	2	0(0.2)	705	1.6
V8	12	0(1.9)	42	0.1(6.7)	342	0.8(55.3)	223	0.5(36.0)	0	0(0)	619	1.4
V9	1	0(4.5)	3	0(12.1)	12	0(12.1)	9	0(34.9)	0	0(1.4)	26	0.1
V10	57	0.1(4.6)	157	0.3(12.8)	628	1.4(51.4)	377	0.8(30.9)	2	0(0.2)	1220	2.7
V11	19	0(6.3)	29	0.1(9.2)	172	0.4(55.2)	91	0.2(29.1)	1	0(0.2)	311	0.7
V2~V11	5196	11.5(22.3)	2272	5.0(9.8)	8640	19.2(37.2)	5127	11.4(22.0)	2021	4.5(8.7)	23256	51.6
V3~V11	394	0.9(3.7)	1094	2.4(10.4)	5652	12.5(53.7)	3345	7.4(31.8)	31	0.1(0.3)	10516	23.3
total	11298	25.1	3754	8.3	11081	24.6	7174	12.9	11759	26.1	45065	100

The heavy trucks of V3~V11 were mainly distributed on lane 3 and lane 4, the corresponding equivalent axle weight reached above 90kN. Otherwise that the loading cycles of lane 3 was 28463, and 18180 loading cycles for lane 4. It's demonstrated that axle loading cycles were significantly large on the highway, and concentrated on part of the lanes. It's extremely disadvantage to the fatigue life of steel bridges, particularly the orthotropic steel bridge deck.

4. Fatigue truck models

4.1. One-direction fatigue truck model

A one-direction fatigue truck model has been developed based on the gross vehicle weight, axle spacing, and vehicle lateral distribution. The damage accumulation of representative vehicle models were studied to determine the appropriate number of axles and axle spacing for the standard fatigue truck model. The Palmgren–Miner's rule (Federal Highway Administration 2015) is one of the most widely used fatigue damage accumulation models. It assumes a linear damage accumulation and neglects sequence and mean stress effects. Therefore, the fatigue damage of each stress cycle induced by vehicles is independent. Based on Miner's rule, the fatigue damage contribution *Di* is equal to the damage caused by each represented truck models to the summation damage of all truck models, as shown in Equation 4:

$$D_i = r_i W_{ei}^{\ 3} / \sum r_i W_{ei}^{\ 3} \tag{4}$$

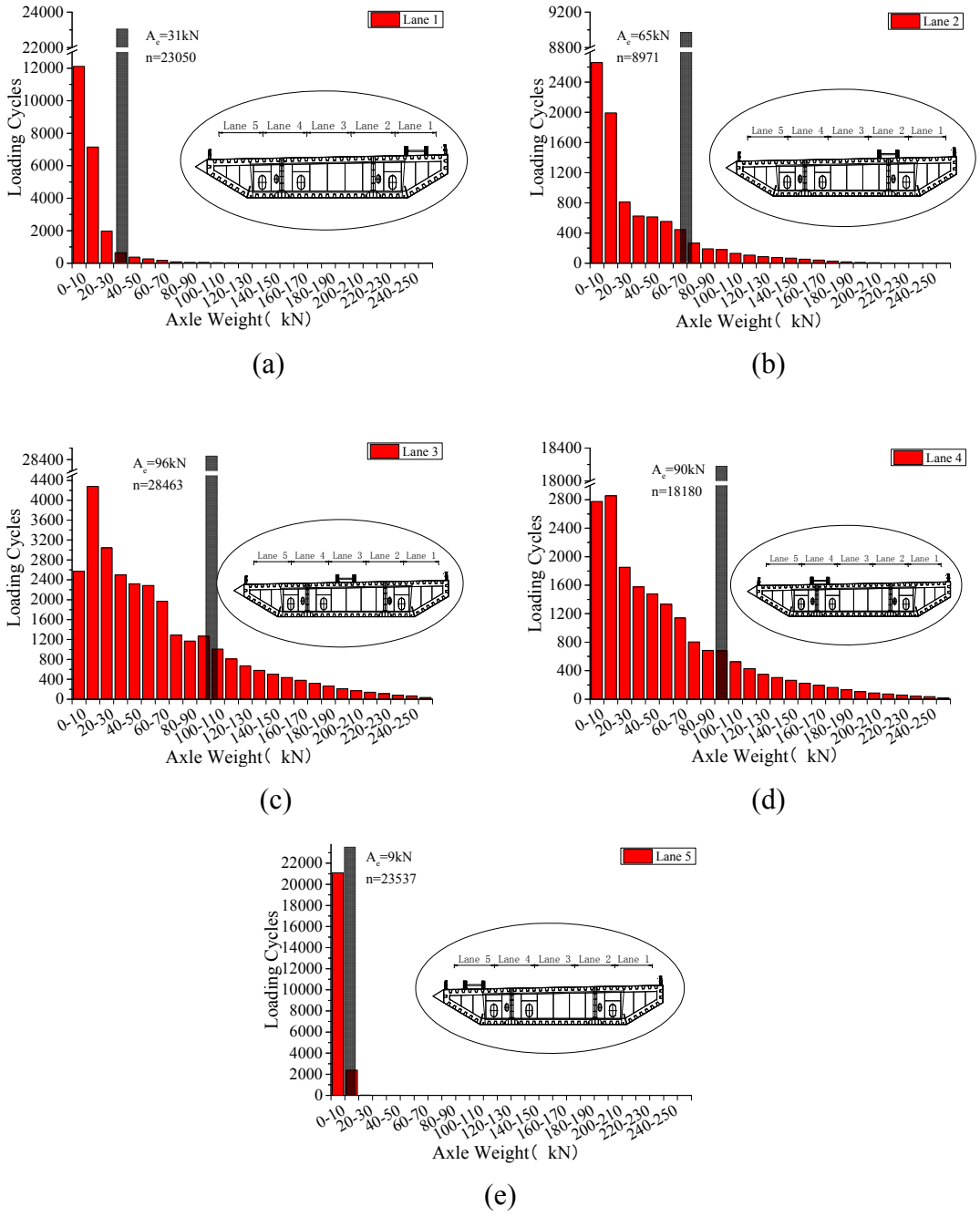

Fig. 7. Axle weight distribution (kN) and equivalent axle weight (kN) on each lane: (a) Lane 1; (b) Lane 2; (c) Lane 3;(d) Lane 4;(e) Lane 5

where *Di* is fatigue damage contribution of ith represented truck model; r_i is the occurrence rate of this represented truck model, and W_{ei} is corresponding equivalent GVW. Table.5 shows the represented truck models' fatigue damage contribution of one-direction vehicular spectrum. Fatigue damage contribution is significantly affected by the gross vehicle weight rather than the

occurrence frequency of the represented truck models. The largest fatigue damage contribution was 53% which induced by 6-axle truck of V10; then followed about 11% by V8 and V11. Although the V2 model occupy about 40% of the one-direction traffic, but the fatigue damage contribution was only 0.5% as its light gross weight. However the daily traffic of V3 was the same as V2, the fatigue damage contribution reached 4.6% as its GVW was 175kN. It's further demonstrated that the 2-axle truck with overloaded condition shouldn't be ignored. The largest fatigue loading contribution truck model of V10 was used as the prototype to evaluate the standard and simplified standard fatigue truck models in this paper.

Table 5. One-direction vehicular spectrum and fatigue loading contribution rate

Model	GVW(kN)	Number	One-direction vehicle spectrum (%)	
			Rate	fatigue Contribution rate
V2	7.7	6800	39.4	0.5
V3	17.5	5355	31.1	4.6
V4	26.9	294	1.7	0.9
V5	27.4	1440	8.4	4.8
V6	40.4	475	2.8	5.1
V7	40.2	698	4.0	7.3
V8	48.5	619	3.6	11.4
V9	63.1	26	0.2	1.1
V10	64.5	1220	7.1	53.0
V11	60.8	311	1.8	11.3

When a truck passed, for directly bearing components, such as rib-deck welding, diaphragm-deck welding and so on, would produce repeatedly stress cycles, that's means each axle would respectively produce a stress cycle, even the closely arranged axles of axle-group. The standard fatigue truck model should be applied to these details. Based on the vehicle load spectrum, the equivalent gross vehicle weight of the recommended standard fatigue truck model was acquired from Equation 2, then it was proportional assigned to axle according to the prototype. It's a 6-axle truck with single front axle, mid two-axle group and rear three-axle group. As the approximately single axle weight of the axle-group, the single axle weight of axle-group was adjust to the same for the sake of convenient application, as shown in Fig. 8(a), and the standard fatigue truck (HS-15) in AASHTO LRFD was also shown in Fig. 8(b). The simplified standard fatigue truck model should be applied to main bearing components or details far away from the directly loading components. The simplified method was coupling the axle-group into one axle, and the combined axle was located in the center of axle-group according to the AASHTO LRFD, as shown in Fig.9.

The front axle weight and mid axle-group weight of the suggested standard fatigue truck model were almost the same as AASHTO LRFD fatigue truck. Although the single axle weight was the same as the code defined, the rear axle-group was comprised of three axles in this paper, the rear axle of simplified fatigue truck model was reached 177kN, that significantly greater than 108kN of the AASHTO LRFD defined. Otherwise, the gross vehicle weight of the fatigue truck model was 330kN in this paper, also significantly greater than 242kN of the AASHTO LRFD defined.

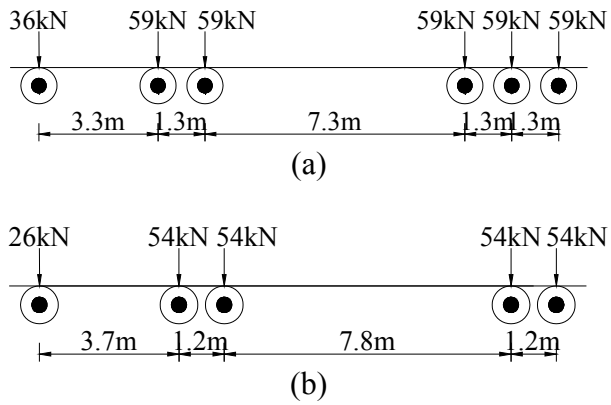

Fig. 8. Suggested one way standard fatigue truck model in comparison with AASHTO standard fatigue truck: (a) Suggested one way standard fatigue truck model; (b) AASHTO standard fatigue truck

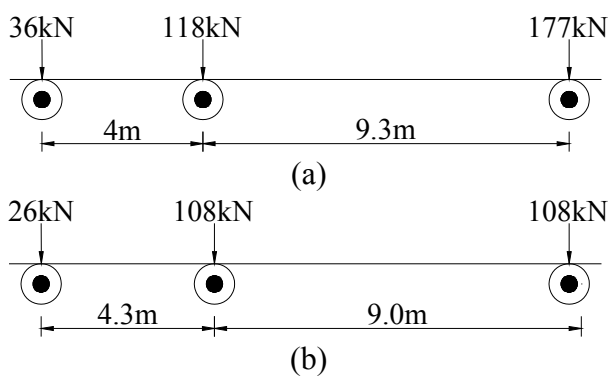

Fig. 9. Suggested one way simplified fatigue track models in comparison with AASHTO simplified fatigue truck: (a) Suggested one way simplified fatigue truck model; (b) AASHTO simplified fatigue truck

4.2. Fatigue truck model on heavy lane 3

A truck is defined as any vehicle with more than either two axles or four wheels as AASHTO LRFD defined. The average daily traffic, including all vehicles, i.e., cars and trucks, is physically limited to about 20000 vehicles per lane per day under normal conditions. The average daily truck traffic can be determined by multiplying the average daily traffic by the fraction of trucks in the traffic. However the truck passage concentrates on part of the lanes would be generally characterized by non-uniform distribution, as the stress influence line is short for orthotropic steel bridge deck, which may cause fatigue cracking concentrated on these heavy traffic concentrated lanes. As stated above that a high fraction of the trucks passage concentrated on part of the lanes with overweight gross weight and axle weight, particularly the lane 3 was the most heavy traffic lane. The fatigue truck model on heavy traffic lane 3 was presented to reasonable estimate the fatigue life of details at this orthotropic steel bridge, as shown in Fig. 10. It's shown that the fatigue truck models on heavy traffic lane have the same axle spacing as the one-direction fatigue truck model but much heavier, and also 1.5 times heavier than AASHTO

fatigue truck, that the gross vehicle weight was reached 365kN. This further demonstrates that the number of average daily truck passage was significantly large on heavy traffic lane, and concentrated on part of the lanes.

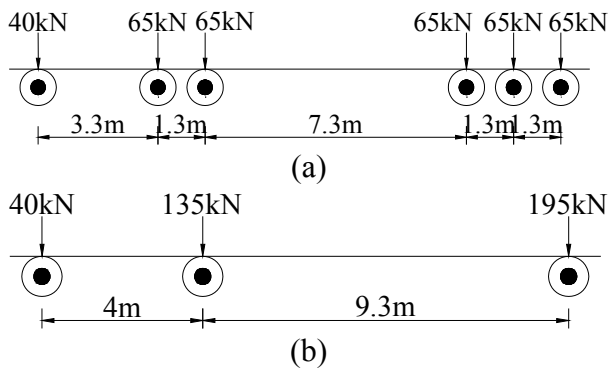

Fig. 10. Suggested fatigue truck models on heavy traffic lane: (a) Standard fatigue truck; (b) Simplified fatigue truck

5. Stress responses at diaphragm cutout

5.1. Finite-element models

For the purpose of investigating the diaphragm cutout cracking at this orthotropic steel bridge on heavy traffic lane, the finite element model of the partial orthotropic steel bridge girder system and sub-model of its deck system were created with linear elastic shell elements using a general purpose FE software ANSYS. The girder model was based on the actual dimension between three hanger sections at mid span in the longitudinal bridge direction, and total length was 24m. The coordinate origin was located at center of north base plate, and the X axis was pointed to the bridge transverse of east(E) direction, and the Y axis was pointed to the bridge vertical upward, as well as Z axis was coincidence with the bridge longitudinal of south(S) direction, as shown in Fig. 11. The translations of X- and Z-axis were constrained at the northern girder section of Z=0, as well as the translation of X-axis was constrained on the longitudinal end (Z=24) to simulate the continuous girder sections. The hangers were simulated as elastic supporters. The boundary conditions used in the girder model were only an approximation of the actual boundaries. However, as the deck system selected in this study were located at mid of the girder model, according to Saint-Venant's principle, the approximation of the boundary conditions was precise enough for the FEM to calculate the stresses around diaphragm cutout. Because the girder model was huge, it was cost too much as adopting fine-mesh division and considering the multiple step load conditions, and also could affect the accuracy of simulation results. Therefore, it was reasonable to construct a smaller sub-model to acquire stress responses of interested details. The aim of the girder model was providing the corresponding boundary conditions for sub-model.

As mentioned above, a high resolution fine-meshed sub-model was adopting to capture the stress response of the structure details. This sub-model was intercepted from mid of girder model on west wheel track line on the heavy lane 3, the sub-model was comprised of 12m length deck plate and four ribs, as well as three diaphragms and corresponding level stiffeners. The sub-model was mapping meshed and a 1mm mesh size element was adopted around 20mm of cutout

to capture the stress distribution around it. Coordinate system origin was moved to northern center of the deck plate for sub-model, and the axis was coincidence with the girder model. The loading conditions were simulated as vehicle moving from north (N) to south (S). The ribs were defined as R17 to R20 from east(E) to west(W), as shown in Fig. 11.

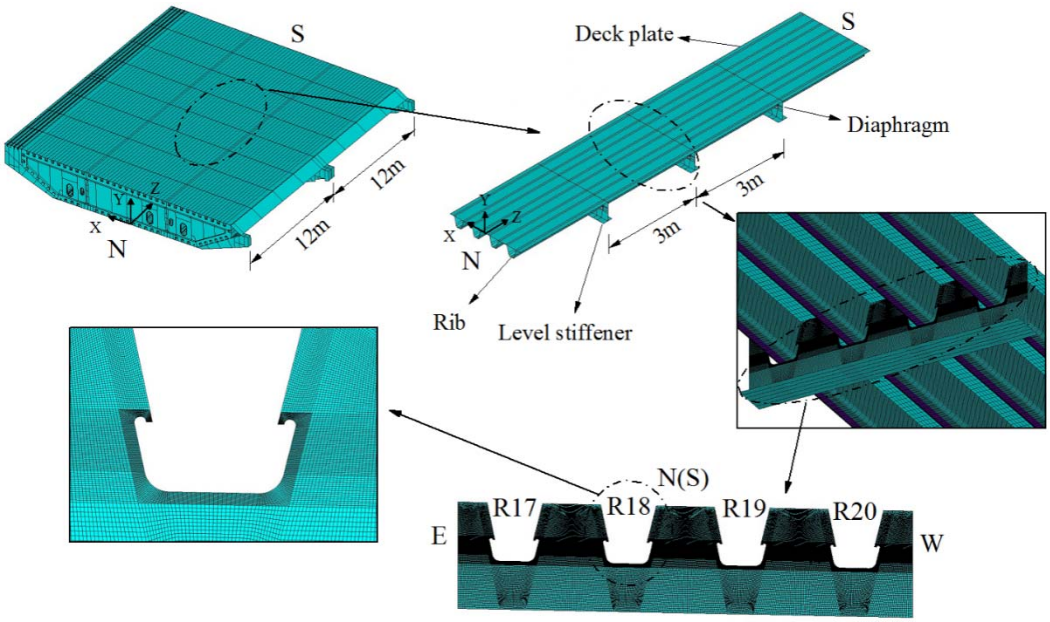

Fig. 11. FEM models

5.2 Loading conditions

As discussed above, the number of average daily truck traffic was significantly large on the roadway, and the truck passage was concentrated on part of the lanes. On the other hand that the local effect was significantly on orthotropic deck, for more reasonable fatigue evaluation of diaphragm cutout, the suggested fatigue truck models on heavy traffic lane as shown in Fig. 10 was used in this paper, its average daily truck traffic was 8045. The AASHTO specifications for the design load of truck load which distributes uniformly over an area of 510×250 mm in the transverse and longitudinal directions. However, considering the possible load distribution of the wearing surface, the effective wheel load area was modified to 610×360mm, as the wearing surface was 50mm thick and a load distribution angle of 45° was considered, as shown in Fig.12(a). For the purpose of investigating the sensitivity of stresses around the cutout in the transverse loading position, 19 transverse load cases were applied, as the Fig.12(b) shows the loading position varying in the transverse direction from the rib-deck welding of R20-E to the rib-deck welding of R17-W. The moving distance was 50mm, and the distance *d* in Fig.12(b) refers to the distance from the center of the wheel load to the coordinate origin of sub-model. Based on the transverse influence lines, three critical driving paths were examined for the stress response around the cutout, i.e., the over-rib wall (LC4), the riding-rib wall (LC7) and in-

between-rib wall(LC10), as shown in Fig. 14. 80 load cases were applied along the longitudinal direction to simulate the movement of the wheel load along the 19 driving paths, forming an array of load cases of 80×19 to simulate the moving of truck wheels. The movement of the longitudinal direction was 120mm. From these longitudinal influence lines it could be obtained that the stress-sensitive length of the driving paths by passage of a wheel load was less than 6m, since the axle-group spaces of suggested fatigue truck model in this paper were 4m and 9.3m, in addition that the front axle is lightweight, that the axle-groups have no little effect on each other. Therefore, it was appropriate to adopt the separately axle-group of the fatigue truck for loading cases. The distance *l* in Fig.12(c) refers to the distance from the center of the axle-group to the coordinate origin of sub-model. When the longitudinal condition number *j*=16,41,66, the center of the axle-group was above the diaphragm. In addition that 15% impact coefficient is considered for wheel load.

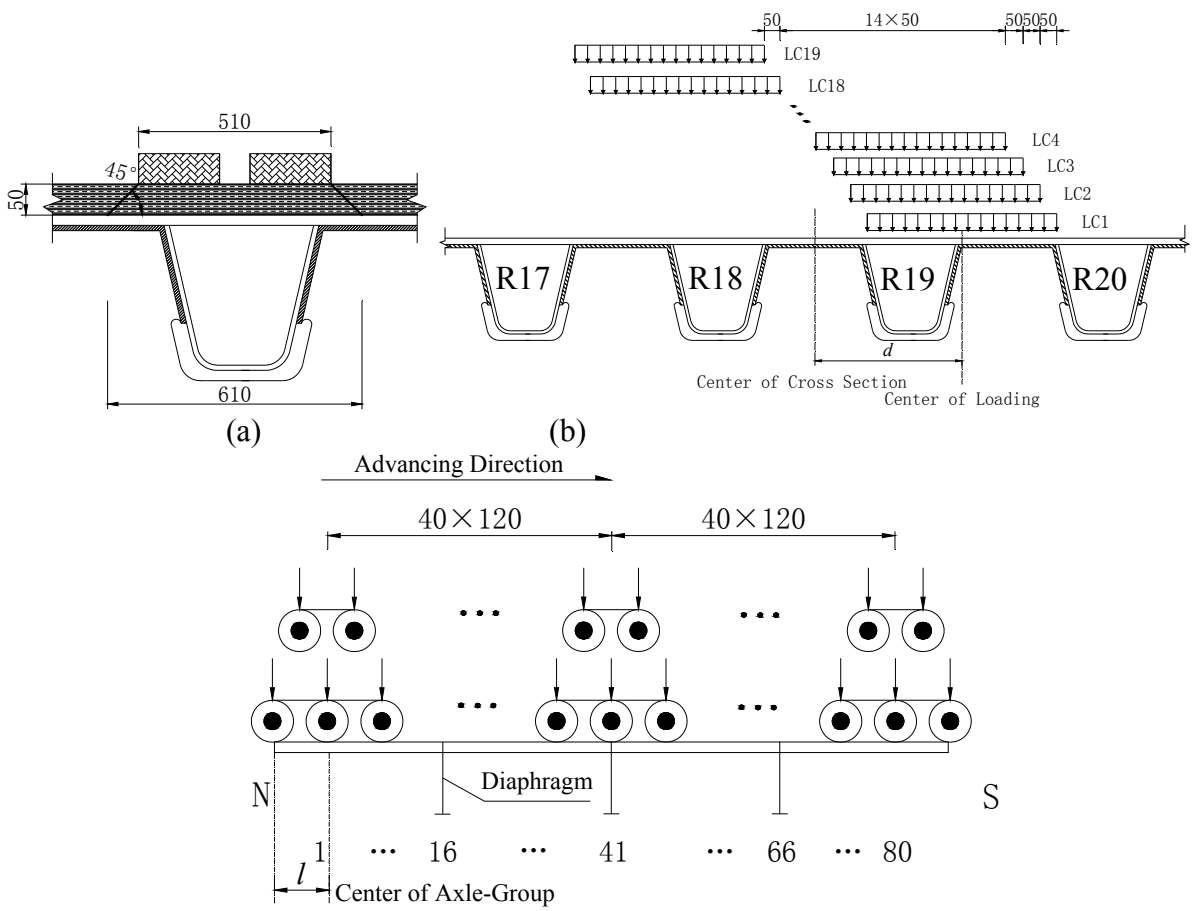

Fig.12. Loading conditions (Unit: mm):(a) Wheel loading;(b) Transverse loading conditions;(c) Longitudinal loading conditions

4.3 Stress Influence surface

The nominal stress approach, hot-spot stress approach and notch stress approach (Federal Highway Administration 2015) were commonly used in steel bridge fatigue analysis. The

corresponding fatigue strength S-N curves and detail categories were defined in each approach. Among them, the AASHTO LRFD specification defined 8 S-N curves to characterize the fatigue strength of structure details in nominal stress approach. However the nominal stress position at cutout is not clearly defined, as an obvious stress concentration was exist at cutout. The researchers generally extract stress at 5mm or 6 mm away from the cutout free edge as the nominal stress. This paper adopted the nominal stress approach to evaluate the fatigue life of diaphragm cutout according to the AASHTO LRFD specification.

The cutout cracking usually initiated between R18 and R19, the R19-E side to be more serious for more exactly. Due to the limited space, the article mainly focuses on the cutout of R19-E, extract stresses around its cutout using the nominal stress approach. Fig. 13 shows the stress response surfaces under individual axle-group loading condition of standard fatigue truck model. It could be shown that the stress response of rear 3-axle group and mid 2-axle group were relatively similar in the same location, as more lightweight of the 2-axle group, the stress response of the 2-axle group was about 18% smaller than the 3-axle group. The most unfavorable condition was LC7 in transverse while *j*=37 in longitudinal, e.t., the center of axle group was 45cm far away from the diaphragm as riding-rib wall condition. It concluded that the local effect was significantly on orthotropic deck, transverse and longitudinal stress influence line were short, which were in two ribs and between two diaphragms respectively, and stress response of cutout was sensitive to wheel load position

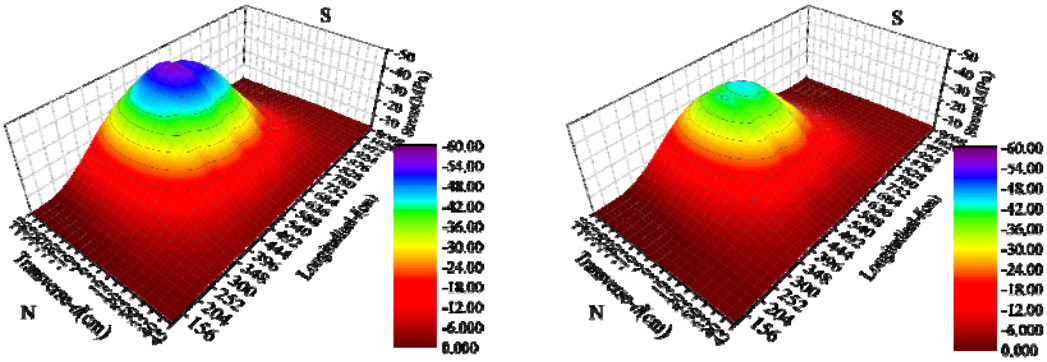

(a) (b)

Fig. 13. Stress response surface under standard fatigue truck model: (a)Rear 3-axle group; (b)Mid 2-axle group

4.4 Transverse stress response

Due to the similar stress response surface of the rear 3-axle group and the mid 2-axle group, as larger stress of the 3-axle group, it's only list the 3-axle group loading results to save space in the following passage. Cutout stresses of rib R18 and rib R19 were extracted at longitudinal unfavorable condition *j*=37, e.t., R18-E, R18-W, R19-E and R19-W, the Fig. 14 shows the north stresses of these four locations. The maximum stress was -56.7MPa while the wheel load was riding-rib wall acting on the corresponding ribs. It can be seen that the transverse influence line was actually short for cutout, which were between two ribs. Once the wheel load act from one rib to another, the stress would decrease largely, and closed to zero while across two ribs.

Consequently, it's suggested that offset lane separator lines should alleviate fatigue crack propagation in the event of crack initiation.

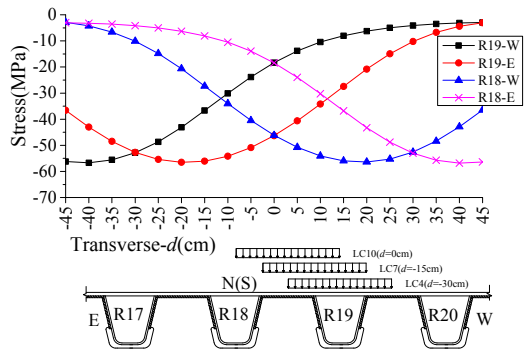

Fig. 14. Transverse stress responses in 3-axles loading

4.5 Longitudinal influence line

Cutout stresses of rib R18 and rib R19, e.t., R18-E, R18-W, R19-E and R19-W, were extracted at transverse unfavorable condition LC7, the Fig. 15 shows the north stresses of these four locations. The axle-group only produced one primary stress range, indicated that the stress response of diaphragm cutout could only identify axle-group, instead of individual axles of the axle-group. It could be found that the longitudinal influence line was actually short for cutout, which equals to the distance between two diaphragms. The distance between mid-axle group and rear-axle group of the suggested standard fatigue truck model was 9.3m, that could respectively produce one primary stress range. As lightweight of the front axle but short distance away from the mid-axle group, that had little effect on the stress range, which could be neglected. These indicated that the standard fatigue truck model should produce 2 or 3 stress ranges at diaphragm cutout. The stress response of cutout was sensitive to the axle load location, even though the cutout at both side of one rib should produce different response stress, e.t., the R19-E and R19-W were -56.1MPa and -36.7MPa respectively, with difference of 34.6%. This may be the result of distortion of the rib around the diaphragm. In addition, the stress was directly dependent on the ribs participation, e.t., the rib R18 wasn't directly undertake the wheel load, the stress was only -27.5MPa at the cutout of R18-W, which 51% smaller than the R19-E. Meanwhile the stress was only -8.1MPa at another side of R18. This indicated that the local effect was significant on orthotropic steel bridge deck.

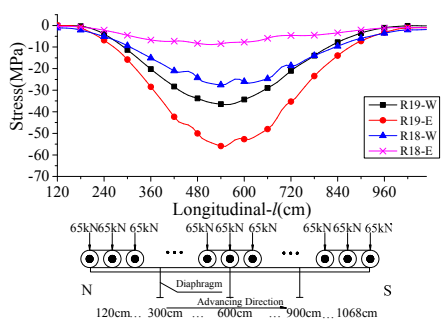

Fig. 15. Stress longitudinal influence line

4.6 Stress distribution around cutout

For steel bridge, the fatigue crack was usually initiated at the stress concentrated location, regardless the stress concentration was due to the geometry or the internal defects of structural details. As for the steel bridge, the stress concentration of structure details was the core issue of fatigue cracking. The fine-meshed sub-model was adopted to capture the stress response around the cutout in this paper, as shown in Fig. 16. From the stress response of the cutout within 20mm, it can be seen that the cutout was in compressive stress. This was mainly due to the effect of vertical compressive stress induced by the wheel load, and it was also in compressive zone above the neutral axis of the diaphragm plate web, so the cutout was in bi-directional compression. There was an obvious stress concentration at cutout as shown in Fig.17, and a significant nonlinear stress occurred there. The stress was showed linear attenuation trend after about 10 mm away from the free edge of cutout.

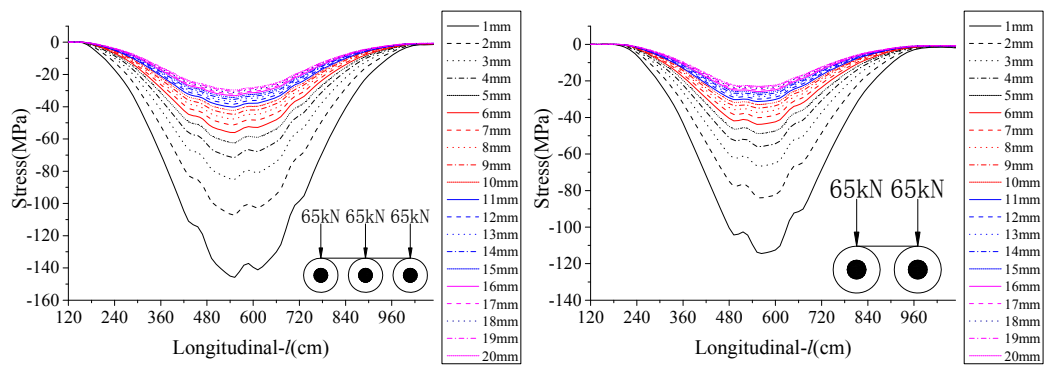

Fig. 16. Stress responses of the cutout

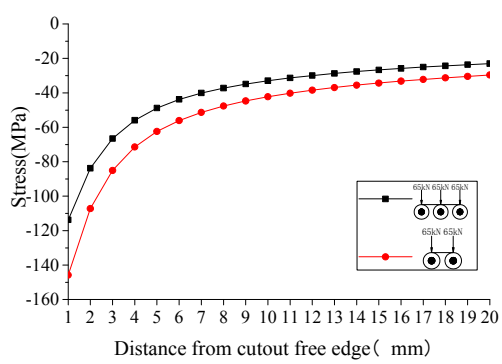

Fig. 17. Stress distribution of the cutout

Fig. 18 shows the stress and deformation contour around cutout, the local effect of diaphragm was significant under the wheel load, and an obvious stress concentration was exist at the minimum net section of cutout. As the rib R19 was directly undertake the wheel load, that its bending deformation happened induced an out-of-plane deformation of diaphragm. Meanwhile the rib rotation causes a larger stress of R19-E. The deformation of diaphragm cutout was quite complicated, an out-of-plane stress was the most prominent as it was directly connected the rib web, and restricted by the diaphragm at the same time, they both work together to form the shear

deformation at the stress concentration location. The further explicit detail was shown in Fig.19, the maximum principal stress direction at the stress concentration location was shown an angle of about 67° to the horizontal direction, the other condition were the same, that means the crack initiation would show an angle of about 23° to the horizontal direction, and propagate to the nearby rib along the path. This was coincidence with the actually cracking at cutout as shown in Fig. 1.

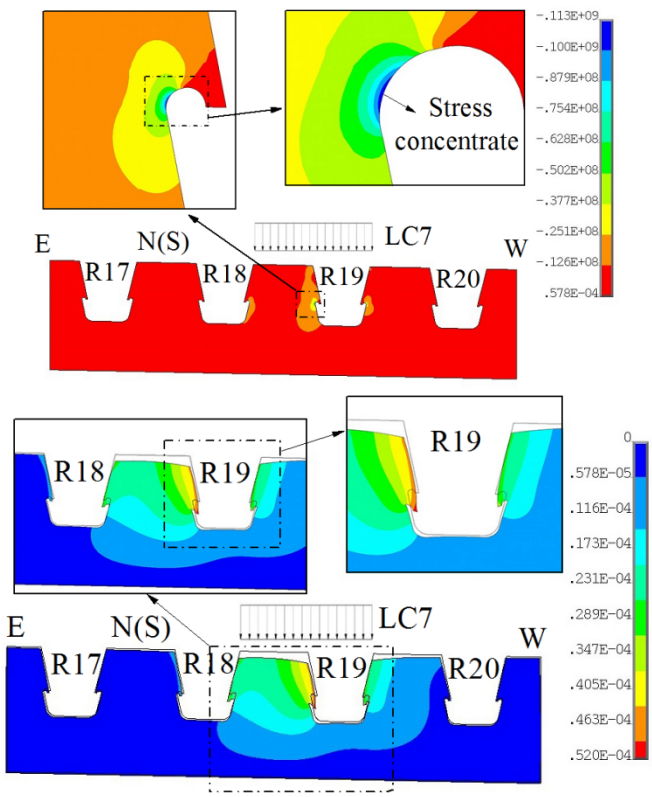

Fig. 18. Stress and deformation contour around cutout

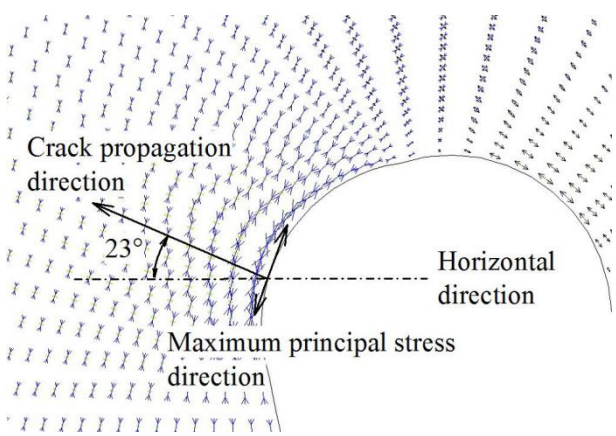

Fig. 19. Principal stress direction around cutout

4.7. Stress responses in different diaphragm

The thin diaphragm plate web due to the inappropriate structure detail designed at early construction of orthotropic steel bridge deck, the hanger diaphragm and other inner diaphragm between hangers were 12mm and 10mm respectively. The Fig.20 shows the stress comparison of the two type diaphragm at most unfavorable condition. It could be seen that the stress response shapes were the same for these two diaphragms, with difference about 14%, e.t., the stress peak of hanger diaphragm was -56.1MPa, while the stress peak of inner diaphragm was -64.9MPa. It's thus clear that the thinner diaphragm would decrease the cutout stress

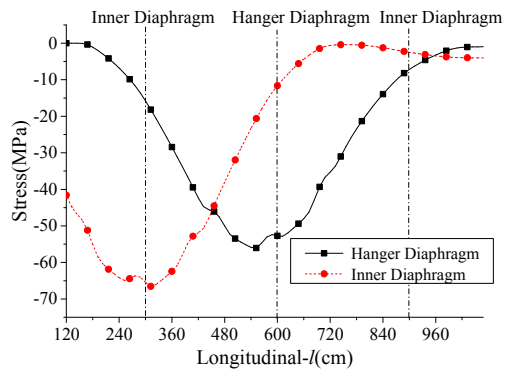

Fig. 20. Stress responses of different thickness diaphragms

4.8. In-plane stress and Out-of-plane stress

As discussed above that an out-of-plane stress was exist at diaphragm cutout. The out-of-plane stress can be explicit as Equation 6, since the north and south stress of the diaphragm cutout were extracted from the element at both sides.

$$\begin{cases} \sigma_{in\text{-}plane} = (\sigma_N + \sigma_S)/2 \\ \sigma_{out\text{-}of\text{-}plane} = (\sigma_N - \sigma_S)/2 \end{cases} \quad (6)$$

where the σ_N and σ_S were the stresses at north face and south face of diaphragm respectively. The Fig.21 shows the in-plane stress and the out-of-plane stress at hanger diaphragm and inner diaphragm under the most unfavorable condition. It could be seen that the in-plane stress was dominated there, and reached the peak while the center of axle-group was just above the diaphragm, e.t., the in-plane stress peaks of hanger diaphragm and inner diaphragm were -54.4MPa and -66.8MPa respectively. The out-of-plane stress was small, and reached the peak while the center of axle-group was 120cm away from the diaphragm, e.t., the out-of-plane stress peaks of hanger diaphragm and inner diaphragm were about ±5.6MPa and ±4.7MPa, which account for about 16.5% and 10.4% respectively in total stresses. This indicated that the thicker diaphragm plate, the higher stress at cutout. Anyhow, the diaphragm cutout was controlled by in-plane deformation, increase the thickness of the diaphragm plate can effectively reduce the total stress at cutout, but the out-of-plane stress would increase relatively. In general, the out-of-plane deformation should not be the critical reason of cracking at cutout.

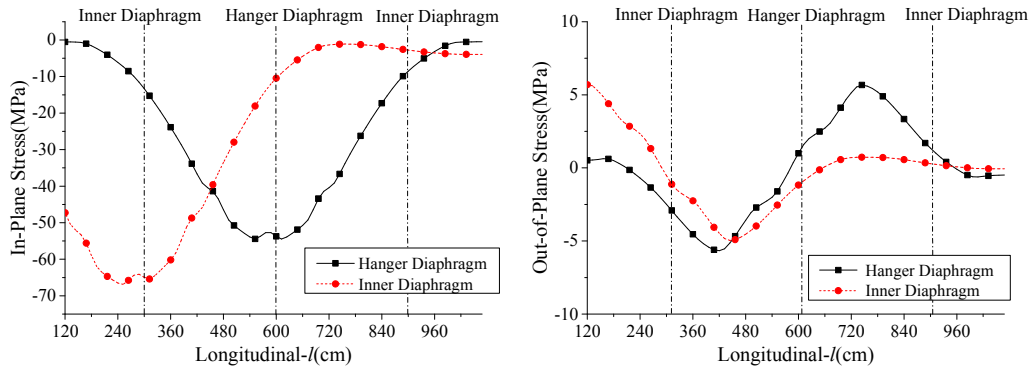

Fig. 21. In-/out-of-Stress of different diaphragms in 3-axles loading

5 Fatigue life assessment

The crack initiation phase is negligibly short in comparison with the crack propagation phase, and the fatigue life of cutout can be approximated by the propagation life of fatigue cracks. The crack propagation life is usually calculated with the Miner's rule (AASHTO 2010). In this study, the fatigue life of cutout was evaluated using the nominal stress approach, which was based on fatigue resistance Class A of the fatigue design S-N curves. However if the edge of cutout wasn't smooth well, the fatigue resistance Class A should degrade to Class B according to the AASHTO LRFD specification. As this early construction of this bridge, the edge of cutout somehow didn't smooth well, so the fatigue resistance Class A and Class B were both used to evaluation. The transverse location of the wheel load was also considered in the fatigue life evaluation (Zhou et al. 2015). A normal distribution with a standard deviation of 250mm was assumed for the transverse location of the wheel load. Three typical cases were considered for the mean location of truck wheels in relation to the three critical driving paths, i.e., the over-rib wall (LC4), the riding-rib wall (LC7) and in-between-rib wall (LC10), as shown in Fig.23. The average daily truck traffic (ADTT), 8045, on the transverse location i is ADTT$\cdot p_i$. The daily cumulative fatigue damage rate (D) is calculated as(Li et al. 2014; Hyong-Bo Sim et al. 2012):

$$D = \frac{ADTT}{C} \cdot \sum S_i^3 p_i \qquad (7)$$

where p_i is the relative frequency of the wheel load located at transverse location i; the C is the constant of the fatigue resistance according to the AASHTO LRFD specification; S_i is the stress range produced by the standard fatigue truck model on the transverse location i. The fatigue life (Y) is then calculated as

$$Y = \frac{1}{365 \cdot D} \qquad (8)$$

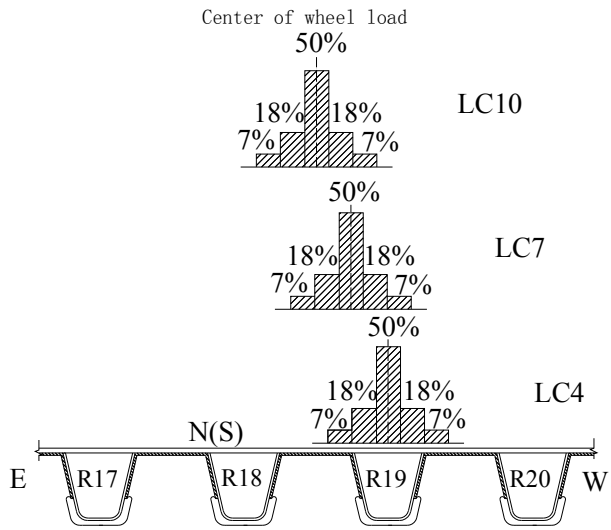

Fig. 22. Transverse distribution of truck wheels

The fatigue life of three typical cases are listed in Table 6, in which the Y_A and Y_B are fatigue life corresponding to the Class A and Class B respectively. It could be seen that the fatigue life were much shorter than the design life, that mainly because of significantly large average daily truck traffic and the remarkably high fraction of overweight truck passage at this bridge. As fatigue life was cubic proportional to stress range, suggested that the transfinite vehicle rectifying work should be strengthen. The fatigue life of the cutout was considerably decreased because of pool smooth edge. The fatigue life of cutout at the inner diaphragm was much shorter than the hanger diaphragm, this mainly because of the inner diaphragm was 10mm thick while the hanger diaphragm was 12mm. The most unfavorable case was LC7 that the fatigue life were only 7.8 years and 10.4 year at R19-E and R19-W, these were identical to the actually cracking time of this bridge. However the actually fatigue cracks were mainly concentrated between rib R18 and R19, speculated that the actual wheel load track should between LC7 and LC10, and the fatigue life were about 6 to 10 years according to the Class A and Class B, which were consistent with the actually crack initiated time and location. In addition, the fatigue life of R19-W and R18-E were much longer than the R19-E and R18-W, which further illustrate the local effect was remarkable at the orthotropic steel bridge deck.

Table 6. Fatigue life assessment (Unit: years)

Location / Condition		Hanger Diaphragm				Inner Diaphragm			
		R19-W	R19-E	R18-W	R18-E	R19-W	R19-E	R18-W	R18-E
LC4	Y_A	15.0	14.1	339.3	6572.4	9.1	8.5	183.5	4019.3
	Y_B	7.2	6.8	162.6	3149.9	4.3	4.1	87.9	1926.3
LC7	Y_A	32.1	13.0	58.6	851.6	10.4	7.8	33.9	520.4
	Y_B	15.3	6.2	28.1	408.2	9.3	3.7	16.2	249.4
LC10	Y_A	128.3	20.1	20.2	126.6	77.5	11.9	12.0	76.8
	Y_B	61.5	9.6	9.7	60.7	37.1	5.7	5.7	36.8

6. Conclusions

In order to investigate the diaphragm cutout cracking at an orthotropic steel bridge on heavy freight transportation highway, the database from a weight-in-motion system located on the steel bridge in South China highway was used to present ten representative vehicle models, with vehicle gross and axle weight, axle spacing, as well as vehicle and axle load distribution on each lane included. It could be seen that the number of average daily truck traffic was significantly large on the highway, and the fraction of truck passage in all traffics was remarkably high. It was also found that a high fraction of the trucks impose on the bridge with overweight gross weight and axle weight, and the truck passage concentrates on part of the lanes.

Based on the rule of equivalent fatigue damage, the six-axle representative truck, which was the dominant vehicle type on fatigue loading, was used as the prototype to derive the proposed standard and simplified standard fatigue truck models, which were proposed targeting to evaluate the fatigue performance of steel bridges. The vehicle loading spectrum and truck models presented in this paper would provide important information for fatigue design and evaluation of steel bridges, especially the orthotropic steel bridge decks on heavy freight transportation highway in China.

The girder section model and sub-model were established by ANSYS, were carried out to investigate the fatigue performance of diaphragm cutout. The research find that the local effect was significantly on orthotropic deck, the axles group could be observed at diaphragm cutout, but the effect of the individual axle of axles group was not apparently. As the cutout was in complex deformation, induced an obvious stress concentration at the minimum net section, the normal direction of maximum principal stress was consistent with the actual cutout cracking direction. Diaphragm cutout was controlled by an in-plane deformation, increasing the thickness of diaphragm could effectively reduce total stresses.

Considering the transverse distribution, the fatigue life of the cutout between R18 and R19 were just 6 to 10 years, which was accordance with the actual bridge cracking time and cracking location. It's demonstrated that the high fraction of the trucks with overweight gross weight and axle weight primary caused the bridge early fatigue cracking, and had a great threat to the operation and durability of steel bridges on such heavy traffic route.

7. Acknowledgements

Financial support for this study is provided by Major State Basic Research Development Program of China (973 Program)(2015CB057702) and China National Science Foundation(51878269), to which the writers gratefully appreciate.

8. References

AASHTO (2010). " AASHTO LRFD bridge design specifications." American Association of State Highway and Transportation Official, Washington, DC.

Federal Highway Administration (2012). "Manual for design, construction, and maintenance of orthotropic steel deck bridges." U.S Department of Transportation Federal Highway Administration, Washington D.C.

Connor, R.J., and Fisher, J.W. (2006). "Identifying effective and ineffective retrofits for distortion fatigue cracking in steel bridges using field instrumentation." Journal of Bridge Engineering, 11(6): 745-752.

Fanjiang G.N., Ye Q, et al. (2004). "Fatigue analysis and design of steel orthotropic deck for Bronx-Whitestone Bridge, New York City." Transportation Research Record: Journal of the Transportation Research Board, 1892(1): 69-77.

Fisher, J.W., et al. (1990). "Distortion-induced fatigue cracking in steel bridges." NCHRP Report. Transportation Research Board, Washington, DC.

Kozy, Brian M, and Connor, R.J. (2010)."Fatigue design of orthotropic steel bridges." Structures Congress, ASCE, Florida, 2014(369):541-553.

Tsakopoulos, P. A., and Fisher, J. W. (2003). "Full-scale fatigue tests of steel orthotropic decks for the Williamsburg bridge." J.Bridge.Eng.,5(323):323-333.

Tsakopoulos, P. A., and Fisher, J. W. (2005). "Full-scale fatigue tests of steel orthotropic panel for the Bronx-Whitestone Bridge rehabilitation." Bridge Structures,1(1):55-66.

Zhou, Y. E. (2006). "Assessment of bridge remaining fatigue life through field strain measurement." Journal of Bridge Engineering, 11(6): 737-744.

Shao Xudong, Yi Dutao, Huang Zhengyu, et al.(2013). "Basic Performance of the Composite Deck System Composed of Orthotropic Steel Deck and Ultrathin RPC Layer" J. Bridge Eng., 18(5):417-428.

Li Ming, Kunitaro Hashimoto and Kunitomo Sugiura.(2014). "Influence of Asphalt Surfacing on Fatigue Evaluation of Rib-to-Deck Joints in Orthotropic Steel Bridge Decks" J. Bridge. Eng.10.1061/(ASCE)BE.1943-5592 .0000610, 04014038.

Xiao Z.G., Yamada,K., and Ya.S.(2008). "Stress analyses and fatigue evaluation of rib-to-deck joints in steel orthotropic decks. " Int. J. Fatigue, 30(8):1387-1397.

Hyong-Bo Sim and Chia-Ming Uang.(2012). "Stress analyses and parametric study on full-scale fatigue tests of rib-to-deck welded joints in steel orthotropic decks. " J. Bridge. Eng.17(5):765-773.

Zhu Zhiwen, Huang Yan et al. (2015). "Investigation on base metal cracking on diaphragm cutout at self-anchored suspension bridges." 4th Orthotropic Bridge Conference Proceedings, Tianjin, China:125-136.

Han Wanshui, Wu Jun, Cai C.S, et al.(2015). "Characteristics and Dynamic Impact of Overloaded Extra Heavy Trucks on Typical Highway Bridges." J. Bridge. Eng. 10.1061/(ASCE)BE.1943-5592.0000666, 05014011.

Zhou, X., Treacy, M., Schmidt, F., Brühwiler, E.,Toutlemonde, F., and Jacob, B.(2015). "Effect on Bridge Load Effects of Vehicle Transverse In-Lane Position: A Case Study." J. Bridge Eng., 10.1061/(ASCE)BE.1943-5592.0000763, 04015020

Consideration on Corrosion Damage Investigation and Maintenance of Pratt Truss Bridge Using for 97 years

Takumi Kanou[1*], Tatsumasa Kaita[2], Shuhei Kawami[3], Yoshiyuki Hirahara[4], Tatsuro Yamane[5], Hiroaki Fukuda[6], Ryoichi Satake[7], and Katashi Fujii[8]

[1] Aratani Civil Engineering Consultants Corporation, Hiroshima, Japan; email: takumi.kanou@aratani.co.jp
[2] Tokuyama College of Technology, Department of Civil engineering and Architecture, Shunan, Japan; email: kaita@tokuyama.ac.jp
[3] Chuden Engineering Consultants Corporation, Hiroshima, Japan; email: kawami@cecnet.co.jp
[4] Doboku Engineering Consultants Corporation, Hiroshima, Japan; email: hirahara@decnet.co.jp
[5] Graduate School of Science and Engineering, Ehime University, Matsuyama, Japan; email: yamane.tatsuro.17@cee.ehime-u.ac.jp
[6] Yokogawa Bridge Corporation, Sakai, Japan; email: h.fukuda@yokogawa-bridge.co.jp
[7] Chuden Engineering Consultants Corporation, Hiroshima, Japan; email: satake@cecnet.co.jp
[8] Graduate School of Engineering, Hiroshima University, Higashi-hiroshima, Japan; email: ken214f@hiroshima-u.ac.jp

[*] : corresponding author

Keywords: Pratt truss bridge; corrosion damage; re-deterioration; maintenance

Abstract: The local corrosion damages on structural member of aging truss bridge are possible to be trigger for serious problem such as whole collapse of bridge from the sight of remaining load bearing capacity. Also, the old truss bridges which are used for about 100 years still be not a little existing in japan. Since these bridges are constructed by using the combined section and the racing bars, it will be thought that the local corrosion will be easy to progress due to water drainage problem on steel surfaces. Therefore, as many as possible of referable data based on actual corrosion cases for aging truss bridge will be required for practical engineers engaging to inspection, strength evaluation and repair design in maintenance. In this study, detailed on-site investigation of an actual Pratt truss bridge which is used for 97 years was conducted in 2016 for clarifying the characteristics of corrosion damage. Main corrosion conditions (such as the maximum corrosion depth, corrosion area, corroded position and so on) of damaged members were measured in this investigation. From the investigation results on corrosion damages, it was found that severe corrosion damages tend to concentrate near joint parts on the vertical members, because rain water and dust accumulates to a little space between the vertical member and sway bracing. The maximum reduction rate of cross-section in this member was 16.4%. Also, a noticeable re-deterioration including the paint stripping was confirmed on some repaired parts despite of just 3 years after repainting.

1. Introduction

The old truss bridges which are used for about 100 years still be not a little existing in japan. The main structure of these old truss bridges is the structure that was combined from some shaped steels and racing bars, and rainwater collects in these joint parts. Therefore, it is thought that local corrosion will be easy to progress. The local corrosion of the structural member is a representative damage factor in aging truss bridge and breaking or buckling of the member may become trigger for serious problems such as the collapse of the whole bridge. However, there are few examples of the detailed corrosion investigation for these aging truss bridges. Therefore, as many as possible of referable data based on actual corrosion cases for aging truss bridge will be required for practical engineers engaging to inspection, strength evaluation and repair design.

In this study, the detailed corrosion damage investigation of an aging Pratt truss bridge carried out clarifying the characteristics of corrosion damages. The characteristics and main cause for corrosion were considered based on the investigation results. Also, some key points to note which includes repaired members are indicated for maintenance of aging truss bridges.

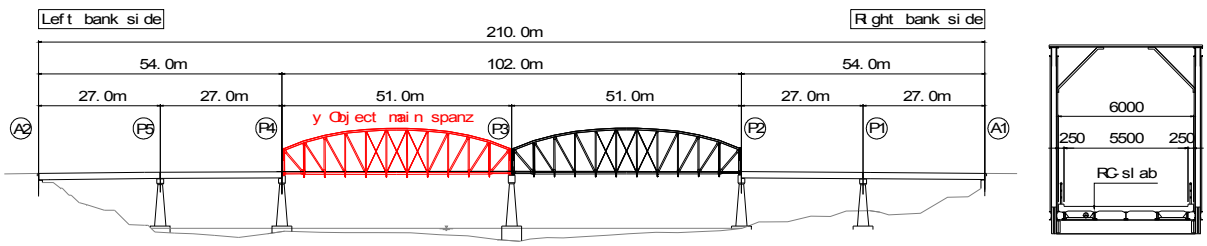

Fig. 1. Dimensions of objective truss bridge

2. Outlines of object bridge

As shown in Fig.1., the investigated bridge in this study is a main span of existing Pratt truss bridge which had been used for 97 years in the mountain area in Hiroshima prefecture. The span length of this bridge is 50.19 m. The members of this bridge are the combination member constructed by riveting channel steels and racing bars. The panel points of this bridge are rigid joints, and the supporting condition is simple support. This bridge built in 1921 but was relocated to current location in 1959 due to river improvement.

From the past maintenance history, it was confirmed that four times of repainting was carried out for 1972 to 2012. However, many corrosion damages which have cross-sectional loss were found in near the joint of structural members at the time of periodic inspection in 2012. Especially, the severe cross-sectional loss due to pitting corrosion was confirmed at some joints between the vertical member and sway bracing. These severe cross-sectional losses have already been repaired with additional plates and HT bolts.

3. Corrosion damages of main structure

3.1. Investigation method

In this study, detailed on-site investigation of this bridge was conducted once again in 2016 for clarifying the characteristics of corrosion damage and progress. In this investigation, main

corrosion conditions (such as the maximum corrosion depth, corrosion area, corroded position and so on) of damaged members in main span of left bank side were measured by using the depth gauge, caliper gauge and the ultrasonic thickness gauge.

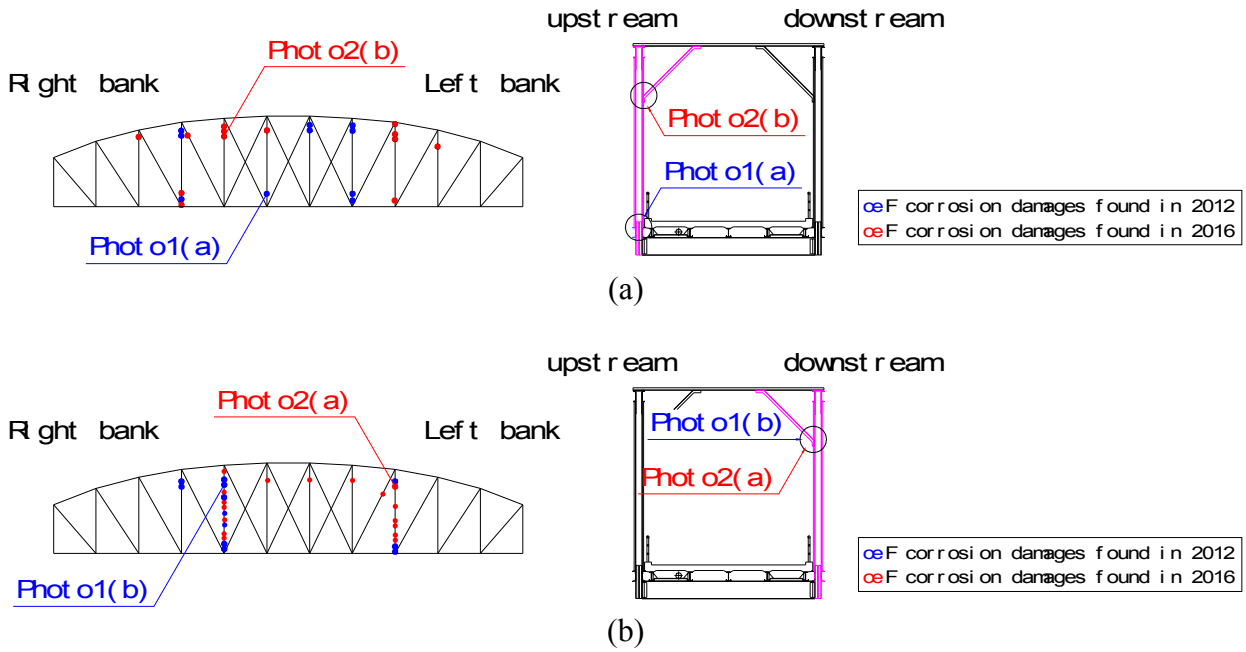

Fig. 2. Distribution maps of severe corrosion damage in main structures: (a) Upstream (South) side; (b) Downstream (North) side

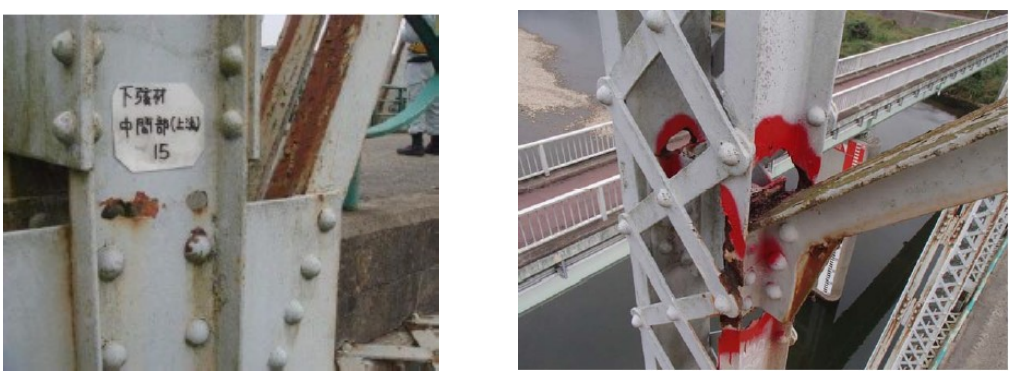

(a) (b)

Photo 1. Examples of corrosion damage on vertical member**:** (a) Groove-like corrosion on boundary between the gusset plate and vertical member; (b) Cross-sectional loss near joint part

3.2. Characteristic of corrosion damages and consideration

Distribution maps of severe corrosion damage in main structures are shown in Fig. 2. In this figure, the blue dots and red dots indicate the results of investigation carried out in 2012 and 2016. Fig. 2(a) and (b) shows the result of upstream and downstream side, respectively. From

these figures, it was clarified that severe corrosion damages concentrate to vertical members in main structures. In Fig. 2(a), the both ends of some vertical members have typical cross-section loss as shown in Photo 1. Photo 1(a) shows groove-like corrosion on boundary between the gusset plate and vertical member, and this corrosion was found the joint near lower chord member. It is thought that this groove-like corrosion progressed from inside to outside because the paint deterioration and water interception in inner surface by gusset plate. Web thickness of channel steel on vertical member may have almost no margin of remaining strength.

(a) (b)

Photo 2. Re-deterioration around repair part: (a) accumulation of muddy dust; (b) Water drainage routes including rust under the joint part

Photo 1(b) shows the cross-sectional loss near joint part between the vertical member and sway bracing. Though the damage in Photo 1(b) has been already repaired with additional plates and HT bolts, many similar corrosion damages were confirmed in 2016. The maximum rate of cross-section loss was 16.4%. Also, many re-degradations due to corrosion were found in these joints, as shown in Photo 2. It is thought that these local corrosions are caused by structural reason. It can be confirmed that the structural detail of joint in Photo 2(a) becomes like a pocket-form, because the sway bracing is inserted to among flanges of the channel steel in vertical member. Therefore, the flowing rainwater along the surface of the sway bracing collects in this pocket with rusts and bird wastes, and a wet state continues for a long time. Moreover, it will be difficult to remove their rusts and wastes perfectly in this pocket before the repainting. Photo 2(b) shows the re-deterioration of the new paint along a drainage route from both edges in the pocket part of the joint. The sedimentation of rainwater and dust was confirmed in the joint, and new paint has already exfoliated after repainting in spite of just 3 years. On the other hand, it will be noticed that the severe corrosion damages as shown in Photo 1 concentrates to specific 2 vertical members in the main structure of downstream side (Fig. 2(b)).

4. Concept on maintenance and life extension for aging truss bridges

In maintenance of an aged steel bridge like the main bridge, it is reasonable to think about the minimum maintenance period to assure safety within the period assuming a short service life of about 10 years. In other words, pay attention to remarkable corrosion damage, repeat partial touch-up repair (repair not requiring large-scale work such as scaffold) and follow-up observation (monitoring) to delay its progress. Thereby reaching the assumed service life. This

means management that keeps the current state by allowing current corrosion damage to some extent.

In inspection (detailed investigation), the dimensions of the corrosion area and the maximum corrosion depth (the size of the through hole) are recorded, and stress calculation (simple evaluation) for each member is performed by framing calculation etc. by using this information. For existing bridges in local areas, the live load assumed from the actual traffic situation is often much smaller than at design time. It is also possible to apply a weight limit that does not impair the actual traffic conditions. Although it is difficult to prevent re-deterioration, it is possible to delay the progress of deterioration by repeating a simple repair like touch-up. By doing so, maintenance should be considered to satisfy the minimum traffic needs with the minimum cost. By doing so, the possibility of service in the next 10 years may be visible.

5. Conclusions

1) In the truss bridge such as the object bridge of this study having a lot of member of framework joint, it is easy to corrode it as the narrow point that rain water and dust are easy to deposit. In addition, because the narrow point remarkably had bad workability of cleaning, the removal of the rust became incomplete, and, it was confirmed after a painting complete change to deteriorate again in a short term.
2) At the bridge of the structure that a lot of member of framework joint are easy to make stagnant rainwater, the measures that thought about a raw water transmission course of rainwater drifting to the material are very important. From this, not only I repair a damage department, but also it may be said that it is posture found for the maintenance of the steel bridge to take measures to exterminate origin of the corrosion.
3) In maintenance of an aged steel bridge like the main bridge, it is reasonable to think about the minimum maintenance period to assure safety within the period assuming a short service life of about 10 years. From this, paying attention to remarkable corrosion damage of re-deterioration, repeating partial touch-up repair to delay the progress, tolerate current corrosion damage to some extent, manage with keeping the current state, at the necessary minimum cost , Maintenance should be considered to satisfy the minimum traffic needs.

6. References

1) Kanou, Kawami, Hirahara, Satake, Kaita and Fujii, 2017. Proceedings of Annual Conference of the JSCE, I (19), 37-38. (In Japanese)

2) Yamane, Kaita and Fujii, 2017. The 15th East Asia-Pacific Conference on Structural Engineering and Construction, Proceedings of EASEC-15

Investigation of Innovative Steel-Concrete Composite and Hybrid Bridge Girders Using Corrugated Steel Web

Balázs Kövesdi[1*], Bence Jáger[2], Péter Hegyi[3], Mansour Kachichian[4], and László Dunai[5]

[1] BME Dept. of Structural Engineering, Budapest, Hungary; kovesdi.balazs@epito.bme.hu
[2] BME Dept. of Structural Engineering, Budapest, Hungary; jager.bence@epito.bme.hu
[3] BME Dept. of Structural Engineering, Budapest, Hungary; hegyi.peter@epito.bme.hu
[4] BME Dept. of Structural Engineering, Budapest, Hungary; kachichian.mansour@epito.bme.hu
[5] BME Dept. of Structural Engineering, Budapest, Hungary; dunai.laszlo@epito.bme.hu

[*] : corresponding author

Keywords: corrugated web, composite girder, hybrid girder, innovative shear connector

Abstract: Experimental and numerical research program is carried out on steel-concrete composite and hybrid girders having trapezoidally corrugated webs at the Department of Structural Engineering at the Budapest University of Technology and Economics in Hungary. The analysed girders are formed by reinforced concrete top flanges and steel (composite) or pre-stressed concrete (hybrid) bottom flanges with steel corrugated web. The shear connectors between the steel-to-concrete junctions are embedded type connections using transverse reinforcement through the web openings or vertical headed studs. The research program includes study of (i) the embedded shear connections by push-out tests; (ii) the bending-shear interaction behavior with special focus on the contribution of the concrete flanges to the shear resistance, (iii) large scale tests to prove the load carrying capacity of the designed bridge girder. The current paper gives general overview on the executed experimental research program having 56 push-out tests, 5 large scale (8 m long) beam and 4 full scale (24 m long) bridge girder tests.

1. Introduction

Composite and hybrid girders with corrugated web are increasingly used in bridge engineering due to its numerous favorable properties. Due to the features of corrugation, the application of corrugated steel webs leads to advantages for hybrid bridge structures. The web has a small stiffness in longitudinal direction, therefore the prestressing force remains in the concrete chords. The resistance against buckling – locally and globally – increases, so the number of stiffeners or diaphragms may be reduced significantly. In comparison to flat web girders there is a high bending stiffness in transverse direction, which can be favorable during manufacturing. Due to the increased stiffness the web thickness may be reduced, therefore the dead load of the structure may be smaller leading to easier and faster building processes especially in case of incremental launching. Another advantage is that the concreting difficulty of thin reinforced concrete webs disappears, which also results in a faster and easier building process. The current research project has the aim to take benefits from these advantages and to improve the efficiency of the conventional pre-cast bridge girders using corrugated web as an alternative solution for bridges in the span range of 20-40 m. The paper gives a brief overview on the executed research work

and gives a summary on the investigations which led to improve the design of corrugated web bridge girders.

2. Innovative shear connectors

Shear connectors are one of the most important part of composite and hybrid girders, therefore special attention is given to their design. Standard based and reliable design methods are mainly available for headed stud connectors. If different connection layouts are applied, the design should be based on experimental background. Based on the literature review lack of experiences and research results have been found in the field of resistance and stiffness of embedded shear connections of corrugated hybrid girders. To contribute to this research an extensive experimental research program has been designed and executed including a total number of 56 specimens with a wide range of structural details to investigate the structural behavior of this connection type. Figure 1 gives an overview on the applied test layout, geometry of the specimens and on the investigated 5 different corrugation profiles. Two different shear connector configurations are investigated in the test program, (i) horizontal headed studs and (ii) perfobond type connections having open cut-outs on the corrugated web using rebars as connectors.

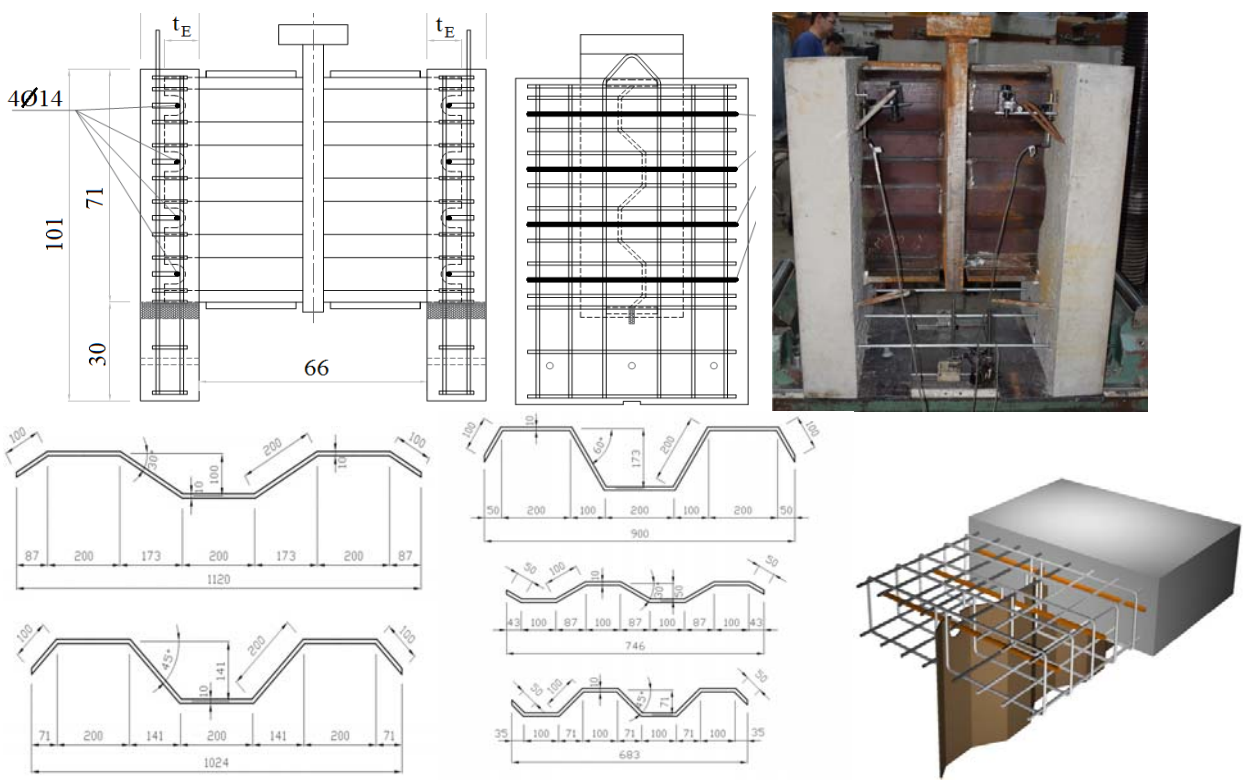

Fig. 1. Test specimen geometries, test layout and corrugation profiles

During the research program 5 different corrugation profiles are investigated with two different embedding depths (100 – 150 mm). Further varied parameters are the diameter, the layout of the applied headed studs and reinforcing bars, the size and number of cut-outs on the corrugated web. For each specimen configurations tests without any mechanical shear connector are also carried out to determine the shear resistance coming from the corrugation profile, as reference. Based on

the test results the shear resistance coming from the corrugation profile is determined as a reference value. The different mechanical shear connectors (headed studs and transverse rebars) give additional shear resistance, which are determined and added to the reference resistance. The final research aim is to develop the resistance calculation method for the design of these innovative shear connectors. Further details on the research results are given in [1].

3. M-V interaction behavior of composite corrugated web girders

3.1. Effect of corrugation on the interaction behavior

Previous studies showed that the M-V interaction behavior of corrugated web girders is more favorable than for conventional flat web girders. Results of previous experiments and numerical studies proved that the combined loading (M-V) does not reduce the bending and the shear buckling resistance of corrugated web girders having steel flanges [2,3]. The M-V interaction behaviour can be neglected in the design of corrugated web girders. However, it is also known, that for girders with heavy flanges, the flange contribution can have a significant effect on the shear buckling resistance, thus on the M-V interaction behavior. It can be the case of composite girders. Therefore, the current research program investigates the M-V interaction behavior of corrugated web girders with concrete upper flange. A total of 8 large scale test specimens are investigated having different M-V interaction pairs. One corrugation profile is tested in the experimental program, which is extended by numerical studies for different corrugation configurations. The obtained failure mode and resistances are presented in *Fig. 2*. Five significantly different M-V pairs are applied in the tests to cover a wide range of the M-V interaction curve and three duplications are executed to check the accuracy of the test results. The red lines on the graph shows the pure bending moment resistance of the composite cross-section and shear buckling resistance of the web alone. The measurements draw the attention on the significant importance of the M-V interaction behavior in case of composite corrugated web girders. Results show that it comes from the fact, that the flange contribution in the shear buckling resistance has a significant role in the structural behavior, which should not be neglected in the design. Further ongoing investigations are studying the flange contribution in the shear buckling resistance of steel and composite girders to improve the M-V interaction curve.

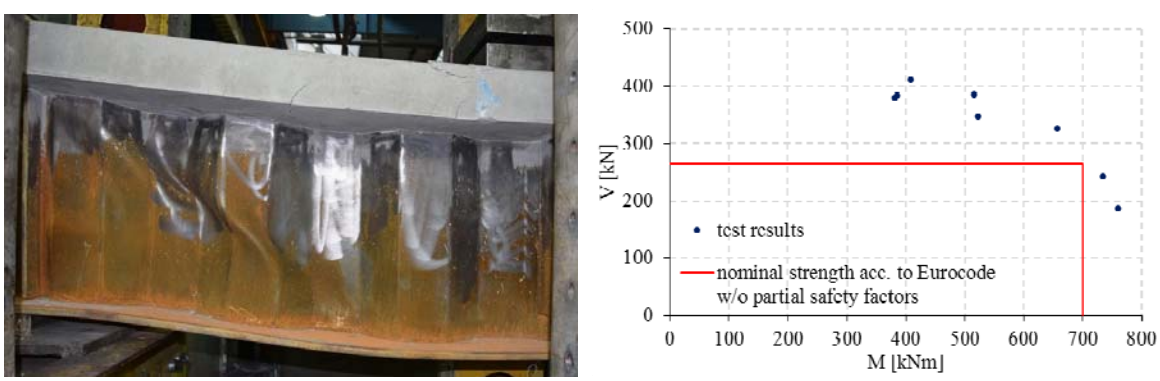

Fig. 2. Obtained failure mode and M-V interaction diagram based on test results

3.2. Full scale tests on innovative bridge girders

The designed bridge girders are tested by a full scale experiments on specimens with 24 m span length. Four test specimens are studied and loaded under three-point-bending and four-point-

bending arrangements until failure. Two composite girders with concrete upper flanges (*Fig. 3*), and two prestressed hybrid girders (*Fig. 4*) are tested having the same corrugation profile. The structural behavior and the load carrying capacity of the specimens are studied in the experimental program. The bending moment resistance of the tested girders with accompanying shear force are measured. The test results proved the accuracy of the design method applied to the design of test specimens. The obtained failure mode was a bending type failure for all tested specimens at the mid-span region with a slight effect of shear. Results proved the applicability of the developed design method and the appropriate detailing of these bridge girders, which have numerous application examples around the word, but it is a novel girder type in Hungary.

Fig. 3. Full scale test of the developed composite bridge girder with corrugated web

Fig. 4. Full scale test of the developed hybrid bridge girder with corrugated web

4. Summary

The BME Department of Structural Engineering executed an experimental and numerical research program on the improvement of composite and hybrid bridge girders using corrugated web. The executed research and their results significantly helps to understand the structural behavior of girders with corrugated web and it improves their design methodologies used in the praxis.

5. Acknowledgement

Funding has been received from Hungarian R&D project under grant agreement *No. GINOP-2.1.1-15-2015-00659*. Support was also given by the *ÚNKP-18-4 and ÚNKP-18-3 New National*

Excellence Program of the Ministry of Human Capacities and by the *János Bolyai Research Scholarship of the Hungarian Academy of Sciences*; financial supports are acknowledged.

6. References

[1] B. Jáger, G. Németh, N. Kovács, B. Kövesdi, M. Kachichian: "Push-out tests on embedded shear connections for hybrid girders with trapezoidal web", *Proc. of 12th International Conference on Advances in Steel-Concrete Composite Structures, ASCCS 2018*, València, Spain, June 27-29, 2018.

[2] B. Kövesdi, B. Jáger, L. Dunai: "Bending and shear interaction behaviour of girders with trapezoidally corrugated webs", *Journal of Constructional Steel Research*, 121, 383-397, 2016.

[3] B. Jáger, L. Dunai: "Flange buckling behavior of trapezoidally corrugated web girders subjected to bending and shear interaction", *Proc. of Annual Stability Conference*, Baltimore, USA, p. 13, 2018.

Behavior of Corroded Steel Beams Strengthened with CFRP Sheets

Jun Wang[1], Ibrahim Bumadian[2], and Yail J. Kim[3]

[1] Department of Civil Engineering, University of Colorado Denver, Denver, Colorado, USA; email: jun.wang@ucdenver.edu
[2] Department of Civil Engineering, University of Colorado Denver, Denver, Colorado, USA; email: ibrahim.bumadian @ucdenver.edu
3 Department of Civil Engineering, University of Colorado Denver, Denver, Colorado, USA; email: jimmy.kim@ucdenver.edu

[*] : corresponding author

Keywords: carbon fiber reinforced polymer; corrosion; steel; strengthening

Abstract: The physiochemical behavior of steel beams retrofitted with carbon fiber reinforced polymer (CFRP) sheets is discussed when subjected to accelerated corrosion. The focus of the present experimental study is on the potential of electricity, corrosion current density (i_{corr}), a change in load-bearing capacity, and failure characteristics. Despite the development of corrosion, the integrity of the CFRP-strengthening system is preserved. Nonetheless, the flexural capacity of the beams decreases due to the deterioration of the CFRP-steel interface. It is recognized that the failure mode is a function of corrosion damage; specifically, a change in the pattern of CFRP-debonding is noticed from discontinuous to gradual progression.

1. Introduction

Steel bridges are vulnerable to corrosion, which can reduce the load-bearing capacity of the members. Once corrosion-induced damage occurs, stress concentrations accelerate the progression of cracking. Technical action is necessary to mitigate such a detrimental consequence before catastrophic failure takes place. Carbon fiber reinforced polymer (CFRP) composites have been used frequently to upgrade reinforced concrete structures with a number of advantages (ACI 2007). Research substantiates that this strengthening technique is also usable for steel members (Hollaway and Cadei 2002). The majority of published papers were concerned with flexural behavior and failure characteristics; as a result, insufficient knowledge exists when it comes to the durability of CFRP-strengthened steel members (Gholami et al. 2013; Zhao et al. 2014).

Electrochemical reactions are responsible for corrosion in steel structures. It is well recognized that the performance of existing infrastructure degrades due to the occurrence of corrosion (Albrecht and Hall 2003; Akgul and Frangopol 2004; Rahgozar 2009). Although CFRP is a promising and non-corrosive material, steel members strengthened with CFRP may still deteriorate due to corrosion. Insufficient information is currently available on how CFRP-strengthened beams behave when subjected to corrosion and corresponding implications. This experimental project discusses the durability aspect of CFRP-strengthened steel beams subjected to accelerated corrosion.

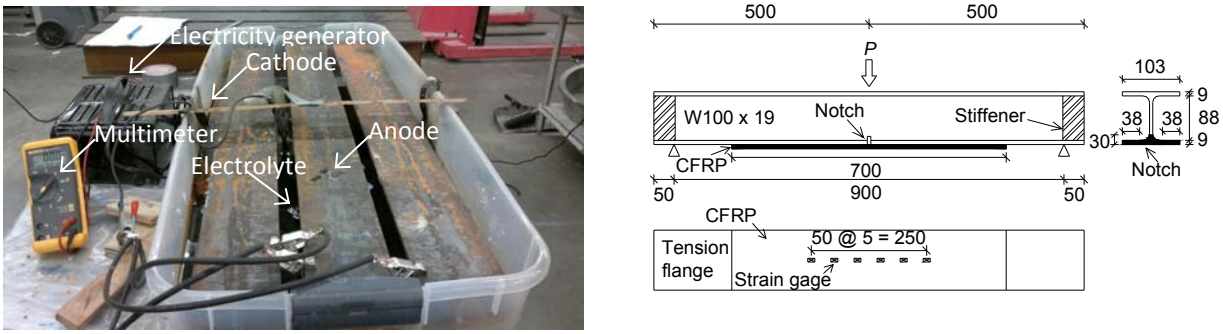

(a) (b)

Fig. 1. Test details: (a) electrochemical process for accelerated corrosion; (b) residual beam testing (unit in mm)

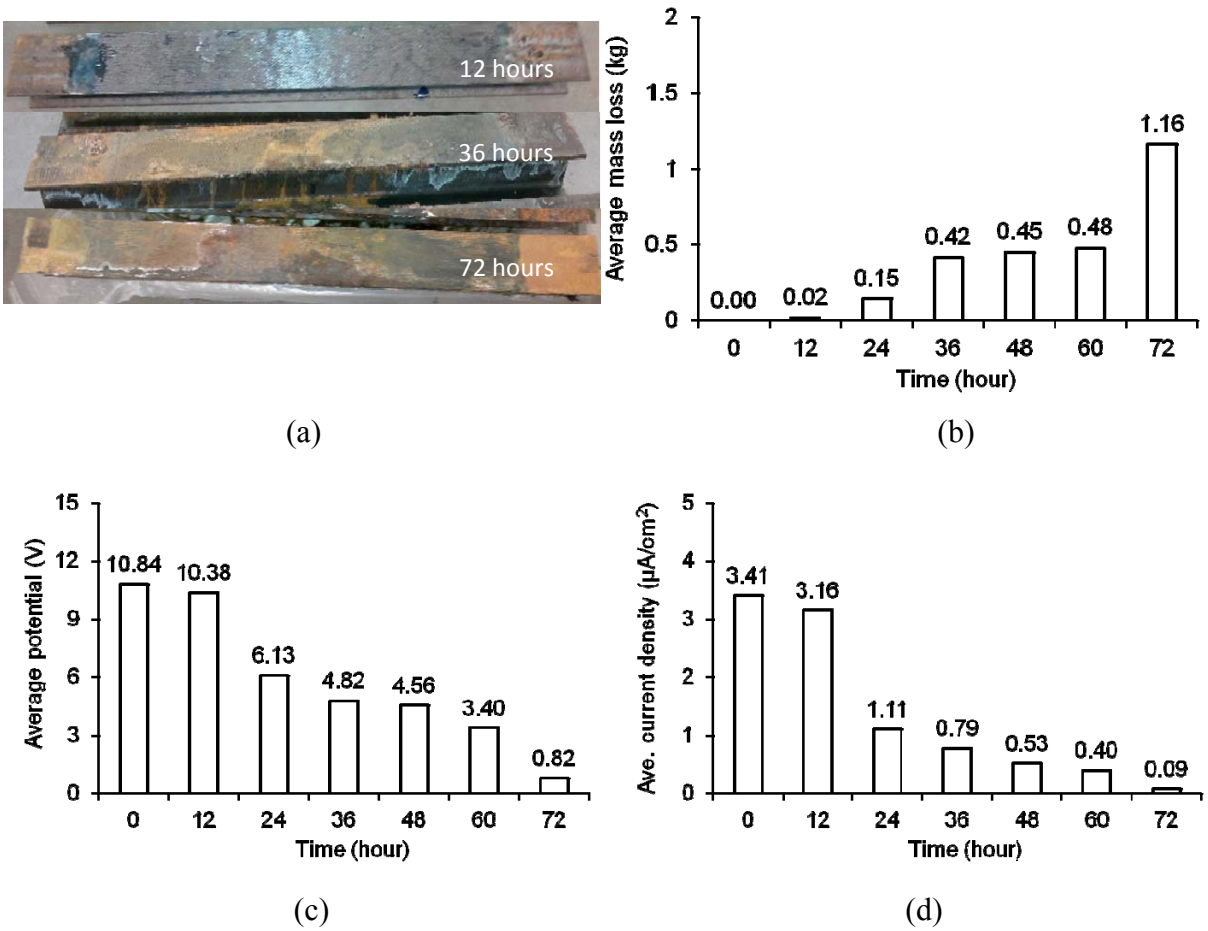

(a) (b)

(c) (d)

Fig. 2. Effects of corrosion: (a) damage progression; (b) mass loss; (c) potential; (d) current density

2. Experimental Campaign

Wide-flange beams made of A992 steel (yield strength = 345 MPa and modulus = 200 GPa) were prepared and strengthened with a single layer of CFRP sheet. The surface of each steel beam (103 mm wide by 106 mm deep by 1,000 mm long) was roughened employing a steel brush to enhance the bond and a notch was created at midspan for damage simulation. Upon curing of the strengthening system, the beams were conditioned in an electrolyte (3.5% sodium chloride solution) alongside a 2A direct current for up to 72 hours, as shown in Fig. 1(a). Three-point bending tests were then conducted to examine the flexural behavior of the conditioned beams (Fig. 1(b)).

3. Test Results

3.1. Effects of corrosion

Figure 2(a) shows the ramifications of the electrochemical reactions. Brown rust was noticed on both ends of the beam exposed to a conditioning period of 12 hours. With an increase in time, significant changes were observed owing to the progression of corrosion. The mass of the beams was measured before conducting a load test and is graphed in Fig. 2(b). The mass loss was marginal up to 12 hours, whereas from an exposure period of 24 hours the loss became conspicuous. It is interesting to note that the loss tended to plateau in the periods from 36 to 60 hours. The average potential dwindled with time, as shown in Fig. 2(c), including a large drop between 12 and 24 hours. Figure 2(d) exhibits the variation of current density (i_{corr}). The anode and electrolyte did not interact properly owing to the formation of the brown rust; as such, the monitored electric properties descended with time.

3.2. Flexural capacity

The flexural capacity of the test beams is comparatively assessed in Fig. 3(a). A transition of corrosion damage was noted from initiation to development: the rates of capacity reduction were 0.4 kN/hr from 0 hours to 36 hours and 0.15 kN/hr from 48 hours to 72 hours. As shown in Fig. 3(b), the capacities of the strengthened beam at 0 and 72 hours were 66% and 13.4% greater than that of an unstrengthened beam, respectively. This fact implies that the bond along the CFRP-steel interface deteriorated due to corrosion.

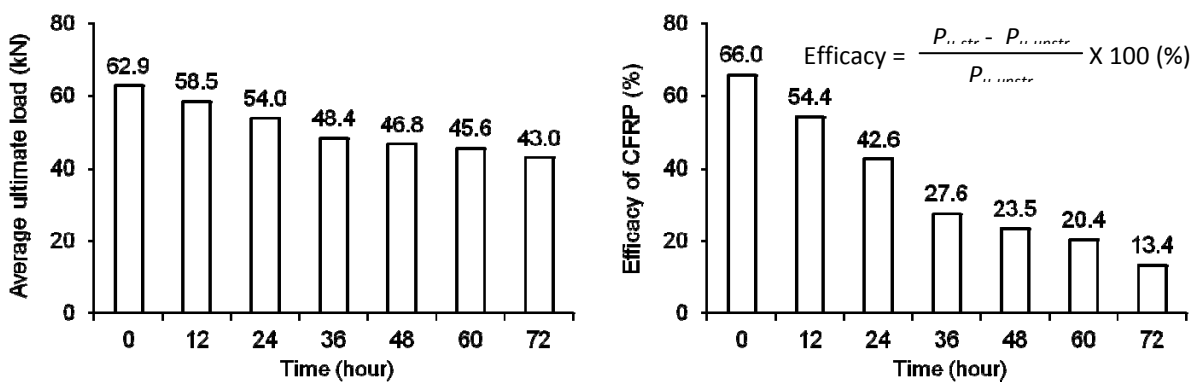

Fig. 3. Variation of flexural capacity: (a) ultimate load versus corrosion time; (b) efficacy of strengthening

3.3. Failure mode

Ductile fracture was noticed for the unstrengthened beam at the notched location (Fig. 4(a)). By contrast, all strengthened beams failed by CFRP-debonding (Fig. 4(b)), accompanied by a change in the debonding pattern from discontinuous to gradual progression contingent upon the level of corrosion. When the debonded beams were further loaded, the notch-induced fracture crack initiated and the beams failed as in the case of the unstrengthened beam.

(a) (b)

Fig. 4. Failure mode: (a) fracture crack; (b) debonding

4. Concluding Remarks

The study was concerned with the durability performance of CFRP-strengthened steel beams with a focus on corrosion damage. The deterioration mechanism of these beams was detailed and their residual capacity was experimentally evaluated. Electric current was reduced as corrosion progressed.

5. References

ACI. 2007. Report on fiber-reinforced polymer (FRP) reinforcement for concrete structures (ACI 440.R-07), Farmington Hills, MI, USA.

Albrecht, P. and Hall, T.T, 2003. Atmospheric corrosion resistance of structural steels, Journal of Materials in Civil Engineering, 15(1), 2-24.

Akgul, F. and Frangopol, D.M. 2004. Lifetime performance analysis of existing steel girder bridge superstructures, Journal of Structural Engineering, 130(12), 1875-1888.

Gholami, M., Sam, A.R.M., Yatim, J.N., and Tahir, M.M. 2013. A review on steel/CFRP strengthening systems focusing environmental performance, Construction and Building Materials, 47, 301-310.

Hollaway, L.C. and Cadei, J. 2002. Progress in the technique of upgrading metallic structures with advanced polymer composites, Progress in Structural Engineering and Materials, 4, 131-148.

Rahgozar, R. 2009. Remaining capacity assessment of corrosion damaged beams using minimum curves, Journal of Constructional Steel Research, 65, 299-307.

Zhao, X.-L., Bai, Y., Al-Mahaidi, and Rizkalla, S. 2014. Effect of dynamic loading and environmental conditions on the bond between CFRP and steel: state-of-the-art review, Journal of Composites for construction, 18(3), A4013005-1.

Materials

Self-Healing of Cementitious Materials by Supply of Ca^{2+} and CO_3^{2-} under Different Temperature Conditions

Risa Sengoku[1], Heesup Choi[2*], and Masumi Inoue[3]

[1] Department of Civil and Environmental Engineering, Kitami Institute of Technology, Hokkaido 090-8507, Japan; email: 59rinda@gmail.com
[2] Department of Civil and Environmental Engineering, Kitami Institute of Technology, Hokkaido 090-8507, Japan; email: hs-choi@mail.kitami-it.ac.jp
[3] Department of Civil and Environmental Engineering, Kitami Institute of Technology, Hokkaido 090-8507, Japan; email: m- inoue@mail.kitami-it.ac.jp

[*] : corresponding author

Keywords: cementitious material; temperature; CO_2 nano-bubble; Ca^{2+}; $CaCO_3$; vaterite

Abstract: This study focuses on the type of $CaCO_3$ crystals produced by the self-healing of concrete. $CaCO_3$ is crystal polymorphism and it's reported that crystal formations can be controlled by the relationship of temperature and pH. Generally, $CaCO_3$ consists of the three kinds, such as calcite, vaterite and aragonite for crystal formation. Vaterite is produced most densely among these, and minute self-healing can be expected. Therefore, an experiment is made for the purpose of establishing the conditions to produce vaterite. It was effective in self-healing to supply specimen with CO_3^{2-} as a nano-bubble as well as supplying Ca^{2+}. In addition, Conditions of the temperature is managed by 20, 40°C and the pH condition was constant at 12.0. The results showed that self-healing occurred and the production of the self-healing was mostly vaterite to a crystal of $CaCO_3$ under the condition of a temperature of 40°C.

1. Introduction

Generally, in concrete, tensile strength is much lower than compressive strength, and crack formation is inevitable. Cracks that exceed the permissible crack breadth leads to problems in terms of structural durability and waterproofing quality [1]. Therefore, appropriate measures must be taken during the initial crack outbreak to prevent such deterioration.

On the other hand, "self-healing" occurs where relatively small cracks in concrete are placed in an environment where water blocks the crack by filling it with a precipitate generated by a natural hydration or rehydration reaction [2]. The self-healing mechanism originates from the Ca^{2+} in concrete reacting with CO_3^{2-} dissolved in water to produce to $CaCO_3$, which fills the cracks. Previous studies have shown that cracks less than 0.1 mm can be occluded [3] via reactions described by the following equations under various pH conditions.

$$H_2O + CO_2 \Leftrightarrow H_2CO_3 \Leftrightarrow H^+ + HCO_3 \Leftrightarrow 2H^+ + CO_3^{2-} \quad (1)$$

$$Ca^{2+} + CO_3^{2-} \Leftrightarrow CaCO_3 \quad (\text{pH water} > 8) \quad (2)$$

$$Ca^{2+} + HCO_3^{-} \Leftrightarrow CaCO_3 + H^+ \quad (7.5 < \text{pH water} < 8) \quad (3)$$

Choi et al. reported that large amounts of $CaCO_3$ precipitates were produced in the specimen as the self-healing of cementitious composite materials produced CO_2 nano-bubbles using CO_3^{2-}, which flowed into the specimen under a continuous water supply [4]. Generally, calcite, vaterite, and aragonite phases are found in crystalline $CaCO_3$. Previous studies have shown that by adjustment of temperature and pH, control of the crystal formation of $CaCO_3$ can be achieved [5, 6]. Normally, the crystal formation of $CaCO_3$ which is produced by $Ca(OH)_2$ bonding with CO_3^{2-} in cement paste is entirely calcite [5, 6]. However, better self-healing is expected from vaterite compared to the calcite, because vaterite exhibits smaller particle size and improved cavity filling abilities [7]. According to the previous studies that vaterite is produced at about 30 to 50 °C. This study focuses on the crystals of $CaCO_3$ produced during self-healing for the purpose of controlling the crystal formation by temperature adjustment. In addition, improved self-healing conditions by supplying Ca^{2+} and CO_2 nano-bubbles were examined. Figure 1 shows a schematic of the process of the self-healing process.

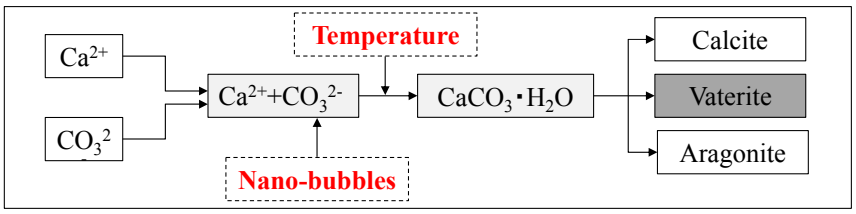

Figure 1. Process of the self-healing.

2. Experimental

2.1 Materials and specimen overview

The major reaction materials produced during the self-healing of cementitious composite materials are controlled by the hydration reaction between cement particles and water [3]. Thus, self-healing performance was evaluated using hardened cement paste in this experiment. Using ordinary Portland cement (C, density: 3.16 g/cm^3, Average particle diameter: 10 μm), specimens were prepared with a water-cement ratio of 0.4. After it was cured at 20±1 °C in a thermostatic chamber for 24 h, it was cured in a tank of 20 °C water from 2 days to 28 days of material age. Figure 2 shows the specimen overview. Specimen was cast on a mold of φ50 × 100 mm, which was removed after 24 h. After curing in water, the specimen was cut into φ50 × 5mm using a cutter.

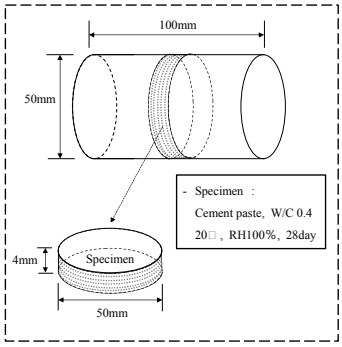

Figure 2. Specimen overview

2.2 Experimental methods

Table 1 shows the factors and experimental conditions. For the self-healing conditions, saturated $Ca(OH)_2$ and the water solution which mixed ethanol (C_2H_5OH) with calcium oxide (CaO) were used to supply Ca^{2+} additionally. It have shown that by using ethanol as an solution, it is expected to delay the reaction between Ca^{2+} and OH^- to promote the reaction between Ca^{2+} and CO_3^{2-} [7]. Based on the previous studies, it employed the method of providing nano-size (average particle diameter: 50nm) bubbles that included CO_3^{2-} in water, as self-healing conditions. Moreover, it determined self-healing conditions by adjusting the temperature at 20 °C as well as 40 °C and pH at around 12.0 so that it could control the cement hydrates to calcite and vaterite. The self-healing method used is as follows (Figure 3). After a specimen was left in each solution while adjusting the temperature, CO_2 nano-bubbles were provided. The time that the specimen was left in the self-healing solution was set to 4 durations, and the time that nano-bubble was supplied was set to be constant for 4 hours. Self-healing performance was evaluated by measuring specimen weight for each time condition (5, 10, 15, 20 h) of CH solution and CE solution with CO_2 nano-bubble solution of 4 hours.

Table 1. Factors and experimental conditions

Self-healing condition	$Ca(OH)_2$ + CO_2Nano-bubble (CH) CaO+Alc+CO_2Nano-bubble (CE)	20°C 40°C
Period	CH, CE(5h) + CO_2Nano-bubble(4h)	Ⅰ
	CH, CE(10h) + CO_2Nano-bubble(4h)	Ⅱ
	CH, CE(15h) + CO_2Nano-bubble(4h)	Ⅲ
	CH, CE(20h) + CO_2Nano-bubble(4h)	Ⅳ

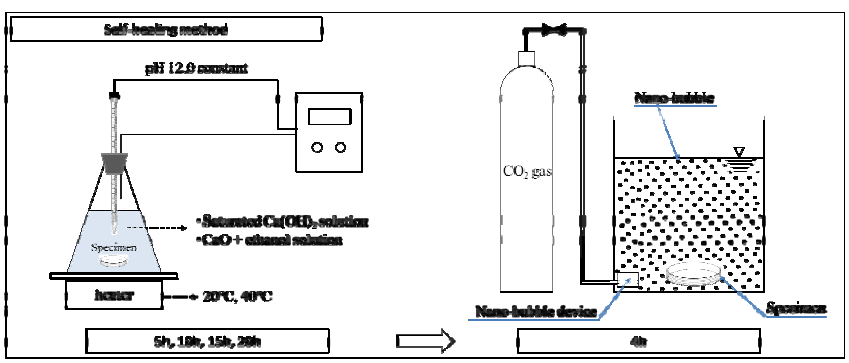

Figure 3. Self-healing method

3. Results and discussion

3.1 Changes in physical properties

Figures 4 and 5 show the weight increase for each self-healing condition. The weight increase for each self-healing period was calculated based on the dry weight of the specimen before self-healing. Regardless of a self-healing temperature condition, the weight increase showed a tendency to increase after self-healing in comparison with before self-healing. In addition, both in the case of 20 °C and 40 °C, the CE series was higher in the weight increase than the CH

series. When it was compared on a temperature condition, the case under the condition of 40 °C showed a tendency that the weight increase was high in comparison with a temperature of 20 °C. Figure 6 show the calculation result of the weight increase ratio after the self-healing in each condition. As the self-healing period increased, the weight increase ratio also showed a tendency to rise. The weight increase ratio of the specimen which self-healed for 24 hours (Ⅳ) was confirmed to increase in the order of CE40>CE20>CH40>CH20. It is presumed that this is due to the higher the temperature of cementitious materials the faster the reaction of Ca^{2+} and CO_3^{2-}. In addition, it is considered that because ethanol was used in the solution, the reaction was promoted and the weight increase ratio of the CE series was higher. Based upon the foregoing, it is thought that more effective self-healing can be expected in using ethanol for a water solution and adjusting the temperature to 40 °C.

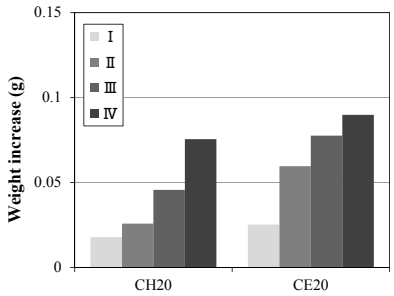

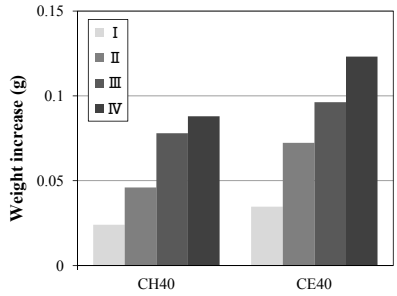

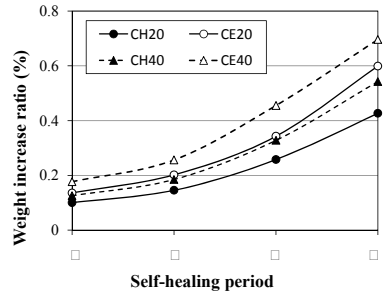

Figure 4. Weight increase (20°C) **Figure 5**. Weight increase (40°C) **Figure 6**. Increase ratio

3.2 Scanning electron microscope (SEM)

The influence that a self-healing condition gave to a crystal formation change of $CaCO_3$ was confirmed by using SEM. Figure 7 shows SEM images of specimens before self-healing, Figures 8 and 9 show SEM images of specimens after self-healing. Crystal formation was judged and estimated by comparing crystal formation and crystal size, which can be confirmed in the previous study [3, 5] with the SEM analysis of this study or the obtained crystal formation. By the observation of the specimen before the self-healing, most of $CaCO_3$ was not observed and confirmed production such as $Ca(OH)_2$ and C-S-H or ettringite. On the other hand, with the specimen after the self-healing, production of C-S-H and $CaCO_3$ were confirmed. It was supposed in particular that calcite was produced in the case of a temperature of 20°C, and vaterite was produced in the case of 40 °C. It is considered that in this way a crystal formation of $CaCO_3$ can be controlled when the temperature of the self-healing is adjusted.

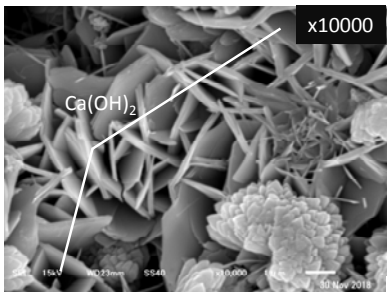

Figure 7. Before self-healing

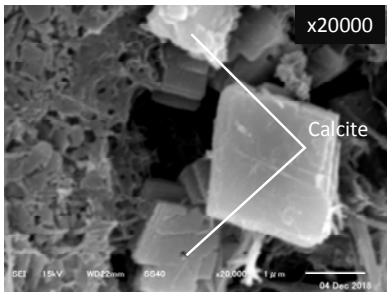

Figure 8. After self-healing (20 °C)

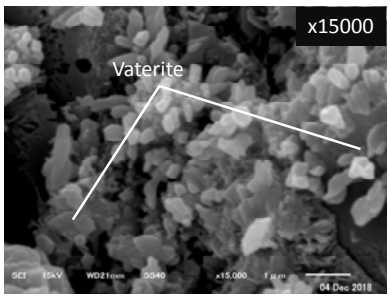

Figure 9. After self-healing (40 °C)

5. Conclusions

In this study, the crystal formations of $CaCO_3$, the main precipitate in concrete self-healing, were examined under various conditions to control crystal polymorphism by temperature adjustment and supplying CO_2 nano-bubbles. The main findings of this study are summarized as follows:

1) When the temperature is controlled to 40 °C using a CE solution, the reaction between Ca^{2+} and CO_3^{2-} is promoted, and the production of $CaCO_3$ inside the cement matrix increased.
2) By controlling the temperature with any solution, calcite was produced at a temperature of 20 °C, and a vaterite which can expect densification of cement matrix among $CaCO_3$ crystals was produced at a temperature of 40 °C.

6. References

[1] Japan Concrete Institute, "Practical Guideline for Investigation", Repair and Strengthening of Cracked Concrete Structure, Japan Concrete Institute, 2013, Tokyo, Japan (In Japanese).
[2] Neville, A.M. Properties of Concrete, Pearson Education Limited, p.328, 1995.
[3] Edvardsen, C. Water Permeability and Autogenous Healing of Cracks in Concrete, ACI Mater. J. 1999, 96, 96-M56, 448–454.
[4] Heesup Choi et al.: change in crystal polymorphism of $CaCO_3$ generated in cementitious material under various pH conditions, conctruction and building materials 188, 2018
[5] Matsumoto, M.; Polymorph control of calcium carbonate by reactive crystallization using microbubble technique, Chem. Eng. Res. Des. 2010, 88, 12, 1624–1630.
[6] Kojima, Y.; Controls of Polymorphism and Morphology of Calcium Carbonate Compounds Formationed by Crystallizing Amorphous Calcium Carbonate Hydrate, J. Ceram. Soc. Japan, 1994, 102, 12, 1128–1136.
[7] Nakayama, K. et al.; Influence of alcohol addition on the specific surface area of calcium hydroxide powder prepared from quicklime –in case of the alcohol-water successive treatment-, Journal of the Association of Materials Engineering for Resources, 2001, 1/2-14

Durability of PCaPC Containing Supplementary Cementitious Materials Manufactured by Steam Curing

Masateru Taniguchi[1*], Kimihiko Amaya[2], and Kenya Maruyama[3]

[1] Nippon P.S Co., Ltd., Fukui, Japan; email: m.taniguchi@nipponps.co.jp
[2] Nippon P.S Co., Ltd., Fukui, Japan; email: k.amaya@nipponps.co.jp
[3] Nippon P.S Co., Ltd., Fukui, Japan; email: kenya.maruyama@nipponps.co.jp

[*] : corresponding author

Keywords: fly ash; blast furnace slag; durability; steam curing; mist curing

Abstract: Recently in Japan, the life-extension of infrastructures and the decrease in environmental loads draw a great attention. Precast prestressed-concrete (PCaPC) structures are normally made of high early-strength Portland cement. In this concern, the replacement of supplementary cementitious materials (SCM) such as fly ash and granulated blast furnace slag has been investigated for practical applications. According to previous studies, it is found that curing conditions significantly affect durability properties of cement-replaced concrete with supplementary materials. In the present study, three kinds of concrete samples are made by replacing 15%-mass with fly ash (FA), 50%-mass with blast furnace slag (BFS), and control one with only high-early strength cement (H). The samples were cured in steam-room for 1 day and then kept under mist for six days. The durability properties are studied by (1) salt water immersion test, (2) freezing and thawing test and (3) air permeability test. Results show that the concrete samples FA and BFS have better durability properties than sample H. It is clarified that the mist-curing is effective for improvement of the durability.

1. Introduction

Concrete containing supplementary cementitious materials (SCM) such as fly ash and ground granulated blast furnace slag is expected be desirable for enhanced durability as compared to non-blended high early strength concrete. This is a main reason why blended cement concrete is extensively applied to precast prestressed concrete (PCaPC) slabs in replacing bridge slabs, especially in the areas where deicing salt is often employed. A recent study describes that the durability of concrete containing SCM depends on curing methods (Nakamura et al. 2016). To ensure early strength development, steam curing is generally adopted for manufacturing PCaPC slabs in one-day cycles. However, few studies are achieved to clarify the durability of steam-cured PCaPC containing SCM. Based on these backgrounds, the present study presents the results and findings of the experiments on the durability of high-early strength concrete (control sample) and SCM-blended concrete samples under the curing conditions for manufacturing PCaPC slabs.

2. Experiments

2.1. Materials and mixture proportions

Table 1 shows the mixture proportions of concrete samples and their properties of the fresh state. Cement is high-early strength Portland cement (H), the ground granulated blast furnace slag

(BFS) has a specific surface area of 6000 by Blaine value, and the fly ash (FA) is of JIS type II (obtained from Tsuruga Thermal Power Station, Hokuriku Electric Power Company). The replacement ratio of BFS is set to 50%, and that of FS is 15%. These ratios are recommended in JIS A 5308 (Ready-mixed Concrete) for prevention of alkali-silica reaction. The water-binder ratio (W/B) of each concrete mix is determined so that all mix types would be at the same strength level, satisfying a design strength of 50.0 N/mm^2 and a 1-day compressive strength of 35.0 N/mm^2. The designed values for fresh properties are 12.0±2.5 cm for the slump and 4.5±1.5% for the air content.

Table 1. Mix proportions and fresh properties of the concretes used

Mix type	Water-binder ratio (%)	SCM[a] replace-ment ratio (%)	Unit weight (per m^3)							Fresh properties	
			Water (kg)	Binder		Fine aggregate (kg)	Coarse aggregate (kg)	SP[b] (%)	Air entraining agent (kg)	Slump (cm)	Air (%)
				Cement (kg)	SCM[a] (kg)						
H	36	--	151	420	--	725.5	1082	2.39	0.050	14.0	4.0
BFS	33	50	151	229	229	704.0	1074	3.21	0.332	13.0	4.8
FA	33	15	151	389	69	699.0	1071	2.29	0.180	14.5	5.2

[a]: supplementary cementitious material
[b]: superplasticizer

2.2. Curing methods of the specimens

The specimens were cured by the procedure commonly used for PCaPC slabs. Steam curing was performed after a specified time period of pre-curing from casting. The forms were removed on the following day, and mist curing was performed until the age of 7 days, by spraying water to keep the specimens wet. The pre-curing time before steam curing was 3 hours for non-blended concrete (H) and blended concrete (FA), and 5 hours for blended concrete (BFS). The maximum temperature and its duration for the steam curing were 55°C for 5 hours for H and BFS, and 60°C for 7 hours for FA. The temperature was increased at 15°C/h for all mix types. Mist curing was performed after the steam curing, in a large curing tent kept at a daily mean temperature of 14.5°C. Then air curing in the outdoor environment followed until the age of 28 days.

2.3. Durability tests

Three kinds tests were performed to examine the durability: air permeability test; freeze-thaw test; and salt water immersion test. The air permeability test was performed by the Torrent method (Torrent, 1995) at the ages of 4 weeks and 13 weeks, measuring the air permeability coefficient at the center and both ends on one side of each square prism specimen (150×150×530 mm). The freeze-thaw test was conducted, following JIS A 1148 (Method A) to measure the relative dynamic modulus of elasticity and the mass loss rate. The salt water immersion test was conducted following JSCE-G572, with the specimens immersed in 10% NaCl aqueous solution for 180 days from the age of 28 days. EPMA (JSCE-G574) was applied to obtain chloride ion distributions for determining the apparent diffusion coefficient. The specimens

were cured in water at a temperature of 20±2°C the day before the freeze-thaw tests and the salt water immersion tests to eliminate influence of the drying of sample surfaces.

3. Test results

3.1. Air permeability

Results of the air permeability tests are shown in Fig. 2. The specimens after curing process were stored indoors at a room temperature of 20±2°C and a relative humidity of 60±5%. Air-permeability coefficients increase with the ages in all samples due to drying. It is observed from visual observation that the surface quality graded at the age of 13 weeks is good or higher. As seen in the graphs, the air-permeability coefficient is the smallest in sample H at the early age. Then the coefficients reach to the same level in all mixtures at the age of 13 weeks.

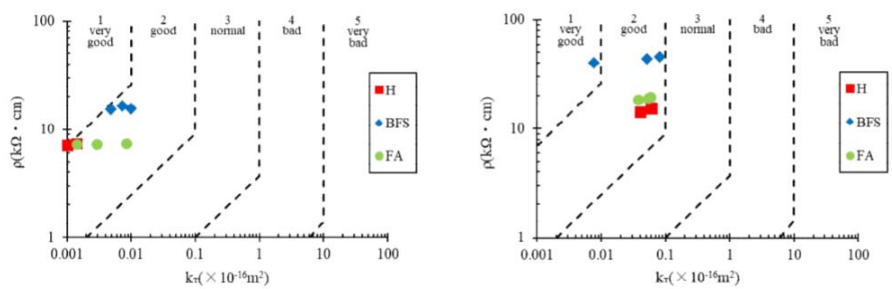

Fig. 2. Results of air-permeability tests: (a) 4 weeks elapsed and (b) 13 weeks elapsed

3.2. Freezing and thawing

Fig. 3 shows results of the freeze-thaw tests. Relative dynamic moduli of elasticity in all the mixtures indicate over 100% still after 300 cycles, with the increase in approximately 5% in BFS samples, in addition to almost 0% mass loss. These results confirm adequate resistance against freezing and thawing in all the concrete samples.

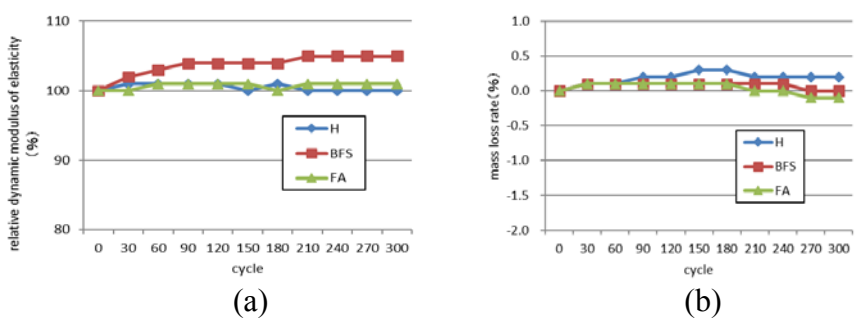

Fig. 3. Results of freezing and thawing tests: (a) relative dynamic modulus of elasticity and (b) mass loss.

3.3. Salt-water immersion

Chloride concentration distributions and apparent diffusion coefficients after 180 days of immersion are given in Fig. 4. As compared to H sample (control), the apparent diffusion coefficient is about 10% in BFS sample, and is about 40% in FA. Thus, results show that the use of SCM leads to an enhanced chloride penetration resistance that is the highest in BFS. Since Pozzolanic reaction of FA sample could be insufficient at the age of 28 days when the salt water immersion test was started, results imply that the resistances of chloride penetration in SCM concrete (BFS and FA) would be even smaller in extended time periods.

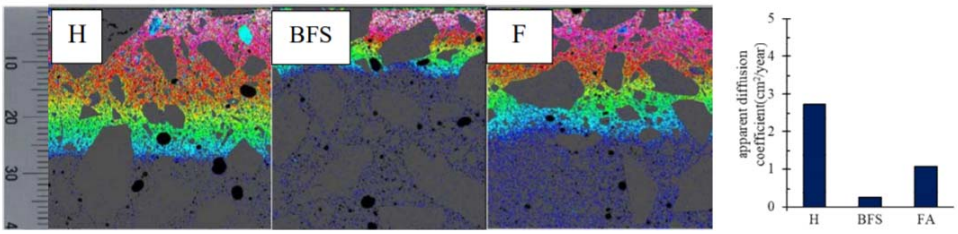

(a) (b)

Fig. 4. Results of salt water immersion tests: (a) chloride penetration depths by EPMA and (b) apparent diffusion coefficients.

4. Summary

Concrete samples containing SCM were prepared by curing in mist until the age of 7 days after steam curing, and three kinds of the durability tests were carried out. All the findings are summarized, as follows:

(1) According to the air-permeability tests, the surface qualities of all the samples are satisfactory, even at the age of 13 weeks, with grades of good and higher.
(2) Adequate freeze-thaw resistances are confirmed in all mix types.
(3) The salt water immersion tests demonstrate the enhanced chloride penetration resistance of the concrete containing SCM (both BFS and FA), compared to the control mix of high-early strength cement. It is suggested that the difference between the two blended cement concretes would be smaller over time in real structures due to the pozzolanic reaction. This is because the reaction of FA concrete could continue for extended periods.

In conclusion, PCaPC poducts containing SMC cured in mist until the age of 7 days after steam curing could present the novel durability. From the viewpoint of environmental impact, therefore, it is desirable to procure supplementary cementitious materials (SCM) available from local suppliers close to the precast product industry.

5. References

Nakamura, E., Kurihara, Y., Suzuki, M. and Koga, H. 2016. Influence of Wet Curing Period on Strength and Durability of Concrete Containing Supplementary Cementitious Materials, Proceedings of the 25th symposium on Developments in Prestressed Concrete, 401-404.

Torrent, R.J. 1995. A method for the rapid determination of the coefficient of permeability of the "covercrete", International Symposium on Non-Destructive Testing in Civil Engineering (NDT-CE), 26-28.

Estimation of Compressive Strength Trends of Recycled Concrete Aggregate Systems through a Statistical Database Analysis

Anuruddha Jayasuriya[1*], Emily Shibata[2], Tola Chen[2], Matthew J. Bandelt[3], and Matthew P. Adams[4]

[1] New Jersey Institute of Technology, Newark, NJ; USA, email: aj464@njit.edu
[2] New Jersey Institute of Technology, Newark, NJ; USA
[3] New Jersey Institute of Technology, Newark, NJ; USA, email: bandelt@njit.edu
[4] New Jersey Institute of Technology, Newark, NJ; USA, email: matthew.p.adams@njit.edu

[*] corresponding author

Keywords: recycled concrete aggregates; compressive strength; database analysis; nonlinear regression; statistical indicators

Abstract: Using recycled concrete aggregate (RCA) as a supplementary material in concrete systems has now become a central focus in the material industry to enhance the sustainability of concrete production and the preservation of natural resources. However, due to the lack of globally accepted technical guidance, long-term durability concerns, and the broad material variability of the aggregate sources, the usage of RCA systems has not been expansively practiced in concrete applications. Consequently, design engineers have no way to predict the mechanical properties of RCA, and thus are reluctant to use the materials without extensive testing. A comprehensive literature review on mechanical properties of RCA systems' compressive strength is presented. The data for RCA properties were obtained from concrete that were cast according to a normal mixing method with RCA replacement for coarse aggregate and using only natural sand. Mechanical properties showed a strong dependency on factors such as effective water-to-cement ratio, recycled aggregate replacement levels, and properties of parent concrete that those recycled aggregates are derived from. Based on the statistical inferences, the variabilities of RCA mechanical performance factors were quantified, and their significant effects were evaluated.

1. Introduction

Recycled concrete aggregate (RCA) systems have been considered as an innovative construction material to reduce carbon footprint, improve economic sustainability, and reduce the construction and demolition (C&D) waste stream. However, the use of RCA systems has not been broadly promoted mainly due to the lack of standardized guidance on methods for mix proportioning design procedures which can predict the mechanical properties of RCA systems, and large variability of the RCA particles derived from demolished concrete. Despite the number of mathematical relationships that have already been developed on the mechanical properties of RCA systems (Xiao *et al.*, 2006; Rahal, 2007; Hoffmann *et al.*, 2012; Lovato *et al.*, 2012; Thomas *et al.*, 2013; Ulloa *et al.*, 2013; Jayasuriya *et al.*, 2018a), the limitations in those parametric ranges and the restricted number of sample sizes adopted in the experiments resulted in low confidence in those prediction tools. Therefore, a large-scale database needs to be constructed covering a wide range of parameters that controls the variability of mechanical

properties in RCA systems. The main motivation of this paper is to establish a basic statistical evaluation by studying the variabilities of the mechanical properties of RCA due to various properties through an extensive database analysis over a wide scope of literature studied.

2. Data collection and analysis procedure

2.1. Development of the database for RCA mechanical properties

In total, over 80 research articles were subjected to a careful review, and the RCA mechanical properties were obtained for compressive strength (850 data), elastic modulus (682 data), flexural strength (197 data), and splitting tensile strength (462 data). Due to space constraints, only compressive strength data will be analyzed here. It was observed that a substantial amount of compressive strength tests was based on standard cube and cylinder specimens, where other properties were included in the database had adopted a consistent testing approach guided by standard code specifications throughout the experiments in the literature. However, due to the large variabilities across the experimental procedures that various authors had adopted, the specimen sizes were different from one experiment to the other imposing a scattered variability in RCA mechanical performance. In addition to the specimen size, there are other mixture proportion factors and aggregate characteristics that were identified during the data collection phase which governed the RCA mechanical properties such as; effective water-to cement ratio, total aggregate-to-cement ratio, RCA replacement level, maximum sizes of RCA particles, natural aggregate, and water absorption capacities of RCA particles and natural aggregate.

2.2. Database analysis results

Based on the data obtained from the literature investigation, the effective water-to-cement ratio and the RCA replacement ratio initiated a higher data variability. Histogram shown in Fig. 1 (a), depicts the effective water-to-cement ratio levels that were adopted in the database, and it followed a right-skewed distribution with an average ratio of 0.48. The adopted effective water-to-cement ratio was mostly controlled by the absorption capacity of the aggregate and, due to the presence of high contents of adhered mortar attached to the natural aggregate, the effective water-to-cement ratio (i.e., free water content) can be decreased in the concrete mix. Therefore, at later stages it may impair the overall fresh and hardened concrete properties of RCA systems quite significantly. The primary key that most of the experiments have used was to bring RCA particles to a saturated surface dry condition by presoaking the aggregates or using RCA particles derived from high strength parent concretes (Xiao *et al.*, 2005a; Xiao *et al.*, 2005b; Rahal, 2007; Ferreira *et al.*, 2011; Ideker *et al.*, 2012; Adams *et al.*, 2016; Zhou and Chen, 2017). These methods significantly improved both the fresh properties (i.e., workability and mixture uniformity) and hardened properties (i.e., shrinkage resistance) as well. Compared to the effective water-to-cement ratio distribution, the RCA replacement ratio showed larger variabilities as shown in Fig. 1(b). It is reasonable to expect this type of larger variability since RCA replacement ratio had not been utilized or quantified according to a guided specification and thus, the distribution of the data showed a scattered characteristic. Although the concrete mechanical performance in an RCA system was greatly influenced by the replacement level, it was numerically studied that the amount of residual mortar content (i.e., adhered mortar content in the system) is the key parameter that primarily controls the RCA mechanical performance (Jayasuriya *et al.*, 2018a; Jayasuriya *et al.*, 2018b). However, utilizing the amount of RCA

replacement levels was seen extremely easy for mix proportioning the aggregate contents as opposed to rigorous experimental procedures to quantify the adhered mortar contents.

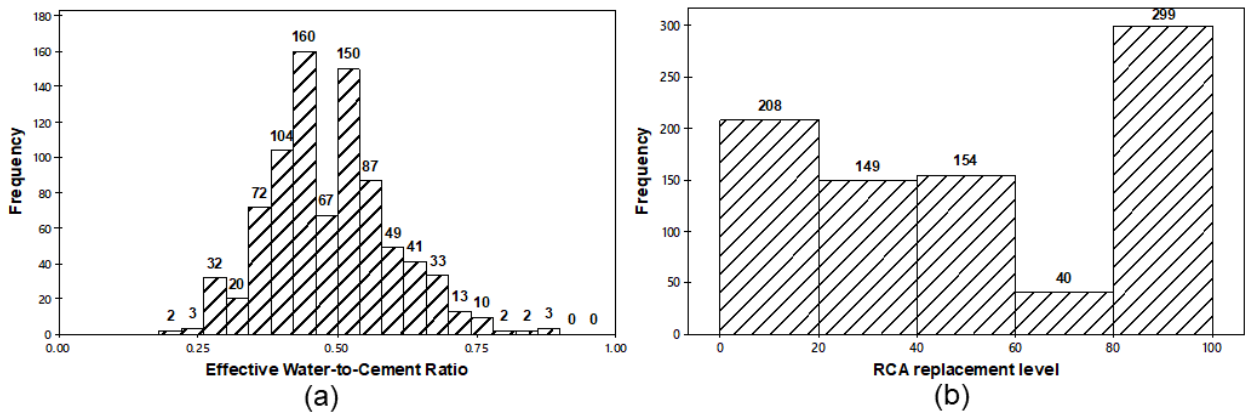

Fig. 1. Histogram distributions in the database; (a) effective water-to-cement-ratio (b) RCA replacement levels

Due to the high variabilities in the RCA replacement levels, the range from 0% to 100% was broken into subsidiary levels where the mechanical performances were studied for 0%, 1-20%, 21-40%, 41-60%, 61-80%, and 100%. For the analysis purposes, the RCA mechanical property trends were observed against the varying effective water-to-cement ratio for each replacement level range mentioned above. Eventually, non-linear regression models were established for those sampling sets of data, and preliminary trends were observed.

2.2.1. Compressive strength database analysis

The database analysis for RCA compressive strength was carried out for cylinder and cube specimens, and it was observed that both testing approaches decayed the compressive strength with increasing effective water-to-cement ratio. The compressive strength data was sampled through a non-linear regression analysis and fitted with exponential decaying functions where four representative fitted models are shown in Fig.2(a) and Fig.2(b) for 0% and 100% replacement levels containing 28-day cube and cylinder strengths respectively. According to Fig. 3, the 28-day compressive strengths of RCA systems were higher when cube specimens were used compared to the cylinder specimens. The highest compressive strength tested (i.e., both cube and cylinder) was shown by those RCA systems that included 1-20% RCA replacement levels. This is indicative of how small amounts of RCA replacements can improve compressive strengths compared to a natural aggregate concrete system (i.e., 0% replacement level). Overall, the compressive strength results exhibited a gradual decrease for RCA replacement level ranges above 20% and it indicated that higher inclusions of replacement levels could depreciate the RCA compressive strength substantially. Considering the 100% RCA replacement level systems, it showed a potential increase in the compressive strengths than that of 61-80% replacement level. This was due to the high contents of adhered mortar in RCA systems and the resulting stiffness compatibility of the material properties contributed to show an improved strength performance. However, such systems did not exhibit much higher compressive strength capacities at greater extents mainly due to the exitance of natural aggregate portions even within the 100% RCA

replacement levels. Eventually, it was observed that the inhomogeneities of material properties controlled the RCA concrete strength characteristics confirming the same context studied by Jayasuriya *et al.*, 2018b.

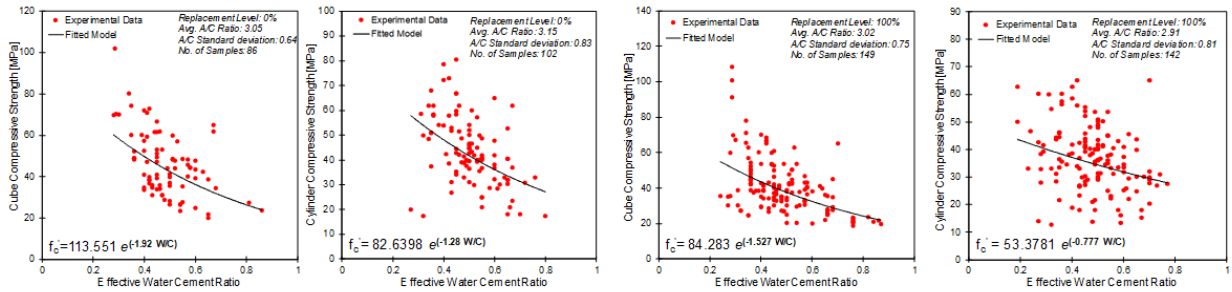

(a) (b)

Fig. 2. Variation of 28-day cube and cylinder compressive strengths with fitted models; (a) 0% RCA replacement level (b) 100% RCA replacement level

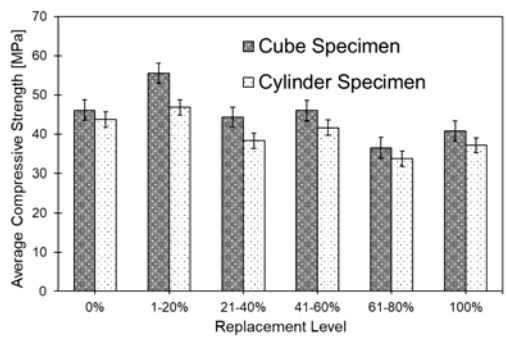

Fig. 3. Comparison of RCA 28-day compressive strengths between cube specimens and cylinder specimens obtained from the database analysis

3. Summary and conclusions

In systems containing RCA, effective water-to-cement ratio and the amount of RCA replacement level showed strong effects on the mechanical properties of RCA systems. The general trends of the mechanical properties behaved inversely proportional to the effective water-to-cement ratio, where the RCA replacement levels showed similar trends with some exceptions. Based on the statistical analysis results, it was evident that the RCA replacement levels below 20% yielded the highest mechanical performances providing a strong implication that the amount of RCA replacement levels could be optimized at 20% or less. However, further understanding on RCA replacement level optimization needs be established upon correct measurements of the adhered mortar contents in the concrete system as it is the most important factor that controlled the mechanical properties. RCA systems with replacement levels 100% showed promising strength performances in all properties due to the reduction of the material heterogeneity. Additionally, utilizing presoaked RCA particles could enhance the long-term strength performance as there will be no relative exchange of water from the aggregates during mixing or hydration process.

4. Reference

Adams, M. P., Fu, T., Cabrera, A. G., Morales, M., Ideker, J. H. and Isgor, O. B. (2016) 'Cracking susceptibility of concrete made with coarse recycled concrete Aggregates', *Construction and Building Materials*. Elsevier Ltd, 102, pp. 802–810. doi: 10.1016/j.conbuildmat.2015.11.022.

Ferreira, L., de Brito, J. and Barra, M. (2011) 'Influence of the pre-saturation of recycled coarse concrete aggregates on concrete properties', *Magazine of Concrete Research*, 63(8), pp. 617–627. doi: 10.1680/macr.2011.63.8.617.

Hoffmann, C., Schubert, S., Leemann, A. and Motavalli, M. (2012) 'Recycled concrete and mixed rubble as aggregates: Influence of variations in composition on the concrete properties and their use as structural material', *Construction and Building Materials*. Elsevier, 35, pp. 701–709. doi: 10.1016/J.CONBUILDMAT.2011.10.007.

Ideker, J. H., Adams, M. P., Tanner, J. and Jones, A. (2012) 'Durability Assessment of Recycled Concrete Aggregates for use in New Concrete', *Transportation Research and Education Center*, (June).

Jayasuriya, A., Adams, M. P. and Bandelt, M. J. (2018a) 'Understanding variability in recycled aggregate concrete mechanical properties through numerical simulation and statistical evaluation', *Construction and Building Materials*. Elsevier, 178, pp. 301–312. doi: 10.1016/J.CONBUILDMAT.2018.05.158.

Jayasuriya, A., Bandelt, M. J. and Adams, M. P. (2018b) 'Simulation of cracking susceptibility in recycled concrete aggregate systems', in Meschke, G., Pichler, B., and Rots, J. G. (eds) *Proceedings of Computational Modelling of Concrete and Concrete Structures (Euro-C 2018)*.

Bad Hofgastein, Austria: CRC Press, pp. 421–428.
Lovato, P. S., Possan, E., Molin, D. C. C. D., Masuero, Â. B. and Ribeiro, J. L. D. (2012) 'Modeling of mechanical properties and durability of recycled aggregate concretes', *Construction and Building Materials*. Elsevier, 26(1), pp. 437–447. doi: 10.1016/J.CONBUILDMAT.2011.06.043.

Rahal, K. (2007) 'Mechanical properties of concrete with recycled coarse aggregate', *Building and Environment*. Pergamon, 42(1), pp. 407–415. doi: 10.1016/J.BUILDENV.2005.07.033.
Thomas, C., Setién, J., Polanco, J. A., Alaejos, P. and Sánchez de Juan, M. (2013) 'Durability of recycled aggregate concrete', *Construction and Building Materials*. Elsevier, 40, pp. 1054–1065. doi: 10.1016/J.CONBUILDMAT.2012.11.106.

Ulloa, V. A., García-Taengua, E., Pelufo, M. J., Domingo, A. and Serna, P. (2013) 'New views on effect of recycled aggregates on concrete compressive strength', *ACI Materials Journal*, 110(6), pp. 687–696.

Xiao, J.-Z., Li, J.-B. and Zhang, C. (2006) 'On relationships between the mechanical properties

of recycled aggregate concrete: An overview', *Materials and Structures/Materiaux et Constructions*, 39(290), pp. 655–664. doi: 10.1617/s11527-006-9093-0.

Xiao, J., Li, J. and Zhang, C. (2005a) 'Mechanical properties of recycled aggregate concrete under uniaxial loading', *Cement and Concrete Research*, 35(6), pp. 1187–1194.

Xiao, J., Li, J. and Zhang, C. (2005b) 'On statistical characteristics of the compressive strength of recycled aggregate concrete', *Structural Concrete*, 6(4), pp. 149–153. doi: 10.1680/stco.2005.6.4.149.

Zhou, C. and Chen, Z. (2017) 'Mechanical properties of recycled concrete made with different types of coarse aggregate', *Construction and Building Materials*, 134, pp. 497–506.

Effects of Seismic Pounding on the Longitudinal Response of Multi-Span Bridges

Donatello Cardone[1*]

[1] University of Basilicata, Potenza, Italy; email: donatello.cardone@unibas.it

[*] : corresponding author

Keywords: multi-span bridges; joints; seismic response; pounding; modeling approaches

Abstract: This paper investigates, from an analytical perspective, the effects of seismic pounding on the longitudinal response of multi-span simply supported deck bridges. A sensitivity analysis is carried out considering three different numerical models: (i) continuous deck bridge (i.e. joints completely closed), (ii) independent spans coupled together only by piers (i.e. joints always open), (iii) adjacent spans linked by compression only gap elements, capturing pounding effects. The model with gap elements is examined taking into account the effects due to interaction between bridge deck and abutment-backfill. The aforesaid different modeling approaches are applied to a case-study represented by a multi-span simply supported deck bridge of the Italian highway. A series of nonlinear response-time history analyses are performed for different earthquake intensity levels. The analysis results clearly point out the effects of seismic pounding on the seismic response of multi-span simply supported deck bridges and the great importance of modeling assumptions concerning joints and abutments.

1. Introduction

The behaviour of joints and abutments can significantly influence the seismic response of multi-span simply supported deck bridges. Especially in case of short bridges, indeed, the closure of the joints in the longitudinal direction, with the consequent mobilization of the abutment backfill can strongly affect the seismic response of the bridge. This paper investigates the sensitivity of the bridge seismic response with respect to joint and abutment modelling approach. Abutments are modelled according to (Caltrans, 2006) specifications, considering both active and passive resistance mechanisms, due to piles-ground and backfill-abutment interaction, respectively. Joints are modelled using compression-only gap elements.

Three different conditions are examined for the joints: (i) joints are completely closed, which brings about a bridge model characterised by a continuous deck, (ii) joints remain always open, which implies a bridge model characterised by independent adjacent spans, coupled together only by the piers and (iii) joints modelled with gap elements. The model with gap elements is developed with and without abutment-backfill effects, in the longitudinal direction. The aforesaid modelling approaches are applied to a real case study.

Comparisons of the analysis results clearly point out the great sensitivity of the seismic response of multi-span simply supported deck bridges to the modeling approaches adopted for joints and abutments.

2. Case study

The Ceraso bridge of the A16 Napoli-Canosa Italian highway was selected as case study. It is a five-span simply supported deck bridge, with span lengths of approximately 33m and 50mm joint width. The bridge is characterized by four RC single shaft piers with hexagonal hollow multi-connected section. Concrete strength and steel yielding are 35MPa and 440MPa, respectively. The bridge has an irregular pier layout, as shown in Fig. 1. The mass of each deck is equal to 720 ton. The pier-deck connections are realised by Neoprene Pads (NP) with 300x600 mm plan dimensions, 50 mm thickness and approximately 1MPa shear modulus.

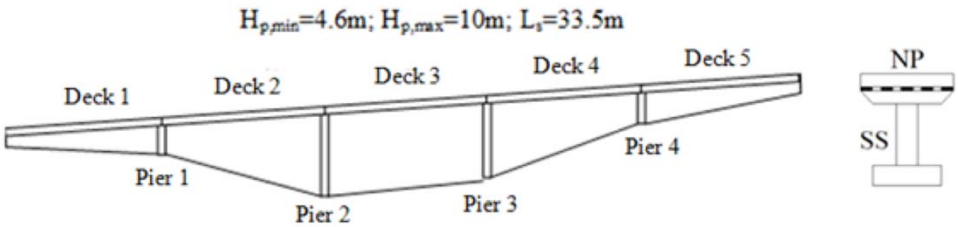

Fig. 1. Schematic layout of the selected case-study

3. Modeling assumptions

According to the Structural Modelling Approach (SCM) approach, the bridge has been divided in five independent rigid diaphragms, modelling the bridge decks, mutually connected by means of a series of nonlinear springs, modelling bearing devices, piers and abutments (see Fig. 2a). Four different models (see Fig. 2a) have been considered. In the first model (C in Fig. 2a), the deck is considered as continuous (joints closed) and the interactions with the abutment backfill are neglected. In the second model (MS in Fig. 2a) joints are supposed to remain always open, which implies a bridge model characterized by independent adjacent spans, coupled together only by the piers. In the third model (MSG in Fig. 2a), the joints present a given clearance. As joints close, pounding between adjacent decks occurs, with a significant redistribution of seismic forces between the piers. The abutment-backfill effects are neglected in the MS and MSG models. Finally, the fourth model (MSGA in Fig. 2a) accounts for both the effects of joint closure and those related to the interaction between deck and abutment-backfill system. Obviously, the last model is the most accurate and realistic to describe the seismic response of multi-span simply supported bridges. The deck mass has been lumped in the centre of mass of each deck. A tributary mass of the pier mass has been also taken into account.

Piers have been modeled with nonlinear springs characterized by a bilinear backbone curve. The lateral force-displacement relationships of the piers have been derived from pushover analysis of beam with hinges elements. The length of plastic hinges has been evaluated according with the formula by (Priestley et al. 1996). Reference to the Takeda degrading-stiffness-hysteretic model (Takeda et al. 1970) has been made to describe the cyclic hysteretic behavior of plastic hinges. In the analysis, P-Δ effects due to gravity loads and premature shear failure have been considered.

A linear viscous-elastic behaviour has been considered for neoprene pads, whose lateral stiffness has been evaluated based on the dimensions (cross section area and thickness) of the pads and

shear modulus, G, of neoprene. The horizontal strength of the bearing system has been evaluated as the lowest between the shear resistance of neoprene pads and the friction resistance between neoprene and concrete sliding surfaces.
Possible effects due to joint closure have been taken into account by means of compression-only link elements with gap (see Fig. 2b). The longitudinal response of the abutment is based on the interaction between bearing devices, abutment back-wall, abutment piles and soil backfill material. Prior to gap closure, the deck force is transmitted through the bearing devices to the abutment wall. After gap closure, the deck pushes directly on the abutment back wall, until the passive backfill pressure is reached. In this study, the horizontal stiffness and ultimate strength of the abutment have been derived from a combination of design recommendations (Caltrans, 2006) and experimental test results on seat-type abutments with piles (Maroney et al. 1993), as a function of the abutment back wall dimensions and pile characteristics.

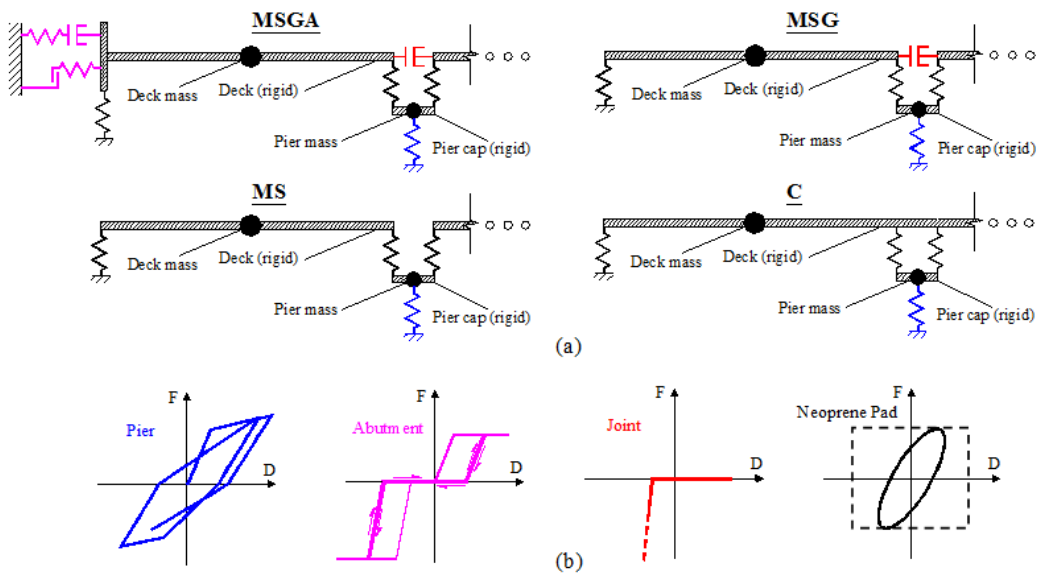

Fig. 2. (a) Bridge models and (b) force-displacement relationships of bridge components.

4. Nonlinear response time-history analyses

Nonlinear Time History Analyses (NTHA) have been carried out with SAP2000_Nonlinear, using a set of 7 accelerograms compatible, on average, with the 5%-damped acceleration response spectrum provided by Eurocode 8 for soil type B (stiff soil), for three different earthquake intensity levels, characterized by PGA = 0.238g, 0.448g and 0.537g, respectively.
Fig. 4 shows the maximum values of pier (left) and deck (right) displacements obtained from NTHA. The results clearly show that the longitudinal seismic behaviour of the bridge is significantly affected by the modelling assumptions. For the continuous deck model, the stiffer piers (n. 1 and n. 4) prematurely collapse at 0.448g while the other piers (n. 2 and 3) remain still elastic. On the contrary, for the models with independent decks, ductility demands are distributed almost uniformly in all the piers, ranging from 2.3 to 2.7 at 0.537g. Considering the closure of the joints and the activation of the abutment-backfill effects, a considerable reduction of the maximum displacements of the central decks and related piers (n. 2 and 3) is observed, with consequent increment of the ductility demands in the stiffer piers (piers n. 1 and 4).

5. Conclusions

The results of this study clearly point out the sensitivity of the longitudinal seismic response of multi-span simply supported deck bridges to the modelling approach adopted for joints and abutments. The closure of the joints and the abutment-backfill effects, in particular, have a great influence on the distribution of the plastic deformations in the piers, thus conditioning the displacement ductility capacity of the bridge and the PGA value associated to the bridge collapse. For this reason, when the seismic assessment of the bridge requires a realistic and accurate evaluation of the seismic behavior of the structure (e.g. in the design of possible seismic retrofit measures), the effects of the joints closure and abutment-backfill interaction should be taken into account in the numerical model. On the contrary, when the seismic assessment of the bridge allows for the use of simplified models (e.g. in the screening and prioritization of a wide bridge inventory) the assumption of continuous deck (joints closed) can be reasonably adopted, in order to reduce the computational efforts, since it brings about a conservative evaluation of the seismic performance of the bridge.

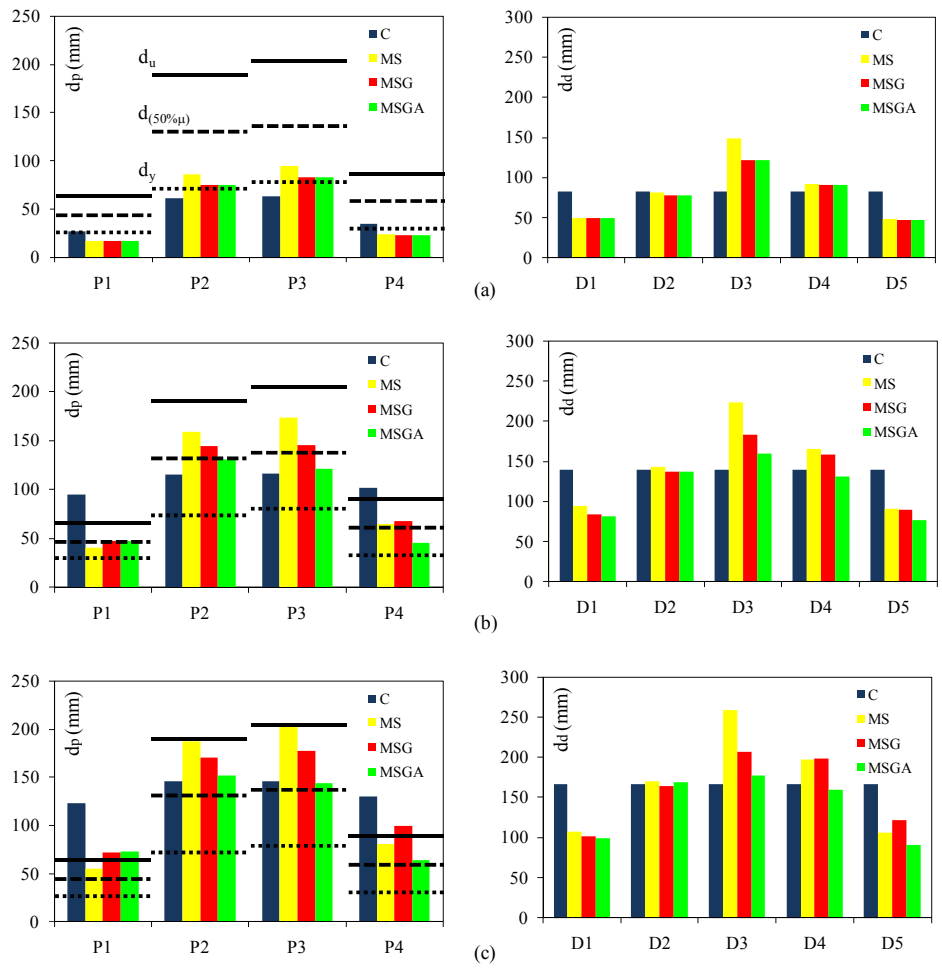

Fig. 4. NTHA results at (a) 0.238g, (b) 0.448g and (c) 0.537g PGA.

5. References

Caltrans (California Dept. of Transportation). 2013. Seismic Design Criteria.

Priestley, M.J.N., Seible, F., and Calvi, G.M. 1996. Seismic Design and Retrofit of Bridges, John Wiley & Sons.

Takeda, T., Sozen, M.A., and Nielsen, N.N. 1970. Reinforced concrete response to simulated earthquakes. Journal of Structural Engineering. 96(12): 2257-2273.

Prediction of Strength and Creep Behavior of Hydrated Cement Components Using Nanoindentation Technique

Hyuk Lee[1*], Vanissorn Vimonsatit[2], and Priyan Mendis[3]

[1] School of Civil and Mechanical Engineering, Curtin University, Western Australia, Australia; email: leehyuk1982@gmail.com
[2] School of Civil and Mechanical Engineering, Curtin University, Western Australia, Australia; email: V.Vimonsatit@curtin.edu.au
[3] Department of Infrastructure Engineering, University of Melbourne, Victoria, Australia; email: pamendis@unimelb.edu.au

[*] : corresponding author

Keywords: cement; nano; indentation; packing density; property

Abstract: The knowledge of the nanostructure of a material and the relationship between its local properties due to the reaction products of the material can be linked to the macroscopic material diversity such as strength and fracture behaviors. Instrument indentation technique is a promising method that provides material responses upon the reversal of touch loading and an access to the elastic properties of the indented material. Despite being well established, the application of the instrumented indentation technique is still difficult to probe directly into the overall material characteristics especially for heterogeneous materials such as hydrated cement and concrete. This paper presents the application of an advanced indentation technique to predict the properties of hydrated cement, including mechanical, microporomechanical and viscoelastic properties using a statistical analysis approach. These properties are essential in delimitating the strength and fracture behaviors of concrete materials.

1. Introduction

The mechanical, micromechanical, and viscoelastic properties of structural materials are important aspects in the designed life of the structure (Neville 2011). The intrinsic properties of hydrated cement primarily define the targeted concrete properties required for engineering applications. Determination of the mechanical, micromechanical and durability properties of hydrated cement demands an in-depth knowledge of its nanostructure and how it is related to the local properties because the hydrated nanostructure form the fundamental building block whose behaviour is expected to delimitate macroscopic material diversity such as strength and fracture behaviours (Lee et al. 2016). Several existing techniques have been used to investigate the properties of the nanostructure of cementitious materials, for example, Tennis and Jennings (2000) provided a microstructural model of OPC that could quantitatively predict the two CSH phases; low density (LD) and high density (HD) CSH. Similarly, Constantidies et al. (2007) determined a mean for quantifying a volumetric proportion of major hydration products of OPC such as capillary porosity (MP), LD CSH, HD CSH, Portlandite (CH) and clinker phases with nanoindentation. This study demonstrates how an indentation technique can be used to predict the strength and creep properties of OPC components.

2. Methodology

The instrumented indentation technique has been extensively studied by several researchers recently (Cheng and Cheng 2004, Oliver and Pharr 2004, Fischer-Cripps 2011, Lee et al 2016). The measurement of hardness H and elastic modulus E of material can be obtained from the relationship between indentation loads P and depth h during loading and unloading (Lee et al. 2016, Lee et al. 2018). The important quantities that must be measured from the $P-h$ curve are the maximum indentation load, P_{max}, the maximum indentation depth, h_{max}, and the elastic unloading stiffness, $S = dP/dh$, which is defined as the slope of the upper portion of the unloading curve. Briefly, we recall that measurement of H and E can be determined by isotropic indentation modulus M from the Hertz contact equation as shown in Equation (1). The scaling relation of the packing density η and M and H leads to finding the solid properties such as stiffness $\lambda = \lim_{\eta \to 1} M$, Poisson's ratio ν_s, cohesion κ, and friction coefficient ξ as presented in Equation (2) (Dormieux et al. 2016)

$$M = \frac{1-\nu^2}{E} \tag{1}$$

$$\begin{aligned} M &= \frac{\sqrt{\pi}}{2}\frac{S}{\sqrt{A_c}} = \lambda \Pi_M(\nu_s, \eta, \eta_0) \\ H &= \frac{P_{max}}{A_c} = \kappa \Pi_H(\xi, \eta, \eta_0) \end{aligned} \tag{2}$$

where A_c is the conatact area which can be expressed in term of indentation contact depth h_c and residual depth h_r as determined by Oliver-Pharr method (Oliver and Pharr, 2004). The Π_M and Π_H are dimensional scaling relating to stiffness and hardness respectively (Lee et al. 2016, Lee et al. 2018). The solid percolation threshold η_0 is the limit that the solid fraction requires for providing the continuous force depth path through the system. With an inverse application between theoretical scaling relationship and experimental values, the total number of phases is identifiable based on a deconvolution technique, and thus the phase properties, M, H, η and the volume fraction can be determined (Lee et al. 2018).

Creep properties can be predicted using the indentation results. The creep compliance rate $\dot{J}_c(t)$ can be expressed (Vandamme and Ulm 2006, Lee et al. 2018) as:

$$\dot{J}_c(t) = \frac{2a(t)}{P_{amax}}\dot{h}(t) \tag{3}$$

$$\dot{h}(t) = x_1 ln\left(\frac{t}{x_2}+1\right) + x_3 t + x_4 \tag{4}$$

$$\dot{J}_c(t) = \frac{1}{Ct}, \quad \text{where} \quad C = \frac{P_{max}}{2a_c x_1} \tag{5}$$

where $a(t)$ is the radius of the projected contact area, $\dot{h}(t)$ is the change in the indentation depth over the holding time, and $x_1, \ldots x_4$ are constants. In Equation (4), the material's related term is only the logarithmic term, therefore, $\dot{h}(t)$ can be replaced by the term x_1/t, C is the contact creep modulus, and $a_c \approx \sqrt{A_c/\pi}$ is the contact radius. Thus, a higher contact creep modulus will lead to a lower logarithmic creep of material.

3. Experimental Procedure

In this investigation, two series of sample were tested, OPC and fly ash based geopolymer mixture. General purpose (Type 1) cement available locally in Australia with water to cement ratio of 0.3 was used to prepare the OPC samples. The OPC samples were cured in lime water at ambient temperature 23 ± 3°C. The average compressive strength has been observed as 94.6 MPa at 28 days curing age. Nanoindentation test has been carried on the three sets of OPC and geopolymer samples at 28 days curing age with minimum 300 indentation points per sample with Berkovich indenter and grid indentation approach (Constantinides et al. 2007).

4. Results and Discussion

The deconvolution results of the modulus M and hardness H based on the mean values of the first peak (MP phase) are: $M = 9.388$ GPa; $H = 0.297$ GPa; the second peak (LD CSH), $M = 16.591$ GPa, $H = 0.700$ GPa; the third peak (HD CSH) $M = 29.818$ GPa, $H = 1.412$ GPa, which are in good agreement with the values reported in literature (Ulm et al. 2007,). For the fourth peak (CH), $M = 48.677$ GPa, $H = 10.495$ GPa, and the clinker, $M = 112.378$ GPa, $H = 14.718$ GPa. the packing density η and the volume fraction (in brackets) of the pores phase (MP), LD CSH, HD CSH, CH and clinker are, $\eta = 0.531 \pm 0.01$ (44%) $\eta = 0.556 \pm 0.01$ (33%) $\eta = 0.595 \pm 0.01$ with (10%), $\eta = 0.627 \pm 0.06$ (7%), and $\eta = 0.780 \pm 0.12$ (5%), respectively.

Based on the microporomechanics approach (Ulm et al. 2007), the solid properties of hydrated products of OPC are: $\lambda = 189.442$ GPa, $\nu_s = 0.499$, $\kappa = 1.300$ GPa, and $\xi = 0.566$. The results of the solid properties of the hydration products of OPC can be understood in the sense of the Drunker Prager strength and Coulomb material model. Thus, the ultimate strength σ_u can be determined as (Vandamme and Ulm 2006):

$$\sigma_0 = 2\kappa \frac{\cos\phi}{1 - \sin\phi} \tag{6}$$

where ϕ is fraction angle. Based on Equation (6), the compressive strength of the MP phase is found to be very close to that of OPC, i.e., $\sigma_0 = 96.5$ MPa and 136.233 MPa for OPC and CSH phases, respectively. With these properties, the Mori-Tanaka and self-consistent schemes enable upscaling the strength properties of structural concrete (Oliver et al. 2003). In order to determine the creep properties using the indentation results, the change in the depth of the holding phase can be fitted with a logarithmic function in Equation (4). In the present case, the long-term contact creep compliance rate was determined as 409.266 GPa, with the average correction coefficient of the fitted curve as 0.986 ± 0.04. The results of the creep compliance rate clearly shows that the rate of the creep compliance sharply decrease after a few days of stressing as shown in Figure 1. The deconvolution results show that for the MP phase, $C = 75.552 \pm 37.754$

GPa; LD CSH phase, $C = 162.201 \pm 37.754$ GPa; HD CSH phase, $C = 333.797 \pm 46.979$ GPa, and CH phase, $C = 663.387 \pm 188.444$ GPa. The results show that the MP phase has the highest creep compliance in OPC which leads to a lower creep modulus. The specific creep after one year from the indentation test was analysed as 18.32 microstrain/MPa which agrees well with the literature (Warner et al. 1998) indicates that creep of OPC after one year is to be around 20 microstrain/MPa.

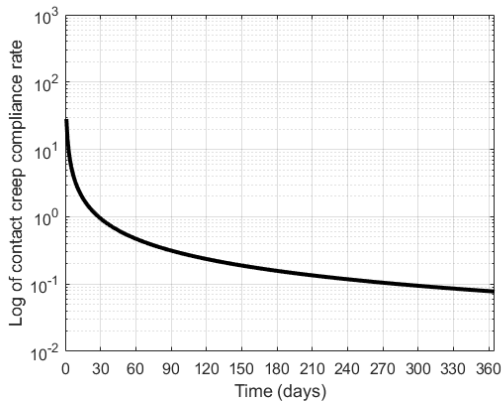

Figure 1. Contact creep compliance rate of OPC

5. Conclusion

The instrumented indentation technique coupled with a statistical analysis, microporomechanics are successfully applied to investigate the local properties and strength of cementitious material which is the matrix in concrete. The known phases, capillary porosity, low density calcium silicate hydrated, high density calcium silicate hydrated, calcium hydroxide and clinker phases, can be quantified. The MP phase in OPC in this case indicates the failure under compression and leads to more creep. With an upscaling approach, the determined properties can be used to predict the strength and creep behavior of concrete in structures where loading is inherently dynamic and repetitive in nature such as bridges.

6. Acknowledgements

This work was supported by Australia Research Council (ARC-DP180100643).

7. References

Cheng, Y.-T. and Cheng, C.-M. 2004. Scaling, dimensional analysis, and indentation measurements. Materials Science and Engineering: R: Reports, 44, 91-149.

Constantinides, G. and Ulm, F.-J. 2007. The nanogranular nature of C–S–H. Journal of the Mechanics and Physics of Solids, 55, 64-90.

Dormieux, L., Kondo, D. and Ulm, F.-J. 2006. Microporomechanics, John Wiley & Sons.

Fischer-cripps, A. C. 2011. Nanoindentation, New York, NY, New York, NY : Springer New York.

Lee, H., Vimonsatit, V. and Chindaprasirt, P. 2016. Mechanical and micromechanical properties of alkali activated fly-ash cement based on nano-indentation. Construction and Building Materials, 107, 95-102.

Lee, H., Vimonsatit, V., Chindaprasirt, P., Ngo, T. and Mendis, P. 2018. Creep properties of cement and alkali activated fly ash materials using nanoindentation technique. Construction and Building Materials, 168, 547-555.

Neville, A. M. 2011. Properties of concrete, Harlow : Prentice Hall.

Oliver, B., Ulm F.J. and Lemarchand E. 2003. A multiscale micromechanics-hydration model for the early-age elastic properties of cement-based materials. Cement and Concrete Research, 33, 1293-1309.

Oliver, W. C. and Pharr, G. M. 2004. Measurement of hardness and elastic modulus by instrumented indentation: Advances in understanding and refinements to methodology. Journal of materials research, 19, 3-20.

Tennis, P. D. and Jennings, H. M. 2000. A model for two types of calcium silicate hydrate in the microstructure of Portland cement pastes. Cement and Concrete Research, 30, 855-863.

Ulm, F. J., Vandamme, M., Bobko, C., Alberto ortega, J., Tai, K. and Ortiz, C. 2007. Statistical indentation techniques for hydrated nanocomposites: concrete, bone, and shale. Journal of the American Ceramic Society, 90, 2677-2692.

Vandamme, M. and Ulm, F.-J. 2006. Viscoelastic solutions for conical indentation. International Journal of solids and structures, 43, 3142-3165.

Warner, R. F., Rangan, B., Hall, A. & Faulkes, K. 1998. Concrete structures, Pearson Education Australia, Frenchs Forest, NSW, Australia.

Physicochemical Study on Strength Characteristics of Mortar with Nitrite-Based Accelerator

A Yoneyama[1], H.S Choi [2*], M Inoue [3], and Y Sudoh[4]

[1] Department of Civil and Environmental Engineering, Kitami Institute of Technology, Hokkaido 090-8507, Japan; email: akimtrice32@gmail.com
[2] Department of Civil and Environmental Engineering, Kitami Institute of Technology, Hokkaido 090-8507, Japan; email: hs-choi@mail.kitami-it.ac.jp
[3] Department of Civil and Environmental Engineering, Kitami Institute of Technology, Hokkaido 090-8507, Japan; email: m-inoue@mail.kitami-it.ac.jp
[4] Chemicals Division Basic Chemicals Department, Nissan Chemical Industries, Ltd., Tokyo 103 -6119, Japan; email: sudouyuuji@nissanchem.co.jp

[*]: corresponding author

Keywords: hydration products; ettringite; C_3A; strength characteristics; fresh properties

Abstract: Calcium nitrite, which is widely used as the main component of a non-freezing agent, promotes the hydration of C_3A and C_3S in cement and has an effect on improving the initial strength of concrete. However, the relationship between hydration products and intensity development is unclear. In this study, examined the freshness, temperature history, strength characteristics and hydration products of mortar with large amount of calcium nitrite added. As a result, the addition of calcium nitrite generated nitrite AFt ($3CaO{\cdot}Al_2O_3{\cdot}3Ca(NO_2)_2{\cdot}10H_2O$) in addition to ettringite, so that good initial strength development (1day) was obtained. On the other hand, It was presumed that the strength characteristics from 3 to 14 days that decreased from the decrease of hydration products such as C-S-H and $Ca(OH)_2$ relatively along with the increase in the amount of AFt.

1. Introduction

When constructing cold-weather concrete, it is necessary to prevent initial frost damage by controlling the temperature of heat curing through the use of a temporary enclosure and heater. In Japan, as a measure to prevent early freezing, early curing is performed adequately to prevent concrete from freezing until its strength reaches 5 MPa after the depositing process, as recommended by the Standard Specifications for Concrete [1] and the Japanese Architectural Standard Specification (JASS5) [2]. On the other hand, when it is difficult to install the temporary enclosure owing to a steep slope at the construction site, a narrow working space, or a strong wind, a non-freezing agent is commonly used to prevent initial frost damage and secure initial strength development through simplified curing [3].

In general, a nitrite-based accelerator is used as the main component of this non-freezing agent. In particular, calcium nitrite ($Ca(NO_2)_2$) chiefly accelerates the hydration process by increasing the solubility of C_3S (alite, $3CaO{\cdot}SiO_2$) and C_2S (belite, $2CaO{\cdot}SiO_2$) and reacts with C_3A (aluminate phase, $3CaO{\cdot}Al_2O_3$) in cement to generate nitrite AFt ($3CaO{\cdot}Al_2O_3{\cdot}Ca(NO_2)_2{\cdot}10H_2O$). These cement hydrates lead to a refinement in cement

hardening; hence, they improve the mechanical properties of concrete in low-temperature environments [4]. A considerable number of studies have been conducted on the effects of a non-freezing agent on the properties of concrete in the initial stage after production. In a low-temperature environment of -10 °C or less, it is necessary to add a larger amount of the non-freezing agent; with this increase, however, the hydration reaction of the C_3A phases progress rapidly from the initial stage. The reaction of C_3A generates a large amount of AFt [5].The purpose of this study is to clarify the correlation between strength development characteristics and hydration products of mortar to which a large amount of nitrite-based accelerator is added.

2. Outline of the experiments

2.1 Materials used and mixing proportions and experimental conditions

The cement materials used are listed in table 1, and the non-freezing agents are listed in Table 2. The mixing proportions and curing temperatures used to prepare the cement materials are listed in Table 3. The water-to-cement (W/C) ratio was 0.5. The standard replacement ratio of conventional accelerators is approximately 4-7% of the unit content of cement (3-5L per 100kg of cement) [4]. Therefore, in this study, more than 7% of calcium nitrite (CN) were defined as replacement ratio of large amount of calcium nitrite and the replacement ratio of CN was 0%, 7%, 9%, 11%, 13%. Also, the temperature of concrete at the time of placing should be 10–20 °C as specified by the Architectural Institute of Japan in “Recommendation for Practice of Cold Weather Concreting” [6]. In this experiments, the material management and mixing of cement mortar were performed in the test condition with control of temperature (10 ± 1 °C) and humidity (85 ± 5 %) from the time of mixing to the test, during 14 days.

2.2 Test method

The temperature of cement mortar was measured immediately after mixing cement mortar. And, the compressive strength (φ50 × 100 mm) was measured after 1, 3, 7, and 14 days. Also, the hydration product was measured using SEM with the specimen of 1 days age (CN0 and CN13) and XRD with the specimen of 1 days and 14days age (CN0 and CN13).

Table 1 Properties of the materials used

Materials (Code)	Properties
Cement (C)	Normal Portland cement, Density: 3.16 g/cm^3
Fine aggregate (S)	No.5 silica sand, Absolute dry density: 2.61 g/cm^3, Water absorption: 0.26%, Fineness modulus: 2.16
Accelerator (CN)	Main component: calcium nitrite; other accelerating components (45% water solution), Density: 1.42–1.44 g/cm^3

Table 2 Properties of the non-freezing agent

Code	Component	Component ratio	pH	Density
CN	$Ca(NO_2)_2$	23.0%	9.3	1.43
	$Ca(NO_3)_2$	22.8%		

Table 3 Mix proportions of mortar

Type	W/C (%)	S/C	Unit content (kg/m^3)			Admixture (C×%)
			W	C	S	CN
CN0	50	2.0	315	631	1262	0
CN7						7
CN9						9
CN11						11
CN13						13

3. Results and discussion

3.1 Compressive strength and mortar temperature

The temperature history are presented in Figures 1 and 3, and the results of the compressive strength test are presented in Figures 2 and 4. In Figure 1, the mortar temperature after mixing tended to be higher as CN was added. In Figure 2, when the specimens were cured at +10 °C immediately after mixing for 1 day, CN0 showed a compressive strength of 3.42 MPa. However, CN11 and CN13 showed compressive strengths 4.95 and 5.09 MPa. From this result, it is assumed that the temperature rise is caused by the reaction of C_3A and NO_2^-. Also, the increase in compressive strength with temperature rise at day 1 is presumed to be increased by NO_2^- reacting with C_3A to generate nitrite AFt ($3CaO{\cdot}Al_2O_3{\cdot}3Ca(NO_2)_2{\cdot}10H_2O$) [9]. In Figure 3, when CN was added, the temperature peak around 20 hours tended to be earlier compared with CN0. In Figure 4, The compressive strength after 3 day tended to decrease when CN was added, the compressive strength at the 14 day, CN0 was 39.5 MPa, but CN11 was 28.3 MPa and CN13 was 24.1 MPa, respectively. From this result, it is presumed that the decrease in strength is due to the decrease of C-S-H and $Ca(OH)_2$with the increase of Aft.

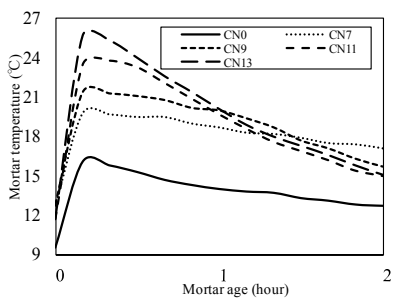

Figure 1 Temperature history (2 hours)

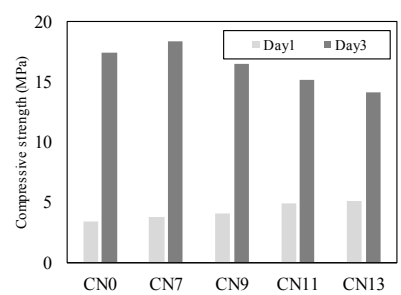

Figure 2 Compressive strength (1 and 3days)

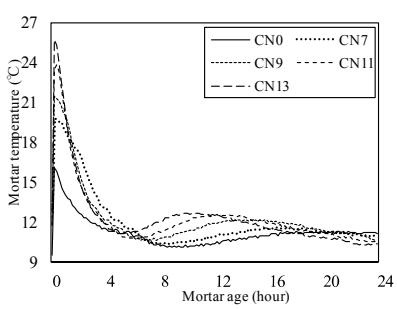

Figure 3 Temperature history (24 hours)

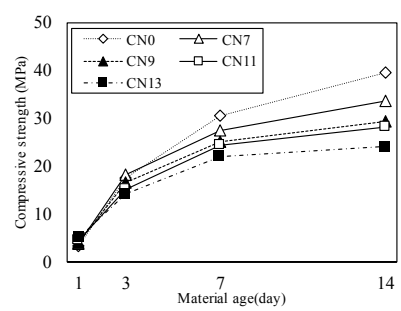

Figure 4 Compressive strength

3.2 Micro evaluation of reactants of C_3A and $Ca(NO_2)_2$

3.2.1 Scanning electron microscope (SEM)

In order to clarify the correlation between hydration product when CN added and compressive strength, hydrated products were confirmed using Scanning electron microscope (SEM). SEM observed CN0 and CN13, and compared differences in the crystal structure, as shown in the SEM images of Figure 5 and 6. The pictures show that at day 1. Observed hydration products were presumed from the crystal form and size that can be confirmed in the previous study [7]. In Figure 5, ettringite and $Ca(OH)_2$ were observed at CN0. On the other hand, in Figure 6, the CN13, nitrite AFt was confirmed in addition to ettringite. Therefore, it was considered that the addition of CN generates a hydrated product which is guess to be nitrite AFt.

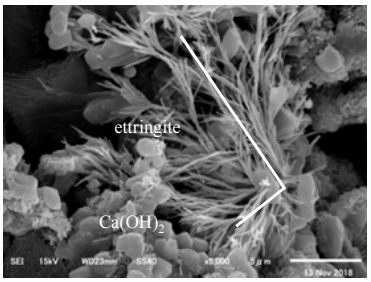

Figure 5 CN0-Hydrate products (×5,000)

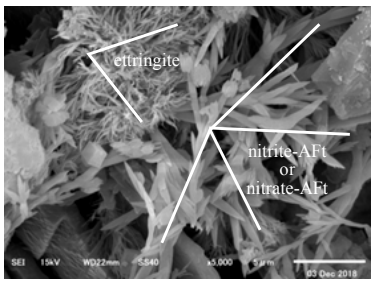

Figure 6 CN13-Hydrate products (×5,000)

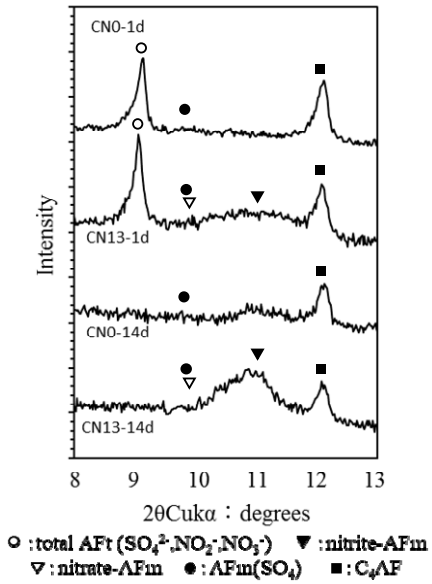

Figure 7 XRD profile

3.2.2 XRD

Figure 7 shows the XRD profiles of calcium aluminate hydrate on CN0 and CN13 on day 1 and day 14. Measurement of XRD was performed at a voltage: 40kV, current: 20mA, scanning range: 2θ=5~65°, step width: 0.02°, and scanning speed: 1° per min. nitrite AFt and nitrite AFm are generated in addition to AFt, when CN was added. According to a previous study, the peak of nitrite AFm appears from 11.23° to 11.04°. In this study, hydrate products were identified in the range of 8~13° [8] [9].

From day 1 in Figure 7, Although AFt is generated in both cases, the peak intensity is higher in CN13 due to the influence of NO_2^- and NO_3^-. Furthermore, nitrite AFm and nitrate AFm were also generated in CN13, and it is considered that these were produced in large quantities at the young ages. It was confirmed that the increase in the amount of AFt produced and the formation of nitrite AFm were obtained by adding CN. As a result, it was presumed that the initial compressive strength increased. On the other hand, from day 14 in Figure 7, AFt was not confirmed in either case. On the other hand, in CN13, it can be confirmed that the peak

intensities of nitrite AFm and nitrate AFm are larger than day 1. It is presumed that AFt reacted with C_3S and a large amount of nitrite AFm and nitrite AFm were formed in the case where CN was added [10]. Also, it is considered that as the production of nitrite AFm and nitrite AFm increased, the amount of hydrated products such as C-S-H gel and $Ca(OH)_2$ decreased relatively and the compressive strength became lower than CN0

4. Conclusions

The aim of this study is to clarify the effect of strength characteristics of concrete when a large amount of nitrite-based accelerator was added. Furthermore, the hydration product was measured at each material age, and the correlations between each item were examined. The following conclusions can be drawn from the investigation:

1) When CN was added, the hydration speed of C_3A and C_3S accelerated, and the heat of hydration increased as the addition amount of CN increased.
2) When CN was added in a large amount, nitrite AFt was generated by reaction of NO_2 and C_3A in addition to ettringite, as a result, the compressive strength at young age was increased.
3) After 3 days, increase of large amount of AFt, and hydrated products such as C-S-H and $Ca(OH)_2$ are decreased relatively. As a result, it was decreased strength to compared CN0.

5. References

[1] Standard Specifications for Concrete Japan Society of Civil Engineers 1991

[2] Japanese Architectural Standard Specifications for Reinforced Concrete Work JASS5 Architectural Institute of Japan 1997

[3] Aakama, T., Inoue, M., Sudoh, U., and Mikami, S. (2012), "Fresh properties and early strength development of concrete using calcium nitrite and water-reducing agents," *Proceedings of the Japan Concrete Institute*, 34(1), 155-159.

[4] Iwasawa, M., Inoue, M., Choi, H., Sudoh, Y., and Ayuta, K. (2016), "Characteristics of concrete using nitrite-based accelerator and chemical admixtures in low-temperature environments," *Proceedings of the 7th International Conference of Asian Concrete Federation*, 1-052, 1-8.

[5] Ramachanran, V.S. (1995), "Concrete Admixture Handbook," *Noyes Publications, U.S.A.*, 741-799.

[6] Practical Guideline for Investigation (2010), "Recommendation for practice of cold weather concreting," *Architectural Institute of Japan,* 57. (In Japanese)

[7] Ramachanran, V.S. : Concrete Admixture Handbook, Noyes Publications, U.S.A., pp.741-799, 1995

[8] M. Balonis et al. : Influence of calcium nitrate and nitrite on the constitution of AFm and AFt cement hydrates. Advanced in Cement Research, Vol. 23, pp. 129-143, 2011

[9] P. Kumar Mehta , Paulo J. M. Monteiro : CONCRETE , Microstructure, Properties, and Materials Second Edition, pp.22-27 , 1997

[10] United States Patent：Inorganic admixtures for mitigating against conversion phenomena in high-alumina cements，1995.1

Determination of Material Frequency from Instrumentation Response

Zafrul Khan[1] and Rafiqul Tarefder[2*]

[1] The University of New Mexico, Albuquerque, USA; email: zkhan@unm.edu
[2] The University of New Mexico, Albuquerque, USA; email: tarefder@unm.edu

[*]: corresponding author

Keywords: wavelet; falling weight deflectometer; instrumentation; frequency; asphalt concrete.

Abstract: This study demonstrates a methodology to determine the response frequency of pavement structure through embedded sensors such as strain gauge. Pavement response data were collected from an instrumented pavement section on Interstate-40 (I-40) in New Mexico. Noise removal schemes such as Savitzky-Golay filter and detrending is applied to the sensor response data to enhance the signal to noise ratio. Using a low-pass FIR filter and Continuous Wavelet Transformation (CWT) on the sensor obtained response spectrum, loading frequency was removed, and only the material response frequency was isolated. Asphalt layer frequency was obtained under the class 9 semi-trailer vehicle and controlled Falling weight Deflectometer (FWD) test. From the results, it is observed that conventional Odemark's based solution overpredicts the frequency of the asphalt layer by 25%, which may lead to inaccurate design of the transportation structures.

1. Introduction

Mechanical properties of asphalt concrete (mostly depends on the frequency and temperature. Complex modulus ($|E^*|$) of AC is determined in laboratory in frequency domain at different temperatures. However, in actual field condition the load is applied on the pavement in time domain. Several methods have been developed by the researchers to convert between time and frequency domain. Mechanistic Empirical (ME) design guide uses Odemark's method to calculate the load pulse time duration (t) and then uses reciprocal of time to calculate the frequency (f). Recent studies showed that this method of frequency calculation may not be accurate (Ulloa et al. 2012)**.** Al-Qadi et al. (2008) and Shafiee et al. (2015) have used vehicle travelling at 60 kmph (37 mph) to determine the loading frequency. Most of the loads in interstates come from class 9 semi-trailer vehicle and average operating speed of these type of vehicle is around 105 kmph (65 mph). Therefore, it is important to obtain the AC layer frequency under the class 9 vehicle operating in the range of allowable speed limit of the interstates directly from the field instrumentation response.

2. Methodology

AASHTOWare ME design guide (ARA Inc 2007)uses Odemark's method to calculate the load pulse time duration (t) and then uses $f = 1/t$ to calculate frequency (f).

$$\left.\begin{aligned} t &= \frac{L_{eff}}{17.6v} \\ L_{eff} &= 2(a_c + Z_{eff}) \\ Z_{eff} &= \sum_{i=1}^{n-1}\left(h_i \sqrt[3]{\frac{E_i}{E_{SG}}}\right) + h_n \sqrt[3]{\frac{E_n}{E_{SG}}} \\ f &= \frac{1}{t} \\ a_c &= \sqrt{\frac{P}{p\pi}} \end{aligned}\right\} \quad (1)$$

where, t = loading time (s), L_{eff} = Effective length (in), v = speed (mph), a_c = radius of contact area (in), E_{SG}= modulus of subgrade, n = number of layers, h_n = thickness of the layer of interest (in), E_n = modulus of the layer of interest (psi), f = loading frequency (Hz), P = Wheel Load, p = contact pressure. This study uses CWT to study the asphalt concrete (AC) layer frequency spectrum under traffic and controlled FWD test loads. This is done due to the time-varying nature of the sensor obtained response signal. The wavelet is a linear transformation (Mallat 1999; Kareem & Kijewski 2002) that decomposes an arbitrary signal *x(t)* via basis function of a parent wavelet *g(t)* through a convolution process by a scale factor of *a* as shown in Eq. (2).

$$W(a,t) = \frac{1}{\sqrt{a}} \int_{-\infty}^{\infty} x(\tau) g^*\left(\frac{t-\tau}{a}\right) d\tau \quad (2)$$

In this study, Morlet weavelet is used for CWT due to is similarity to the Fourier transform.

3. Instrumentation Section

AC layer response from the traffic and the FWD loadings were obtained from the instrumentation section located on I-40 near Albuquerque, New Mexico. Figure 1 shows the location of the sensors at the I-40 instrumentation section. The instrumentation section has a total of 32 sensors. For this study, responses from the horizontal axial strain gages at the bottom of the 11.1-inch Hot-Mix Asphalt (HMA) layer is used.

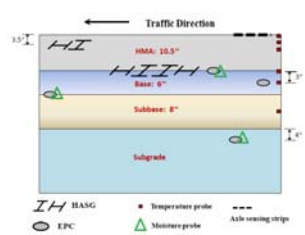

Fig. 1. Cross sectional view of the sensors positions at the instrumentation section

3. Analysis and Discussion

Response of the applied load on the pavement can be obtained through installed sensors and it can be plotted against time. Figure 2(a) shows the response of a horizontal strain gage under the 9-kip FWD load. The signal was detrended and Savitzky-Golay filter (Schafer 2011) was applied to increase the signal to noise ratio as shown in Figure 2(b).

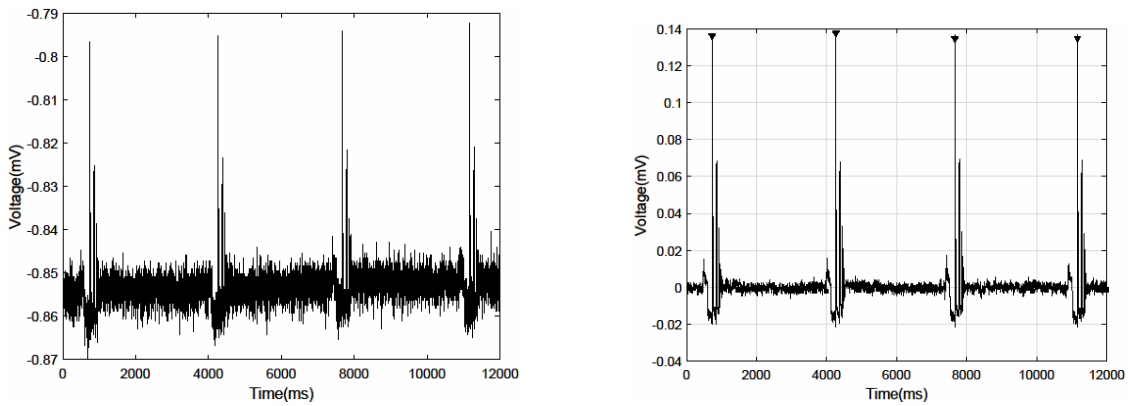

(a) (b)

Fig. 2. Signal Preprocessing (a) Raw Signal (b) Pre-Processed Signal

The loading frequency in FWD test is around 25-30 Hz (Seo et al. 2013). In this study, it is assumed that class 9 semi-trailer vehicle will have a loading frequency in the similar or higher range of FWD test. It is a valid assumption as the FWD 9-kip load simulates the response of a class 9 vehicle traveling in the range of 55 mph (Appea 2003). Figure 3 shows the scalogram of FWD signal with both loading frequency and materials response frequency. It can bee that it has high magnitude frequencies around 25 Hz, 13 Hz and 7.2 Hz. As 25 Hz is the loading frequency, therefore, anything above 25 Hz has been removed using a low pass FIR filter. Figure 4(a and b) shows the scalogram of the AC layer only under class 9 vehicle and FWD 9-kip load. From Fig. 4(a) high magnitude frequency of the AC layer under class 9 vehicle was observed around 17 Hz, and from Fig. 4(b) the value was around 13 Hz. Using the Odemark's method in Eq. (1), AASHTOWare ME predicts the frequency of AC layer to be around 21 Hz under class 9 vehicle.

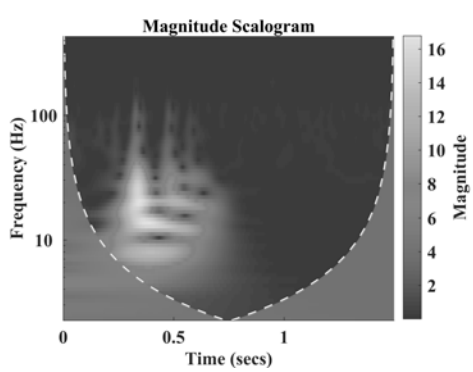

Fig. 3. Scalogram of FWD signal with loading frequency and AC frequency

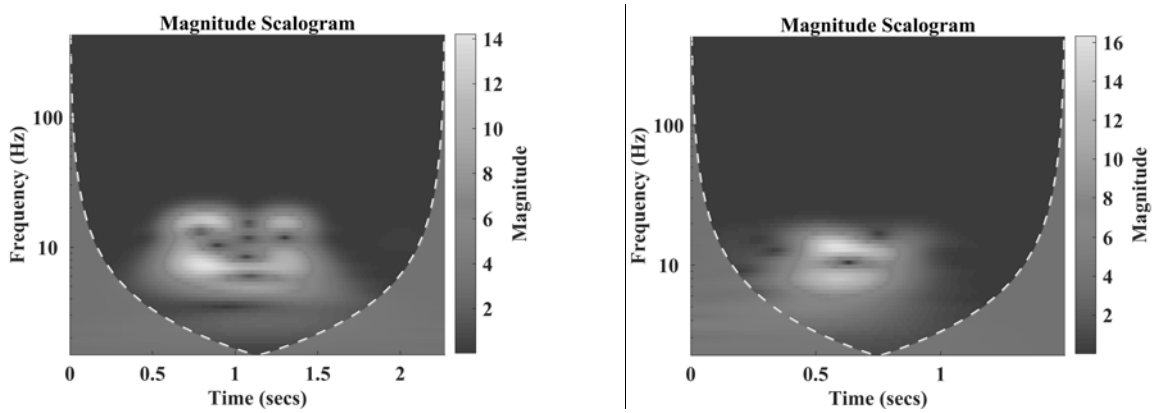

(a) (b)

Fig. 4. Scalogram of AC layer under (a)class 9 semi-trailer vehicle (b) FWD 9-kip load

6. Conclusions

This study successfully uses CWT method to determine the frequency of AC layer under any type of loadings. Tradition Odemark's method overpredicts the AC layer response by around 25%. Accurate determination of the material frequency spectrum is important for continuous health monitoring of the transportation structures.

5. References

Al-Qadi, I. et al., 2008. Accuracy of current complex modulus selection procedure from vehicular load pulse: NCHRP project 1-37a mechanistic-empirical pavement design guide. Transportation Research Record: Journal of the Transportation Research Board, (2087), pp.81–90.

Appea, A.K., 2003. Validation of FWD Testing Results at the Virginia Smart Road : Theoretically and by Instrument Responses. Virginia Polytechnic Institute and State University.

ARA Inc, 2007. Guide for the mechanistic-empirical design of new and rehabilitated pavement structures. Final report, NCHRP Project 1-37A.

Kareem, A. & Kijewski, T., 2002. Time-frequency analysis of wind effects on structures. Journal of Wind Engineering and Industrial Aerodynamics, 90(12–15), pp.1435–1452.

Mallat, S., 1999. A wavelet tour of signal processing, Elsevier.

Schafer, R.W., 2011. What is a Savitzky-Golay filter?[lecture notes]. IEEE Signal processing magazine, 28(4), pp.111–117.

Seo, J. et al., 2013. Estimation of in situ dynamic modulus by using MEPDG dynamic modulus and FWD data at different temperatures. International Journal of Pavement Engineering, 14(4), pp.343–353.

Shafiee, M.H. et al., 2015. Analysis of Loading Frequency in Flexible Pavement Using Fast Fourier Transform. International Journal of Pavement Research and Technology, 8(6), pp.403–409.

Ulloa, A. et al., 2012. Equivalent loading frequencies for dynamic analysis of asphalt pavements. Journal of Materials in Civil Engineering, 25(9), pp.1162–1170.

Bridge Engineering Institute Conference 2019 (BEI-2019)
Honolulu, Hawaii, USA, July 22-25, 2019

Fundamental Study on the Strength Development of Cold-Weather Concrete with Hydronic Heat Curing System

Soki Obara[1], Heesup Choi[2*], Masumi Inoue[3], Yoshio Saito[4], Wataru Inoue[5], and Kenichi Yoshioka[6]

[1] Department of Civil and Environmental Engineering, Kitami Institute of Technology, Hokkaido 090-8507, Japan; email: komachi15daen@gmail.com
[2] Department of Civil and Environmental Engineering, Kitami Institute of Technology, Hokkaido 090-8507, Japan; email: hs-choi@mail.kitami-it.ac.jp
[3] Department of Civil and Environmental Engineering, Kitami Institute of Technology, Hokkaido 090-8507, Japan; email: m-inoue@mail.kitami-it.ac.jp
[4] EXEN Corporation, Tokyo 105-0013, Japan; email: y-saito@exen.co.jp
[5] EXEN Corporation, Tokyo 105-0013, Japan; email: w-inoue@exen.co.jp
[6] Nippon High Strength Concrete Co. Ltd., Hokkaido 060-0003, Japan; email: k.yoshioka@nihonkoatsu.co.jp

[*]: corresponding author

Keywords: cold-weather concreting; hydronic heat curing; strength; cumulative temperature

Abstract: As a new heat curing system for cold-weather concrete, there is a hydronic heat curing system in which high quality and economical curing may be expected by maintaining appropriate temperature environments. The aim of this study is to clarify the strength development characteristics by heat curing, using a hydronic heater in a low-temperature environment. In the experiment, temperature history and compressive strength, hydration products of the concrete were used for heat curing and measured a change over time. As a result, effective temperature management of the concrete is possible by heat curing using this system. In addition, author confirmed that good strength development was obtained because the production of the hydration product increased with hydration promotion.

1. Introduction

For cold-weather concreting, inappropriate curing may reduce its strength and durability due to early frost damage caused by water freezing inside the concrete[1),2)]. Accordingly, in Japan, as a measure to prevent early freezing, early curing is performed adequately to prevent concrete from freezing until its strength reaches 5 MPa after the depositing process, as recommended by the Standard Specifications for Concrete[1)] and the Japanese Architectural Standard Specification (JASS5) [2)]. In this case, in general, correspondence is made by warm curing and heat curing along with the correction of the mix proportion. On the other hand, as shown in Fig. 1, the accelerated heat curing method that is typically adopted in the cold regions is to cover the concrete structure in the construction layer with an insulating tarpaulin and then heated in the inner space using a hot air blower (jet heater). However, this method has been reported to have low heat efficiency and potentially have an adverse impact on the strength development and durability of the concrete structure in the event of a fire or generation of combustion gas (e.g., CO, CO_2) [3)]. Moreover, there is a possibility that the strength of the concrete structure will not be

developed uniformly due to an excessively large or insufficient supply of heat in a localized area, depending on the distance of the heat source[3]. Therefore, the authors propose a heating curing using hydronic heater as a new heating curing method to solve these problems[4]. A hydronic heater is, as shown in Fig. 2, is a device that supplies hot water, which has been heated by a simple boiler installed in an accelerated heat curing unit, to a circulating hose using a pump. The hydronic hose is set up on the surface on which concrete will be placed or outside of the formwork to directly and indirectly heat the concrete structure for the curing process. This system allows an early strength development to prevent early frost damage and early demolding as a means of quality control for cold weather concrete. In addition, it is deemed that by maintaining appropriate temperature and humidity conditions, will be possible to ensure that the resulting concrete is of high quality and that the construction work using the cold weather concrete is economical. The objective of this study is to reveal the characteristics of the strength development of concrete subjected to accelerated heat curing using a hydronic heater in a low temperature environment. Temperature history, compressive strength and hydration products of concrete that were heat cured by using a hydronic heater in a low temperature laboratory were measured.

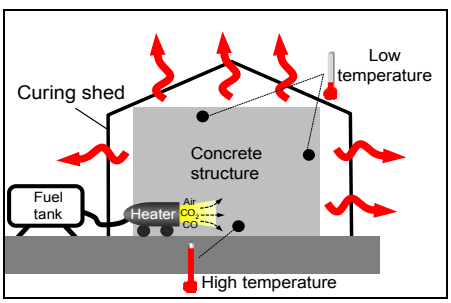

Figure 1. Existing heat curing system

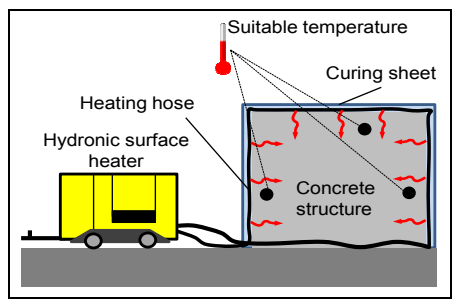

Figure 2. hydronic heat curing system [3,4]

2. Experiment

2.1 Overview of the Experiment

The objective of this experiment is to reveal the characteristics of strength development of concrete subjected to accelerated heat curing using a hydronic heater in a low-temperature environment. Using concrete specimens (φ10×20), the temperature history of the concrete specimens immediately after placing and the compressive strength at each age was measured. In addition, for the Thermo Gravimeter differential thermal analysis (TG-DTA) change over time of the hydration products at each age, after which the correlation of strength were reviewed.

2.2 Experimental Conditions and Materials

Table 1 presents the conditions and parameters of this experiment. It was assumed that the construction work was being performed using cold weather concrete in cold weather, with the external temperature set at -10°C, and the hydronic hose set two conditions: presence, and absence. Fig.3 shows the experimental flow according to the temperature change. During the one-day period (24 h) immediately after concrete placement, curing was performed at a constant temperature of 10°C, in reference to the Standard Specification for Concrete Structures provided by the Japanese Architectural Standard Specification (JASS 5) for the purpose of preventing early frost damage[2]. Then, the ambient temperature was set for each condition, and accelerated

heat curing was carried out using a hydronic heater for 28 days. As for the experimental method, a φ 10×20 cm mold was inserted into an insulating material (styrene board) before the casting of mortar, as shown in Fig. 4. At 24 hours after the casting,

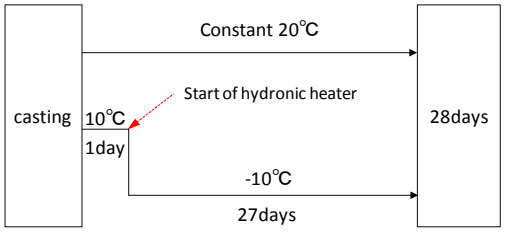

Figure 3. Test flow

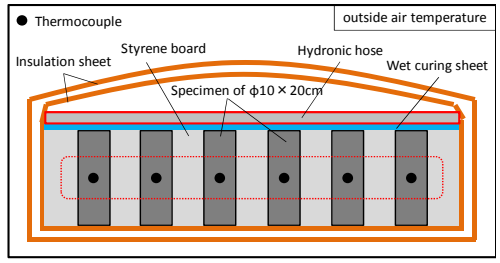

Figure 4. Conception diagram of Test

a hydronic hose was set up at the center of the specimen. Here, with respect to the concrete curing temperature, the surface temperature of the specimen was set at 20±1°C and a temperature of above 20°C×80% was set as the target temperature for the central part and the bottom part between the hoses, in reference to JASS 5[2)]. Moreover, the temperature of the solution inside the hose was set at 70°C in case the external temperature was found to be -10°C, based on a temperature analysis[4)]. Also, as shown in Figs. 4, in order to improve the thermal efficiency for all cases, two layers of insulation sheets were set up on the surfaces of hydronic hose and the mold. In addition, in order to prevent micro-cracks caused by drying shrinkage during the curing period, a wet curing sheet employed in the actual field that satisfied the conditions of the Recommendation for practice of cold weather concreting by the Architectural Institute of Japan[2)] was inserted between the surface of the hydronic hose and the surface of the concrete specimen for the experiment. For the mix proportion of concrete, a general mix proportion of design strength 24 MPa (slump 8cm, Gmax=20mm, W/C=0.52) was used. As shown in Fig. 4, the temperature history of concrete was measured by embedding a thermocouple in the central part of the mold specimen and data loggers were used to measure the temperature history of the concrete every 30 minutes until the age of 3 days. After that, it was measured every 60 minutes until the material age was 28 days.

Table 1. Experimental factors and conditions

Sample		Temperature*	Curing method	Evaluation item	Age (Day)
Constant 20 °C	20_C	-	Insulation sheet (two layer) + Wet curing sheet	- Compressive Strength - Temperature History - Maturity - TG-DTA	1, 3, 7, 28
-10 °C_With hose	(-)10_O	70 °C			
-10 °C_No hose	(-)10_X	-			

3. Results and discussion

3.1 Temperature History

Fig. 5 shows the results of measuring the temperature history. In the case of 20_C, which had been cured at a constant temperature of 20°C, the temperature rose due to the influence of hydration heat immediately after placing and reaching a peak temperature (about 23°C) at one

days of age. After that, the temperature gradually decreased, and after three days of age, the temperature remained around 20°C. On the other hand, (-)10 O for which a hydronic hose was installed, even after 1 day, the temperature increased due to the heat supplied by the hydronic hose, reaching a peak temperature (about 24°C) at 3 days. After that, the temperature gradually decreased, and after 10 days of age, the temperature remained around 16°C. In the case of (-)10_X, for which a hydronic hose was not installed showed the same temperature rise due to the same curing conditions as (-) 10_O for the period from immediately after placing until the end of the 1 day (24 hours), a similar temperature rise was shown by heat of hydration. After 1 day, the temperature suddenly decreased by being exposed to a low temperature environment of -10°C.

3.2 Compressive Strength

Fig. 6 shows the results of measuring the compressive strength at each age and change over time. (-)10 O from the Day 1, compressive strength was measured to be 16.5 N/mm^2 at 3 days, 26.9 N/mm^2 at 7 days, 36.2 N/mm^2 at 28 days. For 20 C, the compressive strength is 32.9N/mm^2 at 28 days. (-)10 O was about 10% higher than 20 C. On the other hand, (-)10 X, from 1 day to 28 days, the compressive strength was measured to be 7.83N/mm^2 3 days, 8.45N/mm^2 7 days, and 9.41N/mm^2 28 days, and showed little improvement in strength after 3 days. After 1 day of age, by being exposed to a low temperature environment of -10 °C, the speed of hydration reactions is reduced by the lower temperature of water reacting with the cement and the strength development decreased.

3.3 Correlation between Compressive Strength and Maturity

Fig. 7 shows the correlation between compressive strength and maturity for each age. The integrated temperature was calculated according to the reinforced concrete work of the Building Construction Standard Specification[4)] (JASS 5). In all of the cases, maturity and compressive strength generally show a linear relationship. Compared to 20 C, (-)10 O in particular exhibited higher strength at low maturity. On the other hand, in the case of (-)10 X, maturity and compressive strength tended to decrease. Generally, in a low temperature environment, the progress of hydration is delayed by the lower temperature of water reacting with the cement during the strength development of concrete. When heat curing using a hydronic heater as suggested in this study, it will be possible to boost the hydration reaction of water reacting with the cement from the early stages of casting in a low temperature environment. As a result, it will be possible to promote the strength of concrete.

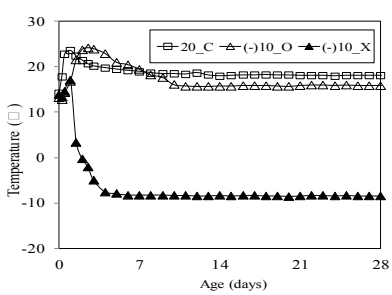

Figure 5. Temperature History

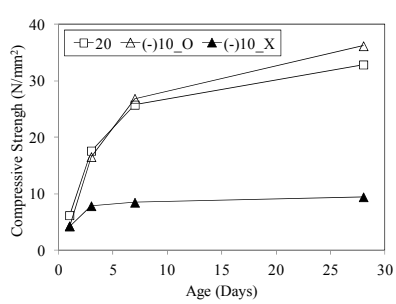

Figure 6. Compressive Strength

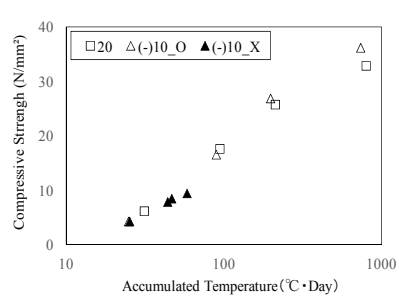

Fig. 7. Correlation

3.4 Quantitative change of Hydration Product

To measure the quantitative change in hydration products of concrete specimens subjected to heat curing by using a hydronic heater, the amount of calcium hydroxide ($Ca(OH)_2$) and C-S-H gel in each case was calculated using Thermo Gravimeter differential thermal analysis (TG-DTA)[6]. Figure 8 shows the results of change over time of the quantitative change of the hydrated product. (-)10 O, in the amount of hydration products increased with age. It is estimated that the hydration of concrete was smooth because the hydronic hose was set up in a low temperature environment. Compared to 20_C, (-)10 O in particular showed a similar tendency. On the other hand, in the case of (-)10 X, as mentioned, above the chemical potential of water reacting with cement decreased. Since the hydration hardly progressed, the production amount of calcium hydroxide ($Ca(OH)_2$) and C-S-H gel decreased.

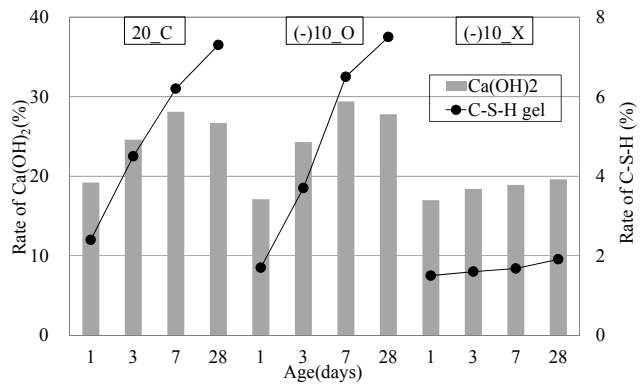

Figure 8. Production amount of hydration product

4. CONCLUSIONS

In this study, an experiment was carried out to clarify the effects of performing accelerated heat curing using a hydronic heater, in a low temperature environment of -10°C, on the strength development of concrete. The knowledge gained from this study is shown below:

1) By installing a hydronic hose on the concrete surface in a low temperature environment, it is possible to effectively control the temperature of concrete and to prevent frost damage by increasing the strength of concrete.
2) It is considered that heat curing by the hydronic hose increases the amount of the hydration product produced, and thereby the strength development by the densification of the hardening concrete structure could be promoted.

5. References

[1] Standard Specifications for Concrete Japan Society of Civil Engineers 1991
[2] Japanese Architectural Standard Specifications for Reinforced Concrete Work JASS5 Architectural Institute of Japan 1997
[3] Cold Weather Concreting with Hydronic Heaters, Journal of American Concrete Institute(ACI), Vol.22, No.4, pp.51-55, 2000
[4] Motoki S. Choi H. Inoue M, etc., A study on curing temperature control of cold weather concrete with energy-saving heat curing systems Cold Region Technology proceedings of Vol.33, pp.59-64, 2017.11

[5] Recommendation for Practice of Cold Weather Concreting. Architectural Institute of Japan 2010
[6] R.Vedalakshmi, et al., Quantification of hydrated cement products of blended cements in low and medium strength concrete using TG and DTA technique, Thermochimica Acta, Vol.407, pp.49-60, 200

Bridge Engineering Institute Conference 2019 (BEI-2019)
Honolulu, Hawaii, USA, July 22-25, 2019

Experimental Study on Mechanical Response of RC Beams Subjected to Freeze–Thaw Action

Takeru Kanazawa[1*]

[1] Hokkai Gakuen University, Sapporo, Japan; email: t-kanazawa@hgu.jp

[*]: corresponding author

Keywords: reinforced concrete; frost damage; load-carrying capacity; failure behavior

Abstract: This study presents the mechanical response of reinforced concrete (RC) beams with and without stirrups subjected to freeze–thaw (FT) action. The experiment showed that the load-carrying capacities of RC beams after FT exposure did not depend on the compressive strength of plain concrete. Plain concrete cylinders subjected to FT action showed approximately the same compressive strengths as that of the non-damaged specimens; nevertheless, RC beams under the same FT environment exhibited clear reductions in load-carrying capacities as well as distinct changes in failure behaviors.

1. Introduction

The mechanical performance of existing reinforced concrete (RC) structures can be adversely affected by freeze–thaw (FT) action. However, the mechanical behaviors of RC members subjected to FT action have received little attention in the past, although several previous studies have investigated the material properties of plain concrete (Hassan et al., 2002; Penttala and Al-Neshawy, 2002). The author reported that RC elements tested in uniaxial compression after FT exposure showed mechanical anisotropy, unlike plain concrete elements (Kanazawa and Sato, 2018). This result suggested that the mechanical response of RC members after FT tests cannot be directly associated with the strength of plain concrete. Therefore, this study investigates the mechanical responses of RC beams subjected to FT action, together with the compressive strengths of frost-damaged plain concrete specimens. Nine RC beams were tested with different reinforcement arrangements and degrees of frost damage.

2. Experimental Program

The mechanical behaviors of RC beams after FT exposure were examined by two-point bending testing of nine beams over the simple span of 1.5 m. As shown in Figure 1, all the test beams have an effective depth (d) of 180 mm and a shear span-to-depth ratio (a/d) of 2.78, where a is the shear span. Three of the test beams (T-control, TC-control, and TCS-control) are not exposed to FT cycles, while the other six beams (T-64, TC-64, TCS-64, T-83, TC-83, and TCS-83) are subjected to different numbers of FT cycles. The symbols T, C, and S denote tensile, compressive, and shear reinforcement, respectively. The subsequent numbers indicate the number of FT cycles. Table 1 lists the mechanical properties of the reinforcing bars. Table 2 shows the mix proportion of the test beams. To increase the frost damage, the water–cement ratio of the concrete is 65% and no air-entraining agent is used. Before the loading test, FT cycling was performed on six RC beams and plain concrete cylinders in a large environmental chamber. Figure 2 shows the history of input temperature in the chamber and the recorded temperature at

the center of the TCS-83 specimen during a cycle. Each FT cycle is 12 h with temperature variation between +20 °C and −15 °C. During FT cycles, the internal recorded temperature at the center of TCS-83 approached −6 °C. Table 3 summarizes the compressive strengths obtained from the plain concrete cylinders (100 mm in diameter and 200 mm in height). The strength of the specimen subjected to 83 FT cycles is somewhat higher than that of the undamaged specimen. This discrepancy may arise from the water supply during FT cycles inducing water-curing. To study the effect of frost damage on the failure modes of RC beams, the flexural reinforcements of all test beams were designed to ensure approximate equivalence of the shear

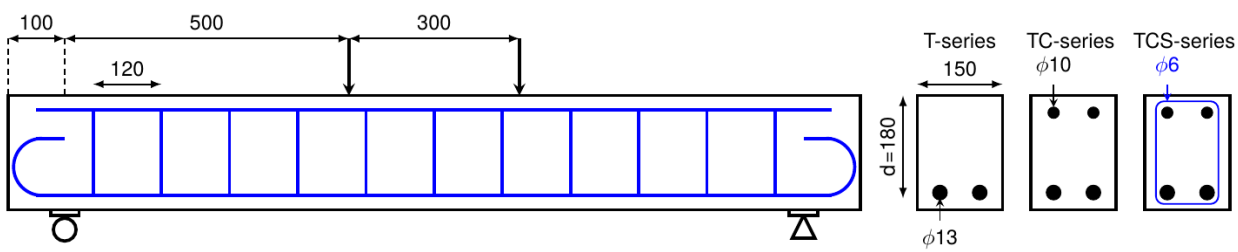

Fig. 1. Details for each series of test beams (all dimensions are in mm)

Table 1. Mechanical properties of reinforcing bars used in test beams

	Young's modulus[a] (GPa)	Yield strength[a] (MPa)
Φ 6	185	363
Φ 10	166	367
Φ 13	174	361

[a]: averaged from three specimens of each diameter

Table 2. Mix proportion of test beams

W/C (%)	Water (kg/m^3)	Cement (kg/m^3)	Sand (kg/m^3)	Gravel (kg/m^3)	s/a[a] (%)	Entrapped air[b] (%)
65.0	170.0	261.5	880.5	1095.8	45.0	2.0

[a]: sand/aggregate ratio
[b]: The measured value was 2.6% during casting.

Table 3. Compressive strengths of plain cylindrical concrete

Number of FT cycles	Compressive strengths (MPa)
0 (Control)	27.4[a]
64	26.5[b]
83	30.6[b]

[a]: average of three specimens
[b]: average of nine specimens

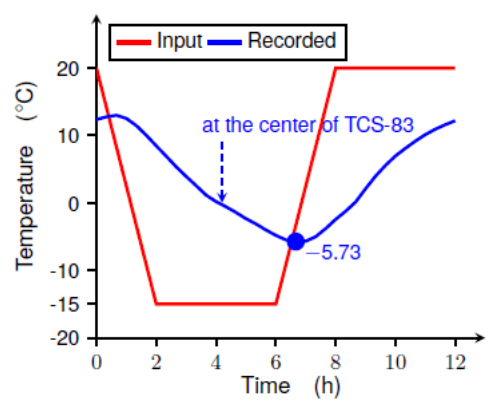

Fig. 2. Temperature histories in a FT cycle

and theoretical flexural capacities. The theoretical flexural capacity was calculated using Japanese standard specifications (JSCE, 2018) as approximately 60.6 kN; the concrete contribution to the shear capacity was determined using Eq. (1) (Niwa et al. 1986) as approximately 58.2 kN:

$$V_c = 0.20\left(p_w f'_c\right)^{\frac{1}{3}} d^{-\frac{1}{4}}\left[0.75 + \frac{0.14}{(a/d)}\right] \tag{1}$$

Here, p_w is the tensile reinforcement ratio and f'_c is the compressive strength of concrete.

3. Results and Discussion

Figure 3 presents schematic crack patterns of all test beams. The crack patterns of T-64, T-83, TC-64, and TC-83 indicate diagonal tensile failure. In comparing the crack distributions between the control and frost-damaged RC beams in both series, fewer cracks are developed in frost-damaged RC beams. This difference may relate to the bond deterioration caused by frost damage. The crack patterns of the TCS series are excluded because they do not differ significantly with and without FT.

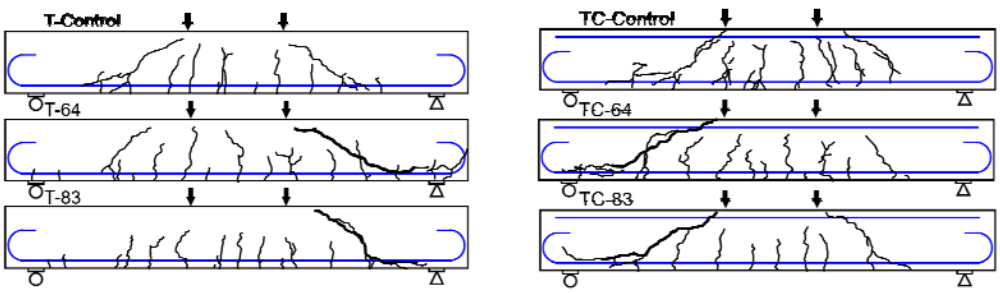

Fig. 3. Crack patterns of test beams: T-series (left) and TC-series (right)

Figure 4 shows the load–deflection relationships for all test beams. The failure modes of the tested beams are listed in Table 4 with some characteristic points in the load–deflection response, such as the maximum load and corresponding midspan deflection. In Fig. 4, the T-series exhibits considerable decreases in the maximum loads as well as corresponding midspan deflection as the frost damage is increased. Although TC-series does not show such a clear reduction, the same tendency is observed.

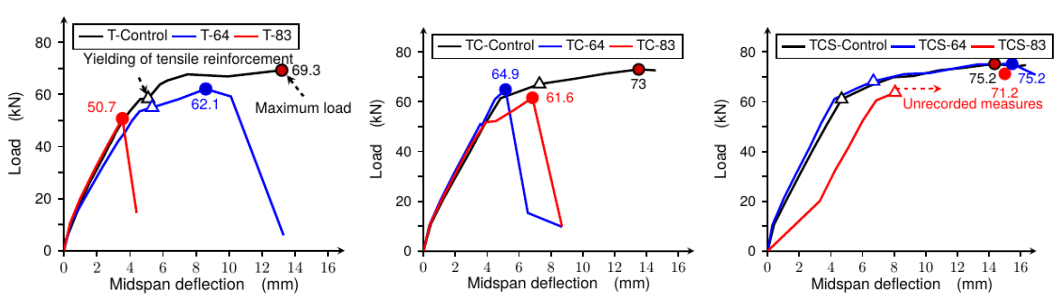

Fig. 4. Load–deflection relationships of all test beams: T-series (left), TC-series (center), and TCS-series (right)

Fig. 4 demonstrates that frost damage has a significant influence on the failure behavior of RC beams without stirrups. Although the compressive strengths of frost-damaged plain concrete are not decreased, the four test beams T-64, T-83, TC-64, and TC-83 present smaller load-carrying capacities as well as more brittle failure characteristics. Reductions in the mechanical properties of plain concrete are not directly associated with the mechanical behaviors of RC beams without stirrups after FT cycles. For the RC beams with stirrups, the load-carrying capacities are not reduced, as shown in Fig. 4.

Table 4. Summary of test results

Series	Number of FT cycles	Maximum loads, L_{max} (kN)	Midspan deflection at L_{max} (kN)	Failure modes
T	0 (Control)	69.3	13.2	Flexure-dominant
	64	62.1	8.60	Diagonal tension
	83	50.7	3.54	Diagonal tension
TC	0 (Control)	73.0	13.5	Flexure-dominant
	64	64.9	5.15	Diagonal tension
	83	61.6	6.84	Diagonal tension
TCS	0 (Control)	75.2	14.4	Flexural
	64	75.2	15.5	Flexural
	83	71.2	- [a]	Flexural

[a]: Deflection was not recorded properly.

4. Conclusion

Frost damage significantly influences the failure behavior as well as the load-carrying capacity of RC beams without stirrups. This mechanical behavior is unlikely to correlate with the strength of plain concrete.

5. Acknowledgements

This study was supported in part by the Obayashi Foundation and Grants-in-Aid for Regional R&D Proposal-Based Program from Northern Advancement Center for Science & Technology of Hokkaido, Japan.

6. References

Hasan, M., Okuyama, H., Sato, Y., and Ueda, T. 2004. Stress-strain model of concrete damaged by freezing and thawing cycles, Journal of Advanced Concrete Technology, 2(1), 89–99.

Japan Society of Civil Engineers (JSCE). 2018. Standard Specifications for Concrete Structures-2017 Design

Kanazawa, T. and Sato, Y. 2018. Constitutive model for cracked and frost-damaged reinforced concrete elements under uniaxial compression, Proceedings of the 8th International Conference of Asian Concrete Federation, 2, 983–991.

Niwa, J., Yamada, K., Yokozawa, K., and Okamura, H. 1986. Re-evaluation of the equation for shear strength of reinforced concrete beams without web reinforcement, Proceedings of JSCE, 372, 167–176.

Penttala, V. and Al-Neshawy, F. 2002. Stress and strain state of concrete during freezing and thawing cycles, Cement and Concrete Research, 32(9), 1407–1420.

Utilization of Marble Dust as Alternative Filler in Microsurfacing Incorporating Type-III Aggregate

Pradipkumar J Gundaliya[1*] and Hiteshkumar A Patel[2]

[1] L. D. College of Engineering, Ahmedabad, India, e-mail: pjgundaliya@ldce.ac.in
[2] Fliegen Wissen Consulting LLP, Ahmedabad, Gujarat, India; Email: metrans2010@gmail.com

[*]: corresponding author

Keywords: microsurfacing, marble dust, testing, mix design, waste utilization

Abstract: Microsurfacing is applied for Pavement Preventive Maintenance. The major materials used to create microsurfacing mix are aggregates, asphalt emulsion, control additive, water and mineral filler as ordinary Portland cement. As ordinary Portland cement is costlier and having higher environmental impact by CO2 Emission while production so there is a need of alternative filler. In this research marble dust is used as an option for OPC to create microsurfacing Mix. Marble dust is produced as mixture with water which is used for cutting of marbles. As northern part of India as very high density of marble treatment industries so huge amount of marble industry waste is generated and create dumping problem. This paper presents results obtained from laboratory investigation of microsurfacing mix. Laboratory investigation performs to determine suitability of marble dust as mineral filler in microsurfacing mix. Laboratory investigation includes determination of setting time, cohesion (30 min), cohesion (60 min) and wet track abrasion test on proposed mix design. Results shows that marble dust can be better option of cement in microsurfacing mix.

1. Introduction

Microsurfacing treatments involve the laying of a mixture of crushed mineral aggregate, polymer-modified asphalt emulsion, mineral filler, water, and an additive to control hardening of the mixture. A self-propelled pug mill mixes the components and lays the mix immediately after mixing – no compaction of the microsurfacing layer is required (Hixon et al. 1993). A microsurfacing layer may be as thin as 3/8 inch (9.5 mm) and is capable of filling wheel ruts up to 1.5 inches (38 mm)or 2 inches (50 mm) deep. Unlike localized treatments such as crack sealing and bump grinding, microsurfacing belongs to a certain category of pavement treatments which includes seal coating and thin HMA overlays. These treatments cover the entire width of the carriageway with an aggregate-bituminous mix. Like all other pavement treatments, microsurfacing is categorized in different ways by different agencies, depending on the purpose of the application, the hierarchy of the supervising jurisdiction, the expenditure involved, and other factors. For the purposes of the present study, microsurfacing is described as a preventive maintenance activity, a categorization that is consistent with most nationwide studies (Geoffroy, 1996). Microsurfacing is normally specified and designed according to IRC:SP:81-2008 or ISSA recommendations. In present scenario cement is used as mineral filler in mix design of microsurfacing. It enhance the breaking time of the modified asphalt emulsion and also work as filler. Improvement in microsurfacing characteristics is often done by use of such mineral filler as cement or lime. In this study, none of the above mineral filler is used; rather, a

waste product, marble dust, resulting from the quarrying and crushing of marble, is utilized. Marble dust is produced as mixture with water which is used for cutting of marbles. As northern part of India as very high density of marble treatment industries so huge amount of marble industry waste is generated and create dumping problem. Utilization of marble dust will reduce costlier and higher environmental impact by CO2 Emission and help us in reducing carbon footprint at some extent. Marble blocks are cut into smaller blocks in order to give the required smooth shape.

2. Materials

In this research type II aggregates were used for in microsurfacing mix. Type II aggregate gradation is used to fill surface voids, address surface distresses, seal, and provide a durable wearing surface. The Source of Type II aggregate was Rajeshree Stone Crusher, Sevaliya, Gujarat. Physical properties of aggregates like water absorption, Sand Equivalent Value and Soundness is determined using IS 2386 Part 3, IS 2720 Part 37 and IS 2386 Part 5 respectively at 25°C temperature. The required physical properties of the aggregate are presented in table 1.

Table: 1 Physical properties of the aggregate

Sample Type	Test Name		
	Water Absorption	Sand Equivalent Value	Soundness (With sodium sulphate solution)
Stone Aggregate (Type II)	1.4	67.5	*Not Required
Test Method	IS 2386 P 3	IS 2720 Part 37	IS 2386 Part 5
Limit as per IRC: SP: 81:2008	Max. 2	Min. 50	Max. 12

The gradation of the aggregate mixture was within the specified limits as determined by IRC:SP:81-2008 for Type II mixture. The actual gradation of the aggregate mixture is as shown in figure 1

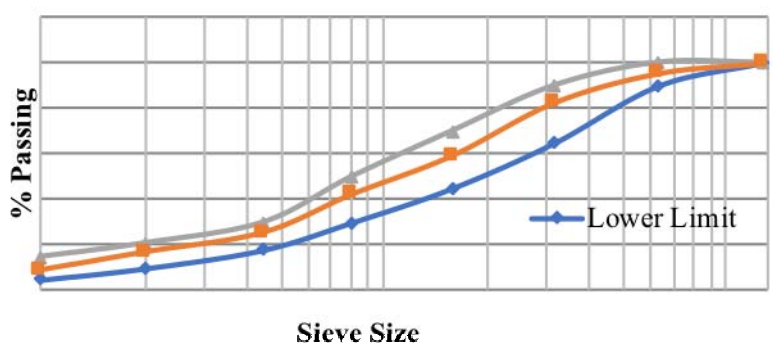

Fig. 1. Type III Gradation curve

The bitumen emulsion used was a cationic bitumen emulsion modified with latex. The Source of Polymer Modified Emulsion is Tiki Tar Industries (Baroda) Limited Its characteristics, which meet the requirements IRC:SP:81-2008 specification, are shown in Table 3.

Table 2. Characteristic properties of polymer modified bitumen emulsion

Test Name	Test Value	Test Method	Limit as per IRC:SP:81:2008
Residue on 600micron IS Sieve (% by mass)	0.039	IS:8887	Maximum 0.05
Viscosity by Say Bolt Furol Viscometer, at 25° C , in sec	23	IS:8887	20 – 100 Second
Coagulation of emulsion at low temperature	Nil	IS:8887	NIL
Storage Stability after 24h , %	1.12	IS:8887	Maximum 2
Particle charge, +ve/-ve	Positive	IS:8887	Positive [+ve]
Test on Residue:			
Residue by evaporation, %	63.9	IS:8887	Minimum 60%
Penetration at 25oC/100g/5s	47.5	IS:1203	40 – 100
Ductility at 27oC, cm	54.6	IS:1208	Minimum 50cm
Softening Point, in oC	59.5	IS:1205	Minimum 57 oC
Elastic Recovery	52.2	IS:15462	Minimum 50%
Solubility in trichloroethylene, %	98.9	IS:1216	Minimum 97%

Table 3. Chemical Composition of marble dust

PARAMETER	UNIT	Test Method Standard	Results Obtained	Specifications As per IRC:SP: 89-2010
Fe2O3+Al2O3+SiO2	%	IS-1727	76.9	70% Min
Sio2	%	IS-1727	62.3	35% Min
Reactive Slice	%	IS-1727	28.7	--
MgO	%	IS-1727	1.7	25 % Max
SO3	%	IS-1727	1.2	2.75 % Max
Na2O	%	IS-1727	1.4	--
Cl2	%	IS-1727	0.02	0.05 Max
Loss of Ing.	%	IS-1727	2.9	5 Max
CaO	%	IS-1727	0.32	--
Phosphorous (P2O5)	%	IS-1727	0.02	--
Potassium (K2O)	%	IS-1727	0.05	1.5 Max
PH	%	IS-1727	7.6	--

3. Mix Design

The mix design was performed according to IRC: SP: 81-2008 specifications. Based on the sieve analysis result and others recommended criteria mentioned in IRC: SP: 81-2008 the material was mix in proportion as aggregate as 100% of total ingredients, marble dust as 1.5%, water as 12%, polymer modified emulation as 13% and Additive as 2.2% of aggregate. The different mixtures were tested for the determination of Mix Time, Consistency, Cohesion, Wet Stripping, Wet Track Abrasion loss, according to IRC: SP: 81-2008 specifications. The mixing is done at temperature of 27°C.

4. Results and Discussion

The results obtained from the use of optional fillers in microsurfacing are showed in Table 6. As it can be seen that Marble dust gave satisfactory results under IRC: SP: 81-2008. The results obtained from experimental investigation shows that Marble Dust gives relatively Better results than that of OPC. Laboratory evaluation Results shows that marble dust provide better cohesion than OPC. After this experimental analysis we can say use of marble dust as alternative mineral filler leads to not only reduce the Overall cost of microsurfacing technology but also reducing the amount of dump of marble dust from earth. Results shows that the mixing time is somehow similar to as of OPC and wet cohesion of Marble dust is more than OPC which shows that it can be suitable filler for microsurfacing mix.

Table 4. Mix Design Criteria for Micro Surfacing

Requirement/Test names	Cement	Marble Dust	Limits as per IRC:SP:81-2008	Test Methods [IRC:SP:81-2008]
Mix Time (seconds)	135	134	120s Minimum	Appendix – 1
Consistency (cm)	2.4	2.3	3cm, Max	Appendix – 3
Wet Cohesion, within 30min; (kg.cm)	14	16	12 kg.cm Min	Appendix - 4
Wet Cohesion, within 60min; (kg.cm)	22	24	20 kg.cm Min	Appendix - 4
Wet Stripping, Pass%	99.5	99.2	90 Min	Appendix – 5

5. Conclusions

The use of Microsurfacing in India for preventive maintenance and surface improvement increased during the last few years. In this paper marble dust was used as optional fillers in order to replace cement in the production of microsurfacing. The results showed that marble dust as optional fillers can be used in place of cement for producing microsurfacing complying with specifications. The use of Fly ash in microsurfacing results in decreasing of their dump in India. It not only reduces the cost of microsurfacing technology but also improve low environmental profile.

6. References

[1] IRC: SP: 81-2008 Tentative Specification for Slurry Seal and Microsurfacing
[2] N. Oikonomou, “Alternative fillers for use in slurry seal”, Global nest journal. 9 (2), 182-186.
[3] Nikolaides, 2000 “The use of fly ash as a substitute of cement in microsurfacing” Waste Materials in Construction, p234 240.
[4] ASTM D3910-90, 1996” Design, Testing and Construction of Slurry Seal, Annual Book of ASTM Standards, Section 4, Construction, Vol. 04.03, Road and Paving Material
[5] International Slurry Surfacing Association (1991), Recommended Performance Guidelines for Microsurfacing, ISSA, A143,Washington D.C.
[6] Dwight Hixon, C and D.A Ooten, 1996. Nine years of microsurfacing in Oklahoma. Transportation Research Record 1392, Transportation Research Board, National Research Council, Washington D.C.

Test and Analysis of Strength of Mass Concrete Based on Equivalent Age

You Lv[1], Wenbo Zhang[2*], Shiteng Zhou[3], Mingjie Mao[4], and Shuangquan Zhao[5]

[1] School of Civil and Hydraulic Engineering, Ningxia University, Yinchuan, China; email: 840537525@qq.com
[2] School of Civil and Hydraulic Engineering, Ningxia University, Yinchuan, China; email: zhangwenbo@nxu.edu.cn
[3] School of Civil and Hydraulic Engineering, Ningxia University, Yinchuan, China; email: 937653273@qq.com
[4] School of Civil and Hydraulic Engineering, Ningxia University, Yinchuan, China; email: maomj@nxu.edu.cn
[5] China Construction Third Engineering Bureau Co.Ltd (Northwest), Yinchuan, China; email: 1847091495@qq.com

[*]: corresponding author

Keywords: equivalent age; compressive strength; core drilling; rebound; mass concrete

Abstract: The core drilling and rebound compressive strength of cured in field mass concrete was studied based on equivalent age. Results show that 91day should be used as the design age for concrete structures under autumn to winter site-curing conditions. At the age of 14day, the core drilling compressive strength of the inner part is clearly higher than that of middle and outer parts. Meanwhile, from the age of 28day to 91day, the test results of inner and outer parts are practically the same, whilst the middle part fluctuates greatly. In addition, compared with the calculating strength of standard curing, the core drilling strength values are stable at the range of 0.84 to 0.88 times, while the rebound strength values are all more than 1.21 times and varies significantly with the age as well. It can be concluded that compared with rebound strength, core drilling strength can reflect actual strength of structural concrete better.

1. Introduction

Testing the compressive strength under standard curing conditions is a common method to evaluate the mechanical properties of concrete. However, standard curing condition is often difficult to be used as the evaluation basis for concrete strength of actual components because of the great difference in maturity between standard curing condition and site-curing condition, which brings great difficulty to site construction and maintenance. Therefore, in this contribution the equivalent age is used to convert the actual curing age into the standard curing age of concrete. Based on equivalent age, the core drilling and rebound compressive strength test results of mass concrete cured on-site, as well as the standard curing concrete at the ages of 14day and 28day, 56day and 91day were analyzed, and the core drilling strength distribution at different depth was investigated. It provides effective reference for the safety construction and maintenance management of concrete project.

2. Experimental program

2.1 Materials and mix proportion

The cementitious materials used in the present study are Ordinary Portland cement (P.O. 42.5R) and fly ash. Chemical composition of fly ash is shown in Table 1. Concrete designed strength is 30 MPa and mix proportion is shown in Table 2. The coarse aggregate is composed of 5 ~ 25mm continuous graded gravel. SM naphthalene series superplasticizer is adopted for water reducing agent, and the dosage is 0.15% ~ 0.6%.

Table 1. Chemical composition of fly ash (%)

SiO_2	Al_2O_3	Fe_2O_3	CaO	MgO	SO_3	K_2O	TiO_2	P_2O_5
40.8	23.9	11.5	9.3	4.19	3.24	2.6	1.88	1.59

Table 2. Mass concrete mix proportion (kg/m^3)

W/B	FA/B	W	C	FA	S	G	Ad
0.46	0.21	175	300	80	755	1040	9.5

2.2 Experimental details

In order to investigate the mechanical properties of mass concrete under autumn to winter site-curing conditions, the concrete cube with a dimension of 1100×1100×1100×mm^3 was casted on the outdoor of Yinchuan city in late October. After 1 day's removal of the mold, the specimens were immediately wrapped tightly with plastic film, then the bubble film was wrapped on the outside for curing until 14day. During the curing period, the air temperature ranged from minus 2.3 °C to 36.6 °C, and the average daily temperature was 12.6 °C. Several cube specimens with a dimension of 100×100×100mm^3 for standard curing were prepared simultaneously. With reference to technical specifications for testing concrete strength by core drilling method (JGJ/T 384-2016), core samples were drilled at the ages of 14day, 28day, 56day and 91day, and each age corresponds to 6 sets of core samples. The length of a single core sample was about 300mm, hence, it was spitted into three cylinders with diameter of φ70 x h70mm, viz. external core, mid core and internal core from the outside to the inside. After the treatment and curing of the core samples, the compressive strength was tested and the strength value was determined. The rebound experiment was conducted in accordance with the technical specification JGJ/T 23-2011. The rebound surface at each age uniformly selected the test area on both dark and sunny surfaces of components. As far as possible, the detection area of concrete at the same age was the same as that of core drilling. The mean value of dark and sunny surfaces was used as the estimated value of rebound strength.

3. Results and analysis

3.1. Estimation of equivalent age and strength

According to the equivalent age (Guo 1989), the actual curing age is converted to the standard curing age, and the strength development is compared and analyzed under the uniform scale according to Eq. (1) and Eq. (2).

$$t_T = \sum_i^n \left(\alpha_T \cdot \Delta t_i\right) \tag{1}$$

$$\alpha_T = \exp\left(4.26 - \frac{375}{68 + T_i}\right) \tag{2}$$

where, t_T is equivalent age; α_T is the age correction coefficient corresponding to temperature i; t_i is the number of days corresponding to temperature i; T_i is the temperature corresponding to temperature i, which is determined according to the average daily temperature. In order to better compare the strength of different detection methods, compressive strength under 28day standard curing is selected as the base to calculate the strength of different equivalent age, as shown in Eq. (3).

$$f_n = f_{28} \frac{\lg n}{\lg 28} \tag{3}$$

Here, f_n is the compressive strength at age n day(n>3); f_{28} is the standard curing strength.

3.2. Core drilling compressive strength

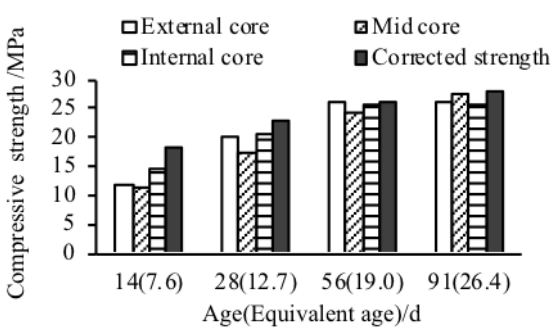

Fig. 1. Core strength

The test results of core drilling compressive strength are shown in Fig. 1. It can be seen that core drilling compressive strength increases constantly while its amplification decreases obviously as the age increases. The core strength of 28day and 91day reached 75.7% and 93.8% of the designed strength respectively, which indicates that mass concrete can reach its designed strength after 91day under autumn to winter site-curing conditions. For each age, there are significant differences between external, mid and internal core. At the early age of 14day, internal core strength is significantly higher than that of the mid and external core. With the growth of age, the strength gap between internal and external core gradually decreases. The reason is that the early hydration rate of cement is fast, the internal temperature of mass concrete cannot be timely distributed, and the high temperature can stimulate the internal cement hydration again, as a result the internal core strength is significantly higher than external core. With the development of age, concrete strength grows slowly and tends to be stable after the cement hydration is coming to an end at 56day. In the process of preparation, mechanical disturbance has a great influence on the inter core results. In order to investigate core strength deviation value at different depth, the difference value between the corrected strength and tested core strength at different depth was calculated, then ratio of the difference value to the corrected strength was obtained. The results are shown in Fig. 2. It can be seen that on 14day, the deviation value between external and mid core is

between 19 ~ 37%. While as the age increases, the deviation value decreases. During the age of 28 ~ 91day, except for mid core of 28day, the deviation value has been reduced to 10% or less. Furthermore, the deviation value of three cores keeps decreasing with the age increasing.

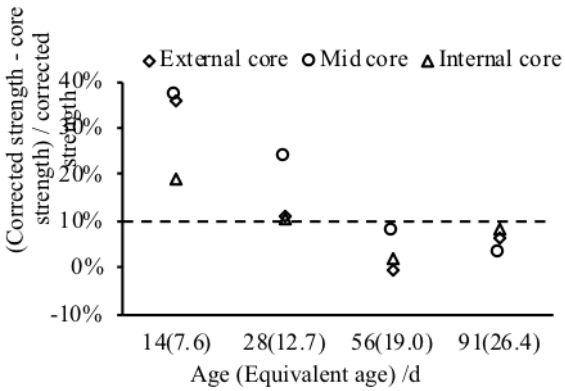

Fig. 2. Core strength deviation value

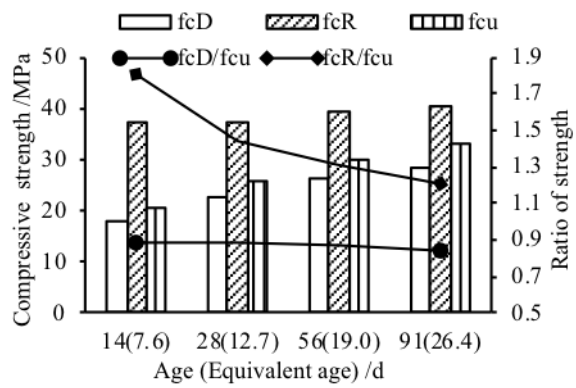

Fig. 3. Comp. strength of different test

In particular, at the age of 91day, the three deviations are between 3 ~ 8%, which tends to be consistent. It can be concluded that when the concrete strength is evaluated by core drilling within 14 days, special attention should be paid to the influence of hydration heat on the core strength at different depth; after 28 days, hydration heat has no significant influence on core drilling strength.

3.3. Comparison of core drilling and the rebound test

In order to compare the compressive strength measured by core drilling and rebound test quantitatively, the calculating standard curing strength corresponding to each equivalent age is obtained according to the method described in section 3.1. The results of core drilling strength (f_{cD}), rebound strength (f_{cR}) and calculating standard curing strength (f_{cu}) are shown in Fig. 3. It can be seen from Fig. 3 that in the age of 14 ~ 91day, both core drilling and rebound strength increase with the age increasing. Core drilling strength and calculated standard curing strength relatively close while rebound strength is much higher than both. Analysis of the strength ratio shows f_{cD}/f_{cu} is range from 0.84 ~ 0.88, which can be considered to be stable at 0.88 within 91day except for a slight decrease to 0.84 on 91day. It is therefore considered that when the relationship coefficient of 1/0.88 is introduced, core drilling strength and calculated standard curing strength can be viewed as essentially equal. However, f_{cR}/f_{cu} decreases continuously from 1.81 to 1.21 with high dispersion. The rebound test is only used to infer strength by measuring the surface hardness of the concrete which does not have a direct and fixed relation with its strength. Therefore, it can be considered that under the same conditions, core drilling strength can better reflect the development trend of concrete strength.

4. Conclusion

(1) Core drilling strength reaches 93.8% of the designed strength on 91day. Thus, 91day should be used as the design age for concrete structures under autumn to winter site-curing conditions.

(2) Despite the same age, the core drilling strength varies at different positions; At the age of 14day, the compressive strength of the inner part is clearly higher than that of middle and outer parts. From the age of 28day to 91day, the test results of inner and outer parts are practically the same, whilst the middle part fluctuates greatly.
(3) Compared with rebound strength, core drilling strength can reflect actual strength of structural concrete better. This study suggests that the relationship coefficient of compressive strength between the core drilling and standard curing test is 1/0.88.

5. Acknowledgment

This work was supported by the Natural Science Foundation of China (51768058, 51568055).

6. Reference

C. Guo. 1989. Maturity of concrete: method for predicting early-stage strength, ACI Materials Journal, 86(4), 341-353.

Experimental Investigation on Flexural Behavior of Textile Reinforced Concrete Composites

Jongeok Lee[1], Changmin Lee[2], Sanghwa Park[3], Jun-Mo Yang[4], Sung Jig Kim[5*], Chunho Chang[6], and Seungyeon Choo[7]

[1] Department of Civil Engineering, Keimyung University, Daegu, South Korea; email: whddjrtnwls@naver.com
[2] Department of Architectural Engineering, Keimyung University, Daegu, South Korea; email: leechangmin92@gmail.com
[3] Department of Architectural Engineering, Keimyung University, Daegu, South Korea; email: tkdehftm88@gmail.com
[4] Department of Civil Engineering, Keimyung University, Daegu, South Korea; email: jm.yang@kmu.ac.kr
[5] Department of Architectural Engineering, Keimyung University, Daegu, South Korea; email: sjkim4@kmu.ac.kr
[6] Department of Civil Engineering, Keimyung University, Daegu, South Korea; email: chunho@kmu.ac.kr
[7] School of Architecture, Kyungpook National University, Daegu, South Korea; email: choo@knu.ac.kr

[*]: corresponding author

Keywords: textile reinforced concrete; textile fabrics; concrete members; flexural behavior

Abstract: The paper introduces an experimental program of investigation on the performance of textile-reinforced concrete (TRC) panel. This new composite material is made with a continuous grid textile fabric incorporated into a cementitious matrix. The TRC panel has been developed to improve the structural performance of RC columns and expedite the construction process in this study. The textile fabrics for the TRC panel are carbon, aramid, and E-glass fibers with various grid dimensions. The mechanical properties under static loading of the composite elements are evaluated through the tensile and flexural testing. The first set of specimens was a normal concrete element without any retrofit. The second set of specimens was strengthened by carbon, aramid and E-glass textile fabric. Testing data are analyzed to investigate the performance of the specimens strengthened with textile fabric compared to the performance of the non-retrofitted elements.

1. Introduction

Recently, there has been a growing interest in the use of textile reinforced concrete (TRC) as a material for constructing new structural members and strengthening or repairing old structures. TRC is a composite material consisting of a cement-based matrix with typically small maximum aggregate grain sizes and high-performance, continuous multifilament yarns made of alkali-resistant glass, carbon, polymer or other materials. By using TRC the tensile strength, ductility, and corrosion resistance of concrete can be increased (Du et al. 2018; Mechtcherine et al. 2016; Mobasher, 2016).

The TRC panel has been developed to improve the structural performance of RC columns and expedite the construction process in this study. The mechanical properties under static loading of the composite elements are evaluated through the tensile and flexural testing.

2. Test program

2.1. Materials

The textile fabrics for the TRC panel are carbon, aramid, and E-glass fibers with various grid dimensions. Two dimensional textiles were woven perpendicularly with the hole spacing of 10 to 25 mm, and then coated with resin. The used textiles are shown in Fig. 1. Premixed type mortar was mixed with water to make concrete matrix. The compressive and flexural strength of the concrete matrix were obtained on the day of testing according to EN 1015-11 on three mortar prisms with 40 × 40 × 160 mm dimensions. The measured average compressive and flexural strength of the concrete matrix were 53.4 MPa and 7.8 MPa, respectively.

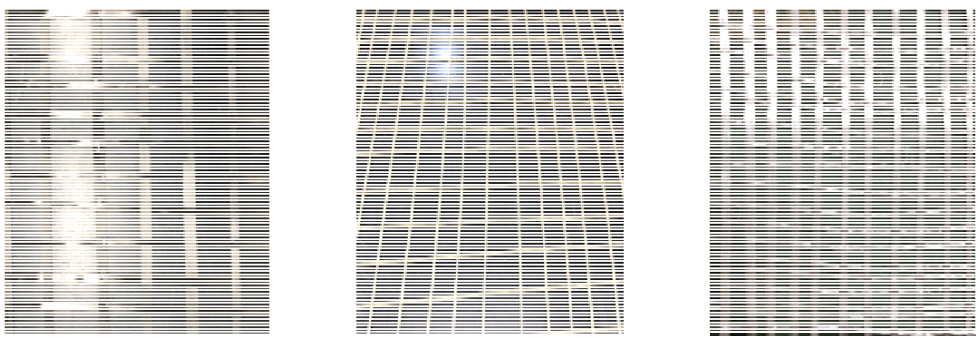

(a) (b) (c)

Fig. 1. Textiles: (a) carbon fiber; (b) aramid fiber; (c) E-glass fiber

2.2. Tensile test

To evaluate the tensile properties of TRC panel, tensile tests were performed. The main variable was the type of textile fabrics, and the results of each variable were compared with those of specimens without textile. Hole spacing of all types of textile was 20 mm. The test specimens were fabricated by installing textiles in the middle of the metal mold with a little tension and casting the concrete. Three specimens were fabricated for each variable, so total twelve tensile test specimens were fabricated. The total length and thickness of the specimen were 400 mm and 16 mm, respectively, and the length and width of the tensile strain measurement region were 200 mm and 60 mm, respectively. Static tensile load was applied by 500kN UTM as shown in Fig 2(a).

2.3. Flexural test

The effects of the type of textile fabrics and hole spacing of textiles on the flexural performance of TRC panel were investigated. Carbon, aramid, and E-glass fibers were used as textile fabrics, and 10 mm, 13 mm, 20 mm, and 25 mm were used as hole spacing of textile. Three specimens were fabricated for each of the 13 variables including the concrete beams without textile, and a total of 39 specimens were fabricated and tested. The test specimen used for the flexural test was with a size (width × length) of 100 mm × 400 mm and its height was 40 mm. All specimens were

fabricated by placing the textiles in the center of the specimen in advance, and casting concrete. A four-point bending test was performed with a span of 300 mm as shown in Fig. 2 (b). A static load was applied until the specimen was failed by UTM with 500 kN capacity.

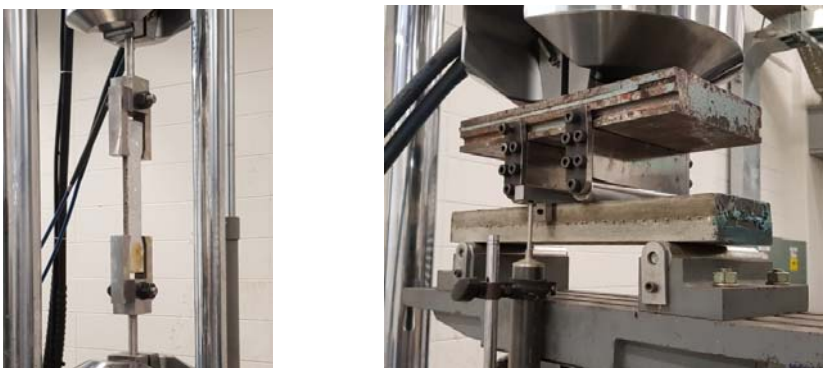

(a) (b)

Fig. 2. Test setup: (a) tensile test; (b) flexural test

3. Test result and discussion

3.1. Tensile test

Fig. 3 (a) shows the tensile stress versus strain relationship curve according to the type of textile fabric. The typical tensile behavior of TRC is shown in four steps in the order of (1) first crack evolution, (2) formation of distributed crack, (3) crack widening, and (4) peak load (Mobasher, 2016). However, in the case of the TRC panels tested in this study, the failure occurred after the step (1), and step (2) did not be reached. The tensile stress increased linearly with the increase of the strain until the first tensile crack occurred. After the first crack, a large decrease of the stress occurred and the tensile strength was not recovered to the first cracking tensile strength. This is because the amount of textile fabric was insufficient for reinforcement of concrete and slip occurred between textile and concrete. The tensile strengths of TRC reinforced with aramid (20AT), carbon (20CT), and E-glass (20GT) fiber fabrics increased to 13.3%, 18.4% and 36.6%, respectively, as compared to tensile specimens without textile reinforcement (NT).

3.2. Flexural test

To describe the flexural behavior of TRC, four states are typically defined: State I (uncracked concrete), State IIA (crack formation), State IIB (crack stabilization), and State III (failure) (Brameshuber, 2006). However, all TRC flexural specimens in this study were failed during State IIA. The flexural stress was linearly increased with the increase of displacement until the first crack occurred at the uncracked stage. The first crack occurred in the pure bending stress zone between the two loading point when the bottom fiber of matrix reached the ultimate tensile strain. In all specimens reinforced with textile, the first cracking strength increased by an average of 27% over the specimens with no textile. Immediately after the first crack, a sudden load reduction occurred. The extent of load drop or so-called delayed load distribution is thought to be a function of the initial geometric waviness of the fabric, reinforcement area and the quality of the bond between the reinforcement and matrix. After the load drop, although the flexural strength increased, it did not progress beyond the first cracking strength. Specimens were failed

after increasing about 42% on average compared with the first cracking strength. This is because the reinforcing ratio of the reinforced textile fabric is low, and it is considered that the modification of type and arrangement of the textile is required to improve the flexural performance of TRC.

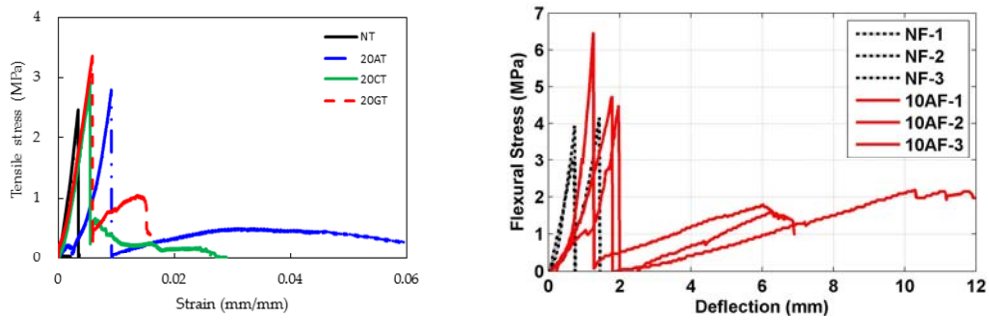

(a) (b)

Fig. 3. Stress-deformation relationship: (a) tensile test; (b) flexural test (10AF)

4. Conclusions

In this study, tensile test and flexural test were performed on TRC panel specimens with variables of textile fabric and hole spacing. The tensile test and the flexural test showed a tendency to fail without recovering the large load drop after the first cracking. Additional testing is required for TRC panel specimens with modified textile types, reinforcement ratios, and textile arrangement methods.

5. Acknowledgements

This research was supported by a grant(18RDRP-B076268-05) from R&D Program funded by Ministry of Land, Infrastructure and Transport of Korean government.

6. References

Brameshuber, W. 2006. Textile reinforced concrete: state of the art report of RILEM committee 201-TRC, RILEM Publications, Bagneux, France.

Du, Y., Zhang, X., Zhou, F., Zhu, D., Zhang, M., and Pan W. 2018. Flexural behavior of basalt textile-reinforced concrete, Construction and Building Materials, 183, 7-21.

EN 1015-11. 1999. Methods of test for mortar for masonry – part 11. determination of flexural and compressive strength of hardened mortar, Brussels: Comité Européen de Normalisation.

Mechtcherine, V., Schneider, K., and Brameshuber, W. 2016. Mineral-based matrices for textile-reinforced concrete, Textile Fibre Composites in Civil Engineering, Elsevier, Woodhead Publishing Limited, 25-43.

Mobasher, B. 2016. Textile fiber composites: testing and mechanical behavior, Textile Fibre Composites in Civil Engineering, Elsevier, Woodhead Publishing Limited, 101-150.

CFD Simulations of Flow around a Square Cylinder with Varying Aspect Ratio

Hanbin Yang[1], Wanli Yang[2*], Chuan-Jiang Zhang[3], Jing Kou[4], and Qiao Li[5]

[1] Department of Bridge Engineering, School of Civil Engineering, Southwest Jiaotong University, Chengdu, China; email: 1059729782@qq.com
[2] Key Laboratory of High-speed Railway Engineering, Ministry of Education, Chengdu China; School of Civil Engineering, Southwest Jiaotong University, Chengdu, China; email: 68360903@qq.com
[3] School of Civil Engineering, Southwest Jiaotong University, Chengdu, China. email: 1366609089@qq.com
[4] Department of Bridge Engineering, School of Civil Engineering, Southwest Jiaotong University, Chengdu, China, email: 996602942@qq.com
[5] Department of Bridge Engineering, School of Civil Engineering, Southwest Jiaotong University, Chengdu, China. email: ql3721@163.com

[*]: corresponding author

Keywords: open foam; square cylinder; drag coefficient; flow pattern

Abstract: The flow filed around a square floating caisson of sea-crossing bridge foundation is complicated and receives few attentions. This paper investigates the flow around a vertical surface-piercing square cylinder with varying aspect ratio, the effects of free surface and free end are considered simultaneously. The investigations were conducted numerically by RANS simulation with $k\omega$-SST turbulent model using OpenFoam. The simulations were carried out for square cylinder with aspect ratio ($AR = H / D$, H is the immerged depth of the square cylinder, D is the side length of square cylinder, respectively) ranging from 1 to 5 at Reynolds numbers 1×10^4. The simulation results show that drag coefficient increases with aspect ratio. Flow separates from the leading corner of the square cylinder and then reattaches onto the surface of the two sides of the square cylinder. From the time-averaged streamline in horizontal plane, two pairs of the recirculation can be observed in the horizontal plane right below the free surface. One pair is in the two sides of the cylinder and the other one is behind the cylinder in the near wake. And in the vertical plane, a large recirculation is found right below the bottom of the cylinder, and a small one behind the cylinder in the near wake. The flow pattern is significantly influenced by aspect ratio.

1. Introduction

Floating caisson, which plays a role of discharging water and providing a dry construction environment, is an important measure to ensure the safety and quality of deep-water bridge foundation construction. As summarized by Krishna et al. (2004), the construction and installation of caisson generally consist of the flowing stage, i.e. (a) Being constructed at the dockside before being towed to site, it is the first stage. (b) Being towed to site. (c) Installation of mooring system. (d) Caisson construction. As construction progressed, the draft of the caisson increases continuously until touchdown. (e) Touchdown and submergence. The touchdown sequence is carefully orchestrated to ensure that the caisson is landed at the target location. Flow

around the floating caisson has the following characteristics in the towing process: (1) The aspect ratio ($AR = H / D$, H and D are, respectively, the immerged depth and diameter of a floating caisson) is very small. The transverse section size of floating caisson is tens of meters or even close to 100 meters. (2) The influence of free surface cannot be ignored because the top of the floating caisson is higher than the free surface in the sinking process. (3) The influence of the free end of floating caisson cannot be ignored.

Investigations on the combined effects of the free-surface and free end on finite cylinders have been given far less attention, although the related structures exist widely in many engineering applications, such as spar platform, offshore floating wind turbine, etc. Gonçalves et al. (2015) presented thorough experimental results for varying aspect ratios AR = 0.1 ~ 2 and varying Reynolds numbers Re = 10000 ~ 50000. The results show the decreased drag force coefficient with decreasing aspect ratio, as well as the decreased Strouhal number. Fukuoka et al. (2016) discussed in detail the influence of Reynolds number, aspect ratio and Froude number on the hydrodynamic forces of circular cylinders. The results show that the root mean square coefficients of streamwise and transverse forces decrease with decreasing Reynolds number, Froude number and aspect ratio, and the drag coefficient increases with increasing Froude number and aspect ratio. These conclusions are in agreement with Gonçalves et al. (2015). Benitz et al. (2016) investigated the flow around cylinder with more larger aspect ratio (AR = 1 ~ 19) on the base work of Gonçalves et al. (2015), their results show that drag coefficient decreases with decreasing aspect ratio, and the free surface is dominant when aspect ratio is lower than 3.
However, to the best of our knowledge, the study of the combination influence of free surface, free end for square cylinder is few. In the present work, the flow around a vertical surface-piercing square cylinder with varying aspect ratio is investigated, and the effects of free surface and free end are considered simultaneously. The investigations will conducted numerically by RANS simulation with $k\omega$-SST turbulent model using OpenFoam. The simulations were carried out for square cylinder with aspect ratio ($AR = H / D$, H is the immerged depth of the square cylinder, D is the side length of square cylinder, respectively) ranging from 1 to 5 at Reynolds numbers 1×10^4 .

2. Numerical simulation method

2.1. Basic equations

The 4.0 version of OpenFOAM was used for all numerical simulations, for more details please refer to Weller et al. (1998). The Reynolds averaged equations for mass conservation and momentum equation are, respectively:

$$\nabla\cdot\vec{U}=0 \tag{1}$$

$$\frac{\partial\vec{U}}{\partial t}+(\vec{U}\cdot\nabla)\vec{U}=-\nabla P+\nabla\cdot\left\{(\nu+\nu_T)(\nabla\vec{U}+\nabla\vec{U}^T)\right\} \tag{2}$$

which $\vec{U}$ is velocity vector, P is the density normalized pressure, ν is the kinematic viscosity and ν_T is the turbulent viscosity. The $k\omega$-SST turbulent model proposed by Menter (1994) is used. VOF method is used to capture the free surface.

2.2. Numerical computation domain and boundary conditions

Fig. 1 illustrates the computational domain. The centre of the square cylinder is 30*D* away form the inlet and 40*D* from the outlet. The blockage is only 5%, and its effect can be ignored. The air height is 2*D* and water depth is 10*D*. The immerged depth of square cylinder up to 5*D*, so the free end of the square cylinder is far enough from the bottom to avoid the effect of the bottom. The square cylinder surface is set as no-slip condition, and the bottom and the lateral wall are set as slip condition. Inlet is set as velocity-inlet $\vec{U}=(0.1,0,0)$, and zero gradient for outlet. The top wall is set as pressure-outlet condition. For pressure condition, zero gradient is used for the other walls. (D=0.1m, ν=10^{-6}m^2/s)

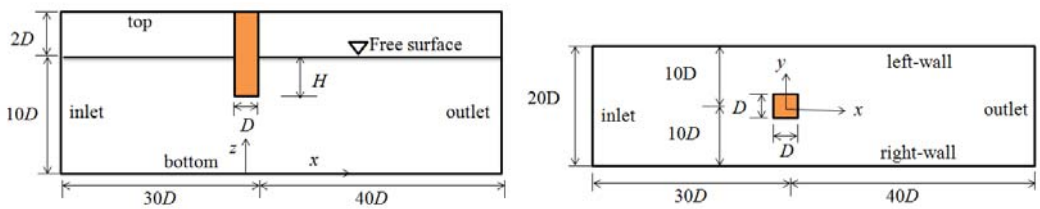

(a) side view (b) top view

Fig. 1. Computational domain

3. Results

Fig. 2 shows the relationship between the drag coefficient C_d and aspect ratio. As can be seen from the figure, the drag coefficient increases with aspect ratio. C_d~1.1 for AR=1 is much smaller than the AR=10, which C_d=2.7(can be assumed as infinite, which has no free end). It indicates that the effect of free end significantly decreases the value of C_d.

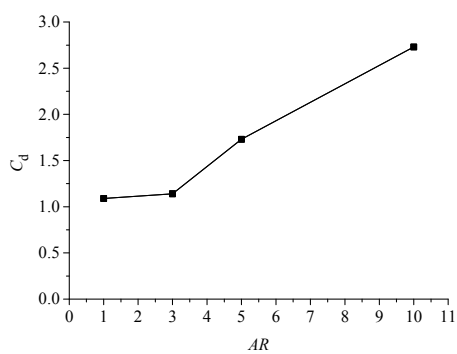

Fig. 2. The relationship between C_d and aspect ratio

Fig. 3 shows the time-averaged streamline in the horizontal plane at half immersed depth. All the cases have the similar pattern. The approaching flow separates at the leading corner, and the recirculation is formed at the two sides of the cylinder as well as a bigger recirculation can be found in the near wake behind the square cylinder. The flow is accelerated outside the two lateral recirculation regions, and low velocity regions lie in the recirculation. For AR=1~5, the length of recirculation behind the cylinder increases with AR. And the length of recirculation of AR=10, is much shorter. It indicates that the free end affects the recirculation behind the square cylinder significantly.

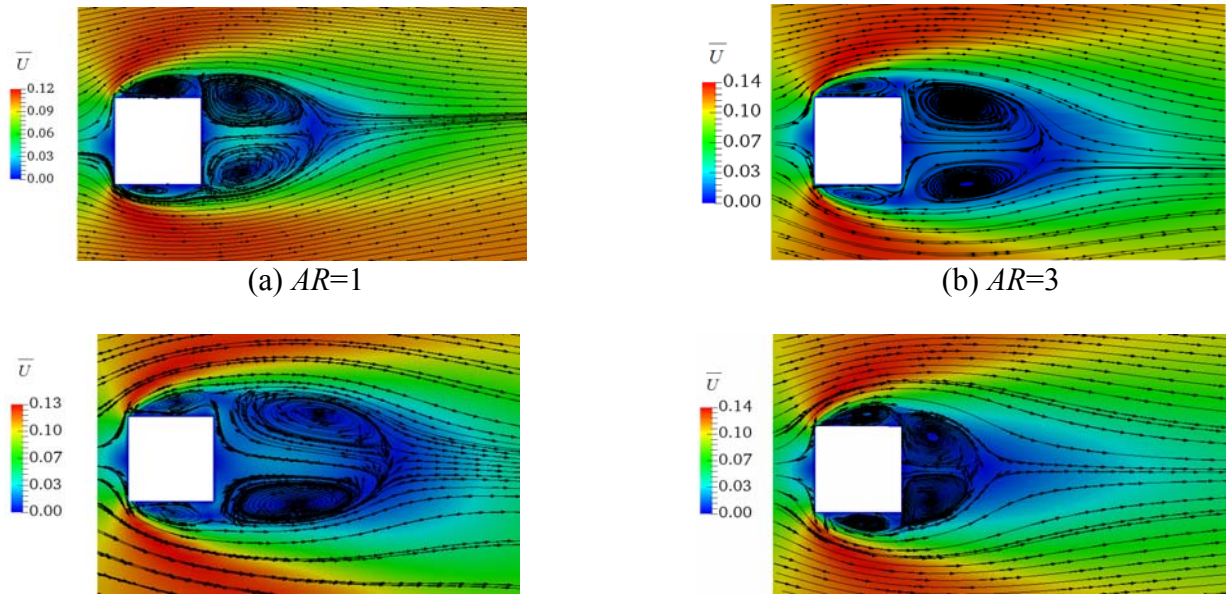

(a) AR=1 (b) AR=3

(c) AR=5 (d) AR=10(no free end)

Fig. 3. The time-averaged streamline in horizontal plane (at half immersion, namely0.5AR), which colored with velocity

Fig.4 shows the time-averaged streamline in the vertical plane(y=0 plane). Flow separates at the leading edge, and two time-averaged vortices can be observed, a small one just below the free end and a larger one behind the square cylinder. Part of the flows on the left of a dividing streamline reverses its direction and impinges on the surface of square cylinder, and most of the flows just go downstream. The dividing line for AR=5 is obviously different from AR=1 and AR=3, a saddle point can be observed (red circle).

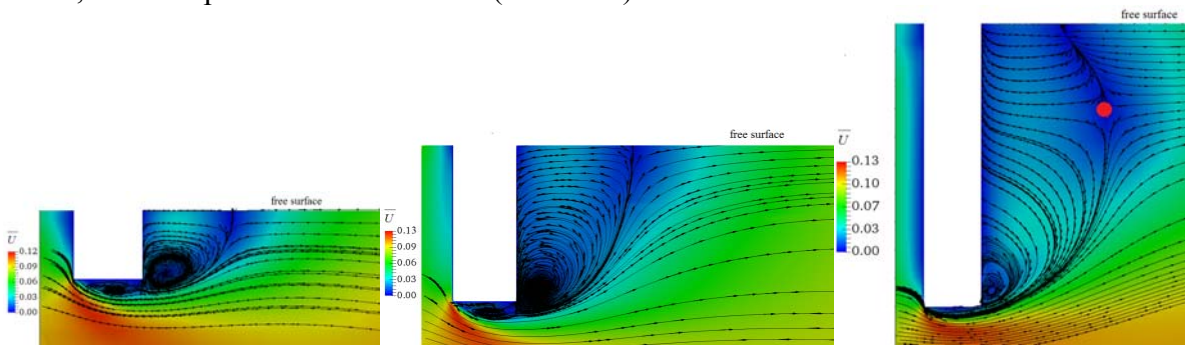

(a)AR=1 (b)AR=3 (c)AR=5

Fig. 4. The time-averaged streamline in vertical plane(y=0), which colored with velocity

4. Conclusions

Numerical simulations were carried out to investigate the flow around a square cylinder with various aspect ratios(AR=1~10) at Reynolds number Re = 1×10^4. The combined effects of the free surface, free end were considered simultaneously. The main conclusions are summarized as:

(1) C_d is significantly influenced by the effect of free end. The drag coefficient increases with aspect ratio.

(2) From the time-averaged streamline in horizontal plane, two pairs of the recirculation can be observed in the horizontal plane right below the free surface.

(3) In the vertical plane, a large recirculation is found right below the bottom of the cylinder, and a small one behind the cylinder in the near wake. The flow pattern is significantly influenced by aspect ratio.

5. References

Gonçalves, R.T., Franzini, G.R., Rosetti, G.F., Meneghini, J.R., Fujarra, A.L.C., 2015. Flow around circular cylinders with very low aspect ratio. Journal of Fluids & Structures 54, 122-141.

Krishna, M.S., Chakrabarti, P., Chakrabarti, S.K., Mukkamala, A., Anavekar, N., 2004. Overview of Tacoma Narrows Bridge Floating Caisson Design, ASME 2004 23rd International Conference on Offshore Mechanics and Arctic Engineering. American Society of Mechanical Engineers, pp. 465-478.

Menter, F.R., 1994. Two-equation eddy-viscosity turbulence models for engineering applications. AIAA journal 32 (8), 1598-1605.

Weller, H.G., Tabor, G., Jasak, H., Fureby, C., 1998. A tensorial approach to computational continuum mechanics using object-oriented techniques. Computers in Physics 12 (6), 620-631.

Characterization of Nano-Particle Reinforced Epoxy Coatings for Structural Corrosion Mitigation

Xingyu Wang[1], Xiaoning Qi[2], Matthew Pearson[3], Mingli Li[4], Zhibin Lin[5*], and Dante Battocchi[6]

[1] Department of Civil and Environmental Engineering, North Dakota State University, Fargo, ND 58108 USA; email: xingyu.wang@ndsu.edu
[2] Department of Coatings and Polymeric Materials, North Dakota State University, Fargo, ND 58108 USA; email: xiaoning.qi@ndsu.edu
[3] Department of Civil and Environmental Engineering, North Dakota State University, Fargo, ND 58108 USA; email: matthew.pearson@ndsu.edu
[4] Department of Civil and Environmental Engineering, North Dakota State University, Fargo, ND 58108 USA; email: mingli.li@ndsu.edu
[5] Department of Civil and Environmental Engineering, North Dakota State University, Fargo, ND 58108 USA; email: zhibin.lin@ndsu.edu
[6] Department of Coatings and Polymeric Materials, North Dakota State University, Fargo, ND 58108 USA; email: dante.battocchi@ndsu.edu

[*]: corresponding author

Keywords: corrosion control and mitigation; nano-particle reinforced coating; durability; graphene nanoplatelets; civil structures

Abstract: Metallic structures, such as bridges and pipelines, rely on effective corrosion protection, such as protective surface coatings that establish a physical barrier layer between the substrate and environment, hereby maintaining their smooth operation and enhancing their service life. Even though several commercially coating systems have used as structural coatings, the major problem is no simple solution that can offer long-term and cost-effective barriers against corrosion. Coatings with low damage tolerance often end up with premature degradation and eventually failure. In this study, new high-performance coatings were developed by incorporating graphene nanoplatelets (GN) in the polymer resins for enhancing resistance to abrasion as well as corrosion resistance. The results demonstrated that the GN-based coatings exhibited a significant improvement in resistance to abrasion and corrosion inhibition property. With the increase of nanoparticle contents, large agglomeration was observed by scanning electron microscopy (SEM).

1. Introduction

Metallic civil structures, including highway bridges and oil/gas pipelines, are often exposed to harsh environments and thus are vulnerable to corrosion (Wang et al., 2016; Pan et al., 2017; Gui et al., 2017; Pan et al., 2018; Lin et al., 2018). Although protective surface coatings have been accepted as one of corrosion control methods to protect these civil structures, data shows that cost associated with corrosion still responds for over $20 billion in these metallic civil structures. Such huge cost during annual structural coating maintenance at each State transportation agencies highlights the deficiencies of the existing protective coatings. One of the major problems for structural coating is the low damage tolerance. For these reasons, the inclusion of nanoparticles as an additives in the coatings has been confirmed as great potential applications

(Xie et al., 2005; Miller et al., 2010; Monetta et al., 2015; Wang et al., 2019; Wang et al., 2018) to enhance the damage tolerance in terms of higher resistance to abrasion as well as higher tensile strength.

Along this vein, we tend to study the corrosion resistance and abrasion resistance of the graphene-loaded epoxy coating. The high-speed disk and ultrasonication were used to disperse the nanoparticles, while the coating properties, including abrasion resistance and the barrier performance, were assessed for structural applications.

2. Experimental Program

Graphene nanoplatelets (from Cheap Tubes Inc.) was used without any modification in this study, while EPON™ Resin 828 (from Hexion Inc.) was used for the primer. Two dispersion methods were carried out to enhance the dispersion and alignment of graphene nanoplatelets in the epoxy matrix. The curing agent was added after the mixture was cooled down to the room temperature. The total solution was mixed with a 10-min mechanical stirring at speed of 400 rpm. Samples with graphene nanoplatelets at 0.5, 1.0, 3.0, 5.0, 7.0 wt.% were made with both dispersion methods. As a comparison, the bare epoxy sample was prepared as controlling group. The samples were characterized by the barrier performance using electrochemical impedance spectroscopy (EIS) measurement and the abrasion resistance using the Taber abraser method.

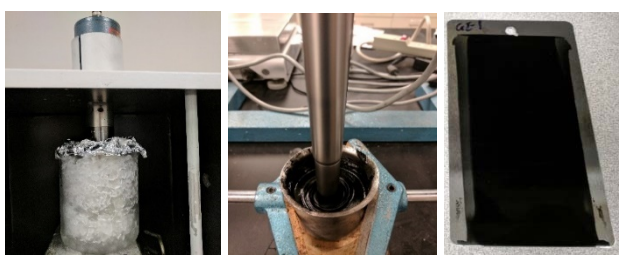

(a) (b) (c)

Fig. 1. Sample preparation: (a) Ultrasonicate; (b) High-speed mixer; and (c) Coated test panel

3. Results and Discussion

3.1. Barrier properties of the nanomodified coating

The corrosion resistances of the GN-based epoxy coatings were determined by potentiostac EIS test, as shown in Fig. 2. Clearly, the 0.5 % and 1.0 % groups exhibited the higher impedance modulus as compared to the pure epoxy (reference). The Zmod values were almost one and half of degrees higher than the pure epoxy. A degradation of the corrosion resistance was observed with the higher concentration of graphene. The Zmod started to decrease in the GN-based epoxy coating with 3.0, 5.0, and 7.0 wt. % of graphene due to particle agglomeration (see Fig. 3).

3.2. Abrasion resistance of the nano-modified coating

Mass loss and wear index were used to calibrate the abrasion resistance of the coatings. As shown in Fig. 4 (a), the results clearly indicated that the graphene-loaded epoxy with higher particle contents could provide enhanced resistance for abrasion, particularly at 500-cycle abrasion. In comparision, Fig. 4 (b) showed that incorporating graphene nanoplatelets was

effective in abrasion resistance by maximum decrease of the wear index about 19%. The highest reinforcement was observed at graphene concentration of 1.0 wt.%. No significant influence of wear index was observed once the concentration exceeding 3.0 wt.%.

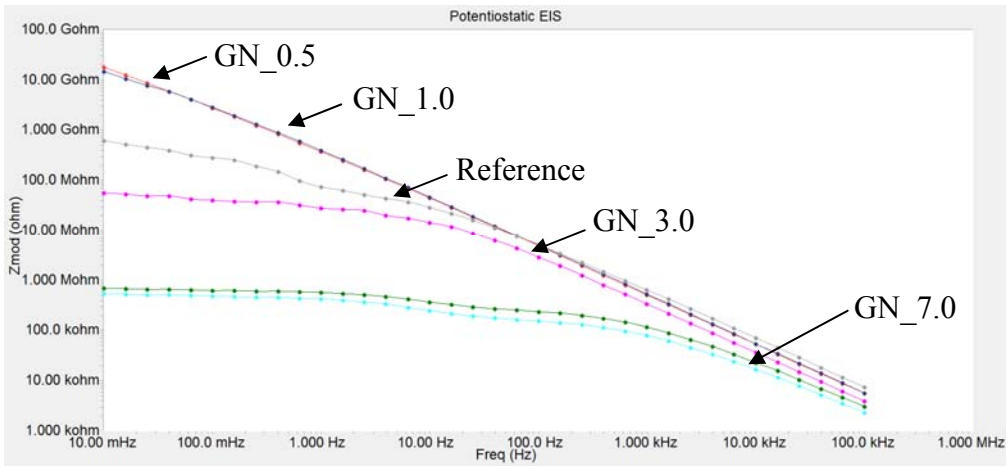

Fig. 2. Impendence curves of the GN-based epoxy coatings

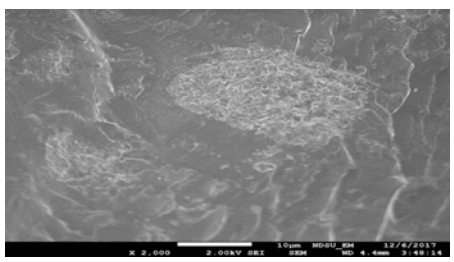

Fig. 3. Agglomeration observed by SEM image in the GN_3.0 (Wang et al. 2019)

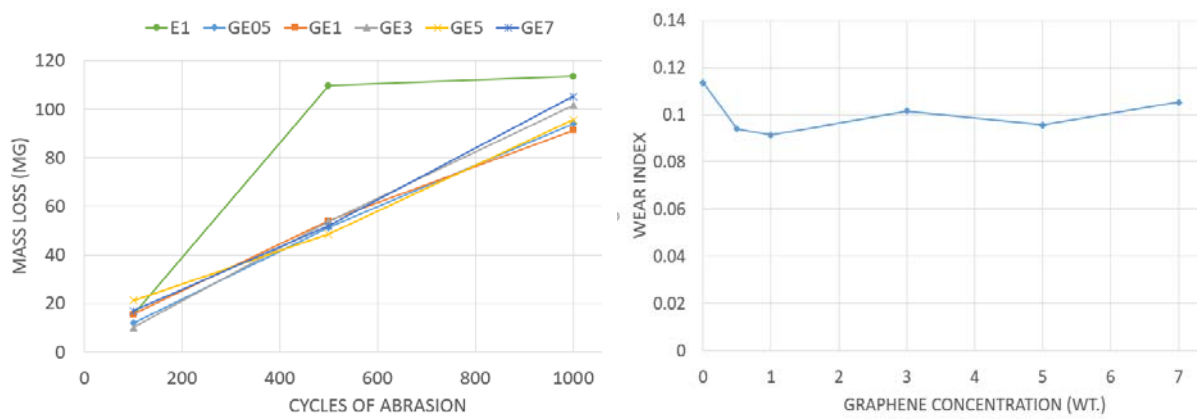

(a) (b)

Fig. 4. (a) Mass loss and (b) Wear index of the GN-based epoxy coatings

4. Conclusions

We investigated the graphene-loaded coatings for structural corrosion control and mitigation. The results demonstrated that the coatings reinforced with a small content of nanoparticles could achieve high resistance to abrasion as well as corrosion resistance. Without surface treatment, the large agglomeration of nanoparticles was observed by SEM image, which mainly responded for the reduction of corrosion resistance.

5. Acknowledgments

The authors gratefully acknowledge the financial support provided by ND DOC Venture Grant, USDOTs (DTPH5616HCAP03, 693JK318500010CAAP and 693JK31850009CAAP). The work presented in this paper was also conducted with partial support from North Dakota State University and the Mountain-Plains Consortium, a University Transportation Center funded by the U.S. Department of Transportation. The results, discussion, and opinions reflected in this paper are those of the authors only and do not necessarily represent those of the sponsors.

6. References

Gui, G., Pan, H., Lin, Z., Li, Y., Yuan, Z. 2017. Data-driven support vector machine with optimization techniques for structural health monitoring and damage detection. KSCE Journal of Civil Engineering, 21, 523–534.

Lin, Z., Pan, H., Wang, X., Li, M. 2018. Data-driven structural diagnosis and conditional assessment: from shallow to deep learning. In Sensors and Smart Structures Technologies for Civil, Mechanical, and Aerospace Systems 2018, International Society for Optics and Photonics, 10598, 1059814.

Miller, S.G., Bauer, J.L., Maryanski, M.J., Heimann, P.J., Barlow, J.P., Gosau, J.-M., Allred, R.E. 2010. Characterization of epoxy functionalized graphite nanoparticles and the physical properties of epoxy matrix nanocomposites. Composites Science and Technology, 70, 1120–1125.

Monetta, T., Acquesta, A., Bellucci, F. 2015. Graphene/epoxy coating as multifunctional material for aircraft structures. Aerospace 2, 423–434.

Pan, H., Ge, R., Xingyu, W., Jinhui, W., Na, G., Zhibin, L. 2017. Embedded Wireless Passive Sensor Networks for Health Monitoring of Welded Joints in Onshore Metallic Pipelines. In ASCE 2017 Pipelines.

Pan, H., Gui, G., Lin, Z., Yan, C. 2018. Deep BBN Learning for Health Assessment toward Decision-Making on Structures under Uncertainties. KSCE Journal of Civil Engineering 22, 928–940.

Wang, X., Qi, X., Lin, Z., Wang, J., Gong, N. 2016. Electrochemical Characterization of the Soils Surrounding Buried or Embedded Steel Elements. In ASCE Pipelines, 110–116.

Wang Xingyu, Xiaoning Qi, Zhibin Lin and Dante Battocchi. 2018. Graphene-Reinforced Composites for Protective Coatings for Oil and Gas Pipelines. Nanomaterials, 8, 1-14

Wang Xingyu, Xiaoning Qi, Zhibin Lin and Dante Battocchi. 2019. Characterization of Graphene Reinforced Epoxy Coatings for Internal Surface of Oil and Gas Pipelines. In ASCE Pipelines.

Xie, X.-L., Mai, Y.-W., Zhou, X.-P. 2005. Dispersion and alignment of carbon nanotubes in polymer matrix: a review. Materials Science and Engineering: R: Reports, 49, 89–112.

Mechanical Properties of Fly Ash Concrete at Early Age for Predicting Thermal Stress of Bridge Pier and Abutment

Yoichi Mimura[1*], Vanissorn Vimonsatit[2], Itaru Horiguchi[3], and Isamu Yoshitake[4]

[1] National Institute of Technology, Kure College, Kure, Japan; email: mimura@kure-nct.ac.jp
[2] Curtin University, Perth, Australia; email: v.vimonsatit@curtin.edu.au
[3] National Institute of Technology, Kure College, Kure, Japan; email: horiguti@kure-nct.ac.jp
[4] Yamaguchi University, Ube, Japan; email: yositake@yamaguchi-u.ac.jp

[*]: corresponding author

Keywords: fly ash; early age; tensile creep; elastic strain; Young's modulus; stress/strength ratio; superposition method

Abstract: Mechanical properties are important for predicting tensile stress, which causes thermal cracking of bridge piers and abutments. Fly ash, a by-product from coal-fired power plants, has been recently used to reduce such thermal cracks. The present study focuses on the tensile mechanical properties of concrete mixed with fly ash at early age. The tensile creep tests with the stress/strength ratio of 30% and 40% were conducted at the age of 3 days, and the loading was sustained for 14 days. Most investigations assume a constant elastic strain during creep test. This study takes a consideration of Young's modulus development during creep test to distinguish actual creep and elastic strains (superposition method). The test results confirmed that creep strain has been underestimated based on the previous assumption (constant elastic strain).

1. Introduction

Controlling cracks due to hydration heat is an important issue for concrete engineers in order to construct durable structures. Thermal cracks often penetrate cross section and cause serious degradation in wall type structures such as bridge piers and abutments. An accurate prediction of thermal stress requires tensile properties at early age, such as strength, Young's modulus and creep. Elastic strain is normally assumed constant for evaluation of creep behavior of mature concrete. However, elastic strain at early age decreases as developing of ages.

Fly ash (FA), a by-product from coal-fired power plants, has been recently used to reduce thermal cracks. Concrete mixed with FA has different development of mechanical properties from concrete without FA. This study examined tensile creep considering stiffness development of FA concrete at early age.

2. Experimental Program

The concrete materials and mixture proportions in this study are given in Table 1. Normal concrete with the water to cement ratio of 55% as shown in Table 1 is generally used for infrastructures in Japan. The amount of FA used in the present study was 20% by mass of the cement of the normal concrete. The dog-bone shaped specimen for the tensile creep test is shown in Fig. 1(a). A mold strain gauge having a thermometric function was embedded at the center of the cross-section. A cylindrical specimen (100 mm diameter x 200 mm long) was used for splitting tensile test (JIS A 1113, 2006) and compression test for Young's modulus. After casting,

all specimens were carried into a curing room to be cured at a room temperature of 20 ± 1 °C for 24 hours before demolding. After that, the specimens were cured underwater in a water tank (16 ± 1 °C) installed in the curing room until load tests were to be carried out at the age of 3 days.
The test setup of the tensile creep test in the present study is shown in Fig. 1(b). A weight was placed on the tip of the steel arm for loading. The loading apparatus was installed in the water tank in the curing room. The tensile creep test was conducted in water in order to eliminate the drying shrinkage.

Table 1. Concrete materials and mixture proportions

Property	Materials	Proportion (kg/m^3)		Density (g/cm^3)
		Normal concrete	FA concrete	
I.D.	---	NX[b]	FAX[b]	---
Water (W)	Tap water	165	165	1.00
Cement (C)	OPC	300	240	3.16
Fly ash (FA)	Class II (JIS A 6201)	0	60	2.24
Fine aggregate (S)	Crushed sand	844	833	2.62
Coarse aggregate (G1)	Crushed stone 20-15 mm	499	493	2.67
Coarse aggregate (G2)	Crushed stone 15-5mm	499	493	2.67
Admixture (Ad1)	AE water reducing agent	3.00	2.40	1.07
Admixture (Ad2)[a]	AE agent for fly ash	0	16.8	1.04

[a]: diluted solution (diluted 100 times with water)
[b]: X means stress/strength ratio (30% or 40%)

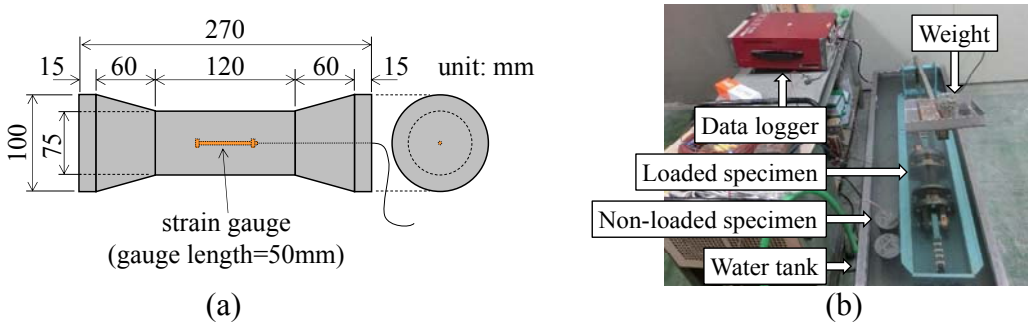

Fig. 1. Dog-bone shaped specimen and test setup of the tensile creep test: (a) dog-bone shaped specimen; (b) test setup of the tensile creep test

The non-loaded specimen was also placed in the tank. Measurement was carried out at one-hour intervals. The loading started at the age of 3 days, and was sustained for 14 days. According to Davis-Granville's principle, creep strain is proportional to loading stress in the range of around 1/3 of strength, so the loading stress in this study was set to 30% or 40% of the splitting tensile strength at the loading. The strain at temporary unloading was recorded in order to measure the elastic strain during the creep test. Three specimens were used for each tensile creep test. The Young's modulus was examined during the tensile creep test. The Young's modulus was evaluated from the gradient of the regression line, which was obtained from the stress-strain relationship in the range of less than the splitting tensile strength (Mimura et al. 2018).

3. Test Results and Discussion

Fig. 2 shows the results of Young's modulus and examples of strain behavior. The Young's modulus at the age of 3, 5, 7, 10, 14 and 17 days is shown in Fig. 2(a). The Young's modulus of FA concrete is lower than that of the normal concrete during the tensile creep test.

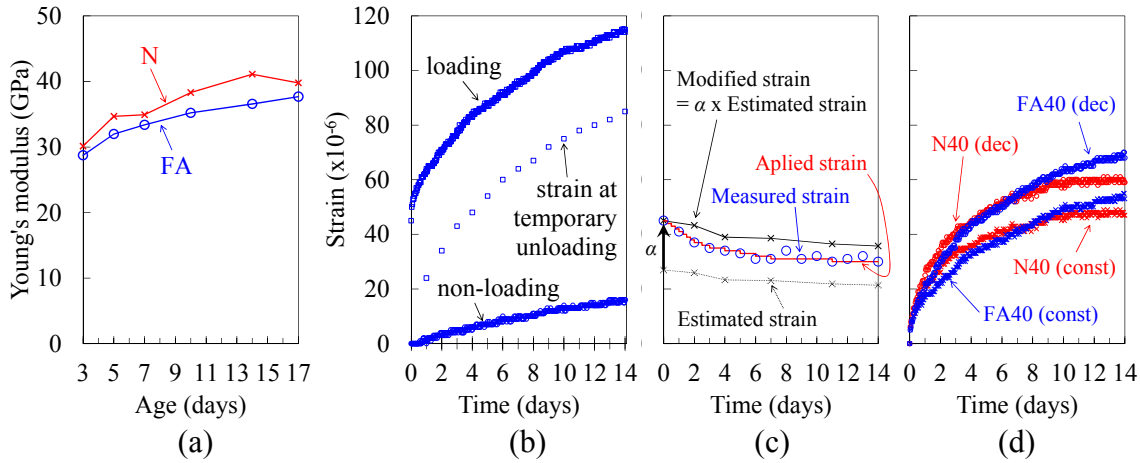

Fig. 2. Examples of strain behavior of FA40 and Young's modulus: (a) Young's modulus of normal concrete and FA concrete; (b) measured strain of loaded specimen and non-loaded specimen; (c) decreasing elastic strain during the tensile creep test; (d) Creep strain of N40 and FA40 based on the constant elastic strain or the decreasing elastic strain

Fig. 2(b) shows the strain behavior of the loaded specimen and non-loaded specimen of FA40. The elastic strain decreased during the tensile creep strain shown in Fig 2. (c). Estimated strain was calculated by dividing the loading stress with the Young's modulus. The estimated strain was not equal to the strain at the loading, so the modified strain was evaluated by multiplying the ratio α of the measured strain to the estimated strain at the loading. The elastic strain for creep evaluation was determined based on the measured elastic strain obtained from the temporary unloading. To estimate the basic creep, the strain of the loaded specimen was subtracted the elastic strain and the strain of non-loaded strain based on superposition method. In this study, two sets of elastic strain were used for creep behavior. One was assumed constant, and the other was the decreasing elastic strain shown in Fig. 2(c). The measured elastic strain shown in Fig. 2(c) was decreased from 45 x 10^{-6} to 30 x 10^{-6}. Fig. 2(d) shows the creep behavior based on the constant elastic strain or the decreasing elastic strain of FA40 and N40. In FA40, the decrease in the elastic strain of 15 x 10^{-6} at 14 days corresponded to 22% of the creep strain based on the decreasing elastic strain. The decrease in the elastic strain of N40 was 12 x 10^{-6}, this was 20% of the creep strain. These results indicate that decrease in elastic strain due to the stiffness development should not be ignored in the evaluation of creep behavior at early age.

The specific creep, which can be obtained by dividing the creep strain by the loading stress, was evaluated. Fig. 3 shows the result of the specific creep behavior based on the decreasing elastic strain. The specific creep of N30 is shown in Fig. 3(a). The experimental data in Fig. 3(a) was obtained from three dog-bone shaped specimens. The three specific creep behaviors were similar,

and the difference between the experimental data of the specific creep and the average value was 2.6 x 10^{-6}/MPa on average. As shown in Fig. 3(b), the difference of experimental data of FA30 and average was greater than that of N30 and was 3.7 x 10^{-6}/MPa. FA30 had the average difference of the specific creep from N30 of 3.7 x 10^{-6}/MPa. Fig. 3(c) presents the specific creep of N40. One was relatively similar to N30, and the others were approximately 2-3 times than N30. The two specific creep behaviors of FA40 until 6 days were almost equal to that of FA30, and the other one was around 1.8 times of FA30 at 14 days. These results indicate that creep strain with the stress/strain ratio of 40% might be nonlinear to loading stress. In addition, the specific creep of N30 and N40 at 14 days almost converged, and the specific creep of FA30 and FA40 was increasing at 14 days yet.

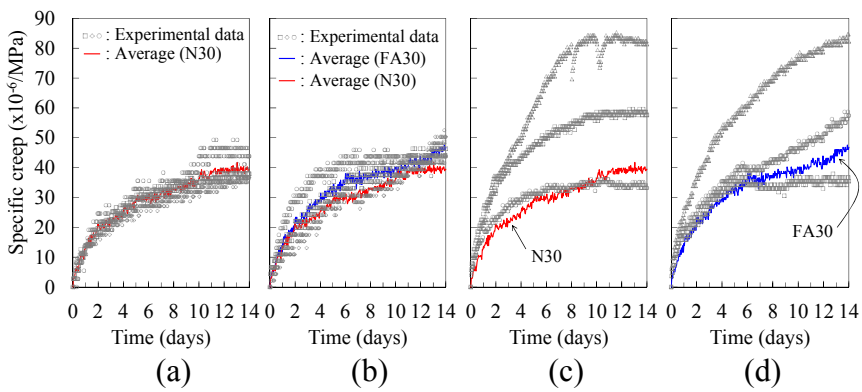

Fig. 3. Specific creep behavior based on the decreasing elastic strain: (a) N30; (b) FA30; (c) N40; (d) FA40

4. Conclusion

This paper presents the tensile mechanical properties of FA concrete at early age for thermal stress prediction of bridge piers and abutments. The elastic strain decreases approximately 20% during the tensile creep test. This result indicates that the creep behavior based on constant elastic strain is an underestimation of actual creep with decreasing elastic strain, so the stiffness development should not be ignored in creep evaluation at early age. The creep strain with stress/strength ratio of 40% might be nonlinear to loading stress.

5. Acknowledgments

The authors would like to thank Mr. Y. Watanabe (former student of National Institute of Technology, Kure College) and the Chugoku Electric Power Co. Ltd.

6. References

JIS A 1113. 2006. Method of Test for Splitting Tensile Strength of Concrete (in Japanese), Japanese Industrial Standard.

Mimura Y., Vimonsatit V., Watanabe Y., Horiguchi I. and Yoshitake I. 2018. Tensile Creep of Fly Ash Concrete at Early Age Considering the Young's Modulus Development, Proceedings of ASEA-SEC-4, MAT-08-1-MAT-08-6.

Bridge Engineering Institute Conference 2019 (BEI-2019)
Honolulu, Hawaii, USA, July 22-25, 2019

Effect of Mycelium on Self-Healing Bio-Concrete

Aparna Deokar[1], Anuja Kamat[2*], and Joe Radecki[3]

[1] Littleton Public Schools, Littleton, MA, USA; email: adeokar.2023@littletonps.org
[2] Wentworth Institute of Technology, Boston, MA, USA; email: kamata@wit.edu
[3] Wentworth Institute of Technology, Boston, MA, USA; email: radeckij@wit.edu

[*]: corresponding author

Keywords: self-healing; mycelium; bridge repair; bio-concrete; fungi; construction; materials

Abstract: While concrete is an excellent building material, concrete is also known to crack. When water enters the cracks and freezes, it expands making the crack wider. When subjected to repeated freeze-thaw cycles, the concrete structure rapidly deteriorates. Repairing the cracks in concrete can be expensive. Also, sometimes the cracks might be in hidden locations and the hazards of unnoticed concrete cracks are well known. *Self-healing bio-concrete* involves introducing fungi into concrete. When the cracks form, the biological material will react to fill the cracks. This will stop the cracks from getting wider and, also "heal" the concrete. This will increase the life of concrete structures which would be great for the environment. Self-healing bio-concrete is the future of concrete in bridge construction because it will reduce the maintenance cost and may also reduce the hazards caused by inaccessible / unnoticed cracks. This paper presents preliminary results of experiments conducted by students and faculty and suggests a direction for future work.

1. Introduction

Concrete is the most used construction material in the world, but across the world, every day, new cracks develop in concrete structures. Water from precipitation enters these cracks and freezes, causing the cracks to enlarge (Mamlouk & Zaniewski 2016; Scientific Principles 2019). More water can enter, freeze, and expand until a bridge is destroyed (Menon et al. 2017). *Bio-concrete*, a type of concrete that is embedded with bacterial spores, can repair these cracks when they are still small, saving a lot of money that is spent to repair larger cracks. This project's aim is to find out if mycelium, a type of filamentous fungi, will affect concrete cracks in the same way. Scientists are still trying to find out how bio-concrete works so that they can make concrete more sustainable (Jonkers & Schlangen 2007). This project will investigate the effects of adding different amounts of mycelium to concrete in different stages on the percentage of concrete cracks reduced.

Traditional bio-concrete is concrete that is embedded with bacterial spores. It is also usually mixed with an organic nutrient that contains calcium. Bio-concrete can repair its own cracks before they expand and become very expensive to fix. It can do this by lying dormant in concrete until it is activated by water dripping inside a crack. After activation, it produces limestone ($CaCO_3$), which repairs the crack by filling it and goes dormant again. Since bacterial spores can repair concrete cracks, it could be possible that mycelium could do the same. The main issue with placing such organisms in concrete is the inherent properties of concrete. High pH levels,

in the range of 13 on the pH scale, limited food sources, and limited oxygen access means most organisms lack the ability to survive and more importantly expand / reproduce. Reproduction is necessary for the success of self-healing concrete as cracking is a continuous process which parallels the life of the concrete structure. Some research (Menon et al. 2017) has been conducted in testing the fungi that have the chemical makeup to withstand such an environment, but no extensive tests have been completed. This research will look to test mycelium's ability to expand and reproduce when mixed in and added to concrete.

Mycelium is a filamentous fungus made from a network of hyphae, which are white threadlike filaments (Editors 2019). Since mycelium can produce calcium carbonate, it could theoretically be used in bio-concrete. This potential advancement in bio-concrete has not yet been explored by researchers in the field. While concrete is mixed, mycelium spores and its organic nutrients would be added to the mix. After water trickles into the cracks, the spores would be activated, and make calcium carbonate precipitates, which would fill the cracks. Then, the mycelium will go dormant again. Existing structures could also be sprayed with the mycelium spores along with the nutrients so that the same process would occur to them.

The hypothesis for this project is that if activated mycelium (a filamentous fungi) is mixed with concrete, the mycelium will reduce the percentage of crack size. This hypothesis was developed because mycelium produces hyphae, which has filaments that expand while activated (Editors 2019). The hyphae could grow to fill concrete cracks. To test this hypothesis, five different samples were made which is explained in the next section.

2. Experimental Setup

The experimental setup consisted of five samples (Fig.1). Each sample was a cylinder, 4 inches in diameter and 8 inches in height. The five samples were: (1) a cylinder made of only mycelium, (2) a cylinder made of activated mycelium added to concrete during the initial mixing, (3) a cylinder made of dormant mycelium added to concrete during the initial mixing, (4) a cylinder of concrete with dormant mycelium added to the cracks, and (5) a cylinder made of only concrete.

Fig. 1. Samples 1-5 on the day of mixing concrete and mycelium (*Sample 1*: Mycelium, *Sample 2*: Concrete + Activated Mycelium, *Sample 3*: Concrete + Dormant Mycelium, *Sample 4*: Cracked Concrete + Dormant mycelium, *Sample 5*: Concrete)

Mycelium: This sample consisted of only mycelium. The dormant mycelium was activated for 5 days. Then, organic matter was added, and the mycelium was put in an air-tight cylinder. This was a control specimen to ensure that the mycelium was active and growing in the test environment

Concrete + Activated Mycelium: In this sample, the mycelium was first activated (for 5 days). Then, the mycelium was added when the concrete was mixed. The proportion of Mycelium mix to Concrete was measured as 1:7. After the concrete was mixed, it was allowed to set for 3 days. Then, the cylinder was put in a compression testing machine and cracked. The ability of the mycelium to fill the crack was observed over the next several days.

Concrete + Dormant Mycelium: In this sample, the dormant mycelium was directly added when the concrete was mixed. The proportion of Mycelium mix to Concrete was measured as 1:7. This sample was allowed to set for 3 days. Then, the cylinder was put in a compression testing machine and cracked. The cylinder was then exposed to organic matter to encourage activation of mycelium in the cracks. The ability of the mycelium to fill the crack was observed over the next several days.

Cracked Concrete + Dormant Mycelium: In this sample, the concrete cylinder was made and allowed to set for 3 days. Then, the cylinder was put in a compression testing machine and cracked. The dormant mycelium was inserted in the cracks along with the organic matter to activate it.

Concrete: This sample consisted of only concrete. The concrete cylinder was cracked after two days. This sample was then kept in the test environment as a control specimen.
Sample 1 and sample 5 were control specimen. The mycelium (activated and dormant) was mixed into the concrete in samples 2 and 3 respectively. The purpose of these samples was to evaluate the efficiency of mycelium to repair cracks in bio-concrete. The purpose of sample 4 was to evaluate if mycelium would be an appropriate medium to repair cracks in conventional concrete.

3. Observations

The samples were observed for 10 days. The mycelium growth was consistent in each sample. Fig.2 shows the mycelium growth on the last day of observation.

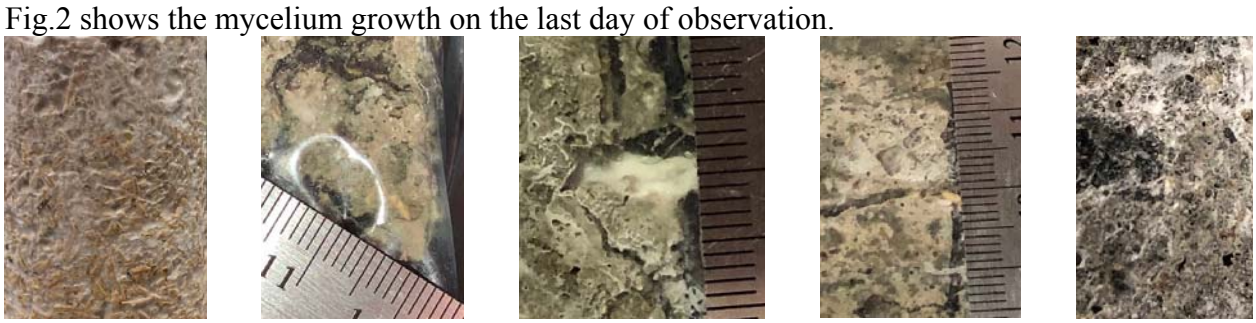

Sample 1 Sample 2 Sample 3 Sample 4 Sample 5

Fig. 2. Samples 1-5, 13 days after mixing (10 days after cracking).

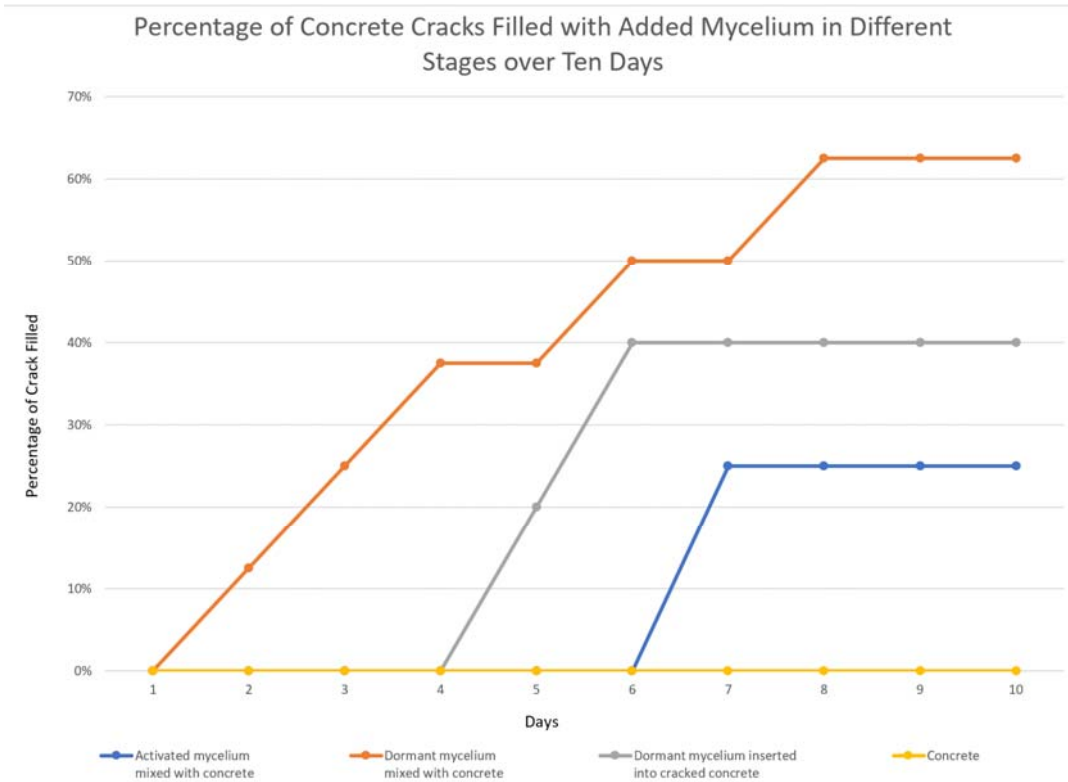

Fig 3. Shows the differences in percentage of cracks filled across the concrete samples, measured throughout the duration of the experiment.

Sample 1: Mycelium in the form of a goo-like substance (white) can be clearly seen on Sample 1 (control).

Sample 2: The mycelium growth was not very obvious. However, after breaking open the cylinder, the mycelium streaks could be clearly seen.

Sample 3: The mycelium growth can be seen very clearly. The crack was filled over 50% with mycelium.

Sample 4: There was very little mycelium growth on the surface.

Sample 5: There was no mycelium on this sample. It was a control specimen.

Fig 3 tracks the growths that formed to fill the cracks in the concrete. It can be concluded that the sample with dormant mycelium mixed with concrete resulted in the most efficient results in terms of the cracks being filled quickly and having the highest percentage of crack filled.

To better understand the ability for the cracks to be filled in the future, volumetric testing as when as characteristics of the growth material will need to be tested to accurately describe the process happening inside the concrete mix. Further testing will allow for the growth material to be tested for strength properties both independently, and in fellowship with the housing concrete

5. Conclusion

When mycelium spores are added to concrete during mixing, the cracks fill up in the presence of organic material. This will stop the cracks from getting wider and, also "heal" the concrete. Adding dormant mycelium produces far better results than adding activated mycelium to the concrete. The life of concrete structures would increase, which would be great for the environment. This will be the future of bridge construction because it will reduce the maintenance cost and may also reduce the hazards caused by inaccessible / unnoticed cracks.

Existing cracks in concrete structures when sprayed with the mycelium spores and nutrients did not fill the cracks. This could be because it was difficult to completely get the mycelium inside the cracks. In future, this experiment should be repeated with a different set up where the mycelium can be fully inserted in the concrete.

Although more tests are required to see the full extent of the mycelium's capabilities as it comes to filling in larger cracks as well as how long the fungi can reproduce before needing potential treatment/replacement; this research was successful in confirming that mycelium could survive in concrete for the allotted time and produce hyphae to fill voids left by external compressive forces on the cylinders.

6. Acknowledgements

The authors would like to acknowledge and thank Mrs. Valerie Finnerty of Littleton Public School for her support during this project

7. References

Editors, 2019. Mycelium. Encyclopaedia Britannica. Available at: www.britannica.com/science/mycelium.

Jonkers, H.M. & Schlangen, E., 2007. Self-healing of cracked concrete: A bacterial approach. In Proceedings of FRACOS6: Fracture Mechanics of Concrete and Concrete Structures. Catania, Italy, pp. 1821–1826.

Mamlouk, M.S. & Zaniewski, J.P., 2016. Materials for Civil and Construction Engineers, Hoboken, NJ: Prentice Hall.

Menon, R.R. et al., 2017. Screening of fungi for the application of self-healing concrete. ArXiV, p.21. Available at: https://arxiv.org/pdf/1711.10386.pdf [Accessed March 1, 2019].

Scientific Principles, 2019. Scientific Principles. Available at: matse1.matse.illinois.edu/concrete/prin.html.

Mechanical Anchoring of Reinforcing Bars to Enhance the Ductility and Constructability of RC Members

Kenji Yoshitake[1*], Hiroki Ogura[2], Naoyuki Araki[3], Yuuri Yoshimura[4], and Kazutoshi Hirata[5]

[1] Technology Planning Div., SHIMIZU Corp., Japan: yoshitake@shimz.co.jp
[2] Institute of Technology, SHIMIZU Corp., Japan: ogura_h@shimz.co.jp
[3] Civil Engineering Technology Div., SHIMIZU Corp., Japan: araki_n@shimz.co.jp
[4] Civil Engineering Technology Div., SHIMIZU Corp., Japan: yoshimura_u@shimz.co.jp
[5] Reinforcing Bar Business Div., Dai-ichi High Frequency Co., Ltd., Japan: k-hirata@dhf.co.jp

[*]: corresponding author

Keywords: mechanical anchoring; T-headed bars; ductility; cyclic Loading column tests

Abstract: Recently, the demand for enhancing the ductility of structural members has greatly increased due to the publication of the mechanical anchoring method guideline. Therefore, we improved the anchor plate shape of T-headed bars, and cyclic loading column tests with two types of rebar arrangements were carried out, with attention focused on load carrying capacity after the ultimate displacement. It was verified that improved T-headed bars function sufficiently as shear reinforcement and enhance the ductility under both conditions.

1. Introduction

Since the Hyogo-ken Nanbu Earthquake, the number of shear reinforcements and tie hoops has increased in civil structures. With the increase of reinforcing bars, the assembly of reinforcing bars subject to bending, such as those with standard hooks for shear reinforcement, is extremely difficult, which reduces the work efficiency of the reinforcing bar arrangement. Furthermore, the large number of reinforcing bar bends, including the standard hooks which stick out of concrete surfaces, would make it difficult to place hose outlets or vibrators for compacting into the bar arrangement. Therefore, the congested arrangement was found to be a cause of less work efficiency in arrangement of reinforcing bars and filling capacity of concrete. Some mechanical anchoring methods of reinforcing bars have been developed and 'Recommendations for Design, Fabrication and Evaluation of Anchorages and Joints in Reinforcing Bars' was published (JSCE 2007). The authors developed the anchorage method to use T-headed bars (TH25), which have increased diameter at the bar ends formed by high-frequency induction heating, instead of the standard hooks as shown in Photo 1(a) (Shioya et al. 2002, Yoshitake et al. 2008). This method has been successfully applied to many actual structures and contributes to improving the quality and work efficiency of concrete structures. Recently, the demand for enhancing the ductility of structural members has greatly increased due to the

(a) TH25 (b) THL

Photo 1. T-headed bar

Table 1. Test parameters and results

Specimen	Application	Anchorage element	Compressive strength (N/mm^2)	Tensile strength (N/mm^2)	Young's modulus (kN/mm^2)
Ro-F	Road	Standard hook	27.3	2.5	28.5
Ro-T	Road	T-headed bar	27.8	2.8	27.8
Ra-F	Railway	Standard hook	25.2	2.4	26.1
Ra-T	Railway	T-headed bar	28.2	2.8	29.1

Table 2. Test results of reinforcing bar

Specification	Application	Yield strength (N/mm^2)	Tensile strength (N/mm^2)	Young's modulus (kN/mm^2)
D29 (SD345)	axial rebar	389	586	200
D13 (SD345)	intermediate tie	366	574	179
D13 (SD345)	hoop tie transverse rebar	390	545	189

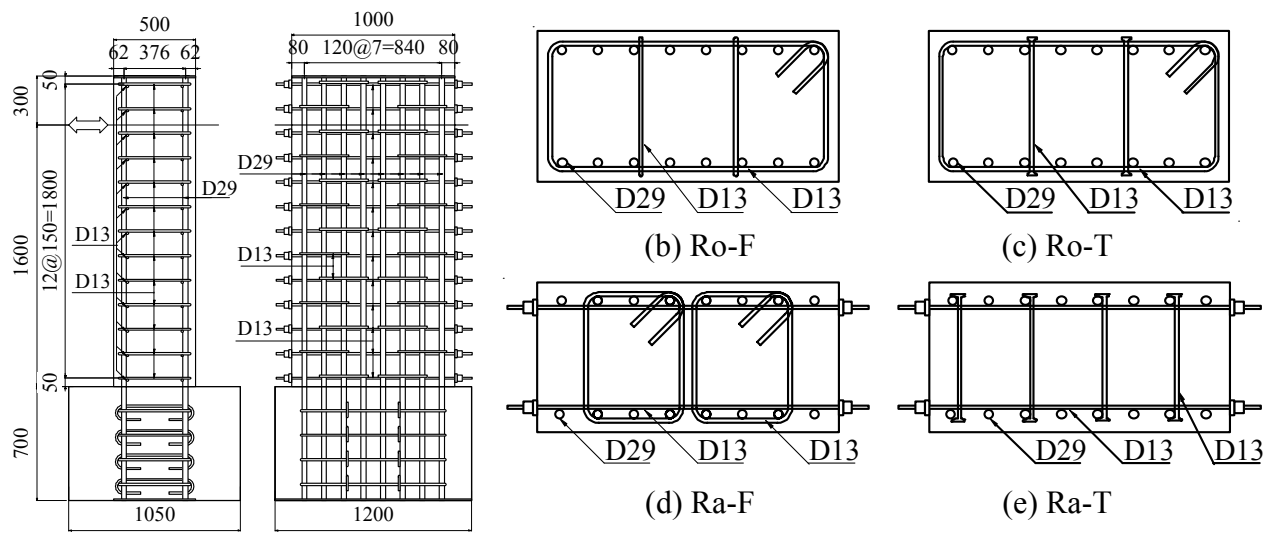

(a) Frontal and lateral view (Ra-F)

Fig. 1. Dimensions and arrangement of reinforcing bar

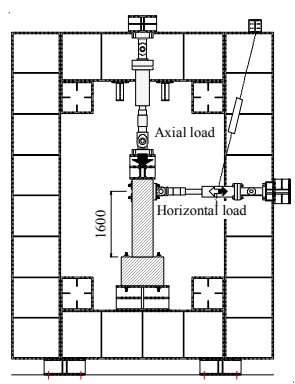

Fig. 2. Loading apparatus

publication of the mechanical anchoring method guideline (MLIT 2016). Therefore, we improved the shape of the anchor plate of T-headed bars (THL) as shown in Photo 1(b). THL has a longer plate side to restrain the reinforcing bar to enhance the ductility. This paper describes the results of reverse cyclic loading column tests to investigate the load carrying capacity of the column using THL after the ultimate displacement.

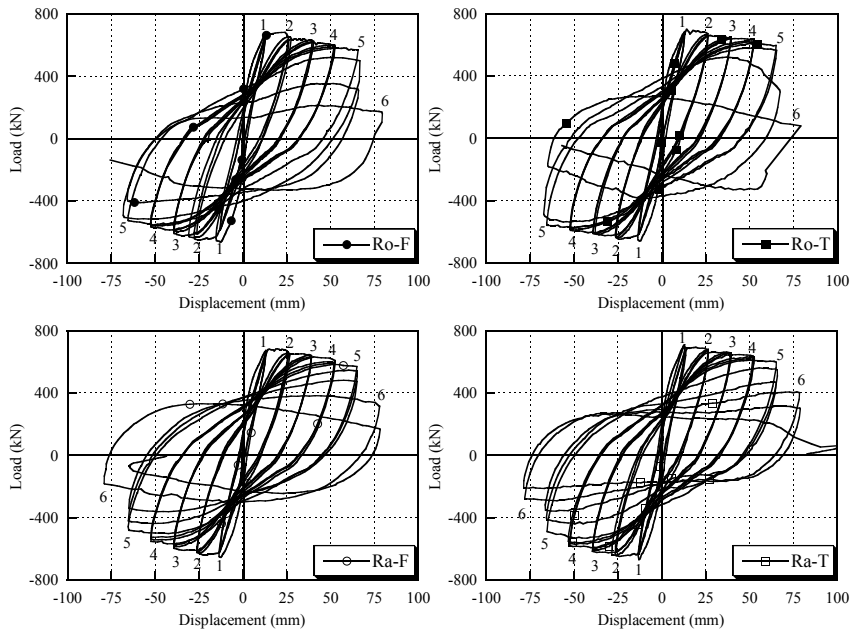

Fig. 3. Load-displacement relationship

2. Outline of tests

Table 1 and Figure 1 show the overview of the specimens, and the configuration of specimens and arrangement of the reinforcing bar. The specimens had a length of 1,900 mm and widths of 1,000 mm and 500mm, respectively. Four different types of specimens in different applications and with different bar anchor end shapes for shear reinforcement were provided. There were two configurations of reinforcing bars: Ro-F and Ro-T were modeled for road structures and Ra-F and Ra-T were for railway structures. The main and shear reinforcement ratios were 1.2% and 0.34, respectively. SD345 grade reinforcing bars were used for reinforcements. The transverse reinforcing bars for Ra-F and Ra-T were fixed to steel plates at the ends of the specimens. The shear span to depth ratio of specimens was specified as 3.7. The shear capacity of the column (V_y) was 1,056kN, while the contributions of the concrete (V_c) and the shear reinforcements (V_s) were 564kN and 492kN, respectively. The flexural yield load of the column was 668kN. A reverse cyclic horizontal displacement was applied to the specimens with a constant axial force as shown in Figure 2. The standard control displacement (δ_y) was set as 13mm using the experimental yield displacement of Ro-F. The axial compressive stress was set as 3.5 N/mm^2 for clarifying the effect of the shear reinforcing bars on the ductility. The loading test was continued until the axial load was maintained. Horizontal displacements at various portions of the specimens and strain at the reinforcing bars were measured. Tables 1 and 2 show the material test results of the concrete and reinforcing bars which were used.

3. Experimental results and discussions

Figure 3 and Photo 2 show the relation between horizontal load and displacement at the horizontal jack and the failure mode, respectively. The load shown in Figure 3 corrected the P- δ contribution. At the 1 δ_y cycle, flexural cracks occurred and axial reinforcing bars began to yield.

A rapid fall in the load was observed due to the buckling of the axial reinforcing bar and disintegration of the cover concrete at the 5 δ_y cycle for all specimens.

(a) Ro-F (b) Ro-T (c) Ro-F (d) Ro-T

Photo 2. Failure mode

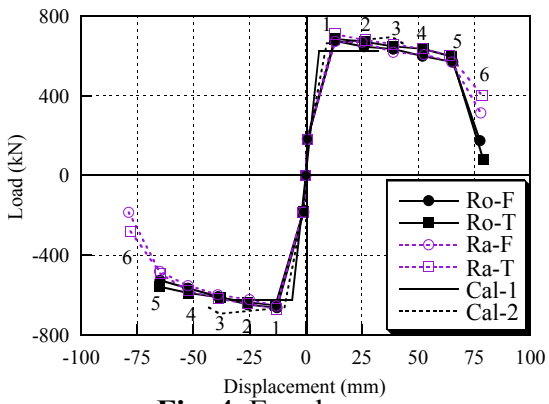

Fig. 4. Envelope curve

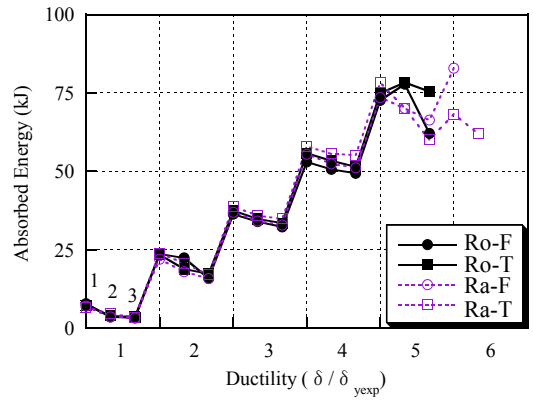

Fig. 5. Absorbed energy

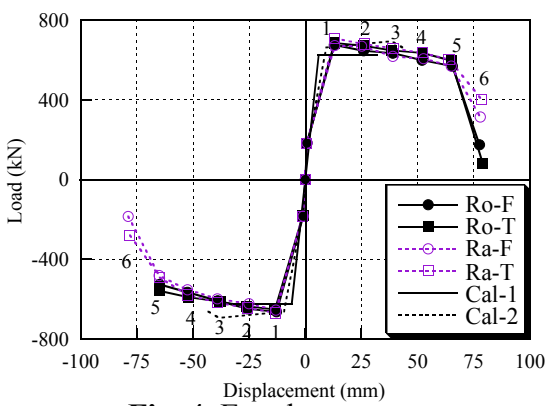

Fig. 4. Envelope curve

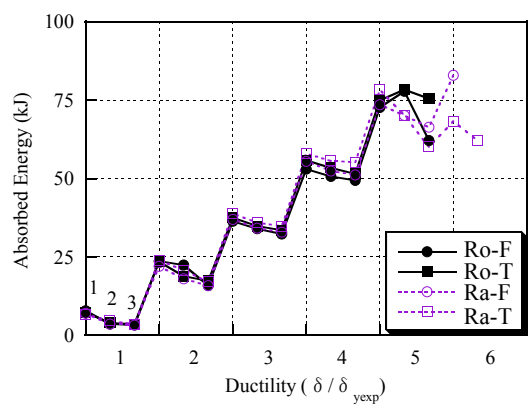

Fig. 5. Absorbed energy

The cycles that did not maintain the axial force were the first cycle of the 6 δ_y for Ro-F and Ro-T, the second cycle of the 6 δ_y for Ra-F and the third cycle of the 6 δ_y for Ra-T. Damage to the core concrete due to the opening of the standard hooks for Ro-F and Ra-F and the anchorage plates that had slipped from the restrained reinforcing bars for Ro-T and Ra-T was observed. Figure 4 shows the envelopes of cyclic load-displacement relations with calculated results using road and railway specifications (Japan Road Association 2002, Railway Technical Research Institute 1992). All specimens exhibited almost the same maximum load, which positively

agreed with the calculated results, and the ductility was higher than calculated results. Ra-F and Ra-T had higher load carrying capacity at the 6 δ_y cycle compared to Ro-F and Ro-T. Figure 5 shows the absorbed energy, which is defined as the area under load and displacement curves for each cycle. Ra-F and Ra-T had higher absorbed energy capacity compared to Ro-F and Ro-T. The confined effect of the transverse reinforcing bar located inside the axial reinforcing bars was observed. The test results showed that T-headed bars had load carrying performance equivalent to that of semicircular hooks even for both road and railway reinforcing bar arrangements after the ultimate displacement.

4. Conclusion

We improved the shape of T-headed bars (TH25) and developed the THL, which has a longer plate side to restrain the reinforcing bar to enhance the ductility. This paper describes the results of reverse cyclic loading column tests to verify the ductility of the column using THL. As a result, it was confirmed that THL functioned sufficiently as shear reinforcement and the load carrying performance was equivalent to semicircular hooks even for both road and railway reinforcing bar arrangements after the ultimate displacement. It was also confirmed that the reinforcing bar arrangement for railway structures had higher load carrying performance and absorbed energy capacity compared to that for road structures due to the difference of the confined effect.

5. References

Japan Road Association (2002), Specifications for highway bridges, Part V Seismic Design

Japan Society of Civil Engineers (2007), Recommendations for design, fabrication and evaluation of anchorages and joints in reinforcing bars [2007] (in Japanese)

Ministry of Land, Infrastructure, Transport and Tourism (2016), Guideline for design and arrangement of reinforcement for mechanical anchorages (in Japanese)

Railway Technical Research Institute (1992), Standard specification for seismic design of structures for railways (in Japanese)

Shioya, T., Higuchi, Y. Shiokawa, H. and Takagishi, M. (2002), "RC beam test using T-headed bars under shear, flexure and compression", The first fib Congress 2002, Session 7, 45-52.

Yoshitake, K., Ogawa, A, Dewa, K., Maenosono, T. and Takagishi, M. (2008), "Structural performance of RC beams using T-headed bars as shear reinforcement under static and fatigue loading", The 3rd ACF International Conference-ACF/VCA 2008

Modeling Concrete Pavements for Bending Stresses Considering Linear and Nonlinear Thermal Gradients

Rafiqul A. Tarefder[1*] and Gauhar Sabih[2]

[1] Department of Civil Engineering, University of New Mexico, Albuquerque, New Mexico, USA; Corresponding Author. email: tarefder@unm.edu
[2] Department of Civil Engineering, University of New Mexico, Albuquerque, New Mexico, USA; email: gsabih@unm.edu

[*]: corresponding author

Keywords: concrete; temperature; thermal gradient; coefficient of thermal expansion; nonlinear; finite element

Abstract: Temperature gradient through the thickness of the concrete pavement slab results in slab curling and induces longitudinal bending stresses in the slab. Historically temperature distribution or gradient has been considered linear, though it can be nonlinear in many cases. In this study, numerical modeling is conducted to compare the bending stresses due to nonlinear temperature to those due to the linear temperature distribution. It became evident from the results that the nonlinear temperature results in higher stress levels up to 34% in the top fibers and lower stress levels up to 36% in the bottom fibers in comparison to the linear temperature. These increased stress levels may result in higher pavement distresses during the design service life and the pavement may not perform through its designed life and thus it is emphasized that nonlinear thermal gradient should be incorporated in numerical modeling to achieve accuracy in concrete pavement analysis.

1. Introduction

Concrete pavements are subjected to traffic and environmental loading which induces distresses in the pavement slab. Besides other factors, pavement temperature is an important factor in concrete pavement design, and especially, daily temperature fluctuations within the concrete slab significantly influence the pavement behavior. A temperature gradient exists between the top and bottom of the concrete pavement slab which results in thermal curling, producing thermal stresses in the pavement. Westergaard (1927) was the first to provide an analytical solution for thermal stresses in concrete pavements. The major restrictive assumption was to consider linear temperature gradient through the slab thickness. Teller and Sutherland (1935) found that the temperature distribution through the thickness of the pavement slab is nonlinear. Bradbury (1938) extended Westergaard's work to derive an approximate solution to determine maximum stresses in finite concrete slab. Lang (1941) found that the difference in stresses between nonlinear and linear temperature gradient is not significant enough to be considered in pavement analysis. Later, numerous researchers discovered and emphasized the significance of temperature nonlinearity as it affects pavement performance. Choubane and Tia (1992) found that assuming a linear temperature profile may lead to a significant amount of errors in computing thermal stresses in comparison to the nonlinear temperature distribution. While most of the researchers

worked on thermal curling with a linear temperature gradient, very few have conducted investigations with nonlinear temperature profiles of concrete pavement slabs.

2. Objective

This study evaluates the effects of linear and nonlinear temperature distribution on the thermal bending stresses in the top and bottom fibers of a concrete pavement slab.

3. Comparison of Thermal Stresses due to Linear Temperature Profile

The effects of linear temperature distribution on the thermal bending stresses are evaluated. The temperature differential found by Choubane and Tia (1992) are retained in this study. The simulations are conducted in *ABAQUS version 6.14-1*, and the results are compared with the analytical, and numerical studies conducted by previous researchers. The slab dimensions were 20 ft long, 12 ft wide and 9 in thick. The material properties used are the elastic modulus of 4500 ksi, Poisson's ratio of 0.2, CTE of $6x10^{-6}$ in/in/°F, concrete unit weight of 150 pcf, and modulus of subgrade reaction assumed as 300 psi/in. The simulations are conducted in 2D using CPS4R elements available in *ABAQUS* and the elastic foundation is used for subgrade.

3.1. State of Longitudinal Bending Stress with Linear Temperature Profile

The linear temperature distribution is incorporated with the material properties given previously, and the single pavement slab is considered with no doweled joints. As expected, the maximum longitudinal bending stress occurs at the center of the pavement slab, both during day time and night time. The stress profile is also linear. The comparison of maximum bending stress through the thickness of the slab is shown in Figure 1 for day time. During the day time, maximum stress is obtained at 1 PM when the temperature differential is maximum. With positive thermal gradient during the day time, downward curling is observed with compressive stresses at the top half of the slab and tensile stresses at the bottom half of the slab. The maximum stress is 393.4 psi at 1 PM. The negative temperature gradient during the night time resulted in upward curling with maximum tensile stress at the top of the slab and maximum compressive stress at the bottom. The maximum stress level is 102.4 psi at 2 AM.

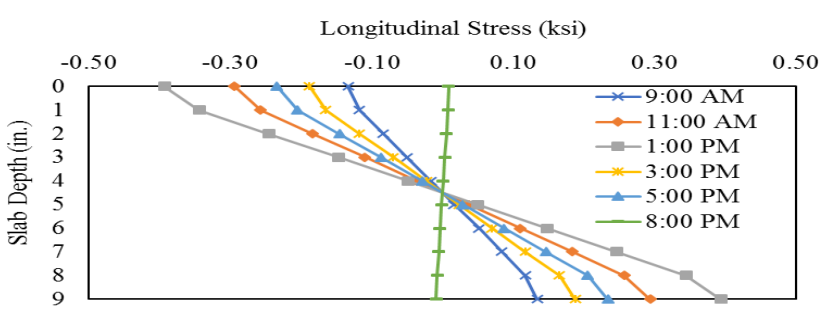

Fig. 1. Stress Comparison During Day Time with Linear Temperature Profile

3.2. Comparison of Stress Data with Previous Studies

The results are compared with the previous studies including the analytical solution by Westergaard (1927) and 3D FE analysis conducted by Aure (2013). This analysis shows that the results of longitudinal bending stress are on the lower side as compared to the other two methods.

With respect to the analytical method, the stress values of this study are around 23% lower, which could be due to simplifying assumptions of the analytical method. With regards to the 3D analysis, 70% of the results of this study are within 13.6% difference. However, the stress profile through the thickness of the pavement slab matches perfectly to the previous studies. With this analysis, it can be deduced that the FE idealization used in this study works well and can be further used for nonlinear thermal modeling.

4. Numerical Modeling with Nonlinear Thermal Gradient

Choubane and Tia (1992) captured the temperatures in JPCP using thermocouples embedded in the pavement slab and suggested a quadratic equation for temperature distribution as follows:

$$T = A + Bz + Cz^2 \quad (1)$$

where A, B, and C are coefficients that were determined from the measured data; T is the temperature in °F; Z is the pavement slab depth, with $Z = 0$ at the top of the slab and $Z = h$ at the bottom of the slab; h is the pavement slab thickness. The same coefficients, temperature differential, and the quadratic profile are retained in this study. The temperature distribution (day time) is shown in Figure 2. The analysis shows that all of the temperature profiles during day and night are nonlinear with the same temperature differential as in the linear profiles. These nonlinear temperature distributions may affect the stress values through the thickness of the slab based on the nonlinearity.

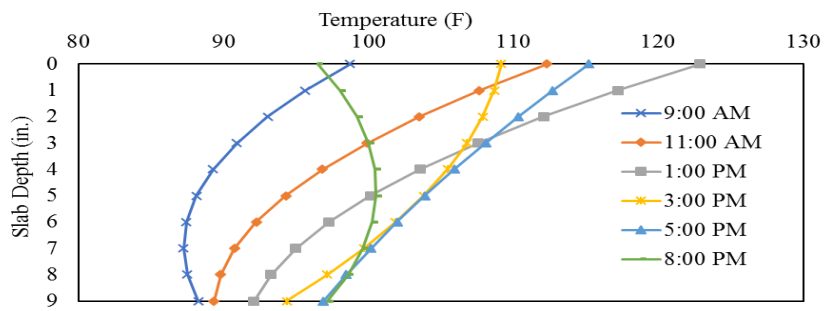

Fig. 2. Nonlinear Temperature data (day time)

4.1. State of Longitudinal Bending Stress with Nonlinear Temperature Distribution

The comparison of longitudinal bending stress results is presented in Figure 3 for day time. It is evident that the stress profile with nonlinear temperature is highly different as compared to the stresses with linear temperature distribution. During the day time, with a positive temperature gradient, the pavement slab curls downward inducing compressive stresses in the top half of the pavement slab and tensile stresses in the bottom half of the pavement slab. The maximum stresses occur at the top and bottom center of the slab. The maximum compressive stress of 464 psi is found at 1 PM with the highest temperature differential. During the night time, with a negative temperature gradient, the slab shows upward curling resulting in tensile stresses at the top and compressive stresses at the bottom of the pavement slab. The maximum stress at night time is 122 psi at the top of the slab and occurs at 2 AM. The stress values are different than the ones with linear temperature distribution.

4.2. Comparison of Nonlinear Cases with Previous Studies

The results of FE simulations with nonlinear temperature distribution are compared with the previous studies conducted by Choubane and Tia (1992), and Aure (2013). The comparative results show that the results of the present study match well with the previous studies. The stress values at the top of the slab are within 64% to 109% of the previous studies and the bottom stresses are within a range of 60% to 142%. The stress profiles through the thickness of the slabs are exactly similar to the previous studies, which validates the FE idealization of the present study.

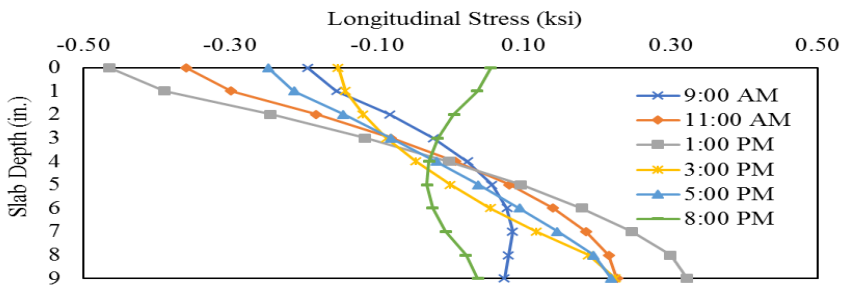

Fig. 3. Stress Comparison During Day Time with Nonlinear Temperature Profile

4.3. Comparison of Bending Stresses with Linear and Nonlinear Temperatures

The stress profiles with nonlinear temperature and linear temperature are analyzed and it is observed that the linear temperature profile underestimates the stresses at the top of the slab and overestimates the stresses at the bottom in almost all of the simulated scenarios. This confirms the findings from the previous research conducted by Aure (2013). Most of the bending stresses at the top surface of the slab has values of 5% to 85% higher than the stresses with linear temperature. The bottom bending stresses with nonlinear temperature are 7% to 106% lower than the linear cases.

5. Conclusion

Numerical modeling is conducted to evaluate the effects of nonlinear thermal gradient on the bending stress levels in concrete pavements. It is found that nonlinear temperature distribution results in higher stress levels, up to 34%, in the top fiber of pavement slab in comparison to the linear temperature profile. The stress levels in the bottom fiber of the pavement slab reduces with nonlinear temperature, compared to linear temperature. With these results, it is emphasized that nonlinear temperature gradient should be incorporated in numerical analysis of concrete pavements for accurate analysis and design of concrete pavements.

6. References

Westergaard, H. M. 1927. Analysis of stresses in concrete pavements due to variations of temperature. Proc. Hwy. Res. Board, 6, National Research Council, Washington, DC, 201-215.

Teller, L. W., and E. C. Sutherland. 1935. Observed Effects of Variation in Temperature and Moisture on the Size, Shape, and Stress Resistance of Concrete Pavement Slabs. Public Roads, 16(9), Bureau of Public Roads, Washington, DC, 169-197.

Bradbury, R. D. 1938. Reinforced Concrete Pavements, Wire Reinforcement Institute, Washington, DC.

Lang, F. C. 1941. Temperature and Moisture Variations in Concrete Pavements. Proc., Hwy. Res. Board, 21, 260-272.

Choubane, B., and M. Tia. 1992. Nonlinear Temperature Gradient Effect on Maximum Warping Stresses in Rigid Pavements. Transp. Res. Rec. 1370, Transportation Research Board, National Research Council, Washington, DC, 11-19.

Aure, T. W. 2013. Numerical Analysis of Cracking in Concrete Pavements Subjected to Wheel Load and Thermal Curling. PhD Dissertation.

High-Strength Grouting Materials for the Internal Prestressing System Using a Hollow-Type Tendon

Takafumi Mihara[1], Ryosuke Anami[2], Takashi Yamane[3], and Isamu Yoshitake[4*]

[1]: Kyokuto Kowa Corporation, Hiroshima, Japan; email: mihara@kkn.co.jp
[2]: Yamaguchi Univ., Ube, Yamaguchi, Japan; email: AnamiRyosuke@yucivil.onmicrosoft.com
[3]: Kyokuto Kowa Corporation, Hiroshima, Japan; email: tyamane0414@krc.biglobe.ne.jp
[4]: Yamaguchi Univ., Ube, Yamaguchi, Japan; email: yositake@yamaguchi-u.ac.jp

[*]: corresponding author

Keywords: internal anchorage; grout; hollow-type prestressing tendon; strengthening

Abstract: An internal strengthening system, which embeds a post-tensioned PC tendon into the wedge-shaped anchorage of an existing concrete member, has been developed and examined in our previous studies. The previous investigations examined the use of a rigid prestressing bar for the strengthening system. In practical applications of the system, adequate backspace is often required for installing the rigid bars into the existing concrete members. In case of narrow workspaces, the hollow corrugated pipe covered with wire-cables must be useful for installing. Furthermore, the inner pipe of the tendon can be used as a grouting pipe. The focus of the present study is to develop a suitable grouting material for the internal strengthening system using the hollow-type prestressing tendon. A horizontal grouting test was conducted by using 5 meters long corrugated pipes of 10 mm internal diameter. Segregation in some kinds of tested grouting materials was observed. Compressive strength was also examined using the grouting materials which passed for 5 m without material-segregation even at the end of the corrugated pipe. Some grouting materials achieved 90 MPa or higher, that required for the internal anchorage of the system. The paper presents suitable grouting materials for the hollow-type prestressing tendon based on these fundamental tests.

1. Introduction

Most existing concrete members in civil infrastructures gradually deteriorate by various factors caused from the surrounding environmental condition. The deteriorated concrete members require regular strengthening and/or upgrading. It is well known that post-tensioned prestressing system is a reliable method for strengthening concrete members. A new system using post-tensioned prestressing bar embedded in the wedge-shaped anchorage (see Fig.1) has been developed to strengthen internally existing concrete members (Mimoto et al. 2016a; Mimoto et al. 2016b). The previous study confirmed that the post-tensioned prestressing bar can be firmly anchored in the internal wedge hole filled with high-strength mortar. It should be noted that adequate backspace is often required for installing a rigid post-tensioning tendon into the existing concrete members. Such conventional prestressing bars may not be applicable in narrow workspace such as footing of bridge pier under the ground (see Fig.2). To increase applicability of the strengthening system, the present study focuses on a hollow-type prestressing tendon, which is flexible hollow corrugated pipe covered with prestressing wire cables. The flexible tendon can be installed into the concrete hole even at narrow work space. In addition, the

corrugated pipe can be used as a grouting pipe for the internal anchorage. The present study aims to developing a suitable grouting material for the hollow-type prestressing tendon.

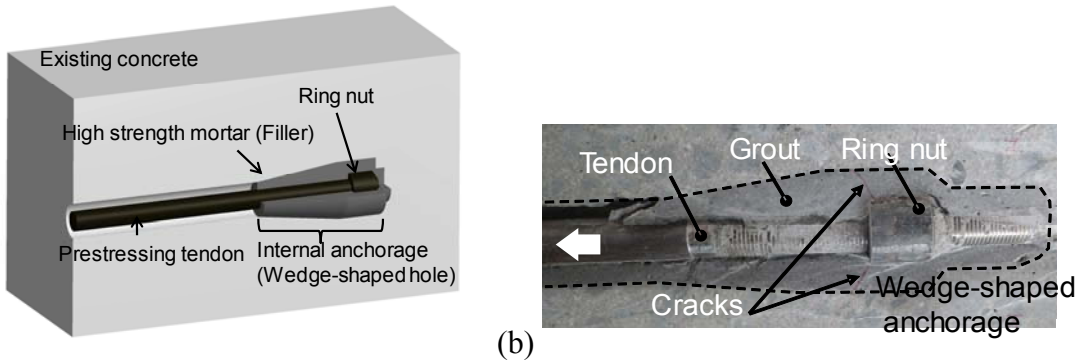

Fig. 1. Developed internal anchorage: (a) schematic of the anchorage; (b) cut section

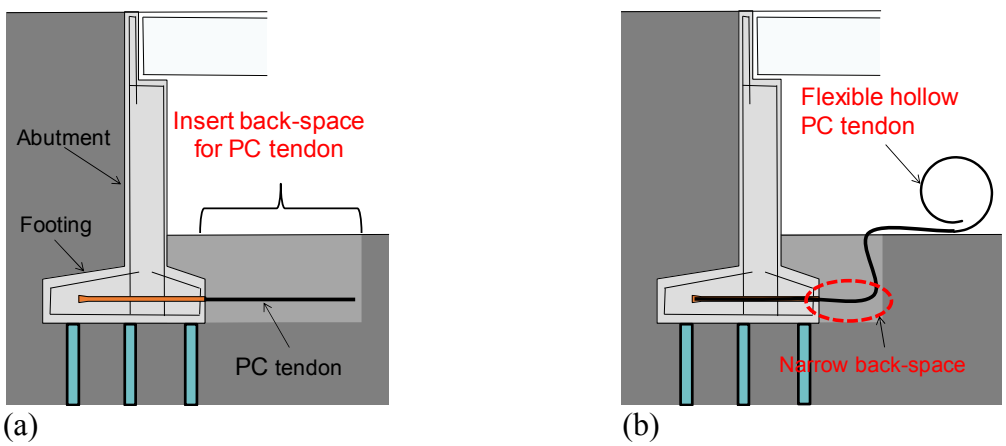

Fig. 2. Application for bridge footing: (a) rigid PC tendon; (b) flexible PC tendon

2. Materials

2.1. Hollow-type prestressing strand

Figure 3 presents the hollow-type prestressing strand used in the experimental study. The tendon consists of the corrugated steel-pipe of 10 mm inner diameter and 9 wires of 6.2 mm diameter. The dimensions of the corrugated pipe are described in Fig.4.

(a) (b)

Fig. 3. Flexible prestressing tendon: (a) hollow-type strand; (b) cross-sectional view

2.2. Grouting materials

Table 1 gives the mixture proportions of grouting materials. The study prepared high strength mortar and cement-paste as well as three pre-mixed materials. Mixture No.0 is the grouting material for the rigid prestressing tendon. The physical and chemical components of the pre-mixed materials can not be released herein because of the commercial contact with the manufactures.

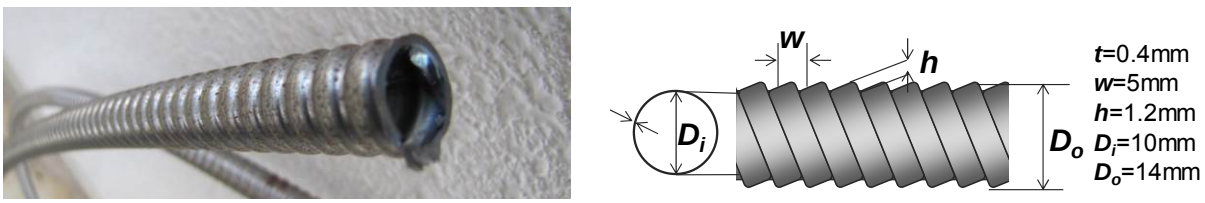

(a) (b)

Fig. 4. Corrugated pipe: (a) photo of the pipe; (b) dimensions

Table 1. Mixture proportions of grouting materials

No.	*w/cm*	Water (W)	Cement (C)	Filler (F)	Fine agg.	HRWRA[c]	SRA[d]
0	0.12	1.2 kg/mix	10 kg/mix[a]			0	0
1	0.20	2.0 kg/mix	10 kg/mix	N/A	N/A	*cm**1.4%	0
2	0.20	2.0 kg/mix	9.5 kg/mix	0.5 kg/mix[b]	N/A	*cm**1.5%	W*1.5%
3	0.20	2.0 kg/mix	9.0 kg/mix	1.0 kg/mix[b]	N/A	*cm**1.5%	W*1.5%
4	0.20	2.0 kg/mix	10 kg/mix[a]		N/A	0	0
5	0.26	2.6 kg/mix	10 kg/mix[a]		N/A	0	0

[a]pre-mix material; [b]silica-fume; [c]high-range water reducing agent; [d]shrinkage reducing agent

3. Grouting and filling tests

3.1. Test method

Figure 5 shows the grouting and filling tests. The grouting test for the corrugated pipe of 5 m long was conducted using an electric pump (Max: 2000 cm^3/min). The study obtained grouting material from the end of the corrugated pipe of 5 m long; and made three cylindrical specimens (50 mm diameter x 100 mm height) for each material. The required 7-days compressive strength (f'_{7d}) for the filling material of anchorage is 90 MPa or higher. To examine the adequate strength, the study conducted compressive strength test by using these specimens at the age of 7 days. In addition, the filling test was performed by using the wedge-shaped acrylic pipe and the hollow-type prestressing tendon. To observe the grouting condition into the anchorage, the filling material was grouted horizontal and 20 degree upward.

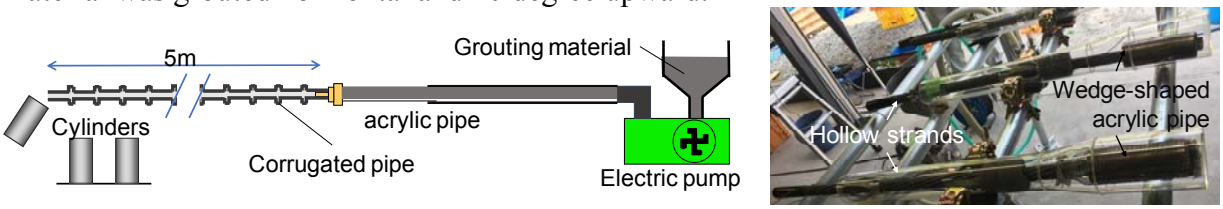

(a) (b)

Fig. 5. Test conditions: (a) grouting test; (b) filling test

3.2. Test results

Table 2 presents the test results. All grouting materials tested in the study achieved the compressive strength of 90 MPa or higher that is required for the wedge-shaped anchorage. The conventional high-strength mortar (No.0) and the plain cement paste (No.1) hardly passed to the corrugated pipe of 5m long because of material-segregation in the pipe. The cement pastes incorporating silica-fume (No.2, 3) completely passed to the pipe of 5m long, however, material segregation at the pipe-end was observed in the grouting test of No.3. It should be noted that the grouting materials (No.2, 4, 5) passed for 5m corrugated pipe without segregation achieved the required strength. The filling test using the hollow-type prestressing tendon confirmed the full-filling condition even in the horizontal wedge-shaped anchorage. Based on the fundamental tests, it can be concluded that the filling materials (No.2, 4, 5) are useful for the hollow-type prestressing tendon of horizontal grouting.

Table 2. Test results

No.	Flow[a] (mm)	5m long grouting	Segregation	f'_{7d} (MPa)	Filling condition
0	189	Incomplete	N/A	109.6 [b] / --	N/A
1	>300	Incomplete	Yes	104.5 [b] / --	N/A
2	244	Complete	No	118.7 [b] / 132.7 [c]	Full
3	193	Complete	Yes	90.1 [b] / 45.2 [c]	N/A
4	265	Complete	No	113.0 [b] / 103.0 [c]	Full
5	163	Complete	No	103.6 [b] / 98.4 [c]	Full

[a] table flow-test; [b] the materials obtained from the mixer; [c] the grouted materials for 5m long.

4. Conclusions

The study examined the grouting material for the hollow-type prestressing tendon. The conclusions of the experimental study are summarized below:

(1) The conventional high-strength mortar is not appropriate for the grouting material for the hollow-type prestressing tendon.
(2) Even if the grouting material can pass into the corrugated pipe, grouting condition without material segregation should be confirmed because the actual filling condition in the internal anchorage is hardly examined.
(3) The grouting and strength tests confirmed that the filling materials (No.2, 4, 5) are useful for the hollow-type prestressing tendon of horizontal grouting.

References

Mimoto, T., Sakaki, T., Mihara, T. and Yoshitake, I. 2016a, Strengthening system using post-tension tendon with an internal anchorage of concrete members, Engineering Structures, 124, 29-35.

Mimoto, T., Yoshitake, I., Sakaki, T. and Mihara, T., 2016b, Full scale flexural test of jointed concrete members strengthened with post-tension tendons with internal anchorage, Engineering Structures, 128, 139-148.

Experimental Study on Autogenous Healing Property by Further Hydration of Cementitious Materials Incorporating Inorganic Binder

Byoungsun Park[1*], Bong Chun Lee[2], Sang-Hwa Jung[3], Young Cheol Choi[4], Sung-Won Yoo[5]

[1]: Korea Conformity Laboratories, Seoul, Korea; pbs0927@kcl.re.kr
[2]: Korea Conformity Laboratories, Seoul, Korea; leebc@kcl.re.kr
[3]: Korea Conformity Laboratories, Seoul, Korea; jsh2593@kcl.re.kr
[4]: Gachon University, Seongnam, Korea; zerofe@gachon.ac.kr
[5]: Gachon University, Seongnam, Korea; imysw@gachon.ac.kr

[*]: corresponding author

Keywords: Autogenous Healing; Cementitious Materials; Further Hydration; Isothermal Calorimetry; Scanning Electron Microscopy

Abstract:
In this study, the autogenous healing properties of the cementitious materials by further hydration were investigated. In addition to ordinary Portland cement (OPC), fly ash (FA), ground granulated blast-furnace slag (GGBFS), silica fume (SF) and crystalline admixture (CA) were used as inorganic binders. The hydration heat was measured by isothermal calorimetry in order to analyze the autogenous healing potential by further hydration of unreacted binder according to age and kind of inorganic binder. It was confirmed that the cumulative heat production by further hydration changes depending on the type of inorganic binder, and the cumulative heat production of specimen incorporating GGBFS was the highest. Also, it was confirmed that the cumulative heat production decreased as the age increased. Results of water flow test showed that the autogenous healing performance was improved when mixed with other binders compared to OPC. From the results of SEM analysis, it was confirmed that calcite and amorphous were the main compounds of self-healing materials.

1. Introduction

In general, concrete has a property that can heal cracks autogenously. This is called autogenous healing (Reinhardt, 2003; Granger, 2007; Yang, 2009). The autogenous healing consists of two mechanisms. The first is the further hydration of the unreacted binder in cracks and the second is the precipitation of calcite by the reaction of Ca^{2+} and CO_3^{2-}. The autogenous healing performance of cementitious materials depends on the type of binder and the age of concrete, because the amount of unreacted binder in the cracks varies (Sisomphon, 2012). When the unreacted binder is reduced, the autogenous healing performance due to further hydration decreases (Tittelboom, 2012). In this study, we conducted a study to evaluate the self-healing potential of unreacted cement clinker in cement paste by further hydration. Powder samples containing unreacted binder were prepared by pulverizing the hardened paste and cumulative heat production by further hydration was measured using isothermal calorimetry. Water flow test was performed to evaluate the self-healing performance and SEM also was performed to analyze the chemical composition of the self-healing material in the crack.

2. Experimental Program

2.1. Materials

In this study, ordinary Portland cement (OPC), fly ash (FA), ground granulated blast-furnace slag (GGBFS), silica fume (SF) and crystalline admixture (CA) were used as inorganic binders. Table 1 shows chemical composition of raw materials measured by X-ray fluorescence (XRF). Density of OPC, GGBFS, FA was investigated as 2,100kg/m^3, 3,120kg/m^3, 2,950kg/m^3, respectively.

Table 1. Chemical compositions of the raw materials

	OPC	GGBFS	FA	SF
SiO_2	18.55	29.13	53.73	74.91
Al_2O_3	4.41	11.82	20.05	0.26
Fe_2O_3	3.23	0.44	5.57	0.97
CaO	62.13	42.51	3.36	0.19
MgO	2.04	2.43	0.91	0.86
K_2O	1.22	0.52	1.45	0.91
Na_2O	0.26	0.2	0.96	0.73
TiO_2	0.27	0.59	0.98	-
MnO	0.2	0.23	0.07	0.13
P_2O_5	0.13	-	0.26	0.03
SO_3	3.03	3.34	0.45	0.20
SrO	-	0.05	0.10	0.01

Table 2 shows mixture proportions used in this study. The mixture proportions were determined to evaluate the effect of GGBFS and FA substitution rate and the type of SCMs on self-healing potential. In this experiment, a paste specimen with a W/B ratio of 0.4 was used.

Table 2. Mixture proportions

	OPC	FA	GGBFS	SF	CA
Plain	100				
Mix 1	85	15			
Mix 2	70	30			
Mix 3	67	30			3
Mix 4	70		30		
Mix 5	40		60		
Mix 6	90			10	

2.2. Test Methods

In this study, specific heat flow was measured using isothermal calorimetry to evaluate the self-healing potential of further hydration of unreacted binder and penetrated moisture in the crack of paste (Tittelboom, 2012). The paste specimens were fabricated to have a W/B ratio of 0.40 and a size of 10 mm×10 mm×10 mm according to the mixture proportions shown in Table 2. In order to simulate further hydration of unreacted binder, paste specimens were prepared and pulverized to prepare samples. The crushed powder was sieved with a sieve of 200 μm size to prepare a sample to be used for compounding. After mixing 10g of the powder and 4g of tap water, about

5g of paste was put into the ample, and the mass was measured and the specific heat flow by further hydration was measured during 72 hours. The water permeability test was performed to compare the results of specific heat flow measurement with further hydration. The water permeability test was performed with reference to the experimental method of Park et al. (Park, 2018). In the experiment, 100×50 mm circular paste specimens were used, which were fabricated by mixture proportions shown in Table 2. Cracks were induced by the method of measuring the tensile strength and were adjusted to a crack width of 0.25 mm using a copper wire.

3. Results and Discussion

3.1. Isothermal calorimetry

Fig. 1 shows cumulative Heat of further hydration measure by isothermal calorimetry. Experimental results show that the cumulative heat increases with time. Cumulative heat of Plain was the highest and cumulative heat of Mix 1 and Mix 2 containing FA was decreased. Mix 3 using a crystalline admixture showed an increase in cumulative heat. The cumulative heat of Mix 5 was higher than that of Mix 4. This result shows that cumulative heat was increased slightly when the amount of GGBFS was increased.

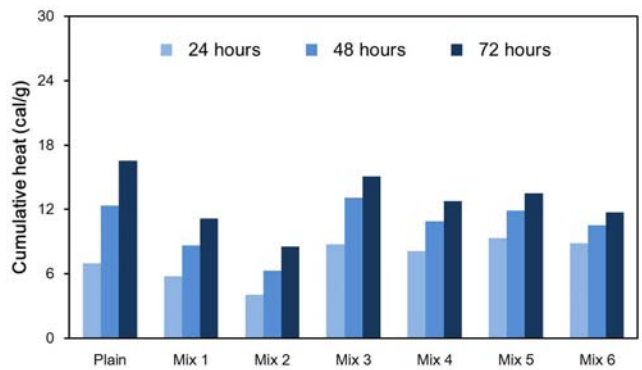

Fig. 1. Cumulative Heat of further hydration measure by isothermal calorimetry

3.2. Water permeability test

Fig. 2 shows water flow reduction ratio during 14 days. In the graph, the water flow reduction ratio of Mix 3 using the crystalline admixture was the largest. Mix 2 and Mix 3 showed no significant difference in OPC, but using crystalline admixture improved self-healing performance. This is because the further hydration on the crack surface was promoted by the crystalline admixture. Mix 4 and Mix 5 containing GGBFS showed excellent self-healing performance and water flow reduction ratio was higher with increasing GGBFS content. The water flow reduction ratio of OPC was the lowest, which was found to be different from the results of isothermal calorimetry test. It was found that the crack self-healing was influenced not only by the amount of unreacted clinker but also by the kind of self-healing material produced.

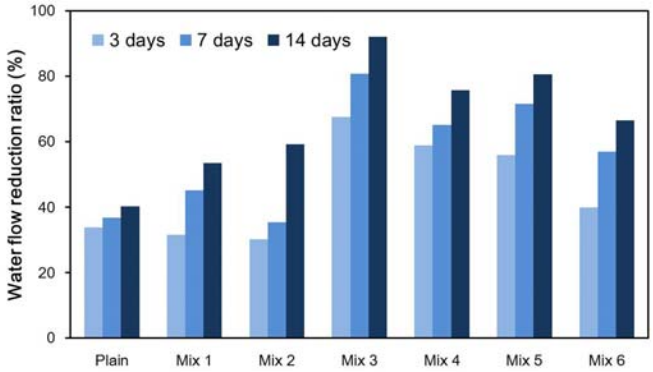

Fig. 2. Water flow reduction ratio

4. Conclusions

In this study, a study was conducted to evaluate the self-healing potential depending on the kind of inorganic binder. Experimental results using the 7th day specimen showed that the cumulative heat of Plain was the highest. Cumulative heat was the lowest in the case of FA containing specimen, but cumulative heat increased when incorporating crystalline admixture. In case of GGBFS, cumulative heat was increased compared to FA, but it was decreased compared to Plain. Water flow test showed that Mix 3 with crystalline admixture had the highest self-healing performance and Plain had the lowest self-healing performance. As a result, it was confirmed that not only the amount of unreacted clinker but also the kind of the self-healing product precipitated in crack surface affected the crack self-healing.

5. Acknowledgement

This research was supported by a grant (19SCIP-B103706-05) from Construction Technology Research Program funded by Ministry of Land, Infrastructure and Transport of Korean government. And this work was also supported by the Korea Institute of Energy Technology Evaluation and Planning (KETEP) and the Ministry of Trade, Industry & Energy(MOTIE) of the Republic of Korea (No. 20161120200190).

6. Reference

Reinhardt, H.W. and Jooss, M. 2003. Permeability and self-healing of cracked concrete as a function of temperature and crack width, Cement and Concrete Research, 33, 981–985.

Granger, S., Loukili, A., Pijaudier-Cabot, G. and Chanvillard, G. 2007. Experimental characterization of the self-healing of cracks in an ultra-high performance cementitious material: mechanical tests and acoustic emission analysis, Cement and Concrete Research, 37, 519–527.

Yang, Y., Lepech, M.D., Yang, E.H. and Li, V.C. 2009. Autogenous healing of engineered cementitious composites under wet–dry cycles, Cement and Concrete Research, 39, 382–390.

Sisomphon, K., Copuroglu, O. and Koenders, E.A.B. 2012. Self-healing of surface cracks in mortars with expansive additive and crystalline additive, Cement and Concrete Composites, 34, 566-574.

Tittelboom, K.V., Gruyaert, E., Rahier, H. and Belie, N.D. 2012. Influence of mix composition on the extent of autogenous crack healing by continued hydration or calcium carbonate formation, Construction and Building Materials, 37, 349-359.

Park, B. and Choi, Y.C. 2018. Quantitative evaluation of crack self-healing in cement-based materials by absorption test, Construction and Building Materials, 184, 1-10.

Wind and Vibration

Time-Varying Wind Load Estimation of Stayed Cables Based on Minimum- Variance Unbiased Estimation

Huili Xue[1], Yin Luo[2], and Hongjun Liu[3*]

[1] Harbin Institute of Technology, Shenzhen, China; email: xuehuili0413@126.com
[2] Harbin Institute of Technology, Shenzhen, China; email: yin_luo@outlook.com
[3] Harbin Institute of Technology, Shenzhen, China; email: liuhongjun@hit.edu.cn

[*]: corresponding author

Keywords: stayed cable; wind load; minimum-variance unbiased estimation

Abstract: Stayed cable is one of the main components in cable-stayed bridge. And it is generally large span, light weight, small damping and low natural vibration frequency. Wind load is one of the main lateral loads for stayed cables. Therefore, it is important to monitoring wind load and wind induced effects on stayed cables. However, with the limitation of the measurement equipment and measurement methods, real-time measurement of wind load on the cables is difficult to achieve. In comparison, acceleration responses are easier and more accurate than that of wind load. In this study, a minimum-variance unbiased estimation method is developed to identify time-varying wind load of stayed-cables from measured acceleration responses. The fluctuating wind speed process is simulated by the auto-regressive model method. The formula derivation of recursive identification equations are obtained in state space. The recursive identification approach includes three parts: time update, estimation of wind load on the stayed cable, and measurement update. A 93 m cable is chosen as an example to validate the feasibility and accuracy of the proposed method. Numerical simulation results indicate that the proposed algorithm can be used to estimated wind load of stayed cables from wind induced acceleration responses accurately and effectively.

1. Introduction

Stayed cable is sensitivity to the wind load because it has large span, light weight, small damping and low natural vibration frequency. Wind load becomes one of the main lateral loads for stayed cables. However, with the limitation of the measurement equipment and measurement methods, real-time measurement of wind load on the structures is difficult to achieve. In comparison, acceleration responses measurement are easier and more accurate than that of wind load. Therefore, it is necessary to establish a method for identification of wind load on stayed cables from measured acceleration responses.

Chen and Li estimated the wind load on the twelve-story structure based on a general statistical average algorithm (Chen and Jie, 2001). Kang and Lo proposed the discretized governing equation to estimate the wind load on an elevated tower (Kang and Lo, 2002). Law et al. identified the wind load on a 50 m guyed mast based on the regularization method (Law et al., 2005). Hwang et al. estimated the modal wind load based on Kalman filter method with limited measured responses (Hwang et al., 2011). Zhi et al. estimate the wind load on the super-tall building based on the Kalman filter method (Zhi et al., 2017). Gillijns and Moor addressed the

minimum variance unbiased estimation method for estimating the unknown input (Gillijns and Moor, 2007). In this paper, a time-varying wind load identification method is developed based on the minimum variance unbiased estimation algorithm. The feasibility of the proposed method is validated through numerical analysis of a 93 m stayed cable subject to wind load.

2. Proposed algorithm

The second-order differential equation of motion of an n degrees of freedom structure can be given by

$$\boldsymbol{M}\ddot{\boldsymbol{x}}(t)+\boldsymbol{C}\dot{\boldsymbol{x}}(t)+\boldsymbol{K}\boldsymbol{x}(t)=\boldsymbol{F}(t) \tag{1}$$

where $\boldsymbol{M}$, $\boldsymbol{C}$, $\boldsymbol{K}$ are $n\times n$ mass, damping, and stiffness matrices of the structure, respectively. $\ddot{\boldsymbol{x}}(t)$, $\dot{\boldsymbol{x}}(t)$, and $\boldsymbol{x}(t)$ are $n\times 1$ structural acceleration, velocity, and displacement responses vectors, respectively. $\boldsymbol{F}(t)$ is the $n\times 1$ wind load vector. The state vector consists of structural displacement and velocity can be given by:

$$\boldsymbol{Z}(t)=\left[\boldsymbol{x}^{\mathrm{T}}(t)\ \ \dot{\boldsymbol{x}}^{\mathrm{T}}(t)\right]^{\mathrm{T}} \tag{2}$$

Then Eq. 1 can be expressed in state space at time $t=(k+1)\Delta t$ as follows:

$$\boldsymbol{Z}_{k+1}=\boldsymbol{A}_k\boldsymbol{Z}_k+\boldsymbol{B}_k\boldsymbol{F} \tag{3}$$

in which $\boldsymbol{A}_k=(\boldsymbol{I}_{2n\times 2n}+\Delta t[\begin{matrix}\boldsymbol{0}_{n\times n} & \boldsymbol{I}_{n\times n}\\ -\boldsymbol{M}^{-1}\boldsymbol{K} & -\boldsymbol{M}^{-1}\boldsymbol{C}\end{matrix}])$, $\boldsymbol{B}_k=\Delta t\begin{bmatrix}\boldsymbol{0}_{n\times n}\\ -\boldsymbol{M}^{-1}\end{bmatrix}$.

The measurement responses are structural acceleration responses and the measurement equation at $t=k\Delta t$ can be given as:

$$\boldsymbol{y}_k=\boldsymbol{D}_k\boldsymbol{Z}_k+\boldsymbol{G}_k\boldsymbol{F}_k+\boldsymbol{v}_k \tag{4}$$

where $\boldsymbol{D}_k=\left[-\boldsymbol{M}^{-1}\boldsymbol{K}\quad -\boldsymbol{M}^{-1}\boldsymbol{C}\right]$, $\boldsymbol{G}_k=\left[-\boldsymbol{M}^{-1}\right]$. $\boldsymbol{v}_k$ is a $n\times 1$ Gaussian measurement noise vector with zeros mean and covariance matrix, where $\boldsymbol{R}_k\delta_k=E[\boldsymbol{v}_k\boldsymbol{v}_k^T]$ is the Kroneker delta.

Based on the minimum variance unbiased estimation method, wind load and unmeasured structural responses and be estimated as follows:

Time update

$$\hat{\boldsymbol{Z}}_{k|k-1}=\boldsymbol{A}_{k-1}\hat{\boldsymbol{Z}}_{k-1|k-1}+\boldsymbol{B}_{k-1}\hat{\boldsymbol{F}}_{k-1} \tag{5}$$

$$\boldsymbol{P}^{\boldsymbol{Z}}_{k|k-1}=\left[\boldsymbol{A}_{k-1}\quad \boldsymbol{B}_{k-1}\right]\begin{bmatrix}\boldsymbol{P}^{\boldsymbol{Z}}_{k-1|k-1} & \boldsymbol{P}^{\boldsymbol{ZF}}_{k-1|k-1}\\ \boldsymbol{P}^{\boldsymbol{FZ}}_{k-1|k-1} & \boldsymbol{P}^{\boldsymbol{F}}_{k-1|k-1}\end{bmatrix}\begin{bmatrix}\boldsymbol{A}^T_{k-1}\\ \boldsymbol{B}^T_{k-1}\end{bmatrix} \tag{6}$$

Estimation of unknown wind load

$$\boldsymbol{P}_k^{\boldsymbol{e}} = \boldsymbol{D}_k \boldsymbol{P}_{k|k-1}^{\boldsymbol{Z}} \boldsymbol{D}_k^T + \boldsymbol{R}_k \tag{7}$$

$$\boldsymbol{M}_k^* = \left[\boldsymbol{G}_k^T (\boldsymbol{P}_k^e)^{-1} \boldsymbol{G}_k\right]^{-1} \boldsymbol{G}_k^T (\boldsymbol{P}_k^e)^{-1} \tag{8}$$

$$\hat{\boldsymbol{F}}_k = \boldsymbol{M}_k (\boldsymbol{y}_k - \boldsymbol{D}_k \hat{\boldsymbol{Z}}_{k|k\text{-}1}) \tag{9}$$

$$\boldsymbol{P}_k^{\boldsymbol{F}^*} = \boldsymbol{M}_k^* \boldsymbol{P}_k^{\boldsymbol{e}} (\boldsymbol{M}_k^*)^T = \left[\boldsymbol{G}_k^T (\boldsymbol{P}_k^{\boldsymbol{e}})^{-1} \boldsymbol{G}_k\right]^{-1} \tag{10}$$

Measurement update

$$\boldsymbol{K}_k^* = \boldsymbol{P}_{k|k-1}^{\boldsymbol{Z}} \boldsymbol{D}_k^T (\boldsymbol{P}_k^{\boldsymbol{e}})^{-1} \tag{11}$$

$$\hat{\boldsymbol{Z}}_{k|k}^* = \hat{\boldsymbol{Z}}_{k|k-1} + \boldsymbol{K}_k^* [\boldsymbol{y}_k - \boldsymbol{D}_k \hat{\boldsymbol{Z}}_{k|k\text{-}1} - \boldsymbol{G}_k \hat{\boldsymbol{F}}_k^*] \tag{12}$$

$$\boldsymbol{P}_{k|k}^{\boldsymbol{Z}} = \boldsymbol{P}_{k|k-1}^{\boldsymbol{Z}} - \boldsymbol{K}_k^* (\boldsymbol{P}_k^{\boldsymbol{e}} - \boldsymbol{G}_k \boldsymbol{P}_k^{\boldsymbol{F}} \boldsymbol{G}_k^T)(\boldsymbol{K}_k^*)^T \tag{13}$$

$$\boldsymbol{P}_k^{\boldsymbol{ZF}} = (\boldsymbol{P}_k^{\boldsymbol{FZ}})^T = -\boldsymbol{P}_{k|k-1}^{\boldsymbol{Z}} \boldsymbol{D}_k^T (\boldsymbol{M}_k)^T \tag{14}$$

3. Numerical simulation

A 93m stayed cable is chosen as an example to check the effectiveness of the algorithm. The cable is assumed to be constant cross section and with a damping vector of 20 kN/m/s installed transversely at its midlength. The axial stiffness (EA) is assumed to be 1458408 kN and the flexural stiffness (EI) is 1305.8 kN-m^2. The mass is assumed to be 170.622 t/m^3. The tension force is 5017 kN. The mass, stiffness, and damping matrices are calculated according to Armin(Mehrabi and Tabatabai, 1998). In this numerical simulation, the fluctuating wind speed is simulated according to auto-regressive model method and the spectral density used to simulate the fluctuating wind speed is Davenport spectrum. The vertical wind profile is taken as the power law and the exponent α is 0.12. According to Chinese National Load Code the reference height is set to be 10 m and the mean wind speed at the reference height is 38.9 m/s. The simulated fluctuating wind speed on the thirtieth and sixtieth node are shown in Fig. 1. The comparison of the power spectral density of the simulated fluctuating wind speed on the thirtieth and sixtieth floor are shown in Fig. 2. It can be seen that the simulated power spectrum density curve matches very well with Davenport spectrum. The density of air ρ is assumed to be 1.23 kg/m^3. The drag coefficient C_H of the structure is set to be 0.7. The equivalent diameter D of the stayed cable is 0.2m. The angle of installation of the stayed cable β is 21.78^0. Then, the simulated wind load can be calculated as

$$w(z,t) = \frac{1}{2}\rho v^2(z,t) C_H D \sin^2\beta \tag{15}$$

The measured structural acceleration responses are numerical calculated based on Newmark-β method and superimposed with 2% RMS white noise. The initial value of the state vector is $[0\ 0\ \cdots\ 0\ 0]_{99\times1}$ and the initial error covariance of the state vector is set to be $I_{99\times99}$. The covariance of measurement noise is $I_{99\times99}$. The identified wind load on the thirtieth and sixtieth

node are shown in Fig. 3. The identified wind load are very close to the real value. The proposed method can estimate the time-varying wind load on the stayed cables accurately.

4. Conclusion

An efficient method for identification of time-varying wind load on the stayed cable has been presented in this paper. The feasibility and accuracy of the proposed approach have been assessed through numerical simulation of a 93m cable. Comparison studies show that the identified results are very close to the real values. Results indicate that the proposed algorithm can be an effective approach for identifying wind load on stayed cables.

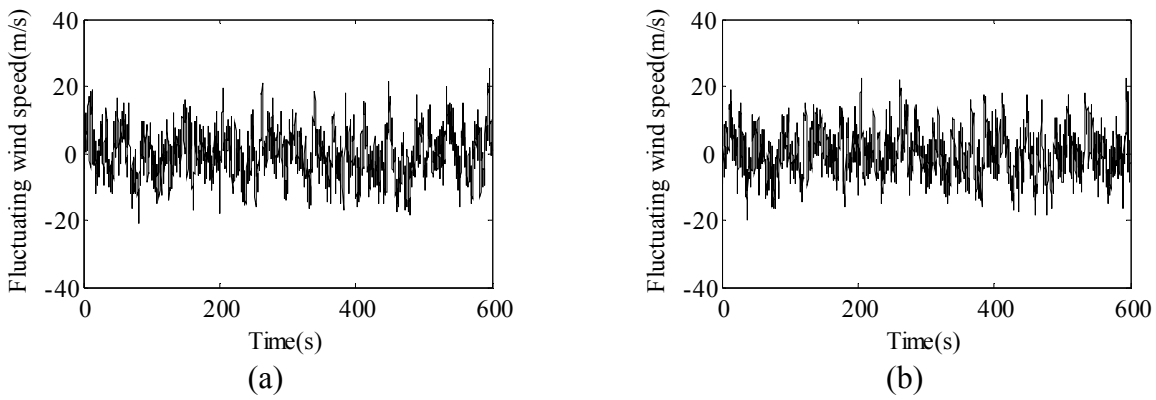

Fig. 1. Simulated fluctuating wind speed: (a) on the thirtieth node; (b) on the sixtieth node

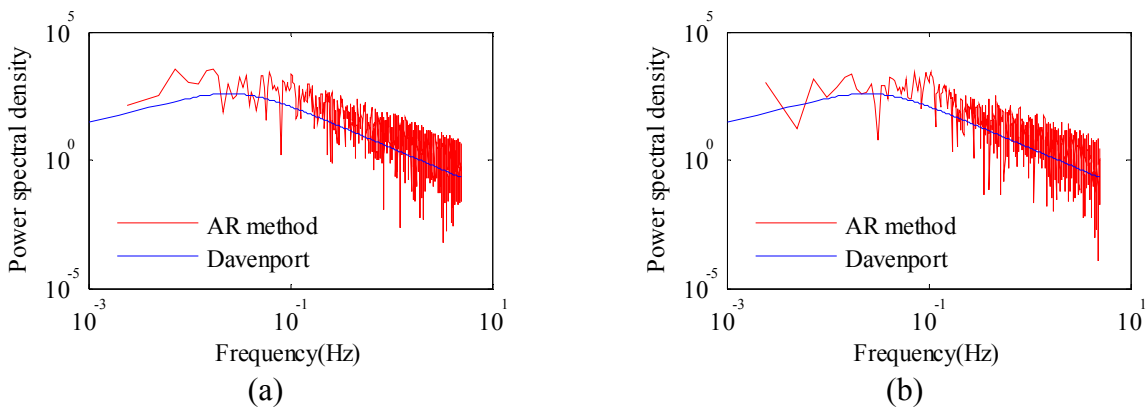

Fig. 2. Comparison of power spectrum density of fluctuating wind speed: (a) on the thirtieth node; (b) on the sixtieth node

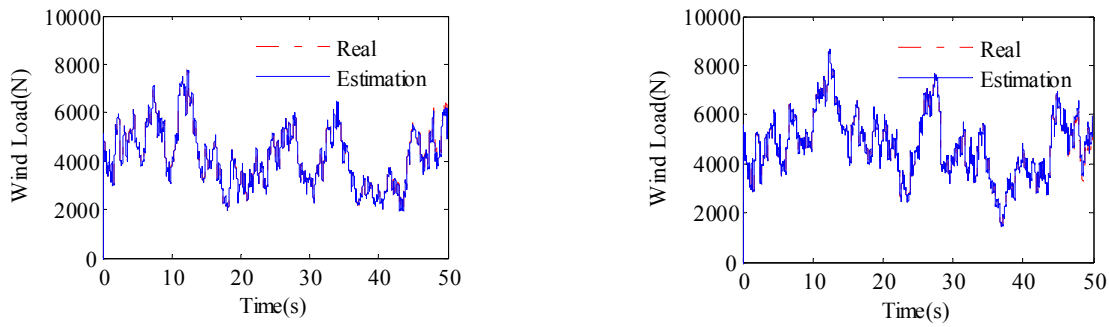

Fig. 3. Comparison of time-varying wind load between exact wind load and estimated values: (a) on the thirtieth node; (b) on the sixtieth node

5. Acknowledgments
This work is supported by the Shenzhen Knowledge Innovation Programme (Grant Nos. JCYJ20170413105418298, JCYJ20170811153857358).

6. References

Chen, J. and Li, J. 2001. Study on wind load inverse of tall building, Chinese Quarterly of Mechanics.

Gillijns, S. and Moor, B. D. 2007. Technical communique: Unbiased minimum-variance input and state estimation for linear discrete-time systems with direct feedthrough, Automatica, 43(5), 934-937.

Hawng, J. S., Kareem, A., and Kim, H. 2011. Wind load identification using wind tunnel test data by inverse analysis, Journal of Wind Engineering & Industrial Aerodynamics, 99(1), 18-26.

Kang, C. C. and Lo, C. Y. 2002. An inverse vibration analysis of a tower subjected to wind drags on a shaking ground, Applied Mathematical Modelling, 26(4), 517-528.

Law, S. S., Bu, J. Q., and Zhu, X. Q. 2005. Time-varying wind load identification from structural responses, Engineering Structures, 27(10), 1586-1598.

Mehrabi, A. B. and Tabatabai, H. 1998. Unified Finite Difference Formulation for Free Vibration of Cables, Journal of Structural Engineering, 124(11), 1313-1322.

Zhi, L. H., Fang, M. X., and Li, Q. S. 2017. Estimation of wind loads on a tall building by an inverse method, Structural Control & Health Monitoring, 24(4).

Free Vibration and Dynamic Behavior of Stay Cable with Shear Thickening Fluid Damper

Yi Liu[1], Kun Lin[2*], Annan Zhou[3*], and Chenchao Huang[4]

[1] School of Civil and Environmental Engineering, Harbin Institute of Technology, Shenzhen 518055, China; email: liuyi_hitsz@outlook.com
[2] School of Civil and Environmental Engineering, Harbin Institute of Technology, Shenzhen 518055, China; email: linkun@hit.edu.cn
[3] Civil and Infrastructure Engineering, School of Engineering, RMIT University, Melbourne, VIC 3001, Australia; email: annan.zhou@rmit.edu.au
[4] School of Civil and Environmental Engineering, Harbin Institute of Technology, Shenzhen 518055, China; email: huang_cc_hitsz@qq.com

[*]: corresponding author

Keywords: STF damper; cyclic test; dynamic performance; loading frequency; cable vibration control

Abstract: Stay cable is a vital component of cable-stayed bridges, which features large span, high flexibility and low damping. The vibration control of stay cables has been studied to ensure the normal service condition of cable-stayed bridges. In this paper, a novel self-adaptive full-scale damper with shear thickening fluid (STF) was designed and applied to the mitigation of undesired cable vibration. The STFD was manufactured according to the traditional viscous double-ended piston damper structure. A series of experiments were designed to study the dynamic properties of STFD. In the tests, loading was a sinusoidal wave at different frequencies but a constant amplitude. It was observed that the output damping force of STFD significantly increased as the velocity increased. A general differential equation for the cable with a STFD was developed to solve the eigenvalue problem of the system by the finite difference method. Then, the modal frequencies and damping ratios of the stay cable can be calculated. The effectiveness of STFD is validated by a comparison with viscous damper (VD).

1. Introduction

Shear thickening fluid (STF) is non-Newtonian fluid and the rheological characters of which change abruptly when the fluid encounters impact loads (Barnes, 1989). The STF has been utilized to generate novel structure for impact protection or vibration mitigation, such as STF fiber cloths (Pinto et al. 2016; Lu et al. 2015), STF rotational brakes (Tian et al. 2017) and STF dampers (STFDs) (Zhang et al. 2008; Wei et al. 2018). Many studies have been conducted to evaluate the dynamic performance of the STFs and STFDs. Fischer (Fischer et al. 2007; Fischer et al. 2006) integrated STFs into composite structures in order to tune part stiffness and damping capacity under dynamic deformation. Zhou (Zhou et al. 2015) fabricated a novel prototype STFD and described its nonlinear behavior in a shear-thickening and solid-like state with a dynamic model. Yeh (Yeh et al. 2014) studied the variation of the STFDs′ damping coefficient and the

energy dissipation with various amplitudes and vibration frequencies. However, there is no existing research works has been related to application of STFD for cable vibration control.

In this study, a nanoparticle-based STF samples were fabricated and studied first. Then, the dynamic properties of the STFD employing nanoparticle-based STF were studied in laboratory under different loading frequencies with constant amplitude of 20mm. Then, the cable-STFD numerical model was constructed and studied. The effectiveness of STFD was validated by comparing with the vibration control of a viscous damper (VD) attached to the same cable.

2. The STFD experiment and results

STF samples with a mass fraction of 20% were used for rheological tests (Lin et al. 2019). An STFD was designed and manufactured for the proposed experimental study. The STFD consists of double-ended piston rod and an annular gap. Fig. 1 show the prototype and a schematic of the designed STFD in this research. Fig. 2 shows the schematic configuration and a photograph of the experimental setup for the cyclic testing. Numerous cyclic tests were conducted to investigate the behaviour of the STFD under various sinusoidal loading conditions with a constant amplitude of 20 mm. Eight different loading frequencies (0.01 Hz, 0.1 Hz, 0.5 Hz, 1.0 Hz, 1.5 Hz, 2.0 Hz, 2.5 Hz, 3.0 Hz) were imposed. The damping forces of the STFD under various loading frequencies is listed in Table 1. The relationship between STFD force (kN) and loading frequencies (Hz) can be fitted by using Eq. 1.

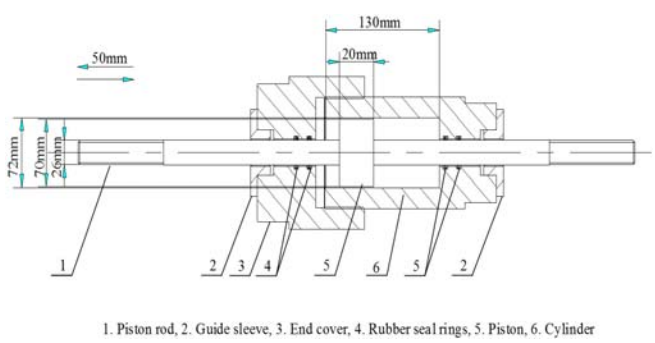

Fig. 1. Dimensions of the STFD

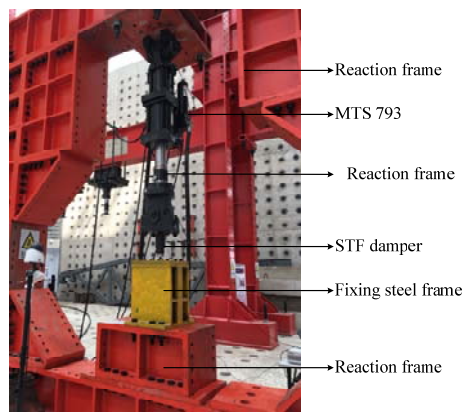

Fig. 2. Schematic photograph of experiment setup

Table 1. STF damper force under different loading frequencies.

Freq. (Hz)	0.01	0.1	0.5	1.0	1.5	2.0	2.5	3.0
Force (kN)	3.46	5.41	9.73	12.66	16.63	17.04	16.99	16.96

$$\mathrm{F}(f) = 3.46 + 12.38 \cdot f - 2.69 \cdot f^2 \tag{1}$$

3. Comparison of VD and STFD

Fig. 3 shows a schematic drawing of a cable with length L, tension T and mass per unit length m. An STFD is installed in the transverse direction at a close distance from the left end of the cable. The distance from the damper to the left end is $x_1 = L\text{-}x_2$. The corresponding governing differential Eq. 2 is:

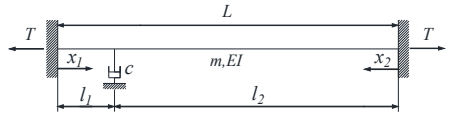

Fig. 3. A model of a taut cable with an attached STFD

$$\frac{\partial^2}{\partial x^2}\left(EI\frac{\partial^2 v}{\partial x^2}H\right)-H\frac{\partial^2 v}{\partial x^2}-h\frac{d^2 y}{\partial x^2}+k'v+c'\frac{\partial v}{\partial t}+m\frac{\partial^2 v}{\partial t^2}=0 \tag{2}$$

A practical stay cable was chosen selected herein this section to investigate the performance of cable-STFD system under free vibration conditions. The parameters of this cable are shown as following (Mehrabi and Tabatabai, 1998): the length of cable L = 93 m; axial stiffness of cable EA = 1458408 kN; flexural stiffness EI = 1305.8 kNm^2; cable mass per unit length m = 113.748 kg/m; applied tensile force along cable T = 5017 kN. The damper location is proposed at 0.05 L from the left end of the cable. To evaluate the effectiveness of the STFD in more actual conditions, the dynamic response of the cable with a STFD was calculated under free vibration condition. Cable with a traditional VD was studied for comparation. The max damping forces of both dampers were set as equal for conveniently comparing the effectiveness.

Fig. 4 shows the free vibration responses of the cable induced by an initial displacement. The vibration of the cable with STFD decays more sharply than the cable with VD. The vibration of the cable with STFD is eliminated in 50s, which is only 1/3 of the free vibration duration of the cable with VD. The cable-VD system was exponential linear decay and the cable-STFD system was linear decay. Fig. 5 shows the STFD produced a combination of friction and viscous damping more obviously. At the beginning of the decay (cycle 2), the damping force kept a high value in the whole cycle, which indicated that the performance of STFD was similar to friction dampers. The shape of the hysteresis loop was rectangle. At cycle 26, the max damping force in the whole cycle did not change but the duration decreased, which indicated that the VD character gradually exhibited, and the friction damper character faded. The shape of the hysteresis loop turned to be ellipse. At cycle 44, the force-displacement character of STFD was almost like that of VD and the height of the hysteresis loop turned to be lower. The force-displacement Fig. of VD kept ellipse in the whole decay.

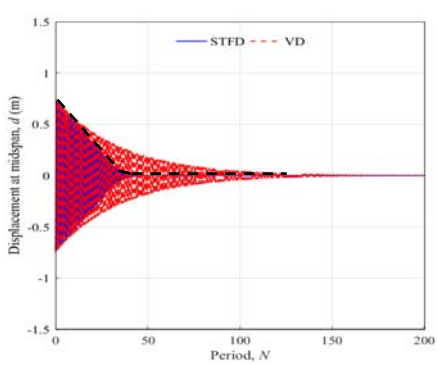

Fig. 4. Displacement time history at mid-length of cable with STFD and VD

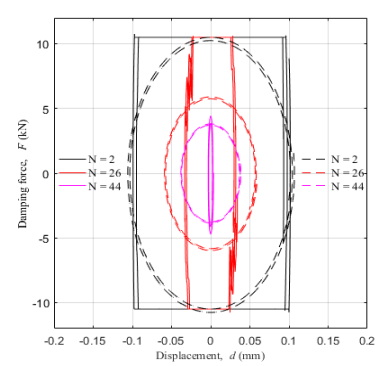

Fig. 5. Damping force and displacement at STFD and VD

4. Conclusions

In this study a smart STFD was designed and manufactured, and its dynamic performance was examined by MTS under various sinusoidal loading conditions with a constant amplitude of 20 mm. According to the dynamic test results of STFD and previous researches related to cable vibration control, the numerical model of cable-STFD was constructed and studied. Comparing with the cable-VD system in this paper, the effectiveness of vibration control for STFD was validated. The decay duration of cable-STFD is only 1/3 of that of VD-cable system. The performance of STFD in this research changed. At the beginning of the decay, STFD showed friction damper properties, and at the end of the decay, STFD showed VD characters.

5. Acknowledgements

This work is support by the National Nature Science Foundation of China (Grant Nos. 51608153, 51608335, 51508135), the Shenzhen Knowledge Innovation Programme (Grant Nos. JCYJ20170413105418298, JCYJ20170811153857358).

6. References

Barnes, H.A. 1989. Shear-thickening (dilatancy) in suspensions of nonaggregating solid particles dispersed in newtonian liquids, Journal of Rheologym, 33(2), 329-66.

Fischer, C., Braun, S.A., Bourban, P., Michaud, V., Plummer, CJG, M Nson, J.E. 2006. Dynamic properties of sandwich structures with integrated shear-thickening fluids, Smart Materials and Structures, 15(5), 1467-75.

Fischer, C., Bennani, A., Plummer, CJG, Michaud, V., Bourban, P., Jacquelin, E., et al. 2007. Shear thickening fluids as a tunable damping element: experimental results and modeling, Proceedings of Spie the International Society for Optical Engineering, 52513.

Lin, K., Liu, H., Wei, M., Zhou, A. and Bu, F. 2019. Dynamic performance of shear-thickening fluid damper under long-term cyclic loads, Smart Materials and Structures, 28(2019), 025007.

Lu, Z., Wu, L., Gu, B., and Sun, B. 2015. Numerical simulation of the impact behaviors of shear thickening fluid impregnated warp-knitted spacer fabric, Composites Part B: Engineering, 69, 191-200.

Mehrabi, A.B. 1998. Unified Finite Difference Formulation for Free Vibration of Cables, Journal of Structural Engineering, 124(11), 1313-1322.

Pinto, F. and Meo, M. 2016. Design and Manufacturing of a Novel Shear Thickening Fluid Composite (STFC) with Enhanced out-of-Plane Properties and Damage Suppression, Applied Composite Materials, 24(3), 643-660.

Tian, T. and Nakano, M. 2017. Design and testing of a rotational brake with shear thickening fluids, Smart Material Structures, 26, (0350383).

Wen, M., Lin, K., and Guo, Q. 2018. Modeling mechanical properties of a shear thickening fluid damper based on phase transition theory, Epl-europhys Lett, 121 (500015).

Yeh, F., Chang, K., Chen, T., Yu, C. 2014. The dynamic performance of a shear thickening fluid viscous damper, Journal of the Chinese Institute of Engineers, 37(8), 983-94.

Zhang, X.Z., Li, W.H., and Gong, X.L. 2008. The rheology of shear thickening fluid (STF) and the dynamic performance of an STF-filled damper, Smart Materials and Structures, 17, (0350273).

Zhou, H., Yan, L., Jiang, W., Xuan, S., and Gong, X. 2015. Shear thickening fluid-based energy-free damper: Design and dynamic characteristics, Journal of Intelligent Material Systems and Structures, 27(2), 208-20.

Investigation on Effect of Aerodynamic Characteristics of Trains on the Viaduct with Various Bridge Cross Sections under Crosswinds

Kehui Yu[1,2], Xuhui He[1,2], Lei Yan[1,2*], and Yongming Huang[1,2,3]

[1] School of Civil Engineering, Central South University, Changsha, China
[2] National Engineering Laboratory for High-speed Railway Construction, Changsha, China email: leiyan@csu.edu.cn
[3] School of Traffic and Transportation Engineering, Central South University, Changsha, China

[*]: corresponding author

Keywords: bridge deck, wind tunnel test, aerodynamic characteristics

Abstract:
In order to investigate the influence of the bridge deck with non-uniform cross sections on the aerodynamic characteristics of the China Railways High-speed (CRH) train, a typical single-box girder bridge is selected as a case study. The aerodynamic characteristics of CRH train are tested and analyzed, with the wind tunnel test by using the pressure measuring device. The aerodynamic parameters of the train-bridge system are obtained by comparing the results of different bridge section models and experimental conditions. The surface pressure distribution of the model has been measured, and the aerodynamic coefficient of the train at different rail positions with different bridge section models are discussed. The results show that the 3D effect caused by the change of bridge shape have outstanding influence on the aerodynamic characteristic of the train.

1. Introduction

In recent years, many researchers have investigated the train-bridge system under crosswind action, by using computational fluid dynamics and wind tunnel test. And considering the influence of train position, wind barriers or other parameters. On the one hand, the existence of the train on the bridge changes the section shape of the bridge, and subsequently, the aerodynamic forces on the bridge. On the other hand, the train may be submerged in the separated flow induced by the bridge deck, which may cause the aerodynamic forces to be quite different from that of a train on the ground[1]. However, the parameterization of the wind load on the train-bridge system due to the change of bridge shape has rarely been reported. In this paper, a continuous single box girder bridge and the China Railways High-speed (CRH) train were selected for this research. According to the shape of the bridge, the L/6 section of the main span was selected as the research object. In order to research how the shape change of the bridge working on the aerodynamic effect of the train.

2. Wind tunnel test

2.1. Experiment details

All section models adopt 1/40 geometric scale ratio. The section shape of the bridge model is similar, but the beam height is different. Different test sections can be defined by their main beam aspect ratio *B/H*. The model length is 2 m, the total width of the bridge is 0.3125 m, the

height is 0.184 ~ 0.39 m. The train's height is 0.0875 m, the width is 0.0845 m, the length-width ratio is greater than 2. Schematic diagram of main girder segment model and its main dimensions are shown in Figure 1.

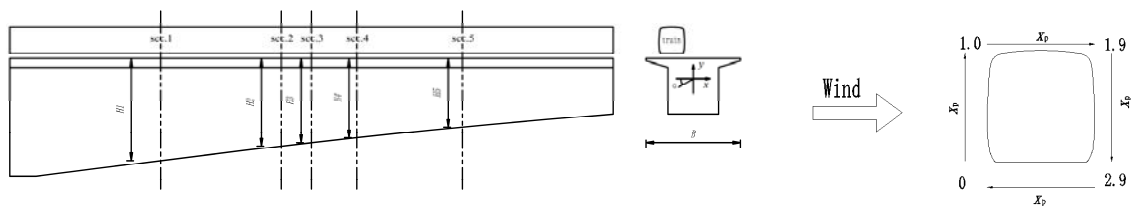

(a) (b)

Fig. 1 (a) Bridge sections of the non-uniform cross model, (b) pressure taps of the train.

According to different driving positions and test objects, it can be divided into four test case. The operating conditions are shown in table 1. The test was carried out under the uniform flow, and the aerodynamic coefficients of trains with different shapes and sections at the respective angles of attack of $-12^0 \sim 12^0$ were measured with the same step pressure.

Table 1. Test case details

case	Relative position	Bridge section model	α (^{0})	U (m/s)
1	Vehicle on upstream	Uniform section	$-12^0 \sim 12^0/2$	18
2		Non-uniform section		
3	Vehicle on downstream	Uniform section		
4		Non-uniform section		

3. Results and discussion

3.1. Aerodynamic characteristics

The time-average and fluctuating aerodynamic force coefficients of the vehicle at Re=1.05E5 are shown in Fig.1 & Fig.2. Fig.1 shows that the time-average aerodynamic coefficients of four cases are different. Especially, for the bridge-deck with non-uniform cross section case. The train on the upstream track cases (case 1 and case 2), for $0^0<\alpha<12^0$, C_D decrease, C_L and C_M increase, and for case 2 the time-average aerodynamic coefficient of test section 1~5 on the train are different obviously, compared to case 1. And for the train on the downstream track cases (case 3 and case4), the C_D is only about half value of the train on the upstream track cases with the same bridge deck section model. And for $-4^0<\alpha<4^0$ in case 4, the time-average aerodynamic coefficient of the train section 1~5 are different. And the aerodynamic coefficient of the first test section is obviously large than the other test section on the train, where the height of the bridge deck is the highest in all test sections.

Fig.2 shows that the fluctuating aerodynamic coefficients of the vehicle. And under the same working condition, the fluctuating aerodynamic coefficient of each test section changes with the wind attack angle by the same rule, but the C_L of the train on downstream track cases, the peak value is at wind attack angle 2^0 for case 3, which is at wind attack angle -4^0~2^0 for case 4 for

different test sections. The variable bridge section model has significantly influence on the aerodynamic coefficient of the train.

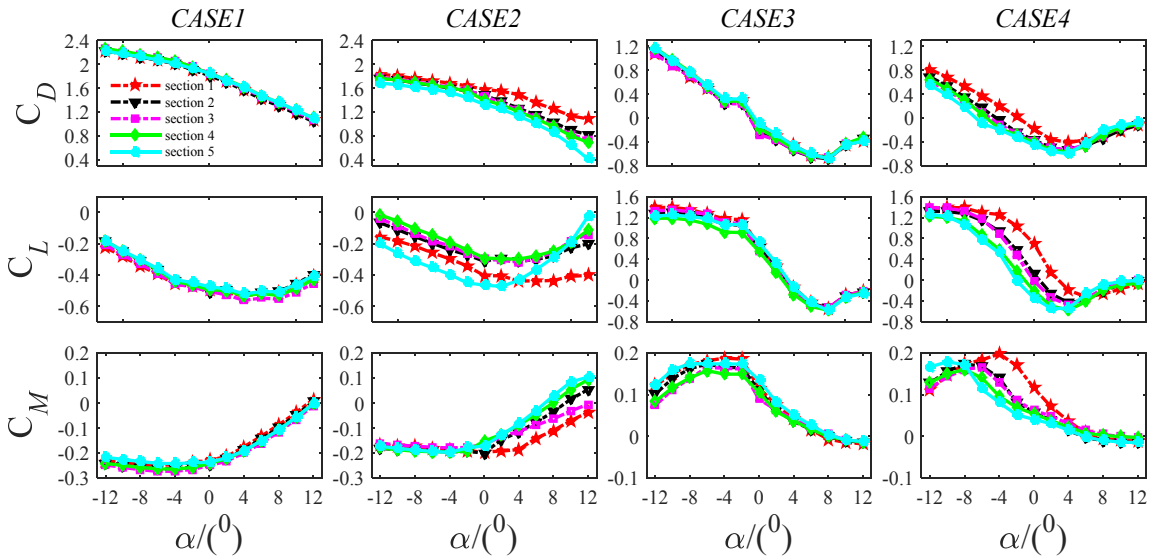

Fig. 1. Time-average aerodynamic coefficients of the train prism with α=-12°~12°/2

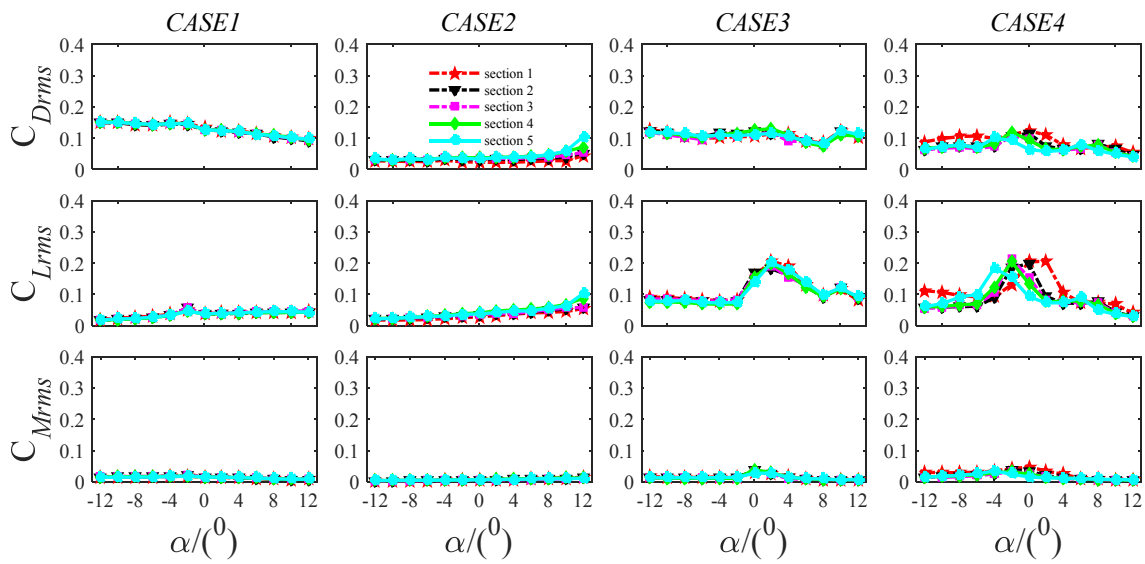

Fig.2. Fluctuating aerodynamic coefficients of the train prism with α=-12°~12°/2: (a) C_L of case 2, (b) C_L of case 4.

3.2. Pressure distribution

Fig.3 shows the experimental results of single train cases with α = 0°(cases 1-4). The wind pressure coefficient values of different test sections on the upstream track are close with each other. And the change trend is consistent with the change of the location of the test points. When the train is on the upstream track, the minimum negative pressure occurs on the separation of the

vehicle-bridge system facing the incoming flow with the value about -3.875 (case1) and -3.122(case2) in all test sections. And Fig.3 case 3 and case 4 shows the experimental results with single train on the downstream track. Due to the train is only a quarter of the height of bridge deck, and the train is submerged in the separated flow induced by the bridge deck. The tested pressure coefficient of the oncoming flow side points are negative. The minimum negative pressure coefficient on the windward surface is -3.921 in case 3. And the minimum negative pressure coefficient on the top surface is -3.582 in case 4. The mean aerodynamic forces of the test sections on the train of the variable cross-section bridge model are greatly different. Due to three-dimensional effect of the bridge section model, which will weaken the interaction aerodynamic interference between the vehicle-bridge system.

Fig.4 shows the fluctuating pressure coefficients of the train prism with α = 0° (cases 1-4). And the test result shows that the train on the downstream track cases has peak value about 0.63 (case 3) and 0.67 (case 4) on the arc-shaped transition, which is located between the windward side and the top side. And for the train on upstream track cases, the maximum value is located on the bottom side, due to the interaction mechanism of the train-bridge system.

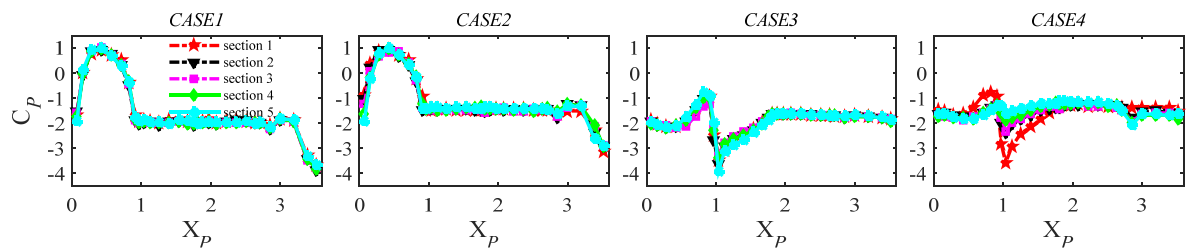

Fig. 3. Distributions of the time-average pressure coefficients of the train prism with α = 0°.

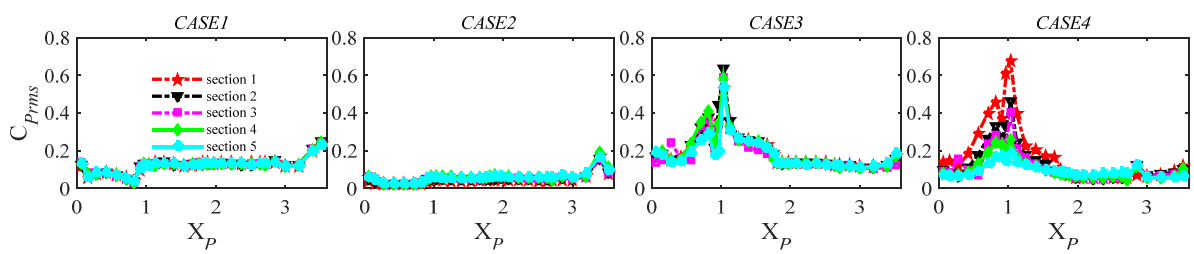

Fig. 4. Distributions of the fluctuating pressure coefficients of the train prism with α = 0°.

4. Conclusions

The aerodynamic characteristics of the train are significantly affected by the change of the bridge shape. And the train on the downstream track cases, the aerodynamic forces of the train may be affected by the separate flow of the bridge obviously. Especially for the test point on the train, which is located on the arc-shaped transition, between the windward side and the top side.

5. References

[1] X.H He, Y.F. Zou, H.F. Wang, and et al. Aerodynamic characteristics of a trailing rail vehicles on viaduct based on still wind tunnel experiments, Journal of wind engineering and industrial aerodynamics, 2014. 135 22-33.

Application of Eddy Current Damping TMD to Control the Human-Induced Vibrations of Two Long-span Suspension Footbridge

Huawei Niu[1*], Jinlin Chen[2], Xugang Hua[3], and Zhengqing Chen[4]

[1] Key Laboratory for Wind and Bridge Engineering of Hunan Province, College of Civil Engineering, Hunan University, Changsha, China; email: n iuhw@hnu.edu.cn
[2] Key Laboratory for Wind and Bridge Engineering of Hunan Province, College of Civil Engineering, Hunan University, Changsha, China; email: 1 044526133@qq.com
[3] Key Laboratory for Wind and Bridge Engineering of Hunan Province, College of Civil Engineering, Hunan University, Changsha, China; email: c exghua@hnu.edu.cn
[4] Key Laboratory for Wind and Bridge Engineering of Hunan Province, College of Civil Engineering, Hunan University, Changsha, China; email: z qchen@hnu.edu.cn

[*]: corresponding author

Keywords: suspension bridge; footbridge; human-induced vibration; tuned mass damper; eddy current damping; vibration control

Abstract: In the present paper, two case studies of the application of the eddy current damping tuned mass damper (ECD-TMD) to suppress the human-induced vibrations of the flexible footbridges are presented. The lengths of the main span of the two footbridges are 430m and 350m respectively, and the widths of the deck are both 6.0m. Firstly, the target modes related to the potential human-induced vibration system were analyzed and evaluated by finite element analysis (FEA). Secondly, the TMD system was designed to control the potential human-induced vibration. The design method and the ECD-TMD configuration are discussed. Thirdly, a series of dynamic tests are performed to identify modal properties of the bridge for fine-tuning of tuned mass dampers. Then, the ECD-TMDs are installed and evaluated by experiments. Finally, the frequencies and damping ratios of the footbridges are discussed before and after the ECD-TMDs were installed on the footbridges. The marked frequency variances between the measured data and the calculated results by FEA are investigated and studied. The results show that the damping ratios for lateral modes increases appreciably after the installation of the ECD-TMDs.

1. Introduction

With the improvement of people's aesthetic pursuit of urban landscape and bridge, and the development of light-weight and high-strength materials, pedestrian bridges are developing in the direction of larger span and more flexible. This makes the problem of pedestrian-induced vibration of pedestrian bridges increasingly prominent. Vibration reduction design has gradually become a very important part of the design process of modern long-span pedestrian bridges. The excitation source of pedestrian-induced vibration of pedestrian bridge is the vertical, lateral and longitudinal dynamic walking force produced by pedestrian walking. The frequency of vertical walking force mainly distributes in 1.2~2.4 Hz. And the frequency of lateral walking force is mainly distributed in 0.6~1.2 Hz. When some modal frequencies of the structure are within the sensitive frequency range, human-induced vibration may occur. The installation of tuned mass dampers has been proved to be an effective measure to control human-induced vibration by

many engineering cases. Tuned mass dampers (TMD) and viscous dampers were used to control human-induced lateral and vertical vibration in the Millennium Bridge in London, UK. The damping ratio of the first-order lateral bending mode of the main span reaches 20% after the dampers were installed[1]. After TMD was installed on Mianyang No. 1 Bridge, the lateral modal damping ratio increased more than 6 times, and the vertical bending modal damping ratio reached 5%. No large vibration phenomenon was observed[2]. In the present paper, one case study of the application of the eddy current damping tuned mass damper (ECD-TMD) to suppress the human-induced vibrations of the flexible footbridges is presented.

2. Introduction of the Yuntiandu Bridge

Located in the scenic area of Zhangjiajie Grand Canyon, Yuntiandu Bridge is a pedestrian suspension bridge with a single span and simple anchor structure. The main cable span is 430m and the vertical span ratio is 1/10. The stiffening girders of the bridge are box steel longitudinal and transverse girders. In order to improve the torsional stiffness and wind resistance of the structure without affecting the landscape effect, the largest proportion of variable width space structure in the world was applied for the first time. The transverse spacing of the main cable at the middle of the span is 8.194m, while the transverse spacing of the main cable at the East and West pylons is 50m and 45m respectively. The width of the stiffening beam varies linearly from 6 m in the mid-span region (275 m in length) to 15 m in the supports at both ends, as shown in Figure 1. The maximum number of people on the bridge is designed to be 800.

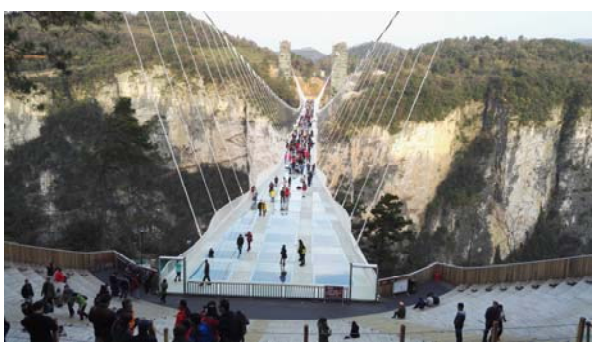

Fig. 1. The Yuntiandu Bridge

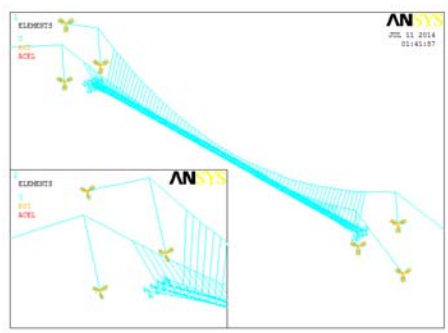

Fig. 2. Finite model of the Yuntiandu Bridge

3. Design of TMD System

In order to obtain the dynamic characteristics of the bridge, a finite model is established based on the large general software ANSYS, as shown in Figure 2. It is found that three lateral bending mode frequencies of the bridge are near the sensitive frequency of pedestrian-induced vibration, as shown in Table 1.

Table 1. Dynamic Characteristic Summary Table

Modal order	Frequency calculated by finite element method (Hz)	Frequency measured by field test (Hz)	Modal mass (kg)	The critical number
12	0.66	0.76	847981	539
22	1.02	1.16	431222	741
32	1.43	1.66	239494	696

The lateral vibration of pedestrian bridges is mainly due to lateral dynamic instability. In this paper, the critical number of dynamic instability of the bridge is estimated based on the Dallard formula established from the test results of the Millennium Bridge in London[1], as shown in Table 1. From Table 1, it can be seen that the critical instability number is less than that of the design number. TMD should be installed to prevent lateral dynamic instability of the bridge.

The vibration reduction effect of TMD depends on the precise tuning of its frequency. Therefore, after the completion of the bridge, dynamic field test was carried out, and the test results were used as the basis for the final design of TMD. A vibrator was used in field test as shown in Figure 3. And the frequency measured by field test is shown in table 1.

Fig. 3. The picture of the field test

Based on the finite element analysis and field test results, the parameters of TMD are designed according to the principle of maximum acceleration minimization[3], as shown in Table 2.

Table 2. Optimum parameters of TMD for each mode

Modal order	Modal parameters of pedestrian bridge			Basic parameters of TMD		
	Frequency (Hz)	Mass（kg）	Mass ratio (%)	Frequency (Hz)	Mass（kg）	Damping ratio (%)
12	0.76	847981	2.4	0.75	20000	9.4
22	1.16	431222	2.0	1.15	8500	8.5
32	1.66	239494	2.8	1.64	6800	10

ECD-TMD is a kind of TMD which uses eddy current damper to provide damping. Eddy Current Damping Element is composed of Permanent Magnet and Conductor Plate. When ECD-TMD works, the conductor plate cuts the magnetic line of the permanent magnet, produces a force that hinders the relative motion of the two and generates eddy current in the conductor plate. The eddy current immediately generates heat and dissipates energy in the conductor plate, and finally converts the mechanical energy of structural vibration into heat energy. Compared with traditional viscous dampers, eddy current dampers have the following advantages: 1. No additional stiffness. 2. Low starting friction 3. Good durability.

Due to the limited installation space, each set of TMDs is divided into several TMD units with the same frequency and damping ratio. For example, the TMD for controlling the 12th mode

vibration is divided into 20 TMD units. The effective mass of each TMD unit is 1000kg and the total mass is 2000kg. In theory, the separated TMD system has the same vibration reduction effect as a single TMD with the same mass. TMDs installed on the Yuntiandu Bridge is shown in Figure 5.

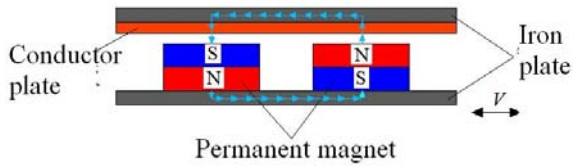

Fig. 4. Composition of Eddy Current Damper

Fig. 5. TMDs installed on the Yuntiandu Bridge

4. Evaluation of Vibration Reduction Effect

Comparing the modal damping ratio of the bridge before and after TMD installation is an effective means to evaluate the vibration reduction effect. Therefore, after all TMDs are installed, the acceleration response values of the bridge under TMD locking and normal working conditions are tested respectively.

Case 1: Leave one TMD working normally, the other TMDs are locked with blocks, shake the TMD working normally, make the bridge vibrate. After the vibration reaches a certain amplitude, lock the TMD working normally quickly with blocks, and measure the acceleration response of free attenuation of the bridge.

Case 2: Let all TMDs work normally and shake a TMD to make the bridge vibrate. When the vibration reaches a certain amplitude, stop shaking, and measure the acceleration response of free attenuation of the bridge.

Based on the measured acceleration response of the bridge, the calculated damping ratios of the bridge are summarized in Table 3.

Table 3. Damping ratios of the bridge

Modal order	Damping ratio in Case 1(%)	Damping ratio in Case2(%)
12	0.78	4.01
22	0.5	2.68
32	0.9	2.60

From Table 3, it can be seen that the damping ratio of the bridge increases obviously after TMD installation, and the effect of vibration reduction is very good.

5. Conclusions

According to the characteristics of the pedestrian suspension bridge with long-span space cable plane studied, a TMD vibration reduction scheme is proposed. The field test results show that the

damping ratio of the control mode has been significantly improved after the vibration reduction system is installed.

6 References

[1] Dallard P, Fitzpatrick T, Flint A, Le Bourva S, Low A, Ridsdill RM et al.2001. The London Millennium footbridge. The Structural Engineer. 79(22):17—33.

[2] Hua Xu-gang, Wen Qing, Chen Zheng-qing , Yang yong, Wang Wen-xi, Niu Hua-wei.2016. Design and experimental validation of structural vibration control of a curved twin-deck cable-stayed bridge subject to pedestrians. Journal of Vibration Engineering.29(5):822-829.

[3] Soong TT, Dargush,G.F. 1997. Passive energy dissipation systems in structural engineering. John Wiley& Sons,Inc, NewYork,NY.

Prediction of Vibration Responses of Large-Span Bridges using Gaussian Process Regression Approach

Fuyou Xu[1*], Xiangyu Bo[2], and Xingliang Ma[3]

[1] School of Civil Engineering, Dalian University of Technology, Dalian, China; email: fuyouxu@hotmail.com
[2] School of Civil Engineering, Dalian University of Technology, Dalian, China; email: boxvsyu@163.com
[3] School of Civil Engineering, Dalian University of Technology, Dalian, China; email: xingliangma@hotmail.com

[*]: corresponding author

Keywords: large-span bridge; vibration response prediction; Gaussian process regression; displacement; acceleration.

Abstract: A novel approach using the machine learning strategy of Gaussian process regression (GPR) is proposed to predict the bridge vibration responses at the positions where sensors are not arranged. This approach is characterized by adaptively selecting hyper-parameters and providing outputs with clear probabilistic meaning. Sutong Bridge, a China cable-stayed bridge with a main span length of 1088m is numerically modeled by finite element program. Under the excitations of simulated wind loads, the dynamic responses at all nodes are obtained and used as data source to demonstrate the applicability and accuracy of the GPR approach.

1. Introduction

In recent years, with the development of structural materials and engineering technology, bridge engineering have expanded rapidly, and large numbers of long-span bridges have sprung up. To date, more than 30 kilometer-level bridges have been built up. It is necessary to apply health monitoring systems (HMS) to improve real-time damage identification and status assessment during the construction and operation of bridges, so as to reduce the probability of accidents[1]. Many larges bridges have installed HMS to collect the concerned parameters such as the vibrations, forces, stresses, temperature fields, etc. However, the amount of sensors for most HMSs is less than 1500. Sensors are arranged at the most interested positions for the sake of cost[2]. Thus, the responses at overwhelming majority locations cannot be directly monitored. Even worse, some data may be deficient due to the failure of data collection, transfer, and/or storage system. Therefore, it is significant to develop efficient prediction approaches for spatial extension and data recovery.

This paper uses the machine learning method: Gaussian process regression (GPR)[3] as basis, to propose an approach for predicting the bridge vibration responses at the positions where sensors are not arranged or the data are lost or invalid. Comparing to other machine learning methods, GPR is more competitive in adaptively selecting hyper-parameters and offering results with clear probabilistic meaning. Sutong Bridge, a China cable-stayed bridge with a main span length of 1088m, is numerically modeled by finite element program. The random wind fields are

simulated. Under the excitations of simulated wind loads, the dynamic responses at all concerned nodes are obtained, which can be used as training and checking data source to demonstrate the applicability and accuracy of the proposed approach.

2. Gaussian Process Regression

A Gaussian Process (GP) $f(x)$ is uniquely determined by its mean function $m(x)$ and covariance function $\Sigma(x,x')$ as

$$f(x) \sim GP[m(x), \Sigma(x,x')] \tag{1}$$

where x and x' are indices. The mean function and the covariance function have no fixed forms, and can be set according to experience or sample information at hand. Measured records are often contaminated by sampling noises. If the noises are assumed to be Gaussian and white, the measured records can be expressed as $y = f(x) + \varepsilon$, where ε is Gaussian white noise with zero mean and σ_n^2 variance. Then,

$$y \sim GP[m(x), k(x,x')] \tag{2a}$$

$$k(x,x') = \Sigma(x,x') + \sigma_n^2 \delta(x,x') \tag{2b}$$

where $\delta(\cdot)$ is the Dirac function. Assuming that $Y = [y_1, y_2 \ldots y_m]$ and $Y^* = [y_1^*, y_2^* \ldots y_m^*]$ are known training set outputs and unknown testing set outputs, respectively, and both Y and Y^* come from the same GP, and thus their joint distribution obeys

$$\begin{bmatrix} Y \\ Y^* \end{bmatrix} \sim N\left\{ \begin{bmatrix} M \\ M^* \end{bmatrix}, \begin{bmatrix} K & K' \\ K'^T & K^* \end{bmatrix} \right\} \tag{3}$$

where N represents the Gaussian distribution; M and M^* are the mean value vectors of Y and Y^*. K, K^* and K' are the covariance matrices for the training set, testing set, and training-testing set, respectively. Y is the given training data, and the conditional distribution of $Y^*|Y$ is of interest. Since the joint distribution of (Y, Y^*) and the marginal distribution of Y are known, $Y^*|Y$ can be inferred as

$$Y^*|Y \sim N\left[M^* + K'^T K^{-1}(Y - M), K^* - K'^T K^{-1} K^*\right] \tag{4}$$

Equation (4) represents the posteriori distribution of testing set conditioning on training set. The mean of $Y^*|Y$ is taken as the output of Y^*, it possess clear probabilistic meaning, which is an important advantage compared with other machine learning methods.

The hyper-parameters θ in the mean and the covariance functions can be estimated by maximizing the log likelihood of Y. The distribution of Y follows $N(M,K)$ so that its log likelihood is expressed as

$$L = \log p(Y|X,\theta) = -\frac{1}{2}\log|K| - \frac{1}{2}(Y-M)^T K^{-1}(Y-M) - \frac{n}{2}\log(2\pi) \tag{5}$$

In Eq. (5), X is known training set inputs, and L is only related to θ. Using the conjugate gradient descent method, θ can be easily estimated.

3. Finite Element Analysis

Sutong Bridge is located in Jiangsu Province, whose main span is 1088m long and main tower is 300m high. It is a double-tower steel box girder cable-stayed bridge with double cable plane. Using AYSYS software, the three-dimensional finite element model of Sutong Bridge is established. BEAM 4 element is used to simulate the main girder, piers and towers, LINK 10 element is used to simulate the cables. Based on the spectral representation method[4], the fluctuating wind speed field is simulated. The target auto-power spectral density (APSD) is Kaimal spectrum, the target cross-power spectral density (CPSD) is determined using Davenport coherence function. Along the longitudinal direction, 68 simulation points are uniformly arranged on the main girder. Along the vertical direction, 11 simulation points are uniformly arranged with a 28m interval on each tower. The arrangement of the simulation points is bilateral symmetry based on the midspan, points on left half span are shown in Fig. 1. The simulated wind speed time history at 1# point is plotted in Fig. 2a, its APSD and CPSD between 1# and 2# points are estimated and compared with the targets in Fig. 2b and 2c. It can be seen that the wind field simulation performance is very good.

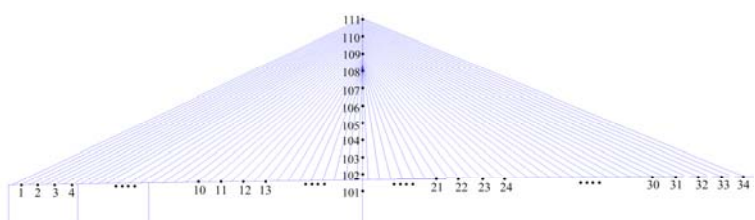

Fig. 1. Simulation points arrangement

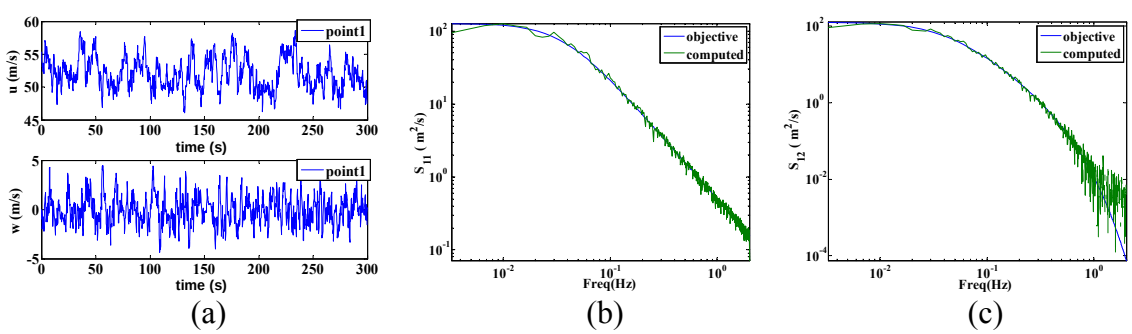

Fig. 2. Simulated wind speed: (a) time history; (b) APSD comparison; (c) CPSD comparison

Based on the quasi-steady aerodynamic theory, the simulated fluctuating wind speeds are converted into the buffeting force. Together with the static wind force that determined by the mean wind, they are applied to the finite element model. Each node on the model can be considered as a sensor. The acceleration and displacement responses at each sensor are recorded and will be used to demonstrate the ability of GPR on predicting vibration response of bridge.

4. Prediction of Acceleration and Displacement Response

Due to the limited space, only one computational example is provided here to show the prediction effect. The results at five nodes on main girder are selected as the data source, the relative positions of these nodes are shown in Fig. 3a. Assuming that only the data at the four corner pints are measured, we make predictions of the acceleration and displacement time histories at the center point E. We propose a new prediction approach that builds a series of independent GPR models to predict the responses for each time instant. For example, at time instant t, model GPR(t) is trained by taking the location coordinates of the known points as inputs and the corresponding responses as outputs. GPR(t) is only used to predict the responses of the interested positions at t. For time instant $t+1$, a new model GPR(t+1) is trained. This approach takes advantage of GPR's powerful ability in generalization and in handling problems with a small sample size. The time-invariant inputs and time-varying outputs are used to train the time-varying GPR models for prediction. The new approach uses a series of time-variant models, each model is independently trained and only deals with the prediction at its specified time instant. It is not affected by the variations of the loading field with time. Thereby it can be used in the non-stationary cases, such as the field measurements of HMS on real bridge.

Using the proposed approach, the acceleration and displacement time histories at the center point are predicted. For each time instant, the mean function and covariance function of the GPR model are set as the constant and neural network kernel function, respectively, and the hyper-parameters are solved by the conjugate gradient descent method. The results are shown in Fig. 3b and 3c. In order to clearly show the comparison and difference, only 37.5 s (150 data) are offered. It can be seen that the predictions match closely to the objectives, from which the high accuracy of the present GPR-based approach is demonstrated. In fact, even the distances among Points A-E are much larger, the prediction accuracy can also be ensured. In addition, the reference point and prediction point number can use any other values, e.g., 5 12 50..., etc.

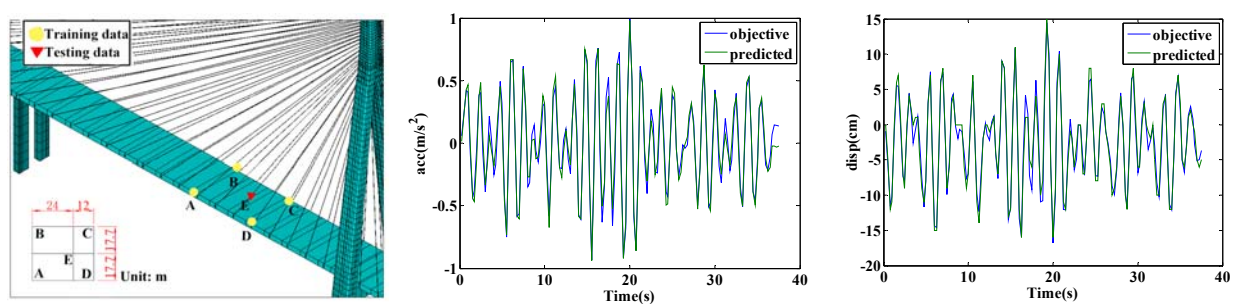

(a) (b) (c)

Fig. 3. Prediction results: (a) sensor arrangement; (b) accelerations; (c) displacements

5. Conclusion

A GPR-based approach for predicting vibration responses of large-span bridges is proposed in this paper. The approach can adaptively select hyper-parameters and offer results with clear probabilistic meaning. In addition, it uses time-varying GPR models for time history prediction, and thereby can be applicable to non-stationary cases. Based on finite element analysis, the computational results of Sutong Bridge under wind load are obtained. Taking them as data source, an example for predicting the acceleration and displacement time histories is provided. The prediction results demonstrate the feasibility and high accuracy of the proposed approach. By the aid of the proposed approach, more useful and interested data can be generated and the sensor amount can be largely reduced.

6. References

[1] Xu, F. Y., Zhang, M. J., Wang, L., Zhang, J. R. 2016. Recent Highway Bridge Collapses in China: Review and Discussion. Journal of Performance of Constructed Facilities,30(5):04016030

[2] Balageas, D., Fritzen, C. P., Güemes, A. 2001. Structural health monitoring. Structural Engineering Mechanics & Computation, 6531(8), 1185-1193.

[3] Rasmussen, C. E., Williams, C. K. I. 2005. Gaussian Processes for Machine Learning (Adaptive Computation and Machine Learning). The MIT Press.

[4] Deodatis G., 1996. Simulation of Ergodic Multivariate Stochastic Processes. Journal of Engineering Mechanics, 122(8):778-787.

Vertical Vortex-Induced Vibration Control of Long-Span Bridges Using the Multiple Eddy Current Tuned Mass Dampers

Zhiwen Huang[1*], Xugang Hua[2], and Zhengqing Chen[3]

[1] Key Laboratory for Wind and Bridge Engineering of Hunan Province, Changsha China; email: zwhuang213@hnu.edu.cn
[2] Key Laboratory for Wind and Bridge Engineering of Hunan Province, Changsha China; email: cexghua@hnu.edu.cn
[3] Key Laboratory for Wind and Bridge Engineering of Hunan Province, Changsha China; email: zqchen@hnu.edu.cn

[*]: corresponding author

Keywords: vortex-induced vibration; bridge; vibration control; tuned mass damper; eddy current damper

Abstract: In this paper suppression of the vertical vortex-induced vibration of long-span bridges by using the multiple eddy current tuned mass damper (MECTMD) is theoretically studied. The MECTMD employ the plane eddy current damper as the damping element, for its longevity and low maintenance requirements. The vertical vortex-induced force is assumed as a harmonic loading, and the displacement magnifying factors (DMF) of the girder with the MECTMD is derived in the modal coordinate. Then minimizing the maximum value of DMF of the girder is selected as the optimization objective, and the optimal parameters of MECTMD are obtained by employing the Genetic Algorithm. Based on these optimal parameters, the plane eddy current dampers, which are composed of the permanent magnets, the conductive plate, primary back iron and secondary back iron, are carefully designed.

1. Introduction

Long-span bridges are susceptible to vertical vortex-induced vibration at low wind velocity even below 10m/s , famous example of which are Storebælt Suspension Bridge , Xihoumen Suspension Bridge , Trans-Tokyo Bay Bridge and Rio-Niteroi Bridge. Although the vortex-induced vibration is self-limiting, large vibration may occur to the long-span bridges due to their low mechanical damping and light weight, resulting in human discomfort and structural fatigue problem. Therefore, it is of great importance to suppress the excessive vortex-induced vibration of long-span bridge by employing practical measures. Aerodynamic or mechanical measures are often used to mitigate the vortex-induced vibration of long-span bridges. The former typically consists of guide vanes, flaps and fairings that modify the shape configuration of the girder and air flow around it, while the latter provides additional damping to the girders. One of the commonly used mechanical measures is the application of tuned mass damper (TMD) on a bridge girder. For example, sixteen TMDs were installed in the girder of Trans-Tokyo Bay Bridge to control the vortex-induced vibration in the first and second vertical mode (Fujino and Yoshida, 2002). Oil dampers were utilized as the damping element for these TMDs, and the TMD parameters were determined by a complex eigenvalue analysis of the bridge-TMD system, whose target logarithmic damping was set to be 0.22 for the first two modes. Since more than ten

tuned mass dampers may be needed to suppress vortex-induced vibration of long-span in a single vibrational mode, it is favorable to design their parameters by using the multiple tuned mass damper (MTMD) theory, which can further improve the control effectiveness and robustness of the traditional tuned mass damper. Additionally, the oil dampers, which is commonly used as the damping element for TMD, may suffer from the problem of fluid leakage as recently emerged in several bridges, which may detune TMDs from optimum damping. Eddy current damping (ECD) is another effective mechanism for dissipating kinetic energy (Huang et al., 2018). In its simplest form, ECD device consists of conductive plate and magnets. Compared with oil damper, one notable advantage of ECD is that no fluid inside the damper and the generation of damping is independent of friction, potentially making it longevity and lower maintenance requirement.

In the present study, suppression of the vertical vortex-induced vibration of a long-span suspension bridges by using the multiple eddy current tuned mass damper (MECTMD) is theoretically studied. The MECTMD employ the plane eddy current damper as the damping element, for its longevity and low maintenance requirements. The vertical vortex-induced force is assumed as a harmonic loading, and the displacement magnifying factors (DMF) of the girder with the MECTMD is derived in the modal coordinate. Then minimizing the maximum value of DMF of the girder is selected as the optimization objective, and the optimal parameters of MECTMD are obtained by employing the Genetic Algorithm. Based on these optimal parameters, the plane eddy current dampers, which are composed of the permanent magnets, the conductive plate, primary back iron and secondary back iron, are carefully designed.

2. Displacement magnifying factor (DMF) of the Bridge-MECTMD system

The MECTMD is used to suppress the vortex-induced vibration of a long-span suspension bridge in the fifth vertical mode. The natural frequency of the fifth vertical mode is 0.230Hz, and its inherent damping ratio is 0.5%. Fig.1 depicts the corresponding normalized modal shape function of the bridge girder, and as shown in Fig.2, twenty-four ECTMDs are installed in the bridge girder at three individual regions, denoted by A, B and C, where the modal displacements reach nearly 1.0. Additionally, since the girder composed of two separated box, the twenty-four ECTMDs are divided into two groups with the same parameters. The vortex-induced force is assumed as a harmonic loading for simplicity, thus DMF of the bridge girder under vortex-induced excitation can be derived in the modal coordinate by employing the MTMD theory (Kareem and Kline, 1995),

$$H\left(i2\pi\omega\right) == \frac{1}{E+iF} \tag{1}$$

$$E = 1-\beta^2-\beta^2\sum_{n=1}^{N}\mu_i\left[\frac{1-\alpha_i^2+4\zeta_i^2\alpha_i^2}{\left(1-\alpha_i^2\right)^2+4\zeta_i^2\alpha_i^2}\right] \tag{2}$$

$$F = 2\zeta_s\beta-\beta^2\sum_{n=1}^{N}\mu_i\left[\frac{2\zeta_i\alpha_i^3}{\left(1-\alpha_i^2\right)^2+4\zeta_i^2\alpha_i^2}\right] \tag{3}$$

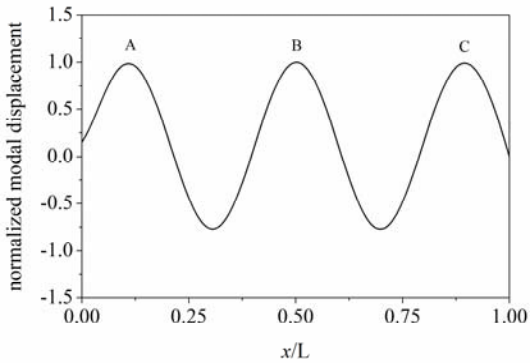

Fig. 1. Normalized modal shape function of the fifth mode of a suspension bridge

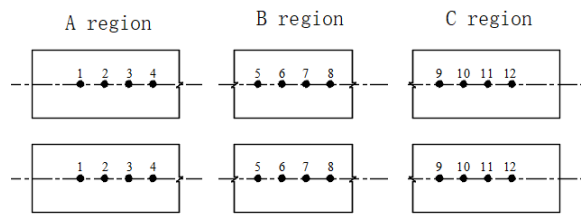

Fig. 2. Installation position of the MECTMD in the bridge girder

where $\beta=f/f_s$, denotes the ratio of excitation frequency and natural frequency of the mode under control; α_i denotes the ratio of the excitation frequency and the natural frequency of the ith eddy current tuned mass damper (ECTMD); ζ_i and ζ_s denotes the damping ratio of ith ECTMD and the bridge, respectively; N denotes the number of the ECTMD; $\mu_i=M_i/M_s$, denotes the generalized mass ratio of the ith ECTMD, where,

$$M_i = m_i\phi^2\left(x_i\right), \quad M_s = \int_{st} m\left(x\right)\phi^2\left(x\right)\mathrm{d}x \tag{4}$$

where m_i denotes the auxiliary mass of the ith ECTMD; $\phi(x_i)$ denotes the modal displacement, where the ith ECTMD is installed; $m(x)$ and $\phi(x)$ denotes the mass distribution function and modal shape function of the bridge, respectively.

3. Parameter optimization of the MECTMD

In order to reduce displacement response of bridge girder under vortex-induced excitation, the minimal value of MDF of bridge girder is choose as the optimization objective. In consideration of the design, manufacture and installation of MECTMD in practical engineering, all the ECTMD are designed with the same damping ratio and stiffness. In the optimization procedure, the total mass ratio of MECTMD is assumed to be 1%, and a Matlab-based Genetic Algorithm are employed to obtain the optimal parameters of MECTMD, including the frequency range, the center frequency ratio and the damping ratio, as shown in Table.1. It is noted that in order to reduce the strokes of the ECTMDs and improve their control robustness, the damping ratio in final design has been amplified by two times compared with the optimal one, that is, ζ_i=0.030. For these two cases, the peak of DMF of the girder are calculated versus the error of natural frequency as shown in Fig.3, it can be seen that increasing the damping ratio of ECTMD really makes it control performance more robust, with only a slight decrease in effectiveness

Table 1. The parameters of MECTMD obtained from the GA Algorithm

frequency range (Hz)	damping ratio	center frequency ratio	DMF
0.0329	0.015	0.9945	10.5250

4. Detail design of the MECTMD

Based on the optimal parameters in the last section, the damping coefficient of each ECTMD can be calculated, and results are shown in Fig.4 It can be seen that the damping coefficients of the twelve ECTMDs is closely spaced, ranging from 593 N·s/m to 737 N·s/m. A schematic of the ECTMD is given in Fig.5 It can be seen that two ECDs are used in the ECTMD, each of which is composed of two NdFeB permanent magnets mounted on the mass block, a conductive plate and a back iron. All the structural parameters of the twelve ECTMDs are the same except the air gap between the permanent magnet and the conductive plate, by which the damping coefficient of the ECD can be finely adjusted, as shown in Fig.6. Through electromagnetic finite element analysis the structural parameters of the ECD can be obtained: the remanence of permanent magnet B_r=1.4T; the dimension of the permanent magnet is $L\times W\times H$=35 mm×70 mm×20 mm; the center-to-center distance of permanent magnet D=42mm; the conductive plate is made of Al, whose conductivity is $\sigma_c=3.7\times10^7$S; The back iron is made of Steel1010 with a height of h=10mm; the air gap varies from 1.5mm to 3.5mm.

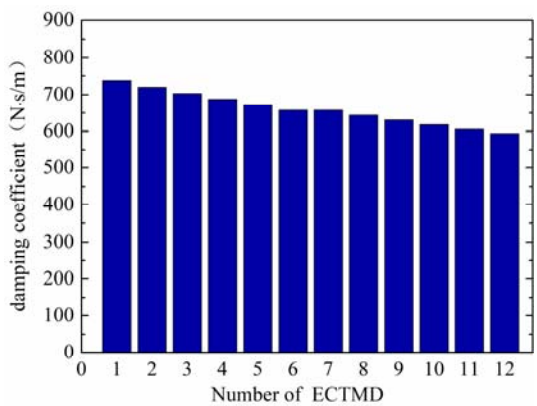

Fig. 3. damping coefficient of ECTMDs

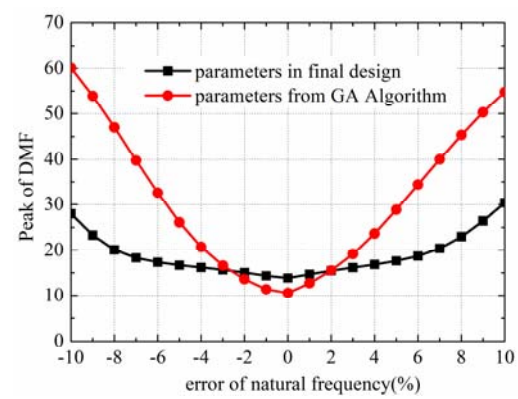

Fig. 4. robustness analysis of MECTMD

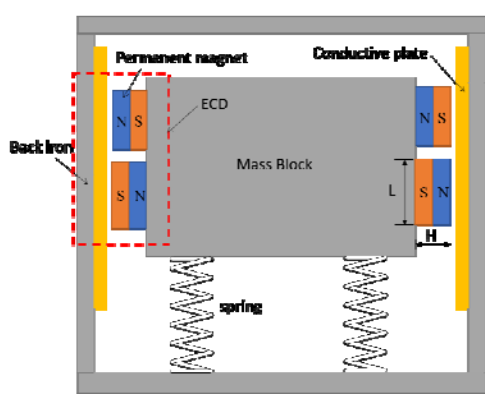

Fig. 5. Schematic of ECTMDs

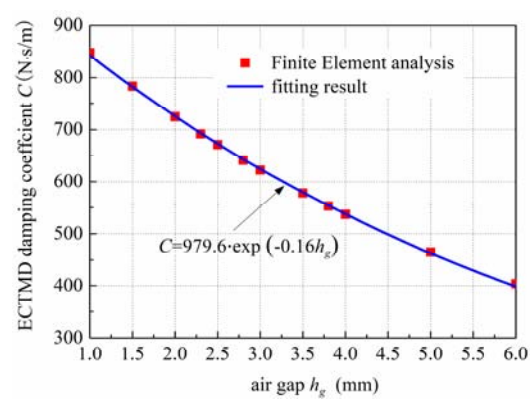

Fig. 6. damping coefficient of ECTMD versus air gap

5. References

FUJINO, Y. & YOSHIDA, Y. 2002. Wind-induced vibration and control of Trans-Tokyo Bay crossing bridge. Journal of Structural Engineering, 128, 1012-1025.

HUANG, Z., HUA, X., CHEN, Z. & NIU, H. 2018. Modeling, Testing, and Validation of an Eddy Current Damper for Structural Vibration Control. Journal of Aerospace Engineering, 31, 04018063.

KAREEM, A. & KLINE, S. 1995. Performance of multiple mass dampers under random loading. Journal of Structural Engineering, 121, 348-361.

Effects of Central Buckle on Flutter Stability of Long-Span Suspension Bridge

Yan Han[1*], Kai Li[2], and C.S. Cai[3]

[1] School of Civil Engineering, Changsha University of Science & Technology, Changsha, China, e-mail: ce_hanyan@163.com
[2] School of Civil Engineering, Changsha University of Science & Technology, Changsha, China, email:1012056203@qq.com
[3] Department of Civil and Environmental Engineering, Louisiana State University, Baton Rouge, USA, email: cscai@lsu.edu

[*]: corresponding author

Keywords: long-span suspension bridge; central buckle; flutter stability; self-excited force; time-domain

Abstract: To investigate the effects of central buckle on the flutter stability of long-span suspension bridges, the Aizhai Bridge in China was selected as an example to demonstrate the analysis procedure. Four different connection options between the main cable and the girder at the mid-span position, namely, a short suspender, one pair of flexible central buckles, three pairs of flexible central buckles, and one pair of rigid central buckles, were considered and their effects on the dynamic characteristics of long span suspension bridges were studied. Then, based on the formulation of self-excited forces in the time domain and APDL(ANSYS Parametric Design Language) offered by ANSYS, the time-domain flutter analysis was realized. Finally, the influences of the central buckles on the flutter stability of the bridge were investigated. The results show that the central buckles can significantly increase the frequency of the longitudinal floating of the bridge and have greater influence on the frequencies of asymmetric lateral bending and asymmetric torsion than on that of symmetric ones. The rigid central buckle can largely increase the frequency of asymmetric torsion. The central buckles have negligible impact on the critical flutter velocity due to that the flutter mode of the Aizhai Bridge was coupled with the symmetric vertical bending and the symmetric torsion. However, it has certain impact on the flutter mode and the three-dimensional flutter states of the bridge, which benefits the flutter stability.

1. Introduction

Since the wind-induced collapse of the original Tacoma Narrows Bridge in the United States in 1940, taking what measures to improve the dynamic characteristics and the global stiffness of main girder of long-span suspension bridges has always been the focus of bridge engineering. One of the effective measures to enhance the global stiffness of long-span suspension bridges is to install the central buckle connecting the main cable and the stiffening girder at the mid-span position (Gao et al. 2007; Xu et al. 2008). Although the central buckles have been applied to many long-span suspension bridges in China in recent years for improving the mechanical performance of the short suspenders at the mid-span position, there are very limited studies on the influences of central buckle on the performance of suspension bridges (Wang et al. 2009; Qin et al. 2014; Wang et al. 2015; Liu et al. 2017). Xu et al. (2008; 2010) studied the influence of

different central buckles on the dynamic characteristics of the SiduRiver Bridge, a long-span suspension bridge, by using the finite element method, and found that the central buckles can increase the frequencies of the longitudinal floating and the first asymmetric torsion modes. There are few studies focused on the influence of central buckle on seismic response of the bridge (Wang et al. 2011; Xu et al. 2010). Meanwhile, there are very few studies concentrated on the influence of central buckle on wind-induced vibration (Wang et al. 2010; 2014), it was found that the central buckle can greatly reduce the vertical buffeting displacement of the deck and the longitudinal displacement of the towers when the wind speed changes from 10 m/s to 40 m/s. Based on the above literature review, the effects of central buckle on the flutter stability of long-span suspension bridges were rarely reported and it is necessary to investigate the influences of central buckle on the flutter stability of suspension bridges, which can provide certain references for the extensive use of central buckles in long-span suspension bridges in the future.

2. Finite element modeling

The Aizhai Bridge is a single-span suspension bridge located in a mountainous area in China with a main span of 1,176 m (steel truss girder) and two side cable spans of 242 m and 116 m. For obtaining the dynamic characteristics of the bridge accurately, a refined spatial-truss-girder model of the Aizhai Bridge was established using ANSYS software in the global coordinate system of *X*, *Y*, *Z*, as shown in Fig.1, with 84,085 nodes and 76,846 elements.

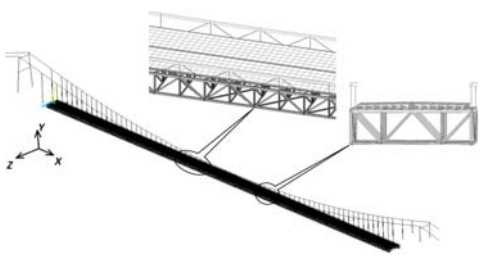

Fig. 1. The refined spatial-truss-girder model

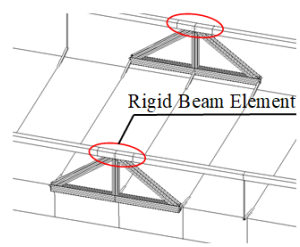

Fig. 2. Rigid Central Buckle of Model FM-D

For investigating the influences of the central buckle on the flutter stability of the suspension bridge, four different connection options are applied between the main cable and the girder at the mid-span position corresponding to the four different finite element models, as defined in Table 1. The rigid central buckle for the model FM-D was simulated with spatial beam element BEAM188, as shown in Fig. 2.

Table 1. Number for four different finite element models

Model number	FM-A	FM-B	FM-C	FM-D
Connection structure	A short suspender	One pair of flexible central buckles	Three pairs of flexible central buckles(prototype)	One pair of Rigid central buckles

3. Flutter Stability Analysis

3.1 Time-domain flutter analysis method

The self-excited forces per unit span can be expressed in terms of impulse response function and the aerodynamic lift force induced by the vertical motion can be written as follows:

$$L_{seh}(t)=\frac{1}{2}\rho U^2\left[A_1 h(t)+A_2\frac{B}{U}\dot{h}(t)\right]+\frac{1}{2}\rho U^2\sum_{n=4}^{m}A_n\int_{-\infty}^{t}e^{-\frac{d_n U}{B}(t-\tau)}\dot{h}(\tau)d\tau \tag{1}$$

Similarly, the expressions for the other self-excited force components $L_{se\alpha}$, M_{seh} and $M_{se\alpha}$ can be obtained. After obtaining the time-domain expressions of all the aerodynamic self-excited forces, the time-domain flutter analysis can be performed by using APDL offered by ANSYS. The computing time step was given 0.01s after the time-step independence testing.

3.2 Flutter analysis

The damping ratio of the steel structure is usually taken as 0.5%, i.e., ζ=0.5%, when the structural damping is considered in aerodynamic analysis. Fig. 3 shows the vertical and torsional displacement responses, respectively, of the mid-span for the model FM-C under 0° wind attack angle at the wind velocity of 94.6 m/s. It can be seen that the amplitudes of vertical and torsional displacements all tend to be constant, thus 94.6 m/s is the critical flutter wind velocity of the model FM-C when the structural damping ratio is 0.5%. This obtained critical flutter wind velocity is very close to 95.1 m/s, obtained from the wind tunnel testing, which proves the reliability of the simulation results. The critical flutter velocity and the corresponding frequency for the four models are summarized in Table 2, and it can be found that all the three different central buckles almost have no effect on the critical flutter velocity when the structural damping is considered. It is mainly because that the flutter mode of the bridge is a coupled mode of the first symmetric vertical bending and first symmetric torsion, but the central buckle has negligible effect on the natural frequencies of these two modes

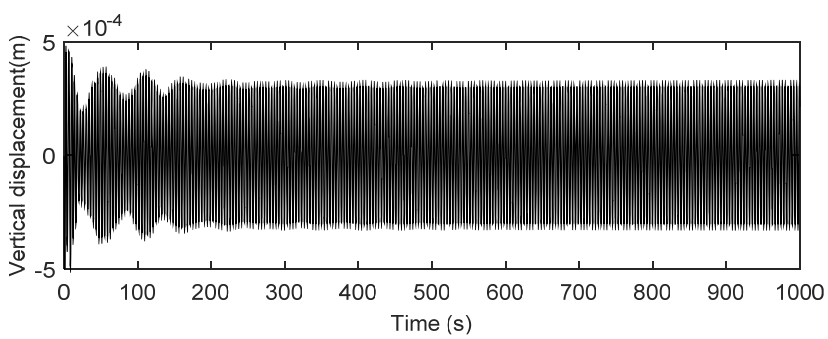

Fig. 3. Vertical displacement response of FM-C at mid-span (critical state, U=94.6m/s, ζ=0.5%)

Table 2. Flutter critical state comparison of the four models (ζ=0.5%)

Model	FM-A	FM-B	FM-C	FM-D	Result of Wind Tunnel Test(FM-C)
Critical flutter velocity (m/s)	94.4	94.6	94.6	94.5	95.1
Frequency(HZ)	0.2578	0.2578	0.2578	0.2578	-

To investigate the flutter synchronization characteristics and compare the effects of the different central buckles on the flutter stability, the phase differences of the vertical displacement responses between the mid-span and the other positions of the main girder were obtained by signal processing technology, as shown in Fig. 4. For the model FM-A, it can be found that the phase differences increases with the increase of the distance between the mid-span and the other positions, reaching the maximum of about 25 degree and is symmetrical about the mid-span. It indicates that the farther the distance is, the weaker the synchronization is. Comparing models FM-A, FM-B, FM-C and FM-D, it can be seen that the change pattern is disturbed due to the asymmetry of the central buckles of the three models and the different types of the central buckle have little effects on the phase difference. The central buckles increased the phase difference of the left side of the main span with the maximum up to 40 degree, resulting in the asymmetry of the phase difference about the mid-span. Thus, the asymmetric central buckles tend to disturb the synchronization of the vertical vibration of the main girder along the span, which is good for the flutter stability.

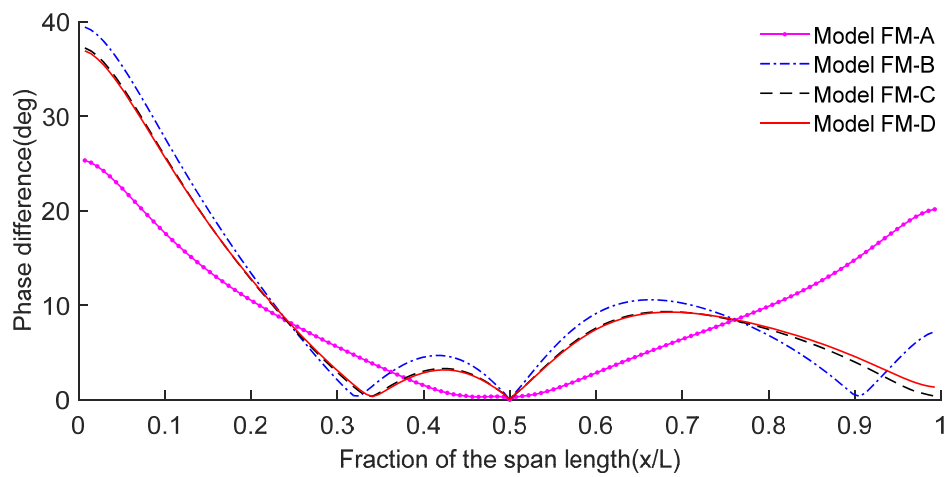

Fig. 4. Phase differences of the vertical displacement responses between the mid-span and the other positions of the main girder (critical flutter state, ζ=0.5%)

4. Conclusions

The rigid central buckle can largely increase the frequency of asymmetric torsion. The central buckles have negligible impact on the critical flutter velocity due to that the flutter mode of the Aizhai Bridge was coupled with the symmetric vertical bending and the symmetric torsion.

5. References

Gao Jian, Liu Gao, Zeng Yu. (2007), "Design of central buckle of Balinghe steel truss suspension bridge in Guizhou"/The 2007 China Bridge Academic Conference. Beijing: People's Transportation Press, 101-106. (in Chinese)

Xu Xun, Qiang Shizhong, He Shuanghai. (2008), "Influence of Central Buckle on Dynamic Behavior and Response ofLong-span Suspension Bridge Under Vehicle Group Excitation". *China Journal of Highway and Transport*, 21 (6): 57-63. (in Chinese)

Wang Hao, Li Aiqun, Guo Tong et al. (2009) "Accurate stress analysis on rigid central buckle of long-span suspension bridges based on submodel method", *Science in China Series E: Technological Sciences*, 52(4), 1019-1026.

Qin F J, Di J, Dai J, et al. (2013), "Influence of Central Buckle on Dynamic Behavior of Long-Span Suspension Bridge with Deck-Truss Composite Stiffening Girder". *Advanced Materials Research* , 838-841:1096-1101.

Wang Da, Deng Yang, Liu Yang, (2015) "Influence of central buckle on suspension bridge dynamic characteristics and driving comfort", *Journal of Central South University*, 22(8), 3108-3115.

Liu Zhongxiang, Guo Tong, Huang Lingyu, et al. (2017), "Fatigue life evaluation on short suspenders of long-span suspension bridge with central clamps". *Journal of Bridge Engineering*,22 (10): 04017074.

Xu Xun, Qiang Shizhong. (2010), "Influence of Central Buckle on Dynamic Behavior and Seismic Response of Long-span Suspension Bridge". *Journal of the China Railway Society*,32 (4): 84-91. (in Chinese)

Numerical Simulation of Flutter Instability of Lingding Suspension Bridge with LES Turbulence Model

Zhiwen Liu[1*], Zhengqing Chen[2], Guoping Xu[3], and Jun Xu[4]

[1] Hunan Provincial Key Lab forWind Engineering and Bridge Engineering, College of Civil Engineering, Hunan University, Changsha, China, e-mail: zhiwenliu@hnu.edu.cn
[2] Hunan Provincial Key Lab forWind Engineering and Bridge Engineering, College of Civil Engineering, Hunan University, Changsha, Hunan, China, e-mail: zqchen@hnu.edu.cn
[3] CCCC Highway Consultants Co., Ltd., Beijing, China, e-mail: guopingxu@hpdi.com.cn
[4] CCCC Highway Consultants Co., Ltd., Beijing, China, e-mail:x861@163.com

[*]:corresponding author

Keywords: suspension bridge; streamlined box girder; thin plate; flutter instability; LES

Abstract: In present paper, a novel numerical method with large-eddy simulation turbulence model (LES) based on user-defined functions (UDFs) and dynamic mesh techniques of ANSYS Fluent was presented. As a validation case, the numerical simulation of aero-elastic instability a thin plate with aspect ratio of 22.5 at 0° attack angle under smooth flow condition was conducted firstly. Thereafter the flutter instability of a bridge deck section of Lingding suspension bridge was investigated. The research results shown that the numerical prediction flutter critical wind speed of the thin plate and bridge deck section with safety barriers and guardrails agrees well with the experimental results separately. The two-dimensional LES turbulence model is suitable to model the aerodynamic characteristic of bridge deck with safety barriers and guardrails et al., which is of quasi-two-dimensional flow around the bridge deck.

1. Introduction

Aerodynamic performances of bridge deck, such wind loads, buffeting, vortex-induced vibrations, galloping and flutter stability, are the important issues for wind-resistant design of long span bridges. A lot of experimental investigations on flutter instability, identification methods of flutter derivatives of bridge decks were conducted by many researchers in the last five decades (Scanlan and Tomko, 1971; Sakar, Jones, et al., 1994; Jones, Scanlan et al., 1995; Singh, Jones et al., 1996). With the development of computational fluid dynamics (CFD), numerical simulations of aerodynamic performances of bridge deck were conducted in the last three decades. Bruno et al. conducted a study for evaluating the capability of 2D numerical simulation for predicting the vortex structure around a quasi-bluff bridge deck using laminar, Reynolds-Averaged Naviers-Stokes (RANS) turbulence models and LES model separately. The study confirms the importance of safety-barriers modeling in the analysis of bridge aerodynamics (Bruno, 2002). The fluid-structure interaction mechanisms due to wind action on either a stationary or a moving long-span bridge deck were investigated using the ALE formulation by Frandsen (Frandsen, 2004). Larsen and Walther (1998) investigated aerodynamic characteristics of five generic bridge deck sections with two-dimensional DVM. It should be mentioned that many researchers have investigated the aerodynamic performances of the main deck sections without subsidiary facilities on the bridge decks. As pointed by Bruno et al. (2003), it is

important for analyzing aerodynamics of the bridge decks to model subsidiary facilities. This paper presented a novel numerical method using two-dimensional LES turbulence model to investigate the aerodynamic performance of bridge deck section with subsidiary facilities.

2. Numerical method

2.1. Governing equations for fluids and bridge deck

The filtered equations of incompressible fluid can be written as follows,

$$\frac{\partial \rho}{\partial t}+\frac{\partial(\rho \overline{u}_i)}{\partial x_i}=0 \tag{1}$$

$$\frac{\partial}{\partial t}\left(\rho \overline{u}_i\right)+\frac{\partial}{\partial x_j}\left(\overline{u_i u_j}\right)=-\frac{\partial \overline{p}}{\partial x_i}+\upsilon \frac{\partial}{\partial x_j}\left(\frac{\partial \overline{u}_i}{\partial x_j}+\frac{\partial \overline{u}_j}{\partial x_i}\right) \tag{2}$$

where $i, j=1,2$ denote the Cartesian coordinate direction x, y, and the overbar denotes the spatial average over a grid volume (V) or the surface average over a cell face (i, j) of the volume. $\overline{p}$ is the filtered pressure, ρ is air density $\rho=1.225 kg/m^3$, υ is the uniform kinematic viscosity which is assumed constant with a value of $1.5\times10^{-5} m^2/s$ for air at 20^oC, u_i is the Cartesian components of the velocity field, and $\overline{u_i u_j}$ is the non-linear term. The non-linear term are given by Smagorinsky-Lilly model as

$$\rho\overline{u_i u_j}=\rho\overline{u}_i\overline{u}_j+2\mu_T\overline{S}_{ij}+\frac{1}{3}R_{kk}\delta_{ij},\ u_T=\rho(C_S\Delta)^2(2\overline{S}_{ij}\overline{S}_{ij})^{1/2},\ \overline{S}_{ij}=\frac{1}{2}\left(\frac{\partial \overline{u}_i}{\partial x_j}+\frac{\partial \overline{u}_j}{\partial x_i}\right) \tag{3}$$

where C_s is the sub-grid scale stress constant (taken here 0.1 as Ref.[14]) and $\Delta=(\Delta x\Delta y)^{1/2}$ defined by the grid spacing. The bridge deck is simplified as a model with two-degree of freedom system which mounted on elastic springs with viscous dashpots appropriate to the structural mode of vibration under consideration.

2.2. Modeling of fluid-structure interaction

A two-dimensional large eddy simulation of turbulent flow past the structures will be used to solve the equations of fluid. The dynamic mesh technique is employed to simulate the FSI of bridge deck under wind action. To analyze the structural responses of the bridge deck section with 2DOF under wind action, the equations of structural motion were integrated using Newmark-β method.

3. Numerical Results

3.1. Aerodynamic instability of thin plate

The numerical simulations of aero-elastic responses of the thin plate with aspect ratio of 22.5 under different wind velocities were conducted to validate the proposed method in present paper, as shown in Fig.1. The mass of the thin plate per unit length is $m=11.25 kg/m$. The mass

moment of inertia is $I_m = 0.2828 kg \cdot m^2 / m$. The circular frequencies of the vertical and torsional vibration modes are 12.11rad/s and 19.0rad/s separately. The damping ratios of the vertical and torsional vibration modes are 0.5%. After the grid and time step independence testing, the 0.0005s time step was choose for the further numerical simulation.

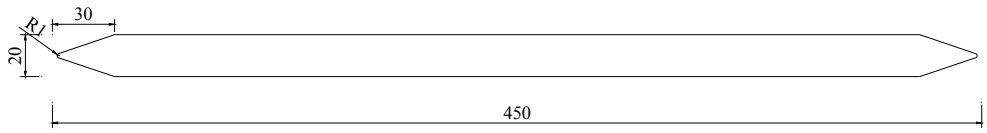

Fig. 1. Thin plate section (unit: mm)

Table 1. Flutter critical wind velocities of the thin plate

Parameters	LES (present paper)	Theory results	Experimental results(Xiang H.F. , 2005)
Flutter critical wind velocity, Vcr (m/s)	15.0~16.0	15.96	16.5
Flutter critical circular frequency (rad/s)	14.9~15.4	15.6	15.6

3.2. Aerodynamic instability of bridge deck section with safety barriers and guardrails

The bridge deck of Lingding Bridge (LDB), which is a three-span suspension bridge with a main span of 1666m and two side spans of 530m under construction in China. Figure 2 shows the general arrangement and the deck cross-section of the bridge. In order to compare with the wind test results, it is determined that the geometric scale ratio of the main beam section is 1/70, and the wind speed scale is 1/5. The numerical simulation parameters of the bridge deck section model are given in Tab.1.

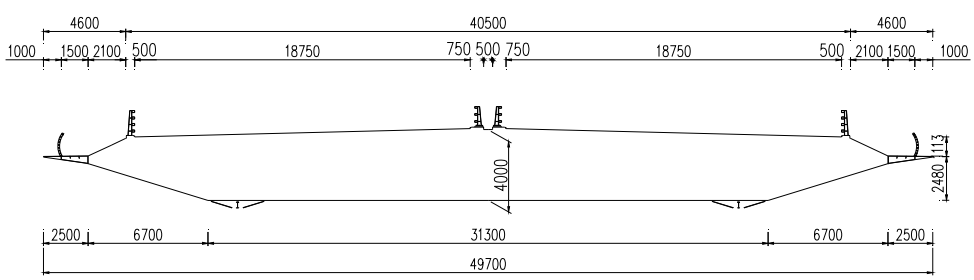

Fig. 2. Main deck cross section of LDB (unit: mm)

The grid near the deck section is divided into two parts. The triangular mesh is adopted in the deformation area near the deck section, and the structured grid is used in the outer area of the computation domain, so as to improve the quality of mesh generation. The first height of the grid close to the main deck section is about $4.0 \times 10^{-5} B$. The total number of the grid is 358871. The Smagorinsky constant is Cs=0.10. The time step is 0.0002s.

Table 2. Dynamic parameters of the LDB

The parameters and units	Bridge structure (Prototype)	Model Scale	Numerical model
Mass per meter, m (kg/m)	42.411×10^3	$1/70^2$	8.6553
Mass moment of inertia, I_m (kg.m^2/m)	9.838×10^6	$1/70^4$	0.4097
Vertical bending frequency, f_h (Hz)	0.1000	14	1.4000
Symmetry torsional frequency, f_α (Hz)	0.2228	14	3.1180
Damping ratio vertical bending mode, ξ_h (%)	0. 5	1	0.5
Damping ratio torsional mode, ξ_α (%)	0.5	1	0.5

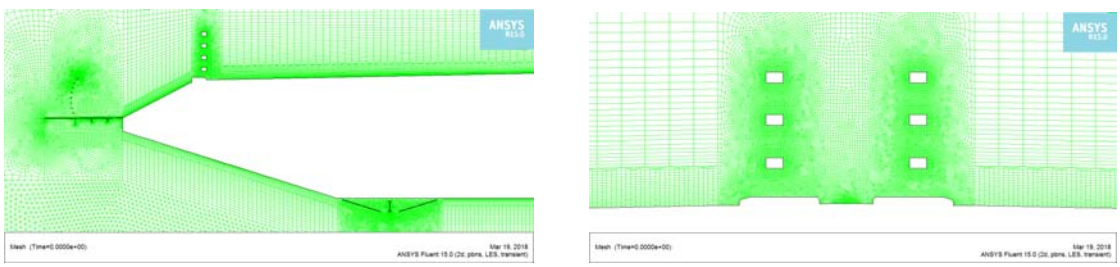

(a) (b)

Fig. 3. Grid of the LDB deck section with safety barriers and guardrails: (a) Grid near the windward of the bridge deck; (b) Grid near the central safety barriers

The time histories of the vertical displacements and rotational angles of the bridge deck section under 15.0m/s and 15.5m/s wind at 0° attack angle are given in Figure 4 separately. The numerical results and the wind tunnel experimental results of flutter critical wind speeds of the bridge deck section are given in Table 2. The numerical results agree well with the experimental results.

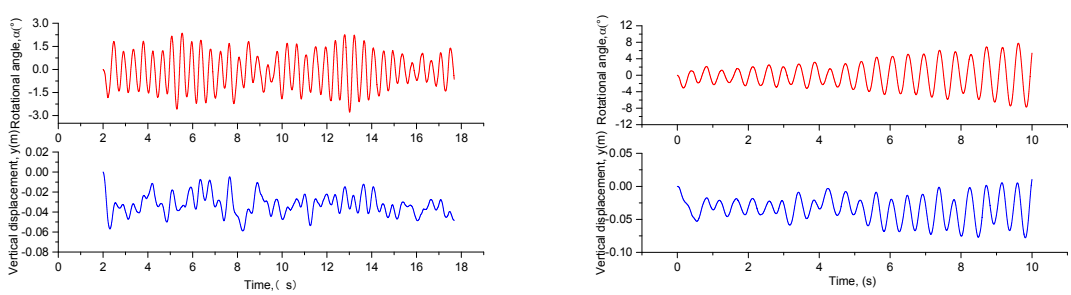

(a) (b)

Fig. 4. Wind-induced vibration responses of the bridge deck section under 15.5m/s and 15.0m/s wind at 0° attack angle: (a) V=15.0m; (b) V=15.5m/s

Table 3. Numerical and experimental results of flutter critical wind speeds of the bridge deck

Wind attack angle(o)	Flutter critical wind speed, Vcr (m/s)		Relative error (%)
	Numerical results	Experimental results	
0	77.5	74.9	3.47

4. Conclusions

The numerical simulation method of FSI of the bridge deck with two-dimensional LES turbulence model using dynamic mesh techniques is presented in this paper. The numerical prediction flutter critical wind speed of the thin plate and bridge deck section with safety barriers and checking car rails agrees well with the experimental results separately. It can be concluded that the two-dimensional LES turbulence model is suitable to model the aerodynamic and aero-elastic characteristic of bridge deck with safety barriers and checking rails et al., which is of quasi-two-dimensional flow around the bridge deck.

5. Acknowledgements

This research works has been supported by National Natural Science Foundation of China (No.51478180, 51778225). The authors fully acknowledge the support received.

6. References

1. Bruno, L., Khris, S. 2003. The validity of 2D numerical simulation of vortical structures around a bridge deck. Mathematical and Computer Modeling, Vol.37, 795-828
2. Frandsen J. B. 2004. Numerical bridge deck studies using finite elements, Part I : flutter. Journal of Fluids and Structures, Vol.19, 171-191
3. Larsen, A., Wather, J.H. 1998. Discrete vortex simulation of flow around five generic bridge deck sections. Journal of Wind Engineering and Industrial Aerodynamics, Vol.77 & 78, 591-602
4. XIANG Hai-fan, et al. 2005. Modern Theory and Practice on Bridge Wind Resistance. Beijing: China Communications Press (in Chinese)

Monitoring and NDT

A New Method for Vibration-Based Damage Detection in Structural Health Monitoring Using Autonomous UAVs

Efstathios Polydorou[1*], Des Robinson[2], Su Taylor[3], and Patrick McGetrick[4]

[1] Queen's University Belfast (QUB), Belfast; email: S.Polydorou@qub.ac.uk
[2] Queen's University Belfast (QUB), Belfast; email: des.robinson@qub.ac.uk
[3] Queen's University Belfast (QUB), Belfast; email: S.E.Taylor@qub.ac.uk
[4] Queen's University Belfast (QUB), Belfast; email: p.mcgetrick@qub.ac.uk

[*]: corresponding author

Keywords: bridge engineering; damage detection; unmanned aerial vehicles; vibration-based health monitoring; computer vision

Abstract: Increasing awareness of economic and social impacts on civil infrastructure through deterioration mechanisms and extreme events, has led to the need for the development of advanced methods to monitor the health condition of structures. To ensure the operational safety of infrastructure, structural health monitoring (SHM) systems have been developed and widely used in bridges and buildings, to better understand the structural response and damage identification under dynamic loads. Vibration-based Damage Detection (VBDD) is a global non-destructive evaluation technique, which is used to detect sudden changes of the dynamic characteristics of a structure subjected to an excitation source. In this way, the presence of damage at an early stage can be detected and located, which provides insights into the health condition of a structure as to whether the damage is at a dangerous level. With the recent advances in sensor technology, many contact-based and non-contact methods have been developed for damage detection, localization and quantification. The traditional VBDD technique is the use of accelerometer contact sensors, which require significant time and cost for cable installation, data acquisition and inspection. Non-contact methods such as static cameras, have limitations due to equipment immobility or physical obstacles (i.e. lakes, rivers) which increase the field of view. This is particularly prominent when implemented in high-rise buildings and long span bridges. Recent advancements in the aviation technology has led to the use of unmanned aerial vehicles (UAV) for the visual inspection of structures. UAVs are equipped with GPS and high-resolution cameras and have the ability to access hard to reach areas that would otherwise be dangerous for inspection measurements. This paper presents the experimental results of a new technique for vibration-based damage detection using unmanned aerial vehicles. The proposed method combines UAVs, computer vision and processing techniques for damage detection and assessment in beams. Cantilever beams of 3000 mm (length), 76 mm (depth) and 74 mm (width) were used in the experimental program. The beams were subjected to different changes in mass and damage configurations. The collected displacement time histories obtained using the drone and the high- speed camera were processed to obtain the acceleration responses. The results obtained show the potential use of drones to build reliable SHM systems as a cost effective and time processing solution for the monitoring long span bridges and structures.

1. Introduction

To ensure both safety and structural integrity, it is of paramount importance to monitor the health condition of structures by detecting the location and extent of damaged zones. Damage detection is mainly associated with loss in stiffness, which influences the dynamic properties of a structure and consequently the natural frequencies. Structural health monitoring (SHM) involves the monitoring of dynamic characteristics of structures using digital devices such as accelerometer sensors, microcontroller-based data acquisition systems etc. (Goyal and Pabla 2016; Wei et al. 2013). By utilizing these devices, it is possible to monitor the dynamic properties of structures such as modal frequencies, modal shapes and damping ratio. In many cases, the condition assessment of bridges, may require access to critical areas due to physical obstacles (i.e. lakes etc.) which would prevent the inspectors to undertake vibration measurements in different locations (Polydorou et al. 2018). A potential solution to these concerns is the use of unmanned aerial vehicles (UAVs), known as drones, equipped with high resolution digital cameras to measure the displacements and derive the acceleration responses (Hassanalian and Abdelkefi 2017). One of the major challenges for measuring the accelerations for assessing damage detection, is the stabilization of the UAV camera and the implementation of advanced image processing and computing algorithms. This paper presents the results of an experimental test series to assess damage detection on cantilever beams using UAVs, by developing a stabilization and image processing methodology. The frequency responses of healthy and damaged cantilever beams are presented and compared with those measured using a high-speed camera.

2. Experimental procedures

In this study, a cantilever timber beam was used with cross-section dimensions of 76 mm in depth and 74 mm in width and a length of 3500 mm. The cantilever beam was clamped at the one end using two steel grips whereas the other end was kept free for exciting the cantilever beam. The damage scenario considered in the experiments involved saw cuts in two locations of the beam, dimensions of 200 mm length and 30.8 mm depth (40% the depth of the beam). The saw cuts were located 120 mm and 170 mm away from the free end of the beam. The displacement versus time history was measured using a multi-rotor Phantom 4 Professional, which operated at a frame rate of 120 frames per second (fps) at a resolution of 1920x1080 pixels. The results obtained using the UAV were compared using a high-speed camera, operated at frame rate of 250 fps at a resolution of 1024x1024 pixels. As soon as the videos were recorded by the UAV, tracking algorithms and inverse analysis were used to stabilize the videos and the displacements were obtained using digital image correlation (DIC) algorithms. Fig. 1 shows the experimental setup during the tests.

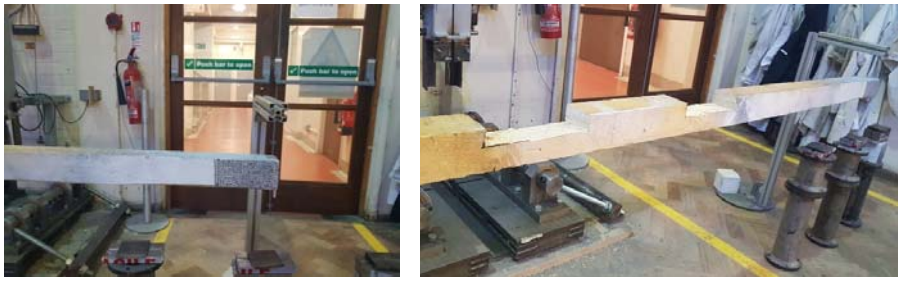

Fig. 1. Test setup used in the experiments

3. Discussion of the results

The displacement versus time histories recorded using the UAV and the high-speed camera were filtered using a low pass Butterworth filter at 11 Hz and double differentiation techniques were applied to obtain the acceleration versus time responses. The acceleration spectrum frequency domain was then studied using Fast Fourier Transformation (FFT). Fig. 2 shows the acceleration versus time response and the corresponding frequency spectrum of the healthy state of the cantilever beam, obtained using the high-speed camera.

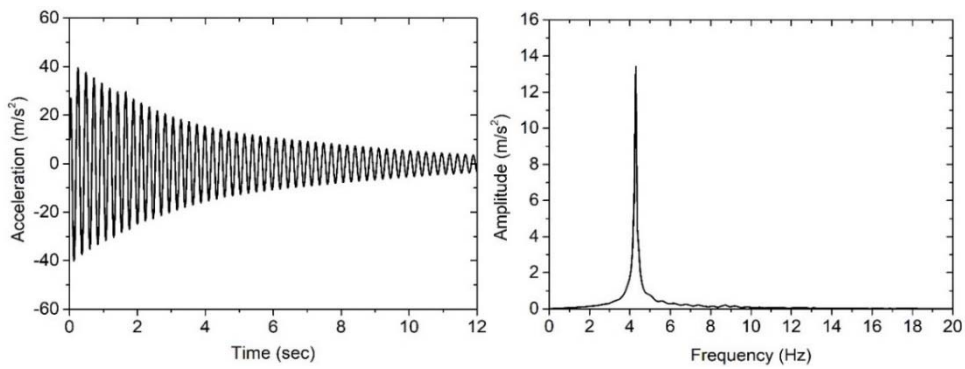

Fig. 2. Acceleration versus time history obtained using the high-speed camera

The analysis of the frequency spectrum showed that there is only one dominant frequency in the range below 11 Hz, representing the first vibration mode. The frequency of the undamaged beam was measured to be 4.287 Hz, which was validated using structural dynamics analytical calculations (Tedesco et al. 1999). The comparison of the frequencies between the high-speed camera and the UAV for the undamaged beam is presented in Fig. 3.

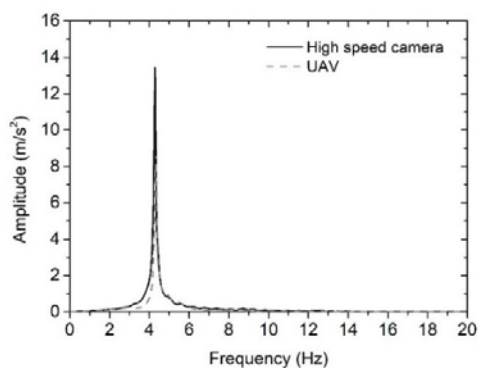

Fig. 3. Comparison of frequency responses using the high-speed camera and the UAV for the undamaged beam

The FFT revealed that the dominant frequency for the undamaged beam obtained using the UAV was 4.330 Hz, with a difference of 0.99% in comparison to the frequency obtained using the high-speed camera. Additionally, it was found that the accuracy in the frequency measurements was influenced by the movement of the UAV due to its flight stability. Therefore, stabilization of

the acceleration measurements played a major factor in eliminating any uncertainties that would lead in erroneous measurements. Fig. 4 shows the frequency spectrum of the damaged beam. The frequencies obtained using the high-speed camera and the UAV were 4.072 Hz and 4.084 Hz respectively, with a frequency difference of 0.29%. The change in stiffness was found to contribute to a change in the natural frequency for the first mode, with a difference of 5.85% between the undamaged and damaged beam, as obtained using the UAV. The percentage difference caused by the damage was around 0.26 Hz, which was bigger than the difference between the high-speed camera and the UAV.

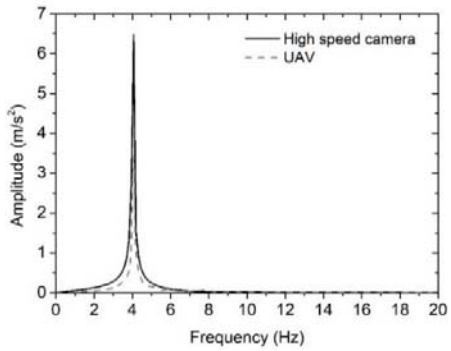

Fig. 4. Spectra of acceleration response with identified damage location measured using the high-speed camera and the UAV

4. Conclusions

In this paper, a camera vibration-based method was demonstrated using aerial unmanned vehicles to study the damage detection characteristics in cantilever beams. The natural frequency of 4.072 Hz measured by the UAV agreed with the frequency measured by the high-speed camera with a difference of 0.29%. The stabilization technique was found to significantly minimize the in-plane and out-of-plane translations and rotations for a single camera system mounted to the UAV. This technique combined with digital image correlation and a speckle pattern applied to the beam, revealed that the displacements and accelerations can be measured with satisfactory accuracy, with low signal to noise ratio. This study presented the efficiency of this method to measure the displacements by the UAV camera for vibration-based damage detection and provides a useful tool for its potential applicability in the field of structural health monitoring.

5. References

Goyal, D. and Pabla, B. S. 2016. Development of non-contact structural health monitoring system for machine tools, Journal of Applied Research and Technology, 14(4), 245–258.

Wei, L., Zhou, Z. D., Huang, J., and Tan, Y. G. 2013. FBG-based non-contact vibration measurement and experimental study, International Journal of Precision Engineering and Manufacturing, 14(9), 1577–1581.

Tedesco, J.W., McDougal, W.G., and Ross, C.A. 1999. Structural Dynamics: Theory and Applications, Addison Wesley Longman.

Polydorou, S., Robinson, D., Treanor, G., Taylor, S. and McGetrick, P. 2018. Use of visual unmanned aerial vehicles (UAVs) for bridge monitoring, Proceedings of the 10th International Conference on Short and Medium Span Bridges, Quebec City, Canada, 1-10.

Hassanalian, M. and Abdelkefi, A. 2017. Classifications, applications and design challenges of drones: A review, Progress in Aerospace Sciences, 91, 99-131.

Study on Stress Detection Method of Prestressed Steel Strands Based on Ultrasonic Guided Waves

Junchao Zheng[1], Zuohua Li[2*], Jun Teng[3], Chunkai He[4], Wei Lu[5], and Nanxi Liu[6]

[1] Harbin Institute of Technology, Shenzhen, China; email: zhengjunchao@stu.hit.edu.cn
[2] Harbin Institute of Technology, Shenzhen, China; email: lizuohua@hit.edu.cn
[3] Harbin Institute of Technology, Shenzhen, China; email: tengj@hit.edu.cn
[4] China Academy of Building Research Shenzhen Branch, Shenzhen, China; email: hechunkai@cabr.com.cn
[5] Harbin Institute of Technology, Shenzhen, China; email: lizuohua@hit.edu.cn
[6] Harbin Institute of Technology, Shenzhen, China; email: liu_nanxi@foxmail.com

[*]: corresponding author

Keywords: non-destructive testing; ultrasonic guided waves; stress detection; prestressed steel strands

Abstract: The safety of prestressed concrete structures, in which steel strands work as the main stress components and bear the complex load and erosion, directly involves the security of both environment and users. During the long term service, the stress state and damage degree of steel strands are related to the safety and durability of prestressed concrete structures. Therefore, it is of great significance to realize non-destructive and in-service measurement of stress in steel strands. In this paper, the theoretical analysis on the detection method of steel strands stress based on ultrasonic guided waves is carried out. For simplicity, the stress of the whole steel strand is approximately represented by the stress of a single center wire, and the problem of guided wave propagating in the multi-wire steel strand is simplified as the problem of guided waves propagating in a center straight wire. The influence of mechanical and geometric characteristics of prestressed steel strand on the selection of optimum excitation frequency of guided wave is studied theoretically. The corresponding relationship between the applied stress and the group velocity of the L (0, 1) mode of ultrasonic guided waves is established. For steel strands with different diameters, the theoretical analysis on stress detection of steel strands based on ultrasonic guided waves is carried out, concerning the optimum excitation frequency of guided wave. This paper shows the potential and the suitability of the ultrasonic guided waves method for evaluating the stress levels in the prestressed steel strands.

1. Introduction

The prestressed tendons in prestressed concrete structures mainly include prestressed steel wires, prestressed steel strands and prestressed reinforcements, all of which can be regarded as slender steel members. The most widely used prestressed tendons are seven-wire steel strands, which are made of six peripheral helical steel wires wrapped around the center straight steel wire with a certain lay angle. This geometric composition results in different tensile stress values of the center wire and helical wires of the seven-wire strand. However, through theoretical analysis and experimental verification, the stress values are close between peripheral helical steel wire and center straight wire under axial tensile condition (Chaki, 2009). In this paper, the problem of

guided wave propagating in multi-wire steel strands is simplified as the problem of guided waves propagating in slender circular bars. The sensitivity of longitudinal mode parameters to axial stress in low frequency range is concerned to discuss the feasibility of stress detection method of steel strands based on ultrasonic guided waves.

2. Theoretical principle

Although the structure of the seven-wire strand is more complicated than that of a single wire, the stress difference between the center straight wire and the peripheral helical wire is very small. Thus, the stress value of the center straight wire can be used to represent that of the whole steel strand approximately. In this way, the problem can be simplified to that of ultrasonic guided waves propagation in a slender circular bar, in which the acoustoelasticity will be used.

2.1. Longitudinal mode of ultrasonic guided waves in a circular bar

The center wire is regarded as an isotropic elastic cylinder. According to the Pochhammer-Chree frequency equation (Meitzler, 1961), the dispersion curve of the longitudinal mode of ultrasonic guided waves in an isotropic elastic cylinder with traction-free boundary conditions can be solved by the following three equations (Chen, 2001):

$$\frac{2\alpha}{a}\left(\beta^2+k^2\right)J_1\left(\alpha a\right)J_1\left(\beta a\right)-\left(\beta^2-k^2\right)^2 J_0\left(\alpha a\right)J_1\left(\beta a\right)-4k^2\alpha\beta J_1\left(\alpha a\right)J_0\left(\beta a\right)=0 \tag{5}$$

$$\alpha^2=\omega^2/C_L^{\ 2}-k^2 \tag{6}$$

$$\beta^2=\omega^2/C_T^{\ 2}-k^2 \tag{7}$$

where a is radius of center wire; k is wavenumber; J_0 and J_1 are Bessel function of the first kind of order 0 and 1, respectively. C_L and C_T are the longitudinal wave velocity and the transverse wave velocity of the infinite elastic solid under uniaxial tensile stress, respectively. According to equation (1) ~ (3), for given values of a , C_L and C_T , the dispersion curve of the L (0, 1) mode of ultrasonic guided waves can be obtained by numerical calculation, as shown in Fig. 1.

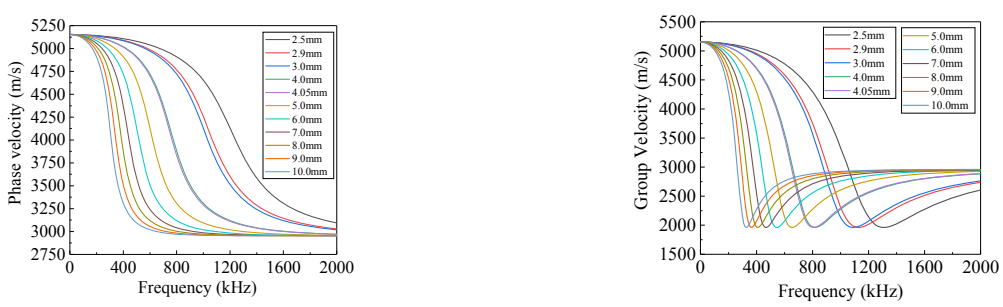

(a) (b)

Fig. 1. Phase velocity and group velocity dispersion curves of first longitudinal mode of steel circular bars with different diameters under non-stress (diameter changes from 2.5mm to 10.0mm): (a) Phase velocity dispersion curve; (b) Group velocity dispersion curve.

2.2. Theory of acoustoelasticity

The velocities of waves propagating along the waveguide, subjected to uniaxial tensile stress, are given (Murnaghan, 1937; Hughes and Kelly, 1953) as

$$C_T = \sqrt{\frac{\mu}{\rho} + \frac{4\lambda + 4\mu + m + \lambda n/(4\mu)}{\rho(3\lambda + 2\mu)}\sigma} \tag{8}$$

$$C_L = \sqrt{\frac{\lambda + 2\mu}{\rho} + \frac{\lambda + 2l + (\lambda + \mu)(4\lambda + 10\mu + 4m)/\mu}{\rho(3\lambda + 2\mu)}\sigma} \tag{9}$$

where ρ is mass density of the strand; σ is tensile stress applied on the center wire; λ and μ are Lame's elastic constants of propagation medium; l, m, and n are Murnaghan's third-order elastic constants of propagation medium. For the calculation, the material constants of previous study (Chen, 2001) are taken as follow:

ρ=7800kg/m^3; λ=115.9GPa; μ=79.9GPa; l=-248GPa; m=-623GPa; n=-714GPa;

The relationship curves between C_L, C_T and σ can be calculated, which are shown in Fig. 2.

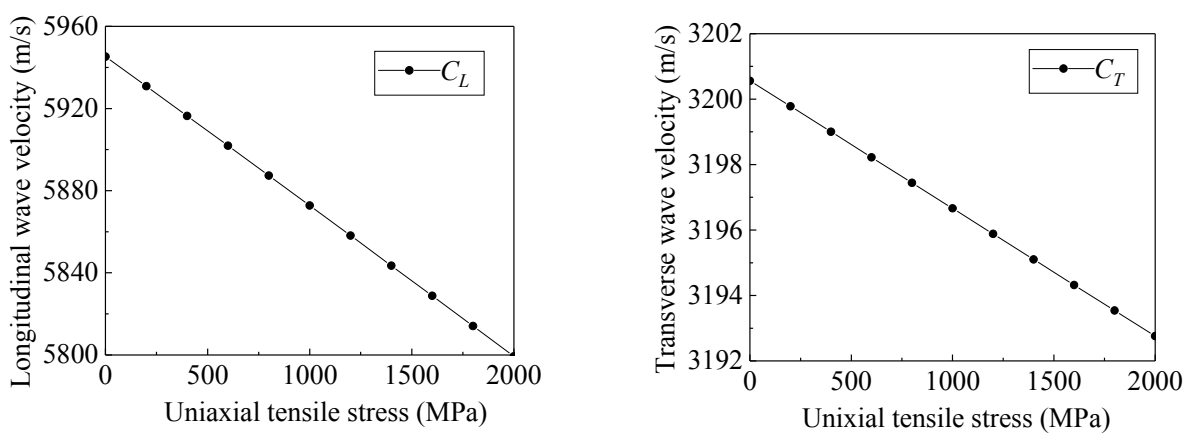

(a) (b)

Fig. 2. Relationship curves between wave velocity and uniaxial tensile stress: (a) Longitudinal wave velocity with stress; (b) Transverse wave velocity with stress.

From Fig. 2, it can be found that the relationship between the velocity of longitudinal wave and the uniaxial tensile stress is approximately linear in the stress range of 0~2GPa. The dispersion curves of longitudinal mode under different stresses will be obtained by using the C_L and C_T corresponding to the different stresses obtained in this section.

2.3 Acquisition of the relationship between stress and wave velocities of the center wire

By introducing the acoustoelastic effect, the C_L and C_T in the Pochhammer-Chree dispersion equation are adversely proportional to the uniaxial tensile stress. Thus, the dispersion curves corresponding to the center wire of certain diameter can be obtained under different stresses. The relationships between velocities of the L (0, 1) mode of ultrasonic guided waves and the uniaxial tensile stress applied on the center wire are obtained as shown in Fig. 3.

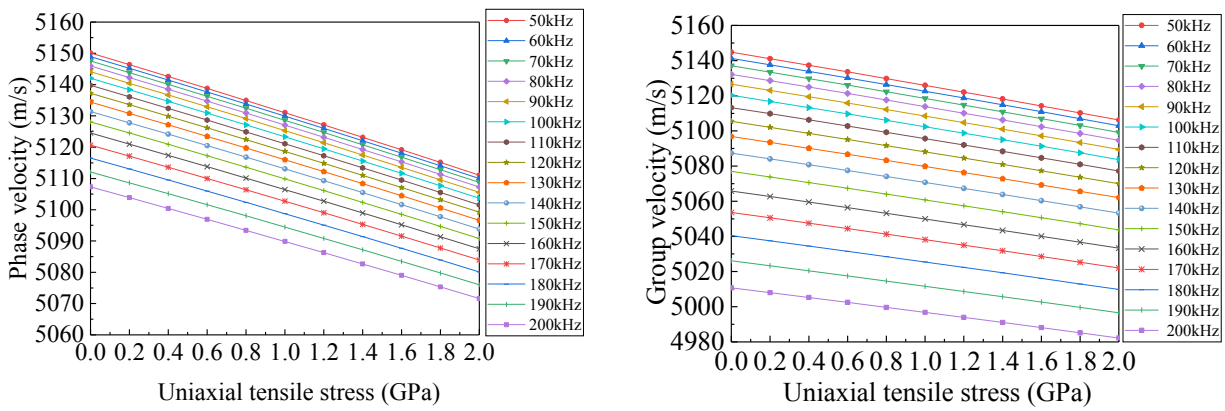

(a) (b)

Fig. 3. Relationship between wave velocities of first longitudinal mode of steel circular bars with diameter = 5mm and uniaxial tensile stress: (a) Relationship between phase velocity and stress; (b) Relationship between group velocity and stress.

Fig. 3 shows that both phase velocity and group velocity of the first longitudinal mode of guided wave have an approximate linear negative correlation with the uniaxial tensile stress in the stress range of 0~2GPa. Further work will be carried out on the experimental basis.

3. Conclusions

In this paper, the simplified problem that of ultrasonic guided waves propagation in a slender circular bar is solved in theory. Based on the calculated results, it can be found that with the increase of the diameter of the steel strand, the faster the wave velocity decreases with the increase of the frequency. When the theory of acoustoelasticity is introduced to study the relationship between stress and wave velocities, it can be found that both phase velocity and group velocity of the first longitudinal mode of guided wave have an approximate linear negative correlation with the uniaxial tensile stress in the stress range of 0~2GPa.

4. References

Chaki, S. and Bourse, G. (2009). Guided ultrasonic waves for non-destructive monitoring of the stress levels in prestressed steel strands. Ultrasonics, 49(2), 162–171.

Meitzler, A. H. (1961). Mode Coupling Occurring in the Propagation of Elastic Pulses in Wires. The Journal of the Acoustical Society of America, 33(4), 435–445.

Murnaghan, F. D. (1937). Finite Deformations of an Elastic Solid. American Journal of Mathematics, 59(2), 235.

Hughes, D. S. and Kelly, J. L. 1953. Second-Order Elastic Deformation of Solids. Physical Review, 92(5), 1145–1149.

Chen, H.-L. (Roger), and Wissawapaisal, K. 2001. Measurement of Tensile Forces in a Seven-Wire Prestressing Strand Using Stress Waves. Journal of Engineering Mechanics, 127(6), 599–606.

Tensile Force Measurement of PC Strands Using Ultrasonic Guided Waves Generated by Magnetostrictive Transducers

Hong Min Seung[1*], Jae-Ha Park[2], and Seung Hyun Cho[3]

[1] Center for Safety Measurement, Korea Research Institute of Standards and Science (KRISS), Daejeon, South Korea; email: shm@kriss.re.kr
[2] Center for Safety Measurement, Korea Research Institute of Standards and Science (KRISS), Daejeon, South Korea; email: jhpark4.0@kriss.re.kr
[3] Center for Safety Measurement, Korea Research Institute of Standards and Science (KRISS), Daejeon, South Korea; email: seungcho@kriss.re.kr

[*]: corresponding author

Keywords: tensile force; guided waves; seven-wire-strand; PC strands

Abstract: The tensile force of PC strands should regularly be measured to evaluate the safety of large structures such as bridges. For the measurement, a method based on a classical vibration testing is widely used in the fields, which is an indirect measurement method having relatively poor accuracy. Although EM sensors, which are based on the magneto-elastic phenomenon of ferromagnetic materials, can be used as an alternative, a bothersome calibration process is necessary before use. In this research, hence, we newly propose a method for measuring tensile force of PC strands with ultrasonic guided wave transduction. To this end, a magnetostrictive transducer technique is considered to generate and measure ultrasonic guided wave in a PC strand. The developed transducer is based on a magnetostriction phenomenon of ferromagnetic materials and is designed to be installed onto a seven-wire-strand without any bonding layer between the transducer and the specimen. The measured guided wave signals are obtained by varying the applied tensile force on a seven-wire-strand installed a universal testing machine. The signals are analyzed in the frequency domain and it can be observed that the specific frequency response varies according to the applied force. By doing so, a relation between the applied force and the frequency response of guided waves can be obtained as a characteristic function of a seven-wire-strand. With the obtained characteristics, we can estimate the applied tensile force of the seven-wire-strands having identical dimension and material property. To check the effectiveness of the proposed method, a series of experiment are carried out. The experiment results show that the measured tensile force with the proposed method agrees well with that of the load cell sensors in a universal testing machine. With further theoretical and experimental investigations, the proposed method will possibly be used in industrial field applications in the future.

1. Introduction

Evaluating tensile forces of PC strands is important to secure the safety of cable supported structures such as bridges. Especially, monitoring the change of the initially supplied tensile strength is a key element of structural maintenance. A vibration method based on a conventional modal testing is usually preferred to measure tensile forces of PC strands. However, this is an indirect measurement process and has relatively poor accuracy. Although elasto-magnetic

sensors are also used using a varying magnetization property according to the applied stress of strands, it always requires a time-consuming sensor calibration process before installation.
Hence, to overcome the disadvantages of the above-mentioned methods, a new tensile force measurement method of strands is proposed based on an ultrasonic guided wave transduction as a promising alternative. After analyzing the measured guided wave signals in the frequency domain, the applied tensile force can be extracted according to a specific relation. More importantly, a magnetostrictive transducer technique (Kwun et al. 1994) is considered to effectively generate and measure ultrasonic guided waves in PC strands. In this study, the proposed method is experimentally confirmed using a seven wire strand, which is a widely used component of strands, under various tensile loads. The results are shown to be in good agreement with the load cell data.

2. Proposed method

A pair of magnetostrictive transducers is developed for a pitch-catch guided wave transduction in a seven wire strand. One is used as a transmitter and while the other is used as a receiver. The transducers are specially designed and fabricated to be effectively installed on the strand. As shown in the experimental setup in Fig. 1(a), the strand is installed in the universal testing machine (UTM) to control and vary the tensile loads on the strand. Other specifications for experiments are depicted in Fig. 1(b). Using the experimental setup, a successful guided wave transduction can be obtained with respect to various loads as shown in Fig. 1(c) and (d). It can be seen that the guided waves are clearly measured in the time domain and those waveforms change according to the different loading condition.

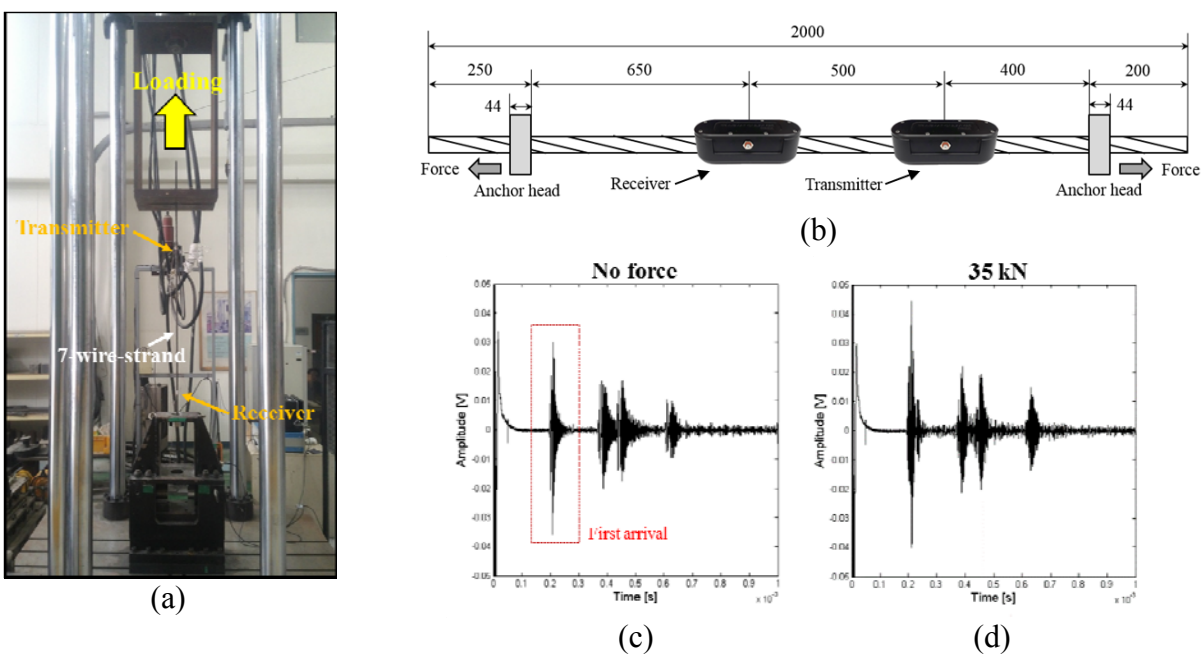

Fig. 1. Experimental setup and measured guided wave signals: (a) seven wire strand installed in UTM with the developed guided wave transducers; (b) details of the experimental setup; (c) measured guided wave signals under no loading condition and (c) 35 kN, respectively.

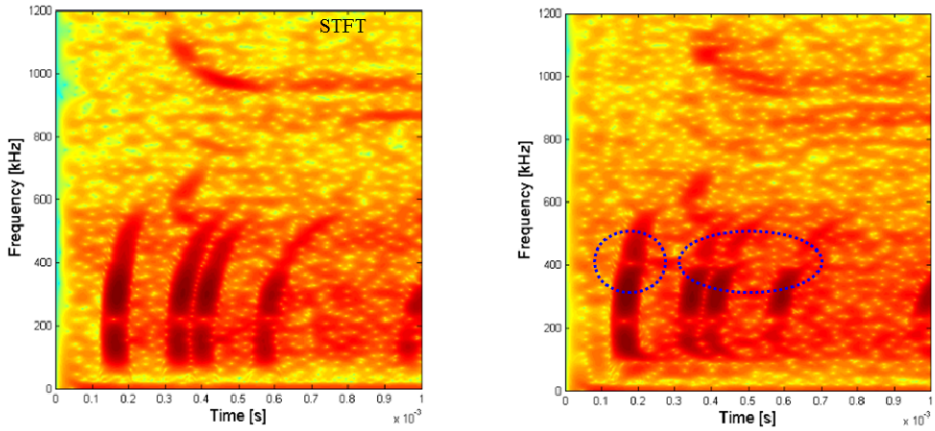

(a) (b)

Fig. 2. Short time Fourier transform results of the measured signals for (a) no loading condition and (b) 35 kN, respectively.

To examine the differences of the measured signals with various loading conditions, the frequency spectrograms based on the short time Fourier transform (STFT) are compared as shown in Fig. 2. As indicated dotted circles in Fig. 2(b), a suddenly weakened response is observed at a specific frequency range by supplying 35 kN tensile load on the strand. After analyzing this phenomenon for various load conditions, a specific relation between the frequency characteristics of guided waves in the strand and tensile loads can be achieved. Using this relation, the tensile force is extracted from the measured signals. The measured tensile force values based on the proposed method are in good agreement with those of load cell installed on the UTM.

3. Conclusion

A new approach for measuring tensile forces of a seven wire strand is proposed ultrasonic guided wave transduction. To facilitate the proposed method, a magnetostrictive transducer is specially designed and installed to generate and measure guided waves in a seven wire strand. To confirm the effectiveness of the proposed method, experiments are carried out using UTM for inducing various tensile load conditions of the strand. Through the experimental investigation, the validity of the propositions is successfully confirmed by comparing the measured tensile force values with the load cell data indicated in the UTM. To employ the method for practical situation, further analytical investigations and utilizations for various types of strands will be conducted.

4. References

Kwun, H and Teller, C.M. 1994. Magnetostrictive generation and detection of longitudinal, torsional, and flexural waves in a steel rod, Journal of the Acoustical Society of America, 96(2), 1202-1204.

Structural Health Monitoring: Predicting the Thermal Response and Identifying Anomalous Behavior of a Cable-Stayed Bridge Using Artificial Neural Networks

Jian Chen[1*], Harry W. Shenton III[2], and Michael J Chajes[3]

[1] Dept. of Civil & Env. Eng., Univ. of Delaware, Newark, DE, USA; email: jianchen@udel.edu
[2] Dept. of Civil & Env. Eng., Univ. of Delaware, Newark, DE, USA; email: shenton@ udel.edu
[3] Dept. of Civil & Env. Eng., Univ. of Delaware, Newark, DE, USA; email: chajes@udel.edu

[*]: corresponding author

Keywords: Structural Health Monitoring; Artificial Neural Network; Thermal Response Prediction; Gaussian Distribution; Threshold Values

Abstract:
Structural health monitoring (SHM) is increasingly being used to monitor the structural condition of various civil infrastructures. When doing this, an important question that needs to be addressed is when does anomalous data represent changes in condition of the structure being monitored. For long-span bridges, it is well known that thermal effects produce significantly larger deformations than those caused by live loads. This paper examines the thermal induced response of the Indian River Inlet Bridge (IRIB), a cable-stayed bridge in southern Delaware in the US, and how it can be used to assess bridge performance. Temperature-based (TB) methodologies have been used to successfully predict the thermal response of experimental trusses in a controlled laboratory environment (i.e. no effects of live loads on the structure). In this study, to demonstrate that the methodology is applicable to in- service bridges whose response includes "noise" from live loads (i.e. traffic and wind), data collected from the IRIB over a 3-year period was evaluated. Within the TB framework, three artificial neural networks (ANNs) were trained and used to predict bearing displacements of the IRIB due to thermal loads. The effectiveness of the ANNs was evaluated, and statistical damage detection thresholds were defined by analyzing prediction errors (PEs). The results suggest that using the ANN algorithm within a TB framework can be effective at accurately predicting bearing displacements and at setting threshold values for anomalous behavior detection.

1. Introduction

Bridges are an essential component of highway infrastructure systems. The majority of US bridges were built before the 1950s and are reaching the end of their design service life. Transportation agencies evaluate bridge safety through visual inspection and the computation of bridge load ratings. The visual inspections are expensive, time-consuming and rely heavily on qualitative information. The advent of robust SHM systems presents the opportunity to gain useful quantitative information in a relatively economic manner and use it to improve bridge evaluations. In long-term SHM, daily and seasonal temperature variations cause the majority of the observed deformations in long-span bridges (Koo et al. 2013). There are two approaches to deal with temperature effects contained in SHM data. The first approach removes the temperature effects by treating them as undesirable noise in the measurements. This approach makes it harder to identify anomalous behavior (Laory et al. 2011). The second approach,

referred to as utilizes the temperature effects as being the primary factor effecting bridge responses. TB methodologies have been studied both using numerical models and through experiments (Yanold et al 2015; Kromanis et al. 2017), and the results indicate that TB methodologies can accurately predict thermal response as long as the thermal loading is known.
This paper presents a model-free damage detection approach based on an ANN algorithm in combination with TB methodology. The model-free approach allows engineers to analyze SHM measurements directly without the need for a complex finite element model. Instead, it requires that the ANN algorithm is trained using in-service data collected from the "healthy" or undamaged structure. In this way, it can identify anomalous response data that can represent a change in condition from the "healthy" or "normal" state. This paper focuses on temperature and related bearing displacement data. The trained ANNs are shown to accurately predict the IRIB bearing displacements, and effective threshold values for detecting anomalous behaviors are determined. The results can be used by infrastructure owners to improve the practical application of SHM.

2. Structural health monitoring system in IRIB

A comprehensive SHM system was installed on the IRIB, a cable-stayed bridge in southern Delaware in the US, when it was built in 2012. The system, which collects data 24/7, includes 70 strain sensors, 44 accelerometers, 9 tiltmeters, 3 bearing displacement sensors, 2 anemometers and 16 chloride sensors. Displacements at each of the two expansion joints (north and south end) and at the one moveable pylon bearing (south pylon) are measured using Cleveland Electric Labs displacement transducers (the displacements are labeled as D_E1, D_E2 and D_E3). Temperature data across the bridge is collected by 18 temperature sensors. The data used in this work was continuously collected from March 2015 to March 2018. Since this is very early in the life of the bridge, it is considered to represent the "normal" state.

3. Artificial neural networks (ANN)

ANNs are mathematical models inspired by neurophysiology. The basic processing unit of the ANN is a neuron. In a neuron, the arriving inputs, multiplied by the connection weights, are first summed and then passed through a transfer function to produce the output for that neuron. Neurons are interconnected with each other by summing the inputs from previously connected neurons. Once the summing inputs exceed a specific limit value, the neuron is activated. It then generates a new input and passes it on to the network. Based on known inputs and outputs, a training process for bearing displacement prediction, called supervised learning, can be executed. In each training step, the prediction error (PE) is used to adjust the weight (w_i) in the network. This type of supervised training algorithm is called a backward propagation network. Quantitative threshold values are desired to distinguish normal and abnormal behaviors of a bridge in practical applications. When using ANNs to make predictions, the distribution of resulting PEs should follow a normal distribution, should have a zero mean and a constant standard deviation (i.e., sigma). Both 3-sigma and 6-sigma are common criteria for determining if a PE is statically significant. These two criteria can be used to establish threshold values for PEs of bearing displacements. A quantile-quantile (Q-Q) plot is used to test the normality of the PEs. When the PEs follow a normal distribution, the points on the Q-Q plot lie on a positive diagonal line.

4. Analysis

4.1. Data pre-processing

Data pre-processing is an essential step in generating high accuracy ANNs. The raw SHM datasets are pre-processed to eliminate data outliers and noise. Inter-quantile range (IQR) analysis is employed to classify if a value at the center of the moving window is an outlier. The detected outliers are replaced by corresponding median values in the moving window. The second step is to remove the "noise" in the raw data. The primary noise in the raw thermal response data is caused by live loads. Due to the lack of traffic monitoring data, and the complexity of the bridge, it is a challenge to remove the live load noise. Since temperature changes slowly, using average displacement values over a time window is an effect way to minimize the live load effects on the data. By comparing training results coming from 10 minute, 1 hour, and 6 hour averages, data averaged every hour led to the most accurate predictions. Data normalization is another step to be used to facilitate the learning process of ANNs. Doing so allows all inputs in a comparable range to be scaled. The most popular normalization method, which is utilized in this paper, involves centering the inputs on zero by subtracting the mean from the inputs and dividing the data by its standard deviation. In case of information leak, the calculated mean and standard deviation of normalization are only computed based on training data.

4.2 ANNs training

For each bearing displacement sensor, a unique ANN is trained and tested using the pre-processed data. To evaluate the bearing condition, about 1 month of continuous data is reserved at the end of the three year data set and analyzed by the trained ANNs. The left pre-processed data is divided into training data, validation data and test data. All the training, validation and test data, although mutually exclusive, are composed of measurements spread over the entire data. 70% of the data is used as training data, 20% as validation data, and 10% data as test data. The Root Mean Standard Error (RMSE) is a common and powerful error metric to evaluate the performance of the ANNs. The RMSE is given by Eq. 1.

$$\text{RMSE} = \sqrt{\sum_{i=1}^{N}(Output_i - Actual_i)/\ N} \qquad (1)$$

where $Output_i$ is the bearing displacement predicted by ANN; $Actual_i$ is the actual measured bearing displacement; and N is the number of measurements in the test data.

5. Results

Three ANNs were trained separately for the three bearings. The performance of the ANNs is evaluated using the RMSE. As shown in Table 1, the RMSEs for the bearing displacements are 1.79, 1.76 and 1.15. Compared to the range of bearing displacements, all of the predicted error percentages (i.e., RMSE/ displacement range) are quite small. The results show that the ANNs can accurately predict bearing displacement with the knowledge of actual temperatures and further indicates that the TB methodology is feasible for in-service structures.

Table 1. ANN result summary

Gauge No.	Displacement Range (mm)	RMSE	Predicted Error (%)
D_E1	[-59.1, 138.7]	1.79	0.90%
D_E2	[-141.0, 9.3]	1.76	1.17%
D_E3	[-22.0, 41.0]	1.15	1.83%

The PEs of each ANN were analyzed to establish threshold values representing "normal" behavior. The nature of the PEs distribution was first evaluated using the Q-Q plot technique. For example, the PEs of D_E2 approximately follow a straight line and so the PEs are assumed to be normally distributed (Fig.1). In evaluating SHM data, 3-sigma and 6-sigma values are suggested for use in determining two warning thresholds, yellow and red respectively. The yellow threshold is meant to indicate a situation that is rare and should be noted while the red threshold indicates a level that so rarely should rarely occur that more immediate investigation of the bearings is warranted. The PEs for D_E2, along with corresponding yellow and red warning thresholds, are illustrated in Fig 2. Since all of the PEs for D_E2 are within the yellow warning threshold limit, it is concluded that no anomalous structural behavior has occurred. The normal state threshold values for all three bearings are summarized in Table 2.

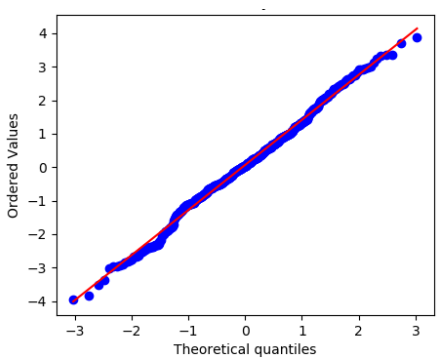

Fig. 1. Q-Q plot for PEs of D_E2

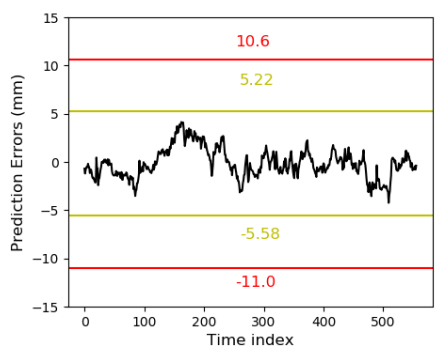

Fig. 2. PEs of D_E2 with threshold values

Table 2. Threshold values summary

Gauge No.	3-Sigma (99.73%)		6-Sigma (99.99%)	
	Lower	Upper	Lower	Upper
D_E1	-4.95	5.37	-10.1	10.5
D_E2	-5.58	5.22	-11.0	10.6
D_E3	-3.25	3.59	-6.67	7.01

6. Conclusion and future work

This paper has shown how the TB methodology, combined with ANNs, can effectively predict bearing displacement of a long span bridge due to thermal effects. The paper has also shown how threshold values for continuous SHM data can be established and used to indicate structural performance anomalies that should be more closely monitored or investigated. The methodology includes two phases. The first phase is training the neural networks to accurately predict the bearing displacement. The second phase is analyzing PEs and establishing threshold values using Gaussian distribution analysis. From the results, the following conclusions can be drawn:

1. TB methodologies can be successfully applied to in-service structures.
2. ANNs can be used to accurately predict bearing displacement due to temperature effects.
3. Effective threshold values can be set and used to identify anomalous structural behaviors.

For the IRIB, while the ANNs accurately predicted the bearing displacement, and statistical threshold values were defined, no anomalous response was observed (as would be expected with a relatively new bridge). Future work will focus on damage simulation to investigate the sensitivity of the method in identifying anomaloaus data corresponding to structural deterioration.

7. References

KOO, K.Y., BROWNJOHN, J.M.W., LIST, D.I. and COLE, R., 2013. Structural health monitoring of the Tamar suspension bridge. *Structural Control and Health Monitoring,* 20(4), pp. 609-625.

KROMANIS, R. and KRIPAKARAN, P., 2017. Data-driven approaches for measurement interpretation: analysing integrated thermal and vehicular response in bridge structural health monitoring. *Advanced Engineering Informatics,* 34, pp. 46-59.

LAORY, I., TRINH, T.N. and SMITH, I.F.C., 2011. Evaluating two model-free data interpretation methods for measurements that are influenced by temperature. *Advanced Engineering Informatics,* 25(3), pp. 495-506.

YARNOLD, M.T. and MOON, F.L., 2015. Temperature-based structural health monitoring baseline for long-span bridges. *Engineering Structures,* 86, pp. 157-167

New Tools for Evaluating Concrete Bridge Decks: High-Speed Acoustic Impact-Echo and Vertical Electrical Impedance Testing of the Longest Bridge in Utah

W. Spencer Guthrie[1*], Tenli Waters[2], Jared S. Baxter[3], Lorin Hendricks[4], and Brian A. Mazzeo[5]

[1] Department of Civil and Environmental Engineering, Brigham Young University, Provo, Utah, USA; email: guthrie@byu.edu
[2] Department of Civil and Environmental Engineering, Brigham Young University, Provo, Utah, USA; email: tenliwaters@gmail.com
[3] Department of Electrical and Computer Engineering, Brigham Young University, Provo, Utah, USA; email: jaredbaxter5@gmail.com
[4] Department of Electrical and Computer Engineering, Brigham Young University, Provo, Utah, USA; email: maxwellhendricks@gmail.com
[5] Department of Electrical and Computer Engineering, Brigham Young University, Provo, Utah, USA; email: bmazzeo@byu.edu

[*]: corresponding author

Keywords: acoustic impact-echo; bridge deck; chloride; concrete; vertical electrical impedance

Abstract: High-speed acoustic impact-echo and vertical electrical impedance testing devices have been recently developed at Brigham Young University as new tools for rapidly evaluating the condition of concrete bridge decks. Both devices are capable of testing a full lane width at speeds that do not require stationary traffic control. While the acoustic impact-echo device detects the presence of delamination in the bridge deck surface, the vertical electrical impedance device measures the quality of protection against chloride ingress provided to the top mat of reinforcing steel by any deck overlays, the original concrete cover, and any epoxy coatings on the steel itself. These tools were utilized in a project in which the longest bridge in the state of Utah, USA, was evaluated to determine the appropriate scope of repair.

1. Introduction

Understanding the degree of deterioration of a bridge deck is important for determining appropriate maintenance and rehabilitation strategies (Guthrie et al., 2007). To this end, two new tools have been developed at Brigham Young University for rapidly evaluating the condition of concrete bridge decks. These include high-speed acoustic impact-echo and vertical electrical impedance testing devices (Mazzeo et al., 2017; Mazzeo and Guthrie, 2018), which are both capable of testing a full lane width at speeds that do not require stationary traffic control. While the acoustic impact-echo device detects the presence of delamination in the bridge deck surface, the vertical electrical impedance device measures the quality of protection against chloride ingress provided to the top mat of reinforcing steel by any deck overlays, the original concrete cover, and any epoxy coatings on the steel itself.

The objective of this work was to demonstrate the utility of both devices for rapidly collecting impact-echo and impedance data and using the results to strategically guide chloride concentration sampling and coring at selected locations. In particular, these new tools were used

to determine the appropriate scope of repair for the longest bridge in the state of Utah, USA. The bridge, which was constructed in two phases in 1970 and 1976, was 9.8 m wide and 944 m long. An approximately 30-mm-thick concrete overlay was placed in 1976, and a thin-bonded polymer overlay about 10 mm thick was applied to the bridge deck in 2005. With 28 spans, the bridge carries one lane of eastbound traffic and one lane of westbound traffic over several railroad tracks and roads, as well as a river.

2. Procedures

The testing, which occurred during the summer of 2017, involved several steps. High-speed acoustic impact-echo testing, which did not require any form of traffic control, was performed five times in each of the two lanes, with deliberate transverse offsets being applied in successive passes to ensure that a majority of the surface area within each lane was interrogated. For a given pass, each of the six channels, which were about 0.5 m apart in the transverse direction as illustrated in Figure 1(a), applied two impacts every 25 to 50 mm in the longitudinal direction for an estimated total of more than 433,000 impacts per pass. Each pass along the length of the bridge required between 78 and 84 seconds, corresponding to a range in speed from 45 to 48 km/h. With customized data collection and analysis software, the acoustic impact-echo testing data were analyzed immediately, and maps of the deck were generated to identify areas of delaminated and intact concrete.

Under a moving traffic control operation, vertical electrical impedance testing was then performed. With four probes positioned across the majority of the width of each lane, as shown in Figure 1(b), data were collected at a rate of approximately 98 samples per second per probe and at a frequency of 189 Hz, consistent with recommendations developed in previous research (Argyle, 2014). Vertical electrical impedance testing in each of the two lanes required 28 and 25 minutes, respectively, corresponding to a range in speed from 2.3 to 2.4 km/h. Maps of the deck were generated to identify areas of low and high protection against chloride ingress.

(a) (b)

Fig. 1. Deck testing using (a) acoustic impact-echo and (b) vertical electrical impedance devices

Beyond six randomly selected test locations on the surface of the bridge deck, an additional 13 test locations were strategically selected for chloride concentration testing and coring, under a stationary traffic control plan, based on the results of the acoustic impact-echo and vertical electrical impedance testing. All combinations of delaminated and intact concrete and low and high impedance magnitudes were deliberately included to allow investigation of a wide range of possible deck conditions. Chloride concentrations were determined at 25-mm depth intervals to a target depth of 150 mm, and the concrete overlay thickness and the depth of delamination, where observed, were measured from the cores.

3. Results

The results of the deck testing included acoustic impact-echo, vertical electrical impedance, chloride concentration, and core data. Example maps of the acoustic impact-echo and vertical electrical impedance data are presented in Figure 2 for one of the 150-m sections of the deck. As needed for display and analysis purposes, a cubic interpolation function was used to generate values between the locations of actual measurements in the maps. The spatial accuracy of the data was approximately 1.2 m in both the longitudinal and transverse directions based on the limitations of the differential global positioning system used for data collection. In the acoustic impact-echo map, the results are overlaid on an aerial image of the deck, and green highlighting shows the specific paths that were interrogated. The magnitude of the acoustic response is represented with a red circle of varying diameter at locations of suspected delamination; therefore, an increasing circle diameter indicates an increasing probability of delamination but not necessarily a larger delamination size. When multiple paths overlap, which is indicated by an increased intensity of green highlighting, and the same delamination is identified more than once, the intensity of the red highlighting increases to show greater confidence in the existence of that delamination. The acoustic impact-echo data indicate that 11 percent of the total interrogated deck area was delaminated and that the delaminations were distributed relatively uniformly across the deck.

In the vertical electrical impedance map, areas characterized by lower reinforcing steel protection are marked in red, while areas characterized by higher reinforcing steel protection are marked in blue. Although universal thresholds for impedance magnitude have not been established, the data can be divided into three categories. Specifically, impedance magnitudes less than 4, between 4 and 5, and higher than 5 were defined as “low,” “medium,” and “high,”

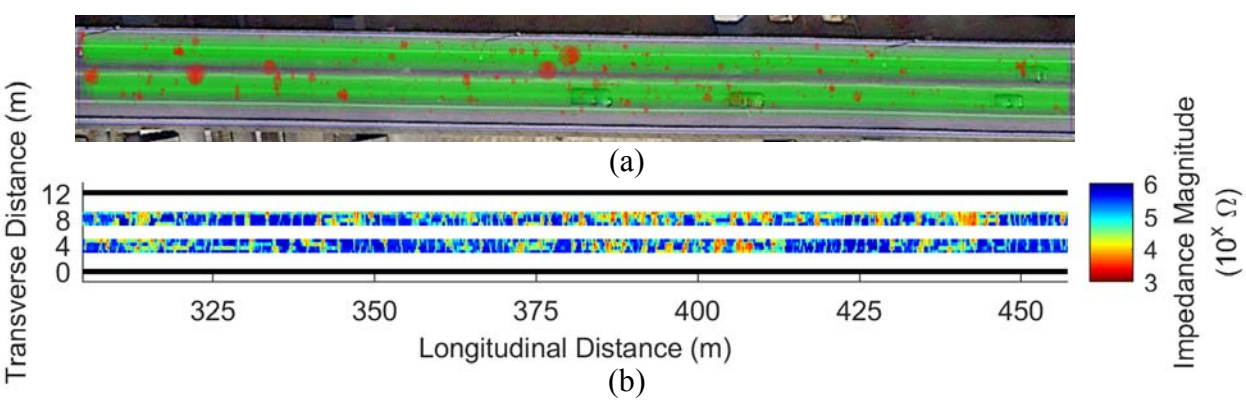

Fig. 2. Example maps for (a) acoustic impact-echo data and (b) vertical electrical impedance data

respectively (an impedance magnitude of 5, for example, indicates an actual impedance value of 10^5 Ohms). With these definitions, 10, 29, and 62 percent of the total interrogated deck area exhibited low, medium, and high impedance magnitude, respectively.

Although the average chloride concentration at the top mat of reinforcing steel was determined to be comparatively low at 0.5 kg of chloride per cubic meter of concrete from the results obtained for the randomly selected test locations, seven of the 19 test locations evaluated in this project had chloride concentrations at the top mat of reinforcing steel that equaled or exceeded the generally accepted threshold of 1.2 kg of chloride per cubic meter of concrete at which corrosion of black bar is initiated. Nonetheless, the data suggest that the corrosion process had not yet advanced to the stage at which the formation of rust at the top mat of reinforcing steel was governing the occurrence of delamination on the bridge deck. Instead, the results of coring indicate that delaminations were originating at or near the interface between the 30-mm-thick concrete overlay and the original concrete deck surface. Thus, while corrosion-induced delaminations may have existed on the bridge deck, a main cause of delamination appeared to be a separation of the concrete overlay from the underlying deck.

4. Conclusion

This work demonstrated the utility of the new acoustic impact-echo and vertical electrical impedance devices for rapidly collecting data and strategically guiding chloride concentration sampling and coring at selected locations. The condition of the bridge deck was characterized using the collected data, which were then utilized to develop an appropriate repair strategy for the bridge deck.

5. Acknowledgments

The authors acknowledge HDR, the Utah Department of Transportation, and the Utah Science Technology and Research Initiative for funding.

6. References

Argyle, H. M. 2014. Sensitivity of electrochemical impedance spectroscopy measurements to concrete bridge deck properties, M.S. thesis, Brigham Young University, Provo, UT.

Birdsall, A. W., Guthrie, W. S., and Bentz, D. P. 2007. Effects of initial surface treatment timing on chloride concentrations in concrete bridge decks, Transportation Research Record, 2028, 103-110.

Guthrie, W. S., Linford, E. T., and Eixenberger, D. 2007. Development of an index for concrete bridge deck management in Utah, Transportation Research Record, 1991, 35-42.

Mazzeo, B., Baxter, J., Barton, J., and Guthrie, W. S. 2017. Vertical impedance measurements of concrete bridge deck cover condition without a direct electrical connection to the reinforcing steel, AIP Conference Proceedings, 1806, 080004.

Mazzeo, B. A., and Guthrie, W. S. 2018. Algorithms for highway-speed acoustic impact-echo evaluation of concrete bridge decks, AIP Conference Proceedings, 1949, 030010.

Inspection of Quality of Concrete of Load-Bearing Structure and Use of New Materials for Reconstruction, Bridge across VLTAVA River at Zvikov

Stanislav Rehacek[1*], David Citek[2], and Jiri Kolisko[3]

[1] Klokner Institute, Prague, Czech Republic; email: stanislav.rehacek@cvut.cz
[2] Klokner Institute, Prague, Czech Republic; email: david.citek@cvut.cz
[3] Klokner Institute, Prague, Czech Republic; email: jiri.kolisko@cvut.cz

[*]: corresponding author

Keywords: Bridge; Visual Inspection; Compresion Strength; Carbonation; UHPC

Abstract: This paper is introducing results of diagnostic survey of bridge no. 121-007 across Vltava river near Zvikov, focusing on assessment of quality of concrete mix used for load-bearing structure of the bridge after more than 50 years of operation and assessment of reconstruction works (monolithic assembly of central joints of main fields) executed in 1996.

1. Description of the Structure

The bridge is situated on the Zvíkovské podhradí - Kučeř road over the Vltava river valley. The bridge was constructed still before the filling of the artificial lake created by the Orlík Dam at the beginning of the 1960s, and it was put into operation in 1963. The four-span bridge was constructed by using the cantilevered concrete work construction method from the main central pillars which were constructed still in the original non-risen river bed. The edge pillars of the bridge stand on the river banks. The span between the central pillar and the edge pillars is 84 metres, between the edge pillar and the support it is 42 metres. The bridge is approximately 253 metres long. The height of the road above the original Vltava river water level oscillates from 70 to 75 metres [3, 4].

Bridges constructed by using the cantilevered concrete work construction method with joints in the middle of the spans were most frequently used in the 1960s. In the course of time it was clear that the long cantilevers tend to drop because of concrete creeping. For this reason, the joints in the middle of the spans were cancelled on the bridge in 1996, and for structural stress reasons new joints were carried out in the bases of edge pillars (P2 and P4). A part of this renovation was also installation of free pre-stress cables into individual chambers. The cables are placed in a wrapper tube (PE Ø 90 x 5.4 mm). The cables with a length of 130.6 m are alternated above the central pillar (P3). There are altogether 6 cables in each of the chambers, always 3 along each wall. They are conducted above each other, in the alternation place (P3 pillar) they are arranged side by side for the reason of anchorage into the transverse beams [5].

2. Visual Inspection of the Bearing Structure

The visual inspection of the bearing part of the bridge structure was carried out within the framework of the construction and technical surveys. The visual inspection was made from the MOOG platform, type MBI 70-1/S.

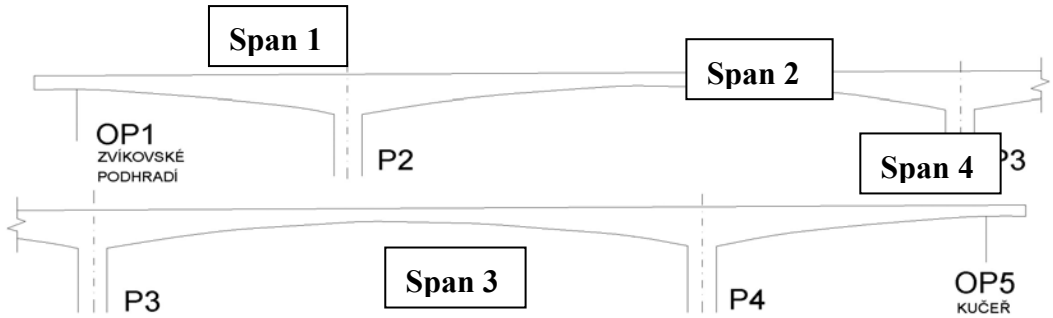

Fig. 1. Marking of individual parts of the bridge structure.
(OP = support; P = pillar)

The most visible failures revealed by the visual inspection include:

a) Concrete surface degradation especially at the cantilever ends, in these places the concrete cover layer of the reinforcement falls off, which is associated with subsequent surface or even medium corrosion of the exposed reinforcement.
b) On the sides and lower faces of the chambers and on the lower face of the cantilevers it is possible to see leachates caused by leaking, especially in the area of construction joints. In these areas it is possible to register leachates of the binding material. Occasionally it is also possible to observe vertical cracks on the surface of the chambers (sides) and on the cantilevers, with a width of 0.05 – 0.15 mm, very rarely even 0.2 mm. These cracks are very likely to correspond with the position of the reinforcement and its possible corrosion. On concrete surfaces (chambers, cantilevers) it is occasionally possible to see gravel pockets and places where concrete was not sufficiently compacted during construction.
c) On external areas (lower face and sides of the chambers and lower face of the cantilevers) it is occasionally possible to observe reinforcement with very small or zero coverage, and it is possible to observe surface or even heavy corrosion of this reinforcement. This corrosion concerns, however, concrete reinforcement. The pre-stress reinforcement is placed in major depths, and therefore it is highly probable that it is not affected by corrosion.
d) Inside the chambers, especially in the upper face (top) it is possible to observe reinforcement with very small or even zero coverage, and this reinforcement is subject to surface, locally even heavy corrosion there.
e) Occasionally it is possible to find vertical cracks on the anchoring transversal ties, the crack width being 0.05 - 0.15 mm, in one place up to 0.25 mm.
f) On internal surfaces of chambers it is possible to clearly see leachates caused by infiltrations (probably due to previous lack of tightness of the water-proofing system), especially in the area of dilatation and work joints. At the time of visual inspections these infiltrations were inactive.
g) A joint is situated in the middle of the spans 2 and 3; this joint has become monolithic and is treated with screeding material. No failures have been found in this area (cracks, deformations, concrete crushing etc.).
h) No significant failures have been found in the middle of the chamber in the area of the monolithic joint in the middle of the spans 2 and 3 (cracks, concrete crushing, deformations etc.).

3. Concrete

3.1. Concrete compression strength – summary

Test core holes (Ø approx. 75 mm) were used for the purpose of destructive tests of concrete compression strength. Non-destructive tests of concrete compression strength were carried out on reinforced-concrete structures of the bridge, internal and external faces of the chambers. The tests were deployed evenly along the structure.

Table 1. Summary of concrete compression strength test results

Diagnosed structural elements		Concrete compression strength (MPa)		Variation coefficient v*	Strength classes, i.e. concrete marks according to different standards	
		Test mean value	Characteristic		ČSN EN 1992	Documentation requirement [3, 5] Mark (class)
Chambers	non-destructive	59.3	55.1	4.3	C 50/60	400 (C 30/37)
	destructive	60.6	55.6	11.6	C 50/60	

From the concrete compression strength tests it is possible to state that concrete of the above stated structures is satisfactory and markedly exceeds concrete requirements according to the design documentation provided [3, 5].

4. Measurement of forces in free pre-stressing reinforcement Cables

Since during renovation of the bridge over the Vltava river no H90-HC elasto-magnetic sensors were installed on free pre-stressing cables, as it is the case on the bridge over the Otava river, it was necessary to wind a new sensor in this case. If the value of relative sensitiveness of the EM sensor is known, it is possible to determine, quite simply and exactly, the deviation of the force in arbitrary cables of the same type from the force in the reference cable in which the force value is known. For this purpose it is necessary to install the reference EM sensor on the reference cable (in this case it is necessary to additionally wind it thereon) and to measure the magnetic flux (modern apparatuses already measure the magnetic flux directly), if possible in multiple work points. Then the same EM sensors should be wound onto the cables in which it is necessary to find out the value of the force with regard to the reference cable, and then only the flux values are to be compared.

Ob the basis of measurements carried out on the bridge over the Vltava river it is possible to state in general as follows:

a) The force in the K23 cables on the bridge over the Vltava river is, within the framework of the measurement uncertainty (approx. +/- 5% due to the dispersion of magnetic properties of cables and because of the temperature) the same as in the K23 cables on the bridge over the Otava river.
b) It was necessary to link the measurement on the bridge over the Vltava river to measurement of free cables on the bridge over the Otava river from which it is possible to state in general as follows:

c) The results of force measurement on both the ends of the freely conducted K23 and K24 cables confirm their right function. The forces in the sections measured diminished on average by 44 kN between 1994 and 2015.
d) With regard to the measurement methodology used in 1994 (the EM sensors were not equipped with an embedded thermometer yet, the measuring apparatus did not have a self-calibration function) it is necessary to count on measurement uncertainty of about +/- 70kN and on a temperature influence. Since the cable temperature during measurement on 11 May 2015 is some 15 ° C (estimation) lower than the temperature at the time of cable stressing, the force values measured are probably higher (by 50 to 100 kN) than the actual force in the cable. The reference sensor is unable to exclude the temperature influence and dispersion of elasto-magnetic characteristics of cables.
e) The change in the pre-stressing force found out in the section measured is smaller than the uncertainty of this type of measurement, which is caused by the type of the measurement apparatus and temperature influence.

5. Use of modern Materials during rehabilitation

The diagnostics of the structure provides the structural engineer and the investor with ground materials for the subsequent method of the structure rehabilitation. The actual rehabilitation of the bridge structure can be carried out in many ways. The extent and method of rehabilitation depends on the nature of the structure and its aim is to increase its durability and lifetime. At present, Ultra – High Performance Concrete (UHPC) tends to be used always more and more often for such rehabilitation interventions in the world. This cement-composite, fine-grain material with minimum content of pores, homogeneous structure features high durability, lifetime and excellent material properties. UHPC compression strength is 150 MPa and higher. From the viewpoint of reinforcing or rehabilitation of structural details this material is suitable especially thanks to its favourable consistence. It is possible to modify the mixture and to optimise it as self-compactable, self-levelling as well as thixotropic. In order to ensure tensile properties and residual strength after occurrence of a crack, the mixture is reinforced with dispersed reinforcement in the form of steel or plastic fibres. In the case of rehabilitation of bridge structures, the material is used in several ways. A rather frequently used method is rehabilitation and reinforcing of pillars. The unconsolidated and degraded concrete layer is removed from the existing pillars and the UHPC envelope is applied onto the surface. With regard to excellent cohesion of both materials, material properties, resistance to effects of frost and defrosting chemicals this layer forms a protective envelope and increases the structure durability. The surface layer of the elements reinforced this way increases also resistance to a possible impact of a vehicle.

Another manner of use of UHPC in the case of rehabilitation and reinforcing of bridge structures is exchange or reinforcing of the bridge decking. The application method is very similar as in the case of pillars. The unsatisfactory bridge decking or a part thereof is removed and replaced with a layer of highly resistant UHPC. This layer is, after regrinding, either directly ascendable for vehicles (U.S.A.) or it serves as a base for insulation and ordinary bridge superstructure (Europe). In special cases it is possible to use UHPC also as pouring compound for making the structure monolithic in the places of supports, joints or for coupling of prefabricated elements of the structure. In these cases the matter concerns an individual design with a maximum use of all

excellent properties – compression strength, residual tensile strength, consistence and especially durability. The material has been developed in the Czech Republic for last 10 years. The experience from new UHPC structures starts to be used now in a greater extent in the case of rehabilitations and reinforcing of structures. Also in the case of the described bridge one of the variants is rehabilitation of structural parts just by making the joints monolithic with the help of UHPC.

6. Conclusion

Overall assessment of the bridge structure condition:
In general it is possible to state that bearing structures do not have any obvious structural deficiencies.

a) With regard to the time of construction of the bridge, mainly external surfaces of the concrete of the chambers and cantilevers are locally degraded on the surface.
b) On the sides of the chambers and on the lower face of cantilevers it is possible to see irregularities arising due to shifting/deformation of the formwork, as well as horizontal and vertical work joints, in the surroundings of which cement grout flowed out, which led to the exposure of gross aggregate. On the sides of the chambers and on their lower face it is possible to find places where cement grout overflowed due to the lack of tightness in the formwork. These defects can be classified as workmanship defects.
c) In-depth degradation of concrete and heavy corrosion of concrete reinforcement occur only on a very rare basis (cantilevers, external surfaces of chambers).
d) In the area of the joints situated in the middle of the spans 2 and 3 which were made monolithic we did not find any significant visible defects which would indicate development of earlier deflection (before making them monolithic and installation of free pre-stressing cables in 1996) in this area.
e) The structural change in operation of the bearing structure made in 1996 fulfilled its mission.
f) Free cables laid additionally meet their function and the change in the pre-stressing force decrement detected is within the range of tolerances and measurement precision.
g) It is possible to state that the condition of the bridge structure found out currently does not affect the load bearing capacity of the bridge.

7. Acknowledgements

This contribution is the result of the research supported by the grant projects of Ministry of Industry and Trade, No: FV 20472.

8. References

[1] Technical report no.: 1500 J 073 - Construction and technical research supporting the bridge structure no. 121-007, Bridge across Otava river, Klokner Institute, CTU in Prague, 06/2015.
[2] TP 72: Diagnostic survey of bridges PK, Pontex spol s r. o., December 2008.
[3] Bridge leaflet: Bridge across Vltava river in Zvikov, Bridge no. 121-007, 1 page, submitted by the Client.
[4] The bridge inspection, Bridge no. 121-007, Bridge across Vlatava river, Pisek district, made by Správa a údržba silnic Jihočeského kraje (Roads management and maintenance - South-Bohemia region, december 2013.

[5] Scanned drawings (plan view, cross sections and details) total of 44 pages, ProMo spol. s r.o., the project of reconstruction of the bridge across the Otava near Zvikov, a project to supply competition in May 1993, submitted by the client representative Bc. Pavla Pulcová.

Bridge Engineering Institute Conference 2019 (BEI-2019)
Honolulu, Hawaii, USA, July 22-25, 2019

Non-Destructive Evaluation Tests Using Elastic Wave Methods for Existing RC Deck Slabs Reinforced with Steel Plate Bonding

Shin Suzuki[1*], Koki Terasawa[2], Shinichi Hattori[3], and Toshiro Kamada[4]

[1] Osaka University, Osaka, Japan; email: shin_suzuki@civil.eng.osaka-u.ac.jp
[2] Osaka University, Osaka, Japan; email: Terasawa@civil.eng.osaka-u.ac.jp
[3] Osaka University, Osaka, Japan; email: Hattori_Shinichi@civil.eng.osaka-u.ac.jp
[4] Osaka University, Osaka, Japan; email: kamada@civil.eng.osaka-u.ac.jp

[*]: corresponding author

Keywords: impact elastic-wave method; RC deck slabs; steel plate bonding method

Abstract: RC deck slabs of road bridges strengthened with steel plate bonding method entail a problem of difficulty in visual investigation from the bottom. In this study, the impact elastic wave method was adopted as a non-destructive technique to detect cracking and other defects within a RC slab, with tests being conducted on the slab of an actual bridge strengthened with steel plates. Measurement was made from the top and bottom surfaces of the RC slab. As to the impact elastic wave measurement from the bottom surface, the consistency between the test results and the results of analysis on a 3D model using finite elements was confirmed. The authors then proposed an effective evaluation technique by utilizing the differences in frequency responses, which vary depending on the depth of the damaged layer, based on the results obtained from measurement on both sides of the slab.

1. Introduction

Steel plate bonding onto the bottom surfaces of RC slabs is a method of strengthening road bridge slabs widely used in Japan. However, this method makes it difficult to carry out visual inspection from the bottom side of slabs. It is therefore strongly desired to develop a new inspection technique to allow detection of damage occurring within RC slabs. In these circumstances, research is under way on non-destructive techniques for effective detection of cracking and delamination within RC slabs, which adversely affect their load-bearing capacity and durability. However, few studies have conducted tests on slabs bonded with steel plates. With this as a background, the authors applied the impact elastic wave method to the top and bottom surfaces of a RC slab of an actual bridge with steel plate bonding to investigate the possibility of detecting internal damage.

2. Experiment overview

2.1. Slab under test

Horizontal cracking in RC slabs generally tends to occur at the level(s) of either or both of the upper and lower reinforcement (Figure 1). It was therefore considered effective to investigate horizontal cracking by the impact elastic wave method both from the top and bottom surfaces. Therefore, measurement was conducted from the top and bottom surfaces of the bridge under test, Bridge A, located along a major road in Kobe, Hyogo Prefecture. Figure 2 shows this continuous steel plate girder bridge. As shown in Figure 3, the RC slab of Bridge A was strengthened with

steel plate bonding approximately 18 years ago. The bridge was subsequently subjected to detailed inspection, with the results posing concern over progressed damage. It was therefore decided to conduct research by nondestructive testing. In this study, the research covered the PA-PB span measuring 30.100 m in length and 27.500 m in width. The slab thickness was 190 mm. The design strength of concrete was f'_{ck} = 24 N/mm^2. The thickness of steel was 4.5 mm. Epoxy resin was injected at the interface with the bottom surface of the RC slab.

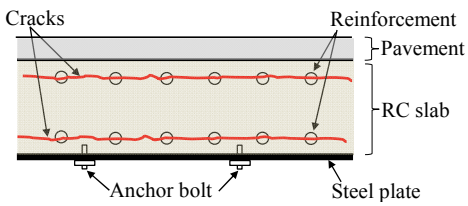

Fig. 1. Property view of cracks

Fig. 2. Situation of bridge A

Fig. 3. Condition of steel plate

2.2. Measurement from the top surface of the slab

Elastic wave measurement from the top surface of the slab was carried out by tightly attaching an acceleration sensor on the top surface of the pavement and striking a point near the sensor with a small steel hammer to input elastic waves. An acceleration sensor with a flat frequency response sensitivity at 3 Hz to 30 kHz was used in this study. The elastic waves generated by the blow repeat multiple reflections between the top and bottom surfaces, demonstrating a specific dominant frequency that corresponds to the slab thickness. The depth of the slab or horizontal cracking can be estimated by determining the frequency profile from the received time-series waveform by fast Fourier transformation and reading the peak frequency recognized on the obtained spectrum[1)]. Measuring points were basically set at 1 m intervals in the bridge axis and transverse directions on each of the lanes in the span. Twenty longitudinal measurement lines were set on 6 lanes (approximately 3 lines per lane). With 30 transverse measurement lines, the measurement points totaled 600 on the span. Note that the slab was drilled at 10 points showing clear peaks on the spectra to confirm the presence/absence of horizontal cracking. The elastic wave propagation rate of concrete was measured using the drilled cores.

2.3. Measurement from the bottom of the slab

Measurement from the bottom of the slab was conducted on a mobile work platform in regard to the driving lane where the slab is assumed to be under heavier loads due to heavier traffic with relatively large vehicles. Hammering tests were conducted beforehand on the areas around the measurement points to ascertain contact between the steel plate and concrete, and measurement was carried out where the steel plate is in contact with concrete. Impacts were applied using steel balls 9.6, 12.5, or 19.0 mm in diameter, while the same acceleration sensor as that used on the top surface received the elastic waves near the impact points.

3. Test results

3.1. Measurements on the top surface of the slab

Figure 4 shows a contour diagram of the depth of defects calculated from the peak frequency of the received wave spectrum at each measurement point. Though no peak corresponding to the upper level of reinforcement was found in the received wave spectra, 88 out of the 600 points

(14.7%) showed peaks corresponding to the lower level reinforcement. The areas of 160 ≤ D < 205 correspond to horizontal cracking near the lower level reinforcement. In the span under analysis, defects were found to be dispersed over the entire area. In the range where defects were suspected by impact testing, horizontal cracking was actually found to exist by drilling cores at six points. Figures 5 and 6 show as examples the received spectra at Points A and B, respectively, where horizontal cracking was recognized (the values beside the red arrows in the figures represent the estimated depth of horizontal cracking). Note that the elastic wave propagation rate of concrete was 3,200 m/s. The depth of horizontal cracking estimated by the impact elastic wave method at the above-mentioned measurement points is given in Table 1 in comparison with the actual crack depth measured by drilling.

3.2. Measurement from the bottom surface of the slab

Prior to actual testing, impact response analysis was carried out based on finite elements to ascertain the frequency characteristics of received waves when the impact elastic wave method was applied from the bottom surface of the slab across a steel plate. Figure 7 outlines the model used for the analysis. The size of concrete portion was 1,000 mm in length, 1,000 mm in width, and 200 mm in thickness. An epoxy layer and steel plate 4 mm and 4.5 mm in thickness, respectively, are placed on top of the concrete. An anchor bolt is driven to a depth of 50 mm in the center of the model. Horizontal cracking is provided at different depths of 40 mm to 200 mm (equivalent to sound concrete) from the bottom of concrete, with the increment being 10 mm. Figure 8 and Table 2 show the input waveform of impact elastic waves and physical properties of the materials, respectively. Assuming an impact from a steel ball of 12.5 mm in diameter, a pulse wave with a contact time of 60 μs is set as the input waveform. Both the input and output points of waveforms are set on the steel plate. The output is assumed to be acceleration waveforms with an output time interval of 1 μs and an output point number of 10,000. Frequency analysis was conducted by applying fast Fourier transformation to time history waveforms from which the time between 0 to 75 μs was excluded to eliminate the effect of surface waves resulting from the impact. Figure 9 shows a typical spectrum of received waves demonstrating a peak frequency. Figure 10 shows the frequencies that showed clear peaks on the spectra. In the range of the

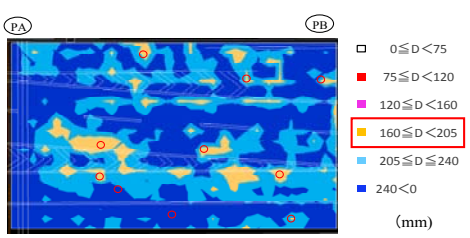

The red circle in the figure shows the hole drilling point.

Fig. 4. Contour map of damage depth

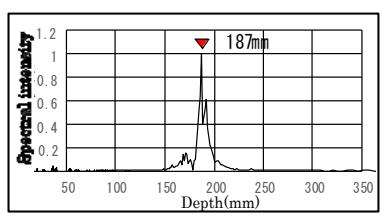

Fig. 5. Received spectrum (Point A)

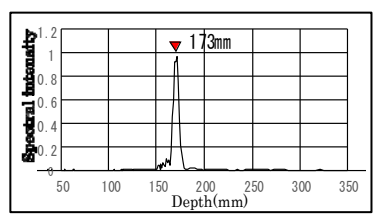

Fig. 6. Received spectrum (Point B)

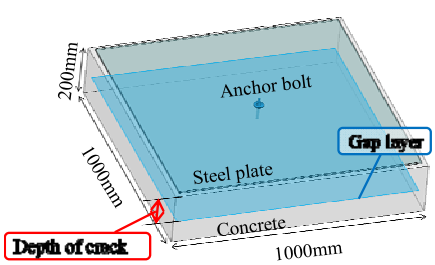

Fig. 7. Analysis model

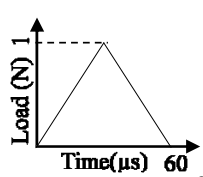

Fig 8. Input waveform

Table 1. Measured and estimated value

	Core No.	Measured depth of cracks(mm) a	Result of investigation(mm) b	Difference (mm) b-a
1	B	180	187	7
2	C	165	173	8

Table 2. Physical properties

	Density (g/cm3)	Elastic modulus (GPa)	Poisson's ratio
Concrete	2 .3	30	0.2
Steel	7.85	200	0.3
Epoxy resin	1 .2	1.5	0.34

crack layer depth of 40 to 100 mm (the depth of lower reinforcement is roughly 45 mm), the peak frequency was found to increase as the crack depth decreased. It is therefore inferred that, when horizontal cracking exists near the lower reinforcement of the slab, the peak frequency tends to be higher than that of a thoroughly sound area. This is apparent by comparison with the peak frequency at a crack depth of 200 mm, which is equivalent to the thickness of a sound slab shown in Fig. 11. In view of this analysis results, the results of field investigation are described as follows: Since the measurement from the bottom surface was conducted after the investigation from the top surface, the presence of defects was known beforehand. For this reason, a relatively sound area and an area with possible cracking in the PA-PB span were taken as the subjects. Figure 11 shows the results of measurement at three and two points selected from the sound and possibly cracked areas. Twenty strikes were applied to each measurement point. Since the data scattered, the data from 10 strikes were extracted by the cross-correlation technique. Figure 11 shows the averages of 60 strikes on the sound phase and 40 strikes on the possibly cracked area.
This figure reveals that the peak frequency tends to be higher at points with horizontal cracking than at sound points regardless of the steel ball diameter. This tendency is particularly significant with a steel ball diameter of 12.5 mm. This is presumably because the wavelength of elastic waves input by a steel ball of this size is suitable for inducing multiple reflections between the bottom surface of the slab and horizontal cracking.

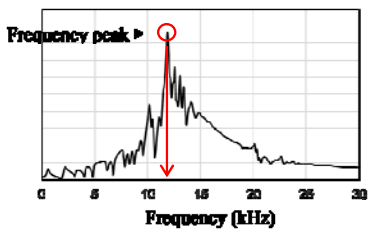

Fig. 9. Example of frequency spectrum

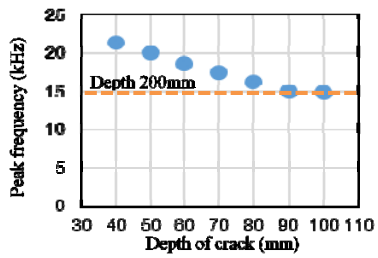

Fig. 10. Analysis result

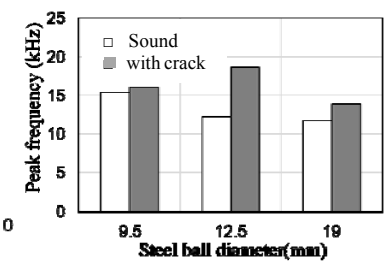

Fig. 11. Peak frequency

4. Conclusion

The results of this study are summarized as follows:

(1) The results of tests from the top surface of the RC slab by the impact elastic wave method agreed relatively well with the results of core drilling.

(2) The depth of horizontal cracking can be roughly ascertained in an appropriate manner by the measuring method adopted in this study.

(3) The presence of horizontal cracking near the level of the lower reinforcement of the slab (around a depth of 45 mm from the bottom) was confirmed.

(4) In the investigation from the bottom surface of the RC slab with steel plate bonding, the authors were able to see a possibility of estimating the state of internal damage by devising the method of inputting elastic waves and an appropriate evaluation index for received waves, as well as comprehensively evaluating the results of measurement both from the top and bottom surfaces.

5. References

1) S. Uchida, T. Kamada, K. Yamamoto, H. Mae and H. Onishi, "Effect of Impact Manners on Detection of Horizontal Cracks in RC Slabs by Impact-Elastic Wave Methods," Proceedings of the Concrete Structure Scenarios, JSMS, Vol. 9, pp. 31-38 (2009)

Non-Destructive Evaluation of RC Bridge Elements Using Ground-Penetrating Radar and Ultrasonic Pitch and Catch Techniques

Wael Zatar[1*] and Hai Nguyen[2]

[1] College of Information Technology and Engineering, Marshall University, Huntington, West Virginia, United States; email: zatar@marshall.edu
[2] College of Information Technology and Engineering, Marshall University, Huntington, West Virginia, United States

*: corresponding author

Keywords: ground-penetrating radar (GPR); ultrasonic pitch and catch (UPC); validation reinforced-concrete slab; embedded reinforcements; image reconstruction; 3D visualization.

Abstract: This study aims at evaluating reinforced concrete (RC) bridge elements using two non-destructive evaluation (NDE) techniques, namely ultrasonic pitch and catch (UPC) and ground-penetrating radar (GPR). An overview of major NDE techniques was provided. A validation test for a RC slab specimen with embedded steel rebars and wire meshes was conducted to understand the advantages and limitations associated with the UPC and GPR techniques. The high-resolution electromagnetic GPR technique was found effective to accurately locate almost all embedded reinforcements within the 3D slab volume being tested. On the other hand, the UPC technique is capable to detect only the rebars with large diameters while the wire meshes with a small diameter were completely undetected. However, unlike the image obtained from the GPR data, 3D visualization reconstructed from the UPC's data showed very strong reflections of the slab bottom. The UPC technique usually requires multiple-point scanning for the targeted survey areas, resulting in a time-consuming data collection and processing. The research team recommended the combined use of the GPR and UPC techniques to comprehensively assess RC bridge elements, where the GPR is used to fast determine the suspicious regions while the UPC technique is used for an in-depth inspection/evaluation.

1. Introduction

About 26 percent of the highway bridges in the United States are in need of repair or replacement, and a large number of these deficient bridges are reinforced or pre-stressed concrete structures (hereafter mentioned as 'concrete structures'). The corrosion of reinforcing steel and prestressing strands is one of the major causes of deterioration, reduced durability or even failure of reinforced and prestressed concrete bridge structures. Corrosion does not only destroy the smooth riding quality of the bridge deck but it could eventually compromise the structural integrity and safety of the bridge. Although visual inspection is a fast, convenient, inexpensive, versatile and simple testing technique for in-situ inspection of concrete structures, it typically limits the inspector to examine discontinuities on surface only and rely heavily on subjective assessments, which may significantly differ from one inspector expert to another (Kaiser and Karbhari 2004, Zatar and Nguyen 2017). This research aims at identifying the feasibility of using GPR and UPC techniques for condition assessment of concrete structures.

2. NDT Methods for Examining Concrete Structures

Non-destructive testing (NDT) of concrete structures is becoming increasingly important due to the aging and deterioration of civil infrastructures, e.g. bridges, roadways, airports and buildings, etc. Advanced NDT techniques facilitate fast, cost effective and reliable condition assessment of existing infrastructure to ensure public safety (Büyüköztürk 1998). Major NDT techniques used for examining concrete structures include acoustic impact testing, penetrant testing, ultrasonics, radiographic testing, thermographic testing, magnetic particle testing, Eddy current testing, half-cell potential testing, microwave (radar) testing, optical methods (fiber optics), acoustic emission, and ground-penetrating radar. Each NDT technique has its own advantages and limitations. For example, the thermographic testing method can generate a rapid mapping of large surface areas but it is susceptible to temperature fluctuations and requires a highly uniform heat source. As another example, acoustic emission method allows continuous lifetime monitoring and remote data acquisition, and it is relatively inexpensive. However, it is extremely difficult to interpret and structure must be under controlled loading condition (Kaiser and Karbhari 2004 and Kaiser et al. 2004). Based on the literature reviews of the advantages and disadvantages of the key NDT techniques, the GPR and UPC techniques were selected to examine the condition of concrete structures in this study.

2.1. Ultrasonic Pulse-Echo and Pitch-Catch Techniques

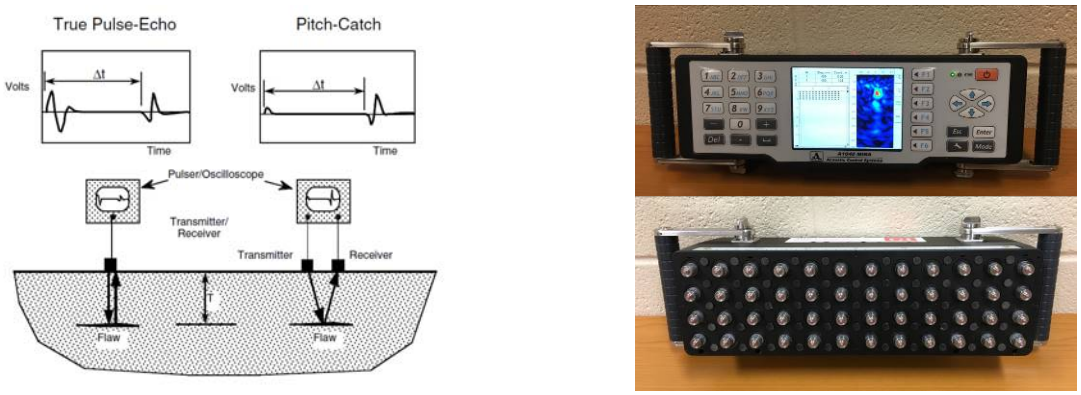

(a) (b)

Fig. 1. (a) Traditional ultrasonic pulse-echo and pitch-catch techniques (Malhotra and Carino 2003); (b) A pitch-catch ultrasonic testing device (MIRA Tomographer)

In a traditional pulse-echo testing, a transmitter introduces a stress pulse into an object at an accessible surface. The pulse propagates into the test object and is reflected by flaws or interfaces. The surface response caused by the arrival of reflected waves, or echoes, is monitored by either the transmitter acting as a receiver (true pulse-echo) or by a second transducer located near the pulse source, a.k.a. 'pitch–catch' (Malhotra and Carino 2003). Figure 1 illustrates the principle of these echo methods.

2.2. Ground Penetrating Radar (GPR)

GPR is a well-accepted electromagnetic technique that uses radar waves to image the subsurface. The most common form of GPR measurements deploys a transmitter and a receiver in a fixed geometry (Fig. 2a), which are moved over the surface to detect reflections from subsurface features (Jol 2008). Three basic visualization modes of a GPR signal include A-scan, B-scan, and C-scan. The A-scan is a single waveform that provides a punctual information about the subsurface configuration. The B-scan represents a set of consecutive radar waveforms along a particular direction while the C-scan provides an amplitude map at a specific time of data collection (Benedetto et al. 2017). An example of the A- and B-scan images of the steel reinforcing rebars embedded in a concrete slab is shown in Fig. 2b.

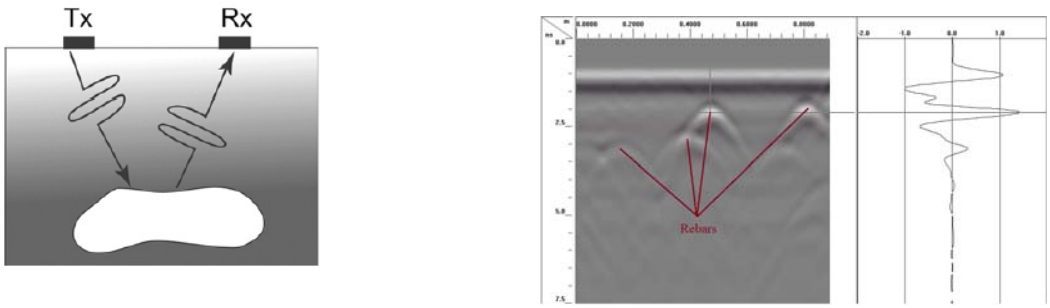

(a) (b)

Fig. 2. (a) Basic principle of GPR (Jol 2008); (b) B-scan (left) and A-scan (right) images of steel reinforcing rebars

3. Validation Test of Reinforced-Concrete Slab with UPC and GPR Techniques

A reinforced-concrete (RC) slab was designed and fabricated, as shown in Fig. 3, for the purpose of conducting the validation test. The slab dimensions (width × length × depth) measured after casting were 1,060 × 1,060 × 185 mm. Steel reinforcing bars of varying diameters (rebars #3, #4, #7) and two meshes of 3-mm steel wires were embedded in the RC slab. The goal was to investigate the effects of rebar sizes on the performance of the 3D visualization with the GPR and UPC techniques. As another test parameter, the steel reinforcing rebars and wire meshes were placed at different depths in the RC slab.

(a) (b)

Fig. 3. Validation RC slab: (a) layout of reinforcements; and (b) slab after casting.

The 3D visualization results using both the GPR and the UPC techniques are shown in Fig. 4. It should be noted that, while the depth of the reconstructed region in Fig. 4a was 250 mm, the one in Fig. 4b was only 150 mm. The reason was to eliminate the reflection from the bottom of the slab for a better view of the rebars and wire meshes. As can be observed, the 3D visualization of the GPR data in Fig. 4a precisely revealed most of the reinforcing rebars and wire meshes within the 3D slab volume being tested. One of the rebars was not well displayed because it was positioned close to the edge of the tested region and the radar aperture was, therefore, limited for that rebar. In addition, the reflection from bottom of the slab was not clear in the 3D image reconstructed from the GPR data. In case of the 3D images obtained with the UPC technique (Fig. 4b), only the rebars with large diameters were displayed and the wire meshes were completely undetected. However, unlike the image obtained from the GPR data, 3D visualization reconstructed from the UPC's data showed very strong reflections of the slab bottom. The rebars appeared smaller in the UPC's 3D image can be attributed to the difference in the wave length of the pulses employed by the UPC and GPR techniques.

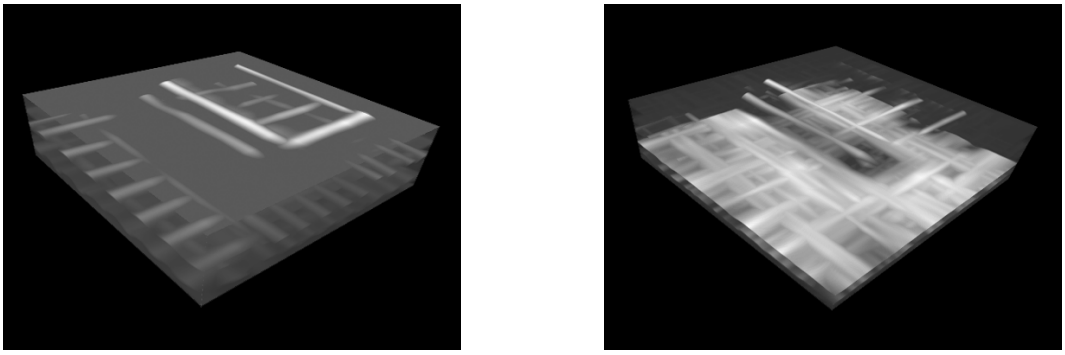

(a) (b)

Fig. 4. 3D visualization of the validation slab: (a) from GPR; (b) from UPC

4. Concluding Remarks

GPR and UPC techniques are powerful for evaluating concrete bridge elements. The GPR technique allows a high-accuracy and rapid data collection where the data can be employed to generate 2D and 3D visualizations of embedded reinforcements and defects. The UPC technique can be used to visualize the RC bridge structures, but the data collection process usually takes a longer time than the GPR. The combined use of the GPR and UPC techniques is recommended for a comprehensive and effective assessment of RC bridge elements.

5. References

Benedetto, A., Tosti, F., Ciampoli, L.B. and D'Amico, F., 2017. An overview of ground-penetrating radar signal processing techniques for road inspections. Signal processing, 132, pp. 201-209.

Büyüköztürk, O., 1998. Imaging of concrete structures. Ndt & E International, 31(4), pp.233-243.

Jol, H.M. ed., 2008. Ground penetrating radar theory and applications. Elsevier.

Kaiser, H. and Karbhari, V.M., 2004. Non-destructive testing techniques for FRP rehabilitated concrete. I: a critical review. International Journal of Materials and Product Technology, 21(5), pp. 349-384.

Kaiser, H., Karbhari, V.M. and Sikorsky, C., 2004. Non-destructive testing techniques for FRP rehabilitated concrete. II: an assessment. International Journal of Materials and Product Technology, 21(5), pp. 385-401.

Malhotra, V.M. and Carino, N.J., 2003. Handbook on nondestructive testing of concrete. CRC press.

Zatar, W. and Nguyen, H., 2017. Condition Assessment of Ground-Mount Cantilever Weathering-Steel Overhead Sign Structures. Journal of Infrastructure Systems, 23(4), p.05017005.

Effects of Mass and Excitation of Live Load on the Modal Frequencies of Bridges in Structural Health Monitoring

Chien-Chou Chen[1*], Wen-Hwa Wu[2], and Yu-Jie Chen[3]

[1] National Yunlin University of Science & Technology, Taiwan; email: ccchen@yuntech.edu.tw
[2] National Yunlin University of Science & Technology, Taiwan; email: wuwh@yuntech.edu.tw
[3] National Yunlin University of Science & Technology, Taiwan; email: b10316012@yuntech.edu.tw

*: corresponding author

Keywords: excitation effect, mass effect, live load, modal frequencies, bridges

Abstract: The objective of this study aims to systematically explore the effects of mass and excitation of live load on the modal frequencies of bridges. Two PC-box girder bridges, one steel bridge, one steel arch bridge, and one pedestrian suspension bridge were chosen to conduct 24-hour continuous measurements of ambient vibration of bridge deck. A recently developed stochastic subspace identification methodology equipped with an alternative stabilization diagram and a hierarchical sifting process was applied to identify the modal frequencies from the measured ambient vibration signals of these five bridges. The cross-examination results show that the identified modal frequencies are affected principally by the relaxation of boundary condition induced by live load. No clear correlation is observed between the identified modal frequencies and temperature in these measurement cases.

1. Introduction

To maintain the serviceability and safety of bridges, it is essential to learn about their structural condition whenever necessary. Several vibration-based methods recently developed have demonstrated their performance on condition assessment and damage detection of bridges. However, the accuracy of such techniques in practical applications strongly depends on the variation of modal parameters caused by the effect of environmental factors such as temperature, wind and so on. For a single-pylon steel cable-stayed bridge with main span length of 330 m, it was elucidated in a recent work by the authors that the traffic intensity is obviously the most crucial environmental factor to the variation of a few identified frequencies of the bridge deck (Chen, 2017). To further explore this observation, two PC-box girder bridges, one steel girder bridge, one arch bridge and one pedestrian suspension bridge were selected to perform similar study. A recently developed covariance-driven stochastic subspace identification (SSI) methodology equipped with an alternative stabilization diagram and a hierarchical sifting process was utilized to identify the modal frequencies from the measured ambient vibration signals of these five bridges (Wu, 2016). The root-mean-square (RMS) of the measured ambient vibration signal was taken to serve as the indication of structural response level. The correlation coefficients between the identified frequencies and the RMS vibration response or temperature were calculated to determine the most crucial factor to alter the modal frequencies of the bridges. In addition, a load test and corresponding finite-element analysis were performed on one of PC-box girder bridges to assess the effects of mass and excitation of live load on the variation of modal frequencies of the bridges.

2. Ambient vibration measurements and identification of modal frequencies

To collect the ambient vibration signal of each investigated bridge, a measurement system, composed of six to seven high-accuracy velocimeters produced by Tokyo Sokushin Co., Ltd., was installed on its bridge deck. The arrangement of measuring points was based on the identification requirement of major vertical bending modes. 24-hour continuous collection of ambient vibration signal was carried out for each measurement with sampling rate of 100Hz. Then, the SSI analysis was conducted with these measurements to identify one set of modal parameters every 30 minutes, and there are 48 sets of identified modal parameter per measurement. The determination of modal parameters with SSI analysis conventionally requires constructing stabilization diagram to observe the stability of identified results with the increasing value of system order parameter n under a designated value of time lag parameter i. Nevertheless, the performance of stabilization diagram for the applications in civil structures can be significantly affected by the selection of time lag parameter. An effort was made by the authors to resolve this discrepancy in identifying the modal parameter of a stay cable. It was indicated that the ambient vibration signal of cable would be nearly periodic function with the quasi-period close to the period of the first cable mode. Even for the measurements on the other structures with irregular distributed modal frequencies, this criterion is still practically applicable. Therefore, if the choice of time lag parameter is larger than the period of the first cable mode divided by the sampling period of measurement, stable identification results can be ensured. Inspired by this criterion, an alternative stabilization diagram was proposed which exhibits the gradually increased time lag parameter i along the ordinate and the corresponding modal frequencies along the abscissa under an assigned value of system order n. The alternative stabilization diagram has been also validated to hold the advantage in less interference from superfluous modes.

With the alternative stabilization diagram to efficiently provide modal frequencies, the authors further developed the robust algorithm to implement three stages of hierarchical sifting process such that closed values in three categories of modal parameters including frequencies, damping ratios, mode shape vectors can be grouped together. The stage of hierarchical sifting process is attempted to extract the clustered frequency values for each mode presented in the stabilization diagram. The stage of sifting begins with sorting all the frequency values appearing in the stabilization diagram in an ascending order. Each clustered group of frequency values after sorting would potentially correspond to the stable modal frequency value for a specific mode. The criterion of the maximum difference of each clustered group of frequency values can be further imposed to guarantee that each extracted group of frequency values would reach an acceptable level of concentration. Since all the clustered groups corresponding to different modes has been classified in the first stage, the second stage to sift close damping ratios for each mode is relatively simple. For each group passing the first stage, all the damping ratios corresponding to its N frequency values are next sifted in the second stage with similar techniques to filter N/2 most closed values. The N/2 frequency values and their associated damping ratios of each mode eventually go to the third stage for examining the consistency of their corresponding mode shape vectors. To tackle this problem, an average distance index was defined to carry out the third stage of sifting process on the mode shape vectors, which is the average distance of normalized mode shapes to the other ones in the same group. If G represents the number of remained mode shape vectors passing the sifting criterion in the third stage

another criterion $G \geq N/4$ is further enforced to guarantee that each extracted group passing the three stages of sifting has a satisfactory number of consistent mode shape vectors.

3. Results and discussion

The first investigated bridge is a four-span PC box girder unit of a long elevated expressway, with standard span length of 50 m. The supporting conditions of the girder are hinged constraint at three central piers and roller constraint at two end piers, with pot bearings. The aforementioned sensor system was deployed on the first span of this bridge unit to take 24-hour continuous ambient vibration signal of bridge deck. In the same time, air temperature was also recorded. For every 30-minute ambient vibration signal of bridge deck, after going though all three sifting stages as described in the previous subsection, the corresponding modal frequencies, modal damping ratios, and mode shape vectors in each clustered group can be averaged to determine the identified modal parameter for each mode. The identified frequencies of the first three vertical bending modes are around 1.871 Hz, 2.344Hz and 5.523 Hz, with maximum variation of 3% within 24 hours. The continuous identified frequencies of these three modes are compared with RMS velocity and air temperature to examine their correlations. It is clear to observe that the trends of identified frequencies of these three vertical bending modes highly correlates with that of the RMS response in a negative manner but hardly correlates with air temperature. The corresponding correlation coefficients from the first bending mode to the third one are -0.83,-0.69 and -0.60. The analysis result also indicates that temperature effect is not significant on the variation of the identified modal frequencies. Nevertheless, several works in literature have indicated that temperature effect is an important environmental factor influencing the alteration of modal frequency. To further explore temperature effect, a three-span steel girder bridge with the main span length of 56 m is adopted for another analysis of environmental effect on the change of modal frequency. The bridge are rigidly connected to two central piers and supported by movable pot bearings on two end piers. Four obvious vertical bending modes can be identified with frequencies about 1.949 Hz, 2.584Hz, 5.656 Hz and 6.272 Hz, also having maximum variation of 3% during measurement period. The results of correlation analysis are similar to those of aforementioned bridge. The modal frequencies are negatively correlated with RMS responses and the correlation coefficients from the first mode to fourth mode are -0.81, -0.53, -0.52 and -0.34. However, the correlation analysis still exhibits that there is no distinct correlation between the modal frequencies and the recorded temperature.

From the studies of the first two investigated bridges, it could be roughly concluded that for the assessment of environmental effects, live load is more important than temperature on the variation of modal frequencies of mid-span girder bridges. Although all the identified modal frequencies reveal the negative correlation with live load, they have quite different magnitudes. Therefore, it is questionable to conclude that the alteration of modal frequencies is caused only by the mass effect of live load. Besides that, the roughly estimated variation percentages of modal frequencies are all much lower than 3% for the total live load on the bridges. Referring to related literatures, it is mentioned that the induced excitation of live load could change the boundary condition of bridges, and, accordingly, prompt the variation of modal frequencies. To verify the possibility of the excitation effect of live load, a load test was executed on a nearly completed PC-box girder bridge, which is the first unit of a long highway bridge, with six spans of standard length of 50 m. The girder is rigidly supported at two central piers and simply

supported with movable pot bearings on the other piers. The load test, including two static load cases and two dynamic load cases, were carried out on the first span of the bridge unit, next to abutment. Two trucks were arranged to generate the loading patterns required for the test. In addition, an ambient vibration measurement was also conducted before the load test to provide the status without any loading on bridge for reference. Because all the measured vibration signals were very small only one vertical bending mode with a frequency of around 4Hz could be clearly recognized. To numerically assess the change of boundary condition, a finite element model of the bridge unit was constructed in which a linear spring element and a rotational spring element were used to simulate different constraint conditions of the movable pot bearings. The results of the load test and corresponding finite element analysis demonstrate that the identified and analytical frequencies are quite consistent and decrease when truck number or truck speed increases, but the effect from truck speed is much stronger than from truck number. In addition, for the dynamic load test with higher truck speed the input values of spring constant in corresponding finite element model is smaller. This can be reasonably explained by considering possible relaxation of boundary condition from pot bearing mechanism under large response of the deck excited by moving truck. The finite element analysis also points out that the frequencies of some modes are not sensitive to the alteration of spring constant. This could provide a practical explanation why the corresponding correlation coefficients for all the identified frequencies with the RMS response are diverse. To extensively explore the excitation effect of live load on the variation of modal frequencies, a steel tied-arch bridge with span length of 60 m was selected to perform 24-hour ambient vibration measurement. The arch is supported by hinged pot bearing at one end and movable pot bearing at the other end. Four clear frequencies of vertical bending modes near 1.921 Hz, 2.719 Hz, 4.000 Hz and 6.094 Hz can be obtained, with the maximum variation range of 3% in 24 hours. All the modal frequencies are correlated with the RMS response in a negative manner. The correlation coefficients from the first mode to fourth mode are -0.180, -0.779, -0.235 and -0.834. Roughly speaking, the analysis results of the arch bridge are similar to those of the girder bridges. The last investigated object is a pedestrian suspension bridge with span length of 180m. The 24-hour ambient vibration data were collected for the identification of modal parameter of the bridge. In addition, live load was also recorded. The live load was estimated in accordance with the number of the tourists on the bridge. Four distinct vertical bending modes can be identified and the corresponding frequencies are approximately 0.282 Hz, 0.419 Hz, 0.796 Hz and 0.960 Hz. Because the RMS velocity and total live load have similar trend of variation during the measurement period, the coefficients of the identified modal frequencies with these two factors are pretty close. The strongest one is -0.883 and the weakest one -0.154. To assess the effects of mass and excitation of live load, a finite element bridge model was constructed to analytically evaluate the variation of modal frequencies contributed by total live load or the relaxation of boundary condition. The results clarify that the effects of mass and excitation of the pedestrians on the bridge to the variation of modal frequencies are almost same.

4. References

Chen. 2017, Assessment of environmental effects in scour monitoring of a cable-stayed bridge simply based on pier vibration measurements, *Smart Structures and Systems*, 20(2), 231-246.

Wu. 2016, Application of Stochastic Subspace Identification for Stay Cables with an Alternative Stabilization Diagram and Hierarchical Sifting Process, *Structural Control and Health Monitoring*, 23, 1194-1213.

An FRP–FBG Smart Stay Cable for Real-Time Tension Monitoring

Zhenwei Zhou[1], Chunfeng Wan[2*], Youliang Ding[3], Yongsheng Song[4], Liyuan Huang[5], Siyuan Li[6], and Jiapei Meng[7]

[1] Southeast University Key Laboratory of Concrete and Prestressed Concrete Structure of Ministry of Education, Nanjing 211189, China; email: zzwdndx@163.com
[2] Jiangsu Advanced Institute of Seismic Resistant Technology for Mechanical and Electrical Equipment, Xingzhuang Industrial Park, Lishui District, Nanjing 211200, China; email: wan_seu@163.com
[3] Jiangsu Advanced Institute of Seismic Resistant Technology for Mechanical and Electrical Equipment, Xingzhuang Industrial Park, Lishui District, Nanjing 211200, China; email: civilding@163.com
[4] Jiangsu Advanced Institute of Seismic Resistant Technology for Mechanical and Electrical Equipment, Xingzhuang Industrial Park, Lishui District, Nanjing 211200, China; email: song1984419@163.com
[5] Key Laboratory of Concrete and Prestressed Concrete Structure of Ministry of Education, Southeast University, Nanjing 211189, China; email: huangliyuan_seu@126.com
[6] Key Laboratory of Concrete and Prestressed Concrete Structure of Ministry of Education, Southeast University, Nanjing 211189, China; email: seusiyuan@163.com
[7] Key Laboratory of Concrete and Prestressed Concrete Structure of Ministry of Education, Southeast University, Nanjing 211189, China; email: c-mengjp@vanke.com

*: corresponding author

Keywords: FBG sensor; stay cable; health monitoring; cable tension

Abstract: The safety of stay cable is very important for the operation of bridges, and the real-time monitoring of cable tension is necessary. In this study, an FBG strain sensor was installed in the FRP compound materials bar, and the bar was inserted into the hollows of steel wires and fixed with the steel wires together at the anchorages of the cable. The stretching test is presented to verify the advantages of the smart cable for cable tension monitoring. Meanwhile, the results demonstrated that the quantity of the cable tension could be perfectly real-time monitored by the FRP-FBG smart stay cable. Nevertheless, direct monitoring the strain of the steel wire cannot exactly record the tension changes.

1. Introduction

Cable-stayed bridge transfers bridge dead weight and live load to the towers through stayed cables. The cable tension determines the reasonability in bearing forces and girder alignment, so it's very necessary to monitoring the cable tension for the safe running of the cable-stayed bridge. At present, there are two kinds of monitoring methods widely used in engineering: one is to install sensors outside the cables, the other is to embed sensitive elements inside the cables. However, a series of problems such as the low survival rate of components and insufficient monitoring range need to be solved. Recently, applications of FBG sensors for monitoring of cable tension have been proposed. A smart stay cable assembled with optical fiber Bragg grating

(OFBG) strain and temperature sensors was also proposed and developed for some practical bridges (Li et al. 2009, Huang et al. 2013, He et al. 2013). In this paper, a kind of cables installed with an FBG sensor was also developed, and the principle, the encapsulation process of the smart cable were introduced. Moreover, the monitoring performance was verified by experiment, and compared with the direct monitoring method.

2. Fabrication of smart stay cable

Recent developments in FBG sensors have provided an excellent choice for civil engineers owing to their small dimensions, better resolution and accuracy, wide temperature operating range, and excellent ability to transmit signals over long distance (Moyo et al.). In view of the vulnerability of fiber grating sensors, a package method is adopted to improve the survival rate of fiber gratings. The fabrication of FRP-FBG bar as shown in Fig. 1, Open a small slot of 0.3 mm in the FRP bar along the length direction, then put the FBG sensor in the slot and encapsulate it with epoxy resin glue. Then the smart bar is implemented parallel to the steel wires of the cable, and the stained condition of cable could be monitored due to the conjunct deformation of the smart bars and steel wires. The main instruments and software used in the preparation of intelligent cables are seven-wire, 5mm-diameter steel strands, 6 mm-diameter FRP bar, FBG sensor, optical fiber fusion splicer, SM130 modulation, and demodulation instrument, MOIENLIGHT software, etc. Furthermore, due to the poor shear performance of FRP, jaw vice anchorage cannot be used directly. The anchoring of stay cables is shown in Fig. 2. In this experiment, the anchor cable was anchored by pouring epoxy resin glue into the anchor cavity of the custom anchor.

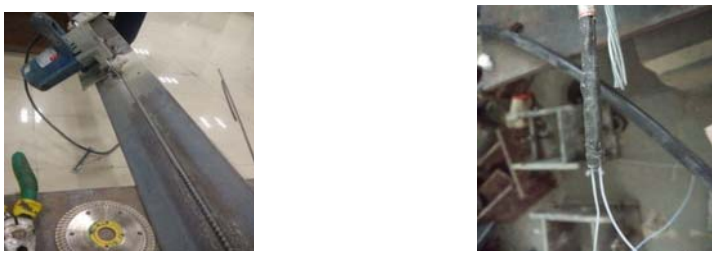

(a) (b)

Fig. 1. The package of FRP-FBG smart bar: (a) FRP bar slotted; (b) FRP-FBG smart bar package

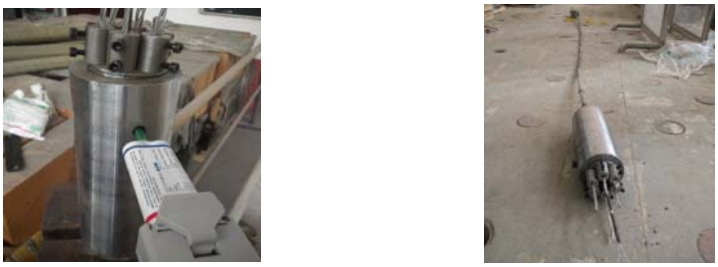

(a) (b)

Fig. 2. The encapsulation of stay cable: (a) the anchor installation and grouting; (b) the whole stay cable in the lab

3. Tension monitoring

The test stay cable is a 7-wire 1860 strand. The diameter, cross-section area, and Young's modulus are 15.24 mm, 139.82 mm^2 and 1.95×10^{11} Pa, respectively. To ensure safety, the maximum load of this loading is about 70% of the ultimate load of steel strands, that is, about 18 t. The load was applied in cycles of loading and unloading, and the scheme is as follows: about 30% (7.8 t) of the ultimate load of the steel strands is pretensioned firstly, then unloaded to about 10% (2.6 t). The loading is started step by step, and it is about 1 t in each stage. During this loading, it also should be noted that the load for 2 min each time and then record the wavelength after unloading and a stand of 2 min. The cable tension monitoring is shown in Fig.3. The experiment is divided into two parts: one is to monitor the tension of the steel strand which directly adheres to the FBG sensor, and the other is to monitor the tension of the FRP-FBG smart stay cable.

(a) (b)

Fig. 3. Cable tension monitoring: (a) Direct monitoring stay cable; (b) Monitoring the FRP-FBG smart stay cable

The stay cable direct monitoring results are listed in Table 1. The analysis of the monitoring data shows that the FBG sensor cannot directly monitor the cables effectively. Furthermore, The FRP-FBG smart stay cable monitoring results were also obtained and are listed in Table 2. Fortunately, the conclusion shows that the measuring precision of FRP-FBG smart stay cable is high and it can be applied in the tension monitoring of practical stay cable.

Table 1. The stay cable direct monitoring results

Actual value T_a (t)	2.67	3.51	4.72	5.66	6.69	7.63	8.68
Monitoring value T_b (t)	2.03	2.54	3.27	3.87	4.52	5.12	5.78
$(T_b- T_a)/T_a*100\%$	31.53	38.19	44.34	46.25	48.01	49.02	50.17

Table 2. The FRP-FBG smart stay cable monitoring results

Actual value T_a (t)	1.84	2.96	3.90	4.87	6.17	6.89	7.92
Monitoring value T_b (t)	1.85	2.98	3.94	4.90	6.22	6.97	8.08
$(T_b- T_a)/T_a*100\%$	0.54	0.68	1.02	0.62	0.81	1.16	2.02

4. Conclusion

An FRP-FBG smart stay cable is fabricated in this paper. Carry on indoor model simulation experiment; the test results are analyzed, the accuracy, validity, and feasibility of the FRP-FBG smart stay cable are demonstrated. In contrast, the measured cable force is considerably less than the actual tension when the FBG sensor was directly pasted on the steel strand.

5. Acknowledgements

The research was supported by the National Key Research and Development Program of China (No. 2017YFC0840200) and the National Natural Science Foundation of China (No. 51578140).

6. References

Li, H., Ou, J.P., and Zhou, Z. 2009. Applications of optical fiber Bragg gratings sensing technology-based smart stay cables, Optics and Lasers in Engineering, 47(10), 1077-1084.

Huang, M., Zhou, Z., Huang, Y., and Ou, J.P. 2013. A distributed self-sensing FRP anchor rod with built-in optical fiber sensor, Measurement, 46(4), 1363-1370.

He, J., Zhou, Z., and Ou, J.P. 2013. Optic fiber sensor-based smart bridge cable with functionality of self-sensing, Mechanical Systems and Signal Processing, 35(1), 84-94.

Moyo, P., Brownjohn, J.M.W., Suresh, R., and Tjin, S.C. 2005. Development of fiber Bragg grating sensors for monitoring civil infrastructure, Engineering Structures, 27, 1828-1834.

Bridge Scour Identification Based on Ambient Vibration Measurements of Superstructures and its Practical Application

Wen Xiong[1*], Feiquan Li[2], Xuefeng Zhang[3], Xuntian Hou[4], and C.S. Cai[5]

[1] Department of Bridge Engineering, School of Transportation, Southeast University, Nanjing, 211189, China; email: wxiong12@hotmail.com
[2] Zhejiang Provincial Highway Administration Bureau, Hangzhou, 310009, China; email: 555660@qq.com
[3] Research Institute of Highway Ministry of Transport, Beijing, 100088, China; email: 28144484@qq.com
[4] Zhejiang Provincial Highway Administration Bureau, Hangzhou, 310009, China; email: 555668@qq.com
[5] Department of Civil and Environmental Engineering, Louisiana State University, Baton Rouge, LA 70803, USA; email: cscai@lsu.edu

[*]: corresponding author

Keywords: bridge scour; cable-stayed bridges; vibration; superstructures; identification

Abstract: A scour identification method was developed for existing bridges based on ambient vibration measurements of superstructures. The Hangzhou Bay Bridge, a super-long cable-stayed bridge, was selected to illustrate the application of this method due to its high scour potential. First, through the acceleration sensors installed on the girder and pylon, two ambient vibration measurements were respectively conducted in 2013 and 2016. By applying the modal analysis on two measurements, the natural frequencies of different orders corresponding to different mode shapes of the superstructure were obtained. Then, by tracing the change of two dynamic features between two measurements, the variation of the support boundary at the foundation of the Hangzhou Bay Bridge was detected and thus the foundation scour was qualitatively identified. Subsequently, a FE model of the bridge considering soil-pile interaction was established to further identify the scour depth quantitatively. The stiffness of the soil springs representing the support boundary of the bridge was first identified by the model updating. The principle for successful identification is to make the simulation best fit the measured natural frequencies which are insensitive to the sour. Based on the updated FE model, the scour depth was second identified by updating the depth of supporting soils. The principle of model updating termination is to make the simulation best fit the measured natural frequency changes which are sensitive to the sour. A comparison to the underwater terrain map of the Hangzhou Bay Bridge was finally carried out to verify the accuracy of the identification. This practical application shows that the proposed method for identifying bridge scour based on the ambient vibration measurements of the superstructure is both effective and convenient.

1. Introduction

Bridge scour is a significant concern in the world. In the last 30 years, more than 1,000 bridges collapsed, and approximately 60% of these failures are related to the scour of foundations in the United States (Deng and Cai 2010; Xiong et al. 2012). The catastrophic collapse of the Schoharie

Creek Bridge in New York in 1987 was caused more by the cumulative effect of pier scour of glacial till than the severe flood that ultimately caused its collapse. The Los Gatos Creek Bridge over I-5 in the state of California collapsed because of local pier scour during a flood event, but the underlying cause was the channel degradation from the previous 28 years of service. Therefore, it is desirable to develop an effective and economical method or technique to identify the bridge scour.

The existing studies show that it is feasible to establish an effective relationship between the scour effect and the dynamic features obtained from the vibration signals of bridge superstructures (Zarafshan et al. 2012). However, most of the previous studies focus on the theoretical analysis on the proposed vibration-based methods based on either the analytical solutions or Finite Element (FE) models. Further research is still necessary in numerous aspects to significantly improve their application's reliability and accuracy in actual scour identification for the field bridges. It is generally believed that the last mile to the success of such vibration-based method to identify the scour is the investigation on the real bridges under actual scour condition and field environment.

The present study aims to develop a scour identification method for existing bridges based on ambient vibration measurements of the superstructure. The Hangzhou Bay Bridge, a super-long cable-stayed bridge, was selected to illustrate the application of this method due to its high scour potential. First, through the acceleration sensors installed on the girder and pylon, two ambient vibration measurements were respectively conducted in 2013 and 2016. By applying the modal analysis on the measurements of each time, the natural frequencies of different orders and corresponding mode shapes of the superstructure were secondly obtained. Then, by tracing the change of the two dynamic features between the two measurements, the variation of the boundary support from the foundation of the Hangzhou Bay Bridge was detected and thus the foundation scour was identified. According to the pre-updated FE model, the specific scour depth was finally identified by varying the depth of supporting soils to best fit the change of the natural frequencies, which are sensitive to the souring, between the two measurements. A comparison to the underwater terrain map of the Hangzhou Bay Bridge was also carried out to verify the identified bridge scour depth.

2. The Hangzhou Bay Cable-stayed Bridge

The Hangzhou Bay Bridge is a large-scale bridge across Hangzhou Bay in the eastern coastal region of China with the total length of 36 kilometers. It consists of a super-long cable-stayed bridge with the main ship-channel and a large quantity of beam bridges (Fig. 1). This cable-stayed bridge is selected to conduct the ambient vibration measurement and in the following study the Hangzhou Bay Bridge only refers to this cable-stayed bridge if not otherwise specified.

The Hangzhou Bay Bridge has one main span along with four side spans, each measuring 70m, 160m, 448m, 160m, and 70m, respectively. The connection between the girder and pylon is designed as a semi-floating system. The side spans are additionally supported by the auxiliary piers in order to improve the dynamic behavior in the daily service time. The pylon of the Hangzhou Bay Bridge is design as a diamond-shaped structure, whose height is 178.8 m from the base level to the top and 138.575m from the girder. The cable system consists of 28 pairs of

stay cables on each side of the pylon and is arranged in the double-plane as a semi-fan shape. The main girder is primarily supported by the cable system and also sits on a horizontal beam of the pylon. The flat steel box is applied as the girder's cross-section, which has 3.5m height and 37.1m width (Fig. 2).

Fig. 1. View of the bridge

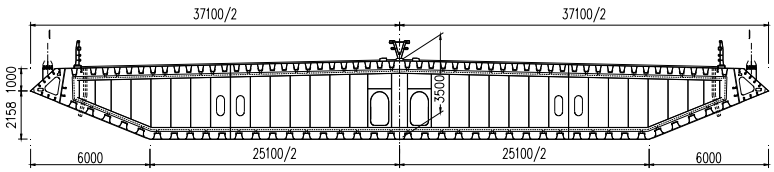

Fig. 2. Cross-section of girder (Unit: mm)

3. Qualitative Identification of Scour

Two ambient vibration measurements for the Hangzhou Bay Bridge were conducted in 2013 and 2016 to obtain its dynamic features. The measurements were taken covering the interior of the steel box girders at the main and side spans and the pylon structures above the pile cap. All the vibration measurements for the Hangzhou Bay Bridge were conducted under the ambient excitation with no traffic interruption. Duration of 20min was adopted for each time of recording with a sampling rate at 100Hz. The modal analysis using the subspace iteration method was applied to the filtered vibration signals. The natural frequencies of the first eleven orders of the Hangzhou Bay Bridge were extracted from each measurement and provided in Fig. 3. The mode shapes of the first eleven orders of the Hangzhou Bay Bridge can also be obtained using the subspace iteration method based on the ambient vibration measurements. Fig. 4 compares the two mode shapes of the girder with the same typical order (e.g. the 1st order of vertical bending mode) extracted by the measurements of 2013 and 2016, respectively. Based on the analysis above, it can be concluded that: (1) the scour development of the Hangzhou Bay Bridge was qualitatively identified by tracing the change of both the natural frequencies and mode shapes between the two measurements of 2013 and 2016; (2) both the natural frequencies and mode shapes of the low order modes can provide more sensitive scour identification than those of high order; (3) the pylon presents more sensitive changes of natural frequencies and mode shapes to the scour than the girder does, even for the high orders.

4. Quantitative Identification of Scour

The quantitative scour identification was further conducted in the following three steps: (1) First, a FE model was established as the object for the model updating; (2) Second, the soil stiffness (stiffness of soil-pile springs) was identified by best fitting the scour-insensitive vibration modes and updated in the FE model; (3) Using the model with the updated soil stiffness the scour depth (soil level) was finally identified by best fitting the scour-sensitive vibration modes. Fig. 5 plots the variation of D_2 (difference between the simulated and measured natural frequency changes of scour-sensitive vibration modes) along with the increasing Δh (scour depth) from 0m to 7m. As can be seen from Fig. 5, the D_2 decreases with the progressive scouring until the Δh reaches the increment of 4.5m. The simulation by the FE model with the scour depth increment of 4.5m very approaches the actual occurring of the foundation between two measurements. Therefore, the scouring of the Hangzhou Bay Bridge from 2013 to 2016 was successfully identified as the

increment of 4.5m. Such scour identification method by model updating based on the measurements worked very well in the present case study. The documented results (NHBBD 2016) from the underwater terrain map (Fig. 6) verify the accuracy of the proposed scour identification based on the ambient vibration measurements.

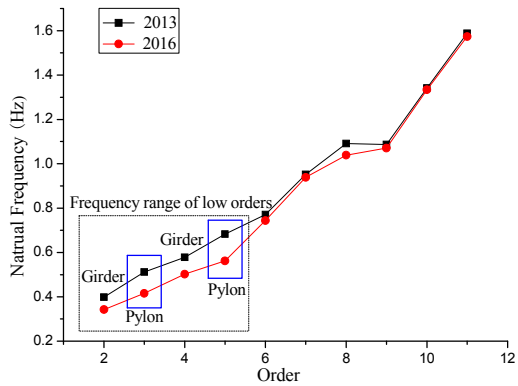

Fig. 3. Natural frequencies in two measurements

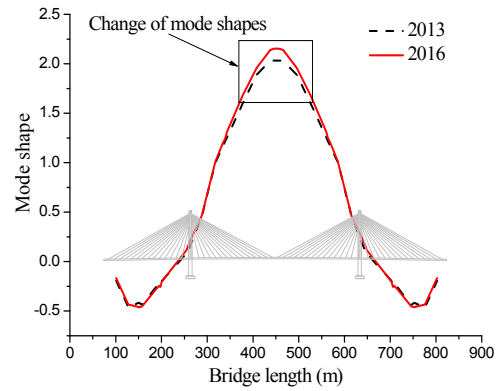

Fig. 4. The change of the mode shapes

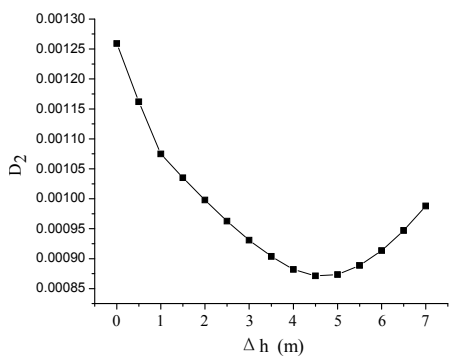

Fig. 5. Variation of D_2 along with the increasing Δh

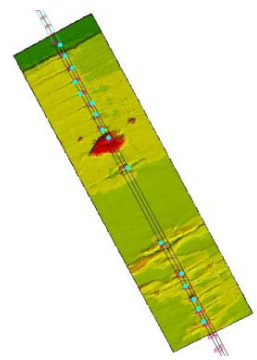

Fig. 6. Underwater terrain map

5. Concluding Remarks

This study shows the great potential for the use of the ambient vibration of the superstructure in identifying the bridge scour. Tracing the dynamic changes based on the ambient vibration measurements of the superstructure can both qualitatively and quantitatively identify the presence of the scour. Once applied in practice, this vibration-based scour identification does not require any underwater devices and operations and could be easily integrated to a routine assessment task for bridges.

6. References

Deng, L. and Cai, C. S. 2010. Bridge Scour: Prediction, Modeling, Monitoring, and Countermeasures - Review. Practice Periodical on Structural Design and Construction, 15(2), 125-134.

Xiong, W., Cai, C. S., and Kong, X. 2012. Instrumentation design for bridge scour monitoring using fiber Bragg grating sensors. Applied Optics, 51(5), 547-557.

Zarafshan, A., Iranmanesh, A., and Ansari, F. 2012. Vibration-Based Method and Sensor for Monitoring of Bridge Scour. Journal of Bridge Engineering, 17(6), 829-838.

NHBBD (Ningbo Hangzhou Bay Bridge Development Co., Ltd.). 2016 Monitoring results for the local scour depth around the foundation of Hangzhou bay bridge. Report No.: 2013-2016, Zhejiang Surveying Institute of Estuary and Coast, Hangzhou, China.

Bridge Engineering Institute Conference 2019 (BEI-2019)
Honolulu, Hawaii, USA, July 22-25, 2019

Halls River Bridge Bulkhead-Seawall Replacement Challenges and a Way Forward

Richard Hunter[1], Thomas Cadenazzi[2], Keith Ellis[3], and Steven Nolan[4*]

[1] Wesley Chapel, FL. USA; email: RHunter@ACP-FL.com
[2] University of Miami, Coral Gables, FL. USA; email: txc470@miami.edu
[3] Florida Department of Transportation - District 1 & 7 Geotechnical Office, Bartow, FL. USA; email: Keith.Ellis@dot.state.fl.us
[4] Florida Department of Transportation–State Structures Design Office, Tallahassee, FL. USA; email: Steven.Nolan@dot.state.fl.us

*: corresponding author

Keywords: bulkhead; CFRP; GFRP; prestressed concrete; seawall

Abstract: The Halls River Bridge project included the replacement and widening of the existing bulkhead-seawall system. The existing 1954 system utilized shallow tipped concrete sheet piles with deadman pile anchors, presumably due to the shallow subsurface limestone rock strata. With the 2016 bridge replacement it was desired to utilize a cantilevered bulkhead system and eliminate the tie-back anchors due to both constructability and long-term maintenance concerns. Soil borings at the site indicated near surface difficult driving conditions through weathered limestone, which typically preclude the use of a conventional jetting installation method for precast concrete sheet piling. Plan notes were added to the contract documents making the contractor aware that trenching for the installation of the precast concrete sheet piles may be necessary. Additionally, the precast concrete sheet piles where to be prestressed and reinforced with innovative materials, CFRP and GFRP respectively, for enhanced durability. The bid prices received on the project were significantly higher than the historical cost average, indicating that bidders were aware of the installation risks and additional cost of the FRP materials During construction operations, the contractor attempted several installation alternatives, including: dynamic and vibratory driving; pre-punching; and pre-auguring, before reverting to the suggested trenching installation method. This paper explores the difficulties incurred during installation of the cantilevered bulkhead, the versatility of the FRP-PC components that were eventually modified, and the potential mitigation strategies for owners with similar challenges on future projects. A modified FRP-RC/PC soldier pile wall system and other emerging solutions will be presented with an emphasis on highlighting improvements that have become possible with the refinement of design parameters for FRP materials under sustained loading in both the first edition of AASHTO Guide Specification for the Design of Concrete Bridge Beams with CFRP Systems, and the AASHTO Bridge Design Guide Specification for GFRP Reinforced Concrete (2nd Edition).

1. Introduction

The Halls River Bridge project included the replacement and widening of the existing bulkhead-seawalls. The existing 1954 system utilized shallow tipped thin concrete sheet piles with deadman pile anchors. Presumably this system was chosen due to the presence of a shallow subsurface limestone rock strata and unrestricted access for tie-back and deadmen installation for

the first bridge at the site. With the 2016 bridge replacement it was desired to utilize a cantilevered bulkhead system and eliminate the tieback anchors due to both constructability and long-term maintenance concerns. Similar anchored wall systems experience severe distress at the anchor connection due to corrosion of the precast tie-beams. Local examples include City of St Petersburg Pier Reconstruction 2017, and Sunshine Skyway South Seawall Rehabilitation 2018.

2. Halls River Bridge Geotechnical and Environmental Conditions

Halls River Bridge (HRB) is located in Citrus County, Florida. The US Department of Agriculture, Soil Conservation Service (USDA-SCS) identified the primary physiographic feature in the project area as the Gulf Coastal Lowland. The lowlands consist primarily of sand and clayey sand underlain by limestone and dolomite. Corrosion parameter testing of the soil and water at the project site indicated a moderately to extremely aggressive environment for corrosion.

During the design phase, a total of four Standard Penetration Test (SPT) geotechnical borings were performed to depths of 75 to 100 feet. The encountered soils were consistent with the soil profile identified by the (USDA-SCS), generally consisting of five to ten feet of fine sand and slightly silty fine sand. The surficial sands were underlain by highly weathered limestone (SPT N-Values on the order of 2 to 30) interbedded with layers of competent weathered limestone (SPT N-Values of 67 to refusal, 50 blows for 0 inches of penetration).

3. Original 1954 HRB Bulkhead-Seawall Design

Bulkheads constructed in coastal environments in Florida, typically consist of cantilevered or anchored concrete sheet pile walls with cast-in-place caps. Anchored wall systems typically use precast RC tie-beams with isolated sheet piles as deadman. While the concrete cover on sheet pile wall systems does provide a temporary barrier against chloride intrusion in uncracked concrete, it is not impermeable so eventually the reinforcing and prestressing carbon-steel will corrode. This project utilized innovative materials such as GFRP reinforcing and CFRP prestressing to eliminate this corrosion risk.

The proposed new bridge had a wider footprint due to the addition of sidewalks and upgraded shoulders on both sides. This required the bulkhead walls to be configured with an out-to-out distance of 92-feet to accommodate all of the geometric constraints. It was decided during the design phase to use a cantilever-wall design to avoid conflicts with the existing 1954 anchored-walls, which used deadman and precast beam tie-backs. The new cantilever-wall design also reduced constructability concerns when installing the proposed wall while still allowing passage of traffic over the existing 30.5-feet wide bridge.

While the cantilever-wall design provided many benefits, the soil borings reveled a significant disadvantage – with a relatively high limestone layer, as discussed above. This soil information was further confirmed with an additional four SPT borings taken to a depth of 15-feet for the nearby temporary walls. The embedment of the proposed cantilever walls was specified to be 23-feet which meant that the wall tips should have been within the sand and highly weathered limestone layers at most locations. It was determined that the disadvantage of the near-surface hard limestone layer did not outweigh the advantages of using the cantilever-wall design. Several

Contract Plan notes alerted the contractor to the anticipate difficult installation of these sheet piles due to the presence of compacted/dense soils, hard clay and limestone. The contractor was advised that specialized equipment and/or installation methods, including the use of preformed pile holes, punching and/or other methods might be required.

4. Modifying the HRB Bulkhead-Seawall Design

During the bulkhead-seawall construction, the contractor encountered difficulty with the installation from the first day, and was not able to install the sheet pile walls in a timely manner to meet the contract schedule. A variety of methods were attempted but the construction rate resulted in significant project delays. Only 466 linear feet (7.5%) of the total 6,251 linear feet of sheet pile wall could be installed in the first 6 months of the contract. During this same period, approximately half of wall needed to be completed to meet the schedule for the first phase of the bridge replacement. Additional borings were taken to determine if the soils at the wall locations being installed were significantly different than what was revealed during the design phase of the project, but the new borings only confirmed the soil parameters found with the previous borings.

After extensive coordination with the contractor, it was decided to revise the wall design to an anchored-wall system that allowed the embedment to be reduced from 23-feet to 12-feet. By this time all of the precast sheet pile wall elements had been cast. As such, off-cuts of the original CFRP-PC/GFRP-RC sheet pile lengths were utilized for the deadman-anchors. Due to the short lead-time and the contractor's preference for stainless steel over CFRP strands, the tie-back anchors utilized 31803 alloy bars and 316 alloy turnbuckles to ensure that all the wall components would continue with the goal of minimizing the corrosion risk. The reduction in embedment significantly increased the sheet pile installation rate, although the installation of the deadman-anchors complicated construction due to their close proximity to both the existing structure and embankment (during the first phase) and then a portion of the newly constructed embankment and structure (during the second phase).

Additional changes were made by the designers to help reduce the cost of the walls both during the design phase and construction. The first design change was reducing the number of CFRP prestressing strands in each sheet pile. The first version of FDOT Standard Index D22440, matched the number and size of CFRP strands to achieve the standard 1,000-psi unit prestress after losses to prevent cracking the concrete section during handling and service loads. Since no carbon-steel was being used in these sections, the second version reduced the number of strands to provide a unit prestress (after losses) to 710-psi minimum. This pre-compression reduction was justified based on the allowable increase in maximum service tension stresses up to the limit permitted for benign environments under AASHTO (2016), rather than limit for extremely corrosive environments, which is typically only applicable to carbon-steel.

A second cost reduction change made during construction, allowing a "hybrid" section to be used in the portion of the wall that was not submerged in brackish water. These "hybrid" sheet piles utilized carbon-steel prestressing strands in the center of the sheet pile sections but still utilized the GFRP reinforcing stirrups near the surface. Even though the carbon-steel prestressing strand does create an opportunity for corrosion, the risk is sufficiently offset by the significantly increased concrete cover (5½-inches).

5. Lessons Learned

While installing sheet piling using preformed pile holes, punching, trenching and/or other methods is possible, it is technically challenging, expensive, and time consuming. Contractors may have difficulty in correctly estimating the effort, in both costs and time needed to complete this work. Serious consideration should be given in lengthening bridges in order to eliminate these walls when at all possible. Using alternative wall types, such as pile or shaft supported or secant-pile walls should also be considered to minimize the constructability issues.

6. Alternative Corrosion-Resistant systems

6.1. Soldier Piles and GFRP-RC Flat Panels

Traditionally, soldier pile and panel bulkheads are a popular bulkhead configuration in southeast Florida where there is a shallow subsurface layer of moderately hard rock (Miami Limestone/Oolite). The soldier (or king) pile system allows preformed or bored pilot holes to assist driving vertical prestressed piles to a minimum tip elevation to secure the toe of the wall. These solider piles support vertical precast concrete panels via direct bearing on the back face of the pile. For taller exposed wall heights, typically greater than 9 feet, battered bracing piles are installed to restrain the top of the wall and the connection with the soldier pile is encapsulated in a reinforced concrete cap for a pseudo-anchored wall system. The bulkhead toe is typically protected from scour with rubble riprap, which usually extends beyond the bracing pile (when present) also providing subsurface protection from larger water vessels. The durability of these systems can be enhanced with the simple substitution of FRP reinforcing and prestressing. This durability enhanced bulkhead-seawall system is currently being utilized on two projects in south Florida for the FDOT (23rd Ave North over Ibis Waterway, and US 41 over North Creek bridge replacements).

6.2. Fiberglass Profiled Sheet Piles

Fiberglass composite sheet pilings are well studied in literature and to date, there are many applications of this technology in waterfront wall systems. Fiberglass corrugated profile sheet piles are typically pultruded panels interlocked with each other through a pin-eye connection on both ends to form a continuous wall. The wall thickness is approximately 0.1 in. for the webs and 0.2 in. for the flanges (Shao et al., 2002). Compared to steel, fiberglass composite panels are 3-times thinner (typical steel sheet piles are 0.4 in. to 0.5 in. thick), and approximately 4-times lighter than steel for the same cross-sectional area, which makes them favorable for construction during shipping and handling, but subject to greater deflections with their lower stiffness. Kouadio, 2001 proved that the tensile strength ranges from 27 ksi for webs to 62 ksi for the flanges, while the tensile modulus can range from 1740 ksi for web to 4350 ksi for flanges (Kouadio, 2001). Such material properties are estimated to be at least four times higher than that of alternative panels made of vinyl materia1s (Bdeir, 2003). However, compared to steel, fiberglass pultruded sheet piling still present a major design challenge due to their low flexural modulus, which can exhibit large deformations in excess of traditionally tolerated design limits. Installations of these systems is typically limited to granular or soft soils due to the limited driving resistance, and were therefore not a good option for the HRB site.

6.3. Prestressed Concrete Sheet Piles

Prestressed concrete (PC) sheet piles are commonly used for permanent bulkhead-seawalls, and can be divided into two categories: flat concrete sheet piles and corrugated concrete sheet piles. While corrugated sheet piles are the most common profile for steel sheet piles, they are rarely produced in prestressed concrete. The main drawback of reinforcing with FRP rebar and strands compared to carbon-steel rebar and strands is the initial cost. Unlike fiberglass pultruded sheet piles, the service limit state deflections are less effected by the FRP component tensile moduli and more dependent on the constituent concrete due to the assumed uncracked service limit state. Also, recent updates to the 2nd Edition of the AASHTO LRFD Bridge Design Guide Specifications for GFRP-Reinforced Concrete (2018), have increased the sustained load tension limits for GFRP rebar further improving design efficiency for applications in cracked concrete (RC or partially prestressed) at the service limit state. FRP-RC/PC structures are expected to have less maintenance and longer service life compared to traditional carbon-steel RC/PC options, and thus present long-term economic benefits (Cadenazzi et al., 2019). Additionally it is expected that the FRP higher initial cost will diminish in time as these materials become more common and market share and competition increases. Beyond the configuration of the CFRP-PC/GFRP-RC sheet piles used at HRB, the following two systems under development are promising alternatives:

6.3.1 MILDGLASS for Prestressed Concrete: An innovative solution under development is the MILDGLASS prestressed concrete technology (Nanni, et al., 2019). MILDGLASS is a GFRP strand prototype currently being investigated for its potential use in less demanding prestressed concrete applications. Currently carbon FRP (CFRP) has been the preferred solution for corrosion-resistant prestressing applications (Spadea et al., 2018), however GFRP may be an efficient alternative since it does not require the same high levels of pre-tensioning as CFRP strands, which directly alleviates some of the main constructability and safety issues during stressing operations. Additionally, GFRP strands have significantly reduced cost compared to their CFRP counterpart, mostly due to the lower embodied energy, making GFRP strands a competitive, sustainable and durable alternative. The GFRP strand under investigation does not alter the conventional manufacturing process at the precast plant, allowing the same procedures and techniques currently applied to steel prestressed concrete tensioning and construction.

6.3.2 PRECOPAL Corrugated GFRP-PC Sheet Piles: PRECOPAL is an innovative project under the European Union's Horizon 2020 research and innovation program (Precopal, 2019). PRECOPAL technology aims to provide a new sustainable type of prestressed, steel-free sheet pile, along with its enhanced mechanical characteristics given by the full corrosion-resistant GFRP bars, in combination with a minimum of 13-ksi (90 MPa) concrete compression resistance. The innovation of PRECOPAL, compared to existing solutions, is the integration of prestressed 0.55-inch diameter GFRP bars that replace the traditional steel and avoid any corrosion, targeting a 100-year service life. Each sheet pile element is approximately 26 to 46-feet long, 3-feet wide, 5-inches thick, and connected with the adjacent sheet pile by an innovative hollow PVC cylindrical joint system which minimizes water permeability.

9. Conclusion

Valuable insight was gained during the demonstration project for the Halls River Bridge replacement. FRP-PC/RC solutions are expanding and provide viable and adaptable applications with less concerns regarding the further durability that arises due to unanticipated construction challenges, damage, and mistakes. The increased initial acquisition costs should be easily offset with future maintenance cost savings and extended design life. Continued development of FRP-PC/RC solutions, refinement of design guidance, and full adoption of FRP design codes will continue to improve cost efficiency in the near future.

10. References

Bdeir, Z. (2003). Deflection-based design of fiber glass polymer (FRP) composite sheet pile wall in sandy soil.

Kouadio, K. S.P. (2001). "Durability of Fiberglass Composite Sheet Piles in Waterl". McGill University, Montreal, Quebec.

Nanni, A., Rossini, M., Dotelli, G., & Spadea, S. (2019). MILDGLASS: GFRP Strands for Resilient Mild Prestressed Concrete. NCHRP-IDEA Project 208, Annual Progress Report: New IDEAS for Highway Systems (pp. 246–248). Washington, DC: Transportation Research Board.

Precopal (2019). European Union Horizon 2020 Grant Agreement No. 790367.
Retrieved from: http://www.sigmac.it/en-US/precopal

Shao, Y., Giroux, C., & Bdeir, Z. (2002). Determination of EI for pultruded GFRP sheet pile panels. In Proc. 3rd Inter. Conf. on Composites in Infrastructure (ICCI'02), Omipress (CD-ROM) (p. 10).

Cadenazzi, T., Dotelli, G., Rossini, M., Nolan, & Nanni, A. (2019). Life Cycle Cost and Life Cycle Assessment Analysis at the Design Stage of a FRP Reinforced Concrete Bridge in Florida. ASTM, Advances in Civil Engineering Materials.

Spadea, S., Rossini, M., & Nanni, A. (2018). Design Analysis and Experimental Behavior of Precast Double-Tee Girders with CFRP Strands. PCI Journal, January-February.

Influence of Camera Resolution and Distance in Measuring Structural Displacements Using Unmanned Aerial Vehicles for Applications in Bridge Engineering

Efstathios Polydorou[1*], Des Robinson[2], Su Taylor[3], and Patrick McGetrick[4]

[1] Queen's University Belfast (QUB), Belfast; email: S.Polydorou@qub.ac.uk
[2] Queen's University Belfast (QUB), Belfast; email: des.robinson@qub.ac.uk
[3] Queen's University Belfast (QUB), Belfast; email: S.E.Taylor@qub.ac.uk
[4] Queen's University Belfast (QUB), Belfast; email: p.mcgetrick@qub.ac.uk

[*]: corresponding author

Keywords: unmanned aerial vehicles; structural displacements; computer vision; bridge engineering; image processing

Abstract: Measurement errors analyzing the displacements in structures (i.e. bridges) using static camera techniques, is commonly related to camera resolution, distance between the camera and the measuring object, digitization, post-processing methods and procedures of analyzing the displacements. In the case of using unmanned aircrafts, known as drones, stabilization becomes an issue where the frame by frame must be analyzed separately. This paper investigates the errors associated with measuring structural displacements in simply supported beams in relation to the camera resolution, field of view and digitization of the images acquired from the unmanned aircrafts. Four incremental weights were used to apply the load on the mid-span of the beam and the vertical displacements were measured using displacement sensors. In this study, a commercially available unmanned aircraft suitable for structural bridge inspections, imaging equipment and advanced image processing techniques were implemented. Accounting for stationary and hovering test measurements, tests were carried out and processed using tracking and image correlation algorithms. It is shown that the unmanned aircraft can be employed to measure the mid-span displacements with relatively high accuracy when computer vision methods are applied. This paper demonstrates the efficiency of the unmanned aircraft camera to measure the displacements at wider fields of view and a comparison of camera resolution characteristics is presented.

1. Introduction

Monitoring static and dynamic displacements in bridge structures is important for collecting quantitative information related to the effective condition assessment and structural safety evaluation (Feng et al. 2015). In structural health monitoring (SHM), the displacements are measured using contact or non-contact sensors. Linear Variable differential transducers (LVDTs) is the most common sensor used to measure the displacements in short span bridges over accessible surfaces. However, LVDTs are unsuitable in places where access in surfaces is not possible (Xu et al. 2016). Non-contact type sensors such as laser vibrometers were used in previous studies to measure the dynamic displacements in bridges. However, measurement errors were reported to be in the range between 5 mm to 10 mm (Fukuda et al. 2010; Ribeiro et al. 2014; Nassif et al. 2005; Casciati and Fuggini 2011). With the advancements in non-contact

devices, vision-based sensors such as high-resolution cameras were implemented in SHM, to measure the displacements in bridges. However, camera sensors are not suitable in inaccessible areas due to the limitations in the field of view (FOV). Unmanned aerial vehicles (UAVs) is a new technology which has not yet implemented for identification and health assessment of bridges in the field of SHM (Polydorou et al. 2018). This is due to the many challenges involved with the stabilization and image analysis including camera resolution, field of view, digitization and other factors, to eliminate measurements errors. Therefore, these errors need to be quantified during the analysis procedures to avoid misinterpretation of the results. The aim of this study was to assess the effect of the resolution and the field of view between the camera and the surface of the beam on the displacement measurements using autonomous UAVs.

2. Experimental methods

The tests were performed on a simply supported polystyrene foam beam with cross-sectional dimensions (Width x Depth) equal to 100 mm x 100 mm. The total length of the beam was 2000 mm with a clear span of 1600 mm. The beam was supported by two rollers and was loaded to the middle section using four circular steel plates, weight of 0.382 grams each. Prior to testing, small targets were used in different locations, in-plane and out-of-plane, to track the stationary positions in 3D space and correct the movement of the drone using inverse analysis. The UAV used in this study was a Phantom 4 Professional, with 1-inch sensor camera, which recorded the videos using resolutions at 1280x720 pixels, 1920x1080 pixels and 3840x2160 pixels (no digital zoom was used). During flight, the UAV was hovering parallel to the tested beam and video measurements were recorded from a field of view of 1 meter, 2 meters and 3 meters away from the front surface of the beam. The recording data collected using the UAV was sampled at 30 Hz and compared to a linear variable differential transducer which was positioned in the mid-span of the beam, sampled at 1 Hz. A static camera was also used to measure the displacements, operating at a frame rate of 30 Hz and with a resolution of 1920x1080 pixels (Polydorou et al. 2018). The experimental test setup of the beam is shown in Fig. 1.

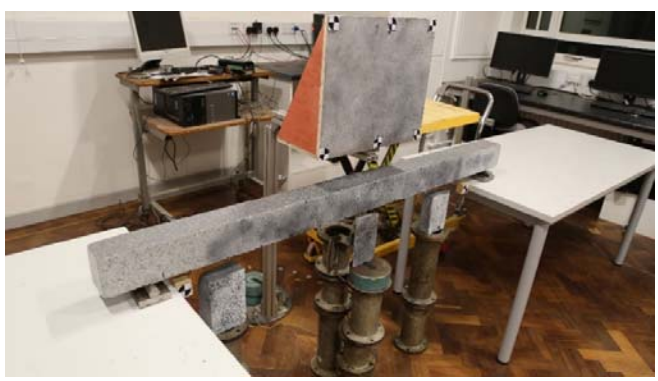

Fig. 1. Test setup used in the experiments

3. Discussion of the results

Fig. 2 presents the vertical displacement versus time histories measured using the displacement sensor, static camera and the raw video footage recorded from the UAV. The displacements were derived using digital image correlation, by tracking the planar surface motion in the mid-span of

the beam with a 29 pixels subset size and a 3 pixels step size. During the testing procedures, the UAV experienced significant movement due to difficulties in detecting dual satellite connectivity and GPS in the indoor environment. As a result, fluctuations involving unstable movement in the mid-span displacement of the beam were presented when using the UAV. To correct this excessive movement, the motion of the stationary targets was tracked using digital image correlation algorithms and stabilized using inverse analysis algorithms. This procedure was performed to consider the in-plane and out-of-plane translations and rotations.

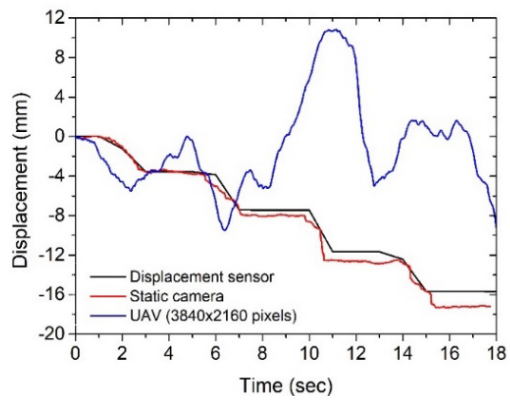

Fig. 2. Displacement versus time history using the displacement sensor, static camera and the raw video footage from the UAV at a field of view of 2 meters

As soon as the video recordings were stabilized, further tests were carried out to investigate the effect of resolution on the displacement measurements. For a field of view of 1 meter, the resolution was found to have less effect on the displacements up to the third loading, compared to the static camera. In the fourth loading, the absolute error of the displacements between the UAV (resolution of 1920x1080 pixels) with the static camera and LVDT was found to be 0.53 mm and 2.78 mm respectively. In contrast, the absolute difference in the displacement measurements for resolutions of 1280x720 pixels and 3840x2160 pixels were 0.18 mm and 1.94 mm. It must be noted that the obstacle avoidance sensors were deactivated during the test to achieve a closer field of view at 1 meter. The displacement sensor showed higher variation, which could be attributed to the accuracy of the sensor. At a field of view of 2 meters, the maximum absolute displacement was found to be 0.1 mm in the first loading, 0.24 mm in the second loading, 0.31 mm in the third loading and 0.38 mm in the fourth loading using a resolution of 1280x720 pixels, compared to the static camera. Moreover, at a field of view of 3 meters, a small amount of noise was presented in the displacement histories. The maximum difference was observed to occur in the second loading case for the 1280x720 pixels resolution, with an absolute displacement of 0.72 mm. Both resolutions of 1920x1080 pixels and 3840x2160 pixels showed differences less than 0.30 mm.

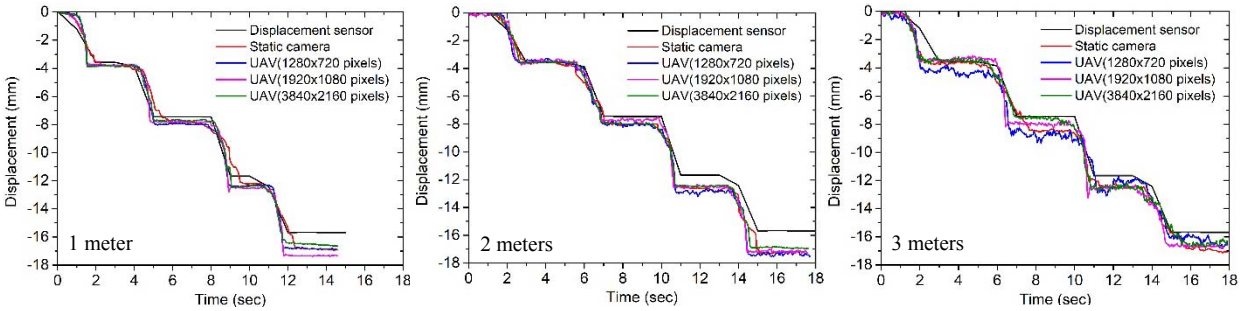

Fig. 3. Effect of resolution and FOV on the displacement versus time histories using the UAV

Using the lowest resolution (1280x720 pixels), the displacements recorded from a field of view of 1 meter and 2 meters were found to follow the same trend. It was noticed that the displacements measured from a field of view of 3 meters presented fluctuations with steep changes. In the case of a resolution with 1920x1080 pixels, the displacement versus time histories measured from field of views of 1, 2 and 3 meters followed a similar trend, with a maximum absolute difference of 0.4 mm in the fourth loading (3 meters). For higher resolutions (3840x2160 pixels), it was found that the maximum absolute difference in displacement was 0.33 mm when the field of view was 1 meter and 2 meters.

4. Conclusions

This paper presented the results of an experimental study to investigate the influence of resolution and field of view on the displacement measurements of a simply supported beam using UAV technology. This study highlighted that the displacements can be obtained with high accuracy from a short distance of 2 meters and relatively low resolution. Higher field cause noise and fluctuations in the displacements with increased uncertainty in accuracy. It was also concluded that issues may arise using LVDTs concerning accuracy and non-linearity response of the sensor.

5. References

Feng, D., Feng, M. Q., Ozer, E., and Fukuda, Y. 2015. A Vision-Based Sensor for Noncontact Structural Displacement Measurement, Sensors (15), 16557-16575.

Fukuda, Y., Feng, M. Q., and Shinozuka, M. 2010. Cost-Effective vision-based system for monitoring dynamic response of civil engineering structures, Structural Control and Health Monitoring, 17(8), 918-938.

Nassif, H. H., Gindy, M., and Davis, J. 2005. Comparison of laser Doppler vibrometer with contact sensors for monitoring bridge deflection and vibration, NDT & E International, 38(3), 213-218.

Casciati, F., and Fuggini, C. 2011. Monitoring a Steel Building using GPS Sensors, Smart Structures and Systems, 7(5), 349-363.

Polydorou, E., Robinson, D., Treanor, G., Taylor, S. and McGetrick, P. 2018. Vision-based deformation and free vibration measurements of beams using Unmanned Aerial Vehicles (UAVs), Proceedings of the Civil Engineering Research in Ireland (CERI 2018), Dublin, Ireland.

Ribeiro, D., Calçada, R., Ferreira, J., and Martins, T. 2014. Non-contact measurement of the dynamic displacement of railway bridges using an advanced video-based system, Engineering Structures, 75, 164-180.

Xu, Y., Brownjohn, J. M. W., Hester, D., and Koo, K. Y. 2016. Dynamic Displacement Measurement of a Long-Span Bridge Using Vision-based System, Proceedings of the 8th European Workshop on Structural Health Monitoring (EWSHM), Bilbao, Spain.

Bridge Engineering Institute Conference 2019 (BEI-2019)
Honolulu, Hawaii, USA, July 22-25, 2019

Bridge Fleet Asset Management Strategy Utilizing Innovative Performance Measurement Technology to Maximize Performance

Paul Westcott[1], Michael Bennon[2], and Brian Westcott[3*]

[1] Cornell University, Ithaca NY USA; email: pbw42@cornell.edu
[2] Stanford University Global Project Center, Stanford, CA USA; email: mbennon@stanford.edu
[3] Intelligent Structures, Inc, Menlo Park CA USA; email: bwestcott@intellistruct.com

*: corresponding author

Keywords: asset management; performance measurement

Abstract: Aging bridge infrastructure is placing increased budget demands on bridge owners to operate and maintain their bridge fleets at an acceptable level of performance over their life cycle. The US Federal Highway Administration is implementing law in 2019 that requires states to develop and implement a compliant highway and bridge asset management plan. The FHWA defines "Asset management is a strategic and systematic process of operating, maintaining, and improving physical assets, with a focus on engineering and economic analysis based upon quality information, to identify a structured sequence of maintenance, preservation, repair, rehabilitation, and replacement actions that will achieve and sustain a desired state of good repair over the lifecycle of the assets at minimum practicable cost." Failure to have a strategic plan and budget that is fully funded will result in loss of the maximum Federal share on National Highway Performance Program (NHPP) projects and activities carried out by the State shall be reduced to 65% for that fiscal year. Fortunately, there is a convergence of innovative new technologies for measured bridge structural performance (MBP) of bridge assets along with pending changes in bridge codes that allow new strategies for bridge life cycle management resulting in significant cost reduction of bridge asset management. This paper will discuss the development of various bridge asset life cycle management strategies for a fleet of bridges that balances total mobility, risk and economics of bridge fleet management. The asset management strategy utilizes a total bridge condition index along with historical deterioration trends to assist owners in calculating the bridge network value over a twenty-year planning horizon. The evaluation of various asset management strategies and life cycle cost analysis as a measure of value to the bridge network. The bridge asset management strategies incorporate the traditional decisions on preservation, repair, rehabilitation, and replacement while also incorporating the options provided using innovative real-time bridge performance monitoring, SHM and decision support. Several strategic asset management scenarios are evaluated for application to fleets of bridges in a region of California. These strategies are analyzed to show the trade-offs and benefits to mobility, risk and budget expenditures

1. Introduction

Major changes to bridge fleet asset management are being driven by the US Federal Highway Administration implementing new law in 2019 that requires states to develop and implement a long-term compliant highway and bridge asset management plan. Fortunately, there is a convergence of innovative new technologies for measuring bridge structural performance (BSP)

of bridge assets along with pending changes in bridge codes that allow new strategies for bridge life cycle management. Resulting in both improved bridge performance and significant cost reduction of bridge asset management.

2. Bridge State and Risk

The conventional method of determining bridge state is based on utilizing visual inspection information combined with the design and age of the bridge resulting in an engineering judgement of the present condition or state of a bridge. The result is a bridge rating reflected by a sufficiency rating, load rating or other defined rating system which is a representation of the risk. Visual inspection is the primary method of bridge review used in all countries rating systems. The accuracy of visual inspection has limitations but historically has been the only economic method that could be applied to all bridges in a fleet. In a study of visual inspection: *" From the routine inspection tasks, it was observed that routine inspections are completed with significant variability. As an example, on average, four or five different condition ratings were assigned to each element. It is predicted that only 68 percent of the condition ratings will vary within one rating point of the average. Similarly, it is predicted that 95 percent of the condition ratings from bridge inspections will be distributed over five contiguous condition ratings, centered about the average. Also, it was observed that condition ratings are generally not assigned through a systematic approach." (1)* A report that reviewed the difference between load-ratings based on live load test with measured bridge parameters using sensors, to the load ratings of the bridges based on visual inspection showed that 85% were significantly higher from the live load test results but that 15% were lower than the conservative engineering judgement had rated. This confirming the inaccuracy of visual inspection as a rating method. (2)

Table 1. Rating of Bridges Using Live Load Testing
Canadian Live Load Testing Summary Report 1975-2010

Bridge Material Types	Sample Size	Results	Conclusion
Steel, Concrete, and Timber	102 total	81 higher rated 14 decreased 7 other type of testing	85% improved (81/95)

Canadian Bridge Test results – 1975 – 2010 Aftab Mufti PhD and Baidar Bakht PhD.

This was further supported by work done by the Massachusetts DOT that showed when a set of 29 bridges were live load tested the result was a 0 to 60% improvement or average of 30% increase in load rating when measured versus depending on visual inspection. (3) This benefit of measured bridge performance is acknowledged by the transportation industry: *"There is a growing consensus on the need to transition to data driven objective fact-based decision-making in managing highway infrastructures. Achieving this will require the use of sensing, simulation and information technologies to obtain, visualize and interpret quantitative performance data from bridges."* (4) Canada is transitioning to measured performance and has proposed a revised set of bridge codes that reflect the additional accuracy of adding live-load testing and further continuous monitoring to the assessment of a bridge's state of performance. *(5)* The results of transitioning to a system of measured performance will ultimately increase the

utilization of the full life cycle of a fleet of bridges and result in more productive use of the valuable bridge assets.

3. Bridge Life Cycle Management Strategy

States have used limited implementations of SHM and live load testing on selective bridges to reduce risk and make improved bridge asset management decisions. New York State DOT has used live load testing to open restricted bridges. (6) A Canadian province, Manitoba Infrastructure, has incorporated a bridge life cycle management strategy on a set of major bridges that incorporates Structural Health Monitoring (SHM) and designed rehabilitation to increase mobility, reduce risk with a reduced budget spend. Manitoba has extended 50 year design life to 80 + years using this bridge asset management strategy (7). The Manitoba strategy implements continuous performance monitoring and live load tests to understand how a bridge structure is behaving under known loads followed with rehabilitation at 40 to 50 years. This strategy has been restricted to a few major bridges due to the historic high cost of Generation 1 (Gen 1) SHM. Gen 1 SHM has consisted of developing a custom solution for each bridge application through the integration of sensors for measurements that are wired into a common data acquisition system. The data acquisition system sends the data to a central data center which archives all the measurements for future analysis. The data is stored and queried as needed to perform specific analysis. Gen 1 systems have high installation and operating costs. (8) To use digital measurements and structural health monitoring incorporated as a tool for the entire fleet of bridges requires an innovative Generation 2 (Gen 2) approach to bridge performance measurement BPM at a much lower cost with advanced analytics to allow use of this information to support decisions on the bridge fleet without adding a huge team of engineers to utilize all the additional information. Gen 2 technology based on semiconductor sensors, mesh networks on the bridge, edge computing, wireless communication, IoT (Internet of Things), with low power requirements allowing operation with solar power. Data is gathered, and analytics performed partially at the bridge to reduce communication requirements and is then sent wirelessly to a cloud computing environment. An enterprise bridge fleet performance asset management platform operates in the cloud allowing real-time bridge dashboards, performance analytics and machine learning that are used to manage an entire fleet of bridges. An emerging strategy for bridge asset management allows for a transition to a measured fact-based system utilizing a fleet performance asset management platform. This strategy is depicted in the graph of figure 2. The strategy is based on the life cycle of a bridge and the information on the bridge state of performance over time. The figure has the X axis as time with the historic design life of a bridge shown as 50 years and the goal of extending bridge life to 100 years. The Y axis is the Bridge Performance on a scale of 0 to 100 and can be either the SR or other rating (based on visual inspection) that transitions to a measured bridge performance index PI (based on measured state). There is a point when the bridge falls below the accepted minimum operating performance that is shown as the Operational Performance Threshold (OPT). This is the point when the bridge needs to be closed and rebuilt. The state of the bridge is shown through 4 lines that degrade over time.

The solid blue line is the bridge design life cycle as designed with a level of operational performance that falls below the standard at 50 years. Since there is a factor of safety built into the design life which also incorporates the reliability of the known state due to visual inspection. The solid red line depicts the actual performance state of the bridge over its life cycle (P-Actual).

The two blue dotted lines show the high-performance range (P-High) and low performance range (P-Low) for a fleet of bridges.

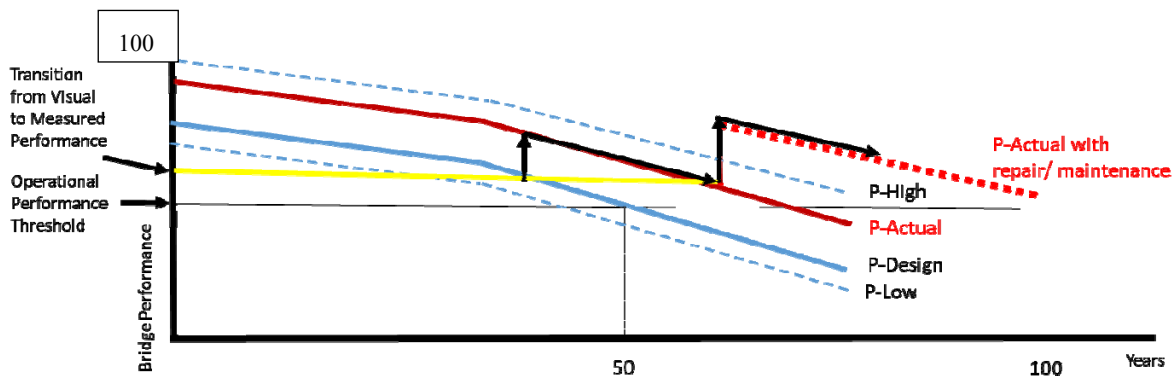

Fig. 2. Bridge asset management strategy

The new bridge management strategy utilizing Gen 2 bridge performance measurement and a PI is implemented as follows. During the first years of bridge life cycle a bridge performance is assessed using conventional visual inspection and operational performance is stated as the SR (shown as the blue line). If conventional life cycle management was incorporated the bridge would continue to deteriorate until it reached a state where it was below the OPT and would be rebuilt. The new measured performance strategy uses a different approach. Once the SR reaches a determined transitional threshold that is determined by the known variability due to visual inspection the method of assessment of bridge performance transitions from visual inspection to measured state through BPM combined with visual inspection (shown as the green line intersection with bridge state). At this point the bridge has installed a BPM system and a live load test is run to determine a new calibrated PI for the state of the bridge. The measured bridge state is monitored over a time period and the method of rehabilitation that is required is determined by utilizing the analytics available for bridge components (example: girder strain-acceleration) as well as the overall operation of the bridge system (example: load sharing). Rehabilitation is implemented (point 4) which improves the bridge state to a higher level which is incorporated into an adjust PI. The bridge continues to be monitored to measure state and rate of deterioration allowing the 100 year or greater life cycle bridge.

4. Economics of Bridge Fleet Management Strategy – Sacramento District 67

Sacramento bridge district was chosen to represent a bridge fleet for analysis of the two bridge policies: Scenario 1. Tradition bridge management with rebuilding at end of life and Scenario 2. Innovative bridge management incorporating measured performance based on monitoring and SHM assessment combined with preventive rehabilitation earlier in the bridge life cycle for life cycle extension. The Sacramento fleet modeled has 473 bridges with a starting average SR of 84.3. The factors used for the model as shown by figure 2 are:

Table 2. Factors used

Transition factor	45	Bridge Policy
Operation Performance Threshold	30	Bridge Policy
Annual rate of deterioration	1.4	Straight line over 50 year life
Bridge Rebuild cost (sq/m)	$6000	Industry data /
Ratio Rebuild /rehabilitation cost	4.5	FHA Transportation (9)
Annual Cost for Monitoring and Analysis Gen 2	$25,000	Industry RFP - Quotes
Annual Cost for Monitoring and Analysis Gen 1	$125,000	Industry RFP – Quotes (GEN 1= 10 times cost of Gen 2 Monitoring and Analysis)

Scenario 1 – rebuilding bridges at end of life when an operational threshold is reached (SR=30)
Scenario 2 – GEN 2 monitor at SR=45 and rehabilitate 4 years after start of monitoring

Table 3. Scenarios

Scenario 1	10 yr	15 yr	20 yr		Scenario 2	10 yr	15 yr	20 yr
Bridges Rebuilt	12	4	10		Bridges rehab	30	11	42
					Bridges Monitor	34	53	83
Cost for period	$76.4	$23.2	45.3		Cost for period	$31.8	$22.2	$49.6
Total Cost	$144.9				Total Cost	$102.7		
Ave. SR	73.3	67.0	61.1		Ave. SR	73.6	67.7	63.1
					NPV (7% discount)	$21		
					IRR	30%		

The results showed a significant budget savings from implementing Scenario 2 -measured performance over Scenario 1 traditional methods with the total cost difference of $42 million, a NPV (at 7%) of $21 million and a annual IRR of Scenario 2 over 1 of 30%. When GEN 1 technology was used for these scenarios the result was a negative result of an NPV of – $7 million. The factors used for this model are conservative and show the result of innovation allowing new strategies are shown. Previously with old GEN 1 SHM data acquisition a strategy as described would not be feasible. The results are consistent with other work on monitoring end of life bridge assets (10).

5. Conclusion

An inflection point for bridge fleet management has arrived. The combination of federal requirements for long term planning and BPM for a fleet of bridges has mandated managers look for different policies for bridge asset management. Combining the changes required by the Transportation MAP 21 with the new economics of bridge performance measurement and analytics created by IoT based Gen 2 systems create an environment for rapid innovation, improved fleet performance, with lower budgets and higher bridge asset life cycle productivity.

Organizational change required to implement this technical innovation is as important as the technology behind it. Bridge owners must understand the trade-off between increased IT spending and better asset management. Bridge codes must be updated and institutionalized to allow the use of measured performance. Successful innovation and transformation of bridge fleet management policy will ultimately be dependent on leadership to this new strategy.

6. References

1. Reliability of Visual Inspection for Highway Bridges, Volume I: Final Report Publication Nos.: FHWA-RD-01-020 and -021 FHWA Contact: Glenn Washer, HRDI-10, (202) 493-3082
2. Mufti, A and Bakht, B. Canadian Live Load Testing Summary Report 1975-2010, SIMTrec University of Manitoba Fall 2017
3. Heath, D. R., Richard, C. Benefits of Live Load Testing and Finite Element Modeling in Rating Bridges. Presented at MassDOT Innovation and Tech Transfer Exchange, Worcester, MA March 12, 2015.
4. Transportation Research Board Working Group Meeting – Washington D.C. January 2017 (4)
5. Mufti, A, Bakht,B, Horosko, A, and Eden R, A Case for Adding An Inspection level Related to SHM for Bridge Evaluation by CHBDC, 10th International Conference on Short and Medium Span Bridges, Quebec City , Quebec, Canada July 31, 2018
6. Hag-Elsafi, Osman, Kunin, Jonathan. Load testing for Bridge Rating dean's Mill Over Hannacrois Creek, Special report 147 TRANSPORTATION RESEARCH AND DEVELOPMENT BUREAU New York State Department of Transportation February 2006
7. Eden, R. Utilizing SHM systems to better manage our highway structure assets. Presented at Intelligent Sensing for Innovative Structures SHM Workshop, Winnipeg, MB, Canada, May 5 2014.
8. Lovejoy, Steven. Applications of Structural health Monitoring to Highway Bridges, Oregon DOT SHM Seminar 2008
9. US DOT Federal Highway Administration. Financial Planning for Transportation Asset Management Overview Pg. 54 February 2015
10. Westcott, P. and Azhari, F. THE ECONOMICS OF INTEGRATING INNOVATIVE MONITORING TECHNOLOGIES INTO BRIDGE MANAGEMENT POLICY TRB committee AHD35 Standing Committee on Bridge Management. TRB 96th Annual Meeting Compendium of Papers Transportation Research Board 96th Annual Meeting Location: Washington DC, United States Date: 2017-1-8 to 2017-1-12 Report/Paper Numbers: 17-04030

Monitoring Steel Bar Corrosion Based on Distributed Optical Fiber Sensing Technology

Fujian Tang[1*], Hao Tian[2], and Hong-Nan Li[3*]

[1] State Key Laboratory of Coastal and Offshore Engineering, School of Civil Engineering, Dalian University of Technology, Dalian, China; email: ftang@dlut.edu.cn
[2] State Key Laboratory of Coastal and Offshore Engineering, School of Civil Engineering, Dalian University of Technology, Dalian, China; email: th15229775476@163.com
[3] State Key Laboratory of Coastal and Offshore Engineering, School of Civil Engineering, Dalian University of Technology, Dalian, China; email: hnli@dlut.edu.cn

*: corresponding author

Keywords: corrosion; chloride; concrete; optical fiber; cracking

Abstract: Optical frequency domain reflectometry (OFDR) distributed optical fiber is employed to monitor non-uniform corrosion distribution of steel bar. Mortar cylindrical specimen containing steel bar (12 mm diameter) is fabricated. After moisture curing for 28 days, optical fiber is wrapped onto the mortar cylinder with a spacing of 100 mm, and the cylinder is then embedded in river sand and subjected to accelerated corrosion tests. To keep a corrosive environment, 3.5 wt.% NaCl solution is periodically sprayed onto the river sand. During the accelerated corrosion test, the strain of optical fibers generated due to steel bar corrosion is recorded with an OFDR-based interrogator from LUNA Technologies. Results show that non-uniform corrosion of steel bar results in different size of cracks on mortar surface which are captured by the optical fiber. Therefore, OFDR distributed optical fiber can effectively monitor the non-uniform corrosion of steel bar.

1. Introduction

Chloride-induced reinforcement steel corrosion is one of the main causes of reinforced concrete (RC) structural deterioration in marine environment or subjected to de-icing salt attack. It is estimated that the annual corrosion-induced direct maintenance and capital cost of concrete highway bridges was estimated to be $4.0 billion in 2002 in the U.S. alone (Koch et al, 2002). The indirect cost of corrosion due to traffic delay and loss of productivity was estimated to be as high as 10 times that of direct corrosion cost (Koch et al, 2002). Corrosion causes concrete cracking, concrete-steel bond loss, mechanical degradation of steel bars, and consequently reduction in the carrying capacity of RC structural members and systems (Tang et al, 2014). Therefore, it is necessary to develop sensors or sensing instruments to monitor steel bar corrosion in RC structures.

Over the past two decades, optical fiber sensors have been proposed to monitor steel corrosion in RC structures due to its advantages over traditional techniques, such as compactness, high precision and stability, electromagnetic immunity and possibility of being inserted in large sensor networks (Li, et al, 2004). Fiber Bragg grating (FBG) sensors are proposed to indirectly monitor steel corrosion in concrete by measuring the corrosion induced strain change (Gao et al,

2011). By coating a thin layer of Fe-C coating, or nano iron/silicate on the surface of long period fiber grating (LPFG), the corrosion-induced mass loss is quantitatively correlated with the change of the resonant wavelength, which in turn is used to monitor corrosion-induced mass loss of steel bars in RC structures (Huang et al, 2015; Chen et al, 2016, 2017; Tang et al 2018). However, these optical fiber corrosion sensors based on FBG or LPFG can only be used to monitor corrosion at a point and are unable to monitor corrosion distribution in space. For large civil engineering infrastructures such as oversea bridges, corrosion of steel bar develops non-uniformly in space and over time. Therefore corrosion sensors that can be used to monitor corrosion distribution in space need to develop.

Different from point measurement based on FBG or LPFG sensors, distributed optical fiber sensors such as optical frequency domain reflectometry (OFDR) can measure distribution of some physical parameters along the length of an optical fiber such as strain, stress, vibration, temperature, refractive index, and son on (Ding et al, 2018). It has attracted tremendous attention because of its high spatial resolution and large dynamic range. The purpose of this study is to investigate the performance of OFDR optical fiber for distributed corrosion monitoring of steel bar in mortar cylinder.

2. Experimental details

Mortar cylindrical specimen is prepared and tested as shown in Fig. 1a. It has a length of 900 mm with a diameter of 30 mm. Grade HRB 400 steel bar with a diameter of 12 mm and a length of 1100 mm is used. Mortar was prepared by mixing Portland cement, tap water and river sand with a ratio of 1.0:0.45:1.0. The mortar cylinder specimen was cast by using a PVC pipe with an inside diameter of 30 mm. After moisture curing for 28 days, optical fiber was wrapped around the mortar cylinder with a spacing of 10 mm. After wrapping, a layer of Marine epoxy resin was applied to make sure the fiber is bonded with the mortar cover and to protect the fiber from damage during corrosion test.

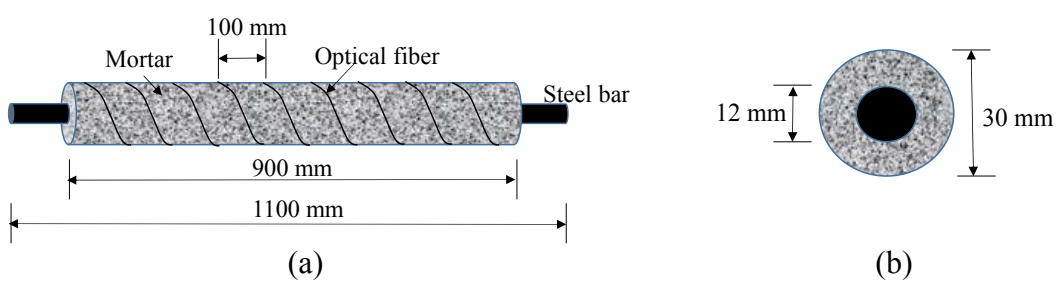

Fig. 1. (a) Dimension of mortar cylinder specimen and wrapping of optical fiber; (b) cross-sectional overview of mortar cylinder specimen.

Accelerated corrosion test (ACT) was used, and the test set-up is schematically illustrated in Fig. 2. A plywood container was fabricated and used to place the mortar cylinder specimen for corrosion test. The container was filled with river sand and its inside was sealed with plastic sheet to prevent leakage of salt water during the tests. For the ACT, the steel bar was connected with the positive end of a power supply and a graphite rod was connected with the negative end.

A constant electrical current was applied to produce a corrosion current density around 300 μA/cm^2. During the test, 3.5 wt.% NaCl solution was sprayed periodically onto the river sand to keep a corrosive environment. Distributed strain of the optical fiber during the test was recorded with an OFDR-based interrogator from LUNA Technologies.

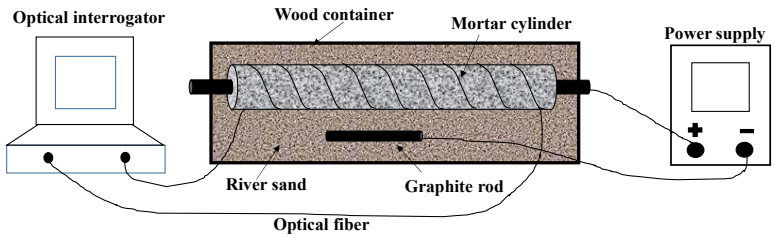

Fig. 2. Accelerated corrosion test set-up.

3. Results

Fig. 3 shows the change of the measured strain from the optical fiber attached on the mortar cylinder surface as a function of test time. It can be observed that after 3 hours of corrosion test, some peaks started to appear which correspond to the cracking of mortar cover. This is because the tensile stress of mortar cover generated due to the expansion of corrosion products at the steel bar-mortar interface reaches its tensile strength and results in mortar cover cracking. The cracking strain of the mortar is around 100 με, which is consistent with results from other research. With an increase of corrosion time, the peaks increase with different rates, which is attributed to the non-uniform corrosion occurred on the steel bar.

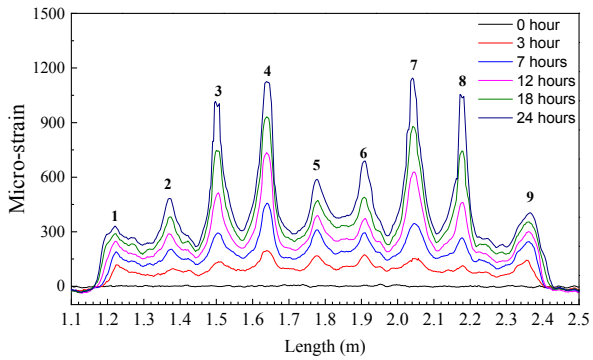

Fig. 3. Change of strain during the first 24 hours of accelerated corrosion test.

Fig. 4a shows the change of measured strain corresponding to peak 7 in Fig. 3. It increases linearly in the first 30 hours, and then its slope started to decrease and remained stable. This is because with an increase of mass loss of steel bar, the mortar becomes softened due to propagation of cracking, resulting in reduced rate of cracking development. Fig. 4b shows the crack on mortar cover corresponding to peak 7 after accelerated corrosion test.

(a) (b)

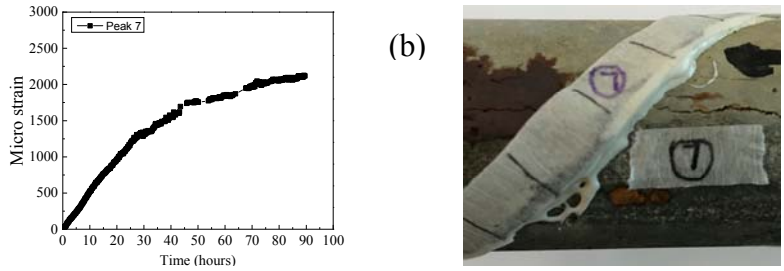

Fig. 4. (a) Change of mortar surface strain over time and (b) the crack present on the mortar surface after corrosion test corresponding to peak 7 in Fig. 3.

4. Conclusions

In this study, corrosion of steel bar embedded in mortar cylinder is monitored by using an OFDR distributed optical fiber with high spatial resolution. Accelerated corrosion test is performed on mortar cylinder specimen, and test results show that steel bar corrosion causes mortar cover cracking which can be captured by the OFDR optical fiber. Different peaks of strain are observed which correspond to different size of cracks due to non-uniform corrosion of steel bar.

5. Acknowledgements

This study was financially supported by the National Natural Science Foundations of China (No. 51878119), the National Key R&D Program of China (2016YFC0701108), the Innovation Fund for Young Scholars from the State Key Laboratory of Coastal and Offshore Engineering at Dalian University of Technology (No. LY18B3), and the Fundamental Research Funds for the Central Universities of China under No. DUT17RC(3)076. The discussion and opinions expressed in this paper are those of the authors and do not necessarily represent those of the sponsors.

6. References

Chen Y., Tang F., Bao Y., Tang Y. and Chen G. 2016. A Fe-C coated long-period fiber grating sensor for corrosion-induced mass loss measurement, Optics Letters, 41(10), 2306-2309.

Chen Y., Tang F., Tang Y. O'Keefe M.J. and Chen G. 2017. Mechanism and sensitivity of Fe-C coated long period fiber grating sensors for steel corrosion monitoring of RC structures, Corrosion Science, 127, 70-81.

Ding Z., Wang C., Liu K., Jiang J., Yang D., Pan G., Pu Z. and Liu T. 2018. Distributed optical fiber sensors based on optical frequency domain reflectometry: a review, Sensors, 18, 1072.

Gao J., Wu J., Li J. and Zhao X. 2011. Monitoring of corrosion in reinforced concrete structure using Bragg grating sensing, NDT & E International, 44(2), 202-205.

Li, H., Li D. and Song G. 2004. Recent applicator of fiber optic sensors to health monitoring in civil engineering, Engineering Structures, 26(11), 1647-1657.

Huang Y., Tang F., Liang X., Chen G., Xiao H. and Azarmi F. 2015. Steel bar corrosion monitoring with long-period fiber grating sensors coated with nano iron/silica particles and polyurethane, Structural Health Monitoring, 14(2), 178-189.

Koch G.H., Brongers M.P.H., Thompson N.G., Virmani Y.P. and Payer J.H. 2002. Corrosion costs and preventative strategies in the United States, Publication No. FHWA-RD-01-156, NACE International, Houston, TX, USA, 2002.

Tang F., Chen G. and Yi W. 2014. Corrosion-induced concrete cracking, steel-concrete bond loss, and mechanical degradation of steel bars, Advanced Materials Research 919-921, 1760-1770.

Tang F., Chen Y., Li Z., Tang Y. and Chen G. (2018). Application of Fe-C coated LPFG sensor for early stage corrosion monitoring of steel bar in RC structures, Construction and Building Materials, 175, 14-25.

Equivalent Compressive Strength of Fly Ash Mortar under Low Water-Binder Ratio

Shiteng Zhou[1], Wenbo Zhang[2*], Mingjie Mao[3], and You Lv[4], and Yixi Xu[5]

[1] School of Civil and Hydraulic Engineering, Ningxia University, Yinchuan, China; email: 937653273@qq.com
[2] School of Civil and Hydraulic Engineering, Ningxia University, Yinchuan, China; email: zhangwenbo@nxu.edu.cn
[3] School of Civil and Hydraulic Engineering, Ningxia University, Yinchuan, China; email: maomj@nxu.edu.cn
[4] School of Civil and Hydraulic Engineering, Ningxia University, Yinchuan, China; email: 840537525@qq.com
[5] Shanghai Construction Engineering Design and Research Institute, Shanghai, China; email: 1791065943@qq.com

*: corresponding author

Keywords: low water-binder ratio; fly ash mortar; equivalent strength; compressive strength

Abstract: In order to provide a reasonable mixing design method of the equivalent compressive strength of fly ash concrete, under a series of low water-binder ratio of 0.24, 0.28 and 0.32, the compressive strength of mortar with fly ash content of 0%, 30%, 50% and 70% were discussed. According to the test results, two types of equivalent compressive strength were obtained: One is fixing the water-binder ratio to 0.32 or 0.28, equivalent compressive strength of 60 MPa and 70MPa can be obtained by keeping the fly ash content within 30%, respectively. And the other one is when the fly ash content is more than 30%, in the case of increasing the fly ash content by 20%, the equivalent compressive strength of around 50 MPa can be achieved by means of reducing water-binder ratio by 0.04, correspondingly. In addition, according to the response surface analysis method, the relational model between compressive strength and water-binder ratio as well as fly ash content was fitted to obtain the prediction curve of equivalent strength of mortar at 28d. It can be observed from the model that the peak of compressive strength in the model appears when the fly ash content is about 20%.

1. Introduction

As is known to all, fly ash (FA) is primarily used as a substitute for cement in various applications, which often leads to a decrease in the mechanical properties of concrete. In most cases, if the FA content exceeds a certain value, e.g. 30%, it will result in a significant decline in concrete strength grade. That is, most of the researches on FA concrete were not carried out under the equal compressive strength. However, in the design, as well as construction and life management of concrete structures, the determination of a certain compressive strength grade is the most fundamental premise. From this point of view, it is more meaningful to discuss other properties of concrete within the same compressive grade. Therefore, it is necessary to further study the mechanism of equivalent compressive strength and its influencing factors.

In recent years, the performance of concrete under equal compressive strength conditions has been paid more and more attention. He et al. (2011) made the equal strength concrete by adjusting the water-binder (W/B) ratio and the FA content under the condition of invariability of sand ratio and total amount of cementitious material. Moreover, the effects of concrete constituents on internal relative humidity and self-shrinkage were studied. However, the design method of equal compressive strength, especially the relationship between FA content and W/B in high volume FA concrete, is still insufficient and remains open to discussion. In the present study, under a series of low W/B of 0.24, 0.28 and 0.32, the compressive strength of mortar with FA content of 0%, 30%, 50% and 70% were discussed.

2. Experimental program

The cementitious materials used in the present study are ordinary Portland cement (P.O. 52.5R) and fly ash. The physical and chemical properties of FA are given in Table 1. The fine aggregate is natural river sand with a fineness modulus of 2.71. The water reducing agent is a polycarboxylic acid superplasticizer, the water reducing rate is 30%.

Table 1. Chemical Composition and Physical Properties of Fly Ash (%)

Al_2O_3	SiO_2	Fe_2O_3	CaO	K_2O	SO_3	SrO	Fineness	Water consumption	Loss on ignition
28.00	50.70	6.67	5.01	2.61	2.58	0.14	5.40	97.00	3.90

Mortar specimens with size 40×40×160mm^3 were cured in water of 20±2°C until the age of testing, namely: 3d, 7d and 28d. For all the mixing proportions, the unit dosage of cementitious materials was fixed to 616kg/m^3, and the mass ratio of sand to cementitious materials binder is 1.1. In addition, the unit dosage of water reducing agent was 2% by weight of gelled material. Test method specified in Chinese standard GB/T 17671-1999, which is identical with ISO 679:1989, was carried out to determine the compressive strength.

3. Results and Discussion

3.1. Compressive Strength

The compressive strength of FA mortar with different W/B ratio is shown in Fig. 1. It can be observed that the compressive strength increases obviously with the decrease of W/B ratio and FA content, and the strength growth varies apparently between 3d to 7d and 7d to 28d. For a given W/B ratio, taking 0.32 as an example, when the FA content is 0% and 50%, the strength increments between 3d to 7d and 7d to 28d are almost the same, respectively, while when the FA content is 30% and 70%, the strength increment between the two periods is evidently different. Thus, it is difficult to find out any relationship between strength increment and curing time when the amount of FA changes. Hence, in order to study the effect of FA content and W/B ratio on the compressive strength of mortar, on the basis of the before mentioned reasons as well as referring to the common practices of current specifications, the 28d compressive strength was selected as the object of discussion.

3.2. Influence of W/B ratio and FA content on compressive strength

At 28d of age, the increment rates of compressive strength at W/B ratio of 0.28 and 0.24 were calculated based on the results of 0.32 W/B ratio (as 100%). The results are shown in the solid dots in Fig.2. At a W/B ratio of 0.28, when the replacement rate of FA is 0 and 30%, the

compressive strength increment rate is 116.87%, 120.41%, respectively. Under the replacement rate of 50% and 70%, the increment rate up to 134.53% and 143.26%, respectively. It is clear that the when the FA content is higher than 50%, the compressive strength increases significantly when the W/B ratio decreases from 0.32 to 0.28. The strength increment ratio is further improved as reducing the W/B ratio to 0.24, which is as high as 221.22% at a FA content of 70%. In short, for the mortar which FA content is above 50%, reducing W/B ratio has a remarkable effect on the strength increment, while its influence is not obvious when FA content is below 30%.

In order to investigate the influence of FA content on compressive strength, the strength reduction ratio calculated according to the variation of FA content is also provided under each W/B ratio, as shown in Fig. 2 (hollow points). It can be seen that under the W/B ratio of 0.32 and 0.28, when the FA content varies between 0 and 30%, the compressive strength reduction ratio is 8.04% and 5.26%, respectively, which has little effect on strength. Whilst as the FA content up to 50% and 70%, the strength reduction ratios are all higher than 20%, which has a significant effect on the strength reduction. When the W/B ratio is 0.24, it can be found that the results are quite different from those mentioned above. Under this W/B ratio, the strength reduction rate is stable in the range of 13.03% to 16.23% although the FA content has changed greatly from 0% to 70%, which indicates that the strength approximately decreases linearly with the increase of FA content.

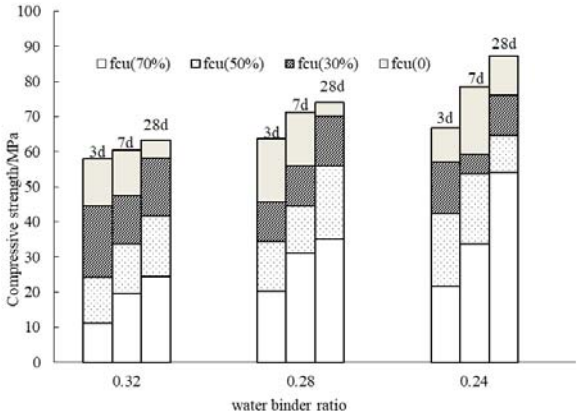

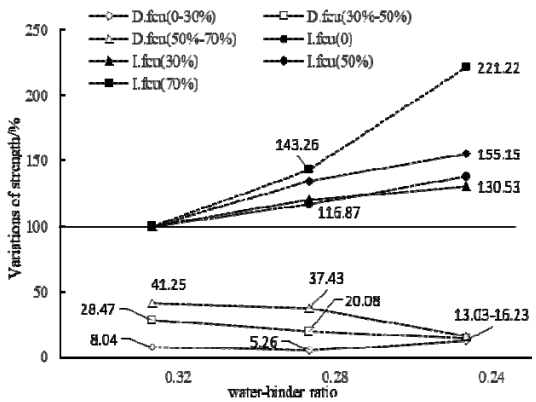

Fig. 1. Variation of compressive strength with age **Fig. 2**. Variations of compressive strength

Table 2. Classification of equivalent compressive strength of mortar

Classification	Water-binder ratio	FA content/%	Compressive strength/ MPa (Strength ratio)
Univariate 1	0.32	0	63.4 (1.00)
	0.32	30	58.4 (0.92)
Univariate 2	0.28	0	74.1 (1.00)
	0.28	30	71.6 (0.96)
Bivariate	0.24	70	54.2 (1.00)
	0.28	50	56.1 (1.03)
	0.32	30	58.4 (1.08)

It can be seen from the above analysis, within the scope of this study, it is possible to achieve the equivalent compressive strength under the premise of adjusting the W/B ratio and the FA content simultaneously. The present study obtains two types of equivalent compressive strength groups, namely, univariate and bivariate groups, which are shown by Table 2. Firstly, the univariate groups refer to obtained equivalent strength when the FA content varies between 0% to 30% on the condition of fixing W/B ratio to 0.32 or 0.28. Besides, for the bivariate group of simultaneous change of W/B ratio and FA content, it can be found that the strength decline caused by 20% increase in FA content can be recovered by reducing the W/B ratio by 0.04. It should be point out that the strength error of equivalent strength mentioned here is 10%.

3.3. Prediction of equivalent compressive strength

In order to study the influence rules of W/B ratio and FA content on mortar strength, according to the existing data, the three-relationship model was fitted. The relationship model is shown in Fig. 3(a), and the goodness of fit is 0.9775. It can be seen that the peak compressive strength occurs when the FA content is about 20%. And formula is as follows

$$f_c = 10^{-m}$$
$$m = 7.95\times10^{-5}\cdot r^2 + 6.29\cdot(\mathrm{W/B})^2 + 0.04\cdot r\cdot \mathrm{W/B} - 0.01\cdot r - 2.48\cdot \mathrm{W/B} - 1.68$$

where, r is the replacement rate of FA (%); W/B is the water-to-binder ratio; and f_c is the compressive strength.

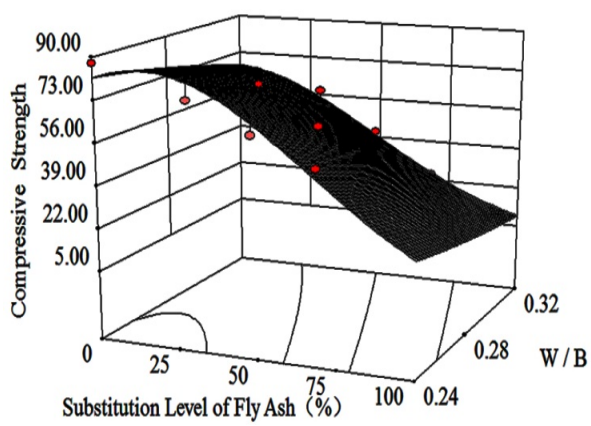

Fig. 3. (a) The model of mortar compressive strength

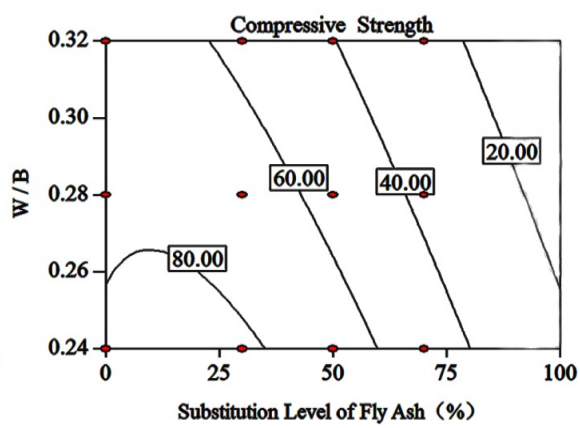

Fig. 3. (b) The prediction curve of equivalent mortar

The prediction curve of equivalent compressive strength at 28d age is also obtained, as shown in Fig.3 (b).

4. Conclusions

(1) When the FA content is higher than 50%, the reduction in W/B ratio is especially effective in enhancing the compressive strength.

(2) When the FA content and W/B ratio varies between 30%-70% and 0.32-0.24, respectively, in order to obtain equivalent compressive strength, if the FA content is increased by 20%, the W/B ratio should be reduced by 0.04 correspondingly.

(3) The prediction model proposed in this paper establishes the formula on the influence of W/B ratio and FA content on mortar strength. In addition, the compressive strength reaches the peak value as the FA content is about 20%.

5. Acknowledgements

This work was supported by the Natural Science Foundation of China (51768058, 51568055).

6. References

Z. He, C. Qian, G. Qian, F. Meng, F. Cheng, X. Gao, Y. Zhuang. 2011. Influence of concrete constituents on autogenous shrinkage and interior relative humidity of concrete at same compressive strengths, Journal of Functional Materials,42(02), 222-225.

Load Characteristics

Bridge Engineering Institute Conference 2019 (BEI-2019)
Honolulu, Hawaii, USA, July 22-25, 2019

A Bimodal Distribution Function for Truck Loads Including Overloads

Bora Jang[1*] and Jamshid Mohammadi[2]

[1] Sharma & Associates, Inc, Countryside, IL, USA; email: bjang5@hawk.iit.edu
[2] Department of Civil, Architectural and Environmental Engineering, Illinois Institute of Technology, Chicago, IL, USA; email: mohammadi@iit.edu

*: corresponding author

Keywords: truck overloads; weight-in-motion data; statistical models; bimodal distribution function; goodness-of-fit test; damage assessment

Abstract: This study presents a bimodal distribution function suitable for representing truck loads including the contribution from overloads. Overloads refer to truck weights in excess of the 356 kN (80 kips). Overload trucks often appear as a sizeable portion of truck populations on highways. As truck populations grow, there is a potential for increase in the frequency of overloads as well. In applications when damage estimations of transportation facilities such as pavements and bridges are desired, theoretical models providing a reasonable representation of truck load populations including overloads will be useful. This is especially true considering the fact that overloads, although less frequent in the entire load population, cause damage at an accelerated rate to pavements and bridges. Load populations mostly exhibit an inconsistent pattern - often with two or more distinct peaks. Mixed probability distribution models consisting of two functions (bimodal models) have been tried in the past and appear to offer a better solution for truck load populations. In this study, several truck load populations for 5-axle vehicles were acquired from the States of Illinois and Michigan and used to demonstrate the suitability of bimodal distribution models in representing the data. The goodness-of-fit tests such as Kolmogorov-Smirnov (K-S) and Anderson-Darling (A-D) methods were used to demonstrate the suitability of the bimodal functions to represent the data. The results show that a combination of beta and lognormal distribution can conveniently be used as a suitable model to represent the truck load populations that were analyzed in this study. The mathematics of the goodness-of-fit test, especially for the A-D method, is presented to show the applicability of this method.

1. Introduction

Truck load data play an important role in condition assessment and life-cycle management of transportation systems such as pavements and bridges. For condition assessment of these systems, a realistic estimation of wear and tear and damage accumulation as a result of the repeated application of truck loads is needed. Damage assessment for a given systems can be done by using truck load data directly in a discrete format. However, such a method will be limited to the system for which the truck load data is available. Furthermore, since the data is used in a discrete format, the frequencies of load occurrences can only be described with specific ranges. Each range will have an upper and lower limit; and any other load value within the limits must be approximated with either the upper or the lower limit. In addition, many highway bridges in operation today have been built for lower truck weights than current design load of 356 kN (80 kips) used in the highway bridge design practice. The passage of overloads can accelerate the

rate of damage to bridges shortening their service lines (Jang and Mohammadi, 2017; 2018). A more versatile and realistic approach in damage assessment can be achieved when the frequency of overloads is properly accounted for, and considered in, a load population model. This can be achieved by using a theoretical model that best represents the truck load data including overloads. The advantage of using a theoretical truck load data model is that (1) it affords the formulation of the damage assessment independent of the type of structure and in a rather theoretical format; and (2) the model would allow the continuity in the load data and eliminates the issues with the discrete data ranges as described.

2. Truck load distribution including overloads

The intensity and frequency of load occurrences in the population vary to a great extent for a given class of trucks. As shown in Fig.1, and described earlier, load populations mostly exhibit an inconsistent pattern - often with two or more distinct peaks. The reason being attributed to the variety of loads in the population; and in most cases, the appearance of two peaks may be because of a combination of loaded and empty truck in the data. Furthermore, load data also contain overload frequencies. Studies on the effect of truck load on highway systems have shown that truckload spectra often contain occurrences of overloads and in certain cases, overloads are rather frequent in which they may significantly affect the service life of bridges (Mohammadi and Shah, 1992; Jang and Mohammadi, 2017; 2018).

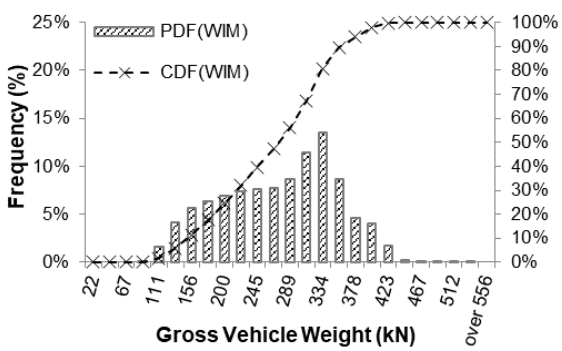

Fig. 1. Frequency distribution of truck weight for 5-axle truck from WIM data (adopted from IDOT from June, 2014 to May, 2015)

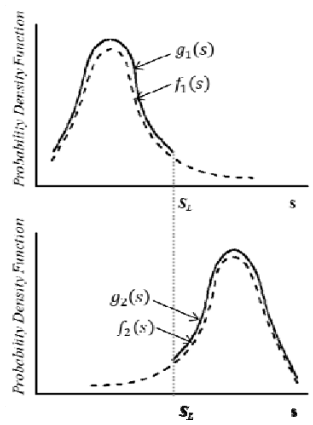

Fig. 2. Schematics of mixed density function with consideration for the common load (S_L)

3. Proposed bimodal distribution

In general, in modeling the truckload data, often a single probability distribution function cannot be used to represent the entire population. Models representing gross vehicle weight with two peaks are referred to as bimodal distribution functions. A bimodal distribution indicates a need for two different continuous probability distributions. Several studies (e.g., Mohammadi and Shah, 1992; Timm et al., 2005) suggest that a mixed probability function is necessary to describe the truckload distribution because of the characteristic of the data as described. In the case of a combination of two distribution models, the overall truckload data is divided into two parts with a common load, S_L, representing the boundary between the two functions. In developing the mixed distribution model, it was decided to use beta and lognormal distributions because of (1)

the fact that they only accept positive values; and (2) they have also been recommended by others (e.g., Mohammadi and Shah, 1992). Fig. 2 describes the concept of bimodal probability function with consideration for the common load. The flowchart in Fig. 3 demonstrates the proposed bimodal distribution using the Weigh-In-Motion (WIM) data.

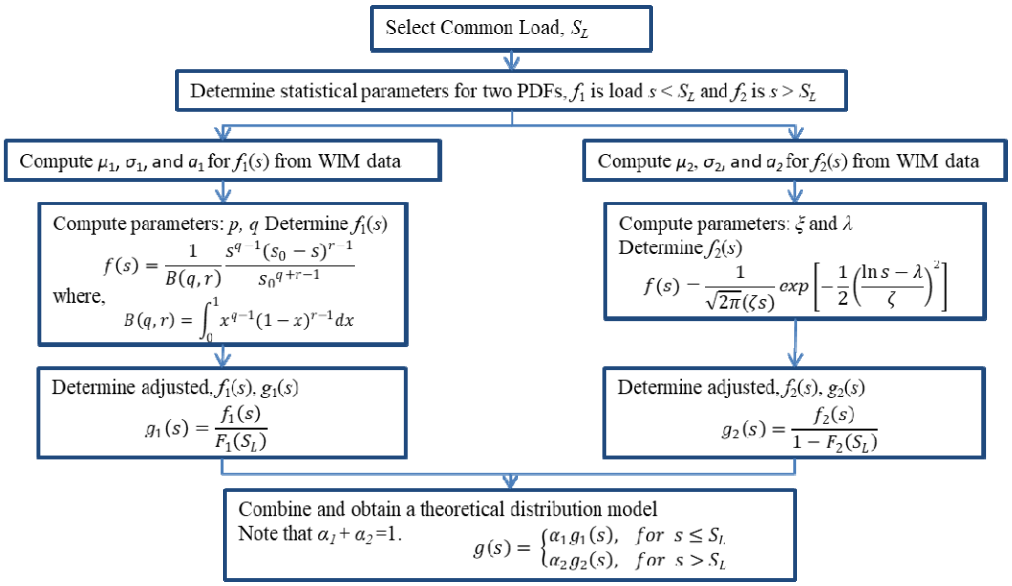

Fig. 3. Flowchart for obtaining a suitable statistical truck load distribution model

4. Goodness-of-fit tests

The validity of a selected distribution model is verified statistically by goodness-of-fit tests. In this study, the Kolmogorov-Smirnov (K-S) and Anderson-Darling (A-D) tests (Ang and Tang, 2007; Anderson and Darling, 1954; Stephens, 1979) are conducted for the proposed theoretical distributions.

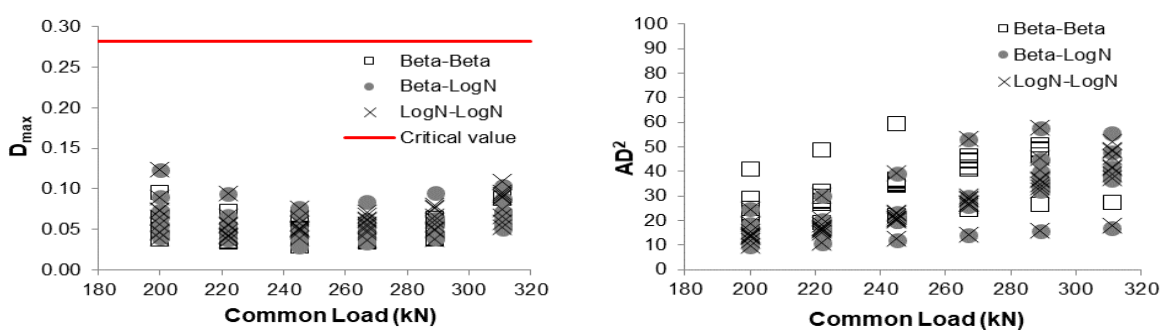

(a) (b)

Fig. 4. Results of K-S and A-D tests with various common loads and combinations of mixed distribution for the nine WIM stations: (a) K-S test; (b) A-D test

Both the K-S and the A-D tests are based on the cumulative probability distribution function of data and by calculating the difference between the observed and the theoretical distributions. The

A-D test has advantages over the K-S test; and it may be applicable specific to the WIM data, since the sample-size is very large. Since most overloads occur at the tail of the pertinent probability density function, the A-D test offers another advantage in the sense that it considers multipliers (weights) for values at the tail. The load spectra of the WIM data are modeled using several possible combinations of beta and lognormal distributions and examined by K-S and A-D tests. Fig. 4 represents the result of K-S and A-D tests. For analyses conducted in this study, and at least within the limitations of the data from the Illinois and Michigan truckloads, it is reasonable to conclude that a combination of the beta and lognormal distributions with the common load of 200 kN (45 kips) is a suitable theoretical distribution for truckload data (including the overloads). The frequency and cumulative probability distribution for the observed WIM data and the theoretical model for two of the nine WIM stations (for which the data was acquired) are illustrated in Fig. 5.

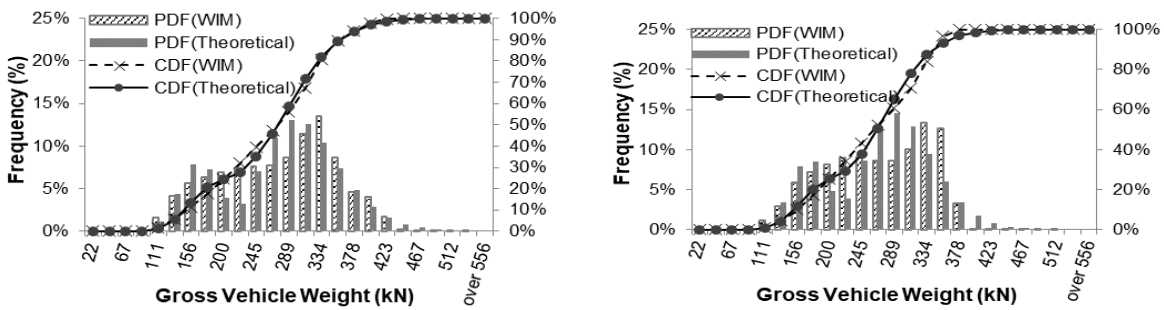

(a) (b)

Fig. 5. The frequency and cumulative probability distribution for the observed WIM data and the theoretical model for the two different WIM stations

5. Summary and Conclusion

In this study, statistical tests for validity of distribution models for truck load populations are described. Mixed distribution models to represent the truck load populations are suggested to account for the trends observed in WIM data. Specifically, a beta-lognormal combination presents a favorable mixed distribution model. The study further enhances the statistical load analysis process by introducing using A-D test in addition to the more traditional K-S test. In applications when a load distribution is needed for damage estimation, a mixed distribution model for situations where WIM data is available is proposed in this study.

6. References

Anderson, T.W. and Darling, D.A. 1954. A Test of Goodness of Fit, Journal of the American Statistical Association, 49(268), 765-769.

Ang, A.H. and Tang, W.H. 2007. Probability Concepts in Engineering – Emphasis on Applications to Civil and Environmental Engineering, John Wiley & Sons, Inc.

Jang, B. and Mohammadi, J. 2017. Bridge rating modification to incorporate fatigue damage from truck overloads, Bridge Structures, 13(2-3), 101-107.

Jang, B. and Mohammadi, J. 2018. Significance of fatigue damage from overload trucks on bridge load rating, MATEC Web of Conferences, 165, 10005.
Mohammadi, J. and Shah, N. 1992. Statistical Evaluation of Truck overloads, Journal of Transportation Engineering, 118(5), 651-665.

Stephens, M.A. 1974. EDF Statistics for Goodness of Fit and Some Comparisons, Journal of the American Statistical Association, 69(347), 730-737.

Timm, D.H., Tisdale, S.M., and Turochy, R.E. 2005. Axle load spectra characterization by mixed distribution modeling, Journal of Transportation Engineering, 132(2), 83-88.

Influence of Reinforced Concrete Slabs with or without Steel Fibre on Fatigue Behavior

Jingyuan Li[1], Qiuning Yang[2*], Mingjie Mao[3], Dongmeng Shan[4], and Wenbo Zhang[5]

[1] School of Civil and Hydraulic Engineering, Ningxia University, Yinchuan, China; email: 1249786278@qq.com
[2] School of Civil and Hydraulic Engineering, Ningxia University, Yinchuan, China; email: 2541316330@qq.com
[3] School of Civil and Hydraulic Engineering, Ningxia University, Yinchuan, China; email: 1401281929@qq.com
[4] School of Civil and Hydraulic Engineering, Ningxia University, Yinchuan, China; email: 467614539@qq.com
[5] School of Civil and Hydraulic Engineering, Ningxia University, Yinchuan, China; email: zhangwenbo@nxu.edu.cn

Keywords: steel fibre; fatigue behavior; dosage of steel fibre; static

Abstract: This paper investigates the fatigue behavior of reinforced concrete deck slab with or without steel fiber, and predict the fatigue life of reinforced concrete deck slab with steel fibre. The punching test was carried out before the fatigue test. Then the capacity of working load in fatigue test was determined based on the result of punching test. By analyzing and comparing different failure pattern of the specimens, steel bar strain, crack width and central residual deflection to study fatigue behavior, experimental results show that directly adding volume at a rate of 0.38% steel fiber, steel bar strain was reduced by 7%, and the crack width decreased by 44%, the rate of crack growth was reduced by 51%, and due to the slab's stiffness was increased by adding steel fiber, the central residual deflection 34% smaller than the reinforced concrete slabs. Adding 0.38% steel fiber can increase the ultimate capacity of static load by 8%, but it can reduce the fatigue life decrease.

1. Introduction

All kinds of slabs will be fatigue failure by the numbers of cyclic load, especially bridge deck slabs. Fatigue loading is caused by moving wheels and is characterised by a high number of load cycles which may exceed 100 million over the service life of a bridge (Schläfli, 1998). Such a severe loading scenario can significantly influence the structural performance of the deck slabs owing to stiffness degradation and damage accumulation. Fatigue failure is a brittle failure that occurs without warning in several cases, it cause continuous bridge collapse and catastrophic casualties. Thus, fatigue behavior has become an important index for bridge detection and evaluation. It is important that study fatigue behaviour of reinforced concrete slab. So far, there are several experiments have investigated the effect of reinforcing ratio, loading range, types of load (i.e. pulsating and moving load) and size of slabs on the fatigue strength of the reinforce concrete deck slabs (Perdikaris, 1989; Graddy, 2002; Matsumoto, 2006). However, there is little research on influence of adding steel fibre on fatigue behaviour of reinforced concrete slabs. Ahsan Parvez has studied the influence of steel fiber on fatigue performance of railway sleeper (Parvez, 2017). The results were different from the expectation. The addition of steel fiber did not improve the fatigue behaviour of sleeper. The support and stress of sleeper and slab are

different, So it still needs further research that the effect of steel fiber on the fatigue behaviour of concrete slab. In this paper, the influence of steel fiber on the fatigue performance of concrete slabs is analyzed and studied from three aspects of steel strain, crack and central residual deflection, and the research results of Ahsan Parvez are verified.

2. Experimental program

2.1 Specimens design

The loading object made in this experiment is a bidirectional plate. Main parameters are shown in Table.1. In the Table, RC means reinforced concrete and SF means steel fibre reinforced concrete. The wavy shear steel fiber with a length-diameter ratio of 37 is adopted in SF. According to The Technical Specification Of Fiber Concrete Structure (CECS 38-2004), the volume rate of steel fiber should not be less than 0.35% (28kg/m3) in general. In this experiment, the dosage of steel fibre is 35kg/m3, namely, the volume rate is 38%. In tensile and compressive side, the Φ12II steel fibre was used. Mechanical properties of reinforcement are shown in Table 2. Adopting grid reinforcement which is more favorable for improving punching capacity, as shown in Fig. 1.

Specimen	Sectional effective height/mm	Reinforce ratio/%	Steel fibre dosage/%	Comprehensive strength（28d）/MPa	Tensile stress（28d）/MPa	Concrete strength
RC	115	0.64	0	36.2	2.14	14.3
SF	115	0.64	0.38	35.62	2.95	14.3

Table 1. Main parameter of specimen

Table 2. Mechanical properties of steel bar

Type	Diameter (mm)	Yield (N/mm^2)	Tensile stress (N/mm^2)	Elastic modulus（$\times 10^5$ N/mm）
HRB400	12	400	540	2.0

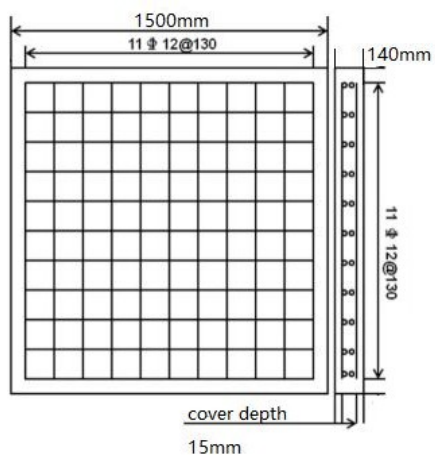

Fig. 1. Reinforcement diagram and sectional diagram of the specimen

2.2. Loading method

A loader with a stroke of 200mm and a thrust of 500kN is used. The loading plate is 100mm × 100mm×30mm square steel plate. Owing to reduce friction, a rubber pad of 100mm×100mm×3mm is inserted between the loading plate and the specimen. The support is simply supported by a round steel bar with a diameter of 50mm and a length of 800mm. Span is 1300mm. The diagram of loading device is shown in Fig. 2. During the loading process, the static strain gauge was used to measure the strain of concrete and reinforcement in the compression and tension area of the specimen plate. Using displacement meter to record the central deflection deformation. After the failure , the angle of the underside of the punching cone and the distribution of crack development were observed. Different tests and results are shown in Table 3. In the Table, RC, RC-1 and RC-2 are identical, SF, SF-1 and SF-2 are identical. In this experiment, all fatigue loads were sinusoidal load with equal amplitude, and loading frequency is 1Hz.

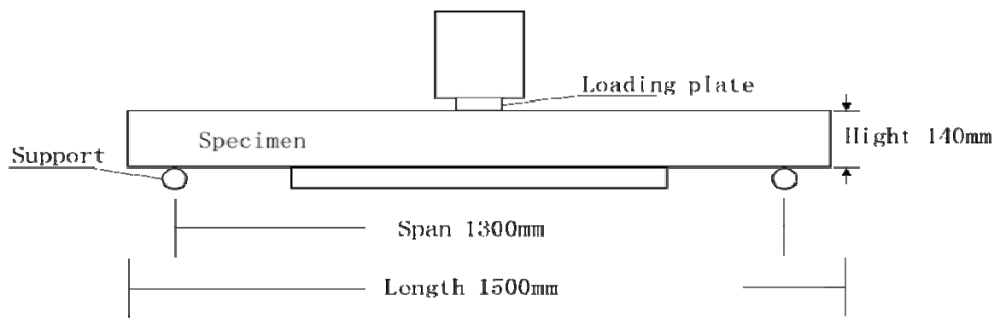

Fig. 2. Fatigue loading device

Table 3. Loading method and results

specimen No.	Test type	Static load capacity/kN	Min-Max Load range/%	Number of cycles to failure
RC	Static	288	——	——
SF	Static	313	——	——
RC-1	Cyclic	288	13-67	26449
SF-1	Cyclic	313	13-67	6700
RC-2	Cyclic	288	13-61	320000
SF-2	Cyclic	313	13-61	171258

3. Test result

3.1. Failure mode

Fig. 3 is the failure of the bottom of RC and SF under fatigue load of different stress range. As can be seen from Fig. 3, both specimens were subjected to fatigue damage. During the first loading, cracks at the bottom of the specimen developed and developed from the loading center to the surrounding area. The farther the crack is from the loading center, the narrower the crack width is. However, due to the stress redistribution, some regions may be different from the law. By comparing RC and SF, it can be found that the crack in RC is wider than that in SF.

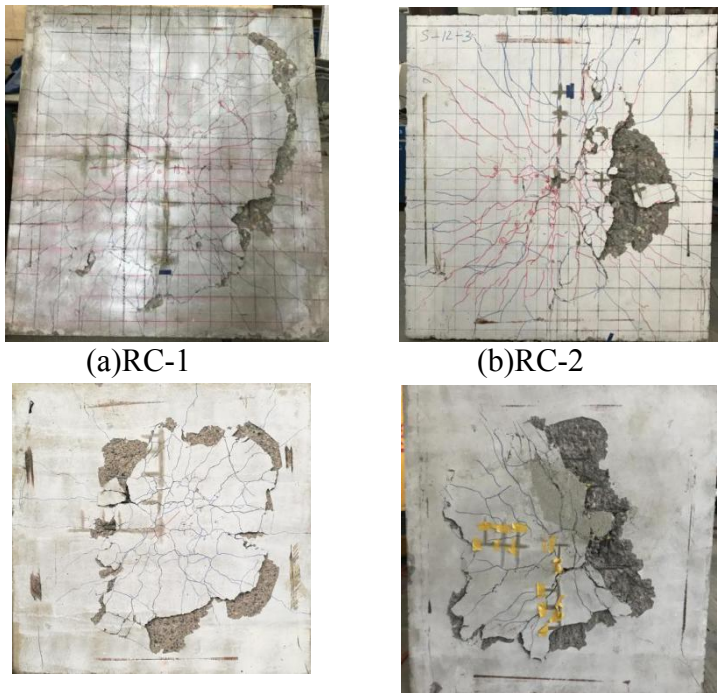

(a)RC-1 (b)RC-2

(c) SF-1 (d)SF-2

Fig. 3. Failure condition of bottom

3.2. Steel strain

Fig. 4 shows the relationship between the maximum tensile strain of the reinforcement and the number of cycles. There was an initial rapid increase in the reinforcing steel bar strains in the first few hundred cycles of the fatigue tests and then after the strain in reinforcing bars became steady or exhibited a very mild gradual increase until the sudden jump in the strain prior to fatigue failure. By comparing the experimental results of steel bar strain, it can be found that under the same stress range, the steel bar strain of reinforced concrete slab is 9% higher than that of reinforced concrete with steel fiber.

3.3 Cracks

In Fig. 7, (a) and (b) are respectively the relationship between the maximum width of crack at the same location of RC-2 and SF-2 and the number of load cycles. As can be seen from the Fig. 8, the crack widths of the two specimens at a distance of 5cm from the loading center showed a trend of rapid increase, then decrease and then increase, while the crack widths of the two specimens at a distance of 10cm from the loading center increased steadily with the increase of cycles number. Comparison of different specimens shows that the crack width of SF-2 is significantly smaller than that of RC-2. According to the linear fitting calculation, the slope of RC-2 and SF-2 in Figure 7 (b) is 0.0467 and 0.0222, respectively. It can be found that the addition of steel fiber can effectively reduce the width of the crack and inhibit the growth of the crack.

3.4. Center residual deflection

In fatigue test, center residual deflection produced because stiffness of specimen degenerate and cracks of bottom grow. The Fig. 9 shows that residual deflection increases with the increase of cycles number, and mainly produce within ten thousand times early loading, with the rise of cycles times after steady increase, before specimen damage increased dramatically. The central residual deflection of reinforced concrete slabs is higher than that of steel fiber reinforced concrete slab.

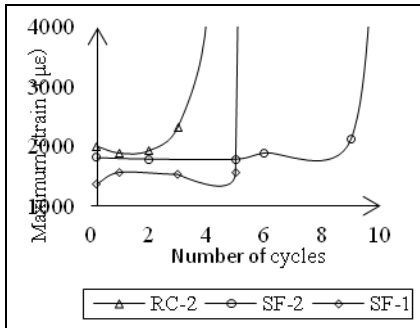

Fig. 4. Maximum tensile strains in the reinforcing steel bars versus number of cycles at maximum load

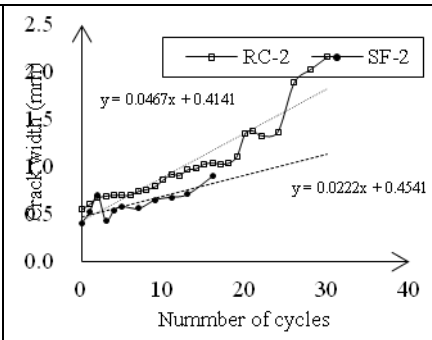

Fig. 5. The crack width versus number of cycles

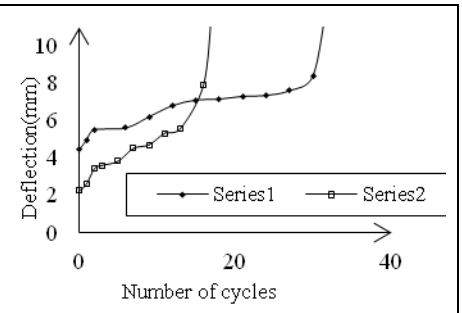

Fig. 6. The center residual deflection versus number of cycles

4. Predict fatigue life by S-N curve

There are three different approaches for fatigue life prediction: S – N curve, fracture mechanics and damage accumulation models that can be used for fatigue assessment of steel elements. However, the concept of S-N curves has gained popularity and, owing to its simplicity is widely adopted by design codes. S-N curve have also been successfully used for fatigue assessment of steel bars in bridge deck slabs. In order to accurately describe the S-N curve, Stüssi submit the formula (1)

$$\Delta\sigma = \frac{R_m + \alpha N^{\beta} \Delta\sigma_{\infty}}{1 + \alpha N^{\beta}} \tag{1}$$

where

$\Delta\sigma$: stress range during the fatigue test; R_m: ultimate tensile strength; N: number of load cycles up to failure or up to end of the test; $\Delta\sigma_{\infty}$: fatigue limit; and αβ: geometrical parameters. The model given by Eq. (1) depends on two geometrical parameters which should be estimated, and on two material parameters which are supposed to be known. The estimation of the two geometrical parameters of the Stüssi model is performed by applying a linear regression. Consider that Eq. (1) can be written also as

$$\alpha N^{\beta} = \frac{R_m - \Delta\sigma}{\Delta\sigma - \Delta\sigma_{\infty}} \tag{2}$$

Taking logarithm in Eq. (2) leads to

$$\log(N)=\frac{1}{\beta}\log\left(\frac{R_m-\Delta\sigma}{\Delta\sigma-\Delta\sigma_\infty}\right)-\frac{1}{\beta}\log(\alpha). \tag{3}$$

Make $X=\log\left(\frac{R_m-\Delta\sigma}{\Delta\sigma-\Delta\sigma_\infty}\right)$, $Y=\log(N)$, Eq.(3) can be written as follows

$Y=AX+B$, where $A=\frac{1}{\beta}, B=\frac{1}{\beta}\log(\alpha)$

The parameters A and B can be determined from the experimental data of fatigue failures by applying a linear regression model. Then,

$\alpha=e^{-\frac{B}{A}}, \beta=\frac{1}{A}$

Substitute the fatigue test data of steel fiber concrete in formula, we can get that $A=9.132, B=10.43$.

So, $\alpha=0.319, \beta=0.11$,(1)can be written as $\Delta\sigma=\frac{313+0.292N^{0.102}\times 87}{1+0.292N^{0.102}}$

(3) can be written as $\log(N)=9.09\times\log\left(\frac{313-\Delta\sigma}{\Delta\sigma-87}\right)+4.55$.

5. Conclusion

In this experimental, by comparing fatigue behavior of reinforced concrete and steel fibre reinforced concrete whose volume of steel fibre is 0.38% we can drew the conclusion as follows:

- Adding steel fiber can make the slabs subject to load more uniform and avoid the local failure caused by the uneven distribution of stress inside the reinforced concrete slabs. It also can effectively reduce the strain in the reinforcement and avoid premature failure of the reinforcement. It can improve the tensile strength of concrete, reduce the width of cracks and inhibit the growth of cracks.
- Adding steel fibre can reduce the center residual deflection, improve stiffness of slabs. Adding 0.38% steel fibre can increase the ultimate capacity of static load by 8%. However, due to increase the ultimate capacity of static load and fatigue load of test lie on ultimate capacity of static load, fatigue load of test also increase. According to the fatigue formula in paper, it can be found that the capacity of impact fatigue life.

6. Acknowledgment
This study was supported by the National Natural Science Foundation of China (51468052) and the Special Project for Scientific and Technological Cooperation with Foreign Countries of Ningxia Province of China (2018BFH03002). Their results were fundamental to this study.

7. Reference

Graddy J C, Kim J, Whitt J H, et al. 2002. Punching-shear Behavior of bridge decks under fatigue loading[J]. Aci Structural Journal, 99(3):257-266.

Matsumoto T, Suthiwarapirak P. Fatigue Analysis of RC Slabs and Repaired RC Slabs Based on Crack Bridging Degradation Concept[J]. Journal of Structural Engineering, 2006, 132(6):939-948.

Parvez A, Foster S J. Fatigue of Steel-Fibre-Reinforced Concrete Prestressed Railway Sleepers[J]. Engineering Structures, 2017, 141:241-250.

Perdikaris P C, Beim S R, Bousias S N. Slab continuity effect on ultimate and fatigue strength of reinforced concrete bridge deck models[J]. Aci Structural Journal, 1989, 86(4):483-491.

Schläfli, Max, Brühwiler, Eugen. Fatigue of existing reinforced concrete bridge deck slabs[J]. Engineering Structures, 1998, 20(11):991-998.

Zanuy C, Maya L F, Albajar L, et al. Transverse fatigue behaviour of lightly reinforced concrete bridg

Effect of Varying Axial Loads on Shear Behavior of Reinforced Concrete Columns

Siyun Kim[1], Sung Jig Kim[2*], Chunho Chang[3], and Jun-Mo Yang[4]

[1] Department of Architectural Engineering, Keimyung University, Daegu, South Korea; email: kimsiyun1989@gmail.com
[2] Department of Architectural Engineering, Keimyung University, Daegu, South Korea, email: sjkim4@kmu.ac.kr
[3] Department of Civil Engineering, Keimyung University, Daegu, South Korea; email: chunho@kmu.ac.kr
[4] Department of Civil Engineering, Keimyung University, Daegu, South Korea; email: jm.yang@kmu.ac.kr

*: corresponding author

Keywords: RC column; variable axial load; seismic performance; shear capacity

Abstract: This paper investigates the effect of varying axial loads on shear strength of RC columns by comparing the recently conducted experimental results and existing column test data. In the experimental investigation, a total of five specimens were constructed and tested in order to assess the structural behavior of RC columns subjected to lateral as well as various axial loading patterns. The test results in this study and available column test data are statistically analyzed and discussed by comparing with the existing shear strength models in terms of the impact of axial loads on failure mode and shear behavior of RC columns.

1. Introduction

Vertical members of RC structures are subjected to axial actions due to gravity loads but also to combined varying axial force, moment and shear forces when excited by earthquake ground motion. The combined effect of overturning and multi-axial input leads to significant variation in axial loads on columns. Since the axial load affects shear and moment capacity of RC columns, the effect of the varying axial loads on columns should be considered in the design and assessment. However, most of experiments for RC columns were conducted with constant axial loads. Only a few tests have been conducted with variable axial load and fewer still with an axial loading pattern that was uncoupled from horizontal demands. Thus, most of shear strength models for RC columns in current design codes and predictive approaches have a limitation to consider the effect of varying axial loads.

Many researches indicated that the varying axial loads could significantly affect the behavior of RC columns (Kim et al. 2018). However, only a few experimental validations with variable axial load exists (Esmaeily and Xiao, 2004). Hence, the test results in this study analyze by comparing with the existing shear strength models in terms of the impact of axial loads on failure mode and shear behavior of RC columns.

2. Previous Shear Strength Models

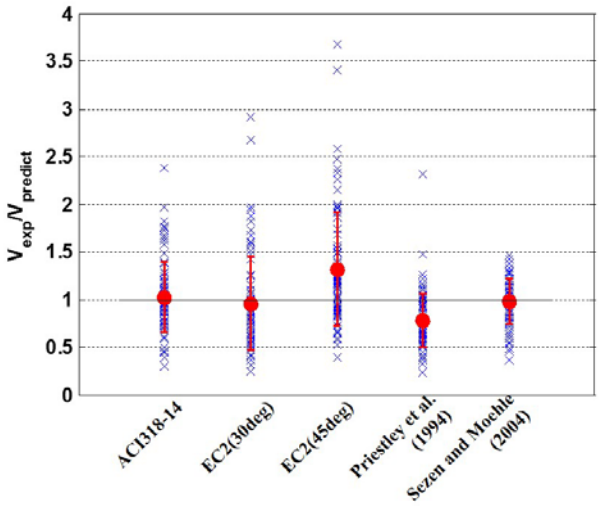

Fig. 1. Ratio of measured to calculated shear strength for different models

To analyze the shear capacity of RC columns under varying axial load, The shear strength models by ACI318-14, Priestley et al.(1994), Sezen and Moehle (2004) are employed. The shear strength model proposed in ACI318-14 provides a different design equation depending on the direction of axial load (tension and compression). Priestley et al.(1994) proposed the shear strength model using an arch mechanism proportional to axial load. The shear strength model proposed by Sezen and Moehle (2004) provides the axial load as the parameter in the square root at the shear strength of the concrete contribution. Also, the shear strength model except ACI318-14 includes the coefficient considering displacement ductility. To analyze the characteristics of the proposed shear strength models, a total of 54 experimental data of RC column with constant axial load were collected from the PEER center. Comparing the experimental and predicted results, the shear strength model proposed by Sezen and Moehle(2004) predicted relatively accurately as shown Fig. 1.

3. Experimental Program

As detailed in Table 1, the applied initial axial load for all specimens was 10% of the column capacity ($0.1f'_cA_g$, 243kN). The constant compressive axial load was applied to the reference specimen (CA10R), while the variable axial loads imposed on the rest of specimens. The variable axial load histories for specimens VA15H and VA20H were designed to replicate the forces caused by overturning moment due to horizontal ground motion. Thus, the axial load was directly proportioned to the applied lateral loads. Applied varying axial loads for specimens VA20V1 and VA20V2 were designed to replicate the forces caused by vertical ground motion. The important characteristics of axial loads of vertical members due to vertical ground motion have higher magnitude and frequency contents compared to those caused by horizontal ground motion. Note that the maximum compressive force for both specimens is 20% of axial compressive capacity of the column due to limitation of testing facilities.

4. Shear Capacity Estimation

The shear strength of RC column subjected variable axial load showed the effect of the magnitude and frequency of the axial load. As the axial load increased, the shear strength increased, while the opposite tendency was reversed. Particularly, ductility ratio of all specimens subjected variable axial load clearly showed reduction. To estimate the shear capacity of the RC column subjected to variable axial loads, the shear strength models by ACI318-14 as well as the predictive approaches by Priestley et al.(1994), Sezen and Moehle(2004) are utilized. As shown in Fig. 2, the shear capacity was estimated by using various methods and compared to shear demand from the experiment.

Table 1. Test specimens

Specimen	Mechanical properties	Axial load			
		Type	***Description***	***Magnitude Range*** (f_{ck}·A_g)	***Period Ratio*** (T_h/T_v)
CA10R	**Concrete strength** 26.6 MPa **Longitudinal rebar ratio** 2.55% (8-D19) **Transverse rebar volumetric ratio** 0.60% (D10@200mm)	Constant	Constant axial load	0.10	-
VA15H		Variable	Proportional to lateral displacement	0.05~0.15	1
VA20H		Variable		0~0.20	1
VA20V1		Variable	Varying frequency	0~0.20	1
VA20V2		Variable		0~0.20	2

The shear strength model proposed by Priestley et al.(1994) was highly predicted in all specimens. The shear capacity proposed by ACI318-14, Sezen and Moehle(2004) was similar to the shear demand for specimens with constant and proportionally increased axial load, while the shear demand of specimens proportional reduction of axial load exceeded the shear capacity. It is clear that the measured shear demand exceeds the estimated capacity in some shear strength models when the variable axial load of the characteristics of vertical ground motion is considered. Particularly, the shear strength was not predicted at all in the case of variable axial load with high frequency compared to the lateral force. Also, the shear capacity proposed by Priestley et al.(1994), Sezen and Moehle(2004) using the reduction factor with the ductility was more decreased after yielding, while no consideration is given to the response of RC columns according to the variable frequency of axial load. The shear capacity by various the shear strength models decreases significantly as the axial load increases, while the shear demand is less affected by the axial load variation.

4. Conclusion

The paper presents the experimental and analytical investigation of the seismic performance of RC columns subjected to varying axial loads considering the characteristic of overturning moment and vertical ground motion. The damage of specimens subjected to variable axial loads appeared to be severe compared to the specimen subjected to the constant axial load. Depending on the amplitude of axial loads, the maximum lateral force was reduced up to 13.77%. Conversely, the maximum lateral forces when subjected to the peak axial load increased up to 5.30%, resulting in the fluctuation of hysteresis loop. In addition, due to the reduction of ultimate displacement, the estimated ductility of the specimens subjected to variable axial loads is less than the case of the constant axial load. The estimated shear capacity by utilizing the design code and predictive approaches has a discrepancy with the measured shear demand of RC column subjected variable axial load. Particularly, the available shear strength models cannot predict the capacity well for the specimen subjected to a high axial force variation. And then, it is necessary to develop the shear strength model that can consider the magnitude and frequency of axial load.

5. Acknowledgment

The research was supported by a grant(19DRMS-B146826-02) from Development of Customized Contents Provision Technology for Realistic Disaster Management Based on Spatial Information Program funded by Ministry of the Interior and Safety of Korean Government.

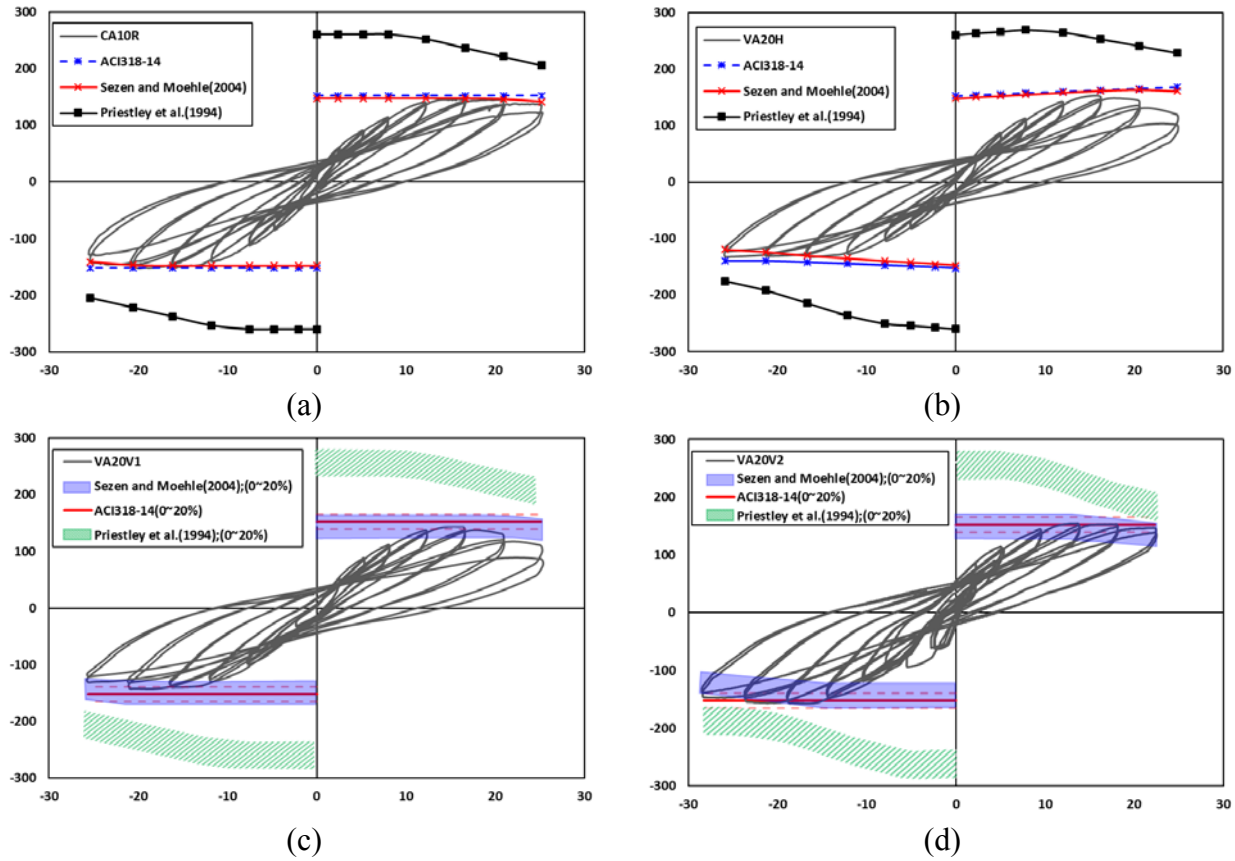

Fig. 2. Shear capacity estimation; (a) CA10R; (b) VA20H; (c) VA20V1; (d) VA20V2

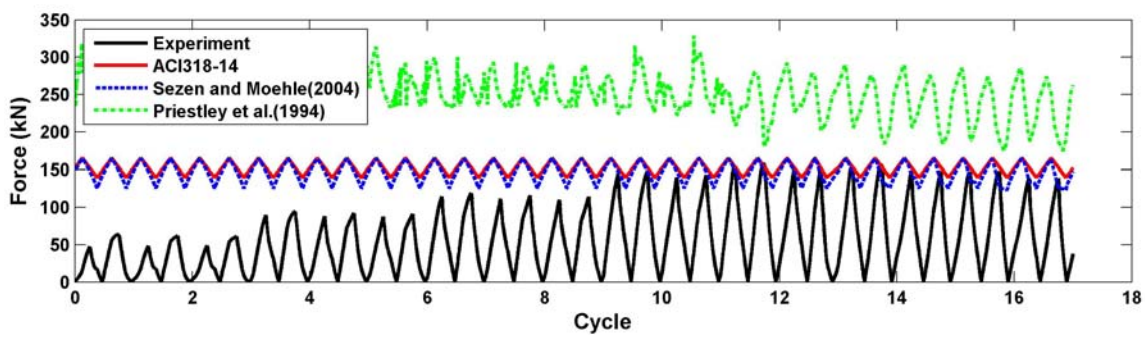

Fig. 3. Prediction of shear strength in each cycle; VA20V2

6. References

Kim, S., Kim, S.J., and Chang, C. 2018. Analytical assessment of the effect of vertical ground motion on RC frames designed for gravity loads with various geometric configurations, Advances in Civil Engineering, 2018.

Esmaeily, A. and Xiao, Y. 2004. Behavior of reinforced concrete columns under variable axial loads, Structural Journal, 101(1), 124-132.

ACI (American Concrete Institute). 2014. Building code requirements for reinforced concrete, ACI318-14.

Priestley, M.N., Verma, R., and Xiao, Y. 1994. Seismic shear strength of reinforced concrete columns, Journal of Structural Engineering, 120(8), 2310-2329.

Sezen, H. and Moehle, J.P. 2004. Shear strength model for lightly reinforced concrete columns, Journal of Structural Engineering, 130(11), 1692-1703.

Quantification of Uncertainties in Diagnostic Load Test Data

Christos Aloupis[1*], Michael J. Chajes[2], and Harry W. Shenton III[3]

[1] Department of Civil and Environmental Engineering, University of Delaware, Newark, DE, USA, email: chr.aloup@gmail.com
[2] Department of Civil and Environmental Engineering, University of Delaware, Newark, DE, USA, email: chajes@udel.edu
[3] Department of Civil and Environmental Engineering, University of Delaware, Newark, DE, USA, email: shenton@udel.edu

[*]: corresponding author

Keywords: bridges; SHM; testing; uncertainty; variability

Abstract: The management and maintenance of cable-stayed bridges requires a major investment of human and financial capital. The utilization of structural health monitoring (SHM) systems to collect data during regularly conducted diagnostic load tests is an efficient and cost effective method for improving the accuracy of ongoing bridge evaluations. In order to know when changes in response are significant, it is essential to know the inherent variability of the response data. The Indian River Inlet Bridge (IRIB), a 533-meter long cable stayed bridge, was opened for traffic in 2012. From the very early stages of the design process, the Center for Innovative Bridge Engineering (CIBrE) at the University of Delaware (UD) worked with the Delaware Department of Transportation (DelDOT) and their design-build team of Skanska and AECOM to design and install a comprehensive SHM system to help monitor bridge performance. The installed system is fiber-optic based and contains more than 120 sensors of varying type distributed throughout the bridge. The system, which not only collects data continuously during normal operation, is also being utilized to collect data during regularly scheduled diagnostic load tests. Over its first six years of service, six diagnostic load tests have been conducted on the bridge. The initial three tests were used to establish a baseline response for the bridge. The three additional tests, along with all planned future tests, are being compared to the baseline to determine if the bridge condition has changed. This paper focuses on quantifying the variability in the diagnostic load test data. Only by understanding the inherent variability of the data can one determine if a change in response is likely due to a change in condition. The causes of variability being considered include sensor accuracy, effects of vibration, environmental effects, and effects of variable load placement.

1. Introduction

Conducting diagnostic load tests, where predefined service loading is applied to a bridge, in a controlled environment, is a well-documented method used to evaluate the response of typical short-to-medium span bridges. The cost to instrument and perform diagnostic load tests on long-span bridges is much greater and as a result, diagnostic load tests are typically conducted on them. However, the installation of a permanent structural health monitoring system during the bridge construction can significantly reduce the cost of such load tests and allow them to be economically conducted at periodic intervals.

By utilizing periodic load tests, the bridge owner may be better able to determine changes in bridge response, since the collected data can be compared with initial data from the bridge that represents the healthy condition. Therefore, to keep track bridge response over a series of load tests, and to evaluate bridge condition, baseline load test response should be established (Al-Khateeb et al., under review). After establishing the baseline, the next step is to establish a threshold for a change in response that would signify a change in bridge condition as opposed to inherent variability. To do this, one must first establish the magnitude of the variability that could occur during the load test and is not due to a change in condition.

In the IRIB, a SHM system was installed during its construction and is being used to collect bridge response data for long-term in-service monitoring. To date, six diagnostic load tests have been conducted on the bridge, each involving numerous truck passes involving from one to six trucks. The first test was conducted at the time the bridge was opened to traffic, the second was conducted after six months of service, the third after one year of service, the fourth after two years of service, the fifth after four years of service, and the sixth after six years of service (future tests are scheduled to occur every two years). Since the bridge is still quite new, little change in condition is expected. Regardless of this, no two load tests produce identical datasets. This paper seeks to evaluate and quantify the variability in response data among the six load tests and explain what factors may be causing the variability, and provides suggestions as to how some of the variability might be reduced. Finally, by understanding the variability, future response can be better evaluated in an attempt to differentiate changes in structural condition from inherent test variability.

2. Variability during load tests

Four sources of response variability during identical load tests have been identified as (a) variability due to differences in the bridge's environment, (b) variability due to measurement noise, (c) variability due to imperfect replication of truck loading passes, and (d) unexplained effects.

(a) Environmental related variability: Differences in the weather (temperature and wind) between tests may result in changes in structural response and in wind induced vibrational response. To reduce these effects, load tests can be conducted after the sunset, at times of the year with mild temperature, and during times with little to no wind. The fact that each individual load pass takes only a few minutes helps to reduce variability due to thermal effects.

(b) SHM system measurement noise: Data from any testing system has noise and only a certain level of accuracy. Manufactures provide sensor accuracy information, and data collected with no traffic can help quantify this form of variability (it is important to do this when there is no wind).

(c) Imperfect load replication: When conducting load tests with moving trucks, perfect replication cannot be achieved. Trucks will have different weights and weight distributions, there is variability in the path that the truck(s) follow, and when side-by-side trucks are used, there is variability in their relative transverse and longitudinal position.

(d) Unexplained effects: This represents unexpected phenomena that are not bridge condition related. In our case, we noticed that the readings of several did not return to their initial (or zeroed) reading. The cause of this has yet to be determined, but the variation in response readings caused by this situation is unlikely to be related to a permanent change in bridge condition.

3. Truck configurations during tests

During the load tests, multiple configurations of trucks were used to load the bridge. Test protocols were developed to define configurations that were used during each test to evaluate bridge performance. Additional configurations were used in some tests to investigate specific issues, such as repeatability. The load test protocol includes single truck passes in which the single truck crosses in either one of the four, or in one of the two shoulders. The protocol also includes passes in which four side-by-side trucks cross, or six side-by-side trucks cross (see Figure 1). During each load test, for each pass configuration, duplicate passes are conducted to ensure repeatability.

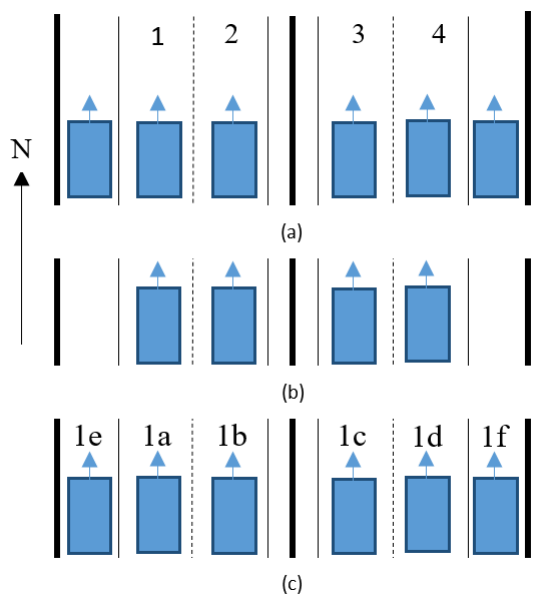

Fig. 1. Trucks configurations with (a) six trucks side-by-side, (b) four trucks side-by-side and (c) the different single truck passes

4. Quantification of variability

Having identified four causes of variability, we will now discuss the magnitude of the variability based on the six conducted load tests. These tests not only provide a plethora of data to evaluate bridge condition and to establish the response corresponding to the healthy condition of the bridge, they also enabled us to quantify the aforementioned testing variability. The two sensors selected for this study are (1) the strain sensor placed at the bottom of west girder and located at the center of the midspan (S_W8), and (2) the strain sensor at the quarter span of the backspan (S_W22), as can be seen on Figure 2. The first two factors discussed, variability due to environmental conditions (primarily wind), and variability due to system measurement noise, are

hard to separate and were evaluated together. This was done using measured ambient response that took place before and load trucks were on the bridge but after ambient traffic was stopped. Using a window of 10 seconds before trucks get on the bridge, and using at least 18 passes from each load test, there are 3 minutes of ambient noise that can be analyzed for each load test. For all six test, the maximum strain range measured during the ambient condition was 14.5 με for sensor S_W8 and 15.1 με for sensor S_W22. To reduce this range the data was smoothed using a moving average of 25 data points (data is taken at 15.6 Hz). After the smooth process the maximum strain range was 2.3 με and 2.5 με, respectively.

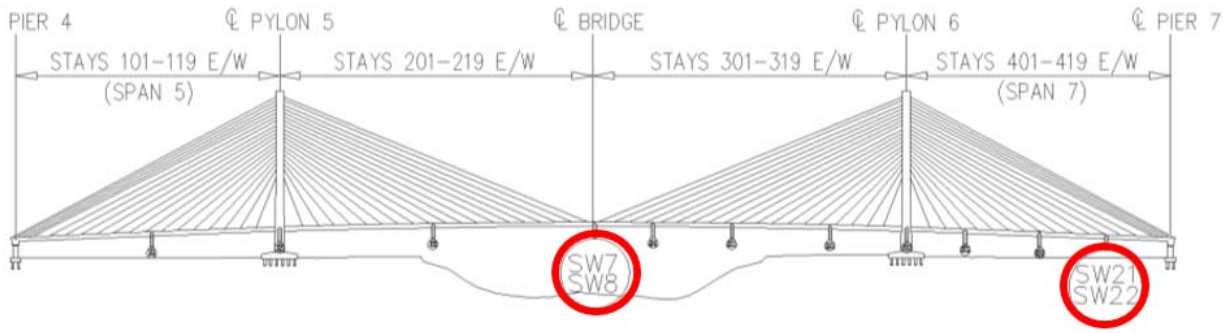

Fig. 2. Key strain sensors on edge girder

For the variability associated with lack of perfect replication, single truck passes (and the concept of superposition) were used to assess the variation that could be expected for multiple side-by-side truck passes occur (in the load test, both four trucks side-by-side and six trucks side-by-side are used). For each test, while the weight of trucks and weight distribution on their axles is similar, they are not the same. To minimize this variability, the recorded strain response is normalized using the average truck weight for the test as compared to the average truck weight of the baseline test. This helps to minimize the variability due to different weights between load tests. Even so, the variability in weight between trucks in a single test, and the result of having the heaviest truck close to the edge girder as opposed to the lightest truck, leads to a predicted variability in strain of 0.69 με for S_W8 and 0.63 με for S_W22.

Also effecting variability associated with lack of perfect replication is the effect of variations in the lateral position of the truck between tests. To evaluate this, the average of the peak points for each of the lanes were used. It could be assumed that the average of multiple passes will be a pass from the middle of the lane dividing by the difference of strains between two consecutive lanes. The effect that the lateral variability of the load truck results in strains on the girder varying by 0.35 με/ft for S_W8 and 0.27 με/ft S_W22. For a six side-by-side truck pass, and assuming that a truck could follow a path offset from the center of the lane by 1 ft, and since this offset could be on both sides, the truck could have a lateral offset of 2 ft (Figure 3). At the same time, when a truck is offset to one side it also tends to affect the trucks next to it. Therefore, it is reasonable to assume that all trucks will move laterally by the same amount. This leads to a strain variability due to lateral position variability of the trucks for sensors S_W8 and S_W22 of 4.2 με and 3.2 με, respectively.

Part of the variability results from the longitudinal configuration of the trucks. It is very difficult to ensure that the moving trucks cross exactly adjacent to each other (i.e. all having the same longitudinal position on the bridge). During the test some of the side-by-side trucks will be slightly ahead of, or behind, the other side-by-side trucks (see Figure 4). In order to assess this variability), a Monte Carlo (MC) simulation of 1,000 replicates was conducted. First, the sensitivity of the peak girder strain to longitudinal movements of the truck were determined. Using this, MC simulations were used to calculate the maximum peak strain value that would result from different configurations. In that simulation, the trucks were limited to being at most 2 feet ahead of or behind of transverse line, and their variation within that shift was assumed to following a normal distribution. By moving this transverse line relatively to the line that would cause the peak strain assuming all trucks were in a straight line, the variation of the peak strain due to longitudinal offset of adjacent trucks was simulated. From the 1,000 replicates, the top 90% were used in order to eliminate outliers and extreme conditions. Based on this analysis, the variability in strain due to the variability of longitudinal truck alignment was calculated to be 4.4 με for S_W8 and 3.5 με for S_W22.

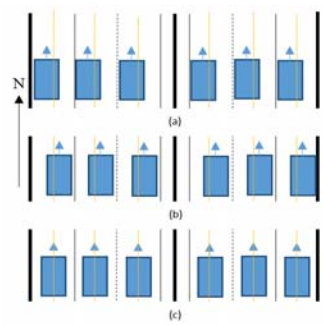

Fig. 3. Lateral displacement of trucks with (a) being 1 foot offset to the west, (b) 1 foot to the East and (c) passing from the center of the lanes

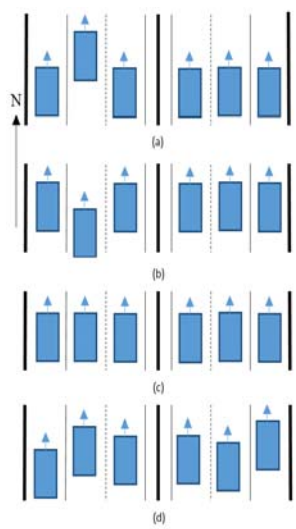

Fig. 4 Longitudinal configuration of trucks during passes where on (a) one truck is ahead, (b) one truck is following, (c) all trucks are in a straight line and (d) trucks are passing randomly

Finally, following the six side-by-side trucks passes, the strain readings of sensor S_W22 did not return to the original reading (unlike the strain data for S_W8 which did return to the original reading). The residual strain ranged from 3.4 με to 7.4 με, and as a consequence, the variability due to this "unexplained" phenomena is taken as a difference of the limits, or 4.0 με.

5. Conclusions

To quantify the variability of strain data that is present even when there are no changes in bridge condition, multiple load tests should be conducted. The tests should include both passes with full loading of the bridge (trucks in all lanes and shoulders), and single truck passes that would be used to evaluate the aforementioned variabilities. Once the variabilities of all the various sources of variability have been evaluated, they must be combined to get a final threshold value. This combination could be computed using the square root of the sum of the squares of all of the sources of variability, excluding the residual strain which should be added directly. In this case, using this method for combining the four variabilities, leads to a threshold for the key sensors S_W8 and S_W22 of 6.52 με and 9.46 με, respectively.

6. References

Al-Khateeb, H.T., Shenton, H.W., Chajes, M.J., and Aloupis, C. (under review). "Structural Health Monitoring of a Cable-Stayed Bridge Using Regularly Conducted Diagnostic Load Tests," Frontiers in the Built Environment, Bridge Engineering Section.

Experimental Study on Noise Reduction of a U-Shaped Rail Transit Bridge

Xiaodong Song[1*] and Qi Li[2]

[1] School of Transportation, Southeast University, Nanjing 211189, China; email: xdsong@seu.edu.cn
[2] Department of Bridge Engineering, Tongji University, Shanghai 200092, China; email: liqi_bridge@tongji.edu.cn

*: corresponding author

Keywords: rail transit bridge; noise reduction; field test; noise barrier; floating ladder track

Abstract: Rolling noise and structure-borne noise radiated from the bridge are two major sound sources of urban rail transit bridges. To reduce the total noise level of urban rail transit bridges, efficient noise mitigation measures are needed. In this paper, three noise mitigation measures are used for a U-shaped rail transit concrete bridge, including the installation of noise barrier, the use of absorbing panel, and the installation of floating ladder track. A field test is then conducted to study the corresponding noise reduction effect of the above-mentioned measures. It is found that the noise barrier is more efficient to control the rail noise, especially in the space where the rail noise is not shielded by the bridge. The absorbing panel has insignificant effect on the total noise level. The floating ladder track can significantly reduce the bridge vibration, but the severe vibration of the ladder track may become a major sound source. Appropriate mitigation measures should be chosen for noise reduction of urban rail transit concrete bridges.

1. Introduction

Rolling noise and structure-borne noise radiated from the bridge are two major sound sources of urban rail transit bridges. To control the noise level of urban rail transit lines, a lot of experimental study has been conducted. A series of field tests were conducted to investigate the noise reduction of four steel bridges with different noise mitigation systems, including the use of rail absorbers, bridge absorbers, soft rail fastening system, and soft elastomeric pads (Venghaus et al, 2012). Related technologies were also used to reduce the noise radiated from steel railway bridges in Germany, and the associated noise reduction effects were investigated by field tests (Stiebel et al, 2015). A full-scale bridge model was used to investigate the reduction effect of the bridge with floating ladder track and floating concrete deck (Watanabe et al., 2012). GFRP plates and rapid hardening concrete were used to reduce the structure-borne noise of steel bridges in Japan (Lin et al, 2013) and the harmer impact test showed a noise reduction of 5 to 15 dB can be achieved after strengthening. An impact hammer test was used to compare the vibration and noise radiation of a steel girder with wood sleepers and a steel girder with concrete deck (Saito et al, 2015). The high-performance damping material was used to reduce the railway noise in Austria (Koller et al, 2012), and the test showed a reduction of 2 to 4 dB can be achieved for ballast tracks. In this study, a series of field tests were conducted to study the noise reduction effect of three noise mitigation measures on urban rail transit bridges, including the installation of noise barrier, the use of absorbing panel, and the installation of floating ladder track.

2. Experimental study

A U-shaped girder bridge (Fig. 1) used in shanghai metro line was selected here for experimental study. The abovementioned noise mitigation measures were used for the U-shaped girder bridge. The effect of noise barrier and sound absorbing panel was investigated by first installing and then removing the noise barrier and absorbing panel (Fig. 2). Two span bridges (span 1 and span 2) were selected in the field test to investigate the effect of the floating ladder track. The floating ladder track is installed in Span 2 (Fig. 3), while for Span 1, there is no floating ladder track. Microphones were used to record the sound pressure levels during the train pass by.

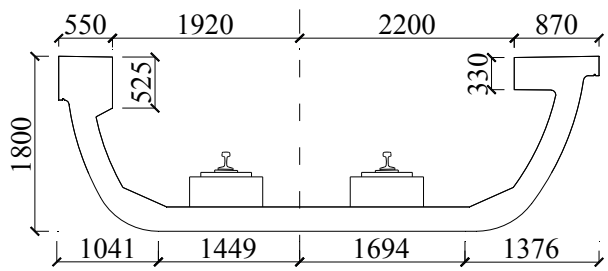

Fig. 1. Cross section of the U-shaped girder bridge (unit: mm)

Fig. 2. Photo of the noise barrier and absorbing panel

Fig. 3. Photo of the floating ladder track

2.1. Noise barrier and sound absorbing panel

Figure 4 shows the sound pressure spectrum with different field points. It can be found that the noise barrier and sound absorbing panel has insignificant effect on the sound pressure level at field point underneath the bridge (P1), where the rolling noise and structure-borne noise radiated from the ladder track is shielded by the U-shaped girder bridge. For field point above the bridge (P2), where the rail noise and sleeper noise play a more important role, the total noise level can be effectively controlled, and the total noise reduction at P2 is about 6 dB by using the noise barrier and absorbing panel. It can be found from Fig.4 the low frequency noise (less than 200 Hz) can be hardly controlled by the noise barrier used in this study. Fig. 4 also shows the effect of the sound absorbing panel on the noise level is very small. Only about 1 dB reduction can be observed by using the sound absorbing panel.

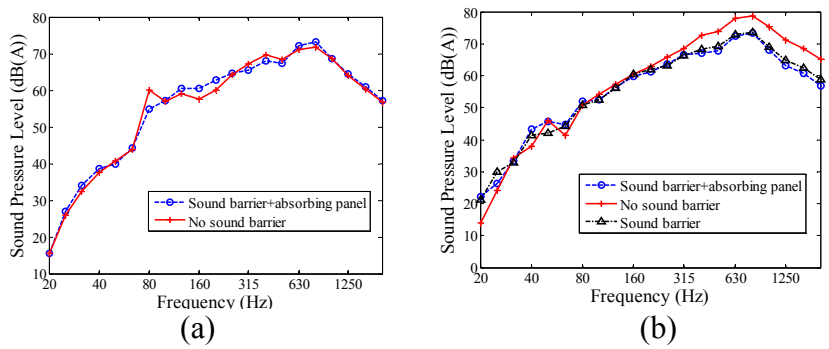

Fig. 4. Sound pressure levels during the train pass by: (a) P1, beneath the bridge; (b) P2, above the bridge

2.2. Effect of floating ladder track

Figure 5 shows the sound pressure levels radiated from the bridge with and without the floating ladder track. Generally, the sound pressure levels at different field points can be effectively reduced above 40 Hz with the installation of the floating ladder track, due to the reduction of the vibration of bridge, and the reduction of the total noise level is about 5 dB. However, it should be noted the noise reduction effect may be overestimated due to the difference of the roughness excitation and related parameters between the two span bridges, especially for field points above the U-shaped girder (P2), where the rail noise may be dominant.

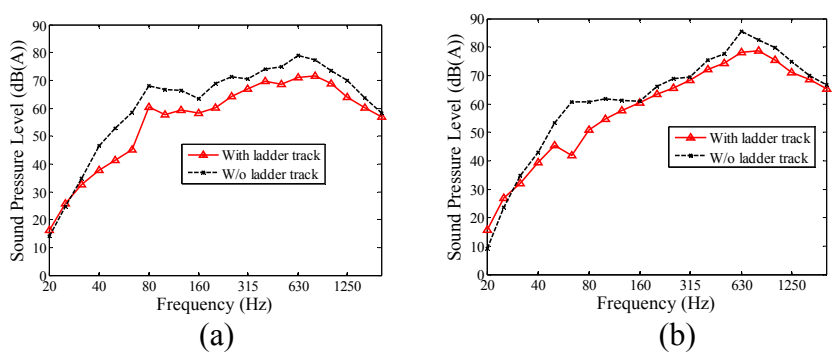

Fig. 5. Sound pressure levels during the train pass by: (a) P1, beneath the bridge; (b) P2, above the bridge

3. Conclusions

A field test was conducted to study the effects of three noise mitigation measures on the noise radiation of a U-shaped rail transit bridge. The conclusions of the study can be drawn as follows:

(1) The noise barrier is efficient to control the rail noise, but the influence on bridge noise is insignificant.

(2) The noise absorbing panel has insignificant influence on the total noise level.

(3) The floating ladder track can reduce the vibration transmitted to the bridge, leading to smaller noise radiation from the bridge.

4. References

Koller G., Kalivoda M.T., Jaksch M., Muncke M., Oguchi T., and Matsuda Y, 2012. Railway noise reduction technology using a damping material, Noise and Vibration Mitigation for Rail Transportation Systems, 118, 159-166.

Lin W., Yoda, T., Taniguchi N., and Hansaka M., 2013. Performance of strengthened hybrid structures renovated from old railway steel bridges, Journal of Constructional Steel Research, 85, 130-139.

Saito M., Sugimoto I., and Sasaki E., 2015. Experimental study on noise reduction effect of installing concrete deck on existing steel girders, International Journal of Steel Structures, 15, 205-212.

Stiebel D., Lölgen T., and Gerbig C., 2015. Innovative measures for reducing noise radiation from steel railway bridges, Noise and Vibration Mitigation for Rail Transportation Systems, 126, 409-416.

Venghaus, H., Balmer, P., Muncke, M., and Poisson, F., 2012. Noise reduction of steel bridges with non ballast tracks, Noise and Vibration Mitigation for Rail Transportation Systems, Notes on Numerical Fluid Mechanics and Multidisciplinary Design, 118, 339-347.

Watanabe T., Sogabe M., Asanuma K., and Wakui H., 2012. Development of silent steel railway bridge equipped with floating ladder track and floating reinforced concrete deck, Noise and Vibration Mitigation for Rail Transportation Systems, 118, 211-219.

Bridge Pier Deformation Due to Road Construction and Heavy Trucks

Hanyong Liu[1], Chengyin Liu[2*], and Haichang Yu[3]

[1] Research Institute of Highway Ministry of Transport, Beijing, China; email: hy.l@rioh.cn
[2] Department of Civil and Environmental Engineering, Harbin Institute of Technology, Shenzhen, China; email: chengyin.liu@hit.edu.cn
[3] Department of Civil and Environmental Engineering, Harbin Institute of Technology, Shenzhen, China; email: yuhaichang@stu.hit.edu.cn

*: corresponding author

Keywords: heavy trucks; pier-pile-soil model; pile displacement

Abstract: When heavy transport trucks pass underneath a bridge, the moving load may cause additional stress and deformation on the adjacent piles, and possible girder collapse due to the displacement of bearing on top of pier. In this paper, the performance of bridge piers is studied on a real condition that mud transport trucks passing on an artificial pavement underneath a continuous beam bridge on soft soil field. A three-dimensional pier-pile-soil model is established in ABAQUS, according to the field condition. The displacement of pile is obtained and compared with those obtained by the M method by assuming a concentrated force and a moment act on the top of the pile. Then, a parametrical study is performed to discuss the influence of subgrade excavation, road construction and heavy truck passage on pile displacement, respectively. At last, countermeasure to reduce pier deformation is suggested.

1. Introduction

In recent years, as transportation network becomes denser, there have been more and more construction and heavy traffic underneath existing bridges. Those heavy loads acting on the foundation under the bridge will lead to additional deformation of the pile, or even serious accidents such as partial damage or bridge collapse. Under the horizontal load, the pile and soil constitute an extremely complex interaction system under the constraint of external conditions.The m method is widely used because of its convenience and is listed in the “Code for Pile Foundation of Port Engineering” (1998). In terms of vehicle loads, predecessors have focused on vehicle loads on bridges, vehicle-bridge coupling, vehicle-bridge collision under bridges, large-area surcharge on adjacent piers and so on (Abdelkarim and Eigawady, 2017). Many scholars at home and abroad have also used finite element software to establish two-dimensional and three-dimensional finite element models to study the influence of surface displacement, track irregularity, vertical dynamic stress of subgrade and train speed on subgrade (O'brien and Rizos, 2005). But generally speaking, there are few studies about the influence of vehicle under the bridge on the performance of the pier.

In this paper, the performance of bridge piers in the condition of road construction and heavy traffic underneath the bridge is studied for a realistic case. A three-dimensional finite element model of “pier-pile-soil” is established, and verified according to the m method. Then the effects of subgrade excavation, road construction, and heavy truck passage on the performance of bridge

piers are investigated. Finally, safety suggestions are provided in the present paper in order to reduce risks in similar practice.

2. Establishment and Verification of FE Model

2.1. Establishment of FE Model

In order to transfer spoil, a project in Shenzhen needs to build a temporary road under a multiple-span continuous bridge to meet the traffic of vehicles. The temporary road is shown in Figure 1. Since the bridge field is a soft soil area, earthwork filling near the bridge may affect the safety of the bridge. According to relevant bridge management regulations, it is necessary to consider the impact of road construction and heavy truck passages on the safety of bridge piers.

Fig. 1. Temporary road

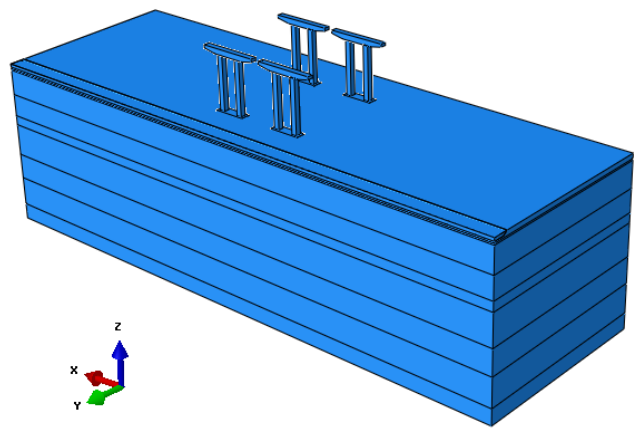

Fig. 2. The semi-structural model

According to the results of on-site drilling, in-situ testing and indoor soil test, the physical and mechanical parameters of each soil layer on the site are obtained. The material parameters of pier, pile, cushion cap and top cap can be obtained from the bridge blueprint. After considering factors such as grid density, impact range, vehicle spacing, structure symmetry and computational efficiency. The semi-structural model was eventually adopted, the model size changed to 180m×60m×50m, as shown in Figure 2.

2.2. Verification of FE Model

The plan view of piles is shown in Figure 3. By setting specific conditions, that is, Assume that a force of 200KN and a moment of 200KN·m act on the top of the pile #1 and the direction is away from the road, the deformation curve along the bridge of pile #1 is shown in black curve in Figures 4. On the other hand, for the above conditions, the theoretical solution of pile displacement can be obtained by m method, as shown in the red curve in Figure 4. The trend of the two curves is roughly the same. It is noted that the maximum displacement on the top of pile is concerned herein. The relative error of the displacement of the two at the top of the pile is only 4.3%. Therefore, through comparison with the theoretical solution, the developed 3D finite element model can be safely used for simulation investigation in this paper.

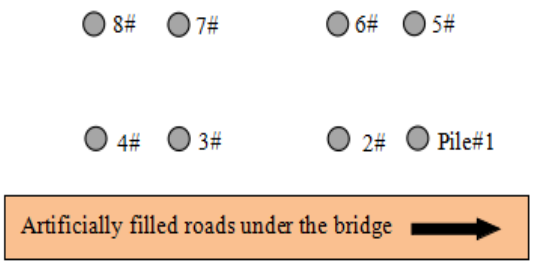

Fig. 3. The plan view of piles

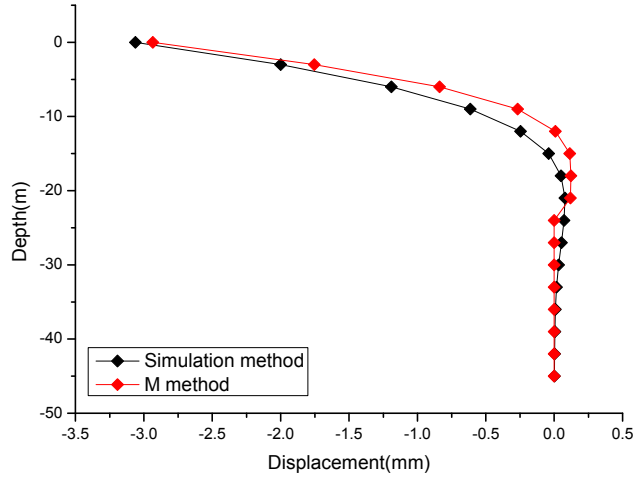

Fig. 4. Displacement of pile #1 along the bridge

3. Simulation Analysis of Road Construction and Heavy Truck Passage

Through the "birth and death unit" function of ABAQUS, we can simulate the construction of artificial filled road. It is estimated that the number of mud trucks per day is about 2000, and the equivalent uniform load of the maximum wheel pressure is about 20KPa, which acts on the pavement of 10m wide. Since the influence of road construction and heavy truck on piles is mainly along the bridge direction, the displacement of piers along the bridge direction in each stage are shown in Figure 5.

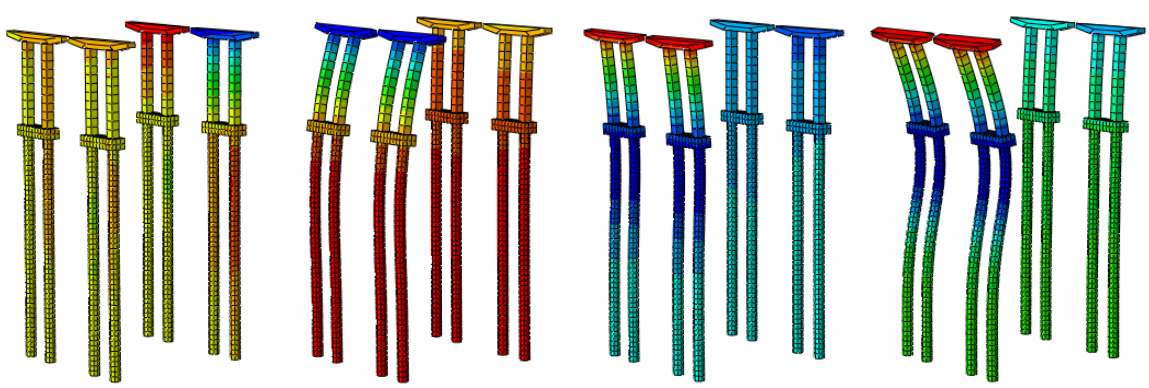

(a) (b) (c) (d)

Fig. 5. Bridge displacement during road construction and heavy truck passage: (a) Before subgrade excavation; (b) After subgrade excavation; (c) After road construction; (d) After loading of vehicle

The entire simulation process is divided into four main phases in chronological order, including before subgrade excavation, after subgrade excavation, after road construction and after loading of vehicle. Since the deformation of each pile is consistent, the deformation of pile #1~#4 is obviously larger than that of pile 5#~8#. Therefore, the deformation of pile #1 along the bridge direction is taken as an example. The displacement of the pile #1 at each stage is shown in Fig. 6. Before the excavation, the pile can be regarded as vertical; after excavation, due to the unloading

action, the upper part of the pile is away from the subgrade, and the middle and lower part is biased toward the subgrade; after the road construction, the whole pile is away from the subgrade, and the maximum deformation occurs at a depth of 8m; after the vehicle load, the pile is further away from the subgrade, and the maximum deformation reaches about 7.3mm. It can be seen that the vehicle load is the most important factor causing the deformation of the pile throughout the process. According to the "Technical code for building pile foundations" (2008), the allowable horizontal displacement of piles at ground level is 6 mm for horizontal displacement sensitive structure. Therefore, specific countermeasures need be taken to reduce the displacement at the top of the pile, such as setting steel sheet piles between the road and the adjacent piles.

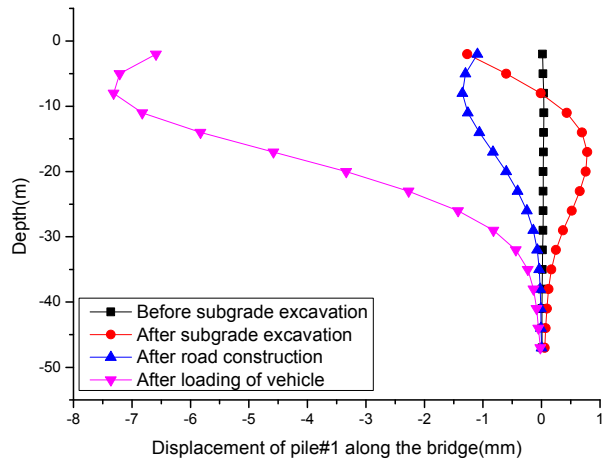

Fig. 6. The displacement of the pile#1 at each stage

4. Conclusions

This paper studies the influence of heavy truck passing underneath bridge on the performance of the pier and pile. A 3-D FE model of pier-pile-soil is established, and the performance of bridge pile is analyzed in terms of subgrade excavation, road construction and heavy truck passage. The results show that the heavy truck passage is the key to ensure the safety of bridge structure. Current design code was found to be non-conservative and countermeasures are suggested to reduce the risk of bridge collapse in similar practice.

5. References

Abdelkarim O.I. and Eigawady M.A. 2017. Performance of bridge piers under vehicle collision, Engineering Structures, 140, 337-352.

JTJ254-98 Codes for pile foundation of harbour engineering. 1998.

JGJ94-2008 Technical code for building piles. 2008.

O'brien J and Rizos D.C. 2005. A 3D BEM-FEM methodology for simulation of high speed train induced vibrations, Soil Dynamics and Earthquake Engineering, 25 (4), 289-301.

Experimental Study on Tsunami Force on Residential House

Wanli Yang[1], Chuanjiang Zhang[2*], Hanbin Yang[3], and Qiao Li[4]

[1] Key Laboratory of High-speed Railway Engineering, Ministry of Education, Chengdu 610031, China; School of Civil Engineering, Southwest Jiaotong University, Chengdu 610031, China. E-mail: 68360903@qq.com
[2] Department of Structural Engineering, School of Civil Engineering, Southwest Jiaotong University, Chengdu 610031, China. E-mail: 1366609089@qq.com
[3] Department of Bridge Engineering, School of Civil Engineering, Southwest Jiaotong University, Chengdu 610031, China. E-mail: 1059729782@qq.com
[4] Department of Bridge Engineering, School of Civil Engineering, Southwest Jiaotong University, Chengdu 610031, China. E-mail: ql3721@163.com

[*]: corresponding author

Keywords: tsunami; residential house; dam break; tsunami force; calculation formula

Abstract: Tsunami is an extreme disaster that has given rise to massive loss of coastal structures such as residential houses and bridges because of the complexity and unpredictability of the tsunami. In this study, the dam-break wave was carried out to simulate the tsunami wave to investigate the impacting process on a house model, which represents the prototype house with the dimensions of 8m in length, 8m in width and 5m in height. Both the wet bed cases with initial downstream water depth of 2cm and dry bed cases were conducted. Results show the time histories of the wet and dry bed cases can be generally divided into four stages, i.e. impacting stage, fluctuation stage, quasi-stable stage and decreasing stage. And generation mechanisms of the forces in different stages are discussed. Because the drag effect of the downstream initial water in wet bed case is greater than the friction of the flume bottom in dry bed case, the tsunami bore in wet bed has slower velocity and larger wave front slope than that in dry bed case, introducing the relatively later arrival time of the tsunami bore at the house model and larger impacting force for the wet bed case. The maximum tsunami force happens in the impacting stage when wave height is larger, but happens in the fluctuation or quasi-stable stages when wave height is smaller for the wet bed cases. For the dry bed case, the maximum tsunami force happens in the quasi-stable stage. Further, the estimation equations of the maximum tsunami force on square house are suggested, which could also be referred by square columns of bridges.

1. Introduction

Tsunami is an extreme disaster that has given rise to massive loss of coastal structures such as residential houses and bridges because of the complexity and unpredictability of the tsunami forces. Tsunami waves and the resulted forces on structures have received wide attentions and have been studied by many scholars. Dam break wave is similar to tsunami wave and is convenient to be generated in the lab, therefore it is often used to simulate tsunami wave. Ritter (1892), Keulegan (1950), Dressler (1952), Whitham (1955), Stoker (1957), Lauber and Hager (1998) and Chanson (2005,2006) proposed the dam break theory for the study of

theoretical solutions. The dam break theory provided a theoretical basis for the later tsunami research. Over time, many studies have been conducted on the interaction between tsunamis and structures. Yeh (2005), Fujima (2009) et al. studied the characteristics of tsunami forces on house. Lukkunaprasit (2008), Triatmadja (2012), Hartana (2015) et al. carried out studies on the effect of door and window opening ratios on the tsunami force on houses. Thomas (2011), Oshnack (2009) et al. carried out studies on the effect of breakwater on tsunami force. Osti (2010) and Yanagisawa (2010) also carried out studies on the effect of mangroves on the tsunami forces on sea homes. The research on the interaction between tsunami and residential house is relative seldom, which needs to be further studied. Therefore, tsunami force on residential house is investigated in this study experimentally.

2. Experimental Set-up

Experiments were carried out in the tsunami wave flume at Southwest Jiaotong University, Chengdu, China. The flume is 10.72m in length, 1.485m in width and 0.60m in depth. And the flume is divided into the upstream region of 4.58m in length and the downstream region of 6.14m in length by a dam gate. A steel tank for water storage is right below the glass flume, and an aluminum sluice gate is installed at the downstream end and will be quickly opened when the wave front reaches the downstream end, so the water can flow freely and fall into the water storage below to delay the reflection influence of the downstream wall. Dam break wave is generated by rapidly lifting the gate upward by the lever installed at the top of the gate, shown in Fig.1. The duration of the gate lifting process varies from 0.25s to 0.35s in different cases, which is slightly longer than the "sudden removal" criterion recommend by Lauber and Hager (1998) but is already short enough to simulate a sudden removal of the gate.

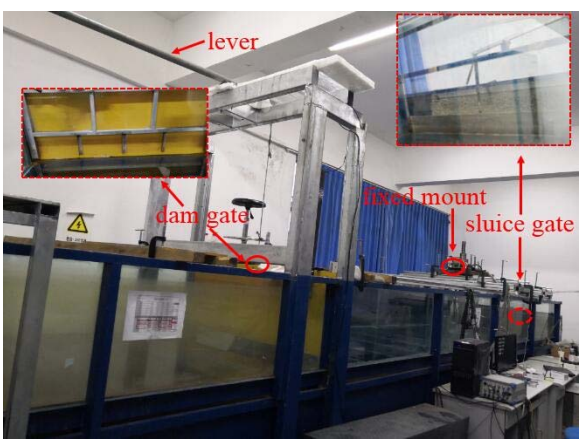

Fig. 1 Flume and its accessibilities

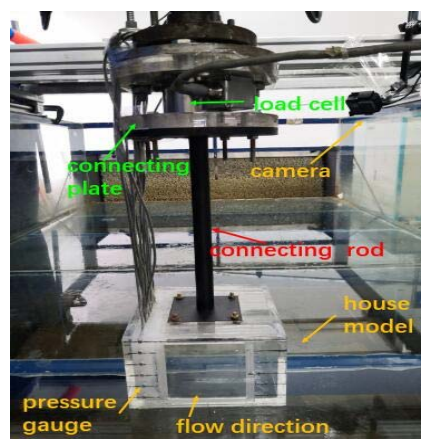

Fig. 2 Schematic of the installation

In this experiment, the prototype of the house is a one-story house with a length of 8m, a width of 8m and a height of 5m. The length scale ratio is 1:40. Then the length, width and height of the house model are respectively 20cm, 20cm and 12.5cm. The block ratio, defined as the ratio of flume width to house model width, is 7.425, the blocking effect is ignorable according to Wei (2016). The top surface of the house model is connected to the load cell (ATI, si-130-10, 1000HZ) through an iron bar with diameter of 2.5cm, shown in Fig. 2. The upstream edge of the housing model is located 4m away from the dam break gate. The gap

between the bottom of the house model and the flume bottom is 2mm so that the house model does not touch the bottom of the flume when dam break wave impinging on the house model.

Tsunami waves break near the coastline due to the shallowed water depth then rush onto the land in the form of a series of bores. Always the first bore might be not the biggest. In other words, the house may be inundated partially before the biggest tsunami bore arrives. Therefore, two kinds of physical experiments, i.e. one with initial downstream water (wet bed) and another without downstream water (dry bed), were conducted in this study. The wet bed cases and the dry bed cases are listed in Tab.1 and Tab.2 respectively. Note that the experimental cases are named as "d_4-d_3", and the variables defined in Tab.1 and Tab.2 are demonstrated in Fig. 3 (a) and (b) respectively.

Table 1. Wet bed cases and variables

Case	d_4 (cm)	d_3 (cm)	d_0 (cm)	U (m/s)	V_2 (m/s)	Fr_f	Fr_s	Re ($\times 10^{-6}$)
4-2	4	2	13	1.085	0.724	2.450	0.944	1.448
6-2	6		20.3	1.401	1.051	3.136	1.186	2.103
8-2	8		28.7	1.717	1.374	3.876	1.387	2.748
10-2	10		38	2.030	1.692	4.583	1.559	3.385
12-2	12		48.3	2.344	2.009	5.292	1.714	4.018

Note: $d_4 = d_2 - d_3$, d_2 is incoming wave height, d_3 is initial downstream water depth, d_0 is upstream water depth, U is wave front velocity, V_2 is velocity in quasi-sable stage, $Fr_f = U/\sqrt{gd_3}$ is wave front Froude number, $Fr_s = V_2/\sqrt{gd_2}$ is Froude number in quasi-sable stage, $Re = V_2 b/\upsilon$ is Reynolds number. $g = 9.81 m/s^2$ is the acceleration of gravity, b=0.2m is width of the house model, $\upsilon = 1\times10^{-6}$ is kinematic viscosity of the water body.

Table 2. Dry bed cases and variables

Case	d_4 (cm)	d_3 (cm)	d_0 (cm)	U (m/s)
4-0	4	0	13	1.21
6-0	6		20.3	1.64
8-0	8		28.7	2.07
10-0	10		38	2.49
12-0	12		48.3	2.90

Note: $d_4 = d_2 - d_3$, d_2 is incoming wave height, d_3 is initial downstream water depth, d_0 is upstream water depth, U is wave front velocity.

3. Analysis of model test results

The in-line tsunami force F_x is the focus of this study, although the forces in other direction and moments are measured simultaneous, they are not discussed here. The time histories of F_x for the wet bed cases are shown in Fig. 4 (a). Generally, the time histories can be divided into four stages, including the impacting stage, the fluctuation stage, the quasi-stable stage and the decreasing stage caused by the influence of the boundary wall, as shown in Fig. 4 (a). The

tsunami force in the impacting stage is mainly caused by the impingement of tsunami bore on the front surface of the model in the extremely short instant, which is characterized as vertical

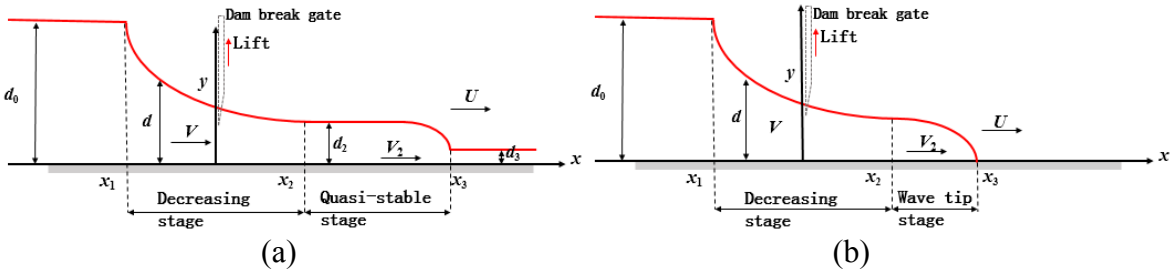

Fig. 3. The definitions of the variables: (a) in wet bed case; (b) in dry bed case

lines rising from zero in the time history curves. The tsunami force in fluctuation stage is mainly affected by the combined action of the impingement, the runup of tsunami bore on the front surface and the pressure acting on the rear surface of the house model. And the tsunami force in the quasi-stable stage is mainly caused by the difference of the water lever at the front and rear surfaces of the house model, in other words, it is caused mostly by the static pressure on the front and rear surfaces. Also the static pressure difference is responsible for the generation of the tsunami force in the decreasing stage, which is not concerned in this study.

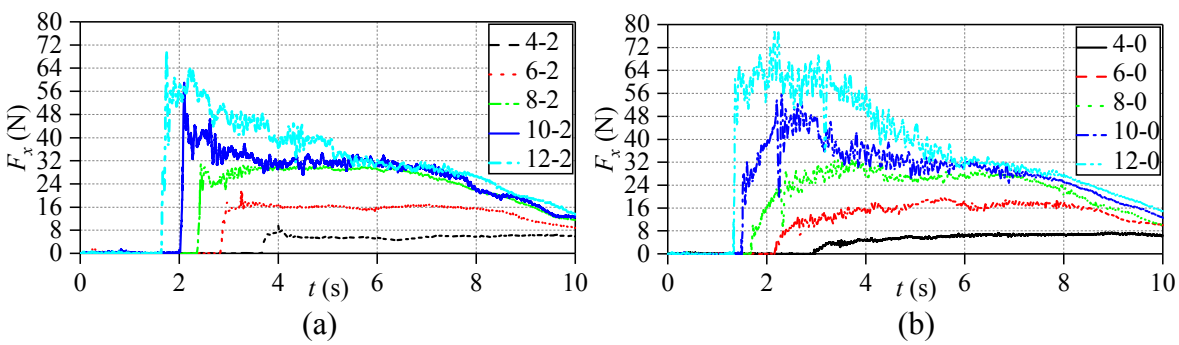

Fig. 4. Time histories of tsunami force F_x: (a) time histories of tsunami force F_x for the wet bed cases; (b) time histories of tsunami force F_x for the dry bed cases

Generally, the time histories of tsunami force F_x for the dry bed cases have the similar characteristics to that of the wet bed cases, shown in Fig. 4 (b). But the differences also exist, detailed as: (1) compared with the wet bed cases sharing the same initial wave height, shorter arrival times are observed in the dry bed cases because the drag effect of the dry bed (friction of the flume bottom) is weaker than drag effect of initial downstream shallow water. For example, the impacting force occurred at 1.6s in the dry bed case 10-0 and occurred at 2.0s in the wet bed case 10-2, approximately. (2) compared with the wet bed cases, the impacting stages are not obvious when the wave height is small, i.e. the cases 4-0 and 6-0. When the wave height is larger, i.e. the cases 8-0, 10-0 and 12-0, the impacting stage is obvious but the amplitude of the impacting force is smaller than that of the wet bed case sharing the same

wave height. For example, the amplitudes of the impacting forces of the cases 12-0 and 12-2 are 64 N and 69 N respectively. The main reasons are believed to be: the relatively smaller wave front slope and the 2mm gap between the house model bottom and flume bottom in the dry bed cases, because the initial downstream water in the wet bed cases increases the wave front height and wave front slope and, for the dry bed cases the lower part of the wave front may pass through the gap but not directly impinge on the front surface of the house model, which does happen in the wet bed cases. (3) The impacting force magnitude is smaller than the maximum value of the fluctuation or quasi-stable stage for all the dry bed cases. And the impacting force magnitude is smaller than the maximum value of the fluctuation or quasi-stable stage only when the wave height is larger for the wet bed cases.

Further, the maximum value of tsunami force $F_{x\text{-}max}$ in the whole stages and the tsunami force mean value in quasi-stable stage $F_{x\text{-}sta,ave}$ of the wet bed cases were calculated and shown in Fig. 5 (a). It can be observed that $F_{x\text{-}max}$ increases with the wave height. $F_{x\text{-}max}$ is slightly larger than $F_{x\text{-}sta,ave}$ when the wave height is smaller, but greatly larger than $F_{x\text{-}sta,ave}$ when the wave height is larger, i.e. the cases 10-2 and 12-2, because the $F_{x\text{-}max}$ happens in the impacting stage, which remarkably larger than the mean value of the forces in quasi-stable stage. And when the wave height is smaller, the maximum force happens in the fluctuation stage, i.e. the cases 4-2 and 6-2, which are marked with squares in Fig. 5 (a). This is because when the incoming wave is small, both the wave height and the wave front velocity is small, and the impinging force is small, while the free surface effect in the subsequent fluctuating section is prominent. And also the mean value of tsunami forces in quasi-stable stage increases with the incoming wave height.

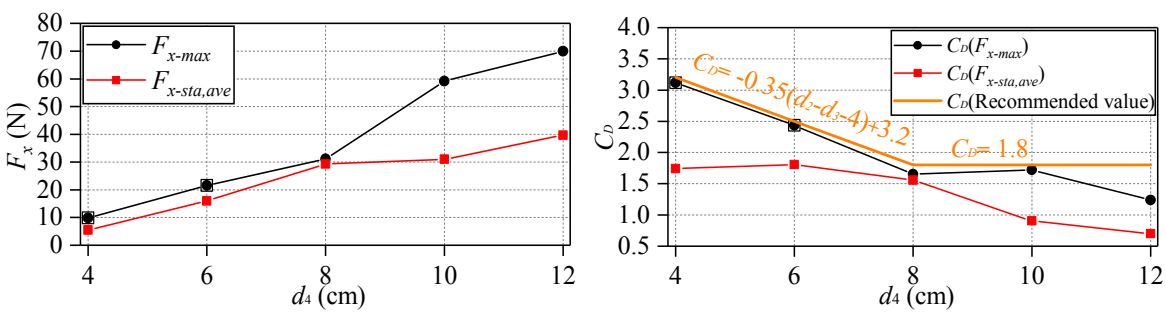

(a) (b)

Fig. 5 The variation of tsunami force with d_4: (a) compare of the maximum values between the whole stages $F_{x\text{-}max}$ and the mean value of tsunami forces in quasi-stable stage $F_{x\text{-}sta,ave}$ for the wet bed cases; (b) compare of coefficient C_D of the maximum value force of the whole stages and average value of quasi-stable stage for the wet cases

Dived by $\frac{1}{2}\rho b d_2 V_2^2$, the tsunami force F_x is nondimensionalized as coefficient C_D, shown in Fig. 5 (b). The coefficient C_D no matter related to $F_{x\text{-}max}$ or $F_{x\text{-}sta,ave}$ decreases with the increase of the incoming wave height. This is because the free surface effect decreases with the increase of the incoming wave height. The curve fitting in the form of polyline is suggested to describe the change of the C_D related to $F_{x\text{-}max}$. Then the maximum tsunami force on the house

model can be estimated by Eq.(1), and the drag force coefficient C_D can be estimated by Eq.(2) and Eq.(3).

$$F=\frac{1}{2}C_D\rho b d_2 V_2^2 \quad (1)$$

$$C_D=-0.35(d_2-d_3-4)+3.2\ ,\ (d_2-d_3)/d_3<4 \quad (2)$$

$$C_D=1.8\ ,\ (d_2-d_3)/d_3\geq 4 \quad (3)$$

Similarly the maximum value of tsunami force $F_{x\text{-}max}$ in the whole stages and the tsunami force mean value in quasi-stable stage $F_{x\text{-}sta,ave}$ of the dry bed cases were calculated. The maximum value $F_{x\text{-}max}$ of the wet bed and dry bed cases are compared in Fig. 6 (a). The results show although there are some differences in wave flow patterns between the wet bed and dry bed cases, the maximum values of tsunami force are almost the same. Also compare of the tsunami force mean values in quasi-stable stage $F_{x\text{-}sta,ave}$ between the wet bed and dry bed cases were conducted and shown in Fig. 6 (b), results indicate they agree with each other very well. Therefore, the Eq.(1), (2) and (3) are also valid for the tsunami force estimation for the dry bed cases.

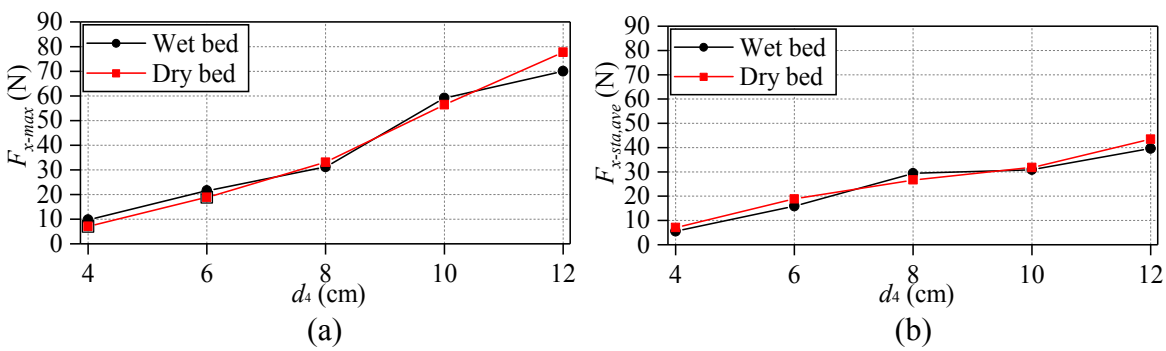

Fig. 6. Compare of the tsunami force: (a) compare of the maximum values of whole stages Fx_{max} between the wet and dry bed cases; (b) compare of the tsunami force mean values in quasi-stable stage $F_{x\text{-}sta,ave}$ between the wet bed and dry bed cases

4. Conclusions

The tsunami force on the model of a prototype house with dimensions of 8m in length, 8m in width and 5m in height was investigated by physical experiments. The tsunami bore was simulated by dam break bores through lifting the gate which separating the upstream impound water and downstream dry bed or wet bed with 2cm initial water. The main conclusions obtained in this study are:

1. The time histories of both the dry bed and wet bed cases can be divided into four stages: impacting stage, fluctuation stage, quasi-stable stage and deceasing stage.
2. The magnitude of the impacting force of the wet bed case is larger than that of the dry bed case sharing the same wave height with wet bed case.

3. The magnitude of the impacting force is larger than the maximum force of the fluctuation or quasi-stable stages when wave height is larger for the wet bed cases, but it is smaller than that when the wave height is smaller.
4. The impacting stage disappears when the wave height is smallar and magnitude of the impacting force is weakened when the wave height is larger for the dry bed case.
5. The arrival time of the dam break bore (the impacting time) in dry bed is earlier than that in wet bed case with the same wave height.
6. The drag effect of the downstream initial water in wet bed case is greater than the friction of the flume bottom in dry bed case, which introduces a higher wave front with larger slope in the wet bed, finally leads to the difference between time histories of the tsunami force between the dry bed and wet bed cases.
7. The wet and dry bed cases have almost the same maximum tsunami forces during the whole stages, and also have almost the same mean values of tsunami forces in the quasi-stable stages.
8. The calculation equations of tsunami force on square house are suggested for both the wet and dry bed cases.

More wet bed cases with different downstream initial water depth should be conducted to check the validation of the proposed calculation equations, and the tsunami force on house with different length-width ratio also should be investigated in the next. And the study of tsunami force on the square house also provides a reference for the square columns in bridges.

5. Acknowledgements

This work is supported by the National Natural Science Foundation of China [Grant nos. 51678491, 51478390], and thanks go to the Science and Technology Planning Project of Sichuan Province with Grant No. 2017JY0003.

6. References

Chanson H. Tsunami surges on dry coastal plains: Application of dam break wave equations[J]. Coastal engineering journal, 2006, 48(04): 355-370.

Como A, Mahmoud H. Numerical evaluation of tsunami debris impact loading on wooden structural walls[J]. Engineering Structures, 2013, 56: 1249-1261.

Dressler R F. Hydraulic resistance effect upon the dam-break functions[M]. National Bureau of Standards, 1952.

Fujima K, Achmad F, Shigihara Y, et al. Estimation of tsunami force acting on rectangularstructures[J]. Journal of Disaster Research, 2009, 4(6): 404-409.

Hartana,Murakami K.Numerical and Experimental Simulation of Two Phase Tsunami FlowThrough Buildings with Openings[J], Journal of Earthquake

Keulegan G H. Wave motion[J]. Engineering hydraulics, 1950.

Lauber G, Hager W H. Experiments to dambreak wave: Horizontal channel[J]. Journal of Hydraulic research, 1998, 36(3): 291-307.

Lukkunaprasit P,Chinnarasri C,Ruangrassamee A, et al. Experimental Investigation of Tsunami Wave Forces on Buildings with Openings[M]. Solutions to Coastal Disasters 2008: Tsunamis. 2008:82-93.

Oshnack M E, Aguíñiga F,Cox D,et al. Effectiveness of small onshore seawall in reducing forcesinduced by Tsunami bore: large scale experimental study[J]. 2009.

Osti R, Tanaka S, Tokioka T. The importance of mangrove forest in tsunami disaster mitigation[J]. Disasters, 2010, 33(2): 203-213.

Ritter A. Die fortpflanzung der wasserwellen[J]. Zeitschrift des Vereines Deutscher Ingenieure, 1892, 36(33): 947-954.

Stoker, J.J. Water Waves. Interscience[M]. New York, 1957

Thomas S, Cox D. Influence of finite-length seawalls for tsunami loading on coastal structures[J].Journal of Waterway, Port, Coastal,and Ocean Engineering,2011, 138(3): 203-214.

Triatmadja R, Nurhasanah A. Tsunami force on buildings with openings and protection[J]. Journal of Earthquake and tsunami, 2012, 6(04): 1250024.

Wei Z, Dalrymple R A. Numerical study on mitigating tsunami force on bridges by an SPH model[J]. Journal of Ocean Engineering and Marine Energy, 2016, 2(3): 365-380.

Wilkinson F. Coastal design and tsunami mitigation for shelter/house reconstruction on the west coast Aceh[C]//International symposium–Disaster reduction on coasts. Monash University, Melbourne. 2005: 14-16.

Whitham G B. The effects of hydraulic resistance in the dam-break problem[J]. Proc. R. Soc. Lond. A, 1955, 227(1170): 399-407.

Yanagisawa H, Koshimura S, Miyagi T, et al. Tsunami damage reduction performance of a mangrove forest in Banda Aceh, Indonesia inferred from field data and a numerical model[J]. Journal of Geophysical Research: Oceans, 2010, 115(C6).

Yeh, H., Robertson I, Preuss J. Development of design guidelines for structures that serve as tsunamivertical evacuation sites[M]. Washington State Department of Natural Resources, Division of Geology and Earth Resources, 2005.

Service Life

Probabilistic Corrosion-Fatigue Life Assessment of Concrete Bridges

Yafei Ma[1*], Zhongzhao Guo[2], Lei Wang[3], and Jianren Zhang[4]

[1] Changsha University of Science and Technology, Changsha China; email: yafei.ma@csust.edu.cn
[2] Changsha University of Science and Technology, Changsha China; email: guozzhao@163.com
[3] Changsha University of Science and Technology, Changsha China; email: leiwlei@hotamail.com
[4] Changsha University of Science and Technology, Changsha China; email: jianrenz@hotmail.com

*: corresponding author

Keywords: bridge engineering; corrosion; fatigue crack growth; seasonal environment

Abstract: This paper proposes a novel framework for the probabilistic life prediction of aging concrete structures under seasonal corrosion-fatigue damage based on the fracture mechanics and equivalent initial flaw size concept. A series of fatigue crack growth tests of steel bars in air and solution environment are conducted to simulate the fatigue crack growth behavior of rebar in different seasons. The framework includes three critical deterioration stages: corrosion initiation-pure fatigue crack growth, competition between corrosion pit growth and fatigue crack propagation, and structural failure. The chloride ingress, cyclic load, corrosion pit growth, concrete cracking, seasonal environment variation and corrosion pit induced-stress concentration are considered. Following that, an uncertainty model is established to incorporate various uncertainties associated with the load and environment. The characteristics of different stages are discussed. Several conclusions and future work are drawn based on the proposed study.

1. Introduction

Corrosion is one of the main influential factors for the deterioration of reinforced concrete (RC) structures in coastal and deicing salt environment. Some highway bridges are also subjected to cyclic load, and corrosion will enhance the fatigue damage accumulations (Ma et al. 2018). Corrosion fatigue of aging RC bridges has been identified as one of the most important failure patterns (Coca et al. 2011). Therefore, the fatigue life prediction is a critical issue for the design and maintenance plan of RC bridges. To perform corrosion-fatigue analysis, Bastidas-Arteaga et al. (2009) proposed a mechanical model for corrosion fatigue life prediction of RC bridges, in which the corrosion pit growth and transition from pit to fatigue crack growth were considered as the main mechanism. However, the morphology of corrosion pit is quite random, and considering the corrosion pit as an initial crack may not satisfy the requirement of fracture mechanics and crack growth analysis. In practical engineering, the corrosion pits act more like notches (Ma et al. 2014; 2017) and affect the fatigue crack propagation. Additionally, corrosion-induced concrete cover cracking and the seasonal environment variation made the interaction more complicated, and few studies included these influential factors in the theoretical corrosion-fatigue analysis.

This study is the first time to perform corrosion fatigue life prediction for existing RC bridges considering the effect of seasonal environment. This paper is organized as follows. First, the entire prediction procedure is divided into three critical stages: corrosion initiation-pure fatigue crack growth, competition between corrosion pit growth and fatigue crack propagation, and structural failure. Following this, a probabilistic method is performed to include various uncertainties for the corrosion fatigue life prediction. Finally, some conclusions and future work are drawn based on the proposed study.

2. Coupled corrosion-fatigue model

2.1 Corrosion initiation and pure fatigue crack growth

Chloride ingress results in a depassivation of reinforcement and induces corrosion initiation of steel bar. The corrosion initiation time T_{ini} is determined as

$$T_{ini} = \frac{C_0^2}{4D_{cl}}\left[erf^{-1}\left(1-\frac{C_{th}}{C_s}\right)\right]^{-2} \tag{1}$$

where C_0 is the concrete cover thickness, C_s is the surface chloride concentration, erf( ) is the error function, C_{th} is the threshold chloride concentration, and D_{cl} is the chloride diffusion coefficient in concrete. The fatigue crack growth of steel bar with microscopic defects before corrosion initiation is considered in this study. The fatigue crack length at T_{ini} can be obtained by

$$T_{ini} = \frac{1}{f}\int_0^{N_{ini}} dN = \frac{1}{f}\int_{a_i}^{a_{ini}} \frac{1}{C_a\left(\Delta K - \Delta K_{th}\right)^{m_a}} da \tag{2}$$

where N_{ini} is the number of load cycles at T_{ini}, f is the traffic frequency, a_i is the equivalent initial flaw size, a_{ini} is the fatigue crack length corresponding to N_{ini}, ΔK is the stress intensity factor range, C_a, m_a and $\Delta K_{th,a}$ are estimated from crack growth test under non-corrosive environment. The a_{ini} is required and can be obtained when T_{ini} and f are determined.

2.2 Competition stage considering seasonal corrosion effect

Currently, it is still difficult to accurately predict the corrosion rate due to concrete cover cracking. Ma et al. (2014) suggested an acceleration coefficient to consider the corrosion activation caused by concrete cracking. The corrosion pit depth $p(t)$ can be determined as

$$p(t) = \begin{cases} 0.0116R_0\int_{T_{ini}}^{t} i_{corr}(t)dt, & t > T_{sp,\lim} \\ 0.0116R_0\int_{T_{ini}}^{T_{sp,\lim}} i_{corr}(t)dt + 0.0116R_0k_{ac}\int_{T_{sp,\lim}}^{t} i_{corr}(t)dt, & t > T_{sp,\lim} \end{cases} \tag{3}$$

where $T_{sp,lim}$ is the time to severe cracking, $T_{sp,lim}=T_{ini}+T_{cr}+T_{cp}$, T_{cr} is the first cracking time of concrete cover induced by corrosion, T_{cp} is the time from the cracking to limit width, k_{ac} is an acceleration coefficient. The pit growth rate can be obtained by taking the derivative of Eq. (3). The effect of seasonal environment variation on fatigue crack growth is considered in this paper, which is a very complex influential factor and shown as follow

$$da/dt = \begin{cases} C_a(\Delta K - \Delta K_{th,a})^{m_a} f, & spring \quad and \quad summer \\ C_b(\Delta K - \Delta K_{th,b})^{m_b} f, & autumn \quad and \quad winter \end{cases} \tag{4}$$

where C_b, m_b and $\Delta K_{th,b}$ are estimated from corrosion fatigue crack growth test. The competition time T_{com} between corrosion pit growth and crack growth can be determined by

$$T_{com} = [N_0 + n \bullet N_{half} + N_{com,end}] \tag{5}$$

where N_0, N_{half} and $N_{com,end}$ are the number of load cycles from T_{ini} to first environment stage, at a load frequency for half year and in the last calculation item of competition stage, respectively.

2.3 Structural failure stage

After the competition, the fatigue crack growth dominates the deterioration of RC bridges. If the competition ends in spring-summer stage, the structural failure time T_{det} can be estimated by

$$T_{det} = \frac{1}{f}\left[\int_{a_i}^{a_{k1}} \frac{1}{C_a\left(\Delta K - \Delta K_{th,a}\right)^{m_a}} da + \int_{a_{p1}}^{a_{q1}} \frac{1}{C_b\left(\Delta K - \Delta K_{th,b}\right)^{m_b}} da \cdots \int_{jn,kn}^{a_c} \frac{1}{C_{a,b}\left(\Delta K - \Delta K_{th,a,b}\right)^{m_{a,b}}} da\right] \tag{6}$$

where a_{k1}, a_{p1}, a_{q1} are the integration upper and lower bound in different environment stage, a_c is the critical crack length, $C_{a,b}$, $m_{a,b}$ and $\Delta K_{th,a,b}$ mean the parameters corresponding to certain environment stage.

3. Application example

The proposed model is used to a simply supported RC bridge beam with a span of 10 m. Fig. 1 shows the details of the cross-section and the arrangement of reinforcement. The fatigue effect is simulated by a random truck axles load P applied at the middle of the span with a daily traffic frequency f. It is assumed that P follows a lognormal distribution. The values of 50, 100, 200 and 500 cycles/day are used to clarify the influence of traffic frequency on the prediction result.

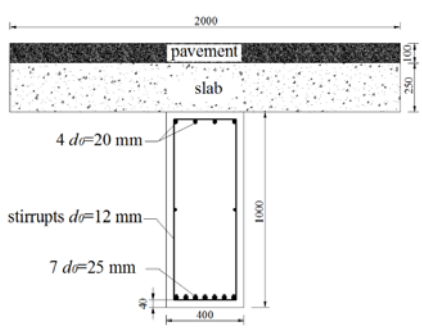

Fig. 1. Configuration of the bridge beam (unit: mm)

The mean and COV of the variables used for probabilistic analysis can be found in references such as (Stewart 2009 and Ma et al. 2014). Monte Carlo simulation is conducted and 500,000 samples are performed.

4. Results and discussion

The total lifetime of RC bridge is the sum of the three stages. Fig. 2 shows the total lifetime of RC bridge under different aggressiveness levels and various traffic frequencies. The lifetime follows a lognormal distribution with a mean varying between 15.56 and 161.32 years and SD varying between 5.18 and 74.89 years, respectively. The mean and the SD decrease as the traffic frequency and aggressiveness level increase. Fatigue crack growth rate increases under a higher traffic frequency, resulting in a reduction in the determination stage. In addition, it is also expected that increasing aggressiveness level leads to a decrease in the determination stage. The reinforcement fractures in a shorter period.

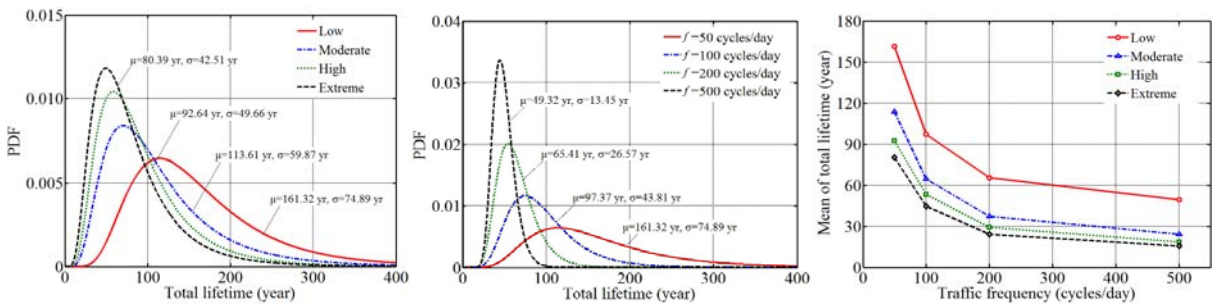

(a) (b) (c)

Fig. 2. Total lifetime: (a) PDFs under various aggressiveness levels and f =50 cycles/day; (b) PDFs under low aggressiveness level and various traffic frequencies; (c) mean of total lifetime

5. Conclusions

The coupled action of corrosion and fatigue significantly reduced the remaining service lifetime. Fatigue crack growth rate increased under a higher traffic frequency, resulting in a reduction in the determination stage. In addition, it is also expected that increasing aggressiveness level leads to a decrease in the determination stage. The reinforcement fractures in a shorter period.

6. Acknowledgments

The work is financially supported from the National Natural Science Foundation of China (51508036, 51478050), the Scientific Research Fund of Hunan Provincial Education Department (17B012), and the Training Program for Excellent Young Innovators of Changsha (kq1802012). The support is gratefully acknowledged.

7. References

Bastidas-Arteaga, E., Bressolette, P., Chateauneuf, A., and Sánchez-Silva, M. 2009. Probabilistic lifetime assessment of RC structures under coupled corrosion–fatigue deterioration processes. Structural Safety, 31(1), 84-96.

Coca, F.J.O., Tello, M.U.L., Gaona-Tiburcio, C., Romero, J.A., Martínez-Villafañe, A., Maldonado, E., and Almeraya-Calderón, F. 2011. Corrosion fatigue of road bridges: a review. International Journal of Electrochemical Science, 6(8), 3438-3451.

Ma, Y., Wang, G., Su, X., Wang, L., and Zhang, J. 2018. Experimental and modelling of the flexural performance degradation of corroded RC beams under fatigue load. Construction and Building Materials, 191, 994-1003.

Ma, Y., Wang, Q., Guo, Z., Wang, G., Wang, L., and Zhang, J. 2017. Static and fatigue behavior investigation of artificial notched steel reinforcement. Materials, 10(5), 532-545

Ma, Y., Wang, L., Zhang, J., Xiang, Y., Peng, T., and Liu, Y. 2014. Hybrid uncertainty quantification for probabilistic corrosion damage prediction for aging RC bridges. Journal of Materials in Civil Engineering, 27(4), 1-10.

Ma, Y., Xiang, Y., Wang, L. Zhang, J., and Liu, Y. 2014. Fatigue life prediction for aging RC beams considering corrosive environments. Engineering Structures, 79, 211-221.

Stewart, M.G. 2009. Mechanical behaviour of pitting corrosion of flexural and shear reinforcement and its effect on structural reliability of corroding RC beams. Structural Safety, 31(1), 19-30.

Analysis of Serviceability of Existing RC Beams after 20 Year's Service in Seasonal Frozen Areas

Yixing Ding[1] and Yanmin Jia[2*]

[1] School of Civil Engineering, Northeast Forestry University, Harbin and China; email: dyx0011@foxmail.com
[2] School of Civil Engineering, Northeast Forestry University, Harbin and China; email: yanminjia2008@126.com

[*]: corresponding author

Keywords: existing RC beams; materials inspection; corrosion reinforcement; carrying capacity; finite element method

Abstract: An investigation of the behavior of 3 full-scale reinforced concrete (RC) beams that have served in seasonal frozen areas for two decades is presented in this paper. Rebound value, carbonization depth, concrete cover depth, corrosion potential, bending and shear capacity of the beams were tested. The results of both bending and shear carrying capacity test still meet requirements of specifications. However, the materials inspection illustrates that reinforcement cannot be effectively protected because of the excessive depth of carbonization of concrete and the corrosion of reinforcing steel began to appear. Necessary maintenance measures for the beams are required. Based on the data of above tests the constitutive behaviors of the corrosion reinforcement, constitutive model of concrete considering carbonization and exponential damping friction model for bond relation between reinforcement and concrete were chosen to realize the nonlinear finite element (FE) models of the test beams via ABAQUS software. The deflection and strain data calculated by the model exhibit good agreement with the experimental results. Existing carrying capacity of RC beams can be evaluated by finite element method on the basis of materials inspection.

1. Introduction

After a bridge has been put into operation, with the lapse of time, such diseases as aging or destruction may gradually appear. For a lot of existing bridges, especially dangerous bridges, it is impossible to fully dismantle and rebuild them, because it is neither scientific nor realistic. A more practical and effective method to accurately assess the bearing capacity of an existing bridge for assuring it to meet present transport requirement. Because creepage and shrinkage are marked during the first 10-15 years, the internal forces of RC structures are redistributed, some reinforcements more easily yield. During the subsequent several dozens of years, the reliability decreases slowly. After 50-60 years, serious corrosion may cause the reliability of concrete structure to decrease greatly again(Guo et al., 2016).

In the paper, three RC beams having served for 20 years in a seasonal frozen soil region were detected, including the perfectness degree of concrete strength, carbonization and corrosion. All above data can be obtained by nondestructive testing. The bending capacity and shear capacity were researched by destructive tests. In addition, a finite element model established by

ABAQUS to discuss the possibility of applying concrete carbonization and index damping friction model for forecasting the bearing capacity of RC beams on basis of material detection.

2. Experimental program

The test beams have served in the seasonal frozen soil region for 20 years, the calculation span is 7.52m. M-1 and M-2 were tested for their bending capacity, load was applied symmetrically at both points 0.7m away from span center; S-1 was tested for its shear capacity, the load points were located at the place 1m away from the bearing centerlines on both ends. The thickness of the protection layer at the span center of the test beams are too thin to protect steel bars; the largest ratio of the carbonization depth and the thickness of the protection layer can reach 0.7 and the durability is quite affected. The potential detection result on reinforcement shows that the rustiness probability is 5%. Due to the deep carbonization depth, the concrete strength determined by rebound test can only indicate the strength status of concrete is in good condition. For M-1, longitudinal crack, exposed reinforcement and serious rustiness exist; for M-2, many vertical and lateral cracks exist, stirrup seriously rusts, main reinforcement rusts by a little; for S-1, concrete peel-off position superimposes the load application point.

3. Finite element analysis

3.1. Constitutive model on concrete

ABAQUS damage plasticity model was used for concrete. Previous test results have shown that the peak strain of the carbonized and non-carbonized concrete are basically equal, the ultimate compressive strength increases by 16%-26%, while the ultimate strain reduces by about 20%(Geng and Yuan 2006). Considering the Rebound value of test beams, the constitutive model of concrete is revised by increasing ultimate strength and reducing ultimate strain. Concrete destruction criterion adopts the 4-parameter destruction criterion proposed by Jiang Jianjing (Jiang and Lu, 2005) by referring to Ottosen 4-parameter strength criterion.

3.2. Constitutive model on reinforcement

$$\sigma_{s,c}=\begin{cases} E_s\times\varepsilon_{s,c} & \left(0<\varepsilon_{s,c}\le\dfrac{1-1.104\rho}{1-\rho}\times\dfrac{f_y}{E_s}\right) \\ \dfrac{1-1.104\rho}{1-\rho}f_y+\dfrac{\varepsilon_{s,c}-\dfrac{1-1.104\rho}{1-\rho}\times\dfrac{f_y}{E_s}}{e^{-2.203\rho}\varepsilon_{su}-\dfrac{1-1.104\rho}{1-\rho}\times\dfrac{f_y}{E_s}}\times\left(\dfrac{1-1.125\rho}{1-\rho}f_u-\dfrac{1-1.104\rho}{1-\rho}f_y\right) & \left(\dfrac{1-1.104\rho}{1-\rho}\times\dfrac{f_y}{E_s}<\varepsilon_{s,c}<e^{-2.203\rho}\varepsilon_{su}\right) \end{cases} \tag{1}$$

The present test research shows that, following the increase of reinforcement corrosion rate, the elasticity modulus of reinforcement failed to change apparently, while the yielding strength, the ultimate strength, the yielding strain, the intensified strain and the ultimate strain changed toward negative direction. On basis of test research data and research achievements on the constitutive model of corroded reinforcement, Yu (2014) proposed a physical model on the stress-strain relationship of slightly corroded reinforcement and established a constitutive model on the inlaid reinforcement of slightly corroded RC structures, as shown in Eq. 1.Where ε_{su} is ultimate strain of non-corroded steel rebar; and f_y is the yield stress of non-corroded steel rebar; ρ is the percentage mass loss of the steel rebar.

3.3. Contact conditions

In the model, normal behavior adopts interference contact, in which the contact pressure is the exponential function of surface gap. In surface contact, contact pressure can be transferred between two surfaces; if surfaces are separated to proper distance, the contact pressure may decrease to zero. Then, the contact pressure transferred between surfaces increases exponentially following the decrease of gap. Tangential behavior adopted the formula proposed by Amleh (Amleh and Ghosh, 2006) in which the friction coefficient shows exponential relationship from static friction to dynamic friction, in addition, an ideal mathematic expression on the exponent decay friction model was provided in Eq. 2. The three parameters μ_s, μ_k and d_c are calibrated as 1, 0.4 and 0.45, respectively1, 0.4 and 0.45 (Lundgren and Gylltoft, 2000).

$$\mu = \mu_k + (\mu_s - \mu_k)\exp(-d_c \dot{\gamma}_{eq}) \tag{2}$$

4. Model validation

The load-displacement curves of bending test shows that the increase trend of deflection calculation value and test value are basically consistent and gradually become large following the increase of load. When the load respectively reaches 325.43kN and 342.67 kN, the test beams are destroyed, the loads are just the ultimate loads of the test beams. The concrete crushing load obtained by finite element calculation is 303.85kN, and the calculation result with the constitutive model of uncarbonated concrete is 287.81kN. It shows that it is feasible to forecast the bending performances of slightly corroded RC beams by using the finite element model considering the carbonization and slip of peripheral concrete.

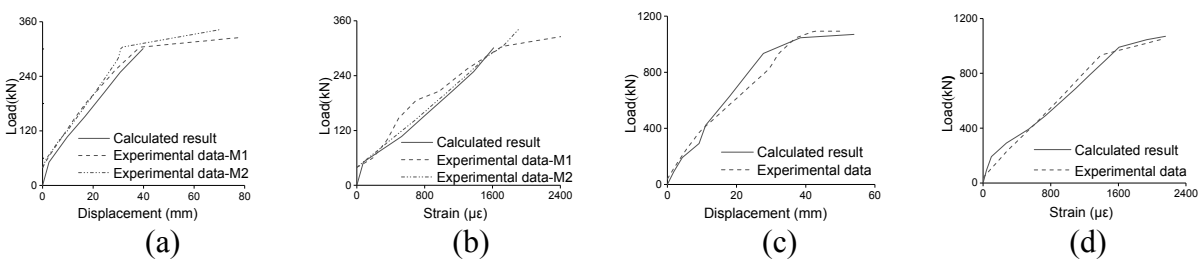

Fig. 1. Measured and calculated data of mid-span section of test beams: (a) displacement of bending test; (b) strain of longitudinal reinforcement in bending test; (c) displacement of shear test; (d) strain of longitudinal reinforcement in shear test

The strain of the longitudinal reinforcement and loading deflection of each stage of load used for the shear test beam coincide well with the simulative values. When load is increased to 1092.70kN, the concrete at the upper edge of the loading point is crushed, at the time, the actually-measured reinforcement strain sharply changes, the finite element calculation value is1069.68KN, which coincides well with the test result, at the same time the calculation result without considering carbonization is 1022.15kN. It shows that the result of considering carbonization is more accurate. In addition, it also indicates that the ultimate bearing capacity of a slightly corroded over-reinforced concrete beam increases following the increase of the carbonization degree.

5. Conclusion

In the paper, the appearance, sizes and material status of three 8m RC hollow plate beams that have served for 20 years in seasonal frozen area were firstly detected, concrete peel-off exists, the reinforcement at partial peel-off locations corrodes seriously, however, the potential result is excellent, no corrosion activity is found at the complete structure; the mechanical performances of concrete are excellent, however, the carbonization degree is serious, the thickness of the protection layer is not sufficient to prevent reinforcement from being corroded. On basis of the material data obtained by NDT, ABAQUS model was established by considering carbonization, corrosion and slip, the calculation results coincide well with the bending and shear test results. The result shows that the calculation values obtained by using the numerical modeling theory after considering concrete carbonization, slight reinforcement corrosion and exponential slip model can basically meet the demand for analyzing slightly corroded RC beam. After twenty years of service, due to carbonization the strength increases, and the bending and shear capacity are strengthened. Partial concrete peel-off and reinforcement corrosion appearing in the test beam less affect the integral bearing capacity. On the other hand, the reinforcement corrosion activity of the test beams shall be frequently monitored, in addition, necessary durability maintenance measures shall be taken.

6. References

Amleh, L. and Ghosh, A. 2006. Modeling the effect of corrosion on bond strength at the steel–concrete interface with finite-element analysis. Canadian Journal of Civil Engineering, 33, 673-682.

Geng, O. and Yuan , G. L. 2006. Study on The Stress-Strain Relationship of Carbonation Concrete and the Flexural Performance of The Carbonized Reinforced Concrete Beam. Industrial Construction, 44-46+79.

Guo, T., Chen, Z., Liu, T. and Han, D. 2016. Time-dependent Reliability of Strengthened PSC Box-girder Bridge Using Phased and Incremental Static Analyses. Engineering Structures, 117, 358-371.

Jiang, J. J. and Lu, X. Z. 2005. Finite Element Analysis of Concrete Structures, Tsinghua University Press.

Lundgren K. and Gylltoft K. A model for the bond between concrete and reinforcement. Magazine of Concrete Research, 2000, 52(1):53-63.

Yu, H. C., Tao, Q. L. and Hu, Y. Theory of Numerical Model for Light Corroded RC Components. The Second International Conference on Large Building Steel and Composite Structures, 2014 Shanghai, China.

Crack Propagation of Concrete Bridge Which Were Made by the New Quality Assurance System in Japan

Hiroki Hayashi[1] and Tatsuya Nukushina[2*]

[1] Tokuyama College of Technology, Yamaguchi, Japan; email: nukushina@tokuyama.ac.jp
[2] Tokuyama College of Technology, Yamaguchi, Japan; email: c13hayasi1h@tokuyama.kosen-ac.jp

[*]: corresponding author

Keywords: concrete structure; crack; crack width; crack length; crack detection

Abstract: Civil engineers consisting of ordering, building, designing and material manufacturing academics made “The quality assurance system check-sheet” and the quality of structures was seen to have improved because of it. In the past, there were many structure cracks at the time of construction, so a form was created to collect data and note important information. However, some structures whch were made using the quality assurance system still developed cracks after only a few years had passed. These crack widths were over 0.2 millimeters in size and so it was thought that action should be taken to improve the quality assurance system. An investigation into the cracks found in certain structures was carried out as a result. For this investigation a selection of bridges in Yamaguchi prefecture, Japan were selected. During this investigation, it was discovered what went wrong during construction, such as the distance between reinforcements, construction methods used and the concrete composition. With this information it is possible to improve the quality assurance system even further. This quality assurance system is now being considered to be put into use by all of the Prefectures in Japan and even the Japanese ministry of land. By continuing to accumulate data to improve the current database of Yamaguchi Prefecture structures, it can provide insights to allow construction of longer lasting structures in the future. Therefore, structures that had existed for over 10 years were also investigated. One of these structures called Kagawa IC has changed a lot since construction, and now features many large cracks which provided interesting results.

1. Introduction

Conventionally, concrete structures are generally excellent in durability and it is considered a semi-permanent maintenance-free material. However, there are large quantities of concrete structures which were built when Japan had experienced high economic growth that are now suffering from early deterioration. And now faced with the long-term population decline in Japan, it is important to maximize long-lasting structures economically. For the above reason, civil engineers in Yamaguchi prefecture, Japan, who are academics in ordering, building, designing and material manufacturing decided to make "The quality assurance system" and the quality of engineering structures were seen to have been improved as a result. In particular, they recorded defects such as cracks that had occurred during the beginning of the construction and compiled them into databases. Those databases were published publically so that industry, government and academia could benefit from the results together. Yamaguchi Prefecture created the

"Construction situational awareness check-sheet" which is summarizing the key points from the status check at the time of construction. It was highlighted by the ministry and a lot of local governments as a new innovation of concrete. Nowadays, construction projects which are based on this system have been expanded to all parts of Japan. Though most structures which were made using the quality assurance system over the past several years are considered to be more durable, there can still be issues with cracks forming. For example, some structures have been found to contain cracks wider than 0.2mm, which is considered dangerous by the Japanese ministry of Land, Infrastructure, Transport and Tourism. Because of this, we investigated the long-term cracks of structures that were made by the quality assurance system, and then collated our findings with the extensive database created during the time of construction. By doing so, it is possible to verify the presence or absence of conditions during construction that can lead to future cracking.

2. System and Database

During the construction work, if it is determined that harmful cracking has occurred, it would be necessary to take on additional labor costs to cover the investigation and any repairs that may be needed. It means to avoid unnecessary costs is very important to the suppress any causes of future cracking. To find out more information, Yamaguchi Prefecture, conducted a test installation. The test structure, was constructed physically using the prefecture's own crack suppression system instead of relying on any simulations. It is has helped during both pre-examination and post-examination by providing realistic data. A loop with the configuration of the "PDCA cycle of Crack Control System in Yamaguchi Prefecture" [1] is shown in Fig. 1. The system aims to suppress cracks through the cooperation of all of the departments involved. In addition, the "Construction situational awareness check-sheet" was opened to the public in the form of a check sheet consisting of 27 carefully selected items. The result of the check sheet has been published on the website of the Technical Management Division and is regularly providing useful information to builders.

2.1. Analysis of Database

In this study, two bridge structure groups were formed in Yamaguchi Prefecture. The first studied structures that were around 2 years old, and the second studied structures that were around 10 years old. There are two reasons for this. Firstly, there are a lot of the bridge structures that had been constructed over 10 years ago, and many of them had harmful cracks at the time of construction. Even though many of these structures existed for over 10 years, there was almost no documented information to find on them. The other reason that structures that were less than 2 years old weren't selected was that structures can change a lot in their first year since most cracks form around this time and are then expanded during the winter. For the above reasons, the surveyed bridge structure group of 2016, 2017 and 2007 are shown in Table 1. The surveyed bridge structure has a significant influence on its durability. In this study, we conducted a cracked investigation using a crack scale. To get our results we measured three spots on each of the cracks, and calculated their average width. Also, crack length has measured by the convex. Crack sketches that compare the investigated cracks with the construction drawings have since been made and are now also stored in the database along with the initial cracks that occurred during construction. With this it is easy to compare how much the crack's widths and lengths have progressed.

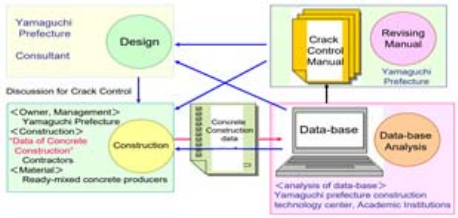

Fig. 1. The crack control system [1]

Table 1. The surveyed bridge structure

Year	The name of the bridge	Season (month)	Crack width (mm)
2007	48 streams	3	0.35
	Otsukasokudo	5	0.20
	Matsuzaka	3	0.35
	Kagawa IC	7	0.25
2016, 2017	Shinkogawa	4	0.20
	Tojo	8	0.20

4. Result and Discussion

In this study, there were 6 structures used for the survey as shown in Table 1. We chose to use just 3 of them which were "Tojo", "Kagawa IC" (Fig. 2) and "48 streams bridge" (Fig. 3). The reason for choosing these structures was that they would give us a wide range of results to use as they each have a different creation date, number of cracks, crack width and crack length. "Tojo" and Fig. 2 were investigated two times in summer and winter. Those two structures have harmful initial cracks, and they are progressing. Even though "Tojo" was built recently, 4 out of 6 piers have over ten cracks in them. However, Fig. 3 which has stood for over ten years, has no crack progress. Because of this, it was decided that comparing the three bottoms of the bridges would be better.

4.1. A Relationship between the Results and System of each Visual Evaluation of Bridges

The crack area per unit area of the three structures is shown in Fig. 4. "Tojo" only passed by two years, but it has many initial cracks to compare with other 2 bridges, and has progressed dramatically such a short time. One of the causes might be the season in which it was constructed. Construction details of three structures is shown in Table 2. The construction for this structure happened in the summer, so the temperature of concrete and amount it expanded were higher than usual. When the temperature of concrete later decreased, it shrank. The stress from this reaction can cause cracks to form throughout the concrete. In addition, no record exists about the temperature of concrete on the database (Table 2). The initial temperature of concrete, being under 35 degrees, is thought that important for preventing a temperature crack or workability in Japan.

The number of cracks has been increasing a little for ten years at the Kagawa IC (Fig. 2) to compare with "Tojo" that passed by only 2 years. However the 48 streams bridge (Fig. 3) has

Fig. 2. Kagawa IC

Fig. 3. 48 streams bridge

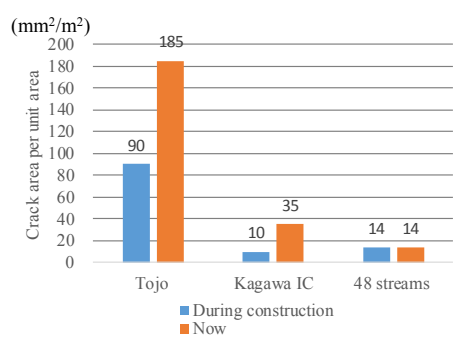

Fig. 4. Crack area per unit area of three structures

discovered that prevented expansion of the cracks for ten years. One reason might be that is that it used a well thought out method of curing (Table 2). Initial cracks had a 19 days leaving period of curving forms, and a 14 days curing period. The method of curing used was curing forms and curing mat + spray curing. Because it was considered that the average temperature was 2-5 degrees when the concrete was placed in February. On top of this they also conducted heat curing and applied a curing sheet to the construction scaffolding. When the concrete surface hardened, it was covered with a curing mat and sprayed. The curing method influences the surface quality, so these are theorized to be the reason behind the prevented expansion of the cracks. The biggest difference between Kagawa IC and other two structures are that the new quality assurance system had not yet been completed. Data about Kagawa IC is almost the same as 48 streams bridge such as the water-cement ratio and slump. In addition, the concrete placed in April, and the type of cement used is the same as in Fig. 4. However, the initial cracks progressed over 10 years. This construction had been created using an early incomplete version of the new assurance system, which may explain the reason for the differences in cracking between 2 near identical structures.

Table 2. Construction details of three structures (Portland blast furnace cement type B)

	Tojo	Kagawa IC	48 streams
Water-cement ratio (%)	53	54	54
Unit water content (kg/m^3)	165	162	163
Unit cement content (kg/m^3)	311	300	302
Slump (cm)	12	8	8
Placing interval between the lift (day)	20	25	21
Placing month	August	April	February
Temperature (℃)	30	8.8	5.9
Concrete temperature (℃)	—	16	11.0
Method of curing (Surface of placing)	Curing mat + Spray curing	Curing mat + Spray curing	Curing mat + Spray curing
Curing period (day)	7	10	14

5. Conclusions

The cracks on bridge structures which were constructed using the new quality assurance system in Yamaguchi Prefecture, Japan were measured and assessed. They were then compared to information in the database and the results of this investigation are that strict adherence to basic precautions or meticulous initial preventive measures during construction are very important for preventing long term cracks in concrete. Some structures which were constructed using this system have still deteriorated at an early stage. As a result, it was discovered that it is necessary to improve the welding conditions and methods of construction used, as they can help improve the long-term durability of structures.

6. Reference

[1] Akira HOSODA, Makoto NINOMIYA, Takahiro TAMURA, Kazuhiko HAYASHI, “Improvement of Covercrete Quality by Crack Control System in Yamaguchi Prefecture in Japan”, The 8th Int. Symposium on Social Management Systems SSMS2012-Disaster Prevention and Reconstruction Management, SMS12-3835, May 2012.

Bridge Life-Cycle Cost Analysis with Effects from Overloads and Fatigue Damage

Bora Jang[1*] and Jamshid Mohammadi[2]

1 Sharma & Associates, Inc, Countryside, IL, USA; email: bjang5@hawk.iit.edu
2 Department of Civil, Architectural and Environmental Engineering, Illinois Institute of Technology, Chicago, IL, USA; email: mohammadi@iit.edu

*: corresponding author

Keywords: truck overloads; fatigue damage; bridge life-cycle cost analysis; bridge load rating; damage assessment

Abstract: Life-cycle cost analyses are often considered in bridge management in conjunction with the decision-making process for bridge maintenance, rehabilitation, or replacement. A major portion of a bridge life cycle cost is associated with maintenance and rehabilitation that occur periodically. An accurate estimate for these costs requires a better understanding, and proper modeling of, deterioration rate of a bridge's components throughout its useful time. The deterioration rate is affected by the structural type and design, volume and intensity of traffic, damage as a result of continuous use and fatigue, and the plan for scheduled maintenance. Various measures may be used to describe the deterioration in a structure. However, specific to bridges, generally, the bridge condition rating is used as an index to represent deterioration. When using the condition rating in bridge life cost analysis and management, special attention will need to be paid in regard to the potential for accelerated fatigue damage that can occur because of frequent use of overloads on the bridge. Overload trucks constitute a sizeable portion of truck load populations on many of our nation's highways. As truck populations grow, there is a potential for increase in the frequency of overloads on highway bridges as well. With a sufficient number of overloads, there is a potential for accelerated damage to fatigue-critical structural components resulting in a reduction in bridge service lives and increasing the bridge life cycle cost. Hence, the intensity and number of overloads occurrence result in an increase in the maintenance and rehabilitation frequency and also their associated costs. In this study, an index representing the fatigue life expended (FLE) due to truck overloads is introduced and used as a driving factor in the deterioration curve to incorporate the significance of fatigue damage from overloads in the decision-making strategies in maintenance and rehabilitation and in bridge management.

1. Introduction

Overload trucks constitute a major portion of truck load populations on many arterial routes and highways. Specific to bridges, the increase in the frequency of overloads may trigger shortening of service life of critical components because of fatigue damage, considering the fact that fatigue damage accelerates at higher loads. This is especially important to older bridges that have been designed for loads lower than the standard for current highway bridge design in the United States (Jang and Mohammadi, 2017 and Jang, 2018). It is indicated that the fatigue life expended (FLE) is significantly affected by the annual rate of truck traffic growth and the percentage of overloads in the entire truck load population (Jang and Mohammadi, 2018). To incorporate the significance

of fatigue damage from overloads in bridge management applications, the "fatigue index factor" introduced by Jang (2018) may be used. Life-cycle cost analyses are often considered in bridge management in conjunction with the decision-making process for bridge maintenance, rehabilitation, or replacement. A major portion of a bridge life cycle cost is associated with maintenance and rehabilitation that occur periodically. An accurate estimate for these costs requires a better understanding, and proper modeling of, deterioration rate of a bridge's components throughout its useful time (Moses et al., 1987). If the condition rating in bridge life cost analysis and management is used, special attention will need to be paid in regard to the potential for accelerated fatigue damage that can occur because of the frequent use of overloads on bridges. Overloads and their potential for accelerated fatigue damage may in fact become a major cost item in the bridge overall life-cycle cost, if not addressed properly. In this study, the fatigue index factor is used as an additional parameter in life cycle cost analysis and bridge management. The procedure via which this factor is incorporated in the analysis is described and illustrated.

2. Bridge Life-Cycle Cost Analysis (BLCCA)

The life-cycle cost analysis (LCCA) is an engineering economic analysis tool. It is used to quantify the differential costs of alternative investment options for a given construction project. It is therefore used to study new construction projects and examine preservation strategies for existing structures. The bridge life-cycle cost analysis (BLCCA) is conducted to minimize costs over the long-term life of bridges (Hawk, 2003). The procedure of BLCCA shown in Fig. 1 is to (1) establish alternative options for a project; (2) determine activity timing for each alternative; (3) estimate agency and user cost; and (4) determine life-cycle costs. For each alternative, the output may be demonstrated graphically as shown in Fig. 2. The slope in the graph represents the deterioration rate of a bridge component or system. Each peak indicates the significance of a preventive measure such as a maintenance or rehabilitation action.

Fig. 1. BLCCA methodology steps

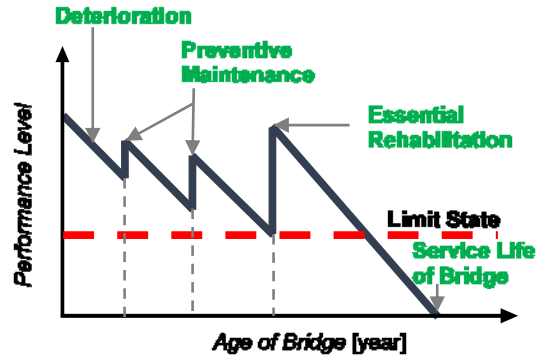

Fig. 2. BLCCA output for each alternative

In general, the bridge rating (whether obtained as a subjective measure by an inspector or through structural analyses) can be used for determining the deterioration rate. Among various parameters affecting the deterioration of bridge condition, live loads are most significant. And of course, the effect of the live load can well be accelerated when loads larger than the legal limits (i.e., overloads) are frequently applied. Overloads can produce a reduction in capacity or service

life of bridges potentially leading to direct agency and user costs as well as to an increased risk of future damage or failure (Jang, 2018).

3. Application of fatigue index factor for estimating deterioration rate

The deterioration rate is affected by the structural type and design, volume and intensity of traffic, damage as a result of continuous use and fatigue, and the plan for scheduled maintenance. Various measures may be used to describe the deterioration in a structure. However, specific to bridges, generally, the bridge condition rating is used as an index to represent deterioration. Typical deterioration models are often shown as a curve for bridge rating with negative incremental slopes. Such curves illustrate the situation when no actions (repairs or rehabilitations) are applied on the structure. The rating based on subjective condition assessment (condition rating) or analytical methods (analytical rating) can be to construct these curves. If analytical rating is considered, rating values will need to be converted to measures that describe condition rating, since the deterioration curves currently available are mainly for condition rating. Fig. 3 represents a bilinear function for the fatigue index factor as proposed by Jang, 2018. This factor can simply be implemented in modifying the bridge ratings (to account for fatigue damage) and establishing a revised deterioration curve accordingly for use in BLCCA.

4. Illustrative example of BLCCA applications

For illustrative purposes, a simply supported steel girder bridge with a welded cover plate (Category E in fatigue details) is considered in which the *ADTT* and the percentage of overloads in truckload population are 2623 and 10.5%, respectively, for this example. Three different scenarios for the condition rating are considered. These are (Case I) no maintenance is used; (Case II) maintenance without a fatigue index factor applied; and (Case III) maintenance with the fatigue index factor applied. Fig. 4 presents the results of life-cycle cost analysis for the example bridge. Obviously, if some maintenance and rehabilitation is performed, the service life of bridge is to be extended to 135 and 117 years, respectively, depending on whether or not the fatigue index factor is considered. With no maintenance, the service life is at 87. In a more detailed analysis, the results of BLCCA for the example bridge can be compared by using the value index (*VI*) model. The concept of the *VI* model was proposed by Mohammadi, Guralnick, and Yan in which a single parameter can be represented to quantify the value of an alternative for bridge life-cycle cost analysis with consideration for the bridge condition, time and cost. The function of *VI* model is written in the following equation (Mohammadi et.al., 1995).

$$VI = \frac{rt}{c} = \frac{A_s}{c} \tag{1}$$

In which r is the rating, t is time, c is the cost, and A_s is the area under the rt curve (i.e., the bridge deterioration curve). The underlying concept of the *VI* model is that the increase in r and t results in an improvement in value index. However, the variable r is related to the cost, c. Thus, this model is used as an objective function and its result produces an optimum value of *VI* that can be used in decision-making procedure and estimation of an optimum time intervals between scheduled maintenance or rehabilitation. In this example, the cost, c, is assumed as a unit cost for all the three cases and the quantity *VI* is determined by computing the area under each deterioration curve. To simplify the problem, a linear deterioration function is used. Fig. 5

represents *VI* for each case. For case II and III, the value index *VI* = 639 and 514 respectively, which are higher than *VI* = 380 obtained for case I. As expected, the service life of the bridge is extended for those two cases due to several maintenance or rehabilitation actions. The *VI* for case II has the highest among the three cases. However, it is not desirable since the potential for fatigue damage from overloads has not been incorporated in the process. This means this *VI* value is not a true representative of the situation, if indeed frequent overloads are applied on the bridge. It is evident that the fatigue damage from overloads results in reducing the service life of the bridge and increasing the bridge-life cycle cost.

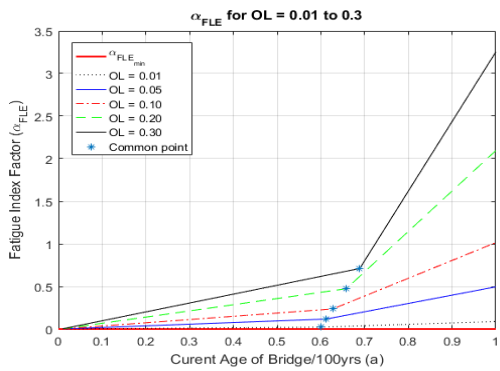

Fig. 3. Bilinear function of fatigue index

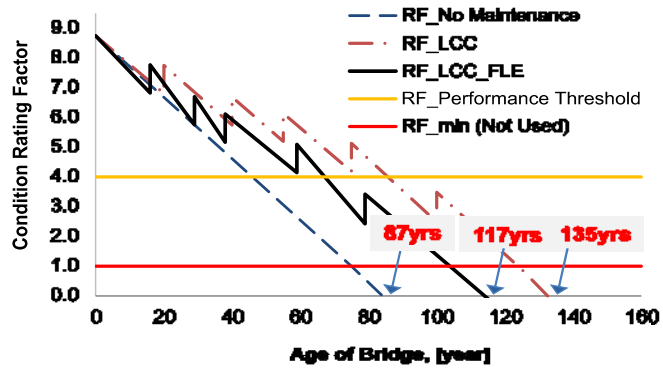

Fig. 4. Results of life-cycle cost analysis

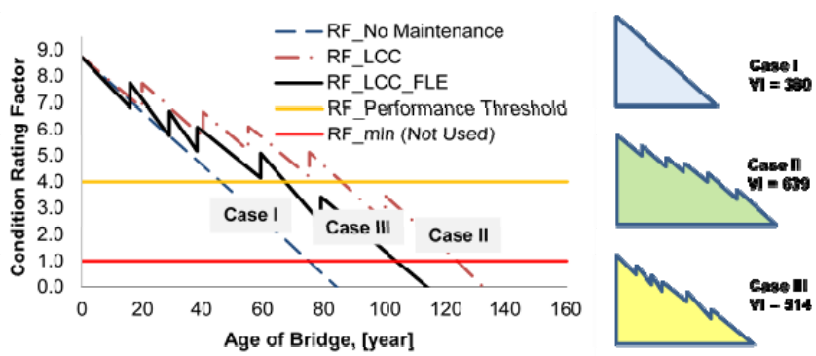

Fig. 5. Value index (*VI*) for three cases

5. Summary and Conclusion

In this study, the use of the fatigue index in the bridge rating with consideration for the fatigue damage potentials from overloads is suggested in BLCCA and in making decision for a maintenance and rehabilitation scheduling. This offers a more realistic procedure for BLCCA by incorporating fatigue damage effects in the deterioration curves. When used in BLCCA, the fatigue index will affect the analysis outcome, which is expected to result in more realistic estimates for future maintenance and repair costs.

6. References

Jang, B. and Mohammadi, J. 2017. Bridge rating modification to incorporate fatigue damage from truck overloads, Bridge Structures, 13(2-3), 101-107.

Jang, B. and Mohammadi, J. 2018. Significance of fatigue damage from overload trucks on bridge load rating, MATEC Web of Conferences, 165, 10005.

Jang, B. 2018. Bridge rating with considerations for fatigue Damage effect from truck overloads, doctoral dissertation, Illinois Institute of Technology, Chicago, IL.

Mohammadi, J., Guralnick, S.A., and Yan, L. 1995. Incorporating Life-Cycle Costs in Highway-Bridge Planning and Design, Journal of Transportation Engineering, 121(5), 417-424.

Moses, F., Schilling, C.G., and Raju, S.K. 1987. Fatigue evaluation procedures for steel bridges, NCHRP Report 299, Transportation Research Board, Washington, D.C.

New Directions for RC: Avoiding Time-Bombs in Our Coastal Structures

Marco Rossini[1], Steven Nolan[2*], Ivan Lasa[3], and Antonio Nanni[4]

[1] University of Miami, Coral Gables, FL. USA; email: mxr1465@miami.edu
[2] Florida Department of Transportation–State Structures Design Office, Tallahassee, FL. USA; email: Steven.Nolan@dot.state.fl.us
[3] Florida Department of Transportation – State Materials Office, Gainesville, FL. USA; email: Ivan.Lasa@dot.state.fl.us
[4] University of Miami, Coral Gables, FL. USA; email: nanni@miami.edu

*: corresponding author

Keywords: concrete bridges; corrosion-resistant; durability; fiber-reinforced polymer; FRP

Abstract: Within the last century, coastal structures for infrastructure applications have traditionally been built with timber, structural steel, and/or steel-reinforced/prestressed concrete. Given asset owners' desire for increased service-life; reduced maintenance, repair and rehabilitation liability; resilience; and sustainability, it has become clear that traditional construction materials cannot reliably meet these challenges without periodic intervention. Fiber-Reinforced Polymer (FRP) composites have been successfully utilized for durable bridge applications for more than three decades, demonstrating their ability to provide a reduced maintenance costs, extend service life, and significantly increase design durability. This paper explores these applications, related specifically to internal reinforcement for concrete structures in both passive (RC) and pre-tensioned (PC) applications, and contrasts them with the time-dependent effect and cost of corrosion in coastal transportation infrastructure. Recent development of authoritative design guidelines within the US and international engineering communities will be summarized and case-studies comparing traditional RC/PC verses FRP-RC/PC will be presented to show the sustainable (economic and environmental) advantage of composite structures in the coastal environment.

1. Introduction

Within the last century, coastal structures for infrastructure applications have traditionally been built with timber, structural steel, and/or steel-reinforced/prestressed concrete. Given owners' desire for increased service-life; reduced maintenance, repair and rehabilitation liability; resilience; and sustainability, it has become clear that traditional construction materials cannot reliably meet all these challenges without periodic intervention. Although some of the conventional construction materials can provide improved service life for reinforced concrete structures, it is understood that these will still require corrective repairs or replacement in order to reach their intended service lives. Otherwise, the safe use of these will be compromised. The total annual cost of corrosion in the United State was reported as $276 billion in 2002. In the world's second largest economy (China), the annual cost of corrosion was similarly estimated at ¥2 trillion (approximately US$290 billion) (CAS 2014). It was further estimated that the annual direct cost for maintenance for concrete bridge decks due to corrosion of the reinforcement in the United States is around $2 billion, and another $2 billion are spent for maintenance on concrete

substructures due to the same reason (FHWA, 2002). Although the corrosion on bridge decks is mainly due to the use of de-icing salts, almost all the corrosion deterioration on bridge substructures is due to exposure to seawater.

2. The Inevitability of Corrosion in Coastal Structures

The time-dependent effect and cost of corrosion in coastal transportation infrastructure is of extreme concern to owners of structures near the coastline. Repairs due to corrosion of reinforcing steel in concrete is estimated to be the most expensive repairs performed on coastal structures (Cadenazzi et al. 2019). Either by direct contact with the water on structures such as bridges, docks, or seawalls, or by exposure to saltwater sprays on structures close to the coast line, chlorides accumulate on the surface of the concrete and then slowly diffuse inside the concrete until it reaches the reinforcement. At that point, corrosion starts. Typically, the reinforcement in concrete remains in a passivated state produced by the high alkalinity of the concrete. However, when chlorides reach high concentration at the reinforcement level, very localized acidic conditions develop, and pitting corrosion locally penetrates the passivation film. Furthermore, when carbonation hinders concrete passivation, the presence of chlorides fosters general corrosion over the entire surface of the reinforcement. Corrosion degrades the reinforcement until the structural integrity of the concrete component is compromised. The condition is further aggravated since as the reinforcement corrodes, it expands producing cracks and splitting of the concrete, which promotes faster access of chlorides onto the reinforcement surface and eventual delamination of the concrete cover. Several mitigations techniques such as denser concretes, increased concrete covers, or topical treatments to seal the concrete are recognized and are used in industry to mitigate the penetration of chlorides in the concrete. However, these mitigation strategies only delay the onset of corrosion. Eventually, the steel rebars in the reinforced concrete will corrode.

3. Drastic Consequences Demand Different Solutions

There is no disputing the need for corrosion mitigation solutions for existing structures. There will never be sufficient budget to replace all the deficient infrastructure with new durable, resilient solutions. However, for those replacements that are feasible, it is a disservice to society to continue building strategic infrastructure with materials that have proved not able to weather the challenge of time. The rational solution is to eliminate the possibilities of corrosion completely rather than delay it. Fiber-Reinforced Polymer (FRP) composites have been successfully utilized for durable bridge applications for more than a quarter century, demonstrating their ability to provide reduced maintenance cost, extended service life, and significantly increase design durability. FRP reinforcement is made from continuous fibers, typically glass, basalt, carbon, or aramid. Fibers are impregnated with a polymeric thermosetting resin, typically vinyl ester, epoxy, or acrylic. The fibres provide tensile strength, and the resin acts as a binder. The role of an FRP reinforcement manufacturer is to combine fibers and resin into pultruded composite bars. During pultrusion, fibers are impregnated with resin and drawn through a heated die from which they emerge as a semi-final product. Then, various surface preparation techniques can be employed to enhance the bond of the FRP bar to the concrete. In addition, a number of small-diameter composite bars can be twisted into a single strand for prestressed concrete (PC) applications. Being a non-ferrous material, FRP is non-corrosive and impervious to chloride attack.

Recent development of authoritative design guidelines for both FRP-RC and FRP-PC within the US (AASHTO, 2018a & 2018b) and Canada (CSA, 2010 & 2019) complement and enhance the existing repository of international design guidance (JSCE 1998, ACI 2004, *fib* 2007, ACI 2015).

4. Case Study Examples

Case-studies show the sustainable (economic and environmental) advantage of composite structures in the coastal environment:

4.1. Ulenbergstrasse Bridge, Düsseldorf, Germany 1986 (GFRP-PC)

World's first vehicular bridge using FRP E-glass tendons with polyester resin and polyamide coating for protection against chemical and mechanical attack (Wolff & Miesser 1989).

4.2. Shinmiya Bridge, Japan 1988 (CFCC-PC)

World's first CFCC prestressed concrete bridge located adjacent to the Sea of Japan. Constructed as a replacement for a 21-year old prestressed concrete bridge suffering severe corrosion deterioration. Additional beams were set adjacent to the structure for in-place weathering and the test to destruction in 1994 and 2017. The flexural strengths exceeded the original beams by 20%-25%, presumable due to concrete strength gain and compression-controlled failure mode (Nguyen et al. 2018).

4.3. Beddington Trail Bridge, Calgary, Alberta 1993 (CFCC & CFRP-PC)

The first highway bridge in North American with FRP prestressing. This is a two-span skewed bridge using CFCC tendons and Leadline strands for precast/pretensioned bulb-T girders (Rizkalla and Tadros 1994). Three girder lines contained CFCC and three CFRP single strands.

4.4. Hall's Harbor Wharf, Bay of Fundy, Nova Scotia 1999 (GFRP-RC)

The Hall's Harbor Wharf was the first marine structure in Canada to be built using ISIS Canada technology and design concepts (Newhook et al. 2000). The structure is located on the Bay of Fundy shore in Nova Scotia, and comprises GFRP reinforced precast concrete panels, and concrete pile cap beams reinforced with a hybrid GFRP-steel bar system (Mufti et al. 2005).

4.5. McKinleyville Bridge, West Virginia 1998 (GFRP-RC).

McKinleyville Bridge was one of the first bridge decks to use GFRP rebar in the US. GFRP bars were extracted from the bridge after 15 years of service life, showing good durability performance (Gooranorimi & Nanni 2017). Other bridges that followed include Gills Creek Bridge, O'Fallon Park Bridge, Salem Ave Bridge, Bettendorf Bridge, Cuyahoga County Bridge, Sierrita de la Cruz, Thayer Road Bridge, and Bourbon County Bridge.

4.6. Val-Alain Bridge, Quebec 2004 (GFRP-RC)

Val-Alain Bridge was the first completely steel-free decks in Canada. In 2015, concrete cores were taken and the encapsulated GFRP bars evaluated to assess durability (Benmokrane et al. 2018). Other early Canadian bridges with partial replacement include Joffre Bridge

(Benmokrane et al. 2000), Chathman Bridge (Aly et al. 1997), Crowchild Trail Bridge (Tadros et al. 1998), and Waterloo Creek Bridge (Tsai & Ventura, 1999).

4.7 Halls River Bridge, Homosassa, FL 2018 (GFRP-RC & CFRP-PC)

Halls River Bridge is a five-span vehicular bridge entirely constructed using corrosion-resistant solutions and mostly FRP reinforcement. The structure includes CFRP-PC bearing piles, CFRP-PC/GFRP-RC sheet piles, hybrid HSCS-PC/GFRP-RC sheet piles, GFRP-RC pile bent caps and bulkhead caps, a GFRP-RC bridge deck, GFRP-RC traffic railings, GFRP-RC approach slabs, and a GFRP-RC gravity wall. The unprecedented variety and completeness of the material and structural solutions deployed make the Halls River Bridge an invaluable source for data. To this end, monitoring protocols have been implemented at the design and construction stages and are implemented through the service life of the structure. A Life-Cycle Cost analysis was performed by (Cadenazzi et al. 2019), proving a complete FRP-RC/PC design to be the least impacting solution from both an economic and environmental perspective over an estimated service life of 100-years.

5. Conclusion

Over more than 30 years of field applications in bridge structures, FRP reinforcement has proved to be a reliable and durable material, able to answer the owners' demand for increased service-life, reduced maintenance costs, resilience, and sustainability. More than 270 bridges have been completed using FRP reinforcement in the US and Canada (ACMA, 2016) and more than 23 of these include CFRP prestressing in the US (Yamamoto, 2018), providing a number of successful case studies to the structural engineering community and eliminating the ever-present risk of corrosion.

6. Acknowledgements

The first and fourth authors gratefully acknowledge the financial support from "Sustainable concrete using seawater, salt-contaminated aggregates, and non-corrosive reinforcement" Infravation, 31109806.005-SEACON.

7. References

AASHTO. 2018. "AASHTO LRFD Bridge Design Guide Specifications for GFRP-Reinforced Concrete" (2nd ed.). Washington, DC: American Association of State Highway and Transportation Officials.

AASHTO. 2018. "AASHTO Guide Specifications for the Design of Concrete Bridge Beams Prestresssed with CFRP Systems" (1st ed.). Washington, DC: American Association of State Highway and Transportation Officials.

ACMA. 2016. "List of GFRP Reinforced Bridges in North America". Arlington, VA: American Composites Manufacturers Association.

ACI, 2004. "ACI 440.4R-04(11) Prestressing Concrete Structures with FRP Tendons (Reapproved 2011)".

ACI, 2015. "ACI 440.1R-15 Guide for the Design and Construction of Structural Concrete Reinforced with Fiber-Reinforced Polymer (FRP) Bars".

Aly, A., Bakht, B. and Schaeffer, J. 1997. "Design and Construction of Steel-fee Deck Slab in Ontario," Annual Conference of Canadian Society for Civil Engineering, V. 6, pp. 81-90.

Au, A. and Mermigas, K. 2018. "Performance of GFRP Composite Slab-On-Concrete Girder Bridge – 10 Years After Construction Based on Load Tests", Proceedings of 10th International Conference on Short and Medium Span Bridges, CSCE/CSGC, Quebec City, Quebec, Canada.

Benmokrane, B., Rahman, H. and Mukhopadhyaya, P. 2000. "Use of Fiber Reinforced Polymer Reinforcement Integrated with Fiber Optic Sensors for Concrete Bridge Deck Slab Construction," Canadian Journal of Civil Engineering. V. 27, No. 5, pp. 928-940.

Benmokrane, B., Nazair, C., Loranger, MA., Manalo, A. 2018. "Field Durability Study of Vinyl-Ester–Based GFRP Rebars in Concrete Bridge Barriers, Journal of Bridge Engineering", ASCE, SSN1084-0702.

CAS. 2014. "Corrosion Status of China and the Control Strategy Research," Chinese Academy of Sciences, Beijing, China, www.cas.cn.

Cadenazzi, T., Dotelli, G., Rossini, M., Nolan, S., & Nanni, A. 2019. "LCC and LCA Analysis at the Design Stage of an FRP Reinforced Concrete Bridge in Florida". Advance in Civil Engineering Materials.

CSA. 2019. "Canadian Highway Bridge Design Code CAN/CSA-S6-19 (in press). Canadian Standards Association (CSA), Mississauga, Ontario, Canada.

CSA, 2010. "Canadian Highway Bridge Design Code CAN/CSA-S6S1-10", Canadian Standards Association (CSA), Mississauga, Ontario, Canada.

FHWA. 2002. "Corrosion Costs and Preventive Strategies in the United States", Publication No - RD-01-156, Federal Highway Administration Turner-Fairbank Highway Research Center, McLean, VA.

fib, 2007, "FRP Reinforcement in RC Structures," Bulletin No. 40, Federal Institute of Technology, Lausanne, Switzerland.

Gooranorimi, O., & Nanni, A. 2017. "GFRP Reinforcement in Concrete after 15 Years of Service". Journal of Composites for Construction, 21(5), 04017024.

JSCE, 1998, "Recommendation for Design and Construction of Concrete Structures Using Continuous Fiber Reinforcing Materials," Japan Society of Civil Engineer, Tokyo, Japan.

Mufti, A., Onofrei, M., Benmokrane, B., Banthia, N., Boulfiza, M., Newhook, J., Bakht, B., Tadros, G., and Brett P. 2005. "Durability of GFRP Reinforced Concrete Field Structures" SP-230-77: Compendium from 7th-FRPRCS, pp 1361-1367.

Newhook, J.P., Bakht, B. and Mufti, A.A. 2000. "Design and Construction of a Concrete Marine Structure Using Innovative Technology", 3rd International Conference on Advanced Composite Materials in Bridges and Structures. Canadian Society for Civil Engineering, pp. 777-784.

Nguyen, H.T, Masuya, H., Ha, T.M., Fukada, S., Hanaoka, D., Kobayashi, K., Koida, E. 2018. "Long-Term Application of Carbon Fiber Composite Cable Tendon in Prestressed Concrete Bridge-Shinmiya Bridge in Japan", 3rd International Conference on Civil Engineering and Materials Science, MACEX Web Conference, Volume 206, 2018.

Tadros, G., Tromposch, E. and Mufti, A. A., 1998, "Superstructure Replacement of Crowchild Trail Bridge," edited by L. Dunaszegi, Calgary, Alberta, Canada. 5th International Conference on Short and Medium Span Bridges, Calgary, Alberta, Canada, pp. 499-506.

Tsai, P. and Ventura, C.E., 1999, "Waterloo Creek Bridge Project", Field Assessment Report No. 2, University of British Columbia, Canada.

Wolff, R. and Miesser, H.J, 1989. "New materials for prestressing and monitoring heavy structures", Concrete International 11(9): 86–89.

Yamamoto, Y. 2018. "CFCC Update", Presentation at 2018 Florida Transportation Builders' Association Construction Conference, Orlando Florida. Retrieve 1/31/2019, https://ftba.com/2018-construction-conference-presentations/

Field Testing

Experimental and Analytical Capacity Evaluation before Strengthening of Missouri Bridge P0058

Eli S. Hernandez[1] and John J. Myers[2*]

[1] Missouri S&T, Rolla, MO, USA; email: eli.hernandez@mst.edu
[2] Missouri S&T, Rolla, MO, USA; email: jmyers@mst.edu

[*]: corresponding author

Keywords: Bridge evaluation; dynamic load allowance; girder distribution factor; load rating

Abstract: Load rating is the capacity evaluation methodology that bridge managers employed to prioritize actions on a bridge structure. These actions include (1) repair; (2) rehabilitation; (3) strengthening; and (4) replacement of a bridge structure. Load posted Bridge P0058 was scheduled for strengthening of its main carrying members. A diagnostic load test was conducted before the strengthening work was executed to determine if the load rating capacity of the bridge superstructure can be increased. The bridge was instrumented at several locations with LVDTs, and the lateral distribution factors were obtained using the recorded data. The compressive strength of the bridge's main carrying members was obtained by means of non-destructive tests (NDT). The load rating capacity was estimated analytically and experimentally, and field results revealed that the bridge possessed a larger capacity than suggested by analytical predictions. However, the higher experimental rating was not large enough to remove the bridge's load posting.

1.Introduction

Field testing permits the verification of design and analysis assumptions such as actual lateral load distribution, dynamic load allowance (impact factor), influence line position, degree of composite action, and unintended support restraint. Although, field testing applications may sometimes be hindered by costs, time, test truck requirements, traffic interruptions, safety, difficulty to access a bridge structure and difficulty to install sensors, it is the most accurate approach. Load testing permits to: (1) better understand the response of bridges fabricated with innovative designs and new construction technologies; (2) evaluate the response of posted and deteriorated bridges; and (3) evaluate a bridge's response to permit and nonstandard vehicles (ACI 2016). In general, the American Association of State Highway and Transportation Officials (AASHTO) Manual for Bridge Evaluation (MBE) defines two different options for load testing: diagnostic load tests and proof load tests (AASHTO 2010). Independently of the method employed to conducting a strength evaluation (analytical or experimental), load rating a bridge structure involves good "engineering judgment" to guarantee that the rating results minimize the economic impacts on the community served by the bridge without sacrificing the public's safety at the same time. Determining the actual girder lateral distribution factor of a bridge is fundamental to obtain a valid load rating factor of a bridge (Kim and Nowak 1997). The focus of this study centered on conducting a flexural capacity evaluation (analytical and experimental) of Bridge P0058's main reinforced concrete (RC) supporting members.

2. Bridge Description

Bridge P0058 [Fig. 1(a)], built in 1951, along Highway 142 in Howell County, Missouri, spans the Myatt Creek river. The bridge carries one-way traffic and has four spans supported by three simply supported reinforced concrete (RC) beams. Spans 1 and 2, located on the west side of the bridge, are 11.43 m (37.5 ft) long, and spans 3 and 4 are 8.38 m (27.5 ft) long. The total bridge length is 39.62 m (130.0 ft) with no skewed angle. The slab thickness is 150 mm (6 in.), and RC beams spaced 2.16 m (7.1 ft) on center support it. Bridge P0058 was selected from a list of candidate bridges considered structurally deficient according to MoDOT inspection data. In the most recent condition assessment, Bridge P0058 received a deck/sup/sub rating of 4/4/6 (4 means poor, and 6 satisfactory). Due to the age and condition, Bridge P0058 is currently load posted. The total deck width is 5.23 m (17.2 ft) with a curb-to-curb roadway of 4.27 m (14.0 ft).

(a) (b)

Fig. 3. Bridge P0058. (a) Sideview; (b) trucks acting on Bridge P0058 during diagnostic tests.

3. Diagnostic Load Test

The bridge instrumentation consisted of linear variable differential transducers (LVDTs) installed at midspan sections of spans 1 and 4's girders. An LVDT was deployed at each girders' center line to record its vertical deflection during the static tests. These load configurations were applied on the bridge's superstructure to determine the experimental lateral load distribution of span 1's girders. During the static tests, two trucks loaded with gravel were used to load span 1 as shown in Figures 1(b) and 2.

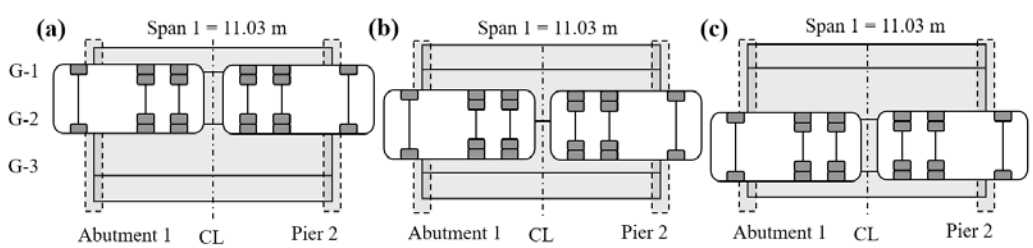

Fig. 4. Load configurations: (a) stop 1; (b) stop 2; (c) stop 3. Conversion factor: 1 m = 3.28 ft.

4. Test Results

During the static load tests, midspan's vertical deflections were recorded with LVDTs. The load distribution factor of the interior and exterior RC beams was estimated as follows:

$$LDF_i = n\frac{\delta_{Gi}}{\sum_{i=1}^{k}\delta_{Gi}} \quad (1)$$

where LDF_i = load distribution factor of *ith* girder obtained from field deflections; δ_{Gi} = vertical deflection of the *ith* girder at midspan (Table 2); n = number of lanes loaded = 1; and k = number of girders. The experimental load distribution factors (LDF) are reported in Table 2.

Table 2. Midspan vertical deflections (mm) and experimental load distribution factor (LDF)

Span	Stop	δ_{G1}	δ_{G2}	δ_{G3}	LDF_1	LDF_2	LDF_3
1	1	20.3	20.8	12.4	0.38	0.39	0.23
1	2	13.7	20.3	15.2	0.28	0.41	0.31
1	3	10.2	18.5	17.3	0.22	0.40	0.38

5. Bridge Evaluation

The rating factor of a bridge component can be estimated analytically according to the AASHTO LFR approach (AASHTO 1994) in the following manner:

$$RF = \frac{M_n - A_1 M_D}{A_2 M_L (1+I) DF} \quad (2)$$

where RF = rating factor; M_n = nominal moment capacity; M_D = dead load moment; M_L = live load moment effect caused by the rating vehicle (HS20 truck); I = impact factor; DF = distribution factor; A_1 and A_2 = factors for dead and live load, respectively. A_1 = 1.3 (operating and inventory levels); A_2 = 1.3 (operating level); and A_2 = 2.16 (inventory level). The analytical distribution factors were determined using the AASHTO Bridge Standard Specifications (AASHTO 2002), Art 3.23.2.2[3] (footnote f). The impact factor was determined as follows:

$$I = \frac{50}{3.28L + 125} \quad (3)$$

where I = impact factor (maximum is 0.3); and L = span length (m).

The experimental load distribution factors (Table 2) were employed to enhance bridge P0058's rating factor. Table 2 summarizes the analytical and experimental data used to determine the rating factor of the bridge. The experimental compressive strength reported in Table 3 was obtained using a Schmidt hammer. Some calculations are omitted for the sake of brevity; however, the moment values used in the subsequent computations are listed in Table 4. The values of the live-load moment (M_L) were determined using the AASHTO LFD HS20 rating loading as a measurement of the bridge performance (inventory and operating levels). The experimental and analytical rating factors are reported in Table 5.

Table 3. Bridge load rating data

Parameter	Interior Girder (Span 1)	Exterior Girder (Span 1)
Analytical		
b_f (mm)	2159	1549
d (mm)	503	503
A_s (mm^2)	7297	7297
F_y (MPa)	227	227
f'_c (MPa)	21	21
DF	1.153	0.776
I	0.30	0.30
M_{n_A} (kN-m)	719.7	706.8
Experimental		
DF	0.41	0.38
f'_c (MPa)	41.3	41.3
M_{n_E} (kN-m)	736.05	729.6

Table 4. Bridge P0058 analytical moments

Parameter	Interior Girder (Span 1)	Exterior Girder (Span 1)
M_D (kN-m)	267.5	227.8
M_L (kN-m)	377.4	253.9

Table 5. Bridge P0058 load rating results

RF	Interior Girder (Span 1)	Exterior Girder (Span 1)
Analytical		
$LR_{(INV)}$	0.45	0.75
$LR_{(OPR)}$	0.76	1.24
Experimental		
$LR_{(INV)}$	0.67	0.80
$LR_{(OPR)}$	1.11	1.34

6. Concluding Remarks

A pre-strengthening load test was successfully performed on the superstructure of Bridge P0058 to obtain an experimental evaluation of the bridge's superstructure. By incorporating site-specific data measured during this diagnostic load test, a more precise load rating was obtained in comparison to the theoretical load rating values obtained following the AASHTO LFR procedure. The load rating capacity was estimated analytically and experimentally, and field results revealed that Bridge P0058 possessed a larger capacity than suggested by theoretical predictions. However, the higher experimental load rating was not large enough to remove the bridge's load posting limit.

7. References

American Association of State Highway and Transportation Officials (1994). *Manual for Condition Evaluation of Bridges*, Washington, DC.

American Association of State Highway and Transportation Officials (2002). Standard Specifications for Highway Bridges, Washington, DC.

American Association of State Highway and Transportation Officials (2010). The Manual for Bridge Evaluation (2nd Edition) with 2011, 2013, 2014 and 2015 Interim Revisions, Washington, DC.

American Concrete Institute (2016). "Report on Flexural Live Load Distribution Methods for Evaluating Existing Bridges." ACI 342R-16, Farmington Hills, MI.

Kim, S. and Nowak, A. S. (1997). Load distribution and impact factors for I-girder bridges. J Bridge Eng 97-104.

Feasibility of Collapse Test on the Nieuwklap Bridge

Eva Lantsoght[1,2*], Yuguang Yang[3], Cor van der Veen[4], and Dick Hordijk[5]

[1] Universidad San Francisco de Quito, Quito, Ecuador; elantsoght@usfq.edu.ec
[2] Delft University of Technology, Delft, the Netherlands: E.O.L.Lantsoght@tudelft.nl
[3] Delft University of Technology, Delft, the Netherlands: Yuguang.Yang@tudelft.nl
[4] Delft University of Technology, Delft, the Netherlands: C.vanderveen@tudelft.nl
[5] Delft University of Technology, Delft, the Netherlands: D.A.Hordijk@tudelft.nl

*: corresponding author

Keywords: collapse testing; field testing; flexure; reinforced concrete, shear, slab bridge

Abstract: The Nieuwklap Bridge is a 7-span reinforced concrete slab bridge that is scheduled for demolition. Since a large number of reinforced concrete slab bridges in the Netherlands are found to have insufficient shear capacity upon assessment, such bridges have been studied extensively over the past decade. To better evaluate the structural behavior and ultimate capacity of slab bridges, it was suggested to test the Nieuwklap Bridge to collapse. Since collapse tests are expensive and involve large risks, an extensive feasibility study is necessary. Testing of the Nieuwklap Bridge would be interesting if the assessment shows that the bridge is representative for the shear-critical slab bridges in the Netherlands, and if the test can be carried out safely. An assessment of the bridge in an end span and middle span at two levels of approximation is carried out, and the maximum load required to cause collapse is estimated. The outcome of the feasibility study is that the required loads for collapse are large when a plasticity-based model is used. Furthermore, the Nieuwklap Bridge is not shear-critical and thus not representative of the shear-critical slab bridges in the Netherlands. As such, collapse testing is recommended against.

1. Introduction

The live loads in the recently introduced Eurocodes are larger than the previously used national codes in the Netherlands, and the axle spacing is smaller. At the same time, the shear capacity according to Eurocode is smaller than according to the old Dutch code. The result is that a large number of reinforced concrete slab bridges in the Netherlands are found to have an insufficient shear capacity upon assessment (Lantsoght et al., 2013a). Scale models of such bridges have been studied extensively in the past in the laboratory (Lantsoght et al., 2013b). A previous collapse test on a reinforced concrete slab bridge resulted in insufficient load to reach collapse in the first span, and reaching of yielding of the steel combined with a large settlement of the support in the second span (Lantsoght et al., 2016). The previously tested bridge was an integral bridge, of which the restraint at the end supports could not be quantified, which complicated the analysis. The previous experience showed that, if a collapse test should result in information about the shear capacity of reinforced concrete slab bridges, an extensive feasibility study is necessary prior to testing, to see if the test can fulfil the goals of the study.

2. Definition of test goals

To better evaluate the structural behavior and ultimate capacity of reinforced concrete slab bridges, it was suggested to test the Nieuwklap Bridge to collapse. Since collapse tests are expensive and involve large risks, an extensive feasibility study is necessary to evaluate if the test can meet the stipulated goals. First of all, the goals of the test should be clear. The goal of the collapse test would be twofold: 1) testing a shear-critical reinforced concrete slab bridge to study the actual behavior of such a structure, and 2) possibly achieving a shear failure of a reinforced concrete slab bridge outside of laboratory conditions, in a safe way. To verify if these goals can be met during the test, the feasibility study should answer two questions: 1) Is the Nieuwklap bridge, which has been made available for testing, representative of the shear-critical reinforced concrete slab bridges in the Netherlands?, and 2) Is the required load for testing reasonable so that a safe execution of the test is possible?. To answer these questions, the feasibility study should focus on two topics: 1) the assessment of the bridge with all load and resistance factors, and 2) the estimation of the actual capacity of the bridge based on average material properties and based on the current state-of-the-art regarding the load-carrying behavior of concrete slabs.

3. Description of bridge

The Nieuwklap Bridge, located in the province of Groningen in the Netherlands, is a 7-span reinforced concrete slab bridge, built in 1941. The bridge is situated on the connection between the cities Groningen and Leeuwarden, close to Aduarderzijl. The total length of the bridge is 101 m, with end spans of 11.2 m and middle spans of 14.14 m. The total width is 14.31 m, accommodating a carriageway of 7.25 m, sidewalk of 1 m on both sides, and bike path of 2.53 m on both sides. The thickness of the slab varies between 650 mm at the supports and 631 mm at midspan for the end span and 620 mm at midspan for the middle spans. The skew of the bridge is 8°. The results of core testing showed that the characteristic compressive strength of the concrete is 60 MPa. The steel type used for the bridge is not reported, but given the period of construction, the options can be narrowed down to QR 220 (characteristic yield strength f_{yk} = 220 MPa) or QR 240 (f_{yk} = 240 MPa) steel. The sagging moment reinforcement ratio in the end spans is 1.06%, the sagging moment reinforcement ratio in the middle spans is 1.08 %, and the hogging moment reinforcement ratio is 1.5%.

4. Feasibility study: assessment

To answer the question if the Nieuwklap bridge is representative for the shear-critical reinforced concrete slab bridges, assessment calculations are carried out at two Levels of Approximation (fib, 2012). The first Level of Approximation is a spreadsheet-based method, similar to a hand calculation, for identifying which bridges do not fulfil the code requirements for shear, called the Quick Scan (Vergoossen et al., 2013). The second Level of Approximation uses a linear finite element model to find the shear stresses and bending moments. The Quick Scan does not consider bending moment, so that for the assessment for the failure mode of bending moment, only the results for the second Level of Approximation are available. The considered load combination is self-weight, superimposed dead load (asphalt), and the Eurocode live loads (design tandem in each lane and distributed lane load). The load factors for the RBK Usage level (Rijkswaterstaat, 2013) are used; these load factors are calibrated to a reliability index of 3.3 with a reference period of 30 years (Steenbergen and Vrouwenvelder, 2010). The outcome of the

assessment is expressed in terms of the Unity Check, which is the ratio of the load effect from the factored load effect to the factored capacity for the failure mode under consideration. When the Unity Check is larger than 1, the bridge does not fulfil the code requirements. **Table 6** shows the results for the Unity Check for shear and bending moment for span 1 (representative of an end span), and span 2 (representative of a middle span). The following conclusions can be drawn from these results: 1) the middle spans are more critical than the end spans; 2) bending moment has the larger Unity Check, and is thus the governing failure mode; 3) the bridge fulfils the requirements for shear; and 4) the concept of Levels of Approximations, where increasing Levels lead to sharper assessment works for this considered bridge. These results thus answer the question if the Nieuwklap Bridge is representative of the Dutch shear-critical slab bridges: it is not.

Table 6. Results of assessment of Nieuwklap bridge

	Unity Check for shear		Unity Check for bending moment
Span	LoA I	LoA II	LoA II
End span	0.45	0.43	0.85
Middle span	0.65	0.52	0.88

5. Feasibility study: required loads for collapse

To answer the question if the test can be carried out in a safe manner, the maximum load that would lead to a shear failure or flexural failure should be determined. These calculations are carried out based on average material properties, and uses the load combination of self-weight, asphalt, and a single testing tandem without load factors. QR22 steel is assumed. The total load on a single testing tandem necessary to reach failure in the end and middle span for loading at a shear- and flexure-critical position are given in Table 7. For the shear-critical position, both the maximum load for the failure mode of shear and flexure are reported. For all calculations, a saw cut between the slab and the sidewalk (which has a larger depth and contains shear reinforcement) is assumed, so that the behavior of the slab can be isolated for study. The results show that the required loads are reasonable, based on the resistance models for shear and flexure from the codes. However, based on the Extended Strip Model (Lantsoght et al., 2017), a plasticity-based method for the determination of the maximum load on reinforced concrete slabs which combines the effects of shear and flexure, it is found that the required loads to reach failure are much higher than based on the models from the code. This observation can be explained by acknowledging the fact that the resistance models from the codes are for beams, not for slabs, and thus do not take transverse load redistribution into account (Lantsoght et al., 2015). The answer to the second question, whether testing to failure can be done safely is thus: “maybe”.

Table 7. Maximum required load on tandem to cause considered failure mode.

Failure mode	P_{tot} (kN) – end span	P_{tot} – middle span
Bending moment	1969	1844
Shear	3547	2490
Bending moment at shear-critical position	2276	3330
Extended Strip Model	4459	5390

7. Summary

This paper shows the feasibility study for testing to collapse of the Nieuwklap Bridge, a continuous reinforced concrete slab bridge. The feasibility study addresses two questions: 1) Is the Nieuwklap bridge representative of the shear-critical reinforced concrete slab bridges in the Netherlands; and 2) Can a test be carried out safely? To answer the first question, an assessment according to Dutch practice is carried out. The result of this assessment is that flexure is the governing failure mode for the bridge and that both end and middle spans fulfil the new code requirements for shear. To answer the second question, the maximum load to cause collapse of the end and middle spans is estimated based on average material properties and all load factors are omitted. The calculation is carried out based on the regular code equations and with a plasticity-based model. The maximum load calculated based on the regular code equations is reasonable, which would indicate that the test can be carried out safely. The maximum load calculated with the plasticity-based model is significantly larger, as it takes slab behavior into account. The answer to the second question is thus that it may be possible to carry out the test safely. Since the feasibility study shows that the bridge is not shear-critical, the recommendation was not to test this bridge to collapse. This structured approach can be used for the preparation of collapse tests on bridges, as well as for the preparation of diagnostic and proof load tests.

8. Acknowledgment

The authors are grateful for the funding received from the Province Groningen for this research.

9. References

FIB 2012. Model code 2010: final draft, Lausanne, International Federation for Structural Concrete.

LANTSOGHT, E., VAN DER VEEN, C. & DE BOER, A. 2016. Shear and moment capacity of the Ruytenschildt bridge. IABMAS 2016.

LANTSOGHT, E. O. L., VAN DER VEEN, C., DE BOER, A. & ALEXANDER, S. D. B. 2017. Extended Strip Model for Slabs under Concentrated Loads. ACI Structural Journal, 114, 565-574.

LANTSOGHT, E. O. L., VAN DER VEEN, C., DE BOER, A. & WALRAVEN, J. 2015. Transverse Load Redistribution and Effective Shear Width in Reinforced Concrete Slabs. Heron, 60, 145-180.

LANTSOGHT, E. O. L., VAN DER VEEN, C., DE BOER, A. & WALRAVEN, J. C. 2013a. Recommendations for the Shear Assessment of Reinforced Concrete Slab Bridges from Experiments Structural Engineering International, 23, 418-426.

LANTSOGHT, E. O. L., VAN DER VEEN, C. & WALRAVEN, J. C. 2013b. Shear in One-way Slabs under a Concentrated Load close to the support. ACI Structural Journal, 110, 275-284.

RIJKSWATERSTAAT 2013. Guidelines Assessment Bridges - assessment of structural safety of an existing bridge at reconstruction, usage and disapproval (in Dutch), RTD 1006:2013 1.1. Utrecht, the Netherlands.

STEENBERGEN, R. D. J. M. & VROUWENVELDER, A. C. W. M. 2010. Safety philosophy for existing structures and partial factors for traffic loads on bridges. Heron, 55, 123-140.

VERGOOSSEN, R., NAAKTGEBOREN, M., 'T HART, M., DE BOER, A. & VAN VUGT, E. 2013. Quick Scan on Shear in Existing Slab Type Viaducts. International IABSE Conference, Assessment, Upgrading and Refurbishment of Infrastructures. Rotterdam, The Netherlands.

Applicability and Constructing of Whole Analytical Model for Aging Truss Bridge to Evaluate Load Bearing Capacity in Maintenance

Shuhei Kawami[1*], Tatsumasa Kaita[2], Tatsuro Yamane[3], Hiroaki Fukuda[4], Ryoichi Satake[5], Yoshiyuki Hirahara[6], Takumi Kanou[7], and Katashi Fujii[8]

[1] Chuden Engineering Consultants Corporation, Hiroshima, Japan; email: kawami@cecnet.co.jp
[2] Tokuyama College of Technology, Department of Civil engineering and Architecture, Shunan, Japan; email: kaita@tokuyama.ac.jp
[3] Graduate School of Science and Engineering, Ehime University, Matsuyama, Japan; email: yamane.tatsuro.17@cee.ehime-u.ac.jp
[4] Yokogawa Bridge Corporation, Sakai, Japan; email: h.fukuda@yokogawa-bridge.co.jp
[5] Chuden Engineering Consultants Corporation, Hiroshima, Japan; email: satake@cecnet.co.jp
[6] Doboku Engineering Consultants Corporation, Hiroshima, Japan; email: hirahara@decnet.co.jp
[7] Aratani Civil Engineering Consultants Corporation, Hiroshima, Japan; email: takumi.kanou@aratani.co.jp
[8] Graduate School of Engineering, Hiroshima University, Higashi-hiroshima, Japan; email: ken214f@hiroshima-u.ac.jp

[*]: corresponding author

Keywords: FEM analysis; analytical model; steel pratt truss bridge; maintenance

Abstract: Maintenance of aging infrastructures is becoming more serious problem in Japan. In Japan, when evaluating the load bearing capacity of the aging bridge analytically in maintenance, it is common to be evaluated the remaining strength in unit of structural member. However, it will be thought that the finite element analyses using whole bridge modeling may be more reasonable for clarifying in maintenance management. The main objective of this study is to confirm an applicability of analytical whole bridge model to estimate the load bearing capacity of the aging whole bridge by comparing the field loading test results with the analysis results. The analytical object in this study is an aging Pratt truss bridge (97 years old) with severe corrosion damages. In the field loading test, 2 dump trucks with 80kN weight were used as live-load considering the current load limitation of this bridge. The analytical model in this study was constructed by shell elements with 4 nodes to consider the actual corrosion damages of main structure. The analytical conditions were set to same as the field loading test. From the comparison of test and analytical results, both results of axial stresses by live load were almost the same although these members have corrosion damages, and the differences were within 1MPa. Moreover, the vertical displacements of main truss structures were also almost matched. Therefore, the validity of this analytical model constructed by shell elements considering the corrosion wastage was confirmed by comparison with the field loading test of the actual bridge.

1. Introduction

Maintenance of aging infrastructures is becoming more serious problem in Japan. In Japan, when evaluating the load bearing capacity of the aging bridge analytically in maintenance, it is common to be evaluated the remaining strength in unit of structural member. However, it will be

thought that the finite element analyses using whole bridge model may be more reasonable for clarifying in maintenance management, because some past studies show that the whole bridge has enough load bearing capacity comparing with the remaining strength of each member in the initial design. The main objective of this study is to confirm a validity of analytical whole bridge model to estimate the load bearing capacity of the aging steel truss bridge by comparing the field loading test results with the analysis results.

2. Outline of Analytical Bridge

The analytical object in this study is an aging Pratt truss bridge (97 years old) with severe corrosion damages. The span length of this bridge is 50.19 m. Fig. 1 shows the side view of the main span. The members of this bridge are the combination member constructed by riveting channel steels and racing bars. The panel points of this bridge are rigid joints, and this bridge is supported by simple shoes. In this bridge, many corrosion damages occurr at the joint between the members (Yamane et al. 2017). Also, severe cross-sectional losses confirmed at that time had been already repaired using additional plates.

3. The Applicability of Analytical Whole Bridge Modeling

3.1 Field Loading Test

In the field loading test, 2 dump trucks with weight about 80kN were used as live-load considering the current load limitation of this bridge. Fig. 2. shows the layout and dimensions of dump trucks in loading test. The dump trucks was loaded on positions shown in Fig. 3. Also, the strain on main truss structure and floor members were measured near the vertical member V9 which has severest corrosion damage. The deflections of whole bridge were measured as vertical displacement in the center of each panel points of lower chord members. Fig. 4 shows all measurement points.

Fig. 1. Side view of main span

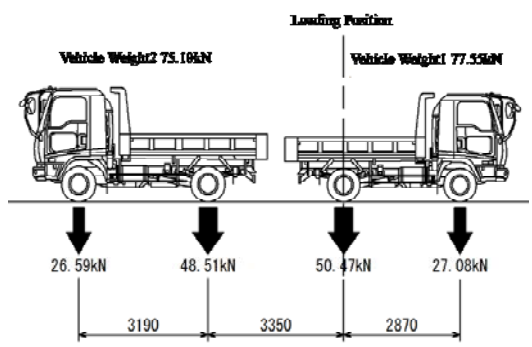

Fig. 2. Loading vehicles

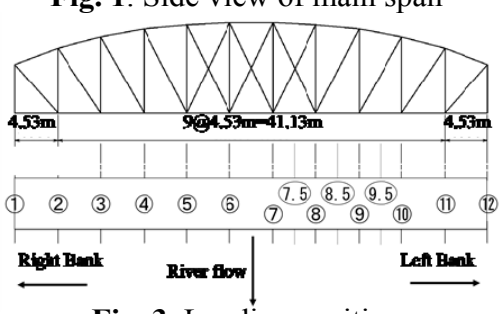

Fig. 3. Loading position

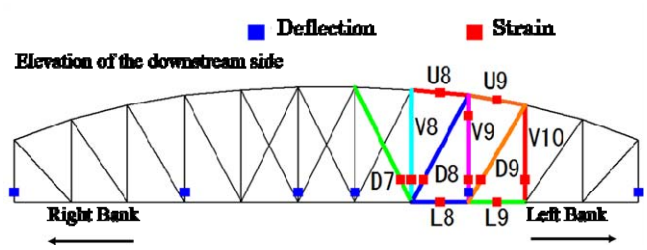

Fig. 4. Measurement points of deflection and strain

3.2 FEM Analysis

Fig. 5 shows the analytical model. The size of each element is set to 50 mm to 100 mm square. The material properties of the steel were assumed to be elastic modulus E=210 [GPa], yield stress σ_y=245 [MPa], and Poisson's ratio ν=0.3. The stress-strain relation was assumed the perfect elasto-plasticity. Boundary conditions were set to simple shoes. All riveted joints were modeled as the rigid state. The RC slab is not modeled, because it is not structural member for main loads. In this study, all corroded regions were assumed as simple rectangular shape. The maximum corrosion depth obtained from the field measurement was uniformly reflected to corroded regions in analytical model. The dead-load of the RC slab was loaded as an external force on the stringer. As shown in Fig. 2, the live-load was loaded as an external force on the same condition as the test.

3.3 Comparison of Loading Test and Analytical Results

Fig. 6 shows the axial stress in main truss members obtained from loading test and analytical results. The axial stress of the test results was calculated from the average strains in a same section. The axial stress of the analytical results was also calculated corresponding same section. From Fig. 6, both results of axial stress by live load were almost the same although these members have corrosion damages, and the differences were within 1MPa. The maximum live-load stress by 2 dump trucks with weight around 80kN is around 10MPa, and the maximum stress acting on a member added in the dead-load stress is estimated about 50MPa.

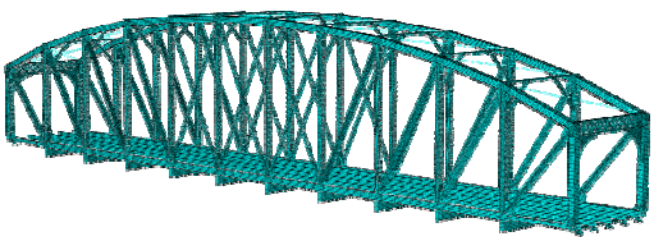

Fig. 5. Analytical model

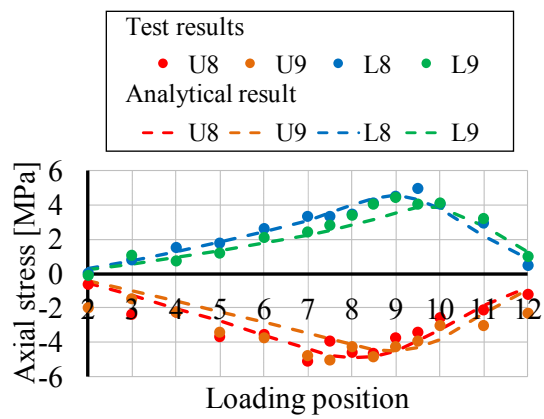

(a)

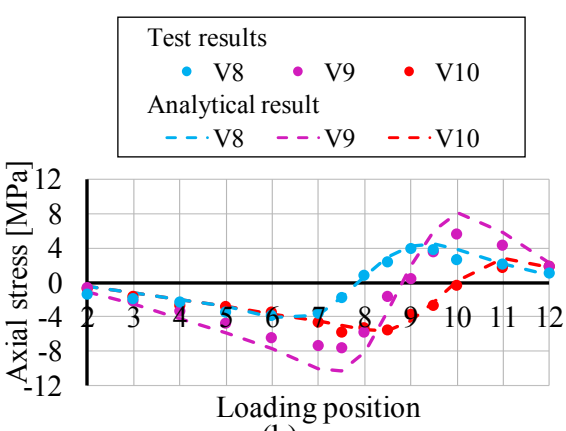

(b)

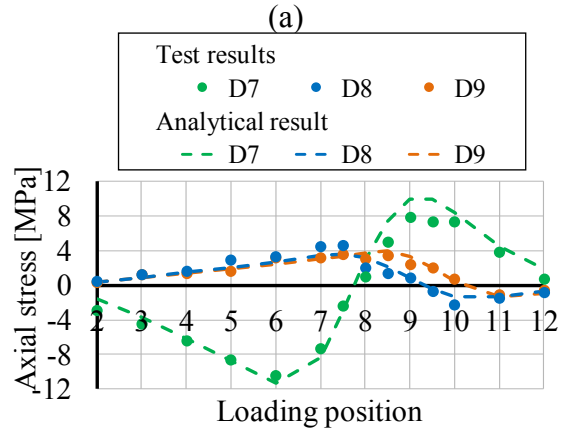

(c)

Fig. 6. Comparison of the axial stress in truss members: (a) chord members; (b) vertical members; (c) diagonal members

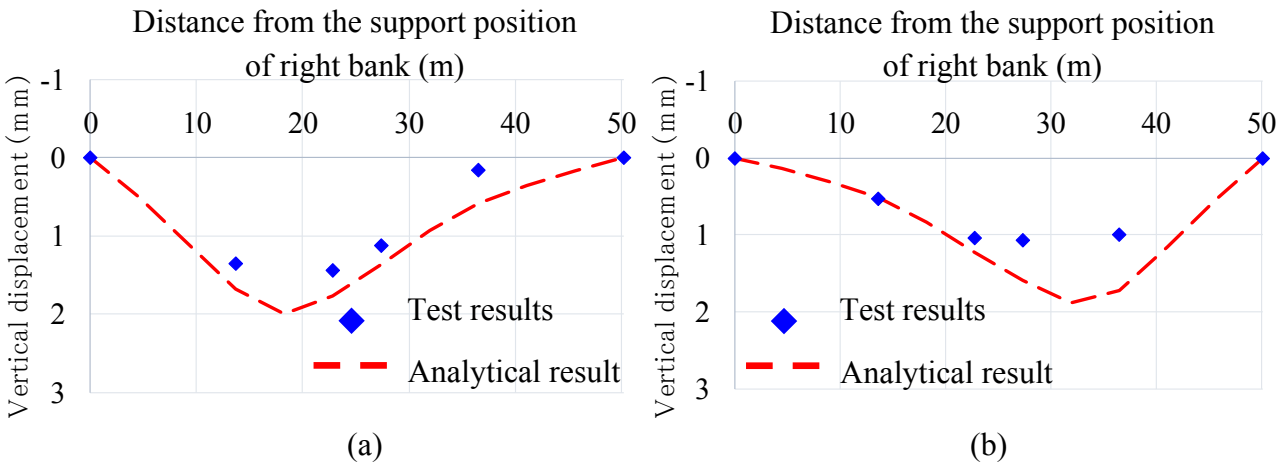

Fig. 7. Deflection behavior of main truss structure loaded the live-load: (a) loading position 5; (b) loading position 9

Fig. 7 shows the vertical displacements of main truss structure loaded the live-load at loading position 5 and 9. As shown in Fig. 7, the vertical displacement of analytical result was greater about 0.8mm at the maximum than test results, because the simple shoes in actual bridge was difficult to rotate due to use long time against the bearing rotated in analytical model. However, the vertical displacements of main truss structure were also almost matched. From the mentioned above, the validity of this analytical model constructed by shell elements considering the corrosion wastage was confirmed by comparison with the field loading test of the actual bridge.

4. Conclusions

This paper presented the whole bridge model of the aging steel truss bridge using shell elements by the comparison of test and analytical results. The main conclusions obtained from this study are as follows:

1) Test and analytical results of axial stresses by live load were almost the same although these members have corrosion damages, and the differences were within 1MPa. Moreover, the axial stress of structural member in 80kN weight were used as live-load considering the current load limitation of this bridge was confirmed that acted stress did not reach to the yield stress.
2) It is thought that the bearing of simple shoes in actual bridge was different from Analytical model, but the vertical displacements of main truss structures in test and analytical results were also almost matched.
3) From the comparison of loading test and analytical results, the applicability of this analytical model constructed by shell elements considering the corrosion wastage was confirmed.

5. References

Yamane, T., Kaita, T. and Fujii, K. 2017. Basal Study on Analytical Prediction of Original Load Bearing Capacity for an Aging Truss Bridge by Using Whole Bridge Model, Proc. of EASEC-15, pp.1906-1913.

Field Loading Test on Aging Pratt Truss Bridge with Severe Corrosion Damages

Yoshiyuki Hirahara[1*], Shuhei Kawami[2], Tatsumasa Kaita[3], Takumi Kanou[4], Hiroaki Fukuda[5], Tatsuro Yamane[6], Ryoichi Satake[7], and Katashi Fujii[8]

[1] Doboku Engineering Consultants Corporation, Hiroshima, Japan; email: hirahara@decnet.co.jp
[2] Chuden Engineering Consultants Corporation, Hiroshima, Japan; email: kawami@cecnet.co.jp
[3] Tokuyama College of Technology, Department of Civil engineering and Architecture, Shunan, Japan; email: kaita@tokuyama.ac.jp
[4] Aratani Civil Engineering Consultants Corporation, Hiroshima, Japan; email: takumi.kanou@aratani.co.jp
[5] Yokogawa Bridge Corporation, Sakai, Japan; email: h.fukuda@yokogawa-bridge.co.jp
[6] Graduate School of Science and Engineering, Ehime University, Matsuyama, Japan; email: yamane.tatsuro.17@cee.ehime-u.ac.jp
[7] Chuden Engineering Consultants Corporation, Hiroshima, Japan; email: satake@cecnet.co.jp
[8] Graduate School of Engineering, Hiroshima University, Higashi-hiroshima, Japan; email: ken214f@hiroshima-u.ac.jp

*: corresponding author

Keywords: Maintenance; Field lording test; steel Pratt truss bridge; corrosion damage

Abstract: In Japan, the importance of maintaining and managing infrastructure is increasing. Especially, more reasonable maintenance existing road bridges will be important as technical issues. However, there are few experimental studies that focused on actual damaged conditions and the effectiveness of repaired members in an existing bridge. In this study, the Field loading test of an aging Pratt truss bridge was conducted for comparing the measured live-load stress and strain with practical design values. The effectiveness of repair and safety of members were confirmed by loading test, because this existing bridge which had been used for about 100 years has many corrosion damages including some repaired members by using the additional plates. In the field loading test, 2 dump trucks with 80kN weight were used as live-load considering the current load limitation of this bridge. Also, the strain of main truss structure and floor members were measured near the severest vertical member. The deflections of whole bridge were measured as vertical displacement in the center of each panel points of lower chord members. The practical design values were referred the analytical results of plane framework which commonly uses in structural design of Pratt truss. From the experimental results, because the deflection and stress level of the main structure were smaller in the experimental value than that of practical design values, it was confirmed that there as a considerable margin of load bearing capacity in the situation where the current load limitation was applied. For the repaired members, since the actual stress of the additional plates and the base material when loading the live load were almost the same, the stress was transmitted normally to the repair section and the effectiveness of the additional plate repair was also confirmed did it.

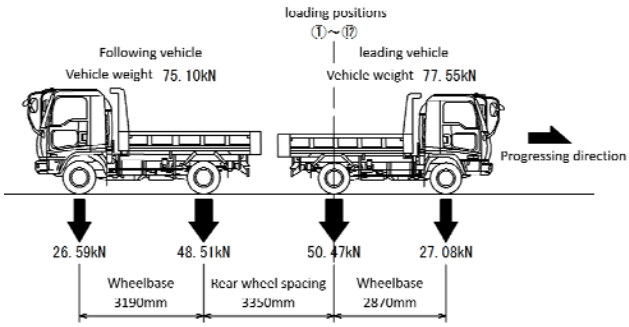

Fig. 1. Axle weight of the vehicles

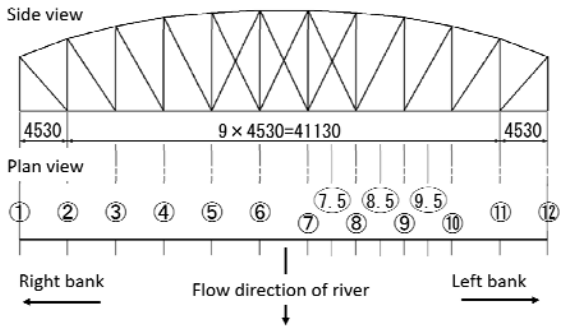

Fig. 2. Loading position

1. Introduction

In Japan, the importance of maintaining and managing infrastructure is increasing. Especially, more reasonable maintenance existing road bridges will be important as technical issues. However, there are few experimental studies that focused on actual damaged conditions and the effectiveness of repaired members in an existing bridge. In this study, the Field loading test of an aging Pratt truss bridge was conducted for comparing the measured live-load stress and strain with practical design values.

2. Outline for Targeted Bridge

The truss bridge which was targeted in this study is an actual curved Pratt truss bridge which had been used for 97 years in Japan. The span length of this bridge is 50.19 m. The members of this bridge are the combination member constructed by riveting channel steels and racing bars. The panel points of this bridge are rigid joints. The weight of vehicles that can pass this bridge is limited less than 8 tons due to severe corrosion damages. In this bridge, many corrosion damages have occurred at the joint between the members. Furthermore, maximum cross section reduction rate is 16.4%. Severe cross-sectional loss at the joint between the vertical member and sway bracing were confirmed at periodic inspections in 2012. The severe cross-sectional loss has already been repaired with additional plates.

3. Field loading test

3.1. Outline of Loading Test

In this study, static loading test was carried out using experimental vehicles whose axle weights were adjusted. In addition, strain of each member and the deflection of the bridge were measured. As shown in Fig. 1, From the consideration of current traffic restriction, 2 dump trucks with 80kN weight used as loading condition. As shown in Fig. 2, the loading positions are on the panel points No.1 to 12 and the intermediate points of No. 7 to 10. These loading positions are based on the rear wheel position of the leading vehicle. Fig. 3 shows the measurement points of strain and vertical deflection of main structure. Since the corrosion damage was occurring intensively in vertical member V9 of this bridge, the strain gauges were set to structural members around V9.

3.2. Measurement Results of Deflection

Fig. 4 shows an example result of the measured vertical deflection in the case of the loading position No. 6. The plotted points in Fig. 4 show deflections measured by field loading test. The

red line is the deflection which was calculated from the plane frame analysis in practical design.

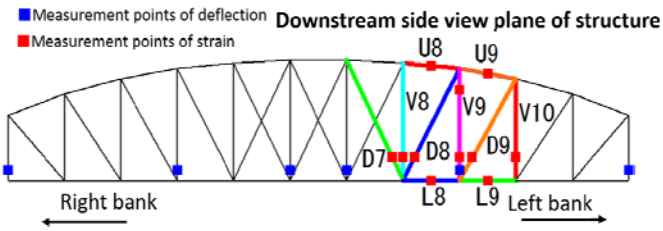

Fig. 3. Measurement points of strain and deflection

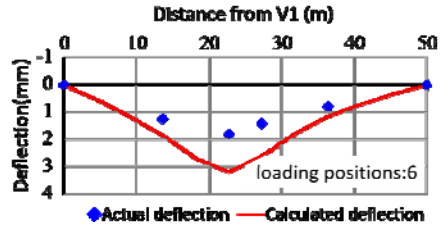

Fig. 4. Deflection curve diagram

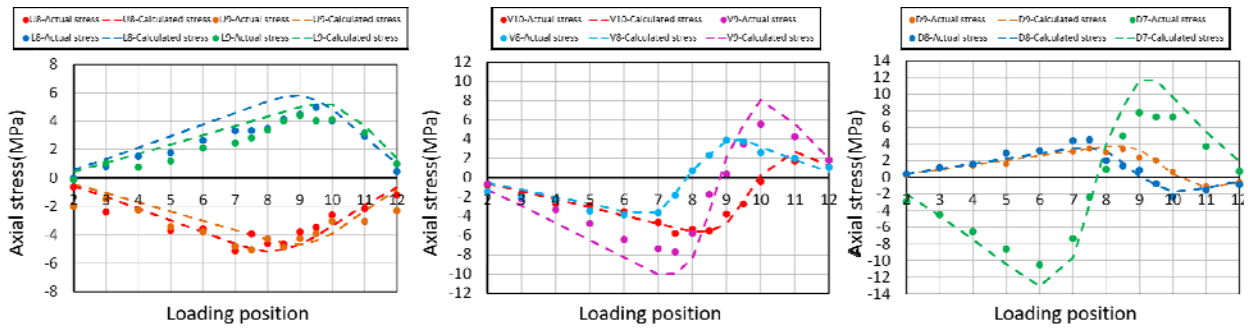

(a) (b) (c)

Fig. 5. Axial stress of structural members: (a) Upper and lower chord members; (b) Vertical members; (c) Diagonal members

The plane frame analyses are assuming to be simple supported and pin jointed truss. In the frame analyses, the deflection was calculated by assignment the load using the influence line. As shown in Fig. 4, though the deflection by loading test tends to be similar to that of the frame analysis, it is a little small. The reason for this is that the support conditions of the plane frame analysis are assumed the simple support, so the rotation at the support is free, however actual bridge is difficult to rotate by the aging deterioration.

3.3. Axial Stress Behavior of Main Member

Fig. 5 shows the axial stress obtained from axial strain due to live load at each loading position. The plotted points in Fig. 5. are axial stress calculated by results of the field loading test. The broken lines are the axial stress calculated by the plane frame analyses. As shown in Fig. 5, it can be confirmed that both axial stress on each structural member tends to be similar value with the deference of about ± 1 MPa. However, the test results in L8 and L9 were little smaller than calculated values, because a part of live load stress will act to stringers under RC slab. And, the test results of V9 and D7 were also little smaller than calculated values. The reason of this is the thought that the stress distribution in section was changing depending on load increase. Also, the strain gauges of V9 and D7 had to set to center of the rivet holes in section due to workability. As shown in Fig. 5(b), the axial stress occurred in V9 by two vehicles having a weight of about 80 kN is about 8 MPa at the maximum. The dead load stress estimated by FEM analysis for this bridge is 33.75 MPa (Yamane et al. 2018). The axial compressive force acting on V9 was calculated to be 121.8 kN based on this result. In contrast, if calculated as a pinned member and

cross section reduction rate is 16.4%, the buckling load is 409.0 kN. From this result, it is considered that there is comparative margin for the load bearing capacity of the member under the current weight limit.

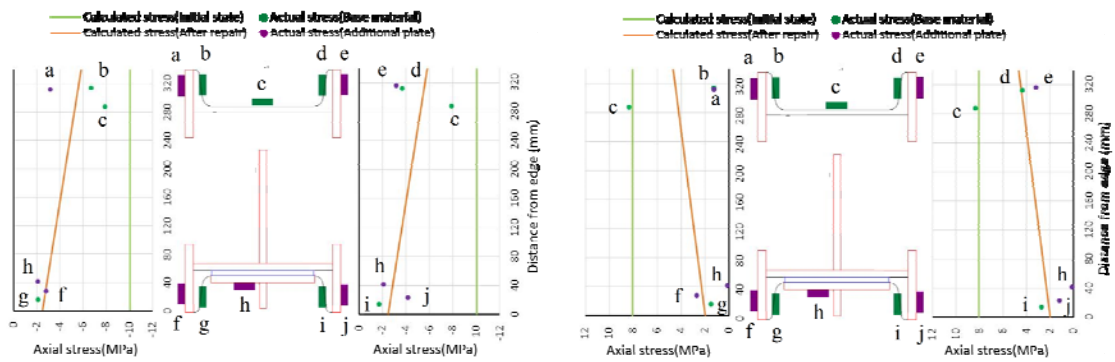

(a) (b)

Fig. 6. Axial stress state on repair section: (a) Under maximum compressive force (-34.7 kN); (b) Under maximum tensile force (27.9kN)

3.4. Stress state of repair section

Fig. 6 shows the axial stress state of the repair section when the maximum compressive force (-34.7 kN) and the maximum tensile force (27.9 kN) occurred in the repair member in this field loading test. In these Figures, the plotted points are the actual stress measured on the additional plates and base materials, and the linear lines show the calculation results by frame analyses assuming the initial state and after repair respectively. From these figures, the bending stress caused by the eccentric distance will be added to the calculated stress of after repair. For the repaired members, since the actual live-load stress on the additional plates and the base materials were almost the same, it was confirmed that the live-load stress was normally transmitted from original section to the repair section. From this fact, the effectiveness of additional plates repair was confirmed.

4. Conclusions

In this study, the Field loading test of an aging Pratt truss bridge was conducted for comparing the measured live-load stress and strain with practical design values (the results from 2-dimensional frame analysis). The main conclusions obtained from this study are as follows:

1) From the comparison of both results on vertical deflection, it was confirmed that the actual deflection near loading point was clearly smaller than analytical results near loading point. These facts may appear the influences of the aging deterioration for pin shoes and bending stiffness of RC slabs.
2) The actual compressive stresses in upper chord members were almost the same to the results of frame analysis. However, the actual tensile stresses in lower chord members were smaller than analytical results, because a part of main load may be acting to stringers. Also, in V9 and D7, it will be thought that the stress difference of both results was occurred due to a change in stress distribution around rivets in cross-section which was constructed by using

L-sharp steels and channel steels according to load increase.

3) Since the buckling load of V9 including corrosion damages was estimated about 3 times the acting compressive force, it was thought that there is comparative margin for the load bearing capacity of the member under the current weight limit.
4) For the repaired members, since the actual live-load stress on the additional plates and the base materials were almost the same, it was confirmed that the live-load stress was normally transmitted from original section to the repair section.

5. References

Yamane, T., Fukuda, H., Kawami, S., Satake, R., Hirahara, Y., Kanou, T.,Kaita, T. and Fujii, K. 2018. Estimation of remaining load bearing capacity for aging steel pratt truss bridge using FEM, The 78th Annual Meeting of the JSCE, I-054, pp.107-108. (In Japanese)

Bridge Engineering Institute Conference 2019 (BEI-2019)
Honolulu, Hawaii, USA, July 22-25, 2019

Assessment and Repair of Damaged Prestressed Girders

Azam Nabizadeh[1] and Habib Tabatabai[2*]

[1] University of Wisconsin - Milwaukee, Milwaukee, USA; email: azam@uwm.edu
[2] University of Wisconsin - Milwaukee, Milwaukee, USA; email: ht@uwm.edu

*: corresponding author

Keywords: bridge, prestressed girders, damage, repair, serviceability, strength, FRP, stress check

Abstract: Accidental impact due to over-height vehicles (primarily at the bottom flange) and unintended construction-related damage during deck removal processes (mainly at the top flange) are the primary modes of damage to prestressed concrete bridge girders that are unrelated to long-term deterioration. There is significant information available in the literature regarding accidental damage to prestressed girders due to over-height vehicles. However, those studies do not address the problem of estimating service stresses in damaged prestressed girders and may not provide comprehensive user tools to address various aspects of assessment and repair of damage. A comprehensive software program (Prestressed Bridge Assessment, Repair, and Strengthening - PreBARS) has been developed to assess serviceability and strength of girders under undamaged, damaged, and repaired conditions. This program addresses top and bottom flange damage cases and currently incorporates the girder sizes and details used by the Wisconsin Department of Transportation. The program calculates bridge loads, distribution factors, prestress losses, as well as strength and service stresses for prestressed bridge I girders and side-by-side box girders. A specific set of procedures have been developed to calculate changes in section properties and service stresses following damage. The effects of patching, internal strand splices, external carbon fiber reinforced polymer (CFRP) reinforcement, as well as a combination of these methods, are considered for repair. PreBARS can evaluate the effects of various levels of damage on the strength and serviceability of prestressed girders.

1. Introduction

Impact damage to precast prestressed bridges can range from minor scrapes to severe structural damage and may occur on both the exterior and interior girders. Impact damage can damage concrete and/or pre-stressing strands. Therefore, repair techniques require awareness of proper concrete repair methodologies, prestressing strand replacement, and possible restoration of prestressing in concrete (Shanafelt and Horn, 1985). Corrosion damage can be one of the long-term consequences of impact damage, due to exposure of strands to the environment. There is significant detailed information available in the literature regarding accidental damage to prestressed girders due to over-height vehicles. Detailed guidelines have been proposed that address assessments and classification of damage as well as specific repair techniques and procedures for a variety of damage conditions. Notable examples include NCHRP Report 280 (Shanafelt and Horn, 1985), NCHRP Report 226 (Shanafelt and Horn, 1980), and a PhD dissertation by Kassan (2012). Feldman et al. (1996) assessed impact damage reports for the Texas DOT. Harries et al. (2009) investigated repair methods for prestressed bridges in a major

report to the Pennsylvania DOT. Harries et al. (2009) discussed the NCHRP 280 report and reviewed their assessment processes. They also conducted a survey of practice in North America. However, these and other studies do not address the problem of estimating service stresses in damaged prestressed girders, and do not provide detailed procedures or software regarding the various aspects of assessment and repair of damage. Externally-bonded Carbon Fiber Reinforced Polymers (CFRP) can be an effective technique for restoring the flexural capacity and stiffness of damaged bridge girders (Klaiber, 2003; Miller, 2006; Rosenboom and Rizkalla, 2006). In this project, the Prestressed Bridge Assessment, Repair and Strengthening (PreBARS) software program is designed to analyze cross sections of prestressed concrete bridge girders at strength and serviceability limit states under undamaged, damaged and repaired conditions. Damage could be at the bottom flange of the girder due to an over-height truck impact, or to the top flange of the girder during removal of deck slab during re-decking operations. Repair options embedded in the PreBARS program include patching, internal strand splices, and CFRP external reinforcement, either individually or in combination. PreBARS is developed within the Microsoft excel using its VBA (visual basic application) capability. The program simulates the pre- and post-damage conditions in prestressed concrete bridge girders and estimates section properties as well as moment strength and service level stresses for the desired cross section based on the provisions of the 8th edition of the AASHTO LRFD Bridge Design Specifications (AASHTO 2017). Simply-supported and continuous span bridges (up to three spans) can be modelled. The maximum programmable length of each span is 160 ft, with an overall maximum bridge length of 480 ft. Various properties are calculated at 1-ft increments over the entire length of the bridge. In its initial (2018) state of development, shear and negative moment effects as well as fatigue are not considered in the PreBARS program.

2. User input data

The user is asked to input the basic bridge information including span length(s), girder type (I-girder or box girder), girder size, girder spacing, strand pattern, slab thickness (structural and initial wearing surface), thickness of build-up over the top flange, barrier type, sidewalk area (if any), compressive strength of girder and slab concretes, skew angle, etc. The standard Wisconsin Department of Transportation (WisDOT) girder sizes, strand patterns, barrier types, etc. are embedded into the current version of the software and can be selected by the user. The user provides information regarding damage to the prestressed girder (at the point of maximum damage) by first specifying whether bottom or top damage has occurred, and then specifying whether any strands have been severed. The user should provide information on CFRP repairs (if any) and patch information.

3. Calculation of loads

The program determines moment and shear influence lines to calculate AASHTO LRFD moments and shears. Fig. 1 shows an example Strength I moment envelope for a prestressed concrete girder bridge with three equal spans of 120 ft.

4. Generation of Undamaged, Damaged, and Repaired Sections

A cross section of a girder from a bridge is modeled within the excel spreadsheet, in which cells representing 0.5 in x 0.5 in square blocks make up the cross section with identifying cell values and colors. Girder concrete, deck concrete, prestressing strand, patch material, CFRP, strand

splices, etc. are given unique numbers in cells corresponding to their specific position(s). With the approach of allocating numbers and coordinates to each cell, the section properties, stress and strength can be automatically calculated for undamaged, damaged, and repaired sections.

Fig. 1. Example of Strength I moment envelope for a three-span bridge.

When the girder type, size and strand pattern is selected by the user (from pull-down menus), the undamaged cross-section is automatically generated by the program. The girder cross-section is populated in a specific worksheet based on the predefined geometry of the girder. An example of the Wisconsin 72W girder is illustrated in Fig. 3a. Common strand patterns for all Wisconsin standard I-girders and box girders are predefined within the PreBARS program.

PreBARS can simulate damage (symmetrical or unsymmetrical damage) in prestressed sections. Loss of prestressing strands and concrete (through spalling and cracking) is modelled through the elimination of cross-sectional elements (zeroing out of affected spreadsheet cells) using mouse clicks on the computer screen. The damage is simulated through simple deletion of cell contents in the damaged areas. Fig. 3b and Fig. 3c show example simulations of damage to bottom and top flanges of a prestressed girder, respectively. Repair are simulated and analyzed in the PreBARS program by first "adding" patch repair materials to the damaged section. All cells representing damaged concrete areas (which were earlier zeroed out due to loss) would be replaced with content representing patch materials. All cells containing severed strands are automatically populated with a unique numerical value. If an internal strand splice were to be applied on any of the severed strand, a different value is allocated to the corresponding cells. The user would select which of the severed strands should be spliced and would manually over-write the existing pre-existing cell value. The user also has the option to specify the use of CFRP for repair and strengthening. The user would select the location of CFRP (soffit, the two sides of web, the side faces of bottom flange), and the program automatically assigns a specific number to the selected CFRP cell location(s).

5. Service and Strength Limit State Calculations

A new set of procedures are developed (based on a differential approach) to calculate service stresses in undamaged, damaged and repaired conditions considering the redistribution of stress

during damage, effects of preloading, patching and CFRP applications, etc. Detailed information on service stress calculations are provided by Tabatabai and Nabizadeh (2019). Strength calculations are performed for undamaged, damaged, and repaired states using the strain compatibility approach. Strain limits in concrete and CFRP are considered and stress-strain behavior of prestressing steel and concrete is modeled. Strains, curvatures, and stresses are calculated at the strength limit state (Tabatabai and Nabizadeh 2019).

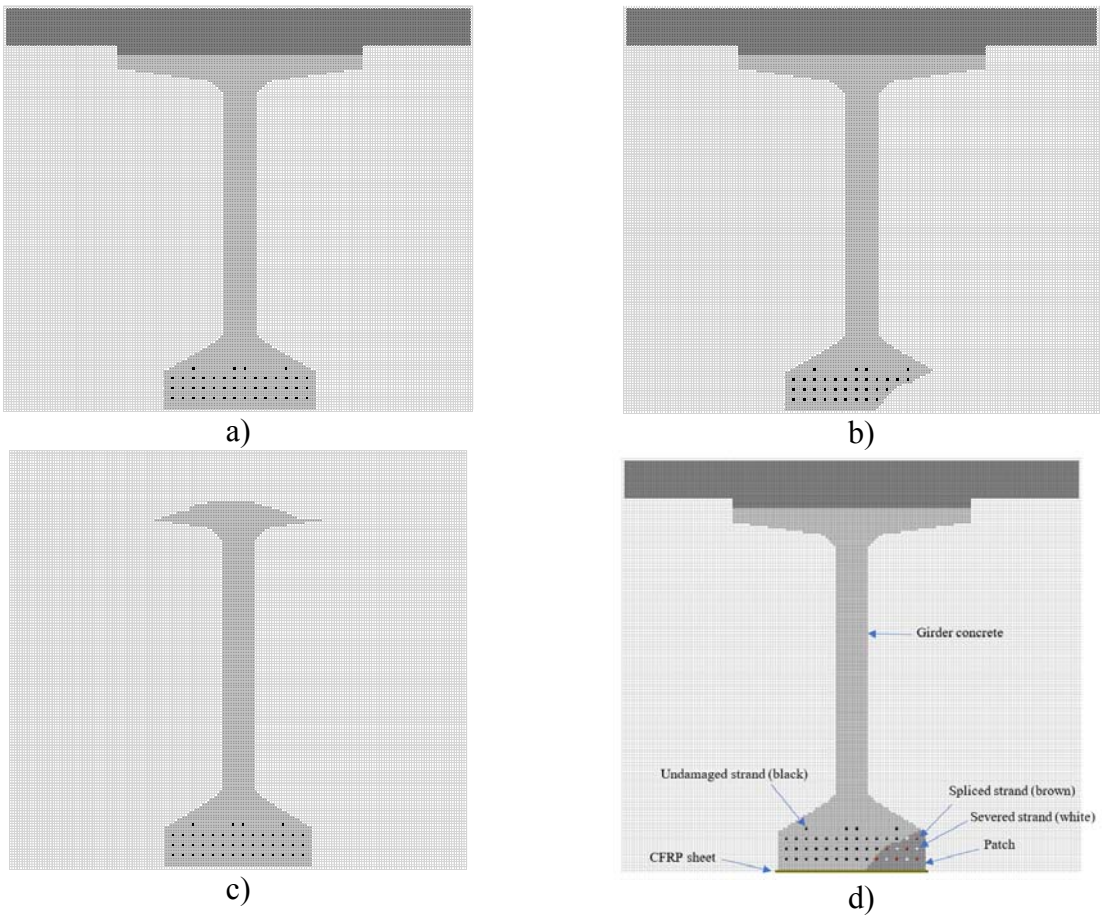

Fig. 3. a) Undamaged section configuration, b) Bottom damaged section configuration, c) Top damaged section configuration, and d) Repaired section with CFRP at the bottom.

6. Summary

A comprehensive software program (PreBARS) has been developed to assess service stresses and strength for undamaged, damaged and repaired precast prestressed bridge girders. Detailed information on the development of software program, case studies, procedures for service stress calculations, etc. are provided in a research project report to the Wisconsin Department of Transportation (Tabatabai and Nabizadeh, 2019). The current (2019) version of the program incorporated sections and details used in Wisconsin. Sources and types of damage are categorized and defined. A detailed set of proposed guidelines are provided to help with decisions regarding assessment of damage, structural calculations, and repair decisions.

7. Acknowledgements
This research was funded through the Wisconsin Highway Research Program by the Wisconsin Department of Transportation and the Federal Highway Administration under Project # 0092-17-02. The contents of this paper reflect the views of the authors and not necessarily those of the sponsors. The authors are grateful for the support of WisDOT and the members of the Project Oversight Committee.

8. References

AASHTO. Guide Specifications for Design of Bonded FRP Systems for Repair. 1st Edition, American Association for State Highway and Transportation Officials, Washington D.C., 2012.

Feldman, L.R., Jirsa, J.O., Fowler, D.W. and Carrasquillo, R.L., 1996. Current practice in the repair of prestressed bridge girders.

Harries, K.A., Kasan, J. and Aktas, J., 2009. Repair methods for prestressed girder bridges (No. FHWA-PA-2009-008-PIT 006). Pennsylvania. Dept. of Transportation.

Kasan, J.L., 2012. On the repair of impact damaged prestressed concrete bridge girders (Doctoral dissertation, University of Pittsburgh).

Klaiber, F.W., Wipf, T.J. and Kempers, B.J., 2003, August. Repair of damaged prestressed concrete bridges using CFRP. In Proceedings of the 2003 Mid-Continental Transportation Research Symposium, Ames, Iowa.

Miller, A.D., 2006. Repair of Impact-Damaged Prestressed Concrete Bridge Girders Using Carbon Fiber Reinforced Polymer (CFRP) Materials.

Rosenboom, O. and Rizkalla, S., 2006. Behavior of prestressed concrete strengthened with various CFRP systems subjected to fatigue loading. Journal of Composites for Construction, 10(6), pp.492-502.

Shanafelt, G.O. and Horn, W.B., 1980. Damage evaluation and repair methods for prestressed concrete bridge members. NASA STI/Recon Technical Report N, 81.

Shanafelt, G.O. and Horn, W.B., 1985. Guidelines for Evaluation and Repair of Prestressed Concrete Bridge Members. NCHRP Report, (280).

Tabatabai H., Nabizadeh A., 2019. Strength and Serviceability of Damaged Prestressed Girders. WisDOT Report. Project #0092-17-02. Madison, WI.

Environmental Effects and Others

Scour Stability Evaluation of Bridge Pier Considering Fluid-Solid Interaction

Po-Wei Chen[1], Tzu-Kang Lin[2*], and Chu-Chieh Jay Lin[3]

[1] National Chiao Tung University, Hsinchu Taiwan; email: e2171918@gmail.com
[2] National Chiao Tung University, Hsinchu Taiwan; email: tklin@ntu.edu.tw
[3] AECOM Technology Inc., Los Angeles United States; email: bei_institute@outlook.com

*: corresponding author

Keywords: bridge scour; stability evaluation; fluid-solid interaction; soil spring

Abstract: As the development of human civilization, transportation has become an indispensable part of daily live, which form a large demand on river crossing bridges. Due to typhoon or flooding, scour at bridge piers poses huge threat to stability, bearing capacity and other performance of bridge foundation. For traditional static evaluation, however, fluid behavior is simplified by linear force distribution when current force is considered, which may cause the overestimate of stability because of the negligence of nonlinear force generated by down flow, wake verities and other fluid behavior in the vicinity of pier. In order to consider the complicated fluid impact, finite element simulation is applied in this study by creating a fluid-solid interaction (FSI) system. In FSI system, simulation result for both fluid and solid system is transferred to each other at each time interval. In this way, the force generate by fluid system can be added back to solid system to estimate the dynamic response of pier. In this study, a scaled single pier scour test is conducted by both experimental test and finite element program. By analyzing the dynamic data collected in experimental test, the natural frequency of pier at each scour depth can be defined, which is later compared to results from numerical simulation. According to the low error of natural frequency, the established FSI system is able to conduct pier scour simulation correctly while considering fluid-solid interaction, and can be further applied in practical engineering bridge simulation, which will be applied as a guideline for bridge and traffic control that supports disaster prevention and evacuation while flood strikes bridges.

1. Introduction

A survey (Shirhole and Holt 1991) in U.S. indicated that around 60% of bridge failure mode belongs to hydraulic while only 3% belongs to seismic, and a similar result was found in other survey in Taiwan. Scour, where the characteristic is classified as hydraulic, happened at pier while water flows by and causes lost of bed material near piers. Studies had shown how scour effects stability, bearing capacity and other performance of bridge foundation. Prendergast L.J. et al. (2013) builds numerical and realistic model for scaled and full-scale pile models. Analyzing the model response excited by an impulse force, loss of structure natural frequency, which implies a lower constraint, can be observed while scour happened. Focusing on pier of offshore wind turbine, Prendergast L.J. et al. (2015) and Tseng W.C. et al. (2018) both conclude that natural frequency drops and deformation increases while pier lost vicinity bed material by structure response and numerical model respectively.

Complicated fluid behavior in the vicinity of pier is simplified as a linear force in most building regulations. For studies about flow pattern and vortex around cylinder or scoured pier, Brücker C. (1995) plotted 3D vorticity downstream of a cylinder by Digital-Particle-Image-Velocimetry (DPIV) scanning technique. Graf W.H. & Yulistiyanto B. (1998) measured the velocity and vorticity fields around cylinder, describing the fluid behavior at pier vicinity. Akilli H. and Rockwell D. (2002) observed Kármán vortex and other vortex formations in shallow water. Graf W.H. and Istiarto I. (2002) measured the velocity field alone upstream and downstream of scaled pier model. These researchers concluded that fluid behavior of water at pier vicinity, especially pier with scour, is highly nonlinear, and velocity and vorticity fields change alone time and distance from pier. Normally, the fluid behavior might be minor comparing to live load and dead load of bridge. However, bridge failure might happened due to overestimation of stability while severe scour happened, which performances of pier are relatively worse.

2. Scaled model experiment

As barely study used fluid-solid combined numerical model to simulate a bridge pier, a scour experiment of a scaled hypothetical structure is conducted to provide a simulation target for FSI system in this study, verifying the capability of ANSYS that simulates the complicated interaction between fluid field and multi-degree-of-freedom (MDOF) system composed of bridge pier and soil springs. In the scaled model experiment, a 37m by 1m sink with 1.2m-depth is set to have a constant flow rate of 2.5m/s as watercourse (see Fig. 1(a)) while a pier with 0.49m-caisson-foundation (see Fig. 1(b)) having initial embedded depth by 0.099m (see Fig. 2).

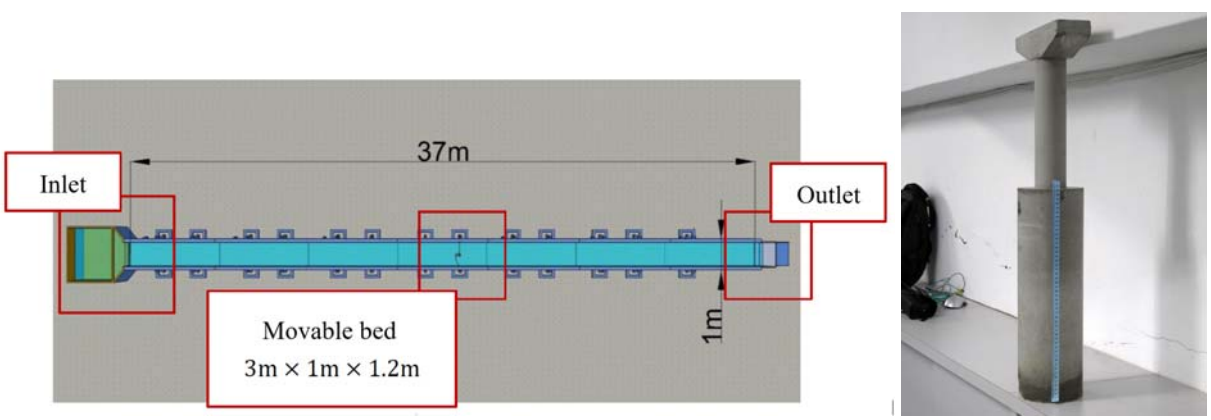

(a) (b)

Fig. 1. (a) The sink for experiment; (b) the scaled pier model

Ambient vibration is collected in three axes by 3 velocity meters set on top of pier model. In order to analyze the dominant frequency of pier alone time series, Short-time Fourier Transform (STFT) (Eq. 1), using 2048-point Hanning window with 50% overlap as window function, is applied in this study. According to the result of experiment (see Fig. 2), several sets of data, buried depth at 8, 6, and 5 cm which having main frequency at 10.76, 10.41, and 10.21 Hz, respectively, is select for numerical simulation.

$$X(\tau,\omega)=\int_{-\infty}^{\infty}x(t)w(t-\tau)e^{-i\omega t}dt \tag{1}$$

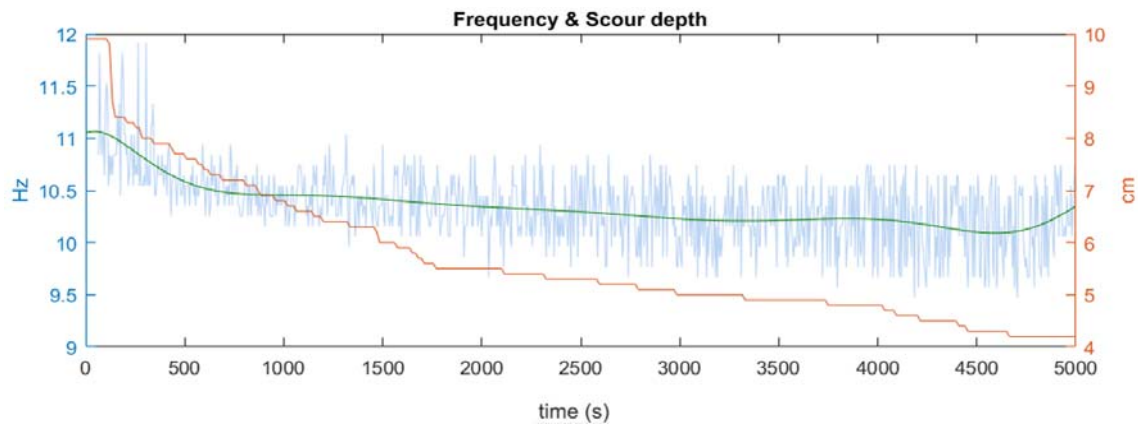

Fig. 2. dominant frequency(blue line) and scour depth(red line) of pier model

3. Numerical simulation

A numerical model is built by FSI system in ANSYS, and soil springs is set horizontally and vertically on the lower part of model to simulate soil pressure applied to the pier (see Fig. 3(a)(b)), and is removed according to the scour condition. In order to prevent model collapse and calculation error, a linear increment velocity of flow rate is applied in this simulation. As seen in Fig. 3(c), two free decay signals, having same vibration period, can be observed from the response on top of model at the very start and end of linear increment velocity of flow rate, and are later used in defining the natural frequency of pier model.

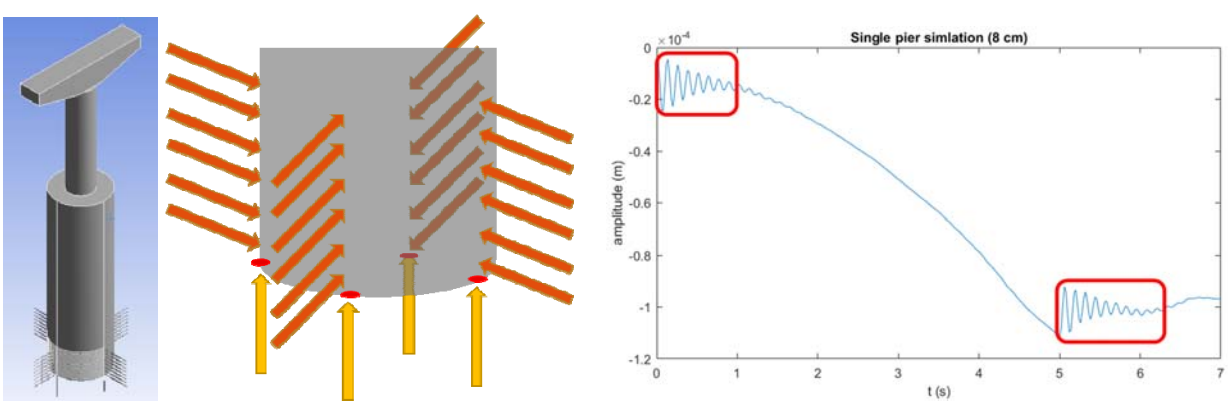

(a) (b) (c)

Fig. 3. (a)(b) Numerical model of scaled pier build in ANSYS; (c) response at the top of model

By analyzing the model response in simulation, natural frequency of model at each scour condition are shown in Table 1. Natural frequency of model in both experiment and simulation drops while buried depth decrease, caused by scour and removing soil spring, which reflects the reduce of soil constraint. FSI system shows its capability and applicability on pier scour

simulation with a low error percentage of model natural frequency. The error might come from the negligence of friction between pier and soil, which underestimates the constraint condition.

Table 1. Simulation result

Buried depth (cm)	8	6	5
Freq. (experiment)	10.76	10.41	10.21
Freq. (simulation)	10.77	10.07	9.70
Error	0.1%	3.2%	5.0%

4. Conclusion

According to the result of simulation, pier scour simulation can be conducted with FSI system in the consideration of fluid behavior. The low simulation error, which is under 5%, of natural frequency of pier model represents that the established model can correctly simulate behavior of a scaled pier buried in riverbed, meaning which demonstrates the feasibility of conducting full-scale simulation for the dynamic characteristic including displacement and angle of inclination of piers of a practical structural. In the future, a numerical model in full-scale will be constructed to represent a practical engineering bridge, and scour stability considering fluid-solid interaction will be evaluated. The result can be applied to disaster prevention and traffic control while flood strikes.

5. References

Shirhole, A.M. and Holt, R.C. 1991. Planning for a comprehensive bridge safety program, Transportation Research Record, 1290.

Prendergast, L.J., Hester, D., Gavin, K., and O'Sullivan, J.J. 2013. An Investigation of the Changes in the Natural Frequency of a Pile affected by Scour, Journal of sound and vibration, 332(25), 6685-6702.

Prendergast, L.J., Gavin, K., and Doherty, P. 2015. An investigation into the effect of scour on the natural frequency of an Offshore Wind Turbine, Ocean Engineering, 101, 1-11.

Tseng, W.C., Kuo, Y.S., Lu, K.C., Chen, J.W., Chung, C.F., and Chen, R.C. 2018. Effect of Scour on the Natural Frequency Responses of the Meteorological Mast in the Taiwan Strait, Energies, 11(823), 1-18.

Brücker C. 1995. Digital-Particle-Image-Velocimetry (DPIV) in a scanning light-sheet: 3D starting flow around a short cylinder, Experiments in Fluids, 19, 255-263.

Graf, W.H. and Yulistiyanto, B. 1998. Experiments on flow around a cylinder; the velocity and vorticity fields, Journal of Hydraulic Research, 36(4), 637-654.

Graf, W.H. and Istiarto, I. 2002. Flow pattern in the scour hole around a cylinder, Journal of Hydraulic Research, 40(1), 13-20.

Akilli, H. and Rockwell, D. 2002. Vortex formation from a cylinder in shallow water, Physic of Fluid, 14(9), 2957-2967.

Modal Frequency and Damping Identification of Stay Cables with Ambient Vibration Measurements Based on a Bayesian Approach

Zhouquan Feng[1*], Yafei Wang[2], Chao Yang[3], Zhiwen Liu[4], and Zhengqing Chen[5]

[1] Key Laboratory for Wind and Bridge Engineering of Hunan Province, College of Civil Engineering, Hunan Univ., Changsha, China; email: zqfeng@hnu.edu.cn
[2] Key Laboratory for Wind and Bridge Engineering of Hunan Province, College of Civil Engineering, Hunan Univ., Changsha, China
[3] Key Laboratory for Wind and Bridge Engineering of Hunan Province, College of Civil Engineering, Hunan Univ., Changsha, China
[4] Key Laboratory for Wind and Bridge Engineering of Hunan Province, College of Civil Engineering, Hunan Univ., Changsha, China
[5] Key Laboratory for Wind and Bridge Engineering of Hunan Province, College of Civil Engineering, Hunan Univ., Changsha, China

[*]: corresponding author

Keywords: Stay cable; ambient vibration; modal frequency; damping ratio; Bayesian approach

Abstract: Stay cables are one of the most critical structural components in cable-stayed bridges and their dynamic characteristics play important roles in the construction, monitoring and control of cable-stayed bridges. We propose a Bayesian frequency domain approach for modal parameter identification of stay cables using ambient vibration measurements. The proposed approach obtains not only the optimal values of the modal parameters but also their associated uncertainties, calculated from their posterior probability distribution. Calculation of the uncertainties of identified modal parameters is very important when one plans to proceed with probabilistic analysis and design based on modal estimates. An experiment on a stay cable of Sutong Bridge is presented to verify the proposed approach. Ambient vibrations of the stay cable are measured using an accelerometer. From ambient measurements, the optimal values and their standard deviations of the modal frequency and damping ratio of the stay cable are extracted.

1. Introduction

Stay cables are one of the critical members of the cable-stayed bridges that play an important role of supporting the decks. However, the stay cables are sensitive to various vibrations induced from external sources such as traffic, wind and rain-wind due to their inherent low damping (Ni et al. 2007). To solve these hazardous vibration problems, various countermeasures have been developed. One of the effective ways is to install dampers near to the anchorages of stay cables (Chen et al. 2003). In order to analysis the vibration mechanism, optimally design the damping system and verify the performance of cable dampers, the modal parameters of the stay cables especially the modal frequency and damping ratio should be accurately identified. The modal parameters of the stay cables can be identified either using ambient vibration data or free vibration data. The free vibration data are usually obtained by sudden release of the exciter that performs sine sweeping and resonance tests. This kind of test can generate sufficient amplitude of vibrations and thus renders high signal to noise ratio. However, the tests require more

instruments including the cable exciting system that is not easy to be installed and the excitation force is not harmonic motion but unsymmetrical motion in upward and downward directions (Lee et al. 2010). On the other hand, the ambient vibration data are readily obtained by the sensors mounted on the cables. However, the signal to noise ratio is low and the uncertainties should be properly quantified. In this paper, a Bayesian spectral density approach is proposed to identified the modal frequencies and damping ratios and their associated uncertainties are quantified as well (Katafygiotis and Yuen, 2001). An experiment on one stay cable of Sutong Bridge is presented to verify the proposed approach.

2. Bayesian spectral density approach

2.1. Dynamics of linear systems

Consider a linear dynamic system with N_d degrees of freedom and equation of motion:

$$\boldsymbol{M}\ddot{\boldsymbol{x}}(t) + \boldsymbol{C}\dot{\boldsymbol{x}}(t) + \boldsymbol{K}\boldsymbol{x}(t) = \boldsymbol{F}(t) \tag{1}$$

where $\boldsymbol{M}$, $\boldsymbol{C}$ and $\boldsymbol{K}$ are the mass, damping and stiffness matrix, respectively; $\boldsymbol{F}$(t) is the external excitation that can be modeled as zero-mean Gaussian white noise with spectral intensity matrix $\boldsymbol{S}_F(\omega) = \boldsymbol{S}_0$. Based on the relationship between the original co-ordinates and the modal co-ordinates, one obtains the uncoupled modal equations of motion:

$$\ddot{\boldsymbol{q}}_r(t) + 2\zeta_r\omega_r\dot{\boldsymbol{q}}_r(t) + \omega_r^2\boldsymbol{q}_r(t) = \boldsymbol{F}_r(t), \quad r=1,\ldots,N_d \tag{2}$$

Assume that the measurement $\boldsymbol{y}_N = \{\boldsymbol{y}(n), n = 1, \ldots, N\}$ contains N_0 channels of structural response, contaminated by the measurement noise $\boldsymbol{s}(n)$

$$\boldsymbol{y}(n) = \boldsymbol{L}_0\boldsymbol{x}(n) + \boldsymbol{s}(n) \tag{3}$$

where $\boldsymbol{y}(n) \in \mathbb{R}^{N_0}$ is the measurement at the nth time step; $\boldsymbol{L}_0\boldsymbol{x}(n)$ is the concerned structural response (e.g., displacement or acceleration) at the same time step, where $\boldsymbol{L}_0$ denotes an $N_0 \times N_d$ observation matrix, comprised of zeros and ones. Herein, the measurement noise is modeled as zero-mean Gaussian white noise process vector.

Let $\boldsymbol{\theta}$ denote the full set of modal parameters to be identified. It consists of the modal frequencies f_r and damping ratios ζ_r of the concerned modes, the partial mode shapes $\boldsymbol{\phi}(r)$ including only the components at the observed degrees of freedom of the concerned modes, the upper triangles (diagonal inclusive) of $\boldsymbol{S}_0$ and the modeling error $\boldsymbol{s}_z$.

2.2. Statistical characteristics of response power spectral density

It has been proved in (Yuen et al. 2002) that the spectral density matrix estimator

$$\boldsymbol{S}_{y,N}^{M}(\omega_k) = \frac{1}{M}\sum_{m=1}^{M} Y_N^{(m)}(\omega_k)Y_N^{*(m)}(\omega_k) \tag{4}$$

follows a central complex Wishart distribution of dimension N_0 with M degrees of freedom. Also, note that in the special case of a single-degree-of-freedom (SDOF) oscillator or in the case of a

MDOF system with only one measured DOF (N_0=1), the distribution becomes a Chi-square distribution with 2M degrees of freedom. That is,

$$p\left(S_{y,N}^{M}(\omega_k)\right) = \frac{M^M |S_{y,N}^{M}(\omega_k)|^{M-1}}{(M-1)!\,|E[S_{y,N}(\omega_k)]|^M} exp\left(-\frac{M S_{y,N}^{M}(\omega_k)}{E[S_{y,N}(\omega_k)]}\right) \tag{5}$$

Assume that in a resonance frequency band the response is dominated by one single mode and only the spectral density data in this band are used for modal identification.

$$E\left[S_{y,N}(\omega_k)\right] = \frac{s_f}{(\beta_k^2-1)^2+(2\zeta\beta_k)^2} + s_\varepsilon \tag{6}$$

where s_f is the spectral density of the modal force, s_ε is the spectral density of modelling error, $\beta_k = \omega/\omega_k$. Furthermore, the matrices $S_{y,N}^{M}(\omega_k)$ and $S_{y,N}^{M}(\omega_l)$ are independent for $k \neq l$, that is

$$p\left[S_{y,N}^{M}(\omega_k), S_{y,N}^{M}(\omega_l)\right] = p\left[S_{y,N}^{M}(\omega_k)\right] p\left[S_{y,N}^{M}(\omega_l)\right] \tag{7}$$

2.3 Identification based on spectral density estimates

Here we using only one sensor to collect the vibration data of stay cables, and then the auto-spectral densities are calculated. It is assumed that the spectral density set $S_\Gamma = \{S_{y,N}^{M}(\omega_k), k = k_1, \dots, k_2\}$ formed over the frequency band $\Gamma = [k_1\Delta f, k_2\Delta f]$ is employed for modal analysis. According the Bayes's theorem, the posterior probability density function (PDF) of θ given S_Γ is

$$p(\theta|S_\Gamma) = cp(S_\Gamma|\theta)p(\theta) \tag{8}$$

Assuming a uniform (constant) prior distribution is used for θ, the optimal modal parameter vector $\hat{\theta}$ can be obtained by minimizing the objective function defined as $L(\theta) = -\ln[p(\theta|S_\Gamma)]$. It is convenient to write the objective function in terms of the 'negative log-likelihood function' (NLLF) as

$$L(\theta) = M\sum_{k=k_1}^{k_2} \ln|E[S_{y,N}(\omega_k)]| + M\sum_{k=k_1}^{k_2} \frac{S_{y,N}^{M}(\omega_k)}{E[S_{y,N}(\omega_k)]} + c_1 \tag{9}$$

The NLLF can be obtained by constrained numerical optimization without much computational effort, which can be done by using the function 'fmincon' in MATLAB.

2.4 Posterior uncertainty of modal parameters

The most probable parameter vector $\hat{\theta}$ can be obtained by minimizing $L(\theta)$, while the covariance matrix of the modal parameters can be obtained by taking the inverse of the Hessian of $L(\theta)$ evaluated at $\theta = \hat{\theta}$, i.e., $\Sigma(\theta) = [H(\hat{\theta})]^{-1}$. The elements of $H(\hat{\theta})$ can be calculated either analytically as shown in (Yan and Katafygiotis, 2015) or using finite difference approach.

3. Application of Bayesian spectral density method

An accelerometer was mounted on a long stay cable of Sutong Bridge to collect the ambient vibration signals, the sampling frequency is 100Hz, and the data duration is 24 hours. The first 8 modes of this stay cable are identified using the Bayesian spectral density method, and the results are tabulated in Table 1. Not only the optimal values of modal frequency and damping ratio are obtained, but also the uncertainties (standard deviation and coefficient of variation) are quantified.

Table 1. Identification results for one set of data

Mode / Parameter	#1	#2	#3	#4	#5	#6	#7	#8
frequency	0.2368	0.4745	0.7122	0.9517	1.1913	1.4298	1.6752	1.9164
SD	0.0007	0.0007	0.0010	0.0011	0.0012	0.0012	0.0013	0.0012
COV	0.0028	0.0015	0.0014	0.0012	0.0010	0.0008	0.0008	0.0006
damping	0.0062	0.0044	0.0060	0.0051	0.0042	0.0037	0.0035	0.0046
SD	0.0025	0.0014	0.0013	0.0011	0.0010	0.0008	0.0007	0.0005
COV	0.4049	0.3230	0.2159	0.2213	0.2275	0.2138	0.2109	0.1076

Note: SD: standard deviation; COV: coefficient of variation

4. Conclusions

A Bayesian approach is proposed in this paper to identified the modal frequencies and damping ratios of stay cables based on ambient measurements. Not only the optimal values of the modal parameters are obtained but also their uncertainties are quantified by standard deviations. Calculation of the uncertainties of identified modal parameters is very important when one plans to proceed with probabilistic analysis and design based on modal estimates. An experiment on a stay cable of Sutong Bridge is presented to illustrate the practicability of the proposed method. The results of operational modal analysis can be used for cable condition assessment and robust vibration control based on statistical methods.

5. Acknowledgements

The research is funded by National Natural Science Foundation of China (Grant No.51708203), the Open Research Fund Program of Guangdong Key Laboratory of Earthquake Engineering and Application Technology (grant No.2014B030301075-02), and the Fundamental Research Funds for the Central Universities (Grant No.531118010047). The authors are grateful to these supports.

6. References

Ni, Y. Q. , Wang, X. Y. , Chen, Z. Q. , & Ko, J. M. . (2007). Field observations of rain-wind-induced cable vibration in cable-stayed Dongting Lake bridge. Journal of Wind Engineering and Industrial Aerodynamics, 95(5), 303-328.

Chen, Z. Q. , Ko, J. M. , Ni, Y. Q. , & Spencer, B. F. . (2003). MR damping system on Dongting Lake cable-stayed bridge. Proceedings of the SPIE, Volume 5057, p. 229-235

Lee, J. J. , Kim, J. M. , Ahn, S. S. , & Choi, J. S. . (2010). Development of a cable exciter to evaluate damping ratios of a stay cable. Ksce Journal of Civil Engineering, 14(3), 363-370.

Katafygiotis, L. S., & Yuen, K. V. (2001). Bayesian spectral density approach for modal updating using ambient data. Earthquake Engineering & Structural Dynamics, 30(8), 1103-1123.

Yuen, K. V., Katafygiotis, L. S., & Beck, J. L. (2002). Spectral density estimation of stochastic vector processes. Probabilistic Engineering Mechanics, 17(3), 265-272.

Yan, W. J., & Katafygiotis, L. S. (2015). A two-stage fast bayesian spectral density approach for ambient modal analysis. part i: posterior most probable value and uncertainty. Mechanical Systems & Signal Processing, 54-55, 139-155.

Bridge Engineering Institute Conference 2019 (BEI-2019)
Honolulu, Hawaii, USA, July 22-25, 2019

Design and Construction of Deck Slab Replacement for Highway Bridges

Rikiya Murakami[1*] and Takashi Yamane[2]

[1] Kyokuto Kowa Corporation, Hiroshima, Japan; email: rmurakam@kkn.co.jp
[2] Kyokuto Kowa Corporation, Hiroshima, Japan; email: tyamane0414@krc.biglobe.ne.jp

*: corresponding author

Keywords: deck slab replacement, precast prestressed concrete (PC) deck slab, salt damage

Abstract: This paper presents an overview and special considerations of concrete deck slab renovation work performed on expressway bridges in Japan. Bridge deck slab replacement involves replacing the existing reinforced concrete (RC) deck slab with partially pretensioned precast concrete deck slab. Improvements in the materials, design, and manufacturing of the newly installed deck slabs all contribute to enhancing the durability of the road: ground granulated blast-furnace slag was mixed in with the concrete; crack width and stresses were controlled based on the service conditions and structural location; and measures such as deck slab curing in water tanks immediately after manufacturing were taken. During construction, deck replacement was carried out simultaneously at two locations, using two teams of workers moving from the center of the bridge toward the ends, to minimize the effect on highway traffic.

1. Introduction

At present, the highways in Japan have extended to a total length of around 9,000 km since opening more than 50 years ago in 1963, and about 40% (about 3,700 km) of the roads have been in service for over 30 years. In bridges, deterioration from salt damage due to deicing agents (sodium chloride) in winter and from fatigue due to the increased numbers of large vehicles have become more pronounced. To address this, the expressway companies, acting as administrators, have launched the "Expressway Renewal Project" and have undertaken large-scale renovation and repair since 2016. This paper presents a description of concrete deck slab renovation projects performed in Japan, along with their features and special considerations. As an example of the construction work, we showcase a 127-meter-long 3-span continuous steel plate girder bridge that opened for service over 40 years ago.

2. Description of the bridge

Table 1 shows the bridge specifications. The bridge side elevation is shown in Fig. 1.

Table 1. Bridge specifications

structure	3-span continuous plate girder
length of bridge	127.130m
span length	3 @ 42.000m
effective width	9.750m
skew	θ=90°00'00"
gradient	5.000% ～ 2.474%
cross slope	8.00%

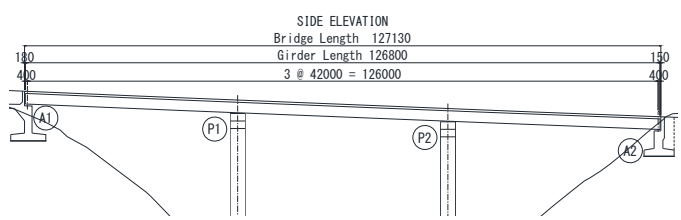

Fig. 1. Bridge side elevation

3. Deck slab structure

Figure 2 shows the cross-section of the existing RC deck slab before replacement, while Fig.3 shows the cross-section of the precast PC deck slab after replacement. The thickness of the existing RC deck slab before replacement is 210 mm, while the thickness of the PC deck slab after replacement is 230 mm to provide a concrete cover and tendon spacing in accordance with current standards.

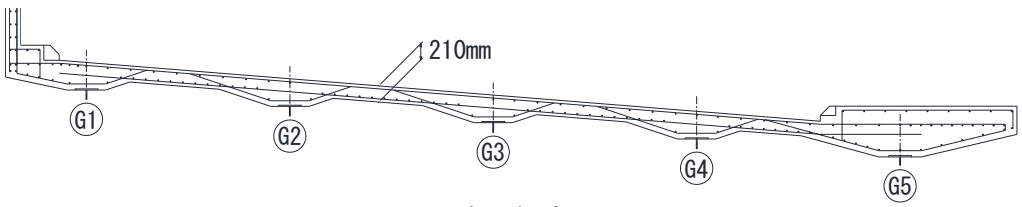

Fig. 2. Cross-section before repracement

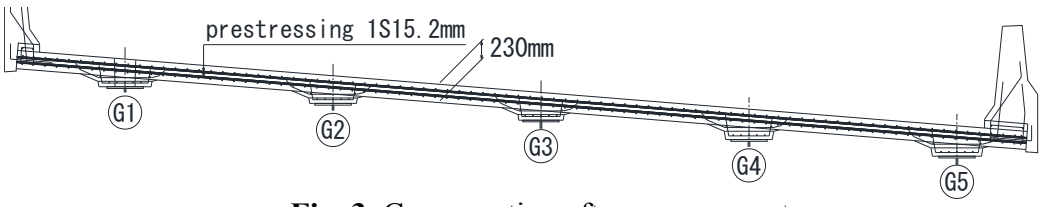

Fig. 3. Cross-section after repracement

4. Materials

The compressive strength of the concrete used is 50 N/mm^2. In addition, a concrete mix with 50% of the cement volume replaced by ground granulated blast-furnace slag (specific surface area of 6,000 cm^2/g) with a high salt blocking property was adopted. Because the initial curing is important in enhancing the salt blocking effect, steam curing was carried out, followed by water tank curing for 3 days in a special curing tank. Figure 4 shows the water tank curing.

Fig. 4. Water tank curing of the deck slab

5. Design

5.1. Deck slab design

The deck slab was designed as an RC structure in the bridge axial direction and as a precast PC structure in the direction transverse to the bridge axis. The design of the precast PC structure used the control procedure shown in Table 2, which depends on use condition. The procedure performs the design with three constraints, depending on the use condition of the bridge: (1) tensile stress is prohibited, (2) tensile stress occurs but flexural cracks are prohibited, and (3) flexural cracks occur but crack widths are kept within a limit. This control procedure has essentially been standardized for the design of highway bridges and is called the “prestressed reinforced concrete (PRC) structure” in Japan.

Table 2. Stress control methods

structural location	control method
dead load action	prevent generation of tensile stress
live load action	prevent cracks
wind load action	control crack width
collition load action	control crack width

5.2. Deck slab arrangement

The precast PC deck slab was designed to be arranged by combining two slab types, square- and trapezoid-shaped slabs, as shown in Fig.5. Trapezoidal slabs are slabs placed to adjust the slab arrangement in the direction of horizontal alignment and to adjust along the skew angle of the bridge ends; all other standard portions consist of square slabs. Slabs were joined together by pouring concrete with the same compressive strength as the precast PC deck slab between adjacent slabs.

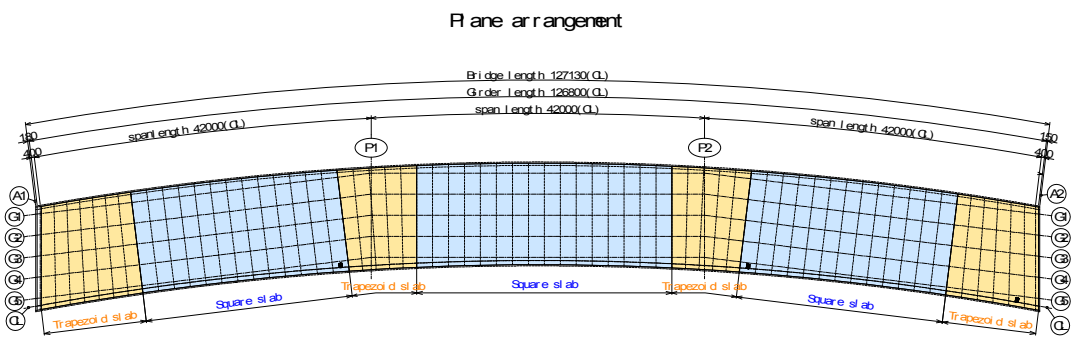

Fig. 5. Precast PC deck slab arrangement plan

6. Construction

6.1. Construction flowchart and work schedule

Figure 6 shows the construction work schedule. All the work was completed in 67 working days from the beginning of construction until completion.

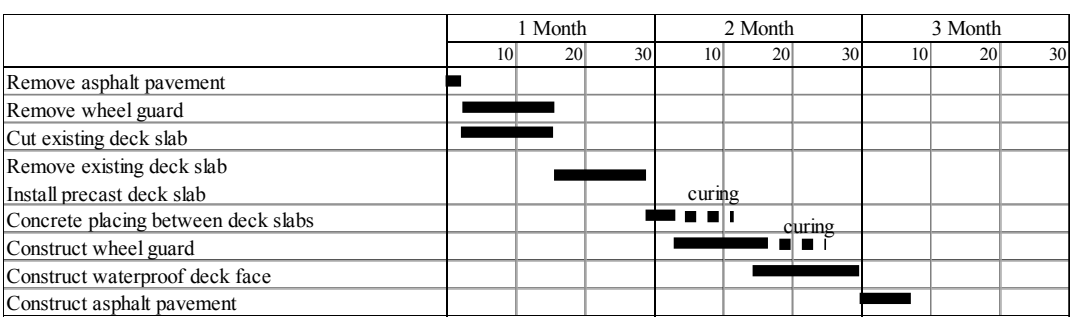

Fig. 6. Construction work schedule

6.2. Removal of existing deck slab and erection of precast PC deck slab

Removal of the existing deteriorated deck slab was performed by cutting the existing slab at regular intervals and then using hydraulic jacks to dismantle and remove discrete areas of the

existing slab from the main girder, as shown in Fig.8 After removing the existing deck slab, dowel bars and other rebars remaining on top of the steel girder flange surface were cut and removed, after which the surface was sanded and rustproofed, as shown in Fig.9, and the precast PC deck slab was erected. The replacement work continued by repeating the removal and erection procedures. Construction work started from the center of the bridge, as shown in Fig.7, and proceeded with the replacement by separating the work into two groups that moved toward both ends of the bridge (at about 8 m/day for each group). Figure 10 shows the precast PC deck slab erection.

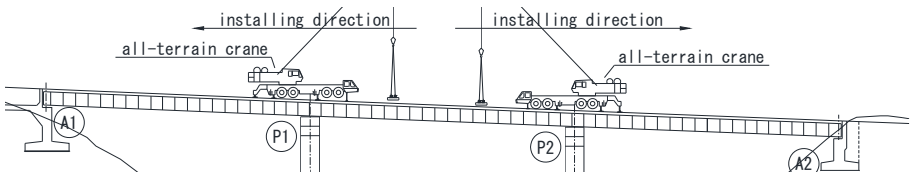

Fig. 7. Deck slab erection sequence

Fig. 8. Dismantling the existing slab

Fig. 9. Sanding and cleaning the girder top

Fig. 10. Deck slab erection

6.3. Precast PC deck slab and main girder joint

The precast PC deck slab and main girder joints were connected by stud dowels, as shown in Fig. 11. After erecting the precast PC deck slab, stud dowels were welded and the gaps between the slab and main girder were filled with mortar. After the mortar hardened, the stud dowel holes were then filled with concrete with the same compressive strength as the girder to join the deck and main girder together.

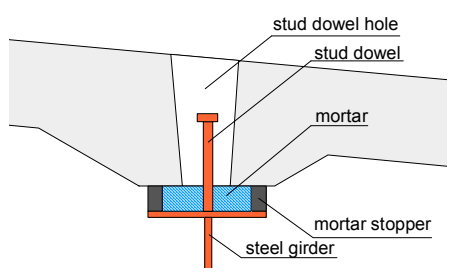

Fig. 11. Joining of the deck slab and girder details

7. Measures to improve durability

7.1. Edge treatment of the deck slab waterproofing layer

The edge of the deck slab waterproofing layer at the interface with the wheel guard is a region prone to water leakage if there is stagnant rainwater, so the waterproofing layer was extended to 30mm above the corner of the wheel guard, as shown in Fig. 12. Since the exposed section of the waterproofing layer uncovered by pavement tends to

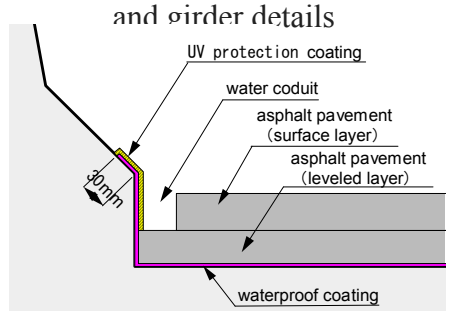

Fig. 12. Extent of deck slab waterproofing treatment

deteriorate due to ultraviolet rays, this section was protected by a durable coating material resistant against ultraviolet rays.

7.2. Concrete joint location at the wheel guard

If there is a concrete construction joint between the deck slab and the wheel guard near the bottom of the slope where water is likely to stagnate, there is a risk that water will leak from the concrete joint when the deck slab waterproofing layer has deteriorated in the future. Therefore, when constructing the precast PC deck slab, concrete was cast to form a raised area in the deck slab to join to the wheel guard and be a part of it, as shown in Fig.13. This raised the elevation of the concrete joint and thereby reduce the risk of water leakage.

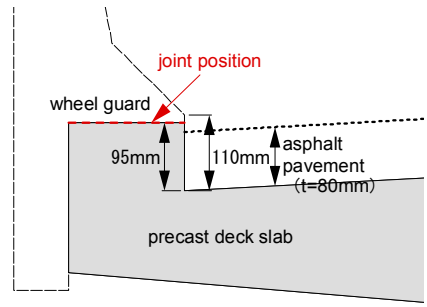

Fig. 13. Casting to join the deck and wheel guard

8. Conclusion

The Expressway Renewal Project is essential for sustaining Japan's infrastructure. We will continue to engage in renovation and repair and pursue more effective design and construction in the future to maintain these efforts over the long term.

Temperature Effect of CFG Composite Foundation in China Island Permafrost Region

Yongcheng Ji[1], Wei Li[2*], Yunfeng Ma[3*], and Yanmin Jia [4*]

[1] School of Civil Engineering, Northeast Forestry University, Harbin and China; email: yongchengji@outlook.com
[2] Department of Civil Engineering, University of Colorado Denver, USA; email: alice12383@126.com
[3] Chongqing Water Resources and Electric Engineering College, Chongqing and China; email: mayunfeng@163.com
[4] School of Civil Engineering, Northeast Forestry University, Harbin, China; email: yanminjia2008@126.com

[*]: corresponding author

Keywords: island permafrost region; cement fly-ash gravel (CFG) composite foundation; heat exchange; concrete raft; CFG piles

Abstract: Freezing and thawing circulation mainly cause the deterioration of subgrade soil performance in permafrost region, especially in the island permafrost region. With the advantage of the high construction speed, low cost, and the advantages of high carrying capacity, Cement Fly-ash Gravel (CFG) composite foundation is an effective method to strengthen the subgrade soil integrity in the permafrost region. Generally, the CFG composite foundation mainly consists of two parts: concrete raft and CFG piles. Based on the island permafrost region field test in Yisui expressway (China), this paper explains the behavior of heat exchange between the CFG composite foundation and frozen soil. Several temperature sensors are embedded to measure the temperature variation of the concrete raft, CFG piles, and frozen soil among CFG piles. The concrete raft temperature is simulated by finite element software ABAQUS, and concrete hydration heat is considered. The model analysis result shows that the concrete raft is sensitive to the field temperature vary due to the thin thickness. CFG piles concrete pouring also influences original frozen soil temperature. Furthermore, the CFG composite foundation settlement is monitored during temperature varies. Compared with the settlement differences before and after CFG composite foundation construction, the interaction between frozen oil and CFG piles is explained. This research indicates that CFG composite foundation, effectively minimizing the impact of the settlement, can be applied to subgrade treatment in the island permafrost region.

1. Introduction

With the development of infrastructure construction in recent years, more and more researchers focus on the foundation treatment in the permafrost region. Pile foundation is playing an important role on the poor geological condition treatment, especially seasonal frozen soil exists in the island permafrost region. Seasonally frozen soil is very sensitive to temperature, and the long-term strength is far lower than the instantaneous strength. The frozen soil freezing and thawing cycle mainly causes non-homogeneous deformation of soils in permafrost region, especially in island frozen zone. This phenomenon leads to elevation of ground is not always

consistent in the changing of the seasons, which serious influences stability of highway foundation construction. With the advantages of the high construction speed, low cost, and high carrying capacity, CFG (Cement Fly-ash Gravel Pile) composite foundation is widely used in structure poor foundation treatment. CFG composite foundation system contains CFG piles, concrete raft, and frozen soil interlayer. The compression pressure provided by CFG pile can effectively resist frozen soil deformation. The Concrete raft is used to connect all CFG piles into integration that greatly reduced the uneven sedimentation for frozen soil subgrade. All these technologies can effectively solve the stability of foundation in the permafrost region.

2. Field Experimental Program

Pile foundation mechanics analysis has made many achievements, such as the mathematical model, the numerical simulation method, and experimental test research. However, most researches focus on pile foundation linear and nonlinear static analysis, and little research considers pile-soil temperature analysis, especially CFG composite foundation temperature analysis.

2.1. Experimental Concrete Raft Temperature Field

In order to understand the temperature impact during CFG pile composite foundation construction period, one island frozen soil sections are selected, which located in Yisui expressway. In these sections, the high adhesive strength of CFG pile composite foundation is innovatively used to deal with island-frozen soil. Yisui CFG pile composite foundation design figure is shown in Figure 1. This research measures the temperature of CFG piles and frozen soil interlayer during one freezing and thawing cycle, and also CFG piles settlement is monitored. The CFG pile is 6 m length by 0.4 m diameter, and space between two piles is 1.2 m. Vibration settling tube filling is used in field pile construction.

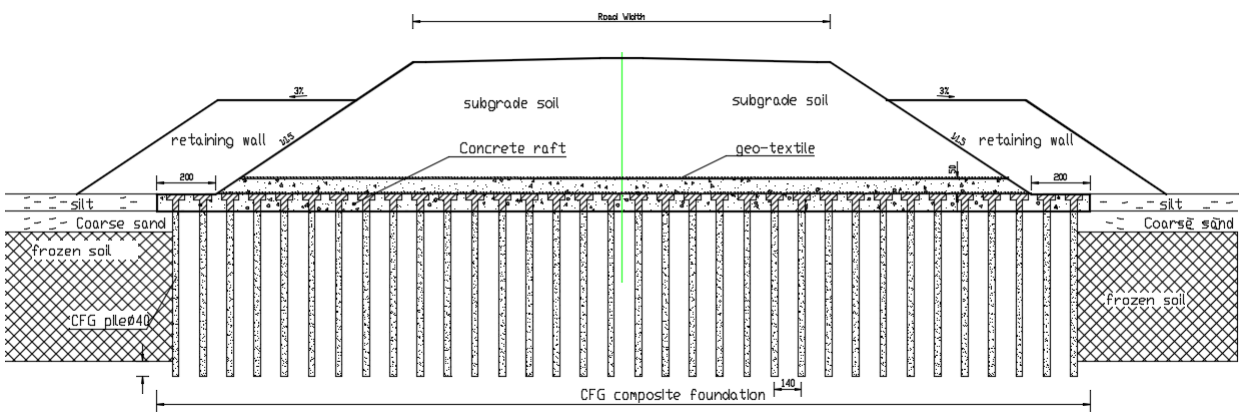

Fig. 1. CFG composite foundation (Unit: cm)

Each concrete raft connects with 16 CFG piles, and a 0.05m CFG pile length is penetrated into a raft to guarantee the rigid connection. Because of symmetric features, this research set 14 test points in a quarter raft and the arrangement diagram is shown in figure 2. During casting the concrete, the temperature is monitored every 1 hour until peak value is reached, and then measured every 2 hours from peak value time to 7 days concrete curing time. The ground surface

temperature range is between 6 ℃ and 10 ℃ based on the temperature data collection. The concrete raft mold temperature is 18.54 ℃ when casting the concrete.

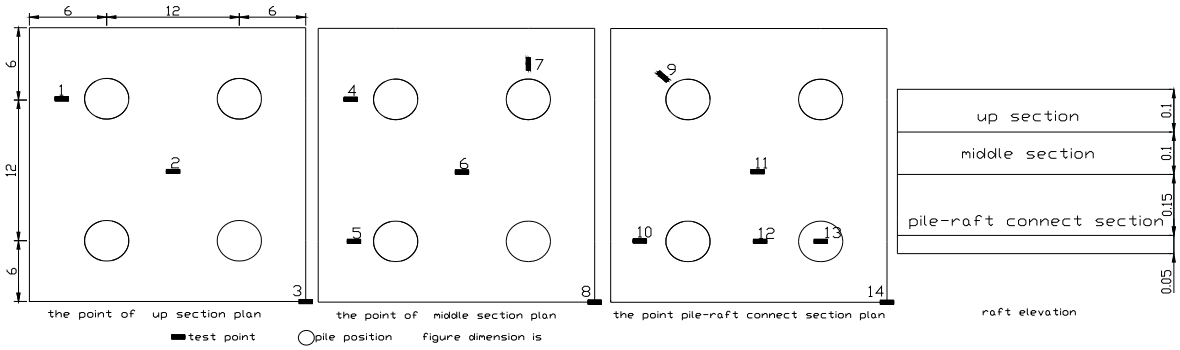

Fig. 2. Raft-pile interface test point arrangement diagram (Unit: m)

2.2. Experimental CFG Piles Temperature Field

Based on the geological survey data and monitoring needs, five temperature sensors are embedded into CFG pile and frozen soil, respectively. Frozen soil temperature sensors located in the central layer of soil and interface of two layers soil, and CFG pile temperature sensors located in the same elevation as frozen soil temperature sensors. These two types of temperature sensors are monitored temperature up to one year, and detail information shows in figure 3.

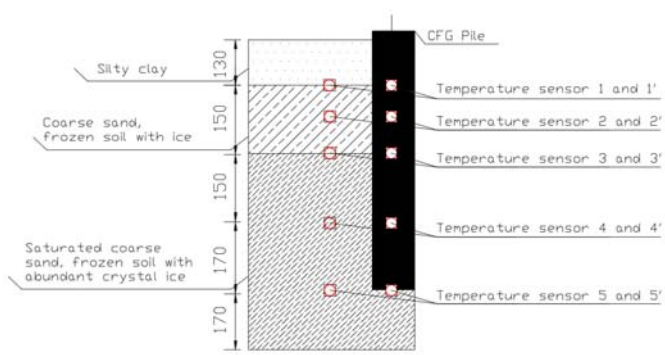

Fig. 3. Temperature sensors layout in CFG pile and frozen soil (Unit: cm)

2.3. Theoretical Temperature Field

Concrete hydration heat is a transient heat transfer process, and the transient heat conduction differential control equation can be expressed as (Zhang et al. 2008; Zheng et al. 2009):

$$\frac{\partial T}{\partial \tau} = a\left(\frac{\partial^2 T}{\partial x^2} + \frac{\partial^2 T}{\partial y^2} + \frac{\partial^2 T}{\partial z^2}\right) + \frac{\partial \theta}{\partial \tau} \tag{1}$$

where T is the temperature; a is conductivity temperature coefficient; τ is time; θ is adiabatic temperature rise. Heat transfer equation establishes the relationship among temperature, space and time in the objects. In order to get a solution of heat transfer equation, the corresponding initial conditions and boundary conditions need to be determined. The initial condition is the initial instantaneous temperature distributed in the object internal. Contact boundary condition

between the concrete surface and ambient air can be described by the third boundary condition (Zhang et al. 2005):

$$T(x,y)\big|_{\tau=0} = T_1 \tag{2}$$

$$-\lambda \frac{\partial T}{\partial n} = \beta(T - T_a) \tag{3}$$

where λ is a coefficient of thermal conductivity; n is outside surface normal direction; β is surface heat emission coefficient. Considered the different heat transfer way among the raft, air, and ground, the different coefficient of thermal conductivity is used. A finite element program (Abaqus) is used to simulate the concrete raft temperature effect, and a quarter of raft (24 m by 24 m) is selected due to symmetric. The concrete raft casting temperature field is transient and solves it by implicit analysis.

3. Result and Discussion

3.1. Concrete Raft Temperature Field Analysis

The center part of the concrete raft temperature mainly depends on concrete casting temperature and cement hydration heat in adiabatic conditions. Due to center concrete heat dissipation is the slowest and lower influenced by outside when compared with other locations, and it can well reflect the distribution of concrete hydration heat temperature. Figure 4 (a) gives the relationship of the raft center test point 8 (figure 2) between Abaqus simulation and field measuring value. The temperature data simulation has a good agreement with actual monitor temperature. The concrete temperature fluctuations appear the peak temperature value in 28 hours, and have a declining tendency in the next 140 hours. It can be divided into two stages from the temperature curve. The first phase is a powerful reaction stage from 0 to 100 hours, and the combined effect of concrete casting and cement hydration heat caused higher temperature. The second phase is a steady stage from 100 to 170 hours, and turned to a slow heat dissipation process until close to atmospheric temperature. The concrete heat dissipation mainly occurs between raft top surface and atmosphere. Thus, test points 3, 8, 14 (figure 2) are selected to analyze the relationship of the concrete temperature field between the raft and atmospheric temperature, and the results are showed in Figure 4 (b). The test point 3 thermal disturbances are highly influenced by atmospheric temperature, and point 8 influenced by atmospheric temperature is smaller. The test point 14 basic have no influence from atmospheric temperature. After 18 hours from poured concrete, the temperature of test point 3 decreases obviously, and then it appears a rising process, and the peak temperature is 24.57 ℃. Based on basic heat conduction fundamental law, the test point 14 is 0.05 m higher than the ground surface, which means a quantity of heat from internal concrete through the thermal transfer way transfer to the foundation that contact with the raft. The concrete temperature nearby test point 14 show a downward trend and no apparent temperature peak is observed. Test points 12, 13, and 14 (figure 2) are selected to study the pile raft interface and its surrounding temperature field, as shown in Figure 5 (a). Due to heat transfer rates varies for different materials, the pile raft interface temperature is lower than its surrounding frozen soil temperature in the whole experiment stage. After concrete cast, the pile raft temperature interface has declined in 12 hours, and the trend tends to slow. Similarly, the test point 13 temperature is similar as its surrounding temperature, but the temperature fluctuations amplitude of the test point 13 is higher than test point 12 and 14. The biggest temperature

difference between CFG pile and raft occurred in 12 hours after concrete poured. Figure 5 (b) also elucidate the temperature of point 14 and 12 almost the same, but the temperature of point 13 is lower than point 12 and 14 at this time from pile-raft interface model.

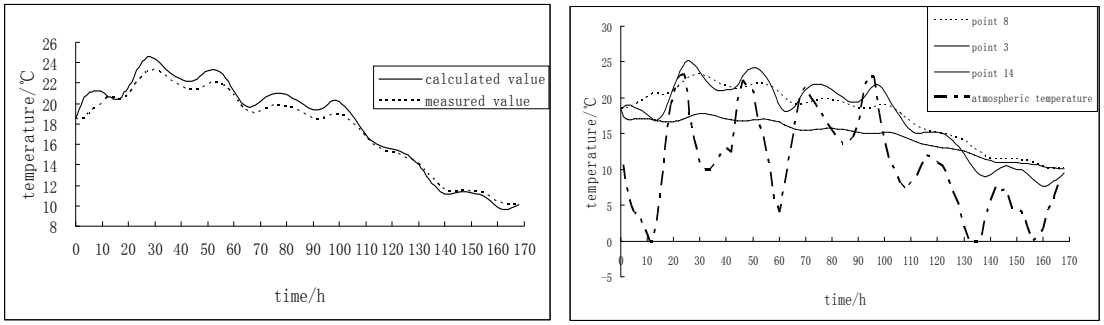

(a) (b)

Fig. 4. Temperature Data: (a) Raft Center point; (b) Concrete Raft and Atmospheric

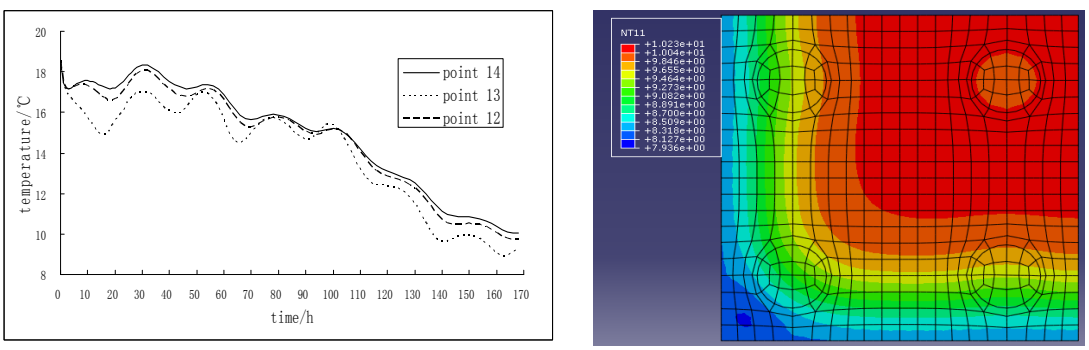

(a) (b)

Fig. 5. Pile-raft interface temperature: (a) temperature curve for test point 12, 13, and 14; (b) Abaqus pile-raft interface model at 12 hours

3.2. CFG Piles Temperature Field Analysis

In order to represent a freeze-thaw cycle, four time nodes are selected to collect temperature data, which are 1). Initial condition; 2). CFG piles casting complete on August 3, 2009 (frozen soil thawing condition); 3). Permafrost frozen soil under the freezing condition on January 5, 2010; 4). The CFG pile composite foundation fills complete on August 3, 2010 (frozen soil thawing condition). All the monitoring temperature data are shown in figure 6.

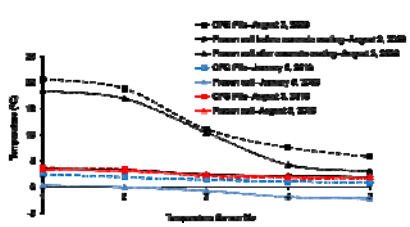

Fig. 6. CFG Pile and Frozen Soil One Cycle Temperature Data

Figure 6 shows the frozen soil temperature increases rapidly before and after CFG piles casting (August 3, 2009). The reason is mainly caused by high initial concrete temperature (25 ℃) and concrete hydration heat. The frozen soil transferring from thawing state to frost heave state causes frozen soil volume expansion, and vice versa. Temperature stress between pile and soil is gradually disappeared with the decreasing of temperature difference. Based on Composite modulus method (Li et al. 2007), the theoretical value of final deformation in subgrade soil is 6 mm, and the measured deformation of CFG pile composite foundation for one year is 4 mm, which meets the design requirements.

4. Conclusion

By monitoring a freezing and thawing cycle in CFG pile composite foundation, it can be concluded that the bearing capacity of the CFG pile is mainly depended on the pile side friction under the influence of temperature. CFG pile negative friction force is an upward force that prevents deformation between soil and pile. The lateral deformation of CFG pile is also restricted by piles-raft interaction, which leads to soil vertical deformation decrease. The established of FEA raft-pile model can simulate the actual temperature field very well, and provide the evidence for temperature control. The raft concrete temperature highly depends on outside temperature because of relatively thin thickness. Raft top section mainly provides a heat transfer platform for inside concrete, and temperature varies keeps consistent with atmospheric temperature. Although temperatures of pile-raft interface lower than its surrounding, the variation of amplitude is larger. All these observations explain the heat transfer process in the CFG pile composite foundation system.

5. References

Zhang, Y.X. and Huang, D.H. 2008. Solution precision of concrete temperature fields with finite difference method, Journal of Shanghai University, 1, 16-56

Zheng, H.Y. and Qin, Z.G. 2009. Application of ABAQUS in computing temperature field and creep thermal stress field of concrete, The China science and technology paper online, 2, 1-10.

Zhang, L.L. and Zhao, L. 2005. Temperature Field Finite Element Analysis of Pier Concrete, Journal of Chongqin University, Chongqing, 3, 1- 5.

Li, P.Y. and Wu, W.J. 2007. CFG pile composite foundation settlement calculation method analysis, Journal of Shanxi architecture, 5, 2-6.

FRP Composites

Bridge Engineering Institute Conference 2019 (BEI-2019)
Honolulu, Hawaii, USA, July 22-25, 2019

The Seismic Retrofit of the Dog Creek Bridge Using Both Steel and Advanced Composites Materials

Scott F. Arnold[1*]

1 Fyfe Co. LLC, San Diego, USA; email: sfarnold@aegion.com

[*]: corresponding author

Keywords: composite casing; steel jacket; fiber reinforced polymer

Abstract: The Dog Creek Bridge is located along Interstate 5 in Shasta County, California within the Shasta-Trinity National Forest. The open-spandrel concrete arch bridge is 682 feet long and the longest span is 299.9 feet. It was built in 1956 and then rehabilitated in 1989. In the summer of 2017 the bridge received a seismic retrofit that incorporated both conventional materials (e.g. concrete and steel) and advanced composite materials (i.e. carbon fiber reinforced polymers). The design and detailing were prepared by the California Department of Transportation. The retrofit included large elliptical steel jackets for the rectangular columns and then incorporated a carbon fiber reinforced polymer to strengthen the arch ribs. Construction access was provided by suspended stages from the deck above creating a unique working platform suspended above the forest below. This paper will review the spirit of the design, the various techniques employed and the construction challenges that were overcome. Special attention will be given to the pros and cons of using steel jackets as compared to advanced composite jackets on reinforced concrete, as determined by full and large-scale structural testing.

1. Introduction

There are many ways to retrofit reinforced concrete structural elements. Traditionally these members (e.g. columns, beams, arch ribs) were retrofitted by providing additional steel reinforcing and concrete to the existing structure. In the late 1980's the University of California at San Diego began to test and validate the use of steel jackets to retrofit bridge columns. These tests were quite successful and started to be implemented by Caltrans fairly quickly. One of the problems with the steel jackets was that they could not achieve the required performance goals for rectangular sections without changing the section shape to be elliptical or circular. The research and development at UCSD, in conjunction with Fyfe Company, immediately began to investigate the use of advanced composite materials as an alternate to steel jackets. Many advantages were realized but one of the main reasons was the ability to keep the existing section shape. This was especially important to maintain the aesthetics of arch bridges such as the Dog Creek Bridge.

2. Steel Jackets

Due to the size of the approach columns (4-ft x 8.5-ft) and their location (See Figures 1, 2 & 3), Caltrans determined that they would use the steel jackets. The combined weight of these jackets was approximately 93,500 lbs (42,411 kg) and each section required a crane to get them into place (See background of Figure 3 below). The jacket segments must then be welded together prior to having the space between the existing column and the steel jacket fully grouted.

Fig. 1 & 2: Installed Steel Jackets on the Approach Columns with Welded Seams

Fig. 3: Project Overview

3. Advanced Composite Jackets

The advanced composite jackets, often referred to by Caltrans as Composite Casings, were composed of high-strength carbon fiber sheets saturated with an epoxy matrix. The carbon fiber reinforced polymers (CFRP) were able to be transported by hand to the suspended scaffolding without the need for heavy equipment. The system is unidirectional and is built up in layers to achieve the final design thickness. The final installed thickness for this project was approximately 3/8" (9mm). Once the jacket is installed and allowed to cure for approximately 24-hours, two-coats of paint are applied to provide the required color (See Figures 4 & 5). A special anchorage detail was required to develop the system where the CFRP jacket was interrupted by the spandrel columns that connect to the arch rib.

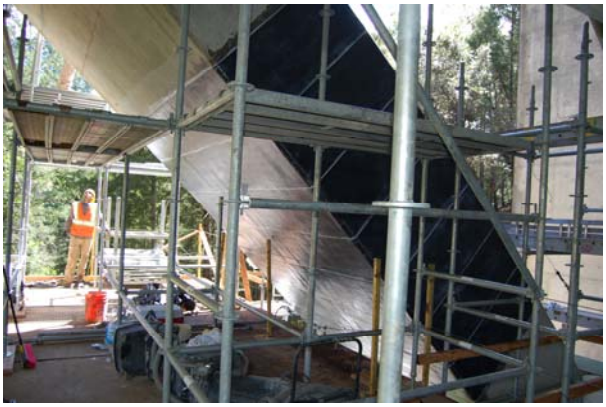


Fig. 4 & 5: Installed CFRP on the Arch Ribs

4. Conclusions

The Transportation Research Board recently released a study on materials such as fiber-reinforced polymer composites and high-performance concrete, concluding that they have been able to reduce infrastructure life-cycle costs and decrease construction times. The Federal Highway Administration's Innovative Bridge Research and Construction Program found that, because of those benefits, the materials are increasingly gaining acceptance within state highway bridge programs. The Dog Creek bridge is a great example of the use of both conventional and advanced technologies to address seismic deficiencies. The goal of the project was to achieve these performance goals while maintaining the aesthetics of the bridge and minimizing the disruption to the sensitive environment. The total cost of the project was approximately $1.3 million USD.

5. References

Transportation Research Board, 2019. Performance of Bridges That Received Funding Under the Innovative Bridge Research and Construction Program, A report of the National Academies of Sciences, Engineering, and Medicine.

Priestley, M.J.N, Seible, F., July 1991. Seismic Assessment and Retrofit of Bridges.

Bridge Engineering Institute Conference 2019 (BEI-2019)
Honolulu, Hawaii, USA, July 22-25, 2019

Cyclic Loading Test of Flexural RC Member Embedding Bond-Improved High Modulus CFRP Rods

Hiroaki Hasegawa[1], Yoshiki Onari[2], Kodai Shimose[3], and Isamu Yoshitake[4*]

[1] Mitsubishi Chemical Infratec, Tokyo, Japan; email: hasegawa.hiroaki.ms@m-chemical.co.jp
[2] Yamaguchi Univ., Ube, Yamaguchi, Japan; email: OnariYoshiki@yucivil.onmicrosoft.com
[3] Yamaguchi Univ., Ube, Yamaguchi, Japan; email: ShimoseKodai@yucivil.onmicrosoft.com
[4] Yamaguchi Uni., Ube, Yamaguchi, Japan; email: yositake@yamaguchi-u.ac.jp

*: corresponding author

Keywords: CFRP rod; fatigue; cantilevered slab; bridge deck; strengthening

Abstract: The study aims at development of a strengthening technique using high modulus carbon fiber reinforced polymer (CFRP) rods for cantilevered bridge deck slabs subjected to wheel loads. The high modulus CFRP rods have little shear-resistant ribs, hence the bond performance in concrete is significantly low. The study improves bond strength by attaching glass fiber reinforced polymer (GFRP) ribs to the CFRP rod. The bond-improved CFRP rods have relatively small diameter even though the attachment of GFRP ribs, so it can be embedded even into general concrete cover (30-50 mm) by using high strength mortar. The advantage implies that near-surface mounted (NSM) technique is applicable for the strengthening with the high modulus CFRP rods. To simulate general cantilevered bridge decks, the study prepared 10 RC beam specimens of 160 mm thick. A pseudo negative bending test was conducted by using the reversed slab which embeds the CFRP rods. The study investigates failure mechanism and fatigue durability of the strengthened RC members subjected to cyclic loads. The result in the cyclic loading test achieved 2 million cycles in the practical load range. The study confirmed adequate high durability of the cantilevered RC deck slab strengthened with NSM-CFRP rods.

1. Introduction

Cantilevered deck slabs of highway bridges are frequently subjected to negative bending moment due to wheel and wind loads. Most of the cantilevered slabs in Japan is constructed as reinforced concrete (RC) structure. It is occasionally reported that the cantilevered RC slabs have been deteriorated in accordance with traffic cyclic loads. Near-surface mounted (NSM) technique using carbon fiber reinforced polymer (CFRP) is an effective strengthening method for such damaged RC members (Yoshitake, et al. 2010). The NSM strengthening technique using CFRP rods, which have elastic modulus of 450 GPa or higher, can decrease deformation of the cantilevered slabs and stress of steel reinforcing bars in concrete. High modulus CFRP rods are generally manufactured by PULTRUSION method. Hence, it is hard to add shear-resistant ribs to surface of the CFRP rod. Most concern is the bond performance of CFRP rod without ribs. To improve bond performance of the high modulus CFRP rods, the authors have developed CFRP rods having ribs of glass fiber reinforced polymer (GFRP). Bond strength of the CFRP rods was examined in a pull-out test, and the NSM strengthening effect was confirmed in the static loading test using RC flexural members in our previous investigations (Hasegawa et al., 2016; Kuroda et al. 2016; Hasegawa et al. 2018).

The foci of this study are to investigate failure mechanism of the bond-improved CFRP rods in concrete subjected to cyclic loading, and to examine fatigue durability of the strengthened beam. This paper presents the fatigue properties of the cantilevered RC members embedding high modulus CFRP rods.

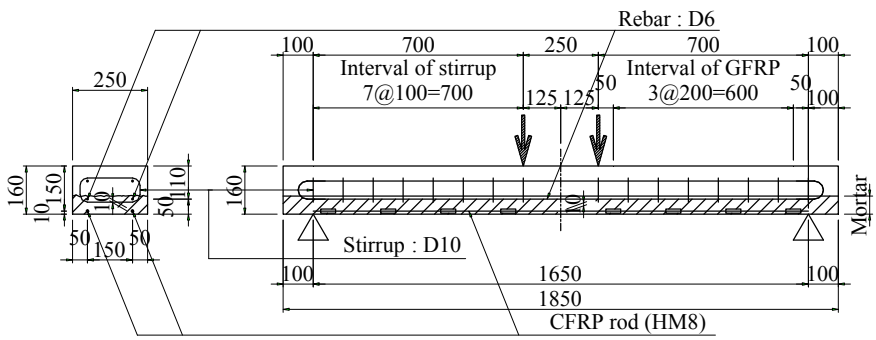

Fig. 1. Detail of beam specimen

2. Test procedure

2.1. Beam specimens

The study prepared 10 RC beams of 160 mm thick, the minimum thickness for bridge deck slabs in Japan. Dimensions of the beam were 160 mm thick x 250 mm width x 1850 mm long (Fig. 1). Two RC beams were the control specimen for static loading test, and four beams were used in the static and cyclic loading tests respectively. For the NSM-CFRP beam specimens, concrete cover of 50 mm was removed, the surface was glued with an epoxy adhesive as shown in Fig. 2 (b). Two CFRP rods were placed on the top-surface filled with high strength mortar as shown in Fig. 2 (c), (d).

2.2. Bond-improved CFRP rod

The study used high modulus CFRP rod of 8 mm diameter. To increase bond strength, GFRP ribs of 1.5 mm thick were attached to the CFRP rod with an interval of 200 mm or 300mm. The GFRP rib was tightly coiled around the rod without glue such as epoxy adhesive. The study prepared two sorts of GFRP ribs of 50 mm and 75 mm long. Fig. 2 (a) shows the CFRP rod with GFRP ribs.

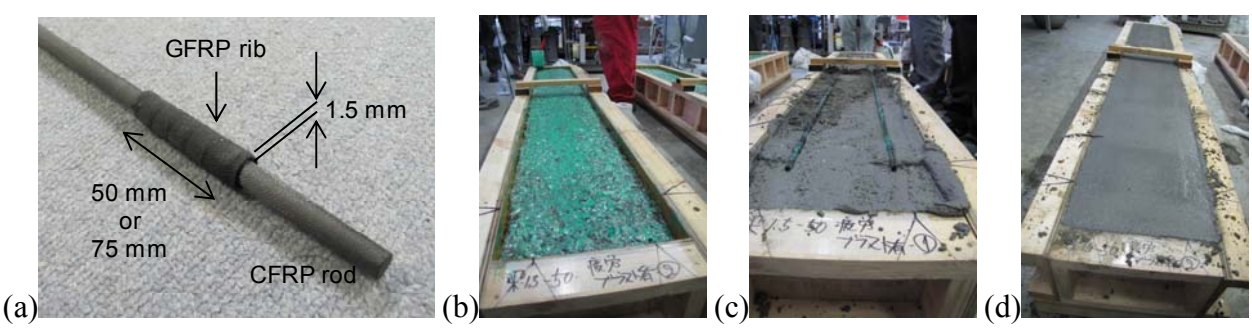

Fig. 2. CFRP rod and beam specimen: (a) CFRP rod with GFRP ribs; (b) epoxy-coated concrete surface; (c) CFRP ribs embedded into the covering mortar; (d) surface finish of covering mortar.

2.3. Loading program and test parameters

Fig. 3(a) shows schematics of cantilevered bridge deck slab and its simulated loading system. The beam specimens were designed to simulate rebar arrangement of the cantilevered deck, and were reversed for the flexural test. The pseudo negative bending test is presented in Fig. 3(b). Table 1 gives the loads in the cyclic loading test. The maximum load of 22.0 kN (F1) is the rebar allowable force calculated in accordance with Japanese design code.

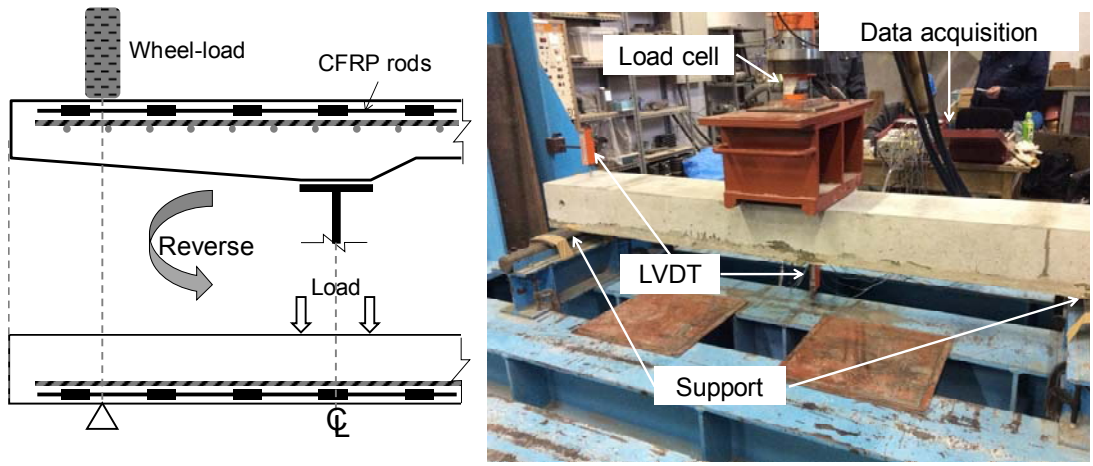

(a) (b)

Fig. 3. Loading method: (a) schematics of cantilevered deck slab; (b) flexural loading test

Table 1. Test parameters and results

No.	Specimen I.D.	Rib length / Interval	Max. load	Average	Max. deflection		Failure
S1	Control-1	-	15.4 kN	15.3 kN	9.68 mm		Flexure
S2	Control-2	-	15.1 kN		11.43 mm		Flexure
S3	GD-1.5-50	50 mm / 200 mm	65.8 kN	62.8 kN	8.80 mm		Flexure
S4	GD-1.5-50	50 mm / 200 mm	59.8 kN		7.71 mm		Flexure
S5	GD-1.5-75	75 mm / 300 mm	58.1 kN	60.4 kN	7.18 mm		Flexure
S6	GD-1.5-75	75 mm / 300 mm	62.8 kN		8.10 mm		Flexure
			Load (vs.P_s[a])		Cycles	P_{ps}[b]	
F1	GD-1.5-50	50 mm / 200 mm	6.28-22.0 kN (0.10-0.35)		$2x10^6$	67.8kN	Flexure
F2	GD-1.5-50	50 mm / 200 mm	6.28-47.1 kN (0.10-0.75)		$1.4x10^5$	-	Flexure
F3	GD-1.5-75	75 mm / 300 mm	6.04-36.3 kN (0.10-0.60)		$2x10^6$	64.8 kN	Flexure
F4	GD-1.5-75	75 mm / 300 mm	6.04-45.3 kN (0.10-0.75)		$2x10^6$	58.8 kN	Shear

a: load bearing capacity (average) in the static test; b: maximum load in the post-fatigue test

3. Test results and discussion

3.1. Fatigue durability

The study conducted the static loading test prior to the cyclic loading test. Table 1 summarizes the test results. The load bearing capacities (P_s) were 62.8 kN for GD-1.5-50 and 60.4 kN for GD-1.5-75, respectively. The loads (P_s) were significantly higher than the load bearing capacity (15.3 kN) of the control beam without CFRP rods.

The cyclic loading test results were also given in Table 1. Except for the test of F2, other fatigue loading tests achieved two million cycles. Note is that the cyclic loading test of F2 may not show the fatigue durability because the failure was due to the loading program.

3.2. Post-fatigue test

The static loading test was conducted by using the beams (F1, F3, F4) which achieved two million cycles of loading. The maximum loads in the post-fatigue test were almost equal to the load-carrying capacity in the static loading test. Upon completion of the post-fatigue test, the cover mortar was removed to observe the damage of CFRP rods with GFRP ribs. The visual inspection confirmed the failure of CFRP rod at the concrete crack, and the adequate bonding of GFRP ribs even after the cyclic loading of two million.

Fig. 4. Visual inspection: (a) removal of mortar; (b) failure of CFRP rod; (c) little bond-damage

4. Conclusions

This paper reported the cyclic loading test of the cantilevered RC members embedding bond-improved CFRP rods of high modulus. The conclusions of the study are summarized below:

(4) The static test confirmed the excellent load carrying capacity of the CFRP-strengthened beam.
(5) The cyclic loading and post-fatigue tests confirmed high durability of the cantilevered RC deck slab strengthened with NSM-CFRP rods.
(6) It was confirmed that GFRP ribs were firmly bonded to CFRP rod even after two million cyclic loadings.

5. References

Hasegawa, H., Hisabe, N., Kuroda, Y. and Yoshitake, I., 2016, Flexural behavior of a cantilevered RC slab strengthened with NSM CFRP rods, Proceedings of ACMBS-VII.

Hasegawa, H., Hisabe, N., Onari, Y. and Yoshitake, I., 2018, Improvement of mechanical shear resistance of high modulus CFRP rod with GFRP ribs, Proceedings of the 9th International Conference on FRP Composites in Civil Engineering.

Kuroda, Y., Hasegawa, H., Hisabe, N. and Yoshitake, I., 2016, Strengthening effect of a CFRP rod having ribs for a cantilevered slab, Proceedings of 6th International Conference of GEOMATE, 420-425.

Yoshitake, I., Kim Y.J., Yumikura K. and Hamada S. 2010, Moving-wheel fatigue for bridge decks strengthened with CFRP strips subject to negative bending, Journal of Composites for Construction, 14(6), 784-790.

A Numerical Investigation of a Hybrid GFRP-Concrete Beam under Static Loading

Zongjun Li[1], Amar Khennane[2*], and Paul Jonathan Hazell[3]

[1] School of Engineering and Information Technology, The University of New South Wales, Canberra, Australia; email: zongjun.li@adfa.edu.au
[2] School of Engineering and Information Technology, The University of New South Wales, Canberra, Australia; email: a.khennane@adfa.edu.au
[3] School of Engineering and Information Technology, The University of New South Wales, Canberra, Australia; email: p.hazell@adfa.edu.au

[*]: Corresponding author

Keywords: numerical analysis; hybrid structure; finite element model; flexural capacity

Abstract: The concept of combining two or more conventional materials into a hybrid structural system has been developed widely in bridge engineering applications. The optimal design of the combination can utilize the demand characteristics of each material in the place where they perform best in a hybrid system. This study presents a numerical investigation of a hybrid beam made of a rectangular hollow pultruded profile filled with concrete. A finite element model has been developed by using the commercial software ABAQUS to simulate the flexural behaviour of this hybrid beam under static loading condition. Two material models, one for concrete and the other for fiber-reinforced polymer, are employed to define the nonlinear response of the hybrid member. The bond properties based on the surface-base cohesive behaviour are implemented in this model. The numerical results including the load deflection curves and the flexural capacity are compared and verified with the experimental data from literature. The validated numerical model is used to analyse the sequence, propagation and development of the damage in this hybrid beam.

1. Introduction

The concept of combining different conventional materials into a hybrid structural system has been widely adapted in bridge engineering applications. The most commonly used conventional materials in hybrid structures are timber, steel, fiber reinforced polymers (FRP), and concrete. These materials are chosen for their inherent qualities such as strength, availability, cost, durability, and so on. An optimal design of the combination of these materials can utilize the desired characteristics of each material to perform to the best of its abilities in a hybrid system and achieves the criteria it was designed for. Among the conventional materials, FRP composite materials has been widely recognized as promising elements by the bridge industry. The use of FRP composites cannot only reduce the total weight but they also increase the overall durability of the structures. The latter makes them particularly suitable to be combined with other materials (Deskovic et al., 1995; Canning et al., 1999; Correia et al., 2007; Teng et al., 2007; Keller et al., 2007; Khennane, 2009; Chakrabortty et al., 2011; Ferdous et al., 2015; Satasivam and Bai, 2016; Sun et al., 2018).

The present study focusses on the design of a hybrid beam consisting of a rectangular hollow pultruded glass fiber reinforced polymer (GFRP) composites filled with concrete. The aim is to numerically investigate its suitability as a bridge girder by studying its flexural behaviour under static loading. A nonlinear finite element model (FEM) was developed and calibrated to analyse the experimental results from the literature (Ferdous st al., 2013). In particular, the FEM was used to reveal the cracking pattern and failure modes within the concrete hidden inside the pultruded profile.

2. Experimental program

To validate the numerical model of the hybrid GFRP-concrete beam, the experimental results reported in (Ferdous et al., 2013) are used. Three hybrid beams were cast with base-plates on both ends. These hybrid beams were tested along the weak axis under a four-point bending test to evaluate their flexural behavior. The total length of each beam was 2000 mm and the span length was 1440 mm. The schematic diagram of the experimental setup is shown in Fig. 1.

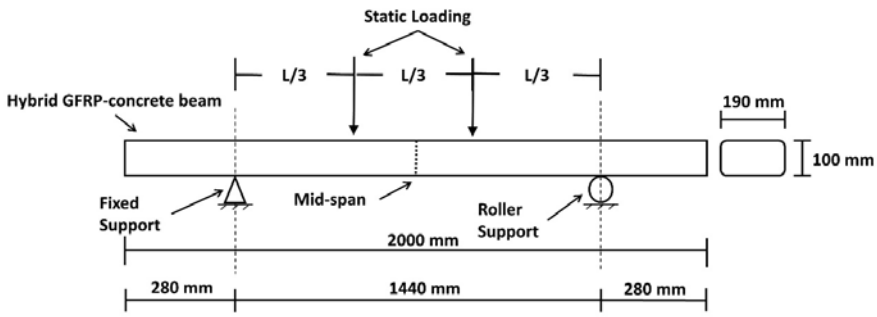

Fig. 1. Schematic diagram of the experimental setup (Ferdous et al., 2013)

3. Numerical anaylsis

A nonlinear FEM was developed using the commercial software ABAQUS to simulate the flexural behaviour of the hybrid GFRP-concrete beam. The linear eight-node three-dimensional solid elements and eight-node quadrilateral in-plane general-purpose continuum shell elements were used to model the concrete and the GFRP respectively. The concrete is modelled using the damaged plasticity (CDPM) model available in Abaqus. Damage initiation in the FRP is modelled according to the Hashin criterion also available in Abaqus. The detailed input parameters and materials' properties are shown in Table 1. The bond properties based on the surface-base cohesive behaviour are implemented in this analysis.

3.1. Numerical results

A comparison of the load-displacement curves between the numerical and the experimental results is illustrated in Fig. 2. The numerical result of the fully bonded FEM (without implementation of bonding cohesive behaviour) is also presented to compare. As shown, the ultimate failure load from the debonding model is 125 kN, and the ultimate failures from the experimental tests are 120, 111 and 115 kN. The relative differences is 8 % between the numerical and experimental results.

Table 1. Material properties and input parameters in CDPM and FRP

Materials' properties			Input parameters		
Concrete	E (GPa)	30.0	CDPM	β	38°
	ν	0.18		m	1
	f_c	57.0		f_b/f_c	1.12
	f_t	4.0		γ	0.666
FRP	E_1 (GPa)	28.9	FRP	X^T (MPa)	301.2
	E_2 (GPa)	3.5		X^C (MPa)	310.8
	G_{12} (GPa)	3.0		Y^T (MPa)	29.8
	ν	0.21		Y^C (MPa)	32.0
	ε_f	0.011		S^L (MPa)	33.0
	ε_c	0.013		S^T (MPa)	33.0
	G_{mt} (N/mm)	11.5		G_{ft} (N/mm)	55.0
	G_{mc} (N/mm)	11.5		G_{fc} (N/mm)	95.0

The flexural behaviour predicted by the debonding model is similar to the experimental one. The hybrid beam behaved in a purely elastic fashion until approximately 10 % of the total load, and then the response became non-linear until failure. As predicted in the numerical analysis, the failure of the beam was initiated at the center of the GFRP composites in the early loading stage. As the load continues, the shear cracks started to appear. The cracking patterns in the concrete were governed by the shear failure, and the cracks were following a diagonal direction from the bottom to the top surface. The ultimate failure of the beam occurred because of debonding failure at the interface between the concrete and the GFRP composites on the bottom side. This behaviour is reasonably simulated, and is in accordance with the experimental observations.

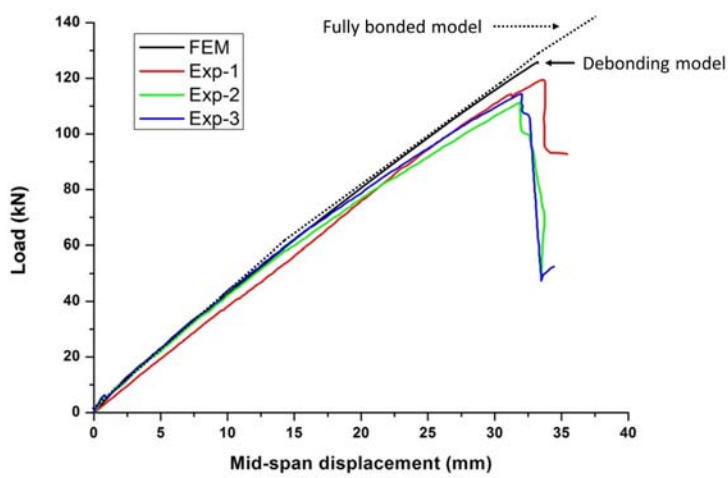

Fig. 2. Comparison between numerical and experimental results for load-displacement curves

4. Conclusion

In this study, the static flexural behaviour of the hybrid GFRP-concrete beam was investigated numerically in the commercial software ABAQUS. A nonlinear FEM was developed using the FRP progressive damage model and CDPM to simulate the static performance of the hybrid

beam. The numerical results, consisting of ultimate failure load, load-displacement curves and failure modes, presented a good and reasonable agreement with the experimental program. The sequence, propagation and development of the damage were well predicted in the numerical analysis.

5. References

Canning, L., Hollaway, L., and Thorne, A.M. 1999. Manufacture, testing and numerical analysis of an innovative polymer composite/concrete structural unit, Proceedings of the Institution of Civil Engineers-Structures and Buildings, 134**,** 231-241.

Chakrabortty, A., Khennane, A., Kayali, O., and Morozov, E. 2011. Performance of outside filament-wound hybrid FRP-concrete beams, Composites Part B-Engineering, 42**,** 907-915.

Correia, J.R., Branco, F.A., and Ferreira, J.G. 2007. Flexural behaviour of GFRP–concrete hybrid beams with interconnection slip, Composite Structures, 77**,** 66-78.

Deskovic, N., Triantafillou, T.C., and Meier, U. 1995. Innovative Design of Frp Combined with Concrete - Short-Term Behavior, Journal of Structural Engineering-Asce, 121**,** 1069-1078.

Ferdous, W., Khennane, A., and Kayali, O. 2013. Hybrid FRP-concrete railway sleeper, 6th International Conference on Advanced Composites in Construction. ACIC 2013, Sep 10th.

Ferdous, W., Manalo, A., Khennane, A., and Kayali, O. 2015. Geopolymer concrete-filled pultruded composite beams - Concrete mix design and application, Cement & Concrete Composites, 58**,** 1-13.

Keller, T., Schaumann, E., and Vallee, T. 2007. Flexural behavior of a hybrid FRP and lightweight concrete sandwich bridge deck, Composites Part A: Applied Science and Manufacturing, 38**,** 879-889.

Khennane, A. 2009. Manufacture and testing of a hybrid beam using a pultruded profile and high strength concrete, Australian Journal of Structural Engineering, 10**,** 145-155.

Satasivam, S. and Bai, Y. 2016. Mechanical performance of modular FRP-steel composite beams for building construction, Materials and Structures, 49**,** 4113-4129.

Sun, G., Chen, D., Wang, H., Hazell, P.J., and Li, Q. 2018. High-velocity impact behaviour of aluminium honeycomb sandwich panels with different structural configurations, International Journal of Impact Engineering, 122, 119-136.

Teng, J.G., Yu, T., Wong, Y.L., and Dong, S.L. 2007. Hybrid FRP-concrete-steel tubular columns: Concept and behavior, Construction and Building Materials, 21**,** 846-854.

Bond Behavior of FRP Bars in Air-Entrained Concrete

Sandor Solyom[1*], Anna Szijarto[2], and György L. Balázs[3]

[1] Department of Construction Materials and Technologies, Budapest University of Technology and Economics, Budapest, Hungary; email: solyom.sandor@epito.bme.hu
[2] Dept. of Const. Mat. and Technologies, Budapest Uni. of Technology and Economics, Hungary; email: anna.szijarto.bme@gmail.com
[3] Dept. of Const. Mat. and Technologies, Budapest Uni. of Technology and Economics, Hungary; email: balazs.gyorgy@epito.bme.hu

*: corresponding author

Keywords: bond; FRP bars; air-entrained concrete; test setup; surface profile

Abstract: An extensive experimental work has been performed to study the effect of air-entraining admixtures (AEA) on the bond behavior of FRP bars in concrete. The experimental program was designed to study the effect by using different test setups (traditional and modified pull-out tests), four concrete mix designs (range of compressive strength: 35 to 77 MPa) and FRP bars with different surface profiles (ribbed, indented, sand coated, and sand coated with helically wrapping), thus a whole overview of the AEA can be accomplished. Results along with the discussion are summarized in this paper. AEA slightly affects the bond behavior, while the bond failure mode is not affected. Due to the admixture, pours are formed at the FRP-concrete interface that reduces the bond strength depending on surface type and concrete strength. Furthermore, the test setup influences the bond strength, being generally lower in case of modified pull-out test.

1. Introduction

During the last decades the degradation of reinforced concrete (RC) structures has increased. Among the most important degradation induced factors are the corrosion of steel reinforcement and the concrete degradation due to the freeze-thaw cycles (Bertolini et al. 2014). To reduce the obsolescence of RC structures due to the corrosion of steel bars and the concrete degradation induced by freeze-thaw cycles, FRP reinforced air-entrained (AE) concrete appear as a promising solution (Nanni et al. 2014).

Fibre Reinforced Polymer (FRP) bars became an alternative to those of traditional steel as internal reinforcement of concrete structures especially when their corrosion resistance is of high importance. FRP bars show good mechanical properties and have low specific weight. AE concrete has increased resistance (Neville, 1995) against the freeze-thaw cycles due to the entrapped (equally distributed) pours. To ensure the composite behavior of FRP reinforced elements, proper interaction must be mobilized between the concrete and FRP bars. However, there is no study available on the effect of the additional pours induced by air-entraining admixture (AEA) on the bond behavior of FRP bars.

2. Experimental study

Two different small-scale pull-out test types (
Fig. **8**) were chosen to investigate the bond behavior of FRP bars in concrete, namely the traditional pull-out (P-O) test (i.e. ACI 440.3R 2004) and the modified, so called direct tension (DT) pull-out test (more details can be found in Sólyom et al. 2018).

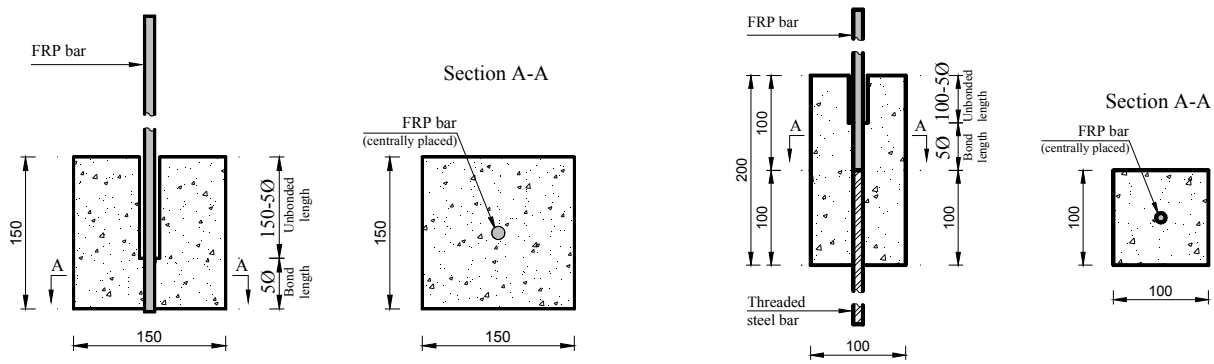

Fig. 8. Schematic representation of test specimen, dimensions are in mm: pull-out (left) and direct tension pull-out (right) test specimens (Sólyom et al. 2018). Dimensions are in mm.

2.2. Materials

Specimens with four different concrete compositions (Table 8) were prepared in laboratory. The concrete compressive tests were carried out on three cubic specimens (150 mm) (EN 12390-3 2009). The concrete average properties are summarized in Table **9**. BASF MasterGlenium C300 superplasticizer was used to set the consistency of concrete to flow class F4 (EN 12350-5 2009). As air-entraining admixture Sika Air-260 was applied.

Table 8. Concrete mix design for 1 m^3 (quantities are in kg)

Symbol	Cement (CEM II/B-S 42.5)	Water	Sand (0-4 mm)	Coarse aggregate		Air-entraining admixture
				(4-8 mm)	(8-16 mm)	
C1	300	195	824	366	641	0
C1A	320	189	793	352	617	0.48
C2	400	160	824	366	641	0
C2A	420	155	789	351	614	0.67

Table 9. Concrete compressive strength

Symbol	Average	St.dev.[a]	C.o.V.[b]
	(MPa)	(MPa)	(%)
C1	35.23	2.47	7.0
C1A	36.56	3.33	9.1
C2	76.77	8.48	11.1
C2A	72.95	7.17	9.8

[a]: Standard deviation
[b]: coefficient of variation

Fig. 9. Typical FRP bars applied in this study (Note: photos are not to the same scale)

Various types of FRP bars (Fig. 9) were used to study the effect of AEA on the bond behavior of FRP in concrete. Commercially available FRP bars with different surface types were chosen to be used in this study to investigate, if the AEA effect on bond strength changes with the surface profile. Bars with the following surface profile were applied: ribbed (Ri), indented (In), sand coated (SC) and sand coated with helically wrapping (SC+HW) (Fig. 9, from left to right). Additionally, bond tests were also performed on deformed steel bars as well, for comparison.

3. Experimental results

Experimental results for specimens prepared with C1 and C1A concrete mixes are summarized in Table 10, including the average bond strength ($\tau_{b,max}$), as well as the standard deviation (St.Dev) and coefficient of variation (C.O.V) of the individual results. Particularly, the bond strength is defined considering uniform bond stress distribution along the bond length. After failure specimens were split to analyze the bond failure mode, which is also reported in Table 10.

Table 10. Pull-out test results (C1 and C1A concrete mixtures)

Specimen symbol	Surface profile[a]	Nominal diameter	C1			C1A			Failure mode
			$\tau_{b,max}$	St.Dev[b]	C.o.V[c]	$\tau_{b,max}$	St.Dev[b]	C.o.V[c]	
		(mm)	(MPa)	(MPa)	(%)	(MPa)	(MPa)	(%)	
AB8	Ri_A	8	23.64	1.76	7.43	20.43	0.37	1.82	bar/concrete
AG12	Ri_B	12	15.13	1.32	8.73	14.86	1.87	12.59	bar/concrete
SG8	In	8	10.75	1.97	18.36	9.56	0.62	6.53	concrete
VG6	SC	6	26.51	1.07	4.03	22.33	1.01	4.52	bar surface
PG6	SC+HW	6	21.9	0.71	3.24	19.07	4.33	22.68	bar/concrete
PG8	SC+HW	8	19.36	2.14	10.60	16.12	1.31	8.14	bar/concrete
S6	Ri	6	13.06	0.56	4.28	12.41	1.13	9.10	concrete

[a]: Ri = ribbed; In = indented; SC = sand coated; SC+HW = sand coated and helically wrapped;
[b]: standard deviation; [c]: coefficient of variation;

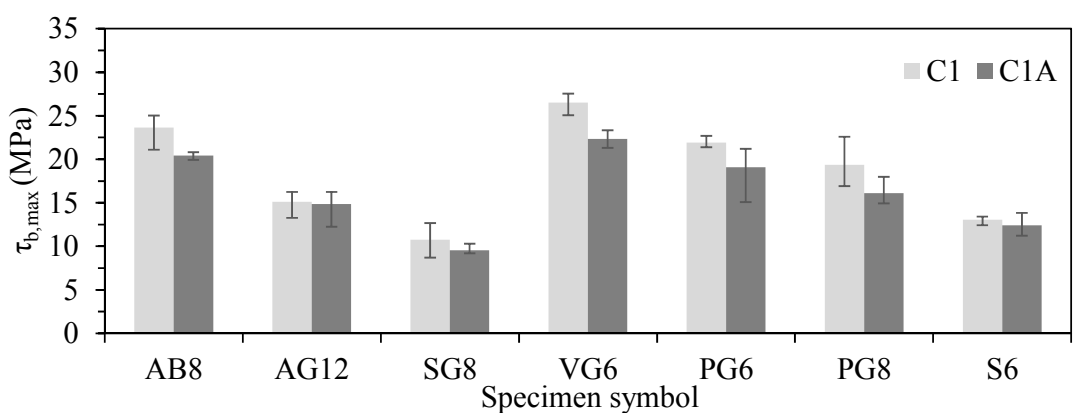

Fig. 10. Bond strength results: C1 and C1A concrete mixtures (for symbols see Table 10)

For better interpretation the results of Table 10 are reported in Fig. 10 as well. It is visible that due to the added AEA, the bond strength of specimens prepared with C1A are always lower than the ones with C1, however the average decrease is of low magnitude. In average, 7% and 10% of bond strength decrease is observed for C1-C1A and C2-C2A mixes, respectively. The most important decrease was observed for indented and sand coated with helically wrapping bars (Fig. 11). The effect of concrete strength increase on the bond strength is similar in concrete mixes with (C1A-C2A) or without (C1-C2) the AEA.

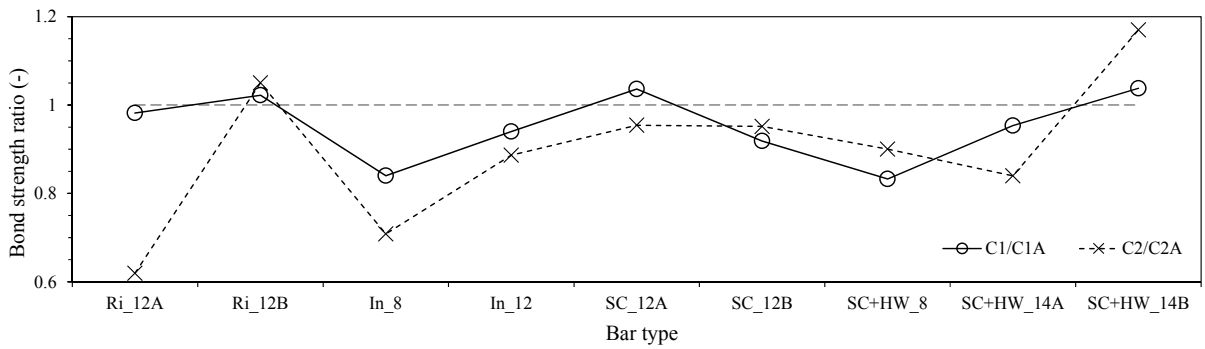

Fig. 11. Ratio between the bond strength results in normal and air-entrained concrete (Symbols: see Table 10)

4. Conclusions

In this paper an experimental program to study the effect of air-entraining admixtures (AEA) on the bond behavior of FRP bars in concrete is presented. To achieve a proper overview of AEA effect different test setups (traditional and modified pull-out tests), four concrete mix designs (range of compressive strength: 35 to 77 MPa) and FRP bars with different surface profiles (ribbed, indented, sand coated, and sand coated with helically wrapping) were applied.

Based on the results of the experimental work, it can be concluded that AEA does slightly affect the bond behavior of FRP bars. Owing to the AEA, pours are formed at the FRP-concrete interface that reduce the bond strength. In average, 7% of bond strength decrease is observed for C1 and C1A mixes, while 10% for C2 and C2A. In particular, the bond strength decrease due to the added AEA is the highest in case of indented and sand coated with helically wrapping bars. Furthermore, the test setup influences the bond strength, being generally lower in case of direct tension pull-out test. Finally, bond failure mode is not affected, all specimens failed by pull-out of FRP bars.

5. Acknowledgements

Supported by the ÚNKP-18-3 New National Excellence Program of the Ministry of Human Capacities.

6. References

ACI 440.3R, 2004. Guide test methods for Fiber-Reinforced Polymers (FRPs) for reinforcing or strengthening concrete structures, ACI Committee 440.

Bertolini, L. et al., 2014. Corrosion of Steel in Concrete: Prevention, Diagnosis, Repair Second Edi., Weinheim, Germany: Wiley-VCH.

EN 12350-5, 2009. Testing fresh concrete. Part 5: Flow table test.

EN 12390-3, 2009. Testing hardened concrete. Part 3: Compressive strength of test specimens.

Nanni, A., De Luca, A. & Zadeh, H., 2014. Reinforced Concrete with FRP Bars, Boca Raton, FL: CRC Press - Taylor & Francis Group.

Neville, A.M., 1995. Properties of concrete Fourth edi., Essex, England: Longman Group Ltd.

Sólyom, S., Di Benedetti, M. & Balázs, G.L., 2018. Effect of surface characteristics of FRP bars on bond behavior in concrete. ACI SP, 327, p.41.1-41.20.

Bridge Engineering Institute Conference 2019 (BEI-2019)
Honolulu, Hawaii, USA, July 22-25, 2019

Heavy CFRP Fabric Deployment for Repair of Impacted PC Bridge Girder on Interstate 64 in Kentucky

Abheetha Peiris[1] and Issam Harik[2*]

[1] Kentucky Transportation Center, University of Kentucky, Lexington, Kentucky USA; email: Abheetha.Peiris@uky.edu
[2] Department of Civil Engineering, University of Kentucky, Lexington, Kentucky USA; email: Harik@uky.edu

[*]: corresponding author

Keywords: CFRP retrofit; impact damage; PC girder; bridge repair; heavy fabric

Abstract: An exterior beam of a prestressed concrete bridge girder over Interstate 64 (I-64) in Kentucky was damaged due to an over-height truck impact. The damaged section spanned two of the three eastbound lanes of the highway. Several prestressing strands were cut-off and others were bent. In addition, shear reinforcing bars in the vicinity of the impact were cut-off. Heavy carbon fiber reinforced polymer (CFRP) unidirectional fabric was deployed to replace the load carrying capacity lost due to the severed prestressing tendons. The fabric, selected for flexural strengthening, has a capacity of 535 kN (120,000 lbs) per 300 mm (1 ft). U-wraps of tri-axial braided quasi-isotropic CFRP fabric (0°, $\pm$ 60°) was selected for shear strengthening and served as containment of crushed concrete in the event of future over-height impacts. The retrofit design is based on the capacity of the beam prior to the impact, following the impact, and following the retrofit. The manuscript will discuss in more details the evaluation of the impacted beam, the retrofit analysis and design, and the field repair stages.

1. Introduction

Damage to bridge beams from over-height truck impacts affects the safety of traffic on both the bridge and the roadway that passes beneath it. Damage caused by impacts includes cracking of beams, damage to reinforcement and/or prestressing strands, yielding of steel, spalling of concrete, and failure of joints and connections. Many traditional methods of repair and retrofit of RC and PC bridge girder damages can be costly and time-consuming due to the location of the damage and traffic impacts. Fiber Reinforced Polymer (FRP) materials have emerged over the last few decades as a reliable and effective method of externally strengthening bridge beams, especially concrete bridges. Among FRP materials, Carbon FRP (CFRP) has been the primary material used to repair and retrofit bridge girders impacted by over-height trucks. CFRP in the form of externally bonded CFRP (EB-CFRP) pultruded laminates and wet layup sheets/fabric has been used successfully to repair and strengthen bridges with impact damage. A recent National Cooperative Highway Research Program report (Harries and Miller, 2012) highlighted these methods of utilizing CFRP for PC bridge retrofit. The paper presents the field application of a heavy CFRP fabric of 757 g/m^2 (22.3 oz/yd^2) in multiple layers to retrofit an impact damaged PC I-girder.

2. Bridge and Damage Details

The impact damaged four-span PC I-girder bridge was built in 2011 on US 60 over Interstate 64 (I-64) in Clark County, Kentucky. The outside girder over eastbound I-64 was damaged by an over-height truck impact. The damaged section spanned the right two lanes of the four-lane eastbound interstate highway. The over-height truck impact produced some concrete spalling on the front side of the girder (Figure 1) and exposed 10 prestressing tendons within the girder's bottom flange. Seven prestressing strands were severed in the impact. The AASHTO Type VI Precast PC girder is 40.7 m (133' 6") long and 1.68 m (5' 6") deep. The prestressing steel is grade 270 low-relaxation steel of tensile strength 1860 MPa (270 ksi). The strands are 12.7 mm (0.5 in.) diameter with an area of 107.7 mm^2 (0.167 in^2). There are a total of 53 prestressing strands within the bottom flange of the girder, with the seven strands affected by the impact representing 13.2% of the total prestressing steel.

Fig. 1. Impact damage to bridge over I-64: (a) damage location over I-64, (b) front-bottom view

3. Retrofit Design

Following an inspection, the capacity of the girder before and after the impact damage was calculated based on AASHTO specifications (AASHTO, 2011). As the bridge was constructed in 2011, a load rating was carried out for an HL-93 design live load on the exterior girder of the bridge. The calculated AASHTO load rating and moment capacities, for both Inventory and Operating levels of service, for the undamaged and damaged girder are provided in Table 1.

Table 1. Girder details

Girder State	Moment Identification	Moment Capacity		FRP Stress (f_f/f_{fu})	Inventory Rating	Operating Rating
		kN-m	k-ft			
Undamaged	$M_{nO\text{-}AASHTO}$	16,920	12,480	-	1.11	1.44
Damaged	$M_{nD\text{-}AASHTO}$	14,781	10,902	-	0.85	1.10
Retrofit	$M_{nR\text{-}AASHTO}$	16,621	12,259	0.29	1.07	1.39
	$M_{nR\text{-}ACI}$	16,784	12,380	0.40	1.10	1.42

The chosen heavy unidirectional CFRP fabric, with a weight of 757 g/m^2 (22.3 oz/yd^2), had a design tensile strength of 2,344 MPa (340 ksi) and a manufacturer-specified tensile modulus of 139 GPa (20,200 ksi). Given the width of the bottom flange of the PC girder, two strips of fabric — each 305 mm (12 in) wide — were to be placed side-by-side on the underside of the bottom flange of the impacted beam. Additional 152 mm (6 in) strips were to be placed on the two vertical faces on either side of the bottom flange. Each strip was to have three layers of fabric. The CFRP fabric strips immediately in contact with the concrete spanned a total of 3.7 m (12 ft) along the beam bottom flange. Each subsequent layer was to be 914 mm (36 in) less in length than the layer beneath it and placed symmetrically over the preceding layer. U-wraps of tri-axial braided quasi-isotropic (0°,+/- 60°) carbon fabric were selected for additional shear strengthening and to serve as containment for crushed concrete in the event of future over-height impacts. The CFRP U-wraps are also expected to increase the capacity of the unidirectional heavy CFRP fabric strengthening system by anchoring the fabric ends.

4. Retrofit Analysis and Construction

To better study the behavior of the impacted exterior PC girder at the different stages (i.e., undamaged, damaged, retrofit), a moment-curvature analysis was carried out. First, analysis of the undamaged girder was carried out. For the damaged girder, the section properties were modified to account for the loss and change in centroid location of the prestressing steel. For the retrofitted beam, the section was further modified to include the CFRP material. The calculated retrofit moments calculated based on both AASHTO (AASHTO, 2012) and ACI (ACI, 2008) were found to be in good agreement with the analysis curve for the retrofit girder (Figure 2).

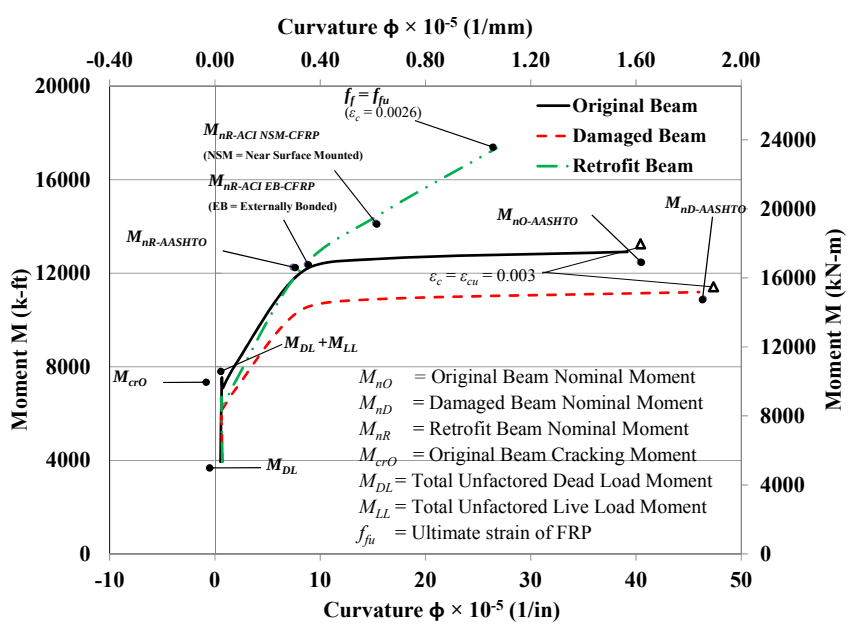

Fig. 2. Moment-Curvature analysis results

The retrofit work was carried out by a Kentucky Transportation Cabinet (KYTC) bridge maintenance crew using two man lifts. The first phase of the repair involved replacing the deteriorated concrete and returning the girder to its original shape. Once the first layer of unidirectional fabric was applied (Fig. 3.a), additional saturating epoxy was rolled onto the top of

the fabric prior to applying the subsequent layer of saturated heavy CFRP fabric. Following the application of the heavy CFRP fabric, the triaxial carbon fabric was applied using the same wet layup method (Fig. 3.b). Two days following the CFRP strengthening, after the saturating epoxy had sufficiently cured, a UV protective coating was applied over the retrofit area.

(a) (b)

Fig. 3. CFRP retrofit: (a) Application of heavy CFRP fabric layer, (b) Application of triaxial CFRP fabric U-wraps

5. Summary and Conclusions

An exterior girder of a PC bridge over I-64 in Kentucky was damaged due to an over-height truck impact. This paper discussed the retrofit design, which used heavy unidirectional CFRP fabric for flexural strengthening of the damaged bridge girder. Three layers of the heavy CFRP fabric were utilized to replace the capacity lost due to the impact damage. A moment-curvature analysis was carried out and the results compared with current design guidelines from AASHTO and ACI for flexural strengthening utilizing externally bonded CFRP. The personnel who carried out the retrofit construction did not encounter any difficulties handling and placing the heavy CFRP fabric. The retrofit was able to replace almost all of the moment capacity lost due to the impact damage.

6. References

AASHTO. 2012. Design of Bonded FRP Systems for Repair and Strengthening of Concrete Bridge Elements, 1st Edition, American Association of State Highway and Transportation Officials, Washington, D.C.

AASHTO. 2011. The manual for bridge evaluation, 2nd Edition, American Association of State Highway and Transportation Officials, Washington, D.C.

ACI Committee 440. 2008. Guide to the Design and Construction of Externally Bonded FRP Systems for Strengthening Concrete Structures, ACI 440.2R-08, American Concrete Institute, Farmington Hills, MI.

Harries, K.A. and Miller, R. 2012. Updated Research for Collision Damage and Repair of Prestressed Concrete Beams, NCHRP 20-07/Task 307, Transportation Research Board, Washington, D.C.

Development of Efficient Anchorage Systems for Flexural Strengthening of Concrete Bridge Planks using FRP Materials

Bahaa Al-Atta[1,2*], Robin Kalfat[3], Riadh Al-Mahaidi[4], and Alaa Al-Mosawe[5]

[1] Swinburne University of Technology, Melbourne, Australia; email: balatta@swin.edu.au
[2] University of Baghdad, Baghdad, Iraq
[3] Swinburne University of Technology, Melbourne, Australia; email: rkalfat@swin.edu.au
[4] Swinburne University of Technology, Melbourne, Australia; email: ralmahaidi@swin.edu.au
[5] Swinburne University of Technology, Melbourne, Australia; email: aalmosawe@swin.edu.au

[*] : corresponding author

Keywords: FRP; Concrete; Patch anchors; Bidirectional Fibers; Anchorage

Abstract: A widely-used method for flexural strengthening of reinforced concrete (RC) structures is the use of fiber-reinforced polymer (FRP) materials as externally-bonded reinforcement. FRP materials have several advantages over traditional materials in terms of their tensile strength, low cost, durability and ease of application. However, a commonly-documented failure mode of externally-bonded systems is premature FRP debonding. The aim of this study is to present a new FRP patch anchorage system, which can be used to mitigate the commonly-observed failure modes of intermediate crack-induced (IC) debonding. Although patch anchors have shown their effectiveness in suppressing FRP debonding when used in shear strengthening applications, this study explores their effectiveness in flexural strengthening. An experimental program is presented where this anchorage type is trialed, and its effectiveness is discussed

1. Introduction

Strengthening with fiber-reinforced polymer (FRP) materials has become one of the main methods used in repairing and retrofitting existing structures. Existing reinforced concrete (RC) structures built in the last century are showing deficiencies such as reinforcement corrosion, concrete degradation and damage resulting from aging. Further, population growth and heavier freight vehicles have increased both the traffic volume and vehicle weight bridges are required to carry, resulting in many becoming overloaded (Al-Mahaidi & Kalfat 2018). FRP materials can be used for strengthening different structural components for flexural, shear, torsion and axial loads. Despite the wide popularity of the use of FRP for strengthening purposes, the efficiency of RC members strengthened with FRP materials remains highly dependent on the bond properties between the FRP and the concrete. Various debonding failure modes may occur prior to the ultimate tensile strength of the FRP material being reached, including intermediate flexural or shear crack-induced (IC) debonding, end concrete cover separation, end interfacial delamination and shear-induced debonding (Kalfat, Al-Mahaidi & Smith 2013). In order to avoid premature failure mechanisms, design guidelines such as ACI 440.2 (2017) and the Concrete Society Technical Report No. TR55 (2012) place strict limitations on the maximum FRP strain which may be used in design. These strain limitations are typically 35-50% of the FRP fiber rupture strain for flexural strengthening and 10-25% in the case of shear strengthening (Kalfat, Al-

Mahaidi & Smith 2013), and represent a major under-utilization of the tensile strength characteristics of FRP materials (Zhang, Smith & Kim 2012). Improvement of the bond performance between the concrete and FRP using anchorage systems is an important area of research that addresses the limitations of FRP debonding. One anchorage system which has been used successfully for shear strengthening was developed by Al-Mahaidi & Kalfat (2011) and Kalfat and Al-Mahaidi (2012). It uses ±45° bidirectional fiber patches to anchor FRP laminates and suppress the end debonding failure mode. Patch anchors have been demonstrated to improve the efficiency of shear-strengthened members by 93-109% (Kalfat and Al-Mahaidi 2014)and have been implemented in large-scale shear strengthening projects including the West Gate Bridge project and the M80 Western Ring Rd in Melbourne, Australia. This paper investigates the efficiency of using patch anchors to suppress IC debonding of RC slabs strengthened using FRP in flexure. Although patch anchors have shown great effectiveness when used for enhancing the bond between the concrete and the FRP for beams under shear actions, there is a lack of understanding of the performance of these type of anchors for beams and slabs under flexure (Kalfat, Al-Mahaidi & Smith 2013).

2. Experimental Program

2.1 Specimen Design

The experimental program was developed in a way analogous to previous studies by Smith et al. (2011) on FRP anchors for comparative purposes. The specimens were six slabs 2700mm long x 400mm wide x 150 mm deep. Each slab was longitudinally reinforced with 2 x M10 mm diameter bars and 14 transverse tie bars of the same diameter. Three groups of slabs were developed with two specimens in each group. The first group was a control group consisting of two RC slabs, i.e. C-1 and C-2. The second group of specimens (S-1 and S-2) consisted of two RC slabs strengthened in flexure using two layers of FRP unidirectional fabric sheets totalling 100mm in width, 0.454mm in thickness (0.227mm per layer) and 2200mm in length. The third group of specimens (SA-1 and SA-2) involved two specimens of RC slabs strengthened using the same configuration as specimens S-1 and S-2, however four patch anchors were introduced. One specimen was anchored with bidirectional patch anchors (SA-1) while the other specimen was anchored with quad-directional patch anchors (SA-2). Each patch anchor was 400 wide x 300 mm long. Patch anchors were placed in protentional debonding zones. i.e. two patches at the ends of the FRP laminate and two patches below the point loads in the intermediate regions. Before applying the FRP sheets to the specimens, the RC slabs were sandblasted to improve the bonding properties. They were later cleaned of any remaining dust and debris using a brush and vacuum cleaner. FRP sheets and patches were cut to size and transferred to the location of application. Since only FRP fabric sheets were used in this series of experiments, a saturant type of epoxy was used to saturate both FRP sheets and patches. In the case of the anchored slabs, the patches were saturated and applied to the specimens in their pre-marked locations. Next, two layers of unidirectional FRP sheet were saturated and applied on top of the first layer of patches. A second layer of patches was impregnated and applied on top of the FRP sheets to sandwich them. The specimens were then left at room temperature for curing.

2.2 Test Set-up

A steel test frame was designed with special supports in order to perform the four-point bending tests upside down as depicted in Figure 1 below. This was to ensure that the tension side of the

specimens was facing upwards so that image correlation photogrammetry could be used to capture the strain distributions along the length of the FRP laminates. The steel reaction frames at each end of the specimen provided downward-acting reactions provided by horizontal steel crossheads connected to steel roller bearings. Both supports allowed for rotation and longitudinal movement during testing. The load was applied using a 500 kN MTS actuator connected to a steel plate bolted to the strong floor of the laboratory. The actuator was welded to a spreader beam that distributes the load to two-point loads spaced 800mm apart. When the frame was assembled and the slab was put on top of the spreader beam, there was a gap of 40 mm between the soffit of the slab and the supports. Hence, 40 mm of the stroke was used to lift the slab until it touched the supports. The rest of the stroke was used to apply the force on the slab. Strain gauges were installed on the tension side of the slab to measure the strain along the FRP sheets. Laser extensometers were used to measure the maximum mid-span deflection of the specimens.

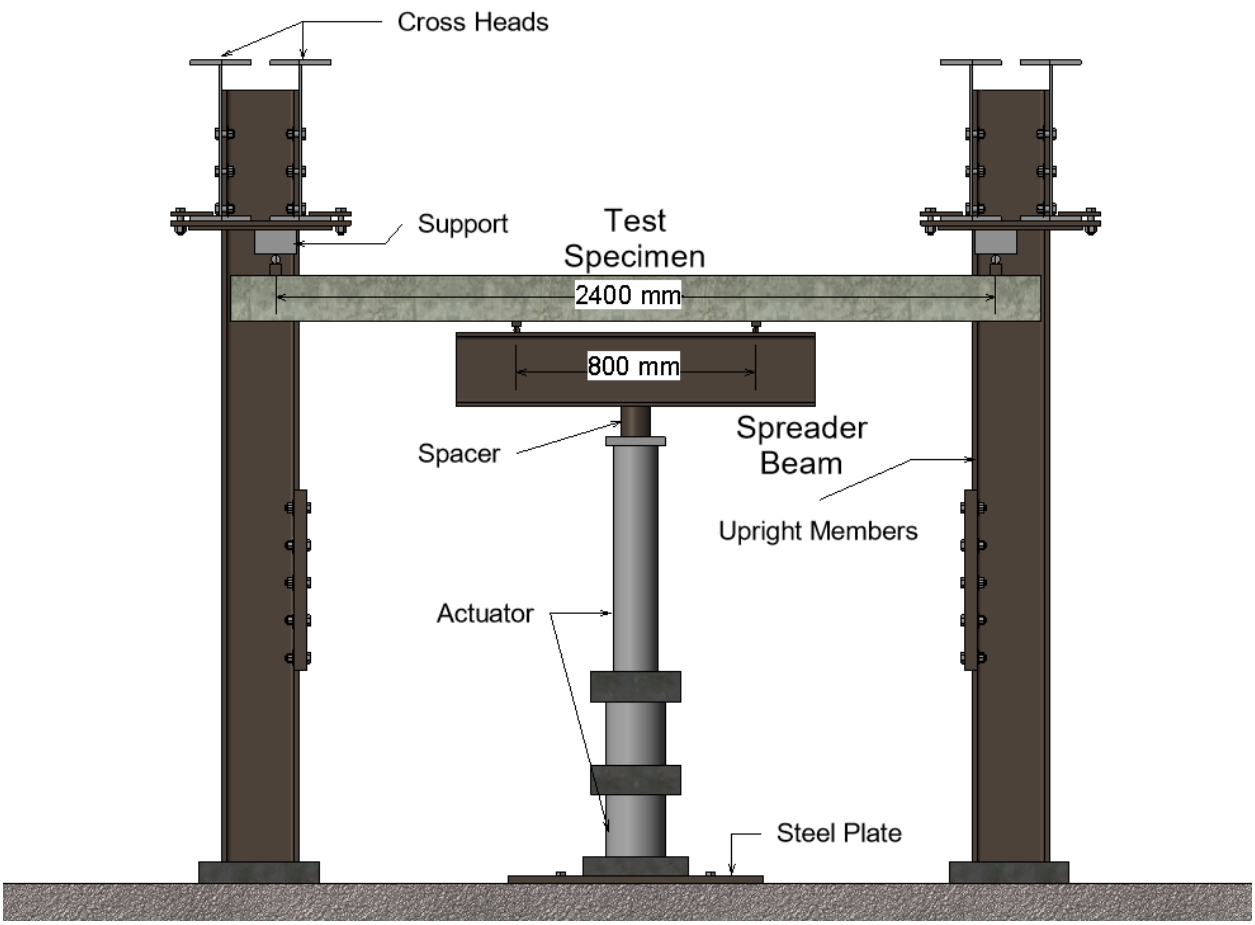

Figure 1. Test set-up

2.3 Material Properties

After the slabs were tested, cores were taken from the slabs to test the compressive strength of the concrete. Slabs C-1, C-2, S-1 and S-2 were found to have a compressive strength of 50 MPa, while slabs SA-1 and SA-2 had a compressive strength of 70 MPa. This discrepancy in concrete

strength was due to improper supply of concrete by the batching plant. The steel reinforcement bars had a tensile strength of 500 MPa an elastic modulus of 200000 MPa.
The unidirectional FRP sheets had a tensile strength and an elastic modulus of 4900 MPa and 230 GPa respectively, while the bidirectional FRP patches had a tensile strength of 3790 MPa and tensile modulus of 230 MPa. On the other hand, the quad-directional patches had a tensile strength of 4510 MPa and modulus of elasticity of 230 MPa. The tensile strength of the saturant epoxy was also tested and found to be 29.5 MPa, which is almost identical to the manufacturer's reported value of 30 MPa.

3. Results and Discussion

The RC slabs C-1 & C-2 exhibited ductile behavior and failed with a maximum load of 30 kN. The slabs continued to deflect beyond a displacement of 70mm but the test was stopped after 120mm as a sufficient level of deformation had been reached. The second group of slabs, S-1 & S-2, had stiffer load deflection curves. Both slabs exhibited IC mode failure, as shown in Figure. The FRP sheets debonded at a load of 60 kN and a deflection of 40 mm.

Figure 2. Mode of failure (Specimen S-2)

The slabs anchored with patch anchors, SA-1 and SA-2, showed better performance in terms of both ductility and load capacity. The patch anchors enhanced the performance of the strengthened slabs and delayed debonding failure. The load capacity and deflection increased to 78 kN and 58 mm respectively. Although the patches did not show any sign of debonding, the FRP sheets in the areas between the patches showed partial debonding (refer to Figure). The slabs finally failed by shear in the concrete. After the strengthened and anchored slabs failed, the load dropped back to the capacity of the unstrengthened specimen. However, the test was stopped at this point as the aim of the test was to measure the efficiency of patch anchors. Results have also shown that FRP strengthening and anchoring had impacted the cracking load of the slabs. The cracking load has increased from C-1 and C-2 to S-1 and S-2 reaching its maximum values in the anchored specimens, SA-1 and SA-2. The following figures and table summarize the results of this series of experiments

Figure 3. Mode of failure (Specimen SA-3)

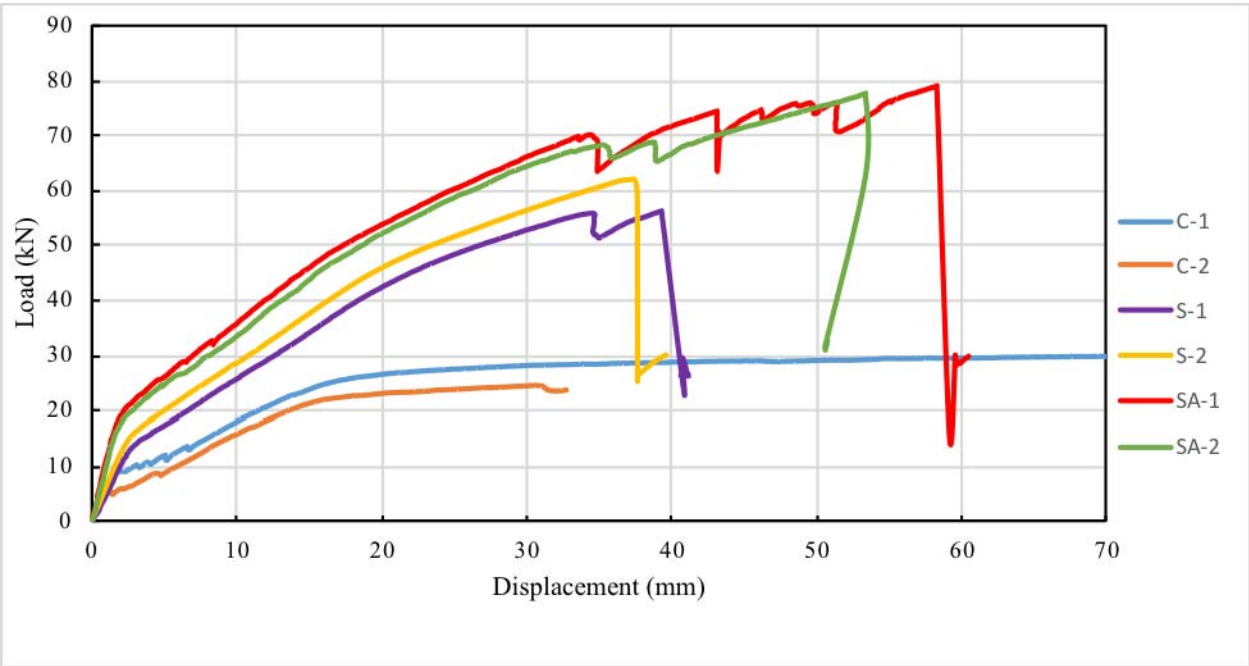

Figure 4. Load- deflection curves

Table 1. Summary of results

Slab	Peak Load (kN)	Cracking Load (kN)	Peak Strain (με)[a]
C-1	28.2	5.2	-
C-2	24.5	9.0	-
S-1	57.3	13.5	8000
S-2	63.2	15.4	8663
SA-1	79.5	20.0	11375
SA-2	77.0	17.5	11161

[a]: Peak deflection and peak strain were measured at point of peak load

4. Conclusion

The effectiveness of patch anchors in enhancing the ductility and load capacity of RC slabs strengthened with FRP sheets has been investigated in this paper. Patch anchors increased the load capacity and the maximum FRP strain by 25 % and 26 % respectively, compared with the unanchored specimens (S1 & S2). Both type of anchors, bidirectional and quad-directional patches, showed similar performance, with the bidirectional patches showing a little more ductile behavior. Both anchored specimens failed by a combination of shear failure leading to IC debonding in the vicinity of the shear crack.

5. Acknowledgment

The joint scholarship support provided to the first author by Iraqi Ministry of Higher Education and Scientific Research and Swinburne University of Technology is gratefully acknowledged. The authors wish to acknowledge the technical support provided by staff of the Smart Structures Laboratory of Swinburne University of Technology.

6. References

ACI 440.2R. (2017). Guide for the Design and Construction of Externally Bonded FRP Systems for Strengthening Concrete Structures, American Concrete Institute, Farmington Hills, Michigan.

Al-Mahaidi, R & Kalfat, R. (2018), *Rehabilitation of concrete structures with fiber-reinforced polymer*, Oxford : Elsevier.

Al-Mahaidi, R & Kalfat, R (2011), 'Investigation into CFRP laminate anchorage systems utilising bi-directional fabric wrap', *Composite Structures*, vol. 93, no.4, pp. 1265-1274.

Concrete Society Technical Report No. 55, Design guidance for strengthening concrete structures using fibre composite materials, Second Edition, The concrete Society, Surrey, UK, ISBN 1 904482 14 7 (2012).

Kalfat, R, Al-Mahaidi, R & Smith, ST (2013), 'Anchorage Devices Used to Improve the Performance of Reinforced Concrete Beams Retrofitted with FRP Composites: A State-of-the-Art Review', *Journal of Composites for Construction,* vol. 17, no. 11, pp. 14-33.

Kalfat, R, Al-Mahaidi, R (2014), 'Experimental investigation into the size effect of bidirectional fiber patch anchors in strengthening of concrete structures', *Composite Structures*, vol.112, pp. 134-145.

Smith, ST, Hu, S, Kim, S & Seracino, R 2011, 'FRP-strengthened RC slabs anchored with FRP anchors', *Engineering Structures*, vol. 33, no. 4, pp. 1075-1087

Zhang, HW, Smith, ST & Kim,SJ (2012), 'Optimisation of carbon and glass FRP anchor design', Construction and Building Materials, vol.32, pp. 1-12.

Strengthening of Concrete Bridge Girders with Concavely-Curved Soffit Using Fiber Reinforced Polymer

Khattab Al-Ghrery[1,2*], Robin Kalfat[3], Nazar Oukaili[4], Alaa Al-Mosawe[5], and Riadh Al-Mahaidi[6]

[1] Swinburne University of Technology, Melbourne, Australia; email: kalghrery@swin.edu.au
[2] University of Baghdad, Baghdad, Iraq; email: kalghrery@swin.edu.au
[3] Swinburne University of Technology, Melbourne, Australia; email: rkalfat@swin.edu.au
[4] University of Baghdad, Baghdad, Iraq; email: nazar.oukaili@coeng.uobaghdad.edu.iq
[5] Swinburne University of Technology, Melbourne, Australia; email: aalmosawe@swin.edu.au
[6] Swinburne University of Technology, Melbourne, Australia; email: ralmahaidi@swin.edu.au

[*]: Corresponding author

Keywords: concrete bridges; curved soffit; fiber reinforced polymer; flexure strengthening; design

Abstract: Recently composite materials have been increasingly used in different structural engineering applications. The research reported here focuses on the performance of concavely-curved soffit reinforced concrete beams strengthened by carbon fiber reinforced polymer (CFRP). CFRP composites used to strengthen reinforced concrete members with curved soffits generally try to straighten under load, resulting in normal tensile stress at the interface between the adhesive and the concrete. Therefore, these structural members may experience premature CFRP de-bonding due to the high concentration of tensile stresses generated by the induced curvature. Interfacial cracking followed by de-bonding is the dominant failure mode. The objective of this research is to study experimentally the effect of soffit curvature on de-bonding failure mode, deformability and load capacity of reinforced concrete beams strengthened with CFRP. A testing program including eight simply-supported beams 2.7 m length was conducted to determine the influence of concavity on the performance and capacity of these types of structural members. CFRP laminates and sheets were used for external strengthening, and all specimens were tested under three-point monotonic static loading up to failure.

1. Introduction

Many reinforced concrete (RC) bridge structures around the world were built more than 70 years ago and some need to be upgraded to increase their traffic capacity. Increasing traffic capacity leads to increases in traffic load and deterioration. Strengthening deteriorated structures is necessary to sustain new applied loads or to enhance degraded elements. Conventional methods of strengthening include, replacing the degraded element, attaching external steel plates, external post-tensioning and using steel jacks where applicable. These methods are time-consuming, they add more loads to the members, and they need mechanical lifting during the application process. Over the last few decades, strengthening of structures using fiber reinforced polymers (FRP) technique has attracted structural engineers, due to their high strength-to-weight ratio, ease of installation, corrosion resistance and minimum maintenance requirements (Al-Mahaidi and Kalfat 2018). A significant amount of research has been carried out on the failure mechanism of flat soffit RC beams strengthened with FRP (Gao et al. 2005; Pham and Al-Mahaidi 2004; Wu

and Niu 2007; Yao and Teng 2007). However, despite the popularity of this strengthening system, the failure behavior of curved soffit RC beams strengthened with FRP remains an area of limited study. Therefore, there is a crucial need to conduct experimental destructive tests to assist in understanding the behavior of curved soffit RC beams at serviceability and failure stages. Based on (Aiello et al. 2001; Eshwar et al. 2005) testing, ACI 440.2R (2017) recommends anchoring the FRP to the curved soffit to avoid delamination if the curvature exceeds 5 mm per meter. Based on (Porter et al. 2003; Eshwar et al. 2005) testing, TR55 (2012) set a curvature limit of 3 mm per meter when strengthening using fabric-based-systems as they tend to closely follow the profile of the concrete. And 5 mm per 1 meter when strengthening using plate-based-systems because they tend not to follow the profile of the concrete. Curved soffit RC bridges exist worldwide, Figure 1 shows the Swan St. Bridge in Melbourne, Australia and the FRP strengthening carried out on it.

Figure 1. Swan Street Bridge, Melbourne, Australia

2. Research Significance

This study shows that a soffit curvature of 20 mm per 1 meter significantly reduces the efficiency of a RC beam strengthened with FRP.

3. Experimental Program: Materials and Strengthening Procedure

Eight beams were tested in this research program. Three were flat soffit RC beams; one was un-strengthened, one was strengthened with CFRP laminates and one strengthened with CFRP sheets. These three flat soffit RC beams were considered as control beams. The other five beams were fabricated with a curvature of 20 mm per 1 meter extending over 2 meters; one was un- strengthened, two identical beams were strengthened with one layer of CFRP fabric and two similar beams were strengthened with CFRP laminate.

3.1. Material Properties

All tested beams were manufactured from one concrete batch and similar deformed steel bars (10 and 12 mm in diameter). Tests were carried out on the constituent materials to determine their mechanical properties. The concrete compressive strength was determined in accordance with ASTM C39 (2018), where the cylinder compressive strength at 60 days was 48.7 MPa. Three deformed steel bars of each size were exposed to uniaxial tensile tension in accordance

with ASTM A615/A615M (2018). The average yield strength, ultimate strength, and modulus of elasticity for both sizes were: 580, 554; 701, 636; and 202000, 201000, respectively.
The tensile strength and Young's modulus of elasticity for CFRP fabric and CFRP laminate are shown in Table 1, as reported by the manufacturer.

Table 1. CFRP mechanical properties

Material	Elastic Modulus (MPa)	Tensile Strength (MPa)	Thickness (mm)
CFRP Fibre (BASF MasterBrace)	230000	4900	0.337
CFRP Laminate (BASF MasterBrace)	165000	3000	1.4

3.2. Test Specimen Details

All beams were designed in accordance with AS5100 (2017) and ACI318-14 (2014). Configuration and reinforcement details of the flat and curved beams are shown in Figure 2. All tested beams were 2700 mm in length and 140 mm wide. All beams were designed with equal section dimensions at mid-span (260 mm depth). The curved soffit beams had a curvature of 20 mm per 1 meter distributed over the central part of the beam of 2000 mm chord length.

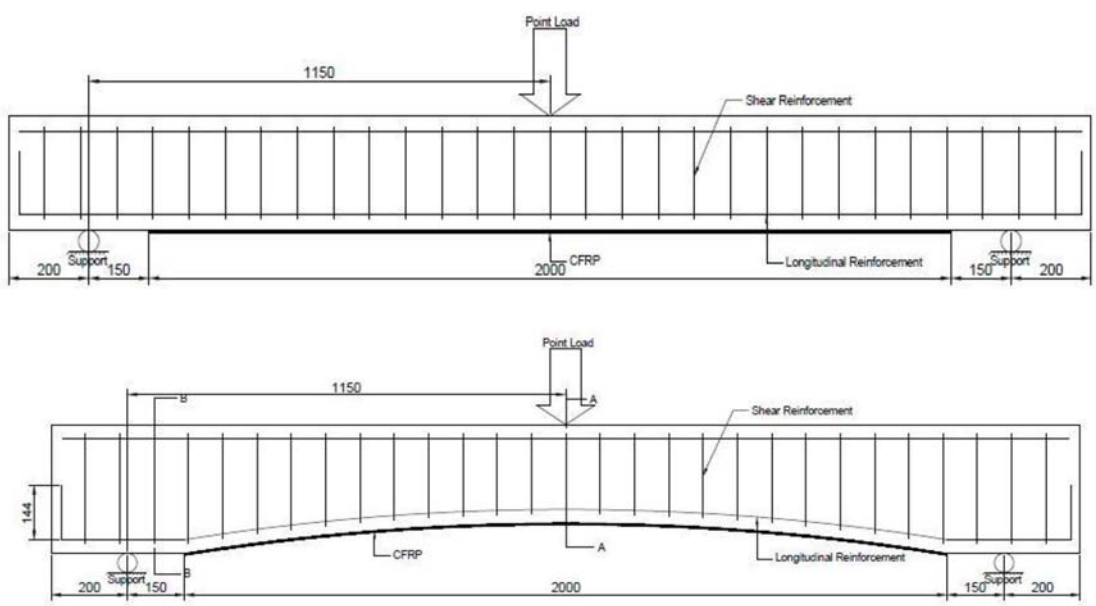

Figure 2. Flat and curved soffit beams (elevation view)

All beams were reinforced in tension and compression with three 12 mm and two 12 mm in diameter steel deformed bars, respectively. Shear stirrups were provided at 90 mm c/c spacing with 10 mm diameter bars. See Figure 2 and 3.

3.3. CFRP Installation

All strengthened beams were turned upside down for ease of installation. The process of applying CFRP composites consisted of two major steps: surface preparation and CFRP bonding. In the first step, the RC beams bonding surface was sandblasted to give a sandpaper surface. MasterBrace P3500 primer was applied to the surface of all strengthened beams with a brush to fill any gaps or small cracks. The primer was left to cure for 30-60 minutes to give a tacky nonporous surface.

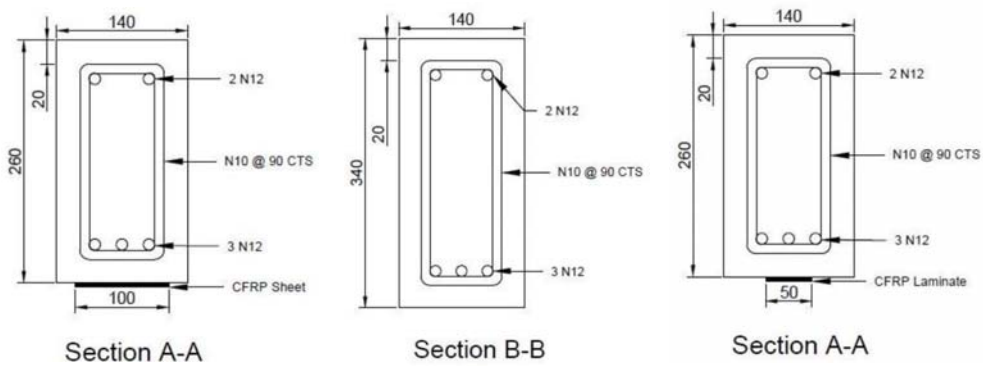

Figure 3. Cross-section of both curved and flat beams

The second step involved cutting fabric sheet to 100 mm in width and 2000 mm in length using scissors. MasterBrace P4500 saturant was prepared by mixing part A and part B using a slow-speed (300-600 rpm) mixer. The CFRP sheet was fully impregnated with the saturant using a plastic scraper and then placed on top of the primer. The second step involved applying CFRP laminate to the beams. CFRP laminate was cut beforehand into plates 50 mm wide and 2000 mm long plates using an electrical saw. MasterBrace P4000 adhesive was prepared by mixing the two parts using a mixer for 5 minutes. The laminate adhesive was equally applied to the CFRP plates to form a layer 3 mm thick. Next, the CFRP laminate was placed on top of the primer and pressed down by hand to form a thin layer of adhesive. All specimens were left to cure for eight days at room temperature. The installation sequence is shown in Figure 4.

Figure 4. Installation sequence of CFRP

4. Test Set-up and Test Procedure

All beams were loaded in three-point bending with a clear span of 2300 mm. The beams were loaded using an MTS actuator with 500 kN load capacity and a piston stroke of 150 mm. The displacement control test was carried out upside-down, as shown in Figure 5. The beam was held from the top by two steel support blocks, while the hydraulic actuator was placed underneath the beam and the stroke was upward. The beams were loaded at a rate of 2 mm per minute for the entire test time. Three micro-laser displacement sensors were placed to obtain the displacement at mid-span and support sections. In addition, seven electrical strain gauges were installed along the CFRP axis to measure the strain during loading.

5. Test Results

Control beam FC exhibited typical under-reinforced failure. As the load increased beyond the cracking load, flexural cracks started to increase in number, width, and depth. The steel in the tension zone yielded at a load of 68 kN and the peak failure load was 78 kN. Both flat soffit beams FS and FL failed by intermediate span-induced crack de-bonding (IC). Both beams showed a reduction in deflection and crack width and an increase in capacity compared to the control beam. As load increased, flexural cracks increased, leading to high interfacial stresses between the concrete and the CFRP. This resulted in complete CFRP delamination starting from the mid-span section and propagating towards the supports.

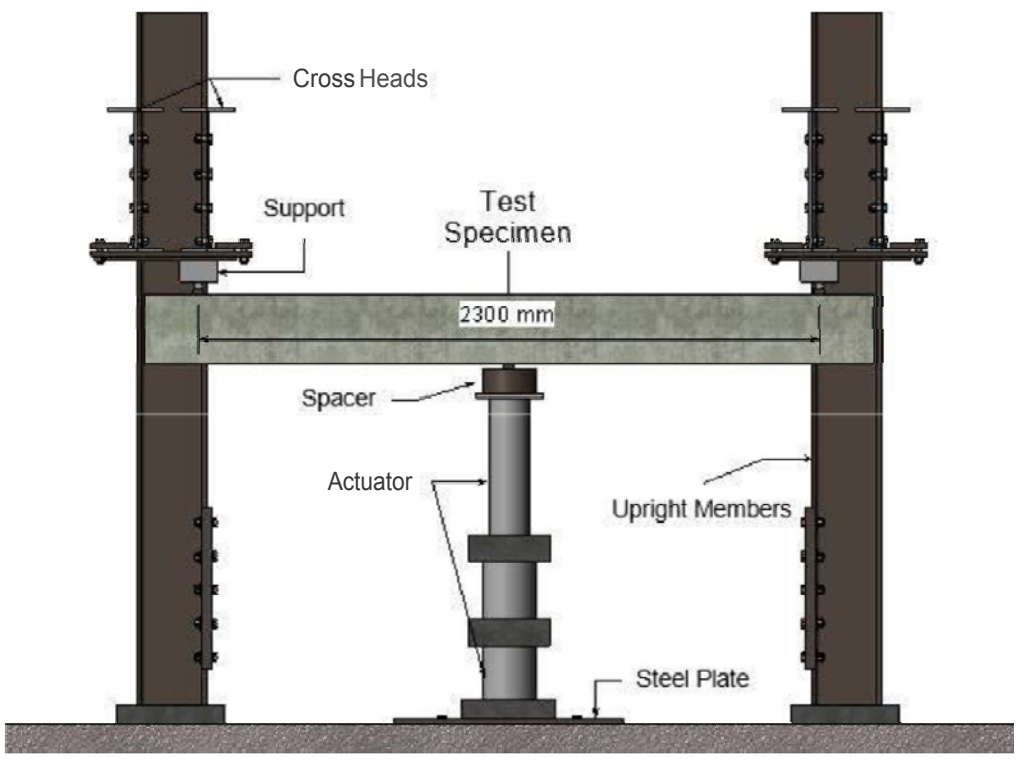

Figure 5. Upside-down test set-up

The control curved beam CC failed in a similar manner to FC. However, the peak load for CC was lower than that for FC (73 kN) due to the existing bend in the tension reinforcement. Beams CS-1 and CS-2 failed by IC debonding and recorded a reduction in ultimate capacity of 86 kN and 85 kN, respectively. Delamination started from the mid-span section and propagated towards the CFRP end. Similar failure was observed in beams CL-1 and CL-2. However, their ultimate capacity showed the same reduction as the CS beams. CL-1 and CL-2 failed at 88 kN and 90 kN respectively, as shown in Table 2. Figure 6 shows the load-displacement behavior of all the tested beams at mid-span. Load and displacement were calibrated at the beam's self-weight level since the test was conducted upside-down.

Beam	FRP strengthening type	*Rise (mm)	*Cord (mm)	*Radius (mm)	Pu(kN)	Change over flat un-strengthened (%)	Change over curved un-strengthened (%)
FC	None	0	0		78		
FS	Sheet	0	0		105	34.6	
FL	Laminate	0	0		107	37.2	
CC	None	80	2000	6260	72		
CS-1	Sheet	80	2000	6260	86	10.3	19.4
CS-2	Sheet	80	2000	6260	85	9.0	18.1
CL-1	Laminate	80	2000	6260	88	12.8	22.2
CL-2	Laminate	80	2000	6260	90	15.4	25.0

*

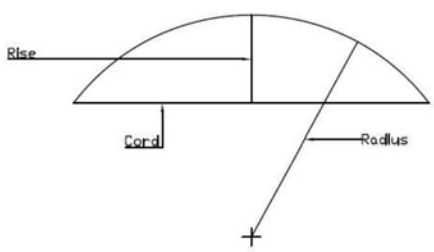

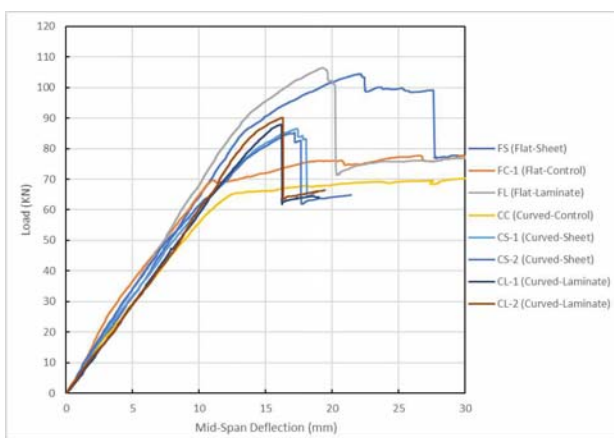

Figure 6. Load vs. mid-span deflection for all beams

6. Conclusions

In this experimental program, the behavior of curved soffit RC beams strengthened with CFRP laminates and sheets was investigated. A significant increase in the capacity of all strengthened beams ranging from 18% to 37% was observed. All retrofitted beams failed by intermediated span induced crack de-bonding. These cracks were a combination of flexural and flexural-shear cracks. A curvature of 20 mm per 1 meter significantly reduces the efficiency of FRP strengthening and further research is needed to set a limit for the curvature of strengthened beams. It was noted that beams strengthened with CFRP laminate performed slightly better than those strengthened with CFRP sheet in term of ultimate capacity. All retrofitted beams retained their original strength after CFRP de-bonding

7. Acknowledgment

The joint scholarship support provided to the first author by Iraqi Ministry of High Education and Scientific Research and Swinburne University of Technology is gratefully acknowledged. The authors wish to acknowledge the technical support provided by staff of the Smart Structures Laboratory of Swinburne University of Technology.

8. References

ACI Committee 318 (2014), Building Code Requirements for Structural Concrete and Commentary. Detroit, American Concrete Institute.

ACI Committee 440 (2017), Guide for The Design and Construction of Externally Bonded FRP Systems for Strengthening Concrete Structures. Detroit, American Concrete Institute.

ASTM: A615/A615M (2018). "Standard Specification for Deformed and Plain Carbon-Steel Bars for Concrete Reinforcement" ASTM Standard, American Society for Testing Materials, USA.

ASTM: C39/C39M 2018. "Standard Test Method for Compressive Strength of Cylindrical Specimens" ASTM Standard, American Society for Testing Materials, USA.
Australian Standard 5100 (2017), Bridge Design. Sydney, Standards Australia.

Aiello, M, et al. 2001,'Bond Analysis of Curved Structural Concrete Elements Strengthened using FRP Materials', in FRPRCS-5: Fibre-reinforced plastics for reinforced concrete structures Volume 1, pp. 399-408.

Al-Mahaidi, R and Kalfat, R 2018, 'Chapter 3 - Fiber-Reinforced Polymers and Their Use in Structural Rehabilitation', in Rehabilitation of Concrete Structures with Fiber-Reinforced Polymer, Butterworth-Heinemann, pp. 15-2 0.

Porter, D, et al. 2003, Effectiveness of FRP Plate Strengthening on Curved Soffits.

Eshwar, N, et al. 2005, 'Effectiveness of CFRP Strengthening on Curved Soffit RC Beams', Advances in Structural Engineering, vol. 8, no. 1, pp. 55-68.

Gao, B, et al. 2005, 'Prediction of concrete cover separation failure for RC beams strengthened with CFRP strips', Engineering Structures, vol. 27, no. 2, pp. 177-189.

Pham, H, Al-Mahaidi, R 2004, 'Experimental investigation into flexural retrofitting of reinforced concrete bridge beams using FRP composites', Composite Structures, vol. 66, no. 1, pp. 617-625.

Wu, Z, Niu, H 2007, 'Prediction of Crack-Induced Debonding Failure in R/C Structures Flexurally Strengthened with Externally Bonded FRP Composites', Doboku Gakkai Ronbunshuu E, vol. 63, no. 4, pp. 620-639.

Yao, J, Teng, JG 2007, 'Plate end debonding in FRP-plated RC beams I: Experiments', Engineering Structures, vol. 29, no. 10, pp. 2457-2471.

Application of FRP for Strengthening of Precast Segmental Bridge Construction of Motorway No. 6 in Thailand

Sukit Yindeesuk[1*], Phanthira Chanachompu[2], and Panatchai Chetchotisak[3]

[1] Department of Highways, Bangkok Thailand; email: sukit.uiuc@tonsukit.com
[2] Department of Highways; Bangkok Thailand; email: c.phanthira@gmail.com
[3] Rajamangala University of Technology Isan, Thailand; email: panatchaich@gmail.com

*: corresponding author

Keywords: precast bridge construction; construction stage; FRP; strut-and-tie; bridges

Abstract: Recently, the construction of highways and motorway in Thailand increases rapidly due to the economic and city expansion and development. Motorway No.6 in Thailand is designed and under constructed to connect the Bang Pa-in and Nakhon Ratchasima in North Eastern Thailand. A section of the motorway is designed to be elevated viaduct (6 traffic lanes) using the dual sections of precast segmental box girder system as superstructure supported by the T-shape single column pier along the depress median of the highway No.2. The construction of superstructure utilizes the launching gantry operated on the top of the pier and performs the span by span construction where the precast segments are served from the ground using full trailer trucks. The longitudinal prestressing system of the viaduct is composed of 10 tendons of 19- strands of 15.2mm in diameter (in span and continuous prestressing tendons) to sustain the service load conditions. The prestressing operation is performed in one direction from the fist span to the next span to complete the 7 continuous spans of 310 m expansion length. Since the erection of the precast system along the route of the viaduct uses multiple launching gantrys moving in the same direction to reduce the construction time, the reversed direction jacking operation of prestressing tendons of the last 2 spans of the adjacent continuous viaducts is required. To ensure the strength of the existing pier segments of the viaduct when performing the reversed direction jacking operation, the evaluation of the existing pier segment subjected to the prestressing forces for the reversed jacking operation is required using special methods e.g. strut-and-tie model (STM) and FEA and the recommendation of ACI 440 and AASHTO LRFD. This paper presents the application and effective use of FRP for strengthening of pier segments subjected to the reversed prestressing operation from design phase to construction in details

1. Introduction

Due to the traffic volume and economic growth of Eastern Thailand, Motorway No.6 is designed and under constructed to connect the Bang Pa-in and Nakhon Ratchasima in North Eastern Thailand. A section of the motorway is designed to be elevated viaduct (6 traffic lanes) using the dual sections of precast segmental box girder system as a superstructure which are one of the major new developments in bridge engineering (Rombach,2002). The superstructure is erected by using launching gantry and supported by the T-shape single column pier along the depress median of the highway No.2 as illustrated in Fig.1.0a.

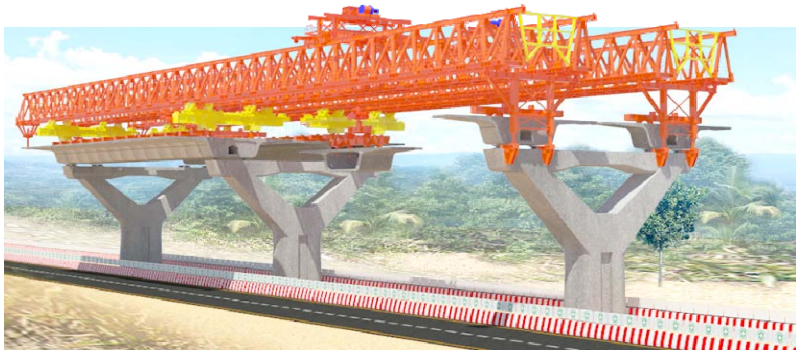

(a)

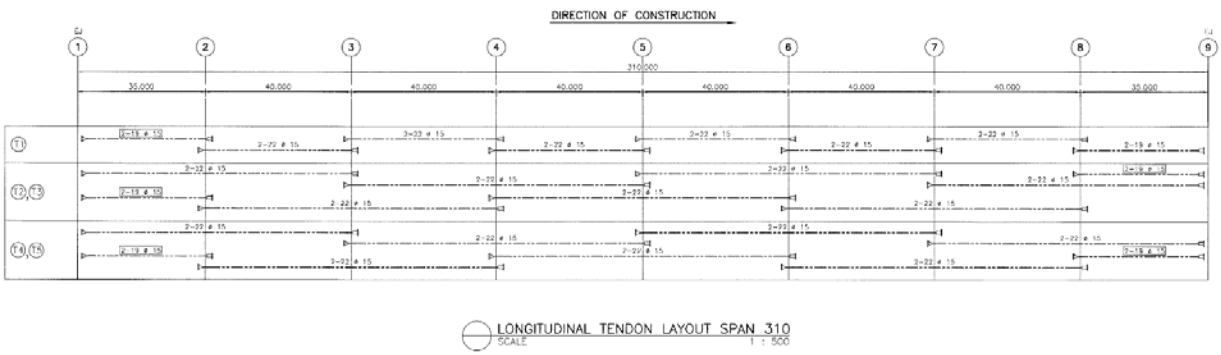

(b)

Fig. 1. Typical precast segmental box girder structures and construction of motorway no.6 (Thailand): (a) Launching gantry over T-shape pier; (b) Prestressing tendon configuration

The construction of superstructure utilizes the launching gantry operated on the top of the pier and performs the span by span construction where the precast segments are served from the ground using full trailer trucks. The longitudinal prestressing system of the viaduct is composed of 10 tendons of 19-strans of 15.2mm in diameter (in span and continuous prestressing tendons) to sustain the service load conditions. The prestressing operation is performed in one direction from the fist span to the next span to complete the 7 continuous spans of 310 m expansion length as illustrated in Fig.1.0b. Since the erection of the precast system along the route of the viaduct uses multiple launching gantrys moving in the same direction to reduce the construction time, the reversed direction jacking operation of prestressing tendons of the last 2 spans of the adjacent continuous viaducts is required. To ensure the strength of the existing pier segments of the viaduct when performing the reversed direction jacking operation, the evaluation of the existing pier segment subjected to the prestressing forces for the reversed jacking operation is thus required to perform for the safety reason.

2. D-Regions of pier segment designed and strengthening using STM

It is well known that pier segments are recognized as D-Regions where the strain distribution is nonlinear (Yindeesuk, S. and Kuchma, D.A., 2009) and strut-and-tie model (STM) is needed for design of the regions. For STM, a load-resisting truss is idealized to carry the

forces through the D-regions to its supports (Kuchma et al, 2008). To design the new structures, code provisions for design of D-Regions by STM has been developed and recognized by designers e.g. AASHTO LRFD Bridge Design Specification (AASHTO, 1994) and ACI Building Code (ACI Committee 318, 2002) where the compression and tensile forces are resisted by compression strut and tension ties or the reinforcement in the structure, respectively. For the repair and rehabilitation purposes of D-Regions using Fiber Reinforced Polymers (FRPs), very limited number of research and code of practices have been addressed (Mohammed, 2018). To demonstrate the application of STM for FRP strengthening of pier segment, the guide for the design and construction of externally bonded FRP systems (ACI 440.2R-08, 2008) for slender beam is adopted for D-Regions. The force transfer mechanism within D-regions is solved by using STM as per AASHTO LRFD for concrete and reinforcement while the calculation of FRP strength with its reduction factor is performed based on ACI 440. The design procedure of pier segment using STM is proposed as follows:

- Idealized the D-regions of pier segment
- Adopt stress distribution of D-region from FEA for STM shape
- Generate STM shape for load transfer mechanism of pier segment
- Perform STM analysis using linear elastic to determine truss forces
- Check strut and nodal zone capacity based on AASHTO LRFD.
- Quantify the required reinforcement and FRP (ACI 440) to resist the tensile forces in ties.
- Produce construction drawing

3. Strengthening of Pier Segments using CFRP

Based on the proposed design procedure, the strengthening of pier segment is performed. Fig.2.0a illustrates the STM design of pier segment subjected to the jacking force of reversed prestressing systems. Both transverse and longitudinal force transfer case are considered in the design. To obtain the most accurate capacity of FRP for design, the test matrix of FRP materials is performed based on ACI440 Including the FEA validation. The tested FRP properties for design are as follows: 1) Modulus of elasticity = 190,000 MPa. 2) Tensile strength of fibers = 3,600 MPa. 3) Elongation at break = 1.7% The proposed design for strengthening of pier segment has been applied to the existing pier segments prior to stressing operation of reversed tendons as illustrated in Fig. 2.0b. Currently, the construction of superstructure with the strengthened pier segments is completed and the structure has shown no evidence of distresses and performed excellent behavior.

4. Conclusion

In this paper, the practical use of STM for design of FRP strengthening of actual pier segments is presented. The ACI 440 guide of slender beam strengthened using FRP is adopted for calculation of FRP tensile strength while the capacity of concrete strut and nodal zone is designed based on AASHTO LRFD. The performance of the design was validated by FEA and the real construction sequences. The results showed that the pier strengthening designed by the proposed procedures performed the great behavior without the sign of distresses.

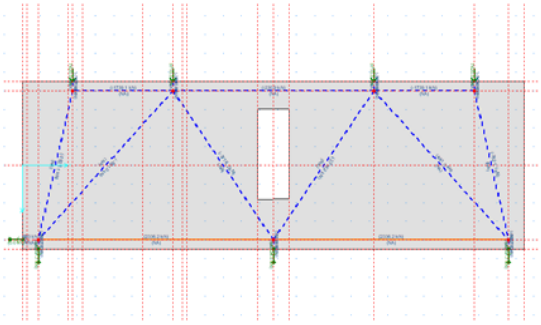

(a)

(b)

Fig. 2. Strengthening of Pier Segments using CFRP designed by STM: (a) STM shape and analysis (Top Side); (b) CFRP application on pier segment prior to stressing operation

5. References

AASHTO, 1994. AASHTO LRFD Bridge Design Specifications, American Association of State Highway and Transportation Officials, 1091 pp.

ACI Committee 318, 2002. Building code requirements for structural concrete (ACI 318-02) and
commentary (318R-02), American Concrete Institute, 443 pp.

ACI 440. 2R-08, 2008. Guide for the design and construction of externally bonded FRP systems for strengthening concrete structures, American Concrete Institute, 80 pp.

Mohammed, K. 2018. Strut and tie modeling of deep beams shear strengthened with FRP lamiates, Composite Structures,193, 247-259.

Rombach, G. 2002. Precast segmental box girder bridges with external prestressing design and construcction, INSA Rennes, 1-15.

Yindeesuk, S. and Kuchma, D.A. 2009. Automated design and analysis procedure for effective structural performance of D-Regions in reinforced concrete structures, Proceedings of the Conference of the Computational Techniques.

Kuchma, D.A., et al. 2008. Experimental validation of the strut-and-tie method for complex regions, ACI Structural Journal, 105(3), 578-589.

Basalt FRP-RC Standardization for Florida DOT Structures

Steven Nolan[1*], Chase Knight[2], and Raphael Kampmann[3]

[1] Florida Department of Transportation – State Structures Design Office, Tallahassee, FL. USA; email: Steven.Nolan@dot.state.fl.us
[2] Florida Department of Transportation – State Materials Office, Gainesville FL. USA; email: Chase.Knight@dot.state.fl.us
[3] FAMU-FSU, Tallahassee FL. USA; email: kampmann@eng.famu.fsu.edu

*: corresponding author

Keywords: basalt, BFRP, composite reinforcing, corrosion-resistant, rebar, standards

Abstract: Fiber-reinforced polymer bars are emerging as a viable economical solution to eliminate corrosion degrading of reinforced concrete (RC) structures caused by chloride attack in both coastal and cold weather locations. The corrosion mechanism is similar in these divergent environments due to the presence of chlorides: within seawater along the coastal fringe of 20 states; and within deicing chemicals used in most of the other US states. Significant improvements in manufacturing techniques and resin matrix materials have occurred in recent years enabling exploitation of the superior properties of Basalt FRP rebar that is now available. The Canadian Standards Association will shortly be adopting BFRP rebar for concrete structures in their next update to the Canadian Highway Bridge Design Code. FDOT under their Transportation Design Innovation initiative is committed to providing resilient, sustainable, cost effective and scalable solutions to the aging infrastructure challenge. The provision of multiple material options for corrosion-resistant rebar is foreseen as a positive development to encourage competition, further innovation and provide a redundant supply chain for FRP materials, especially as wider deployment occurs. A significant amount of inferior BFRP products are reportedly now available on the world market due to the lack of standards, underlying the need and urgency for establishing robust standards in the US. This paper describes the need and development of standard (guide) design specifications, and standard material and construction specifications for basalt fiber-reinforced polymer (BFRP) bars for the internal reinforcement of structural concrete on FDOT projects.

1. Introduction

Fiber-reinforced polymer bars are emerging as a viable economical solution to eliminate corrosion degradation of reinforced concrete (RC) structures caused by chloride attack in both coastal and cold weather locations. Although Paul Dh`e first produced basalt fibers in the United States, in 1923 (Dh´e, 1923; Colombo et al., 2012), the technology did not gain traction in the US due to initial production difficulties and more profitable opportunities with glass fibers. Specifically, after the manufacturing process for glass fibers was successfully industrialized in Toledo, Ohio, by Games Slayter in 1933 (Slayter, 1938), the major fiber producers in the US abandoned basalt fiber research in favor of glass products (Faruk et al., 2017). Extensive research on basalt fibers was later conducted in the former Soviet Union, during the cold war (Jamshaid and Mishra, 2016), for military purposes in a search for ballistic resistant textiles.

After the Soviet Union collapse in 1991, these research projects were declassified (in 1995) and released for civilian applications. In consequence, basalt fibers are a recent development in the engineered construction industry and most basalt fiber producing companies are still located in countries that use to be associated with the Eastern Bloc (Zych and Wojciech, 2012).

2. Basalt FRP Rebar Manufacturing

Significant improvements in FRP manufacturing techniques and resin matrix materials have occurred in recent years enabling exploitation of the superior properties of Basalt FRP rebars. Different processes have been developed to combine the basalt fibers and resin for the efficient production of fiber reinforced polymer rebar. The typical production method is pultrusion, however the production method is not yet standardized leading to different rebar products from each manufacturer. Pultrusion is a relatively simple and reliable process for the manufacture of BFRP bars, particularly for the straight rods. Other production processes are available as discussed in Patnaik, 2009, potentially less reliable, but possibly better suited for complicated bent shapes or mesh products.

Pultrusion is a continuous molding process combining fibers and thermosetting resin, with a constant cross-sectional architecture. The fibers are continuously pulled from rovings, passing through a wetting operation (impregnated) usually in a liquid resin bath. Inside the pultrusion die, a controlled temperature promotes resin hardening while the heat activates the curing or polymerization of the thermoset resin. The fixed cross section of the pultrusion-dies, ensure tight dimensional control of FRP rebar. Inside the heating die, the rebar reacts chemically and solidifies under an exothermic reaction morphing from a heterogenous liquid stage to a gel stage, until finally the solid state is reached. To achieve a sufficient bond between concrete and the rebar in its end use, an additional process is required to provide surface enhancement features (You et al., 2015). Surface enhancement includes: formed ribs; machined grooves; sand coating; helical wrap; or combinations of these. The final product is cut to length at the end of the pultrusion process is only constrained by logistics such as storage and transporting limitations. Coiling is also possible when smaller diameters are produced (ACI Committee 440, 2007).

Various studies have identified possible weaknesses in existing products and provide recommendations for standardization requirements. Scanning electron microscope (SEM) analysis can be used to show qualitatively when porosity and voids are present with FRP rebars. Based on these observations ElSafty et al. (2014) recommended improvements to the manufacturing process to reduce and/or eliminate these defects. Borges et al. (2015), studied the influence of resin bath temperature on the properties of pultruded FRP rebars with polyester resin. It was shown that temperatures between 86°F to 122°F (30°C to 50°C) were suitable for the production process. Higher temperatures lead to a low viscosity and inadequate wetting of the fibers before entering the heating die. The recommended curing temperature for resins is about 350°F (177°C) according to Joshi et al., 2003. More commonly, epoxy based resins are the preference for BFRP due to improved durability and mechanical performance in a concrete bound environment.

3. Standards for BFRP-RC

A significant amount of BFRP products are reportedly now available on the world market, with a wide range of performance properties due to the lack of uniform standards. This highlights the need and urgency for establishing robust standards in the US to ensure reliability and instill confidence in asset owners and designers. Some significant progress has already been completed for developing a US based code of practice using the current GFRP rebar Guide Specifications as a framework (AASHTO 2018, ACI 2015).

The American Concrete Institute Committee 440 (ACI 440) initially led the North American effort to address the technical implementation for FRP rebars by developing and publishing test methods, specifications, and design guidelines (ACI Committee 440, 2006, 2008a, 2008b, 2012, 2013, 2015). The 2008 version of ACI 440 (ACI Committee 440, 2008b) and the 2010 version of the Canadian Standards Association (CSA) Specifications for Fiber Reinforced Polymers (CAN/CSA, 2010) were developed to standardize glass, carbon, and aramid FRP bars. CSA has recently led the western effort for developing specifications and design guidelines for BFRP. The new CSA S807-19 (CAN/CSA, 2019) standard will include FRP bars made from basalt fibers, which highlights the current interest of this material and the confidence of a commercialized availability (Vincent et al., 2013). Similarly, ASTM Committees D30 and D20 have addressed the emergence of FRP rebar technology by developing test methods (ASTM-International, 2015) intended to characterize GFRP rebar, that can also be applied to BFRP rebar. Recently, ASTM D7957-17 was published with specific guidelines for solid round glass fiber reinforced polymer bars for concrete reinforcement (ASTM-International, 2017). In addition, the FDOT has developed documents to regionally aid in the design and implementation of FRP rebar, specifically expanding Specifications Section 932 (FDOT, 2014 & 2018), and implementing the Fiber Reinforced Polymer Guidelines (FDOT, 2015).

While different production techniques and processes exist today in the FRP rebar market, the established acceptance criteria allow manufacturers to target specific properties. Nevertheless, BFRP rebars have been produced before these acceptance criteria were available, and so manufacturers have often followed very individual mechanical properties and proprietary production sequences. Accordingly, the market is currently very diverse with unique products, and new manufacturers can enter the market quickly due to relatively low start-up costs.

It is therefore desired to add BFRP rebar specific criteria to the AASHTO guidelines and specifications as soon as practical to ensure product reliability, encourage US manufacturing, and increase competition and redundancy in the material supply chain. Transportation agencies and asset owners are becoming increasingly interested in BFRP composites because of broader exposure in the western hemisphere and production technology improvements which have led to improved mechanical properties such as: fatigue endurance; creep rupture resistance; strength; and elastic modulus. The environmental benefits of lower embodied energy and a longer service life compared to steel are also gaining interest. Some recent guideline and specification developments for BFRP rebar are summarized in the following:

3.1. AC454 - 2015

The International Code Council Evaluation Services, approved the proposed addition of BFRP rebar to their Acceptance Criteria AC454 "Fiber-Reinforced Polymer Bars for Internal Reinforcement of Concrete Members" (ICC-ES, 2014) in 2015. This allows structures designed according to the requirements of the International Building Code (IBC), and most state adopted versions of this model code, to be realized with BFRP rebar technology.

3.2. State Transportation Innovation Council (STIC) Incentive Project, 2018 - 2019

FDOT under their Transportation Design Innovation (TDI) initiative provides guidance for FRP technology infrastructure solutions (https://www.fdot.gov/structures/innovation/FRP.shtm). One goal of the TDI initiative is to provide multiple material options (including the adoption of BFRP) for corrosion-resistant rebar, which encourages market competition and product innovation, and should provide a redundant supply chain of FRP materials as wider deployment occurs. The FHWA funded STIC Incentive project (STIC-0004-00A) is developing standard design (guide) specifications, and standard material and construction specifications for BFRP rebars for 2020 adoption.

3.3. CAN/CSA 807 & S6 - 2019

The Canadian Standards Association will be adopting BFRP rebar for concrete structures in the next update to their "Specifications for fibre-reinforced polymers" (CAN/CSA 807-19), followed by adoption in the Canadian Highway Bridge Design Code (CAN/CSA S6-19)

Table 2A
Grades of FRP straight bars and grids corresponding to their minimum modulus of elasticity, GPa

	Grade I		Grade II		Grade III	
Designation	Individual bars	Bars in a grid	Individual bars	Bars in a grid	Individual bars	Bars in a grid
AFRP	50	40	70	60	90	80
BFRP	50	40	60	50	70	60
CFRP	80	70	110	100	140	130
GFRP	40	30	50	40	60	50

Fig. 1. Proposed grades of FRP bars per CAN/CSA S807-19 public review copy

4. BFRP-RC Structures

Some recent examples of structures that have been successfully constructed with BFRP rebar in Florida, are summarized below:

4.1. Port Miami Tunnel Entrance Walls (Watson Island), Miami - 2014

BFRP reinforcement bars #2.5 and #4 (8 mm and 12 mm) were utilized in Watson Island Retaining Walls 5 and 6 (Fig. 2) as an FDOT demonstration project, with a research plan for monitoring long-term performance and durability. The retaining walls were originally designed with Grade 60 carbon-steel reinforcement. The contractor initiated redesign, proposed BFRP

bars in substantial conformance with the AASHTO LRFD Bridge Design Guide Specifications for GFRP-RC Bridge Decks and Traffic Railings (2009). The wall shape, dimensions, and class of concrete remained the same as the original plans. An FDOT research plan includes extraction of cores to evaluate any changes in the physical and chemical properties of BFRP rebar, concrete, and interfaces between them. Sampling and analysis for this research project is scheduled to begin in 2019.

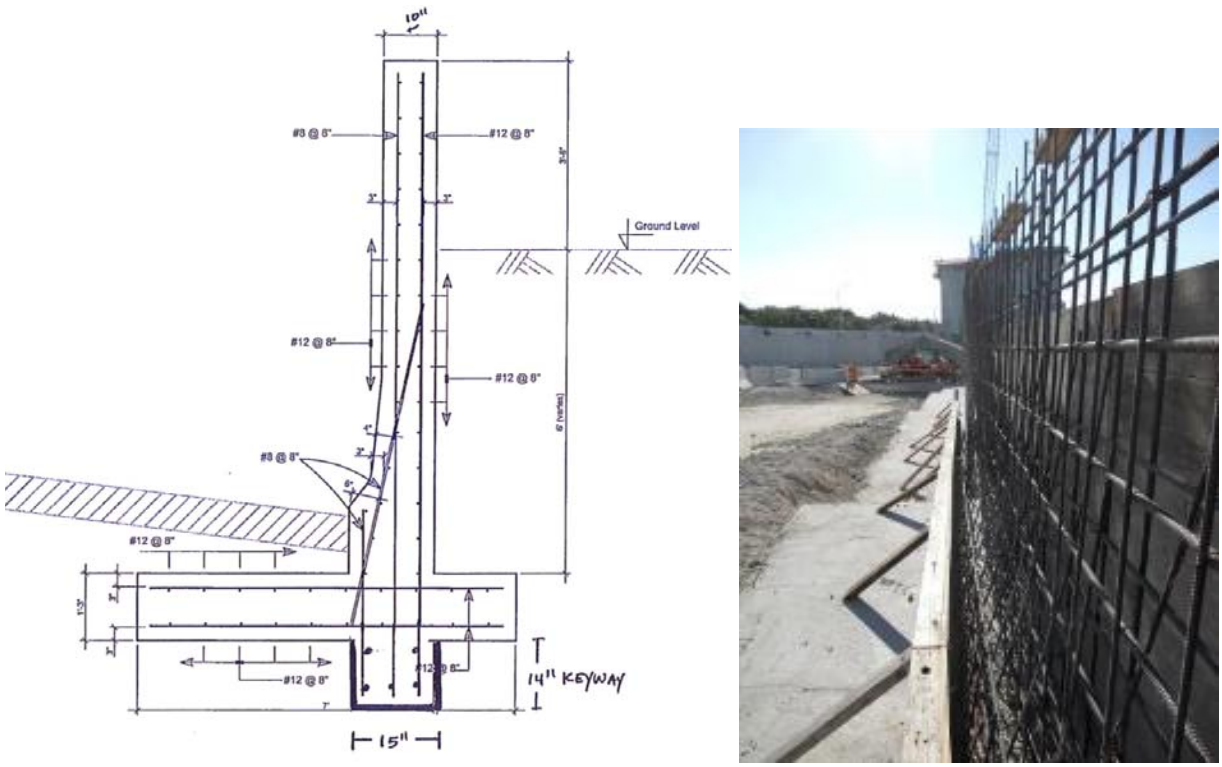

(a) **(b)**

Fig. 2. (a) Typical Cross-section of Retaining Walls 5 and 6 with BFRP Reinforcement (Bar sizes in mm); (b) Wall 6 under construction.

4.2. IROX Drainage Structures, Lee County - 2014

Five precast drainage structures (ditch bottom inlets and junction boxes) were constructed using BFRP rebar as a direct replacement for Grade 60 carbon-steel rebar as originally designed. The structures are inside or near retention ponds which experience seasonal wet/dry cycles. Fig. 3(a) shows the locations of three structures that were visually inspected in December 2018, with no external evidence of cracking or deterioration observed. Fig. 2(b) shows images of one of the retention pond structures.

4.3. Innovation Pedestrian Bridge, Miami - 2016

This bridge on the University of Miami (UM) campus combines different FRP materials (basalt, glass, and carbon) and novel composite manufacturing technologies (continuous closed stirrups

and automated-preassembled cages) within the following elements: auger-cast piles; cast-in-place pile caps and back walls; precast prestressed girders; and, cast-in-place deck topping and curbs. FRP was deliberately chose to demonstrate UM's commitment to innovation and sustainability for a pedestrian bridge and BFRP was heavily featured. Eight 40-foot long, 16-inch diameter auger-cast piles were reinforced with a prefabricated cage of six #6 BFRP bars and bespoke spirals. The cages (in the shape of an octagon) were prefabricated at the composite manufacturer's plant and delivered to the site, ready for installation with only man-power.

(a) **(b)**

Fig. 3. BFRP-RC drainage structures: **(a)** Plan view locations of 3 retention pond overflow

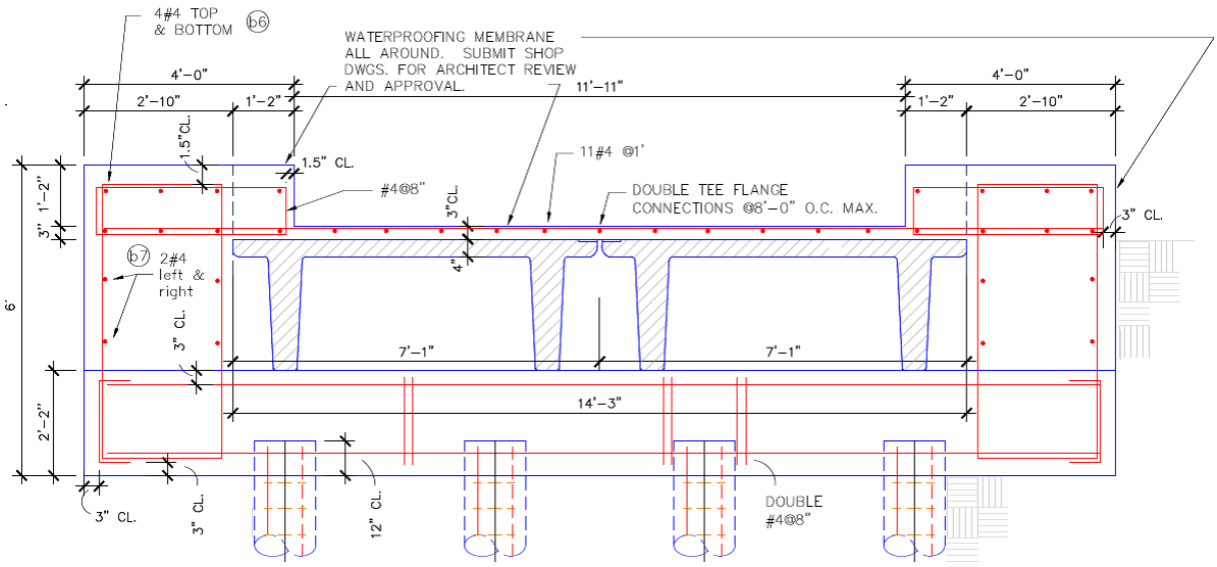

Fig. 4. (a) Typical cross-section of Innovation Bridge with BFRP reinforcement in the piles, caps, double-tee stems and flanges, deck overlay and curbs.

The pile caps and backwalls were mostly reinforced with closed (bespoke) BFRP stirrups and straight bars. The two double-tees girders were prestressed with CFRP strands and BFRP shear and supplemental reinforcing. The reinforcement grids for the stems and flanges were made of

pre-assembled interwoven BFRP bars (#3 and #4, respectively). The cast-in-place, 3-inch concrete deck topping was also reinforced with a grid of #3 BFRP bars in both directions while the curbs consisted of a combination of closed (bespoke) #4 BFRP transverse stirrups and straight longitudinal BFRP rebars.

4.4. Halls River Bridge, Homosassa - 2018

The Halls River Bridge replacement project is the first of its kind for a vehicular bridge in Florida. The bridge was predominantly designed and constructed using a variety of non-metallic reinforcement materials. In addition, it features 400 linear feet of sacrificial test blocks constructed monolithically with the bulkhead-seawall coping along the north and south abutments. These test blocks are reinforced with several types of FRP rebars, including BFRP rebar (#5). The test blocks are designed to be removed for testing and analysis after various periods of exposure. Fig. 5 shows the typical positioning of the test blocks after construction. The test blocks allow for natural exposure to brackish water in the splash zone. The first set of test blocks were removed in November 2018 and are currently being evaluated as a benchmark for long-term comparison. An example Life-Cycle Cost (LCC) analysis was performed by Cadenazzi et al. 2018, to highlight the economic advantage of FRP in similar structures and environments.

(a) **(b)**

Fig. 5. Typical position of test blocks: (a) High tide at HRB (test bock outlined); (b) Benchmark test blocks cut and ready for extraction.

5. Conclusion

Several demonstration projects in Florida, and many others around the world, have shown the versatility and practicality of BFRP rebar for structural applications. Commercial manufacturers have exhibited the capacity to accommodate a variety of geometric challenges and respond to asset owner's needs. Researchers have validated the mechanical properties, and while durability research continues, the current limits in the available GFRP-RC guide specifications appear appropriately conservative for initial deployment of BFRP-RC in the US. LCC analysis can currently be utilized by designers to show the benefits of BFRP-RC alternatives, while future refinement of the durability models can provide additional economy, as will industry innovation,

fueled by an increase in market share, and demand by asset owners for more sustainable infrastructure.

6. References

AASHTO (2012). Guide Specifications for Design of Bonded FRP Systems for Repair and Strengthening of Concrete Bridge Elements. American Association of State Highway and Transportations Officials

AASHTO (2018). LRFD Bridge Design Guide Specifications for GRFP-Reinforced Concrete. American Association of State Highway and Transportations Officials

ACI Committee 440 (2006). Guide for the Design and Construction of Structural Concrete Reinforced with FRP Bars, (440.1R-06). American Concrete Institute.

ACI Committee 440 (2007). Report on Fiber-Reinforced Polymer (FRP) Reinforcement for Concrete Structures, (440R). American Concrete Institute.

ACI Committee 440 (2008a). Guide for the Design and Construction of Externally Bonded FRP Systems for Strengthening Concrete Structures, (ACI 440.2R-08). American Concrete Institute.

ACI Committee 440 (2008b). Specification for Carbon and Glass Fiber-Reinforced Polymer Bar Materials for Concrete Reinforcement, (ACI 440.6-08). American Concrete Institute.

ACI Committee 440 (2012). Guide Test Methods for Fiber-Reinforced Polymer (FRP) Composites for Reinforcing or Strengthening Concrete and Masonry Structures, (ACI 440.3R-12). American Concrete Institute.

ACI Committee 440 (2013). Specification for Carbon and Glass Fiber-Reinforced Polymer (FRP) Materials Made by Wet Layup for External Strengthening of Concrete and Masonry Structures, (ACI 440.8-13). American Concrete Institute.

ACI Committee 440 (2015). Guide for the Design and Construction of Structural Concrete Reinforced with Fiber-Reinforced Polymer (FRP) Bars, (ACI 440.1R). American Concrete Institute.

ASTM-International (2017). Standard Specification for Solid Round Glass Fiber Reinforced Polymer Bars for Concrete Reinforcement, (ASTM D7957 / D7957M – 17). West Conshohocken, PA.

Borges, S. G., Ferreira, C. A., Andrade, J. M., and Prevedello, A. L. (2015). “The influence of bath temperature on the properties of pultruded glass fiber reinforced rods.” Journal of Reinforced Plastics and Composites, 34(15), 1221–1230.

Colombo, C., Vergani, L., and Burman, M. (2012). “Static and fatigue characterisation of new basalt fibre reinforced composites.” Composite Structures, 94, 1165–1174.

CAN/CSA. (2010). Specifications for Fibre Reinforced Polymers: CAN/CSA-S807-10, Canadian Standard Association.

CAN/CSA. (2019). Specifications for Fibre Reinforced Polymers: CAN/CSA-S807-19, Canadian Standard Association (in press).

ElSafty, A., Benmokrane, B., Rizkalla, S., Mohamed, H., and Hassan, M. (2014). "Degradation assessment of internal continuous fiber reinforcement in concrete environment", Florida Department of Transportation.

Faruk, O., Tjong, J., and Sain, M. (2017). "Lightweight and Sustainable Materials for Automotive Applications." Tyler & Francis Group, LCC.

FDOT. (2014). "Nonmetallic Accessory Materials for Concrete Pavement and Concrete Structures", Dev932FRP. FDOT Developmental Specification, Revision 7-16-14.

FDOT. (2015). "Fiber reinforced polymer guidelines (FRPG)." Structures Manual - Volume 4. Florida Department of Transportation.

FDOT. (2018). "FDOT Standard Specification for Road and Bridge Construction", Section 932. Florida Department of Transportation.

ICC-ES. (2014). "Acceptance Criteria for Glass Fiber-Reinforced Polymer (GFRP) Bars for Internal Reinforcement of Concrete Members." Acceptance Criteria 454, International Code Council Evaluation Services

ICC-ES. (2017). "Acceptance Criteria for Fiber-Reinforced Polymer (FRP) Bars for Internal Reinforcement of Concrete Members." Acceptance Criteria 454, International Code Council Evaluation Services

Jamshaid, H. and Mishra, R. (2016). "A green material from rock: basalt fiber - a review." The Journal of The Textile Institute, 107(7), 923–937.

Joshi, S. C., Lam, Y., and Tun, U. W. (2003). "Improved cure optimization in pultrusion with pre-heating and die-cooler temperature." Composites Part A, 34, 1151–1159.

Nanni, A., De Luca, A., and Jawaheri Zadeh, H. (2014). FRP Reinforced Concrete Structures – Theory, Design and Practice. CRC Press.

Patnaik, A. (2009). "Applications of Basalt Fiber Reinforced Polymer (BFRP) Reinforcement for Transportation Infrastructure." The University of Akron.

Slayter, G. (1938). "Method and apparatus for making glass wool." Patent 2,133,235, United States Patent Office.

Vincent, P., Ahmed, E., and Benmokrane, B. (2013). "Characterization of basalt fiber-reinforced polymer (BFRP) reinforcing bars for concrete structures." Specialty Conference on Material Engineering & Applied Mechanics, 3rd, MEC–111–1 – MEC–111–10.

You, Y.-J., Kim, J.-H. J., Kim, S.-J., and Park, Y.-H. (2015). "Methods to enhance the guaranteed tensile strength of gfrp rebar to 900 mpa with general fiber volume fraction." Construction and Building Materials, 75, 54 – 62.

Zych, T. and Wojciech, K. (2012). "Study on the properties of cement mortars with basalt fibres." Brittle Matrix Composites 10, 155–166.

Basalt Characterization from Commercial Quarries on Hawaii Island and Feasibility Study Results for a Continuous Basalt Fiber Manufacturing Operation

Rodrigo Romo[1*] and Kyla Defore[2]

[1] Pacific International Space Center for Exploration Systems, Hilo USA; rfvromo@gmail.com
[2] Pacific International Space Center for Exploration Systems, Hilo USA; deforeky@hawaii.edu

[*]: corresponding author

Keywords: basalt characterization; continuous basalt fiber (CBF); sintering

Abstract: The Pacific International Space Center for Exploration Systems (PISCES) is a state agency of the State of Hawai'i attached to the Department of Business, Economic Development and Tourism (DBEDT). PISCES' objectives are to promote the aerospace industry in the state of Hawai'i and/or to support economic development through technologies/processes related to research work in Planetary exploration, especially In-Situ Resource Utilization (ISRU). In ISRU research, PISCES has been exploring how to use Hawaiian basalt as a feedstock in manufacturing and construction for lunar or Mars applications. Sintered basalt samples have resulted in materials possessing mechanical characteristics superior to those of concrete. However, variations in the chemical composition of basalts used have produced a wide range of results in the products of sintered materials. In response, PISCES has collected and analyzed the chemical composition of basalt from various sources on the island to characterize and better identify which samples product the best sintered materials. As part of an economic development initiative, PISCES contracted the consulting firm SMA to conduct a feasibility study to determine whether a Continuous Basalt Fiber (CBF) manufacturing plant would be a viable venture in Hawaii. CBF manufactured in Hawaii could be used in-state or exported for use in the production of pultruded FRP products like rebar, woven fabrics for composite applications, shells for concrete-filled tubes or other structural/strengthening applications. This paper will show the results of the basalt characterization research PISCES has conducted and the results of the CBF market feasibility study performed by SMA.

1. Hawaiian Basalt as a Feedstock for Manufacturing and Construction

Between 2015 and 2016, PISCES in collaboration with NASA's Swamp Works developed interlocking paver tiles made of sintered Hawaiian basalt to robotically build a vertical take-off & vertical landing (VTVL) pad. The basalt used for the tiles was a product of a Hawaii Island quarry. These tiles were constructed using sub-150µm basalt fines with no additives. The fines were packed into a ceramic mold and placed into a kiln, then sintered at 1,149^{o}C. The mechanical properties of the resulting material exceeded those of residential concrete and met the requirements of the test (Table 1). Additional sintering tests of the basalt fines at a higher temperature 1,176.6^{o}C produced a different material with significantly stronger mechanical properties (Table 1). PISCES is currently continuing research in this field.

Table 1. Structural Properties of Hawaiian Sintered Basalt

Sintering Temp	Density (g/cm^3)	Compressive Strength[1] (MPa)	Flexural Strength (MPa)
1,149^{o}C	1.699	21.48	4.93
1,176^{o}C	2.64	212.54	40.35

2. Characterization of Basalt Obtained from Commercial Quarries

PISCES began experimenting with basalt sintering using basalt aggregate from only one local quarry. When basalt from other quarries was used for testing to compare results, fines from other locations produced widely varying results in structural characteristics. So far, PISCES has sintered and analyzed basalt aggregate from four quarries on Hawaii Island. For both thermal profiles shown above, quarries 1 and 3 created the most cohesive bricks whereas quarries 2 and 4 created bricks with structural problems like cracking and crumbling. Figures 1a & 1b below show all four quarried materials sintered at 1,149^{o}C and 1,176^{o}C. So far, only material from quarry 1 and quarry 4 have been sintered at 1,176^{o}C, and only quarry 1 has been sintered at grain sizes larger than 125 µm producing bricks with a textured surface.

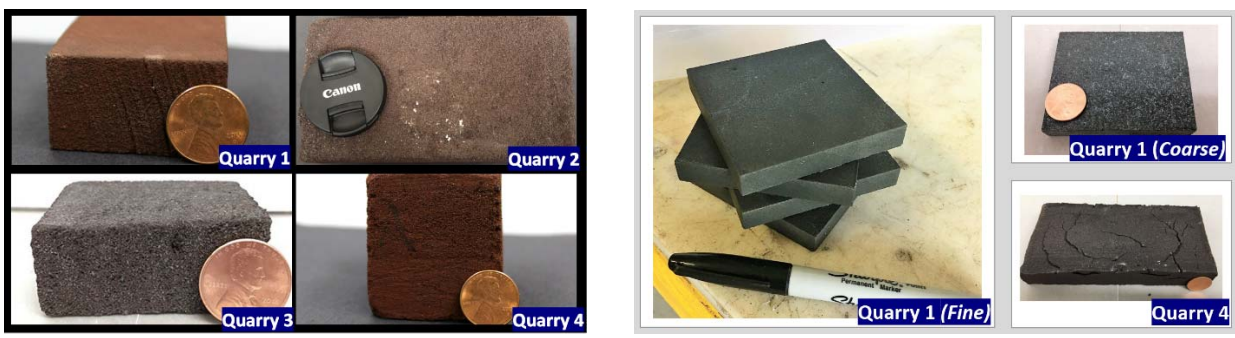

(a) (b)

(b)

Fig. 1 (a). Basalt aggregate from four Hawaii Island quarries sintered at 1,149^{o}C produced various qualities of bricks depending on their source. (b). Basalt aggregate from quarries 1 & 4 sintered at 1,176^{o}C produced various qualities of brick depending on source location and grain size.

Due to the variation in brick quality from each quarry, it was important to investigate the chemical makeup of each aggregate sample to determine if there were any significant differences between them. Energy Dispersive X-Ray Fluorescence (EDXRF) analysis was used to gauge the chemical composition of each sample. Table 2 illustrates the chemical profiles of aggregate samples from each of the four quarries. Testing results showed that samples from quarries 2 and 4 (which produced poor-quality bricks) contained significantly higher amounts of MgO. These samples are thought to contain minerals abundant in MgO such as Forsterite Olivine. Forsterite has a melting point of 1,898.9 °C. It was assumed that Forsterite would not sinter at the current thermal profiles, possibly resulting in points of weakness and lesser-quality bricks.

[1] Compressive Strength and Flexural Strength (Modulus of Rupture) tests were performed by NASA's Engineering Directorate Laboratories and Test Facilities Division, Kennedy Space Center, FL in accordance with ASTM C133.

Table 2. EDXRF Chemical Abundance Values for Island Quarries

	Na_2O%	MgO %	Al_2O%	SiO_2 %	K_20 %	CaO %	TiO_2 %	FeO%	Fe_2O_3 %	MnO %	P_2O_5%
Quarry 1	*2.4*	*6.78*	*13*	*50.4*	*0.35*	*10.1*	*1.77*	*10.5*	*11.69*	*0.17*	*0.26*
Quarry 2A	*2.34*	*8.89*	*12.3*	*49.5*	*0.34*	*9.61*	*1.71*	*10.7*	*12.21*	*0.16*	*0.3*
Quarry 2B	*1.71*	*18.6*	*8.76*	*46.1*	*0.22*	*6.73*	*1.22*	*12*	*13.74*	*0.17*	*0.3*
Quarry 3	*2.39*	*5.45*	*13.4*	*51*	*0.4*	*10.6*	*1.93*	*10.4*	*11.77*	*0.16*	*0.26*
Quarry 4	*2.17*	*13.3*	*11.2*	*47.6*	*0.28*	*7.87*	*1.5*	*11.5*	*12.98*	*0.17*	*0.31*

3. Continuous Basalt Fiber Manufacturing Feasibility Study for Hawai'i.

As part of its core objective to develop and diversify Hawaii's economy, PISCES contracted SMA[2] to conduct a comprehensive market feasibility study. The study's main goal was to determine if a Continuous Basalt Fiber (CBF) manufacturing operation in Hawaii County could benefit the local economy. The study looked at many factors including the projected market growth of the CBF industry worldwide, the current supply and demand of CBF, and the necessary costs of running such an operation in Hawaii. The basalt samples collected at four commercial quarries in Hawai'i indicated that two locations (Quarries 1 & 3) possessed the chemical makeup within, or close to, the desirable parameters required for basalt fiber extrusion (Table 3). Coincidentally, these were the quarries that produced the higher quality sintered material.

Table 3. Recommended Composition of Basalt for CBF Extrusion[3] (%)

Source	SiO_2	Al_2O_3	CaO	MgO	$NA_2O + K_2O$	TiO_2	Fe_2O_3 + FeO	Others
Excelement.com	50-60	14-19	5-10	3-5	3-5	0.5-3.0	9-14	0.05-1.0
Quarry 1	50.4	13	10.1	6.78	2.75	1.77	22.19	
Quarry 3	51	13.4	10.6	5.45	2.79	1.93	22.17	

According to SMA's analysis, the CBFmarket was worth $178 million in 2018 and is expected to grow to $405 million in the next decade. The current market is dominated by Chinese and Russian CBF manufacturers. Some production is happening in Europe and a plant in the U.S. is expected to begin operations this year. SMA's analysis incorporated a 30-year financial model for a 6,600 metric-ton plant producing various types of CBF roving. The model was based on prices of $1.50, $2.50 and $4.00 per pound of low, medium and high-quality roving. Based on these assumptions and an estimated average selling price of $2.38 per pound of basalt roving, the venture would produce roughly $1 billion in free cash flow and $450 million in net income during the 30-year operating period of the plant. The study identified that the main obstacles a Hawaii-based CBF operation faces include but are not limited to:

- High energy costs;
- High labor costs;
- Shipping costs to and from Hawaii.

The next step in this process is to locate a facility where Hawaiian basalt from local quarries can be tested and validated for its fiber making quality. PISCES is now seeking companies and/or laboratories to complete this goal.

[2] SMA Inc. 18400 Von Karman Ave, Ste 500. Irvine, CA 92612. www.smawins.com

[3] Chemical constituents of basalt rocks; www.excelement/basalt-fibre-technology/

Effect of the Fiber Content on the Tensile Strength Properties of Basalt Fiber Reinforced Polymer Rebars

Alvaro Ruiz Emparanza[1*], Raphael Kampmann[2], Francisco De Caso[3], and Antonio Nanni[4]

[1] Department of Civil & Environmental Engineering, University of Miami, Miami (FL), USA. email: alvaro.ruiz@miami.edu
[2] Department of Civil & Environmental Engineering, FAMU-FSU College of Engineering, Tallahassee (FL), USA. email: kampmann@eng.famu.fsu.edu
[3] Department of Civil & Environmental Engineering, University of Miami, Miami (FL), USA. email: fdecaso@miami.edu
[4] Department of Civil & Environmental Engineering, University of Miami, Miami (FL), USA. email: nanni@miami.edu

[*]: corresponding author

Keywords: BFRP; basalt fiber, fiber content; tensile strength; corrosion

Abstract: The long-term performance of steel reinforced concrete structures is limited by the corrosion of the steel reinforcing bars (rebars). Recently, continued efforts have emerged to implement alternative reinforcing materials in substitution of steel to extend the lifespan of concrete structures. The use of basalt fiber reinforced polymer (BFRP) rebars as internal reinforcement of has increased significantly in the last years, mainly due to the corrosion resistance and its beneficial mechanical properties. BFRP rebars are composite materials made of continuous basalt fibers embedded longitudinally in a resin matrix. The fiber to resin proportion is different for every commercially produced rebar type, with a minimum fiber content of 70% (by weight/mass) per ASTM D7957. The aim of this project was to evaluate the effect of the fiber content and its impact on the tensile strength properties of the BFRP rebars. Accordingly, the fiber mass content, the cross-sectional area, and the tensile strength of three different rebar types were tested and compared. Preliminary results show, that a direct relation exists between fiber to resin proportion, and the tensile strength of BFRP rebars.

1. Introduction

In the process of moving toward a sustainable and long-lasting infrastructure, composite materials are gaining importance to be used as internal reinforcement in concrete structures, substituting the traditional black steel to avoid corrosion issues. Composite rebars are fiber reinforced polymers (FRP) and compared to steel, they have higher strength (2-3 times higher), they are lightweight (4 times lighter), but most importantly, they don't suffer corrosion. To-date, the most commonly used fiber types are carbon (for pre-stress applications) and glass (for mild reinforcement); however, the use of basalt fibers is increasing exponentially due to relatively simpler production process compared to glass. Basalt fibers are produced using a continuous process similar to the glass fibers, but with the difference that the basalt fibers are extracted from a single raw material (melted basalt rock), while the glass fibers are made combining different constituents (silica sand, oxides of boron, aluminum, etc.). In addition, aramid fibers are also used by some manufacturers but are not as common as carbon, glass or basalt. Among the resins,

epoxy and vinyl-ester are the ones that are mainly used in the production of FRP rods (Nanni, De Luca and Zadeh, 2014). For the production of these composite materials, the quality of the raw materials (fibers and resin) is of high importance, but also the proportions of each constituent are critical. The fibers are the load carrying elements, while the resin is responsible for the strength transfer between the fibers, as well as for protecting them against damaged over time.

Due to the increase of the use of basalt fiber reinforced polymer (BFRP) rebars, many researchers around the world have worked on the characterization and durability assessment of these composite materials (Serbescu, Guadagnini and Pilakoutas, 2014; Wu *et al.*, 2014; Dong *et al.*, 2016, 2017; Wang, X. L. Zhao, *et al.*, 2017; Wang, X.-L. Zhao, *et al.*, 2017). However, to the best knowledge of the authors, the effect of the fiber/resin ratio on the strength properties of the BFRP rebars has not been documented in the literature. To-date, no material standard specification exists for BFRP rebars, but the one existing for glass FRP rebars, ASTM D7957 (ASTM International, 2017), sets the minimum fiber mass content to a minimum of 70%. To determine the fiber mass content, two methods are referenced in ASTM 7957: 'ASTM D2584 - Standard Test Method for Ignition Loss of Cured Reinforced Resins' (ASTM International, 2018) and the 'ASTM D3171 - Standard Test Method for Constituent Content of Composite Materials' (ASTM International, 2015). The aim of this paper is to correlate the fiber content of BFRP rebars with their tensile test properties.

2. Methodology

For the evaluation of the effect of the fiber content on the tensile test properties of BFRP rebars, rebars from three different manufacturers were tested (A, B, C). Two rebar sizes were evaluated: #3 and #5. Manufacturer A provided two rebar types per size (A-1 and A-2), made of different resins but same fibers. Manufacturer B provided # 3 rebars only, while manufacturer C provided # 5 rods only. Four different physio-mechanical properties were tested: cross-sectional area, fiber content, tensile strength and modulus of elasticity. The research scope included 5 repetitions per test (tensile test, fiber content test and cross-sectional area test), rebar type (A, B and C) and size (#3 and #5), leading to a total of 90 test repetitions. The specimen preparation and the tests were accomplished according to the relevant ASTM standards. ASTM D7205 was followed for the tensile tests: due to the low strength capacity on the transverse direction of the BFRP rebars compared to the longitudinal one, both specimen ends were protected using steel pipes filled with expansive grout. The fiber mass content tests were conducted according to ASTM D2584, while ASTM D792 was followed to evaluate the cross-sectional area. Figure 1 shows the test setup for both the tensile (left) and the fiber content (right) tests.

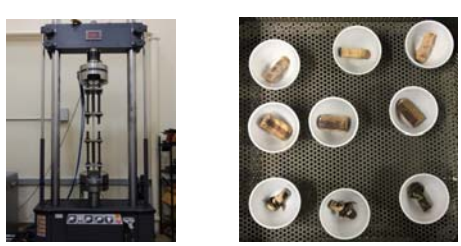

Figure 1. Tensile test setup (left) and fiber content test specimens being burnt inside the furnace (right)

3. Results and Discussion

The obtained results were analyzed and statistically evaluated and as summarized in Table 1. Both the tensile strength and E-Modulus were calculated using the measured area values. It can be seen that the physio-mechanical properties for the two types of rebars for manufacturer A, were similar, while they differed significantly from the rebars provided by manufacturers B and C.

Table 1. Summary of the experimental results

Rebar Size	Rebar Type	Measured Area		Fiber Content		Tensile Peak Load		Tensile Strength		E-Modulus	
		Mean	COV	Mean	COV	Mean	COV	Mean	COV	Mean	COV
		in^2	%	%	%	kip	%	ksi	%	10^6 psi	%
#3	A-1	77.29	0.49	71.78	0.32	17.19	5.70	146.63	5.70	6.99	3.10
	A-2	77.73	0.26	75.27	0.18	19.78	2.60	167.81	2.60	6.66	2.50
	B	55.56	0.45	75.48	1.12	14.06	3.70	166.79	3.70	7.94	3.80
#5	A-1	225.62	0.35	75.54	0.06	52.34	5.80	144.30	5.80	6.46	5.60
	A-2	231.00	0.85	75.49	0.06	49.15	8.00	140.28	8.00	5.74	7.00
	C	192.41	0.17	84.80	0.06	47.37	3.80	162.30	3.80	7.20	2.40

To better understand the correlation between the fiber content and the tensile properties of the BFRP rebars, the tensile strength and the E-Modulus were plotted with respect to the fiber content (see Figure 2 and 3). The average tensile strength values for the different rebar types are shown in Figure 2, grouped by rebar size. Each of the three data points per rebar size represents the average tensile peak stress with respect to the average fiber content of the five repetitions per rebar type. The maximum fiber content was obtained for manufacturer C (#5 rebars) with about 85%, while A-1 rebars had the least relative amount of fibers. However, all rebar types exceeded the minimum fiber content (70%) defined by ASTM D7957. In general, it can be inferred that the tensile capacity increases with increasing fiber content. These results indicate that the tensile strength is mainly governed by the amount of fibers, though a minimum amount of resin is needed to properly transfer the stress between fibers. For this reason, the resin type appears to also affect this property as it can be seen in rebar types A-1 and A-2, which had almost identical fiber contents but different resin types. However, the tensile strength for A-1 was about 6.5% higher than the one for A-2.

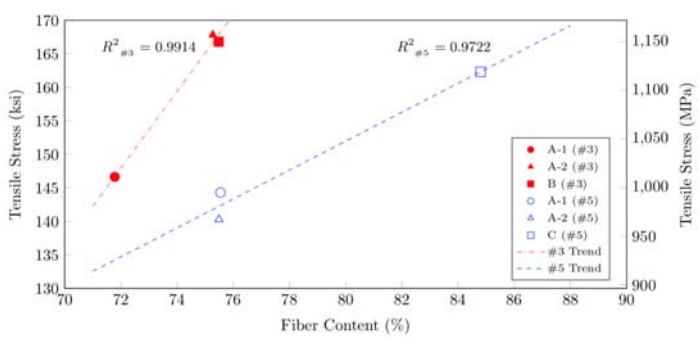

Figure 12. Tensile stress with respect to the fiber content

In Figure 3, the E-modulus was plotted versus the fiber content. In this case, based on the tested specimens, the authors did not find any relation between the E-modulus and the fiber content.
In general, the E-modulus tended to increase with the increase of fiber content, though the values appeared to be more scattered.

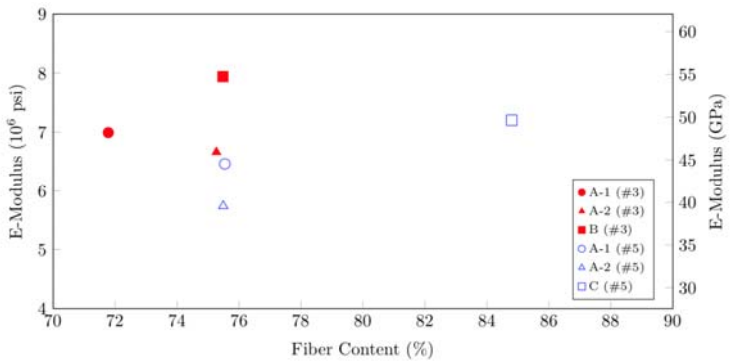

Figure 13. E-Modulus with respect to the fiber content

The resin type also appeared to affect the E-Modulus. Both #5 rebar types produced by manufacturer A (type A-1 and A-2) were produced using the same fiber type but different resins, and even if they had comparable fiber contents, the E-Modulus varied about 12.5% between each other.

4. Conclusions

In this paper the correlation between the fiber content and the tensile properties of BFRP rebars was evaluated by testing dissimilar rebar types and sizes (#3 and #5) produced by three different manufacturers. For all rebar types and sizes, the cross-sectional area, the fiber content, the tensile strength, and the E-Modulus were calculated. From the obtained results it could be seen that a linear correlation exists between the tensile strength and the fiber content: the higher the fiber content, the higher the tensile capacity of the rebar. This leads to the conclusion that the tensile response of the BFRP rebars is directly related to the amount of fiber, though the resin type (responsible for the stress transfer between fibers) also has an effect. This was substantiated by the 6.5% difference in peak tensile stress for A-1 and A-2 rebars, which differed only by the resin type. The E-modulus also tended to increase with the increasing fiber content, though no clear trend was found. In this case too, the E-Modulus appeared to be affected by the resin type: a difference of about 12.5% was found between the E-Modulus of type A-1 and A-2 rebars.
To better assess the relation between the tensile properties and fiber content of BFRP rebars, more rebar types and sizes should be tested. In addition, tests on each of the constituents (fibers and resin) independently would be beneficial to assess the effect that these raw materials may have in the general performance of the rebars.

5. Acknowledgments

The authors acknowledge the financial support of the Florida Department of Transportation (FDOT) and the guidance provided by its staff Chase C. Knight, Ph.D. and Steven Nolan, P.E.

6. References

ASTM International (2015) 'ASTM D3171 - Standard Test Methods for Constituent Content of Composite Materials'. doi: 10.1520/D3171-15.2.

ASTM International (2017) *ASTM D7957 - Standard Specification for Solid Round Glass Fiber Reinforced Polymer Bars for Concrete Reinforcement*. doi: 10.1520/D7957.

ASTM International (2018) *ASTM D2584 - Standard Test Method for Ignition Loss of Glass Strands and Fabrics*. doi: 10.1520/D2584-11.2.

Dong, Z., Wu, G., Xu, B., Wang, X. and Taerwe, L. (2016) 'Bond durability of BFRP bars embedded in concrete under seawater conditions and the long-term bond strength prediction', *Materials and Design*, 92, pp. 552–562. doi: 10.1016/j.matdes.2015.12.066.

Dong, Z., Wu, G., Zhao, X. L. and Wang, Z. K. (2017) 'A refined prediction method for the long-term performance of BFRP bars serviced in field environments', *Construction and Building Materials*, 155, pp. 1072–1080. doi: 10.1016/j.conbuildmat.2017.07.154.

Nanni, A., De Luca, A. and Zadeh, H. (2014) *Reinforced Concrete with FRP Bars*. doi: 10.1201/b16669.

Serbescu, A., Guadagnini, M. and Pilakoutas, K. (2014) 'Mechanical characterization of basalt FRP rebars and long-term strength predictive model', *Journal of Composites for Construction*. American Society of Civil Engineers, 19(2), p. 4014037.

Wang, Z., Zhao, X.-L., Xian, G., Wu, G., Raman, R. K. S., Al-Saadi, S. and Haque, A. (2017) 'Long-term durability of basalt-and glass-fibre reinforced polymer (BFRP/GFRP) bars in seawater and sea sand concrete environment', *Construction and Building Materials*. Elsevier, 139, pp. 467–489.

Wang, Z., Zhao, X. L., Xian, G., Wu, G., Singh Raman, R. K. and Al-Saadi, S. (2017) 'Durability study on interlaminar shear behaviour of basalt-, glass- and carbon-fibre reinforced polymer (B/G/CFRP) bars in seawater sea sand concrete environment', *Construction and Building Materials*, 156, pp. 985–1004. doi: 10.1016/j.conbuildmat.2017.09.045.

Wu, G., Dong, Z., Wang, X., Zhu, Y. and Wu, Z. (2014) 'Prediction of Long-Term Performance and Durability of BFRP Bars under the Combined Effect of Sustained Load and Corrosive Solutions', *Journal of Composites for Construction*, 19(3), p. 4014058. doi: 10.1061/(ASCE)CC.1943-5614.0000517.

The Use of Geopolymer Concrete and GFRP Materials for an Innovative Wharf Structure

Thomas Glasby[1], John Day[2], Michael Kemp[3*], and Rohan McElroy[4]

[1] Wagners EFC Pty Ltd, Australia
[2] Wagners EFC Pty Ltd, Australia
[3] Wagners CFT Pty Ltd, Australia; email: michael.kemp@wagner.com.au
[4] icubed consulting engineers, Australia

[*]: corresponding author

Keywords: CFT; EFC; glass fibre reinforced polymer; GFRP; geopolymer concrete; U-girders; wharf

Abstract: The design and construction of a new Wharf facility at the Wagners cement site in Brisbane Queensland features an innovative approach to building materials that delivers significant advancements in both environmental and engineering performance. The wharf deck superstructure is comprised of 191 no. prefabricated panels that span between 8 and 12 metres over steel headstock beams. The panels are a unique hybrid structural system developed over many years by Wagners R&D division initially for use in pedestrian and road bridges. The system has been adapted and further developed for the challenging conditions of a marine wharf structure. Each of the panels consist of:

- pultruded composite fibre girders that provide the tensile beam spanning capacity,
- geopolymer concrete engaged deck that acts as a compression flange while locking the girders together,
- glass fibre reinforced polymer (GFRP) reinforcing bar in the concrete deck to form a completely non-metallic structure that is risk free for marine exposure borne corrosion,
- vastly reduced embodied carbon emission compared to conventional materials.

The hybrid deck superstructure described above represents a new approach using high technology building materials to deliver efficient, low maintenance and low CO_2 emission engineering structures. This paper describes the design and manufacture of the prefabricated deck units and the necessary testing and material properties validation that were undertaken on this structural system and its component materials over many years.

1. Introduction

A new Wharf facility constructed at Wagners cement site on the Brisbane River, Queensland will enable the direct berthing of cement clinker ships that carry up to 35,000 tonnes cargo. This facility will replace the current arrangement of berthing clinker ships at the Port of Brisbane and road freighting clinker to the cement site. Figure 1 shows the location and overall layout. The subject of this paper is the Wharf's deck which features a new and innovative approach to building materials and delivers significant advancements in both environmental and engineering performance.

The Wharf's deck is comprised of 191 no. prefabricated panels that span between 8 and 12 metres over steel headstock beams. The panels are a unique hybrid structural system developed over many years by Wagners R&D division initially for use in pedestrian and road bridges. The system has been adapted and further developed for the challenging conditions of a marine wharf structure. The wharf deck layout is shown in Figure 1. Each of the panels consists of:

• pultruded composite fibre U-girders that provide the tensile beam spanning capacity,
• geopolymer concrete engaged deck that acts as a compression flange while locking the U-girders together,
• glass fibre reinforced polymer (GFRP) reinforcing bar in the concrete deck to form a completely non-metallic structure that is risk free for marine exposure,
• vastly reduced embodied carbon emission compared to conventional steel and concrete materials.

The hybrid deck superstructure described above represents a new approach using high technology building materials to deliver efficient, low maintenance and low CO2 emission engineering structures. This paper describes the design and manufacture of the prefabricated deck units and the necessary testing and material properties validation that were undertaken on this structural system and its component materials.

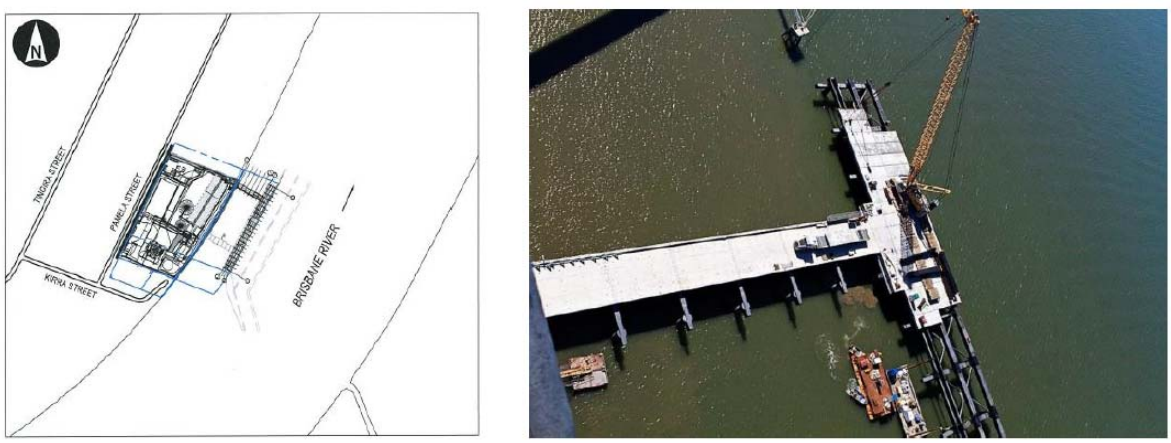

Fig. 1 Locality plan and aerial photograph while under construction – Wagners cement wharf

2. Use of novel engineered materials

Three novel engineered materials have been used in the design of the prefabricated deck units – geopolymer concrete, glass fibre reinforced polymer (GFRP) reinforcement and glass fibre reinforced polymer U-girders (CFT). The arrangement is shown in figure 2.

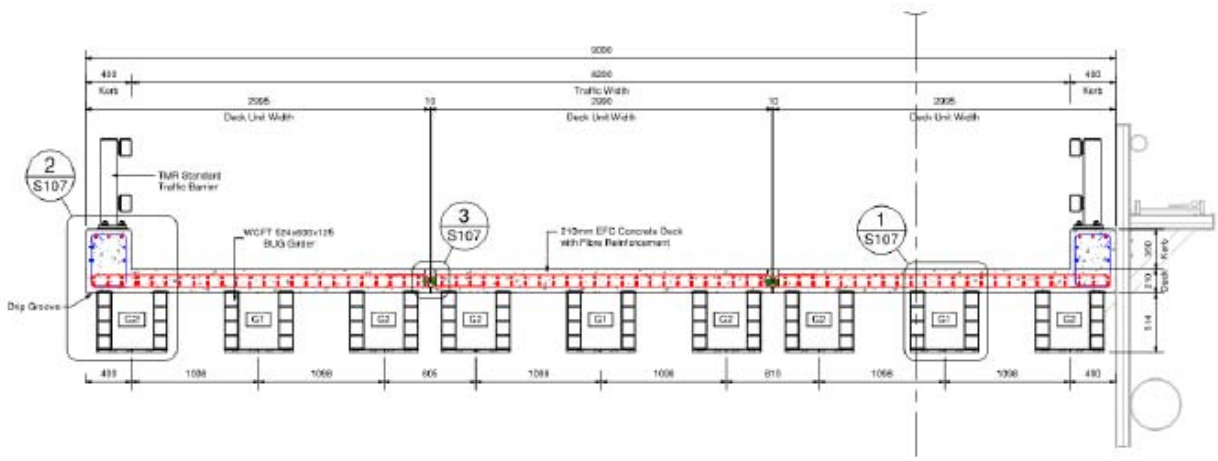

Fig. 2 Typical deck unit cross section and images of completed deck units

2.1. Geopolymer concrete

While alkali activated slag concrete has a history dating back to the 1930's in Eastern Europe (Roy 1999), geopolymer concrete is still deemed a relatively new technology in modern concrete construction. The proprietary geopolymer concrete mix (Wagners Earth Friendly Concrete® - EFC) used in this project follows over 10 years of work by Wagners developing a commercial product that is produced and handled in a similar manner to conventional concrete. It contains absolutely no Portland cement. The binder consists of ground granulated blast furnace slag (GGBS) complying to AS 3582.2 (2016), fly ash complying to AS 3582.1 (2016) and a proprietary geopolymer hardener solution. Comprehensive testing and independent R&D studies have shown EFC to possess many significant performance and durability benefits over conventional cement based concrete, including 30% higher flexural strength, low drying shrinkage, low heat of reaction and very high resistance to chemical attack.

Previous significant project examples of this proprietary geopolymer concrete include load bearing precast reinforced floor beams in a multi storey building (Bligh & Glasby 2013) and heavy duty aircraft pavements in Australia's newest public airport (Glasby et al 2015). The project mix was developed to suit placement through heavily congested reinforcing layers and achieve the design strength requirements:

• Minimum flexural strength of 6.0 MPa at 28 days, tested to AS 1012.11
• Characteristic compressive strength of 50 MPa at 28 days, tested to AS 1012.9

The demanding strength criteria and rheological (flow) properties were able to be achieved using a 10 mm maximum aggregate size EFC that still achieved over 6.0 MPa flexural strength and 50 MPa characteristic compressive strength in 28 days. High flexural strength in comparison to conventional concrete is a benefit of the EFC geopolymer that was able to be used in the FE design of the prefabricated hybrid deck elements. The mix also satisfied the demand of high production precast by attaining the minimum 20 MPa lift strength in typically 15 hours without any artificial heating. An image of a deck unit being cast with EFC using a kibble is shown in Table 1.

2.2. Glass fibre reinforced polymer (GFRP) reinforcing bars

GFRP has a very important role to play as reinforcement in concrete structures that will be exposed to harsh environmental conditions where traditional steel reinforcement could corrode, especially in marine and other salt laden environments. GFRP reinforcing bars are gradually finding wider acceptance as a replacement for conventional steel reinforcement as it offers a number of advantages. Detailed laboratory studies of samples taken from reinforced concrete structures, aged from five to eight years old, have confirmed that GFRP has performed extremely well when exposed to highly corrosive marine field conditions (Kemp and Blowes 2011).

The GFRP reinforcing bars used in this project are made of E-Glass and a polymer resin matrix in a pultrusion manufacturing process. The GFRP bars are post-cured to set the thermosetting polymer matrix to prevent remoulding of the material at elevated temperatures. GFRP bar can come in a number of sizes with some standard and non-standard varieties. The prefabricated deck units' design and construction utilised 16mm, 19mm and 22mm diameter bars.

GFRP bars have a high tensile modulus and low modulus of elasticity compared to standard G500 reinforcing steel. They are also characterised by their light-weight and inherently brittle nature meaning that bars cannot be manually bent on site and do not yield like a typical steel bar. Instead, GFRP bars are designed with large factors of safety on their ultimate design to prevent brittle failure mechanisms developing. An overloaded under-reinforced steel reinforced slab will show warning signs of approaching failure, such as large deformations and crack widths. A well designed GFRP beam at overload will undergo an over-reinforced failure mechanism with the concrete failing in compression and exhibiting warning signs of oncoming structural collapse.

The GFRP reinforced geopolymer concrete slabs for the wharf deck units were designed in accordance with Canadian Standard CSA S806 (2012). This standard outlines methods for manufacturing requirements, designing beams and slabs for ultimate and service loads, testing of

reinforcing bars and testing the bar and slab interactions. Three of the general governing concepts of this code include:
1. Ensuring the governing failure mode is from crushing failure of the concrete and not GFRP bar rupture failure.
2. Limiting GFRP bar strains to 0.002 and stresses to 25% of characteristic tensile strength for serviceability loading criteria, and
3. Including additional safety reduction factors and rules regarding the ultimate limit state moment resistance of the slabs to prevent sudden collapse mechanisms.

A comparison of typical properties of GFRP rebar and standard G500 rebar is shown in Table 1 below, along with images of the GFRP during manufacture of the deck units.

Material Type	Modulus of Elasticity	Tensile Modulus	Shear Modulus	Material Density
G500 Steel Rebar	200 GPa	500 MPa	80 MPa	7850 kg/m3
GFRP Rebar	~46 GPa	752 MPa	150 MPa	2030 kg/m3

Table 1 Comparison of standard mild steel vs. GFRP reinforcing bar

2.3. Glass fibre reinforced polymer (GFRP) U-girders

Fibre reinforced polymers have proven themselves as the material of choice in high performance applications such as the Aerospace and Marine industries. As the use of Fibre reinforced polymers have become more common their benefits have been realised by other industries and their use and acceptance by civil engineers has greatly increased in recent years (Benmokrane and Ali 2018). Fibre reinforced polymers offer high strength, low weight, and long service lives as they are not prone to corrosion, rot or shrinkage unlike other materials more traditionally used by the construction industry. The product used for the U-girders in the prefabricated deck units was a proprietary GFRP material manufactured and supplied by Toowoomba Queensland based company, Wagners Composite Fibre Technology (WCFT). This company has been instrumental

in expanding the use of fibre reinforced polymers in Australia and throughout the World, exporting products to locations such as the USA, New Zealand, Russia, and Malaysia.

WCFT use the 'Pultrusion Process' to manufacture proprietary GFRP sections branded CFT, figure 3. Electrical-Corrosion Resistant (ECR) Type Glass is used because it is a high-grade material with excellent strength performance, workability and chemical resistance (Ely et al 2001). The ECR fibres are bound in a vinyl ester resin which provides the best structural solution at an economical cost. WCFT supported by icubed consulting have been producing CFT sections for use in a multitude of applications for 14 years. Table 2 shows the comparison between the CFT material properties and concrete, timber and steel.

Mechanical Properties of Typical Construction Materials							
Material	Young's Modulus	Shear Modulus	Density	Ultimate Tensile Strength	Ultimate Compressive Strength	Nominal Shear Strength	Poisson's Ratio
	GPa	GPa	kg/m^3	MPa	MPa	MPa	
CFT	36.3	8	2030	610	485	84	0.28
Steel	200	80	7600	300	~170	~180	0.30
Concrete	~30	12	2400	3-5	25-60	6-17	0.2
Timber	7-21	13	500-700	10-40	20-50	4-20	0.2-0.5

Table 2 Mechanical properties comparison of GFRP with typical construction materials compiled by icubed consulting

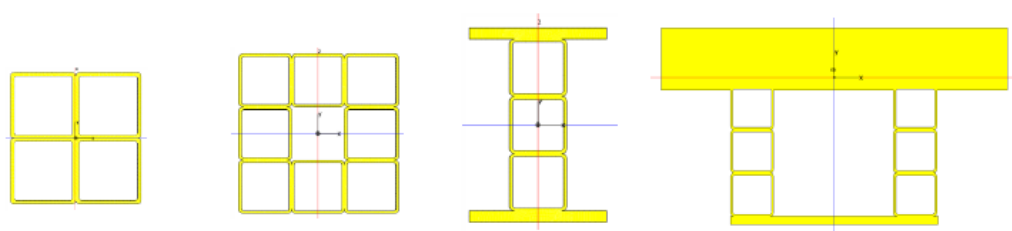

Fig. 3 Typical CFT section profiles
(bonded square section, bonded box section, bonded I-beam, bonded U-Girder)

3. Wharf deck structural system

3.1 Interaction of CFT girders and EFC geopolymer concrete

The Wharf project and a number of AS5100 rated road bridges around Australia currently use the technology of CFT U-Girders integrated with a reinforced concrete slab wearing surface. These two technologies coupled together provide a 'composite' beam section. The modules act in the following manner:

1. The concrete slab acts as the top flange for the section by transferring compression stresses (under downward loads).
2. The CFT U-Girder acts as the webs transferring shear and longitudinal stresses, and,
3. The 24mm thick GFRP flange acts as the bottom flange to distribute longitudinal / extreme fibre stresses.

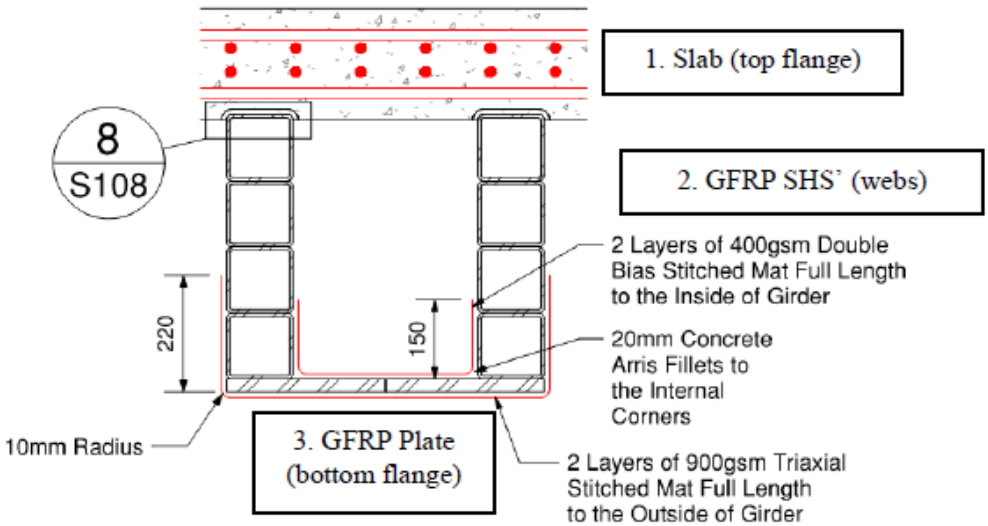

Fig. 4 Typical CFT U-Girder Cross Section

These actions can be seen in the cross-sectional stress graphs for a specific load case on the Wharf deck units, figure 5. The graph on the left shows the longitudinal shear stress values under maximum bending moment, while the graph on the right shows shear stresses across the section under maximum shear force.

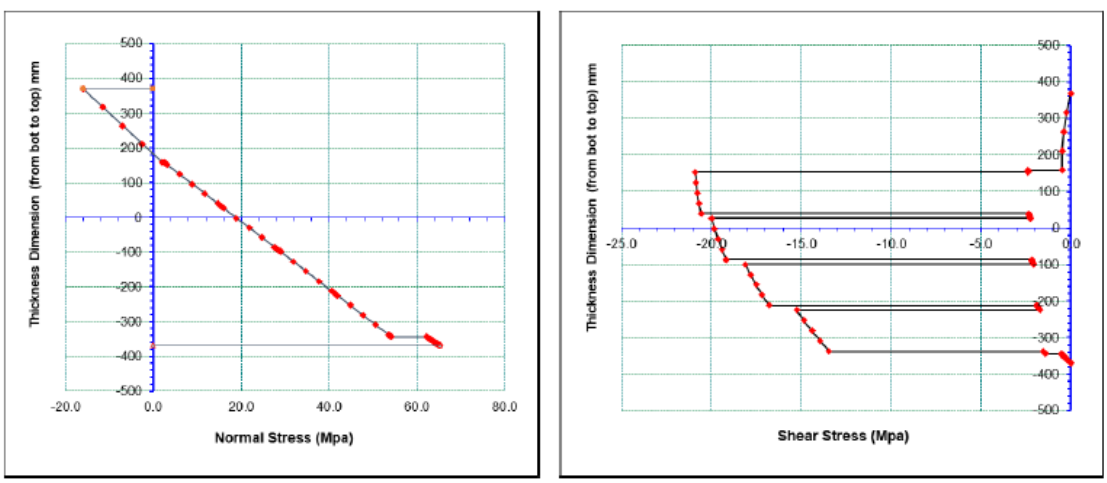

Fig. 5 Visual representation of longitudinal and shear stresses in the CFT U-Girder

The composite action of this member acts in the same manner as a typical reinforced concrete slab and Universal Beam (UB) floor system and can be seen in thousands of building projects across Australia. The use of composite floor slabs can be found in multistorey residential and commercial buildings, shopping centres, industrial warehouses, car parks and road and pedestrian bridges.

3.2 Neutral axis location

A critical design component of the CFT U-girders was the derivation of the neutral axis location. The neutral axis is the point at where longitudinal stresses change from compression to tension, or vice versa, under bending. It is characterised by a point of zero longitudinal stress. The below diagram from icubed's software shows the neutral axis sitting above the soffit of the concrete. Longitudinal tensile stresses may form in the concrete from the position of the neutral axis to the soffit of the concrete. These bending induced tensile stresses are required to be limited to the concrete's tensile stress capacity. This longitudinal tensile force will transfer through the tension zone of the concrete soffit, to the aggregate shear key located between the concrete slab and the top two rows of CFT U-girders. The aggregate shear key is made up of 10-12mm coarse aggregate that is washed, dried and adhesively bonded to the pultrusion top flange using a vinyl-ester resin. Best practice is to size the neutral axis to be positioned as close to the aggregate shear key as possible. This will ensure that tensile stresses in the unreinforced section of the concrete soffit are kept to a minimum.

Fig. 6 neutral axis calculation by icubed consulting and image showing aggregate shera key surface on U-girders

3.3 Prying of U-girders and concrete infill

During the detailed design of the Wharf, icubed consulting undertook a finite element (FE) model of the interaction between the U-girders and the EFC geopolymer infill blocks between each U-girder at their support location. This analysis was undertaken using ANSYS and specifically looked into the surface contact between the walls of the U-girders and the wall of the concrete infill blocks. The model showed that under high vertical loads the U-girders and the concrete infill panels may separate (delaminate) without a vertical shear key. In lieu of the shear key, due to added cost and manufacturing time, icubed and WCFT adopted a simple bolted stainless-steel rod that would act as a tension tie to prevent the U-girders and concrete infill blocks from prying under high loads.

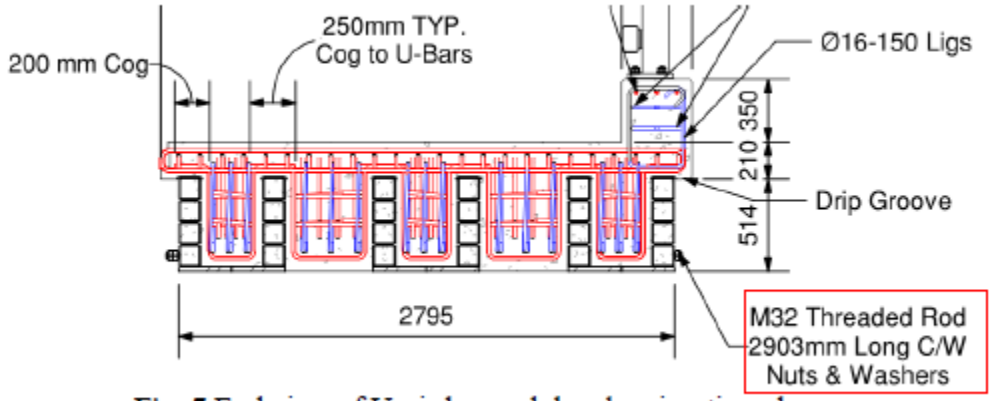

Fig. 7 End view of U-girder modules showing tie rod

3.4 Design Forces on Wharf structure

The Wharf structure has been designed to withstand some significant vertical and horizontal loads. The loads applied to the Wharf have been derived from detailed meetings with the Wharf operator focusing on their requirements over the design life of the structure. The main deck was designed to AS 4997 'Guidelines for the design of maritime structures' (2005) with a deck load classification of Class 25. The Wharf was also designed to AS 5100 'Bridge design code' (2004) and allowance was made for specific client requested structures and vehicles, summarised in table 3:

AS 4997	AS 5100	Client Requested
25 kPa UDL	W80 wheel load	40t moxy
500kN PL over 1200x1200mm sq.	A160 axle load	80t fully loaded hopper
SM1600	SM1600 design vehicle	35t straddle carrier
HLP	HLP design vehicle	forklifts
50t SWL mobile crane		Conveyors and transfer towers
		Liebherr LR1280 tracked crane for construction

Table 3 Vertical loading criteria for Pinkenba Wharf

One of the largest vehicle loads on the Wharf would be the 300t capacity crawler crane used exclusively for construction processes. The crane allowed the wharf to be constructed in sequence as each time a set of decks was installed, the crane was able to move forward and prepare the next bent, figure 8. All crane movements on the Wharf were accompanied by bog matts, which are large timber pads bolted together, to prevent the treads from damaging the wearing surface. Once the crane reached the jetty / wharf transition zone, large steel plates, as well as the bog matts, were laid to prevent damaging the wearing surface.

Fig. 8 Mobile crane tracking on the wharf deck during construction

3.5 Horizontal loading on the Wharf

In addition to the vertical loads outlined above, the Wharf structure is also required to resist a number of significant horizontal actions. These include:

1. 1 in 500-year flood and wave loading, including large debris mats. a. Uplift loads
   b. Downward loads
   c. Lateral loads
   d. Log/object impact loads

2. 40,000t moored vessel
   a. 80t bollard mooring loads (in multiple directions) from vessel
   b. 92t fender pile reactions from vessel

To accurately model and understand the horizontal actions imposed on the wharf, icubed consulting undertook a number of detailed finite element models in Strand7. The Strand7 models included developing the super-structure (EFC deck and CFT U-girders) as plate and brick elements and the sub-structure (structural steel transfer beams, headstocks, piles and bolts) as beam elements. A 3D screenshot of one of these models can be found below in Fig. 9 Strand7 FEA model the Wharf.

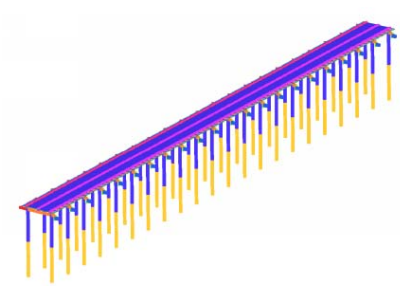

Fig. 9 Strand7 FEA model the Wharf

The horizontal load-response mechanism of the Wharf is complicated and required detailed analysis of both transverse and longitudinal actions through the deck. The EFC deck acts as a large diaphragm to share these loads across multiple bents. The results of the modelling indicated that longitudinal forces along the Wharf showed high tension and compression forces at joint locations while transverse forces across the Wharf showed high shear at joint locations. One of these graphical results can be seen below, figure 10:

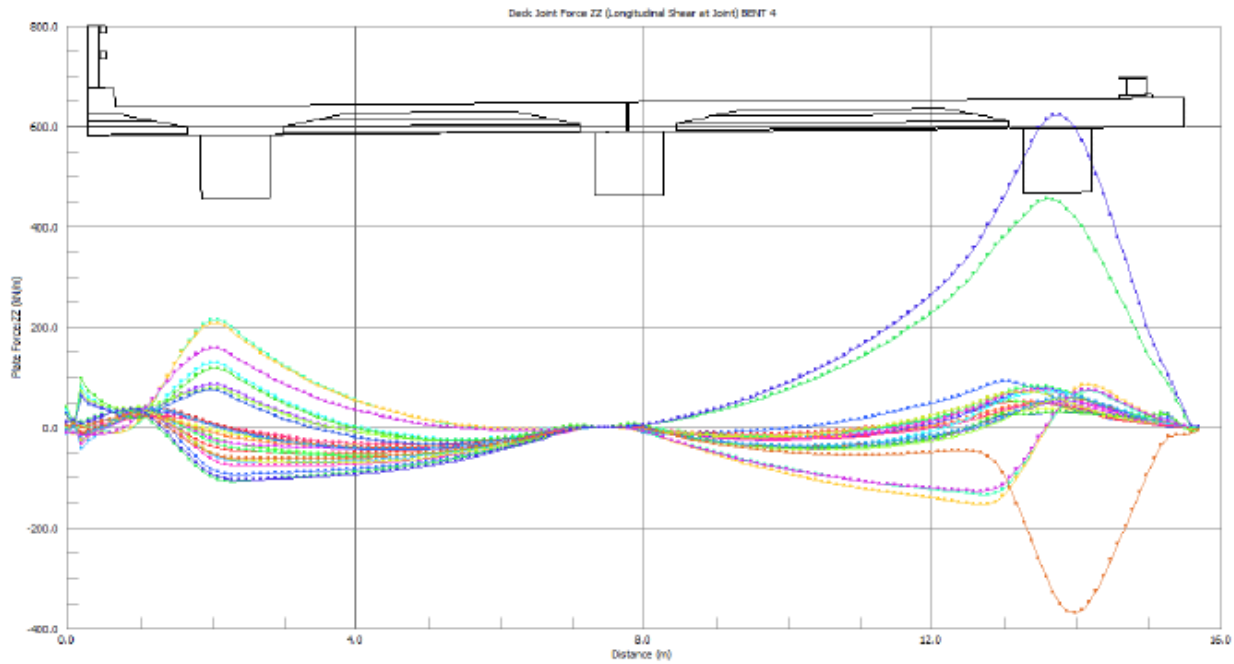

Fig. 10 Longitudinal shear at joint. LHS shows land side of wharf, RHS shows quay side (high forces from bollard loads)

3.6 Other environmental loads

In addition to the loading outlined above, the Wharf was also designed for 1-in-500-year wind event and 1-in-500-year earthquake event. Due to the magnitude of the horizontal actions from flooding, waves, debris and mooring of the vessels, the wind and earthquake load cases did not govern the design. The strand7 models also assessed thermal expansion and contraction of the varying materials on the wharf (steel, GFRP and geopolymer concrete) and estimated time dependant movement of the concrete over a 30-year period.

3.7 Creep and fatigue loads

Creep and fatigue were assessed for both GFRP reinforced EFC geopolymer concrete and for the CFT U-girders. Creep and fatigue calculations were undertaken for the concrete slab to AS 3600 (AS 2009) and for the GFRP materials to Eurocomp 'Structural design of polymer composites'(Clarke 1996).

3.8 Full-Scale Testing Program

Due to the relatively new-age technology used in the design and construction of the Wharf, icubed consulting requested a detailed testing program be undertaken to validate the theoretical design. The testing program was broken up into five key tests:

- Test 1: aggregate shear key tension test
  - To test tensile capacity of concrete
  - Ultimate tensile capacity of shear key from direct tension (wave uplift) loads
- Test 2: GFRP reinforcing and concrete deck capacity
  - Test ultimate moment capacity
  - Test ultimate shear capacity
  - Test ultimate punching shear capacity
  - Test ultimate bending capacity of slab
  - Test fatigue performance of slab over 2e6 cycles
  - Test long-term creep performance
  - Test longitudinal shear key capacity
  - Measure crack widths
- Test 3: full scale U-girder and concrete deck test
  - Test ultimate moment capacity
  - Test ultimate shear capacity
  - Test ultimate bending capacity of slab
  - Test fatigue performance of slab over 2e6 cycles
  - Test long-term creep performance
  - Test longitudinal shear key capacity
- Test 4: GFRP reinforcing bar tests
  - Test tensile modulus
  - Test elastic modulus
  - Test shear strength
  - Test ultimate tensile strength
  - Deriving GFRP bond coefficient
- Test 5: U-Clip joint capacity
  - Test shear and tension across U-clips in construction joints between each deck module.

Selected modelling and testing images, figures 11 - 13, show the good alignment achieved through this process.

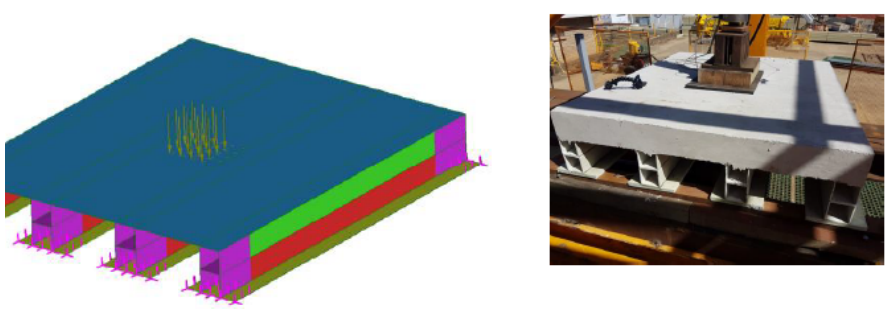

Fig. 11 Test 2: Strand7 FEA Model – GFRP rebar/concrete capacity and associated test rig

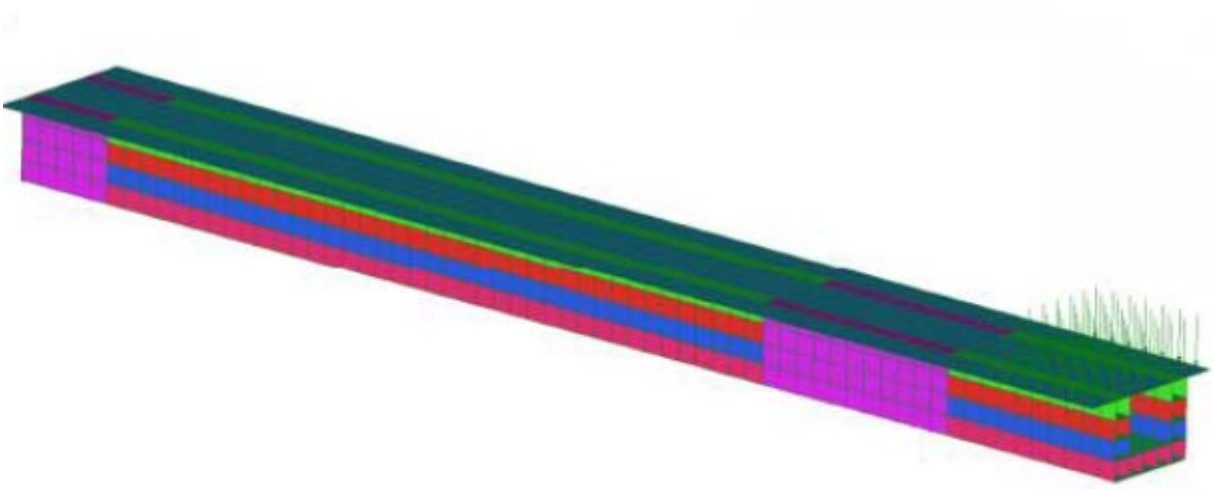

Fig. 12 Test 3: Strand7 FEA model – U-Girder cantilever performance

Fig. 13 Test 3: Actual cantilever testing being undertaken on full scale prototype

3.9 Cambering / serviceability description

The 12m long deck units forming the jetty section of the Wharf were designed with a 50 mm pre-camber in them while the 6m span modules that formed the long ship berthing section were designed as flat with no pre-camber. Cambering of the pre-cast modules for longer spans allows for imposed and environmental factors to occur without permanent sag in the U-girders. The

calculation of pre-camber required is based on a consideration of the following items: dead load, live load, creep, fatigue, shrinkage, and thermal movement.
The above load cases were calculated manually and then input into Strand7 FE analysis. The vertical deflection reading at mid-span of the modules were then extracted into Microsoft Excel and summed to provide an overall required pre-camber for each module. The 6m span modules experienced zero pre-camber requirements due to the shorter span. This also assisted construction and pre-casting of the most labour-intensive portion of the Wharf.

3.10 Design life of the Wharf

The wharf facility has been designed for a 50 year design life in accordance with AS 4997 (2005). WCFT have had three significant U-girder bridge designs installed in the USA and Australia for over 13 years. These three bridges to date have had no maintenance or remedial works undertaken.

- o Wellcamp quarry access bridge, Toowoomba, Australia – installed 2003
- o New Oregon Road Bridge, Erie County, USA – installed 2004
- o Taromeo Creek Bridge, D'Aguilar Highway, Australia – installed 2005

3.11 Interaction of Wharf deck and the sub-structure

The prefabricated deck elements also required an appropriate load path to transfer vertical and horizontal actions into the steel sub-structure, and then into the river bed. The simplest solution for this issue was to install stainless steel hold down bolts across the entire wharf. Each bolt was installed in the webs of the U-girder and were full-strength butt welded to the sub-structure hot-rolled steel elements and treated accordingly. This configuration is shown below in figure 14.

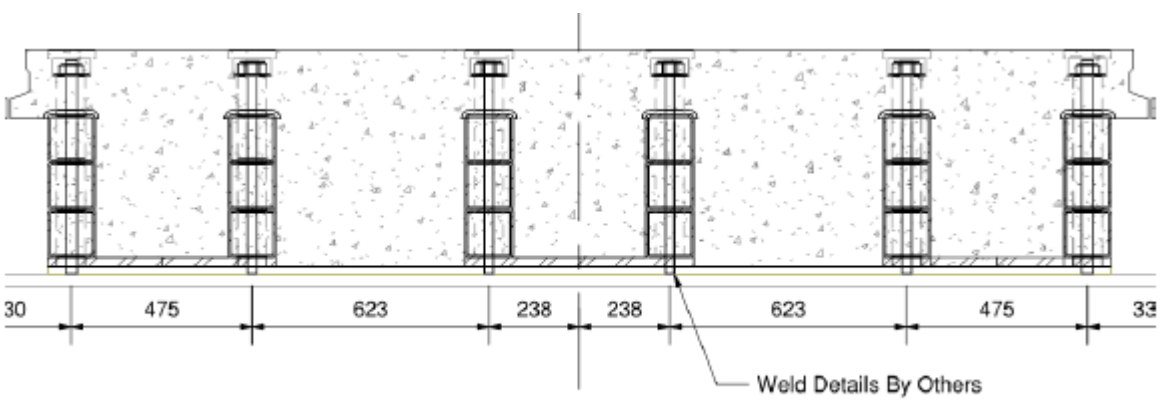

Fig.14 Positioning of a typical set of stainless steel hold down bolts

In the preliminary design phase of the project, icubed consulting undertook detailed hand calculations and simple beam structure models in Microstran to estimate the required bolt actions on the wharf. This proved to be too conservative so the hold down bolts were included as part of the greater FE modelling of the Wharf. Modelling the bolts in Strand7 allowed for accurate bolt force distributions across the deck modules which aided in providing a highly refined design outcome. The bolt groups with the highest loads on the Wharf were located at the 80t deck bollards and would be required to shed the large uplift and shear loads to the sub-structure portal

frame. Outside of the wharf bolting arrangement, large bolts were also required on the 84m long jetty, which acts as a large cantilevered structure for flood and debris loads. The extremely large bending moments at the abutment resulted in large force couples on the bolts. An extracted graph of the bolt shear forces at the abutment can be found below in figure 15:

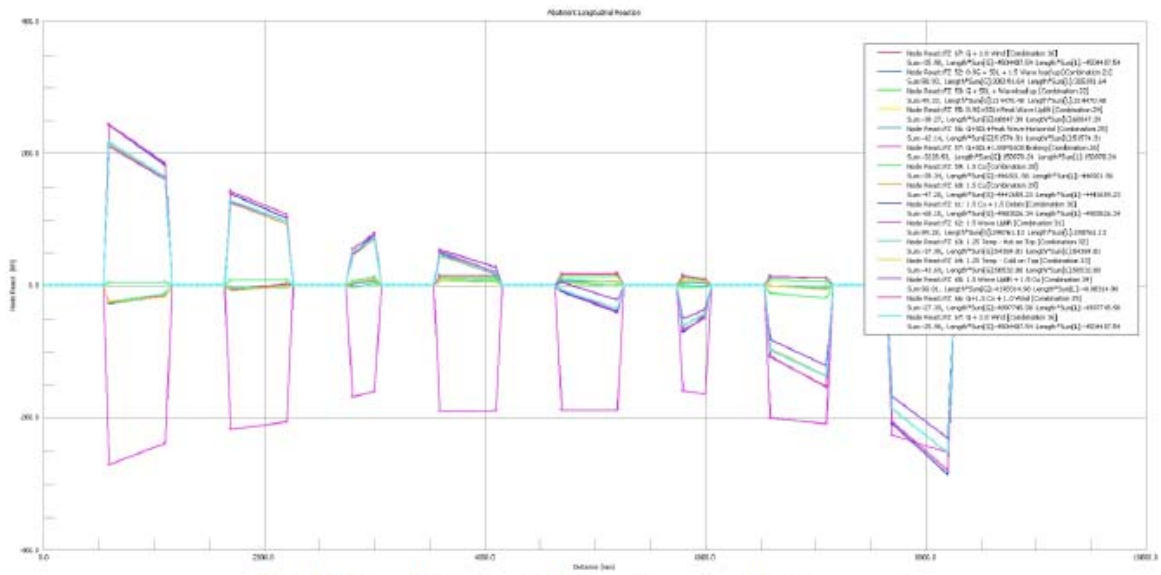

Fig. 15 Strand7 abutment bolt reactions visualised in a graph

3.12 Flexible filler end treatment

Another major design consideration for the hold down bolts was their fixity conditions at each end. The deck modules made allowance for a 75mm diameter grout hole for the hold down bolts to sit in. Grouting each hole with a high-strength, low-shrinkage grout would essentially result in a pinned-pinned end connection on a simply supported beam. To avoid the excessively high shear forces associated with this indeterminate model, icubed consulting undertook a localised FE model in ANSYS. This model looked at the stiffness requirements of a fully grouted end connection and also the stiffness of a flexible filler end connection. The results of the ANSYS model provided two key parameters to proceed with the design of the Wharf in Strand7:

1) The stiffness values for grouted and flexible filler end conditions were input into icubed's Strand7 FEA models to complete the hold down bolt design forces.
2) The ANSYS model looked at fatigue performance of the stainless steel over the working life of the Wharf. The predicted fatigue life of the bolts provided an upper-bound number of cycles for a fully loaded Moxy vehicle. The outcome of this analysis also drove the minimum bolt size requirements.

3.13 Post-Tension cables

Also discussed in Section 3.11 was the interaction of the super-structure deck with the steel sub-structure frame. Part of this design process also looked at the long-term performance of the deck construction joints to reliably transfer shear and tension loads from vessel and flood forces. The tension arching loads at both the quay-side and land-side of the wharf were in excess of 80t each. To help prevent unravelling and cracking of the high-strength grouted construction joint, icubed

opted to install 4 no. 15.2mm dia. post-tension cables on each side of the Wharf. These cables would be greased and sheathed, non-grouted, and post-tensioned. Once the cables are in tension, the deck diaphragm would continuously act in compression and will be prevented from opening up due to adverse berthing impacts for its design life. Visual representation of this arching action in the deck diaphragm can be seen below in figure 16.

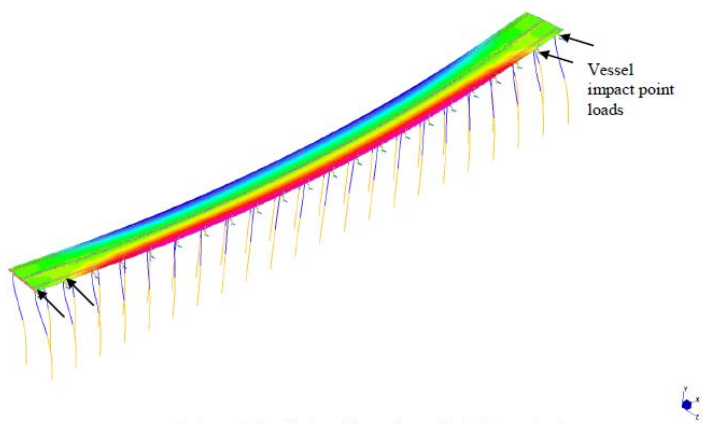

Fig. 16 Strand7 view of wharf deck arching actions – fender impact load case

4. Environmental benefits

The three novel engineered materials chosen for this project produce a significant improvement in environmental performance. In summary these include:

• The proprietary geopolymer concrete, EFC, contains no ordinary Portland cement and as a result achieves vastly reduced carbon emissions compared to conventional cement based concrete (Davidovits 2013). It contains a binder which also uses two common recycled wastes from other industries – GGBS and fly ash.
• Geopolymer concrete has a range of performance and durability benefits compared to conventional concrete that extend the life of concrete structures and reduces unplanned maintenance.
• GFRP reinforcing bars eliminate the risk of degradation of reinforced concrete via steel corrosion. This extends the life of concrete structures and reduces unplanned maintenance.
• CFT U-girders are high tensile strength, light weight and non-metallic / non-corrodable. These properties can deliver an efficient structure with long life and reduced unplanned maintenance.
• A life cycle assessment study by UNSW found that an I-Beam that is made from pultruded fibre composite has an environmental impact which is 76% less than that of a cold-formed stainless steel (316) I-Beam. This equates to a lessening on the effects towards human health, the ecosystem quality and resource use during its life cycle (Kara and Manmek 2009)

4.1 Carbon Emission (reduction) for the prefabricated deck units

An internal company report by the author (Glasby 2017) analysed this new technology wharf deck structure for the reduction in carbon emissions compared to a conventional 'business as usual' design in structural supporting steel with an in situ cast reinforced concrete deck. A

reference conventional design is provided by Sullivan (2017) in his thesis titled "Assessment of the Benefits of GFRP in Wharf Construction" which used this cement wharf as its subject matter.

Sullivan developed an alternative conventional design using code compliant concrete deck with steel reinforcing bar supported on structural steel beams. The deck design consisted of structural steel I-beams with steel shear studs welded to the top flange with an engaged in situ poured 50 MPa concrete slab that forms the deck surface. Steel member sizes to suit the two different spans of the wharf and jetty structure are:

• Jetty sections: 12 m spans. 6 no. steel girders, 700WB173, with 65mm long studs spaced at 145 mm along the girder. The concrete slab was 220mm thick, reinforced with SL102 structural steel mesh top and bottom (50 mm cover), and N16 steel reinforcing bars central spaced 200mm along the deck.
• Wharf sections: 8 m spans. 6 no. steel girders, 610UB125, with 65mm long studs spaced at 130mm along the girder. The concrete slab was 220mm thick, reinforced with SL102 structural steel mesh top and bottom (50 mm cover), and N16 steel reinforcing bars central spaced 200mm along the deck.

The emission reduction is shown below in Table 3 which is an extract from the internal report (Glasby 2017). These calculations show that there is an enormous CO2eq greenhouse

ITEM - Conventional Deck Design	CO_{2eq} (t)	Alternative - Wagners	CO_{2eq} (t)
Jetty steel girder - 700WB173	174.4	Jetty prefabricated panel - CFT girders	52.3
Jetty steel girder - 15.9 mm shear studs	2.9	N/A	
Jetty - 50 MPa grade concrete in deck (cement only)	54.6	Jetty prefabricated panel - EFC geopolymer concrete (binder only)	10.9
Jetty - N16 reinforcing bar in concrete deck	12.0	Jetty prefabricated panel - GFRP rebar in EFC geopolymer concrete	3.6
Jetty - SL 102 reinforcing mesh in concrete deck	17.6	Jetty prefabricated panel - GFRP rebar in EFC geopolymer concrete	5.3
Wharf steel girder - 610UB125	676.0	Wharf prefabricated panel - CFT girders	202.8
Wharf steel girder - 15.9 mm shear studs	17.3	N/A	
Wharf - 50 MPa grade concrete in deck	667.8	Wharf prefabricated panel - EFC geopolymer concrete (binder only)	133.6
Wharf - N16 reinforcing bar in concrete deck	66.9	Jetty prefabricated panel - GFRP rebar in EFC geopolymer concrete	20.1
Wharf - SL 102 reinforcing mesh in concrete deck	97.0	Jetty prefabricated panel - GFRP rebar in EFC geopolymer concrete	29.1
TOTAL	**1786.4**		**457.6**
Reduction from conventional deck			**1328.7**

Table 3 CO_{2eq} emissions reduction – Wharf deck structure

5. Conclusion

The Wharf deck structure described in this paper represents the next generation in high technology building materials and will serve as a demonstration case for long life, low maintenance and extremely low CO2 emission engineering structures. The materials combination of geopolymer concrete, GFRP reinforcing bar and CFT U-bar girders have been successfully applied to the challenges of a heavily load wharf structure.

The application of these materials in an innovative engineering design has delivered a wharf structure that has performed well against the client's key criteria of – economy, fit for purpose, speed of construction and reducing the environmental impact. This paper has shown how new engineered materials that may not be covered by design codes can be designed using manufacturing test data supported by appropriate R&D studies and full scale prototype models to provide the necessary level of confidence and reliability. The innovation displayed in this project is the result of many years of collaboration between engineering consultant and product developer / manufacturer and may be a useful example for others.

6. References

AS 3600 (2009), Concrete structures. Standards Australia, Sydney.

AS 4997 (2005), Guidelines for the design of maritime structures. Standards Australia, Sydney.

AS5100 (2017), Bridge design series. Standards Australia, Sydney.

AS 3582.1 (2016), Supplementary cementitious materials Part 1: Fly ash. Standards Australia, Sydney.

AS 3582.2 (2016), Supplementary cementitious materials Part 2: Slag—Ground granulated blast furnace. Standards Australia, Sydney.

Benmokrane, B. and Ali, A.H. (2018), Durability and long-term performance of fiber-reinforced polymer as a new civil engineering material. International Congress on Polymers in Concrete (pp. 49-59), Springer, Cham.

Bligh, R. and Glasby, T. (2013), Development of geopolymer precast floor panels for the Global Change Institute at University of Queensland. Proceedings Concrete Institute of Australia Biennial Conference, Concrete 2013 – Understanding Concrete, Gold Coast, Australia.

Clarke, J.(Ed) (1996), Structural design of polymer composites eurocomp design code and handbook. E & FN Spon, London, UK.

CSA S806 (2012), Design and construction of building components with fibre-reinforced polymers. CAN/CSA-S806-02, Canadian Standards Association (CSA), Mississauga, Ontario.

Davidovits, J. (2013), Geopolymer cement review 2013. Geopolymer Institute website, <www.geopolymer.org/library/technical-papers/21-geopolymer-cement-review-2013>, accessed 20-2-20178.

Ely, T., Armentrout, D. and Kumosa, M. (2001), Evaluation of stress corrosion properties of pultruded glass fiber/polymer composite materials. Journal of composite materials, 35(9), pp.751-773.

Glasby, T. Day, J. Genrich, R. & Aldred, J. (2015), EFC geopolymer concrete aircraft pavements at Brisbane West Wellcamp Airport. Proceedings Concrete Institute of Australia Biennial Conference, Concrete 2015 – Construction innovations, Melbourne, Australia.

Glasby, T. (2017), Reduction of greenhouse gas emissions in Wagners cement wharf project. Internal company report, Wagners, Toowoomba.

Kara, S. and Manmek, S. (2009), Composites: calculating their embodied energy. UNSW, Sydney

Kemp, M. and Blowes, D. (2011), Concrete reinforcement and glass fibre reinforced polymer. Queensland Roads Journal, no.11, pp.40-48.

Roy, D.M. (1999), Alkali-activated cements - opportunities and challenges. Cement and Concrete Research vol.29, pp.249–254.

Sullivan, B. (2017), Assessment of the benefits of GFRP in wharf construction. PHD Thesis, Griffith University, Brisbane.

Bridge Engineering Institute Conference 2019 (BEI-2019)
Honolulu, Hawaii, USA, July 22-25, 2019

Bond-to-Concrete Characteristic of Basalt Fiber Reinforced Polymer Rebars

Raphael Kampmann[1]*, Tim Schneider[2], and Srichand Telikapalli[3]

[1] FAMU-FSU College of Engineering, USA; email: kampmann@eng.famu.fsu.edu
[2] Fachhochschule Mnster, Germany; email: tim.schneider@fh-muenster.de
[3] FAMU-FSU College of Engineering, United States of America; email: st15d@my.fsu.edu

*: Corresponding author

Keywords: basalt; BFRP; bond; bond-to-concrete; surface enhancement

Abstract: Due to historical developments, fiber reinforced polymer (FRP) materials in the United States are mostly based on glass (GFRP) or carbon (CFRP) and the majority of reinforcing bars (rebars) for concrete structures are made with GFRP. Recently, basalt-based composites gained traction as these materials have been successfully used in Russia and China, and because U.S.- based FRP manufacturers and distributers have started to use basalt fibers for various rebar products. BFRP rebars are now considered because of the low production cost compared to CFRP rebars and due to improved chemical resistance, a higher tensile strength, and a higher modulus of elasticity compared to GFRP rebars. As the production of BFRP rebars is yet to be standardized, manufacturers around the world have produced various BFRP rebar types with different surface enhancements that affect the bond-to-concrete performance in various ways. For this study, it was the goal to evaluate the design-critical bond-to-concrete property for dissimilar BFRP rebar types through pullout tests according to ASTM D 7913 in an effort to characterize the bond performance of various surface conditions. The evaluated independent test variable was the bond interface — created through the various rebars types with sand coat, helical wraps and traditional steel lugs — while the measured dependent variables included the free-end slip, load-end slip, bond stress development, and interface stiffness. The results showed that the bond stiffness and rebar slip behavior are dependent on the surface enhancement features; while rebars with surface deformation presented a ductile rebar slip behavior, sand-coated surface lead to sudden failure. Likewise, the strength capacity of the BFRP rebar-concrete interface was affected by the surface enhancement features, and rebars with a deformed surface attained the highest bond capacity. Further, the type of resin affected the bond-to-concrete strength of BFRP rebars. Each rebar type lead to a distinctive failure interface and the failure modes suggested that the pullout behavior of BFRP rebars differs significantly from the pullout behavior of traditional steel rebars due to the transverse material stiffness.

1. Introduction

Throughout the past decades, concrete structures in coastal environments have deteriorated faster than expected. Besides a significant increase in traffic volume and traffic loads, exposure to salt-water and harsh environments has led to increased corrosion of traditional reinforcement bars. While corrosion results in tensile strength losses, the volumetric expansion of rust causes surface cracks and spalling, which destroy the protective (high pH) concrete layer. Generally, these effects lead to deterioration and may induce structural failure with significant financial implications and personal losses. To reduce these risks and to increase the service life of bridges

and infrastructure elements, noncorrosive internal reinforcement alternatives, such as fiber reinforced polymers (FRP) rebars, have been developed and they appear to be a viable option for concrete structures in harsh environments (Benmokrane and Ali, 2016; Vincent et al., 2013).
FRP rebars are manufactured from different fiber types (glass, carbon, aramid or basalt), which are bound together with various resins, for example polyester, vinyl ester or epoxy (Sólyom and Balázs, 2015). Besides corrosion resistance, other benefits, such as high tensile strength, magnetic transparency, low unit weight (about one-third of steel), reduced transportation costs, ease of handling on the job site, etc., have sparked a great interest in the construction industry. Recent research projects and demonstration structures — e.g., Halls River Bridge replacement in Florida — have shown that FRP rebars are advantageous for many aspects and that the technology has the potential for standardized use in construction projects (Rossini et al., 2018). Similar to the Halls River Bridge replacement, most pilot projects in the United States are generally based on glass (GFRP) or carbon (CFRP) and the majority of rebars for concrete structures are GFRP based. Now, basalt FRP rebars are gaining more attention because of the low production cost compared to CFRP rebars and due to improved chemical resistance, a higher tensile strength, and a higher modulus of elasticity in comparison to GFRP rebars. Basalt (a volcanic rock) is the only needed raw ingredient for the production of basalt fibers; it turns into a molten mass at 1400 °C to 1500 °C and can be formed directly into continuous fibers. Due to the promising characteristics, numerous research projects are conducted to determine the material characteristics and mechanical properties of BFRP rebars (Elgabbas et al., 2013, 2016; Hassan M., 2016; Ali et al., 2019). The bond-to-concrete performance of these rebars is an important material characteristic and research topic because it determines the structural behavior of BFRP reinforced concrete. To ensure proper bond between the BFRP rebar and the concrete, a surface treatment is applied to the FRP rebars, which increases the friction at the bond interface, or improves the interlocking effect. Unlike for traditional black steel rebars, the production of BFRP rebars has not been standardized yet and manufacturers around the world have developed different BFRP rebar products with various surface types and features (sand-coated, helical wraps, lugs, etc.). While the bond-to-concrete behavior of various Glass FRP surface enhancements has already been evaluated in many studies (Fava et al., 2016; Yan and Lin, 2016; Yang and Xu, 2018; Jamalan and Fu, 2018), this property has not been extensively defined for BFRP, and currently, it only can be assumed that Basalt FRP rebars perform similarly.

2. Problem Statement

The bond-to-concrete behavior is one of the most fundamental mechanical characteristics of FRP rebars that affects the quality and durability of concrete structure because it guarantees proper stress transfer between the two materials and ensures uniformity (Sólyom et al., 2015). While the bond-to-concrete performance of traditional black steel rebars (W. A. Slater, 1920; Bilek et al., 2017) and GFRP rebars (Gu et al., 2016; El-Nemr et al., 2016; Yan and Lin, 2016; Islam et al., 2015; Munoz, 2010) has been evaluated in detail, the bond-to-concrete performance of BFRP rebars has not been fully analyzed yet. This BFRP rebar knowledge gap is reflected in current structural design codes; most design standards allow the use of FRP rebars, but generally only permit glass and carbon fiber materials because adjustment factors for these rebar types are available already (AASHTO, 2018). Such adjustment factors are also needed to define the bond properties, because it is reasonable to assume that the diverse BFRP rebar surface treatments lead to dissimilar bond-to-concrete performances and that some surface features provide better

interlocking effects than others. To properly use and implement BFRP rebar technology for infrastructure projects, the bond-to-concrete performance of different rebar products must be evaluated and compared—relative to each other and to traditional steel rebars.

3. Research Significance

To provide additional data and knowledge for the bond behavior of basalt FRP rebars, this study aims to evaluate the bond-to-concrete performance of various BFRP rebars with different surface enhancements. Rebar pullout tests were conducted to quantify and compare the bond strength and bond stiffness due to various surface types and enhancement features. Thereby, this study provides important data for further development of specifications and guidelines for the design of FRP-reinforced structures to facilitate redundant material supply chains, additional alternatives, and market expansion.

4. Methodology

In an effort to characterize the bond-to-concrete performance of various BFRP rebar surface features and to evaluate dissimilar BFRP rebar types relative to each other and relative to the performance of traditional steel rebars, pullout tests according to ASTM D7913 (ASTM International, 2014) were conducted. For this study, # 3 rebars with a nominal diameter of $^{3}/_{8}$ in. (10mm) and three different rebar types (A, B, and C) were tested, whereas one rebar type had two sub-variants (Type-A1 and Type-A2), each was made with a different resin (c.f. Table 1). Control group specimens were made from traditional black steel rebars and were tested to provide benchmark values.

Table 1. Properties of the tested Rebars

Rebar	Surface Treatment	Resin Type	Measured Diameter		Tensile Strength		Elastic Modulus	
			mm	in.	MPa	ksi	GPa	ksi
Type-A1	Sand coating	Epoxy (HE)	10.41	0.410	926	134.2	47.07	6827
Type-A2	Sand coating	Epoxy (HP)	10.19	0.401	1166	169.2	49.64	7200
Type-B	Helical Wrapped	Epoxy	10.25	0.403	839	121.7	37.80	5482
Type-C	Sand coating	Vinyl ester	10.88	0.428	1353	196.3	53.83	7808
Type-D[1]	Surface lugs	Black steel	9.53	0.375	276	40.0	200.00	29 000

[1] Control group (black steel)

Each sample consisted of five specimens for each rebar type, and a total of 25 specimens were tested for this study. The bond interface created by the various rebars (sand-coated, helically grooved, and surface lugs) was defined as the independent test variable. Test constants according to ACI/ASTM were the bond length with five times the nominal diameter of the rebar (47.5mm or $1^{7}/_{8}$ in.), the (via PVC-tubes) de-bonded rebar length, and the concrete properties. The measured dependent variables included the free-end slip, load-end slip, bond stress development, and interface stiffness. All rebar types, independent variables, and the relevant material properties are summarized in Table 1 to provide an overview of the entire test program. Besides the control group of steel rebars (Type-D) all values were experimentally evaluated. As shown in Figure 1, one rebar end was embedded inside the concrete cube — with a 200mm (8 in.) edge length — while the other end was encased in a steel anchor to protect it from transverse failure

due to rebar gripping. To guarantee an accurate bonding length of five times the nominal diameter (48mm or $1^7/_8$ in.), PVC tubes were installed as a bond blocker.

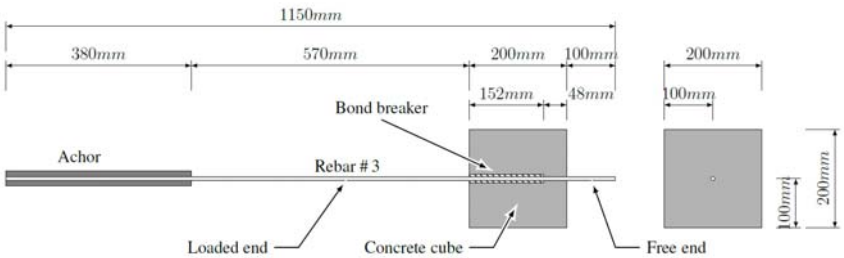

Fig. 1. Specimen with a rebar # 3

According to ASTM D7913 (ASTM International, 2014) the PVC tubes were used at the loaded ends of the rebar to minimize the stress concentration near the loading plate. The rebar displacement relative to the concrete cube was measured at both ends — the free end and the loaded end. While the free end slip was measured with one transducer, the relative displacement at the loaded end was recorded as the average value measured by three transducers in a 120° arrangement. All tests were displacement-controlled with a rate of 0.076 mm/min (0.3 in./min).

4.1. Materials

Photos of the cross section and the surface enhancement for each experimentally tested rebar type (BFRP and steel) can be seen in Figure 2. As seen in the Figure 2, all rebar types had a round solid cross section, but the surface features varied.

(a) Type-A1 (b) Type-A2 (c) Type-B (d) Type-C (e) Type-D (steel)

Fig. 2. Rebar overview

The major physical difference between the rebar types was the surface enhancement features because Type B was helically wrapped, sand coating was used for Types-A and C, and the tradition steel rebars had surface lugs. To reduce variances and to ensure consistency of test results, one single batch of ready-mixed concrete with a guaranteed compressive strength of 31.01 MPa (4500 psi) was used to produce all pullout cubes. Suwannee American type I cement (371 kg/m^3 or 625 lbs./yd^3), A-mining/FDOT Sand (761 kg/m^3 or 1282 lbs./yd^3), A-mining/FDOT# 57 Stone (801 kg/m^3 or 1350 lbs./yd^3), Amining/ FDOT# 89 stone (178 kg/m^3 or 300 lbs./yd^3), tapwater (117 L or 31 gal.), air entrainment (0.015 L or 0.5 oz.), type A water reducer (0.46 L or 15.6 oz), and a retarder (0.28 L or 9.4 oz) were used to batch the concrete mixture.

4.2. Specimen Production and Preparation

For this study, 25 pullout specimens with embedded # 3 rebars were created via horizontal casting with combined molds using form dividers according ASTM D7913 (ASTM International, 2014). For consistency, one single operator placed the concrete in three layers of approximately equal thickness, while a different single operator rodded each layer 25 times with a 16mm 5/8 in. Diameter tamping rod. After each layer was consolidated, a third operator tapped the mold for each specimen with a rubber mallet 5 times. After the top layer was completely consolidated, the free surface was struck off and leveled with a trowel before it was covered to prevent evaporation according to ASTM C192 (ASTM International, 2002). For curing, the specimens remained covered in the molds for 17 days but were removed thereafter to install the anchors at the load end (around the BFRP rebars) according to ASTM D7205 (ASTM International, 2016). In line with test procedure ASTM C39 ASTM International (2003), the compressive strength of five test cylinders (152.4 mm × 304.8 mm or 6 in. × 12 in.) was obtained at the day of pullout testing (more mature than 28 days) with a mean compressive strength of 51 MPa (7396 psi), a standard deviation of 1.39 MPa (201.38 psi), and a coefficient of variation of less than 2.7 %.

4.3. Test Procedure

The bond-to-concrete properties were recorded according to ASTM D7913 ASTM International (2014), which provides a standard test method by means of pullout testing. The tests were conducted under standard laboratory conditions within (23±2) °C [(73±5) °F] and (50±10) % relative humidity, using a 300 kN (66 kip) hydraulically controlled load frame. To properly apply the pullout force to the specimen, the test fixtures shown in Figure 3 were designed. Before installing the LSCTs to measure the rebar slip at both ends, an initial seating load of 272 kN (600 lbs.) was applied to every specimen to generate sufficient stiffness in the system. The force was continuously applied and without shock, all values were recorded with 1000 Hz until the measured force decreased significantly (more than 50 %) and the slippage at the free end of the bar measured at least 2.5mm (0.1 in.). After each test was completed, the concrete block was split open to analyze the failure mode and to measure the precise bond length of each specimen. While the raw data was recoded in LabView software with high data rates, it was written to file at 10 Hz (using appropriate filters). For efficient data analysis and data presentation, the high-speed data was filtered and reduced using R-statistics1 and R-Studio2 software packages. The graphs presented in this paper display the filtered and reduced data, which was verified to match the original raw high-speed data. However, all reported numerical values are based on the raw data and were calculated before any filter was applied.

5. Results

The experimental results obtained through pullout testing are presented in Figure 4 and Table 2, while the modes of failure are shown in Figure 5. The bond stress τ_{max} (MPa or psi) for a circular bar diameter d (mm or in.) is given by Equation 1 in which F represents the recorded pullout load (N or lbs.) and L is the accurately measured bond length (mm or in.).

[1]R.app GUI 1.70 (7434 El Capitan build), S. Urbanek & H.-J. Bibiko, R Foundation for Statistical Computing, 2016
[2]Version 1.1.383 2009-2017 RStudio, Inc.

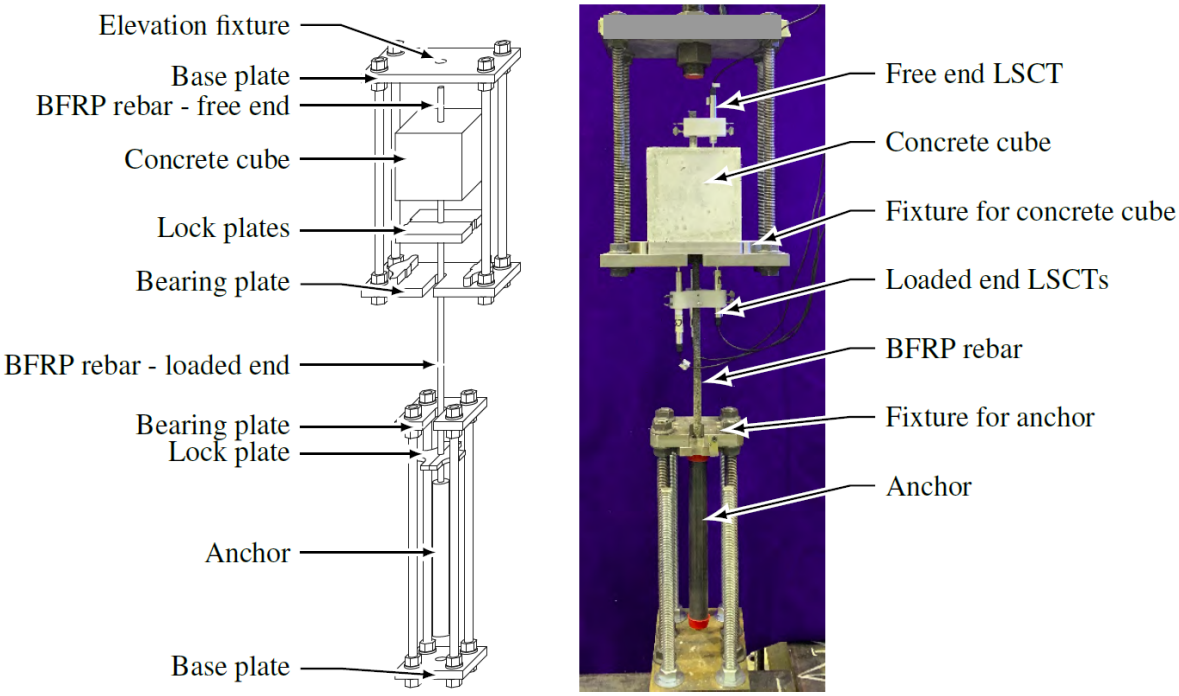

(a) Concept (b) In Laboratory

Fig. 3. Experimental Setup

$$\tau_{max} = \frac{F}{d\pi L} \qquad \text{[MPa or psi]} \qquad (1)$$

The bond stress vs. free end slip behavior is graphed in Figure 4 for all 25 specimens. For clarity, the post failure measurements (at the onset of the 50 % load drop) were removed from these graphs. All tested specimens failed at the rebar-concrete interface in bond rapture, without splitting the concrete open or without tensile failure. Generally, from the graphs it can be seen that each rebar type resulted in a consistent but distinct failure mode with ultimate stresses that were characteristic for each rebar type. Whereas most of the sand-coated rebars (Type-A1, A2 and B) failed suddenly with abrupt pullout, the rebars with a deformed surface (Type-C and Type-D [steel]) showed a soft failure. Likewise, the strength capacity of the BFRP rebar-concrete interface was affected by the surface enhancement features. While steel rebars attained the highest maximum strength values, they were seconded by helically wrapped rebars, which were followed by sand-coated rebars (c.f. Table 2). The initial slope (bond stiffness) of the steel specimens was notably variant with a wide envelope. However, all steel rebar specimens demonstrated a similarly ductile failure after reaching the peak bond stress.

For numerical comparison and concluding values, Table 2 lists the bond minimum stress (∧), the maximum bond stress (∨), the average bond stress (μ), the standard deviation (σ), and the coefficient of variation (CV) for each individual test sample.

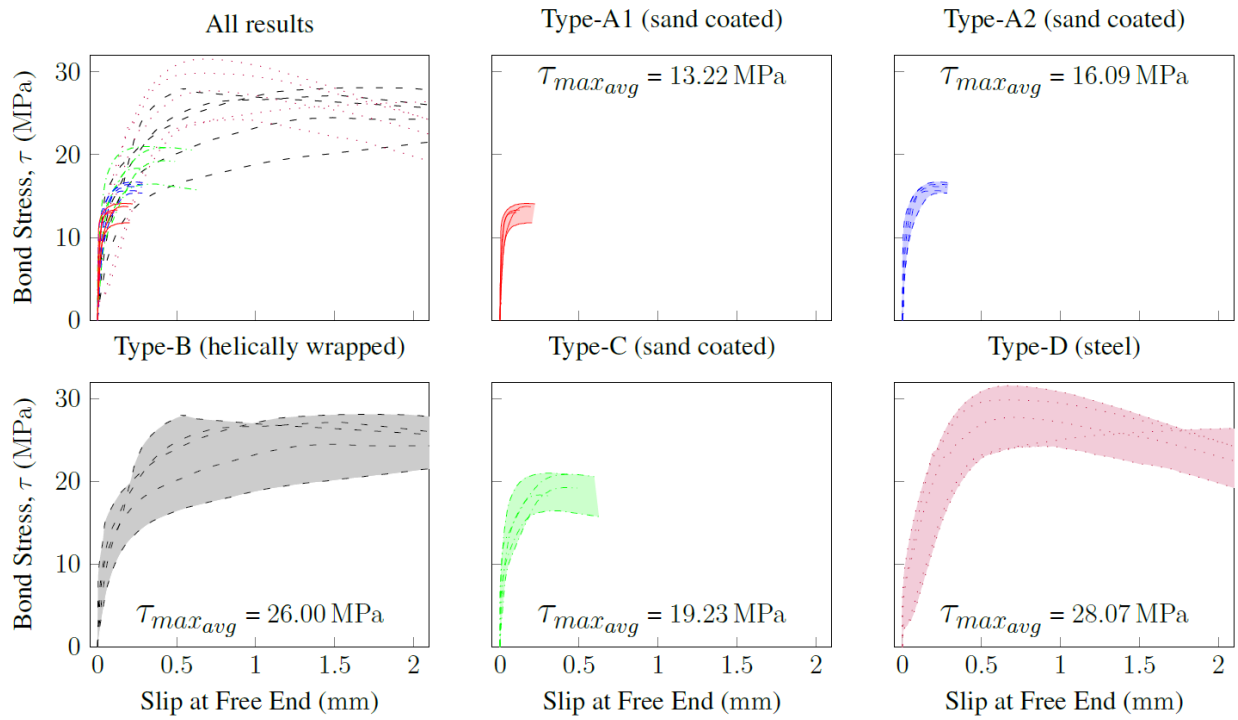

Fig. 4. Free end slip behavior of the tested rebars

Table 2. Bond-to-Concrete strength test statistical values for each sample

Sample Group		Statistical Values								
		Imperial				Metric				
Rebar Type	Resin Type	$\wedge$ ksi	$\vee$ ksi	μ ksi	σ ksi	$\wedge$ MPa	$\vee$ MPa	μ MPa	σ MPa	CV %
A	HE	1.71	2.05	1.92	0.13	11.81	14.15	13.22	0.90	0.07
A	HP	2.24	2.43	2.33	0.08	15.41	16.74	16.09	0.54	0.03
B	Epoxy	3.20	4.08	3.77	0.38	22.08	28.15	26.00	2.64	0.10
C	VinylEster	2.39	3.05	2.79	0.27	16.49	21.04	19.23	1.89	0.10
D	Steel	3.53	4.59	4.07	0.41	24.33	31.65	28.07	2.85	0.10

While Type-A1 and A2 measured the lowest mean bond strength (13.22 MPa or 1.92 ksi for Type-A1 and 16.09 MPa or 2.33 ksi for Type-A2), they also had the lowest variation between individual test results with a standard deviation of less than 1.0 MPa (0.13 ksi) and a CV of 7 % for Type-A1 and 3 % for Type-A2. All other rebar types had the same CV of 10%, whereas Type-D rebars (black steel) measured the highest mean bond strength (28.07 MPa or 4.07 ksi) followed by Type-B rebars (helically wrapped) with a mean bond strength of (26.00 MPa or 3.77 ksi) and Type C (sand-coated) with a mean bond strength of (19.23 MPa or 2.79 ksi). After the pullout tests were completed, the concrete blocks were split in half to further evaluate the failure

mode by analyzing the surface of the rebar and the concrete. Figure 5 exemplifies the different representative failure modes as they were observed for each rebar type.

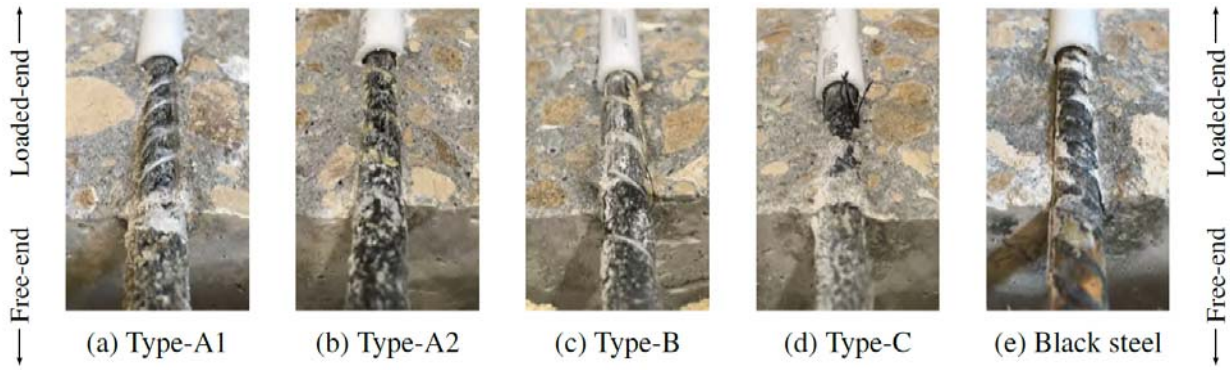

Fig. 5. Overview rebar surface after testing

In Figure 5 can be seen that each rebar type produced different damages dependent on the surface enhancement features. For rebar Types-A1 and A2, de-bonding of the entire sand coat was observed (sand delamination). For rebar Type-B, only the sand layer was pulled off the concrete and the surface deformed slightly, but the helical wraps remained in place. For rebar Type-C, it was noted that the rebar surface was significantly damaged at the loaded end, and that the outer layer was entirely peeled off from the rest of the rebar. Close to the unloaded end, the surface layer of the rebar did not peel off, and most parts of the sand-coated layer remained well-adhered to the bar. The steel rebars did not suffer any visible damages, but fine concrete dust was noted at the surface of the rebar.

6. Analysis & Discussion

The results have shown that a different surface enhancement, as well as different resin types, lead to different bond behavior, and therefore, to different damages at the rebar surface. Besides the resin type, rebar Types-A1 and A2 were made from identical materials and with the same production techniques; however, the maximum bond stress of rebar Type-A2 was more than 20 % higher in comparison to the bond strength of rebar Type-A1. The results within each test sample were considerably consistent (CV of 7 % for rebar Type-A1 and 3 % for rebar Type-A2), which leads to the conclusion that the bond properties are affected by the resin. Similar to the observations made by Ahmed et al. (2018), the sand-coated rebars failed mainly due to damages at the bar surface in the form of abrasion. For these specimens, the concrete strength was high enough, such that the bond strength of FRP rebars was controlled by the shear strength between the fiber layers (Sólyom and Balázs, 2015; Fava et al., 2016), which also is depending on the resin type (Achillides and Pilakoutas, 2004). This uniform peeling off of the surface layer along the whole length of the embedded portion of the bar explains the abrupt failure of these specimens (Munoz, 2010). After delamination, the sanded surface becomes effectively smooth and increasing loads can no longer be resisted (Refai A., 2015). While also sand-coated, the failure mode of Type-C rebars was different, which is assumed to be due to different resin properties. As shown in Figure 5, rebar damages (delamination) were noted at the loaded end, but the sand coat at the free end remained intact. Because delamination was more pronounced

and concentrated at the loaded end, it appears that peeling started from there and moves toward the free end until failure. Due to the pullout test setup, the higher stresses appears at the loaded end, which explains the damage concentration on the rebar surface closest to that end (Refai A., 2015; Kabir and Islam, 2014). Before the bonded area can delaminate completely (moving toward the free end), the increasing bond stresses (due to surface reduction and increasing loads) cause failure at the concrete surface and the rebar is pulled in a sudden manner. Rebar Type-B (with helical wraps) had the highest bond strength of the tested BFRP rebar types (almost twice the average bond strength of rebar Type-A1). These rebars facilitated a softer failure and the fibers did not delaminate, but the rebar deformed slightly in the radial direction and the sand coat was partially rubbed off. Accordingly, it can be concluded that the Type-B rebars were squeezeed through the concrete, because of low transverse stiffness. For this rebar type, the bond strength is mostly generated through the geometrical interlocking effect or by friction between the rebar surface deformations and the concrete (Sólyom and Balázs, 2015; Aiello et al., 2007; Munoz, 2010). The helical wrapping may not be advantageous for rebar tensile strength because the outer layer of the fibers have to be straightened before the entire cross section can be fully activated, but if bond strength needs to be maximized, this interlocking effect appears to be advantages, because it lead to the highest load resistance during pullout testing compared to the other BFRP specimen types tested in this study. These helical wraps are closest to the ribs of the control group Type-D (black steel) specimens, which had an 8 % higher average bond stress than rebar Type-B. Also the bond stress vs. free-end-slip development of the control group was similar to rebar Type-B, but the peak bond stress of the steel rebars occurred earlier (at a lower free end displacement). This is because of the higher transverse stiffness of the steel rebar, which reduces rebar deformation, and therefore, the steel rebars cannot squeeze through the concrete. Instead, it crushed the surrounding concrete at the lugs within the bonded length (Fava et al., 2016). This also explains the concrete dust around the control group Type-D (steel) rebars that was not seen for any of the other rebar types. Generally rebars with a surface deformation (Type-B and Type-D) provided higher bond stress than rebars without a surface deformation (Aiello et al., 2007). These rebar types measured a larger free end slip when they reached the maximum capacity and failed in a ductile fashion, whereas the rebars without a surface deformation showed a more sudden failure. This phenomenon can be traced back to the larger interlock effect, created through the deformed surface of the rebars, which is activated by the slip of the rebar. Generally, pullout tests lead to compression within the concrete—which rarely occurs in practice when a rebar is in tension—and cause a reduction in bond stress of sand-coated rebars, while the opposite is true for deformed rebars (Aiello et al., 2007; Sólyom and Balázs, 2015).

7. Conclusions

For this research project, a total of 25 specimens with a nominal diameter of 10 mm ($^3/_8$ in.) and different surface enhancements (sand-coated, helically wrapped and black steel) were tested according to ASTM D7913 (ASTM International, 2014) in an effort to quantify the bond strength of dissimilar basalt FRP rebars in concrete. Four BFRP rebar types with different surface enhancement features and one traditional steel rebar type were experimentally and statistically evaluated. The load displacement behavior, the failure behavior, and the fracture patterns of all samples (specimen groups) were systematically compared to each other. Based on the findings and the analysis conducted in this research, the following conclusions were drawn:

- Different surface enhancements lead to different bond-to-concrete behavior and performance. Rebars with surface deformations provided a higher bond strength than rebars without a surface deformation.
- The pullout failure mechanism of FRP rebars is significantly different from the pullout failure mechanism of traditional steel rebars, due to the differences in the material transverse stiffness. While the stiff lugs of steel rebars crush the surrounding concrete, BFRP rebars with surface deformations may squeeze through the concrete.
- Basalt FRP rebars with sand coating and without surface deformations predominantly fail due to delamination at the outer rebar surface.
- Sand-coated FRP rebars without surface deformations are more likely to fail in a sudden or brittle fashion, while rebars with surface deformations lead to a more ductile pullout failure behavior.
- The ultimate bond stress of deformed BFRP rebars occurs after significant slip, whereas rebars with sand coating and no surface deformations produce a high initial bond stiffness, but with reduced bond-to-concrete strength due to missing interlocking effects.
- If bond strength needs to be maximized, interlocking effects due to rebar surface deformations (e.g.: through helical wraps) should be considered.
- The resin type impacts the bond-to-concrete performance of BFRP rebars. Though all other constituent materials and production processes may be identical for a specific rebar type, from this study it appears that a variation in resin can lead to a 20% strength difference.

8. Acknowledgements

The authors would like to acknowledge the Florida Department of Transportation (FDOT) for a progressive approach to the implementation of emerging technologies in our infrastructure. Special thanks go to Steven Nolan and Chase Knight for their continues engagement, exceptional support, and outstanding expertise. The opinions, findings, and conclusions expressed in this publication are those of the authors and not necessarily those of the Florida Department of Transportation, or the US Department of Transportation.

9. References

AASHTO (2018). AASHTO LRFD Bridge Design Guide specifications for GFRP-Reinforced Concrete. American Association of State Highway and Transportation Officials.

Achillides, Z. and Pilakoutas, K. (2004). “Bond behavior of fiber reinforced polymer bars under direct pullout conditions.” Journal of Composites for Construction, 8(2), 173–181.

Ahmed, S. A. S., Fahmy, M. F. M., and Wu, Z. (2018). “Experimental study and numerical modeling of cyclic bond and slip behavior of basalt frp bars in concrete.” Journal of Composites for Construction, 22(6), 04018050.

Aiello, M., Leone, M., and Pecce, M. (2007). “Bond performances of frp rebars-reinforced concrete.” Journal of Materials in Civil Engineering, 19, 205–213.

Ali, A. H., Mohamed, H. M., Benmokrane, B., ElSafty, A., and Chaallal, O. (2019). "Durability performance and long-term prediction models of sand-coated basalt frp bars." Composites Part B: Engineering, 157, 248 – 258.

ASTM International (2002). Standard Practice for Making and Curing Concrete Test Specimens in the Laboratory, (C192/C192M). West Consohocken, PA.

ASTM International (2003). Standard Test Method for Compressive Strength of Cylindrical Concrete Specimens, (C39/C39M). West Consohocken, PA.

ASTM International (2014). Standard Test Method for Bond Strength of Fiber-Reinforced Polymer Matrix Composite Bars to Concrete by Pullout Testing, (D7913/D7913M). West Consohocken, PA.

ASTM International (2016). Standard Test Method for Tensile Properties of Fiber Reinforced Polymer Matrix Composite Bars, (D2584-06(2016)). West Consohocken, PA.

Benmokrane, B. and Ali, A. (2016). "Durability of frp rebars in aggressive environments." International Workshop on Seawater Sea-sand Concrete (SSC) Structures Reinforced with FRP Composites 13.

Bilek, V., Bonczková, S., Hurta, J., Pytlík, D., and Mrovec, M. (2017). "Bond strength between reinforcing steel and different types of concrete." Procedia Engineering, 190, 243 – 247. Structural and Physical Aspects of Construction Engineering.

El-Nemr, A., Ahmed, E. A., Barris, C., and Benmokrane, B. (2016). "Bond-dependent coefficient of glassand carbon-frp bars in normal- and high-strength concretes." Construction and Building Materials, 113, 77 – 89.

Elgabbas, F., Ahmed, E., and Benmokrane, B. (2013). "Basalt frp reinforcing bars for concrete structures." Fourth Asia-Pacific Conference on FRP in Structures (APFIS 2013).

Elgabbas, F., Vincent, P., Ahmeda, E. A., and Benmokrane, B. (2016). "Experimental testing of basalt-fiberreinforced polymer bars in concrete beams." Composites Part B, 91, 205–218.

Fava, G., Carvelli, V., and Pisani, M. A. (2016). "Remarks on bond of gfrp rebars and concrete." Composites Part B: Engineering, 93, 210 – 220.

Gu, X., Yu, B., and Wu, M. (2016). "Experimental study of the bond performance and mechanical response of gfrp reinforced concrete." Construction and Building Materials, 114, 407–415.

Hassan M., Benmokrane B., E. A. (2016). "Bond durability of basalt-fiber-reinforced-polymer (bfrp) bars embedded in concrete in aggressive environments." Composites Part B, 106, 262–272.

Islam, S., Afefy, H. M., Sennah, K., and Azimi, H. (2015). “Bond characteristics of straight- and headedend, ribbed-surface, gfrp bars embedded in high-strength concrete.” Construction and Building Materials, 83, 283 – 298.

Jamalan, M. H. and Fu, D. F. (2018). “Numerical analysis on bond strength of FRP re-bars under elevated temperature.” IOP Conference Series: Materials Science and Engineering, 371, 012013.

Kabir, M. and Islam, M. M. (2014). “Bond stress behavior between concrete and steel rebar: Critical investigation of pull-out test via finite element modeling.” International Journal of Civil and Structural Engineering, 5, 80–90.

Munoz, M. B. (2010). “Study of bond behaviour between frp reinforcement and concrete,” PhD thesis, Universitat de Girona.

Refai A., Ammar M. A., M. R. (2015). “Bond performance of basalt fiber-reinforced polymer bars to concrete.” Journal of Composites for Construction.

Rossini, M., Cadenazzi, T., Nolan, S., and Nanni, A. (2018). “Seacon and resilient frp-rc/pc solutions: The halls river bridge.” Italian Concrete Days 2018.

Sólyom, S. and Balázs, G. (2015). “Bond strength of frp rebars.” Concrete Structures, 16, 62–68.

Sólyom, S., Balázs, G., and Borosnyói, A. (2015). “Material characteristics and bond tests for frp rebars.”

Concrete Structures, 16, 38–45. Vincent, P., Ahmed, E., and Benmokrane, B. (2013). “Characterization of basalt fiber-reinforced polymer (bfrp) reinforcing bars for concrete structures.” Specialty Conference on Material Engineering & Applied
Mechanics, 3rd, MEC–111–1 – MEC–111–10.

W. A. Slater, F. E. Richart, G. G. S. (1920). (Tests of Bond Resistance Between Concrete and Steel). Washington Government Printing Office.

Yan, F. and Lin, Z. (2016). “Bond behavior of gfrp bar-concrete interface: Damage evolution assessment and fe simulation implementations.” Composite Structures, 155, 63 – 76.

Yang, S. and Xu, X. (2018). “Discussion on bonding performance between FRP bars and concrete.” IOP Conference Series: Earth and Environmental Science, 189, 032031.

Railway Bridges

Bridge Engineering Institute Conference 2019 (BEI-2019)
Honolulu, Hawaii, USA, July 22-25, 2019

Aerodynamic Interference between High-Speed Train and Truss Girder Long-Span Bridge in Cross Winds

Xuhui He[1], Huan Li[2*], and Hanfeng Wang[3]

[1] Central South University, Changsha and China; email: xuhuihe@csu.edu.cn
[2] Central South University, Changsha and China; email: lihuan2016@csu.edu.cn
[3] Central South University, Changsha and China; email: wanghf@csu.edu.cn

[*]: corresponding author

Keywords: train-bridge system; aerodynamic interference; quasi-reynolds number effect; suppressing effect; shielding effect

Abstract: This paper systematically investigates the interference effects on the aerodynamic properties of the high-speed train and truss girder system via a series of two dimensional wind tunnel tests at Re = 6.24×10^4 (based on the oncoming flow velocity and the height of the train model). Three key parameters are considered in the tests, i.e., angle of attack (α), truss solidity ratio (Φ), and girder aspect ratio (B^*/D^*, width to height ratio). For comparison, the corresponding aerodynamics of the train-only and bridge-only models are also tested. The results indicate that the aerodynamic interference between train and truss girder could be concluded into three categories of effects: the shielding effect, the suppressing effect, and the quasi-Reynolds number effect. Besides, this quasi-Reynolds number effect, sharing almost all the similarities with the classical Reynolds number effect, is sensitive to the variation of α, Φ and B^*/D^* with the inflow Reynolds number (6.24×10^4) remaining constant. For the train model in the train- bridge system (TBS), salient observations are: (a) the shielding effect of the truss member leads to a smaller drag coefficient relative to the train-only model; (b) the suppressing effect on the organized vortex shedding from the bottom of the train, caused by the presence of the bridge deck, results in obvious reductions of both the torsional moment and the three fluctuating coefficients; and (c) the quasi-Reynolds number effect engenders obvious drag crisis and other abruptly-changing forces. Moreover, the span-wise aerodynamics of the train inside truss girder displays a strong 3-dimensional characteristic. For the bridge model in the TBS, the three categories of effects also lead to a smaller drag for the bridge, the behaviors of the lift and moment show a strong dependence on the flow state around the train due to the quasi-Reynolds number effect. Finally, the aerodynamics of the whole train-bridge system tested synchronously is also discussed.

1. Introduction

Compared with other vehicles operated near the ground, high-speed train (HST) is characterized by its larger slenderness ratio (length to height ratio) and higher commercial speed, e.g., the widely used China Railway High-speed 380BL (CRH380BL) with 16 carriages, whose two characteristic parameters are about 108 (larger than that of the world longest railway bridge) and 300km/h, respectively. The operating speed of the China latest HST ("FuXingHao") has been raised up to more than 350km/h, which makes the slender HST more sensitive to the lateral wind disturbance (Cooper 1981; Baker 1986; Khier et al., 2000; Suzuki et al., 2003, 2106; Bocciolone

et al., 2008; Baker et al., 2009; Dorigatti et al., 2015; He et al., 2014 & 2016; Li et al., 2018). Under cross wind, the lateral stability of an HST may be deteriorated by the aerodynamic interference between train and bridge. Besides, the aerodynamics of bridge may also be significantly changed by the presence of HST. In order to improve the current safety criteria, it is meaningful to systematically investigate the aerodynamic interference between HST and truss girder long-span bridge.

2. Wind tunnel test

All experiments were conducted in a close-loop low-speed wind tunnel with the working section of 3m in width, 3m in height, and 15m in length, respectively. More details of the wind tunnel are available in Wang et al. (2016). The tested cases are listed in Table 1. The setups and coordinate systems are shown in Fig. 1.

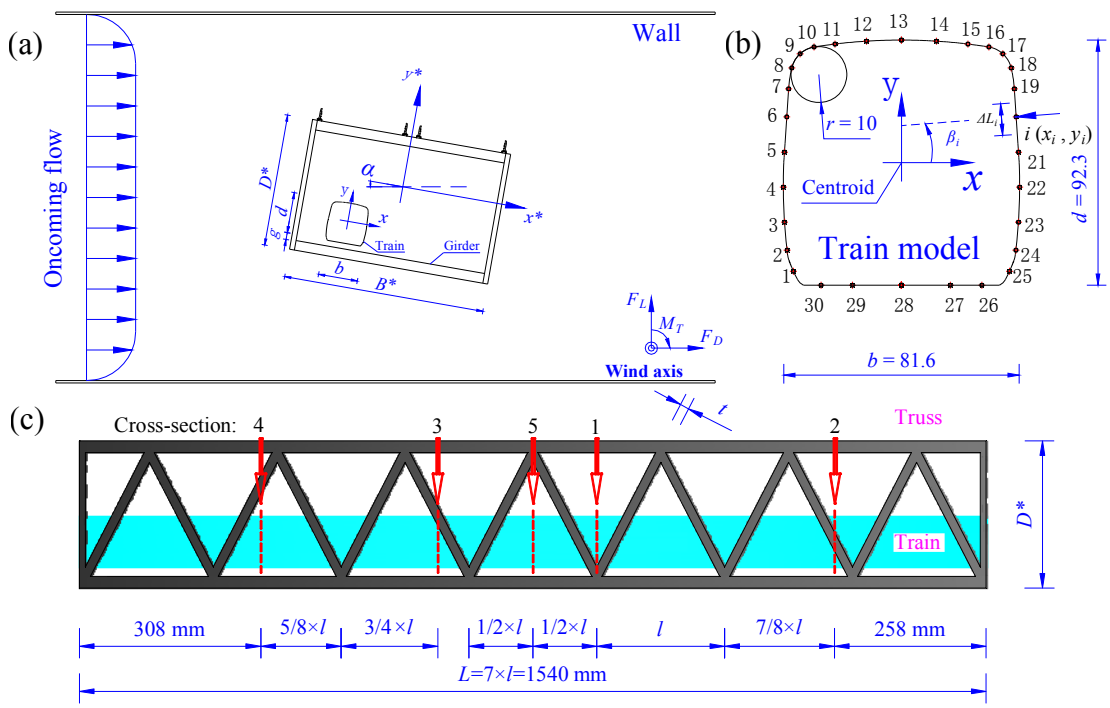

Fig. 1. Experimental details: (a) coordinate systems, (b) arrangements of pressure taps on the train cross section, (c) five pressure tested sections along the span-wise direction.(Unit: mm)

3. Results and discussion

The aerodynamic coefficients of the train model measured by pressure scanner are shown in Fig. 2. It can be observed three critical angles of -4°, 4º and 10º in the range of α (-12° to 12°) of major concerned in bridge engineering. According to the investigation of Li et al. submitted for publication (a), for α = -12° ~ +4°, the aerodynamics of the train-only model behaves similar to the rounded-corner square cylinder, whereas it is aerodynamically the same as a square cylinder in the range of α = 10° - 12°. Moreover, the critical angle of attack α = 4° is to the aerodynamics of train-only model what α = 0° is to a symmetrical cross-section such as square cylinder or a round corner ones.

Table.1. Test conditions

Case	Model	α(°)	Bridge model No.	Φ	B^*/D^*	D^* (mm)	t (mm)
train-only	HST	-12 ~ +12, $\Delta\alpha$ = 2	--	--	--	--	--
train-bridge system	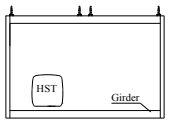	-6 ~ +6, $\Delta\alpha$ = 3	1	0.20	1.0	400	10
			2	0.25	1.0	400	16
			3	0.30	1.0	400	22
			4	0.35	1.0	400	28
			5	0.40	1.0	400	34
			6	0.30	1.3	308	19
			7	0.30	1.6	250	15
			8	0.30	1.9	211	12
			9	0.30	2.2	182	8

In Fig.2, the results of a rounded square cylinder with r/d = 0.07 at Re = 2.70×10^4 (Carassale et al., 2014) are shown here for comparison, which have been parallel shifted to match the critical angle of attack α = 4°. The overall match validates the present experiments.

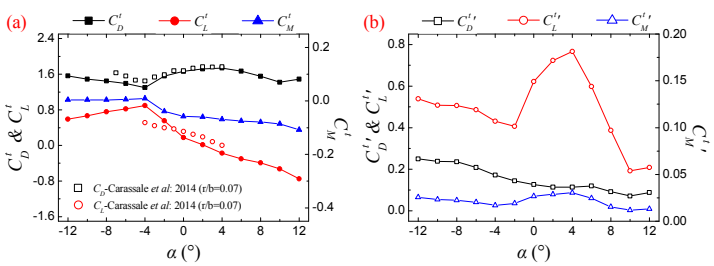

Fig. 2. Aerodynamic coefficients of the train-only model, (a) mean (b) fluctuating.

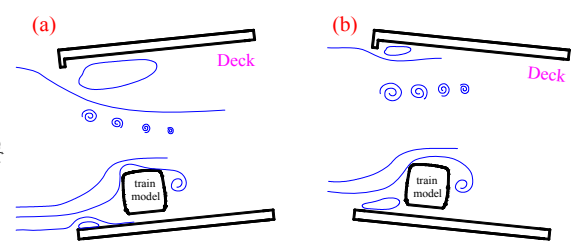

Fig. 3. Flow patterns around the train-bridge system with an increase in α.

Based the pressure distribution, fig. 3 sketches the flow structure around the train model inside the truss girder roughly (Chiu and Squire, 1992; Tamura & Miyagi, 1999; Shimada & Ishihara 2002; Nakayama et al., 2010; Huang et al., 2010; Yen and Yang, 2011; Carassale et al., 2014; Achenbach, 1968; Cadot et al., 2015; van Hinsberg et al., 2017; Cao et al., 2017). In both subfigures, the separation and reattachment at the roof of train model are depicted, and the leading-edge vortex shedding from the upper and lower decks as well as the rough wake structures behind upstream truss members. Fig. 4 illustrates the comparison of aerodynamic coefficients of train model between the train-only and inside-girder cases. An overall observation is that, all the force coefficients are smaller for the inside-girder case than those of the train-only case during the all tested range of angle of attack, except for the $|C_L^t|$ at α = 0° - 3°. The reduction of C_D^t is mainly caused by the shielding effects aforementioned, whereas $|C_L^t|$ and all the fluctuations are mainly decreased by the suppressing effect. Within different ranges of angle of attack, the coefficient reduction percentage varies obviously. This phenomenon shall be attributed to the angle-dependent quasi-Reynolds number effect. For α = 6° and 3°, the corresponding pressure distribution around the upper half train model is similar to that of the circular cylinder and the rounded corner prism in the subcritical Reynolds number range. Thus, the quasi-Reynolds number effect is limited. For α decreasing from 0° to -3°, the aerodynamic properties of the upper half train model resemble to those of the circular cylinder and the

rounded corner prism in the critical Reynolds number range. The quasi-Reynolds number effect causes a further reduction of C_D^t and a large increase rate of C_L^t, which are highlighted by red dash lines in Figs. 4(a) & (b), respectively. Moreover, this effect also leads to a further rising of the three fluctuating coefficients with $C_D^{t\prime}$ and $C_M^{t\prime}$ reach their maximum at α = -3°, while the maximal value of $C_L^{t\prime}$ occurs at α = 0°. For the suppressing effect, the maximums of all the three fluctuating coefficients are still smaller than those of the train-only case, even though the turbulence intensity in the truss girder is obvious increased. With the further decrease of α to -6°, the flow in the boundary layer begins to burst into turbulent with the separated flow still reattaching on the lateral face of the train model, the reduction rate of C_D^t remains unchanged, but the increasing rate of C_L^t begins to fall down. With the end of the transition state, three fluctuating coefficients reduce rapidly. On the other hand, it is noteworthy from Fig 4(c) that $|C_M^t|$ increases significantly (more than 100%) for the inside-girder case, suggesting a potential threat to the operational safety of an HST going through a truss-girder. The interference effects on $|C_M^t|$ is very different from the other aerodynamic coefficients, the major reason for that would be the suppressing effect of the lower deck.

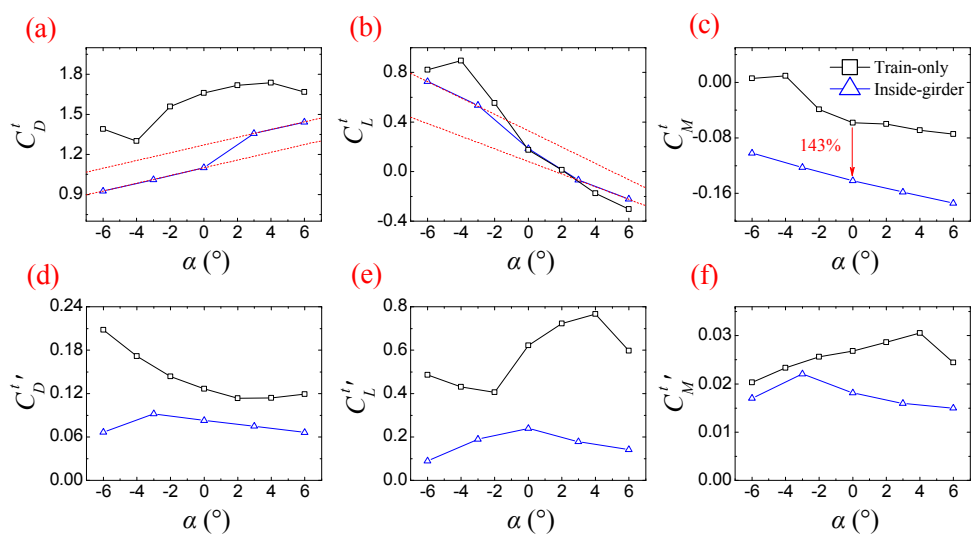

Fig. 4. Comparison of time-average aerodynamic coefficients of train model between train-only and inside-girder cases with Φ = 30%, B^*/D^* = 1.0 and α = -6° ~ 6°.

3. Conclusion

(1) The aerodynamics of the high-speed train and truss girder system are investigated.

(2) The aerodynamic interference between high-speed train and truss girder could mainly be concluded into shielding effect, suppressing effect, and quasi-Reynolds number effect.

4. Reference

Baker, C.J., 1986. Train aerodynamic forces and moments from moving model experiments. Journal of Wind Engineering and Industrial Aerodynamics, 24(3), pp.227-251.

Cooper, R.K., 1981. The effect of crosswinds on trains. Journal of Fluids Engineering, 103(1), pp.170-178.
Khier, W., Breuer, M. and Durst, F., 2000. Flow structure around trains under side wind conditions: a numerical study. Computers & Fluids, 29(2), pp.179-195.

Dorigatti, F., Sterling, M., Baker, C.J. and Quinn, A.D., 2015. Crosswind effects on the stability of a model passenger train—A comparison of static and moving experiments. Journal of Wind Engineering and Industrial Aerodynamics, 138,

Rolling Noise and Bridge Noise from an Elevated Bridge for Urban Road and Rail Transit Traffics

Qi Li[1*], Man-fei Shi[2], Min-jie Gu[3], and Ding-jun Wu[4]

[1] Department of Bridge Engineering, Tongji University, Shanghai, China; email: liqi_bridge@tongji.edu.cn
[2] Department of Bridge Engineering, Tongji University, Shanghai, China; email: 1732272@tongji.edu.cn
[3] Shanghai Municipal Engineering Design and Research Institute (Group) Co., Ltd., Shanghai, China; email: guminjie@smedi.com
[4] Department of Bridge Engineering, Tongji University, Shanghai, China; email: tjwdj@tongji.edu.cn

[*]: corresponding author

Keywords: double deck elevated bridges; urban road; urban rail transit; wheel-rail interaction; noise prediction; sound propagation; noise barriers

Abstract: It is very efficient in land and investment utilization to construction double deck elevated bridges carrying both urban road and rail transit traffics. The characteristic of noise from these elevated traffics is different from that of pure rail traffic. This study aims to develop a noise predicting model allowing the generation and propagation of sound from vibrating rails and bridges. The force method in the frequency domain is applied to obtain the vibration power input to the rails and bridges caused by wheel-rail interaction and rail-bridge interaction. A two-dimensional (2D) vibroacoustic model is used to gain the transferring functions between the sound pressure at the given field points and the vibration power of the rail and bridge. This model includes the sound refection effects of the double deck bridge, the vehicle body and the noise barriers. The radiated noise from the rail-bridge system is then calculated by combining the sound transfer functions with the vibration power of the rail and bridge subjected to wheel-rail rolling excitation. The above noise prediction method is used to obtain the noise fields from pure urban rail transit bridges and combined urban road and rail transit systems. Suggestions are finally provided for the noise barriers for elevated bridges for combined traffics

1. Introduction

Urban rail transit lines and elevated urban roads have become effective means to alleviate traffic congestion in large and medium-sized cities in China. Construction of double deck elevated bridges carrying both urban road and rail transit traffics has become an efficient way of land use and investment. However, the characteristic of noise from these double deck elevated transit traffics is different from that of pure rail traffic. Although the noise from pure rail traffic has been investigated a lot by many researchers (Li et al. 2015; Li et al. 2016; Li and Thompson, 2018; Thompson et al. 2008; Wu and Thompson, 2000), it is necessary to establish a reasonable noise prediction model to predict and mitigate the noise from elevated bridges for combined traffics.

2. Vibration analysis for vehicle-track-bridge coupled system

To calculate the wheel-rail interaction forces above 20 Hz, the influence of the vehicle suspensions can be ignored and the vehicle-track-bridge system can be then simplified into the coupled wheel-track-bridge system shown in Fig. 1. Linear spring-dashpot elements are used in the system to connect the wheel, rail and bridge components to simulate the wheel-rail contact springs, fasteners and bridge supports.

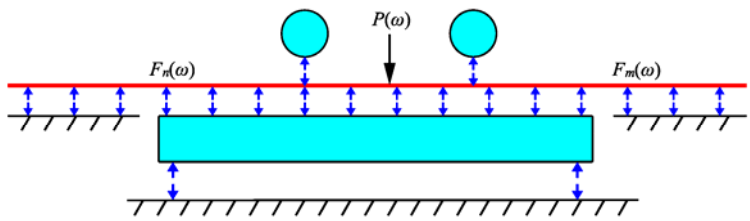

Fig.1. The vehicle-track-bridge coupled system

The internal forces (see Fig. 1) of the spring-dashpots with the system are taken as the basic unknown quantities, and therefore the deformation compatibility condition of the spring-dashpots can be expressed by using the principle of the force method (Li et al. 2016):

$$(\mathbf{Y}_F + \mathbf{Y}_S)\mathbf{F} + \mathbf{Y}_P P = 0 \tag{1}$$

where P is the external force applied on the rail, which is the function of frequency; $\mathbf{F}$ is the unknown force vector of the springs; $\mathbf{Y}_S$ is a diagonal matrix representing the mobilities of the springs; $\mathbf{Y}_F$ is a matrix containing the mobilities of the free rail and bridge without the springs, when subjected to unit spring forces at the connecting points; and $\mathbf{Y}_P$ is the relative velocities between two ends of each spring caused by a unit harmonic excitation on the rail.

Using a track-bridge model without wheels on the rail, spring-dashpot forces for all the rail fasteners can be firstly calculated from Eq. (1). Secondly, the rail mobilities in the track-bridge system can be obtained by summing up the effect of all the spring-dashpot pairs as well as the external force on the structure. Thirdly, the wheel-rail contact forces due to the excitation of random wheel-rail combined roughness in the case of multiple wheels on the rail can be calculated according to the vibration compatibility condition between the wheels and the rail (Li and Thompson, 2018). Fourthly, the power input to the bridge can be then obtained by summing the effects of all the springs connected with the bridge. The spatially averaged mean-square velocity of rail vibration can be obtained directly from the node responses of the rail, and that of the bridge can be approximately obtained by the statistical energy analysis from the power input to the bridge (Thompson, 2008).

3. Acoustic analysis for the rail and bridge

Fig. 2(a) presents a general two-dimensional (2D) vibroacoustic model for the rail and bridge. This model is comprised of structural finite elements for the rail and bridge, fluid finite elements for the air, infinite elements for the exterior air and surface elements of these bodies for the fluid-

structure coupling interface. This model is used to obtain the transferring functions between the sound pressure at the given field points and the spatially averaged mean-square velocity of the rail and bridge. The forces are respectively acted on the rails and the bridge to obtain the transferring functions for rail noise and bridge noise. The radiated noise from the rail-bridge system is then calculated by combining the sound transfer functions with the vibration of the rail and bridge obtained from the method introduced in Section 2.

Fig.2(b) shows the schematic diagram of the mid-span section and the two-dimensional (2D) vibroacoustic model of a double-deck bridge in China. The upper deck carries urban road and the lower deck carries urban rail transit. The rectangle zone of 16 meters by 24 meters in Fig. 2(b) will be discussed in terms of contour of sound pressure level (SPL). Fig. 2(c) gives detailed mesh of the vibroacoustic model. It can be seen from Fig. 2(c) that the road deck, the car body and the noise barriers are all represented by void zones which account for sound reflection but ignore their vibration effects.

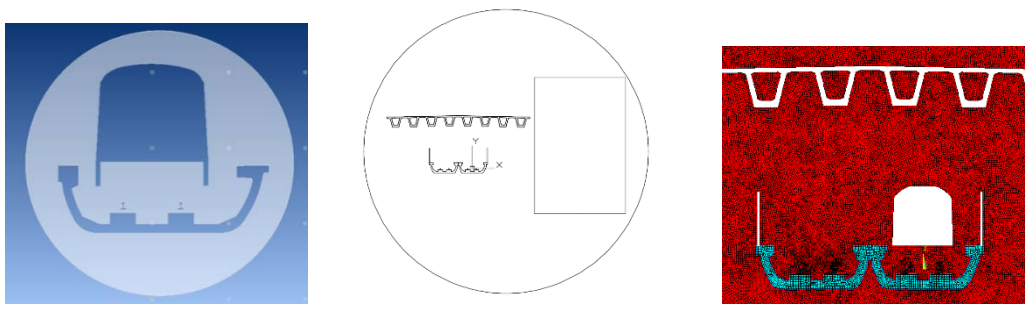

(a) (b) (c)

Fig. 2. Vibroacoustic model of vehicle-track-bridge systems: (a) pure rail transit bridge; (b) double deck bridge; (c) detail mesh for double deck bridge

Fig.3 shows the contour map of difference A-weighted SPL of the double deck elevated bridge and the corresponding U-shaped bridge for pure urban rail transit. It can be seen from the figures that the shielding effect of the overhead urban road obviously blocks the propagation of upward noise from the below bridge and rail. With the effect of the upper deck, the bridge noise in the zone below the track increases by 2-5 dB and the total noise increases by 6-18 dB.

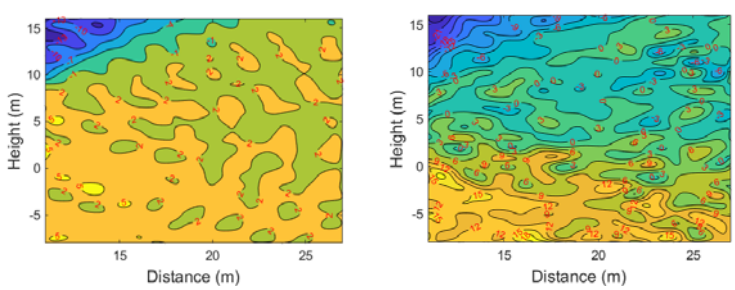

(a) (b)

Fig. 3. The contour map of difference of SPL between the double deck bridge and the pure urban rail transit bridge: (a) bridge noise; (b) total noise

Fig. 4 depicted the spectra of A-weighted SPL for the double deck bridge, pure rail transit bridge and double deck bridge with noise barriers of 2 m above the top of the U-shaped girder. Two positions S1 and S2 are investigated, which are 25 m horizontal from the track center, and 5 m below the track center and 5 m above the track center respectively. It can be observed from Fig. 4 that the shielding effect of the overhead urban road obviously increases the SPL at S1 above 250 Hz. The sound barriers can decrease the noise by about 5 dB at 630 Hz. However, the overhead urban road and the sound barriers have less influence on the SPL at position S2.

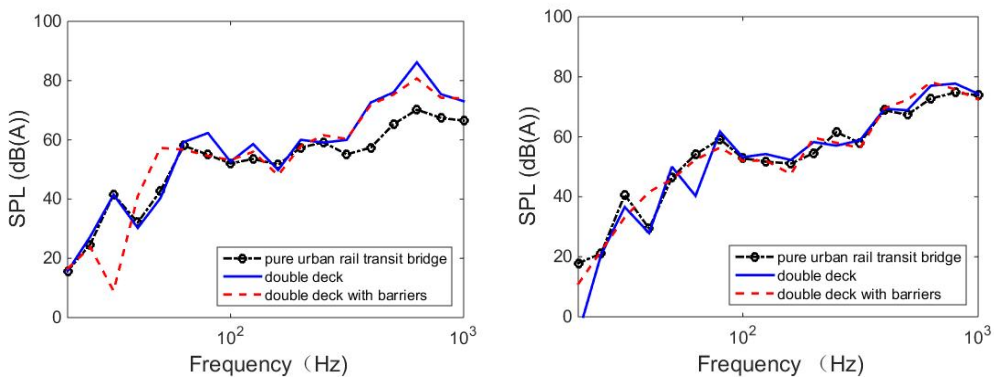

Fig.4. Comparison of SPL for various conditions at two different positions: (a) S1; (b) S2

4. Conclusion and suggestion

This study developed a vibrational model of vehicle-track-bridge interaction system and a two-dimensional vibroacoustic model of the system to predict rail and bridge noise subjected to wheel-rail rolling excitation. The noise radiated from three different systems is then calculated and compared. The results indicate that the shielding effect of the overhead urban road increases both rail and bridge noise below the track center. The sound barriers significantly reduce the noise at some positions but have less effect at others. Reasonable height of the sound barriers should be further explored and applied in practical engineering.

5. Acknowledgements

The study has been supported by the National Natural Science Foundation of China (grant number 51878501).

6. References

Li, X., Liu, Q., Pei, S., Song, L., & Zhang, X., 2015. Structure-borne noise of railway composite bridge: Numerical simulation and experimental validation, Journal of Sound and Vibration, 353:378-394.

Li, Q., Li, W. Q., Wu, D. J., and Song, X. D., 2016. A combined power flow and infinite element approach to the simulation of medium-frequency noise radiated from bridges and rails, Journal of Sound and Vibration, 365:134-156.

Li, Q. and Thompson, D.J., 2018. Prediction of rail and bridge noise arising from concrete railway viaducts by using a multilayer rail fastener model and a wavenumber domain method, Proceedings of the Institution of Mechanical Engineers, Part F: Journal of Rail and Rapid Transit, 232:1326-1346.

Thompson, D.J., 2008. Railway Noise and Vibration: Mechanisms, Modelling and Means of Control. Elsevier.

Wu, T.X., and Thompson, D.J., 2000. The vibration behavior of railway track at high frequencies under multiple preloads and wheel interactions, Journal of the Acoustical Society of America, 108: 1046-1053.

Study on Aerodynamic Characteristics and Running Safety of Train Passing through the Wake of Bridge Tower

Jinfeng Wu[1], Xiaozhen Li[2*], and C.S Cai[3]

[1] Department of Bridge Engineering, Southwest Jiaotong University, Chengdu, China; email: jfwu1y@outlook.com
[2] Department of Bridge Engineering, Southwest Jiaotong University, Chengdu, China; email: xzhli@home.swjtu.edu.cn
[3] Department of Civil and Environmental Engineering, Louisiana State University, Baton Rouge, USA; email: cscai@lsu.edu

[*]: corresponding author

Keywords: aerodynamics; wind tunnel test; moving vehicle; running safety; truss bridge; bridge tower

Abstract: To study the impact of the bridge tower on the aerodynamic characteristics of train, an innovative moving train model test device was designed. Based on this device, a series of wind tunnel tests were performed on a 1:30 scaled model. A truss girder and a typical high-speed train geometry are selected as the experimental prototype with towers placed at both sides of the deck segment. To investigate the influence of the bridge tower on the dynamic responses of train, the wind-train-track-bridge coupling vibration model was used to analyze the responses of the CRH3 train. The results show that the bridge tower has a shielding effect on the train, and the aerodynamic characteristics of the train change considerably when it passes the wake of the tower. The influential width on the aerodynamic coefficient curves is far greater than the width of the tower itself. The train is more sensitive to the shielding effect at a lower wind speed, and the mutation region is wider at a higher train speed. The shielding effect has an adverse impact on both the running safety and riding comfort of the train.

1. Introduction

When a vehicle passes through the tower area, the windward area of the vehicle will change, which may result in deviation, sideslip and rolling of the vehicle. It severely influences the stability of the vehicle as well as the running safety. In recent years, researchers have studied the influencing parameters on aerodynamic characteristics of vehicles with cases of the wake of pylon (Wang et al. 2015), wind barrier (Estébanez et al. 2017) and lane position (He et al. 2016). In this paper, a moving train model test device was designed based on a highway-railway steel truss cable-stayed bridge, and the aerodynamic forces on the train were tested in the XNJD-3 wind tunnel. Then the wind-train-track-bridge spatial coupling vibration method was used to analyze the dynamic responses of train, either considering the influence of bridge tower or not.

2. Effects of bridge tower on aerodynamic characteristics of moving train

2.1. A brief introduction of the wind tunnel test

As shown in Fig. 1, the entire device was located in the XNJD-3 wind tunnel (36 m in length, 22.5 m in width and 4.5 m in height), and the train driven by a synchronous belt can run on a

guide rail at any speed manipulated by a control panel. The steel truss, bridge tower and CRH3 train were constructed based on a geometric scale ratio of 1:30. The train model was composed of 3 independent cars, among which the middle car was set as the force-measured vehicle. Its built-in force balance can record aerodynamic forces when the train passes through the bridge tower under cross wind, and the real-time data will be transferred to the computer through a wireless acquisition instrument connected to the force balance. During the test, the train only ran on the windward track, and it passed the bridge tower with a constant speed.

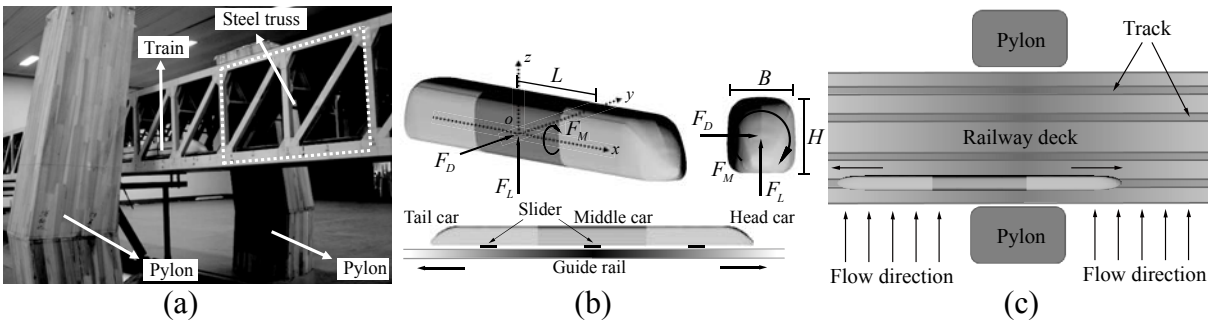

Fig. 1. Wind tunnel test device of moving train model: (a) test device; (b) CRH3 train model; (c) scheme of test.

2.2. Train aerodynamics under different wind speeds

Based on the test results, the aerodynamic coefficients of train at a speed of 8 m/s under different wind speeds are shown in Fig. 2. When the train is passing through the wake of tower, in general, the lift and side coefficient show a downward-upward trend, while the rolling moment coefficient show an upward-downward trend. The mutation in the tower area of these curves are greater under a lower wind speed. The mutation widths of lift and side coefficient are basically the same, which indicates that the influencing width of the tower under different wind speeds is indistinctive.

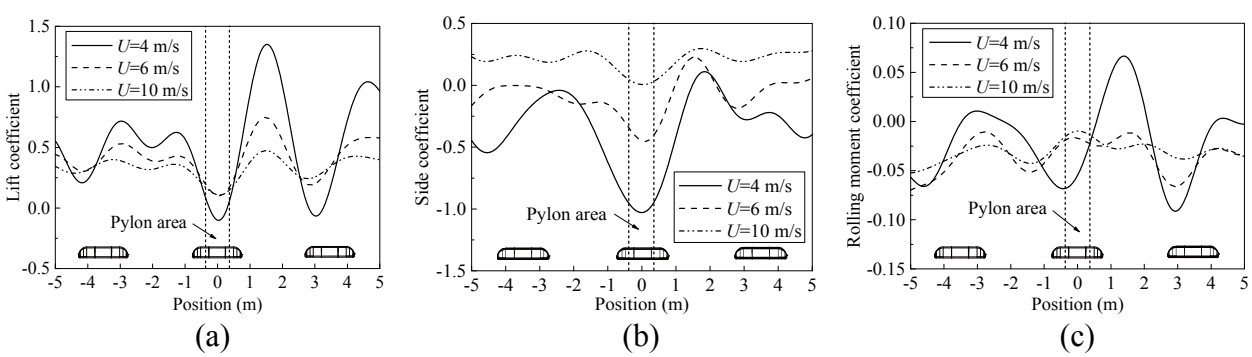

Fig. 2. Train aerodynamic coefficients under different wind speeds (V=8 m/s): (a) lift coefficient; (b) side coefficient; (c) rolling moment coefficient.

2.3. Train aerodynamics under different train speeds

The air flow around the train varies with its speed. The aerodynamic coefficients of the train under different train speeds are shown in Fig. 3, with crosswind speed of 8 m/s. From the side coefficient curves, we can find that the mutations in the tower area under different train speeds are approximately the same, while the mutation width is larger at a higher train speed. The side coefficient even decreases to the negative region in the tower area, which means the direction of the side force on the train changes abruptly due to the wake of bridge tower.

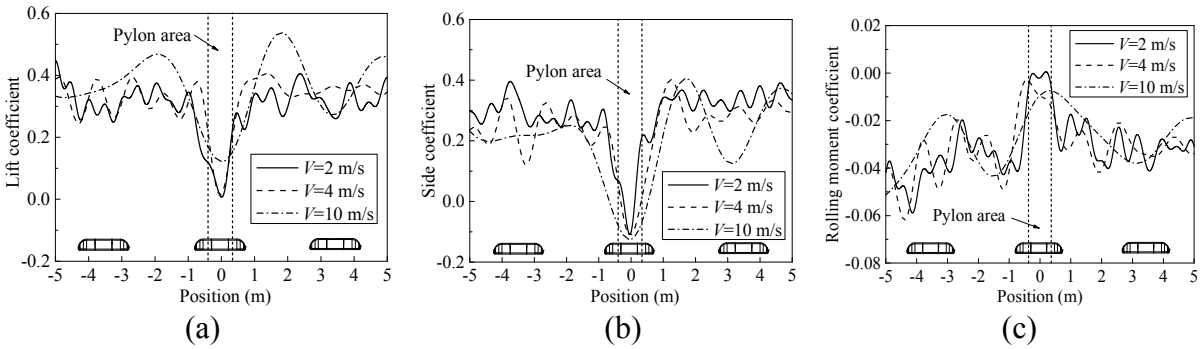

Fig. 3. Train aerodynamic coefficients under different train speeds (U=8 m/s): (a) lift coefficient; (b) side coefficient; (c) rolling moment coefficient.

3. Effects of bridge tower on running safety of train

3.1. Engineering background

As shown in Fig. 4, the highway-railway cable-stayed bridge has a main span of 1092 m, with 4-lane railway on the bottom of the deck of the truss girder. A CRH3 train runs on the windward side at a speed of 324 km/h under a crosswind speed of 30 m/s, and the aerodynamic coefficients of the train and the bridge are from the moving train wind tunnel test results mentioned above.

The wind-train-track-bridge coupling model was used to analyze the responses of the train-bridge system under crosswinds. The wind forces acting on the bridge consider the static force, the buffeting force and the self-excited force, while the wind forces acting on the train only consider the static force and the buffeting force. The self-excited force on train is neglected due to its less obvious pneumatic coupling effect.

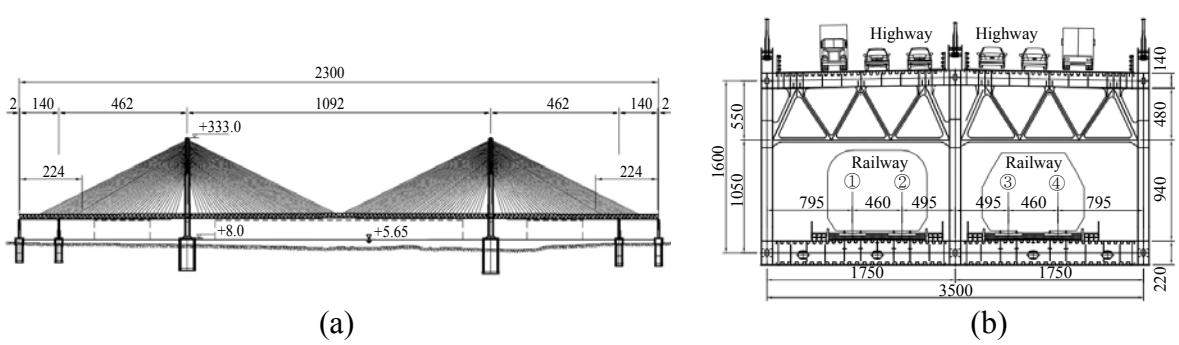

Fig. 4. Layout of bridge spans and lanes: (a) layout of the bridge span (unit: m); (b) cross section of the truss girder (unit: cm).

3.2. Simulation results

Fig. 5 shows the dynamic responses of the first car in the train, which are quite different considering the shielding effect of the tower or not. The responses magnify abruptly with tower considered. The differences on curves illustrate that the mutation of wind loads on the train have an adverse effect on both the riding comfort and running safety of vehicles.

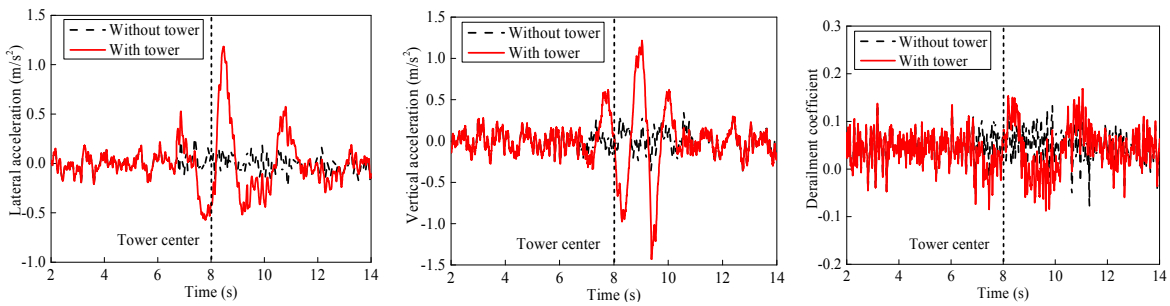

(a) (b) (c)

Fig. 5. Time-history of train dynamic responses: (a) lateral acceleration; (b) vertical acceleration; (c) derailment coefficient.

4. Conclusions

(1) The bridge tower has a shielding effect on the train, and there is mutation in aerodynamic characteristics of train when it passes the wake of tower.
(2) The influential width of the aerodynamic coefficient curves is larger than the width of the tower itself, and the influencing width in the tower area is greater at a higher train speed.
(3) The train is more sensitive to the shielding effect of the tower under a relatively lower crosswind speed.
(4) In the wind-train-track-bridge coupling vibration system, the simulation results will be more realistic when the shielding effect of the tower is taken into consideration.

5. Acknowledgements

This work is financially supported by the National Natural Science Foundation of China (U1434205).

6. References

Alonso-Estébanez, A., Del Coz Díaz, J.J., álvarez Rabanal, F.P. et al. 2017. Performance analysis of wind fence models when used for truck protection under crosswind through numerical modeling. Journal of Wind Engineering and Industrial Aerodynamics, 168, 20-31.

He, X.H., Shi, K., Wu, T., Zou, Y.F., Wang, H.F. and Qin, H.X. 2016. Aerodynamic performance of a novel wind barrier for train-bridge system, Wind & Structures An International Journal, 23.3 171-189.

Wang, B. and Xu, Y. L. 2015. Safety analysis of a road vehicle passing by a bridge tower under crosswinds. Journal of Wind Engineering and Industrial Aerodynamics, 137, 25-36.

Optimization of the Track Position on a Highway and Railway Combined Bridge through Wind Tunnel Testing

Haiquan Jing[1], Xu Zhou[2], Xuhui He[3*], and Yunfeng Zou[4]

1 School of Civil Engineering, Central South University, Changsha and China; email: hq.jing@csu.edu.cn
2 School of Civil Engineering, Central South University, Changsha and China; email: xu_zhou@csu.edu.cn
3 School of Civil Engineering, Central South University, Changsha and China; email: xuhuihe@csu.edu.cn
4 School of Civil Engineering, Central South University, Changsha and China; email: yunfengzou@csu.edu.cn

*: corresponding author

Keywords: train tracks, highway and railway, optimization, wind tunnel test

Abstract: The bridge deck is wide when highway and railway are designed on the same layer. There are various layouts of the train tracks on the deck. In cross winds, the trains will change the flow field around train-bridge system, resulting different aerodynamic forces. This paper investigated the influences of the lateral arrangement of tracks on the aerodynamic characteristics of the train-bridge systems using the model of Jinhai Bridge, and found out the optimal layout scheme of the train tracks.

1. Introduction

As the running speed of train becomes higher and higher, the running safety in strong wind has becoming a concerning problem in civil engineering and transportation engineering[1]. More than 30 accidents of derail and overturn were caused by strong wind in Lanzhou-Xinjiang Railway, China, until 2002 [2]. Similarly, more than 30 accidents of derail and overturn caused by strong wind occurred in Shinkansen Japan until 2006 [3]. The strong wind is more danger for the running train on bridges because the train-bridge coupled vibration enhances the instability of the train. Two types of efforts has been taken by the researchers to improve the running safety of high speed trains. One is to improve the aerodynamic of the train by optimizing its aerodynamic shapes [4~6]; the other one is to improve the side-incoming flow of the train by installing wind barriers[7~9]. Zou[7], Xiang[8], and Zhou[9] investigated the effects of different types of wind barriers on the side-incoming flow and consequently the aerodynamic force coefficients of the train. Recently, the highway and railway combined bridge becomes popular because its cost-effectiveness. Most of the highway and railway combined bridges separate the vehicles and trains at different layers. However, there are also bridges with vehicles and trains on the same layer. When the the vehicles and trains are put on the same layer, the bridges are almost wide and the track position of the train has various layouts. The location of the train significantly changes the air flow and the aerodynamic forces of train and bridge. However, up to now, there are few reports on the the effect the track position on the aerodynamic forces of train and bridge. In the presently study, a case study has been conducted using a 5-span cable stayed bridge in China and

investigate the effect of track position. Finally, it was found out that the track in the center is relatively optimal layout when only considering the wind influence.

2. Engineering Background

Jinhai Bridge is locatedin Zhuhai City, where suffers strong wind every year. According to local meteorological data, from 1993 to 2003, there were 29 typhoon attacked Zhuhai City. In particular, in 2017, the typhoon 'Hato'attacked Zhuhai City. The maximuminstantaneouswind speed of 'Hato'reached 51.9 m/s, which broken the wind speed record of Zhuhai City. Consequently, the Jinhai Bridge has to face numerousstrong winds during its servers life. The main bridge of Jinhai Bridge has four towers with spans of 58.5+116+3×340+116+58.5 m, as Fig. 1 shows. The total length of this bridge is 1371.8 m. The width of the bridgedeck is 49.6 m, including 4 highway lanes and 2 railway tracks. The bridge deck is made of steel box with pick arms on both sides, as Fig. 2 shows. The box girder has three chambers. The roof of the box girder is made of orthotropic steel plate. A diagonal supportis designedevery 3 meters in the box girder and every 6 meters outside the box girder, in longitudinal direction.

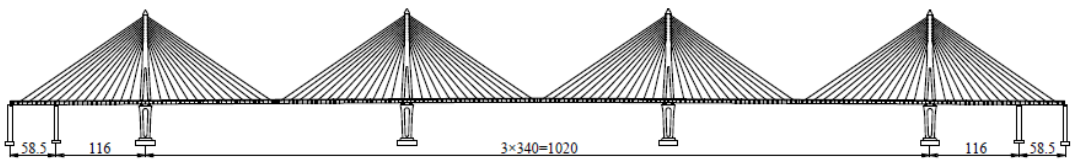

Figure 1. Facade layout of the main bridge of Jinhai Bridge (Unit:m)

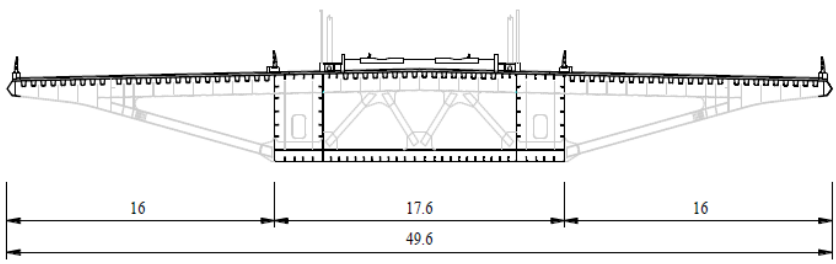

Figure 2. Cross-section of the deck of main bridge of Jinhai Bridge (unit:m)

3. Wind tunnel tests

In the present study, wind tunnel tests were conducted to investigate the location of the train tracks on the aerodynamic forces of the train and train-bridge system. The segment models of both bridge deck and train for wind tunnel tests are shown in Fig. 3. The scale factor of these model is 1/50[10~11]. The bridge model has length of 2.04 m, height of 0.09 m, width of 0.99 m. The ratio of length to width equalsto 2.06. The train model was made according to the body of CRH2, a high speed train in China. It has the same length with bridge model, the height and width of 0.07 m and 0.068 m, respectively. The wind pressure on the bridge and train models is tested by Scanivalve(ZOC33/64PxX2). The testing section is located at the center of the models. The distribution of the pressure taps is shown in Fig. 4. The sample frequency of the scanivalve is set as 625 Hz, and the sampling time is 32 s. The piezometric tubes have interiorand external diameterof 0.6 mm and 1.8 mm, respectively. The total length of the piezometric tubesis less than 1.5 m. Six cases were tested as summarizedin Table 1 and Fig. 5. The wind pressure was measured when the train model was fixed at different positions on the

bridge model. The non-dimensionaldistance (r=S/B*) represents the relative position of the train on the bridge. The accessory structure, including railings, slabs, and tracks, is ignored. The wind speed is set constant as 10 m/s with an attackingangle of 0°.

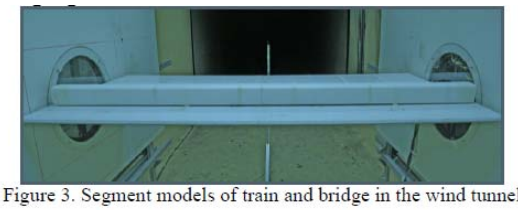

Figure 3. Segment models of train and bridge in the wind tunnel

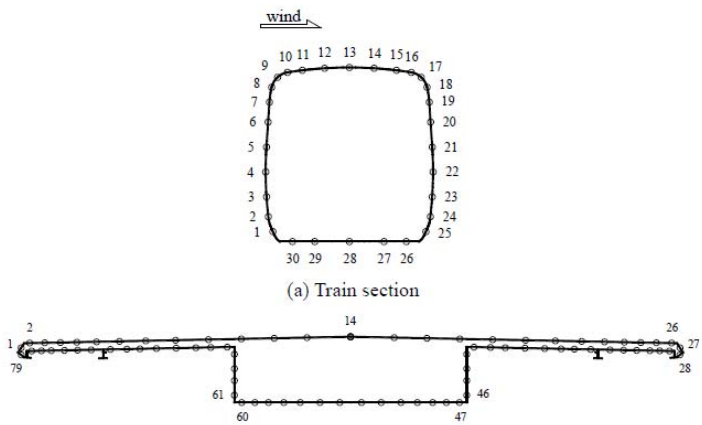

Figure 4. Distribution of pressure taps

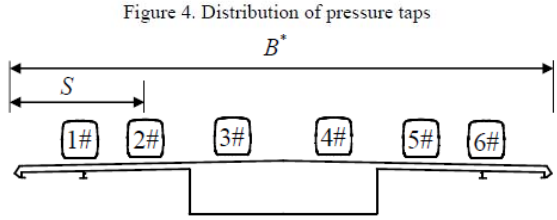

Figure 5. Track positions on the deck

Table 1. Summary of test cases

Case No.	Non-dimensional distance
1#	0.11
2#	0.22
3#	0.41
4#	0.59
5#	0.78
6#	0.89

4. Aerodynamic force coefficients of train and train-bridge system

The aerodynamic characteristics of the train, bridge, and train-bridge system are describedby lift force, drag force, and torsionmoment coefficients. They are defined as follows：

$$\begin{cases} C_D = \dfrac{2F_D}{\rho U^2 H^*} \\ C_L = \dfrac{2F_L}{\rho U^2 B^*} \\ C_M = \dfrac{2M_T}{\rho U^2 (B^*)^2} \end{cases} \tag{1}$$

where, the F_D, F_L, and M_T are drag force, lift force, and torsion moment, respectively; the C_D, C_L, and C_M are three force coefficients; ρ is air density; U represents incoming wind speed; H^* and B^* are representative height and width of the model, respectively. It is worth to note that the height and width of the bridge model are taken as the representative height and width for the train-bridge system.

The wind pressure around the train and bridge models has been measured. The lift, drag, and torsion forces of the train and train-bridge system are then obtained by numerical integration. The aerodynamic force coefficients of the train and train-bridge system are shown in Figs. 6 and 7. When the train moves leeward, both the drag and lift force coefficients of the train-bridge system increases, while the torsion coefficient is relatively stable. From the Case 1# to Case 5#, the drag force coefficient of the train-bridge system increases from 1.5 to 1.95, the lift force coefficient increases from 0 to 0.92. There is a sudden jump in the lift curve from Case 3# to Case 4#.

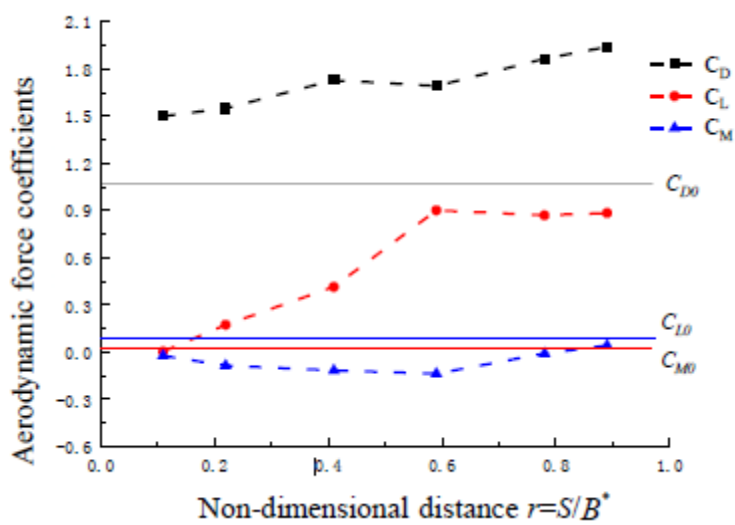

Figure 6. Aerodynamic force coefficients of the train-bridge system when the train is located at different positions. (*C*D0、*C*L0、*C*M0are the drag, lift, and torsion coefficients of the naked bridge)

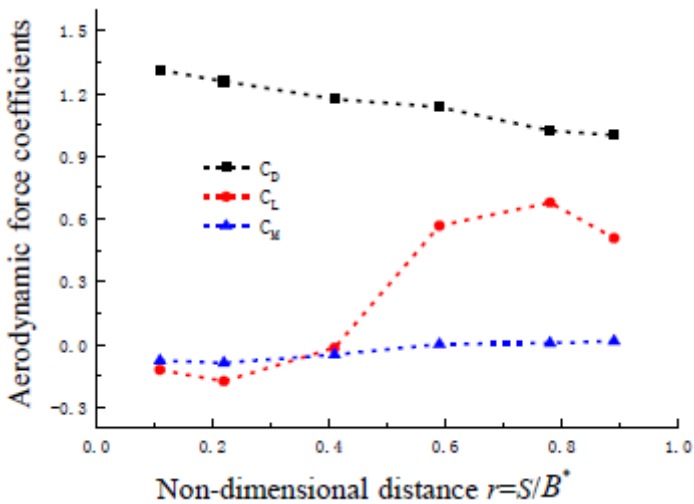

Figure 7. Aerodynamic force coefficients of the train when the train is located at different positions

When the train moves leeward, the drag and torsion coefficients of the train decrease, while the lift coefficient increases. There is a obviously jump in the lift coefficient curve when from Case 3# to Case 4#. However, becausethe drag force and torsion moment play most important roles in running safety of the train and the wind comes from both sides in site, Case 3 and Case4 should be the optimal positions for the train track.

5. Conclusions

In the present study, the effect of track position on the aerodynamic force coefficients of the train and train-bridge system has been investigated through wind tunnel testing. A case study was conducted using the Jinhai Bridge, which arranges highway and railway at the same layer. When the tracks was set at different positions, the wind pressure around the train and the bridge model was measured and the aerodynamic force coefficients were obtainedthrough numerical integration. The main conclusions are drawn as follows：

(a) When the train moves leeward on the bridge, the drag and lift coefficients of the train-bridge system increase, while the torsion coefficient is relatively stable. That means the wind resistance of the train-bridge system reduces when the train moves leeward.
(b) When the train moves leeward on the bridge, the drag and torsion coefficients of the train decrease. That means it is helpful to improve the running safety of the train when the track is located in leeward；
(c) Considering the wind will attack the train/bridge in both sides, for a highway and railway combined bridge, the optimal position of the rail tracks should be the center of the bridge deck.

6. References

[1] He Xuhui, Zou Yunfeng, Zhou Jia, et al.. Effect of wind environment parameters on aerodynamic characteristics and critical wind velocity of vehicle operation. Journal of the China Railway Society 2015, 37(5): 15-20.

[2] Ge Shencang, Yin Yongshun. Field measurement on the velocitylimit criterion for running safety in strong wind of Xinjiang railway. Railway Quality Control 2006, 34(04): 9-11.

[3] Liu Qingkuan, Du Yanliang, Qiao Fugui. Train-crosswind and strong wind countermeasure research in Japan. Journal of the China Railway Society 2008, (01): 82-88.

[4] Tian Hongqi. Train Aerodynamics.China Railway Press, 2007.

[5] Cheli F., Ripamonti F., Rocchi D.,et al.. Aerodynamic behaviour investigation of the new EMUV250 train to cross wind. Journal of Wind Engineering & Industrial Aerodynamics 2010, 98(4-5): 189-201.

[6] Feng Zhipeng. Aerodynamic performance of high-speed train with the train shape design. Southwest Jiaotong University, 2011.

[7] Zou Yunfeng, He Xuhui, Li Huan, et al.. Effect of wind barrier on aerodynamic characteristics for the trailing train under cases of vehicle-bridge coupling. Journal of Vibration Engineering 2016, 29(1): 156-165.

[8] Xiang Huoyue. Study on Wind Protection Effect and Wind Load of High Speed Railway Wind Barrier. Southwest Jiaotong University, 2013.

[9] Zhou Qi, Zhu Ledong, Guo Zhenshan. Numerical simulation for curve windshied barrier effects o wind enviroment around bridge deck. Journal of Wuhan University of Technology 2010, (10): 38-44.

[10] Chen Zhengqing. Bridge Wind Engineering.China Communications Press, 2005.

[11] CCCC Highway Consultants CO., Ltd. Wind Bridge Design Code for Highway Bridges.China Communications Press, 2004.

Crosswind Effects on a Train-Bridge System: Wind Tunnel Tests with a Moving Vehicle

Xuhui He[1], Simin Zou[2], and Teng Wu[3*]

[1] School of Civil Engineering, Central South University, Changsha, China; National Engineering Laboratory for High-Speed Railway Construction, Changsha, China; E-mail: xuhuihe@csu.edu.cn
[2] School of Civil Engineering, Central South University, Changsha, China; Department of Civil, Structural and Environmental Engineering, University at Buffalo, Buffalo, NY 14260, USA; E-mail: simin_zou@csu.edu.cn
[3] Department of Civil, Structural and Environmental Engineering, University at Buffalo, Buffalo, NY 14260, USA; E-mail: tengwu@buffalo.edu

[*]: corresponding author

Keywords: moving vehicle; train-bridge system; wind tunnel test; crosswind; aerodynamic characteristics

Abstract: To better understand the aerodynamic characteristics of the moving vehicle-bridge system, an in-house experimental apparatus was developed in the wind tunnel at Central South University (CSU). The new facility consists of the train, bridge, acceleration-deceleration U-shaped side guide, and positioning system with a winch. The data acquisition system for the pressure measurements was mounted within the train carriage to avoid any aerodynamic interference. A 1:25 scale model of CHR2 running over a simply-supported girder bridge was tested in the wind tunnel. The aerodynamic characteristics of the vehicle-bridge system under various combinations of the crosswind speed, train speed and vehicle location on the bridge were identified. The difference of the pressure distribution on the train windward and top area between static and moving cases was observed. In general, the C_p values of the static train is greater than those of the moving train. Both of the drag force and lift force coefficients of bridge become functions of wind speed due to the presence of the train. The results show that the train movements lead to more complicated aerodynamic interference between the train and the bridge.

1. Introduction

Since the first high-speed (or bullet) train in the 1960s with a speed of 210km/h in Japan, the high-speed trains become an important engineering application in China, Japan, Germany, as well as many other Asian and European countries and regions (Yang et al., 2004). The high-speed railway has been become a crucial approach for intercity and even for intercontinental passenger transportation, for example, “the Belt and Road” initiative proposed and actively advanced in China. It is important to carefully investigate the high-speed railway train-bridge dynamic system under strong wind to guarantee the safety and smooth of train movements. With the increase in speed, the aerodynamic interference become ever more significant. A number of accidents investigations indicated that crosswind may cause the train to overturn. For example, around 30 train accidents occurred from 1899 to 2006 in Japan (Toshishige F., et al, 1999) and a dozen of trains are withdrawn from the schedule each year in China. In addition, accidents of train crash caused by the strong winds were frequently reported in Spain, Switzerland, USA,

France, and India. To reduce the risk of wind-induced railway accidents, European and national standards prescribe detailed specifications.

The bridge, as an important part of the transportation line, will suffer huge losses when subjected to damage. In the strong wind area, the wind load may not only result in the comfort and safety issues of the running train on the bridge but also lead to the large lateral response of the bridge itself. Compared to the static train, the aerodynamic force and moment may be modified for running trains subjected to strong crosswinds. The above-mentioned factors have formed a complicated wind-vehicle-bridge dynamic interactive system. The investigation of the overturning accident on the 40m high Amarube Bridge in Japan has noted that the train and the bridge must be integrated as a whole system in the aerodynamic analysis. In order to explore the aerodynamic characteristics of the vehicle, two types of wind-tunnel tests have been discussed by various researchers, namely stationary and moving train model experiments. The former is a convenient method used to consider the wind direction α=90° (Baker 2001, He et al, 2016). The model was also rotated to change the wind direction in the static tests (Suzuki et al, 2003; Sterling et al 2010). However, these tests do not reflect the real situation of the train operation.

In this study, a moving train on the bridge was intended in the wind tunnel to analyze aerodynamic characteristics of the vehicle-bridge system, where the effects of the wind and train speeds were highlighted. The aerodynamic characteristics of the vehicle-bridge system under various combinations of the crosswind speed (8m/s, 9m/s, 10m/s), train speed (0m/s, 4m/s) and vehicle location (upstream and downstream) on the bridge were comprehensively considered.

2. Experiment setup

To investigate the underlying mechanism of aerodynamics in the static and moving vehicle-bridge system, U-shape slide rail was constructed in the CSU wind tunnel to study the change of the aerodynamics of the vehicle-bridge system due to the motions of train. The selected model of the bridge is a multiple-span simply-supported bridge. This type of bridge is the most commonly used bridge in the construction of the high-speed railway and its test model has a scale ratio of 1:25. The span of the prototype bridge is 32m long, 12.24m wide and 3.628m high. Accordingly, the length, width and height of the bridge model in the wind tunnel are 1.28m, 0.493m, 0.15m, respectively. As shown in Fig.1, the model of the bridge is composed of 5 spans with the railway. Hence, the system of the total bridge length is 5*1.28=6.4m, which is connected to the guide way at both sides of the wind tunnel. The test train model was selected from the prototype China Railways high-speed CRH2 which consists of a head car (1.028m) and a middle car (1m). A nested connection is used between the two cars to conveniently acquire the individual data for each car.

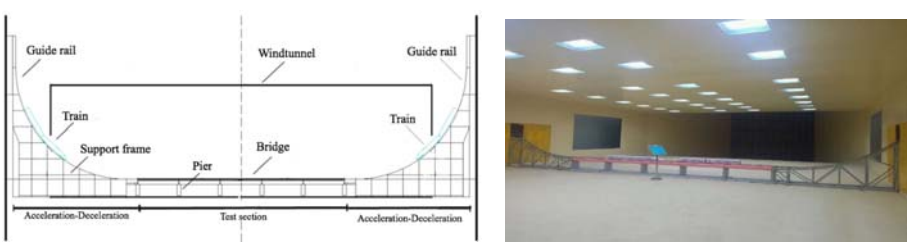

Fig. 1. Moving vehicle-bridge wind tunnel test system

3. Wind tunnel tests of static and moving vehicles

3.1 Mean pressure coefficient of train under static and dynamic tests

This test is aimed at the surface wind pressure distribution of the train under static and moving conditions, respectively, as shown in Figs. 2 and 3. The tests were performed with three wind speeds, two train speeds (including stationary case) and two rail positions. The mean pressure coefficients of static model test results are larger than those of the moving model for the downstream case, especially for points of 3-6. When the train runs on the upstream of the bridge, there is a significant difference in C_p of the static and dynamic trains for wind speed of 8m/s-10m/s. In general, the test result of the stationary model are also larger than those of the moving model. Due to the flow separation and reattachment, the surface wind pressure fluctuation of a train running on the downstream of bridge is more intensive than the upstream case. In addition, the wind pressure on the windward side of train for the upstream case is much greater than the downstream case.

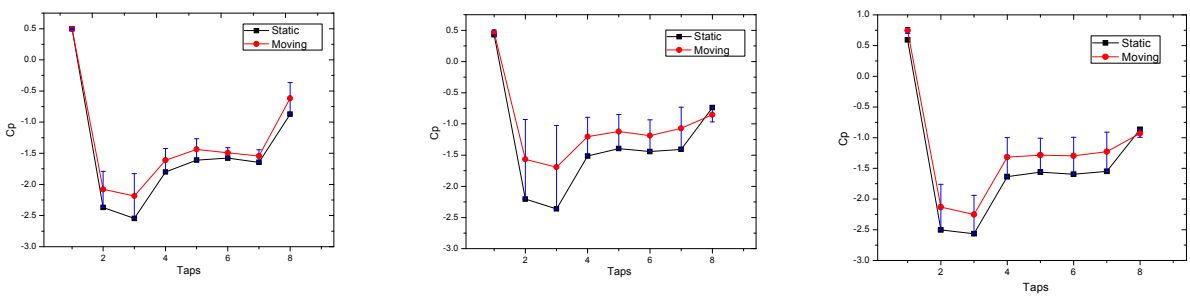

(a) (b) (c)

Fig. 2. Comparison of train at downstream track for various wind speeds: (a) 8m/s; (b) 9m/s; (c) 10m/s

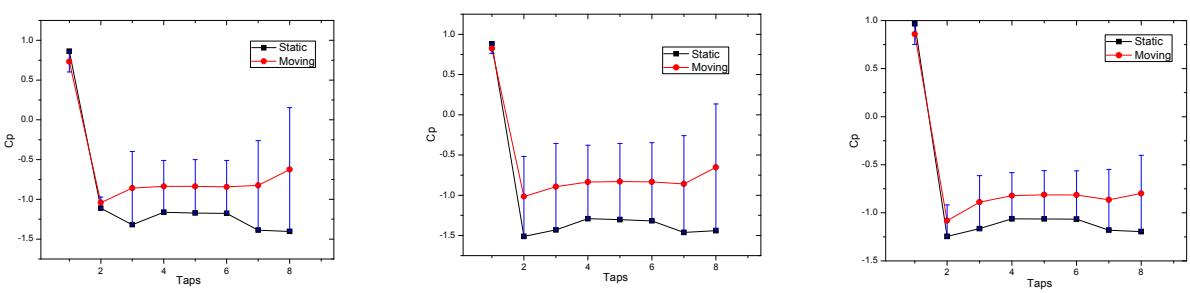

(a) (b) (c)

Fig. 3. Comparison of train at upstream track for various wind speeds: (a) 8m/s; (b) 9m/s; (c) 10m/s

3.2 Bridge aerodynamics with static and moving vehicles

Figure.4 presents a comparison of the aerodynamic force coefficients of bridge measured for stationary and moving CRH2 model tests with various wind speeds (8m/s, 9m/s and 10m/s). It is observed that the data curve changes gently in different wind speeds. Figures 4(b) and (e) present a comparison between the aerodynamic coefficients of the downstream static and moving vehicle cases. Figures 4(c) and (d) present the upstream results measured at V_{car}=0m/s and 4m/s. It is noted the wind speed has little effect on lift force and moment coefficients of the bridge, but the position of train shows a significant effect on the drag force coefficient. In general, the drag and

lift force coefficients increase with the train speed for the upstream case. On the other hand, the lift force coefficient decreases with the train speed for the downstream case.

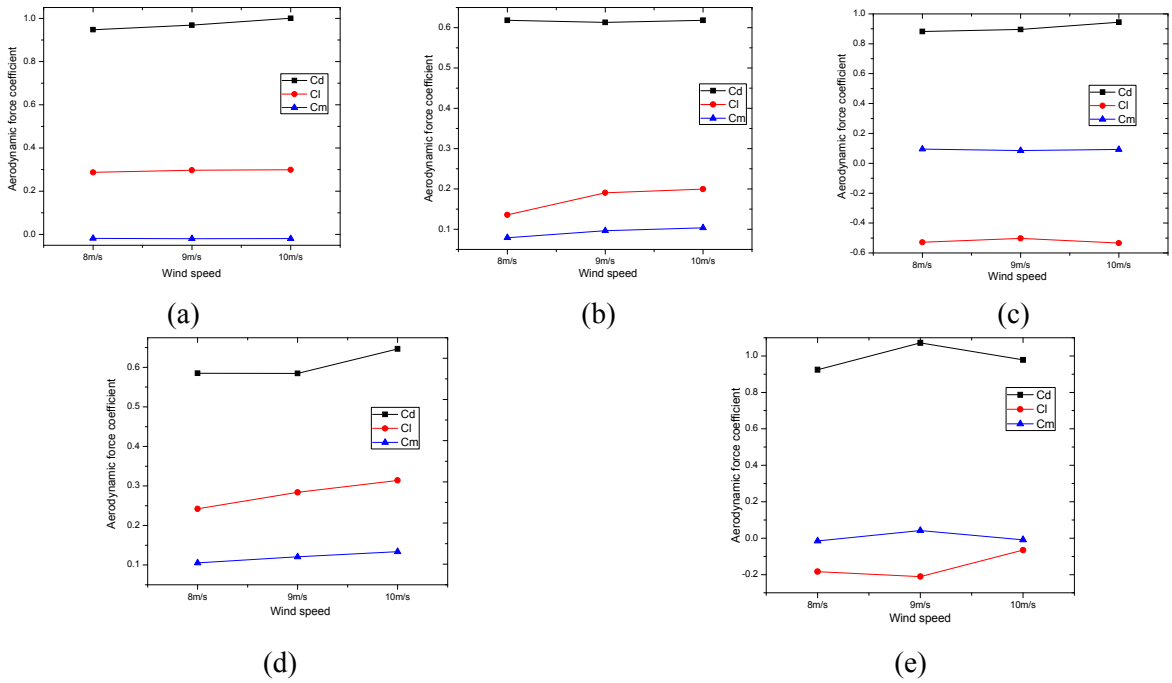

Fig. 4. Aerodynamic coefficient of bridge: (a) No trains; (b) The train stopped on the downstream; (c) The train stopped on the upstream; (d) Average wind pressure coefficient (V_{car}=4m/s, upstream); (e) Average wind pressure coefficient (V_{car}=4m/s, downstream)

4. Concluding remarks

The aerodynamic characteristics based on the measured surface wind pressure distribution on the vehicle-bridge system have been comprehensively studied for the various combinations of wind speed, vehicle speed, and rail position. The main conclusions can be drawn as follows:

- This paper introduced the novel vehicle movement system in the wind tunnel to provide a basis for reliable study on the aerodynamic characteristics of the wind-vehicle-bridge system based on the wind pressure measurements.
- The wind pressure on the moving and static trains C_p generally increases with wind speed, and the values of the static tests are greater than those of the moving tests.
- The drag force coefficient of bridge become larger due to the presence of the train. Furthermore, the movement of the train will cause the drag force and lift force coefficients to be functions of wind speed.

5. References

Baker, C.J. & Hargreaves, D.M. 2001.Wind tunnel evaluation of a vehicle pollution dispersion model. Journal of Wind Engineering & Industrial Aerodynamics, 89.2:187-200.

Yang, Y. B., Yau, J. D., and Wu, Y. S. Vehicle-Bridge Interaction Dynamics. 2004.

Toshishige, F.,and Tatsuo, M. Wind-induced Accidents of Train/vehicles and their measures in Japan. QR of RTRI, 1999, 40(1):50-55.
He, X.H., Shi, K., and Wu, T., et al.2016. Aerodynamic performance of a novel wind barrier for train-bridge system. Wind and Structures, 23(3):171-189.

Suzuki. M, Tanemoto. K, Maeda .T. 2003. Wind tunnel evaluation of a vehicle pollution dispersion model. Journal of Wind Engineering and Industrial Aerodynamics 91,209–218

Sterling, M., et al. 2010. A comparison of different methods to evaluate the wind induced forces on a high sided lorry. Journal of Wind Engineering and Industrial Aerodynamics, 98(1): 10-20.

Earthquake, Dynamics, and Impact

Novel Materials for Design of Earthquake Resilient and Durable Bridges

Ruchin Khadka[1], Jared Cantrell[2], and Mustafa Mashal[3*]

[1] Idaho State University, Pocatello, United States; email: khadruch@isu.edu
[2] Idaho State University, Pocatello, United States; email: cantjare@isu.edu
[3] Idaho State University, Pocatello, United States; email: mashmust@isu.edu

[*]: corresponding author

Keywords: Titanium alloy rods; bridge retrofitting; corrosion resistance; mechanical properties; tensile test

Abstract: Titanium alloy (Ti_6Al_4V) bars have recently found its way into civil engineering applications. Properties such as, high strength-to-weight ratio, ductility, corrosion resistance, low thermal conductivity and modulus of elasticity makes the titanium alloy a promising material for bridge works. In the last few years, several bridges in Oregon have been retrofitted using titanium alloy rods. The staple-like titanium bars were used in this near-surface mounted (NSM) technology to increase the shear and flexural capacities of reinforced concrete. The Oregon Department of Transportation (ODOT) is planning to retrofit more bridges using titanium alloy rods in 2019. There is an on-going research on application of titanium alloy bars in civil infrastructure at Idaho State University (ISU). The Idaho Transportation Department (ITD) is interested in the research at ISU. Phase I of the research at ISU includes materials characterization for titanium alloy rods. This paper presents a summary of results obtained from the tension, Charpy V-notch, Brinell hardness and galling test of titanium alloy rods. Results from testing of grade 150 ksi high-strength steel samples are also presented for comparison.

1. Introduction

Titanium alloy (Ti6Al4V) has been widely used in the areas of aerospace, chemical engineering, marine engineering, medical industry and consumer products. In the past few decades the use of titanium alloys have increased in civil engineering applications. Walt Disney Concert Hall (Los Angeles, USA), Guggenheim Museum (Spain), Kyushu National Museum and Koetsuji Shrine (Japan) are some notable structures. In the bridge sector, the near-surface mounted (NSM) technique using Ti6Al4V alloy reinforcing bars have been successfully tested using full-scale specimens (Higgins and Barker, 2013). Test results have shown four No. 5 hooked titanium bars could double the flexural strength of the test beam. Furthermore, even after complete rupture along the length of the rods, the beam showed reserve capacity as a result of mechanical anchorage of 90-degree hooks provided on each ends of the rods. The replacement of Mosier Bridge in the State of Oregon was estimated to cost US $4.6million and over a year to restore regular traffic. However, the retrofitting project using Ti6Al4V was completed in a few weeks at a cost less than 3% of the estimated replacement cost, and 30% lower than using stainless steel or FRP (Adkins and George, 2017). The installation of staple titanium alloy rods in Mosier Bridge is shown in Figure 1.

Fig. 1. Retrofit of Mosier Bridge (photos courtesy of ODOT and Perryman Company)

Millions of dollars are spent annually to reduce the detrimental corrosion problem in bridge piers and other water-exposed structures. Titanium sheets have very good corrosion resistance to waters containing mineral salts. Nippon Steel and Nittetsu Sumikin Anti-Corrosion Co. Ltd., together, have come up with the "TP method" (titanium-covered petrolatum lining method) to prevent corrosion of such structures. The TP method has longer service life and lower life cycle cost when compared with the conventional FRP methods. This method is used in D Runway of Tokyo International Airport (December, 2010) as shown in Figure 2. The titanium sheet cover panel consists of a nonflammable urethane core sandwiched between a titanium sheet and a painted steel sheet (Tokita, 2014). The titanium alloy offers excellent resistance against chemical, pitting and biological corrosion attributing to durability of bridge components exposed to such environment (K. Kimura, K. Kinoshita, 2002).

Fig. 2. Titanium cover plates (photo courtesy of Nippon Steel & Sumitomo Metal)

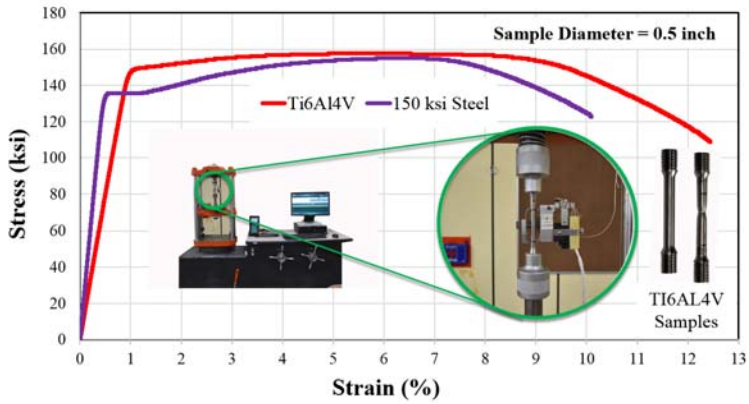

Fig. 3. Stress – Strain diagram of Ti6Al4V and 150 ksi steel

This paper presents a summary of the research at Idaho State University (ISU) on material characterization of titanium alloy rods in accordance with ASTM Standards. Several tests were conducted to quantity mechanical properties of the material. Results from testing of titanium alloy rods are compared with grade 150 ksi high-strength steel rods. For tension test, three identical Ti6Al4V specimens were tested for different diameters (0.5", 0.35", 0.25") as per the ASTM E8. The graphical result of the tensile test of 0.5" diameter specimen is shown in Fi. The results indicate that Ti6Al4V is more flexible and ductile than the 150 ksi steel while having similar yield and ultimate strength. The elongation of Ti6Al4V bars is higher than the steel. The Ti6Al4V specimens before and after the test are also shown in Figure 3. Table 1 presents a

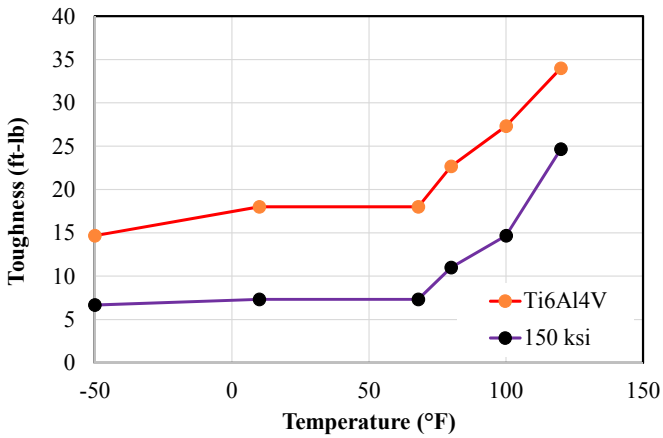

Fig. 4. Charpy V-notch test results

Fig. 5. Galling test setup

Fig. 6. Non-galled Ti6Al4V specimens

Table 11. Tension test results for Ti6Al4V and grade 150 ksi high-strength steel alloy rods

Mechanical Properties	Ti6Al4V	150 ksi high-strength steel
Modulus of Elasticity	1.6×10^4 ksi	2.9×10^4 ksi
Proportionality Limit	140 ksi	132 ksi
Yield Strength	148 ksi	140 ksi
Ultimate Tensile Strength	158 ksi	159 ksi
Fracture Strength	109 ksi	125 ksi
% Elongation Increase	17.5 %	12.7 %
% Reduction In Area	49.2 %	39.6 %

summary of the mechanical properties from tension tests and comparison for titanium alloy rods and grade 150 ksi high-strength steel rods. Following the ASTM E23, the Charpy V-notch test was performed at six different temperatures (-50° F, 10°F, 68°F, 80°F, 100°F, 120°F). As shown in Figure 4, for each temperature the titanium alloy absorbed more energy than the high-strength steel when subjected to an impact loading. Brinell hardness test was performed at the center of each specimen as per the ASTM E10. The hardness was found to be 289 HBW 10/3000. Similarly galling test was performed according to ASTM G98. The threshold galling stress of 150 ksi steel was determined to be 4.33ksi while the self-mated Ti6Al4V did not gall even at a stress of 152.78 ksi. The test surface preparation involved polishing with 600 grit and then 1500 grit followed by cleaning with CSM-3 degreaser. The test setup and post-test specimens are shown in Figures 5-6, respectively. Review of a study for galling-resistant substitute for silicon nickel showed that self-mated Ti6Al4V did not gall under a stress of 40 ksi (Budinski, Kenneth G., Budinski, Michael K. and Kohler, 2003). The bond test and cyclic loading test of Ti6Al4V are currently underway at ISU. The concrete block for bond test is prepared for different values of embedment length (7d, 10d, 15d) and bar diameter (0.75”, 0.5”, 0.38”). Further research at ISU on the use of titanium alloy rods in bridges in seismic regions is planned in Phase 2.

2. References

Adkins, J., George, W., 2017. Titanium Finds a Home in Civil Engineering. Conc. Int. 39, 51–55.

Budinski, Kenneth G., Budinski, Michael K., Kohler, M.S., 2003. A galling-resistant substitute for silicon nickel.

Higgins, C., Barker, L., 2013. Chapter 20 Titanium alloy bars for strengthening a reinforced concrete bridge 225–234.

K. Kimura, K. Kinoshita, K.T. et al., 2002. Application of titanium to construction, civil engineering and ocean development.

Tokita, M., 2014. Expanding in Application of Titanium by Nippon Steel & Sumitomo Metal Corporation.

ASTM E23 (2016) 'Standard Test Methods for Notched Bar Impact Testing of Metallic Materials', ASTM Book of Standards. doi: 10.1520/E0023-16B.2.

Astm G 98-02 (2002) 'Standard Test Method for Galling Resistance of Materials', ASTM Standards. doi: 10.1520/G0098-02R09.2.

E10-12 (2014) 'Standard Test Method for Brinell Hardness of Metallic Materials', in ASTM Book of Standards. doi: 10.1520/E0010-12.Copyright.

E8/E8M − 15a (2015) 'Standard Test Methods for Tension Testing of Metallic Materials', ASTM International. doi: 10.1520/E0008.

Seismic Performance of Precast Segmental Bridge Columns with Resettable Sliding Joints: Feasibility Study

Francis T.K. Au[1*], Y.Q. Liu[2], Y. Yuan[3], Ray K.L. Su[4], and Nelson T.K. Lam[5]

[1] Department of Civil Engineering, The University of Hong Kong, Hong Kong, China; email: francis.au@hku.hk
[2] Department of Civil Engineering, The University of Hong Kong, Hong Kong, China; email: selbyliu@hku.hk
[3] Department of Civil Engineering, The University of Hong Kong, Hong Kong, China; email: fredyhku@connect.hku.hk
[4] Department of Civil Engineering, The University of Hong Kong, Hong Kong, China; email: klsu@hku.hk
[5] Department of Infrastructure Engineering, The University of Melbourne, Australia; email: ntkl@unimelb.edu.au

[*]: corresponding author

Keywords: Concrete bridges; precast segments; prestressing; seismic resistance; wind resistance

Abstract: In an attempt to promote the use of precast segmental bridge columns in regions of moderate to high seismicity, sliding planar joints are adopted to relieve the adverse effects of seismic action. However, despite the ability to survive, the sliding segments often result in noticeable residual relative movements after an earthquake, which require costly repairs. With the increased occurrence of super typhoons, the ability of bridges to resist extreme wind loads is also a concern. It is desirable to improve and provide the system of sliding segments the self-centering capability and sufficient lateral resistance without unduly high prestressing forces. This paper reports the initial findings on an innovative resettable sliding joint system comprising resetting guide keys, concrete interfaces with low coefficient of friction and a partially debonded tendon system. The resetting guide key is essentially a smooth "shear key" with gentle slope. The partially debonded tendon system consists of grouted tendons in ducts provided with soft wrapping around the length of ducts near the interface to allow relative slipping between precast segments during an earthquake. The capabilities in seismic isolation and self-centering of the resettable sliding joint system are investigated both theoretically and numerically. It is found that, with proper choice in the location of resettable sliding joints, the co-existing rocking displacements at the resettable sliding joints during an earthquake are minimal. Key performance indicators, such as the maximum shear forces at the bottom of column, and the residual relative displacements at joints, are reported and assessed.

1. Introduction

Since its debut in Europe, precast segmental bridge construction has become a versatile method due to its economy, efficiency and quality. The method has been further extended from the construction of bridge superstructure to the substructures, i.e. segmental columns. The earlier generation of segmental columns belonged to the emulative system and used connections designed and detailed to make the performance of the precast segmental structure comparable to

that of an equivalent cast-in-place reinforced concrete structure. The success in segmental column construction in the low-seismicity regions has prompted research in seismic-resistant segmental columns (Kurama et al., 2018), where the non-emulative joints, basically dry connections between segments allowing separation, have attracted the attention of researchers.
The gap opening between segments, carefully controlled by specially designed tendon systems, has been utilized to incorporate rocking behavior into the segmental columns so that a comparatively larger drift ratio can be achieved, while minimizing the residual drift and causing limited damage at the same time. Apart from gap opening, relative slipping, the other type of relative movement between segments, has been wisely utilized, resulting in a type of segmental column with hybrid rocking-sliding joint (Sideris, 2012). However, despite better chance to survive, the sliding segments often result in noticeable residual relative movements after an earthquake, which require costly repairs. It is also desirable to improve and provide the system of sliding segments with the self-centering capability and sufficient lateral resistance to extreme wind loads without unduly high prestressing forces. To ensure sufficient capability of seismic isolation and to minimize undesirable residual displacements after sliding, an innovative resettable sliding joint system comprising resetting guide keys, low-friction concrete interfaces, and a partially debonded tendon system is proposed. The capabilities in seismic isolation and self-centering of the resettable sliding joint system are investigated both theoretically and numerically in this paper. Key performance indicators, such as the maximum shear forces and bending moments in the column, and the residual relative displacements at joints, will be reported and assessed.

2. Details of the resettable sliding joint system

In the resettable sliding joint system as shown in Fig. 1(a), the resetting guide keys, low-friction concrete interfaces, and the partially debonded tendon system are essential to its superior seismic performance. The partially debonded tendon system consists of grouted tendons in ducts provided with soft wrapping around the length of ducts near the interface to allow relative slipping. Compared to the fully unbonded counterparts, this partially debonded nature provides higher local restoring tendon forces for control of sliding, and the sensitivity of restoring tendon force to relative movement can be adjusted by changing the wrapping length, while low-friction concrete contact can be achieved by applying lubricant at chemically polished concrete surfaces.

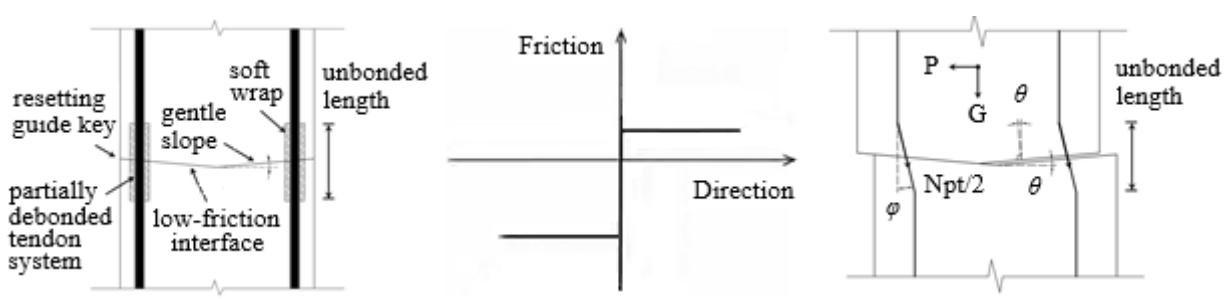

(a) Schematic diagram (b) Asymmetric sliding law (c) Model for analysis

Fig. 1. Details of resettable sliding joint

The resetting guide key is essentially a smooth "shear key" with gentle slope. The merit of this design is that the slope-induced asymmetric sliding behavior helps the sliding segments to self-center themselves especially under reversed cyclic loading such as earthquakes, thus making residual drift hardly noticeable as if the joints were reset after an earthquake. A theoretical analysis of the asymmetric sliding behavior is given below to better understand the resetting mechanism.

3. Theoretical analysis of self-centering ability of resetting sliding keys

Consider two such rigid segments stacked together as shown in Fig. 1(c). The classical friction law is applied and it is assumed for the time being that no rocking will be initiated during the sliding of segments. The slope of the guide key is θ and the angle φ denotes the deviation of unbonded length of tendon from verticality. The symbols P, G and Npt denote the earthquake-induced lateral force, gravity force and tendon force respectively. The analysis of the frictional force at interfaces gives the critical value of coefficient of friction (CoF) as

$$\mu_{\text{critical}} = \frac{P\cos\theta - G\sin\theta - N_{pt}\sin(\theta+\varphi)}{P\sin\theta + G\cos\theta + N_{pt}\cos(\theta+\varphi)} \tag{1}$$

When P changes the direction, its value turns negative but Eq. 1 still holds. Slipping will be initiated when the absolute value of the real CoF abs(μ_{real}) falls below abs($\mu_{critical}$).

Table 1. Trial results based on the theoretical analysis

G	1													
P	0.1	0.3	1	0	-1	-0.3	-0.1	0.1	0.3	1	0	-1	-0.3	-0.1
Npt	1			- [(a)]	1						- [(a)]	1		
θ	2°							5°						
φ	0° [(b)]													
$\mu_{critical}$	0.02	0.11	0.46	-0.03	-0.54	-0.18	-0.08	-0.04	0.06	0.40	-0.09	-0.61	-0.24	-0.14

[(a)] $\mu_{critical}$ is irrelevant to the tendon force
[(b)] $\varphi = 0°$ indicates the original position of segments before movement to that shown in Fig. 1(c)

According to the trials listed in Table 1, if the value of μ_{real} falls between 0.04 and 0.14, the sliding segment will gradually return to its original position under excitation of a $\pm 0.1G$ sinusoidal excitation due to the frictional properties resulting from the 5° inclined surfaces. Incidentally, the energy in the post-peak time-history of an earthquake, normally in the form of considerable rounds of gentle cyclic vibrations, will probably be beneficial to the self-centering of the segmental columns with resetting sliding keys.

4. Numerical investigation on the seismic performance of the resettable sliding joint system

A series of parametric combinations as shown in Table 2 were studied to further verify the proposed system. In this preliminary study, linear response is assumed, and the tendon and concrete outside the unbonded zone are assumed to be perfectly bonded. The column geometry was the same as that of Sideris (2012) and the excitation was scaled to a maximum of 0.5g.

Table 2. Cases studied in simplified numerical simulations

No.	Description
1	Partially debonded, plane, μ = 0.1 [(a)] and low prestress
2	Partially debonded, plane, μ = 0.1 and medium prestress
3	Partially debonded, plane, μ = 0.1 and high prestress
4	Partially debonded, plane, μ = 0.7 [(b)] and medium prestress
5	Partially debonded, 2° keys, μ = 0.1 and medium prestress
6	Partially debonded, 5° keys, μ = 0.1 and medium prestress
7	Unbonded, plane, μ = 0.1 and medium prestress

[(a)] μ= 0.1 is the nominal minimal CoF obtained at grease-lubricated polished concrete surfaces in the companion paper
[(b)] μ= 0.7 is the nominal maximum CoF obtained at concrete dry contact surfaces

Fig. 2(a) shows that cases with partially bonded tendons (Cases 1-6) all have lower sliding movements, residual sliding movements and gap openings than the one with unbonded tendons (Case 7). Those with guide keys with gentle slope (Cases 5-6) have large sliding movements and gap openings, while keeping the residual sliding movements extremely low at the expense of a higher base shear. The sliding time histories shown in Fig. 2(b) indicate that the use of partially debonded tendons helps reduce the large amount of residual sliding displacement at the bottom while the use of guide keys further reduces it. Particularly, Case 5 with 2° guide keys tends to re-center itself in a quicker manner comparing to the other three cases.

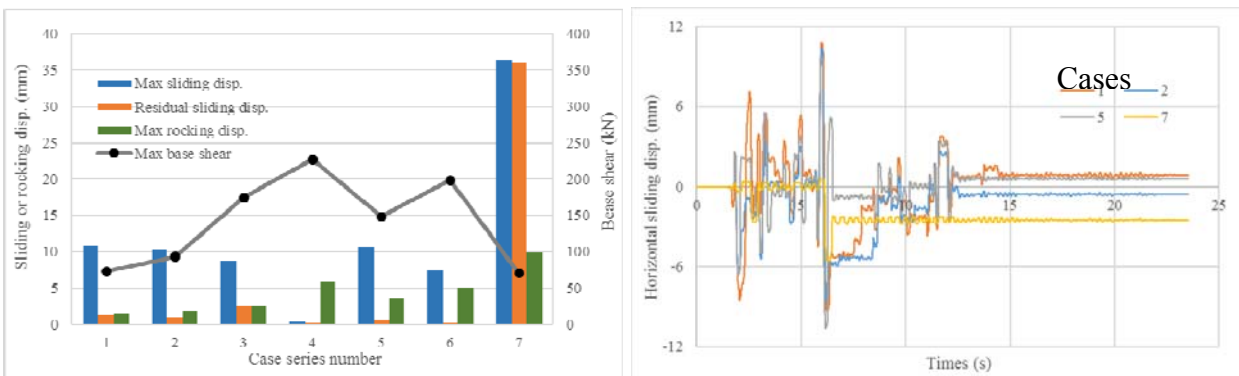

(a) Summary of performance (b) Sliding displacement at bottom joint

Fig. 2. Seismic performance of resettable sliding joint system

It can be inferred from this preliminary study that the arrangement of partially debonded tendon, long-term CoF at concrete interfaces and the geometry of the guide keys are critical parameters in the resettable sliding joints. Further investigation is being carried out to achieve the desirable seismic performance of segmental columns with the proposed resettable sliding joints.

5. Conclusions

Based on theoretical and numerical analyses, the following conclusions can be drawn.

(a) The post-peak self-centering performance of resettable sliding joints was captured and verified to be beneficial to the self-centering behavior of segmental columns.

(b) The adoption of resetting guide key and partially debonded tendon system not only dramatically improved the self-centering ability of the segmental column, but also maintained the seismic isolation feature of the sliding joints in terms of lower maximum base shear.

(c) The low values of initial tendon force and CoF at interfaces facilitated seismic isolation and self-centering performance of the proposed design of segmental columns. Combinations of the initial tendon force and CoF should be as low as possible without compromising their resistance against wind load.

6. References

Kurama, Y.C., Sritharan, S., Fleischman, R.B., Restrepo, J.I., Henry, R.S., Cleland, N.M., Ghosh, S.K. and Bonelli, P. 2018. Seismic-resistant precast concrete structures: state of the art, Journal of Structural Engineering, 144(4), 03118001.

Sideris P. 2012. Seismic Analysis and Design of Precast Concrete Segmental Bridges, PhD Dissertation, Department of Civil, Structural and Environmental Engineering, State University of New York at Buffalo, Buffalo, NY

Effective Use of Lead Rubber Bearing for an Isolated Bridge in Taiwan through Parametric Study

Cho-Yen Yang[1], Chin-Kuo Su[2*], Chia-Ming Chang[3], Chia-Chuan Hsu[4], and Yu-Chi Sung[5]

[1] National Center for Research on Earthquake Engineering, Taipei, Taiwan; email:cyyang@ncree.narl.org.tw
[2] National Center for Research on Earthquake Engineering, Taipei, Taiwan; email: cksu@ncree.narl.org.tw
[3] National Taiwan University, Taipei, Taiwn; email: changcm@ntu.edu.tw
[4] National Center for Research on Earthquake Engineering Taipei, Taiwan; email: chiachuan@ncree.narl.org.tw
[5] National Taipei University of Technology, Taipei, Taiwan; email: sungyc@ntut.edu.tw

[*]: corresponding author

Keywords: isolation, bridge, parametric study, seismic, lead rubber bearing

Abstract: Design of seismically isolated bridges needs a series of considerations to meet various requirements. For example, the space, which accommodates excessive displacements during severe earthquakes, is limited by the sizes or locations of other bridge components, e.g., pier caps, girders, beams, and expansion joints. In Taiwan, isolation bearings are selected from existing product lines of manufactures and rarely customized according to optimized design results. Thus, this culture introduces complicatedness to design an isolated bridge. Therefore, this study carries out a parametric study of an existing isolated bridge in Taiwan and then develops a systematic approach that can guide the design of isolated bridges. First, a simplified two-degrees-of-freedom model, consisting of a pier and rigid-body mass with a connection of a bilinear lead rubber bearing model, is constructed to investigate static and dynamic behavior of a single bridge column element in this bridge. Multiple parameters associated with design criteria and physical limitations are studied to obtain the relationships in terms of seismic performance of this isolated bridge. Then, a design guideline of isolated bridges is established based on the results of the parametric studies. As a result, the redesigned isolated bridge can be more effective than the existing one in regard to the capacity of lead rubber bearings and the overall performance of the bridge.

1. Introduction

Bridges with precast super- and sub-structures are more acceptable and popular in recent years because this sort of bridges can benefit to reduced construction time, lowered environmental impact, improved construction safety, and reduced life-cycle costs. These precast super- and sub-structures, i.e., concrete girders and piers, can be further advantageous to construction automation. To ensure the safety, all these precast components should remain in the elastic range. Thus, isolation bearings provide an option to lower the shear force between the girders and piers in a bridge (Huang et al. 2010). In addition to this feature, the dynamic behavior of these isolation bearings for a bridge is more of interest, i.e., under seismic excitation.

In this study, an existing isolated bridge is reinvestigated to understand the seismic performance as well as to provide some insights that can guide the LRB design of isolated bridges. First, the isolated bridge consists of a continuous girder over multiple spans, and only a critical pier is chosen to construct a simplified model. Then, this model is compared with and validated by a finite element (FE) model established by SAP2000 (CSI 2015). Note that the SAP2000 model represents the entire isolated bridge after construction. The validation process is carried out by comparing seismic responses of both models, and the ground motions used in this process are far-field and obtained from the strong motion stations around this bridge. This validated model is subsequently exploited to evaluate seismic performance of the critical pier and superstructure in terms of the parameters in a LRB. The numerical results show improved seismic performance if appropriate parameters are employed. This investigation also informs the design criteria for a seismically isolated bridge.

2. Layout of isolated bridge and modelling

The bridge selected, as shown in Fig. 1, is 258 m long with an 11-m wide box girder. The bridge deck is continuous over 7 single-column piers and supported by isolation bearings over on the top of pier caps. All piers have an identical cross sections, but the height (H) varies between 8.53 and 8.88 m. The longitudinal and transverse stiffness thus ranges from 46,227 to 50,714 and 52,750 to 59,513 tonf/m, respectively. The total weight of superstructure is approximately 5,247 tf . Two LRBs and a box-type shear key are mounted at the top of each pier. The effective period of the isolated bridge (T_d) is 1.471 sec, while the designed displacement D_d and damping ratio are 0.1445 m and 18.7%, respectively. To numerically examine the seismic performance, a simplified 2DOF model is constructed as shown in Fig. 2 and validated by comparing with a FE model. In this paper, the pier P2 is critical and selected as an example for investigation. In this model, the weight of deck W_d is approximately equal to 1080 tf because the right and left half spans are lumped to form this simplified deck on the pier P2. The weight of the pier P2 W_p is 134.86 tf. The stiffness and inherent damping ratio of pier are 48484 tf/m and 5%, respectively. Moreover, the two LRBs on this pier are identical, and a bilinear model is adopted to portray the force-displacement relationship under seismic excitation (Fig. 3). For each LRB, the designed characteristic strength Q_d and post-yield stiffness K_d are 48 tf and 720 tf/m, respectively. Moreover, the post yielding stiffness ratio is assumed to be 10 in this paper (*i.e.* K_u =10 K_d).

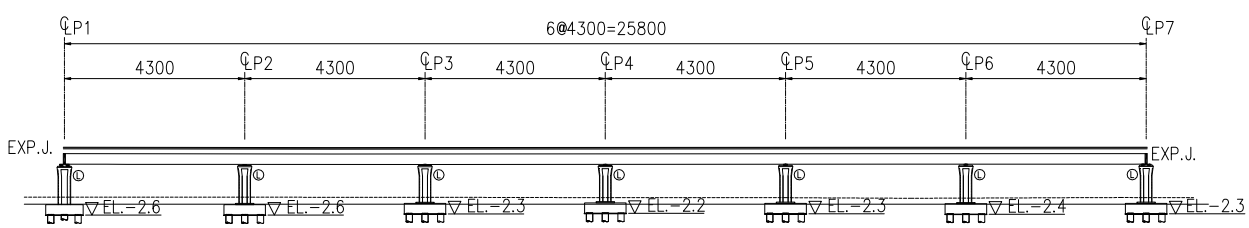

Fig. 1. Longitudinal elevation of the bridge

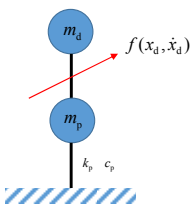

Fig. 2. Simplified 2DOF model

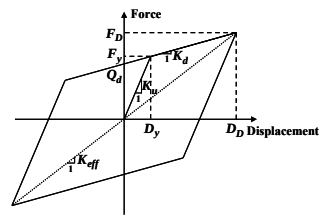

Fig. 3. Bilinear model

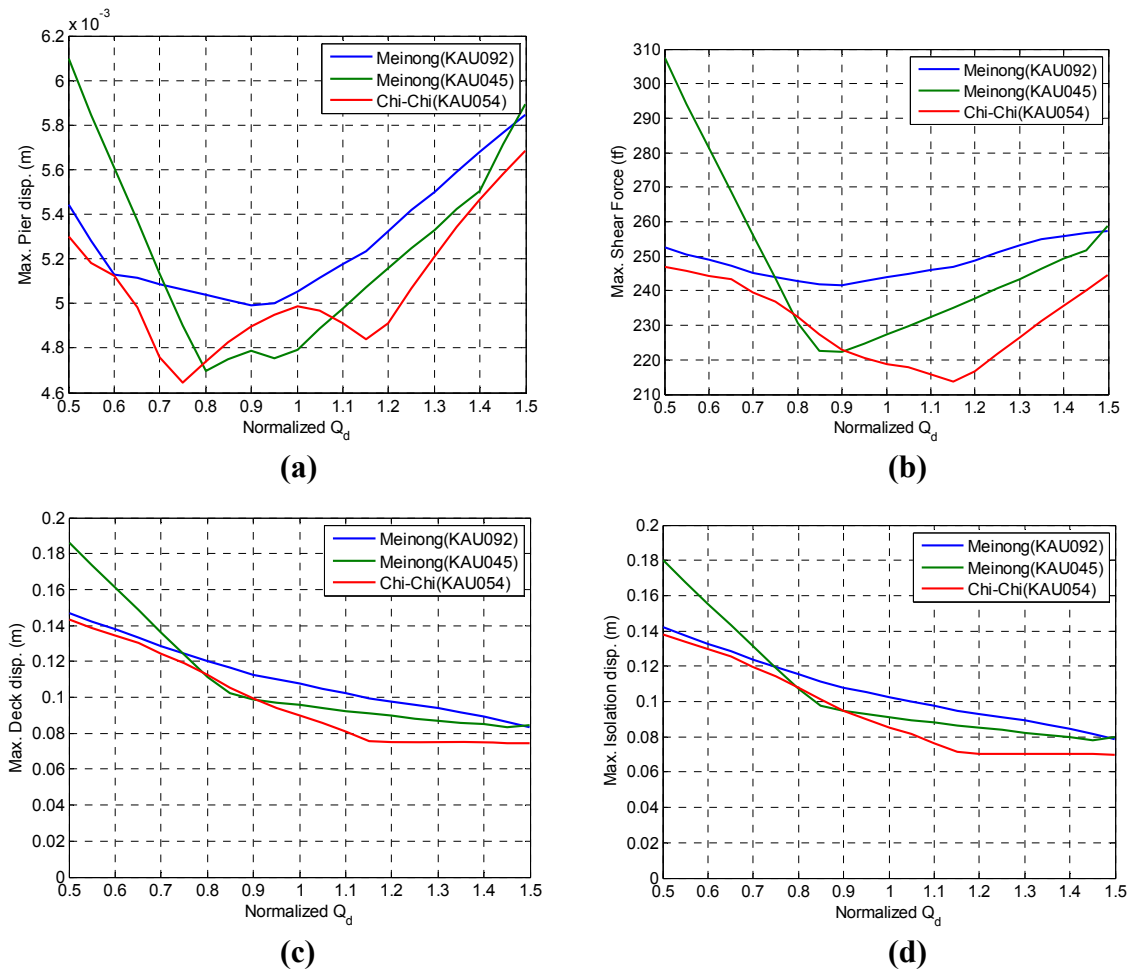

Fig. 4. Sensitivity study of characteristic strength Q_d versus (a) max. pier disp., (b) max. shear force, (c) max. deck disp. and (d) max. isolation disp.

3. Numerical simulation and parametric study

In the numerical simulation, the simplified 2DOF model is compared with the SAP2000 FE model. The ground accelerations used in the simulation are design-spectrum compatible and generated from the stations KAU054 and KAU092 in the 2016 Meinong earthquake event and the station KAU054 in the 1999 Chi-Chi earthquake event. As observed from the results, the pier displacements of the FE model under these excitations are in a range of 0.0053-0.0057 m, and the deviations between two models are -6.99 to -12.00%. Moreover, the maximum deformations of the LRBs from the FE model are 0.0820-0.0920 m, and the differences between two models

are -0.92 to 11.75%. The results also demonstrate small shear forces provided by the LRBs, resulting in a reduced seismic demand of the pier. Also, the maximum isolation forces from the FE model are 207-222 tf, and the differences between two models are 2.26 to 9.57%. The effective LRB stiffness ranges from 2,416 to 2,542 tf/m in the FE model, and the differences between two models are within 5%. As can be found, the differences in pier and deck displacements are relatively larger so as to the maximum LRB deformation and shear force. Still, the overestimated performance leads a conservative design approach, indicating an acceptable simplification of this 2DOF model. In the parametric study, the characteristic strength Q_d is discussed because the capacity of energy dissipation and the trigger of isolation is directly influenced by this strength. Thus, the sensitivity of the characteristic strength is presented as a normalized index by the one in the original design. The ratio of characteristic strength varies from 0.5 to 1.5 with an increment of 0.05, and the elastic stiffness K_u and post-yield stiffness K_d remain the same. The results are demonstrated in Fig. 4. The optimal normalized Q_d values corresponding to the minimum pier displacement are roughly 0.75-0.95. However, the resulting pier displacement is still quite small, and the characteristic strength may be then not sensitive to this index. To investigate the sensitivity of seismic responses, the optimal normalized Q_d values corresponding to the maximum shear force are 0.8-1.15. In this case, the variation of the optimal normalized Q_d is a little bit large, especially in the case of Meinong (KAU045). Therefore, the optimal characteristic strength is close to the design one. In short, the required damping would adjust the characteristic strength accordingly because the sensitivities of the deck displacements and LRB deformations are quite similar. The best design with the smallest deck displacement allows determination of the characteristic strength.

4. Conclusions

In this paper, an existing isolated bridge was investigated to understand the dynamic behavior against earthquakes and to consider redesigning the isolation bearings. A simplified 2DOF model was established and compared with a FE model to validate the prediction of seismic performance. The simulation result of the 2DOF model was slightly different from the FE model; however, the results were conservative for practical applications. The parametric study shows that the characteristic strength indeed influenced the isolation shear force and displacement. Consequently, the design characteristic strength was roughly close to an optimal one, and the isolation displacement can be effectively reduced by increasing the characteristic strength. A trade-off effect between the isolation displacement and isolation shear force was found, meaning that the characteristic strength should be carefully designed.

5. References

AASHTO 2010. Guide Specifications for Seismic Isolation Design, Third Edition, American Association of State Highway and Transportation Officials, 444 North Capitol Street, NW Suite 249, Washington, DC 20001.

Huang, P. H., Chen, H. C., Chen, B. H., Chi, S. R. and Su, C. K. 2010. A Study on the Seismic Isolation System of Bridge in Soft Ground, The Tenth National Conference on Structural Engineering , Tao-Yuan, Taiwan, 1-3 Dec., Paper No. 181(In Chinese).

Computers & Structures Inc. 2015. CSI Analysis Reference Manual For SAP2000, ETABS, SAFE and CSiBridge, Berkeley, California, USA.

Bridge Engineering Institute Conference 2019 (BEI-2019)
Honolulu, Hawaii, USA, July 22-25, 2019

Seismic Reliability Analysis of Energy-Dissipation Bridges with Damper Parameter Uncertainty under Multi-Support Excitation

Shaomin Jia[1], Jin Fan[2*], and M. Ala Saadeghvaziri[3]

[1] Sichuan Agricultural University, Chengdu, China; email: jiashaomin1@163.com
[2] New Jersey Institute of Technology, Newark, New Jersey, USA; email: jf372@njit.edu
[3] New Jersey Institute of Technology, Newark, New Jersey, USA; email: ala@njit.edu

[*]: corresponding author

Keywords: damper; energy-dissipation bridge; Monte Carlo simulation; nonlinear; seismic reliability;

Abstract: Compared to conventional seismic reliability analysis method of structures with uncertainty parameters, this study proposed a new framework of seismic reliability analysis of energy-dissipation bridges with damper parameter uncertainty subjected to stochastic multi-support excitation. The dynamic response of energy-dissipation bridge is a local nonlinear problem because of the hysteresis characteristics of dampers. Regarding its local nonlinearity, an explicit time-domain dimension reduced iteration method was employed to reduce the computing cost in each excitation sample. To further reduce computing cost, an efficient sampling method of rare events, a Hamiltonian Monte Carlo method-based subset simulation algorithm, was employed. Since the stochastics of damper parameter and excitation are independent, the nonlinear stochastic dynamic response analysis of the structure can break into two parts: consideration of damper parameter uncertainty and analysis of determined structure. Damping coefficient was chosen as the uncertain parameter before a specific damper was installed. Twenty-six representative damping coefficients were selected based on Good Lattice Point Set, which is a mathematical method for numerical evaluation of multivariate integrals. Therefore, for each determined damping parameter, dynamic response analysis can be conducted by adopting the explicit time-domain dimension reduced iteration method. Finally, the reliability analyses were conducted both by applying the above framework and conventional seismic reliability analysis method. Maximum longitudinal displacements of the beam of the continuous bridge were taken as the measurements of failure criteria of the structure. Multi-support excitation in the longitudinal direction was taken into consideration. It was found that the proposed framework can significantly reduce the computing cost without reducing the computing accuracy for seismic reliability analysis of energy-dissipation bridges with consideration of damper parameter uncertainty subjected to stochastic multi-support excitation.

1. Introduction

Energy-dissipation bridges are widely used for their improved seismic performance due to the use of seismic protection devices, such as dampers. Structure parameters such as physical and/or geometric parameters are usually not exactly certain. The statistical approaches, e.g. the Monte Carlo simulation method(MCM), and the non-statistical approaches are the two classes of approaches that are used for structures with uncertainties(Li and Chen,2005; Li and Chen, 2006). However, either the computational cost or accuracy has limited them from widely adopted by

engineers, especially for stochastic structures explicit non-linearity under strong ground motions. A new framework aimed at reducing computational cost without sacrificing accuracy was proposed and a numerical example was carried out to verify the efficiency. Multi-support excitations were considered.

2. Methodology

The conventional reliability analysis of a nonlinear stochastic structure , such as MCM method, requires large number of samples that describes the characteristics of both structure randomness and ground motion randomness. The computational cost is relatively high. The proposed framework breakdown the complex process into many parts. Firstly, the characteristics of structure randomness and ground motion randomness are independent from each other. Therefore, a mathematical method called Good Lattice Point Set can be used to describe the stochastic characteristic of the structure. Thirteen groups of representative damping coefficients were selected based on Good Lattice Point Set .And for each selected group, the structure is deterministic, which means the original dynamic reliability problem with damper parameter uncertainty became 13 determined dynamic reliability problems. Secondly, for each of the 13 determined problem, instead of conventional MCM, a Hamiltonian Monte Carlo method-based subset simulation algorithm(HMCM) was employed to generate rare event ground motion samples. HMCM is more efficient in rare event sampling and thus reduced the computational cost. Furthermore, regarding its local nonlinearity of energy-dissipation bridges, an explicit time-domain dimension reduced iteration method (Jia et al, 2019)was employed to further reduce the computing cost in each excitation sample. Multi-support excitations were considered.

3. Numerical Simulation

To verify the efficiency of the proposed framework, MATLAB was used to analyze the energy-dissipation bridge under multi-support excitations. The conventional analysis approach was also conducted using OpenSees and ANSYS.

3.1. Physical and Geometry Parameters of the Bridge

A 3×30m prestressed concrete bridge with continuous constant height girder on a highway is considered in this paper(Fig. 1). The super-imposed dead load is 63 kN/m. Four plate rubber bearings are arranged on each abutment and pier of the bridge, 2 viscous dampers are installed on each abutment. Damping coefficient of vicious damper is 1500 kN/(m/s)$^{0.5}$, shear stiffness of plate rubber bearings in abutments 1 and 4 is 1100 kN/m and in abutments 2 and 3 is 2200 kN/m.

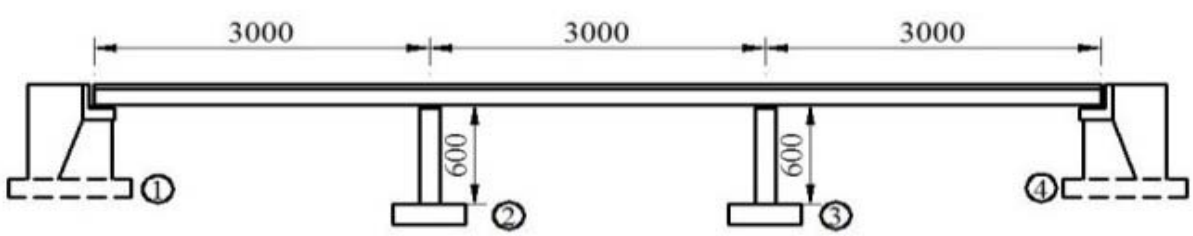

Fig. 1. The bridge layout (unit: cm), pier 1 on soil type 1, pier 3 on soil type 2

3.2. Ground Motion Displacement Power Spectrum and Spatial Correlation

The seismic excitations at different piers are considered as partially correlated. The auto-power spectrum density of the displacement excitation process is given by Clough-Penzien spectrum expressed as (Clough and Penzien,1993):

$$S_{kk}(\omega) = S_0 \frac{\omega_k^4 + 4\zeta_k^2\omega_k^2\omega^2}{(\omega_k^2-\omega^2)^2 + 4\zeta_k^2\omega_k^2\omega^2} \cdot \frac{1}{(\omega_{sk}^2-\omega^2)^2 + 4\zeta_{sk}^2\omega_{sk}^2\omega^2} \tag{1}$$

where S_0 is scale factor, and is set equal to 0.009413 m^2/s^3 (equivalent to seismic fortification intensity of E2 earthquake action level); ω_k, ζ_k are characteristic soil frequency and damping respectively; ω_{sk} and ζ_{sk} are parameters of a second filter. The values of ω_k, ζ_k, ω_{sk} and ζ_{sk} are shown in Table 1, and the auto-power spectrum density functions of the displacement processes for different sites are shown in Fig. 2(a) and one set of ground motion of displacement time history is shown in Fig. 2(b).

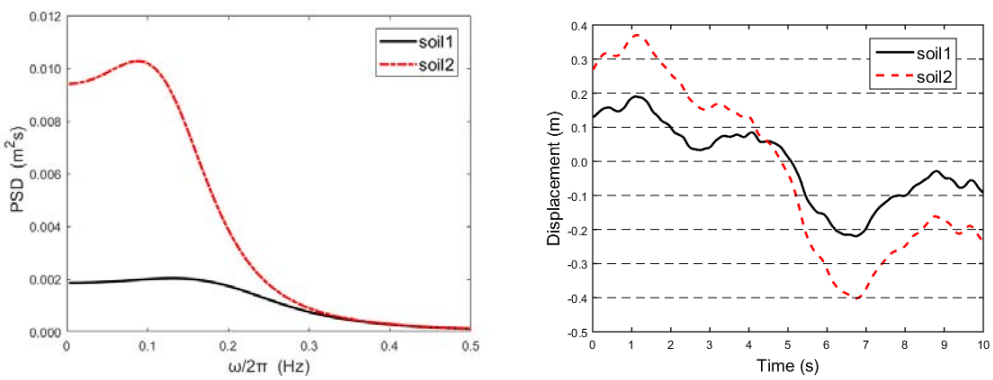

(a) (b)

Fig. 2. (a) Auto-power displacement spectrum; (b) A set of ground motion displacement

Table 1. The parameters of Clough-Penzien spectrum

Soil type	ω_k(rad / s)	ζ_k(rad/s)	ω_{sk}(rad/s)	ζ_{sk}
1 Firm	20.94	0.6	1.5	0.6
2 Medium	10.0	0.4	1.0	0.6

In the simulation of correlated ground motions, the coherent effect between two arbitrary points can be expressed as Eq.2(Luco and Wong 1986), where and $v_s = 600$ m/s .

$$|\rho(\omega,d)| = \exp\left[-\left(\frac{\alpha\omega d}{v_s}\right)^2\right] \tag{2}$$

3.3. Damping coefficients of vicious damper using Good Lattice Point Set

Twenty-six representative damping coefficients were selected based on Good Lattice Point Set (Table 2).

Table 2. representative damping coefficients (unit : kN/(m/s)$^{0.5}$)

θ_{11}	θ_{21}	θ_{31}	θ_{41}	θ_{51}	θ_{61}	θ_{71}	θ_{81}	θ_{91}	$\theta_{10,1}$	$\theta_{11,1}$	$\theta_{12,1}$	$\theta_{13,1}$
1085	1154	1223	1293	1362	1431	1500	1569	1639	1708	1777	1846	1916
θ_{12}	θ_{22}	θ_{32}	θ_{42}	θ_{52}	θ_{62}	θ_{72}	θ_{82}	θ_{92}	$\theta_{10,2}$	$\theta_{11,2}$	$\theta_{12,2}$	$\theta_{13,2}$
1569	1223	1777	1431	1085	1639	1293	1846	1500	1154	1708	1362	1916

4. Numerical Results

Firstly, the validity of explicit time-domain dimension-reduced iteration method was verified by comparing with results obtained from a single run (using a random sample of the stochastic ground motion model) of conventional nonlinear dynamic analysis via Newmark-β algorithm (Wilson 2002). The conventional nonlinear dynamic analysis was conducted on OpenSees and ANSYS. The displacement response histories of beam end of Abutment 1 are shown in Fig. 3(a), and the restoring forces of the damper on Abutment 1 are shown in Fig. 3(b). The failure of the bridge is defined that the displacement of the beam end of the Abutment 1 exceeds $b = 0.26\,\mathrm{m}$. The failure probabilities of each simulation and the total computing time are shown in Table 3. Note that the time for build the models were not considered here.

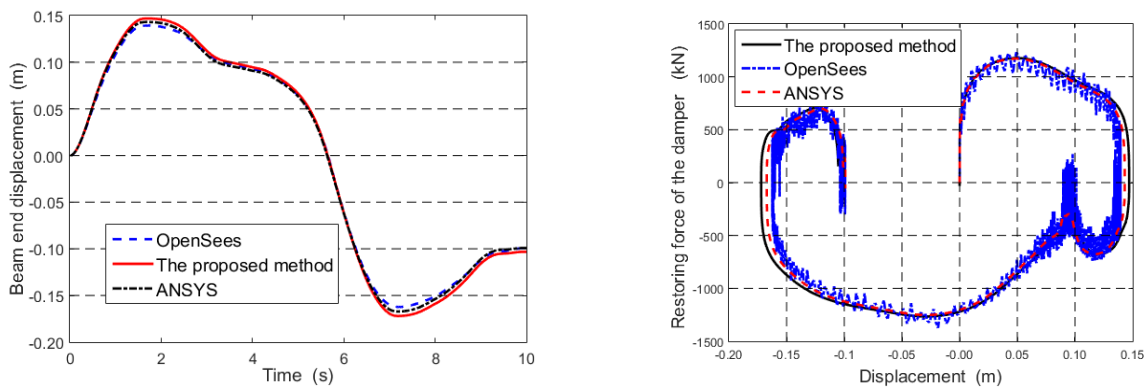

(a) (b)

Fig. 3. (a) Beam end displacements histories of Abutment 1; (b) Restoring forces of the damper of Abutment 1.

Table 3. Failure probability results and calculation times

Computational methods	Sample numbers	Failure probability	Computing time (s)
Traditional stochastic simulation (OpenSees)	30,000	0.0036	120,000
Traditional stochastic simulation (ANSYS)	30,000	0.0036	9,300,000
The proposed method	36,400(13×2800)	0.0038	36,530

5. Conclusion

As shown in Fig.3, the proposed framework has high calculation accuracy compared to conventional methods. The computing time is significantly reduced using the proposed framework. Combining the advantages of explicit time-domain dimension-reduced iteration scheme and the subset simulation approach based on Hamiltonian Monte Carlo method, the proposed framework provides an efficient and reliable way for solving the nonlinear seismic reliability problem of the energy-dissipation bridge structures with viscous dampers (damper parameters were uncertain) subjected to multi-support excitations.

6. References

Clough R.W.& Penzien, J,1993, *Dynamics of structures (2nd ed.*), McGraw Hill, NY, USA.

Jia, S.M, Wang, Z.Q, Fan J., and Ma, H.T,2019.'An efficient monte carlo simulation method for reliability analysis of energy-dissipation bridge structures under multi-support excitations', Unpublished work.

Li, J. and Chen, J. B.,2005.'Dynamic response and reliability analysis of structures with uncertain parameters', *International Journal for Numerical Methods in Engineering*, 62(2), 289–315.

Li, J. and Chen, J. B. ,2006.'The probability density evolution method for dynamic response analysis of non-linear stochastic structures', *International Journal for Numerical Methods in Engineering*, 65(6), 882–903.

Luco, J. E., and Wong, H. L. ,1986. 'Response of a rigid foundation to a spatially random ground motion', *Earthquake Eng. &Struct. Dyn*., 14(6), 891–908.

Wilson E.L., 2002, *Three-Dimensional Static and Dynamics Analysis of Structures*, Computers and Structures, Inc., Berkeley, CA, USA.

Development Length of Reinforcing Bar under Impact Load

Hyeon-Jong Hwang[1*] and Li Zang[2]

[1] Hunan Univ., Changsha, China; email: hwanggun85@naver.com
[2] Hunan Univ., Changsha, China; email: 984782160@qq.com

[*]: corresponding author

Keywords: impact loading; drop hammer test; development length; RC beam; strain rate effect

Abstract: Current design codes specify the development length of a reinforcing bar on the basis of static test results. In the present study, the development length of a reinforcing bar under impact loading was evaluated. Drop hammer test was performed in RC beam specimens to evaluate the effect of impact loading on the bar development length. The test parameters were the drop height of a hammer, hammer mass, rebar diameter, bar development length, and anchorage types. The test results showed that although the bar development length was shorter than the requirement under static loading, longitudinal bars of the beam specimens were yielded under impact loading.

1. Introduction

Recently, structural failures under collision have been a large concern in the design procedures of RC structures. Under impact loading, stress wave induces the local response at the loading point, which generates large inelastic behavior and vibration. The overall response depends predominantly on the loading rate and dynamic behavior of the structural member (Kazunori et al. 2009; Li et al. 2016). The effect of high strain rate on the material properties has been studied on the basis of a large number of dynamic test data of reinforcing bars and concrete (Soroushian and Choi, 1987; Bischoff and Perry, 1991; Ross et al. 1995; Malvar, 1998). Although the strain rate effect on the strength increment of reinforcing bars and concrete was studied, the bond strength between rebar and concrete under impact loading has not been well known. In the present study, drop hammer impact test was performed on RC beam specimens to evaluate the bar bond strength under impact loading. The effects of drop height, hammer mass, bar diameter, and bar development length on the impact responses of RC beam specimens were investigated.

2. Drop hammer test

Fig. 1 shows the RC beam specimens in detail and drop hammer test setup. The beam width was 250 mm, height was 300 mm, and span was 2000 mm. The beam specimens were divided into four groups according to the following two test parameters: longitudinal bar diameter (D18 bar and D25 bar), and bar development length (300 mm and 400 mm). D18 bar (diameter= 18 mm and yield strength= 497 MPa) and D25 bar (diameter= 25 mm and yield strength= 469 MPa) were used for longitudinal bars, and D8 bar (diameter= 8 mm and yield strength= 693 MPa) was used for stirrups. A flat-shaped hammer head with a radius of 100 mm was used. The hammer was dropped at four different elevations for the four groups of specimens. A mass of 272.3 kg was dropped at heights of 3, 6, and 12 m. On the other hand, the 597.3 kg mass was dropped at a

height of 5.47 m, which generated the same impact energy of the mass of 272.3 kg dropped at a height of 12 m.

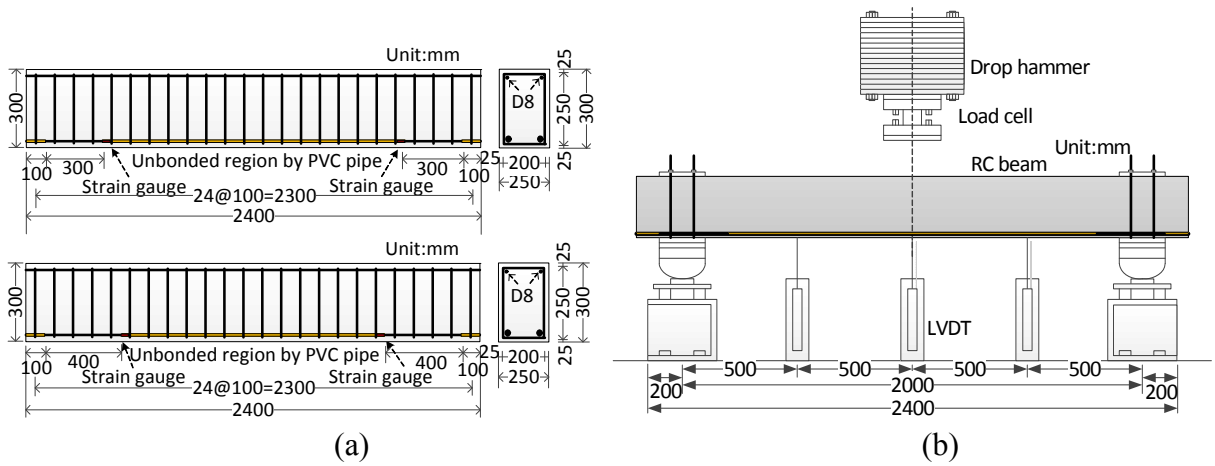

(a) (b)

Fig. 1. Test program [unit: mm]: (a) specimen details; (b) test setup

3. Test results

Fig. 2 shows the failure modes of beam specimens at the end of the test. In the case of the drop height of 3 m, flexural cracks and concrete crushing of the beam top face occurred at the mid-span. As the impact energy increased, diagonal cracks were concentrated on the impact point. Under 12 m drop height, significant local failure occurred at the top and bottom of the beam specimens. Although the same impact energy (5.47 m and 12 m drop heights) caused similar local failure in two group specimens, the beam specimens at the drop height of 5.47 m exhibited more significant damage. Further, in the specimens with D25 bar at larger impact loading (drop height of 12 m and 5.47 m), horizontal cracks occurred along the longitudinal bars due to bond-slip (i.e. bond failure). The beam specimens using D18 bar exhibited flexural failure, while obvious local failure occurred near the impact point in the specimens using D25 bar. Larger rebar ratio of D25 bar increased the compression zone depth of a beam section, which caused early concrete crushing at the top face of the beam. As a result, more significant concrete crushing failure occurred in the specimens using D25 bar.

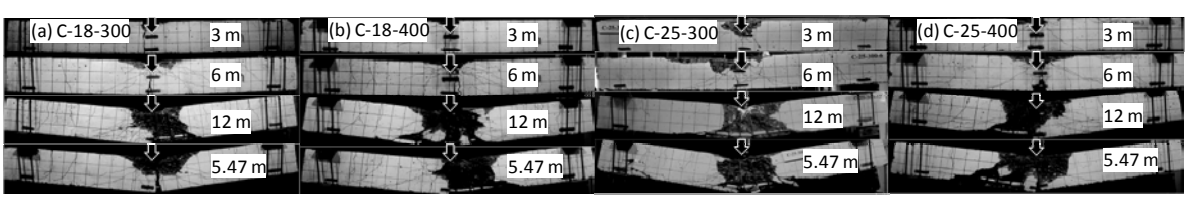

Fig. 2. Failure modes at the end of the test

Fig. 3 shows the strain variation of longitudinal bars according to time. In general, the specimens with the bar development length of 400 mm showed larger strain than that of specimens with the bar development length of 300 mm. Specimens with D18 bar showed almost the same peak

strain of the longitudinal bars regardless of the drop height. The peak strain and residual strain were greater than the dynamic yield strain of D18 bar. This result indicates that the longitudinal bars can be yielded under impact loading even though the bar development length is shorter than the requirement under static loading. However, the specimens with D25 bar showed large discrepancy in the peak strain of the longitudinal bars even though the peak strain was greater than the dynamic yield strain of D25 bar.

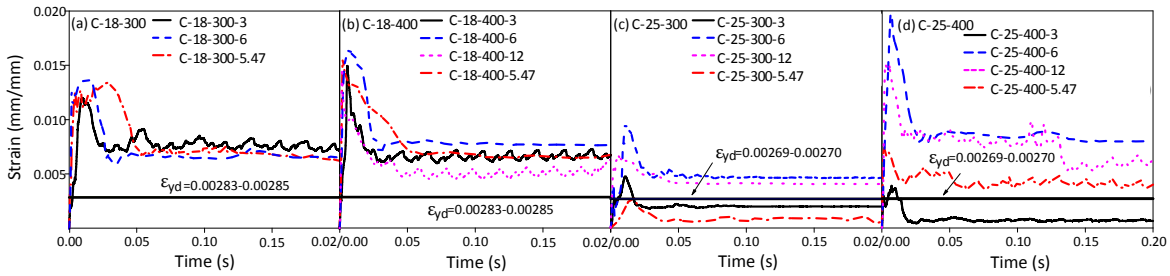

Fig. 3. Longitudinal bar strain according to impact energy

4. Conclusions

In the present study, impact loading test was performed to investigate the effect of strain rate on the bond strength between reinforcing bars and concrete. RC beam specimens using D18 and D25 bars with bar development lengths of 300 mm and 400 mm were tested under four drop heights. The bond strength between reinforcing bars and concrete is increased by strain rate effect under impact loading. As a result, although the bar development length was shorter than the requirement for static loading, the reinforcing bars of test specimens under impact loading were yielded. However, compared to the specimens using D18 bar, the specimens using D25 bar exhibited lower rebar strain, and then bond failure behavior occurred.

5. References

Bischoff P.H., Perry S.H. 1991. Compressive behaviour of concrete at high strain rates. Materials and Structures, 24(6), 425-450.

Kazunori F., Bing L., and Sam S. 2009. Impact Response of Reinforced Concrete Beam and Its Analytical Evaluation. Journal of Structural Engineering, ASCE, 135(8), 938-950.

Li, J., Wu, C., Hao, H., Su, Y., and Liu, Z. 2016. Blast Resistance of Concrete Slab Reinforced with High Performance Fibre Material, J. Struct. Integ. Maint., 1(2), 51-59
.

Malvar L.J. 1998. Review of static and dynamic properties of steel reinforcing bars. ACI Materials Journal, 95(5), 609-614.

Ross C.A., Tedesco J.W., Kuennen S.T. 1995. Effects of strain rate on concrete strength. ACI Materials Journal, 92(1), 37-47.

Soroushian P., Choi K.B. 1987. Steel mechanical properties at different strain rates. Journal of Structural Engineering, ASCE, 113(4), 663-67

Investigation of Pounding Effect for a Seismically Isolated Bridge Based on a Simplified Model

Chin-Kuo Su[1], Chia-Ming Chang[2*], Cho-Yen Yang[3], and Chia-Chuan Hsu[4]

[1] National Center for Research on Earthquake Engineering, Taipei, Taiwan; email: cksu@ncree.narl.org.tw
[2] National Taiwan University and National Center for Research on Earthquake Engineering, Taipei, Taiwan; email: changcm@ntu.edu.tw
[3] National Center for Research on Earthquake Engineering, Taipei, Taiwan; email: cyyang@ncree.narl.org.tw
[4] National Center for Research on Earthquake Engineering, Taipei, Taiwan; email: chiachuan@ncree.narl.org.tw

*: corresponding author

Keywords: isolation; bridge; parametric study; seismic; lead rubber bearing

Abstract: Bridges with seismic isolation can reduce seismic loading transition to the bridge deck due to the flexibility and hysteresis. The relatively low horizontal stiffness of isolation bearings intrinsically lowers shear forces on piers. However, large displacements are expected to occur at the isolation layers during strong earthquakes and may introduce another safety issue to the isolated bridge. To avoid the excessive displacements, durable shear keys are equipped with limited allowable movements for isolation bearings. These shear keys can be hit in extreme earthquake events and then protect the superstructure from failure. Therefore, the objective of this study is to numerically investigate the pounding effect from the superstructure to shear keys in an isolated bridge. First, a simplified model, consisting of a bridge pier and an isolated rigid mass, is developed in the form of a two-degrees-of-freedom system. The seismic isolation considered is lead rubber bearings which are modeled by a bilinear hysteretic force with respect to displacement. The pounding effect employs the conservation of momentum with an appropriate coefficient of restitution. Post contact stiffness is also considered after contact occurs. Several parameters such as the allowable isolation displacements, restitution coefficient, and shear key flexibility are explored in this study. To characterize the pounding effect, time-domain analysis is carried out. As seen in the results, the pounding between the superstructure and shear keys may induce instantaneously high shear forces to both pier and superstructure. The impulsive loading is capable of dissipating energy and lower the responses for an isolated bridge.

1. Introduction

Seismic isolation is a widely acceptable and promising control strategy for bridges because isolation bearings can limit the transmission of horizontal acceleration from the superstructure to the substructure. Most of bridges have a fundamental natural frequency in the range of 0.8-5 Hz. This range aligns with the dominant frequencies of earthquakes and can induce significant responses of bridge structures (Kunde and Jangid 2003). Isolation bearings are installed between the superstructure and substructure, e.g., between the bridge deck and piers, and the fundamental natural frequency of an isolated bridge is shifted away from the dominant frequencies of

earthquakes. Thus, seismic responses of isolated bridges can be effectively reduced. However, excessive displacements can be found in the soft layer of isolation bearings during extremely large earthquake events. Therefore, shear keys in an isolated bridge plays an important role to limit isolation displacements. To understand the effectiveness of these shear keys, the pounding effect (Li *et al.* 2012) should be studied when the isolation bearings contact shear keys.

In this study, the pounding effect of an isolated bridge is investigated. The isolated bridge is first simplified into a single degree-of-freedom (SDOF) pier which supports a rigid-mass deck sitting on a lead-rubber bearing (LRB). The LRB follows the bilinear hysteretic behavior between the displacements and forces. Then, a parametric study is carried out to study the pounding effect in terms of allowable isolation displacements, post contact stiffness, coefficients of restitution, and earthquake intensity. Moreover, the impact model is formed by a spring with the restitution coefficient model, which calculates the relative velocities after impact. The results of this study provide the preliminary investigation of the pounding effect to an isolated bridge.

2. Problem formulation

A bridge shown in Fig. 1 is selected to study the pounding effect of an isolated bridge. This bridge is 258 m long over 7 single-column piers. Two identical isolation bearings are placed on the top of each pier cap. The height of bridge columns varies from 8.53 m to 8.88 m, resulting in 46,227 to 50,714 tf/m longitudinal stiffness and 52,750 to 59,513 tf/m transverse stiffness. The total weight of superstructure is approximately 5,247 tf. The isolation bearings are lead rubber bearings of which each has the properties in terms of bilinear hysteresis, as shown in Fig. 2 and listed in Table 1. To simplify this investigation, only the pier P2 (see Fig. 1) is evaluated in this study. The effective deck mass is 1,080 ton, and the pier mass is 135 ton. The pier stiffness is 48,484 tf/m, and the inherent damping is 5%. In this study, a 2DOF model of the pier P2 is considered to investigate the pounding effect of an isolated bridge, as shown in Fig. 3.

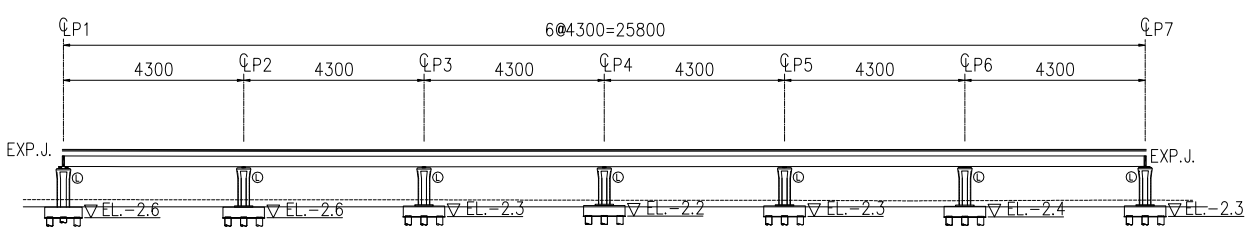

Fig. 1. Longitudinal elevation of the bridge

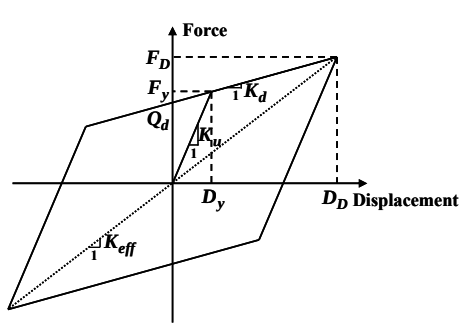

Fig. 2. Bilinear hysteretic model

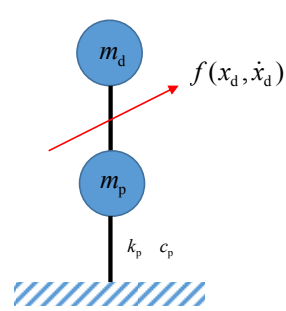

Fig. 3. Isolated bridge model

Table 1. Properties of lead rubber bearings.

Variable	Value
Q_d	96 tf
K_d	1,440 tf/m
D_D	0.1445 m
T_d	1.471 sec
K_{eff}	2,104 tf/m
ξ_{eff}	0.187
K_u	14,400 tf/m

The nonlinear element in this isolated bridge model is the LRB with the pounding effect. This nonlinear force can be written by

$$F_{\text{nonlinear}} = F_{\text{iso}} + F_{\text{pound}} \tag{10}$$

where

$$F_{\text{pound}} = \begin{cases} 0 & , \text{ if } D^{rel} < D^{rel}_{\text{allow}} \\ K_{post} D^{rel} & , \text{ if } D^{rel} \geq D^{rel}_{\text{allow}} \end{cases} \tag{11}$$

and

$$r = \frac{V^{rel}_{after}}{V^{rel}_{before}} \tag{12}$$

$$M_d V^{abs}_{\text{d},before} + M_p V^{abs}_{\text{p},before} = M_d V^{abs}_{\text{d},after} + M_p V^{abs}_{\text{p},after} \tag{13}$$

$F_{\text{nonlinear}}$ is the total nonlinear force; F_{iso} is the shear force provided by the LRB and calculated by the rules in Fig. 3; F_{pound} is the pounding force during impact; K_{post} is the post contact stiffness; D^{rel} is the relative displacement between the deck and pier; D^{rel}_{allow} is the allowable isolation displacement; r is the coefficient of restitution; V^{rel}_{before} and V^{rel}_{after} are the relative velocities between the deck and pier before and after contact, respectively; M_d and M_p are the deck mass and pier mass; $V^{abs}_{\text{d},before}$ and $V^{abs}_{\text{p},before}$ are the absolute velocities of the deck and pier before contact, while $V^{abs}_{\text{d},after}$ and $V^{abs}_{\text{p},after}$ are the absolute velocities of the deck and pier after contact. To explore the nonlinearity of the pounding effect, the post contact stiffness, allowable isolation displacement, and coefficient of restitution are studied in this research.

3. Numerical results

Seismic performance of the isolated bridge is investigated under excitation of the 2016 Meinong earthquake event. The records used in this study are those obtained from the stations KAU006, KAU045, KAU055, KAU092, and KAU100. All recorded ground accelerations are modified to be design spectrum compatible, and different intensities in terms of peak ground acceleration (PGA) are used in the investigation. The PGAs considered in this study is 1.0, 1.5, 2, 2.5, and 3 times of the designed PGA (= 0.24g) for this bridge. Note that only the results obtained from the KAU100 record are presented in this paper. The first variable to be studied is the effect of

allowable isolation displacements, as shown in Fig. 4. The allowable isolation displacements selected include 0.10, 0.15, and 0.20 m. The soft, moderate, and hard impact means the post contact stiffness with values of 10, 100, and 1000 times of the isolation pre-yield stiffness. The coefficient of restitution ranges from 0.2 to 0.8. Note that r = 1 indicates the completely elastic impact, while r = 0 indicates the completely plastic impact. As seen in the results, a small allowable isolation displacement yields worse performance in the moderate earthquakes (i.e., PGA = 0.48 and 0.60 g), but similar performance among different allowable displacements can be found in the severe earthquake (i.e., PGA = 0.72g). For the effect of post contact stiffness, the difference in the pier top displacements is minor among all cases. As for the effect of restitution coefficients, the almost plastic impact (i.e., r = 0.2) results in better performance, especially for the case with the hard impact. To sum up, the investigation concludes that the large post contact stiffness with the almost plastic impact introduces a better pounding effect for this isolated bridge.

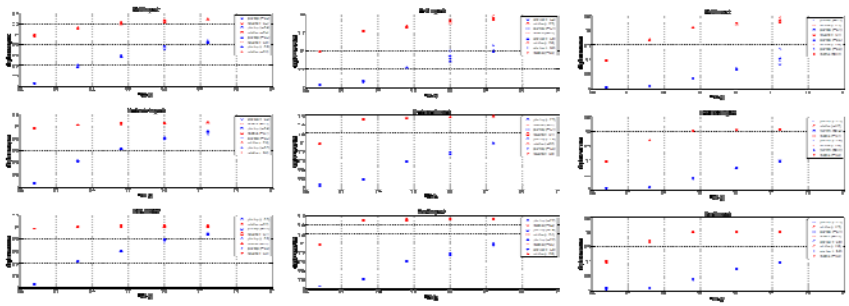

(a) (b) (c)

Fig. 4. Isolation displacements and pier top displacements against different level of earthquakes where the allowable isolation displacement is a) 0.10 m, b) 0.15 m, and c) 0.20 m.

4. Conclusions

In this study, the pounding effect in an isolated bridge was investigated, and several parameters such as the allowable isolation displacements, post contact stiffness, and coefficients of restitution were considered. An existing isolated bridge was selected to be explored in this study, while this bridge was simplified to 2DOF model with nonlinearity at the isolation layer. The bilinear hysteretic model was employed for the lead rubber bearings, and the pounding force was generated from the post contact stiffness and instant momentum changes. As seen in seismic responses of this simplified model, large post contact stiffness with a small restitution coefficient yielded better performance. Meanwhile, a small allowable isolation displacement can worsen performance in the moderate earthquakes. The pounding force was more effective when the earthquake intensity is large.

5. References

Kunde, M.C. and Jangid, R.S., 2003. Seismic behavior of isolated bridges: A-state-of-the-art review. Electronic Journal of Structural Engineering, 3(2), pp.140-169.

Li, B., Bi, K., Chouw, N., Butterworth, J.W. and Hao, H., 2012. Experimental investigation of spatially varying effect of ground motions on bridge pounding. Earthquake Engineering & Structural Dynamics, 41(14), pp.1959-1976.

Bridge Engineering Institute Conference 2019 (BEI-2019)
Honolulu, Hawaii, USA, July 22-25, 2019

Seismic Risk in Idaho and Understanding the Consequences of a Future Large Earthquake on Idaho's Bridges

Mustafa Mashal[1*] and Ali Shokrgozar[2]

[1] Idaho State University, Pocatello, United States; email: mashmust@isu.edu
[2] Idaho State University, Pocatello, United States; email: shokali@isu.edu

[*]: corresponding author

Keywords: earthquakes; sulphur peak earthquake sequence; Idaho bridges; seismic retrofitting

Abstract: Idaho is located in a moderate-to-high seismic region. The Mw 5.3 Sulphur Peak earthquake occurred on September 2 2017. The epicenter of the earthquake was located in the east of Soda Springs in the southeast corner of Idaho. The earthquake caused moderate shaking in southeastern Idaho, northern Utah, and western Wyoming. There were no reports of damage or death following the main shock. An active sequence of smaller aftershocks followed the main shock. This has been uncommon for an earthquake magnitude of this scale. Following the main shock, the United States Geological Surveying (USGS) had a scenario where an earthquake of Mw 7.0 could occur in the region. The area in southeast Idaho has a complex geology, and most of the faults have not been investigated in detail. It is still not known which fault caused the Mw 5.3 Sulphur Peak earthquake. Preliminary indication from USGS suggests that the Mw5.3 earthquake could have been caused by rupture of several different faults with both normal and strike slip mechanisms. Following the earthquake, researchers from USGS and scientists from the University of Utah installed temporary seismic stations to collect data about the earthquake swarm, and understand the active faults characteristics in the region. The research in this paper presents available information on Sulphur Peak earthquake in Idaho. It uses ground motion records from the Sulphur Peak earthquake sequence to build the design spectra in accordance with ASCE 7-16. Findings from spectral analysis and implications from earthquake engineering point of view are discussed. This paper aims to be a step towards understanding the earthquake risk in southeast Idaho and seismic vulnerability of existing bridges. The region has an increasing population, and there is lack of knowledge in understanding the seismic risk of the area and consequences of a future larger earthquake on bridges. Many bridges in Idaho have reached their service life. The effects of large earthquakes on Idaho's civil infrastructure have to be investigated. Retrofitting and replacement of earthquake-prone bridges are vital for the resiliency of communities in Idaho

1. Introduction

Idaho has a complex geology. The presence of active and unknown faults in this part of the country is common. Past strong earthquakes in Idaho include the 1959 Yellowstone earthquake and the 1983 Mount Borah earthquake. These were some of the most severe earthquakes ever recorded in North America. The Sulphur Peak earthquake occurred on September 2 2017 near Soda Springs in Idaho. The moment magnitude of the earthquake was 5.3. Several aftershocks in the order of 4.5-4.9 followed the main shock. The aftershock sequence has continued since then which has been uncommon for an earthquake of 5.3 magnitude. The main shock was felt across a

large area in the region. It did not cause any injuries or damage. Two instruments, one in Pocatello, Idaho, and one in Salt Lake City, Utah, captured the main shock. However, due to distance from the epicenter, the ground motion records showed small accelerations and valuable data were lost. Temporary stations were installed around Soda Springs area in the days after the earthquake. Some of these stations recorded the aftershocks. Figure 1 presents the elastic response spectra from two recorded aftershocks in Soda Springs. For a comparison, the ASCE 7-16 spectra for the same location has also been plotted. It can be noticed that the aftershocks had higher values of spectral acceleration compared to the code. Given the short duration of the aftershocks, they did not cause any damage. The region has the potential for a moment magnitude 7.0 or larger earthquake in the future. This makes southeast Idaho as the most seismically active region in the State. Sulphur Peak earthquake sequence should be considered a wakeup call for assessing the vulnerability of civil infrastructure, especially bridges, in Idaho.

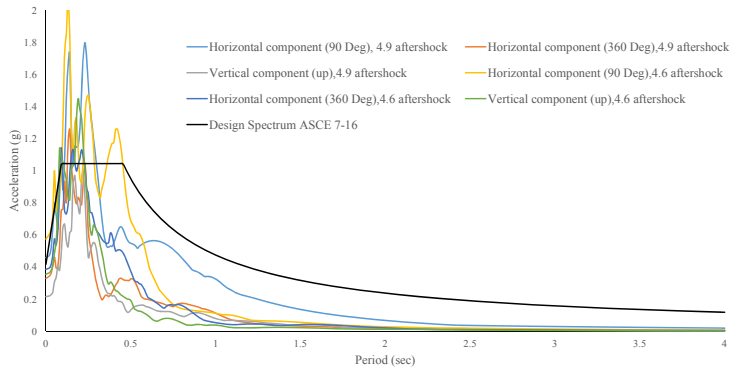

Fig 1. Comparison of 5% damped response spectra for Sulphur Peak earthquake sequence

2. Bridges in Idaho

Reinforced concrete substructure systems are dominant in construction of bridges in Idaho. Most of the bridges in Idaho were designed and constructed in the 1950-1970s. At the time, there were not robust requirements for seismic detailing of the bridges. This was due to lack of knowledge and relaxed building codes. Past earthquakes have shown vulnerability of existing bridges that were not sufficiently detailed to resist earthquake forces (Buckle, 1994) (Palermo et al., 2012). The population of Idaho has been growing fast. Bridges are vital arteries which have to remain functional following an earthquake. The 2017 American Society of Civil Engineers (ASCE) Infrastructure Report Card was "C+" for bridges throughout the country. This was "D" for Idaho's bridges. There are 4,492 bridges in Idaho. 9.1% (411) of the 4,492 bridges in Idaho, are "structurally deficient". This means the condition of these bridges include significant defects. Speed or weight limits have to be enforced to ensure safety and prevent collapse of the structure. Almost half of the bridges (1,848) in Idaho are located on the state highway system; 2,375 are local bridges. The remaining 269 bridges are maintained by federal agencies. Most of these bridges were constructed during the twentieth century for a lifespan of 50-years. 837 bridges on the state highway system (45%) are 50 years or older. The current plan for bridge replacement indicates that in three years' time, the number of bridges that would be 50 years and older will rise to 911; almost 50% of the bridges on the state highway system will be 50 years and older in three years' time. Aging of Idaho bridges is of concern and requires significant investment. To

provide some numbers, there are 1,520 bridges in Idaho that require repairs. The repairs for these bridges is estimated to cost $2.2 billion. Table 1 presents a summary of the top most travelled structurally deficient bridges in Idaho. In addition, Idaho has a harsh climate in the months of winter and corrosion due to chloride/moisture ingress is a major cause for bridge decay, maintenance, and increasing life-cycle cost. The corrosion combined with lack of seismic detailing (Figure 2) make the bridge stock in Idaho more vulnerable to earthquakes. Lack of confinement steel (shear failure) in the potential plastic hinge zones is one of the main concerns for seismic performance of existing reinforced concrete bridges. This is common in many bridges around Idaho. During an earthquake, the longitudinal rebars in the plastic hinge can buckle outward due to lack of confinement bars. This would compromise displacement ductility and the integrity of the plastic hinge. Shear failure followed by compression failure could occur in such circumstances.

Fig. 2. Corrosion and lack of seismic detailing in a typical bridge in Pocatello, Idaho

Table 1. Top Most Traveled Structurally Deficient Bridges in Idaho (ARTBA 2019)

County	Year Built	Daily Crossing	Type of bridge	Location
Bonneville	1957	23,000	Urban minor arterial	SMA 7406, 17th St.
Canyon	1969	19,000	Urban minor arterial	SMA 8353, 16th Ave.
Madison	1971	16,000	Urban other principal arterial	SH 33 over S.FK Teton river
Bannock	1962	15,000	Urban Interstate	I 15 over I 86
Bingham	1965	14,000	Urban other principal arterial	US 26 over snake river, Blackfoot
Bannock	1967	13,000	Urban other principal arterial	STP 7151, Benton St
Canyon	1956	13,000	Urban other principal arterial	STP 7773, 10th Ave.
Ada	1963	11,500	Rural Interstate	I84 over Kuna

3. References

ASCE Infrastructure Report Card (2017). Available at: https://www.infrastructurereportcard.org/.
American Road and Transportation Builders Association (ARTBA) (2017) National Bridge Inventory: Idaho. Available at: https://www.artbabridgereport.org/state-profile/ID.html#inventory.

ASCE 7-16 (2017) ASCE/SEI 7-16 Minimum design loads for buildings and other structures, ASCE standard. doi: 10.1061/9780784412916.

Buckle, I. (1994) The Northridge, California earthquake on january 17, 1994: Performance of highway bridges, Nceer-94-0008.

Palermo, A. et al. (2012) 'Seismic performance of concrete bridges during Canterbury earthquakes', Structural Concrete. doi: 10.1002/suco.201100041.

Seismic Performance of Precast Segmental Bridge Columns with Resettable Sliding Joints: Friction at Interface

Y.Q. Liu[1*], Y. Yuan[2], Francis T.K. Au[3], Ray K.L. Su[4], and Nelson T.K. Lam[5]

[1] Department of Civil Engineering, The University of Hong Kong, Hong Kong, China; email: selbyliu@hku.hk
[2] Department of Civil Engineering, The University of Hong Kong, Hong Kong, China; email: fredyhku@connect.hku.hk
[3] Department of Civil Engineering, The University of Hong Kong, Hong Kong, China; email: francis.au@hku.hk
[4] Department of Civil Engineering, The University of Hong Kong, Hong Kong, China; email: klsu@hku.hk
[5] Department of Infrastructure Engineering, The University of Melbourne, Australia; email: ntkl@unimelb.edu.au

[*]: corresponding author

Keywords: Coefficient of friction; concrete bridges; precast segments; seismic resistance; wind resistance

Abstract: In an attempt to promote the use of precast segmental bridge columns in regions of moderate to high seismicity, sliding planar joints have been adopted to relieve the adverse effects of seismic action. However, despite the ability to survive, the sliding segments often result in noticeable residual relative movements after an earthquake, which require costly repairs. With the increasing occurrence of super typhoons, the ability of bridges to resist extreme wind loads is also a concern. It is desirable to improve and provide the system of sliding segments the self-centering capability and sufficient lateral resistance without unduly high prestressing forces. Similar to the isolation mechanism provided in most of the mechanical sliding bearings, lateral relative sliding displacement is permitted at the sliding joints by dry contact between adjacent segments. To ensure sufficient capability of seismic isolation and to avoid excessive magnitudes of co-existing rocking displacements, it is desirable to keep the coefficient of friction at the segment-to-segment interfaces reasonably low. The challenge is to control the coefficient of friction at the interfaces within a suitable range. The resetting guide keys can be so designed to provide sufficient resistance to wind and other actions. This paper reports some initial experimental investigations on possible ways to achieve a reasonably low coefficient of friction, including (a) lubrication using powder, (b) lubrication using grease, (c) chemical polishing treatment, and (d) combinations of the above. By varying the coefficient of friction within the practical range, the seismic performance of precast segmental bridge columns with resettable sliding joints is studied numerically to identify possible directions for further improvement.

1. Introduction

The success in segmental column construction in the low-seismicity regions has prompted research in the design of seismic-resistant segmental columns, which depends on the non-emulative joints that are basically dry connections between segments allowing separation. The

gap opening between segments, carefully controlled by specially designed tendon systems, has been utilized to incorporate rocking behavior into the segmental columns so that a higher drift ratio can be achieved. Apart from gap opening, relative sliding has been wisely combined so that a type of segmental column with hybrid rocking-sliding joint has been proposed and verified (Sideris, 2012). However, despite the ability to survive, the sliding segments often result in noticeable residual relative movements after an earthquake, which require costly repairs. To ensure sufficient capability of seismic isolation and to avoid excessive magnitudes of co-existing rocking displacements, it is desirable to keep the coefficient of friction (CoF) at the segment-to-segment interfaces reasonably low. The frictional behavior of contact with concrete is a common topic in the field of pavement research, but the main objective there is to provide high-friction concrete surfaces to enhance their skid resistance to the vehicle tires. Linseed oil was applied to modify low-friction concrete-to-concrete surfaces in the semi-interlocking masonry structures (Hossain et al., 2016), while silicone material was applied at the concrete interfaces to temporarily obtain smoother frictional characteristics for bridge pier segments. In horizontal rotation construction of bridges, extremely low CoF under extremely high pressure is temporarily made possible by lubricating contacting polytetrafluoroethylene (PTFE) friction pairs with butter-PTFE powder mixture. It is believed that, with better understanding of the tribology and surface treatment technology, materials like concrete can also achieve low-friction contact with satisfactory durability. This paper reports some initial experimental investigations on selected methods to achieve a reasonably low CoF at concrete contacting surfaces, including (a) lubrication using powder, (b) lubrication using grease, (c) chemical polishing treatment, and (d) combinations of the above. Practical range of CoF will then be adopted in a companion study on the seismic performance of precast segmental bridge columns with resettable sliding joints so as to identify possible directions for further improvement.

2. Experimental details

2.1. Chemical polishing technology — concrete surface hardening

Concrete alone has various limitations in terms of carbonization and abrasion at the surfaces, and this porous material makes it difficult to hold liquid lubricants for a long period. In order to modify the performance of concrete surfaces, engineers in the floor industry normally prefer those surfaces to be chemically densified or hardened followed by proper mechanical polishing, i.e. the chemical polishing technology. Hardeners are essentially fine-sized, highly reactive silicates. When mixed with water, those silicates impregnate the surface of as-cast concrete and react with superficial calcium hydroxide, resulting in hard-to-wear calcium silicate hydrates. Superior performance on dusting, carbonization, water-permeation and especially abrasion will be obtained at the concrete surfaces (Fig. 1(b)) together with exterior improvements such as color and shininess. The chemical polishing technology is vital to facilitate wear-resisting concrete surfaces for column segments, while the two key factors of permeability and roughness for practically achieving durable low-friction contact at concrete interfaces can be modified accordingly.

2.2. Test set-up and procedures

The simplified Couplet Hoff-mann/Stöckl test adopted is shown in Fig. 1(a). A 100 mm cube was placed on a 100 mm × 100 mm × 500 mm beam. Grade 40 concrete with coarse aggregate size of 10 mm was used. The cubes were demolded 1 day after casting and then cured in air for

28 days before testing. In this preliminary study, a hydraulic jack was used in conjunction with a spring scale for convenience in load application and data measurement.

(a) (b) (c)

Fig. 1. Couplet test (a) Schematic diagram; (b) polished specimen; and (c) greased specimen

The experimental program consisted of 9 sets of one-way displacement-controlled tests performed at different vertical load levels and horizontal loading rates as shown in Table 1. The variables investigated include (a) lubrication using PTFE powder or MoS_2 grease (Fig. 1(c)), (b) chemical polishing treatment, (c) moist conditions, and (d) combinations of the above.

Table 1. Description of tests

Set name	O-G [(a)]	O-P	O-D	O-W	P-G [(a)]	P-G [(b)]	P-P	P-D	P-W
Surface	original	original	original	original	polished	polished	polished	polished	polished
Interface	grease	powder	dry	wet	grease	grease	powder	dry	wet
Protocol	loading rates (mm/s): 0.1-0.45-2.0; vertical loads (kg): 7.5-22.5-37.5-66								

[(a)] The grease lubricant was applied two days before testing
[(b)] The grease lubricant was applied a few minutes before testing

Negligible wearing at the contact interfaces was observed and repeating tests could always produce stable outcomes in terms of CoF after a few initial trials. Thus, the first few rounds of data were discarded. Nevertheless, the variations of CoF should be further examined in future.

3. Results and discussion

3.1. Coefficient of friction

According to the results shown in Fig. 2(a), it is obvious that polishing treatment can produce much smoother contact at the concrete interfaces under all testing conditions. Partially attributed to water permeation, the moisture condition seems to have little effect on the frictional behavior of concrete contacts. MoS_2 grease applied at the concrete interfaces surely provides the most desirable low CoF at the concrete contact, but this superior lubricating effect deteriorated quickly in 2 days mainly due to the grease infiltrating into the porous concrete. Nevertheless, the polished surfaces indeed preserved a better quality of grease as the rise of CoF in the case of Grease-b is much smaller than the case of Grease-a.

According to Fig. 2(b), grease lubricated concrete contacts shared a descending trend of CoF under increasing loading rate or vertical load, while the opposite trend was observed in dry concrete contacts. It has to be noted that the CoF measured in cases of the lowest vertical loading

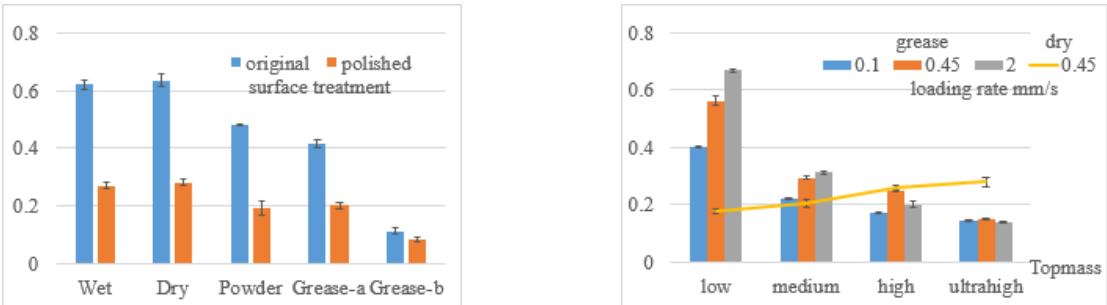

(a) High vertical load and 2 mm/s loading rate (b) Greased and dry cases with polishing

Fig. 2. Results of CoF for various cases

and highest loading speed is even higher than the maximum dry contact CoF, indicating the cohesive forces related to the viscosity of grease.

3.2. Additional observations

An interesting phenomenon was observed during the tests. It was much more difficult to remove the cube from a grease lubricated beam underneath than from a dry or powder lubricated one. The greased interfaces could provide an increasing dynamic CoF as the CoF kept increasing during the sliding of the upper cube. This noticeable amount of vertical "adhesive" force may be attributed to the removal of air at the concrete contact interface, which might in a way explain the relatively high CoF of the grease lubricated case under a low vertical load.

4. Conclusions

Based on the above test results, the following conclusions can be drawn.

(a) Surface treatment is essential to the CoF at the concrete interface and it is recommended to use chemical polishing technology to modify the frictional behavior of concrete contact surfaces.
(b) Polishing and grease lubrication are desirable treatments to obtain an extremely low CoF at concrete surfaces. A reasonably low CoF at the concrete interface can be achieved by polishing and powder lubrication. The CoFs within the range of 0.1 to 0.7 are possible values for further theoretical analyses and numerical simulations.
(c) MoS_2 grease performed quite well in terms of lubricating concrete contact surfaces under high vertical load conditions. Future investigation should be carried out to examine the relationship between grease viscosity and its lubricating effect as well as the possible "adhesive" forces induced by the grease at the concrete interfaces.

5. References

Sideris P. 2012. Seismic Analysis and Design of Precast Concrete Segmental Bridges, PhD Dissertation, Department of Civil, Structural and Environmental Engineering, State University of New York at Buffalo, Buffalo, NY.

Hossain, M.A., Totoev, Y. and Masia, M.J. 2016, Friction on mortar-less joints in semi interlocking masonry, Conference on Brick and Block Masonry – Trends, Innovations and Challenges – Modena, da Porto & Valluzzi (Eds), August 2016.

Bridge Engineering Institute Conference 2019 (BEI-2019)
Honolulu, Hawaii, USA, July 22-25, 2019

A Case of Seismic Performance Evaluation of Dam Gate Piers against Large-scale Earthquake

Tetsuo Fujimoto[1*], Hironori Hiramatsu[2], Ryoichi Fujita[3], and Motoyuki Suzuki[4]

[1] Osaka Institute of Technology, Osaka, JAPAN; email: tetsuo.fujimoto@oit.ac.jp
[2] Eight-Japan Engineering Consultants Inc., Osaka, JAPAN; email: hiramatsu-hi@ej-hds.co.jp
[3] Eight-Japan Engineering Consultants Inc., Osaka, JAPAN; email: fujita-ryo@ej-hds.co.jp
[4] Yamaguchi University, Ube, JAPAN; email: msuzuki@yamaguchi-u.ac.jp

[*]: corresponding author

Keywords: seismic; performance; evaluation; earthquake

Abstract: In Japan, seismic performance the dam body and its related facilities are evaluated according to "Guidelines for Seismic Performance Evaluation of Dams against Large Earthquake (Draft)" established after the Hyogo-ken Nanbu Earthquake which occurred on the 17th of January 1995. This paper describes a case of seismic performance evaluation of dam gate piers which were built by the spillway against large-scale earthquake. The characteristic of the dam gate pier is that it supports both superstructure of bridge and dam gate, and the ratio of reinforcement to cross section is low. It is different from the general bridge pier. Therefore, in this study, the bending and shear strengths of reinforced concrete section were appropriately evaluated, and the structural stability was examined. In addition, the deformation amount of the dam gate pier was also checked from the viewpoint of maintenance of the function to open and close the dam gate. Furthermore, the seismic response of the dam gate pier was calculated by dynamic analysis.

1. Introduction

In Japan, seismic performance the dam body and its related facilities are evaluated after the Hyogo-ken Nanbu Earthquake which occurred on the 17th of January 1995(River Bureau, Japanese Ministry of Land, Infrastructure, Transport and Tourism, 2005). However, like the Fujinuma dam due to the 2011 off the Pacific coast of Tohoku Earthquake which occurred on the 11th of March 2011, the dam's function of store water storage was lost due to a large-scale earthquake, and there was also a serious damage occurred in the downstream area (Tanaka et al., 2012). Therefore, it is required to evaluate seismic performance of existing dams. This paper describes a case of seismic performance evaluation of dam gate piers which were built by the spillway in concrete gravity dam against large-scale earthquake.

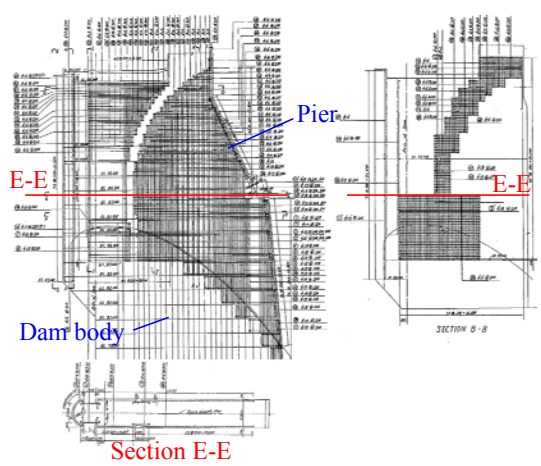

Fig. 1. Bar arrangement of the dam gate pier

2. Outline of dam gate pier

The dam targeted in this study is a concrete gravity dam constructed in 1964, with a dam height of 40m and a crest length of 453m. The dam gate pier is built by the spillway, the height is 16.7m, the bar arrangement is as shown in Fig. 1. The characteristic of the dam gate pier is that it supports both superstructure of bridge and dam gate, and the ratio of reinforcement to cross section is low, the elevation of the base changes in the upstream and downstream direction. It is different from the general bridge pier.

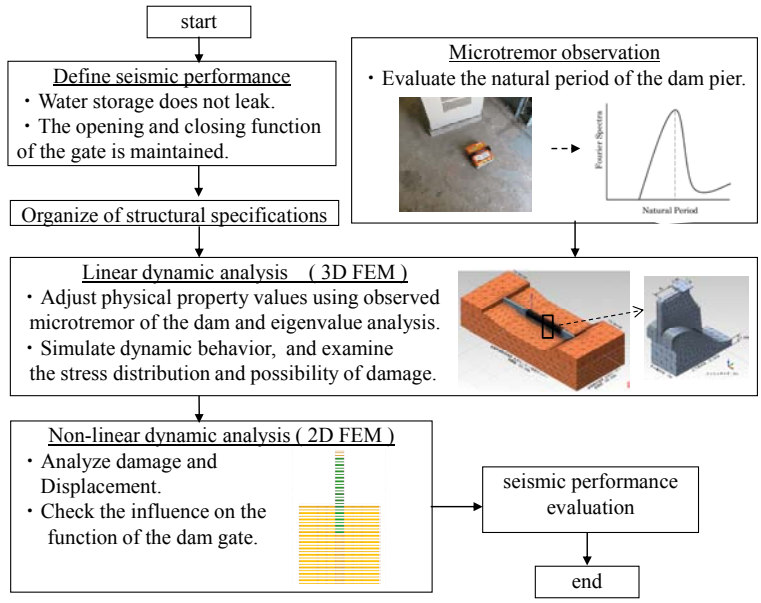

Fig. 2. Flow chart of seismic performance evaluation

3. Seismic performance evaluation of dam gate piers

3.1. Outline of study

Fig. 2 shows the flow chart of this study. In this study, the target seismic performance is to maintain both the water storage function and the opening and closing function of the gate. This study was focused on the loading capacity and the deformation of the dam gate pier. Firstly, the dam body and foundation were modeled by 3-D FEM and the seismic response of the dam gate pier was confirmed by linear dynamic analysis. At that time, in order to improve the accuracy of analysis, using the natural period of the dam gate pier obtained by microtremor observation, it was estimated the elastic modulus of concrete. As a result of linear dynamic analysis, the generated stress of dam gate pier exceeded the allowable value. Therefore, one block of the dam body was modeled by 2-DFEM and the seismic response of the dam gate pier was confirmed by dynamic analysis considering the nonlinearity of the material. The seismic ground motion used in this study was an artificial seismic wave (duration: 24 seconds) having the acceleration response spectra shown in Fig. 3.

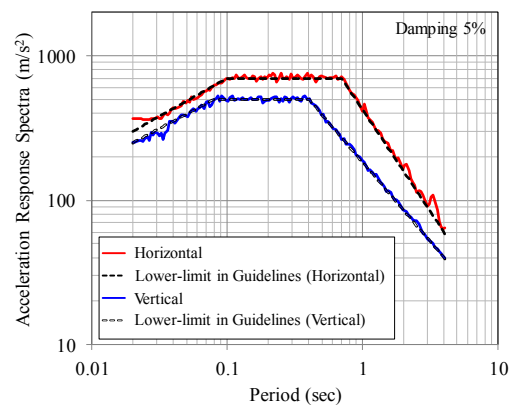

Fig. 3. Acceleration response spectra

Table. 1. Physical properties of the dam body concrete

Unit weight	γ	(kN/m^3)	22.9
Compressive strength	σ_c	(N/mm^2)	19.4
Tensile strength	σ_t	(N/mm^2)	2.33
Elastic modulus	E	(N/mm^2)	23000
Poisson's ratio	ν	(-)	0.126
Damping ratio	h	(%)	10

3.2. Linear dynamic analysis by 3-D FEM model

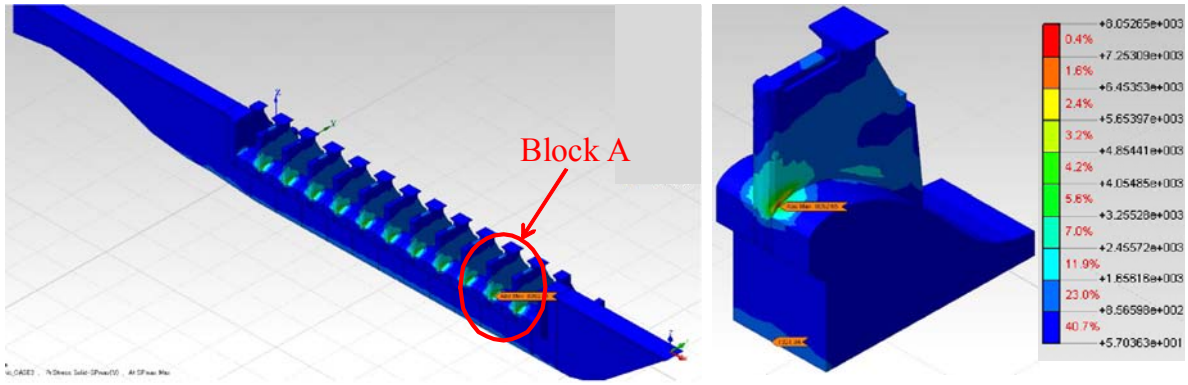

(a) Entire dam body (b) Block A

Fig. 4. The maximum principal stress distribution

The dam body and foundation were modeled by 3-D FEM and the seismic response of the dam gate pier was confirmed by linear dynamic analysis. Physical properties of the dam concrete is as shown in Table. 1. Before linear dynamic analysis, linear static analysis was carried out considering empty weight, hydrostatic pressure, sedimentation pressure, ice pressure, and results were superimposed. The seismic ground motion, three directions of the dam upstream and downstream direction, the dam axial direction, and the vertical direction were input. The seismic hydrodynamic pressure was considered as additional mass based on the concept of Westergaard, H.M., 1933. Fig. 4 shows the maximum principal stress distribution by linear dynamic analysis. The maximum principal stress generated in the dam gate pier tends to increase at the base due to the response of the dam gate pier in the direction of the dam axis. The maximum value (8.05 N/mm^2) exceeds the tensile strength greatly. Therefore, since there is a possibility of damage due to tensile stress at the base of the dam gate pier, the degree of damage was confirmed by dynamic analysis considering the nonlinearity of the material.

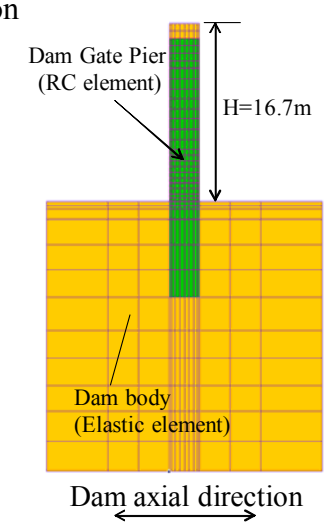

Fig. 5. 2-D FEM model

3.3. Nonlinear dynamic analysis by 2-D FEM model

The analytical model used in the nonlinear dynamic analysis is a 2-D FEM model that models one block of the dam body as shown in the Fig. 5 from the viewpoint of analysis accuracy and cost. This model is characterized by using the reinforced concrete element (RC element, nonlinear) and the unreinforced element (elastic element) in superposition, it is possible to consider the depth of the member and the deviation of the reinforcing bar. For the nonlinearity of reinforced concrete, the model of Maekawa et al., 2003 was applied. For the physical properties of concrete, the damping ratio of the linear

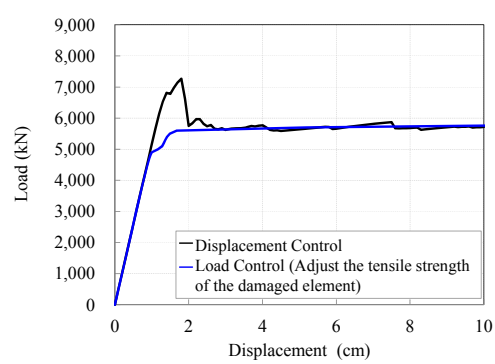

Fig. 6. Relationships load and displacement of section E-E

element is set to 5%, the damping ratio of the nonlinear element is set to 2% based on Japan Road Association, 2017, and the values of Table. 1 are applied otherwise. In checking the loading capacity of the dam gate pier, focused on the strain generated in each element. As the strain showing the ultimate state, tensile strain is 3%, the compression strain is 1%, the shear strain was set to 2%.

Fig. 6 shows the relationship between the load and displacement of the base of the dam gate pier (Fig.1 section E-E) when pushover analysis was performed using the analysis model. The conditions of loading gave 0.1cm/STEP forced displacement in the direction of the dam axis at the top of the gate. When the horizontal displacement is 1.8 cm, the maximum yield strength is 7270kN, after which the yield strength is small. The relationship between this load and the displacement is a behavior found in the RC structure with low reinforcing bar, which occurs when the yield load is smaller than the crack load. If a seismic load is applied to such a structure, in the analysis it is difficult to express the softening behavior after the yield strength has decreased, and the calculation may become unstable in some cases. Therefore, the tensile strength of the concrete at the base of the dam gate pier was reduced so that the relationship between the load and the displacement by the load control is the same as the relationship between the load and the displacement by the displacement control (after the strength reduction).

Fig. 7 shows the crack distribution, reinforcing bar yield distribution, tensile strain distribution by nonlinear dynamic analysis. The dam gate pier causes cracks and yield of reinforcing bars due to tension at the cut-off point. However, the maximum tensile strain is 0.63%, which does not reach the ultimate state. Therefore, it was judged that the loading capacity of the dam gate pier is retained against large-scale earthquake. The maximum response displacement at upper end of the dam gate was 19.6mm and the residual displacement was 0.6mm, and the maximum response displacement exceeded the gap between the gate and the dam gate pier (10 mm). Therefore, it was judged that gate opening and closing operation after the earthquake is possible although the gate and the dam gate pier may contact during the earthquake.

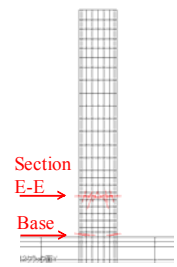

(a) Crack distribution

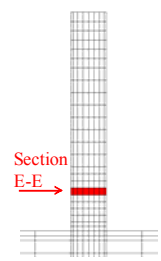

(b) Yield distribution

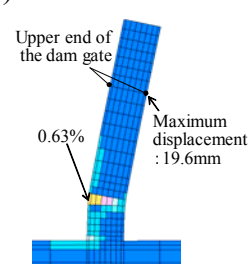

(c) Tensile strain distribution

Fig. 7. Results of non-linear analysis

4. Summary

This paper described a case of seismic performance evaluation of dam gate piers which were built by the spillway in concrete gravity dam against large-scale earthquake. This study was focused on the loading capacity and the deformation of the dam gate pier. For the development of reinforcement methods and effective maintenance, it is important to accumulate cases of seismic performance evaluation in the future.

5. References

Japan Road Association, 2017. Specifications for Highway Bridges, Part V Seismic Design.

Maekawa, K., Pimanmas, A., Okamura, H., 2003. Nonlinear Mechanics of Reinforced Concrete, Spon Press.

River Bureau, Japanese Ministry of Land, Infrastructure, Transport and Tourism, 2005. Guidelines for Seismic Performance Evaluation of Dams against Large Earthquakes (Draft).

Tanaka, T., Tatsuoka, F., Mohri, Y., 2012. Earthquake Induced Failure of Fujinuma Dam, Proceedings of the international symposium on dams for a changing world, 6-47-6-52.

Westergaard, H.M., 1933. Water Pressure on Dams during Earthquakes, Transactions, ASCE, Vol.98, 418-4

Performance of Bridges with Foundation Exposure under Near-Fault Seismic Demands

Shin-Tai Song[1*] and Chih-Chun Huang[2]

[1] Dept. of Civil Engineering, National Chung-Hsing University, Taichung City, Taiwan R.O.C.; email: ssong@nchu.edu.tw
[2] Dept. of Civil Engineering, National Chung-Hsing University, Taichung City, Taiwan R.O.C.; email: nostradamus@livemail.tw

[*]: corresponding author

Keywords: near-fault earthquake; multiple hazards; capacity spectrum; soil-structure interaction;

Abstract: Bridges located in near-fault regions are vulnerable to severe damage during earthquakes, especially if the bridge is suffering from foundation exposure caused by riverbed scour. In this study, the performance of a bridge at different scour depths under near-fault and far- field seismic demands is assessed through the capacity spectrum approach. Given that the bridge was originally designed with sufficient foundation strength, the level of seismic demand required to reach the performance limit remains approximately identical at shallow scour depths. Once the scour depth exceeds a critical level, the seismic performance is controlled by the foundation deformation limit and declines rapidly when the scour depth increases. Results of the study highlight that near-fault ground motions are devastating to bridges suffering from riverbed scour.

1. Introduction

Bridges located in flood-prone regions commonly suffer from serious foundation exposure caused by riverbed scour. Although the serviceability of the bridge may not be directly affected, the loss of surrounding soil reduces the lateral stiffness and strength of the foundation and alters the seismic performance of the structure. When these bridges are subjected to near-fault earthquakes, strong ground excitation with long-duration pulses produces a large inelastic deformation in the columns or piles, causing unexpected damages to the bridge. Given that many bridges located in near-fault regions suffer from serious scour problems, assessing their seismic performance at different scour depths under near-fault seismic demands is relevant.

2. Method

In this study, the performance of a bridge at different scour depths under near-fault seismic demands is assessed by a nonlinear analytical procedure based on the capacity spectrum approach. The capacity spectrum of the bridge bent is constructed on the basis of lateral pushover curve through an approach recommended in ATC-40 (1998). A point corresponding to the performance limit of the bridge is identified in the capacity spectrum for satisfactory seismic performance. The seismic demand imposed on the structure is assessed by utilising the acceleration–displacement response spectrum of a near-fault ground motion recorded at the bridge site. The hysteretic damping effect from structural yielding is considered during the construction of demand spectrum. Maximum seismic demand, which the bridge is able to sustain, can be determined by scaling the demand spectrum to intersect with the capacity spectrum at the

point corresponding to the performance limit. Denoted as PGA_p, the peak ground acceleration of the seismic demand required to reach the performance limit of the bridge is utilised for the characterisation of the seismic performance of the bridge. Variation in seismic performance of the bridge at increasing scour depth is investigated by comparing the PGA_p values at different scour depths. A demand spectrum of a scaled far-field ground motion record at the bridge site is constructed and used for the assessment of the performance of the bridge under the far-field earthquake. The comparison between the near-fault ground motion PGA_p values and the far-field ground motion PGA_p values reveals the influence of near-fault earthquakes on the seismic performance of bridges.

3. Finite Element Model of a Bridge and Seismic Demands

A bridge is designed as an example in this study. The geometry and finite element model of the bridge bent are illustrated in Fig. 1. The expected compressive strength of the concrete is taken as $f'_{ce} = 45$ MPa . Longitudinal and transverse reinforcements are assumed to be provided by A706 steel with an expected yield strength of $f_{ye} = 475$ MPa . The damping ratio of the concrete structure is taken as 5%. The bridge is assumed to be located at a medium sand site with an effective friction angle of $\bar{\phi} = 35^{o}$. The effective damping ratio of the soil-foundation system is assumed to be 10%. The bridge is originally designed with the piles fully embedded in the riverbed with a scour depth of $L_a = 0$ m . The scour depth is assumed to vary from $L_a = 0$ m to $L_a = 6$ m . To ensure a satisfactory seismic performance of the bridge, the inelastic deformation of the foundation is controlled within the *serviceability* limit to prevent any damage to regions that cannot be readily assessed. The inelastic deformation of the column cannot exceed the *damage-control* limit to avoid subsequent replacement of the structure. The recommended limit strains for various performance limit states are available in Priestley et al. (2007). The seismic performance of the bridge is controlled either by the *damage-control* limit of the column or by the *serviceability* limit of the foundation, whichever occurs first in the capacity spectrum.

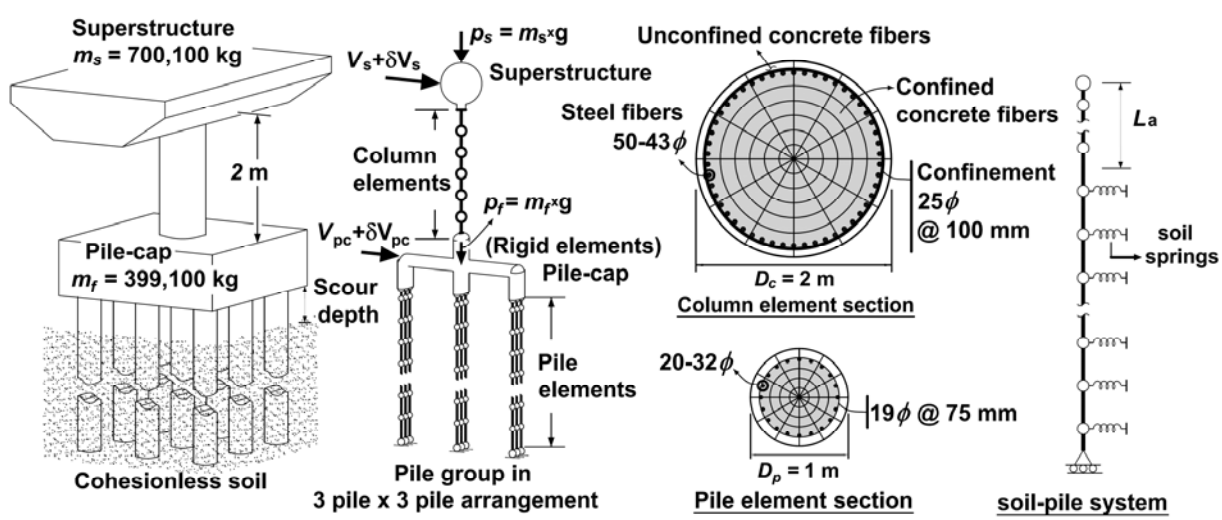

Fig. 1. Geometry and finite element model of a bridge bent

Two earthquake ground motion records are selected from the PEER Ground Motion Database (PEER 2013) as the seismic demand for the performance assessment of the bridge. The near-fault motion was recorded by the TCU102 station at the 1999 Chi-Chi earthquake. The distance from the station to the fault rupture surface is $R_{rup} = 1.5$ km. A ground motion recorded by the same station during the aftershock of the Chi-Chi earthquake is selected as the far-field motion ($R_{rup} = 52.8$ km). Fig. 2 illustrates the acceleration response spectra of the two ground motion records in terms of the spectral acceleration S_a normalized by the peak ground acceleration PGA. The figure shows that the near-fault motion imposes a larger spectral acceleration for structures with a natural period between 0.6 s and 0.8 s or greater than 0.95 s. Consequently, near-fault ground motion is influential to bridges suffering from foundation exposure caused by riverbed scour because of their prolonged natural period.

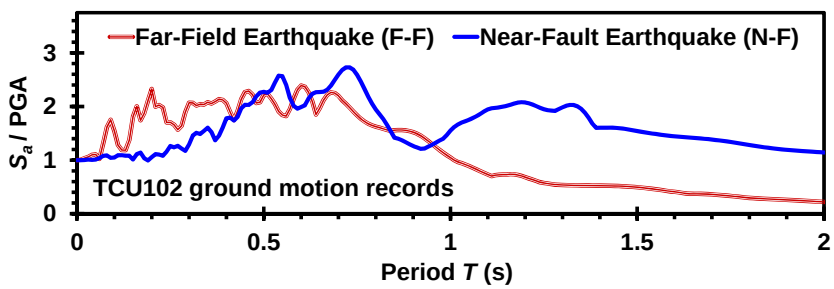

Fig. 2. Acceleration response spectra of a near-fault ground motion and a far-field ground motion

4. Bridge Performance

The capacity spectra of the bridge at scour depths L_a of 0 m and 4 m along with the demand spectra under the near-fault and far-field ground motions are presented in Fig. 3. Before the commencement of riverbed scour, the seismic performance of the bridge is controlled by the *damage-control* limit of the column. The foundation remains elastic before the performance limit of the bridge is reached. When the bridge is subjected to near-fault seismic demands, the peak ground acceleration required to reach the performance limit of the bridge is $PGA_p = 0.83$ g, which is much smaller than that of the far-field seismic demand $PGA_p = 2.59$ g. For a scour depth of $L_a = 4$m , the foundation yields before the bridge column does. The seismic performance of the bridge is controlled by the *serviceability* limit of the foundation. The PGA_p value given by the far-field ground motion is $PGA_p = 2.30$ g. The near-fault ground motion gives a smaller PGA_p value of 0.72 g. Fig. 6 reveals the variation in peak ground acceleration correlated to the performance limit of the bridge at different scour depths. Moreover, the seismic performance limit state of the bridge is specified. When the scour depth is shallower than $L_a = 3.9$ m , the seismic performance limit of the bridge is the column reaching the *damage-control* limit. The peak ground acceleration required to reach the performance limit of the bridge remains approximately the same with increasing scour depths. After the scour depth exceeds $L_a = 3.9$ m , the foundation strength becomes insufficient to protect itself from being damaged. The seismic performance limit of the bridge bent changes from the *damage-control* limit of the

column to the *serviceability* limit of the foundation. The peak ground acceleration required to reach the performance limit of the bridge decreases rapidly with increasing scour depths. While the scour depth varies from $L_a = 0\ \text{m}$ to $6\ \text{m}$, the level of the near-fault seismic demand required to reach the performance limit of the bridge remains approximately 1/3 of the far-field seismic demand required. Near-fault earthquakes are devastating to bridges suffering from riverbed scour.

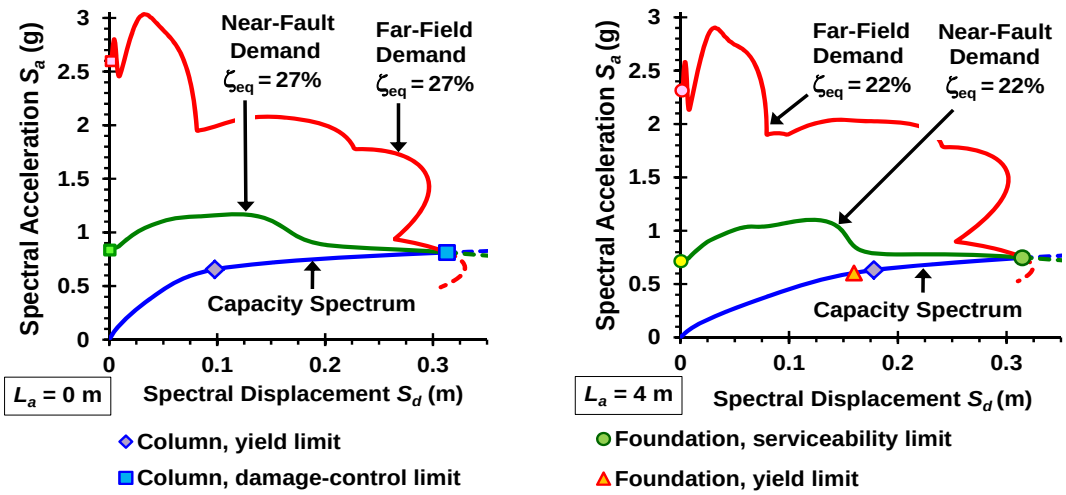

Fig. 3. Capacity and demand spectra of a bridge at scour depths of $L_a = 0\ \text{m}$ and $4\ \text{m}$

Fig. 4. Near-fault and far-field seismic demands correlated to the bridge performance limit

5. Conclusion

Bridge performance at different scour depths under near-fault and far-field seismic demands is assessed through the capacity spectrum approach. A point corresponding to the performance limit of the bridge is identified in the capacity spectrum, and the seismic demand required to reach this performance limit is determined accordingly. The influence of riverbed scour on the seismic performance of a bridge is assessed by comparing the seismic demands correlated to the performance limit at different scour depths. When the scour depth is shallow, the seismic performance is governed by the deformation limit of the column and not significantly affected by riverbed scour. Once the scour depth exceeds a critical level, unexpected foundation damage

controls the seismic performance of the bridge. The seismic demand correlated to the performance limit of the bridge reduces rapidly when the scour depth increases. The comparison of the levels of the near-fault and the far-field seismic demands required to reach the performance limit of the bridge reveals that near-fault earthquakes are devastating to bridges suffering from riverbed scour.

6. References

Applied Technology Council (ATC) 1996. Seismic Evaluation and Retrofit of Concrete Buildings. ATC-40, Applied Technology Council, Redwood City, California, U.S.A.

Priestley M.J.N., Calvi G.M., and Kowalsky M.J. 2007. Displacement Based Seismic Design of Structures, IUSS Press, Pavia, Italy.

Pacific Earthquake Engineering Research Center (PEER). 2013. PEER Ground Motion Database. https://ngawest2.berkeley.edu/

Research on Seismic Performance of Reinforced Concrete Columns with HTRB600 High-strength Bars

Hanbo Zhu[1] and Changqing Miao[2*]

[1] Key Laboratory of Concrete and Prestressed Concrete Structures of Ministry of Education, School of Civil Engineering, Southeast University, Nanjing, China; email: chqmiao@163.com
[2] Key Laboratory of Concrete and Prestressed Concrete Structures of Ministry of Education, School of Civil Engineering, Southeast University, Nanjing, China; email: zhubobo610113@163.com

[*]: Corresponding Author

Keywords: high-strength bars; reinforcing concrete column; low-cyclic experiment; the modified Park-Ang model

Abstract: In common, Application prospects of high strength steel bar in structural seismic design are controversial with high strength but poor ductility. An experiment study was undertaken to investigate seismic performance of reinforced concrete columns with HTRB600 high-strength Bars. In according to equal strength and volume principles of longitudinal and transverse bars, 14 reinforced concrete columns were designed and classified were tested to failure under cyclic loading. The comparison results, including backbone curve, lateral load-carrying capacity, ultimate deformation, ductility, hysteresis energy consumption, degradation of strength and load-deformation relations of columns are presented. Results indicate that, with the increase of axial pressure ratio, the bearing capacity, energy dissipation performance and stiffness of the specimen are obviously improved, but the ductility and total energy dissipation capacity are greatly reduced, and the rate of stiffness degradation is also greatly accelerated. After replacing the HRB400 longitudinal bar with the 630MPa high strength steel bar ultra-high longitudinal bar on the principle of equal strength, the ductility of the specimen is significantly increased, but the energy dissipation performance decreases when the displacement ductility is large. The replacement of steel bars on the principle of equal strength has no significant effect on bearing capacity, hysteresis curve shape, stiffness and strength degradation.

1. Introduction

The higher strength of the steel bars used in the reinforced concrete structure can reduce the amount of steel consumption and improve the economic benefits of the project. Therefore, many countries are promoting the use of high-strength steel bars. ACI 318-14 Building Code (Randall 2013) specifies that the main longitudinal steel in the building structure are Grade 60 (420MPa) and Grade 75 (520MPa) steel reinforcement ; The strength of steel reinforcement in Europe is relatively high. The European CEB-FIP standard code 2010 (Elghazouli 2016) is specified in the strength of 400-600 MPa. At present, China's technical policy (Zhao et al.2015) is to give priority to the promotion of HRB400 steel bars, and actively promote HRB500 steel bars. The application of 600MPa and upper strength steel bars is still relatively short (For convenience of

description, the hot-rolled steel bars with the strength of 600MPa and above are called "high-strength steel bars", and the hot-rolled steel bars of 400MPa and 500MPa grades are called "normal-strength steel bars".). Domestic and foreign scholars have conducted in-depth study on the seismic performance of normal-strength reinforced concrete columns (Wang et al. 2014; Rong et al. 2014;), and get some guiding conclusions. The research on the seismic performance characteristics, damage degradation law and failure mechanism of high-strength reinforced concrete column members is also inadequate (Rautenberg et al.2013; El-Nemr et al.2013). With the development of high-strength steel bars in China, more and more projects will use high-strength steel bars. It is necessary to conduct in-depth research on the seismic performance of concrete members with high-strength steel bars. Based on the previous research of the research group, this paper takes the concrete column with 630MPa high strength steel bar as the research object, and mainly studies the seismic performance of main influencing factors such as axial compression ratio, concrete strength, reinforcement strength and so on. It provides a scientific basis for the promotion and application of 630MPa high strength steel bars.

2. Experimental overview

2.1. Specimen design

In order to study the seismic performance of high-strength reinforced concrete columns, 11 reinforced concrete columns with grade HTRB630 steel bars as test group and 3 reinforced concrete columns with grade HRB400 steel bars as control group were designed and compared with a quasi-static experiment. Among them, the steel bars of equal intensity substitutions are based on the design values of the yield tensile strength specified in related specification. The parameters of the specimen are shown in Table 1. 11 components, Z1~11, are only briefly discussed due to space limitations.

Table 1. Specimen parameters

Column label	Concrete Strength grade	N Axial Compression Ratio	N(kN) Axial pressure	ratio of shear span to effective depth	Longitudinal reinforcement	Longitudinal reinforcement ratio P (%)	Stirrup	Stirrup ratio ρ sv(%)
Z1	C45	0.10	201	5.58	4D14	0.985	C8@100(2)	1.100
Z2	C60	0.25	641	5.58	4D14	0.985	C8@100(2)	1.100
Z3	C45	0.25	502	5.58	4D14	0.985	C8@100(2)	1.100
Z4	C45	0.10	201	5.63	4C18	1.630	C8@100(2)	1.160
Z5	C45	0.25	502	5.63	4C18	1.630	C8@100(2)	1.160
Z6	C60	0.25	641	5.63	4C18	1.630	C8@100(2)	1.160
Z7	C45	0.10	201	5.58	4D14	0.985	D8@150(2)	0.736
Z8	C45	0.25	502	5.58	4D14	0.985	D8@150(2)	0.736
Z9	C60	0.25	641	5.58	4D14	0.985	D8@150(2)	0.736
Z10	C45	0.25	502	5.58	4D14	0.985	D8@100(2)	1.100
Z11	C60	0.25	641	5.58	4D14	0.985	D8@100(2)	1.100

2.2. Material properties and loading process

In accordance with China's materiality test specification, the standard material tests were carried out on three sets of C45 and C60 concrete standard test blocks and three sets of HRB400 and HTRB630 steel test pieces. Before the start of the experiment, the finite element program, OpenSees, was used to simulate the skeleton curve of each test under the monotonic loading according to the measured mechanical properties above, and then calculated yield load $P_{y,c}$ and yield displacement $\Delta_{y,c}$ used the equivalent Elasto-Plastic Energy Method. The experimental lateral force loading mode is equal increment step-by-step loading under variable-amplitude, and under the control of displacement such as $0.4\Delta_{y,c}$, $0.8\Delta_{y,c}$, $\Delta_{y,c}$, $2\Delta_{y,c}$, $3\Delta_{y,c}$, $4\Delta y_{y,c}$ and so on. The first three stages are cycled to 1 cycle, and then each cycle is cycled to 3 cycles until the ultimate load is less than 85% of the peak load. The component is considered to reach the state of destruction.

3. Test results and analysis

The effects of axial compression ratio on the seismic behavior of concrete columns with high-strength steel bars were studied. The Z4, Z5 and Z7, Z8 components were compared and analyzed. The axial compression ratios of the test pieces were different (0.1 and 0.25 respectively). According to the analysis, the axial compression ratio is increased from 0.1 to 0.25; the yield load, peak load and ultimate load of the member are increased by 37%~48%; the displacement ductility coefficient is reduced by 22.2%~32.9%; the shape of hysteresis and skeleton curve has little effect. Although the stiffness of the specimen with high axial compression ratio is larger than that of the specimen with low axial compression ratio; the stiffness degradation rate is faster; the difference between the stiffness of two specimens decreases with the increase of the displacement amplitude; the axial compression ratio has little effect on the strength degradation coefficient. In summary, the increase of axial compression ratio is unfavorable to the seismic performance of concrete columns with high-strength steel bars, which is consistent with the concrete column with normal-strength steel bars.

The effects of the influence of seismic performance of concrete columns with high-strength and normal-strength longitudinal reinforcement in equal strength were studied. The six test pieces of Z4、Z1、Z5、Z3、Z6 and Z2 are divided into three groups for comparison, and each group consists of two columns. The test pieces of each group only have different reinforcement strength grades (the former and latter are HRB400 and HTRB630). After replacing high-strength to normal longitudinal reinforcement under the principle of equal strength substitution, It is found that the bearing capacity, stiffness and strength degradation performance, hysteresis and skeleton curve shape of the specimens with the HTRB630 high-strength longitudinal reinforcement are little different from those of the HRB400 ordinary longitudinal reinforcement. but the displacement ductility increased by 15.41% ~19.68%, and the cumulative energy consumption increased by 25.27%. In general, when the equal tensile strength of the HRB400 longitudinal steel bar is replaced by the HTRB630 longitudinal steel bar, the seismic performance of the components does not change much, but the amount of steel bars is saved.

The effects of the influence of seismic performance of concrete columns with high-strength and normal-strength confined reinforcement in equal strength were studied. The six test pieces of

Z1、Z7、Z3、Z8、Z2 and Z9 are divided into three groups for comparison, and each group consists of two columns. The test pieces of each group only have different reinforcement strength grades (the former and latter are HRB400 and HTRB630). The results show that, after replacing high-strength to normal stirrups under the principle of equal strength substitution, the cumulative energy consumption of the specimens is increased by 28.57% in the late stage of loading, and the energy consumption of the single-cycle is also improved, but the ductility and total energy consumption has dropped significantly. There were no significant changes in bearing capacity, hysteresis shape and strength degradation. In conclusion, when the equal tensile strength of the HRB400 stirrups are replaced by the HTRB630 stirrups, the seismic performance of the test pieces is improved, but the defect of component restraint effect needs to be improved in the future.

The effects of the influence of seismic performance of concrete columns with high-strength and normal-strength confined reinforcement in equal volume were studied. The six test pieces of Z1、Z7、Z3、Z8、Z2 and Z9 are divided into three groups for comparison, and each group consists of two columns. The test pieces of each group only have different reinforcement strength grades in same volume (the former and latter are HRB400 and HTRB630). After replacing high-strength to normal stirrups under the principle of equal volume substitution, the bearing capacity and stiffness of the test pieces have a small drop, but the ductility, the total cumulative and single-cycle energy consumption at the later stage of loading are all improved. Both the decline rate of the strength and the degradation rate of stiffness degradation are slowed down. Among them, the displacement ductility is increased by 5.19%~60.75%, and the cumulative energy consumption capacity is increased by 24.6%. In a word, when the equal volume of the HRB400 stirrups are replaced by the HTRB630 stirrups, the seismic performance of the test piece in the later stage of large displacement amplitude is obviously improved.

3. Conclusion

To summarize, 11 quasi-static tests of 630MPa high strength reinforced concrete columns are carried out, and the effects of axial compression ratio, concrete grade and longitudinal reinforcement on the seismic performance of concrete columns are analyzed. It can be conclude in 4 points as follows:

(1) With the equal strength principle, the seismic performance of the member with high-strength longitudinal bars is only improved in ductility and similar to that of common bars in other performances.
(2) Under the premise of ensuring sufficient hoop restraint efficiency, the equal strength substitution of high-strength stirrups is beneficial to the seismic performance of the column.
(3) With the equal volume principle, the seismic performance of column with high-strength transverse bars is prone to obtaining better seismic capacity such as cumulative and hysteresis energy consumption in the later stages of experimental loading
(4) Replacing stirrup with high-strength bars according to volume principle is prone to obtaining better seismic performance;

4. References

Elghazouli, A., (2016)Seismic design of buildings to Eurocode 8[M]. CRC Press.

El-Nemr, A., Ahmed, E.A., and Benmokrane, B.(2013) Flexural Behavior and Serviceability of Normal-and High-Strength Concrete Beams Reinforced with Glass Fiber-Reinforced Polymer Bars[J]. ACI structural journal, 110(6),USA.

Randall, W. P., (2013): ACI Building Code Requirements for Structural Concrete (ACI-318 14R)[S]. Americal Concrete Insitute, USA.

Rautenberg, J.M., Pujol, S., and Tavallali, H., et al.(2013) Drift capacity of concrete columns reinforced with high-strength steel[J]. ACI Structural Journal, 110(2): 307,USA.

Rong, X., Li, Y.Y., and Zhang, J.X,. Experimental Study and Analysis on Aseismic Performce of High Strength Reinforcement Concrete [J]. Engineering Mechanics, 2014,32(10):99-105, China.

Wang, Q.F., Zheng, J. K., and Zhou, B., et al. (2014) Study on Seismic Behavior of HRBF500 RC Column Based on Hysteretic Energy[J]. China Civil Engineering Journal, (11):22-28, China

Zhao, G.D., Xu, Y.L., and Hua, X.K. (2015): Code for design of concrete structures GB50010-2010. China Architecture & Building Press, China.

Bridge Engineering Institute Conference 2019 (BEI-2019)
Honolulu, Hawaii, USA, July 22-25, 2019

Evaluation of the Seismic Response Regarding the Anchorage between Electrical Cabinet and Concrete Slab in the Power Plant

Sang-Moon Lee[1], Bub-Kyu Jeon[2], and Woo-Young Jung[3*]

[1] Dept. of Civil Engineering, Gangneung-Wonju National University, Gangneung, South Korea email: sunnybob1@naver.com
[2] Seismic Simulation Test Center, Korea Construction and Transport Engineering Development Collaboratory Management Institute (KOCED CMI), Yangsan, South Korea; email: bkjeon79@pusan.ac.kr
[3] Dept. of Civil Engineering, Gangneung-Wonju National University, Gangneung, South Korea; email: woojung@gwnu.ac.kr

[*]: corresponding author

Keywords: electric cabinet, shaking table test, rocking motion, earthquake load, anchorage performance

Abstract: In this study, the performance of an anchorage connecting between electric cabinet and concrete slab installed in the power plant that was investigated by both experiment and numerical analysis. Firstly as the test, cabinet was mounted on the shaking table to confirm the difference in behavior depending on the anchoring method of the cabinet bottom. It used three seismic waves to perform time history tests and resonance search tests before and after time history tests. Secondary as the numerical analysis, the earthquake load was considered as the applied load in the numerical analysis and its results were compared with the experiment data. The FE model was composed of three groups which were the cabinet body, floor jig and anchorage bolt. The interface between cabinet bottom and top of the jig was designed to have the sliding effect by using contact surfaces. In addition, the contact mechanism was applied to the anchor used to connect between the cabinet and the jig. It was shown that there was a difference between the results of the analysis and experiment because the rocking motion occurred at the bottom of the cabinet due to the uplifting behavior confirmed in the experiment. More advanced technique will be studied to present the rocking motion in the numerical analysis in the future.

1. Introduction

As the frequency of large-scale earthquakes occurrence and damage has increased in recent years, the interesting seismic design of various facilities has also growing. Not only the damage to the entire facility was a problem, the damage to non-structural element installed in the affected facility was also found to significantly disrupt the performance of the entire facility. Especially, such as power generation facilities with special purpose cause severe 2nd and 3rd damage and loss of lives if an unstable element malfunctions due to an earthquake.

Fig. 1. Earthquake damage of the non-structural elements

2. Methodology

In this study, there is analyze the behavior characteristics of an anchorage connecting electric cabinet subjected to earthquake loading by using the numerical analysis. The earthquake loads were generated by using the shaking table and its mechanism can be confirmed the model by using experiment data. Numerical analysis results from simulating an electrical cabinet, which is implemented based on Abaqus elements are compared with the experimental results.

2.1. Description of Geometry

The specifications of the cabinet used in the study are shown in Table 1. The Fig. 2 shows the overall setup for the experiment, and the cabinet modeling by using Abaqus program based on Table 1.

Table 1. Test specimens specifications

Specimen Cabinet	Dimension (mm)			Weight (kg)	Fixed
	Length	Width	Height		
Single door	800	800	2,350	480	M16 Anchor (8ea)

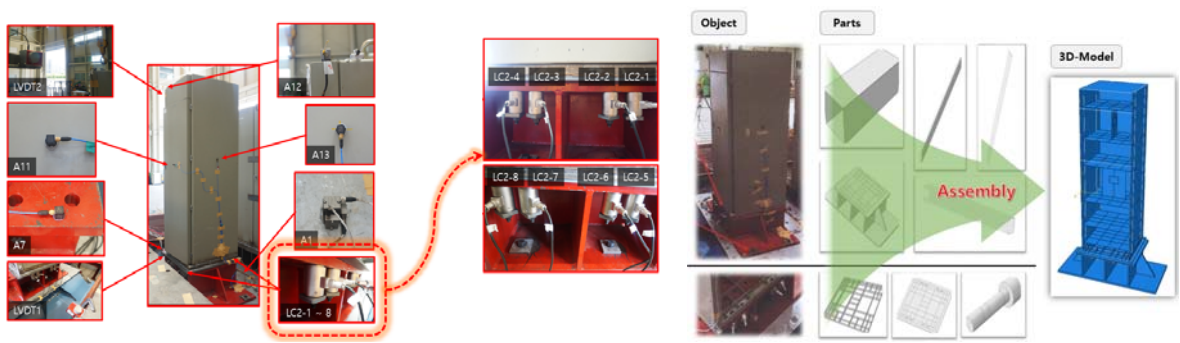

(a) (b)

Fig. 2. Overall description of the cabinet used in the study: (a) the whole system regarding experiment; (b) component for 3D-Model using Abaqus program

2.2. Input earthquake waves

In this study, it was that three seismic waves were used for the experiment. ICC-ES AC156[(1)] RRS (Required Response Spectrum), Nuclear Power Plant Seismic Design Criteria Reg. 1.60[(2)], the acceleration scale of the Uniform Hazard Spectrum (UHS) in Uljin area of South Korea were used. Fig. 3 presents Reg. 1.60 and UHS normalized to 0.67g in the horizontal direction and 0.14g in the vertical direction with respect to the ZPA (Zero Period Acceleration) size of the AC156 RRS according to the equivalent static structural load of the domestic building structure standard. For each seismic wave, the damping ratio was set to 5% in 3 axes using

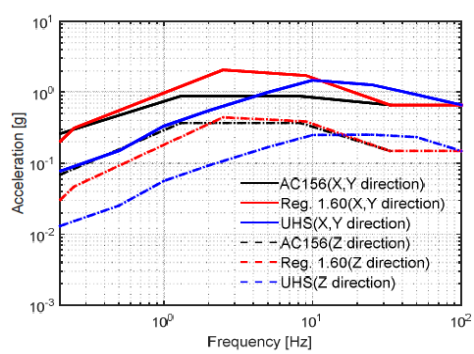

Fig. 3. Required Response Spectrum (5% damping)

horizontal (X, Y) and vertical (Z) RRS. The wave used in the numerical analysis carried out only the most normalize and standard AC 156 among the three waves.

3. Experimental methods and procedures

3.1 Checking resonance frequency

A resonance search experiment was performed with a sine sweep test to check the possible structural deformations before and after the experiment. It was performed once for each axis direction (X), (Y), and (Z) and the magnitude of the acceleration signal was 0.07g in order to minimize the damage of the cabinet. The search range was 1 ~ 50Hz and the frequency increase was 2 octave / min. The procedure of the shaking table experiment is shown in below Table 2.

3.2 Time history test using the shaking table

As shown in Fig. 4, the TRS (Test Response Spectrum) obtained a response measured after the time history experiment by installing an accelerometer for three directions (X, Y, Z) on the bottom of the shaking table.

Table 2. Overall test sequence

Step	Classification	
1	Pre-resonance search test	X
2		Y
3		Z
4	Time history test	Reg.1.60
5		UHS
6		AC 156
7	Post-resonance search test	X
8		Y
9		Z

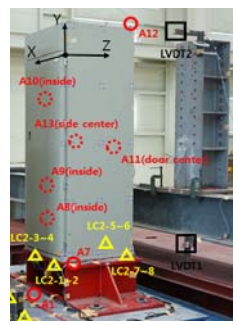

Fig. 4. Sensor location

4. Finite Element Model

4.1. Properties of Material

As shown in below Table 3 presents the material properties applied in the numerical analysis.

Table 3. Properties of Material

Material	Density (ton/mm)	Elastic		Damping (5%)[a]	
		Young's Modulus	Poisson's Ratio	Alpha	Beta
Steel (SS400)	7.85e-09	2.1e+05	0.3	2.7309	9.06e-04

[a]: The values is obtained proceeding Eigenvalue-analysis by using Abaqus program. And then the values required for the numerical analysis were calculated using Matlab program.

4.2. Description of FE Modeling

For the more detail information on modeling, refer to the abstract and the Fig. 2(b).

5. Results and Comparison

5.1. Examining the anchorage load under experiment and analysis

The below Fig. 5(a) and (b) shows the data obtained by using the acceleration response of the accelerometer installed at the main position of the cabinet as a transfer function and that is a showing the absolute maximum value of the anchor pullout regarding the cabinet for each seismic wave. The Fig. 5(c) shows the anchorage load which obtained by using numerical analysis.

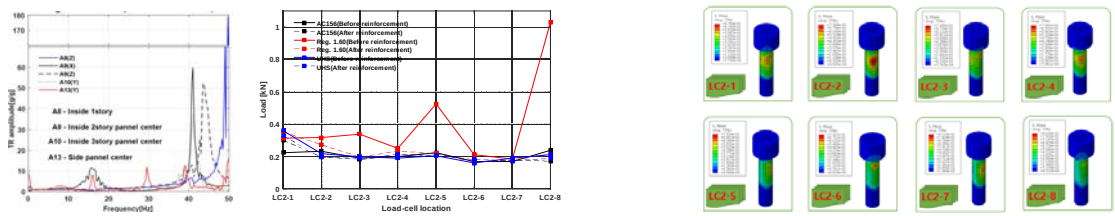

(a) (b) (c)

Fig. 5. Review the impact on the anchors: (a) resonance search test results (TR); (b) Abs. max. anchorage load; (c) anchorage load respectively under numerical analysis

5.2. Comparison results data

The below Table 4 and Fig. 6 presents comparison between test and analysis. As you can see there is slight difference results except LC2-1. Experimental data of LC2-1 shows a lot of difference from other experimental data.

Table 4. Anchorage load respectively

Specimen	Load gauge	Test (kN)	Analysis (kN)
Single door cabinet	LC2-1	0.301	0.136
	LC2-2	0.198	0.148
	LC2-3	0.182	0.148
	LC2-4	0.207	0.143
	LC2-5	0.221	0.151
	LC2-6	0.170	0.147
	LC2-7	0.179	0.163
	LC2-8	0.171	0.174

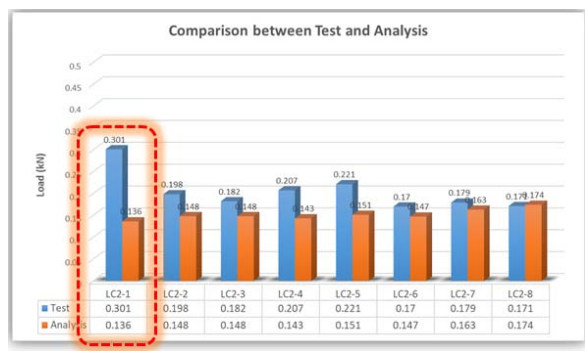

Fig. 6. Comparison between test and analysis

6. Conclusion and remarks

As mentioned above, the experimental and analytical results are somewhat different. For that reason the bottom of the cabinet is subjected to an impact due to the uplifting, which causes cup-like deformation around the anchor bolt. The following suggestions are made for future study.

- Rocking mode should be considered and prevention measures are required by lower plate reinforcement.
- It should be considered of local deformation around the anchor.

- It should be minimize effects such as banging and rattling which is caused by the impact.

7. Acknowledgments
This study was carried out by the research grant support (19IFIP-B128598-03) of the R & D project of the Ministry of Land, Transport and Tourism.

8. References
ICC-ES, 2015, AC156-2010 Acceptance Criteria for Seismic Certification by Shake-table Testing of Nonstructural Components, 2.2(1), 2-4.

2014. REGULATORY GUIDE 1.60 DESIGN RESPONSE SPECTRA FOR SEISMIC DESIGN OF NUCLEAR POWER PLANTS, 2.2(2), 2-4.

2D Analytical Model for the Eddy Current Damping Force and the Application in Seismic Analysis of Bridge

Hongyi Zhang[1*], Longteng Liang[2], and Zhengqing Chen[3]

[1] College of Civil Engineering, Hunan University, Changsha 410082, People's Republic of China; email: zhyzzb25@qq.com
[2] College of Civil Engineering, Hunan University, Changsha 410082, People's Republic of China; email: longteng_liang@163.com
[3] College of Civil Engineering, Hunan University, Changsha 410082, People's Republic of China; email: zqchen@hnu.edu.cn

[*]: corresponding author

Keywords: Structural vibration control, eddy current dampers, analytical modelling, force-velocity characteristics

Abstract: The eddy current damper is a new kind of damping device in civil engineering, dissipating kinetic energy as heat by the eddy current. A 2D analytical model of the eddy current distribution is presented for the eddy current damper, expressed in the form of Fourier series as a function of radial, spatial angle and time. The eddy current force generated by the damper at different working velocity is obtained by integral. Experiments and finite element calculations are conducted to validate the analytical model. Results show that the analytical model is consistent with the finite element model. The eddy current force measured in the test is a bit larger than that calculated, while the changing trends are the same. The nonlinear force-velocity relation of a damper could be obtained through this method. A structural finite element analysis is conducted for abridge with eddy current dampers connected between the girders and abutments, using the nonlinear damping force. Parameters are optimized based on the FEM results

1. Introduction

Structural vibration control by using passive and semi-active energy dissipation devices is critical to improving severability and limiting damage to bridge and building structures when subjected to dynamic loadings such as earthquakes and windstorms. The eddy current damper (ECD) is another effective mechanism for dissipating kinetic energy and vibration control. In its simplest form, ECD device consists of conductive sheet and permanent magnets (PMs), where the relative linear motion between conductive sheet and PMs generates damping forces. Electromagnet can also be used in place of PMs for realization of semi-active control. The ECD has a number of advantages compared to other types of dampers. There is no fluid inside the ECD and the generation of damping is independent of friction, potentially increasing eddy current damper longevity and lowering maintenance requirements. The axial eddy current damper with a rotatable exterior cylinder (A-ECD) shown in Fig. 1 is an improved and more efficient type of ECD, capable of producing a sufficiently large damping force. The working principle of an A-ECD is to transform the linear relative motion between damper's two ends into the rotation of the rotor, through a ballscrew assembly and bearings. The relationship between angular velocity ω and axial linear velocity v is

$$\omega = v \times \frac{2\pi}{Ld} \tag{1}$$

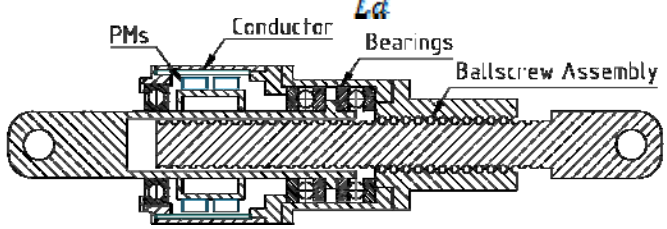

Fig. 1. Axial eddy current damper (A-ECD)

2. Analytical model

2.1. Assumptions

- End effects are ignored, that is, the cylinder is assumed to have infinite axial length compared to the distance between rotor and stator. The problem is therefore simplified to a 2D case. A rotor fixed reference axis is defined as shown in Fig. 2(a).
- The electromagnetic field can be treated as a quasi-static field, ignoring the displacement current.
- All materials are isotropic. The permeability and conductivity are constant. The magnetic saturation and hysteresis loss are neglected. The steel has infinitely large permeability and infinitely small conductivity. Air between the PMs has the same permeability as the PMs.

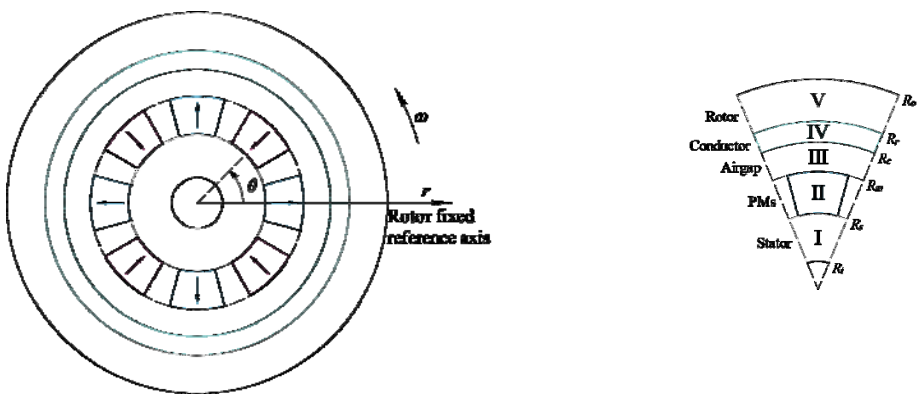

(a) Section view (b) Geometric parameters

Fig. 2. Illustration of key geometric parameters of the rotational parts of the A-ECD

2.2. Governing PDEs

An electromagnetic field can be fully described by the magnetic vector potential **A** along with the electric potential ϕ (a scalar field):

$$\begin{aligned} \mathbf{B} &= \nabla \times \mathbf{A} \\ \mathbf{E} &= -\nabla\phi - \frac{\partial \mathbf{A}}{\partial t} \\ \mathbf{H} &= \frac{1}{\mu_0}\mathbf{B} - \mathbf{M} \end{aligned} \tag{2}$$

where **B** is the magnetic flux density vector, **E** is the electric field vector, **H** is the magnetic field density vector, **M** is the magnetization field vector, μ_0 is the vacuum permeability.

As illustrated in Fig. 2, the cylinder is divided into five regions: stator, PMs, airgap, conductor and rotor. Free current only exists in the conductor. The magnetic hysteresis is ignored in rotor and stator, which are made of steel. Equations in each region are listed below:

$$\begin{cases} \nabla^2 \mathbf{A}^{\mathrm{I}} = 0 \\ \nabla^2 \mathbf{A}^{\mathrm{II}} = -\mu_0 \nabla \times \mathbf{M} \\ \nabla^2 \mathbf{A}^{\mathrm{III}} = 0 \\ \nabla^2 \mathbf{A}^{\mathrm{IV}} = \mu_0 \sigma \dfrac{\partial \mathbf{A}}{\partial t} \\ \nabla^2 \mathbf{A}^{\mathrm{V}} = 0 \end{cases} \tag{3}$$

2.3 Boundary conditions and magnetization vector

At the interface between two media, the perpendicular component of the magnetic flux density is continuous. The parallel component of the magnetic field density is also continuous if there is no surface current at the interface, which only appears at the boundary of a superconductor ($\sigma \to \infty$). At the boundary $r = R_i$ and $r = R_o$, magnetic insulation is set. With the z-component ignored, the magnetization vector of the permanent magnets is expressed by its radial and tangential components. For the radial magnetization pattern:

$$\begin{aligned} M_r(\theta, t) &= \mathrm{Re}\left[\sum_{n=1,3,5\ldots}^{\infty} \frac{4B_{re} \sin\left(\frac{n\pi\alpha}{2}\right)}{\mu_0 n\pi} e^{inp(\theta+\omega t)}\right] \\ M_\theta(\theta, t) &= 0 \end{aligned} \tag{4}$$

where p is the number of pole-pairs, ω is the rotational angular velocity, B_{re} is remanence flux density of PMs, α is the magnet-arc to pole-pitch ratio.

2.4 Induced current distribution

The general solution of Eq(3) could be derived by substituting Eq(4) into the boundary conditions, and the induced current distribution in conductor can be written as:

$$\vec{J}_z(r,\theta,t) = \sum_{n=1,3,5\ldots}^{\infty} J_{zn}(r) e^{inp(\theta+\omega t)} \tag{5}$$

where

$$J_{zn}(r) = \omega\sigma \frac{4B_{re} \sin\left(\frac{n\pi\alpha}{2}\right) p}{\pi} \xi_n R_m \frac{I'_{np}\left(\frac{R_n}{\delta_n}\right) K_{np}\left(\frac{r}{\delta_n}\right) - K'_{np}\left(\frac{R_n}{\delta_n}\right) I_{np}\left(\frac{r}{\delta_n}\right)}{\psi_n} \tag{6}$$

$I_\alpha(x)$ and $K_\alpha(x)$ are *Modified Bessel functions*, and ξ_n and ψ_n are functions of n and geometric parameters, and $\delta_n = \frac{1}{\sqrt{np\omega\sigma\mu_0}} = \frac{1-i}{\sqrt{2np\omega\sigma\mu_0}}$. The Joule heating equation gives the dissipation power of eddy current:

$$P = \iiint_{\text{Region IV}} \frac{1}{\sigma} \mathrm{Re}(\vec{J}_z)^2 \, dV$$

$$= \sum_{n=1,3,5,\ldots}^{\infty} \frac{\pi L}{\sigma} \int_{R_s}^{R_r} |J_{zn}(r)|^2 r \, dr \tag{7}$$

For an eddy current damper, a power balance equation is given by:

$$F \times v = T \times \omega = P \tag{8}$$

3. Experimental validation

The force-velocity relationship of a full-scale A-ECD is measured and compared with the 2D analytical result and FEM result:

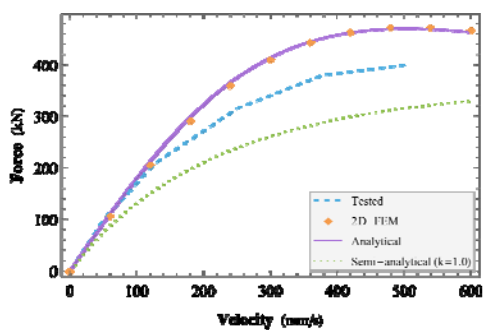

Fig. 3. Eddy current force calculated by different methods

4. Seismic analysis of a suspension bridge with eddy current dampers

A seismic analysis of a suspension bridge, whose longitudinal displacement is under control by eddy current dampers, is conducted. A comparison between the force-velocity curves of an A-ECD and a fluid viscous damper is revealed in Fig. 4.

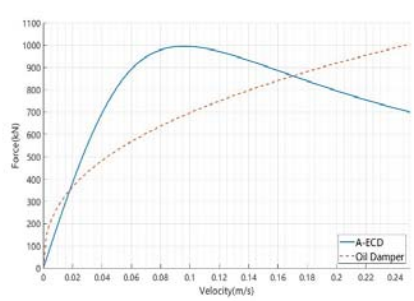

Fig. 4. Force-velocity relationships

El Centro wave is applied to the bridge to estimate the performance of an A-ECD and a fluid viscous damper. The displacement-time curve in shown in Fig. 5. The maximum displacement of the bridge with an A-ECD is 0.0564m, while one with a fluid viscous damper is 0.0611m. The A-ECD is able to provide a good passive control performance for the bridge in an earthquake.

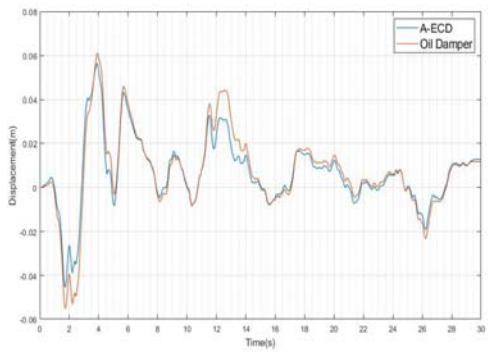

Fig. 5. Longitudinal displacement-time curve of a bridge in seismic analysis

2. Conclusion

In this study, a new kind of rotary ECD with ball screw is developed which amplifies linear motion to rotary motions. Its dynamic characteristics are evaluated by using an analytical approach, and the results are compared with FE simulation and laboratory experiments. A seismic analysis of a suspension bridge with A-ECDs is conducted and the result shows that the A-ECD is able to provide a good passive control performance for the bridge.

Dynamic Characteristics of Continuous Slab Track under Non-Steady Thermal Effects

Gonglian Dai[1], Pengfei Ma[2*], Shiwei Rao[3], and Tong Qiu[4]

[1] School of Civil Engineering, Central South University, Changsha, Hunan, China; email: daigonglian@csu.edu.cn
[2] School of Civil Engineering, Central South University, Changsha, Hunan, China; email: sxtythmpf@csu.edu.cn
[3] School of Civil Engineering, Central South University, Changsha, Hunan, China; email: 2529658865@qq.com
[4] Department of Civil Engineering, The Pennsylvania State University, University Park, PA, USA; email: tqiu@engr.psu.edu

[*]: corresponding author

Keywords: continues slab track; thermal action; non-steady thermal effect; dynamic characteristic

Abstract: Continuous slab track is a new type of track systems in high-speed railways, which looks very much like an infinite slab. In order to study the vibration response of a continuous slab track under non-steady thermal effects and different train speeds, a mechanical model along with the equation of motion for the slab track on a bridge under thermal effects are established based on the principle of total potential energy for a stationary elastic system under dynamic loading. The results obtained from the model show that the natural frequency of the slab track decreases with an increase in the uniform temperature of the slab track. The first natural frequency (f1) of the slab track decreases by 1.5 Hz when the temperature rises by 10 ℃. Considering the extreme temperatures in Jiangxi Province (China), f1 for the lowest temperature (2.1℃) in winter is 75 Hz higher than that for the highest temperature (40.46 ℃) in summer. Under dynamic excitation, the responses of the vertical acceleration and displacement in the slab track are magnified with an increase in the uniform temperature. When the excitation frequency is lower than f1, the thermal effect has a great influence on the vibration transfer in the slab track along the longitudinal direction. It is also found that the attenuation of the vertical vibrations of the slab track tends to slow down with an increase in the uniform temperature.

1. Introduction

With the popularization of high-speed railway and passenger-dedicated lines in China, the dynamic response analysis of continues slab track structure has become an important subject in the field of high-speed railway research [1]. More maintenance and service problems of continuous slab track structure have been encountered. This paper considers that these maintenance problems are closely related to the vibration response of the continuous slab track under the action of non-steady thermal loading and live load. In this paper, based on the analysis of the temperature measurement of a continuous slab track structure for many years, a model for the temperature variation in the slab is developed, and the vibration equation of the structure

under non-steady temperature loading is established by applying the principle of minimum dynamic elastic potential energy [2]. The dynamic response of the structure is also analyzed.

2. Uniform Temperature Variation in Continuous Slab Track Structure

The temperature variation of the continuous slab track is monitored in the field. The positions of the thermometers are shown in Fig. 1. The temperature time history curves can be obtained as shown in Fig. 2. The statistics of the uniform temperature of the cross section can be calculated by the higher-order moment algorithm [3] as shown in Table 1. From the above statistical results, it can be seen that the maximum and minimum uniform temperature of the cross section may reach 40.46 ℃ and 2.1 ℃, respectively for a return period of 100 years.

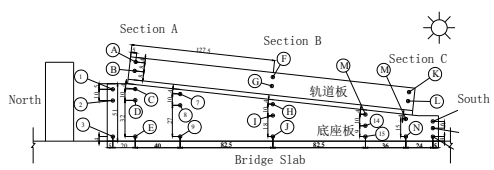

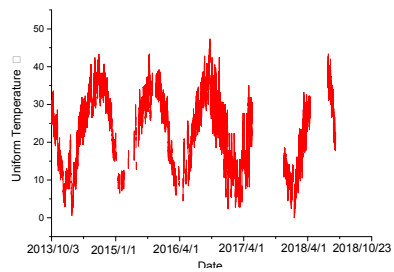

Fig. 1. Measuring Point Arrangement **Fig. 2** Variation of Uniform Temperature

Table 1. Statistics of Uniform Temperature

Probability	Maximum Temperature for Return Period of 100 Years	Minimum Temperature for Return Period of 100 Years	Maximum Temperature For Return Period of 100 Years	Minimum Temperature in Return Period of 100
Characteristic value of Uniform Temperature	40.46℃	2.1℃	39.6℃	3.19℃

3. Elastic Foundation Beam Model of Slab Track Structure under Temperature Loading

Based on the principle of dynamic minimum elastic potential energy [2], this paper establishes the equation, regards slab track as an infinite beam on elastic foundation as shown in figure 3, and simulates the live load as an impact load acting directly on the structure.

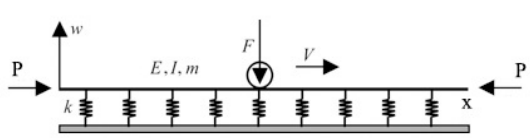

Fig. 3. Continuous Slab Track Model on Infinite Elastic Foundation

$$\Pi = \int_0^l \frac{EI}{2}\left(\frac{\partial^2 w}{\partial x^2}\right)^2 dz + \int_0^l m\frac{\partial^2 w}{\partial t^2} w dz + \int_0^l c\frac{\partial w}{\partial t} w dz + \int_0^l \frac{1}{2} k w^2 dz - Fw - \frac{P}{2}\int_0^l \left(\frac{\partial w}{\partial x}\right)^2 dz \tag{14}$$

where EI is the flexural rigidity of the slab track, w(x, t) is the vertical deflection of beam as a function of time t, m is the mass of the beam per unit length, C is the damping of the structure, k is the elastic foundation coefficient of infinite long beam, F (x, t) is the impact load of vehicle, and P is the axial force caused by temperature effect. The first-order variation of displacement in Eq. (1) is obtained from the principle of minimum dynamic elastic potential energy.

$$\delta\Pi = EI\int_0^l \frac{\partial^2 w}{\partial x^2}\cdot\delta\frac{\partial^2 w}{\partial x^2}dx + \int_0^l m\frac{\partial^2 w}{\partial t^2}\delta w dx + \int_0^l c\frac{\partial w}{\partial t}\delta w dx + \int_0^l kw\delta w dx - F\delta w - P\int_0^l \frac{\partial w}{\partial x}\delta\frac{\partial w}{\partial x}dx = 0 \quad (15)$$

In order to simplify the solution procedure, it is discretized into finite elements and the displacement function w(x) of each element can be multiplied by the shape function **N(x)** and $\mathbf{q_e}$ which represents the vertical displacement and the rotation angle at the both sides of the element as shown in Eqs. (3) and (4).

$$\mathbf{N(x)} = \left\{1-3(\frac{x}{l_e})^2+2(\frac{x}{l_e})^3 \quad x-2\frac{x^2}{l_e}+\frac{x^3}{l_e^2} \quad 3(\frac{x}{l_e})^2-2(\frac{x}{l_e})^3 \quad -\frac{x^2}{l_e}+\frac{x^3}{l_e^2}\right\} \quad (16)$$

where l_e is the length of the element.

$$\mathbf{q} = \{u \quad u' \quad v \quad v'\}^T \quad (17)$$

where u and v are the vertical displacements at both ends of the unit; and u' and $v'$are the rotation angles at both ends of the element. Eqs. (3) and (4) can be substituted into Eq. (2) yielding

$$\delta\mathbf{q_e}^T\bullet\{\int EI\mathbf{N''}^T\mathbf{N''} + k\mathbf{N}^T\mathbf{N} - P\mathbf{N'}^T\mathbf{N'}dx\bullet\mathbf{q_e} + \int m\mathbf{N}^T\mathbf{N}dx\bullet\ddot{\mathbf{q}}_\mathbf{e} + \int c\mathbf{N}^T\mathbf{N}dx\bullet\dot{\mathbf{q}}_\mathbf{e} = F\mathbf{N}^T\} \quad (18)$$

According to Eq. (5), the contribution of equivalent element stiffness matrix $\mathbf{K_{eff}}$ comes from the stiffness of the structure itself, spring stiffness and geometric stiffness

$$\int_e EI\mathbf{N''} + k\mathbf{N}^T\mathbf{N} - P\mathbf{N'}^T\mathbf{N'}dx \quad (19)$$

The element mass matrix **M** is $\int_e m\mathbf{N}^\mathbf{T}\mathbf{N}dx$. The element damping matrix **C** is $\int_e c\mathbf{N}^T\mathbf{N}dx$. The dynamic analysis under the temperature effect is carried out according to

$$\mathbf{K_{eff}q_e} + \mathbf{M}\ddot{\mathbf{q}}_\mathbf{e} + \mathbf{C}\dot{\mathbf{q}}_\mathbf{e} = F\mathbf{N}^T \quad (20)$$

From the deduction of the equations in this section, it can be seen that the increase of uniform temperature of the continuous slab track will lead to the increase of the axial force in the cross section, thus reducing the equivalent stiffness of the cross section.

4. Vibration Analysis of Continues Slab Track under Uniform Temperature

4.1 Variation of Natural Frequencies of Continues Slab Track with Uniform Temperature

According to the statistics of characteristic value of the uniform temperature in Section 2 and the derived Eq. (5), the natural frequency of the structure under different temperature conditions is calculated and shown in Fig. 4. It can be seen from Fig. 4 that the natural frequency of the structure decreases with an increase in the uniform temperature, and the decrease is faster in higher modes.

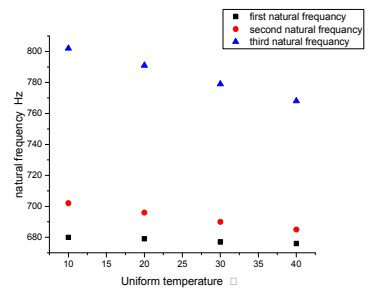

Fig. 4. Variation of Natural Frequency with Uniform Temperature

4.2 Variation of Dynamic Response of Continues Slab Track with Uniform Temperature

In this study, the dynamic excitation is simulated by a single wheel load of 250 kN With a frequency of 500 Hz. Taking the dynamic load and structure parameters into Eq. (5) and assuming a damping ratio of 0.35, the response of the structure under the single-wheel load is calculated and shown in Fig. 5, and the longitudinal propagation of the dynamic response at different temperatures is shown in Fig. 6.

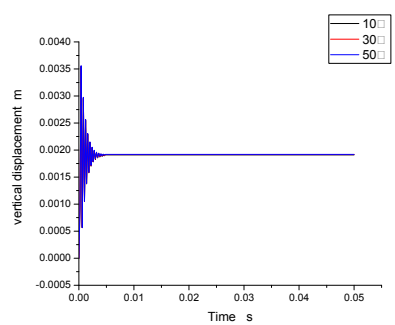

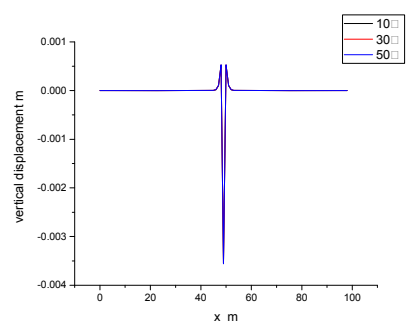

Fig. 5. Dynamic Response under wheel load. **Fig. 6**. Distribution of Displacement

From Fig. 5, the dynamic response of the structure is amplified with an increase in the uniform temperature, the vertical impact increases by 5.3% with a temperature increase of 50 ℃. From Fig. 6, the attenuation of the vertical vibration of the slab track tends to slow down with an increase in the uniform temperature, which is consistent with the conclusion in [4]. When the excitation frequency increases, the vibration travels farther along the longitudinal direction.

5. Conclusion

Through the discussion of the non-steady thermal effect on the dynamic characteristics of continues slab track structure, the following conclusions can be drawn:

(1) From Eqs. (5) and (6), it is concluded that the equivalent element stiffness matrix decreases because of the axial force increasing caused by uniform temperature rising .The natural frequency of the slab track decreases with an increase in the uniform temperature in the slab track. The f_1 of the slab track decreases by 1.5 Hz when the temperature increases by 10 ℃.

(2) From Fig. 5, it can be concluded that increasing the uniform temperature in the structure will amplify the impact response of wheelset to the track plate. When the temperature is increased by 50 ℃, the vertical displacement caused by the impact effect will increase by 2.5%.

(3) From Fig. 6, the attenuation of the vertical vibration in the slab track tends to slow down with increasing uniform temperature.

6. References

[1] Peng Pan, Xiaoyan Lei, Pengfei Zhang, and Shenhua Wu. “Analysis of vertical dynamic characteristics of ballastless track on bridge”. Urban rail transit research,2018,21(03):19-23+27.

[2] Qingyuan Zeng. “The principle of total potential energy with stationary value in dynamics of elastic system”. Journal of Huazhong University of Science and Technology. 2000(01):1-3+14.

[3] Junpu Zhu, Gonglian Dai, Haiting Su, and Jinbao Liang. “Representative Values of Temperature Action of the Box Girder-Track System Based on the Higher-Order Moment Method”.
Journal of Northeastern University Natural Science, 2017,38(08):1195-1200.

[4] Xiaoyan Lei. “Study on critical velocity and vibration boom of reack”.
Chinese Journal of Geotechnical Engineering. 2006(03):419-422.

Laboratory- and Field-Testing

Bridge Engineering Institute Conference 2019 (BEI-2019)
Honolulu, Hawaii, USA, July 22-25, 2019

Anchorage of Epoxy-Coated Rebar Post-Installed Using Chemical Adhesives

Connor Mills[1] and Benjamin Z. Dymond[2*]

[1] Collins Engineers, Inc., Chicago, IL, USA; email: mills372@umn.edu
[2] Dept. of Civil Engineering, University of Minnesota Duluth, Duluth, MN, USA; email: dymond@d.umn.edu

[*]: corresponding author

Keywords: post-installed; rebar; chemical adhesive; epoxy coating; bond strength

Abstract: Post-installed reinforcement is used to connect a new concrete member to an existing concrete structure. Typically, an uncoated reinforcing bar post-installed with a chemical adhesive is used in these applications, which may lead to corrosion. Bridge owners have used, and continue to use, epoxy-coated reinforcing bars in post-installed applications due to its inherent corrosion resistance. Unfortunately, chemical adhesive manufacturers provide tensile bond strengths of their products for use with uncoated reinforcing bars and not for use with epoxy-coated reinforcing bars. This research project examined what effects the epoxy coating had on the tensile bond strength by comparing the results for epoxy-coated and uncoated reinforcing bars. Four different chemical adhesive products were used to post-install both epoxy-coated and uncoated reinforcing bars, a total 48 pullout tests were conducted. Results indicated that the epoxy coating slightly reduced the tensile bond strength of the post-installed reinforcing bars. The ratio of the tensile bond strength of the epoxy-coated reinforcing bars to the tensile bond strength of the uncoated reinforcing bars ranged from 0.94 to 1.04 and varied based on the chemical adhesive manufacturer. Results from *t*-test analyses indicated that differences in the tensile bond strength for epoxy-coated reinforcing bars compared to uncoated reinforcing bars were not statistically different for two of the three of the chemical adhesives that experienced bond failure. A new bond strength reduction factor ($\psi_{e,Na}$) was recommended for use when calculating bond strength in accordance with ACI 318-14 for an epoxy-coated reinforcing bar post-installed using a chemical adhesive.

1. Introduction

Concrete anchors are elements that are used to transmit applied loads into structural concrete. Concrete anchors are divided into two groups based on installation timing: cast-in-place anchors and post-installed anchors. Cast-in-place anchors are installed before the concrete is hardened and post-installed anchors are installed into existing, hardened concrete. Post-installed concrete anchors are further divided into two groups based on the method of restraining the post-installed anchor: bonded and mechanical. Bonded post-installed concrete anchors are divided into two groups by bonding agent: chemical adhesive and grouted. Anchorage systems post-installed with a chemical adhesive can include different anchor elements, such as threaded rods, internally threaded sleeves, or reinforcing bars. This research investigated reinforcing bars post-installed with a chemical adhesive, which have become popular because of their flexibility in retrofit construction applications and in new construction applications. Typically, uncoated reinforcing bars are post-installed with a chemical adhesive. However, uncoated reinforcing bars may corrode in bridge applications, leading some bridge owners specify use of epoxy-coated

reinforcing bars. According to limited research, it is believed that use of post-installed epoxy-coated reinforcing bars could result in different tensile bond strengths compared to post-installed uncoated reinforcing bar (Dicky, 2011; Meline et al., 2006). The purpose of this research was to compare the difference in tensile bond strength of epoxy-coated and uncoated reinforcing bars post-installed with a chemical adhesive.

2. Experimental Program

A total of 48 tests using four chemical adhesive products were conducted to investigate the effect the epoxy-coating has on the tensile bond strength of reinforcing bars post-installed with a chemical adhesive (Mills, 2018). The tests were conducted in accordance with ACI 355.4 (2011) and ASTM E488 (2015); they were performed as confined tests in uncracked concrete (test number 7a from ACI 355.4) to encourage bond failure as the limiting tensile pullout strength. The test jig, built in accordance with ASTM E488 (2015), can be seen in Figure 1. The constant variables for the experimental program were the specified concrete strength of 27.6 MPa (4,000 psi), the reinforcing bar size of #16 (#5), and the embedment depth of 12.7 cm (5 in.) or $8d_b$. The variables that were investigated included the reinforcing bar type (24 tests for epoxy-coated and 24 tests for uncoated), and the chemical adhesive (six tests for each of the four adhesives: A, B, C, and D). The chemical adhesives were selected from a department of transportation Qualified Products List and not specifically selected based on any measurable metric.

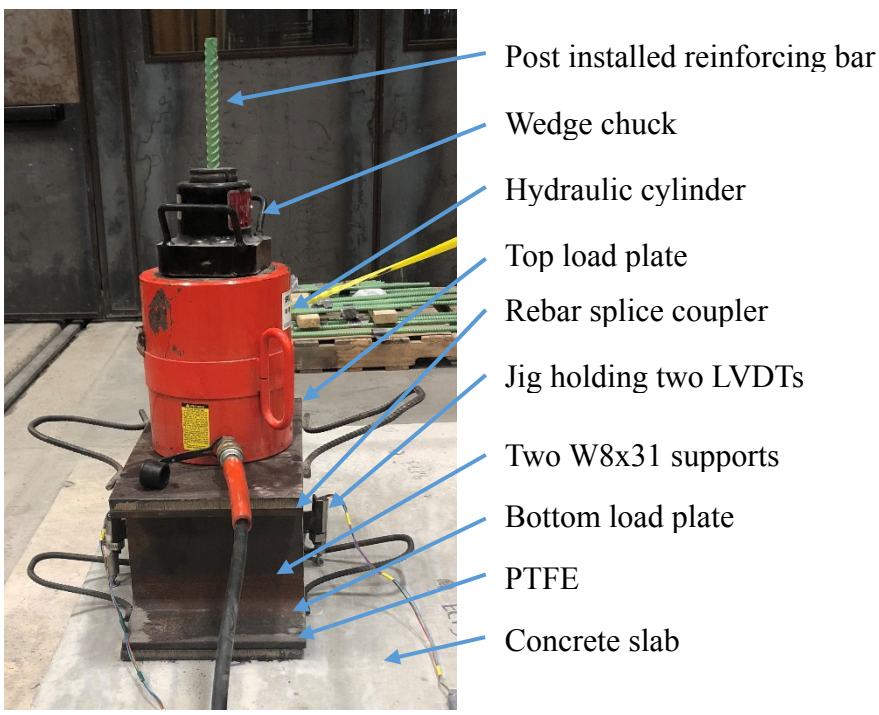

Fig. 1. Tensile pullout test jig constructed in accordance with ASTM E488 (2015) and used to pull out uncoated and epoxy-coated #16 (#5) reinforcing bars embedded 12.7 cm (5 in.).

3. Experimental Results and Discussion

Bond failure was the observed failure mode for the majority of the tests. Typically, bond failure occurred at the interface between the concrete and chemical adhesive for the epoxy-coated

reinforcing bars and bond failure occurred at the interface between the steel and the chemical adhesive for uncoated reinforcing bars. Steel rupture was the observed failure mode for all off the specimens built with chemical adhesive C and for two of the specimens built with epoxy-coated rebar and chemical adhesive D. Data from the tests where steel rupture was observed were not included in the analysis of the experimental results because the purpose of this research was to compare the difference in tensile bond strength of epoxy-coated and uncoated reinforcing bar post-installed with a chemical adhesive and not the differences in steel bar strength. The average tensile bond strength for the epoxy-coated reinforcing bars ranged from 132.60 kN (29.81 kips) to 143.46 kN (32.25 kips), while the average tensile bond strength for the uncoated reinforcing bars ranged from 137.89 kN (31.00 kips) to 140.34 kN (31.55 kips). The ratio of the tensile bond strength of the epoxy-coated reinforcing bars to the tensile bond strength of the uncoated reinforcing bars was 0.94, 0.97, and 1.04 for adhesives A, B, and D, respectively. The average tensile bond strength and the ratios of the tensile bond strength for each of the adhesives are shown in Table 1.

Table 1. Standard deviation analysis comparing tensile bond strength of epoxy-coating and uncoated reinforcing bars.

Adhesive	A		B		D	
Reinforcing bar coating	Epoxy	Uncoated	Epoxy	Uncoated	Epoxy	Uncoated
Tensile bond strength kN (kips)	132.60 (29.81)	140.34 (31.55)	134.87 (31.32)	139.10 (31.32)	143.46 (32.25)	137.89 (31.00)
Ratio of epoxy-coated to uncoated tensile bond strength	0.94		0.97		1.04	
Standard deviation of tensile bond strength kN (kips)	5.47 (1.23)	3.34 (0.75)	4.23 (0.95)	6.54 (1.47)	3.25 (0.73)	5.16 (1.16)
Tensile bond strength reduced by three standard deviations kN (kips)	116.19 (26.12)	130.33 (29.30)	122.19 (27.47)	119.48 (26.86)	133.71 (30.06)	122.42 (27.52)
Ratio of epoxy-coated to uncoated tensile bond strength reduced by three standard deviations	0.89		1.02		1.09	

Results from *t*-test analyses indicated that, statistically, epoxy-coated reinforcing bars post-installed with adhesive A had a lower ultimate tensile pullout strength compared to uncoated reinforcing bars (6% lower). Results from the *t*-test analyses indicated that, statistically, the ultimate tensile pullout strength was the same for both epoxy-coated and uncoated reinforcing bars post-installed using adhesives B and D. Furthermore, analysis considering the standard deviation of the tensile bond strengths was conducted. The average tensile bond strengths of both the epoxy-coated and uncoated reinforcing bars were reduced by three standard deviations to encompass 99% of the normal distribution. The minimum ratio of the reduced tensile bond

strength of the epoxy-coated reinforcing bars to the reduced tensile bond strength of the uncoated reinforcing bars was 0.89, which is shown in Table 1.

4. Conclusions and Recommendations

A broad conclusion could not be drawn in regards to how the epoxy coating affected the tensile bond strength of the post-installed reinforcing bars considering all of the different chemical adhesives in one group. The difference between the tensile bond strength of post-installed epoxy-coated and uncoated reinforcing bars was dependent on the chemical adhesive. Based on the results and analysis of this experimental program, it is recommended that an epoxy-coating modification factor be included when calculating bond strength in accordance with ACI 318 (2014) Equation 17.4.5.1a (Equation 1) for epoxy-coated reinforcing bars post-installed using chemical adhesives. The proposed modification factor would be $\psi_{e,Na}$ = 0.9 for epoxy-coated reinforcing bars or $\psi_{e,Na}$ = 1.0 for uncoated reinforcing bars. The modification factor value of 0.9 was chosen because it encapsulates the lowest ratio of the tensile bond strength of the epoxy-coated reinforcing bars to the tensile bond strength of the uncoated reinforcing bars from the laboratory experimental program (adhesive A ratio = 0.94), while still providing a built-in factor of safety considering results from the standard deviation analysis (adhesive A ratio = 0.89).

$$N_a = \frac{A_{Na}}{A_{Nao}} \psi_{ed,Na} \psi_{cp,Na} \psi_{e,Na} N_{ba} \tag{1}$$

5. References

ACI Committee 318. 2014. Building code requirements for structural concrete (ACI 318-14) and commentary, American Concrete Institute, Farmington Hills, MI.

ACI Committee 355. 2011. Qualification of post-installed adhesive anchors in concrete (ACI 355.4-11), American Concrete Institute, Farmington Hills, MI.

ASTM International. 2015. ASTM E488-15 Standard Test Methods for Strength of Anchors in Concrete Elements, American Society for Testing and Materials (ASTM), West Conshohocken, PA.

Dickey, B. 2011. Development of a design procedure for concrete traffic barrier attachments to bridge decks utilizing epoxy concrete anchors, M.S. Thesis, University of Nebraska Lincoln, Lincoln, NE.

Meline, R. J., Gallaher, M. and Duane, J. 2006. Seismic, creep, and tensile testing of various epoxy bonded rebar products in hardened concrete, Report Number CA06-0247, California Department of Transportation, Sacramento, CA.

Mills, C. 2018. Anchorage of Epoxy-Coated Rebar Using Chemical Adhesives, M.S. Thesis, University of Minnesota Duluth, Duluth, MN.

Experimental Study of RC Beam-Column Joints with Different Bonding Interfaces

Minho Kwon[1], Hyunsu Seo[2], Gyubin Kwon[3], and Jinsup Kim[4*]

[1] Dept. of civil Engineering, ERI, Gyeongsang National University, Jinju, South Korea; email: kwonm@gnu.ac.kr
[2] Dept. of civil Engineering, ERI, Gyeongsang National University, Jinju, South Korea; email: flyfromyou00@gmail.com
[3] Dept. of civil Engineering, ERI, Gyeongsang National University, Jinju, South Korea; email: guseo123486@gmail.com
[4] Dept. of civil Engineering, ERI, Gyeongsang National University, Jinju, South Korea; email: jinsup.kim@gnu.ac.kr

[*]: corresponding author

Keywords: beam-column; different bonding; rubber tube; degradation of cohesion; ductility; un-bonded reinforcement

Abstract: This study was focused on experimental evaluation of RC beam-column joints (L-type and U-type) with different bonding interfaces in the beam area. Due to deterioration of the concrete, the reinforcement inside starts to corrode because there is no longer concrete around it to prevent exposure to the outside environment. Such corrosion causes serious degradation of the cohesion between the reinforcement and the concrete, and the performance capacity of the bonding between concrete and rebar. In this research, the behavior of beam-column joints specimen with different bonding interface were evaluated. The experimental test results show that when L-type and U-type specimens were un-bonded, the maximum strength decreased while the yield displacement increased. The strength decreased due to activity between the rebar and concrete caused by non-bonding, but the ductility increased. The bonded specimens showed both flexural and shear cracks, but the un-bonded specimens showed flexural cracks only. Contrary to the increase in ductility, the strength decreased, which resulted in a lower energy dissipation capacity in the case of un-bonded specimens. From the accumulated energy dissipation, it was indicated that the displacement at yield increased due to the un-bonded rebar, but the energy dissipation did not increase due to the significant strength reduction.

1. Introduction

The beam-column joints are important part in the safety of reinforced concrete structures. Recently, some researches have been conducted on a variety of issues related to evaluation of the seismic performance of joints. Most of them were experimental studies on the performance of beam-column joints. Clyde et al. (2000) and Pantelides et al. (2002) performed cyclic tests on exterior beam-column joints with an axial load. In their research, the joints were designed shear failures before the yield of the beam rebars. The longitudinal and transverse rebar in the beam, and the column transverse rebar, were increased to prevent early degradation of the beam and column, forcing a shear mode of failure in the joint. Hwang et al. (2005) performed tests on exterior joints having different reinforcement details. Their studies were aimed at obtaining elementary data on the RC beam-column joints of reinforced concrete subjected to loss of

cohesion between the steel and concrete due to serious corrosion. This study evaluated the performance of RC beam-column joints with different bonding interface in the beam area. Two types of joints were contacted, U-type and L-type. Rubber tubes were installed over the beam reinforcement in plastic hinge zone to simulate the loss of adhesive capacity. Both the cyclic behavior of the RC beam-column joints were evaluated under lateral cyclic loadings.

2. Experimental test

Seismic performance of RC beam-column joints that had different bonding interfaces between the concrete and reinforcement due to the corrosion was evaluated. The specimens were designed and constructed according to the ACI Committee 318-95 (ACI 318-95, 2011). The section dimensions of the test specimens and the anchorage type and length of the reinforcement were shown in Figure 1.

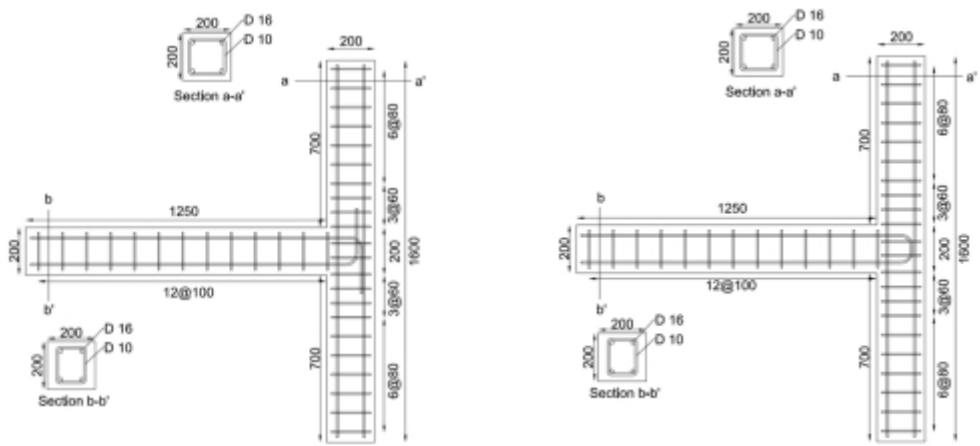

(a) (b)

Fig. 1. Dimension of specimens: (a) L-Type; (b) U-type

The anchorage type affects the destruction of the beam-column joints (Pampanin et al, 2002). Thin rubber tubes were installed in the hinge zone of the beam to simulate un-bonding between concrete and rebar. Four specimens divided two groups were evaluated: two specimens have L-type rebar and the other two specimens have U-type rebar. Each group had two types of interfaces: bonded (LBD and UBD) and un-bonded (LUD and UUD). Yield strength of reinforcement was 400 MPa. The compressive strength of concrete was 24 MPa at 28-day. Test setup for the beam-column speciemens was set up. In order to apply a constant axial load, an oil jack with 200 kN capacity was used. A constant axial load of 84 kN (corresponding to approximately 0.1×Ag×fck) was applied. An actuator with 500-kN capacity was installed in the reaction wall.

3. Results and Discussions

The crack patterns of tested specimens are shown in Figure 2. Both shear and flexural cracks observed in the LBD and UBD, while only flexural cracks observed in the LUD and UUD specimen.

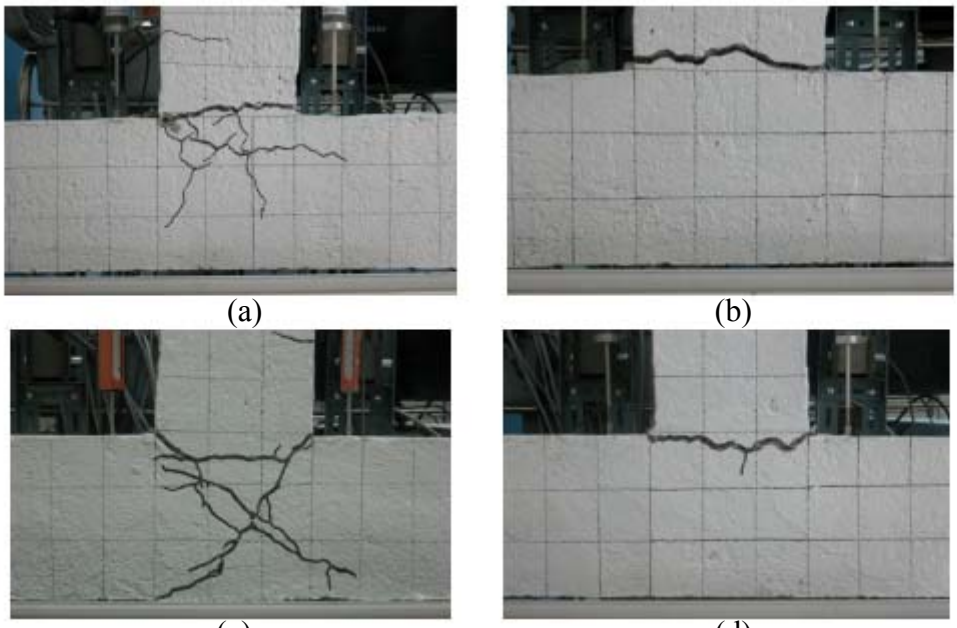

(a) (b) (c) (d)

Fig. 2. Crack distributions at final loading: (a) LBD; (b) LUD; (c) UBD; (d) UUD

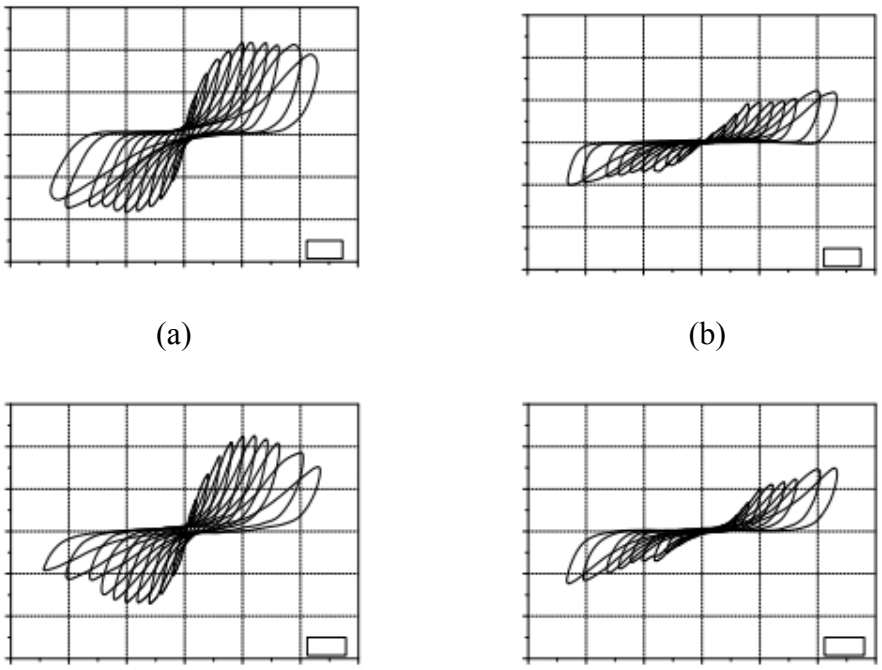

(a) (b) (c) (d)

Fig. 3. Load-displacement relations: (a) LBD; (b) LUD; (c) UBD; (d) UUD

Figure 3 shows the lateral load–displacement relationship of the specimens. Experimental test results are summarized in Table 1. The test results of the strength and displacement of the L- and U-type specimens indicate that the maximum strength of the un-bonded specimens was decreased, and that the displacement at peak strength increased due to slip that occurred in the joint. Moreover, U-type specimens exhibited less strength and greater deformation at the peak than did L-type specimens.

Table 1. Test results at maximum load

Specimen	Max. Load (kN)	Ratio (%)	Disp. (mm)	Ratio (%)
LBD	22.2	100	58.3	100.0
LUD	12.6	56.7	101.0	173.2
UBD	23.0	100	61.4	100.0
UUD	15.5	67.1	115.6	188.3

4. Conclusions

In this research, the behavior of beam-column joints specimen with different bonding interface were evaluated. The experimental test results show that when L-type and U-type specimens were un-bonded, the maximum strength decreased while the yield displacement increased. The strength decreased due to activity between the rebar and concrete caused by non-bonding, but the ductility increased. The bonded specimens showed both flexural and shear cracks, but the un-bonded specimens showed flexural cracks only. Contrary to the increase in ductility, the strength decreased, which resulted in a lower energy dissipation capacity in the case of un-bonded specimens. From the accumulated energy dissipation, it was indicated that the displacement at yield increased due to the un-bonded rebar, but the energy dissipation did not increase due to the significant strength reduction.

5. Acknowledgments

This research was supported by a grant (19SCIP-B146946-02) from Construction technology research program funded by Ministry of Land, Infrastructure and Transport of Korean Government

6. References

American Concrete Institute (ACI-318) 2011, Building Cod e Requirements for Reinforced Concrete, Farmington Hills, MI.

Clyde C, Pantelides CP, Reaveley LD. 2000. Performance-based evaluation of exterior reinforced concrete building joints for seismic excitation, Report PEER 2000/05. Pacific Earthquake Engineering Research Center.

Hwang SH, Lee HJ, Liao TF, Wang KC, Tsai HH. “Role of hoops on shear strength of reinforced concrete beam–column joints”, ACI Structural Journal, 102(3), pp. 445-53 (2005).

Pampanin S, Calvi GM, Moratti M. 2002. Seismic Behaviour of RC Beam-Column Joints Designed for Gravity Loads", 12th ECEE, London, paper n. 726.

Pantelides CP, Hansen J, Nadauld J, Reaveley LD. 2002. Assessment of reinforced concrete building exterior joints with substandard details." Report no. PEER 2002/18. Pacific Earthquake Engineering Research Center (2002).

A Case Study on the Evaluation of Structural Conditions for an Existing Bridge Using Position Sensitive Detector (PSD) Device

Kenji Tada[1*], Masayuki Hyodo[2], Takaaki Miyasaka[3], and Jimmy Oshiro[4]

[1] Just Ltd., Japan; email: tada@just-ltd.co.jp
[2] Graduate School of Sciences and Technology for Innovation, Yamaguchi University, Japan; email: hyodo@yamaguchi-u.ac.jp
[3] Jibansogokenkyujo (Advanced Geotechnical Research Institute). Tokyo, Japan; email: agri@jibansogokenkyujo.com
[4] Environmental Science Corporation, Japan; email: j.oshiro@kankyoscience.com

[*]: corresponding author

Keywords: structural conditions; PSD device; pier; non-contact measuring device; deformation; vibration; attenuation

Abstract: A study for the evaluation of the structural conditions for an existing bridge using position sensitive detector (PSD) technology is presented in this paper. Comparing to other traditional methods, which commonly requires direct contact to the structure with a complex wire deployment, however; non- contact real-time displacement measurement is the best method to assess the structural integrity where other physical characteristics such as velocity and acceleration can be easily derived without deviation. To achieve the above mentioned purpose, the new developed PSD device is applied in this case study. The PSD based displacement measuring system is composed of two parts: the LED targets which emit the spot lights and the PSD V-Cam which captures the spot lights. To verify the performance and reliability of the PSD device, a series of impact test were conducted onto a bridge structure. Moreover, nonlinear dynamic response analysis was performed based on a fine-tuned finite element model. Comparison on both time history and frequency domain analysis has demonstrated that the measured data and the analysis result fit well each other.

1. Introduction

Up to present day, most of the bridge health checks are focused on the structure members and performed with visual inspection. However the conventional health check is unable to offer sufficient information on the integrity of entire structure. To assess the structural integrity, real time high precision deformation measurement is the best method. Based on measured deformation data, valuable information such as the maximum deformations, the vibration characteristics, the fundamental frequency and the attenuation ratio of the bridge structure can be acquired. This case study was performed in Taiya Bridge's piers in Taiwan which is supported on caisson foundations (Figure 1). The river bed level was getting lower year by year resulting in the scouring of foundations. Thus, most of the caisson foundations were seriously exposed and there was a concern about their lateral bearing capacities. In 2009, retrofitting work has been officially determined. To check the effect of retrofitting work, the measurement of its dynamic response before and after the retrofitting work was performed. In this paper, only the data collected before the retrofitting is discussed. In this study, a newly developed PSD device based on non-contact real-time deformation

measurements was used. This device is composed of two parts: the LED targets which emit the spot lights, and the PSD V-Cam which captures the LED targets' spot lights. A single target was mounted onto the side face of the pier's cap beam. A 60 kg timber log (Figures 2 and 3) was employed for the impact. PSD V-Cam was set directly on the ground level outside the caisson foundation. After the data acquisition, FFT analysis was used to acquire the fundamental frequencies. Finally nonlinear dynamic response analysis was performed to simulate the pier's dynamic behavior.

Figure 1. Taiya Bridge View

Figure 2. Impact Test

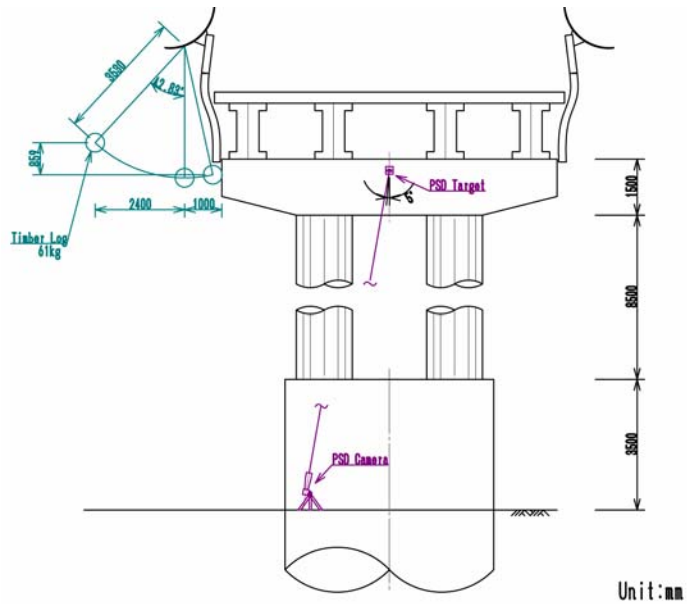

Figure 3. Impact Test Configuration (Pier 31)

2. Impact Test Results

The real time lateral and longitudinal deformation curves at the top of the tested pier 31 (P31) cap beam subjected to consecutive six impact loads are shown in Figure 4.

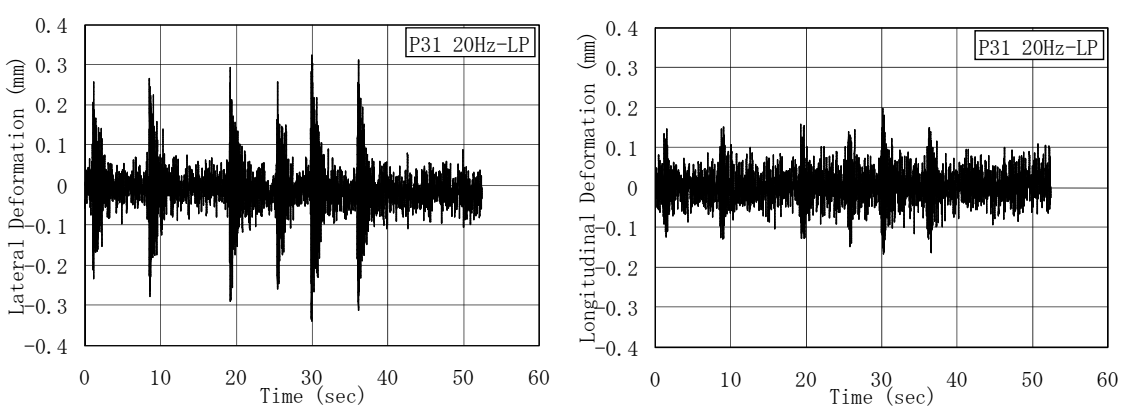

Figure 4. Real Time Deformations at Top of Cap Beam (P31)

The lateral and longitudinal deformation curves caused by the last impact are enlarged and shown in Figure 5. Some observations from this figure are:

1. The maximum lateral deformation is 0.31mm.
2. It takes 0.17sec for the lateral deformation to attenuate to the original status.
3. The lateral attenuation ratio is approx. 0.01.
4. The fundamental frequency in lateral direction is approx. 16Hz.
5. The maximum longitudinal deformation is 0.15mm.

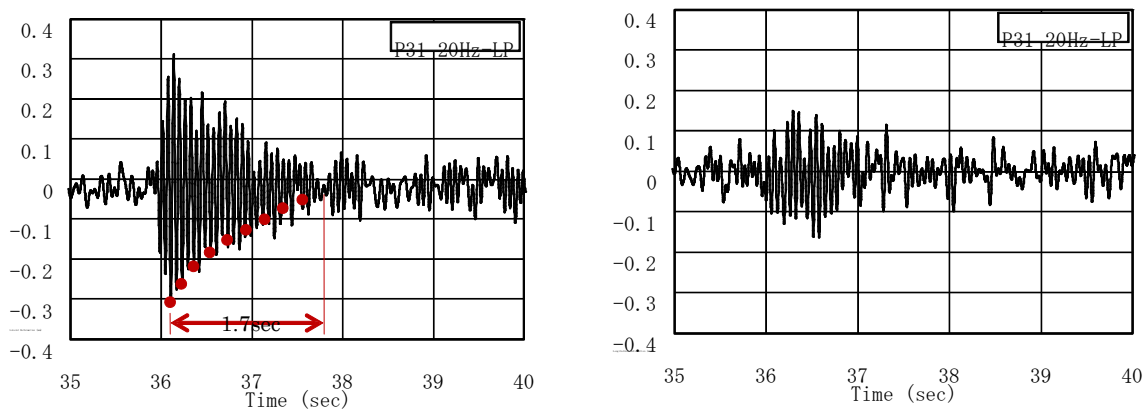

Figure 5. Real Time Deformation at Top of Cap Beam (P31) for the last impact record

The FFT analysis result of P31 is shown in Figure 8. Apparently P31 has a fundamental frequency of 15.7Hz. This frequency is the same as that acquired from the measured deformation curve. This fundamental frequency can also be acquired during the daily traffics loading without applying any impact force. It was considered that this frequency is high enough to assume that this pier is structurally sound. For example, similar analysis for piers 26, 27, 28 revealed low frequencies of 3.5, 0.9 and 0.9 Hz, respectively. These low frequencies may indicate some structural deficiencies in these piers which were actually retrofitted.

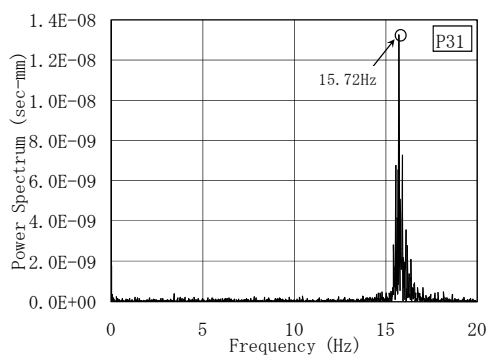

Figure 6. Fundamental Frequency of P31

3. Simulation Analysis

To simulate the pier's dynamic behaviours, Finite Element Method (FEM) Program Midas is employed to perform the nonlinear dynamic response analysis. The pier is modelled by 3 dimension solid element as shown in Figure 6. Material's nonlinear property is considered in the simulation analysis. Input external impact force is shown in Figure 7.

Figure 6. Simulation Model

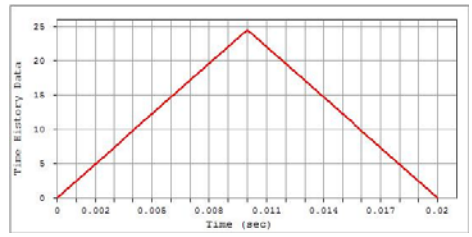

Figure 7. Input Impact force

The first and the second impact test results are simulated. The simulation results are shown in Figure 8. Both figures show that the deformations reach the maximum value soon after the application of the impact force, and then attenuate gradually to their original status. Both cases show that the attenuation rate is very slow and the attenuation ratio is approximate 0.01. The significant difference in the amplitudes of the first wave may be caused by the inefficiency of the real impact. However, the rest of the measured values well agree with the computed values.

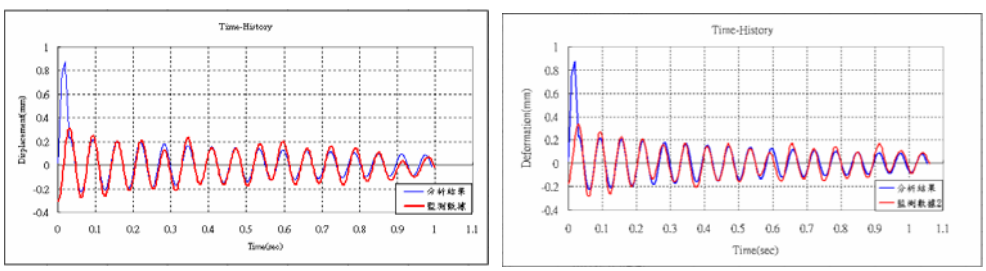

Figure 8. Deformation time histories of P31

4. Conclusions

In this paper, a newly developed PSD method based on dynamic behaviour measuring device and a practical application of this device on a bridge pier health check are introduced. Through this application, followings are concluded.

1. PSD device possesses the capability to precisely measure the dynamic behaviours of bridge pier structures, and to assess their characteristics of deformation, vibration, and attenuation.
2. Comparisons on both deformation time history and fundamental frequency have demonstrated that the measured data and the analysis result fit well each other. The applicability and effectiveness of this measuring method particularly on the bridge substructures to check up their integrity are verified through this study.

5. References

Yu-Chi Sung, Takaaki Miyasaka, Tzu-Kang Lin, Chun-Ying Wang and Chung-Yue Wang; A case study on bridge health monitoring using position-sensitive detector technology; Struct. Control Health Monit. (2011); Published online in Wiley Online Library (wileyonlinelibrary.com). DOI: 10.1002/stc.436

Structural Stability and Fatigue Resistance of Precast Concrete Barriers Installed Using Anchors and Epoxy Resin

Kazuya Sakamoto[1*], Yoshikazu Akira[2], Koji Takewaka[3], and Toshinobu Yamaguchi[4]

[1] Kagoshima University, Kagoshima, Japan; email: sakamoto_k@infratec.co.jp
[2] Kagoshima University, Kagoshima, Japan; email: akira@oce.kagoshima-u.ac.jp
[3] Kagoshima University, Kagoshima, Japan; email: takewaka@oce.kagoshima-u.ac.jp
[4] Kagoshima University, Kagoshima, Japan; email: yamaguch@oce.kagoshima-u.ac.jp

[*]: corresponding author

Keywords: precast concrete; bridge barrier; epoxy resin mortar; steel anchor; reinstallation technology

Abstract: In this study, we focused on the replacement of old concrete bridge barriers with precast concrete barrier using a combination of anchors and epoxy resin mortar to ensure rigid connection between existing foundation slab and the precast member. The structural stability of the whole assembly is determined by applying flexural load. It was found that the cone-shaped fracture strength of the joint was improved by the anchor-epoxy combination. The proposed connection method also showed high fatigue resistance.

1. Introduction

Construction industry in Japan is facing problems of managing several aging structures built during the economic boom. Specifically, bridge and highway barriers used as protective fence and as sound barrier are on the verge of reinstallation. In Japanese highway bridges, roads often exist under high bridges, so falling concrete can cause catastrophes. These deteriorating structures must be repaired or reinstalled. Also, the economic constraints and labor shortages have attracted fast and easy construction methods. From this background, one such technology that can offer easy and quick construction, without affecting the traffic, is the precast concrete technology. In conventional reinstallation using anchors and grouting, the problem of foundation thickness and strength affects the pull out strength of the anchors. Embedding anchors may also be a complicated task due to the densely existing reinforcing bars in the foundation. Therefore, in this study, anchor and epoxy mortar together were used as a method of integrating precast barrier and existing foundation. The adhesive force of the epoxy will also improve the pull out strength required for the embedded anchor. This method is expected to substantially reduce the number of anchors and their embedding depth. The structural performance and durability of the proposed construction method was studied by conducting series of experiment. The performance of the present connection method under fatigue loads was also studied.

2. Pull-out strength

2.1 Experimental

A laboratory model simulating the actual connection was set up as shown in Fig.1(i). D10 threaded bolts were used as anchors. Epoxy mortar was made by mixing epoxy, hardener and a

filler material. The filler helps in reducing the shrinkage of epoxy (Ferdous et al. 2016). A 20mm layer of epoxy mortar above the surface was also made simulating the gap between actual foundation and the barrier. For comparison, 3 specimens were used (a) anchor + epoxy mortar, (b) anchor + non-shrinking mortar and (c) anchor only.

2.2 Results

Cone type fracture was observed in all cases. The pull out load in specimen (a) was 21.9kN, specimen (b) was 13.3kN and specimen (c) was 12.8kN. The pull out strength increased because the effective projection area of cone (Fig.1(ii)) due to cone fracture became larger in anchor-epoxy mortar (Maeno et al. 1992).

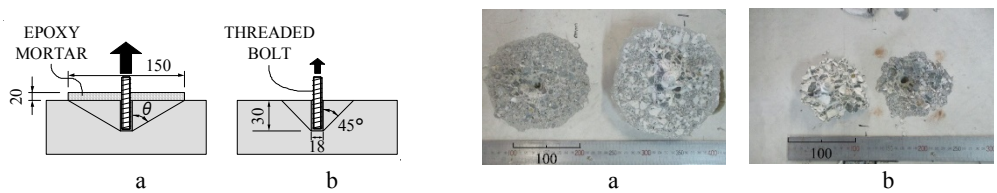

(i) (ii)

Fig. 1. Pull-out cone fracture, (i) specimen setup/cone fracture mechanism (ii) picture after the pull out test

3. Verification of rigidity of connection by static load test

3.1 Experimental

In this test, blocks were prepared simulating the precast member and the existing foundation slab, joined by a method similar to the actual construction. The specimen setup is shown in Fig.2(i) (scale model). The concrete specimens were prepared with mix proportion (in kg/m^3) shown in Table 1 and the average 14-day compressive strength was 41.6MPa.

Table 1. Concrete mix proportion

W/C (%)	Water (W)	Cement (C)	Limestone fine powder	Fine aggregate	Coarse aggregate	High performance water reducing agent
51.5	172	334	201	755	903	5.80

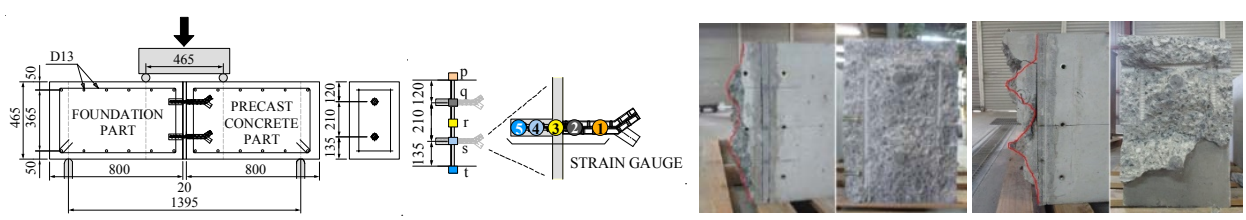

(i) (ii) (iii) (iv)

Fig. 2. (i) loading condition, (ii) location of strain gauges, (iii) failure face of Specimen A, (iv) failure face of Specimen B

Specimen consisted of 2 parts, the foundation part and the precast concrete part each 800×300×465mm^3. Holes with diameter 35mm, depth 90mm were drilled on the foundation

part. Anchors (SD345, D16, and 80mm length) were prefixed in the precast block part. The precast block fitted with anchor was mounted on the foundation part to form a 20mm gap which was later filled with epoxy mortar ("Specimen A"). For comparison, specimens using non-shrinking mortar ("Specimen B") for the gap filling part (anchor grout using epoxy) were prepared and static flexural loading test was carried out in the same way. The static load test was performed as shown in Fig.2(i). The loads at predetermined steps, the strain around the specimen joint and in the anchors until breakage were monitored.

3.2 Test results

The fracture load of Specimen A was 135kN and for specimen B was 70.2kN. The effect of anchor-epoxy combination was significant. The fracture condition is shown in Fig.2(iii)(iv). It was found that the cone fracture angle of specimen A was larger resulting in higher pull-out strength. Fig.3 (i)(ii) show the load-strain relation at the mortar surface around the joint. The position of strain gauges around the joint are shown in Fig.2(ii). In the Specimen A, the strain on the epoxy joint was observed on the compression side and the tension side, but at much higher load without de-bonding until failure at 135kN. The load versus strain was approximately linear up to about 80kN and in the elastic range. Regarding Specimen B, adhesion at the joint was insufficient, and cracks already occurred at the initial stage of loading. The specimen failed at lower loads around the joint with very slight strain at the tension side. The load versus strain in anchors on the tension side are shown in Fig.3(iii)(iv). The position of gauges on the tension anchors are shown in Fig.2(ii). It was found that the strain in the anchor of Specimen A was relatively small up to a load of 100kN, and then increased steeply. This is consistent with the case when the concrete strain on the tension side of the joint decreased when load exceeded 100kN (Fig.3(i)), that is when the anchor began to bear the load simultaneously with the breakdown of the epoxy mortar. In Specimen B, strain quickly developed in the anchor immediately after loading, exceeding 800με. The cone fracture strength of the concrete reached the failure limit. In any case, it was confirmed that the fracture load of Specimen A was about twice as large in comparison, and the effect of the anchor-epoxy system remarkably increased the integrity of the assembly.

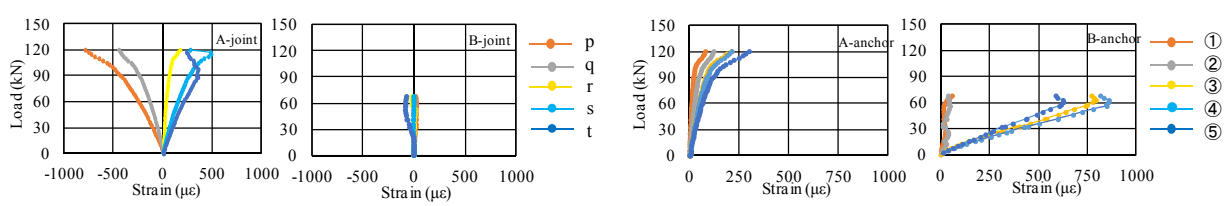

(i) (ii) (iii) (iv)

Fig. 3. Load versus strain, (i) epoxy mortar strain of Specimen A, (ii) non-shrinking mortar strain of Specimen B, (iii) anchor strain in Specimen A, (iv) anchor strain in Specimen B

4. Fatigue resistance test

4.1 Outline of test

Based on the previous studies on the vibration characteristics of actual bridge structure, fatigue resistance test was carried out at a frequency of 3Hz, up to 2 million loading cycles. The repeated loading test was performed with 53.2kN (collision load equivalent prescribed by

the code) (The specifications of railing design. 2004) as the upper limit and 13.5kN as lower limit. At the start of the test and when the number of cycles reached 50000, 500000, 1000000 and 2000000, the loading were stopped, and the static loading test was performed up to the upper limit load (53.2kN). At the time of the static loading, the strain at the joint position was measured, and the presence or absence of cracking etc. was monitored. After 2 million cycles, static loading was carried out until the specimen failed, and compared with specimen not subjected to fatigue cycles.

4.2 Results

Fig.4(i) shows the load-strain relationship at the joint of the specimen for every cyclic stage. No significant change in the load-strain curve was seen even after large repetition. The straight line slope did not change over the course of repetitive load. The maximum strain was equal to the initial value at the start of the test. Specimen did not fail after 2 million loading cycles. The failure load at the final static loading test was 102.5kN, about 76% of the specimen not subjected to fatigue test (Fig.4(ii)). Cone type fracture was observed and the decrease in strength could be due to the fatigue of concrete around the interface of concrete and epoxy mortar.

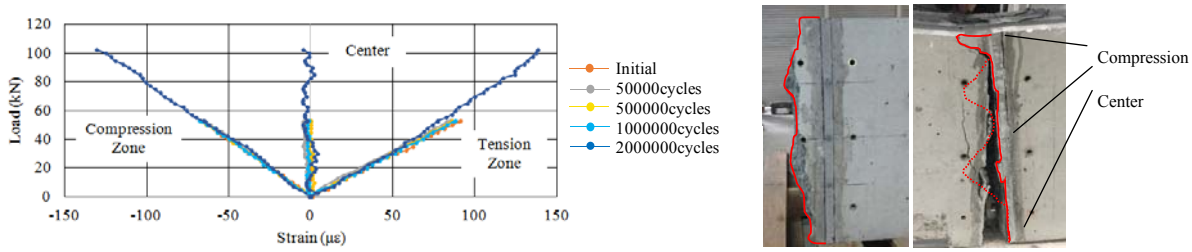

(i) (ii)

Fig. 4. Results of fatigue test, (i) load vs. strain in the epoxy mortar joint, (ii) fractured face, left: specimen not subjected to fatigue, right: specimen subjected to fatigue

5. Conclusion

Performance of the combination of anchor and epoxy resin as a connection technique for precast concrete was investigated. The major observations were:

- Combined use of anchor and epoxy mortar increased the pull out strength thereby increasing the bond between precast concrete members. The rigidity of bolted connections can be further improved by using epoxy as adhesive.
- Epoxy mortar showed high resistance to fatigue. The fracture took place at the concrete region and not in the epoxy mortar region which means that the concrete showed higher fatigue than epoxy mortar.

These results suggest that the technique may be an effective means in situations where there is limitation for anchor embedding depth and /or for the number of anchors.

6. References

Ferdous, W., Manalo, A., Aravinthan, T., and Erp, G. V. 2016. Properties of epoxy polymer concrete matrix: effect of resin-to-filler ratio and determination of optimal mix for composite railway sleepers, Construction and Building Materials, 124, 287-300.

Japan Road Association. 2004. The specifications of railing design (in Japanese)

Maeno, H., Goto, Y., Obata, M., and Matsuura, S. 1992. Ultimate strength of bond-type anchorage under tensile force, Journal of The Japan Society of Civil Engineers, 441/1-18, 185-192 (in Japanese).

Performance Evaluation According to Change of Combined Tensile and Shear Load Acting on Cast-in-Place Anchor Bolt

Yeongseok Jeong[1], Minho Kwon[2*], and Jinsup Kim[3]

[1] Gyeongsang National University, JinJu, South Korea; email: bihimos@gmail.com
[2] Gyeongsang National University, ERI, JinJu, South Korea; email: kwonm@gnu.ac.kr
[3] Gyeongsang National University, ERI, JinJu, South Korea; email: jinsup.kim@gnu.ac.kr

[*]: corresponding author

Keywords: cast-in-place anchor; PN-type bolt; pullout test; tensile-shear force

Abstract: Due to the anchor system is variously used in the construction for the connection between structural and non-structural members, the performance evaluation of the anchor system is very important for the design of structural safety. ACI-18 proposed the design equations for tensile and shear as well as combination load of tensile-shear force. In this study, the combinations of shear and tensile strength prediction of the anchor system based on the code are reviewed through the experimental study. In the experiment study, the loading angle and effective embedded depth was set these experimental parameters. In the experimental conditions of this study, the failure of an anchor under combined loading showed the dominant fracture behavior in shear strength, as the effective embedded depth deepened, this tendency was more pronounced. And if the loading angle of is less than 30°, the shear strength of the anchor material was the major failure mode.

1. Introduction.

Lately the frequency of post-installation anchors has increased due to their ease of construction (Kim and Park, 2016). However, due to reliability of anchor performance and availability of quality control, the construction of the pre-installed anchors is still considered primarily for connections of heavy structures, large frame structures, etc. In particular, earthquakes with a magnitude of 6.0 or higher have occurred in Korea recently, and minor earthquakes have frequently occurred in Korea. For this reason, research is required on conditions where shear and tensile loads are combined to act on anchors, such as earthquakes. In this study, we experimentally investigate the change of anchor performance according to the combination load and the effective embedment depth change for the cast-in-place anchor.

2. Experimental program

Fig. 1 shows the mechanical model of the line anchor under combined load of tension and shear. This section describes the preparation process for the experiment.

2.1. Test parameters

The method of evaluating the performance of anchors embedded in concrete without reinforcement can be calculated using the expression given in ACI318-14. As shown in Fig. **14**1, the failure mode of the anchor is classified as tensile and shear failure, and the strength formula for the failure mode is arranged in Table 1.

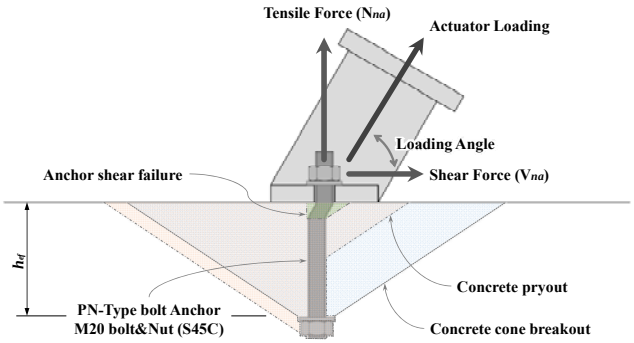

Fig. 14. Test mechanism of cast-in-place anchor

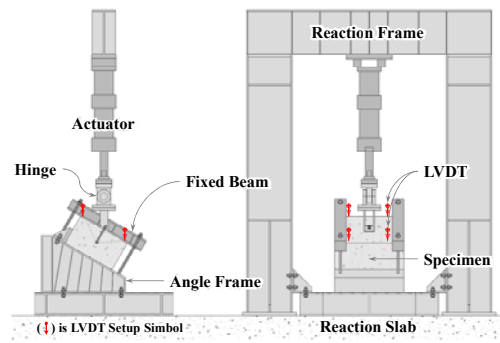

Fig. 2. Loading set up

Table 12. Cast-in-place anchor design equation (ACI 318, 2014; Korea Ministry of Land, 2012)

Tensile strength equation	Shear strength equation
Nominal strength of an anchor $N_{sa} = n A_{se,N} f_{uta}$ Pullout strength $N_p = 8 A_{brg} f_{ck}$ Concrete breakout strength $N_b = k_c \lambda \sqrt{f_{ck}}\, h_{ef}^{1.5} \leq 3.9 \lambda \sqrt{f_{ck}}\, h_{ef}^{5/3}$	Nominal strength of an anchor $V_{sa} = n\, 0.6 A_{se,V} f_{uta}$ Nominal pryout strength $N_p = k_{cp} N_{cb} = 2.0 N_b$ Concrete breakout strength $N_b = \left(0.6 \left(\frac{l_e}{d_a}\right)^{0.2} \sqrt{d_a}\right) \lambda \sqrt{f_{ck}} (c_{a1})^{1.5}$
Interaction of tensile and shear forces	
Traditional shear-tension interaction equation $\left(\frac{N_{ua}}{N_n}\right)^{\zeta} + \left(\frac{V_{ua}}{V_n}\right)^{\zeta} \leq 1.0$	Trilinear simplification interaction equation $\left(\frac{N_{ua}}{\phi N_n}\right)^{5/3} + \left(\frac{V_{ua}}{\phi V_n}\right)^{5/3} = 1.0$

The main factors determining the performance of an anchor in the equation of Table 12 are the cross sectional area of the anchor ($A_{se,N}$, $A_{se,V}$), tensile strength (f_{uta}), effective embedded depth(h_{ef}), variables (l_e, d_a, c_{a1}) and the compressive strength of the concrete (f_{ck}). The purpose of this experimental study is to verify the variation in the performance of the anchors according to the effective depth of the anchor and the loading angle as well as to compare the performances of anchor system between experiments and the design code. Therefore, the effective embedded depth of the anchor and the loading angle was determined as variables in experiment.

2.2. Test specimens and loading setup

The characteristics of the materials used in the test are shown in Table2. The size of the test specimen is designed based on a 200mm specimen. In the design of the test specimen, the width of the specimen is $3h_{ef}$ or more in consideration of the fracture area of the concrete cone failure mode due to the tensile load. The depth of the specimen is $2h_{ef}$ or more considering the strength margin against bending failure. Further, the test specimen is sufficiently secured against destruction by placing reinforcement bars on the concrete block considering the tensile and shear strength of the anchor by ACI formula. Therefore, the concrete block was designed as a reinforced concrete block of 900mm × 700mm × 400mm shows the loading setup and measurement plan of the test. The specimen is firmly secured through the fixed beam and stopper.

The combination of tensile and shear loadings acts as a load combination of fixed ratio according to the change of the loading angle by changing the installation angle of the specimen. The loading angles were considered as 0°, 30°, 60°, and 90°

Table 2. Specimen material property

Concrete	Anchor bolt			
Tensile Strength (MPa)	Bolt No.	Yielding Load (kN)	Ultimate Load (kN)	Cross-section Area (mm^2)
24	M20(S45C)	200	233	245

Table 3. Experiment result and failure mode, calculated combination load

Depth (mm)	Angle (Deg)	Act. Load (KN)	Tensile load (KN)	Shear load (KN)	Failure Mode
100 (ND10)	0°	100.92	0.00	100.92	Concrete pryout
	30°	90.23	45.11	78.14	Concrete pryout
	60°	70.28	60.87	35.14	Concrete cone breakout
	90°	64.07	64.07	0.00	Concrete cone breakout
150 (ND15)	0°	139.99	0.00	139.99	Anchor shear failure
	30°	130.41	65.21	112.94	Anchor shear failure
	60°	138.94	120.33	69.47	Concrete cone breakout
	90°	127.79	127.79	0.00	Concrete cone breakout
200 (ND20)	0°	140.69	0.00	140.69	Anchor shear failure
	30°	128.21	64.11	111.04	Anchor shear failure
	60°	183.69	159.08	91.84	Concrete cone breakout
	90°	207.14	207.14	0.00	Concrete cone breakout

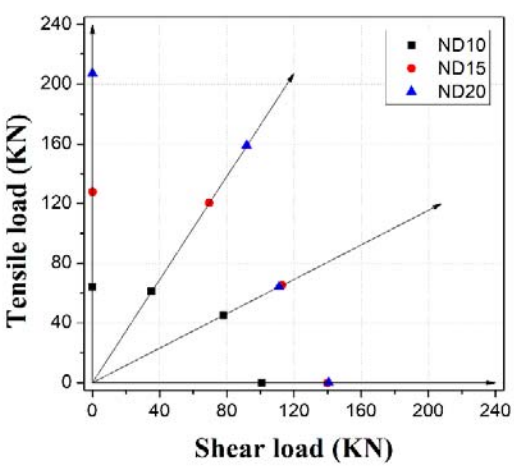

Fig. 3. Shear and tensile load curve

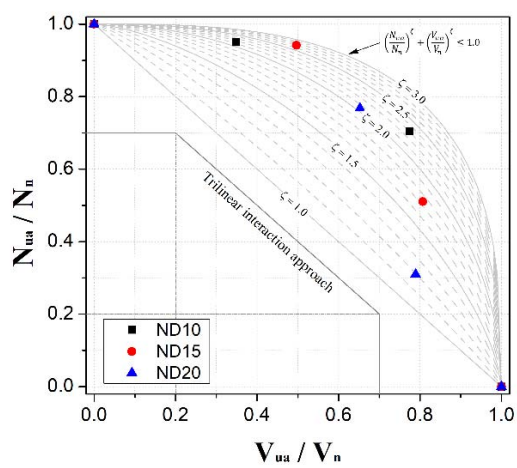

Fig. 4. Interaction of tensile and shear forces

3. Experimental results

Table 3 shows the maximum load of the actuator and the tensile and shear loads acting on the anchor at that time. In the failure mode of Table 3, the ND10 test results show that pryout failure occurs at a loading angle of less than 30°, and concrete breakout failure occurs at more than 60°.

On the other hand, ND15 and ND20 specimens with depths of 150 mm or more had anchor shear failure at loading angle of 30° or less, unlike ND10. The calculated load component of Table 3 is shown in Fig. as the correlation curve between shear load and tensile load. The results of the ND10 specimen show that the peak load on the shear load is greater than tensile load for the same effective embedded depth; however it is not able to observe in the specimen ND15 and ND20 since those specimens show anchor shear failure at loading of less than 30°. In equation of Table 12, the nominal strength of the traditional shear - tension interaction equation is obtained from the experimental result (shear and tensile loads were each calculated at the load angles of 0° and 90°). The results are shown in Fig. as a correlation of N_{ua}/N_n and V_{ua}/V_n. Fig. shows the curves for the coefficient ζ of 1.0 ~ 3.0 in the traditional shear - tension interaction equation at intervals of 0.1 and it also shows a trilinear interaction approach line. In this study, the strength reduction factor φ is 0.7 at the tensile and shear loads according to the experimental conditions. The relationship between the two linear formulas and experimental values is compared. When the shear failure of anchor does not occur, it is found that the experimental value of the traditional shear - tensile correlation expression satisfies the experimental value when ζ is 2.0 or more. On the other hand, when the anchor shear failure occurs, the experimental coefficient ζ tends to drop sharply below 2.0. And the deeper the effective embedded depth, the shear load was increase under the tensile dominant load condition. Trilinear interaction approach line seems to predict the shear failure of the anchor more safely. On the contrary, it tended to underestimate the tensile strength to about 0.7 times or less.

4. Conclusions

In this research, the change of the load combination and the change of the effective embedded depth of the cast-in-place anchor, which are frequently used in connection of heavy equipment, were experimentally studied. The results of the experiment are as follows.

1) "17- Interaction of tensile and shear forces" of ACI 318-14 tend to underestimate tensile strength of anchor. However, this problem is caused by the ratio of the tensile and shear strength of the material. Therefore, it is considered that it is necessary to consider the combined load conditions sufficiently in design.
2) In the experimental conditions of this study, the failure of an anchor under combined loading showed the dominant fracture behavior in shear strength, as the effective embedded depth deepened, this tendency was more pronounced. And if the loading angle of is less than 30°, the shear strength of the anchor material was the major failure mode.

5. Acknowledgment

This research was supported by a grant (19IFIP-B128598-03) from Industrial Facilities & Infrastructure Research Program (IFIP) funded by Ministry of Land, Infrastructure and Transport of Korean government

6. References

ACI Commitee 318. 2014. Building Code Requirements for Structural Concrete (ACI318-14) and Commentary on Building Code Requirements for Structural Concrete (ACI 318R-14). American Concrete Institute.

Korea Ministry of Land, Transport and Marltime Affairs. 2012. Structural Concrete Design Code.

Kim, Ho-Seon, Park, Ji-Hun. 2016. Monotonic Load Test of Post-Installed Anchors subjected to Load Combinations with Different Loading Angles, Journal of the architectural institute of Korea: Structure & construction, 32(1), 15-21.

Bridge Engineering Institute Conference 2019 (BEI-2019)
Honolulu, Hawaii, USA, July 22-25, 2019

Influence of Torsional Stiffness on the Buckling Behavior of Longitudinal Stiffened Plates under Biaxial Stress States

Martin Mensinger[1], Nadine Maier[2*], Joseph Ndogmo[3], and Alexander Stary[4*]

[1] Technical University Munich, Munich, Germany; email: mensinger@tum.de
[2] Technical University Munich, Munich, Germany; email: nadine.maier@tum.de
[3] Technical University Munich; Munich, Germany; email: ndogmo@bv.tum.de
[4] Technical University Munich; Munich, Germany; email: a.stary@tum.de

[*]: corresponding author

Keywords: large scale buckling test; steel bridges; stability; buckling behavior; stiffened plates

Abstract: The influence of the torsional stiffness of longitudinal stiffeners with closed cross sections on the buckling behavior of plates is currently part of scientific research and is controversially discussed with respect to a new standard definition. According to the current state of knowledge, the torsional stiffness has to be neglected for the buckling verification according to EN 1993-1-5 [1]. This is based on the numerical investigations within the background report TWG89 [2]. These investigations were confined only to stiffened panels with constant longitudinal stresses. Additionally, the new test results which were carried out at the Technical University of Munich confirm that there is an influence from torsion on the buckling behavior. Two different shapes of failure were observed during the tests. Main influences are imperfections, the stress ratio and the cross section of the stiffeners. In order to study these influences, a numerical parameter study was carried out.

1. Introduction

Six large-scale buckling tests were carried out 2018 at the Technical University of Munich using longitudinally stiffened plates under biaxial stresses (see Fig. 1). These tests were examined to analyze the buckling behavior during incremental launching.

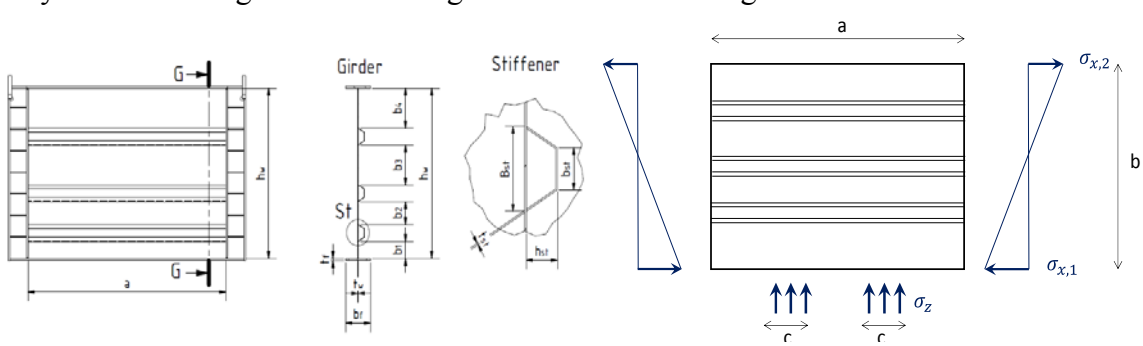

Fig. 1. Geometry and loading of the specimen

Among other things, two different stress ratios σ_z/σ_x were investigated in order to determine the influence of the transverse stress on the buckling behavior in a better way. The test results clearly indicate that there is an influence of the torsional stiffness of the longitudinal stiffeners on the buckling behavior. During the tests, the longitudinal stresses σ_x were first applied to the

specimen. Under the sole effect of these stresses, all specimens were deformed in the direction of the stiffeners. This effect results from the location of the center of gravity. The load introduction of the normal force is in the axis of the web, the center of gravity is above it. This creates a bending moment, which causes tension in the flange of the stiffeners. This results in a positive rotation of the stiffener ϑ, compare with figure 2 on the left. In the next step, the transverse stresses σ_z were applied step by step until failure occurs. Two different cases on the buckling behavior could be observed. In one case, the deformation due to failure goes in the direction of the stiffeners (see Fig. 3, left) which was observed when the longitudinal stresses σ_x applied were dominant. In this case, the rotation of the stiffeners which results from the longitudinal stresses first does not change and the deformation goes in the direction of the stiffener until failure occurs. In the second case, the transverse stresses σ_z were higher, which leads to a change of the rotation of the stiffeners and the failure was initiated in the opposite direction (see Figure 2 middle and Figure 3, right).

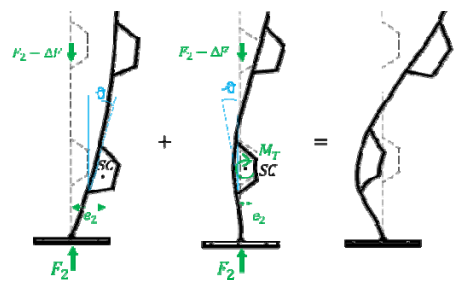

Fig. 2. Moment of torsion

The positive rotation ϑ derives from an asymmetrical arrangement of the stiffeners and/or loading and additionally from the position of the center of gravity. The rotation $-\vartheta$ in negative direction derives from the location of the shear center, which is not in the plate plane; additionally the stress σ_z decreases over the height of the cross section and thus causes a moment of torsion. The differences in the shape of failure could be caused among other things by the stress ratio σ_z/σ_x, imperfections and imperfections due to the execution of the cross sections of the stiffeners.

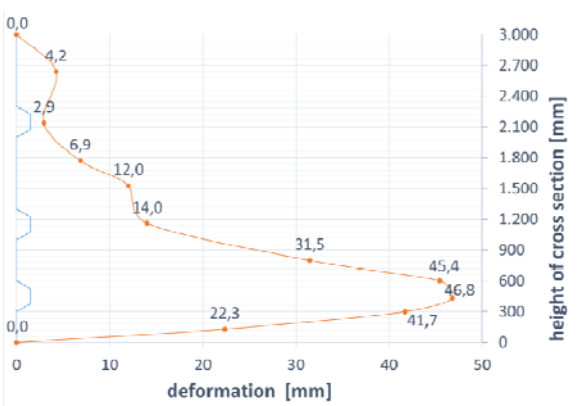

Positive rotation of stiffener (V4)

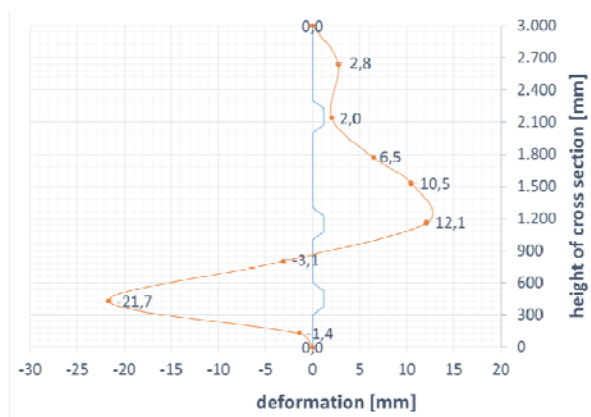

Negative rotation of stiffener (V1)

Fig. 3. Different failure mode during the tests

3. Numerical model

In order to explain the observations from the experiments and to investigate them more precisely, a numerical model with a realistic deformation behavior was created. Thus, conclusions can be deduced on the influence of the torsional stiffness of the stiffeners on the buckling behavior. The basis for the numerical investigations is the first specimen of the test series. An FE-model was created with the ANSYS software, in which a geometric and material non-linear static-mechanical analysis was performed based on an idealized imperfection. The imperfection applied had the shape of the first buckling mode and was scaled on the real imperfections of the specimen which were measured by a 3D Laserscan. This model was validated by achieving load capacity, stresses and deformations from the test result. -To this purpose, the FE-model was compared with the test results and a second FE-model, which was performed with the real imperfections from the 3D-laserscans. The load capacity of the FE-model results from a combination of the applied force F_1 which causes the longitudinal stresses σ_x in the test specimen and the force F_2 which causes the transverse stresses σ_z. At the time of failure, the load difference between the numerical model and the experiment is 8.8%. Therefore, there is a good agreement with the load capacity.

4. Numerical investigations

Adjustments were made to the FE-model with idealized imperfections and their effects were examined. First, new calculations with two different modified stiffeners were performed using the validated FE-model. Once, the stiffeners with closed cross sections were cut open and once open stiffeners with T-shape were used in place of the stiffeners with closed cross section. The stiffeners were dimensioned with the same relative stiffness γ but the torsional stiffness was significantly reduced. The load capacities achieved for the FE-model with cut-open stiffeners and the FE-model with T-shaped stiffeners are compared in Table 1.

Table 1. Load capacities for calculations with different longitudinal stiffeners

	Load capacity [MN]	deviation
Stiffeners with closed cross-section	3,8543	+0,0 %
Cut open stiffeners	3,539	- 8,1 %
T-shaped stiffeners	3,706	-3,7 %

It can be seen that the change in the torsional stiffness of the stiffeners has a negative influence on the load capacity. Interestingly, the change of the torsional stiffness and geometry of the stiffeners does not affect the deformation leading to the failure since all three models fail in the opposite direction of the stiffeners. Next, it was examined which imperfection has an influence on the deformation behavior during failure. The scaling of the imperfection varied from -2.5mm to +2.5mm. The calculations show that the scaling has a large influence on the direction of the deformations. From an imperfection of -1.25mm, the model fails in the opposite direction of the stiffeners, while more positive imperfections lead to failure in the direction of the stiffeners. The imperfection in the area of the lowest stiffener for the considered specimen is at -2.5 mm. Thus, it is far enough in the negative range to lead to a failure in the opposite direction of the stiffeners. Finally, it was examined as to what extent the applied stress ratio σ_z/σ_x affects the failure of the stiffened plate. The stress ratio was changed by varying the applied forces in the geometric and material nonlinear static-mechanical analysis. The investigations were done for closed cross

section stiffeners, as well as for cut-open cross section stiffeners. With a certain stress ratio σ_z/σ_x, a change in the direction of the failure could be confirmed, regardless of the type of stiffener (see Fig. 4 and Fig. 5).

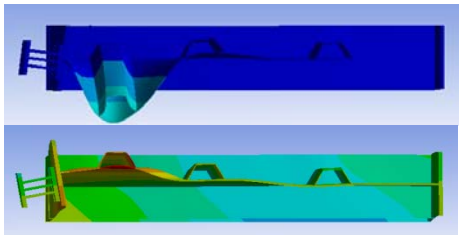

Fig. 4. closed cross-section stiffener
with σ_z/σ_x =0,51
with σ_z/σ_x =0,18

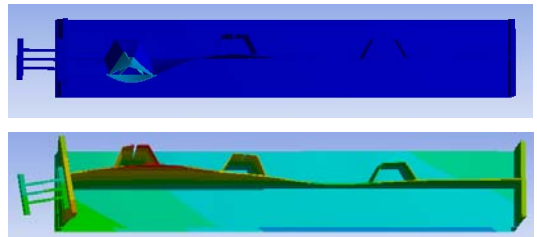

Fig. 5. open cross-section stiffener
with σ_z/σ_x =0,39
with σ_z/σ_x =0,20

For cut open and closed cross section stiffeners, it becomes clear that the deformation behavior of the plate depends strongly on the stress ratio σ_z/σ_x. The calculations have shown that a "large" σ_z/σ_x –ratio leads to a sign change in the deformation in the region of the first stiffener, while a "small" σ_z/σ_x-ratio leads completely to the collapse in the direction of the stiffeners. In addition, a "large" σ_z/σ_x leads to a lower load capacity than a "small" σ_z/σ_x. One reason for this is that with a "small" σ_z/σ_x–ratio under pure longitudinal stresses the plastic region of the material is already reached. In this case, without the presence of the transverse stress (no biaxial load condition), supercritical load reserves can be activated from the membrane effect of the plate and the load capacity can be increased. Meanwhile, with a "large" σ_z/σ_x-ratio the larger transverse load initiates failure much earlier. Finally, it was checked whether the consideration of the torsional stiffness of the closed transverse stiffeners under application of DIN EN 1993-1-5 leads to uncertain results. Various stress conditions were investigated under which failure occurred in and against the direction of the stiffeners. The characteristic load-bearing capacity was applied as an external load. The critical load factors were determined once with the closed transverse stiffeners and once with the cut open stiffeners. In all cases the buckling test was insufficient. Therefore, in these investigated cases, consideration of the torsional stiffness of the stiffeners does not lead to results on the unsafe side. However, the theoretical load-bearing capacity of the models with closed transverse stiffeners is higher, since the critical loads from the linear buckling analyses are higher. In this sense, special cases may occur in which the consideration of torsional stiffness leads to uncertain results.

5. Summary

The numerical investigations showed that the consideration of the torsional stiffness in the tests leads to higher load capacities. Nevertheless, the buckling check using Eurocode 3 is on the safe side under the experimental conditions. The direction of the failure of the plate is hardly influenced by the stiffness of the stiffeners. However, the stress ratio σ_z/σ_x and the imperfections have great influence on the buckling behavior and the direction of the failure. Accordingly, the recommendation to neglect the torsional stiffness of closed cross-sections for the buckling test in accordance with DIN EN 1993-1-5 cannot be accepted completely. The research report TWG83 shows that the results also depend on the aspect ratio of the plate. Therefore, in the next step it is

necessary to include these parameters and further parameters in further investigations in order to be able to make a clear statement. Since torsional stiffness is present in a closed cross-section design of real structures, it would be desirable for the future to develop a design format in which torsional stiffness can be taken into account rather than neglecting an existing torsional stiffness mathematically.

6. References

[1] DIN EN 1993-1-5, Eurocode 3: Bemessung und Konstruktion von Stahlbauten - Teil 1-5: Plattenförmige Bauteile, Dezember 2010.

[2] M. Mensinger, J. Ndogmo and N. Maier, Experimental investigation of buckling modes in longitudinal stiffened plates with biaxial stress state, Munich, Germany: 12th Japanese-German Bridge Symposium, 2018.

[3] A. Stary, Influences from torsion on the buckling behavior of longitudinal stiffened plates, Technische Universität München, 2019

[4] P.O. Martin, T. M. Nguyen, L. Davaine, TWG83, Effect of the torsional inertia of closed section stiffeners on plate buckling in Eurocode 3 Part 1-5

[5] N. Maier, V. Pourostad, J. Ndogmo, M. Mensinger, U. Kuhlmann, Final Report Talbrücke Thulba: Investigation of the buckling behavior of longitudinal stiffened plates under biaxial compession, 2019

Bridge Engineering Institute Conference 2019 (BEI-2019)
Honolulu, Hawaii, USA, July 22-25, 2019

Survival Analysis Approach for Fatigue Reliability Assessment in Bridge Structures

Azam Nabizadeh[1], Habib Tabatabai[2*], and Mohammad Tabatabai[3]

[1] University of Wisconsin - Milwaukee, Milwaukee, USA; email: azam@uwm.edu
[2] University of Wisconsin - Milwaukee, Milwaukee, USA; email: ht@uwm.edu
[3] Meharry Medical College, Nashville, USA; email: mtabatabai@mmc.edu

[*]: corresponding author

Keywords: survival analysis; reliability; bridge; fatigue; remaining service life; steel

Abstract: The Survival analysis approach has long been used for statistical analyses of data from biomedical research. In this approach, a probabilistic evaluation of the time required to reach a milestone (the time-to-event parameter) is conducted using a set of mathematical/statistical tools. Survival analyses are used to quantify the influence of various independent contributing factors (covariates) on the probability of reaching a milestone. This paper discusses the development of survival analysis techniques for probabilistic assessment of fatigue by considering the number of stress cycles as a fictitious "time-to-event" parameter. Currently, fatigue reliability assessments in bridge structures are typically performed by evaluating the statistical distribution of test data for a given detail category and stress range. The number of cycles to failure is treated as a dependent variable while stress range is the independent variable. However, using survival analysis techniques, the number of cycles and the stress range can both be considered independent variables that influence the probability of fatigue failure. The influence of other numerical or categorical parameters can also be modeled. As a comprehensive mathematical platform, survival analyses could provide an effective way to assess the influence of independent covariates on fatigue reliability and the probability of remaining service life.

1. Introduction

The fatigue of engineering materials under repetitive loading is a significant issue affecting the design and durability of components and systems in a variety of engineering-related applications including bridge structures. Many factors can affect the service life of a component or system under repetitive loading, such as the type of structure, loading, connection details, stress state, stress range, surface condition, temperature, and environmental exposure. Although, fatigue has been widely investigated from a micromechanical viewpoint, stochastic processes inherent in fatigue failure make it a random phenomenon (event), and thus probabilistic methods should be employed for fatigue life prediction. Because of their relative simplicity and probabilistic nature, phenomenological (observation-based) models for fatigue analysis can be more attractive for engineers when compared to micromechanical models. Although, these approaches can be complimentary, the phenomenological approach can also be used to verify micromechanical constitutive models (Pyttel et al., 2016). The stochastic nature of fatigue damage is due to variability of fatigue resistance (uncertainties inherent in the material properties and component geometry) and loading process (Shen et al., 2000). Fatigue damage is cumulative with respect to applied cyclic stresses. Cumulative damage theory has been long investigated (Freudenthal and Heller, 1959; Stallmeyer and Walker, 1968; Tanaka and Akita, 1975; Shimokawa and Tanaka,

1980; Tanaka et al., 1980; Manson and Halford, 1981). Many fatigue damage models have been developed which were mostly phenomenological before 1970s and progressed into micromechanical models after the 1970s (Fatemi and Yang, 1998).

In phenomenological fatigue analysis, data on the number of cycles to failure are typically plotted versus stress (or strain) as S-N diagram, also known as Wohler diagram. The stress range or peak stress is commonly considered as an independent variable, and the number of cycles to failure is viewed as a dependent variable. Typically, multiple tests are performed on a component or structure to assess fatigue life under several constant-amplitude stress cycles. The results are usually displayed on a log-log scale, and a linear or multilinear S-N curve is drawn to collectively represent the data. In a wide range of medical and biomedical studies, large-scale data related to various diseases, treatments, and drugs are obtained and analyzed. In such research, probabilistic assessments of time to reach a milestone is frequently considered under the influence of a range of independent numerical and/or categorical parameters. Examples of the time-to-event parameter include patient's age when a disease appears, time to death of a cancer patient since diagnosis, time to recurrence of a disease after treatment, or time for a disease, tumor, or condition to reach a critical stage. The experimental data obtained from observations during research is used to generate the analysis models. Over the last 40-50 years, a powerful set of mathematical/statistical tools have been developed that collectively form the "survival analysis" platform for analysis of time-to-event data (Hosmer et al., 2008; Liu, 2012). Although survival analyses are mostly used in medical and biomedical research, they have also found growing applications in engineering, economics, finance, and other fields. A number of studies have applied survival analysis techniques to bridge structures (Tabatabai et al., 2011; Tabatabai et al., 2015; Tabatabai et al., 2016, Nabizadeh et al., 2018; Nabizadehdarabi, 2015) and medical applications, including development of new survival models (Tabatabai et al, 2007). This paper proposes using survival analysis techniques for probabilistic fatigue analyses by considering the number of cycles of applied stress as a fictitious "time-to-event" parameter.

There are several important issues with the current approach to probabilistic assessment of fatigue and remaining service life: 1) The number of cycles and the stress range can both be considered independent variables that influence the probability of fatigue failure, a fact that is not generally considered in the current approaches. 2) The effect of potential contributing parameters (covariates) other than stress is typically not considered within a single probabilistic analysis. 3) The types of data considered in the analyses are generally not comprehensive. Most commonly, data on run-outs or suspended tests are not included in the statistical analyses, even though they contain valuable information and should be systematically considered in the mathematical model. Furthermore, non-numerical (or categorical) data are typically not considered except as separate analyses. 4) The points along the linear S-N curve (on a log-log scale) are not associated with a uniform probability of failure. In fact, points along these S-N curves could have a wide range of probabilities of failure (Pytell et al., 2016; Albrecht, 1983). 5) The current procedures do not systematically consider the statistical significance of covariates on service life. If a parameter is considered in the fatigue analyses, there should be an objective measure to decide the statistical significance of that parameter and whether it can be omitted from further consideration. The long-standing survival analysis techniques can be applied to the

fatigue problem in bridge engineering applications to address the above shortcomings in the probabilistic assessments of fatigue in bridges.

2. Survival Analysis

Three distinct functions commonly used in survival analysis are (1) survival function S(t) (Eq. 1), (2) probability density function f(t) (Eq. 2), and (3) hazard function h(t) (Eq. 3) [10]:

$$S(t) = P(T > t) = 1 - F(t) \tag{1}$$

$$f(t) = \lim_{\Delta t \to 0} P(t < T < t + \Delta t)/\Delta t \tag{2}$$

$$h(t) = \lim_{\Delta t \to 0} p(t < T < t + \Delta t | T > t)/\Delta t \tag{3}$$

where T indicates the survival time as a random variable, t is the time, and F(t) denotes the cumulative probability of failure at various times. S(t) = 1 at t = 0 and S(t) → 0 as t → ∞. The hazard function, h(t), is the change in probability of failure per unit time at time t assuming survival up to that time (i.e. conditional failure rate). When applied to fatigue problems, the number of applied cycles of stress can be considered as a fictitious time (t) in the survival equations presented here. The choice of baseline statistical distribution (such as Weibull, lognormal, …) must be made for specific types of data at hand; therefore, the appropriate distribution cannot be assumed upfront without first finding the best fit model. Typically, the Akaike Information Criterion (AIC) and goodness-of-fit tests are used to find the best baseline distribution function, as well as the parameters associated with each covariate, using the method of maximum likelihood. As an example, the baseline lognormal probability density function is:

$$f_0(t) = \frac{1}{t\sigma\sqrt{2\pi}} \exp\left\{\frac{-(\ln(t)/\mu))^2}{2\sigma^2}\right\}; t > 0 \tag{4}$$

where parameters μ and σ are the mean and the standard deviation, respectively. The baseline lognormal survival function is defined as:

$$S_0(t) = \frac{1}{2} - \frac{1}{2}\,\mathrm{erf}\left[\frac{\ln(t) - \mu}{\sqrt{2}\sigma}\right] \tag{5}$$

where erf is the Error function. The baseline lognormal hazard function $h(t)$ can be calculated using:

$$h_0(t) = \frac{f(x)}{S(x)} = -\sqrt{2}\sigma^{-\frac{(\ln(t)-\mu)^2}{2\sigma^2}} \frac{1}{\sqrt{\pi}} t^{-1}\sigma^{-1}\left\{-1 + \mathrm{erf}\left[\frac{\sqrt{2}(\ln(t)-\mu)}{2\sigma}\right]\right\}^{-1}; t > 0 \tag{6}$$

The baseline functions must be adjusted to account for the effect of covariates. There are several types of parametric survival models, the most common of which are the Proportional Hazard model (PH) and the Accelerated Failure Time (AFT) model. If the proportionality of hazards is

established (generally through an initial non-parametric Kaplan-Meier evaluation), then the PH model can be used. When the covariates act multiplicatively on the time scale, the AFT model is commonly used. The proportional hazard model has a hazard function $h(t|x,\theta)$ of the form:

$$h(t|x,\theta) = h_0(t)g(x|\theta) \tag{7}$$

where θ is a vector of unknown parameters and x is a p-dimensional vector of covariates. For categorical parameters, x can take values of either 0 or 1. The function $g(x|\theta)$ is a non-negative function of x satisfying the condition that $g(0|\theta) = 1$, and $g(x|\theta) = e^{\sum_{k=1}^{p}\theta_k x_k}$. The survival function $S(t|x,\theta)$ for the proportional hazards model is defined as

$$S(t|x,\theta) = [S_0(t)]^{g(x|\theta)} \tag{8}$$

where the baseline survival function $S_0(t)$ was defined earlier as $S(t)$ in Eq. 5 (for lognormal distribution). The probability density function for the PH model is

$$f(t|x,\theta) = f_0(t)[S_0(t)]^{g(x|\theta)-1} g(x|\theta) \tag{9}$$

where the baseline probability density function $f_0(t)$ was defined earlier as $f(t)$ in Eq. 4 for the lognormal distribution. The AFT model uses a hazard function $h(t|x,\theta)$ of the form

$$h(t|x,\theta) = h_0(tg(x|\theta))g(x|\theta) \tag{10}$$

The AFT survival function is

$$S(t|x,\theta) = S_0(tg(x|\theta)) \tag{11}$$

The probability density function for the AFT model is

$$f(t|x,\theta) = f_0(tg(x|\theta))g(x|\theta) \tag{12}$$

The model parameters are determined using the maximum likelihood estimation by maximizing the likelihood functions. The effect of censored data is considered in the likelihood functions. In the absence of censoring, the log-likelihood function is:

$$LL(\theta : x) = \sum_{i=1}^{n} \ln[f(t_i|x_i,\theta)] \tag{13}$$

where n is the total number of observations. For right-censored data, the log-likelihood function is:

$$LL(\theta : x) = \sum_{i=1}^{n} \left(\delta_i \ln\left[h\left(t_i | x_i, \theta\right)\right] + \ln\left[S\left(t_i | x_i, \theta\right)\right] \right) \quad (14)$$

where $\delta_i = 0$ if the ith observation is right-censored; and $\delta_i = 1$ if otherwise. Fatigue run-out data are right-censored data. Other relationships exist for left-censored and interval-censored data (Tabatabai et al 2011).

3. Summary

This paper proposes the use of long-standing survival analysis techniques for probabilistic assessment of fatigue in bridge structures. The available survival analysis methods can provide a powerful set of statistical tools to address a number of shortcomings in the current probabilistic approaches to fatigue in bridge engineering.

4. References

Albrecht, P., 1983. S-N fatigue reliability analysis of highway bridges. In: Probabilistic Fracture Mechanics and Fatigue Methods: Applications for Structural Design and Maintenance. ASTM International.

Fatemi, A. and Yang, L., 1998. Cumulative fatigue damage and life prediction theories: a survey of the state of the art for homogeneous materials. International journal of fatigue, 20(1), pp.9-34.

Freudenthal, A.M. and Heller, R.A., 1959. On stress interaction in fatigue and a cumulative damage rule. Journal of the Aerospace Sciences, 26(7), pp.431-442.

Hosmer, D.W., Lemeshow, S. and May, S., 2008. Model development. Applied Survival Analysis: Regression Modeling of Time-to-Event Data, Second Edition, pp.132-168.

Liu, X., 2012. Survival analysis: models and applications. John Wiley & Sons.

Manson, S. and Halford, G., 1981. Practical implementation of the double linear damage rule and damage curve approach for treating cumulative fatigue damage. International Journal of Fracture, 17(2), pp. 169-192.

Nabizadehdarabi, A., 2015. Reliability of bridge superstructures in Wisconsin. PhD Dissertation. University of Wisconsin Milwaukee.

Nabizadeh, A., Tabatabai, H. and Tabatabai, M., 2018. Survival analysis of bridge superstructures in wisconsin. Applied Sciences, 8(11), p.2079.

Pyttel, B., Canteli, A.F. and Ripoll, A.A., 2016. Comparison of different statistical models for description of fatigue including very high cycle fatigue. International Journal of Fatigue, 93, pp.435-442.

Shen, H., Lin, J. and Mu, E., 2000. Probabilistic model on stochastic fatigue damage. International Journal of Fatigue, 22(7), pp. 569–572.

Shimokawa, T. and Tanaka, S., 1980. A statistical consideration of Miner's rule. International Journal of Fatigue, 2(4), pp.165-170.

Stallmeyer, J.E. and Walker, W.H., 1968. Cumulative damage theories and application. Journal of the Structural Division.

Tabatabai, H., Tabatabai, M. and Lee, C.W., 2011. Reliability of bridge decks in Wisconsin. Journal of Bridge Engineering, 16(1), pp.53-62.

Tabatabai, H., Lee, C.W. and Tabatabai, M.A., 2015. Reliability of bridge decks in the United States. Bridge Structures, 11(3), pp.75-85.

Tabatabai, H., Lee, C.W. and Tabatabai, M.A., 2016. Survival Analyses for Bridge Decks in Northern United States.
Tabatabai, M.A., Bursac, Z., Williams, D.K. and Singh, K.P., 2007. Hypertabastic survival model. Theoretical Biology and Medical Modelling, 4(1), p.40.

Tanaka, S. and Akita, S., 1975. On the miner's damage hypothesis in notched specimens with emphasis on scatter of fatigue life. Engineering Fracture Mechanics, 7(3), pp.473-480.

Tanaka, S., Ichikawa, M. and Akita, S., 1980. Statistical aspects of the fatigue life of nickel-silver wire under two-level loading. International Journal of Fatigue, 2(4), pp.159-163.

Modeling and Advanced Analysis

Bridge Engineering Institute Conference 2019 (BEI-2019)
Honolulu, Hawaii, USA, July 22-25, 2019

Simplified Analysis of Bridge Pier Caps Using the Strut-and-Tie Method

Pappu Baniya[1] and Serhan Guner[2*]

[1] University of Toledo, Toledo, Ohio, USA; email: Pappu.Baniya@rockets.utoledo.edu
[2] University of Toledo, Toledo, Ohio, USA; email: Serhan.Guner@utoledo.edu

[*]: corresponding author

Keywords: analysis; bent cap; deep beam; pier cap; strut and tie.

Abstract: Around the world, large number of pier caps are used to transfer loads from bridge girders to columns. When analyzed using traditional 'sectional analysis methods,' many pier caps are found to be shear-overloaded, even though they don't exhibit any noticeable cracking or signs of distress. Experimental research shows that deep beams are actually more resilient, failing at much higher loads than those predicted by the sectional method. Since most pier caps qualify as deep beams, it is imperative to employ an appropriate analysis method to obtain more accurate shear capacities to reduce bridge rehabilitation costs. The objectives of this study are 1) to create a specialized 'strut-and-tie method' (STM) that is more accurate and less-conservative for pier caps, and 2) to reduce the complexity of the STM to a level comparable to sectional methods. For this purpose, a solution algorithm and associated computer program, called STM-CAP, is developed. An adaptive graphical solution procedure is employed to facilitate a thorough understanding of the system response while making it possible to alter the model to optimize the calculated utilization ratios. The developed method is verified by modeling eight existing pier caps located in Ohio, USA, and shown to predict 2 to 3 times higher shear capacities than the sectional method for beams with shear span-to-depth ratio (a/d) of 0.50. The predictions from both methods converge as the a/d ratios approach to 3.0. The research results have the potential to result in significant cost savings by requiring fewer pier caps to be rehabilitated, thereby reducing unnecessary construction work and traffic disruption.

1. Introduction

The increase in traffic and transport freight over the past decades has required many modifications to bridges (e.g., bridge deck expansions and addition of lanes), frequently causing them to exceed their original design loads. Bridge Design Codes used around the world (e.g., AASHTO, 2017; CSA S6, 2014; Eurocode 2, 2004) typically contain two main analysis methods for concrete members: sectional method and strut-and-tie method (STM). Sectional method requires checking the shear and moment capacities at critical sections based on the plane-sections-remain-plane hypothesis; STM, on the other hand, does not rely on this hypothesis and thus is suitable for the analysis of deep beams, which exhibit nonlinear strain gradient.

In current civil engineering practice, the sectional method is the most popular method and dominantly used for analyzing and load rating existing pier caps, even if they are deep. Unfortunately, if a deep beam is analyzed by a sectional method, invalid and typically overly-conservative (i.e., low) shear capacities are obtained (Senturk & Higgins, 2010a,b). Thus, the current practice may result in incorrectly identifying cap beams as shear-overloaded while in fact

these beams may have reserve capacities when analyzed by the more-thorough STM analysis method. Yet STM is a graphical method and requires more effort and experience to execute than the sectional method.

2. Research Objectives

There is limited public funding for the rehabilitation and strengthening of overloaded bridges. As such, it is imperative to use the proper STM analysis method to correctly identify and rank the overloaded bridges. The main objective of this study is to explore innovative strategies to reduce the complexity of the STM to a level comparable to sectional methods for analyzing deep cap beams. This research seeks to create a computer program with adaptive graphical capabilities to automatically generate efficient STM models while intuitively educating practicing engineers in the correct use of STM. A secondary objective is to compare the results with the shear strength predictions obtained from the sectional method, in order to understand if sectional methods always underestimate the shear capacities of cap beams; and if so, to what extent.

3. Proposed Method

The Strut-and-Tie Method (STM) is based on the basic concept of load transfer from the point of load application to the support through a set of compressive forces (i.e., struts) and tensile forces (i.e., ties). The proposed methodology determines the model geometry based on the principle that 'the loads applied on the structure is transferred to the supports using the shortest path.' (see Fig. 1a). The top and bottom ties are located at the centroid of the steel reinforcement. At each column, the supports are divided to have a uniform stress distribution (see Fig. 1b).

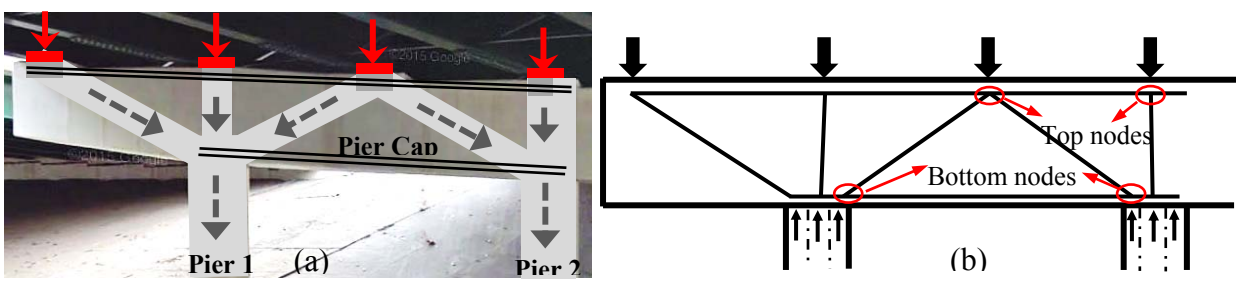

Fig. 1. Determination of the model geometry: (a) a sample pier cap and forces applied; (b) analysis model using the shortest load paths

The matrix stiffness method (e.g., Weaver and Gere, 1990) is used to solve for the indeterminate member forces in struts and ties. The member capacities are calculated as per Section 5.8.2 of AASHTO LRFD 2017. The utilization ratios (UR) (i.e., force divided by capacity) are calculated for each STM element to determine whether the member is overloaded or has a reserve capacity. For example, the UR of 0.69 indicates that the pier cap has 69% of its capacity in use and has approximately 31% reserve capacity remaining. In addition, the proposed method checks the tension bar reinforcement development, 2D nodal stresses, and the concrete stresses under the bearing pads and columns. The URs depend on the efficiency of the STM model created. To optimize the analysis results (i.e., minimize the URs), the proposed method permits adding or removing vertical ties (i.e., stirrups) from each region until the highest overall URs are obtained.

Analysis results are printed graphically to facilitate a more thorough examination of the results while helping the analyst to develop a better understanding of the system response. A generalized solution procedure and associated computer program, STM-CAP, are created. STM-CAP includes 16 modules and more than 5,000 lines of code, and is capable of analyzing pier caps with up to eight columns. More details can be found in Baniya et al. (2019).

4. Verification

The results obtained from STM-CAP are verified with a general-purpose computer-aided strut-and-tie method CAST (Tjhin and Kuchma, 2004). Eight existing bridge pier caps located in Ohio, USA, were modeled using both STM-CAP and CAST. The models for pier cap consisted of a variety of truss models with or without vertical ties. The utilization ratios, member forces, and reactions from each analysis were compared (see Fig. 2 for a sample). STM-CAP and CAST provided identical results in most cases. The largest discrepancy obtained in other cases were less than 5%. Verification with hand calculations indicated that STM-CAP was more accurate in such cases due to more precise input of the bridge geometry.

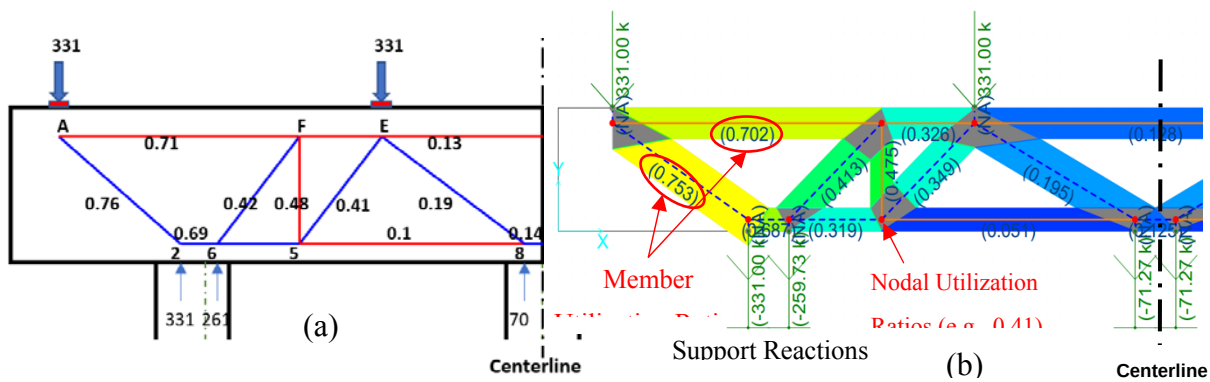

Fig. 2. A sample verification comparison for utilization rations: (a) STM-CAP; (b) CAST

5. Sectional Method Analyses

Sectional analyses of five existing pier caps are performed to compare the shear capacity predictions with the STM-CAP results. The shear utilization ratios obtained from both methods for twenty-one sections with different a/d ratios, and their trendlines, are presented in Fig. 3.

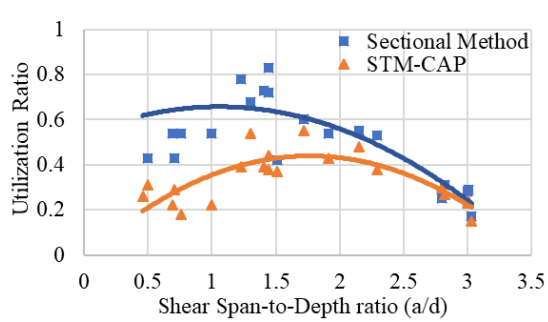

Fig. 3. Comparisons of utilization ratios from 21 sections of five existing bridges

7. Summary and Conclusions

This paper proposed a strut-and-tie method (STM) specifically developed for concrete bridge pier caps. A mathematical procedure, and associated computer program STM-CAP, is created based on the proposed methodology. The developed method is validated by modeling eight existing bridge pier caps with a computer-aided strut-and-tie method. In addition, sectional analysis calculations are performed for 21 sections with the shear span-to-depth ratios (a/d) ranging from 0.45 to 3.0. The developed method predicted lower utilization ratios and higher shear capacities than the sectional method for almost all cases. For lower a/d ratios (e.g., a/d is around 0.50), the STM-CAP predicted two to three times higher shear capacities. With the increase in a/d ratio, the discrepancy between the predictions decreased; the results converged approximately at a/d of 2.8 to 3.0. The proposed method has a general applicability for modeling pier caps and has been shown to provide similar modeling time and effort to the sectional analysis method. The proposed method permits ranking pier caps according to their utilization ratios, enabling limited rehabilitation funds to be directed to the most urgent cases. STM-CAP also indicates the governing failure mode and location of the failure, thereby facilitating the efficient strengthening of cap beams. More details can be found in Baniya et al. (2019).

8. References

AASHTO. 2017. LRFD Bridge Design Specifications, Customary US units, 8th Edition, American Association of State Highway and Transportation Officials, Washington, DC.

Baniya, P., Sharma, A., and Guner, S. 2019 Evaluation of Reserve Shear Capacity of Bridge Pier Caps Using the Deep Beam Theory, Final Report, Ohio Department of Transportation, 120.

CSA S6. 2014. Canadian Highway Bridge Design Code, Canadian Standards Association, Mississauga, Ontario, 833.

Eurocode 2. 2004. Design of Concrete Structures, European Committee for Standardization (CEN), Brussels, Belgium.

Senturk, A. E. and Higgins, C. 2010a. "Evaluation of RCDG Bridge Bent Caps with 1950's Vintage Details - Laboratory Tests." *American Concrete Institute Structures Journal*, 107(5): 534-543.

Senturk, A. E. and Higgins, C. 2010b. Evaluation of RCDG Bridge Bent Caps with 1950's Vintage Details - Analytical Methods, *American Concrete Institute Structures Journal*, 107(5): 544-553.

Tjhin, T. and Kuchma, D. 2004. CAST: Computer-aided strut-and-tie analysis software. Version 0.9.11, University of Illinois at Urbana-Champaign, IL, USA.

Weaver Jr, W. and Gere, J. M. 1990. *Matrix Analysis of Framed Structures.* Third Edition, Van Nostrand Reinhold, New York, USA, 547.

Bond Strength Model of Prestressing Strand Associated with Concrete Splitting

Jianren Zhang[1*], Ju Yi[2], Yafei Ma[3], Lei Wang[4], and Jianxin Peng[5]

[1] Changsha University of Science and Technology, Changsha, China; jianrenz@hotmail.com
[2] Changsha University of Science and Technology, Changsha, China; juyi@csust.stu.edu.cn
[3] Changsha University of Science and Technology, Changsha, China; leiwang@csust.edu.cn
[4] Changsha University of Science and Technology, Changsha, China; yafei.ma@csust.edu.cn
[5] Changsha University of Science and Technology, Changsha, China; yafei.ma@csust.edu.cn

[*]: corresponding author

Keywords: bond strength model; prestressing strand; concrete; splitting

Abstract: An analytical model, which considers the helical structural features of prestressing strand, is proposed to study the bond strength for the concrete splitting failure. Factors that have been experimentally verified to have influences on bond strength, such as concrete compressive strength, strand diameter, friction coefficient, are reflected and applied through theoretical analysis into the model. The predicted results are testified by comparing with experimental data.

1. Introduction

Numerous experimental investigations have been conducted to study the bond between prestressing strand and concrete. Some empirical bond strength models have been established in concrete members based on experimental results (Baran et al. 2012; Ma et al. 2013, 2017). The applicability of these formulas to real structures, however, could be limited due to their high dependency upon test data. Young and Laldji (1988) developed a bond model between steel strand and cement grout in ground anchorages by idealizing the exterior wires of strand as helically lugs along the strand surface. In addition, limited attention has been focused on analytical model to predict bond strength. This study aims to develop an analytical model to predict the bond strength considering the twisted exterior wires of prestressing strand.

2. Derivation of theoretical expressions for bond strength

Bond stress between strand and concrete could be regarded as a uniform shear stress along the bond interface. Thus, the average bond stress τ_b is expressed as

$$\tau_b = F_p \Big/ \left(\frac{4}{3} \cdot \pi \cdot d \cdot l_t \right) \tag{1}$$

where, F_b and d are tensile force and nominal diameter of strand; l_b is the bond length. The seven-wire strand consists of one core wire and six helical wires wrapping around the core one. Within a lay length, which is defined as the distance required to complete one revolution of the strand around the diameter of the conductor, the projections of any cross sections are non-overlapping. A random segment with tiny height of dz, which is shown in Fig. 1(a), is chosen as a representative for mechanical analysis. As Fig. 1(a) shows, a height of dz corresponds to a

rotation angle of $d\alpha$. Assuming the six external wires uniformly wrap around the core wire, the relationship between da and dz is expressed as:

$$\frac{d\alpha}{2\pi} = \frac{dz}{14d} \tag{2}$$

where $14d$ represent a lay length based on ASTM A416 standard.

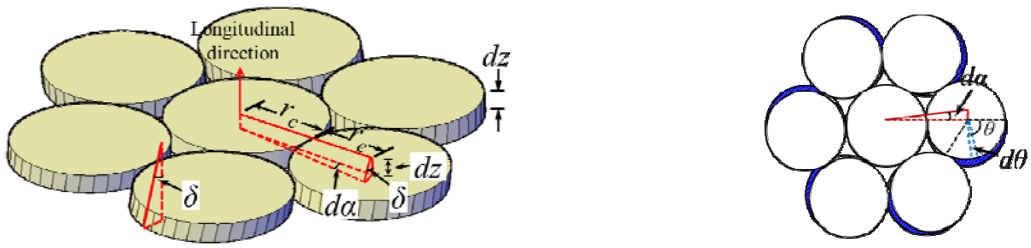

(a) (b)

Fig. 1. Relationship between $d\alpha$ and dz

Fig. 1(b) shows the projection of the two cross sections. The shadow areas are the bearing ribs used for transmission of shear stress. The bearing ribs could be regarded as incomplete crescent shapes, which is similar with that of deformed bars. As for same boundary conditions of the six ribs, one of them was selected as a representative for the force analysis.

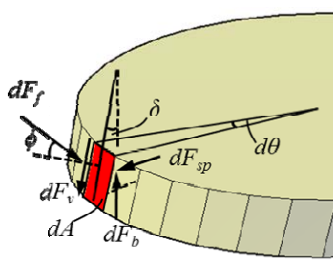

Fig. 2. Force analysis on a single rib

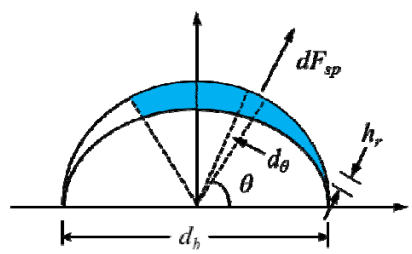

Fig. 3. Effective bearing face on the rib of exterior wires

Fig. 2 shows the forces acting on the face of rib. The rib face has an inclined angle of δ with the axis of the strand. This angle is regarded as 8.7° in accordance with ASTM A416 standard. A shear force dF_v and a friction force dF_f are the forces acting on the rib face. Consider these two forces acting on an area of rib dA, which is subtended by an angle $d\theta$, as shown in Fig. 3. Thus

$$dA = h_r / \sin\delta \cdot d_b / 2 \cdot d\theta \tag{3}$$

where h_r is the height of rib; d_b is the diameter of external wire. The range of θ is [-π/6, π/2]. The shear force dF_v and friction force dF_f can be expressed as:

$$dF_v = f_{coh} dA \tag{4}$$

$$dF_f = f_n dA / \cos\phi \tag{5}$$

where f_{coh} is unit cohesion between bearing face of rib and concrete ,which is estimated as $0.11f_{ct}$ (Cairns and Abdullah, 1996); f_n is normal stress on shear failure plane; ϕ is angle of friction between strand and concrete, which is regarded as 20° in this study (Burgueno and Sun, 2011). These two forces can be resolved into components F_b parallel to and F_{sp} perpendicular to the axis of strand, where

$$-\mathrm{d}F_b + \left(f_n \cdot \frac{dA}{\cos\phi} \right) \cdot \sin(\delta + \tau) + f_{coh} dA \cdot \cos\delta = 0 \tag{6}$$

$$\mathrm{d}F_{sp} - \left(f_n \cdot \frac{dA}{\cos\phi} \right) \cdot \cos(\delta + \tau) + f_{coh} dA \cdot \sin\delta = 0 \tag{7}$$

Integration of Eq. (6) along the bearing face of each rib leads to its contribution to the total strand force F_b

$$F_b = 6\int_{-\pi/6}^{\pi/2} dF_b d\theta = 2\left[\frac{f_n}{\cos\phi} \frac{\sin(\delta+\phi)}{\sin\delta} + f_{coh}\cot\delta \right] \pi h_r d_b \tag{8}$$

where $\pi h_r d_b$ is the area of two complete crescent shapes, which can be expressed as:

$$\pi h_r d_b = 2\left\{ \pi \frac{d_b^2}{4} - \pi \frac{d_b}{2} \left[\frac{d_b}{2} - \left(\frac{d_a + d_b}{2} \right) d\alpha \right] \right\} = \pi d_b^2 d\alpha \tag{9}$$

Integration of Eq. (8) and Eq. (9) leads to F_b within the length of d_z

$$F_b = 2\left[\frac{f_n}{\cos\phi} \frac{\sin(\delta+\phi)}{\sin\delta} + f_{coh}\cot\delta \right] \pi d_b^2 d\alpha \tag{10}$$

Substitution for F_b from Eq. (10) into Eq. (1) leads to bond stress given by Eq. (11)

$$\tau_b = \frac{3}{14}\pi \left(\frac{d_b}{d} \right)^2 \left[\frac{f_n}{\cos\phi} \frac{\sin(\delta+\phi)}{\sin\delta} + f_{coh}\cot\delta \right] \tag{11}$$

3. Confining model of concrete

The confining model of concrete on reinforcement conducted by Uijl and Laldji (1996) is introduced to calculate maximum confining stress on the interface between strand and concrete. In this model, the surrounding concrete is regarded as a thick-walled-cylinder. The resistance of

concrete cover against splitting due to bond is divided into three stages on the basis of concrete cracking degree, namely uncracked stage, partly cracked stage and totally cracked stage. As for the two cracked stages, the tension softening performance of cracked concrete is taken into account. For the uncracked stage, the expression between $\sigma_{t,r}$, which is the tangential stress at radius r, and f_n is expressed as:

$$f_n = \sigma_{t,r} \frac{\left(r_e^2 - r_i^2\right)}{r_i^2} \left(\frac{r^2}{r_e^2 + r^2} \right) \tag{12}$$

where r_i and r_e are the inner radius and outer radius of cylinder, respectively. For the partly cracked stage, The confining stress on interface at partly cracked stage is composed by two parts $\sigma_{r,rs}(LE)$ and $\sigma_{r,rs}(NL)$, which are provided by uncracked concrete and cracked concrete, respectively. The uncracked concrete is regarded as a linear elastic material. As for cracked concrete, a bilinear tension softening behavior is consider to calculate its contribution on confining stress:

$$f_n = \sigma_{r,r_s}(LE) + \sigma_{r,r_s}(NL) = \frac{r_{cr}}{r_s} f_{ct} \left(\frac{c_1^2 - r_{cr}^2}{c_1^2 + r_{cr}^2} \right) + f_{ct} \left[\frac{a \cdot 2\pi\varepsilon_{cr} \cdot r_s}{2n \cdot w_0} \left(\frac{r_{cr}}{r_s} - 1 \right)^2 + b \left(\frac{r_{cr}}{r_s} - 1 \right) \right] \tag{13}$$

where r_{cr} is the radius of crack front; $r_s=d/2$ is the nominal radius of strand; f_{ct} is the tensile strength of concrete; $c_1=r_e$ is the outer radius of cylinder; a and b are constants related to softening behavior of cracked concrete; $\varepsilon_{cr}=f_{ct}/E_c$, where E_c is the elastic modulus of concrete. n is the number of fictitious splitting cracks (n=3), and w_0 is the minimum crack width at concrete failure (w_0 =0.2 mm) (Roelfstra and Wittmann, 1986).

For the totally cracked stage, the calculation of confining stress in the totally cracked stage is the same with that of cracked part in partly cracked stage. It is generally considered that concrete cylinder has reached its maximum confining capacity before the cover was entirely cracked. Thus, the confining stress in the totally cracked stage is not necessary to calculate the ultimate bond strength. Based on Eqs. (12) and (13), the ultimate confining stress on the bond interface can be obtained for various concrete strength and cover depth.

3. Comparison with experimental results

The feasibility of Eq. (13) in calculating the ultimate bond strength is testified by comparing the predicted results with existing experimental data (Baran et al. 2012; Brearley et al. 1990). The comparison results in Fig. 4 show that Eq. (13) is good for predicting the ultimate bond strength of the prestressing strands with diameters of 15.2 mm. The mean ratio of the test results ranges from 0.95 to 1.05, accompanying with the lowest standard deviation of 0.15.

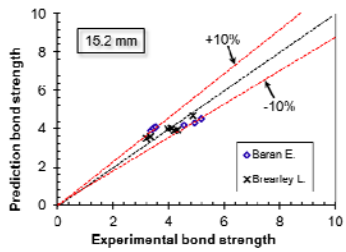

Fig. 4. Comparison of results between prediction and experimental bond strengths

4. Acknowledgments

The work is financially supported from the National Natural Science Foundation of China (Grant No. 51778068), the State Key Development Program for Basic Research of China (Grant No. 2015CB057705), and the Scientific Research Fund of Hunan Provincial Education Department (Grant No. 17B012). The support is gratefully acknowledged.

5. References

Baran E, Akis T., and Yesilmen S. (2012) Pull-out behavior of prestressing strands in steel fiber reinforced concrete. Construction & Building Materials 28(1):362-371.

Brearley, L.M., and D.W. Johnston (1990) Pull-Out Bond Tests of Epoxy-Coated Prestressing Strand. Journal of Structural Engineering 116(8): 2236-2252.

Burgueno R., and Sun Y. (2011) Effects of Debonded Strands on the Production and Performance of Prestressed Concrete Beams. Department of Civil and Environmental Engineering Michigan State University East Lansing, MI, USA, Report No. CEE-RR – 2011/01

Cairns J., and Abdullah R.B. (1996) Bond strength of black and epoxy-coated reinforcement - A theoretical approach. Aci Materials Journal 93(4):362-369.

Ma Y., Zhang J., Wang L., Liu Y. 2013. Probabilistic prediction with Bayesian updating for strength degradation of RC bridge beams. Structural Safety, 44: 102-109.

Ma Y., Guo Z., Wang L., and Zhang J. 2017. Experimental investigation of corrosion effect on bond behavior between reinforcing bar and concrete. Construction and Building Materials, 152, 240-249.

Young A.G., and Laldji S. (1988) Bond between steel strand and cement grout in ground anchorages. Magazine of Concrete Research 40(143):90-98.

Roelfstra PE and Wittmann FH (1986). Numerical method to link strain softening with failure of concrete. In Fracture Toughness and Fracture Energy of Concrete, PP.163-175.

Uijl JAD and Bigaj AJ (1996) A bond model for ribbed bars based on concrete confinement. Heron 41(3):201-226.

Analytical Model to Predict Flexural Capacity of Corroded Prestressed Concrete Beams

Lei Wang[1*], Lizhao Dai[2], Yafei Ma[3], and Jianren Zhang[4]

[1] Changsha University of Science and Technology, Changsha, China; email: Leiwang@csust.edu.cn
[2] Changsha University of Science and Technology, Changsha, China; email: lizhaod@hotmail.com
[3] Changsha University of Science and Technology, Changsha, China; email: yafei.ma@csust.edu.cn
[4] Changsha University of Science and Technology, Changsha, China; email:jianrenz@hotmail.com

[*]: corresponding author

Keywords: prestressed concrete; flexural capacity; corrosion; concrete cracking; bond degradation

Abstract: Strand corrosion can cause the flexural capacity deterioration of prestressed concrete (PC) beams. An analytical model, incorporating the effects of strand cross-section reduction, material deterioration, concrete cracking and bond degradation, is proposed to predict the flexural capacity of corroded PC beams. The effect of flexural cracks is also included in the model. An equivalent bond stress concept is introduced to consider the effect of flexural cracks, which is further implemented into the flexural capacity prediction of corroded PC beams. The proposed model is verified by the experimental results collected from the previous researches. Results show that the proposed model can give an accurate prediction for the flexural capacity of corroded PC beams. Considering the effect of flexural cracks can improve the precision of the prediction model. The flexural capacity deterioration of PC beams depends on corrosion degrees. Strand corrosion less than 5.5% can lead to a slight decrement of flexural capacity. As corrosion progresses, the flexural capacity would exhibit a significant deterioration.

1. Introduction

Steel corrosion in concrete has been considered as one of the main causes of structural deterioration (Ma et al. 2017; 2018). Due to the high-stress level of prestressing strand, the potential dangers of corrosion in prestressed concrete (PC) beams would be much more severe than that in reinforced concrete members (Zhang, and Yuan 2014). The effect of strand corrosion on flexural capacity should be investigated to insure the serviceability and safety of corroded PC beams. Some experimental studies investigated the flexural behaviors of corroded PC beams (Coronelli et al. 2009; Zhang et al. 2017). Based on the load testing, corrosion effects on concrete cracking, ultimate strength and failure mode of PC beams are evaluated. Analytical studies regarding flexural capacity of corroded PC beams have been afforded little attention as compared to experimental studies. Cavell et al. (2001) neglected the effect of bond degradation, and used a strain compatibility theory to study the residual flexural capacity of deteriorating PC beams. Wang et al. (2017) proposed a strain-incompatibility analysis method to evaluate the flexural capacity of corroded PC members, but it failed to consider the effect of concrete

cracking. Corrosion can deteriorate the flexural capacity of PC beams by decreasing strand cross-section, causing material deterioration, inducing concrete cracking and degrading bond strength. All these effects should be included in the prediction of flexural capacity. In addition, the aforementioned studies have not considered the effect of flexural cracks on flexural capacity. The flexural cracks can change the distribution of bond strength along beam length, which further affect the flexural capacity of corroded PC beams. Neglecting the effect of flexural cracks may overestimate the flexural capacity. How to reasonably evaluate the flexural capacity of corroded PC beams still needs to be studied further. This study proposes a model to predict the flexural capacity of corroded PC beams. The effect of flexural cracks is also included in the model. And then, the proposed model is verified by the experimental results collected from the previous researches. Finally, some conclusions are given.

2. Concept of Flexural Capacity Model

For the flexural capacity prediction of corroded PC beams, the effects of strand cross-section reduction and material deterioration can be incorporated into the model with the corrosion loss and degraded constitutive law, while how to consider the effects of corrosion-induced cracking and bond degradation is still a complicated problem. Additionally, the effect of flexural cracks should also be included into the model. In the present study, an analytical model, incorporating these multi-factor effects, is proposed to predict the flexural capacity of corroded PC beams. Corrosion affects the bond behavior by decreasing the strand cross-section and changing the geometrical shape of strand. Moreover, corrosion-induced cracking can degrade the bond strength by reducing the confinement effect of surrounding concrete. Corrosion-induced expansive pressure is employed to reflect the effect of concrete cracking on the bond degradation. Wang et al. (2016) indicated that the bond strength of strand depended on adhesion force, friction force and gear force between strand and surrounding concrete, and the strand's bond mechanism was very similar to that of deformed bar. Therefore, in the present study, a model proposed by Chen and Nepal (2016), which was used to predict the bond stress of corroded deformed bar, is further developed to estimate the bond stress of corroded strand. The bond stress of corroded strand is established from the contributions of adhesion stress, confinement stress and expansive pressure.

How to consider the effect of flexural cracks is another key issue for the flexural capacity prediction. For the corroded PC beam without flexural cracks, it has the same expansive pressure at the different position along beam length. However, when the corroded PC beam is under the ultimate state, the applied loads can lead to concrete cracking. The flexural cracks would change the magnitude of expansive pressure along beam length, as shown in Fig. 1. As Fig. 1 shows, the expansive pressure would mostly release at the crack position, while it would be fully effective at the middle point between adjacent flexural cracks. A linear curve is employed to describe the distribution of expansive pressure between adjacent flexural cracks. In this model, an equivalent bond stress concept is introduced to consider the effect of flexural

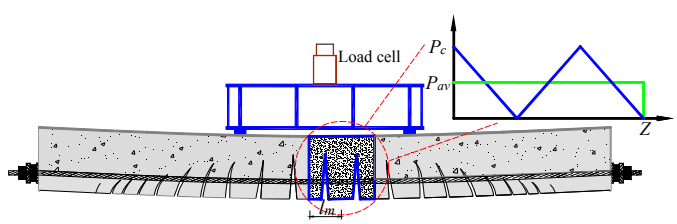

Fig. 1. Expansive pressure along beam length

cracks, which makes it possible to evaluate the bond force of corroded strand for the flexural capacity calculation.

During the loading test, the applied load on PC beams is mainly resisted by the tensile force of strand. Fig. 2 shows the transfer theory of strand force under the applied load. The tension force of prestressing strand (F_p) depends on the effective bond force (F_{eb}), residual bond forces (F_{er}) and effective prestressing force ($F_{e\eta}$) (Wang et al. 2017). For un-corroded PC beams, the bond stress between strand and concrete is perfect. Strand and surrounding concrete are considered to have the consistent strains during the whole loading test. The flexural capacity of un-corroded PC beams can easily be estimated based on the force and moment equilibrium equations.

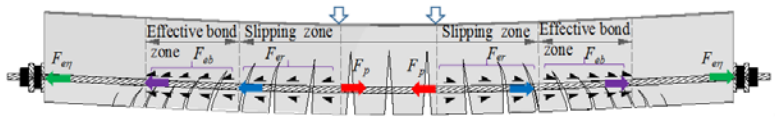

Fig. 2. Schematic of strand force under applied load

For corroded PC beams, corrosion can decrease the bond strength between strand and concrete, which can cause the effective bond zone shifting toward the beam ends to resist the applied loads. More details about the shifting theory of effective bond zone can be seen in Wang et al. (2017). The shifting of effective bond zone would lead to the beam mid-span becoming the slipping zone. The strain of corroded strand in the slipping zone would fail to follow the plane section assumption. How to quantify the incompatible strain between corroded strand and concrete is a key problem for the flexural capacity prediction of corroded PC beams. Studies show that the incompatible strain between corroded strand and concrete can be quantified through introducing a compatibility coefficient (Wang et al. 2017; Zhang et al. 2017). Considering the compatibility coefficient, the conventional strain-compatibility method can be modified to predict the flexural capacity of corroded PC beams.

3. Model Verification

To verify the proposed model for predicting the flexural capacity of corroded PC beams, some experimental results from Zhang et al. (2017) are collected. The relative parameters are listed in Table 1.

Table 1. Comparison between experimental and theoretical results

References	No.	ρ(%)	f_c'(MPa)	M_e(kN·m)	M_{ut}(kN·m)	M_{ct}(kN·m)	M_{ut}/M_e	M_{ct}/M_e
Zhang et al. (2017)	B1	0	31.8	37.8	35.2	35.2	0.93	0.93
	CB1	73.65	31.8	13.5	16.8	14.2	1.24	1.05
	CB2	46.01	31.8	21.0	25.6	23.3	1.22	1.11
	CB3	61.67	31.8	15.9	21.8	19.6	1.37	1.23
	CB4	84.74	31.8	12.3	14.1	11.6	1.15	0.94
	CB5	12.06	31.8	33.0	34.1	31.4	1.03	0.95
	CB6	19.47	31.8	31.5	33.3	29.7	1.06	0.94
	CB7	26.96	31.8	28.8	30.8	27.8	1.07	0.97

Note: ρ is the corrosion loss; f_c' is concrete compressive strength; M_e is the experimental moment; M_{ut} is the theoretical moment un-considering the effect of flexural cracks; M_{ct} is the theoretical moment considering the effect of flexural cracks.

Table 1 gives the theoretical values and experimental results. It is found that the prediction values correlate well with the experimental results. The average errors of M_{ut} and M_{ct} are 15% and 8%, respectively. In general, it is evident that the proposed model can give an accurate prediction for the flexural capacity of corroded PC beams. The precision of the prediction model can be improved by considering the effect of flexural cracks. The flexural capacities under different corrosion losses are shown in Fig. 3. The normalized flexural capacity is defined as the ratio of flexural capacity of corroded PC beams to that of un-corroded PC beams. As Fig. 3 shows, the flexural capacity deterioration depends on corrosion losses, and can be divided into two stages: the slight decrement and significant decrement. Strand corrosion less than the critical value can lead to a slight decrement of flexural capacity. The critical values for the predictions considering and un-considering the effect of flexural cracks are 5.5% and 7.3%, respectively. As corrosion progresses, the flexural capacity exhibits a significant deterioration.

4. Conclusions

An analytical model, incorporating the effects of strand cross-section reduction, material deterioration, concrete cracking and bond degradation, is proposed to predict the flexural capacity of corroded PC beams. The effect of flexural cracks is also included in the model. The experimental results collected from the previous researches are employed to verify the proposed model. Results show that considering the effect of flexural cracks can improve the precision of flexural capacity prediction. Flexural capacity deterioration depends on corrosion degrees. Strand corrosion less than 5.5% can lead to a slight decrement of flexural capacity.

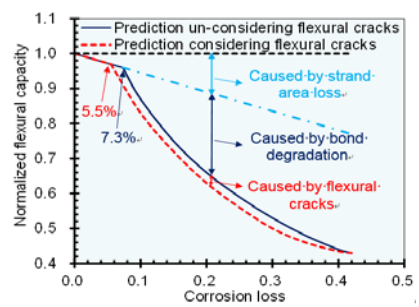

Fig. 3. Flexural capacity and corrosion loss

5. Acknowledgments

The work reported here was conducted with the financial support from the National Natural Science Foundation of China (Grant No. 51678069), the State Key Development Program for Basic Research of China (Grant No. 2015CB057705), the Scientific Research Fund of Hunan Provincial Education Department (Grant No. 17B012), and the Natural Science Foundation of Hunan Province of China (Grant No. 2017JJ3325). Their supports are gratefully acknowledged.

6. References

Ma Y., Guo Z., Wang L., and Zhang J. 2017. Experimental investigation of corrosion effect on bond behavior between reinforcing bar and concrete. Construction and Building Materials, 152, 240-249.

Ma Y., Wang G., Su X., Wang L., and Zhang J. 2018. Experimental and modelling of the flexural performance degradation of corroded RC beams under fatigue load. Construction and Building Materials, 191, 994-1003

Cavell, D.G., and Waldron, P. 2001. A residual strength model for deteriorating post-tensioned concrete bridges. Computer and Structure, 79(4), 361-373.

Chen, H.P., and Nepal, J. 2016. Analytical model for residual bond strength of corroded reinforcement in concrete structures. Journal of Engineering Mechanics, 142(2), 04015079.

Coronelli, D., Castel, A., Vu, N.A., and François, R. 2009. Corroded post-tensioned beams with bonded tendons and wire failure. Engineering Structures, 31(8), 1687-1697.

Wang, L., Zhang, X., Zhang, J., Yi, J., and Liu, Y. 2016. Simplified model for corrosion-induced bond degradation between steel strand and concrete. Journal of Materials in Civil Engineering, 29 (4), 04016257.

Wang, L., Zhang, X., Zhang, J., Dai, L., and Liu, Y. 2017. Failure analysis of corroded PC beams under flexural load considering bond degradation. Engineering. Failure Analysis, 73, 11-24.

Zhang, W., and Yuan, H. 2014. Corrosion fatigue effects on life estimation of deteriorated bridges under vehicle impacts. Engineering Structures, 71(7), 128-136.

Zhang, X., Wang, L., Zhang, J., Ma, Y., and Liu, Y. 2017. Flexural behavior of bonded post-tensioned concrete beams under strand corrosion. Nuclear Engineering and Design, 313, 414-424.

Numerical Investigation of the Effects of Boundary Conditions on Fatigue Behaviors of RC Slab under Moving Wheel Load

Arslan Qayyum Khan[1*], Pengru Deng[2], and Takashi Matsumoto[3]

1 Hokkaido University, Sapporo, Japan; email: arslan.khan146@gmail.com
2 Hokkaido University, Sapporo, Japan; email: pengrudeng@eng.hokudai.ac.jp
3 Hokkaido University, Sapporo, Japan; email: takashim@eng.hokudai.ac.jp

[*]: corresponding author

Keywords: RC slab; fatigue; moving wheel load; boundary conditions; bridging stress degradation

Abstract: To investigate the fatigue behaviors of real RC bridge slabs, a lab-scale RC slab equipped with equivalent boundary conditions (BCs) is normally considered in existing experimental and numerical studies. However, the real grid crack pattern was failed to be captured by the equivalent BCs. In this paper, fatigue analysis is conducted for newly proposed equivalent BCs in addition to the existing equivalent BCs used in the experiment, exploiting an FEM based numerical method based on the bridging stress degradation concept. The analytical results showed that the proposed equivalent BCs have a tendency to predict the cracking pattern well in accordance with real RC bridge slab in contrast to the existing equivalent BCs.

1. Introduction

Owing to space, cost and time limitations, a lab-scale RC slab equipped with equivalent BCs is usually considered in the experimental and numerical researches to predict the fatigue behaviors of RC bridge slab under moving wheel load. However, the equivalent BCs results into the propagation of cracks in diagonal direction originating from the loading point to the corner of supports contrary to grid crack pattern observed in real RC bridge slab. Moreover, the elastic analysis of an RC slab with equivalent BCs exhibits that the bending moment distributions in longitudinal and transverse directions are quite different for applied load at the centre and load applied at other locations in the loading zone contrary to a real RC bridge slab. Therefore, it is essential to investigate the effects of BCs on the fatigue behaviors of RC slab and propose the equivalent BCs capable of predicting the fatigue behaviors of RC slab realistically. In this study, a numerical model based on the bridging stress degradation concept is developed and verified using the experimental study carried out by National Institute for Land and Infrastructure Management (NILIM), Japan (NILIM, 2015). Furthermore, new equivalent BCs are proposed, and the results obtained from analysis of RC slab with proposed equivalent BCs are compared with the experimental and analytical results of RC slab with the existing equivalent BCs. It is found that the proposed equivalent BCs results in the propagation of cracked elements along the longitudinal direction of slab tending to produce grid crack pattern similar to what is observed in real RC bridge slabs, while the existing equivalent BCs results in the crack propagation along diagonal direction towards the corners of supports.

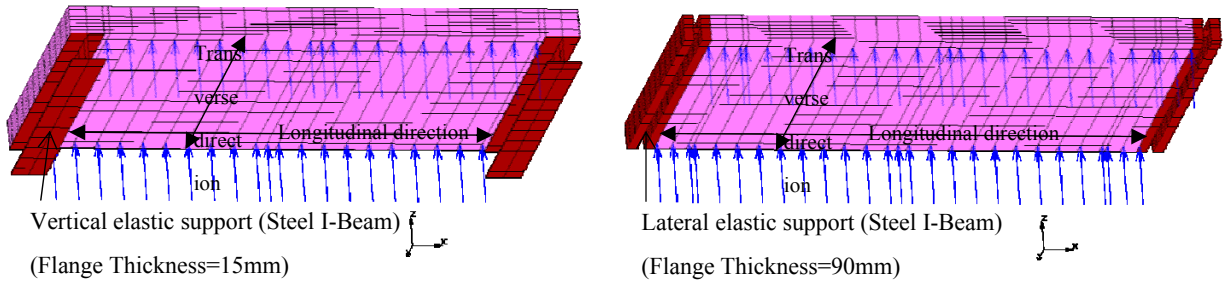

(a) Existing boundary conditions **(b)** Proposed boundary conditions

Figure 1. Illustration of boundary

Table 1. Details of RC slab

Slab Dimensions (mm)			Reinforcement Bars		Steel (MPa)	Concrete (MPa)
Length	Width	Thickness	Main	Distribution		
4500	2800	250	D19@150mm (B)	D16@150mm (B)	f_y=345	f_c'=33.1
			D19@300mm (T)	D16@300mm (T)	E_s=200,000	E_c=27,900

B: Bottom; T: Top

2. Method

A Finite Element Method (FEM) based numerical model is developed to predict fatigue behaviors of RC slab, and smeared crack approach is adopted to represent the distributed cracks. The nonlinear behavior of concrete both in tension and compression is represented by the model proposed by Maekawa et al. 2003. The bridging stress degradation concept (Li and Matsumoto, 1998), the most important part in this fatigue analysis, is introduced as a degradation mechanism of concrete under repetitive loading. The bridging stress degradation equation proposed by Zhang et al. 1999 is employed in this model as follows:

$$\frac{\sigma_N}{\sigma_1} = 1 - (0.08 + 4 \times \delta_{max})\log(N) \tag{1}$$

where σ_N and σ_1 are bridging stress at the *Nth* and the first cycle, respectively. δ_{max} is modified for smeared crack elements in the form of tensile strain (ε_t) and smeared crack element size (l) as $\delta_{max}=\varepsilon_t \times l$. The Giuffré-Menegotto-Pinto model (Menegotto and Pinto, 1973) is used to represent the hysteretic behavior of reinforcement bar under repetitive loading. The slab dimensions, concrete and reinforcement properties are the same as those used in the experiment (NILIM, 2015) as presented in Table 1. The following two cases of equivalent boundary conditions are considered:

1. Existing boundary conditions (Ext. BCs)
2. Proposed boundary conditions (Pro. BCs)

The difference between these two BCs is that the elastic supports (steel I-beams) having flange thickness of 15 mm are vertically placed in the case of Ext. BCs while the elastic supports (steel I-beams) having flange thickness of 90 mm are placed in the lateral direction in the case of Pro. BCs as shown in Figure 1. Due to symmetrical conditions, a half of the slab is modeled and

analyzed using a 3D Finite Element Analysis (FEA) tool MSC/MARC. The following analytical steps are carried out as illustrated in Figure 2: Step 1: Establish the 3D RC slab model and conduct FEA; Step2: modify the material properties of cracked elements due to 1st loading cycle according to the bridging stress degradation equation; Step 3: conduct the FEA for 2nd loading cycle and modify the material properties of new cracked elements; Step 4: repeat the procedure until the final loading cycle and record the analytical results in each cycle of moving load.

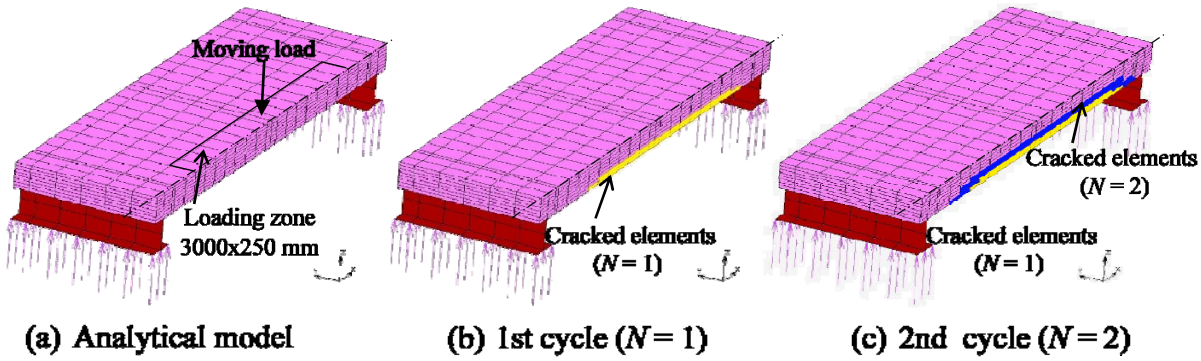

Figure 2. Analytical procedure

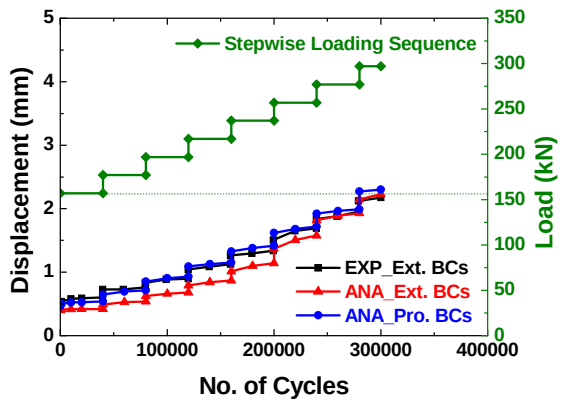

Figure 3. Centre displacement evolution

The loading type is stepwise loading sequence; the initial load is 157 kN and load is increased in intervals with increase in no. of cycles as shown in Figure 3. The final load level is 297 kN and final loading cycle is 300,000.

3. Results and discussions

3.1 Centre displacement evolution

The center displacement evolutions of the RC slab for the Ext. BCs and Pro. BCs are compared with that of obtained from the experiment (Figure 3). The analysis of RC slab with Ext. BCs showed slightly lower centre displacement during initial cycles compared to experimental results because the numerical model is based on the bridging stress degradation phenomenon which is not pronounced during the initial cycles. The similar tendency is observed between analytical results of Ext. BCs and Pro. BCs. However, this difference of centre displacement is reduced with the increase in no. of cycles.

3.2 Propagation of cracked element

In the propagation of cracked elements diagrams, the uncracked elements are shown by white color while the cracked elements are represented by different colors for respective number of loading cycles. For Ext. BCs, the cracks elements are propagated in diagonal direction originating from the loading point towards the corners of supports as shown in Figure 4 (a). The cracked volumes of RC slab after first loading cycle and 300,000th cycle are 0.5% and 42.5% of total slab volume, respectively. Furthermore, the cracked elements propagated up to 5/8th of the RC slab thickness in the vertical direction. However, for the case of Pro. BCs, the cracked elements are found to be spread along the longitudinal directioin of RC slab as shown in Figure 4 (b) contrary to the Ext. BCs case.

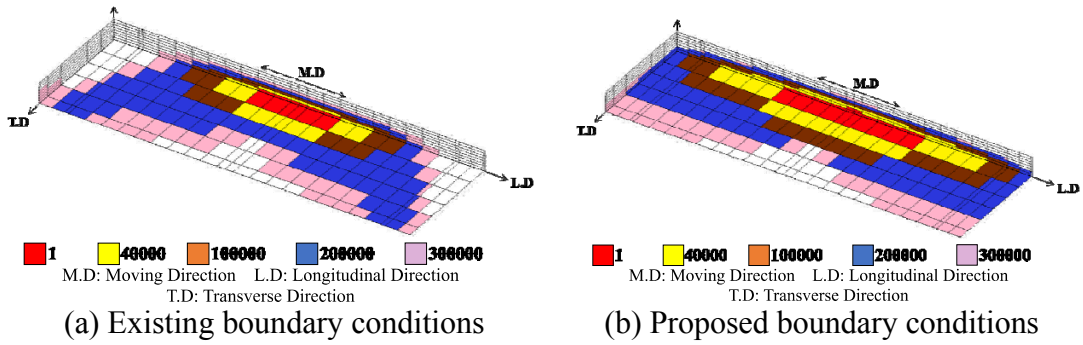

(a) Existing boundary conditions (b) Proposed boundary conditions

Figure 4. Propagation of cracked elements

The similar trend is usually observed in real RC bridge slabs subjected to cyclic loading. The cracked volumes of RC slab after first loading cycle and 300,000th cycle are 1% and 41.1% of total slab volume, respectively, in addition to the cracked elements propagating up to 6/8th of the RC slab thickness in the vertical direction.

4. Conclusions

In this paper, a numerical investigation of the effects of BCs is carried out based on the bridging stress degradation concept for prediction of fatigue behaviors of RC slab under moving wheel load. Moreover, new BCs are proposed and the results are compared with the existing BCs used in the experimental study. Unlike the existing BCs which induces the crack propagation along diagonal direction towards the corners of the supports, the proposed BCs results in the propagation of cracked elements along the longitudinal direction of slab indicating that the real grid crack pattern is more likely to be reproduced with the proposed BCs.

5. References

Li, V. C. and Matsumoto, T. 1998. Fatigue crack growth analysis of fiber reinforced concrete with effect of interfacial bond degradation, Cement and Concrete Composites, 20(5), 339-351.

Maekawa, K., Okamura, H. and Pimanmas, A. 2003. Non-linear mechanics of reinforced concrete, CRC Press.

Menegotto, M. and Pinto, P.E. 1973. Method of analysis for cyclic loaded reinforced concrete frames including changes in geometry and non-elastic behavior of elements under combined normal forces and bending moment, IASBE Proceedings.

National Institute for Land and Infrastructure Management (NILIM). 2015. Research on fatigue durability evaluation for highway bridge concrete slabs. Report no. 844. (In Japanese)

Zhang, J., Stang, H. and Li, V.C. 1999. Fatigue life predication of fiber reinforced concrete under flexural load, International Journal of Fatigue, 21(10), 1033-1049.

Bridge Engineering Institute Conference 2019 (BEI-2019)
Honolulu, Hawaii, USA, July 22-25, 2019

Analytical Study of Ultimate Load Bearing Capacity for an Aging Pratt Truss Bridge using FEM

Tatsuro Yamane[1], Tatsumasa Kaita[2*], Hiroaki Fukuda[3], Shuhei Kawami[4], Ryoichi Satake[5], Yoshiyuki Hirahara[6], Takumi Kanou[7], and Katashi Fujii[8]

[1] Graduate School of Science and Engineering, Ehime University, Matsuyama, Japan; email: yamane.tatsuro.17@cee.ehime-u.ac.jp
[2] Tokuyama College of Technology, Department of Civil engineering and Architecture, Shunan, Japan; email: kaita@tokuyama.ac.jp
[3] Yokogawa Bridge Corporation, Sakai, Japan; email: h.fukuda@yokogawa-bridge.co.jp
[4] Chuden Engineering Consultants Corporation, Hiroshima, Japan; email: kawami@cecnet.co.jp
[5] Chuden Engineering Consultants Corporation, Hiroshima, Japan; email: satake@cecnet.co.jp
[6] Doboku Engineering Consultants Corporation, Hiroshima, Japan; email: hirahara@decnet.co.jp
[7] Aratani Civil Engineering Consultants Corporation, Hiroshima, Japan; email: takumi.kanou@aratani.co.jp
[8] Graduate School of Engineering, Hiroshima University, Higashi-hiroshima, Japan; email: ken214f@hiroshima-u.ac.jp

[*]: corresponding author

Keywords: FEM; aging truss bridge; load bearing capacity; live load; corrosion damage

Abstract: In this study, the objective is to estimate the ultimate load bearing capacity and collapse behavior of the whole bridge by carrying out ultimate load bearing capacity analyses of an aging Pratt truss bridge (97 years old) with severe corrosion damages. The analytical model was constructed by shell elements with 4 nodes to consider the actual corrosion damages of main structure. The live load based on JSHB was loaded at the position where the maximum load against the vertical member with the severest corrosion damage. Then, the live load magnification and the collapse behavior were estimated by increasing the live load until collapse of the bridge. From the analytical results, if it is assuming that additional plate repairs worked effectively, the ultimate load bearing capacity decreased by 7% compared to the bridge when newly constructed. The collapse cause at this case was the local buckling of the area with local corrosion. However, assuming that repairs were not being carried out, the ultimate load bearing capacity decreased by 20% compared to the bridge when newly constructed. The collapse cause at this case was local buckling around the section loss area. When it was halved that the cross-sectional area near the joint with the sway bracing, the ultimate load bearing capacity and collapse behavior did not change very much. However, when it was halved that the cross-sectional area near the panel point with the upper chord member, it was halved that the ultimate load bearing capacity of the whole bridge. Finally, it will be concluded that it is possible to estimate the ultimate load bearing capacity of the steel truss bridge with more accurate consideration of corrosion damage and thickness reduction, by using this analytical model.

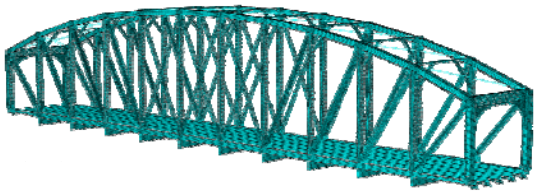

Fig. 1. Analytical model

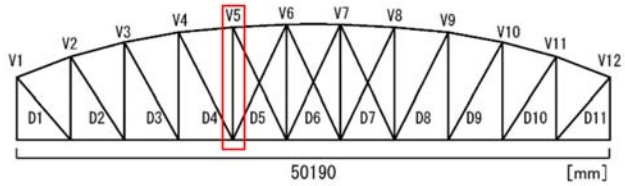

Fig. 2. Axis diagram of the main structure

1. Introduction

Reasonable maintenance of aging infrastructures is becoming more necessary in Japan. In addition, evaluation of load bearing capacity for whole bridge using FEM will be reasonable to maintenance of an aging bridge. Whole bridge models constructed by beam elements are widely used in existing whole bridge analysis of a steel truss bridge. However, that is difficult to evaluate the effects of corrosion damage accurately. This paper presents a whole bridge model that using shell elements to evaluate the effects of corrosion damage of an aging truss bridge accurately. The ultimate load bearing capacity and collapse behavior of the whole bridge are estimated by ultimate load bearing capacity analyses.

2. Outline for Analyzed Bridge

The truss bridge which was analyzed in this study is an actual curved pratt truss bridge which had been used for 97 years in Japan. The span length of this bridge is 50.19 m. The members of this bridge are the combination member constructed by riveting channel steels and racing bars. The panel points of this bridge are rigid joints, and the supporting condition is simple support. In this bridge, many corrosion damages have occurred at the joint between the members (Yamane et al. 2017). In addition, periodic inspections were carried out on this bridge in 2012. Severe cross-sectional loss confirmed at that time had already been repaired using additional plates.

3. Ultimate Load Bearing Capacity Analysis of Whole Bridge

3.1. Analytical Model and Analytical Conditions

Fig. 1. shows the analytical model. The size of each element is set to 50 mm to 100 mm square. The material properties of the steel were assumed to be elastic modulus E=210 [GPa], yield stress σ_y=245 [MPa], and Poisson's ratio ν=0.3. The stress-strain relation was assumed the perfect elasto-plasticity. Boundary conditions were set to be simple support. The rivet joint was modeled as a rigid joint. The RC slab is not modeled, because it is not structural member for main loads. In this study, the corrosion damage region was assumed as simple rectangular shape. The maximum corrosion depth obtained from the investigation results was uniformly reflected in that region. The cross-sectional loss was expressed by erasing elements.

The dead load of the RC slab was loaded as an external force on the stringer. Furthermore, the dead load of steel material was loaded to the whole analytical model as body force. The live load is B live load prescribed in Japan Specifications for Highway Bridges (JSHB) which is loaded on the stringer as external force.(Yamane et al. 2017). The live load was loaded at the position where the most load was applied to the vertical member V5 (Fig. 2.) on the downstream side where severe corrosion damages. In addition, the live load was multiplied by the magnification factor α, and α was gradually increased until the collapse of the whole bridge. The ultimate load bearing capacity of the whole

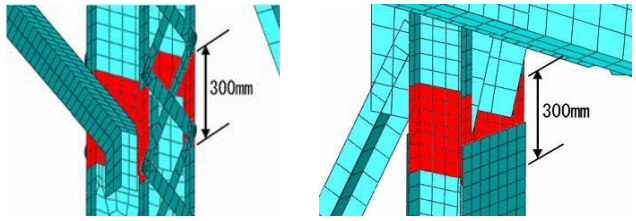

(a) (b)

Fig. 3. The region where the cross-sectional area is halved: (a) Model-4; (b) Model-5

bridge is evaluated by the value of α_{max} when the bridge collapsed. The analyzed models are five models from Model-1 to Model-5. Model-1 is assumed the initial state of this bridge, it has not corrosion. Model-2 to 5 reflect the corrosion damages occurring in this bridge. Model-2 is assumed that the repair section with additional plates has recovered to the same strength as when it was initial strength. Model-3 is assumed to be in a state not repaired by additional plates. Model-4 and Model-5 are based on Model-2. These are models in which the cross-sectional area of the vertical member V5 is partially halved. As shown in Fig. 3., that region is in the respectively range of 300 mm along the axial direction of the member in the vicinities of the junction and the upper chord member.

3.2. Ultimate Load Bearing Capacity and Discussions

In the analytical result of Model-1, when α was increased to 1.7, the full section of diagonal member D5 (Fig. 2.) adjacent to V5 became yielding. The reason for this is that the cross-sectional area of D5 is considerably smaller than that of other members. As shown in Fig. 4.(a), after the full section yielding of D5, the vertical member V4 buckled when α_{max}=3.0 and the whole bridge collapsed. It is considered that the cause of V4 buckling before V5 is because the area of the influence line of V4 is larger than V5. In the analytical result of Model-2, after the full section yielding of D5, local buckling occurred at the lower part of V4 when α_{max} = 2.8(Fig. 4.(b)) and the whole bridge collapsed. There was groove-like local corrosion in this area where local buckling occurred. It can be estimated that the ultimate load bearing capacity has decreased by about 7% from the initial state to the present by comparing the results of Model-1 and Model-2. In the analytical result of Model-3, after the full section yielding of D5, local buckling occurred at the vicinity of the junction with the sway bracing of V4 of upstream side and V5 of downstream side when α_{max}=2.4(Fig. 4.(c)) and the whole bridge collapsed. There was the vicinity of the severe cross-sectional loss where this local buckling occurred. It can be estimated that the ultimate load bearing capacity has decreased by about 20% if repair of the cross-sectional loss was not done by comparing the results of Model-1 and Model-3. In the analytical result of Model-4, as shown in Fig. 4.(d), local buckling occurred where the cross-sectional area is halved. However, this did not become a direct cause of the collapse of the bridge. The reason is assumed that the deformation of the local buckling part was suppressed by the sway bracing. Finally, when α_{max}=2.7, the whole bridge collapsed due to the same cause as Model-2. In the analytical result of Model-5, when α_{max}=1.4, the whole bridge collapsed due to the local buckling occurring at the part where the cross-sectional area is halving as shown in Fig. 4.(e). It is assumed that the part where local buckling occurring largely affects ultimate load bearing capacity because local buckling did not become a direct cause of collapse in Model-4.

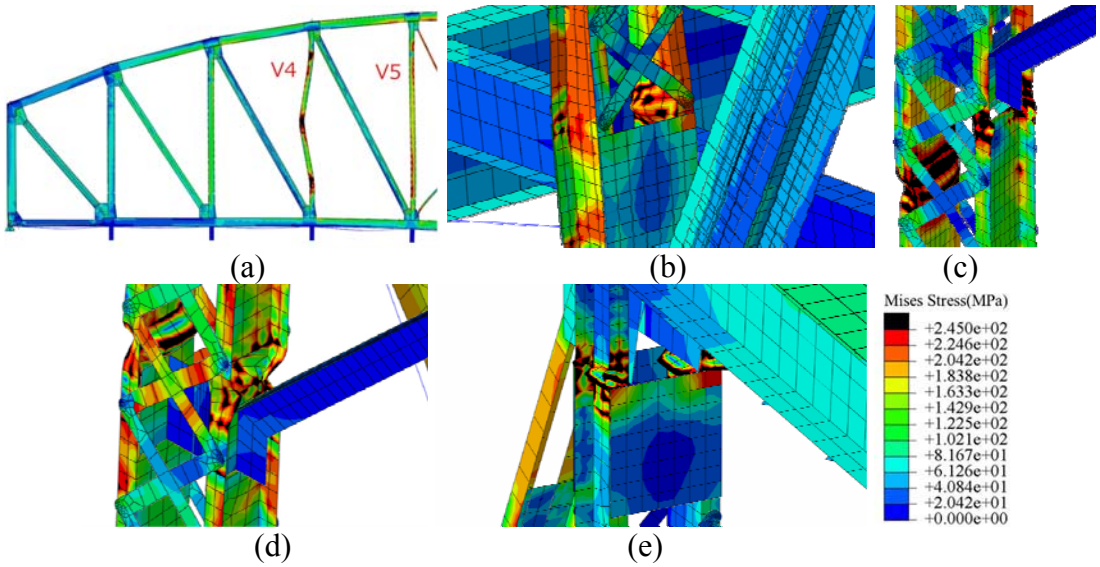

Fig. 4. Buckling behavior of each model: (a) Model-1; (b) Model-2; (c) Model-3; (d) Model-4; (e) Model-5

4. Conclusions

This paper presented the whole bridge model of the aging steel truss bridge using shell elements. Furthermore, the ultimate load bearing capacity analyses were carried out focusing on the vertical member with the severest corrosion damage. The main conclusions obtained from this study are as follows:

- The ultimate load bearing capacity decreased by 7% than the initial state if repairing of additional plate is effective in this bridge. In this case, local buckling in the local corroded part caused collapse of the whole bridge. The ultimate load bearing capacity decreased by 20% than the initial state if repair had not been carried out in this bridge. In this case, local buckling occurred in the vicinity of a severe cross-sectional loss caused the collapse of the whole bridge.
- In case the cross-sectional area near the joint with the sway bracing was halved, the ultimate load bearing capacity and collapse behavior hardly changed. However, in case the halving the cross-sectional area near the joint with the upper chord member, the ultimate load bearing capacity of the whole bridge decreased by half. Therefore, it is assumed that the part where local buckling occurring largely affects ultimate load bearing capacity.
- The analytical model presented in this study can express the effect of corrosion damage and local buckling. Therefore, it is possible to estimate the remaining load bearing capacity of the steel truss bridge can be estimated with more accurate consideration of the effect of corrosion damage and thickness reduction by using such the analytical model.

5. References

Yamane, T., Kaita, T. and Fujii, K. 2017. Basal Study on Analytical Prediction of Original Load Bearing Capacity for an Aging Truss Bridge by Using Whole Bridge Model, Proc. of EASEC-15, pp.1906-1913.

Analytical Estimation on Remaining Load Bearing Capacity of Aging Truss Bridge by Using Whole Bridge Modeling

Ryoko Koyama[1], Tatsumasa Kaita[2*], Tatsuro Yamane[3], and Tsutomu Imai[4]

[1] UBE machinery corporation, ltd., Ube, Japan; email: 36708u@ube-ind.co.jp
[2] Tokuyama College of Technology, Department of Civil engineering and Architecture, Shunan, Japan; email: kaita@tokuyama.ac.jp
[3] Graduate School of Science and Engineering, Ehime University, Matsuyama, Japan; email: yamane.tatsuro.17@cee.ehime-u.ac.jp
[4] Road division, Construction Department, Shunan city government office, Shunan, Japan; email: imai4bb@city.shunan.lg.jp

[*]: corresponding author

Keywords: pony truss; non-linear FEM; shell element; load bearing capacity; collapse behavior

Abstract: Considering the life extension of aging steel bridge, it is important to estimate accurately the remaining load bearing capacity. Even if the bridge with low-traffic state, it is difficult to decide to remove or to stop the bridge because it is an important life infrastructure for users. For the reason, it is considered that estimate the strength against traffic volume and traffic needs will more reasonable and economic maintenance basing on the remaining load bearing capacity. In this study, the finite element analyses focusing on the following two points were conducted for actual pony truss bridge.

1) Confirmation of the safety of the 4-ton truck load which was the result of resident's questionare of actual usage and traffic needs.
2) Grasp of corrosions and members to be emphasized in maintenance management.

In the analysis, the model of the whole bridge by the shell element was used, and the actual corrosion was reflected on the whole bridge. The main conclusions in this study are as follows:

1) Assuming a 4-ton truck load, the stress concentration occurred in the groove-like corrosion at the upper chord member. The safety factor to the yield state of this bridge was estimated as 1.3.
2) It will be estimated that the ultimate load bearing capacity of this bridge has decreased by 24% due to extensive corrosion and severe corrosion accompanied like through holes.

1. Introduction

Recently, the maintenance of aging steel bridges becomes one of the important social problem in Japan. Especially, many local municipalities have strict conditions in terms of financial difficulties and human resources, and it is difficult to keep all the bridges in the good condition. However, even if low traffic volume and short span, regional bridge is the foundation of living and disaster prevention, removal or replacement will not able to be done easily. For the reason, it

is considered that estimating the minimum required load bearing capacity against actual traffic volume and traffic needs may realize more practical and economic maintenance.

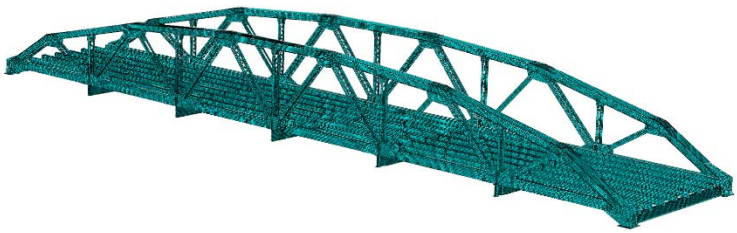

Fig. 1. Analytical model

Table 1. Analytical cases

Analytical cases	Live load	Corrosion dameges
Case-1	truckload (4,6,9,14)	Considered
Case-2	L load in JSHB	Not considered
Case-3		Considered

In this study, the finite element analyses using whole bridge model of an actual aging pony truss bridge which has severe corrosion damages were conducted to estimate the ultimate load bearing capacity and collapse behavior.

2. Whole bridge modeling for finite element analysis

2.1. Outlines of objective steel bridge

The main span of the bridge to be analyzed is simply-supported Warren truss with curved chords and used for 99 years at mountain area in present location. All structural members are constructed by rivet joints combined several simple-shaped steels and many racing bars. The main span is 29.3m and the clear width is 4.5m, respectively. It can be noticed that the maximum height of main truss is kept as low as 2.9m from the considering of pony truss without lateral members. For the traffic needs of this bridge, it is confirmed that up to 4-ton truckload is enough from the viewpoint of daily life and disaster prevention based on the results of the residents questionnaire (Koyama et al. 2017). 27 years have elapsed since the repainting repair last time, and various types of corrosion are distributed throughout the bridge. Especially, severe corrosion damages tend to concentrate on the upper chord members at center span such as groove-like corrosions at the boundary of splice plate and pitting corrosions on the upper flange.

2.2. Whole bridge modeling and analytical conditions

The non-linear finite element analyses in this study were performed by using ABAQUS/Standard 6.14-5. Fig. 1 shows the analytical model in this study. In this model, all main structural members are constructed by the shell element with 4 nodes, and the all rivet joints were modeled as the rigid connection. The size of each shell element was set to under 40mm square in order to consider the corrosion damages which have a certain area. Based on the tensile tests, the material properties were assumed to be elastic modulus E=203.5 [GPa], yield stress σ_y=312.3 [MPa], and Poisson's ratio ν=0.274 respectively. The stress-strain relation was assumed to the perfect elasto-plasticity. For the boundary conditions, the rotations and displacements in all directions are fixed based on the actual state, because all shoes are fixed directly to piers by using 4 anchor bolts in a base plate. The RC slab is not modeled, because it is not structural member for main loads. In the corrosion modeling, the maximum corrosion depth was applied to the entire corrosion area.

2.3. Analytical cases and loading conditions

In all analytical models, the dead load of steel members was acted to entire bridge as the body force. However, the dead load of RC-slab and live load were distributed as external force on all stringers based on the influence lines for reaction force of stringers. Also, 4 analytical cases were prepared depending on loading and corrosion condition as shown in **Table 1.**

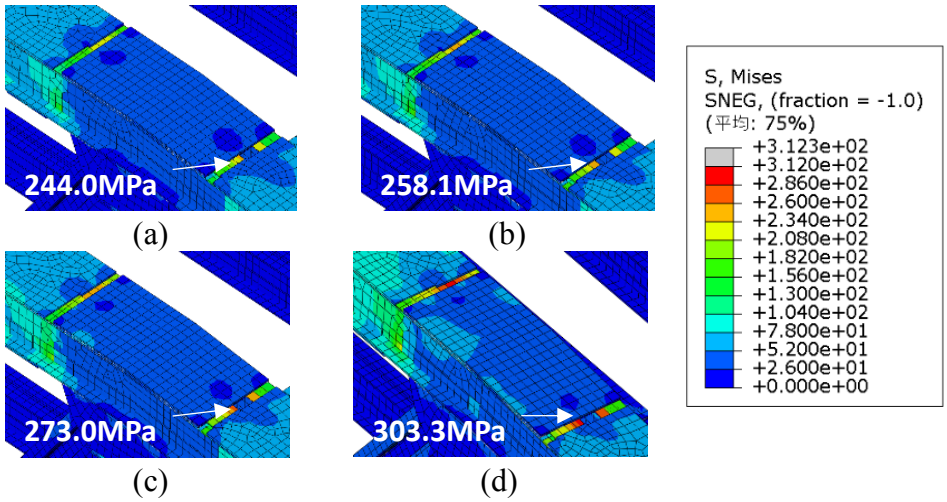

Fig. 2. Mises stress distribution around the groove-like corrosion (Case-1): (a) T-4 truckload; (b) T-6 truckload; (c) T-9 truckload; (d) T-14 truckload

In Case-1, 4 kinds of truckload (T-4~14) assuming severest state were loaded on stringers. T-4 (4-ton) truckload means the actual traffic needs which was based on the questionnaire results for local residents. The loading intensity of each truckload was calculated from the result of dividing the assumed vehicle weight of each load by the occupied area. The truckload was given to the side of road width for increasing the load share in one-sided main truss. Case-2 and Case-3 assumed the L load defined in JSHB (Japan Specifications for Highway Bridges). Here, L load p_1 which means the large-size trailer was excepted from loading condition, because such large vehicles cannot enter to this bridge from the problem on plan shape of connection road. Therefore, only L live load p_2(3.5 kN/m^2) was loaded to analytical model in Case-2~3. Also, the live load was multiplied by the magnification factor α, and α was gradually increased until the collapse of the whole bridge. The ultimate load bearing capacity of the whole bridge is estimated by the maximum magnification factor α_{cr} when the bridge collapsed.

3. Results and discussions

3.1 Truckload

Fig. 2 shows the Mises stress distribution diagram focusing on the groove-like corrosion occurring in the upper chord member at center span when T-4~14 truckload was loaded. The stress arround the groove-like corrosion increases as the truckload increases and concentrates particularly around the through hole. When T-14 truckload was assumed, the stress level reached to almost σ_y. Assuming a T-4 truckload which was the minimum required load for this bridge, the stress generated in this part was 244MPa, and the yield safety factor was 1.3. However, the

corrosion damages in this analytical model were modeled larger than the actual state, and the traffic frequency of 3-ton truckload or more was low. So, it is thought that current state of this bridge will not be serious condition soon. If more life extending is considered, the load restriction of 4-ton and repair to the groove-like corrosion of the upper chord member may come in sight view.

3.2 Ultimate load bearing capacity and collapse behavior

In this section, the ultimate load bearing capacity and the collapse behavior were estimated from the analytical results for Case-2 and Case-3 in which the L load was increased to the ultimate state

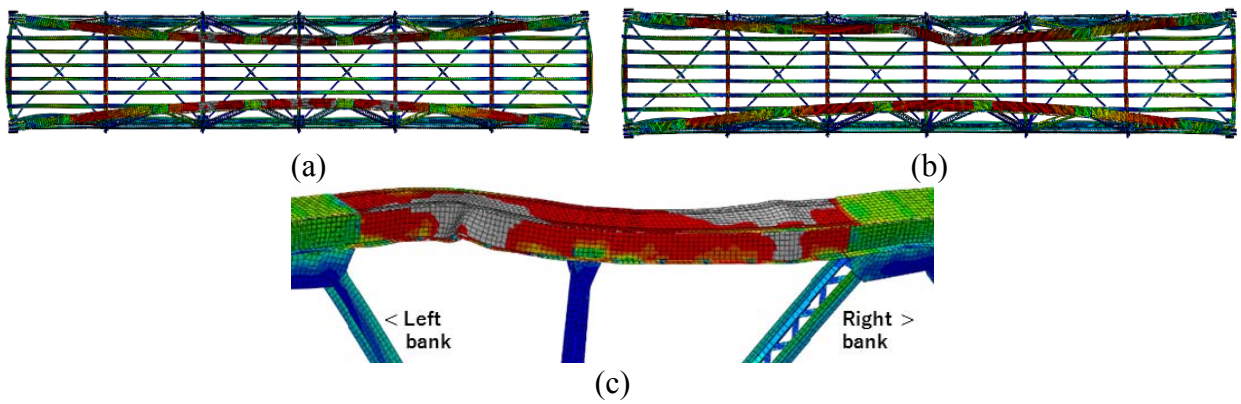

Fig. 3. Deformation (x 20) and stress distribution in ultimate state (Case-2): (a) α_{cr}=6.91 at peak load; (b) α=6.62 after peak load; (c) Out-of-plane buckling of upper chord member

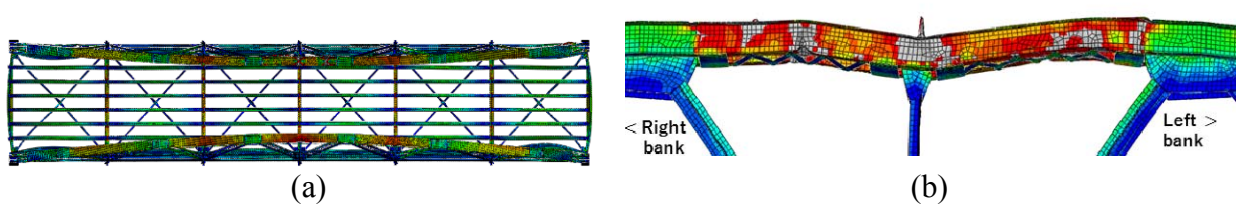

Fig. 4. Deformation (x 20) and stress distribution (α_{cr}=5.28) (Case-3): (a) Plan view; (b) In-plane buckling of upper chord member

by the magnification factor α. From Fig. 3 and Fig. 4, Case-2 without corrosion was disintegrated at α_{cr}=6.91, but Case-3 with corrosion damages collapsed at α_{cr}=5.28. These results will mean that load bearing capacity of whole bridge decreased by 24% due to corrosion for 99 years. Also, in both Case-2 and Case-3, though the buckling was occurred in the ultimate state on same upper chord member at the center span of downstream side, the direction of buckling was different each other. It could be confirmed that the buckling behavior will change from out-of-plane buckling caused by full cross-section yielding to in-plane buckling due to pitting corrosions on upper flange.

4. Conclusions

1) Assuming a 4-ton truck load, the stress concentration occurred in the groove-like corrosion at the upper chord member. The safety factor to the yield state of this bridge was estimated as 1.3. However, it is thought that current state of this bridge will not be serious condition soon.
2) It will be estimated that the ultimate load bearing capacity of this bridge has decreased by 24% due to extensive corrosion and severe corrosion accompanied like through holes.
3) The main collapse trigger of entire bridge was the local buckling toward in-plane direction on an upper chord member at center span. This buckling was caused by a lot of large pitting corrosions on upper flange.

5. References

Koyama, R., Kaita, T., Yamane, T., Kaneshige, K. and Imai, T. 2017. Analytical Estimation on Load Bearing Capacity for Aging Pony Truss Bridge Considering Actual Traffic Conditions, The 15th East Asia-Pacific Conference on Structural Engineering and Construction, Proc. of EASEC-15, pp.1914-1922.

Bridge Engineering Institute Conference 2019 (BEI-2019)
Honolulu, Hawaii, USA, July 22-25, 2019

Analytical Model for Deck-on-Girder Composite Beam System with Multiple Shear Connectors Considering Partial Degree of Composite Action

Mostafa Yossef[1*] and An Chen[2]

[1] Arab Academy for Science and Technology, Cairo, Egypt; E-mail: myossef@aast.edu
[2] Iowa State University, Ames, Iowa, USA; E-mail: achen@iastate.edu

[*]: corresponding author

Keywords: partial degree of composite action; composite beam system; shear lag model; multiple shear connectors

Abstract: In a deck-on-girder composite beam system, the deck and supporting girders work together to effectively provide loading capacity. This system has been widely used for bridges, buildings and other structures. In recent years, Fiber-Reinforced Polymers (FRPs) have been increasingly used as shear connectors to connect the deck and girders due to their non-corrosive properties. However, FRP shear connectors have lower stiffness compared to steel shear connectors, resulting in partial Degree of Composite Action (DCA). Until now, studies on deck-on-girder composite beam system are mainly focused on concrete deck with full composite action. This paper presents a closed-form solution to study the composite beam system with: (1) different DCAs between the deck and multiple supporting steel girders; and (2) decks with orthotropic materials. The analytical model is verified using Finite Element and experimental results.

1. Introduction

The deck-on-girder bridge system is typically composed of deck resting on supporting girders. While the girders are typically made of steel, the deck slab can be made of different materials such as concrete, Fiber Reinforced Polymers (FRP) and timber. The deck slab and girders are connected using shear connectors, which includes steel clamps, bolts and shear studs (e.g., Newmark et al. 1951; Davalos et al. 2011). Until now, the stress across the deck slab is assumed uniform in the design, which is not reasonable since the longitudinal stress over the deck section is non-uniform due to the in-plane shear flexibility of the deck, i.e., shear lag effect as shown in Fig. 1. Partial Degree of Composite Action (DCA) was reported (e.g., Newmark et al. 1951; Davalos et al. 2011), but provided limited guideline to calculate the effective flange width for decks resting on multiple girders. Chen and Yossef, 2015 developed an analytical model to study the effective flange width for deck-on-girder composite beam system considering partial DCA for inner T-beam section. In this paper, this analytical model is extended to include multiple shear connectors considering partial DCA, which is verified using Finite Element (FE) and experimental results.

2. Analytical Model

An analytical model is developed for orthotropic deck rested on multiple girders. Several assumptions are considered including: (1) linear elastic material; (2) symmetric cross-sections;

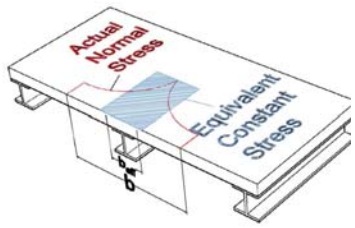

Fig. 1. Effective width (Zou 2008)

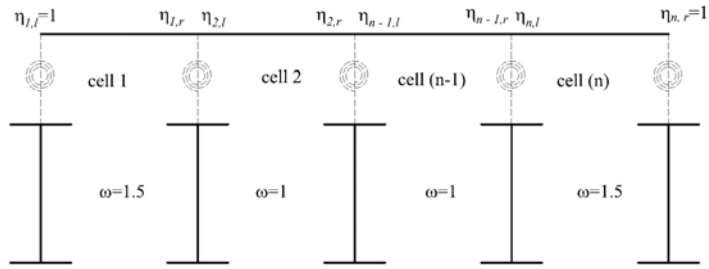

Fig. 2. Multi-cell deck-bridge system showing distribution factors

(3) deformation is neglected, and therefore, the curvature is considered the same for the deck and girders; (4) torsion is not considered; and (5) all shear connectors have the same stiffness. Axial force for the FRP deck can be expressed as (Chen and Yossef, 2015):

$$N_x(x,y)=\sum_{j=1}^{\infty}\left(C_{1j}\cosh(\xi_j y)+C_{2j}\sinh(\xi_j y)\right)\sin(\frac{j\pi x}{a}),\ \xi_j=\frac{j\pi}{a}\sqrt{\frac{\alpha_{66}}{\alpha_{11}}} \tag{21}$$

where C_{1j} and C_{2j} are constants that need to be determined. x is along the span direction, where the panel is simply supported at x=0 and a. α_{11} and α_{66} can be determined based on constitutive relations of the orthotropic plate. Although C_{2j} was assumed to be zero in the previous model based on symmetric boundary conditions, it cannot be neglected in this study for the general case of multi-cell section.

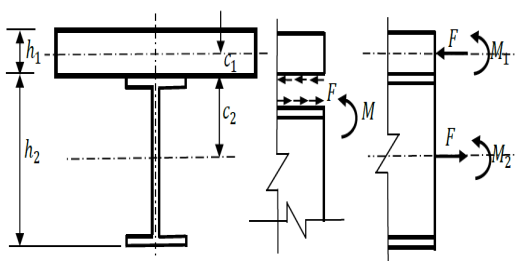

Fig. 3. Axial and bending moment for deck-on-girder system (Chen & Yossef, 2015)

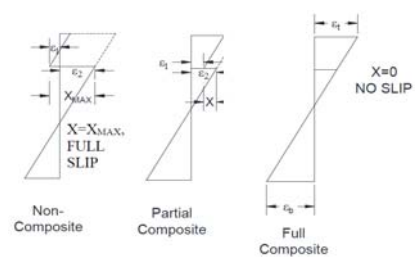

Fig. 4. DCA definition (Lorenz & Stockwell 1984)

Based on boundary conditions, the shear force transferred through connectors F(x) is:

$$F_i(x)=\frac{1}{\eta_i}\sum_{j=1}^{\infty}\frac{-1}{\xi_j}(C_{1j}\sinh(\xi_j\cdot y)+C_{2j}\cosh(\xi_j\cdot y))\sin(\frac{j\pi x}{a}) \tag{22}$$

where η is shear flow distribution factor depending on the shape of the cross-section, *i* can be replaced by r and l which represents right and left sides of the cell, and y is the location of the girder. For a deck on two girders, i.e., single cell, the shear flow distribution factors are equal to one. Based on the equilibrium of the moment as shown in Fig., we have

$$M_1(x)+M_2(x)=\left(\frac{\eta_r+\eta_l}{n}\right)M(x)-\left(\eta_r+\eta_l\right)\cdot F(x)(C^{'}) \tag{3}$$

where $C^{'}$ is the distance between the neutral axis of deck and the neutral axis of the girders, and n is the number of shear connectors for the entire section which can be defined for single cell as $n=\eta_r+\eta_l$. It should be noted that, due to symmetry in single cell section, η_r and η_l are equal to 1 and n is equal to 2. Following similar procedure from Chen and Mostafa, 2015, C_{1j} and C_{2j} can be solved as follows:

$$\begin{bmatrix} C_{1j} \\ C_{2j} \end{bmatrix}=\begin{bmatrix} B_{11}\cdot\cosh(-\frac{\xi_j b}{2})-\frac{1}{\eta_1}\cdot(A_{11}+C_{11})\cdot\sinh(-\frac{\xi_j b}{2}) & B_{11}\cdot\sinh(-\frac{\xi_j b}{2})-\frac{1}{\eta_1}\cdot(A_{11}+C_{11})\cdot\cosh(-\frac{\xi_j b}{2}) \\ B_{11}\cdot\cosh(\frac{\xi_j b}{2})+\frac{1}{\eta_2}\cdot(A_{11}+C_{11})\cdot\sinh(\frac{\xi_j b}{2}) & B_{11}\cdot\sinh(\frac{\xi_j b}{2})+\frac{1}{\eta_2}\cdot(A_{11}+C_{11})\cdot\cosh(\frac{\xi_j b}{2}) \end{bmatrix}^{-1}\cdot\begin{bmatrix} M_{11} \\ M_{11} \end{bmatrix} \tag{4}$$

where

$$A_{11}=\frac{1}{K\xi_j}\left(\frac{j\pi}{a}\right)^2, B_{11}=\alpha_{11}, C_{11}=\frac{\left(\eta_r+\eta_l\right)\cdot(C^{'})^2}{[b\cdot D_{11}+\omega\cdot E\cdot I]\xi_j}, \mathrm{F}_{11}=\frac{1}{[E\cdot A]\xi_j}, M_{11}=\left(\frac{\eta_r+\eta_l}{n}\right)\frac{Q_j\cdot C^{'}}{b\cdot D_{11}+\omega\cdot E\cdot I} \tag{5}$$

K is the connector stiffness, b is the width of the deck between each consecutive girder, and E, A and I are Young's modulus, area and moment of inertia of the steel girder, respectively. ω is beam distribution factor which is introduced to account for the external girders. It is equal to 1.5 and 1 for exterior cells and interior cells, respectively, as shown in Fig. 2.

3. Verification

An FE model was created and validated using experimental results from Zou, 2008. Zou's test consisted of three steel girders (W16x36, Gr50) with a span of 5500 mm and spaced 1200 mm on centers. A 130 mm thick FRP honeycomb deck was connected to steel girders using steel shear connectors at 600 mm on center. Steel bracing was added between the girders to provide lateral support for the flange section as shown in Fig. 5. The panel was loaded to 50% service load at the intersection of middle of right deck and midspan as shown in Fig. 6.

Fig. 5. Bridge model test (Zou 2008)

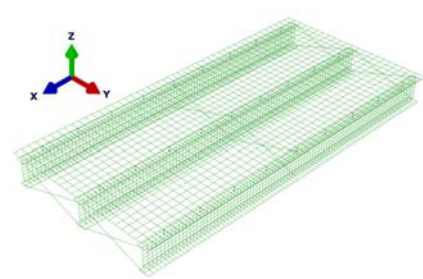

Fig. 6. Finite Element model

Linear elastic FE model using ABAQUS is created using four-node shell elements (S4R) for deck and girder sections. Young's modulus and Poisson's ratio for steel are 200,000 MPa and 0.3, respectively. Equivalent properties of FRP honeycomb panel are shown in Table 1 (Zou 2008).

The FRP deck is connected to the steel girders using CONN3D element where all stiffnesses are set to be rigid except for the longitudinal stiffness, which are varied to obtain different DCAs. Boundary conditions are set to pin and roller at both ends of the girders. Deflection is recorded and compared with experimental results, where good correlation is achieved as shown in Fig.7. The FE model is further used to validate the analytical model, where the load is placed over the girders at the midspan to provide symmetric loading. Different stiffnesses are simulated in both analytical and FE model, where stress and defection results are compared.

Table 1. Equivalent properties of FRP honeycomb panel

E_x (MPa)	E_y (MPa)	$\square_x$	G_{xy} (MPa)
2560	2300	0.303	560

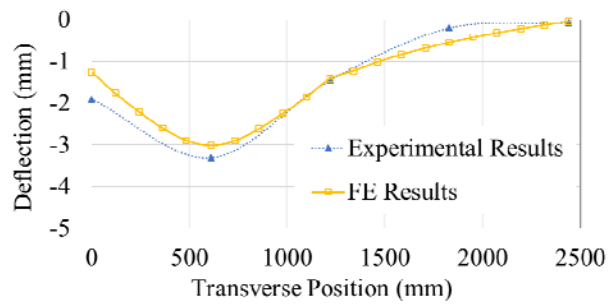

Fig. 7. Midspan deflection of the tested panel

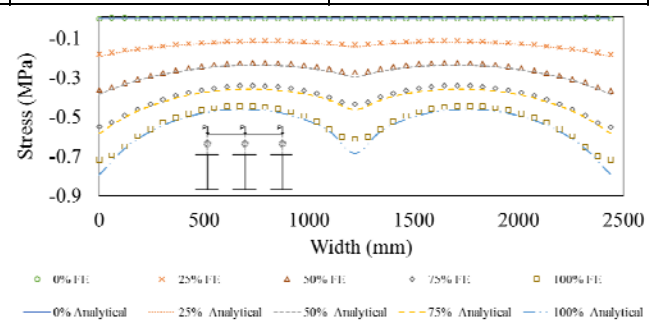

Fig. 8. Stress distribution

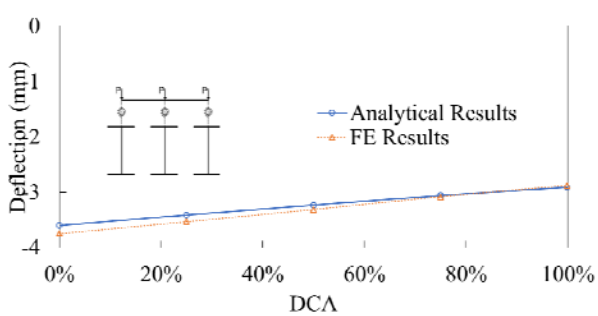

Fig. 9. Deflection

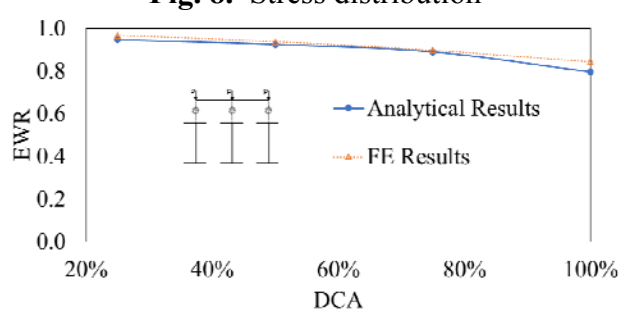

Fig. 10. Effective width ratio (b_{eff}/b) vs. DCAs

4. Results and Conclusions

The stress and displacement results at mid-span from the FE and analytical model for different DCAs are shown in Figs. 8 and 9, respectively, where good correlations can be observed. The shear connector stiffness (K) is chosen to generate 100%, 75%, 50%, 25% and 0% DCAs, respectively. The relationship between Effective Width Ratio (EWR) and DCA is shown in Fig. 10, where good correlation is observed between the analytical and FE results. It can be concluded that the analytical model derived in this study can successfully predict the stress and displacement while taking into account the partial DCA.

6. References

Chen, A. & Yossef, M., 2015. Analytical Model for Deck-On-Girder Composite Beam System with Partial Composite Action. *Journal of Eng. Mech.*, p.4015087.

Davalos, J.F., Chen, A. & Zou, B., 2011. Stiffness and Strength Evaluations of a Shear Connection System for FRP Bridge Decks to Steel Girders. *Journal of Comp. for Const.*, 15(3), pp.441–450.

Lorenz, R.F. & Stockwell, F.W., 1984. Concrete Slab Stresses in Partial Composite Beams and Girders. *AISC Engineering Journal*, 21(3), pp.185–188.

Newmark, N.M., Siess, C.P. & Viest, I.M., 1951. Tests and analysis of composite beams with incomplete interaction. *Proceedings of the Society of Experimental Stress Analysis*, 9(1).

Zou, B., 2008. *Design Guidelines for FRP Honeycomb Sandwich Bridge Decks*. PhD Diss., West Virginia University.

Fragility Curves for a Typical Chilean Highway Bridge

José Wilches[1*], Hernán Santa María[2], Rafael Riddell[3], and Carlos Arrate[4]

[1] Pontificia Universidad Católica de Chile, Santiago, Chile; National Research Center for Integrated Natural Disaster Management CONICYT / FONDAP / 15110017, Santiago, Chile; email: jdwilches@uc.cl
[2] Pontificia Universidad Católica de Chile, Santiago, Chile; National Research Center for Integrated Natural Disaster Management CONICYT / FONDAP / 15110017, Santiago, Chile; email: hsm@ing.puc.cl
[3] Pontificia Universidad Católica de Chile, Santiago, Chile; email: riddell@ing.puc.cl
[4] National Research Center for Integrated Natural Disaster Management CONICYT / FONDAP / 15110017, Santiago, Chile; email: caarrate@uc.cl

[*]: corresponding author

Keywords: highway bridges; seismic design; concrete shear keys; fragility curves.

Abstract: Risk assessment of road transport networks exposed to seismic hazards can be performed using fragility curves. This study uses detailed 2D non-linear analytical models of a representative Chilean bridge to develop fragility curves for risk assessment and to evaluate and calibrate design regulations for different performance objectives. The fragility curves obtained show that the bridges designed using the current Chilean design codes have a seismic performance that depends, to a large extent, on the type of ground on which the bridge is located.

1. Introduction.

During the Maule earthquake (Mw=8.8) about 300 bridges suffered some type of damage (Buckle et al. 2012). Damage ranged from small cracks to the complete collapse of the superstructure. To avoid the occurrence of those damages in future earthquakes, new criteria were considered for the seismic design of bridges in Chile after 2010 (MOP 2017). The main changes were: (a) the addition of a diaphragm connected to the deck and the girders, in order to protect the girders from the pounding against the shear keys, avoiding local damage to the girders and degradation of the lateral stiffness of the deck; (b) the change of the design of the external and internal shear keys in abutments and bents, in order to avoid excessive in-plant rotations and collapse of the deck. One way to evaluate the effectiveness of Chilean bridge seismic design criteria is using fragility curves. Fragility curves are increasingly used in the probabilistic assessment of the seismic risk of road bridges. The objective of this research is to use detailed non-linear analytical models of a typical Chilean bridge to develop fragility curves that can be used in the assessment of the seismic risk of transport networks in the region and evaluate the effectiveness of changes in design provisions.

2. Analytical model.

To define the analyzed bridges, a statistical analysis of the bridges in Chile was carried out using data provided by the Chilean Ministry of Public Works (MOP). The bridges were classified according to the type of material (reinforced concrete, prestressed concrete, and steel), the

number of main girders, and their supporting condition, classified as simply supported or continuous. As shown in Fig. 1, bridges with simply supported, prestressed concrete beams are the most common bridges built in Chile, which comprise 38% of the total. A representative structure of the Chilean road bridges was selected, which can be observed repeatedly throughout the country. A typical interior bent is shown in Fig. 2, which has elastomeric bearings, external shear keys, vertical seismic bars, a cap beam, and columns.

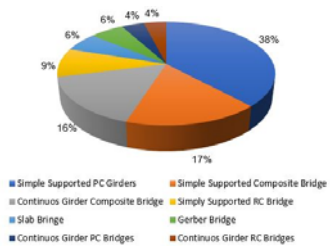

Fig. 1. Distribution of bridges in Chile

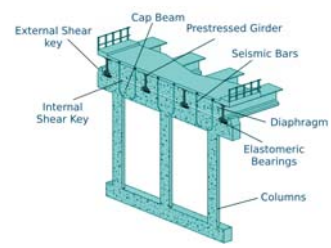

Fig. 2. Structural components of bridge bent

Three configurations of the representative bridge bent (Fig. 3) were designed using the seismic design requirements of the 2008 Bridge Design Code (MOP, 2008), here called BDM2008, of the 2015 code (MOP, 2015), here called BDM and of the 2017 code (MOP, 2017), called BDM2017. Fragility curves were calculated for the three seismic hazard zones and the three soil types defined in those bridge design codes. Configuration A (Fig. 3a) corresponds to the representative bridge as designed before the 2010 earthquake using BDM2008. Configuration B (Fig. 3b) corresponds to the representative bridge with a diaphragm, as designed after the 2010 earthquake using BDM2015. Finally, configuration C (Fig. 3c) corresponds to the bridge as required by the latest version of the Chilean Bridge Design Manual (BDM2017). The OpenSees software (Mazzoni et al., 2006) was used to calculate the non-linear response of the structures designed with the bridge design codes. The analyses were performed using plane non-linear models to represent the transverse response of the bridges. Non-linearities were incorporated into elastomeric bearings (Rubilar et al., 2015), seismic bars (Martínez et al., 2017), internal and external shear keys (Megally et al., 2002), and the cap beams and the columns (Scott et al., 2004). All the models considered the columns fixed to the foundations. The diaphragm was modeled as a rigid element (Mazzoni et al., 2006).

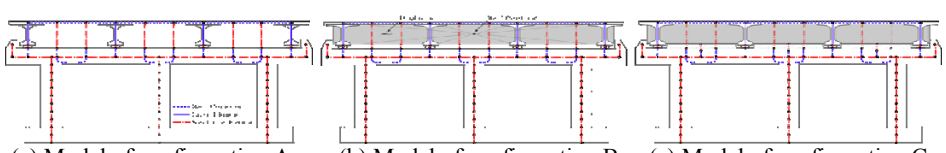

(a) Model of configuration A (b) Model of configuration B (a) Model of configuration C

Fig. 3. Discretization of the finite element models of the bridge bent.

3. Analytical fragility curves.

To obtain the fragility curves, non-linear time-history analyses were performed using 117 horizontal accelerograms (CSN, 2017). The damage states defined for the construction of the fragility curves correspond to the damage modes observed after the 2010 earthquake (Buckel et

al. 2012). Damage state 1 (DS1) corresponds to a residual displacement of the superstructure at the supports greater than 50 mm. Damage state 2 (DS2) corresponds to the displacement produced at yielding of the external shear keys (155 mm for BDM2008, 175 mm for BDM2015, and 195 mm BDM2017). Finally, the damage state 3 (DS3) corresponds to the lateral displacement of the superstructure with respect to the bent that produces collapse of a girder (450 mm for BDM2008, 670 mm for BDM2015, and 890 mm for BDM2017). The fragility curves obtained for the three defined damage states of each bridge configuration are shown in Fig. 4.

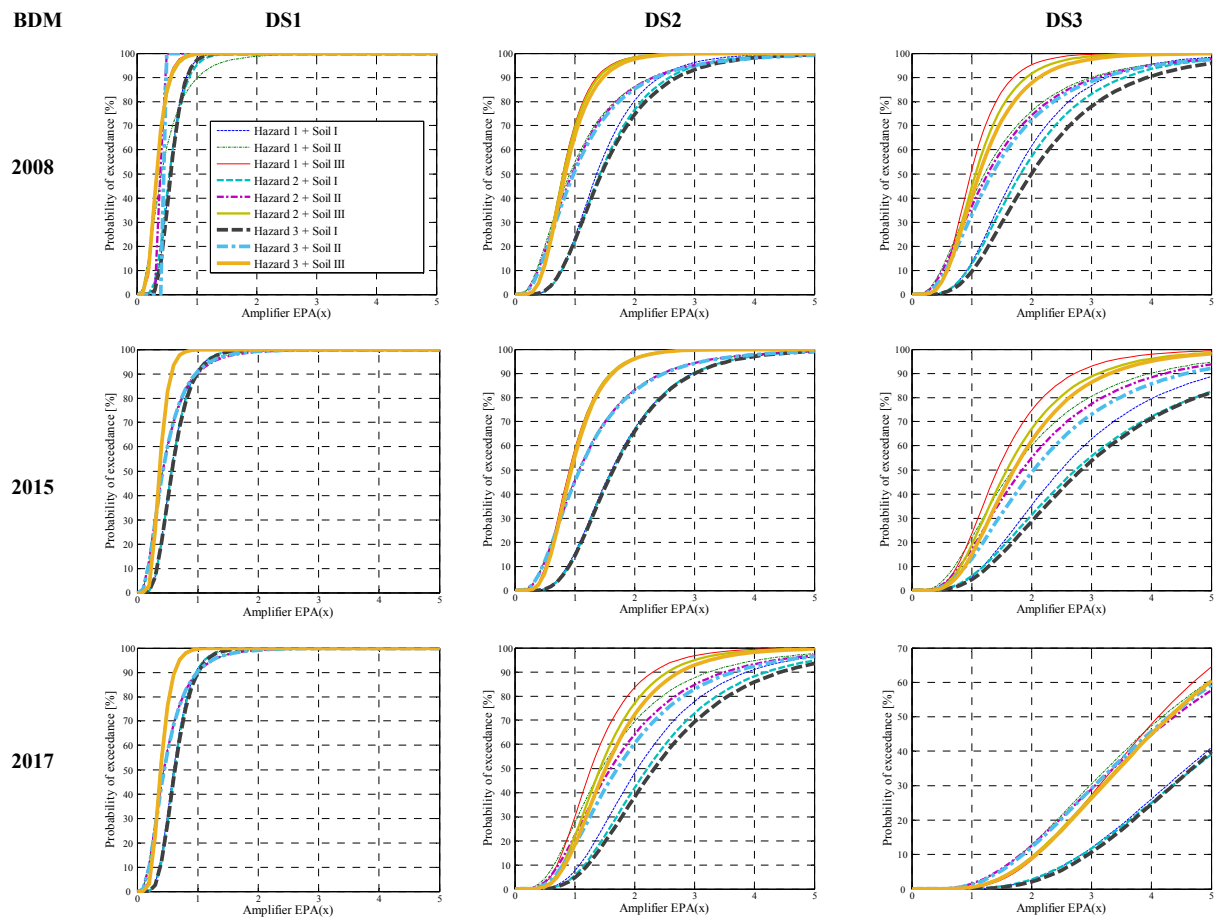

Fig. 4. Fragility curves for the typical bridge

The different fragility curves were calculated for each seismic zone, and type of soil. It can be observed that the fragility curves that result are grouped by the type of soil, which shows that the seismic performance of the bridges in Chile depends mainly on the type of soil in which the bridges are located, regardless of the seismic hazard zone. In addition, the fragility curves for DS1 are similar for all structural configurations. In terms of the effectiveness of the changes in the design criteria, it is observed that the probability of exceeding damage states DS2 and DS3 decreases for the bridge designed using the more recent bridge design manual. The foregoing shows that the regulations have become increasingly secure.

4. Conclusions

In this document, results of an inventory analysis for Chilean bridges are shown, as well as non-linear dynamic analyses were carried out to calculate fragility curves for a Chilean representative bridge. The effect of the changes in seismic design criteria after the 2010 Maule earthquake was analyzed by comparing the fragility curves obtained from bridges designed with different versions of the Bridge Design Manual. Changes in the design criteria resulted in a significant decrease in the probability of collapse due to transverse displacement of the bridges. The fragility curves obtained show that the bridges designed with the current design codes have a seismic performance that depends, to a large extent, on the type of soil on which the bridge is located. Finally, fragility curves can be used to calibrate design regulations to the performance objectives that they pursue. This is particularly important for countries with large recurrence intervals, and therefore cannot calibrate their design codes through earthquake damage observations.

5. References

Buckle, I., Hube, M., Chen, G., Yen, W-H., and Arias, JG. 2012. Structural performance of bridges in the offshore Maule earthquake of 27 February 2010, Earthquake Spectra, 28, 533–552.

CSN, Centro Sismológico Nacional. Records of significant seismic events - Records between 2012 to present (database) 2015. http://evtdb.csn.uchile.cl/ (accessed April 20, 2017).

Martínez A., Hube M., and Rollins K.M. 2017. Analytical fragility curves for non-skewed highway bridges in Chile, Engineering Structures, 141, 530–542.

Mazzoni S., McKenna F., Scott M.H., and Fenves G.L. 2006. OpenSees command language manual. Pacific Earthquake Engineering Research Center.

Megally, S.H., Silva, P.F., and Seible, F. 2002. Seismic response of sacrificial shear keys in bridge abutments. University of California, San Diego.

MOP, Ministerio de Obras Públicas. 2008. Manual de carreteras - Volumen No3 - Instrucciones y criterios de diseño (in spanish). Chile: MOP-DGOP-Direccion de Vialidad.

MOP, Ministerio de Obras Públicas. 2015. Manual de carreteras - Volumen No3 - Instrucciones y criterios de diseño (in spanish). Chile: MOP-DGOP-Direccion de Vialidad.

MOP, Ministerio de Obras Públicas. 2017. Manual de carreteras - Volumen No3 - Instrucciones y criterios de diseño (in spanish). Chile: MOP-DGOP-Direccion de Vialidad.

Rubilar, F.I. 2015. Modelo no lineal para predecir la respuesta sísmica de pasos superiores (in spanish). Pontificia Universidad Catolica de Chile.

Scott, M.H., Franchin, P., Fenves, G.L., and Filippou, F.C. 2004. Response sensitivity for nonlinear beam–column elements, Journal of Structural Engineering, 130, 1281–1288.

Exhibitors and Sponsors

WAGNERS

FDH INFRASTRUCTURE SERVICES
ENGINEERING INNOVATION

AEGION
Stronger. Safer. Infrastructure.

FYFE

Olin™

CRC Press / Balkema
Taylor & Francis Group

KSCE

JPCI
Japan Prestressed Concrete Institute

ice
Institution of Civil Engineers

aci

jci

ACF
Asian Concrete Federation

TRB
TRANSPORTATION RESEARCH BOARD

JSCE


The Bridge Engineering Institute
An International Technical Society
www.beibridge.org